Civil Engineering Research in Ireland 2022 and Irish Transport Research Network 2022

Technological University Of Dublin
25th August 2022

Trinity College Dublin
26th August 2022

Editors: Niall Holmes, Caitriona De Paor And Roger P. West

Assistant Editors: Una Beagon, Cian Desmond, William Finnegan, Ross Higgins, David Igoe, Daniel Mc Crum, Danny Mc Polin, Niamh Power, Tomas O'Flaherty, Fergal O'Rourke

CONFERENCE PROCEEDINGS

ORGANISED BY:

Civil Engineering Research Association Of Ireland (CERAI) and Irish Transportation Research Network (ITRN)

www.cerai.net
CERAI
Civil Engineering Research Association of Ireland
Promoting civil engineering research and practise in Ireland

ITRN.ie
Irish Transport Research Network

Editors: Niall **Holmes**, Caitríona **de Paor** and Roger P. **West**

Assistant Editors: Una **Beagon**, Cian **Desmond**, William **Finnegan**, Ross **Higgins**, David **Igoe**, Daniel **Mc Crum**, Daniel **Mc Polin**, Niamh **Power**, Tomás **O'Flaherty**, Fergal **O'Rourke**

Published in 2022

ISBN 978-0-9573957-5-6

Published by

Civil Engineering Research Association of Ireland

This publication is part of the proceedings of the Civil Engineering Research in Ireland conference held in conjunction with Irish Transportation Research Network conference at Technological University Dublin and Trinity College Dublin, Ireland on 25-26th August 2022.

Printed copies of these Proceedings may be obtained from Dr. Niall Holmes, School of Civil and Structural Engineering, TU Dublin, Bolton Street, Rotunda, Dublin 1, Ireland or by email request to niall.holmes@tudublin.ie

CERAI Board Members 2020 -2022

President: Kieran **Ruane,** MTU

Ex Officio Past Presidents: Jamie **Goggins,** NUIG and Vikram **Pakrashi,** UCD

Treasurer: Jennifer **Keenahan**, UCD

CERI2022-ITRN 2022 Co-Chairs: Niall **Holmes,** TU Dublin and Roger **West,** TCD

CERI2022-ITRN2022 Secretary: Caitríona **de Paor,** TU Dublin

CERI2022-ITRN2022 Treasurer: Bidisha **Ghosh**, TCD

CERI2022-ITRN2022 Public Relations Officer: Aimee **Byrne,** TU Dublin

Elected Board members: Giuseppina **Amato**, QUB, Ciarán **Hanley**, UCC, Vesna **Jaksic,** MTU, Brian **McCann,** ATU Sligo, Patrick **McGetrick**, NUIG, Juan Pablo **Osorio Salas,** TU Dublin

CERI-ITRN2022 Stream Leaders

ITRN 2022: Ross **Higgins**, UL

Bridges: Daniel **Mc Crum**, UCD

Concrete: Daniel **Mc Polin**, QUB

Energy: Fergal **O'Rourke,** DkIT

Environmental: Niamh **Power**, MTU

Geotechnical: David **Igoe**, TCD

New Frontiers: Cian **Desmond**, GDG

Pedagogy: Una **Beagon**, TU Dublin

Structures: Tomás **O'Flaherty**, ATU Sligo

Sustainable Cities and Climate Action: William **Finnegan**, NUIG

Scientific Committee Members 2022

The following are the scientific committee members for the CERI-ITRN 2022 conference:

First Name	Last Name	Affiliation
Aoife	Ahern	University College Dublin
Ciara	Ahern	TU Dublin
Timothy	Aiken	Queen's University Belfast
Giuseppina	Amato	Queen's University Belfast
Tony	Ambrose	Jacobs
Denise	Barnett	Munster Technological University
Bidroha	Basu	Munster Technological University
Una	Beagon	TU Dublin
Zeinab	Bedri	TU Dublin
Edmond	Byrne	University College Cork
Aimee	Byrne	TU Dublin
Paraic	Carroll	University College Dublin
Sean	Carroll	Munster Technological University
Caitríona	de Paor	TU Dublin
Cian	Desmond	GDG
Edelle	Doherty	National University of Ireland, Galway
Wayne	Doherty	Dundalk Institute of Technology
Aidan	Duffy	TU Dublin
Alan	Duggan	Atlantic Technological University, Galway
Bernard	Enright	TU Dublin
John	Gallagher	Trinity College Dublin
Eshmaiel	Ganjian	Concrete Corrosion Tech Ltd
David	Gill	AGL Consulting
Conor	Glennon	National University of Ireland, Galway
Jamie	Goggins	National University of Ireland, Galway
Magdalena	Hajdukiewicz	National University of Ireland, Galway
David	Hester	Queen's University Belfast
Ross	Higgins	University of Limerick
Niall	Holmes	TU Dublin
David	Igoe	Trinity College Dublin
Vesna	Jaksic	Munster Technological University
Denis	Kelliher	University College Cork
Thomas	Kelly	Dundalk Institute of Technology
Zili	Li	University College Cork
Thomas	Lupton	Dundalk Institute of Technology
Bryan	McCabe	National University of Ireland, Galway
Brian	McCann	Atlantic Technological University, Sligo
Liam	McCarton	TU Dublin
Daniel	McCrum	Dundalk Institute of Technology
Patrick J.	McGetrick	National University of Ireland, Galway

First Name	Last Name	Affiliation
Janet	McKennedy	TU Dublin
Cormac	McMahon	TU Dublin
Ciaran	McNally	University College Dublin
Daniel	McPolin	Queen's University Belfast
Asit Kumar	Mishra	National University of Ireland, Galway
Paul	Moran	National University of Ireland, Galway
Salissou	Moutari	Queen's University Belfast
John	Murphy	Munster Technological University
Roisin	Murray	TU Dublin
Sreejith	Nanukuttan	Queen's University Belfast
Ahmed	Nasr	TU Dublin
Patrick	Naughton	Atlantic Technological University, Sligo
Shane	Newell	Atlantic Technological University, Galway
Dervilla	Niall	TU Dublin
Darragh	Noble	TU Dublin
John	O'Donovan	GDG
Tomás	O'Flaherty	Atlantic Technological University, Sligo
Brian	O'Rourke	Munster Technological University
John	O'Sullivan	University College Dublin
Alan	O'Connor	Trinity College Dublin
David	O'Connor	TU Dublin
Leonard	O'Driscoll	Munster Technological University
Richard	O'Hegarty	University College Dublin
Indiana	Olbert	National University of Ireland, Galway
Fergal	O'Rourke	Dundalk Institute of Technology
Juan Pablo	Osorio	TU Dublin
Ruth	Quinn	Atlantic Technological University, Sligo
Ciaran	Reilly	TU Dublin
Kieran	Ruane	Munster Technological University
Mark	Russell	Queen's University Belfast
Peter	Ryan	Dundalk Institute of Technology
Mohammed	Sonebi	Queen's University Belfast
Marios	Soutsos	Queen's University Belfast
Muslim Jameel	Syed	National University of Ireland, Galway
Su	Taylor	Queen's University Belfast
Mark	Tyrer	Collegium Basilea
Amaya	Vega	Atlantic Technological University, Galway
Roger P.	West	Trinity College Dublin

Preface

On behalf of the Civil Engineering Research Association of Ireland (CERAI), we are very pleased to welcome you, in person, to the Civil Engineering Research in Ireland 2022 (CERI2022) conference run in conjunction with the Irish Transportation Research Network (ITRN) 2022 conference. While the pandemic is far from over, with resilience we have learnt to manage and live with it and the time is right to open up again after over two years of almost solely on-line working activity in the academic sector. It is a very important and enormously welcome part of returning to something resembling normalcy.

The Civil Engineering Research Association of Ireland (CERAI) was formed in 2012 with the aim of promoting civil engineering research and practice in Ireland, and their communication to engineering students, academics and practitioners. Its principal activity is the overseeing of the organisation of a biennial conference dedicated to this aim. The first Civil Engineering Research in Ireland (CERI) conference series was held in 2014, growing out of the Concrete Research Ireland (CRI) conferences commenced in 1997 and joint symposia of Bridge and Concrete Research Ireland (BCRI) conferences from 2008. Over the years, the themes of the conference broadened significantly to the ten themes presented in this year's conference. One of these themes is based on the papers of the Irish Transportation Research Network whom we have been delighted to have as collaborators in joint conferences since 2018.

Therefore, this year we are celebrating 25 years of showcasing concrete research at these conferences and the fifth of the much broader CERI conferences, amounting to some 776 published papers in 11 volumes in that time.

We are most grateful to the CERAI Board members and CERI2022 Stream Leaders, listed in the preamble of this book of Proceedings, for their very hard work in preparing for this event. We are also indebted to the staff at the co-hosting institutions, TU Dublin in Grangegorman and Trinity College Dublin, for their assistance in preparing for this two-day event. We are also indebted to our Scientific Committee, also listed herein, for expertly reviewing the abstracts and papers for the conference.

We would like to acknowledge the tremendous support of our long-term conference service providers, Ex Ordo, without whom running this conference would be considerably more challenging. While they did a tremendous job in facilitating going fully on-line for the CERI2022-ITRN2022 in Cork IT, we return now, thankfully, to the more traditional format of an in-person conference.

Given the size and intimacy of our all-island Civil Engineering research community, networking and the introduction of new young researchers have always been the hallmarks of these conferences. We are pleased to note that half of the papers presented at this conference will be by postgraduate researchers, continuing the long-standing traditions of this conference series since 1997.

We would like to thank our Keynote Speakers at this year's conference: Dr Larry Bank, Research Engineer at Georgia Tech's School of Architecture will deliver the Structures stream keynote; the Sustainability keynote will be given by Jennifer Boyer, Vice President of Sustainability at TU Dublin; the Environmental Keynote will be delivered by Laura Burke, Director General of the EPA; Brian Duggan, Director of Inspections at Active Travel England,

will deliver the Transport keynote, opening the ITRN conference; in the Geotechnical theme, with the largest number of papers, Dr Mike Long of UCD and Visiting Professor at NTNU in Norway will deliver the keynote; Prof Brian Norton of TU Dublin and Head of Energy Research at the Tyndall National Institute, UCC will deliver the Energy keynote; the Concrete keynote will be given by Prof John Provis, Professor of Cement Materials Science and Technology at Sheffield University; and Marcos Sanchez, who leads ARUP's European bridge practice, will deliver the Joe O'Donovan Memorial Lecture as the keynote of the Bridges stream. We are hugely honoured to again have such a prestigious panel of Keynote Speakers this year.

Sincere thanks are due to each and every one of our conference sponsors: Arup, Cement Manufacturers Ireland, Ecocem Ireland, Kilsaran, Kingspan, Mattest, Roughan & O'Donovan, the Institution of Structural Engineers, the Irish Concrete Federation, the Irish Concrete Society and Roadstone. Without their support the conference would not be possible, so we are all enormously indebted to them.

We very much hope you engage with and enjoy the many excellent papers on offer at this year's conference, but, equally importantly, that you make time to meet old mentors and friends in person, something, we believe, we have all missed during the extended period of the pandemic.

Niall Holmes and Roger P. West
Co-Chairs, CERI2022-ITRN2022 Conference

Conference Organisers:

Conference Hosts 2022:

Conference Sponsors 2022:

Table of Contents

Concrete

Bridges

Structures

Geotechnics

Transport

Environment

Energy

Pedagogy

New Frontiers

Sustainable cities and climate change

Concrete

Concrete Matters - 25 years of Concrete Research in Ireland Conferences

Roger P. West[1], Mark Richardson[2]
[1]Department of Civil, Structural and Environmental Engineering, Trinity College, University of Dublin, Dublin 2, Ireland
[2]School of Civil Engineering, University College Dublin, Dublin 4, Ireland
email: rwest@tcd.ie, mark.richardson@ucd.ie

ABSTRACT: The 'Concrete Practice in Ireland' (CPI) symposia were initiated in 1965, allowing stakeholders to decennially review significant developments in codes, standards, materials and construction technology. The third symposium introduced a session on research. Presentations from DIT, TCD, QUB, UCC, UCD and UCG led to a consensus at CPI95 that the pace of R&D was such that concrete researchers needed to meet on a more frequent basis. Thus the inaugural Concrete Research in Ireland Colloquium, 'CRI97', was spawned two years later. It provided a platform for island-wide early career concrete researchers to present and publish their work. A further ten such conferences have since occurred, chronicling the advent of new concepts and technologies, paralleling increased capacity in an evolving higher education sector and heralding the present-day biennial Civil Engineering Research in Ireland (CERI) conferences, with nine themes and eight keynote addresses due in the 2022 conference. This paper examines the concrete technology aspects of these conferences, reviewing the research published over the last 25 years. The key trends will be identified, with topics and papers cited, from which significant insights into the successful areas of research may be made. From this, opportunities and global challenges will be identified to inform and nurture career development of early-stage concrete technology researchers in a changing Irish higher education sector. This paper forms a record of impactful concrete research in Ireland, a repository of indigenous concrete knowledge for concrete researchers and practitioners, and a reflective insight on future challenges in an evolving national landscape.

KEYWORDS: CERI; Concrete Research in Ireland

1 INTRODUCTION

Since 1965, every ten years, an Irish concrete practice conference has been held mid decade and that which was held in 1995 [1] had a keynote paper on research developments which prompted the question as to whether or not meeting every decade was frequent enough for updating each other on research matters. What followed was a series of 11 conferences (Figure 1) held roughly biennially, with concrete as a central theme over the subsequent 25 years [2-12] culminating in this conference, the 12th such meeting. As summarised in Table 1, the first four were on concrete themes only, commencing in 1997, whereupon by 2005 sister conferences in bridges and geotechnical engineering , which had been running in parallel for several years, were merged with the CRI colloquia to form a much larger joint conference. Subsequently, with the addition of papers on construction materials other than concrete in 2014, the current day consortium of nine themes (including environmental, energy, pedagogy and new frontiers) are ensconced in the CERAI organisation which was born as a biennial conference under the banner of CERI. The union with Transport Engineering researchers was inaugurated in 2018 under the supplemented title of CERI & ITRN.

The research series is now a two day all-island conference with eight keynotes in the various themes and three parallel sessions presenting over 100 papers, though the pure concrete materials papers have been stable in number at about 15-27 per conference. (Table 1)

The concept of the conferences is not only to present cutting edge research but also to provide postgraduate students and other young researchers with a platform on which to launch their fledgling research topics and this ethos has continued to this day.

The methodology used in researching for this review paper was to assemble all the concrete-related papers over the 11 conferences, some 222 in total, to identify the underlying sub-themes and then to order the discussion and references presented below to match those sub-themes. The aim of the paper is to provide a useful national reference resource to assist researchers and practitioners to quickly identify the relevant themes, papers and their authors on concrete-related topics of interest.

Figure 1. Published proceedings from the biennial conferences.

Table 1. Previous themes: **C**oncrete, **B**ridges, **I**nfrastructure, **G**eotechnical, **M**aterials, **S**tructural, **Ti**mber, **E**nvironmental, **Te**chnology, **T**eaching **& L**earning, **En**ergy, **P**edagogy, **T**ransport, **N**ew **F**rontiers.

Year	Theme	Concrete Papers	Other Papers
1997	**C**	17	0
2001	**C**	20	0
2003	**C**	20	0
2005	**C**	15	0
2008	**C, B, I, G**	15	37
2010	**C, B, I, G, M**	22	56
2012	**C, B, G, M, S**	20	62
2014	**C, B, G, M, S, Ti**	27	61
2016	**C, B, G, M, S, Ti, E, Te, T&L**	27	92
2018	**C, B, G, S, E, P, T**	26	130
2020	**C, B, G, E, En, P, T, NF**	20	109

2 THE PAPERS

2.1 Materials

Cements:

With a recent review [13] of all concrete papers published by Irish authors showing the breadth of topics being researched, more papers have considered aspects of cement types than any other, particularly Pozzolans [14], from Roman cements [15] to the now well-established GGBS [16]. PFA was amongst the first to be considered, continued to this day [17-20] and more recently specialised cements such as spent mushroom compost ash [21, 22], Dolomite powder [23, 24], ceramic waste sludge [25-27] and lime-hemp [28-31]. There is considerable recent interest in geopolymers, that is, making concrete with no Portland cement present, including supplementary cementitious materials (SCMs) of Pozzolans, laterites, metakaolin and calcium aluminates [32-37].

The importance of the effect of utilising SCMs in concrete on strength maturity was realised early on and has continued to be studied [38-41]. Similarly, interest in durability aspects of SCMs has been considerable [42, 43], particularly chlorides [44-46], chemical attack [47-49] and fire [50], although surprisingly, given its importance, carbonation attack does not feature.

In conclusion, papers on the complex but useful software modeller of different cement hydration chemistry have recently been published [51-53].

Aggregates, Admixtures and Rebar:

Amongst graded aggregates [54, 55], fine aggregates such as furnace bottom ash featured early [56-58], and fine recycled aggregates more recently [59]. For coarse aggregates, lightweight aggregate, either more conventional [60] or, more recently, crumb rubber from recycled tyres [61-62], complement the increasing importance of recycled concrete used as aggregate in structural concrete [63-65]. Strength and stiffness properties of concrete depending on aggregate type has also received attention [66-67].

On the admixture front, a small diverse number of papers has been published, including those on plasticising [68], accelerating [41], shrinkage-reducing [69], viscosity modifying [70] and corrosion inhibition admixtures [71].

On rebar alternatives, more conventional FRP [72, 73] and Basalt fibre concretes [74] contrast sharply with timber-concrete [75] and Wireball (3D spherical wire) [76] composites.

2.2 Composites

Fibre-reinforced concrete has become popular for strengthening and/or repair. FRP is well-established [72, 77 and 73], while carbon [78, 79], glass [80] and, more recently, Basalt [81-83] have been used in practice. Ultra-high performance FRC is used in structural concrete particularly for flexural strength [84-87].

Used as an alternative or supplement to rebar, composites been used such as Basalt FRC strips, bars or textiles [74, 88, 89], or as externally bonded laminates [75, 90].

The fibre properties themselves, from dosage to length to alignment to durability have also been shown to be relevant in determining performance [91-95].

2.3 Properties

Workability and Mechanical Strength:

Most papers of interest on the topic of workability involve some aspect of rheology, from the early development of a tool for measuring the rheological parameters [96, 97], to self-compacting concrete [98] and viscosity modifying [70, 99] and plasticising admixtures [68].

The effect of fibres on strength has been examined [81, 100], as had the importance of water and carbon dioxide curing [101-103] complementing the focus on maturity in strength development [41, 104, 105].

High strength concrete is also popular in an Irish context [66, 106], with applications [107] which include the relevance of particle packing in achieving enhanced strength 108].

More specialised topics related to strength, such as active confinement [109, 110], thermal performance [111], vibration properties [112-113] and impact [114-116], have received targeted attention, including a keynote on concrete's impact properties [114].

Movement and Moisture:

The defining of the elastic modulus of concrete for different aggregates [67] is important for most movement types, as it allows prediction of flexural and horizontal deflections [117-119]. Indeed, the phenomena of time-dependent movements [120], including temperature [121, 122], shrinkage [57, 63, 69, 123] and creep [124] have been explored.

The consequences of moisture movement in the drying of slabs [125-127] and the damage caused by early covering with impermeable materials [128] is also of interest in this theme.

2.4 Durability

General:
Two general descriptions of the status of durability for structures and bridges have been published [129, 130] including a keynote on the status of durability specifications [129] .

The role of aggregates and cements in this process has also been researched [43, 54]. Following on from this, the importance of the permeability and sorptivity properties have been emphasised [42, 131].

An important part of durability is the testing of the relevant physical parameters that define performance, especially corrosion activity [132-134]. One aspect of this, cathodic protection, has received some attention [135,136].

Carbonation, Chlorides, and other Specific Forms of Attack:
Surprisingly, there is only one paper which deals with carbonation alone [137] - while this paper does not deal with corrosion affected carbonation, it does infer carbonation ingress rates which are important.

Papers on chlorides form the largest group by far in this category, with 18 papers in total. Specifically, safety assessments, service life and whole life predictions of bridges in marine environments have been made [45, 138-142].

Obtaining the chloride profiles, especially in alkali-activated concrete, is particularly important in understanding the degree of ingress [44, 46,71, 143, 144]. How compressive loading and the diffusion coefficient influence chloride ingress have been examined and modelled [145, 146]. When chlorides are identified as being responsible for corrosion of rebar, several methods of chloride extraction have been successful used [147, 148]. Long-term studies on durability in a marine environment have delivered some useful lessons for future design [149-151].

More recently, there has been considerable interest in the combined effects of carbonation and chloride attack on reinforced concrete, which has been reported on in [152-156].

In relation to other forms of attack, ASR received a lot of attention, largely in the early 2000s, underpinning the development of an understand as to why it is not generally a problem in Ireland [157-160]. Exposure to aggressive chemicals has also been explored [47-49], as has combined chloride and acid attack [95] . A single reference addressed the matter of freeze-thaw resistance [161], with a further two addressing the consequences of fire damage [50, 162]. The electrochemical repair of concrete has been described in [163].

2.5 Products

A range of different cementitiously-based products have been reported on in the publications. Grout rheology [70, 99] and mortars with and without SCMs have been discussed. Papers on cement and fibre type effects on strength, maturity and shrinkage [26, 41, 52, 92, 123] are complemented by papers on application for strength enhancement [88, 164].

The importance of lime mortars to the masonry industry is also discussed [165-167] as have masonry applications in [103, 137, 168].

Self-compacting concrete is well establish in the pre-cast industry and several papers reflect that [23, 24, 55, 98, 105].

2.6 Structures

General Structural Elements:
A keynote [169] and one other paper [170] highlight structural innovations over 40 years and others extracted from the structural concrete themes in the proceedings comprise this section.

Papers on slabs are common, starting with the behaviour of slabs on grade [171, 172], progressing to compressive membrane/lateral action [72, 173, 174] and transverse/shear effects [175-177] as published from the mid 2000s onwards. The introduction of steel fibres and hybrid composites followed [94, 100, 115, 178, 179]. Laboratory testing and modelling of flat slab systems also assumed some importance [180-182].

A variety of beams also feature: high strength partial prestressed [117], BFRP SCC beams [83] and Basalt textile beams [89]. Other composite beams include timber [75] and CFRP laminates [90]. Fatigue testing [183] and modelling of RC deep beams [184] and web openings [185] have also been considered.

Some papers on combined studies of slabs and beams have also been published, principally noting the high performance achieved through the including of steel fibres [85, 86, 91, 186]. The structural behaviour of concrete tanks [121], walls [122], columns [113], piles [187] and corbels [188] also merit noting.

Finally, general concrete structures get a mention in papers on FRP [73, 76] and, most recently, on strut and tie design [189] and demountable structures [190].

Panels and the FlexiArch system:
There were two standout categories of structure which are worthy or special mention, panels and the FlexiArch system.

Research on panels is not new [70, 191] but more recent work on thin precast sandwich panels for retrofitting existing buildings has examined both structural composite action [192-194] and their thermal behaviour, especially when enhanced by PCMs [111, 195, 196]. Other recent work examines formwork liners to enhance geopolymer cladding panels [36].

The FlexiArch system was first mooted as a concept in 2003 [107] and, since then, its genesis has been well-documented, through its introduction [197], its development [198, 199] to its maturation [200, 201].

2.7 Bridges

Although there have been many papers on bridges presented at the said conferences since bridges were introduced as a co-theme in 2008, those papers with a particular focus on concrete have been identified. From a structural viewpoint, compressive membrane and shear actions have been explored [173, 187], while time dependent effects are also of interest [120]. Durability of bridges has been of particular interest [45, 130, 138, 139].

2.8 Design

Sustainability:
Led by two keynotes [202, 203] on performance monitoring in the built environment, sustainability as a topic has had surprisingly few papers as a greater awareness of the vital importance of this topic has been awakened. Aspects of the sustainability of concrete have been considered [37, 204-206]

including its environmental impact [34, 207, 208] and biodiversity [209]. The appearance of concrete especially in the long-term [210, 211] and the consequence of its albedo on internal temperatures [212, 213] have been recognized.

Recent world-wide attention on changing from "deemed to satisfy" to "performance-based" testing [214-216] has also increased because durability is an important aspect of sustainability.

Design Standards:

The last 25 years have encompassed the substantial code changes in concrete design so, inevitably, some papers have aided in this process [184, 217, 218]. New design processes for beams, slabs and columns have been described [130, 219-221].

In another vein, the early use of IT in concrete procurement and design saw some significant advancements which have now become acceptable practices [222-225].

2.9 Other Topics:

Testing:

New laboratory testing methods have featured in recent years in the publications [181, 183, 226, 227] as has in-situ testing/ performance monitoring, including structural health monitoring [178, 179, 196, 203, 228, 229].

Modelling:

Modelling concrete structures is an important part of the design process [134, 193], especially numerical modelling [78, 86, 182]. Finite element modelling is, not surprisingly, popular [76, 190, 193].

Pedagogy:

While pedagogy, as a theme in its own right, has only been recently introduced, there is a small cohort of lecturers who have a keen interest in sharing concrete knowledge on educational matters. Approaches to teaching design using software [223-225, 230] are of interest as is its extension into using software to teach RC detailing [231-233].

Finally, two innovative approaches to integrating concrete laboratories with lectures and making the teaching of statistics for concrete applications more attractive are discussed in [234] and [235].

3 DISCUSSION AND CONCLUSIONS

The rich tapestry of topics reveals the contribution of concrete research in Ireland to teaching, the national industry, state agencies and the international research community. This contribution has been built on resources that are now facing significant challenges.

Regarding physical resources, much of the research was conducted in facilities that formed the combined teaching and research laboratories of civil engineering departments in higher education institutions. The development of high-quality e-learning tools and changed learning styles has reduced the need for fully equipped large scale 'concrete labs' in the teaching role. Maintaining the facilities as solely research laboratories is becoming increasingly difficult to justify financially under current higher education funding models. The pool of human resources is also diminishing and it is increasingly difficult to attract early career technicians and researchers to specialise in concrete technology in the absence of sufficient funding. This is due to a host of factors deserving of a paper in itself!

It would, therefore, be timely for concrete researchers and industry in Ireland to take stock of shared goals measured against current and future resources. It may be worth investing in a formal collaboration and consolidation leading to a national network of specialist concrete laboratories in industry and interested HEIs, which together would constitute a national centre of excellence. This 'centre', distributed geographically but united in a virtual world, could form the basis of a hub in Ireland for tackling concrete related national industry innovations and global sustainability challenges. Such a 'centre' would help to attract technical staff, highly talented engineering graduates and early career researchers to conduct concrete research in Ireland and to join other research centres globally in tackling the vital concrete-related sustainability issues which we undoubtedly all face.

ACRONYMS

BFRC – Basalt Fibre Reinforced Concrete
BIRI – Bridge and Infrastructure Research in Ireland
CERAI – Civil Engineering Research Association of Ireland
CERI – Civil Engineering Research in Ireland
CFRP – Carbon fibre Reinforced Polymer
CRI – Concrete Research in Ireland
FRC – Fibre Reinforced Concrete
FRP - Fibre Reinforced Polymer
GGBS – Ground Granulated Blastfurnace Slag
ITRN – Irish Transport Research Network
PCM - Phase Change Material
PFA – Pulverised Fly Ash
RC – Reinforced Concrete
SCC – Self-compacting Concrete
SCM – Supplementary Cementitious Material

REFERENCES

[1] CPI95, (1995), *Proc. of Concrete Practice in Ireland* 1995, Ed. M. Richardson, pp 177
[2] CRI97, (1997), *Proc. of Colloquium on Concrete Research in Ireland 1997*, Eds. R.P. West and D. O'Dwyer, TCD, Dublin, pp 148.
[3] CRI01, (2001), *Proc. of Colloquium on Concrete Research in Ireland 2001*, Eds. E. Cannon, NUIG, Galway, pp 146.
[4] CRI03, (2003), *Proc. of Colloquium on Concrete Research in Ireland 2003*, Eds. M. Basheer and M. Russell, QUB, Belfast, pp 194.
[5] CRI05, (2005), *Proc. of Colloquium on Concrete Research in Ireland 2005*, Eds. C. McNally, UCD, Dublin, pp 147.
[6] CRI08&BIRI08, (2008), Proc. of Colloquium on Concrete Research in Ireland 2008 and Bridge and Infrastructure Research in Ireland 2008, Eds. E. Cannon, R.P. West and P. Fanning, NUIG, Galway, pp 460.
[7] CRI10&BIRI10, (2010), *Proc. of Joint Symposium on Concrete Research in Ireland 2010 and Bridge and Infrastructure Research in Ireland 2010*, Eds. N.A. Ni Nualainn, D. Walsh, E. Cannon, R.P. West, C. Caprani, B.McCabe, UCC&CIT, Cork, pp 672.
[8] BIRI12&CRI12, (2012), *Proc. of the Bridge and Concrete Research in Ireland Conference 2012*, Eds, C. Caprani, A. O'Connor, DIT&TCD, Dublin, pp 534.
[9] CERI2014, (2014), *Proc. of the Civil Engineering Research in Ireland Conference* 2014, Eds. S. Nanukuttan and J. Goggins, QUB, Belfast, pp 516.
[10] CERI2016, (2016), Proc. of the Civil Engineering Research in Ireland Conference 2016, Eds. J. Goggins, NUIG, Galway, pp 719.
[11] CERI2018&ITRN2018, (2018), Proc. of the Civil Engineering Research in Ireland Conference 2018 and Irish Transport Research Network 2018, Eds. V. Pakrashi and J. Keenehan, UCD, Dublin, pp 892.
[12] CERI2020&ITRN2020, (2020), Proc. of the Civil Engineering Research in Ireland Conference 2020 and Irish Transport Research Network 2020, Eds. K. Ruane and V. Jaksic, CIT, Cork, pp 770.

[13] West R and Gaur G, (2018), "Concrete research in Ireland 2015 to 2017", *Proc of CERI & ITRN 2018*, Dublin, 162 - 171.
[14] Walker R and Pavia S, (2010), "The effect of Pozzolan properties on the properties of building composites", *Proc of CRI 2010 & B&IRI 2010*, Cork, 457- 464.
[15] Pavia S, (2014), "An assessment of some properties of Roman cement", *Proc of CERI 2014*, Belfast, 223 - 228.
[16] Higgins B, Curran M and Spillane J, (2020), "Maximizing the potential use of ground granulated blast furnace slag GGBS) in cement: An Irish investigation", *Proc of CERI & ITRN 2020*, Cork, 156 - 161.
[17] Power E, MacCraith S and Richardson M, (2001), "The influence of peat pulverised fuel ash on the properties of fresh and hardened concrete", *Proc of CRI 2001*, Galway, 11 - 16.
[18] Gavigan D and 'Goggins J, (2010), "Investigation of fly ash from peat fired power stations as a cement replacement in concrete", *Proc of CRI 2010 & B&IRI 2010*, Cork, 531- 538.
[19] Russell M, Basheer M and Kant R, (2012), "Thermal and chemical activation of pulverised fuel ash in Portland cement based systems", *Proc of B&CRI 2012*, Dublin, 235- 240.
[20] Alelweet, O and Pavia S, (2020), "Potential of a low- calcium fly ash (FA) for the production of alkali- activated materials", *Proc of CERI & ITRN 2020*, Cork, 162 - 167.
[21] Russell M, Basheer M, Rao J and Hadi H, (2003), "Potential use of spent mushroom compost ash as an activator for pulverized fuel ash", *Proc of CRI 2003*, Belfast, 99 - 106.
[22] Russell M, Basheer M and Rao J, (2005), "The replacement of gypsum by spent mushroom compost ash in the manufacture of cement", *Proc of CRI 2005*, Dublin, 61 - 70.
[23] Barbhuiya, S and Bashir M, (2005), "Properties of self-compacting concrete containing fly ash and Dolomite powder", *Proc of CRI 2005*, Dublin, 51- 60.
[24] Abdelqader A, Wilson K, Thornton N, McHugh K, Sonebi M and Taylor S, (2020), "Preliminary investigation on the use of dolomitic quarry by-product powders in grouting for self-compacting concrete applications", *Proc of CERI & ITRN 2020*, Cork, 174 - 179.
[25] Kenna F and Archibold P, (2014), "Ceramic waste sludge as a partial cement replacement", *Proc of CERI 2014*, Belfast, 205 - 210.
[26] Farrara L, Deegan P, Pattarini A, Sonebi M, Taylor S and Kelly G, (2016), "Affect of waste ceramic powder on strength development characteristics of cement based mortars", *Proc of CERI 2016*, Galway, 171 - 176.
[27] Archibald P, Russell M and Hoey C, (2016), "The potential use of ceramic waste sludge as a supplementary cementitious material", *Proc of CERI 2016*, Galway, 183 - 188.
[28] Murphy F, Pavia S and Walker R, (2010), "An assessment of the physical properties of lime-hemp concrete", *Proc of CRI 2010 & B&IRI 2010*, Cork, 431 - 438.
[29] Walker R and Pavia S, (2012), "Impact of water retainers in the strength, drying and setting of lime hemp concrete", *Proc of B&CRI 2012*, Dublin, 355 - 360.
[30] Walker R and Pavia S, (2014), "Impact of hydration in the properties of lime hemp concretes made with commercial binder", *Proc of CERI 2014*, Belfast, 211 - 216.
[31] Reilly A and Kinnane O, (2018), "An assessment of the thermal storage capacity of hemp-lime using the transient energy ratio method", *Proc of CERI & ITRN 2018*, Dublin, 196 - 2001.
[32] McIntosh J and Soutsos M, (2014), "Development of a geopolymer binder from the Interbasaltic Laterites of Northern Ireland", *Proc of CERI 2014*, Belfast, 143 - 148.
[33] Oakes L, Magee B, McIlhagger A and McCartney M, (2018), "A simplified mixed design procedure for geopolymer cement mortars based on metakaolin and industrial waste products activated with potassium silicate", *Proc of CERI & ITRN 2018*, Dublin, *Proc of CERI 2018*, Galway, 190 - 195.
[34] Wilkinson A, Magee B, Woodward D and Tretsiakova- McNally S, (2016), "Development of resilient and environmentally responsible highway infrastructure solutions using geopolymer cement concrete", *Proc of CERI 2016*, Galway, 293 - 298.
[35] Lawthar S, McIntosh A, Nanukuttan S, Provis J, Soutsos M and Jose D, (2016), "Understanding the microstructure of alternative binder systems-banahCEM a metakaolin based geopolymer", *Proc of CERI 2016*, Galway, 177 - 182.
[36] Hyde R, West R and Nanukuttan S, (2018), "A study on the impact of a controlled permeability form liner, polymer resin, calcium aluminate cement and heat treatment on the permeability of an ultra-high-performance geopolymer concrete cladding panel", *Proc of CERI & ITRN 2018*, Dublin, 135 - 139.
[37] Alawais A and West R, (2016), "Sustainable concrete with 95% recycled and natural components", *Proc of CERI 2016*, Galway, 347 - 352.
[38] O'Rourke B and Richardson M, (2005), "Improved two-day strengths of Portland Blastfurnace cement", *Proc of CRI 2005*, Dublin, 121- 130.
[39] Reddy J and Richardson M, (2008), "A study of measured and predicted early age in- situ strengths of limestone cement/GGBS concretes", *Proc of CRI 2008 & B&IRI 2008*, Galway, 245 - 252.
[40] Reddy J and Richardson M, (2008), "Early age striking of formwork to GGBS concretes: a proposed decision making tool", *Proc of CRI 2008 & B&IRI 2008*, Galway, 305 - 312.
[41] Korde, C, Crookshank M, West R and Reddy J, (2018), "Temperature and admixture effects on maturity of GGBS mortar for the precast industry", *Proc of CERI & ITRN 2018*, Dublin, 129 - 134.
[42] Snowden, R and Richardson, M, (1997), "Influence of mixed parameters on the permeability of PFA concretes manufactured with PFA sourced in Ireland", *Proc of CRI 1997*, Dublin, 3 - 10.
[43] McNally C and Seymour P, (2010), "Durability aspects of blends of GGBS with CEM I and CEM II/A cements", *Proc of CRI 2010 & B&IRI 2010*, Cork, 637 - 644.
[44] Bondar D, Thompson D, Nanukuttan S, Soutsos M and Basheer M, (2016), "Resistance of alkali activated slag concretes to chloride environments", *Proc of CERI 2016*, Galway, 265 - 270.
[45] Downey S and O'Connor A, (2012), " Influence of corrosion propagation of GGBS concretes on whole life cost of bridge structures in chloride environments", *Proc of B&CRI 2012*, Dublin, 67 - 72.
[46] Basheer M, Ma Q, Nanukuttan S, Bai, Y and Yang C, (2014), "Chloride ingress through alkali- activated slag concretes", *Proc of CERI 2014*, Belfast, 149 - 154.
[47] Coleman D, McNally C, O'Rourke B and Richardson M, (2014), "Performance of GGBS concretes in acidic wastewater environments", *Proc of CERI 2014*, Belfast, 469 - 474.
[48] Thompson D, Holmes N and Reddy J, (2016), "Evaluating a new CEM III/A cement for concrete exposed to harsh acid rich environments", *Proc of CERI 2016*, Galway, 371 - 376.
[49] O'Connell M, McNally C and Richardson M, (2010), "The performance of limestone cements with GGBS exposed to elevated sulfate environments", *Proc of CRI 2010 & B&IRI 2010*, Cork, 619 - 626.
[50] McKenna T, Richardson M and O'Rourke B, (2014), "Mechanical resistance characteristics of GGBS concrete in fire", *Proc of CERI 2014*, Belfast, 367 - 372.
[51] Holmes N, Griffin A, Enright B and Kelliher D, (2018), "Introducing a new cement hydration and microstructure model", *Proc of CERI & ITRN 2018*, Dublin, 202 - 207.
[52] Ogoro E, Kelliher D and Tyrer M, (2020), "Predicting mortar compressive strength using HYDCEM", *Proc of CERI & ITRN 2020*, Cork, 168 - 173.
[53] Holmes N, Kelliher D and Tyrer M, (2020), "Thermodynamic cement hydration modeling using HYDCEM", *Proc of CERI & ITRN 2020*, Cork, 180 - 186.
[54] Basheer L, Basheer M and Long A, (2003), "Role of aggregate grading and size on the durability of ordinary Portland cement concrete", *Proc of CRI 2003*, Belfast, 89 - 98.
[55] Greaves P, Kwasny J and Basheer M, (2010), "Influence of the aggregate composition on fresh and hardened properties of self- compacting concretes", *Proc of CRI 2010 & B&IRI 2010*, Cork, 549 - 556.
[56] Bai Y and Basheer M, (2001), "Influence of furnace bottom ash as fine aggregate on some properties of fresh and hardened concrete", *Proc of CRI 2001*, Galway, 3 - 10.
[57] Bai Y, Darcy F and Basheer M, (2003), "Strength and drying shrinkage properties of concrete containing furnace bottom ash as fine aggregates", *Proc of CRI 2003*, Belfast, 117 - 126.
[58] Bai Y, Russell M and Basheer M, (2010), "Characterization and reactivity investigation of furnace bottom ash for fine aggregate in concrete", *Proc of CRI 2010 & B&IRI 2010*, Cork, 539 - 548.
[59] Collery D, McKenna P, Dunne D and Paine K, (2014), "Strength and deformation characteristics of concrete containing recycled aggregate fines", *Proc of CERI 2014*, Belfast, 333 - 338.
[60] Owens K, by Y, Basheer M, Cleland D and Taylor S, (2010), "Development of structural lightweight, chemically activated blended cementitious concretes with Lytag aggregates", *Proc of CRI 2010 & B&IRI 2010*, Cork, 645 - 652.
[61] West R and McElhinney B, (2008), "Performance of crumb rubber concrete", *Proc of CRI 2008 & B&IRI 2008*, Galway, 363 - 370.
[62] Alawais A and West R, (2018), "Using crumb rubber as an aggregate in a sustainable concrete mix", *Proc of CERI & ITRN 2018*, Dublin, 117 - 122.

[63] Richardson M, Griffin R and Faolain B, (2003), "Drying shrinkage characteristics of recycled aggregate concrete", *Proc of CRI 2003*, Belfast, 127 -136.
[64] Alawais A and West R, (2018), "Pre- treatment of recycled concrete aggregates with silica fume", *Proc of CERI & ITRN 2018*, Dublin, 123 - 128.
[65] Lowe A and O'Flaherty T, (2018), "Effect of recycled concrete aggregates on the performance of structural grade concrete", *Proc of CERI & ITRN 2018*, Dublin, 111 - 116.
[66] Montgomery F and Irvine H, (2001), "Optimizing Northern Ireland's coarse aggregates for use in high strength concrete", *Proc of CRI 2001*, Galway, 17 - 24.
[67] Gao J and West R, (2010), "Assessing the modulus of elasticity of high strength concrete made from different types of Irish aggregates", *Proc of CRI 2010 & B&IRI 2010*, Cork, 557 - 566.
[68] Garcia-Taengua E, Sonebi M, Taylor S, Ferrara L, Deegan P and Pattarini A, (2014), "A study on cement grout rheology: optimum dosage of SP related to their composition and interaction with mineral additions", *Proc of CERI 2014*, Belfast, 217 - 222.
[69] Richardson M, (2001), "Drying shrinkage properties of concrete manufactured in Ireland with and without shrinkage-reducing admixtures", *Proc of CRI 2001*, Galway, 53 - 60.
[70] Sonebi M and Taib A, (2008), "Effect of viscosity modifying agent and silica fume on rheological behavior of cement-based grouts", *Proc of CRI 2008 & B&IRI 2008*, Galway, 265 - 274.
[71] Grimes E, McNally C and Richardson M, (2005), "Influence of amino alcohol inhibitors on corrosion activity in chloride- contaminated reinforced concrete", *Proc of CRI 2005*, Dublin, 109 - 120.
[72] Tharmarajah G, Robinson D, Taylor S and Cleland D, (2008), "FRP reinforcement for laterally restrained concrete slabs", *Proc of CRI 2008 & B&IRI 2008*, Galway, 275 - 280.
[73] Antonopoulou S, McNally C and Byrne G, (2016), "Developing braided FRP reinforcement for concrete structures", *Proc of CERI 2016*, Galway, 189 - 194.
[74] Dal Lago B, Deegan P, Taylor S, Crossett P, Sonebi M, Ferrara L and Patatrini A, (2016), "Pre- stressing using Basalt fibre bars: An experimental investigation on a new frontier of precast concrete", *Proc of CERI 2016*, Galway, 365 - 370.
[75] West R and Holmes- Ievers J, (1997), "The contribution of bond and friction in timber-concrete composite beams", *Proc of CRI 1997*, Dublin, 19 - 24.
[76] Tharmarajah G and Archbold P, (2012), "Nonlinear finite element analysis of FRP reinforced concrete structures", *Proc of B&CRI 2012*, Dublin, 475-480.
[77] Ryan C, West R and Broderick B, (2001), "Wireballs- their genesis and future", *Proc of CRI 2001*, Galway, 25 - 30.
[78] Meehan A and Ruane K, (2016), "An assessment of reinforced concrete members in tension strengthened with near surface mounted CFRP strips", *Proc of CERI 2016*, Galway, 611 - 616.
[79] Fanning P, (1997), "Numerical modeling of RC beams strengthened using CFRP composite materials", *Proc of CRI 1997*, Dublin, 117 - 124.
[80] Cullivan P and Archbold P, (2010), "Load- deflection performance of GFRP reinforced thin FRC panels", *Proc of CRI 2010 & B&IRI 2010*, Cork, 51- 60.
[81] Archibald P, da Costa Santos A and Loonam A, (2016), "The influence of basalt fibers on the mechanical properties of concrete", *Proc of CERI 2016*, Galway, 271 - 276.
[82] Antonopoulou S, McNally C and Byrne G, (2018), "A comparative study on different BFRP rebar design methodologies", *Proc of CERI & ITRN 2018*, Dublin, 759 - 763.
[83] Crossett P, Taylor S, Sonebi M and Ferrara L, (2018), "Ultimate capacity and deflection behavior of BFRP prestressed SCC beam", *Proc of CERI & ITRN 2018*, Dublin, 152 - 155.
[84] English S, Chen J, Soutsos M and Robinson D, (2016), "An experimental study of the shear behavior of ultra-high performance fiber reinforced concrete", 277 - 280.
[85] Wilson W and O'Flaherty T, (2016), "Effect of steel fiber dosage on the behavior of ultra high performance fiber reinforced concrete beams and slabs", *Proc of CERI 2016*, Galway, 259 - 264.
[86] Wilson W and O'Flaherty T, (2018), "Numerical modeling of conventional and ultra high performance fiber reinforced concrete beams and slabs", *Proc of CERI & ITRN 2018*, Dublin, 156 - 161.
[87] He Y, Esmaeele E and Soutsos M, (2020), "Effect of casting method and test setup on flexural characteristics of UHPFRC", *Proc of CERI & ITRN 2020*, Cork, 229 - 233.
[88] D'Anna J, Amato G, Chen J, Minafo G and La Mendola L, (2018), "Experimental investigation on basalt reinforced mortar strips in tension", *Proc of CERI & ITRN 2018*, Dublin, 596 - 600.
[89] O'Leary D, Cadogan D, Ruane K and Jaksic V, (2020), "Retrofitting of reinforced concrete beams strengthened with basalt textile", *Proc of CERI & ITRN 2020*, Cork, 720 - 725.
[90] Harte A, Meade S and McKeever K, (2001), "Flexural strengthening of RC beams using externally bonded CFRP laminates", *Proc of CRI 2001*, Galway, 31 - 38.
[91] Donnelly A, West R, Mohammad A and Grimes M, (2014), "Ultimate structural capacity of very high dosage steel fiber concrete beams and slabs", *Proc of CERI 2014*, Belfast, 311 - 316.
[92] Backus J, Sonebi M, Moore T and Hughes D, (2014), "Effect of fiber type and dosage on early tensile strength of high performance mortar", *Proc of CERI 2014*, Belfast, 317 - 320.
[93] Kenna J, Mulheron M and Archbold P, (2016), "The influence of short fiber additions on the pull out behavior of reinforced concrete", *Proc of CERI 2016*, Galway, 283 - 288.
[94] Cuomo G, West R and Zhang S, (2005), "Demonstrating the alignment of long steel fibers fiber- reinforced concrete slabs, *Proc of CRI 2005*, Dublin, 139 - 147.
[95] Dunne D, Newlands M and Waite A, (2012), "Freeze- thaw resistance of fiber reinforced concrete", *Proc of B&CRI 2012*, Dublin, 49 - 54.
[96] West R and O'Leary R, (1997), " An improved Two- point workability apparatus", *Proc of CRI 1997*, Dublin, 91 - 98.
[97] West R and Cullen R, (2003), "Characteristics of a new hand-held rheology tool, *Proc of CRI 2003*, Belfast, 137 - 146.
[98] Sonebi M, (2005), "Testing segregation and rheology of self- compacting concrete", *Proc of CRI 2005*, Dublin, 81 - 92.
[99] Sonebi M, Adzri K and Taylor S, (2012), "Effect of the type of viscosity-modifying admixtures and metakaolin on the rheology of cement-based grouts", *Proc of B&CRI 2012*, Dublin, 205 - 210.
[100] West R and Cuomo G, (2001), "Strength loss in the wake of a cylinder dragged through a concrete slab", *Proc of CRI 2001*, Galway, 87 - 92.
[101] Killeen C, Goggins J and Hajdukiewicz M, (2018), "Investigation into the correlation between curing temperature and compressive strength gain of concrete", *Proc of CERI & ITRN 2018*, Dublin, 172 - 177.
[102] Owens K, Basheer M and Sen Gupta B, (2005), "Utilization of carbon dioxide from flue gases to improve the compressive strength of cement pastes", *Proc of CRI 2005*, Dublin, 41 - 50.
[103] Gilroy B, Black L, Thompson D, Hogan R and Holmes N, (2020), "Effects of accelerated carbonation curing on CO2 sequestration and on the compressive strength of concrete masonry units", *Proc of CERI & ITRN 2020*, Cork, 137 - 142.
[104] O'Connor A and Perry S, (2001), "Effect of early-age concrete temperatures on strength-maturity relationships", *Proc of CRI 2001*, Galway, 61 - 68.
[105] Deegan P, Sonebi M, Kelly G, Taylor S and Pattarini A, (2016), "Investigation of the maturity and engineering performance of self-compacting concrete for precast elements", *Proc of CERI 2016*, Galway, 255 - 258.
[106] McGuire M, (1997), "High strength concrete using Irish materials", *Proc of CRI 1997*, Dublin, 11 - 16.
[107] Taylor, S, Rankin G and Cleland D, (2003), High strength concrete in flexural and arching theory", *Proc of CRI 2003*, Belfast, 59 - 68.
[108] Wilson W and O'Flaherty T, (2020), "Development and localisation of ultra high performance concrete using a particle packing model", *Proc of CERI & ITRN 2020*, Cork, 131 - 136.
[109] O'Shea C, Niall D, and Holmes N, (2012), "Active confinement of concrete members", 469 - 474.
[110] Suhail R, Amato G, Chen J and McCrum D, (2016), "Heat activated prestressing of shape memory alloys for active confinement of concrete sections", *Proc of CERI 2016*, Galway, 605 - 610.
[111] Niall D, Kinnane O, , West R and McCormack S, (2016), "Mechanical and thermal evaluation of different types of PCM-concrete composite panels", *Proc of CERI 2016*, Galway, 353 - 358.
[112] Noble D, Nogal, M, O'Connor, A and Pakrashi, V, (2014), "Effect of pre-stress force and eccentricity on natural frequencies of prestressed concrete", *Proc of CERI 2014*, Belfast, 427 -432.
[113] Deenihan J and Broderick B, (2010), "Seismic performance of high strength concrete composite columns subject to inelastic flexural loading", *Proc of CRI 2010 & B&IRI 2010*, Cork, 141 - 148.
[114] West R, (2014), "Concrete - making an impact", *Proc of CERI 2014*, Belfast, 303 - 310.
[115] West R and Dousti M, (2014), "Impact resistance of high-dosage steel fiber reinforced concrete slabs, *Proc of CERI 2014*, Belfast, 327 - 332.

[116] Pritchard S and Perry S, (1997), "The response of confined concrete to hard impact", *Proc of CRI 1997*, Dublin, 75 - 82.
[117] Ryan D, O'Dwyer D and O'Connor A, (2003), "Prediction of deflection in partially prestressed post- tensioned concrete beams constructed using high strength concrete", *Proc of CRI 2003*, Belfast, 27 - 36.
[118] Richardson M, (2001), "Redistribution of horizontal movement in airfield pavements: a case study", *Proc of CRI 2001*, Galway, 69 - 78.
[119] MacGiolla A and Richardson M, (1997), "A study of horizontal movements in airfield pavement joints", *Proc of CRI 1997*, Dublin, 35- 42.
[120] Flanagan, J., O'Brien, E. and Samartin, A, (1997), "The prediction of time dependent effects in prestressed concrete bridges", *Proc of CRI 1997*, Dublin, 43 - 48.
[121] Minnehan M and O'Rourke B, (2012) "A finite element study of precast prestressed concrete circular tanks subject to elevated temperatures", *Proc of B&CRI 2012*, Dublin, 409 - 414.
[122] O'Donnell J and Speares A, (2012), "Cracking in concrete walls due to an external temperature load", *Proc of B&CRI 2012*, Dublin, 55- 60.
[123] King C, McEniry J, O'Kiely P and Richardson M, (2012), "The influence of fibrous grass silage extract on the shrinkage properties of cementitious mortars", *Proc of B&CRI 2012*, Dublin, 349- 354.
[124] Barrett D and Cannon E, (2001), "The influence of creep on the risk of thermal cracking in concrete at early ages", *Proc of CRI 2001*, Galway, 45- 52.
[125] West R and Holmes N, (2001), "Experimental investigation of moisture migration in concrete", *Proc of CRI 2001*, Galway, 39- 44.
[126] West R and Holmes N, (2003), "Finite element modeling of moisture movement in concrete floors", *Proc of CRI 2003*, Belfast, 157- 166.
[127] Holmes N and West R, (2010), "Moisture movement in concrete during drying- A review", *Proc of CRI 2010 & B&IRI 2010*, Cork, 73- 82.
[128] Holmes N and West R, (2014), "Performance of vinyl on concrete floors subject to pull off testing", *Proc of CERI 2014*, Belfast, 451-456.
[129] Dhir R, (2008), "Specifying concrete durability: are we getting there?", *Proc of CRI 2008 & B&IRI 2008*, Galway, 3- 14.
[130] Long A, Rankin G, Taylor S and Cleland D, (2003), "Durable concrete bridge decks by design", *Proc of CRI 2003*, Belfast, 3- 14.
[131] O'Dwyer D, (2001), "A preliminary investigation into ferrocement permeability and sorptivity", *Proc of CRI 2001*, Galway, 133- 138.
[132] Basheer M, Nanukuttan, S, Robinson D, Basheer L, McArthur, W, Grattan K, Sun T, McPolin D and Long A, (2008) "Research at Queen's University Belfast on testing and monitoring the durability of concrete structures", *Proc of CRI 2008 & B&IRI 2008*, Galway, 292- 304.
[133] Grattan S, Basheer M, Taylor S, Sun T and Grattan K, (2008), "Monitoring the corrosion of steel reinforcement bars through the use of strain fiber optic sensors and electronic sensor systems", *Proc of CRI 2008 & B&IRI 2008*, Galway, 321- 328.
[134] Downy S, O'Connor A and Shiels E, (2010), "Experimental investigation of corrosion-induced crack propagation in reinforced concrete", *Proc of CRI 2010 & B&IRI 2010*, Cork, 101- 108.
[135] Holmes N, Byrne A and Norton B, (2016), "An overview of the development of cement-based batteries for the cathodic protection of embedded steel in concrete", *Proc of CERI 2016*, Galway, 593- 598.
[136] Ward C, Nanukuttan S and McRobert J, (2014), "The performance of cathodic protection system in reinforced concrete structure: Monitoring and service life modeling", *Proc of CERI 2014*, Belfast, 289- 294.
[137] Byrne A and Nolan E, (2016), "Preliminary investigation into the rate of carbonation of concrete blocks under normal production yard conditions", *Proc of CERI 2016*, Galway, 165- 170.
[138] O'Donovan R, O'Rourke B, Ruane K and Murphy JJ, (2014), "A study of chlorides in a reinforced concrete bridge", *Proc of CERI 2014*, Belfast, 463-468.
[139] Reale T and O'Connor A, (2012), "Future state prediction of reinforced-concrete bridges allowing for chloride-induced deterioration", *Proc of B&CRI 2012*, Dublin, 85- 90.
[140] Evans C and Richardson M, (2005), "Service life of chloride-contaminated reinforced concrete structures", *Proc of CRI 2005*, Dublin, 131-137.
[141] Evans C, Callanan T and Richardson M, (2003), "Service life prediction of concrete exposed to chlorides: a report on work in progress", *Proc of CRI 2003*, Belfast, 187-194.
[142] O'Connor A and Kenshel O, (2008), "Safety assessment of deteriorating concrete structures in marine environments", *Proc of CRI 2008 & B&IRI 2008*, Galway, 313- 320.
[143] McPolinD, Basheer M, Long A, Grattan K and Sun T, (2003), "Obtaining progressive chloride profiles in cementitious materials", *Proc of CRI 2003*, Belfast, 167- 176.
[144] Attari A, McNally C and Richardson M, (2012), "Evaluation of chloride ingress parameters in concrete using Backscattered Electron (BSE) imaging to assess degree of hydration - a proposal", *Proc of B&CRI 2012*, Dublin, 211-215.
[145] Wang J, Basheer M, Nanukuttan S and Bai Y, (2014), "Influence of compressive loading on chloride- ingress through concrete", *Proc of CERI 2014*, Belfast, 475-480.
[146] Callanan T and Richardson M, (2001), "Chloride ingress in concrete: an experimental study of the use of a mathematical model based solely on diffusion coefficients", *Proc of CRI 2001*, Galway, 117- 124.
[147] Bond S, O'Callaghan L, Holmes N and Norton B, (2016), "Using photovoltaics to power electrochemical chloride extraction from concrete", *Proc of CERI 2016*, Galway, 359- 364.
[148] Bond S, Holmes N and Norton B, (2018), "Influence of concrete resistance on electrochemical chloride extraction", *Proc of CERI & ITRN 2018*, Dublin, 178- 183.
[149] Holmes N, Basheer M, Nanukuttan S and Basheer L, (2010), "Development of a new marine exposure site on the Atlantic North-West coast of Ireland", *Proc of CRI 2010 & B&IRI 2010*, Cork, 627 - 636.
[150] Cannon E and Waters R, (2001), "Aspects of the durability of a 65-year old reinforced concrete bridge in an estuarine environment", *Proc of CRI 2001*, Galway, 125 - 132.
[151] O'Donovan R, O'Rourke B, Ruane K and Murphy JJ, (2012), "Reinforced concrete deterioration of a 100 year old structure in a marine environment", *Proc of B&CRI 2012*, Dublin, 217 - 222.
[152] McPolin D, Basheer M, Long A, Grattan K, Sun T and Xie W, (2005), "Fiber optic sensors for monitoring temperature, chloride ingress and carbonation in cementitious materials", *Proc of CRI 2005*, Dublin, 93 - 100.
[153] Backus J, McPolin D, Basheer M and Long A, (2012), "The interaction of multiple mode deterioration by chloride and carbon dioxide in mortars exposed to cyclic wetting and drying", *Proc of B&CRI 2012*, Dublin, 229 - 234.
[154] Backus J, McPolin D, Holmes N and Long A, (2014), "Combined chloride and carbon dioxide ingression in concrete exposed to cyclic wetting and drying", *Proc of CERI 2014*, Belfast, 457 - 462.
[155] Zheng Y, Nanukuttan S and McPolin D, (2018), "A review into the performance of steel reinforced concrete exposed to both carbon dioxide and chloride environments", *Proc of CERI & ITRN 2018*, Dublin, 184 - 189.
[156] Nanukuttan S, (2020), "Effect of carbonation unbound chlorides in different cementitious systems", *Proc of CERI & ITRN 2020*, Cork, 702 - 707.
[157] Richardson M, (1997), "Early experience with ultra- accelerated testing for alkali- aggregate reactivity", *Proc of CRI 1997*, Dublin, 83 - 90.
[158] McNally C and Richardson M, (2001), "Alkali aggregate reaction in Irish concrete: An exploration of the potential existence of a critical alkali threshold", *Proc of CRI 2001*, Galway, 139 - 146.
[159] Hester D, McNally C and Richardson M, (2003), "A study of the influence of slag alkali level on the alkali- silica reactivity of slag concrete", *Proc of CRI 2003*, Belfast, 81 - 88.
[160] Richardson M, (2003), "Developments in minimizing the risk of deleterious alkali- silica reaction", *Proc of CRI 2003*, Belfast, 69 - 80.
[161] Nanukuttan S and McIntosh A, (2018), "Concrete for chloride and acid/biogenic environments: specification, binders, challenges and opportunities", *Proc of CERI & ITRN 2018*, Dublin, 103 - 110.
[162] Montgomery F, (1997), "Observations of fire damage effects on concrete surfaces", *Proc of CRI 1997*, Dublin, 99 - 106.
[163] Cromie J, Abu-Tair A and Lyness J, (1997), "The electrochemical repair of concrete", *Proc of CRI 1997*, Dublin, 55 - 64.
[164] Goggins J and Broderick B, (2003), "The determination of a suitable mortar mix design to fill slender steel hollow sections", *Proc of CRI 2003*, Belfast, 107 - 116.
[165] Pavia S, Fitzgerald B and Tracy E, (2005), "An assessment of lime mortars from masonry repair", *Proc of CRI 2005*, Dublin, 101 - 108.
[166] Pavia S, (2008), "A petrographic study of the technology of hydraulic mortars at masonry bridges, harbours and millponds", *Proc of CRI 2008 & B&IRI 2008*, Galway, 253 - 264.
[167] Patterson R and Pavia S, (2012), "Influence of loading rate and specimen geometry on lime mortar strength", *Proc of B&CRI 2012*, Dublin, 361- 366.
[168] Orr D, (2001), "Characteristics of solid concrete block masonry", *Proc of CRI 2001*, Galway, 93 - 98.
[169] Long, A(2012), "Problems: inspiration for innovative solutions - lessons from over 40 years of reinforced concrete research", *Proc of B&CRI 2012*, Dublin, 3 - 12.
[170] Naughton D, Naughton M, O'Sullivan M and Salawdeh S, (2020), "Analysis and design of a novel heavy-duty precast element", *Proc of CERI & ITRN 2020*, Cork, 119 - 124.
[171] Tchrakian T, O'Dwyer D and West R, (2005), "Investigation of the structural behavior of reinforced concrete slabs on grade", *Proc of CRI 2005*, Dublin, 1 - 8.

[172] O'Dwyer D, West R and Tchrakian T, (2008), "Load capacity of slabs on grade under the action of line loading", *Proc of CRI 2008 & B&IRI 2008*, Galway, 371 - 380.
[173] Shaat A, Taylor S, Cleland D and Rankin G, (2003), "Compressive membrane action in reinforced concrete building and bridge deck slabs", *Proc of CRI 2003*, Belfast, 53 - 58.
[174] Zhang Y, Robinson D, Taylor S and Cleland D, (2005), "Non- linear finite element analysis of compressive membrane action in concrete slabs", *Proc of CRI 2005*, Dublin, 9 - 18.
[175] Cleland D, Gilbert S and Murray K, (1997), "Deep behavior of edge panels in reinforced concrete flat slab structures", *Proc of CRI 1997*, Dublin, 49 - 54.
[176] Hodge D, O'Rourke B and Murphy JJ, (2010), "Finite element modeling of transverse load sharing between hollow core floor slabs", *Proc of CRI 2010 & B&IRI 2010*, Cork, 61 - 72.
[177] Twomey C, O'Rourke B and Hodge D, (2014), "Shear behavior of precast prestressed hollowcore slabs", *Proc of CERI 2014*, Belfast, 373 - 378.
[178] Goggins, J, Newell S, King D and Hajdukiewicz, M, (2014), "Real-time monitoring of a hybrid pre-cast and insitu concrete flat slab system, *Proc of CERI 2014*, Belfast, 321 - 326.
[179] Newell S, Goggins J, Hajdukiewicz M and Holleran D, (2016), "Behavior of hybrid concrete lattice girder flat slab system using in situ structural health monitoring", *Proc of CERI 2016*, Galway, 623 - 630.
[180] Murray K, Clelland D and Gilbert S, (2001), "Flat slabs; a comparison of experimental behavior with equivalent frame analysis", *Proc of CRI 2001*, Galway, 79 - 88.
[181] Newell S, O'Kelly-Lynch G and Goggins J, (2018), "Laboratory testing of the structural behavior of precast concrete lattice girder slabs at construction stage", *Proc of CERI & ITRN 2018*, Dublin, 590 - 595.
[182] Murray K, Cleland D and Gilbert S, (2003 , "The development of a non-linear numerical model to simulate the behavior of reinforced concrete flat slabs in the vicinity of edge columns", *Proc of CRI 2003*, Belfast, 15 - 26.
[183] Barrias A, Casas J and Villalba S, (2018), "Fatigue testing of reinforced concrete beams instrumented with distributed optical fiber sensors (DOFS), *Proc of CERI & ITRN 2018*, Dublin, 729 - 734.
[184] Shinnick D, Walsh D and Ruane K, (2014), "An investigation into the capabilities of design codes to determine the load capacities of RC deep beams", 391 - 396.
[185] Sweeney G and Salawdeh S, (2020), "Design of reinforced concrete beams with web openings", *Proc of CERI & ITRN 2020*, Cork, 223 - 228.
[186] Slevin M, and O'Connor A, (2016), "Interface shear behavior of precast prestressed concrete beams with slender webs in beam and slab bridge construction", *Proc of CERI 2016*, Galway, 617 - 622.
[187] Causer E and Ruane K, (2014), "The behavior of connections in segmental precast concrete pile systems", *Proc of CERI 2014*, Belfast, 379 - 384.
[188] Minahane M and O'Rourke B, (2012), "An investigation into shear reinforcement in reinforced concrete corbels", *Proc of B&CRI 2012*, Dublin, 481 - 486.
[189] Quinn S and Ruane K, (2020), "Finite element appraisal of the strut and tie method for the design of reinforced concrete structures", *Proc of CERI & ITRN 2020*, Cork, 234 - 239.
[190] Fayyad T and Abdelqader A, (2020), "Demountable reinforced concrete structures: A review and future directions", *Proc of CERI & ITRN 2020*, Cork, 218 - 222.
[191] O'Dwyer D, (1997), "Modular construction using ferrocement panels", *Proc of CRI 1997*, Dublin, 25 -34.
[192] Kinnane O, West R, Grimes M and Grimes J, (2014), "Shear capacity of insulated precast concrete facade panels", *Proc of CERI 2014*, Belfast, 385 - 390.
[193] O'Hegarty R, Kinnane O and West R, (2018), "Finite element analysis of thin precast concrete sandwich panels", *Proc of CERI & ITRN 2018*, Dublin, 146 - 151.
[194] Lipczynska J, West R, Grimes M, Niall D, Kinnane O and Hegarty R, (2020), "Composite behaviour of wide sandwich panels with high performance concrete thin wythes with and without Thermomass shear connectors", *Proc of CERI & ITRN 2020*, Cork, 125 - 130.
[195] Niall D, West R, Kinnane O and O'Hegarty R, (2020), "Modeling the thermal behavior of a precast PCM enhanced concrete cladding panel", *Proc of CERI & ITRN 2020*, Cork, 143 - 149.
[196] Niall D, Kinnane O and West R, (2018), "Design and manufacture of a precast PCM enhanced concrete cladding panel for full scale performance monitoring", *Proc of CERI & ITRN 2018*, Dublin, 140 - 145.
[197] Gupta A, Taylor S, Kirkpatrick J, Long A and Hogg I, (2005), "A flexible concrete arch system", *Proc of CRI 2005*, Dublin, 33 - 40.
[198] Quinn D, Gupta A, McPolin D, Taylor S and Long A, (2010), "Development of double radius Flexiarch", *Proc of CRI 2010 & B&IRI 2010*, Cork, 583 - 592.
[199] McNulty P, Taylor S, Robinson D and Long A, (2012), "Development of a 150º skew Flexiarch™ bridge", *Proc of B&CRI 2012*, Dublin, 97 - 102.
[200] Long A, McPolin G, Nanukuttan S and Gupta A, (2018), "FlexiArch: Revolutionises arch construction", *Proc of CERI & ITRN 2018*, Dublin, 93 - 96.
[201] McPolin G, Long A, Gupta A and Cook John, (2018), "FlexiArch: Concept to case histories", *Proc of CERI & ITRN 2018*, Dublin, 97 - 101.
[202] Anthony P, (2010), "Concrete in the built environment, past, present and future), *Proc of CRI 2010 & B&IRI 2010*, Cork, 383 - 396.
[203] McCarter W, (2016), "Concrete: Performance monitoring for sustainable concrete infrastructure", *Proc of CERI 2016*, Galway, 15 - 20.
[204] Jani R, Holmes, N, West, R, Gaughan, K, Liu, X, Orisakwe E, Johnston C, Qu, M, Stella, L, Kohanoff J and Yin, H, (2020), "Characterisation and performance of cement-based thermo-electric materials", *Proc of CERI & ITRN 2020*, Cork, 342 - 347.
[205] Fogarty A and Richardson M, (2020), "Durability and sustainability of pavement quality concrete in airfields", *Proc of CERI & ITRN 2020*, Cork, 150 - 155.
[206] Hajdukiewicz J and Goggins J, (2014), "The influence of heat transfer and storage in structural precast building components on indoor environments", *Proc of CERI 2014*, Belfast,161- 166.
[207] McCaffrey M, Goggins J and Baylor G, (2010), "The use of embodied energy and carbon as indicators of the environmental impact of reinforced concrete structures in Ireland", *Proc of CRI 2010 & B&IRI 2010*, Cork, 653 - 662.
[208] Goggins J, McGovern P, McHugh K and Finnegan W, (2016), "Reducing the environmental impact of concrete products, while at the same time saving money", *Proc of CERI 2016*, Galway, 289 - 292.
[209] Natanzi A and McNally C, (2018), "Ecostructure: concrete design for improved marine biodiversity", *Proc of CERI & ITRN 2018*, Dublin, *Proc of CERI & ITRN 2018*, Dublin, 208 - 211.
[210] Deegan P and O'Connor A, (2010), "Colour variation in finished concrete", *Proc of CRI 2010 & B&IRI 2010*, Cork, 521 - 530.
[211] Deegan P, O'Connor A and Archbold P, (2012), "Measurement of time-dependent color variation in concrete" *Proc of B&CRI 2012*, Dublin, 247 - 252.
[212] Sweeney A, West R and Seymour P, (2012), "Factors affecting the measurement of solar reflectance using an albedometer", *Proc of B&CRI 2012*, Dublin, 241 - 246.
[213] Sweeney A and West R, (2010), "Parameters affecting the albedo effect in concrete", *Proc of CRI 2010 & B&IRI 2010*, Cork, 513 - 520.
[214] Green C, Nanukuttan S and Basheer M, (2014), "A new performance based method for design and maintenance of reinforced concrete structures", *Proc of CERI 2014*, Belfast, 295 - 300.
[215] Nanukuttan S, Holmes N, Srinivasan S, Basheer L, Basheer M, Tang L and McCarter J, (2010), "Methodology for designing structures to withstand extreme environments: performance-based specifications", *Proc of CRI 2010 & B&IRI 2010*, Cork, 663 - 670.
[216] Salawdah S and Ahmad N, (2020), "Performance based design approach for reinforced concrete precast structures", 240 - 246.
[217] Cannon E, (2008), "R.C. column design: a comparison of BS8110 and EN1992 (Eurocode 2)", *Proc of CRI 2008 & B&IRI 2008*, Galway, 351 - 362.
[218] Cannon E, (2008), "Design for flexure: some comparisons between BS8110 and EN1992 (Eurocode 2) requirements", *Proc of CRI 2008 & B&IRI 2008*, Galway, 339 - 350.
[219] West R and Deasy A, (2003), "Sensitivity analysis of beam design to changes in the nationally determined parameters in Eurocode 2", *Proc of CRI 2003*, Belfast, 177 - 186.
[220] Mootoosamy S and O'Donoghue T, (1997), "Comparison of standards in concrete beam design", *Proc of CRI 1997*, Dublin, 65 - 74.
[221] Cannon E, (2005), "An explicit approach to reinforced concrete column design", *Proc of CRI 2005*, Dublin, 19 - 32.
[222] West R and Hore A, (2005), "Benefits of deploying IT in the materials procurement of ready mixed concrete in the Irish construction industry", *Proc of CRI 2005*, Dublin, 71 - 80.
[223] Cannon E and Coyle, B, (1997), "Structural design in concrete: Spreadsheet applications", *Proc of CRI 1997*, Dublin, 141 - 148.
[224] Cannon E and McHugh G, (1997), "Reinforced concrete design and detailing: AutoLISP applications", *Proc of CRI 1997*, Dublin, 133 - 140.
[225] Donoghue B and Orr D, (2001), "Application of computers in prestressed concrete design", *Proc of CRI 2001*, Galway, 109 - 116.

[226] Magee B, M, Nanukuttan S, Hao T and Wu Z, (2014), "A research-based approach to exploring the adoption of novel UK-based concrete test methods in Chinese construction sector", *Proc of CERI 2014*, Belfast, 487 - 492.
[227] Sourav S, Al- Sabah S and McNally C, (2018), "Statistical reliability of the screw pullout test in the assessment of in-situ concrete strength", *Proc of CERI & ITRN 2018*, Dublin, 753 - 758.
[228] Cannon E and O'Byrne C, (2003), "In- situ instrumentation of concrete structures: a case study", *Proc of CRI 2003*, Belfast, 147 - 156.
[229] Sourav S, Al- Sabah S and McNally C, (2016), "Strength assessment of in- situ concrete for the evaluation of structural capacity: state of the art", *Proc of CERI 2016*, Galway, 599 - 604.
[230] Cannon E ,McDonagh A and Burke J, (2010), "Use of 3D modelling and animation in the teaching of concrete structural design", *Proc of CRI 2010 & B&IRI 2010*, Cork, 83 - 92.
[231] Cannon E, (1997), "Concrete reinforcement detailing: Self tutoring using Hypertext", *Proc of CRI 1997*, Dublin, 125 - 132.
[232] Cannon E and Conneely M, (2001), "Development of a computer-aided learning application for reinforced concrete detailing", *Proc of CRI 2001*, Galway, 99 - 108.
[233] Al- Sabah S, Chipperfield J and Falter H, (2018), "A strut-and-tie approach in detailing RC structures", *Proc of CERI & ITRN 2018*, Dublin, 584 - 589.
[234] West R, Taylor D, Burke, M, Grimes M and Hunt S, (2020), "Teaching engineering materials through experiential learning", *Proc of CERI & ITRN 2020*, Cork, 412 - 417.
[235] Gaur G, Shiel P and West R, (2018), "Coping with statistics in concrete technology", *Proc of CERI & ITRN 2018*, Dublin, 690 - 695.

Investigation on fire retardant Concrete with Post Fire Self-Healing features

Ajitanshu Vedrtnam[1,2], William Finnegan[2], Jamie Goggins[2]
[1]Department of Mechanical Engineering, Invertis University, Bareilly, UP, India-243001.
[2]MaREI Research Centre & Ryan Institute, School of Engineering, National University of Ireland Galway, Galway, Ireland
Email: ajitanshu.m@invertis.org

ABSTRACT:

Fire is a notable risk to civil infrastructures and human life. Therefore, civil engineers crave sustainable, safer substitutes of concrete that fulfill fire safety needs without compromising design intent. The present work reports processed-plastic (PET) bottle residuals reinforced cement-based composites (CBCs) having superior post-fire residual compressive performance compared to concrete. The PET bottles are processed using closed container heating and residual condensation (COH-RC) process. The Scanning Electron Microscopy micrographs assisted in identifying possible reasons for the improved post-fire residual compressive performance of CBCs.
It is well-established that fire exposure deteriorates, and selected bacteria can self-heal the cracks in concrete. The concrete rehydration allows recovery of pore structures to some extent but with minor improvement in the mechanical performance. The present work explores the possibility of post-fire self-healing of the concrete for the first time in literature. A novel encapsulation strategy is proposed to protect bacteria incorporated into the concrete samples during fire and later facilitate bacteria activation for self-healing. The pre-and post-fire residual compressive strength of samples is evaluated using the standard method. The article reports concrete deterioration with fire duration and intensity, along with recovery in compressive strength due to self-healing after 28 days in ambient conditions. This article offers a new research direction for fire protection of concrete structures.

KEY WORDS: Bacteria; Concrete; Fire; PET; Self-healing; Waste.

1 INTRODUCTION

The requirement for fire-safe structural materials is evident due to consistent unfortunate fire disasters [1]. Concrete structures are safer than other construction materials such as wood, glasses, composites and steel [2-6]. However, fire exposure deteriorates the concrete properties [7, 8]. The concrete performance in fire is widely studied as the occupant and structural safety depends on concrete behaviour in fire [9-12]. The concrete deteriorates due to cement paste interface and aggregate debonding, aggregate deformation, thermal incompatibility of constituents, cement paste chemical transformation, CSH gel disruption, and internal pressure due to entrapped steam [13]. The performance deterioration of concrete depends on the concrete grade. The lower concrete grade deteriorates lesser in comparison to higher concrete grades [14]. The heating rate and duration also determine concrete performance [15]. Fire-resistant concrete is commercially available these days. The post-fire curing is successful to some extent in improving mechanical behaviour. Besides, active fire control methods such as sprinklers also combat fire in buildings.

Plastic production is peaking all the time and solid plastic waste poising a challenge for the research community. For achieving circular economy and sustainability, it is essential to develop effective methods for converting waste plastics into useful products, as presently, more than 90% of solid plastic waste is either landfilled or incinerated. The efficient utilization of waste plastic in construction products is rewarding but challenging due to compatibility issues. In the present work, the closed container heating and residual condensation method [16] is utilized for producing the waste Polyethylene terephthalate (PET) residual. The PET residual was utilized as reinforcement to produce cement-based composites (CBC) with the aim of achieving fire retardancy.

The application of self-healing concrete is growing commercially. The healing agents that consist of dormant bacterial spores are commercially available. The water penetrates in cracks of the concrete structure, and the dormant bacteria are activated. The bacterial activity results in Calcium Carbonate formation, which self-heals the concrete up to specific dimensions [17]. Since post-fire self-healing is yet not tried in the cited literature, the use of bacteria for post-fire healing is considered the objective of the present work. It is to be noted that protecting bacteria during the fire and further controlled activation of bacteria for self-healing is challenging. A novel encapsulation method is attempted in the present work to achieve this in CBC with bacteria. The present work reports fire-resistant construction products with post-fire self-healing features. These construction products will be a promising alternative with superior safety features to the existing concrete.

2 MATERIAL AND METHODS

The cubical samples of reference concrete, CBC-PET (10% PET by volume) and CBC-PET samples having 10% (by volume) proportions of bacteria + calcium lactate + encapsulation were prepared for fire and compression testing by casting them in wooden moulds (150 mm^3) with the assistance of a vibrator. The samples were removed from the

wooden moulds after 24 hours and cured in water for up to 28 days at 26-32 ºC (ambient conditions). The standard ASTM test procedures are used to evaluate concrete's physical properties.

The cement, sand, aggregate (>19 mm) and water were 345 Kg/m^3, 881 Kg/m^3, 1081 Kg/m^3, and 228 Kg/m^{3,} respectively in the concrete samples. The water to cement ratio was 0.6. The cement, natural sand and aggregate conform to ASTM C150 and ASTM C33-16. The specific gravity and loose density (Kg/m^3) of natural sand and aggregate were 2.39 and 2.61, 2002.4 and 1818.1, respectively. The CBC samples included PET plastic bottle residual to replace the natural sand in 10% by volume. The particle size of the PET residuals was less than 1.18 mm as measured by the sieve analysis.

The PET residual was produced using Constraint Oxygen Heating and Residual Condensation (COH-RC) method. Fig. 1 shows a schematic diagram and plastic recycling products using the COH-RC method. The COH-RC method includes heating plastics at different temperatures into a closed container with air but no air supply during the process and directing the exhaust gases into another chamber filled with water that allows the condensing of exhaust gasses. The temperature range was 500º C to 600º C for 30 minutes. The porous plastic residual includes carbon-rich content that is not converted into exhaust gases during constraint oxygen heating. The porous plastic residual was left in the container where the plastic was heated. The gases are condensed into another closed container filled with water. This condensation process results in three separate layers inside the container of grease, oil and water. The porous plastic residual from PET is shown in Fig. 2. The residual oil and grease are used for biodiesel/foam production and as a lubricant, respectively. However, they are yet not characterized fully to identify their further applications. The residual oil was having flammability and may have many other possible applications. Intensive experimentation is required to achieve the stated objectives in the next section.

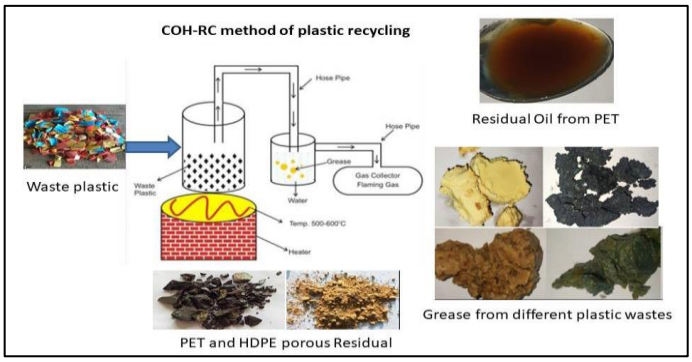

Fig. 1. Schematic diagram of COH-RC method and photograph of residual products.

The PET residual was converted into the powder before using as reinforcement in CBCs.

Figure 2. PET bottle residual.

All the samples were heated for 1 hour in fire (Figure 3 a-c) and also in a furnace following ISO 834 for comparison. Figure 3(d) shows the thermal loading scheme. Figure 4 shows a comparison of time-temperature variation in the furnace and recommended in ISO834.

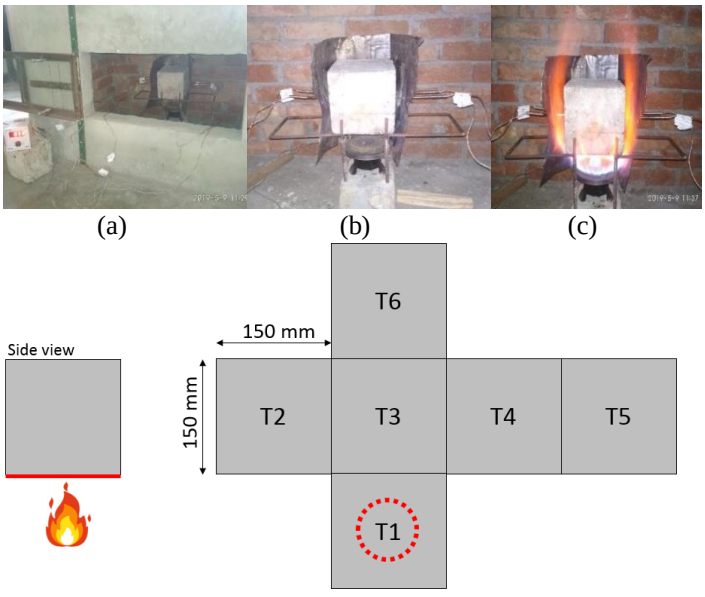

Figure 3. Selected photographs of fire testing for the CBC specimens: (a) furnace view; (b) setup and (c) heating stage, with (d) thermal loading scheme [17].

The surface temperature of the samples was measured using infrared and K-type thermocouples. The non-uniform surface temperature was post-processed to determine the average temperature at the mid of each sample face. In Figure 3(d)):

- T1, average temperature at the bottom (exposed) face;
- T2, T3, T4, T5, four-side cube faces temperatures;
- T6, denoting the top face temperature.

The standard compression testing machine (loading rate = 3 kN/min) was used to determine the residual compressive strength of samples. In addition, the SEM micrographs of the fractured samples were used to establish the structure-property relationship.

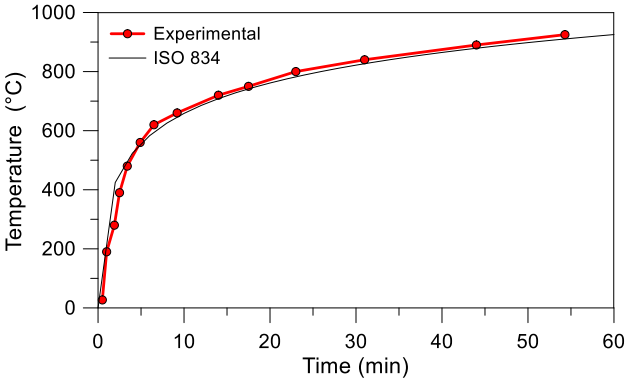

Figure 4. Time-temperature in experiment vs standard ISO 834 fire curve [17].

The CBC-PET samples with gelatine capsules for encapsulating the bacteria as a replacement for the natural sand and coarse aggregates based on filler sizes were Cast. The 400 mg, '#1' size of gelatine capsules immobilized bacteria. The gelatine capsules were filled with 70% bacteria and 30% calcium lactate mixture in the first encapsulation method. These capsules were coated with cement paste as shown in Fig. 5, before their incorporation into the concrete samples.

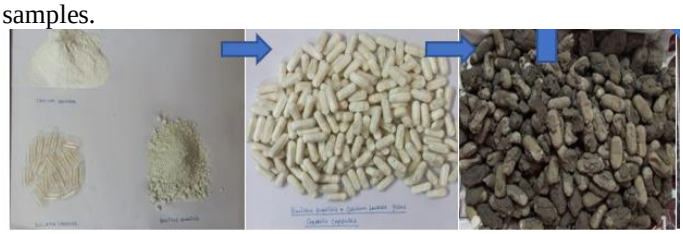

Fig. 5 Cement paste-coated gelatine capsules encapsulating bacteria.

3 RESULTS AND DISCUSSION

The average natural, submerged, and saturated weights of concrete, CBC-PET and CBC-PET with bacteria encapsulation were 2230, 1278, 2276 g, 2180, 1270, 2210 g and 2076, 1242, 2164 g. Figure 6 shows the average time-temperature variation of all faces of the samples when subjected to fire exposure for an hour.

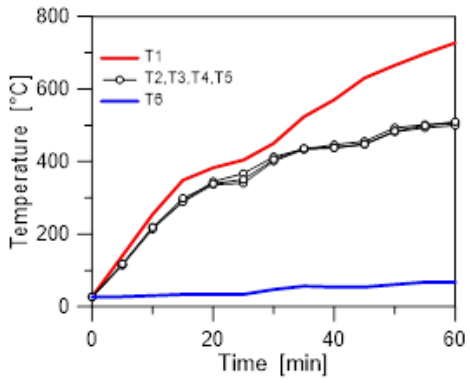

Figure 6. Average Time-temperature variation at all edges of samples subjected to fire.

Fig. 7 shows two infrared thermometer images of the samples during fire exposure. Along with K-type thermocouples, infrared thermocouple images were also used for observing the temperature across the dimensions of the samples.

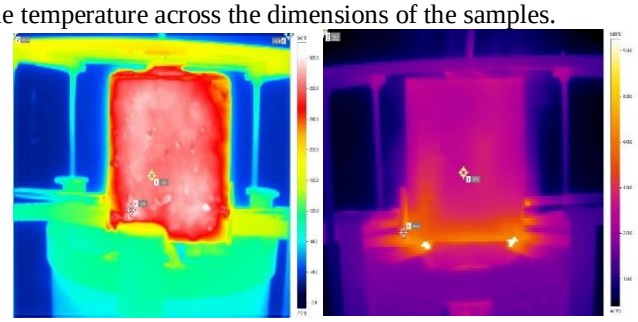

Figure 7. Infrared thermometer Images during Fire exposure.

Fig. 8 shows the images of the sample after fire exposure. It is evident from the images that the bottom face of the samples was severely deteriorated due to fire exposure.

Figure 8. Sample Images post-fire exposure.

Table 1 Compressive strength of Samples pre-, post-fire exposure and post-self-healing

	Average Compressive strength (MPa)		
	Concrete	CBC	
		PET	PET-bacteria
Temperature (°C) / Proportion (%)	-	10	10
27 (ambient)	19.21	18.6	18.4
1h heating in furnace	6.11	7.9	7.4
1h heating in fire	5.77	7.1	6.9
28 days post fire (furnace samples)	6.12	7.96	8.78
28 days post fire (fire exposed samples)	5.81	7.21	8.96

Table 1 shows the average compressive strength of the samples (minimum three of each type) pre- and post-fire exposure and also after keeping samples for post-fire self-healing for 28 days in ambient conditions. Concrete samples had the highest compressive strength, followed by CBC-PET and CBC-PET with bacteria encapsulated samples. The post-fire average residual compressive

strength was the maximum in CBC-PET samples, followed by CBC-PET samples with encapsulated bacteria. For both furnace heating and fire exposure, the concrete samples were degraded most. The possible reason for the better post-fire performance of CBC samples with PET residual could be the limited deterioration due to the presence of carbon-rich burnt porous residual that allowed passage of entrapped steam and observed limited deterioration during the fire. The samples were kept in ambient conditions for 28 days post-fire exposure. The most significant recovery is observed in the samples with bacteria. The post-fire recovery in CC-PET bacteria samples was greater in fire-exposed samples than in furnace-heated samples. The possible reason for the survival of encapsulated bacteria could be the protection of the cement coating on gelatine capsules. During the fire, cement paste might have lost water which causes cracks in the coating. The gelatine might have melted during the fire. Later, the cracks in cement coating might have allowed penetration of moisture and activation of bacteria for self-healing. However, additional investigation is required to confirm the same. Further, the weights of samples post-fire and post-fire recovery were measured. Up to 2% weight gain is observed in CBC-PET with bacteria self-healed samples in comparison to weights just after fire exposure. An insignificant change in weights post-fire and after keeping the samples for 28-days for recovery was observed in concrete and CBC-PET samples. The increase in weight of self-healed CBC-PET with bacteria samples gives an indication of bacteria activation and formation of calcium carbonate in these samples that accounts for better residual compressive strength.

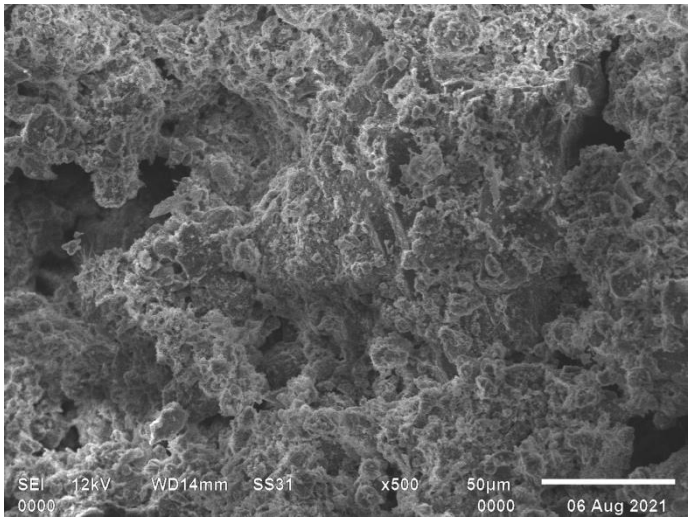

(a)

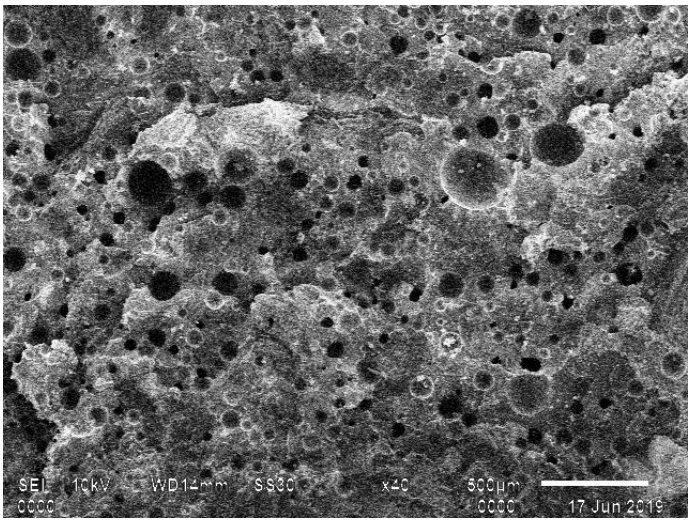

(b)

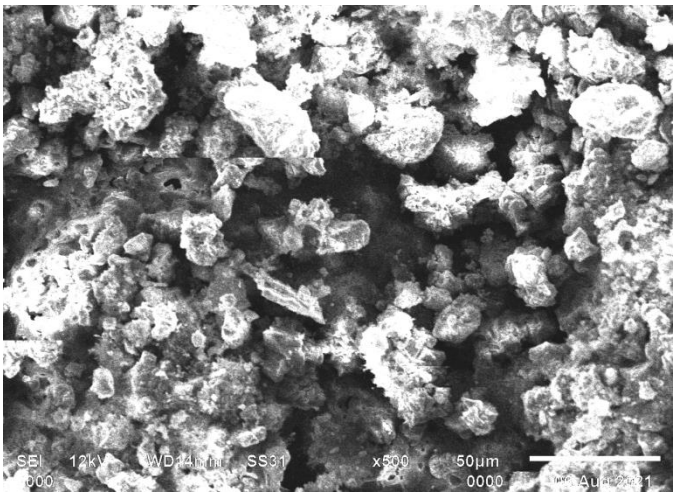

(c)

Figure 9. SEM Images (a) Concrete (b) CBC-PET (c) CBC-PET with encapsulated bacteria.

Fig. 9 shows the SEM images of concrete, CBC-PET and CBC-PET with encapsulated bacteria samples. The SEM image of the CBC-PET sample shows porous phases in comparison to the concrete sample SEM image. This supports the logic that entrapped steam during fire might escape from the CBC-PET samples, resulting in lesser undue internal stresses and lesser degradation of these samples. Fig. 9 (c) shows the presence of coated gelatine capsules. The irregular surface texture is further exaggerated due to the cement paste coating on the gelatine capsule in CBC-PET bacteria encapsulated samples. The post-fire recovery achieved in the current investigation encourages a detailed investigation. A further detailed study is needed to establish the mechanism of post-fire self-healing of encapsulated CBC-PET samples.

4 CONCLUSIONS

The present work reports utilizing PET residual produced by the COH-RC method for producing fire retardant cement-based composites and the possibility of post-fire self-

healing by innovative encapsulation strategies. The performance of concrete, CBC-PET and CBC-PET with encapsulated bacteria were reported during ISO 834 furnace heating and non-uniform direct fire exposure for one h. Following are the main conclusions,

- Concrete samples have the highest compressive strength, followed by CBC-PET samples and CBC-PET with bacteria encapsulated samples.
- CBC-PET residual have the highest residual compressive strength, followed by CBC-PET with encapsulated bacteria and concrete samples.
- The concrete and CBC-PET samples have shown more surface cracks in non-uniform fire exposure compared to furnace heating for the same fire duration.
- CBC-PET samples with encapsulated bacteria gained up to 2% of weight 28 days after curing in ambient conditions from the post-fire weight.
- The CBC-PET samples with encapsulated bacteria regained 7.76% compressive strength in furnace-heated samples and 7.96% in fire-exposed samples.
- The SEM micrographs have shown pours in the microstructure of CBC- PET sample, which has resulted in lesser compressive strength but superior residual compressive strength in CBC-PET samples while compared to concrete samples.

ACKNOWLEDGMENTS

This work is supported by Department of Science and Technology (DST/TDT/WMT/Plastic waste/2021/05) and SFI Ireland.

REFERENCES

[1]. https://www.nfpa.org/News-and-Research/Data-research-and-tools/US-Fire-Problem/Catastrophic-multiple-death-fires/Deadliest-fires-or-explosions-in-the-world

[2]. A Vedrtnam, C Bedon, MA Youssef, M Wamiq, A Sabsabi, S Chaturvedi (2020). Experimental and Numerical Structural Assessment of Transparent and Tinted Glass during Fire Exposure. Construction and Building Materials, Volume 250, 118918, doi: 10.1016/j.conbuildmat.2020.118918

[3]. Wang Y, Wang Q, Wen JX, Sun J, Liew KM. Investigation of thermal breakage and heat transfer in single, insulated and laminated glazing under fire conditions. Appl Therm Eng 2017; 125: 662–72

[4]. Haunting Zhou, Shaoyuan Li, Lu Chen, Chao Zhang, and Fire tests on composite steel-concrete beams pre-stressed with external tendons, Journal of Constructional Steel Research 143 (2018) 62–71

[5]. M. Fan 1, A. Naught on, J. Bregulla, Fire performance of natural fiber Composites in construction, Construction and Building Materials 18 (2004) 505–515.

[6]. Yalinkilic MK, Baysal E, Demirci Z. Role of treatment chemicals in combustion of Douglas fir wood. In: Proceedings of the first Trabzon international energy and environment symposium, July 29–31, Karadeniz Technical University Trabzon, Turkey; 1996. p. 803–809.

[7]. Asif H. Shah, U.K. Sharma, Fire resistance and spalling performance of confined concrete columns, Construction and Building Materials 156 (2017) 161–174

[8]. R.H. Haddad , R.J. Al-Saleh, N.M. Al-Akhras, Effect of elevated temperature on bond between steel reinforcement and fiber reinforced concrete, Fire Safety Journal 43 (2008) 334–343

[9]. Abid M, Hou X, Zheng W, et al. (2017) High temperature and residual properties of reactive powder concrete– A review. Construction and Building Materials 147: 339–351.

[10]. Anand N and Godwin A (2016) Influence of mineral admixtures on mechanical properties of self-compacting concrete under elevated temperature. Fire and Materials 7(40): 940–958

[11]. Li M, Qian C and Sun W (2004) Mechanical properties of high-strength concrete after fire. Cement and Concrete Research 34: 1001–1005.

[12]. Ma Q, Guo R, Zhao Z, et al. (2015) Mechanical properties of concrete at high temperature—a review. Construction and Building Materials 93: 371–383.

[13]. Chu HY, Jiang JY, Sun W, et al. (2016) Mechanical and physicochemical properties of ferro-siliceous concrete subjected to elevated temperatures. Construction and Building Materials 122: 743–752.

[14]. Asif H. Shah, U.K. Sharma, Fire resistance and spalling performance of confined concrete columns, Construction and Building Materials 156 (2017) 161–174

[15]. Thanaraj, D. P., Anand, N., G, P. A., & Zalok, E. (2019). Post-fire damage assessment and capacity based modeling of concrete exposed to elevated temperature. International Journal of Damage Mechanics, 105678951988148. doi:10.1177/1056789519881484

[16]. https://www.nationalgeographic.com/news/2017/07/plastic-produced-recycling-waste-ocean-trash-debris-environment/ (Royal Statistical Society)

[17]. Vedrtnam, A., Bedon, C., Barluenga, G (2020). Study on the Compressive Behaviour of Sustainable Cement-Based Composites Under One-Hour of Direct Flame Exposure. Sustainability, 12(24):10548.

Assessment of Corrosion Damaged Reinforced Concrete Beams Subjected to Shear

David O'Callaghan[1], Kieran Ruane[2]
[1]RPS Consulting Engineers Ltd, Innishmore, Ballincollig, Cork, Ireland
[2]Department of Civil, Structural & Environmental Engineering, Munster Technological University, Bishopstown, Cork, Ireland
email: David.OCallaghan@rpsgroup.com, Kieran.Ruane@mtu.ie.

ABSTRACT: This paper presents a study of the shear behaviour of corrosion-damaged reinforced concrete beams. Shear failure in reinforced concrete members can be sudden and catastrophic in nature. The shear transfer mechanisms that contribute to the shear resistance of reinforced concrete beams were examined in this study with the consequent beam shear failure modes. The purpose of the study was to investigate these issues from the viewpoint of the structural assessor charged with the stewardship of existing structures. The study entailed a laboratory load testing programme of nine damaged beams in association with detailed non-linear finite element modelling of the beams. It was found that the non-linear finite element analyses and the theoretical approaches outlined in current structural assessment codes supported the results obtained from the laboratory testing. It is proposed that the combination of non-linear finite element analysis and modern structural assessment codes provides the optimum approach to the assessment of corrosion damaged reinforced concrete beams for shear resistance.

KEY WORDS: Corrosion damaged reinforced concrete beams, shear failure, non-linear finite element modelling, laboratory testing, structural assessment codes, shear resistance.

1 INTRODUCTION

Reinforced concrete beams must be capable of resisting shear forces originating from their own self weight and external applied loads. Considering the following simply supported concrete beam (see Figure 1) as the applied load is distributed across the span of the beam, the principal compressive stresses take the form of an arch, while the tensile stresses assume the curve of a catenary or suspended cable.

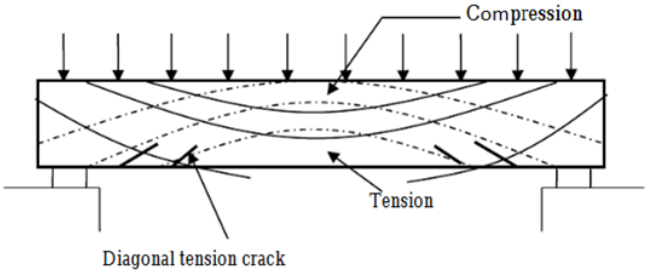

Figure 1 - Principal stresses in concrete beams [1]

Shear forces will typically be greatest near the supports whereas bending stresses tend to be predominant at mid-span. However, shear failure in RC members (more appropriately referred to as diagonal tension failure), is unexpected and catastrophic in nature. Hence, RC beams are designed to ensure that flexural failure occurs before shear failure if the given member is overloaded. This precludes a sudden and brittle failure (Figure 2).

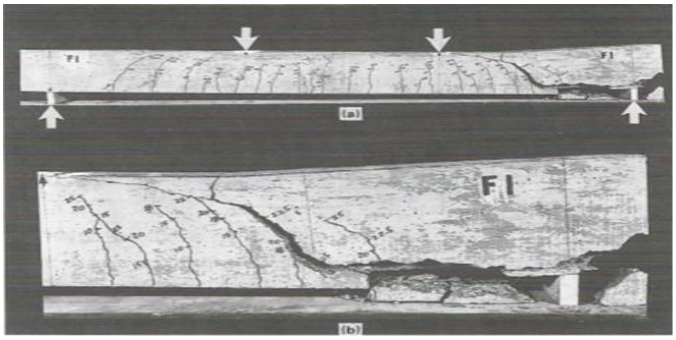

Figure 2 - Shear failure in a RC beam [2]

Previous research highlighted the fact that, due to the positioning of conventional shear reinforcement in RC beams, shear links have less cover than the main longitudinal reinforcement (Figure 3). Furthermore, as the diameter of the shear reinforcement is typically relatively small in comparison to the longitudinal reinforcement, the consequent loss of the cross-sectional area due to corrosion in the shear reinforcement is more significant than that in the longitudinal reinforcement.

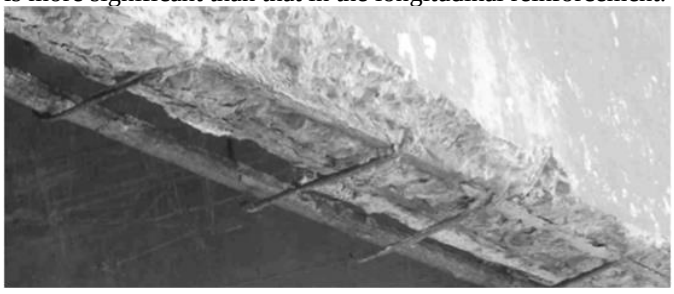

Figure 3 - Exposed shear reinforcement along the bottom of RC bridge beams [3]

It is clear that corrosion of embedded steel reinforcement is a leading factor in the deterioration of aging RC bridges. With this in mind, the inspection of chloride-induced corrosion damage of RC bridge beams focuses on the following four damage stages (see Figure 4).

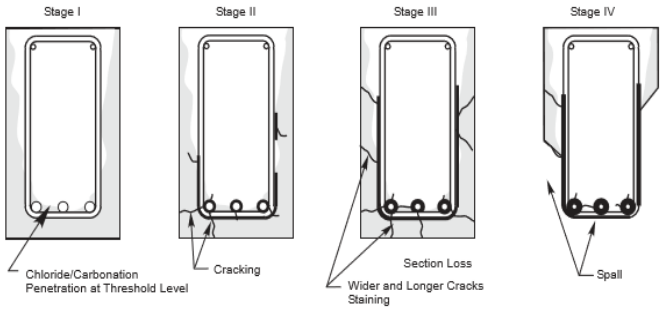

Figure 4 - Four stages of corrosion deterioration in RC bridge beams [3]

The aim of this paper is to present the results of a study of the residual shear capacity of damaged RC beams subjected to shear using modern structural assessment codes, extensive laboratory testing and non-linear finite element analysis.

2 DESIGN PROCEDURES

In total two design procedures IS EN 1992-1-1:2005 (EC2) [4] and AM-STR-06031 (BD 44) [5] along with several research papers were reviewed.

2.1 Analysis and Shear Design to EC2

2.1.1 Shear Resistance of Members Without Shear Reinforcement

The design shear resistance value for $V_{Rd,c}$ is given by Expression 6.2(a) as shown in Equation 1:

$$V_{Rd,c} = [C_{Rd,c}k(100\rho_l f_{ck})^{1/3} + k_1\,\sigma_{cp}]\,b_w d \quad (1)$$

2.1.2 Shear Resistance of Members with Shear Reinforcement

The design shear resistance value for $V_{Rd,c}$ is given by Expression 6.1 as shown in Equation 2:

$$V_{Rd} = V_{Rd,s} + V_{ccd} + V_{td} \quad (2)$$

2.1.3 Vertical Shear Design to EC2

For members with vertical shear reinforcement, the shear resistance, V_{Rd} is the smaller value of Expressions 6.8 and 6.9 as shown in Equation 3:

$$V_{Rd,s} = A_{sw}/s\; z\; f_{ywd}\cot\theta$$

And (3)

$$V_{Rd,max} = \alpha_{cw}b_w\, zv_1\, f_{cd}/(\cot\theta + \tan\theta)$$

2.2 For Structural Assessments to BD 44

Where effective vertical links are present the ultimate shear resistance V_u is given by Equation 8c as shown in Equation 4:

$$V_u = \xi_s v_c b_w d + (f_{yv}/\gamma_{ms})d/s_v A_{sv} \quad (4)$$

3 LABORATORY TESTING

3.1 Test Beam Design

A total of nine test beams were constructed. These consisted of one control beam in perfect condition and the remaining test beams contained progressively worse structural defects to simulate higher levels of corrosion (see Figure 5). The design parameters were selected to represent cross-sectional properties at a shear-critical section at a distance approximately the effective span over four from the support.

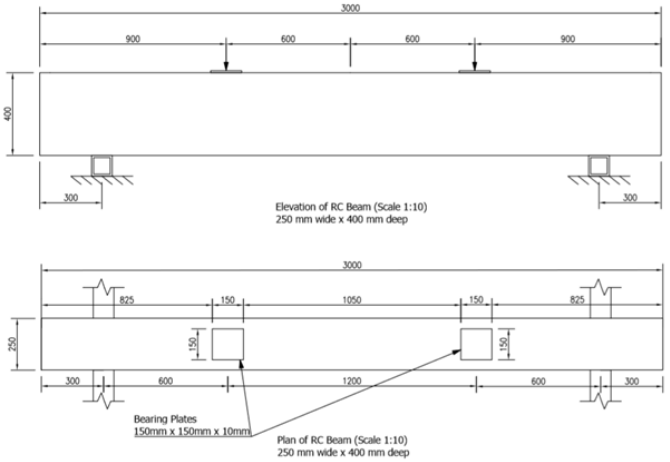

Figure 5 - Selected test beam configuration

The main factor influencing the chosen test beam dimensions was the maximum load capacity of the testing apparatus. The author anticipated that the ultimate shear capacity of the test beams would be in the order of at least 20-30% higher than the respective design figures determined by the design procedures. Hence, the steel reinforcement was arranged to ensure shear failure in the left-hand side of the beams only (see Figure 6). An overview of the reinforcement provided in each test beam is shown below in Table 1.

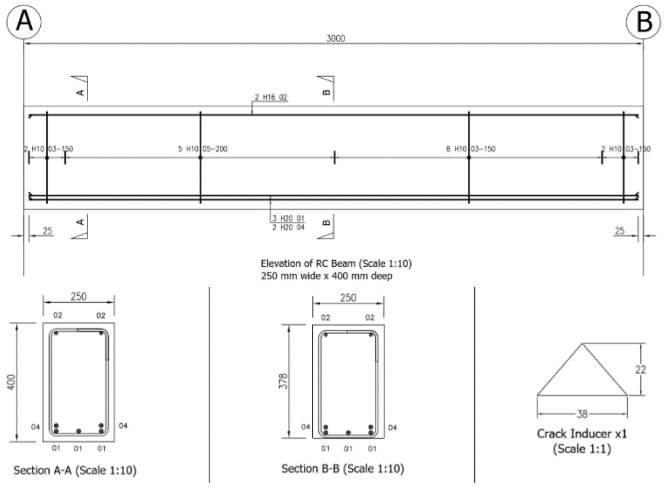

Figure 6 - Test beam steel reinforcement configuration

Test Specimen	Main tension reinforcement (mm^2)	Compression reinforcement (mm^2)	Shear reinforcement (mm^2/m)
Control Beam	1570.8 5 H 20	402.1 2 H 16	785.4 H10 @ 200 mm c/c
Test Beam T1	1570.8 5 H 20	402.1 2 H 16	628.3 H10 @ 250 mm c/c
Test Beam T2	1570.8 5 H 20	402.1 2 H 16	523.6 H10 @ 300 mm c/c
Test Beam T3	1570.8 5 H 20	402.1 2 H 16	502.7 H8 @ 200 mm c/c
Test Beam T4	1570.8 5 H 20	402.1 2 H 16	402.1 H8 @ 250 mm c/c
Test Beam T5	1570.8 5 H 20	402.1 2 H 16	335.1 H8 @ 300 mm c/c
Test Beam T6	1570.8 5 H 20	402.1 2 H 16	282.7 H6 @ 200 mm c/c
Test Beam T7	1570.8 5 H 20	402.1 2 H 16	226.2 H6 @ 250 mm c/c
Test Beam T8	1570.8 5 H 20	402.1 2 H 16	188.5 H6 @ 300 mm c/c

Table 1 - Summary of reinforcement provided in each test beam

A C35/45 concrete mix was used for the test beams and a total of thirty 100mm x 100mm concrete cubes were prepared on the day of the pour. A selection of concrete test cubes was subsequently tested to determine the average compressive strength of the concrete for each test beam after a set number of days and on the day of testing (Table 2).

Tested after No. Days	Average Compressive Strength (N/mm^2)			
	Specimen #1	Specimen #2	Specimen #3	Average
7 Days	41.37	38.06	40.33	**39.92**
14 Days	46.94	46.45	44.13	**45.84**
21 Days	46.36	49.32	50.78	**48.82**
22 Days (CB & T1)	49.44	50.70	51.40	**50.51**
23 Days (T2)	50.88	51.24	50.68	**50.93**
26 Days (T3 & T4)	51.22	52.29	50.88	**51.46**
27 Days (T5 & T6)	51.17	52.04	51.46	**51.55**
28 Days (T7 & T8)	51.55	51.42	52.10	**51.69**

Table 2 - Average concrete compressive strengths

Polyester foil strain gauges were used to measure the strain in selected reinforcement bars within the test beams. The procedure for placing the strain gauges required the reinforcement bar to be grinded locally until flat and cleaned with acetone. The strain gauges could then be placed, wired up and heat wrapped to prevent moisture ingress during the casting of the test beams (Figure 7). Figure 8 illustrates the positioning of the strain gauges.

Figure 7 - Overview of strain gauge application

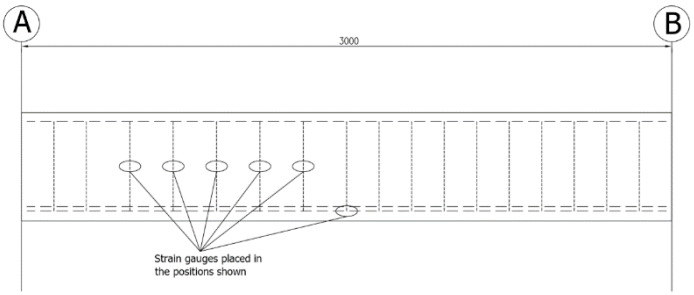

Figure 8 - Strain gauge positions

3.2 *Testing Configuration*

Figure 9 show the test setup in theory and in practice along with all devices required to carry out the destructive testing which include the following:

- 2 no. 55 tonne hydraulic jacks;
- 2 no. load cells;
- 5 no. displacement gauges;
- Several strain gauges;
- Electrically driven hydraulic pump system;
- A system 7000 data logger.

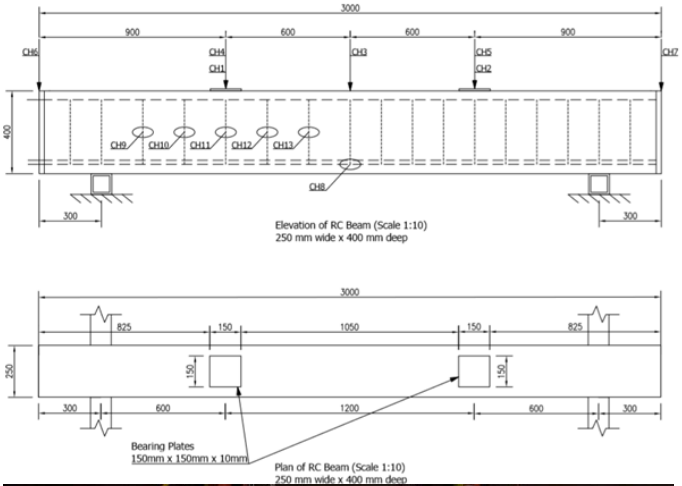

Figure 9 - Testing configuration

3.3 *Test Results*

Load-strain, load/shear-displacement and shear-strain curves were plotted for all nine test beams from the data gathered during the tests. The load was applied in increments until failure of the specimen occurred (Figure 10). A summary of the failure loads is shown in Table 3. Figure 11 illustrates the combined shear-displacement results from all tests.

Figure 10 - Failure of test specimen

Specimen	Applied Load (kN)	Shear force (kN)
Control Beam	670.0	Failed to break
Test Beam T1	662.2	331.1
Test Beam T2	609.6	304.8
Test Beam T3	585.2	292.6
Test Beam T4	547.8	273.9
Test Beam T5	527.8	263.9
Test Beam T6	421.2	210.6
Test Beam T7	376.4	188.2
Test Beam T8	353.2	176.6

Table 3 - Failure loads

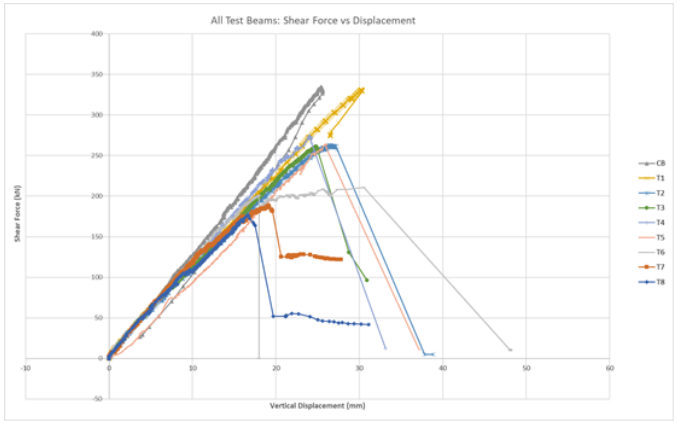

Figure 11 - Shear force vs vertical displacement

4 FINITE ELEMENT ANALYSIS

A series of finite element models were developed to determine the ultimate shear capacity of the test beams using the software LUSAS (Version 16). The finite element analysis mirrored that used in the laboratory testing where the prescribed load was applied incrementally until failure of the model. The analysis utilised plastic material properties for both the steel reinforcement and concrete. A 2D model was utilised to reduce the number of elements and time taken to solve the model (see Figure 12).

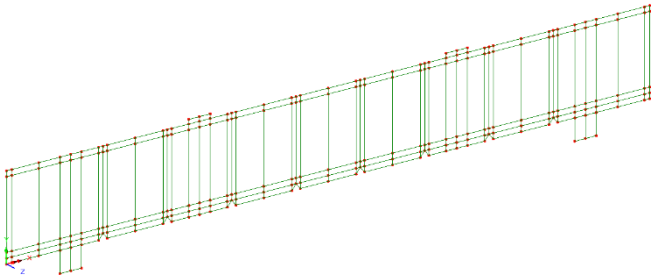

Figure 12 - Geometry of 2D non-linear model

The model was meshed using an 8-noded 2D continuum element (QPM8) using quadratic interpolation. This element was selected over its 4-noded counterpart as it is suitable for analyses where in-plane bending effects are significant. The element was also chosen due to the fact that it is compatible with the 3-noded bar element (BAR3) which was used to represent the steel reinforcement.

Failure of the analysis was governed by the plastic material properties. The Smoothed Multi Crack Model 109 [6] was used to model failure of concrete (see Figure 13) while a Von Mises stress potential model was used to set the yield criterion for the steel (see Figure 14).

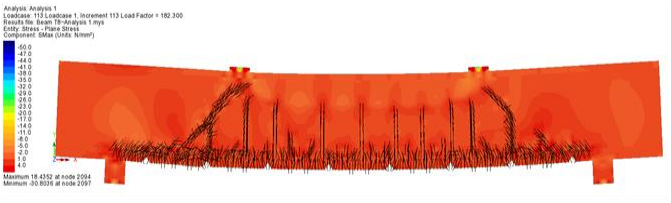

Figure 13 - Contour plot of crack crush pattern at failure

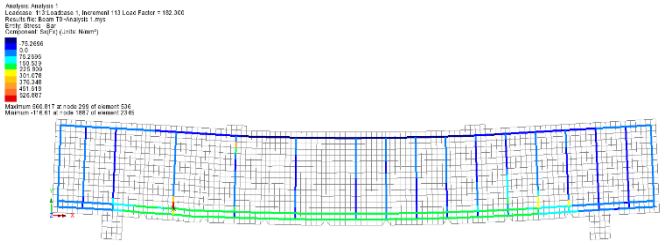

Figure 14 - Contour plot of Von Mises stress at failure

The results of the FEA indicated that failure would occur as a result of the shear reinforcement yielding due to the uniaxial yield stress of the reinforcement being exceeded (see Figure 15).

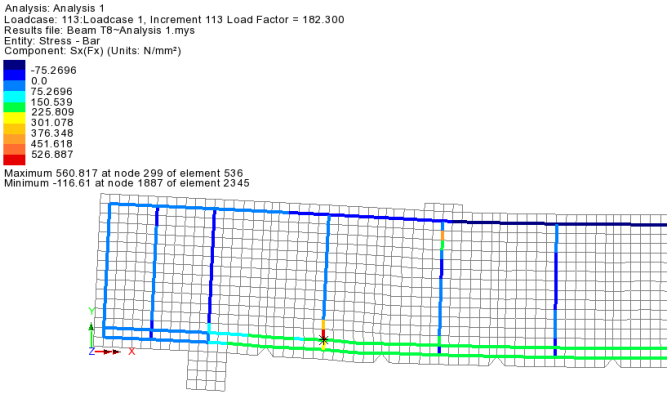

Figure 15 - Predicted failure criteria

Figure 11 illustrates the combined shear-displacement results from all models.

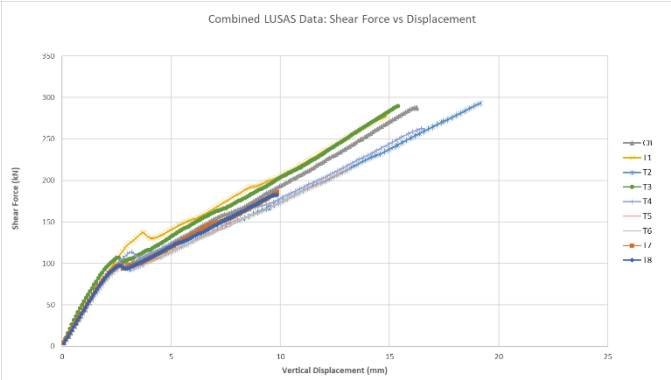

Figure 16 - Shear force vs vertical displacement

5 COMPARATIVE ANALYSIS

5.1 Overview of Results

The results of the laboratory testing and the FEA both indicated that failure as a result of the shear reinforcement yielding was the primary mode of failure (see Figure 17).

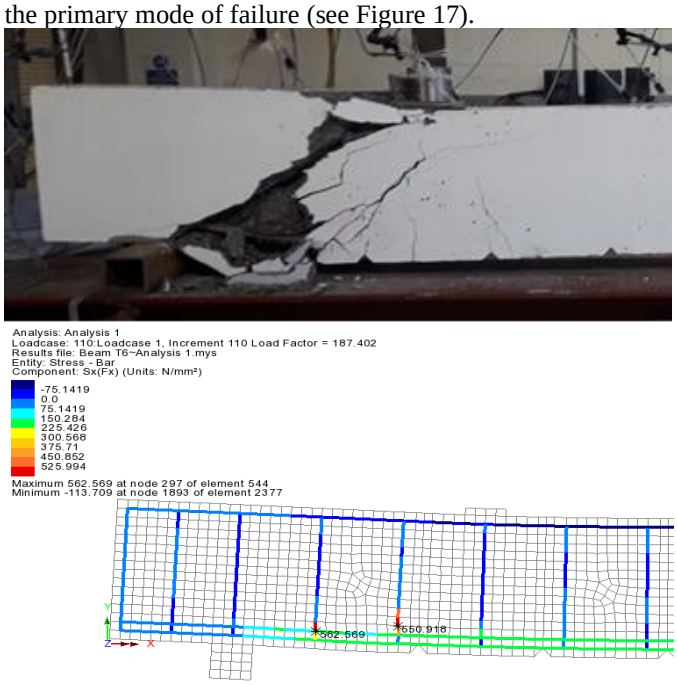

Figure 17 - Test Beam T6 vs LUSAS model failure comparison

Specimen	Max Shear Resistance (kN)			
	Test Failure	LUSAS	BD 44	EC2
Control Beam	Failed to break	288.6	338.6	348.8
Test Beam T1	331.1	278.5	307.7	293.3
Test Beam T2	304.8	293.2	287.6	284.3
Test Beam T3	292.6	289.6	286.1	276.0
Test Beam T4	273.9	262.8	266.2	235.1
Test Beam T5	263.9	213.6	253.0	207.9
Test Beam T6	210.6	187.4	161.4	186.6
Test Beam T7	188.2	248.0	150.0	163.7
Test Beam T8	176.6	182.3	142.5	148.4
Accuracy		92.6%	89.5%	86.5%
Note: All partial factors of safety for BD 44 & EC2 = 1.0				

Table 4 - Maximum shear resistance and average accuracy of each method

Table 4 shows a summary of the data collected from all methods along with the overall accuracy of each method. The results of both the FEA and the laboratory tests display similar trends and there was good correlation between both sets of results for all test beams. Both sets of shear calculations also show a correlation with the laboratory test results. However, BD 44 displayed higher levels of accuracy as opposed to EC2 for the majority of test beams.

It was observed throughout the comparative analysis stage that in all instances, the LUSAS models were behaving as stiffer members compared to the laboratory beams (see Figure 18). This is believed to be due to the fact that the FEA model allows perfect bond conditions between the steel reinforcement and concrete, where, in reality, the bond breaks down as failure approaches.

Figure 18 - Shear force vs displacement results comparison

5.2 Destructive Investigation of Failure Mechanism

A destructive investigation was carried out on the Test Beam T2 to highlight the effects of testing on the test beam, particularly on the shear and longitudinal reinforcement. Figure 19 shows the exposed reinforcement after the surrounding concrete has been removed to enable the reinforcement to be examined.

Figure 19 - Test Beam T2 destructive investigation

It is clear from Figure 19 that the section failed due to excess tension in the shear links which ultimately caused the abrupt and explosive failure. Dowel action of the longitudinal reinforcement was observed by the presence of kinks in the longitudinal reinforcement.

Figure 20 illustrates the reinforcement stresses at the point where the finite element model failure criteria for reinforcement failure was met. The predicted mode of failure in terms of the local yielding of shear links matched the behaviour of the test specimens observed in the laboratory.

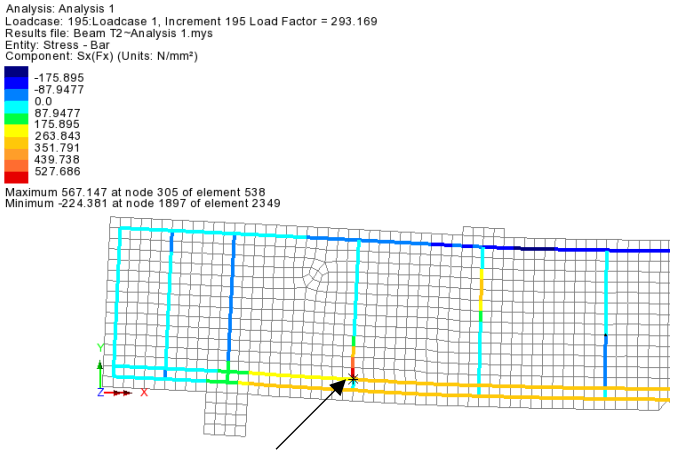

Figure 20 - Predicted failure criteria signifying zone of interest

6 CONCLUSIONS

The literature review established that there is limited experimental data available on the shear resistance of damaged concrete beams. The results of the laboratory testing indicated that with the further increase of applied load, the shear links failed in tension resulting in a sudden and explosive shear failure of the test beams. The mode of failure started with concrete compression failure at the point of load application and once the shear cracks appeared, the aggregate interlock failed, effectively applying all of the shear force to the shear links causing the shear cracks to expand drastically. Finally, the tension failure of the shear links caused the beams to fail in an explosive manner. The FEA analysis and theoretical approaches support the results obtained from the laboratory testing. Plus, the modern structural assessment code BD 44 provides a sound theoretical basis for calculating the shear capacity of damaged concrete beams at structural assessment stage. The combination of non-linear finite element analysis and the modern structural assessment code BD 44 provides the optimum approach to the assessment of corrosion damaged RC beams.

NOTATION

$V_{Rd,c}$	is the design shear resistance of the member without shear reinforcement
$C_{Rd,c}$	coefficient, factor
k	coefficient, factor
ρ_l	longitudinal reinforcement ratio
f_{ck}	characteristic concrete compressive strength
k_1	coefficient, factor
σ_{cp}	concrete compressive stress at centroidal axis due to axial loading or prestressing
b_w	width of the section web
d	effective depth of a cross-section
V_{Rd}	is the design shear resistance of a member with shear reinforcement
$V_{Rd,s}$	is the design value of the shear force which can be sustained by the yielding shear reinforcement
V_{ccd}	is the design value of the shear component of the force in the compression area, in the case of an inclined compression chord.
V_{td}	is the design value of the shear component of the force in the tensile reinforcement, in the case of an inclined tensile chord.
$V_{Rd,max}$	is the design value of the maximum shear force which can be sustained by the member, limited by crushing of the compression struts.
A_{sw}	is the cross-sectional area of the shear reinforcement
s	is the spacing of the stirrups
z	
f_{ywd}	is the design yield strength of the shear reinforcement
ν_1	is a strength reduction factor for concrete cracked in shear
α_{cw}	is a coefficient taking account of the state of the stress in the compression chord
f_{cd}	design value of concrete compressive strength
ξ_s	coefficient, factor
υ_c	is the ultimate shear stress in concrete
f_{yv}	is the characteristic, or worst credible, strength of the shear reinforcement
γ_{ms}	is the material partial safety factor for steel
s_v	is the spacing of the shear reinforcement along the member
A_{sv}	is the cross-sectional area of shear reinforcement at a particular cross-section

ACKNOWLEDGMENTS

The authors would like to thank Mr Jim Morgan and Mr Liam Jones for their assistance with the laboratory testing.

The research reported in this paper was conducted as part of the taught MEng (Structural Engineering) programme at Munster Technological University.

REFERENCES

[1] Mosley, W. H., R. Hulse and J. H. Bungey (2012). Reinforced concrete design: to Eurocode 2, Macmillan International Higher Education.
[2] Nilson, A. H., D. Darwin and C. W. Dolan (2010). Design of concrete structures, McGraw-Hill Science/Engineering/Math.
[3] Higgins, C., W. C. Farrow III, T. Potisuk, T. H. Miller, S. C. Yim, G. R. Holcomb, S. D. Cramer, B. S. Covino Jr, S. J. Bullard and M. Ziomek-Moroz (2003). Shear capacity assessment of corrosion-damaged reinforced concrete beams, Oregon. Dept. of Transportation. Research Unit.
[4] NSAI (2004). I.S. EN 1992-1-1. *Design of Concrete Structures*., National Standards Authority Ireland.
[5] Publications, TÌI. (2014). AM-STR-06031 - The Assessment of Concrete Road Bridges and Structures**:** 92.
[6] London University Stress Analysis System, Theory Manual Volume 1. Version 16.0-2, LUSAS, United Kingdom, 2018.

A solution to bamboo reinforced concrete's bond problem

Méabh Childs, Roger P. West
Department of Civil, Structural, and Environmental Engineering, Trinity College, College Green, Dublin 2
Email : mchilds@tcd.ie, rwest@tcd.ie

ABSTRACT: Bamboo culms have been widely researched as a substitute for steel reinforcement in concrete due to their relatively high tensile strength and many environmental benefits. It has been experimentally shown by various researchers that a lack of bond between the bamboo culms and cement matrix is one of the main inhibitors to the wider use of bamboo reinforced concrete for structural use. This lack of bond strength can cause the bamboo to slip within a concrete element and cease to be effective in taking the tensile stresses when a flexural load is applied to it. The research conducted in this paper develops a solution to this bond problem by cutting notches from reinforcing bamboo culms in appropriate regions of the beam. The purpose of the notches is to improve the anchorage between the two materials by utilising the shear resistance between the concrete in the notches and the surrounding concrete. Tensile tests and pull-out tests were performed on bamboo culms with a range of notch sizes, shapes, and arrangements. The results indicate that the notching arrangement that maximised the bond strength between the cement matrix and the bamboo, without compromising the beams overall tensile capacity, was two parallel, rectangular notches of length 80 mm and depth 2 mm, positioned 50 mm from the end of the culm. It was established with beam flexural loading tests on 600 x100x100 mm unnotched bamboo reinforced concrete beams that a highly workable, recycled aggregate concrete cured at 15°C promoted bond failure due to the low matrix strength. When the two bamboo culms were optimally notched the bond between the two materials was significantly improved and converted the failure mode of the reinforced beam from bond to bamboo tensile failure.

KEY WORDS: Bamboo culms, notch, bond strength, recycled aggregate concrete.

1 INTRODUCTION

Concrete is usually reinforced with steel in structural elements to improve its tensile strength, and to change its failure mode from brittle to ductile. This failure type is an important feature of reinforced concrete as it enables a potential catastrophe to be recognised in advance and avoided, potentially saving many lives. However, steel is a non-renewable resource and is not easily accessible to many projects in developing countries [1]. Steel production also releases greenhouses gases, particularly carbon dioxide. With the increasing threat of climate change, especially to the land and people of developing countries, it is crucial that sustainable construction materials are researched, developed, and implemented.

Bamboo has been widely researched as a substitute for steel reinforcement in concrete due to its high tensile strength, its high strength/weight ratio, its flexibility, and its environmental advantage over steel [2 - 4]. It has been shown that the inclusion of bamboo reinforcement in a concrete beam results in a beam that can be four times stronger in tension than an unreinforced concrete beam [5]. However, the lack of bond strength between bamboo and concrete is one of the main issues inhibiting the wider use of bamboo as reinforcement. This lack of bond can cause the bamboo to slip within a concrete element when a flexural load is applied to it, reducing both the tensile capacity of the element and the predictability of its failure.

The poor bond strength in bamboo reinforced concrete is caused by the lack of frictional or shear resistance between the matrix and the bamboo's surface due to the naturally smooth and cylindrical shape of the bamboo. Many efforts have been made to improve this bond strength, including coating the bamboo culms with epoxy and sand [6], wrapping galvanised iron wire around the culms [7], anchoring the culms with screw nail hooks [8], and cutting notches from the culms. Notches are small indentations cut in the bamboo specimen with the aim that the cement paste and aggregate from the concrete will embed itself in the notch, and the shear resistance between the concrete in the notch and the surrounding concrete will increase the anchorage of the bamboo culm. There has been research conducted on U- and V-shaped notching in bamboo splints [9 - 11], each of which concludes that the inclusion of notches improves the bond between the splints and the concrete. However, there is a lack of research on the bond between concrete beams reinforced with full bamboo culms with notches. The benefits of using full culms rather than bamboo splints are that less time and equipment is required in the preparation of the bamboo for reinforcement.

The aim of this research was to investigate the impact of notches on the bond behaviour of concrete beams reinforced with full Moso bamboo culms. There were a number of experimental stages in developing the combination of notch size, shape, and arrangement that maximised the bond strength between the cement matrix and the bamboo without compromising the beam's overall flexural capacity. The methodology at each stage is described before considering the results of testing on two different notch shapes (Figure 1).

2 METHODOLOGY

This research was conducted in four experimental stages: tensile tests, pull-out tests, flexural loading tests on unnotched bamboo reinforced beams, and flexural loading tests on notched bamboo reinforced beams. In each experimental stage a Universal Testing Machine (UTM) applied a displacement-controlled force to the test specimens until failure occurred or until a displacement of 50 mm was reached. Bamboo culms, available locally, with an approximate diameter of 12 mm were

used throughout. Nodes run transversely through the bamboo's cross-section, and are naturally present at intervals of approximately 200 mm along Moso bamboo culms. The nodes were excluded in the pull-out experiments, where the culms were less than 200mm in length, so that the focus was on the impact of the notches on bonding. However, nodes cannot be excluded in culms longer than 300 mm, so that in the beam flexural loading tests, where the samples are 600 mm long, the nodes were positioned in the central 200 mm of the beams to minimize their impact on the examination of bond failure.

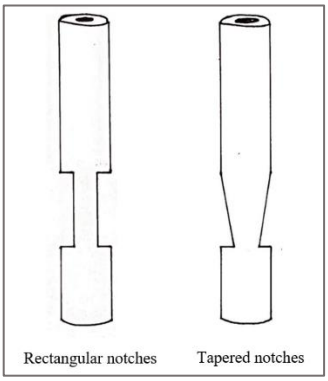

Figure 1: Notched bamboo culms

2.1 Tensile Tests

The aim of these tests was to establish the impact of nodes and notch shapes on the tensile strength of the culm. A tensile force was applied to various bamboo culm types: culms with no nodes or notches in its length, culms with a node halfway along its length, culms with two, parallel, 80 mm long rectangular notches on either side of the culm, and culms with two, parallel, 80 mm long tapered notches on either side of the culm (Figure 1). A steel rod was fixed into each end of the culm to avoid radial crushing of the culm by the jaws of the UTM grip.

2.2 Pull-Out Tests

Two rounds of pull-out test were completed. The purpose of undertaking pull-out tests was to establish the impact of notch shape and size on the bond strength between bamboo and concrete and to determine the notching arrangement that maximised this bond strength. In the first round, the following test specimens were prepared: unnotched culms, culms with two parallel, rectangular notches, and culms with two parallel, tapered notches. Each of the notches was 80 mm long and 4 mm deep and were positioned 50 mm from the ends of the culms. The culms were embedded into concrete cylinders to a depth of 200 mm. The steel rod method of gripping the culm ends used in the tensile tests was unsuccessful, and a new gripping method was developed for the pull-out tests. A 20 mm diameter steel tube was fixed onto the tops of the culms with epoxy. Small indentations were made in the steel to improve the bond between the bamboo, epoxy and the steel, and the tops of the tubes were flattened so that the UTM could easily grip them (Figure 2).

In the second round of pull-out tests, the notched culms were tested again, this time with a depth of 2 mm. The reason for this was to improve the tensile strength of the culm at the notch cutting away less of its cross-sectional area.

Figure 2: Steel tubes and epoxy used to provide grip on the bamboo culms in the pull-out tests

2.3 Flexural loading tests on unnotched reinforced beams

The objective of these tests was to determine the concrete conditions that promoted bond failure in an unnotched bamboo reinforced concrete beam. Fifty-four reinforced beams were tested by 1st Year engineering students in Trinity College as part of their Engineering Materials module. Concrete beams of dimensions 600x100x100 mm were reinforced with two unnotched bamboo culms of length 600 mm (Figure 3), and a flexural load was applied to the beam until failure occurred. The beams were made from concretes of various aggregate types and curing temperatures, as detailed in Table 1. The failure modes of the beams were determined based on their behaviors during loading, their force/displacement plots, by inspecting the cracking patterns of the beams and the movement of the culms within the beams after failure. The concrete that promoted bond failure was 100% recycled aggregate and 50% GGBS concrete cured at 15°C (RAC15) due to its lower cement matrix strength and this was used in the subsequent notched reinforced beams.

Table 1: Experimental conditions for unnotched beam tests

Condition Name	Aggregate Type	Curing Temperature (°C)
RAC15	Recycled	15
RAC30	Recycled	30
FRAC15	Fibre-reinforced RAC	15
FRAC30	Fibre-reinforced RAC	30

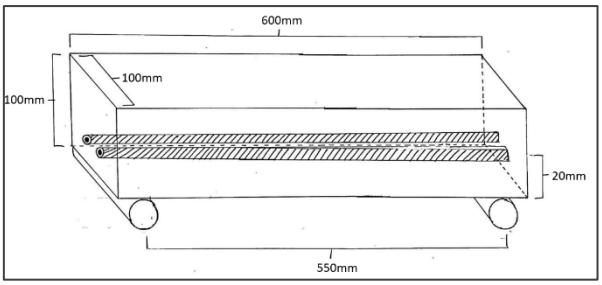

Figure 3: Dimensions of bamboo reinforced concrete beams

2.4 Flexural loading tests on notched reinforced beams

This experimental stage used a similar mix, but without fibres, at 15°C. The optimum notching arrangement established in the pull-out tests (two parallel rectangular notches of length 80 mm and depth 2 mm, positioned 50 mm from each end of the beam; Figure 4) was selected to promote a notched bamboo reinforced beam that would fail in tension rather than due to poor bonding. The dimensions of the beams used in this test were the same as that of the unnotched beam tests. A flexural displacement control load was applied to these beams, compared with the unnotched bamboo reinforced beams as a control.

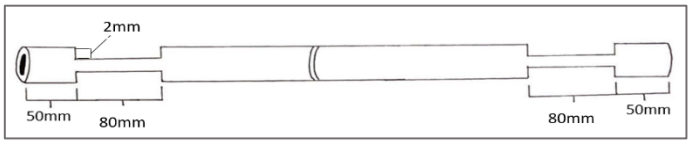

Figure 4: Dimensions of notching arrangement

3 RESULTS AND DISCUSSION

3.1 Tensile Tests

The maximum tensile stress reached by the culms that did not have a node or a notch was 174 MPa, while the maximum tensile stress of the culms with a node was 204 MPa, with wide variability for both. These values could not be taken as the tensile strength of the bamboo culms as in each case failure occurred due to crushing of the ends of the culm by the UTM grip. However, each of the notched culms failed in a tensile manner at the notch locations. The maximum tensile strength achieved in the culm with the rectangular notch was 178 MPa, while that of the culm with the tapered notch was 112 MPa. Although a value for the tensile strength for Moso bamboo could not be determined from this experiment, it was established that the inclusion of notches lowered the tensile strength of the culm locally, which was expected as the cross-sectional area of the culm at the notch is lower. It was clear that an alternative method for gripping the culms would be needed for the next experimental stage, the pull-out tests.

3.2 Pull-out Tests

In each round of pull-out test, there was negligible movement between the steel, epoxy, and the top of the bamboo culm. It was therefore evident that the pull-out behaviour recorded was solely between the bamboo and the concrete. The steel cap was therefore deemed to be a successful gripping method.

3.2.1 Round 1

The bond stresses experienced in the unnotched culm, the rectangular notched culm, and the tapered notched culm test specimens ranged from 0.42-0.6 MPa, 0.73-1.27 MPa, and 0.62-0.83 MPa respectively. In each of the unnotched culms, the whole culm was pulled from the concrete cylinder without any tensile failure along the culm. Classic pull-out behaviour was evident in each of the force/displacement plot, an example of which is displayed in Figure 5. This behaviour is characterized by an increase in applied force as it overcomes the adhesion between the culm and the concrete. A maximum force is reached when the applied force overcomes this

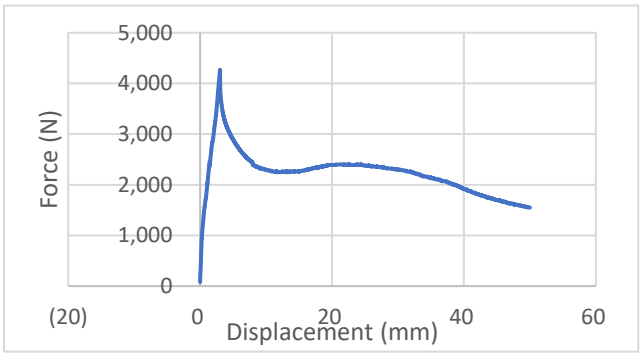

Figure 5: Force/displacement graph showing bond failure of unnotched culms in pull-out tests

adhesion, after which the applied force decreases gradually as the culm is pulled from the concrete cylinder and the culm becomes increasingly easy to pull-out with decreasing embedded length.

In each of the notched culms, the culm snapped at the notch. The section of the culm above the snap was pulled from the concrete, while the section below the snap remained in place with no evidence of pull-out. It was therefore evident from this experiment that the inclusion of notches improved the bond strength between the bamboo and the concrete, promoting tensile failure of the culm at its weakest point, the notch location. This tensile failure by snapping of the culm(s) is represented on a force/displacement plot with a sudden decrease in applied force, as displayed in Figure 6. The impact of the anchorage caused by the notch can be seen on this plot with the applied force remaining close to its maximum value for approximately 4 mm. It was clear that a notch length of 80 mm was sufficient for concrete to enter the notch, however, it was decided that for the second round of pull-out tests, the depth of the notch would be reduced from 4 mm to 2 mm to increase the tensile strength of the culms further.

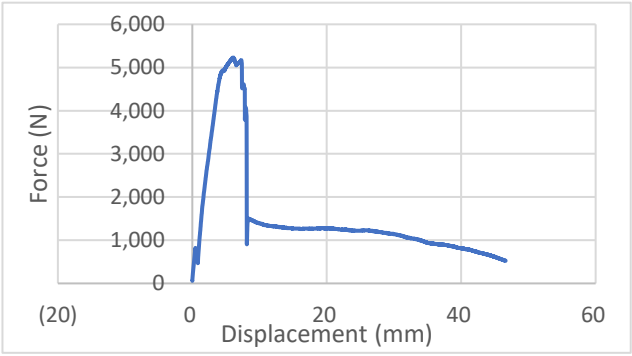

Figure 6: Force/displacement graph showing tensile failure of notched culms in pull-out tests

3.2.2 Round 2

The bond stresses experienced in the rectangular notched culms ranged from 0.64-1.42 MPa, and the bond stress experienced in the tapered notched culms ranged from 0.73-1.73 MPa. The reduction of the notch depth successfully improved the tensile strength of the culms, with most of them failing due to the longitudinal shearing of the bamboo below the notch (Figure

7). This shearing failure indicated that concrete had entered the notch and provided anchorage to the culm as the tensile force was applied to it. The cross-sectional area of the bamboo at the culm was large enough for the bamboo at this area to remain intact, while the concrete in the notch tore through the bamboo under the notch as the culm was pulled from the concrete cylinder. Considering these results, it was decided that a notch of length 80 mm and depth 2 mm would be used as the notching arrangement for the final experimental stage, the notched beam tests. It was also decided that the rectangular notches would be used in the final notching arrangement rather than the tapered notches, mainly because the rectangular notches were easier to cut. With the tapered notches, it was difficult to achieve an even gradient on each side of the culm, and they tended to be cut too deep, decreasing the tensile strength of these culms with these notches.

Figure 7: Embedded end displaying shear failure of culm under notch

3.3 Flexural loading tests on unnotched reinforced beams

The average maximum forces applied to the reinforced beams with concrete types RAC15, RAC30, FRAC15, and FRAC30, were 4.8kN, 5.9kN, 5.0kN, and 7.3kN respectively. The majority of the beams made with concrete cured at 15°C failed due to a lack of bond between the two materials (Figure 8), while most of the beams that were made with concrete cured at 30°C failed in a tensile manner due to the higher concrete strength in bond (Figure 9). It was deduced from this experiment that both the bond strength and the tensile capacity of the beams were notably greater when a stronger concrete cured at 30°C was used. It was therefore concluded that the likelihood of bond failure occurring was highest when the concrete was made with recycled aggregates and cured at 15°C, leading to a weak cement paste. Furthermore, the beams that had the highest workability were more likely to fail in bond due to a higher water/cement ratio. Therefore, a highly workable concrete is required to promote bond failure in a bamboo reinforced concrete beam. This information was used to design reinforced beams in the final experimental stage that were likely to fail due to poor bond, but which would be converted to a tensile failure due to the notching arrangement.

Figure 8: Half of an unnotched reinforced beam displaying bond failure along the culm

Figure 9: Half of an unnotched reinforced beam displaying tensile failure in the culms

3.4 Flexural loading tests on notched reinforced beams

3.4.1 Unnotched Reinforced Beams

It was evident from the results of the unnotched reinforced beam tests that the concrete used successfully promoted bond failure. Each of these beams failed in bond, with the value for bond stress ranging from 0.18 to 0.24 MPa, and a maximum applied force ranging from 2.8 kN to 5.3 kN. The slipping distances of the culms in from the ends of the beams were measured, with the culms moving up to 36 mm into the 600mm long concrete beams (Figure 10). The force/displacement plots also confirmed this failure mode with a classic bond failure behaviour, i.e., an increase in applied force until the concrete cracked, followed by a gradual decrease in applied force with displacement and culm pull-out (Figure 11).

Figure 10: End of beam after bond failure showing inward movement of bamboo reinforcement into the beam

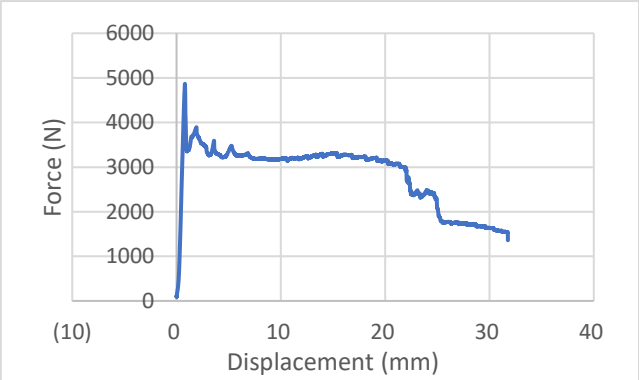

Figure 11: Force/displacement graph showing the bond failure of an unnotched reinforced bamboo beam in a flexural loading test

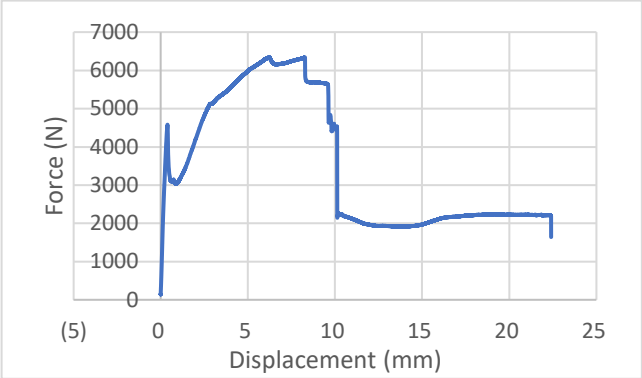

Figure 12: Force/displacement graph showing tensile failure of a notched reinforced bamboo beam in a flexural loading test

Prior to loading in the UTM, a cracking pattern along the length of one of the beams at the position of the reinforcement and around the bamboo reinforcement at the ends of the beam was noticed. It was speculated that the cracking was caused by the absorption of water by the bamboo from the surrounding concrete, causing the bamboo to swell, putting pressure on the concrete causing it to crack. This cracking likely reduced the bond between the two materials. This highlights the importance of water-proofing the bamboo prior to pouring the concrete.

3.4.2 Notched Reinforced Beams

Each of the bamboo reinforced beams featuring the notching arrangement failed in a tensile manner with limited evidence of bond failure. The bond stresses experienced in these beams ranged from 0.23 MPa to 0.36 MPa, with maximum applied forces ranging from 4.4 kN to 6.9 kN. When inspecting the ends of the beams after failure it was evident that little movement of the culms within the concrete had occurred (Figure 12). The largest slipping distance of a culm into the beam was 9mm. In each of these beams tensile failure occurred at the centre of the culms. This tensile failure was represented on the force/displacement plots with sudden drops in the measured restive force capacity (Figure 13).

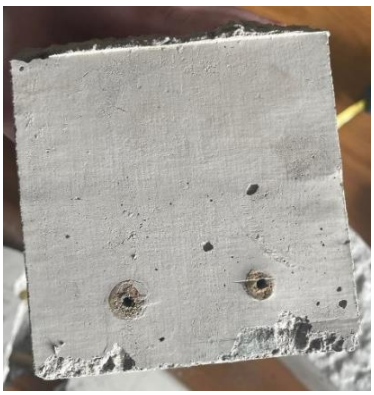

Figure 13: End of beam after tensile failure showing negligible movement of the reinforcement into the beam

The bond strength of the bamboo reinforced concrete beam increased by an average of 33% with the inclusion of rectangular notches in the reinforcement. The tensile stress experienced in the notched culms was also larger than that of the unnotched culms by approximately 22%. However, the most significant conclusion that can be taken from these results is that that the inclusion of the notches in the bamboo reinforcement converted the failure mode of the beams from bond failure to tensile failure. This is an important result as it allows a Moso bamboo reinforced concrete beam to be designed with a more predictable tensile capacity, which can be calculated based on the tensile capacity of the bamboo culms, which, it is recognised, is itself highly variable.

It must be recognised that a small sample size (of six beams) was used in this experiment and given the wide variability of bamboo even within the one species and one bush, these tests should be repeated with a much larger sample size to strengthen these conclusions.

4 CONCLUSIONS

This research has provided evidence of a possible solution to the bond problem which is associated with bamboo reinforced concrete. It was demonstrated that the inclusion of rectangular notches, of length 80mm and depth 2mm in Moso bamboo culms in this case, improved the bond between bamboo and concrete by an average of 33%. The tensile capacity of the beams was also increased with the inclusion of notches in the culms, from 4 kN to 5.5 kN on average. More significantly, the inclusion of these notches converted the failure mode of the reinforced beam from bond failure to tensile failure, thereby utilise fully the bamboo capacity in tension.

This research also developed a new method of gripping bamboo culms in a UTM to mitigate radially crushing of the bamboo ends, that is, a steel cap fixed to the end of the bamboo culm with epoxy. It was evident from the pull-out tests that negligible pull-out occurred between the steel, epoxy, and bamboo. It can therefore be concluded that the bond strength between the epoxy, steel, and bamboo is greater than that of the bamboo and concrete.

With the reduction of the notch depth from 4 mm to 2 mm, the tensile strength of the bamboo culm at the notch location was increased. The failure mode of the bamboo culm in pull-out tests was converted from tensile failure to shear failure of

the bamboo below the notch. This was a preferred mode of failure as it increased the tensile capacity of the culm and reduced the rate of pull-out.

It was then established in the unnotched reinforced beam flexural tests that a highly workable recycled aggregate GGBS concrete cured at 15°C promoted the bond failure of the beam when tested at 7 days. These conditions were replicated in the notched beam tests to create bamboo reinforced concrete beams that were unlikely to fail due to poor bond when flexural loads were applied to them. In these tests, the effectiveness of the notches in the reinforcing culms was evident with the conversion of failure mode from bond failure to tensile failure. This result is significant as it enables a bamboo reinforced beam to be designed with a more predictable tensile capacity.

REFERENCES

[1] Md Ahsan Sabbir, S. M. A. H., Saiada Fuadi Fancy 2011. Determination of Tensile Property of Bamboo for Using as Potential Reinforcement in the Concrete. *International Journal of Civil & Environmental Engineering IJCEE-IJENS*, 11.

[2] Dixon, P.G. & Gibson, L. J. 2014. The structure and mechanics of Moso bamboo material. *J R Soc Interface*, 11.

[3] HARISH SAKARAY, N. V. V. K. T. A. I. V. R. R. 2012. Investigation on properties of bamboo as reinforcing material in concrete. *International Journal of Engineering Research and Applications (IJERA)*, 2**,** 77-83.

[4] YEN, T.-M. & LEE, J.-S. 2011. Comparing aboveground carbon sequestration between moso bamboo (Phyllostachys heterocycla) and China fir (Cunninghamia lanceolata) forests based on the allometric model. *Forest Ecology and Management*, 261**,** 995-1002.

[5] GHAVAMI, K. 1995. Ultimate load behaviour of bamboo-reinforced lightweight concrete beams. *Cement and Concrete Composites*, 17**,** 281-288.

[6] JAVADIAN, A., WIELOPOLSKI, M., SMITH, I. F. C. & HEBEL, D. E. 2016. Bond-behavior study of newly developed bamboo-composite reinforcement in concrete. *Construction and Building Materials*, 122**,** 110-117

[7] DEY, A. & CHETIA, N. 2018. Experimental study of Bamboo Reinforced Concrete beams having various frictional properties. *Materials Today: Proceedings*, 5**,** 436-444.

[8] MAULIDIN, A., MUJIMAN, M. & KASYANTO, H. 2020. Performance of petung bamboo strip with anchor screw nails on the reinforced concrete beams. *IOP Conference Series: Materials Science and Engineering*, 732**,** 012024.

[9] KHATIB, A. & NOUNU, G. 2017. Corrugated bamboo as reinforcement in concrete. *Proceedings of the Institution of Civil Engineers - Structures and Buildings*, 170**,** 311-318.

[10] Budi, A.S., Rahmadi, A.P., Rismunarsi, E., 2017. Experimental study of flexural capacity on bamboo ori strip notched v reinforced concrete beams, in: THE 4TH INTERNATIONAL CONFERENCE ON MATERIALS ENGINEERING AND NANOTECHNOLOGY (ICMEN 2021). THE 4TH INTERNATIONAL CONFERENCE ON MATERIALS ENGINEERING AND NANOTECHNOLOGY (ICMEN 2021).. doi:10.1063/1.4968305

[11] GYANSAH, L. & KWOFIE, S. 2011. Investigation into the Performance of Bamboo Using the Notched and the Un-Notched Specimen. *Research Journal of Applied Sciences, Engineering and Technology 3(4):* 245-251, 2011

Deriving discrete solid phases from CSH-3T and CSHQ end-members to model cement hydration in PHREEQC

Niall Holmes[1,3], Colin Walker[2], Mark Tyrer[1,3] & Denis Kelliher[4]
[1]School of Civil & Structural Engineering, Technological University Dublin, Bolton Street, Dublin 1, Ireland
[2]QJ Science Ltd., Yokohama, Japan
[3]Institute of Advanced Study, Collegium Basilea, Basel, Switzerland
[4]School of Civil, Structural and Environmental Engineering, University College Cork, Cork. Ireland

email: niall.holmes@tudublin.ie; walker.colin@jaea.go.jp; m.tyrer@mtyrer.net; d.kelliher@ucc.ie

ABSTRACT: This paper presents a cement hydration model over time using the CEMDATA thermodynamic database and a series of discrete solid phases (DSP) to represent calcium silicate hydrate (C-S-H) as a ternary (CSH-3T) and quaternary (CSHQ) solid solution.

C-S-H in cement is amorphous and poorly crystalline with a range of molar Ca/Si ratios = 0.6-1.7 and displays strongly incongruent dissolution behaviour where the release of calcium into solution is several orders of magnitude greater than silicon. It is therefore important that any cement hydration model provides a credible account of this behaviour.

C-S-H has been described in the CEMDATA thermodynamic database as a number of binary, ternary and quaternary solid solutions using different end-members with differing levels of complexity. While solid solutions can be included in most modern geochemical software programs, it often leads to a significant increase in computation time.

This paper presents how the two of the more complex C-S-H solid solutions, CSH-3T and CSHQ, available in the CEMDATA database, can be represented by DSP to model cement hydration over time using the PHREEQC geochemical software. By using DSP in place of solid solutions, analysis time is much improved with no loss in accuracy in producing stable phase assemblages and reasonable predictions of pH over time.

KEY WORDS: solid solutions; discrete solid phases; C-S-H; cement; hydration.

1 INTRODUCTION

Solid solutions are homogeneous crystalline structures where one or more atom types or molecules can be partly or wholly substituted on specific lattice sites by moieties of equivalent charge. If the host and substituting moieties are chemically similar, the formation of an ideal solid solution is possible, however, as is usually the case, differences are sufficiently large to cause the formation of a non-ideal solid solution, which can be readily confirmed by the appearance of a miscibility gap [1, 2]. Solid solutions are of great importance in cement chemistry where they can be used to describe the strongly incongruent dissolution behaviour of calcium-silicate-hydrate (C-S-H) gel [3, 4], substitution of SiO_4^{4-} and $4OH^-$ in hydrogarnets [5], and substitution of cationic Al^{3+} and Fe^{3+} and anionic $2OH^-$, 2Cl–, SO_4^{2-}, and CO_3^{2-} components in AFt and AFm minerals [6-8].

If the thermodynamic properties of the unsubstituted, pure end-members are known, it is possible to calculate a series of DSP that can be used to provide a credible thermodynamic model of cement hydration. Work by [9] and [10] demonstrates that DSP can be derived for any ideal or non-ideal solid solution. For example, [10] developed a DSP C-S-H gel solubility model based on two binary non-ideal solid solutions that yielded satisfactory predictions of pH, Ca and Si concentrations for molar Ca/Si (C/S) ratios from 0 to 2.7, the occurrence of portlandite at C/S > 1.65, amorphous silica at C/S < 0.55, and congruent dissolution at C/S = 0.85.

In the current paper, DSP have been derived for the CSH3T (three end-member) and CSHQ (four end member) C-S-H gel solubility models [3], and used to predict ordinary Portland cement (OPC) hydration as a function of time using the CEMDATA thermodynamic database [11] and the PHREEQC geochemical code [12].

2 DERIVATION OF DSP FROM CEMDATA SOLID SOLUTION END-MEMBERS

The first step in deriving a series of DSP is defining the pure end-members and their thermodynamic properties in terms of Gibbs free energy (G, J/mol), enthalpy (H, J/mol), entropy (S, J/K/mol), heat capacity (Cp, J/K/mol) and molar volume (V, cm^3/mol) (see Table 1) [11]. These thermodynamic properties can then be used calculate the solubility constant, log K and its variation with temperature for dissolution reactions of each end-member (Table 2). As shown, the end-members are listed in order of increasing solubility and the analytical expressions describe the variation of log K as a function of temperature (in Kelvin) where *a*, *c* and *d* are calculated as functions of enthalpy (Δ_rH, J/mol), entropy (Δ_rS, J/K/mol) and heat capacity (Δ_rC_p, J/K/mol) of reaction [13] , *b*, *e* and *f* = 0 and *T* is temperature.

$$\log K = a + b\cdot T + c/T + d\cdot\log_{10}(T) + e\cdot T^{-2} + f\cdot T^2 \qquad (1)$$

Each of the end-members shown in Table 2 and their respective analytical expressions are written directly into PHREEQC to suit its data input syntax.

Next, appropriate mole fractions are chosen to discretize the solid solutions and create the series of DSP. In the current paper, mole fraction increments of 0.2 were used to describe the three end-members in the CSH3T model in terms of X_i, X_j & X_k and four end-members in the CSHQ model in terms of X_l, X_m, X_n and X_o), where the sum of the mole fractions in each solid solution must equal 1. Using these mole fractions, the

Table 1 Thermodynamic properties of CSH3T, as taken from the CEMDATA database [11]. Letters assigned to each end-member are shown in parentheses.

Component	G [i]	H [i]	S [ii]	C_p [ii]	V [iii]
CSH3T-TobH (i)	-2561532	-2832974	152.8	231.2	84.960
CSH3T-T5C (j)	-2518659	-2782034	159.9	234.1	79.261
CSH3T-T2C (k)	-2467081	-2722410	167.0	237.0	80.558
CSHQ-TobH (l)	-1668560	-1841498	89.9	141.6	55.0
CSHQ-TobD (m)	-1570891	-1742414	121.8	166.9	48.0
CSHQ-JenH (n)	-2273986	-2506256	142.5	207.9	76.0
CSHQ-JenD (o)	-2169558	-2400704	173.4	232.8	81.0
Ca^{+2}	-552790	-543069	-56.484	-30.923	
$SiO_{2(aq)}$	-833411	-887856	41.338	44.465	
H_2O	-237183	-285881	69.923	75.361	
H^+	0	0	0	0	

[i] J/mol. [ii] J/mol/K. [iii] cm^3/mol.

Table 2 CSH3T and CSHQ end-member properties [11]

CSH3T-TobH (i)
$(CaO)_1(SiO_2)_{1.5}(H_2O)_{2.5} + 2H^+ = Ca^{2+} + 3.5H_2O + 1.5SiO_{2(aq)}$ log K 12.5288
analytical_expression parameters (Equation (1)) [i]
a = -18.8215, *c* = 3282.489718, *d* = 8.22098

CSH3T-T5C (j)
$((CaO)_1(SiO_2)_1(H_2O)_2)_{1.25} + 2.5H^+ = 1.25Ca^{2+} + 3.75H_2O + 1.25SiO_{2(aq)}$ log K 18.1373
analytical_expression parameters (Equation (1)) [i]
a = -18.5190, *c* = 5127.78826, *d* = 7.864154

CSH3T-T2C (k)
$((CaO)_{0.75}(SiO_2)_{0.5}(H_2O)_{1.25})_2 + 3H^+ = 1.5Ca^{2+} + 4H_2O + SiO_{2(aq)}$ log K 25.2708
analytical_expression parameters (Equation (1)) [i]
a = -18.2427, *c* = 7428.082891, *d* = 7.517428

CSHQ-TobH (l)
$(CaO)_{0.6667}(SiO_2)_1(H_2O)_{1.5} + 1.3334H^+ = 0.6667Ca^{2+} + 2.1667H_2O + SiO_{2(aq)}$; log K 8.2866
analytical_expression parameters (Equation (1)) [i]
a = -12.5193, *c* = 2163.381583, *d* = 5.476331

CSHQ-TobD (m)
$((CaO)_{1.25}(SiO_2)_1(H_2O)_{2.75})_{0.6667} + 1.66675H^+ = 0.833375Ca^{2+} + 2.6668H_2O + 0.6667SiO_{2(aq)}$; log K 13.6553
analytical_expression parameters (Equation (1)) [i]
a = -10.9164, *c* = 3959.367696, *d* = 4.563888

CSHQ-JenH (n)
$(CaO)_{1.3333}(SiO_2)_1(H_2O)_{2.1667} + 2.6666H^+ = 1.3333Ca^{2+} + 3.5H_2O + SiO_{2(aq)}$; log K 22.1794
analytical_expression parameters (Equation (1)) [i]
a = -17.10947, *c* = 6470.553982, *d* = 7.107847

CSHQ-JenD (o)
$(CaO)_{1.5}(SiO_2)_{0.6667}(H_2O)_{2.5} + 3H^+ = 1.5Ca^{+2} + 4H_2O + 0.6667SiO_2$ log K 28.730362
analytical_expression parameters (Equation (1)) [i]
a = -15.5918, *c* = 8609.739692, *d* = 6.24251

[i] $a = (\Delta_r S - \Delta_r C_p \cdot (1 + LN(298.15))) / (R \cdot LN(10))$, $b = 0$, $c = (298.15 \cdot \Delta_r C_p - \Delta_r H) / (R \cdot LN(10))$, $d = \Delta_r Cp / R$, $e = 0$, and $f = 0$, where R is the gas constant (8.31451 J/mol/K).

solid phase composition (CaO, SiO_2, H_2O), aqueous reaction components (H+, Ca^{+2}, H_2O, $SiO_{2(aq)}$), mass (g/mol) and volume (cm^3/mol) are determined for each DSP based on the original end-members. The solubility constant is determined for each DSP in the CSH3T and CSHQ models using Equations 2 and 3 respectively.

$$K_{CSH3T} = (K_i \cdot X_i)^{Xi} \cdot (K_j \cdot X_j)^{Xj} \cdot (K_k \cdot X_k)^{Xk} \quad (2)$$

$$K_{CSHQ} = (K_l \cdot X_l)^{Xl} \cdot (K_m \cdot X_m)^{Xm} \cdot (K_n \cdot X_n)^{Xn} \cdot (K_o \cdot X_o)^{Xo} \quad (3)$$

Dissolution reactions and solubility products for the DSP for CSH3T and CSHQ models can be calculated on a spreadsheet and suitably formatted such that the user simply needs to copy and paste directly into the PHREEQC input file. Table 3 and Table 4 shows the resulting DSP for the CSH3T and CSHQ models, respectively.

At this point, the PHREEQC input file is completed and modelling of OPC hydration can begin accounting of the kinetic dissolution of the clinker phases as a function of time [14], oversaturation of the precipitating hydrate phases during the first 12 hours of hydration [15] and the release and uptake of alkali metals (K and Na) by the C-S-H gel [16]. To aid computing time, all input data is defined in an Excel spreadsheet first and pasted directly into PHREEQC.

3 THERMODYNAMIC MODELLING

3.1 OPC Clinker Rate Equations

The oxide compositions of the OPC CEM I cement are shown in Table 5. A normative calculation was undertaken to convert the oxide proportions into the cement clinker phases shown in Table 5. Gypsum is assumed to exist here rather than anhydrite.

The dissolution of the four clinker phases alite (Ca_3SiO_5, C_3S), belite (Ca_2SiO_4, C_2S), aluminate ($Ca_3Al_2O_6$, C_3A), and aluminoferrite ($Ca_4Al_2Fe_2O_{10}$, C_4AF) is described by empirical rate equations proposed by Parrot and Killoh [14] and modified by Lothenbach *et al* [17] which represents the mechanisms of nucleation and growth, diffusion and formation of a hydration shell. The controlling rate (R_t) is the lowest value from Equations (4-6) for any specified hydration time (t) in days. A & A_0 in Equation (4) represent the Blaine fineness and reference surface area ($385 m^2/kg$) respectively. Changes in temperature are accounted for by Equation (7) where T and T_0 are the curing temperature (K) and reference temperature of 293.15 K, respectively. Changes in relative humidity (*RH)* and water/cement (w/c ratio) is accounted for by Equation (8) and Equation (9) respectively where H is a constant and α_{tot} is the total degree of hydration of all four clinker phases. The fraction of clinker hydrated at each time step is given by $\alpha_t = \alpha_t - 1 + \Delta t \cdot R_{t-1}$.Writing Equation (4-9) into PHREEQC proceeds with variable time-steps with only 47 steps required to predict the dissolution of the clinker phases for a simulated 1,000 days of hydration. The constants $K^{1\text{-}3}$, $N^{1,3}$ H, and E_a^m) can be found in [17].

3.2 Dissolution of Oxides Dissolved in OPC Clinker

The model input predefines the molar amounts of the oxide components (K_2O, Na_2O, MgO &, and SO_3) dissolved in the OPC clinker phases (C_3S, C_2S, C_3A &, and C_4AF) using the compositions and method described by [18]. The oxide components therefore proportional to the dissolution of the OPC clinker phases as described above.

Table 3 End-members and DSP for the CSH3T model

Phase	Mole fractions			DSP dissolution reaction	log K (25ºC)	Analytical expression parameters (Eqn. 1)			Vol. cm^3/mol
	i	j	k			*a*	*c*	*d*	
CSH3T-TobH (i)	1	0	0	$(CaO)_1(SiO_2)_{1.5}(H_2O)_{2.5} + 2H^+ = Ca^{2+} + 3.5H_2O + 1.5\ SiO_{2(aq)}$	12.5288	-18.8214	3282.490	8.22098	84.960
3T-DSP$_1$	0.8	0.2	0	$(CaO)_{1.05}(SiO_2)_{1.45}(H_2O)_{2.5} + 2.1\ H^+ = 1.05\ Ca^{2+} + 3.55\ H_2O + 1.45\ SiO_{2(aq)}$	13.4332	-18.9776	3651.678	8.149126	83.820
3T-DSP$_2$	0.6	0.4	0	$(CaO)_{1.1}(SiO_2)_{1.4}(H_2O)_{2.5} + 2.2\ H^+ = 1.1\ Ca^{2+} + 3.6\ H_2O + 1.4\ SiO_{2(aq)}$	14.4799	-18.9962	4020.934	8.079203	82.680
3T-DSP$_3$	0.4	0.6	0	$(CaO)_{1.15}(SiO_2)_{1.35}(H_2O)_{2.5} + 2.3\ H^+ = 1.15\ Ca^{2+} + 3.65\ H_2O + 1.35\ SiO_{2(aq)}$	15.6016	-18.9399	4390.190	8.009281	81.540
3T-DSP$_4$	0.2	0.8	0	$(CaO)_{1.2}(SiO_2)_{1.3}(H_2O)_{2.5} + 2.4\ H^+ = 1.2\ Ca^{2+} + 3.7\ H_2O + 1.3\ SiO_{2(aq)}$	16.7983	-18.8086	4759.446	7.939358	80.400
CSH3T-T5C (j)	0	1	0	$((CaO)_1(SiO_2)_1(H_2O)_2)_{1.25} + 2.5H^+ = 1.25Ca^{2+} + 3.75H_2O + 1.25SiO_{2(aq)}$	18.1373	-18.5190	5127.790	7.864154	79.261
3T-DSP$_5$	0.8	0	0.2	$(CaO)_{1.1}(SiO_2)_{1.4}(H_2O)_{2.5} + 2.2\ H^+ = 1.1\ Ca^{2+} + 3.6\ H_2O + 1.4\ SiO_{2(aq)}$	14.8599	-18.9213	4111.716	8.079203	84.080
3T-DSP$_6$	0.6	0.2	0.2	$(CaO)_{1.15}(SiO_2)_{1.35}(H_2O)_{2.5} + 2.3\ H^+ = 1.15\ Ca^{2+} + 3.65\ H_2O + 1.35\ SiO_{2(aq)}$	15.7862	-19.0603	4480.972	8.009281	82.940
3T-DSP$_7$	0.4	0.4	0.2	$(CaO)_{1.2}(SiO_2)_{1.3}(H_2O)_{2.5} + 2.4\ H^+ = 1.2\ Ca^{2+} + 3.7\ H_2O + 1.3\ SiO_{2(aq)}$	16.8625	-19.0494	4850.228	7.939358	81.800
3T-DSP$_8$	0.2	0.6	0.2	$(CaO)_{1.25}(SiO_2)_{1.25}(H_2O)_{2.5} + 2.5\ H^+ = 1.25\ Ca^{2+} + 3.75\ H_2O + 1.25\ SiO_{2(aq)}$	18.0296	-18.9476	5219.484	7.869436	80.660
3T-DSP$_9$	0	0.8	0.2	$(CaO)_{1.3}(SiO_2)_{1.2}(H_2O)_{2.5} + 2.6\ H^+ = 1.3\ Ca^{2+} + 3.8\ H_2O + 1.2\ SiO_{2(aq)}$	19.3467	-18.6959	5588.739	7.799513	79.520
3T-DSP$_{10}$	0.6	0	0.4	$(CaO)_{1.2}(SiO_2)_{1.3}(H_2O)_{2.5} + 2.4\ H^+ = 1.2\ Ca^{2+} + 3.7\ H_2O + 1.3\ SiO_{2(aq)}$	17.3333	-18.8835	4941.009	7.939358	83.199
3T-DSP$_{11}$	0.4	0.2	0.4	$(CaO)_{1.25}(SiO_2)_{1.25}(H_2O)_{2.5} + 2.5\ H^+ = 1.25\ Ca^{2+} + 3.75\ H_2O + 1.25\ SiO_{2(aq)}$	18.2892	-18.9931	5310.26	7.869436	82.059
3T-DSP$_{12}$	0.2	0.4	0.4	$(CaO)_{1.3}(SiO_2)_{1.2}(H_2O)_{2.5} + 2.6\ H^+ = 1.3\ Ca^{2+} + 3.8\ H_2O + 1.2\ SiO_{2(aq)}$	19.4109	-18.9367	5679.52	7.799513	80.920
3T-DSP$_{13}$	0	0.6	0.4	$(CaO)_{1.35}(SiO_2)_{1.15}(H_2O)_{2.5} + 2.7\ H^+ = 1.35\ Ca^{2+} + 3.85\ H_2O + 1.15\ SiO_{2(aq)}$	20.6984	-18.7145	6048.77	7.729591	79.780
3T-DSP$_{14}$	0.4	0	0.6	$(CaO)_{1.3}(SiO_2)_{1.2}(H_2O)_{2.5} + 2.6\ H^+ = 1.3\ Ca^{2+} + 3.8\ H_2O + 1.2\ SiO_{2(aq)}$	19.8817	-18.7708	5770.30	7.799513	82.319
3T-DSP$_{15}$	0.2	0.2	0.6	$(CaO)_{1.35}(SiO_2)_{1.15}(H_2O)_{2.5} + 2.7\ H^+ = 1.35\ Ca^{2+} + 3.85\ H_2O + 1.15\ SiO_{2(aq)}$	20.8830	-18.8349	6139.55	7.729591	81.179
3T-DSP$_{16}$	0	0.4	0.6	$(CaO)_{1.4}(SiO_2)_{1.1}(H_2O)_{2.5} + 2.8\ H^+ = 1.4\ Ca^{2+} + 3.9\ H_2O + 1.1\ SiO_{2(aq)}$	22.1251	-18.6581	6508.81	7.659668	80.039
3T-DSP$_{17}$	0.2	0	0.8	$(CaO)_{1.4}(SiO_2)_{1.1}(H_2O)_{2.5} + 2.8\ H^+ = 1.4\ Ca^{2+} + 3.9\ H_2O + 1.1\ SiO_{2(aq)}$	22.5051	-18.5832	6599.59	7.659668	81.439
3T-DSP$_{18}$	0	0.2	0.8	$(CaO)_{1.45}(SiO_2)_{1.05}(H_2O)_{2.5} + 2.9\ H^+ = 1.45\ Ca^{2+} + 3.95\ H_2O + 1.05\ SiO_{2(aq)}$	23.6268	-18.5268	6968.85	7.589746	80.299
CSH3T-T2C (k)	0	0	1	$((CaO)_{0.75}(SiO_2)_{0.5}(H_2O)_{1.25})_2 + 3H^+ = 1.5Ca^{2+} + 4H_2O + SiO_{2(aq)}$	25.2708	-18.2427	7428.083	7.517428	80.558

Table 4 End-members and DSP for the CSHQ model

Phase	Mole fractions				DSP dissolution reaction	Log K (25ºC)	Analytical expression (Eqn. 1)			Vol. cm^3/mol
	l	m	n	o			*a*	*c*	*d*	
CSHQ-TobH (l)	1	0	0	0	$(CaO)_{0.6667}(SiO_2)1(H_2O)_{1.5} + 1.3334H^+ = 0.6667Ca^{2+} + 2.1667H_2O + SiO_{2(aq)}$	8.2866	-12.5193	2163.382	5.476331	55.00
Q-DSP$_1$	0.8	0.2	0	0	$(CaO)_{0.700035}(SiO_2)_{0.93334}(H_2O)_{1.566685} + 1.40007\ H^+ = 0.700035\ Ca^{2+} + 2.26672\ H_2O + 0.93334\ SiO_{2(aq)}$	9.1431	-12.4160	2522.579	5.293837	53.60
Q-DSP$_2$	0.6	0.4	0	0	$(CaO)_{0.73337}(SiO_2)_{0.86668}(H_2O)_{1.63337} + 1.46674\ H^+ = 0.73337\ Ca^{2+} + 2.36674\ H_2O + 0.86668\ SiO_{2(aq)}$	10.1418	-12.1704	2881.952	5.111348	52.20
Q-DSP$_3$	0.4	0.6	0	0	$(CaO)_{0.766705}(SiO_2)_{0.80002}(H_2O)_{1.700055} + 1.53341\ H^+ = 0.766705\ Ca^{2+} + 2.46676\ H_2O + 0.80002\ SiO_{2(aq)}$	11.2156	-11.8498	3241.324	4.928858	50.80
Q-DSP$_4$	0.2	0.8	0	0	$(CaO)_{0.80004}(SiO2)_{0.73336}(H_2O)_{1.76674} + 1.60008\ H^+ = 0.80004\ Ca^{2+} + 2.56678\ H_2O + 0.73336\ SiO_{2(aq)}$	12.3643	-11.4542	3600.697	4.746369	49.40
CSHQ-TobD (m)	0	1	0	0	$((CaO)_{1.25}(SiO_2)1(H_2O)_{2.75})_{0.6667} + 1.66675H^+ = 0.833375Ca^{2+} + 2.6668H_2O + 0.6667SiO_{2(aq)}$	13.6553	-10.9163	3959.368	4.563888	48.00
Q-DSP$_5$	0.8	0	0.2	0	$(CaO)_{0.80002}(SiO_2)_1(H_2O)_{1.63334} + 1.60004\ H^+ = 0.80002\ Ca^{2+} + 2.43336\ H_2O + SiO_{2(aq)}$	10.8479	13.6546	3024.214	5.802628	59.20
Q-DSP$_6$	0.6	0.2	0.2	0	$(CaO)_{0.833355}(SiO_2)_{0.93334}(H_2O)_{1.700025} + 1.66671\ H^+ = 0.833355\ Ca^{2+} + 2.53338\ H_2O + 0.93334\ SiO_{2(aq)}$	11.7262	-13.5294	3383.587	5.620139	57.80
Q-DSP$_7$	0.4	0.4	0.2	0	$(CaO)_{0.86669}(SiO_2)_{0.86668}(H_2O)_{1.76671} + 1.73338\ H^+ = 0.86669\ Ca^{2+} + 2.63340\ H_2O + 0.86668\ SiO_{2(aq)}$	12.7545	-13.2543	3742.959	5.437650	56.40

Q-DSP$_8$	0.2	0.6	0.2	0	$(CaO)_{0.900025}(SiO_2)_{0.80002}(H_2O)_{1.833395}$ + 1.80005 H^+ = 0.900025 Ca^{2+} + 2.73342 H_2O + 0.80002 $SiO_{2(aq)}$	13.8737	-12.8882	4102.332	5.255160	55.00
Q-DSP$_9$	0	0.8	0.2	0	$(CaO)_{0.93336}(SiO_2)_{0.73336}(H_2O)_{1.90008}$ + 1.86672 H^+ = 0.93336 Ca^{2+} + 2.83344 H_2O + 0.73336 $SiO_{2(aq)}$	15.1428	-12.3723	4461.705	5.072671	53.60
Q-DSP$_{10}$	0.6	0	0.4	0	$(CaO)_{0.93334}(SiO_2)_1(H_2O)_{1.76668}$ + 1.86668 H^+ = 0.93334 Ca^{2+} + 2.70002 H_2O + $SiO_{2(aq)}$	13.5514	-14.6476	3885.222	6.128930	63.40
Q-DSP$_{11}$	0.4	0.2	0.4	0	$(CaO)_{0.966675}(SiO_2)_{0.93334}(H_2O)_{1.833365}$ + 1.93335 H^+ = 0.966675 Ca^{2+} + 2.80004 H_2O + 0.93334 $SiO_{2(aq)}$	14.4593	-14.4929	4244.594	5.946441	62.00
Q-DSP$_{12}$	0.2	0.4	0.4	0	$(CaO)_{1.00001}(SiO_2)_{0.86668}(H_2O)_{1.90005}$ + 2.00002 H^+ = 1.00001 Ca^{2+} + 2.90006 H_2O + 0.86668 $SiO_{2(aq)}$	15.5330	-14.1723	4603.967	5.763952	60.60
Q-DSP$_{13}$	0	0.6	0.4	0	$(CaO)_{1.033345}(SiO_2)_{0.80002}(H_2O)_{1.966735}$ + 2.06669 H^+ = 1.033345 Ca^{2+} + 3.00008 H_2O + 0.80002 $SiO_{2(aq)}$	16.7726	-13.6858	4963.340	5.581462	59.20
Q-DSP$_{14}$	0.4	0	0.6	0	$(CaO)_{1.06666}(SiO_2)_1(H_2O)_{1.90002}$ + 2.13332 H^+ = 1.06666 Ca^{2+} + 2.96668 H_2O + $SiO_{2(aq)}$	16.3300	-15.5656	4746.229	6.455232	67.60
Q-DSP$_{15}$	0.2	0.2	0.6	0	$(CaO)_{1.099995}(SiO_2)_{0.93334}(H_2O)_{1.966705}$ + 2.19999 H^+ = 1.099995 Ca^{2+} + 3.0667 H_2O + 0.93334 $SiO_{2(aq)}$	17.2833	-15.3655	5105.602	6.272743	66.20
Q-DSP$_{16}$	0	0.4	0.6	0	$(CaO)_{1.13333}(SiO_2)_{0.86668}(H_2O)_{2.03339}$ + 2.26666 H^+ = 1.13333 Ca^{2+} + 3.16672 H_2O + 0.86668 $SiO_{2(aq)}$	18.4774	-14.9245	5464.975	6.090254	64.80
Q-DSP$_{17}$	0.2	0	0.8	0	$(CaO)_{1.19998}(SiO_2)_1(H_2O)_{2.03336}$ + 2.39996 H^+ = 1.19998 Ca^{2+} + 3.23334 H_2O + $SiO_{2(aq)}$	19.1835	-16.4087	5607.237	6.781534	71.80
Q-DSP$_{18}$	0	0.2	0.8	0	$(CaO)_{1.233315}(SiO_2)_{0.93334}(H_2O)_{2.100045}$ + 2.46663 H^+ = 1.233315 Ca^{2+} + 3.33336 H_2O + 0.93334 $SiO_{2(aq)}$	20.2572	-16.0881	5966.610	6.599045	70.40
CSHQ-JenH (n)	0	0	1	0	$(CaO)_{1.3333}(SiO_2)_1(H_2O)_{2.1667}$ + 2.6666H^+ = 1.3333Ca^{2+} + 3.5H_2O + $SiO_{2(aq)}$	22.1793	-17.1094	6470.554	7.107847	76.00
Q-DSP$_{19}$	0	0.8	0.2	0	$(CaO)_{0.93336}(SiO_2)_{0.73336}(H_2O)_{1.90008}$ + 1.86672 H+ = 0.93336 Ca^{2+} + 2.83344 H_2O + 0.73336 $SiO_{2(aq)}$	15.1428	-12.3723	4461.705	5.072671	53.60
Q-DSP$_{20}$	0	0.6	0.4	0	$(CaO)_{1.033345}(SiO_2)_{0.80002}(H_2O)_{1.966735}$ + 2.06669 H+ = 1.033345 Ca^{2+} + 3.00008 H_2O + 0.80002 $SiO_{2(aq)}$	16.7726	-13.6858	4963.340	5.581462	59.20
Q-DSP$_{21}$	0	0.4	0.6	0	$(CaO)_{1.13333}(SiO_2)_{0.86668}(H_2O)_{2.03339}$ + 2.26666 H^+ = 1.13333 Ca^{2+} + 3.16672 H_2O + 0.86668 SiO_2	18.4774	-14.9245	5464.975	6.090254	64.80
Q-DSP$_{22}$	0	0.2	0.8	0	$(CaO)_{1.233315}(SiO_2)_{0.93334}(H_2O)_{2.100045}$ + 2.46663 H^+ = 1.233315 Ca^{2+} + 3.33336 H_2O + 0.93334 $SiO_{2(aq)}$	20.2572	-16.0881	5966.610	6.599045	70.40
Q-DSP$_{23}$	0	0.8	0	0.2	$(CaO)_{0.9667}(SiO_2)_{0.6667}(H_2O)_{1.96674}$ + 1.9334 H^+ = 0.9667 Ca^{2+} + 2.93344 H_2O + 0.6667 $SiO_{2(aq)}$	16.4530	-12.0687	4.890.00	4.899604	54.60
Q-DSP$_{24}$	0	0.6	0.2	0.2	$(CaO)_{1.066685}(SiO_2)_{0.73336}(H_2O)_{2.033395}$ + 2.13337 H^+ = 1.066685 Ca^{2+} + 3.10008 H_2O + 0.73336 $SiO_{2(aq)}$	17.9624	-13.5027	5391.63	5.408395	60.20
Q-DSP$_{25}$	0	0.4	0.4	0.2	$(CaO)_{1.16667}(SiO_2)_{0.80002}(H_2O)_{2.10005}$ + 2.33334 H^+ = 1.16667 Ca^{2+} + 3.26672 H_2O + 0.80002 $SiO_{2(aq)}$	19.6218	-14.7868	5893.27	5.917186	65.80
Q-DSP$_{26}$	0	0.2	0.6	0.2	$(CaO)_{1.266655}(SiO_2)_{0.86668}(H_2O)_{2.166705}$ + 2.53331 H^+ = 1.266655 Ca^{2+} + 3.43336 H_2O + 0.86668 $SiO_{2(aq)}$	21.3720	-15.9800	6394.90	6.425978	71.40
Q-DSP$_{27}$	0	0	0.8	0.2	$(CaO)_{1.36664}(SiO_2)_{0.93334}(H_2O)_{2.23336}$ + 2.73328 H^+ = 1.36664 Ca^{2+} + 3.6 H_2O + 0.93334 $SiO_{2(aq)}$	23.2722	-17.0232	6896.54	6.934769	77.00
Q-DSP$_{28}$	0	0.6	0	0.4	$(CaO)_{1.100025}(SiO_2)_{0.6667}(H_2O)_{2.100055}$ + 2.20005 H^+ = 1.100025 Ca^{2+} + 3.20008 H_2O + 0.6667 $SiO_{2(aq)}$	19.3930	-13.0788	5819.93	5.235327	61.20
Q-DSP$_{29}$	0	0.4	0.2	0.4	$(CaO)_{1.20001}(SiO_2)_{0.73336}(H_2O)_{2.16671}$ + 2.40002 H^+ = 1.20001 Ca^{2+} + 3.36672 H_2O + 0.73336 $SiO_{2(aq)}$	20.9320	-14.4832	6321.57	5.744119	66.80
Q-DSP$_{30}$	0	0.2	0.4	0.4	$(CaO)_{1.299995}(SiO_2)_{0.80002}(H_2O)_{2.233365}$ + 2.59999 H+ = 1.299995 Ca^{2+} + 3.53336 H_2O + 0.80002 $SiO_{2(aq)}$	22.6368	-15.7219	6823.20	6.252910	72.40
Q-DSP$_{31}$	0	0	0.6	0.4	$(CaO)_{1.39998}(SiO_2)_{0.86668}(H_2O)_{2.30002}$ + 2.79996 H^+ = 1.39998 Ca^{2+} + 3.7 H_2O + 0.86668 $SiO_{2(aq)}$	24.5074	-16.7946	7324.84	6.761701	78.00
Q-DSP$_{32}$	0	0.4	0	0.6	$(CaO)_{1.23335}(SiO_2)_{0.6667}(H_2O)_{2.23337}$ + 2.4667 H^+ = 1.23335 Ca^{2+} + 3.46672 H_2O + 0.6667 $SiO_{2(aq)}$	22.4081	-14.0138	6749.87	5.571051	67.80
Q-DSP$_{33}$	0	0.2	0.2	0.6	$(CaO)_{1.333335}(SiO_2)_{0.73336}(H_2O)_{2.300025}$ + 2.66667 H^+ = 1.333335 Ca^{2+} + 3.63336 H_2O + 0.73336 $SiO_{2(aq)}$	23.9924	-15.3729	7251.50	6.079843	73.40
Q-DSP$_{34}$	0	0	0.4	0.6	$(CaO)_{1.43332}(SiO_2)_{0.80002}(H_2O)2.36668$ + 2.86664 H^+ = 1.43332 Ca^{2+} + 3.8 H_2O + 0.80002 $SiO_{2(aq)}$	25.8177	-16.4911	7753.14	6.588634	79.00
Q-DSP$_{35}$	0	0.2	0	0.8	$(CaO)_{1.366675}(SiO_2)_{0.6667}(H_2O)_{2.366685}$ + 2.73335 H^+ = 1.366675 Ca^{2+} + 3.73336 H_2O + 0.6667 $SiO_{2(aq)}$	25.4980	-14.8740	7679.80	5.906775	74.40
Q-DSP$_{36}$	0	0	0.2	0.8	$(CaO)_{1.46666}(SiO_2)_{0.73336}(H_2O)_{2.43334}$ + 2.93332 H^+ = 1.46666 Ca^{2+} + 3.9 H_2O + 0.73336 $SiO_{2(aq)}$	27.2028	-16.1126	8181.43	6.415566	80.00
CSHQ-JenD (o)	0	0	0	1	$(CaO)_{1.5}(SiO_2)_{0.6667}(H_2O)_{2.5}$ + 3H^+ = 1.5Ca^{2+} + 4H_2O + 0.6667$SiO_{2(aq)}$	28.7304	-15.5918	8609.740	6.24251	81.00

$$R_t = \frac{K^1}{N^1}(1-\alpha_t)\left(-ln(1-\alpha_t)\right)^{(1-N^1)} \cdot \frac{A}{A_0} \cdot f(T) \cdot f(RH) \cdot f(\frac{w}{c}) \quad (4)$$

$$R_t = \frac{K^2(1-\alpha_t)^{\frac{2}{3}}}{1-(1-\alpha_t)^{\frac{1}{3}}} \cdot f(T) \cdot f(RH) \cdot f(\frac{w}{c}) \quad (5)$$

$$R_t = K^3(1-\alpha_t)^{N^3} \cdot f(T) \cdot f(RH) \cdot f(\frac{w}{c}) \quad (6)$$

$$f(T) = exp\left[\frac{E_a^m}{R}\left(\frac{1}{T}-\frac{1}{T_0}\right)\right] \quad (7)$$

$$f(RH) = \left(\frac{RH-0.55}{0.45}\right)^4 \quad (8)$$

$$f(\tfrac{w}{c}) = (1+3.333\cdot(\mathrm{H}\cdot\tfrac{w}{c}-\alpha_{tot}))^4; \text{ for } \alpha_{tot} > \mathrm{H}\cdot\tfrac{w}{c} \quad (9)$$

Table 5 Cement oxide and clinker phase proportions

Oxide proportions (wt.%)		Phase composition	
		Phase	g/100g
SiO_2	20.19	C_3S	46.90
Al_2O_3	4.79	C_2S	20.93
Fe_2O_3	2.86	C_3A	7.64
CaO	62.50	C_4AF	8.47
MgO	1.68	Calcite	4.62
Na_2O	0.63	Gypsum	4.19
K_2O	0.16	K_2SO_4	0.26
CaO (free)	1.50	Lime	1.46
CO_2	2.09	Na_2SO_4	0.63
SO_3	2.49	K_2O	0.02
Periclase	0.50	Na_2O	0.34
Blaine fineness (m^2/kg)	419	MgO	1.63
Loss in ignition	2.72	SO_3	2.42

3.3 Accessory Clinker Phases

The remaining accessory clinker phases lime (CaO), calcite ($CaCO_3$), gypsum ($CaSO_4 \cdot 2H_2O$), periclase (MgO), and the alkali metal sulfates (K_2SO_4 & Na_2SO_4) are allowed to reach equilibrium with the pore solution in the first time-step and are immediately available to dissolve and contribute to the precipitation of solid hydrate phases. Due to the immediate availability of free lime, periclase and the alkali metal sulfates for example, result in the precipitation of small amounts of portlandite and gypsum.

3.4 Oversaturation

To increase the solubility of precipitating solid hydrate phases, gypsum, C-S-H gel (as DSP), portlandite, syngenite, brucite and ettringite are assigned a saturation index (SI), given by 0.15(*n*) (Table 6) to account for their oversaturation in the first 12 hours of hydration, where *n* is the number of number of charged aqueous species involved in the dissolution reaction.

3.5 Alkalis binding to the C-S-H

The distribution of the alkali elements K and Na between the pore solution and the C-S-H gel was defined by a distribution coefficient (*Kd*, mL/g) using values of 1.0 and 0.80 for K and Na in the CSH3T model where C-S-H gel having a Ca:Si ratio of 1.5 [19]. For the CSHQ, a *Kd* of 0.42 was used for both on a Ca:Si ratio of 1.8 [19].

3.6 Modelling predictions

The predicted phase assemblages using the CEMDATA database [11] and PHREEQC geochemical software [12] for the CSH3T and CSHQ models are shown in Figure 1 and Figure 2 respectively. As may be seen, thermodynamic modelling predicts the presence of C-S-H, portlandite, hydrotalcite, and ettringite, with small amounts of brucite, hydrogarnet and monocarbonate. The precipitation of monocarbonate helps to stabilize the formation of ettringite, leading to a higher volume (and compressive strength) than if monosulfate was predicted to form. This agrees well with similar observations in the literature [17].

4 DISCUSSION

The above work shows how C-S-H gel solubility can be modelled as a series of DSP, which can be derived from the CSH3T and CSHQ end-members provided in the CEMDATA database. It should be noted however, that a solid solution model is not required to model OPC hydration, which in fact only requires portlandite and a suitable C-S-H gel phase of fixed C/S = 1.6-1.8 and water/Si (H/S) molar ratios = 2.0-2.1. In the DSP model presented in [10], these values are closely matched by the CSH165 phase, which has a C/S = 1.65 and H/S = 2.1167. In the current work, the CSH3T model predicted only the precipitation of 3T-DSP_{18} to represent C-S-H gel, which with a C/S = 1.38 and H/S = 2.38 is not suitable to represent C-S-H gel in hydrated OPC. The CSH3T model should therefore only be used in cement blends where lower C/S ratios are purposefully targeted by the addition of supplementary cementitious materials (SCM). Similarly, the CSHQ model predicted that only Q-DSP_{29} would precipitate to represent C-S-H gel, which has a C/S = 1.64 and H/S = 2.95. In this case the C/S ratio is satisfactory, but the H/S ratio is too large resulting incorrect predictions of the amount of C-S-H gel, free water and pH and so too therefore the dissolution of the solid

Table 6 n values and saturation indices (S.I. = 0.15·n)

Phase	Composition	N	S.I. < 12hrs
Brucite	$Mg(OH)_2$	3	0.45
Ettringite	$Ca_6(Al(OH)_6)_2(SO_4)_3(H_2O)_{26}$	15	2.25
Gypsum	$CaSO_4(H_2O)_2$	2	0.30
Portlandite	$Ca(OH)_2$	3	0.45
Syngenite	$K_2Ca(SO_4)_2(H_2O)$	5	0.75

CSH3T	*n*	SI	CSHQ	*n*	SI
TobH	3.00	0.45	*TobH*	2.00	0.30
3T-DSP_1	3.15	0.47	Q-DSP_1	2.10	0.32
3T-DSP_2	3.30	0.50	Q-DSP_2	2.20	0.33
3T-DSP_3	3.45	0.52	Q-DSP_3	2.30	0.35
3T-DSP_4	3.60	0.54	Q-DSP_4	2.40	0.36
T5C	3.75	0.56	*TobD*	2.50	0.38
3T-DSP_5	3.30	0.49	Q-DSP_5	2.40	0.36
3T-DSP_6	3.45	0.52	Q-DSP_6	2.50	0.38
3T-DSP_7	3.60	0.54	Q-DSP_7	2.60	0.39
3T-DSP_8	3.75	0.56	Q-DSP_8	2.70	0.41
3T-DSP_9	3.90	0.58	Q-DSP_9	2.80	0.42
3T-DSP_{10}	3.60	0.54	Q-DSP_{10}	2.80	0.42
3T-DSP_{11}	3.75	0.56	Q-DSP_{11}	2.90	0.44
3T-DSP_{12}	3.90	0.59	Q-DSP_{12}	3.00	0.45
3T-DSP_{13}	4.05	0.61	Q-DSP_{13}	3.10	0.47
3T-DSP_{14}	3.90	0.58	Q-DSP_{14}	3.20	0.48
3T-DSP_{15}	4.05	0.61	Q-DSP_{15}	3.30	0.49
3T-DSP_{16}	4.20	0.63	Q-DSP_{16}	3.40	0.51
3T-DSP_{17}	4.20	0.63	Q-DSP_{17}	3.60	0.54
3T-DSP_{18}	4.35	0.65	Q-DSP_{18}	3.70	0.55
T2C	4.50	0.68	*JenH*	4.00	0.60
			Q-DSP_{19}	2.80	0.42
			Q-DSP_{20}	3.10	0.47
			Q-DSP_{21}	3.40	0.51
			Q-DSP_{22}	3.70	0.55
			Q-DSP_{23}	2.90	0.44
			Q-DSP_{24}	3.20	0.48
			Q-DSP_{25}	3.50	0.53
			Q-DSP_{26}	3.80	0.57
			Q-DSP_{27}	4.10	0.61
			Q-DSP_{28}	3.30	0.50
			Q-DSP_{29}	3.60	0.54
			Q-DSP_{30}	3.90	0.58
			Q-DSP_{31}	4.20	0.63
			Q-DSP_{32}	3.70	0.56
			Q-DSP_{33}	4.00	0.60
			Q-DSP_{34}	4.30	0.64
			Q-DSP_{35}	4.10	0.62
			Q-DSP_{36}	4.40	0.66
			JenD	4.50	0.68

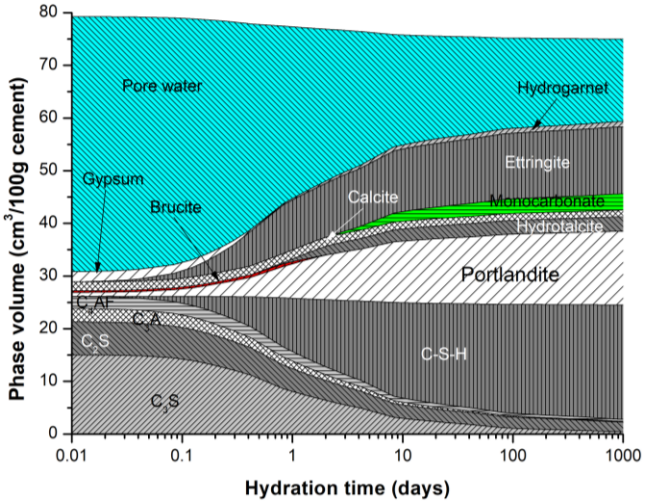

Figure 1 Phase assemblage predictions for the CSH-3T

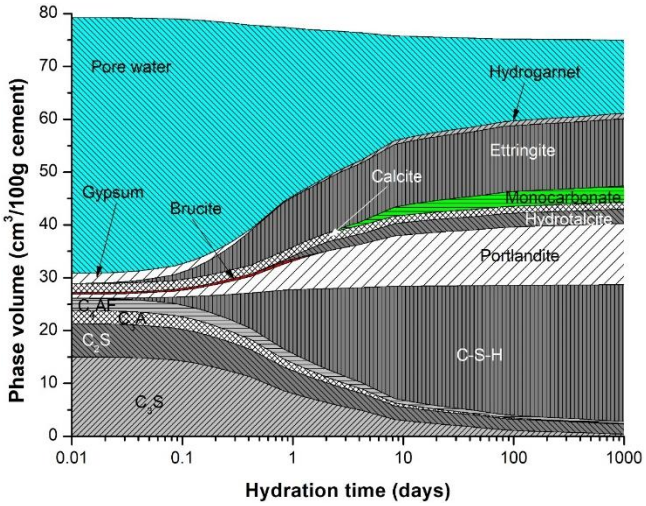

Figure 2 Phase assemblage predictions for the CSHQ

hydrate phases and the composition of the porewater.

Solid solution modelling encompasses all known synthetic ranges of C-S-H gels, which are in fact only needed if portlandite is lost and the Ca/Si ratio in the C-S-H gel is lowered, either by the addition of siliceous SCM or by chemical degradation in increasingly larger volumes of leachate provided by the ingress of groundwater or seawater.

5 CONCLUSIONS

The above work has derived a series of DSP to describe the incongruent dissolution of C-S-H gel from the end-members of two C-S-H gel solubility models, CSH3T and CSHQ, as provided in the CEMDATA thermodynamic database. Both DSP C-S-H gel solubility models were used to simulate the hydration of OPC with the geochemical code PHREEQC. The computational time in both cases was less than one minute with discernible loss in accuracy. While it is possible to model these end-members as sold solutions in PHREEQC, the analysis time is significantly slower. In the case of modelling OPC hydration, only one C-S-H gel phase and portlandite are required thereby making the derivation of the DSP model unnecessary. In the CSH3T model, however, the predicted C-S-H gel composition was C/S = 1.38 and H/S = 2.38, which does not match known C-S-H gel compositions in hydrated OPC. On the other hand, the CSHQ model predicted a C-S-H gel composition with a satisfactory C/S = 1.64, but the predicted H/S = 2.95 was too high. Solid solutions and the derivation of a series of DSP are a thermodynamic credible approach to model the incongruent solubility behaviour of C-S-H gel but are only required for modelling hydration of OPC with the addition of siliceous SCM or for hydrated OPC undergoing chemical attack.

REFERENCES

[1] J. Bruno, D. Bosbach, D. Kulik, and A. Navrotsky, "Chemical Thermodynamics of Solid Solutions of Interest in Nuclear Waste Management," in "Chemical Thermodynamics Vol. 10," North Holland Elsevier Science Publishers B.V., Amsterdam, The Netherlands, 2007.

[2] E. Curti, "Coprecipitation of radionuclides with calcite: estimation of partition coefficients based on a review of laboratory investigations and geochemical data," *Applied Geochemistry*, vol. 14, no. 4, pp. 433-445, 1999, doi: https://doi.org/10.1016/S0883-2927(98)00065-1.

[3] D. A. Kulik, "Improving the structural consistency of C-S-H solid solution thermodynamic models," *Cem. Concr. Res.*, vol. 41, no. 5, pp. 477-495, 2011.

[4] A. Atkinson, J. A. Hearne, and C. F. Knights, "Aqueous chemistry and thermodynamic modeling of CaO-SiO2-H2O gels," *J. Chem. Soc. Dalt. Trans.*, no. 12, pp. 2371-2379, 1989.

[5] T. Matschei, B. Lothenbach, and F. P. Glasser, "Thermodynamic properties of Portland cement hydrates in the system $CaO–Al_2O_3–SiO_2–CaSO_4–CaCO_3–H_2O$," *Cem. Concr. Res.*, vol. 37, no. 10, pp. 1379-1410, 2007.

[6] G. Möschner, B. Lothenbach, F. Winnefeld, A. Ulrich, R. Figi, and R. Kretzschmar, "Solid solution between Al-ettringite and Fe-ettringite $(Ca[Al_{1-x}Fe_x(OH)_6]_2(SO_4)_3.26H_2O$," *Cem. Concr. Res.*, vol. 39, no. 6, pp. 482-489, 2009.

[7] B. Z. Dilnesa *et al.*, "Iron in carbonate containing AFm phases," *Cem. Concr. Res.*, vol. 41, no. 3, pp. 311-323, 2011.

[8] M. Y. Hobbs, "Solubilities and ion exchange properties of solid solutions between the OH, Cl and CO3 end members of the monocalcium aluminate hydrates," Ph.D., Earth Sciences, University of Waterloo, Waterloo, Ontario, Canada, 2001.

[9] D. Kulik, G. D. Miron, and B. Lothenbach, "A structurally consistent CASH+ sublattice solid solution model for fully hydrated C-S-H phases: Thermodynamic basis, methods, and Ca-Si-H_2O core sub-model," *Cem. Concr. Res.*, vol. 151, p. 106585, 2022.

[10] C. S. Walker, S. Sutou, C. Oda, M. Mihara, and A. Honda, "Calcium silicate hydrate (C-S-H) gel solubility data and a discrete solid phase model at 25ºC based on two binary non-ideal solid solutions," *Cem. Concr. Res.*, vol. 79, pp. 1-30, 2016.

[11] B. Lothenbach *et al.*, "Cemdata18: A chemical thermodynamic database for hydrated Portland cements and alkali-activated materials," *Cement and Concrete Research*, vol. 115, pp. 472–506, 2019.

[12] D. J. Parkhurst and C. A. J. Appelo, "Description of Input and Examples for PHREEQC Version 3 - A Computer Program for Speciation, Batch-reaction, One-dimensional Transport and Inverse Geochemical Calculations," USGS, Denver, 2013.

[13] W. Hummel, U. Berner, E. Curti, F. J. Pearson, and T. Thoenen, *Nagra / PSI Chemical Thermodynamic Database 01/01*. Florida, USA: Universal Publishers, 2002, p. 589.

[14] L. J. Parrot and D. C. Killoh, "Prediction of cement hydration," *Brit. Ceram. Proc.*, vol. 35, pp. 41-53, 1984.

[15] B. Lothenbach and F. Winnefeld, "Thermodynamic modelling of the hydration of Portland cement," *Cem. Concr. Res.*, vol. 36, no. 2, pp. 209-226, 2006.

[16] S. Y. Hong and F. P. Glasser, "Alkali binding in cement pastes Part I: The C-S-H phase," *Cem. Concr. Res.*, vol. 29, no. 12, pp. 1893-1903, 1999.

[17] B. Lothenbach, G. L. Saout, E. Gallucci, and K. Scrivener, "Influence of limestone on the hydration of Portland cements," *Cement and Concrete Research*, vol. 38, pp. 848–860, 2008.

[18] H. F. W. Taylor, *Cement Chemistry*. Thomas Telford Publishing, 1997.

[19] S. Y. Hong and F. P. Glasser, "Alkali binding in cement pastes: Part I. The C-S-H phase," *Cement and Concrete Research*, vol. 29, pp. 1893–1903, 1999.

Effect of the early dissolution of Al-phases in reactive industrial wastes, on the setting times and rheology of sustainable binders

Zehao Lei[1], Sara Pavia[1]

[1]Department of Civil, Structural & Environmental Engineering, Trinity College Dublin, College Green, Dublin, Ireland
email: zlei@tcd.ie, PAVIAS@tcd.ie

ABSTRACT: Aluminium-containing minerals in industrial wastes are relatively common, and they have potential as pozzolans or geopolymer precursors for the production of sustainable cements. The availability of reactive Al plays an important role in the early formation of calcium aluminate hydrate or aluminosilicate gel, thereby influencing setting time and rheology. Setting times affect the transport and placement of mortars and concretes. Excessive or insufficient setting times and poor rheology can distress the construction process. Four industrial wastes are studied, including alum sludge (AS), ground granulated blast-furnace slag (GGBS), fluid catalytic cracking catalyst (FCC) and fly ash (FA). They all contain Al and exhibit pozzolanic activity. The early dissolution of Al ions in saturated lime solutions was quantified with colorimetric methods. The relationships between dissolution rate, rheology and setting times were drawn.

The results indicate that the variation in Al ions concentration in the early solution causes considerable differences in setting times. The aluminate wastes (AS) dissolve fast and reach equilibrium in solution within minutes, setting very quickly. On the contrary, the silico-aluminate wastes (FCC, FA) slowly dissolve for hours or even days, taking much longer to set.

The paper concludes that the form in which Al exists can greatly affect the rate of dissolution of aluminium ions. Al present as disordered oxyhydroxides (i.e. AS) readily contributes significant Al ions into the solution, whereas when the Al is present as silicates (mullite in the FA and zeolite in FCC), dissolution is limited and slow, and setting takes much longer.

KEYWORDS: alum sludge (AS); ground granulated blast-furnace slag (GGBS); fluid catalytic cracking catalyst (FCC); fly ash (FA); industrial waste; Al dissolution; Al ions concentration; setting time; workability; sustainable binders.

1. INTRODUCTION

The European Union commits to carbon neutrality by 2050 through the European Climate Law [1]. By 2030, emissions from buildings, waste management, transportation and agriculture shall be reduced by 30% compared to 2005 levels. These sectors are the main contributors to the EU's greenhouse gas emissions, accounting for about 60% of the total EU emissions in 2014 [2]. Concrete, Portland cement (PC) based, is the most heavily used material in the world apart from water [3]. Twice as much PC concretes and mortars are used than all other building materials combined, including wood, steel, plastic and aluminium [4]. The production of PC is blamed for a significant contribution to climate change due to the consumption of energy for calcination (representing 45% of the CO_2 emission) and decarbonisation of calcium carbonate (representing 55% of the CO_2 emission) [5]. As reported, the CO_2 released on PC production can amount to ~7% of the total global CO_2 emissions [6].

At the 2002 World Climate Change Congress in Rio de Janeiro, the concept of "blended cement" was introduced. However, some blended binders such as pozzolan-limes have been used for thousands of years, and others such as blastfurnace slag cements have been used for over seven decades. Blended cements incorporate supplementary cementitious materials (SCMs) to reduce CO_2, usually in the range of 20% when compared to the production of 1 tonne of PC clinker [5]. Typical examples of industrial wastes that can be successfully incorporated in blended cements are ground granulated blast-furnace slag (GGBS) [7, 8], fly ash (FA) [9, 10] and silica fume (SF) [11, 12].

The incorporation of industrial wastes tends to alter the fresh properties of the materials. Concrete's workability decreases with the addition of SF, but increases when featuring FA [13, 14]. It has been claimed that the change in rheology is brought about by the properties of the waste particles. For example, the spherical geometry and smooth surface of FA enhances workability lowering water demand, while ultrafine SF increases water demand [15]. FCC features spherical particles but does not result in a significant reduction in water demand [16].

Other factors such as the organic matter content and the presence of highly reactive phases are known to also influence the fresh properties of composites [17]. It is well known in cement technology that Al dissolves at a faster rate than Si in an alkaline media, largely controlling the setting properties (changes of consistency over time) of the reaction system [17, 18].

Many industrial wastes and tailings have shown potential as SCMs. Abundant studies aim to understand the influence of SCMs on the nature of the hydration products formed, and the strength they developed. However, little research has focussed

on the influence of the chemical properties of SCMs on the fresh properties of mortars and concretes. This paper studies the dissolution of the Al in several industrial wastes, in saturated alkaline solutions made with lime, and establishes its effect on setting times and workability (measured as the water required to reach a specific initial flow).

2. MATERIALS AND METHODS

2.1 SCMs

Alum sludge (AS), spent FCC catalyst (FCC), fly ash (FA), and ground granulated blast-furnace slag (GGBS) from Ireland, NI and Spain are investigated. The AS was dried and ground in a ball mill for 2 hours and the other SCMs were not processed. Raw AS was calcined for 2h to remove organic matter. The AS specimens are named AS/600 and AS/800 according to the calcination temperatures (600-800°C).

2.2 SCM characterization

The chemical composition of the industrial wastes (Table 1) was measured with an X-Ray fluorescence apparatus (XRF). Their vitreous character or amorphousness was estimated with X-Ray diffraction using the powder method. The loss on ignition (LOI) was calculated by calcination between 105 and 1000 °C. A scanning electron microscope (SEM) apparatus was used to study the morphology of the particle components.

2.3 Particle size distribution

The particle size distribution was determined by laser with a Mastersizer 3000 apparatus. The laser diffraction results are represented as cumulative particle size distribution in % by volume.

2.4 Dissolution of the SCMs Al phases in alkaline solutions

The dissolution of the Al phases in the wastes was measured with a colorimetric method. 250 mg of waste were added to a saturated lime solution (pH=12.74, 23.6 °C) in polyethene centrifugal tubes, and shook in a water bath shaker for times ranging from 10 min to 3 days. The high liquid/solid ratio and consistent shaking were designed to minimise re-precipitation and concentration gradients during testing. After each reaction time, the suspensions were centrifuged at 6000 rpm for 5 min. 10 ml of the upper layer solution was mixed with 1 ml of ascorbic acid solution (1 mol/L), 1 ml of HCl (1 mol/L) and 10 ml of acetic acid/sodium acetate buffer. The ascorbic acid solution was added to reduce the interference of iron ions. Eriochrome cyanine R (ECR) was used as an indicator to measure the concentration of Al in the solution. The solution and ECR indicator were mixed with distilled water and shaken for 10 minutes. The resultant solution was analysed with a spectrophotometer and the maximum absorption read between λ=500 and 600 nm.

2.5 Water demand and setting time

A hydrated commercial lime of European designation CL90s was used to prepare the specimens. The water demand of the wastes (or amount of water required to produce a specific flow value) was assessed with the initial flow diameter test in EN 1015-3[19] for mixes of ratio 1:1:3 (SCM: lime: sand).
Due to the significant influence of the w/b ratio on the setting times, pastes were also fabricated with constant w/b ratio. The w/b=0.75 was selected because most SCMs, except for the FA, provided good workability at this range. The water demand of the FA is very low, hence the water content of the FA specimens was adjusted until the sample, upon removing the mould, reached a diameter of 165 mm after 15 table jolts.
The setting times of the different waste-lime pastes was tested in accordance with EN 196-3:2016 [20] using the Vicat apparatus.

3. RESULTS AND DISCUSSION

3.1 Characterisation of the SCMs

The XRF analyses (Table 1) evidenced that the FCC has the highest Al content, and the second highest Si content after the FA. As expected, the alum sludge is Al-rich, and the GGBS contains abundant Si and Ca.
The XRD results show that all the SCMs are either totally or significantly vitreous, therefore their Al and Si phases are active and hence able to dissolve in alkaline conditions. According to the XRD analyses, the FCC is partially amorphous, and its main crystal phase is the zeolite known as faujasite - $(Na_2,Ca,Mg)_{3.5}[Al_7Si_{17}O_{48}]\cdot 32(H_2O)$. The raw AS is totally amorphous and consists of disordered oxyhydroxides, and at 800°C, some of the amorphous phases transform into semicrystalline γ-Al_2O_3. The FA is significantly vitreous and reactive consisting of glass, quartz (SiO_2) and mullite ($2Al_2O_3$. 2 SiO_2), as determined with XRD [22,23].
The GGBS is a totally amorphous and shows outstanding activity. Furthermore, it has ratios of CaO/SiO_2 = 1.41 and Al_2O_3/SiO_2 =0.34, hence significant qualities for the production of alkali activated cements [22,24].

Table 1. XRF results showing the chemical composition of the wastes as % wt. by oxide and loss on ignition.

Chemical composition	GGBS	FA	FCC	AS
SiO_2	32.00	53.41	41.7	3.19
Al_2O_3	12.00	21.18	49.0	28.3
Fe_2O_3	0.45	10.00	1.28	1.03
CaO	42.00	4.14	0.19	0.17
MgO	8.00	1.86	0.07	0.09
Na_2O	0.03	0.70	0.29	0.06
K_2O	0.50	3.24	0.16	0.05
Cr_2O_3	-	0.07	0.05	0.00
TiO_2	0.75	1.35	1.00	0.03
MnO	0.20	0.08	0.01	0.04
P_2O_5	0.42	0.84	0.26	0.08
Others	3.65	3.13	2.50	0.85
LOI (%) at 1000 °C	-	-	3.70	66.1
Al_2O_3/SiO_2	0.37	0.39	1.17	8.87

3.2 Rheology and particle characteristics

With respect to the particle size distribution, the laser diffraction results indicate that the GGBS is the finest SCM while AS is the coarsest (Figure 1). Despite being the finest, the GGBS has the lowest water demand displaying the greatest flowability, much higher than that of AS at the same w/b ratio (Table 2). The reason is that the abundant organic matter in the raw AS (LOI=66%- Table 1) binds the mixing water, lowering workability and raising water demand to attain a given flow.

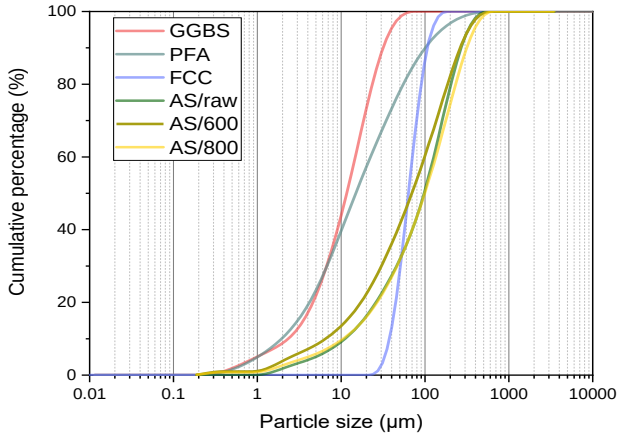

Figure 1. Particle size distribution of the SCMs

Table 2. W/b ratio and initial flow diameter of the SCM-lime pastes.

Notation	w/b ratio	Flow diameter (mm)
AS	0.75	150
AS/600	0.75	Flash set
AS/800	0.75	163
FCC	0.75	185
GGBS	0.75	230
FA	0.60	165

Calcination drastically affects the rheology of the AS (Figure 1 and Table 2). The AS calcined at 600°C reacts with lime rapidly and exothermally which causes flash set (Table 2). This sudden water demand totally disables the flow of the paste. However, when calcined at 800°C, the AS becomes less reactive so that no exothermic reaction takes place, and the avidity for binding mixing water drops, with the consequent improvement in workability. The volatilisation of the organic matter at 800°C significantly enhances the rheology of the pastes.

According to the initial flow tests, the morphology of the particles does not seem to significantly affect the rheology of the materials. For example, the SEM evidenced that the GGBS particles are very angular, and yet their rheology is the best by far (providing the greatest initial flow diameter of all SCMs for a fixed water content-Table 2). Similarly, both the FA and the FCC particles are spherical (Figure 1), and yet the FCC has a considerably greater water demand (it did not exhibit any flowability at a w/b = 0.60). This can be due to the zeolite in the FCC binding water, hence lowering workability.

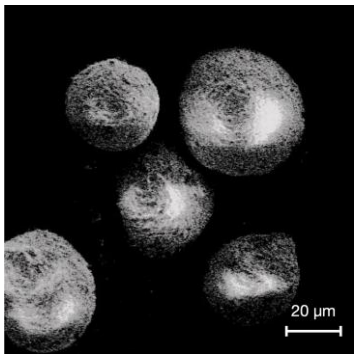

Figure 2. SEM micrograph of the FCC particles

3.2 Dissolution of the Al phases in the SCMs

The dissolution of the Al phases in the various SCMs is significantly different as shown in Figure 3. The AS instantaneously released abundant Al ions into the solution (high Al ions concentrations were measured in the first 10 mins of the reaction). This is due to the high Al and low silica content in the AS (Table 1) and its considerable amorphousness. The pyro-processing of the AS approximately doubled the amount of dissolved Al ions when compared to the raw AS. This is mainly due to the volatilization of the organic matter (66.1% wt in the raw AS) that interferes with the dissolution reaction.
In the AS materials, the dissolution rate drops suddenly at the beginning of the reaction. The reason is that the initial rapid dissolution rate of the AS causes the Al ion concentration to rise quickly and saturate the solution, which leads to the precipitation of reaction products which slows the dissolution reaction.

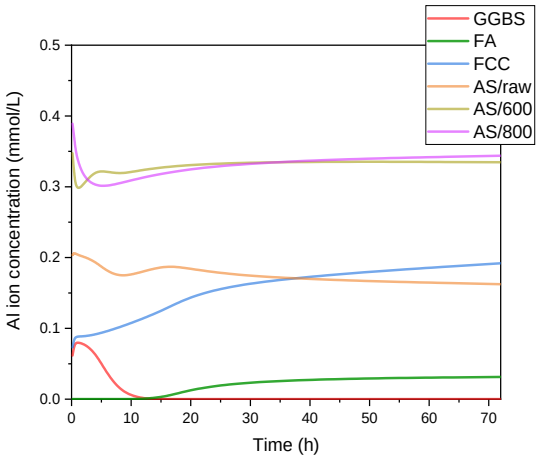

Figure 3. Al ion concentration over time measured with colorimetric methods.

The Al ions dissolution in FCC is moderate (Al_2O_3/SiO_2=1.17). Only low Al ion concentrations were detected in the solution after 10 min of reaction, and the concentration slowly increased with the reaction time (Figure 3). The organic matter content in the FCC lowers the dissolution rate. However, the Al being in

silicate form (bound with Si as the zeolite faujasite) slows down Al dissolution the most. Breaking Si-O bonds requires more energy than breaking Al-O bonds, hence the Si content is much more difficult to dissolve [25].

The FA releases little Al ions into the solution, very low concentrations of Al ions were detected initially, and 24h of reaction were required to detect any substantial concentration, which then slowly increased with the reaction time. The slower dissolution rate is due to the Al (21.18%) being in silicate form as mullite ($2Al_2O_3$. 2 SiO_2), a stable silicate with bonds hard to break.

As expected from its lower Al and higher Si contents (Al_2O_3/SiO_2 =0.37), the GGBS releases little Al ions. Dissolution increased with the reaction time and peaked at around 1 hour. Then the Al ion concentration began to decrease and, after ~8 hours, it was below the detection limit. GGBS is slightly hydraulic, hence the consumption of the Al ions is likely related to its hydraulic activity.

3.3 Setting times and their relationship with Al dissolution and water demand

The setting times of the SCMs-lime pastes are included in Table 3. Due to the hydraulic nature of the GGBS, calcium silicate hydration interferes with the setting, hence the influence of Al dissolution on the setting cannot be discussed. As seen in the workability tests, the AS calcined at 600°C flash sets (Table 2), therefore is not discussed either.

In PC technology, the close relationship between the early Al dissolution, setting and rheology is well known. Among the PC clinker minerals, the aluminates (C_3A - tricalcium aluminate – $3CaO.Al_2O_3$) dissolve and hydrate quickly, having a strong impact on the setting and the rheology of PC mortars and concretes. The hydration of aluminates is highly exothermic, consuming abundant water and producing voluminous hexagonal calcium aluminate hydrates that reduce the distance between particles restricting plastic flow.

The behaviour of the AS materials is similar, including their flash set (when calcined at 600°C). The AS pastes set much faster than the FCC and FA pastes (table 3). This agrees with the rapid dissolution rate of the AS seen above, which causes Al ions saturation in the solution and the early precipitation of reaction products that restrict the plastic flow and cause the setting of the paste. In the AS/800, calcination removes the organic matter which accelerates the Al ions dissolution rate reducing the setting time.

Table 3. Setting times of the SCMs- lime pastes

SCMs	w/b ratio	Initial setting time	Final setting time
AS/raw	0.75	0.30h	1.10h
AS/800	0.75	0.27h	0.57h
FCC	0.75	8.5h	22h
FA	0.60	25h	35h

In the FA, Al only begins to dissolve after 24h of reaction (Figure 3), which is consistent with the initial setting time of FA (25h) and proves that the dissolution of Al triggers the setting.

Even though FA and FCC have similar particle shapes and comparable particle size distributions, the speed at which their Al dissolves is quite different (figure 3), and so are their rheology and setting times (table 3). FCC starts to dissolve Al ions at the beginning of the reaction, whereas FA takes 24h to begin dissolution. Moreover, the dissolution rate of the FCC far exceeds that of the FA.

4. CONCLUSION

The results evidenced that there is a close relationship between the early Al dissolution, setting and rheology in the SCMs studied. The high Al dissolving rate of some SCMs (i.e. the AS) may cause a dramatic increase in water demand and flash setting, whereas a suitable Al source can optimize setting and workability. This paper assists in the selection of such source.

Due to their high amorphousness and Al content, an early release of Al ions into solution was expected from all the SCMs. However, the dissolution rates were very different. From the results, we conclude that three main variables control the early Al ions dissolution in SCMs: the organic matter content, the nature of the Al phases and the amount of silica.

Organic matter: The AS showed very high dissolution rates, but the organic matter in the raw AS depressed dissolution, and calcination removed the organic matter speeding dissolution.

Silica content: Despite being highly amorphous and reactive, the FA and GGBS (Al_2O_3/SiO_2 = 0.39 and 0.37 respectively) dissolve the least Al ions by far, while the FCC (Al_2O_3/SiO_2 = 1.17) dissolves considerably more and the AS (Al_2O_3/SiO_2 = 8.87) dissolves the greatest quantity.

Nature of the Al phases: In the AS, the Al is present as disordered oxyhydroxides that readily dissolve in alkaline conditions. In contrast, silicates such as the mullite in the FA and the zeolite in the FCC, are harder to dissolve and need more reaction time.

According to the workability tests, neither the size nor the morphology of the particles impact the rheology of the materials, but it is the organic matter content and the presence of highly reactive phases that are the main controllers of the rheology of the SCM materials.

ACKNOWLEDGEMENT

The authors would like to thank the China Scholarship Council (No.202007090014) for supporting this research. We greatly appreciate the assistance of our technical staff helping us with testing, especially David McCauley, Patrick Veale, Michael Grimes and Mary O'Shea.

REFERENCE

[1] G. Erbach, 'European climate law', *Regulation (EU)*, p. 1119, 2021.
[2] EU Press Corner, 'Effort Sharing Regulation', *European Commission - European Commission*, Jul. 14, 2021. https://ec.europa.eu/commission/presscorner/detail/en/qanda_21_3543 (accessed May 02, 2022).
[3] V. Khozin, O. Khokhryakov, and R. Nizamov, 'A «carbon footprint» of low water demand cements and cement-based concrete', *IOP Conf. Ser.: Mater. Sci. Eng.*, vol. 890, p. 012105, 2020, doi: 10.1088/1757-899X/890/1/012105.
[4] H. Van Damme, 'Concrete material science: Past, present, and future innovations', *Cement and Concrete Research*, vol. 112, pp. 5–24, Oct. 2018, doi: 10.1016/j.cemconres.2018.05.002.
[5] J. Davidovits, 'False values on CO_2 emission for geopolymer cement/concrete published in scientific papers', *Technical paper*, vol. 24, pp. 1–9, 2015.
[6] A. Hasanbeigi, L. Price, and E. Lin, 'Emerging energy-efficiency and CO_2 emission-reduction technologies for cement and concrete production: A technical review', *Renewable and Sustainable Energy Reviews*, vol. 16, no. 8, pp. 6220–6238, 2012.
[7] K. Ganesh Babu and V. Sree Rama Kumar, 'Efficiency of GGBS in concrete', *Cement and Concrete Research*, vol. 30, no. 7, pp. 1031–1036, Jul. 2000, doi: 10.1016/S0008-8846(00)00271-4.
[8] A. Oner and S. Akyuz, 'An experimental study on optimum usage of GGBS for the compressive strength of concrete', *Cement and Concrete Composites*, vol. 29, no. 6, pp. 505–514, Jul. 2007, doi: 10.1016/j.cemconcomp.2007.01.001.
[9] P. K. Mehta, 'High-performance, high-volume fly ash concrete for sustainable development', in *Proceedings of the international workshop on sustainable development and concrete technology*, 2004, pp. 3–14.
[10] M. D. A. Thomas, *Optimizing the use of fly ash in concrete*, vol. 5420. Portland Cement Association Skokie, IL, USA, 2007.
[11] S. A. Khedr and M. N. Abou-Zeid, 'Characteristics of silica-fume concrete', *Journal of Materials in Civil Engineering*, vol. 6, no. 3, pp. 357–375, 1994.
[12] T. Nochaiya, W. Wongkeo, and A. Chaipanich, 'Utilization of fly ash with silica fume and properties of Portland cement–fly ash–silica fume concrete', *Fuel*, vol. 89, no. 3, pp. 768–774, 2010.
[13] A. Mehta and D. K. Ashish, 'Silica fume and waste glass in cement concrete production: A review', *Journal of Building Engineering*, vol. 29, p. 100888, May 2020, doi: 10.1016/j.jobe.2019.100888.
[14] Y. Zhu, Y. Z. Yang, and Y. Yao, 'Effect of High Volumes of Fly Ash on Flowability and Drying Shrinkage of Engineered Cementitious Composites', *Materials Science Forum*, vol. 675–677, pp. 61–64, 2011, doi: 10.4028/www.scientific.net/MSF.675-677.61.
[15] D. Jiao, C. Shi, Q. Yuan, X. An, Y. Liu, and H. Li, 'Effect of constituents on rheological properties of fresh concrete-A review', *Cement and Concrete Composites*, vol. 83, pp. 146–159, Oct. 2017, doi: 10.1016/j.cemconcomp.2017.07.016.
[16] S. Velázquez, J. Monzó, M. V. Borrachero, L. Soriano, and J. Payá, 'Evaluation of the pozzolanic activity of spent FCC catalyst/fly ash mixtures in Portland cement pastes', *Thermochimica Acta*, vol. 632, pp. 29–36, May 2016, doi: 10.1016/j.tca.2016.03.011.
[17] P. Hewlett and M. Liska, *Lea's chemistry of cement and concrete*. Butterworth-Heinemann, 2019.
[18] P. D. Silva, K. Sagoe-Crenstil, and V. Sirivivatnanon, 'Kinetics of geopolymerization: Role of Al2O3 and SiO2', *Cement and Concrete Research*, vol. 37, no. 4, pp. 512–518, Apr. 2007, doi: 10.1016/j.cemconres.2007.01.003.
[19] EN, '1015-3', *Methods of test for mortar for masonry-Part*, vol. 3, 2007.
[20] EN, '196-3: 2016 Methods of testing cement', *Determination of Setting Times and Soundness. BSI*, 2016.
[21] V. A. Quarcioni *et al.*, 'Indirect and direct Chapelle's methods for the determination of lime consumption in pozzolanic materials', *Revista IBRACON de Estruturas e Materiais*, vol. 8, no. 1, pp. 1–7, Feb. 2015, doi: 10.1590/S1983-41952015000100002.
[22] O. Alelweet and S. Pavia 2019 An Evaluation of the Feasibility of Several Industrial Wastes and Natural Materials, as Precursors, for the Production of Alkali Activated Materials, International Journal of Civil and Environmental Engineering , 13, (12), 2019, p741 - 748
[23] O. Alelweet and S. Pavia, 2020 Potential of a low-calcium fly ash (FA) for the production of alkali-activated materials, Civil Engineering Research in Ireland (CERI) Conf. Cork Institute of Technology, 27- 28th August 2020, Eds Ruane and Jaksic. p162-167.

[24] Alelweet O. and Pavia S., Durability of Alkali-Activated Materials Made with a High-Calcium, Basic Slag, Recent Progress in Materials , 3, (4), 2021, p19 – 45

[25] H. Xu and J. S. J. Van Deventer, 'Ab initio calculations on the five-membered alumino-silicate framework rings model: implications for dissolution in alkaline solutions', *Computers & Chemistry*, vol. 24, no. 3, pp. 391–404, May 2000, doi: 10.1016/S0097-8485(99)00080-7.

Modelling the thermoelectric properties of cement-based materials using finite element method and effective medium theory

Lorenzo Stella[1,2], Conrad Johnston[3], Javier F. Troncoso[4], Piotr Chudzinski[1,5], Esther Orisakwe[1], Jorge Kohanoff[6,1], Ruchita Jani[7], Niall Holmes[7], Brian Norton[8], Xiaoli Liu[9], Ming Qu[9], Hongxi Yin[10], Kazuaki Yazawa[11]
[1]School of Mathematics and Physics, Queen's University Belfast, UK
[2]School of Chemistry and Chemical Engineering, Queen's University Belfast, UK
[3]Pacific Northwest National Laboratory, Richland, WA, USA
[4]Swiss Federal Laboratories for Materials Science and Technology (EMPA), Thun, Switzerland
[5]Institute of Fundamental Technological Research, Polish Academy of Sciences, Warsaw, Poland
[6]Instituto de Fusion Nuclear "Guillermo Velarde", Universidad Politecnica de Madrid, Spain
[7]School of Civil and Structural Engineering, Technological University Dublin, Ireland
[8]Tyndall National Institute, Cork, Ireland
[9]Lyles School of Civil Engineering, Purdue University, West Lafayette, IN, USA
[10]International Center for Energy, Environment & Sustainability, Washington University in St Louis (WUST), St Louis, MO, USA
[11]Birck Nanotechnology Center, Purdue Univeristy, West Lafayette, IN, USA
email: l.stella@qub.ac.uk, conrad.johnston@pnnl.gov, javier.fernandez@empa.ch, niall.holmes@tudublin.ie, p.chudzinski@qub.ac.uk, e.orisakwe@qub.ac.uk, j.kohanoff@upm.es, d18126665@mytudublin.ie, brian.norton@tyndall.ie, liu2251@purdue.edu, mqu@purdue.edu, hongxi.yin@wustl.edu, kyazawa@purdue.edu

ABSTRACT: Because of the thermoelectric (TE) effect (or Seebeck effect), a difference of potential is generated as a consequence of a temperature gradient across a sample. The TE effect has been mostly studied and engineered in semiconducting materials and it already finds several commercial applications. Only recently the TE effect in cement-based materials has been demonstrated and there is a growing interest in its potential. For instance, a temperature gradient across the external walls of a building can be used to generate electricity. By the inverse of the TE effect (or Peltier effect), one can also seek to control the indoor temperature of a building by biasing TE elements embedded in its external walls. In designing possible applications, the TE properties of cement-based materials must be determined as a function of their chemical composition. For instance, the TE properties of cement paste can be enhanced by the addition of metal oxide (*e.g.*, Fe_2O_3) powder. In this paper, a single thermoelectric leg is studied using the finite element method. Metal oxide additives in the cement paste are modelled as spherical inhomogeneities. The thermoelectric properties of the single components are based on experimental data, while the overall thermoelectric properties of the composites are obtained from the numerical model. The results of this numerical study are interpreted according to the effective medium theory (EMT) and its generalisation (GEMT).

KEY WORDS: Cement composites; Thermoelectrics; Seebeck Coefficient; Electrical Conductivity; Thermal Conductivity.

1 INTRODUCTION

Cement-based thermoelectric composites are a novel class of "smart" materials with several potential applications.[1-4] For instance, by means of the Seebeck effect, a temperature gradient across the external walls of a building can be used to generate electricity.

For open circuit conditions, the difference of electric potential, ΔV, established between the two ends of a conductor kept at different temperatures depends on the temperature difference, ΔT, and on a characteristic material property, the Seebeck coefficient, $S = -\Delta V/\Delta T$. In this paper, all Seebeck coefficients are absolute,[5] *i.e.*, they tend to zero as the temperature approaches 0 K, unless stated differently. The Seebeck coefficient of plain (*i.e.*, without additives) hydrated cement paste has been reported as either small (ranging from $S_{\text{cement}} = -1$ μV/K[6] to $S_{\text{cement}} = +2.69$ μV/K[7, 8]) or negligible ($S_{\text{cement}} = 10^{-4} - 10^{-5}$ μV/K[9]). The introduction of a small fraction of additives (usually a few wt%, mixed in dry condition) into the cement paste can largely enhance the magnitude of its Seebeck coefficient.

Wei *et al*. showed an effective Seebeck coefficient, $S_{eff} = +22.07$ μV/K, in Carbon Fibre Reinforced Cement (CFRC) composites with 1.0 wt% carbon fibre.[10] Addition of Expanded Graphite (EG) to CFRC composite gives a maximum $S_{eff} = +11.59$ μV/K at 33 °C.[11] In this case it has been observed a dependence of the effective Seebeck coefficient on moisture content. The authors also showed that in purely Expanded Graphite Cement Composites (EGCC), a $S_{eff} = +20.0$ μV/K can be achieved.[9]

Addition of oxide nanoparticles to CFRC composites boosted the values of the effective Seebeck coefficient of the composite to $S_{eff} = +92.57$ μV/K with 5 wt% Fe_2O_3 or to $S_{eff} = +100.28$ μV/K with 5 wt% Bi_2O_3.[12] Despite the leap in the Seebeck coefficient, the overall figure of merit is only slightly increased because of the limited increase in electrical conductivity upon addition of semiconducting oxides.[12, 13] Ji *et al.* have obtained a stunning $S_{eff} = +2{,}500$ μV/K for cement-based composites with 5 wt% Fe_2O_3 nanoparticles and $S_{eff} = +3{,}300$ with 5 wt% Bi_2O_3 nanoparticles, while Ji et *al.* have obtained $S_{eff} = -3{,}085$ μV/K with 5 wt% MnO_2 nanoparticles.[14] This result has been recently extended to

carbon fibre/MnO_2 composite for which a value of $S_{eff} = -2{,}800$ μV/K with 8 wt% fibre/MnO_2 content has been achieved.[15] In this composite, a largely increased overall figure of merit has been also reported, owing to the good electrical conductivity due to the carbon fibre content.

Despite the growing experimental evidence, numerical models of the thermoelectric properties of cement-based composite materials are scarce.[16]

Assuming that the thermoelectric properties of each component are known, the effective medium theory (EMT),[17] or its generalisation (GEMT),[18-21] can be used to assess the properties of the composite material. Both EMT and GEMT model a composite as a "pseudo-homogenous" material and do not require the microscopic knowledge of the oxide additive distribution. Since the microscopic scale of the composite must not be resolved, models based on either EMT or GEMT are expected to scale more favourably towards real-size (*i.e.*, a few centimetres across[22]) thermoelectric units. To this end, numerical know-how from FEM modelling of traditional thermoelectric units is available, [22-29] and can be easily customised by changing the material properties, when known.

Before applying either EMT or GEMT with confidence to cement-based material, some preliminary validation is in order. In this paper, we have modelled the thermoelectric properties of a cement-based composite material with microscopic resolution and compared the results against the EMT and GEMT predictions.

Ferric oxide, Fe_2O_3, has been used as a representative of the class of oxide materials present in the experimental literature. Simple EMT does not provide a good fit of the properties determined by the microscopic modelling. Although GEMT seems to be more accurate, discrepancies in the fitting of cement-based composite in the saturated and dry conditions suggest some caution. Discrepancies may be due to the averaging procedure used to determine the effective Seebeck coefficient of the cement-based composite material.

2 MATERIAL MODELLING

We model cement-based composites with ferric oxide, Fe_2O_3, as a typical oxide additive. Also known with the name of the naturally occurring mineral hematite, Fe_2O_3 is a semiconductor oxide. At room temperature, the electronic conductivity (unit: S/m) of Fe_2O_3 is extrinsic and the majority carriers are electrons.[30] The electron mobility, $\mu_{Fe_2O_3}$ (unit: $cm^2/V{\cdot}s$), is activated and it depends on temperature, T (unit: K), as

$$\mu_{Fe_2O_3}(T) = (1.998 \cdot 10^5/T)\exp(-0.17/k_BT),$$

where $k_B = 8.617 \cdot 10^{-5}$ eV/K is the Boltzmann constant. The activation energy, 0.17 eV, is appropriate at low temperature ($T < 923$ K).[30] The electrical conductivity is then written as

$$\sigma_{Fe_2O_3}(T) = eN_D\mu_{e,Fe_2O_3}(T),$$

where $e = 1.602 \cdot 10^{-19}$ C is the unit of charge and $N_D = 10^{19}$ cm^{-3} is the notional value of the donor concentration used in this work. For this value of the concentration, $\sigma_{Fe_2O_3}(298.15\text{ K}) = 1.436$ S/m. No precise assessment of the donor concentration has been found in the literature for the Fe_2O_3 microparticles used in cement-based composites.

The Seebeck coefficient also shows a temperature dependence typical of a semiconductor,

$$S_{Fe_2O_3}(T) = -\left(\frac{k_B}{e}\right)\left[\left(\frac{0.17}{k_BT}\right) + g\right],$$

where $g = 3$ for carrier relaxation processes determined by optical phonons scattering.[31] In particular, $S_{Fe_2O_3}(298.15\text{ K}) = -828.7$ μV/K.

We also used the value $\rho_{Fe_2O_3} = 5.26$ g/cm^3 for the density and $\kappa_{Fe_2O_3} = 12.55$ W/m·K for the thermal conductivity of Fe_2O_3. The temperature dependence of these quantities has been neglected.

For the dry cement powder, we have used a density of 3.1 g/cm^3. The density of the hydrated (0.4 water/cement ratio) cement paste with a notional 0.2 porosity is $\rho_{cement} = 2.0$ g/cm^3. The values of the electrical conductivity, thermal conductivity and Seebeck coefficient of the plain (*i.e.*, with no oxide additives) hydrated cement paste have been taken from Jani *et al.*.[6] They are $\sigma_{cement,sat.} = 0.07$ S/m, $\kappa_{cement} = 1.15$ W/m·K and $S_{cement} = -1$ μV/K, where the value of the electrical conductivity corresponds to the pore saturation condition. A much lower value of electrical conductivity, $\sigma_{cement,dry} = 2 \cdot 10^{-4}$ S/m, has been reported for dry hydrated cement paste. All quantities are given at room temperature.

The cement-based composite is modelled as a collection of spherical Fe_2O_3 microparticles inside a matrix of plain hydrated cement paste. The diameter of the spheres is set to 50 μm and superposition between spheres is allowed. Allowing for superposition partially compensates for the lack of dispersion in sphere diameters. In practice, the coordinates of the centre of each sphere are chosen at random within the volume of the composite. A "switch" function, $\phi(x,y,z)$, is defined to smoothly (as a cubic polynomial) interpolate between the value "1" inside each sphere and the value "0" in the matrix. The switch function is then used to define the local properties of the composite, *e.g.*, the local Seebeck coefficient of the composite is defined as

$$S_{comp}(x,y,z) = S_{cement} + \left(S_{Fe_2O_3} - S_{cement}\right)\phi(x,y,z)$$

and the local electrical conductivity as

$$\sigma_{comp}(x,y,z) = \sigma_{cement} + \left(\sigma_{Fe_2O_3} - \sigma_{cement}\right)\phi(x,y,z).$$

The model includes copper contacts at the two ends of the cement-based composite (see Fig.1). The Cu contacts facilitate the implementation of the boundary conditions, especially the open circuit condition. The relevant material properties are $\rho_{Cu} = 8.69$ g/cm^3 for the density, $\kappa_{Cu} = 400$ W/m·K for the thermal conductivity, $\sigma_{Cu} = 5.998 \cdot 10^7$ S/m for the electric conductivity, and $S_{Cu} = 1.83$ V/K for the Seebeck coefficient.[5]

3 COMPUTATIONAL METHODS

The coupled charge and heat transport equations for the geometry shown in Fig. 1 have been solved by means of the Finite Element Method (FEM) as implemented in COMSOL Multiphysics® (version 6.0).[32]

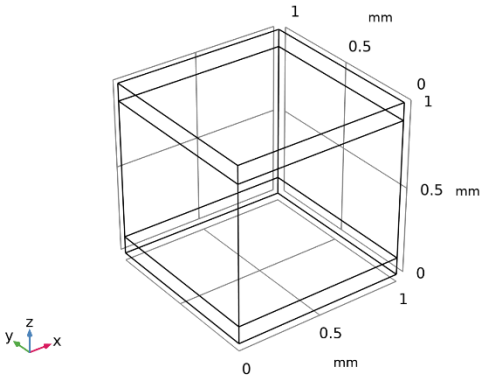

Figure 1. Model geometry. The first surface is the bottom one. The second surface is the interface between the lower Cu electrode and the cement-base composite. The third surface is the interface between the cement-base composite and the upper Cu electrode. The fourth surface is the top one.

The transport equations are:

$$\begin{cases} \nabla \cdot \boldsymbol{J} = 0, \\ \nabla \cdot (-\kappa \nabla T + ST\boldsymbol{J}) = -\boldsymbol{J} \cdot \nabla V, \end{cases}$$

where the electrical potential, V, and the temperature, T, are the unknown fields, and $\boldsymbol{J} = -\sigma \nabla V - \sigma S \nabla T$ is the thermoelectric current density. Because of the thermoelectric effect, the current depends on the gradients of both the electrical potential and the temperature.

The boundary conditions for the model are: $T_{\text{in}} = 298.15$ K and $V_{\text{in}} = 0$ (ground) on the lower Cu electrode surface, $T_{\text{out}} = 298.15 + \Delta T$ (K) and $\boldsymbol{J} \cdot \boldsymbol{n} = 0$ (open circuit) on the upper Cu electrode surface, where $\boldsymbol{n}$ is the normal vector to that surface. We consider three values $\Delta T = 0.1, 0.5, 1.0$ K and then extrapolate to the limit of $\Delta T \to 0$ to compute the effective Seebeck coefficient. Natural boundary conditions for both the electrical potential and temperature are imposed on the lateral surfaces.

Geometries containing different numbers, N_s, of spherical oxide microparticles have been generated. We considered the following values: $N_s = 0$, 100, 200, 300, 400, 500, 600, 700, 800, 900, 1000, 2000, 3000, 4000, 5000, 6000, 7000, 8000, 9000, 10000, and 100000. The cases $N_s = 0$ and $N_s = 100{,}000$ spherical microparticles give the extreme cases of plain hydrated cement paste and pure Fe_2O_3, respectively. A switch function $\phi(x, y, z)$ is generated for each of the cases above and stored on a discretised $100 \times 100 \times 100$ cubic grid. The volume fraction is defined as the average of the "switch" function over the cement-based composite volume. A cubic $50 \times 50 \times 50$ mesh for the whole geometry has been used for all the FEM calculations.

4 RESULTS

The effective Seebeck coefficient of the cement-based composite is estimated as

$$S_{eff} = -\frac{\bar{V}_3 - \bar{V}_2}{\bar{T}_3 - \bar{T}_2},$$

where $\bar{V}_{2,3}$ and $\bar{T}_{2,3}$ are the averages of the electric potential and temperature taken over the second and third surfaces, respectively (see Fig. 1). An estimate of S_{eff} is obtained for each value of ΔT. Note that the isosurfaces of the temperature (see Fig. 2) and of the electric potential (see Fig. 3) are not necessarily parallel and depend on the oxide microparticles distribution. This lack of homogeneity introduces a finite variance in the averages $\bar{V}_{2,3}$ and $\bar{T}_{2,3}$, and a consequent error in the estimator.

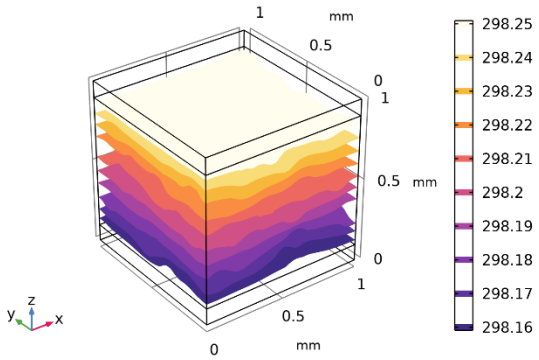

Figure 2. Temperature isosurfaces corresponding to volume fraction of Fe_2O_3 equal to 0.22. The temperature difference between the upper and lower surfaces is $\Delta T = 0.1$ K.

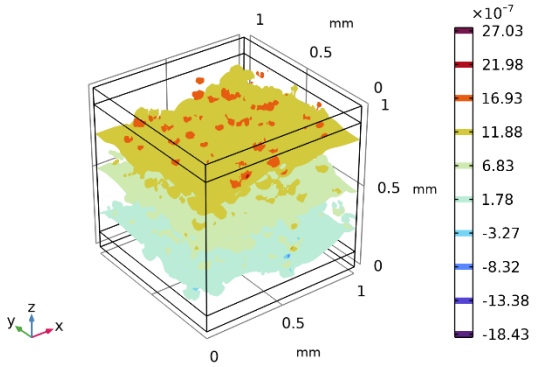

Figure 3. Electric potential isosurfaces corresponding to volume fraction of Fe_2O_3 equal to 0.22. The temperature difference between the upper and lower surfaces is $\Delta T = 0.1$ K.

Numerical results from the FEM calculations are reported in Table 1 and shown in Fig. 4 and 5. Those values have been obtained by extrapolating the numerical values S_{eff} for $\Delta T \to 0$. As expected, the value of the effective Seebeck coefficient grows monotonically with the oxide volume fraction. The values of S_{eff} for dry conditions are always larger than those for saturated conditions. In our model these conditions are only distinguished by the electrical conductivity of the cement paste. For dry conditions the electrical conductivity of the cement paste is much lower than that of the oxide additive. To explain the larger value of S_{eff} for dry conditions, one can tentatively assume that the effective Seebeck coefficient is a "weighted average" of the Seebeck coefficients of the single components.

If the "weight" is proportional to the electrical conductivity of the single components, the Seebeck coefficient of the oxide --- which is larger than that of the hydrated cement paste --- will be given a larger "weight" in the "weighted average" because its electrical conductivity is larger than that of the hydrated cement paste.

We have verified this explanation by computing the "weighted" average Seebeck coefficient, defined as

$$S_{ave} = \frac{\int S_{\text{comp}}(x,y,z)\sigma_{\text{comp}}(x,y,z)\mathrm{d}V}{\int \sigma_{\text{comp}}(x,y,z)\,\mathrm{d}V},$$

where the integrals extend over the volume occupied by the cement-based composite. The values of S_{ave} are reported in Fig. 4 and 5 (blue stars). Although they follow the same trend as S_{eff}, at least qualitatively, there are significant discrepancies.

Table 1. Effective Seebeck coefficients of the cement-based composite with different fractions of Fe_2O_3 microparticles. Values for both saturated and dry conditions are shown for comparison.

Number of microparticles	Volume fraction	Mass fraction	S_{eff} (Sat.) [μV/K]	S_{eff} (Dry) [μV/K]
0	0.00	0.00	-1.00	-1.01
100	0.05	0.14	-3.72	-13.0
200	0.09	0.23	-6.03	-24.3
300	0.15	0.34	-10.3	-43.9
400	0.18	0.40	-12.5	-54.2
500	0.22	0.45	-15.7	-71.0
600	0.26	0.50	-20.0	-91.2
700	0.29	0.55	-24.5	-111
800	0.34	0.61	-30.7	-138
900	0.36	0.63	-32.4	-146
1,000	0.39	0.66	-38.0	-171
2,000	0.63	0.83	-91.0	-372
3,000	0.77	0.91	-158	-539
4,000	0.86	0.95	-228	-651
5,000	0.92	0.97	-340	-729
6,000	0.94	0.98	-440	-759
7,000	0.97	0.99	-561	-787
8,000	0.98	0.99	-667	-803
9,000	0.99	1.00	-722	-812
10,000	0.99	1.00	-783	-821
100,000	1.00	1.00	-829	-829

The estimates for the effective Seebeck coefficient, S_{eff}, from the EMT are obtained by solving the equation[19-21]

$$f_{Fe_2O_3}\frac{\left(\frac{\sigma_{Fe_2O_3}}{S_{Fe_2O_3}}\right)-\left(\frac{\sigma_{eff}}{S_{eff}}\right)}{\left(\frac{\sigma_{Fe_2O_3}}{S_{Fe_2O_3}}\right)+2\left(\frac{\sigma_{eff}}{S_{eff}}\right)}+f_{\text{cement}}\frac{\left(\frac{\sigma_{\text{cement}}}{S_{\text{cement}}}\right)-\left(\frac{\sigma_{eff}}{S_{eff}}\right)}{\left(\frac{\sigma_{\text{cement}}}{S_{\text{cement}}}\right)+2\left(\frac{\sigma_{eff}}{S_{eff}}\right)}=0,$$

where the effective electrical conductivity, σ_{eff}, is obtained by solving the equation

$$f_{Fe_2O_3}\frac{\sigma_{Fe_2O_3}-\sigma_{eff}}{\sigma_{Fe_2O_3}+2\sigma_{eff}}+f_{\text{cement}}\frac{\sigma_{\text{cement}}-\sigma_{eff}}{\sigma_{\text{cement}}+2\sigma_{eff}}=0,$$

where $f_{Fe_2O_3}$ and f_{cement} are the volume fractions of the oxide and hydrated cement paste, respectively. There are no free parameters in the EMT and the theory should be applicable to the case of spherical inclusions.[17, 18] From the EMT, one expects a sharp percolation threshold at $f_c = 1/3$, if the electrical conductivity of the additive component is much larger than that of the host component.[18] This is supposed to be the case for dry conditions, but the sharp percolation threshold predicted by the EMT is not observed in our numerical results. This is a rather puzzling finding which casts some doubt on the accuracy of the numerical estimates of the effective Seebeck coefficient used in this work.

To gain some further insight, we tried to fit the numerical results using the GEMT. The theory has two free parameters, A and t.[18] In particular, the percolation threshold is related to the parameter A by the equation: $f_c = 1/(A+1)$. The estimates for the effective Seebeck coefficient, S_{eff}, from the GEMT are obtained by solving the equations[19-21]

$$f_{Fe_2O_3}\frac{\left(\frac{\sigma_{Fe_2O_3}}{S_{Fe_2O_3}}\right)^t-\left(\frac{\sigma_{eff}}{S_{eff}}\right)^t}{\left(\frac{\sigma_{Fe_2O_3}}{S_{Fe_2O_3}}\right)^t+A\left(\frac{\sigma_{eff}}{S_{eff}}\right)^t}+f_{\text{cement}}\frac{\left(\frac{\sigma_{\text{cement}}}{S_{\text{cement}}}\right)^t-\left(\frac{\sigma_{eff}}{S_{eff}}\right)^t}{\left(\frac{\sigma_{\text{cement}}}{S_{\text{cement}}}\right)^t+A\left(\frac{\sigma_{eff}}{S_{eff}}\right)^t}=0,$$

where the effective electrical conductivity, σ_{eff}, is obtained by solving the equation

$$f_{Fe_2O_3}\frac{\left(\sigma_{Fe_2O_3}\right)^t-\left(\sigma_{eff}\right)^t}{\left(\sigma_{Fe_2O_3}\right)^t+A\left(\sigma_{eff}\right)^t}+f_{\text{cement}}\frac{\left(\sigma_{\text{cement}}\right)^t-\left(\sigma_{eff}\right)^t}{\left(\sigma_{\text{cement}}\right)^t+A\left(\sigma_{eff}\right)^t}=0.$$

The EMT is retrieved from the GEMT when $A = 2$ and $t = 1$. A satisfactory, yet not perfect, fit of the numerical results for dry conditions is obtained by setting $A = 10^4$ and $t = 3.3$ in the GEMT (see Fig. 5). Such a large value of A corresponds to a percolation threshold $f_c \approx 0$, *i.e.*, no percolation at all. Once again this is a puzzling result and may indicate a systematic bias in the estimator used to compute S_{eff}. The same values of the parameters A and t do not yield an equivalently satisfactory fit of the numerical results for the saturated condition (see Fig. 4). Finally, a large value of the GEMT parameter t is also unexpected, as $t = 1$ is usually appropriate for spherical inclusions.[18] As a comparison, two dimensional model based on Random Resistor Networks are in perfect agreement with the GEMT predictions.[33, 34]

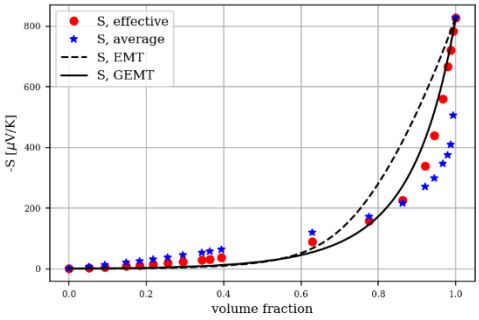

Figure 4. Negative effective Seebeck coefficient (red dots) and negative average Seebeck coefficient (blue dots) as a function of the volume fraction for saturated conditions. The EMT and best GEMT estimates ($A = 10^4$ and $t = 3.3$) are also reported.

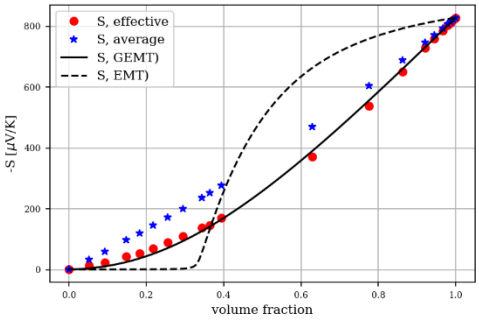

Figure 5. Same as Figure 4, but for dry conditions.

5 DISCUSSION AND CONCLUSIONS

In this paper we have shown preliminary numerical results for the calculation of the effective Seebeck coefficient, S_{eff}, of a cement-based composite material. To this end, a microscopic model of spherical Fe_2O_3 microparticles included into a matrix of hydrated cement paste has been solved by means of the Finite Element Method (FEM) as implemented in COMSOL Multiphysics® (version 6.0). Our numerical results follow the expected qualitative trend with an increasing volume fraction of oxide additives, but they do not display the percolation threshold expected for dry conditions.

A good agreement with the Effective Medium Theory (EMT) was also expected for spherical inclusions, but our results strongly deviate from the EMT predictions for both dry and saturated conditions. Relatively satisfactory regression of the numerical results by means of the Generalised Effective Medium Theory (GEMT) have been obtained, although for rather unphysical values of the GEMT parameters.

While further numerical validation is in order to confirm or not these preliminary results, we note that a potential source of systematic bias can be hidden in our estimator of the effective Seebeck coefficient. To obtain S_{eff}, both the temperature and the electrical potential have been averaged over cross sections of the geometry. Because of the random nature of the oxide inclusions, the isosurfaces of both temperature and electrical potential are not necessarily parallel to the cross sections. As a consequence, the averages may strongly depend on the location of the cross sections. This is in principle a statistical issue which can be fixed by devising a more robust averaging procedure. Research in this direction is ongoing.

ACKNOWLEDGMENTS

This research is supported through a US-Ireland R&D partnership funded by the Department for the Economy of Northern Ireland (DfE, USI 127), Science Foundation Ireland (SFI, 17/US/3424) and the National Science Foundation (NSF, 1805818),

REFERENCES

[1] X. Liu *et al.*, "State of the art in composition, fabrication, characterization, and modeling methods of cement-based thermoelectric materials for low-temperature applications," *Renewable and Sustainable Energy Reviews,* vol. 137, p. 110361, 2021/03/01/ 2021, doi: https://doi.org/10.1016/j.rser.2020.110361.

[2] X. Wang, S. Dong, A. Ashour, and B. Han, "Energy-harvesting concrete for smart and sustainable infrastructures," *Journal of Materials Science,* vol. 56, no. 29, pp. 16243-16277, 2021/10/01 2021, doi: 10.1007/s10853-021-06322-1.

[3] S. Ding, S. Dong, A. Ashour, and B. Han, "Development of sensing concrete: Principles, properties and its applications," *Journal of Applied Physics,* vol. 126, no. 24, p. 241101, 2019, doi: 10.1063/1.5128242.

[4] D. D. L. Chung, "Composites get smart," *Materials Today,* vol. 5, no. 1, pp. 30-35, 2002/01/01/ 2002, doi: https://doi.org/10.1016/S1369-7021(02)05140-4.

[5] N. Cusack and P. Kendall, "The Absolute Scale of Thermoelectric Power at High Temperature," *Proceedings of the Physical Society,* vol. 72, no. 5, pp. 898-901, 1958/11/01 1958, doi: 10.1088/0370-1328/72/5/429.

[6] R. Jani *et al.*, "Characterization and performance of cement-based thermoelectric materials," *Civil Engineering Research in Ireland (CERI) 2020,* 2020.

[7] S. Wen and D. D. L. Chung, "Seebeck effect in carbon fiber-reinforced cement," *Cement and Concrete Research,* vol. 29, no. 12, pp. 1989-1993, 1999/12/01/ 1999, doi: https://doi.org/10.1016/S0008-8846(99)00185-4.

[8] S. Wen and D. D. L. Chung, "Erratum to “Seebeck effect in carbon fiber reinforced cement”," *Cement and Concrete Research,* vol. 34, no. 12, pp. 2341-2342, 2004/12/01/ 2004, doi: https://doi.org/10.1016/j.cemconres.2004.01.010.

[9] J. Wei, L. Zhao, Q. Zhang, Z. Nie, and L. Hao, "Enhanced thermoelectric properties of cement-based composites with expanded graphite for climate adaptation and large-scale energy harvesting," *Energy and Buildings,* vol. 159, pp. 66-74, 2018/01/15/ 2018, doi: https://doi.org/10.1016/j.enbuild.2017.10.032.

[10] J. Wei, Z. Nie, G. He, L. Hao, L. Zhao, and Q. Zhang, "Energy harvesting from solar irradiation in cities using the thermoelectric behavior of carbon fiber reinforced cement composites," *RSC Advances,* 10.1039/C4RA07864K vol. 4, no. 89, pp. 48128-48134, 2014, doi: 10.1039/C4RA07864K.

[11] J. Wei, Q. Zhang, L. Zhao, L. Hao, and Z. Nie, "Effect of moisture on the thermoelectric properties in expanded graphite/carbon fiber cement composites," *Ceramics International,* vol. 43, no. 14, pp. 10763-10769, 2017/10/01/ 2017, doi: https://doi.org/10.1016/j.ceramint.2017.05.088.

[12] J. Wei, L. Hao, G. He, and C. Yang, "Enhanced thermoelectric effect of carbon fiber reinforced cement composites by metallic oxide/cement interface," *Ceramics International,* vol. 40, no. 6, pp. 8261-8263, 2014/07/01/ 2014, doi: https://doi.org/10.1016/j.ceramint.2014.01.024.

[13] J. Wei, Q. Zhang, L. Zhao, L. Hao, and C. Yang, "Enhanced thermoelectric properties of carbon fiber reinforced cement composites," *Ceramics International,* vol. 42, no. 10, pp. 11568-11573, 2016/08/01/ 2016, doi: https://doi.org/10.1016/j.ceramint.2016.04.014.

[14] T. Ji, X. Zhang, X. Zhang, Y. Zhang, and W. Li, "Effect of Manganese Dioxide Nanorods on the Thermoelectric Properties of Cement Composites," *Journal of Materials in Civil Engineering,* vol. 30, no. 9, p. 04018224, 2018, doi: doi:10.1061/(ASCE)MT.1943-5533.0002401.

[15] T. Ji, S. Zhang, Y. He, X. Zhang, X. Zhang, and W. Li, "Enhanced thermoelectric property of cement-based materials with the synthesized MnO2/carbon fiber composite," *Journal of Building Engineering,* vol. 43, p. 103190, 2021/11/01/ 2021, doi: https://doi.org/10.1016/j.jobe.2021.103190.

[16] I. Vareli *et al.*, "High-performance cement/SWCNT thermoelectric nanocomposites and a structural thermoelectric generator device towards large-scale thermal energy harvesting," *Journal of Materials Chemistry C,* 10.1039/D1TC03495B vol. 9, no. 40, pp. 14421-14438, 2021, doi: 10.1039/D1TC03495B.

[17] R. Landauer, "Electrical conductivity in inhomogeneous media," *AIP Conference Proceedings,* vol. 40, no. 1, pp. 2-45, 1978, doi: 10.1063/1.31150.

[18] D. S. McLachlan, M. Blaszkiewicz, and R. E. Newnham, "Electrical Resistivity of Composites," *Journal of the American Ceramic Society,* vol. 73, no. 8, pp. 2187-2203, 1990, doi: https://doi.org/10.1111/j.1151-2916.1990.tb07576.x.

[19] J. B. Vaney *et al.*, "Effective medium theory based modeling of the thermoelectric properties of composites: comparison between predictions and experiments in the glass–crystal composite system Si10As15Te75–Bi0.4Sb1.6Te3," *Journal of Materials Chemistry C,* 10.1039/C5TC02087E vol. 3, no. 42, pp. 11090-11098, 2015, doi: 10.1039/C5TC02087E.

[20] J. Sonntag, "Comment on “Effective medium theory based modeling of the thermoelectric properties of composites: comparison between predictions and experiments in the glass–crystal composite system Si10As15Te75–Bi0.4Sb1.6Te3” by J.-B. Vaney et al., J. Mater. Chem. C, 2015, 3, 11090," *Journal of Materials Chemistry C,* 10.1039/C6TC03140D vol. 4, no. 46, pp. 10973-10976, 2016, doi: 10.1039/C6TC03140D.

[21] J. Sonntag, B. Lenoir, and P. Ziolkowski, "Electronic Transport in Alloys with Phase Separation (Composites)," *Open Journal of Composite Materials,* 2019.

[22] X. Hu *et al.*, "Power generation from nanostructured PbTe-based thermoelectrics: comprehensive development from materials to modules," *Energy & Environmental Science,* 10.1039/C5EE02979A vol. 9, no. 2, pp. 517-529, 2016, doi: 10.1039/C5EE02979A.

[23] K. Huang and F. Edler, "Multiphysics Simulation of Seebeck Coefficient Measurement," *Journal of Electronic Materials,* vol. 51, no. 6, pp. 3276-3287, 2022/06/01 2022, doi: 10.1007/s11664-022-09577-9.

[24] G. Wu and X. Yu, "A holistic 3D finite element simulation model for thermoelectric power generator element," *Energy Conversion and Management,* vol. 86, pp. 99-110, 2014/10/01/ 2014, doi: https://doi.org/10.1016/j.enconman.2014.04.040.

[25] M. Jaegle, "Multiphysics simulation of thermoelectric systems-modeling of Peltier-cooling and thermoelectric generation," in *COMSOL Conference 2008 Hannover*, 2008, no. 6.

[26] E. E. Antonova and D. C. Looman, "Finite elements for thermoelectric device analysis in ANSYS," in *ICT 2005. 24th International Conference on Thermoelectrics, 2005.*, 19-23 June 2005 2005, pp. 215-218, doi: 10.1109/ICT.2005.1519922.

[27] G. Wu and X. Yu, "A Comprehensive 3D Finite Element Model of a Thermoelectric Module Used in a Power Generator: A Transient Performance Perspective," *Journal of Electronic Materials,* vol. 44, no. 6, pp. 2080-2088, 2015/06/01 2015, doi: 10.1007/s11664-015-3664-1.

[28] X. Hu, H. Takazawa, K. Nagase, M. Ohta, and A. Yamamoto, "Three-Dimensional Finite-Element Simulation for a Thermoelectric Generator Module," *Journal of Electronic Materials,* vol. 44, no. 10, pp. 3637-3645, 2015/10/01 2015, doi: 10.1007/s11664-015-3898-y.

[29] D. Ebling, M. Jaegle, M. Bartel, A. Jacquot, and H. Böttner, "Multiphysics Simulation of Thermoelectric Systems for Comparison with Experimental Device Performance," *Journal of Electronic Materials,* vol. 38, no. 7, pp. 1456-1461, 2009/07/01 2009, doi: 10.1007/s11664-009-0825-0.

[30] B. M. Warnes, F. F. Aplan, and G. Simkovich, "Electrical conductivity and seebeck voltage of Fe2O3, pure and doped, as a function of temperature and oxygen pressure," *Solid State Ionics,* vol. 12, pp. 271-276, 1984/03/01/ 1984, doi: https://doi.org/10.1016/0167-2738(84)90156-5.

[31] A. I. Ansel'm, *Introduction to semiconductor theory*. Mir Publishers, 1981.

[32] *COMSOL Multiphysics® v. 6.0*. COMSOL AB, Stockholm, Sweden. [Online]. Available: www.comsol.com

[33] S. Angst and D. E. Wolf, "Network theory for inhomogeneous thermoelectrics," *New Journal of Physics,* vol. 18, no. 4, p. 043004, 2016/04/04 2016, doi: 10.1088/1367-2630/18/4/043004.

[34] A. G. Rösch *et al.*, "Improved Electrical, Thermal, and Thermoelectric Properties Through Sample-to-Sample Fluctuations in Near-Percolation Threshold Composite Materials," *Advanced Theory and Simulations,* vol. 4, no. 6, p. 2000284, 2021, doi: https://doi.org/10.1002/adts.202000284.

Investigation of fresh properties of 3D concrete printing containing nanoclay in forms of suspension and powder

Sandipan Kaushik[1], Mohammed Sonebi[1], Giuseppina Amato[1], Arnaud Perrot[2], Utpal Kumar Das[3]
[1]School of Natural and Built Environment, Queen's University Belfast, Belfast BT7 1NN, United Kingdom
[2]Université Bretagne Sud, IRDL, FRE CNRS 3744, 56100 Lorient, France
[3]Department of Civil Engineering, Tezpur University, Napaam, Tezpur 784028, India
email: skaushik01@qub.ac.uk, m.sonebi@qub.ac.uk, g.amato@qub.ac.uk, arnaud.perrot@univ-ubs.fr, ukrdas@tezu.ernet.in

ABSTRACT: Cement-based additive manufacturing technologies, also known as 3D concrete printing (3DCP), have been under development for more than a decade and many research organisations in academia and the construction sector are now associated with the development of this technology. The present study reveals the feasibility of employing nanoclay both in powder and in suspension of water for 3D concrete printing applications. Because the quality and viability of 3DCP are dependent on how well the nanoclay is dispersed during mixing, a comparison of these two techniques of adding the nanoclay is undertaken in this study. Fresh-state properties of concrete can be tuned to suit the demands of 3D concrete printing, such as shape stability after printing, and ease of pumping and extrusion via a nozzle, by targeting high static yield stress and high fluidity. To assess the effect of the nanoclay on fresh and rheological performance over time, a flow table test and cylindrical slump test were used to measure flowability and static yield stress of a cementitious mortar blend containing fly ash, Portland cement, basalt fibre, and a polycarboxylate polymer-based superplasticizer.

KEY WORDS: 3D concrete printing, nanoclay dispersion, extrusion, shape stability, flowability, static yield stress.

1 INTRODUCTION

Traditionally concrete is poured into formwork and vibrated to construct building components, but technology advancement on self-compacting concrete and sprayed concrete has meant that compaction and formworks can be avoided for some applications. The use of self-compacting concrete (SCC) in construction practices have reduced the need of compaction but SCC still requires formworks which take up significant cost, time, and labour. Moreover, formwork can hardly be reused, and it sometimes act as a constraint to geometry of the structure. Sprayed concrete on the other hand requires a foundation material (natural, like rock in concrete lining tunnels or man-made) to minimise the need for intermediary formwork. The mix proportions are meant to minimise voids by grading the particles, with the biggest size fraction being filled by smaller particles. A high cement concentration is required to allow adhesion and build-up thickness, as well as a lubricating layer around the interior of conveying pipes. Although sprayed concrete reduces the amount of formwork needed, the shape and form of structural components that can benefit from this technique are quite limited [1]. Another technique to overcome constraints due to compaction and formwork is provided by 3D concrete printing (3DCP) which can be used to build concrete components by extruding concrete or mortar in a layer-based manufacturing process [2], [3].

The printable material should behave in such a way that it is fluid enough to flow through a nozzle, hence requires least possible pressure during extrusion. At the same time the material should be stiff enough to retain the shape upon exiting the nozzle and it should not give rise to bleeding during extrusion through the nozzle [4]. The ability to flow easily through a nozzle is however in contrast to the material's ability to remain stiff or buildable. The major indicators of buildability are yield stress, structural build-up of the material, and stability of the cross-sectional form of the layers. Static yield stress provides the initial rigidity of the material enabling it to retain the initial shape whereas structural build-up of material is affected by the rate of flocculation and hydration [6], [7]. It was observed through experimental results that if the rate of structural build-up is slower than the rate of deposition of succeeding layers, the structure will fail [8]. Thus for the material to remain extrudable and buildable it should be flowable yet develop sufficient yield stress simultaneously. That's why some researchers add thickening agent at the nozzle exit to provide both fluidity during pumping and strength after deposit [5].

At microscopic level printable concrete and mortar, like any other cementitious material, exhibit a visco-plastic Bingham behaviour. They can only flow when submitted to a stress larger than a threshold value τ_c, known as yield stress. These materials only flow during the brief pumping/feeding and deposition stages of most printing techniques, and they remain at rest for most of the printing process after deposit. The capacity of these materials to build up an internal structure at rest, known as thixotropy, is a critical property in most printing applications [6]. The ability of cementitious material to flocculate and its ability to nucleate early hydrates at the pseudo-contact sites between the cement grains in the flocculated structure created by cement grains is shown to be responsible for its ability to exhibit a high initial yield stress and build up a stable structure [7]. As a result of this nucleation, weak colloidal connections between cement particles gets transformed into higher-energy interactions. The macroscopic elastic modulus (G) and yield stress (τ_c) rise with an increase in the amount of hydration bridges between percolated cement particles. These fresh parameters change when the mortar is at rest, and experimental data show that $\tau_c(t)$ and G(t) increase as a function of time [8].

Owing to its large specific surface area nanoclay can cover most of the cementitious constituents in the mixture and provide extra nucleation site for structuration to happen apart from cement-cement interaction. The mechanism behind nanoclay interaction with cement paste and its influence on rheology of cement paste has been studied extensively in the literature [9],[10],[11], [12], [13]. While researchers are focused on the mechanism of flocculation, inter particle interaction of clays in cement pastes and its influence on rheology, it's also imperative to study how the printability of mortar containing nanoclay in two different forms (powder and suspension) is affected by the evolution of fresh properties like yield stress, slump flow and density with time.

In this paper the results of slump-flow and yield stress from slump value will be used to evaluate the influence of nanoclay in powder and suspension form on the fresh properties of cementitious mixture. Additionally, extrusion of the cementitious mixture will be used to assess the quality of printed mortar with nanoclay in different dosage and in two different forms to understand the material suitability for 3D concrete printing.

2 EXPERIMENTAL PROGRAMME

Five different mortar mixtures are prepared and tested in this study to assess the effect of dispersion of nanoclay powder (Acti-Gel 208) and suspension (Cimgel 2080), on fresh properties of cementitious material. The values of flow table, cylindrical slump test and density measurement are used to evaluate the ease of extrusion and shape stability of different mixtures.

2.1 Materials

Portland cement of CEM I type and strength of 52.5N as specified by BS EN 197-1: 2011 [15] is blended with fly ash while preparing the cementitious mixtures. The Portland cement and fly ash added in the mixture has specific gravity of 3.12 and 2.21 respectively. Scot ash ltd. supplied the fly ash used in this experiment which conforms to BS EN 450-1:2012 [16]. Fly ash (FA) used here has similar particle size distribution as Portland cement as shown in Figure 1. A constant water-to-binder ratio (w/b) of 0.41 is used for all the mixture in this experiment. A polycarboxylate polymer superplasticizer (SP) with a specific gravity of 1.06 was procured from Larsen building products. This high range water reducer has negligible retardation and air entrainment (<1%) effect. Basalt fibres with specific gravity of 2.65, filament length and diameter of 12.7 mm and 17 µm are used in this experiment. Sand with a maximum particle size of 1.18 mm is used as a fine aggregate here. The sand is obtained by sieving oven-dried sand with particle distribution size between 0 to 5 mm.

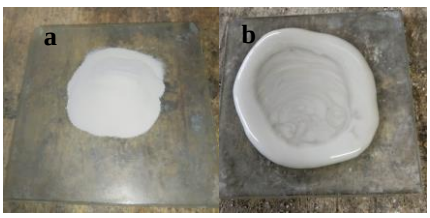

Figure 1. a) Acti-Gel 208 and b) Cimgel 2080.

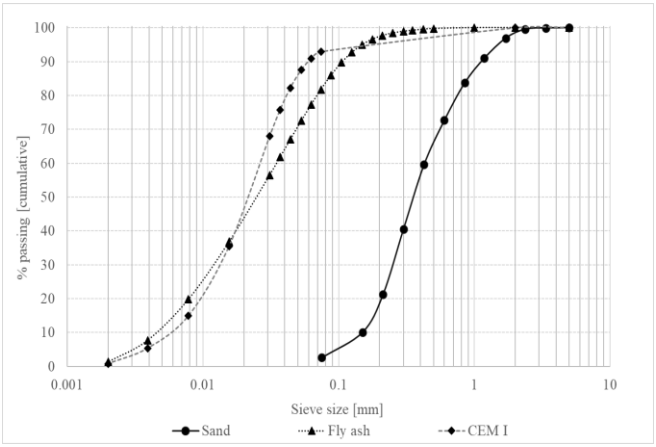

Figure 2. Particle size distribution of sand 0/5 mm, fly ash and CEM I 52.5 N used in this experiment.

Nanoclay is a mineral Acti-Gel 208 which is self-dispersing highly purified magnesium aluminosilicate with its diameter ranging between 1.5-2 µm and radius of 30 nm [17]. It provides superior particle suspension while stabilizing mix designs at a very low dose. It is utilised as a viscosity modifying agent to influence the stability and flow of the cementitious mixture. The same nanoclay is also used in the form of suspension called 'Cimgel 2080' [18] is a high-quality, ready-to-use 'Acti-Gel 208' pre-dispersed in water. It is highly effective in preventing sedimentation without effecting the flow of mixture. Figure 2 shows the two different forms of nanoclay 'Acti-Gel 208' and 'Cimgel 2080'. Table 1 and Table 2 summarizes the chemical and physical properties of the Portland cement, fly ash and nano-clay used in the mixture. The effect of nanoclay in both powder and suspension form on the fresh and rheological behaviour of the cementitious mixture is investigated using three distinct mixes. The chemical composition of CEM I, fly ash and Acti-Gel® 208 is listed in Table 1 below.

Table 1. Chemical compositions of mixture components

Constituents	Cement [%]	Fly ash [%]	Acti-Gel® 208 [%]
SiO_2	19.83	56	55.2
Al_2O_3	4.8	23.3	12.2
Fe_2O_3	3.03	4.7	4.05
SO_3	2.45	-	-
TiO_2	-	-	0.49
CaO	63.12	4.68	1.98
MgO	-	1.92	8.56
K_2O	-	1.7	0.68
Na_2O	-	0.88	0.53
P2O5	-	-	0.65
LOI	3.05	3.52	15.66

Table 2. Physical properties of mixture components

	Cement	Fly ash	Acti-Gel 208
Loss on ignition [%]	3.05	3.52	15.66
Specific gravity	3.12	2.21	2.29
% Passing 45 mm sieve	82	85	-

2.2 Composition of the cementitious mixes

All cementitious mixtures have water-to-binder (w/b) ratio of 0.41. Water absorption of the sand is 0.87% and it is considered when proportioning to achieve the desired w/b ratio. Similarly,

the water used in the mortar mixture is decreased by the precise quantity of water included in the nanoclay suspension ('Cimgel 2080') to achieve the desired w/b ratio. The sand-to-binder ratio (s/b) of 1.5 is same for all cementitious mixtures. To explore the effect of nanoclay on fresh properties, we test mortars with 'Acti-Gel 208' additions of 0.2% and 0.4% by mass of cement and corresponding pre-dispersed suspension of 3 and 6 kg/m^3 of 'Cimgel 2080' respectively. The reference mixture doesn't contain nanoclay. The cementitious mixtures nC_sp1 and nC_pw1 in Table 2, contain nanoclay in the form of suspension of nanoclay and in powder form respectively. All mortar mixture used in the experiment are shown in Table 2 below.

Table 3. Mixture proportions of mortar.

Constituents/Mix		Ref.	nC_sp1	nC6_sp2	nC_pw1	nC_pw2
CEM	[kg/m^3]	641	641	641	641	641
FA	[kg/m^3]	103	103	103	103	103
SP	[kg/m^3]	3	3	3	3	3
BA	[kg/m^3]	2.1	2.1	2.1	2.1	2.1
Sand	[kg/m^3]	1130	1130	1130	1130	1130
Cimgel	[kg/m^3]	-	3	6	-	-
Acti-Gel	[% by mass CEM]	-	-	-	0.2	0.4

2.3 Mixture preparation and testing

The cementitious material is mixed in 2 litre batches in-order to obtain enough material for assessing the fresh properties of mixtures and extrusion of mortar through the nozzle using a battery-operated extruder. Portland cement (CEM), fly ash (FA) and sand are premixed for 30 seconds at low speed of 144 rpm before adding a solution of water and superplasticizer (SP) at temperature of 20±1°C. The time when water and SP is added to cement-based material is considered as zero time. The mortar is then mixed for 1 minute at a low speed. Following this, the mixture is stopped, any lumps of solids are crushed, cement mixture which remained dry along the circumference of the mixing machine thoroughly mixed and basalt fibres are added. Nanoclay (nC) either (Acti-Gel or Cimgel) is then added to the mixture and mixing is continued for another minute at low speed. Mixing speed is then increased to 285 rpm and mixing continued for 4 more minutes. This is to disperse the nanoclay thoroughly in the slurry of mortar mixture. Finally, mixing process continued for 2 more minutes at low speed and mortar is taken out of the mixing bowl for testing. The flow value, yield stress and density of all mortar mixture are recorded every 15 minutes until 1 hour after zero time. The trend in the fresh properties of mortar with time is used to predict the extrusion behaviour of the mixture based on the form and quantity of nanoclay used.

Flow table test is started at 10 minutes from zero time. A cone shaped mould with dimensions of 100 x 70x 60 mm is placed at the centre of a jolting table and then filled with 2 layers of cementitious material compacted with 10 strokes each time. The mould is then removed gently after about 15 seconds and table is jolted 15 times at regular interval. At the end of jolting when the flow stopped, spread of the mortar is measured with a tape in two mutually perpendicular directions to obtain the flow value.

Figure 3. Flow table and cylindrical slump test to determine fresh properties of mortar.

The cylindrical slump test is carried out next. The slump test is performed with a cylinder of height, h=136 mm and diameter, d= 64 mm placed centrally at the centre of the jolting table and filled with two layers of concrete, each layer then compacted with 10 strokes. After the cylinder is filled, extra material is removed using a trowel. The cylinder is gently lifted after approximately 15 seconds taking care of not disturbing the material inside. The height and spread of the shape formed after the removal of mould is measured. The concept of flow regimes for determining yield stress from slump values, a semi-empirical method as discussed by Roussel et al. [19] is utilized to calculate the yield stress (τ). Three different flow regimes defined by calculating the height/radius ratio, can be allocated to cementitious material based on slump and spread values. The conditions for which these flow regimes are defined are: H >> R, H ≈ R and H << R where H denotes the height and R denotes the radius after lifting the mould. For each regime, a different formula is used to calculate the yield stress from the slump values obtained.

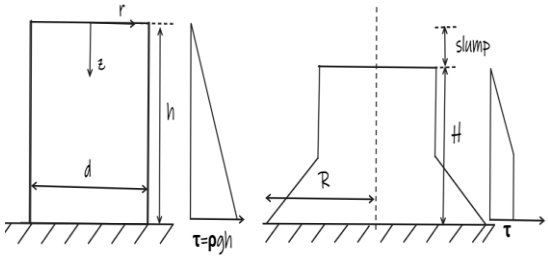

Figure 4. Notations for estimating yield stress from collapse of cementitious material under self-weight after removal of mould.

Finally, measurement of density is necessary to calculated yield stress. The density of mortar mixture is calculated by measuring material weight using the cylindrical mould, a glass plate and scale which gives measurement close to 0.1g. Mortar is filled in two layers and each layer compacted with at least 10 strokes. Extra mortar was removed, and the weight is calculated.

2.4 3D printing with nanoclay in the mortar mixture

As described in the literature [1],[7],[20],[6],[21], extrudability and buildability of cementitious materials are some of the most important features to consider in the early stages of 3D concrete printing. The extrudability of a cementitious material is associated to its ability to pass through a printing nozzle [1] and is therefore dependent on the flowability of the material.

Additionally, while stacking layers on top of each other to build any structural element, a certain level of buildability is essential for printing process to be meaningful. The extruded specimens must develop a capacity to build certain number of layers on top of it, allowing it not to collapse under the self-weight of the layer or subsequent layers [1], [21]. This property of the mortar mixture is achieved when the extruded material exhibits sufficient yield stress. At the same time buildability also depends on the flowability and mix design of the mixture material. Both these properties, buildability and flowability are influenced by the resting time of the mixture and are required for the material to be printable.

A battery-operated aluminium gun has been used for 3D printing of mortar mixtures. The gun can hold about 0.6×10^{-3} m^3 of mortar. The bespoke gun nozzle is designed to have a rectangular shape with size 42x14 mm and a circular shape at the rear end to fit the gun. The nozzle has a ribbed interior surface to provide greater contact between stacked layers.

Figure 5. Printing with the specially developed nozzle and battery-operated aluminium gun

3 DISCUSSION OF RESULTS

3.1 Flowability and yield stress

The flow value of mortar indicates the flowability or workability of fresh mix. Flow value of all the mortar mixtures naturally decreases with time as the mixture loses water due to evaporation, absorption by aggregate or hydration. The greater the interval between mixing and laying the less flowable the mortar becomes. Table 4 below shows the change in flowability and yield stress for all mortars, with negative sign indicating loss from original value. Flow values of the studied mixture are plotted in Fig. 6.

The most significant drops in one hour in flow values were those of the ‘Ref’ mix (from 260 mm to 223 mm) and of the ‘nC_pw2’ mix (from 203 mm to 166 mm). The flow value for ‘nC_sp1’ mix decreased from 219 mm to 196 mm in an hour and was found to be least among all mortars.

It was observed from the flow values that the loss of flowability is less in mortar containing nanoclay suspension in comparison to mortar containing nanoclay in powder form. The mortar containing highest percentage of nanoclay powder (‘nC_pw2’, 0.4% by mass of cement) showed maximum drop in flowability whereas mortar containing lowest amount of nanoclay in suspension (‘nC_sp1’, 3kg/m3) showed the lowest drop in flowability. While ‘nC_pw2’ and ‘nC_sp2’ contain the same amount of nanoclay in form of powder and suspension respectively, the initial flow value is significantly lower and loss of flowability is higher in case of ‘nC_pw2’. This is consistent with findings by other authors [12] that nanoclay is highly dependent on dosage and mode of dispersion.

As shown by [13], at high pressure nanoclay could absorb up to 200% water by its dry mass [13]. Since the powder form was not pre-dispersed in water and it was not fully saturated, it could adsorb the available water due to its high specific surface area. This process of adsorption on its surface is also aided by high pressure exerted during the process of mixing at high shear and could lead to decrease in flow value in early stages.

Table 4. Change in values of fresh properties of mortar in one hour.

Property	Mixture	Initial	Final	Change
Flow value	Ref	260mm	223mm	-37mm
	nC_pw1	217mm	189.5mm	-27.5mm
	nC_pw2	203mm	165mm	-38mm
	nC_sp1	219mm	196mm	-23mm
	nC_sp2	213mm	180mm	-33mm
Yield stress	Ref	981Pa	1374Pa	+393Pa
	nC_pw1	1488Pa	1595Pa	+107Pa
	nC_pw2	1604Pa	1653Pa	+49Pa
	nC_sp1	1440Pa	1587Pa	+147Pa
	nC_sp2	1539Pa	1624Pa	+85Pa

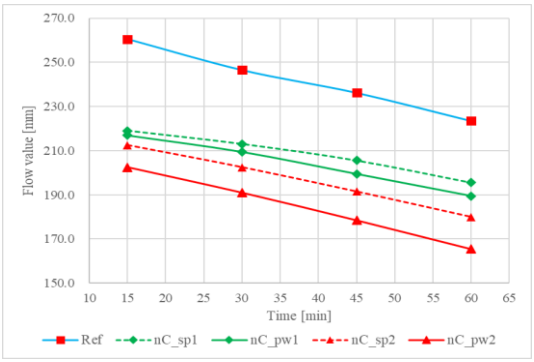

Figure 6. Trend of flow value with time for different mortar mixture containing nanoclay.

As the flow value decreases with time the mortar becomes stiffer and exhibits higher yield stress. The yield stress also increases with increase in dosages of nanoclay in the mixture. The change in yield stress in the 'Ref' mix is higher because there is more water available at the beginning and the mixture has a lower initial yield stress (981 Pa) as compared to other mixtures. The water from the 'Ref' mix was gradually evaporated and absorbed due to hydration. The initial yield stress in more pronounced in the mortar containing nanoclay in powder form. The initial yield stress of 1488 Pa and 1604 Pa is higher in both mortar mixture ‘nC_pw1’ and ‘nC_pw2’ respectively as compared to initial yield stress of 1440 Pa and 1539 Pa for mortar mix ‘nC_sp1’ and ‘nC_sp2’ respectively.

With less nanoclay the flocculation of cementitious material is low, as previous research has shown that clays improve flocculation strength and floc size. In terms of water adsorption, since water content is constant, the presence of any nanoparticles (due to its large specific surface area) will adsorb more water and result in higher yield stress [14],[13]. Although in case of ‘nC_pw1’ and ‘nC_pw2’ mixes the mixing energy and dosages are same as ‘nC_sp1’ and ‘nC_sp2’ respectively, water adsorption on surface of nanoclay powder has influenced the yield stress values.

The ‘nC_pw2’ mix showed the lowest flow values across one hour period, while it exhibited highest yield stress values across the same one-hour period. So, to achieve high yield stress the material loses extrudability. This loss of flow value and yield stress is better pronounced in case of powder form of nanoclay. These properties are interconnected and are related through its viscosity modifying effect using soft and rigid interaction mechanisms described by Roussel et al. [22] and Douba et al. [12]. The correlation between yield stress and flow value in Figure 8 demonstrates the relationship.

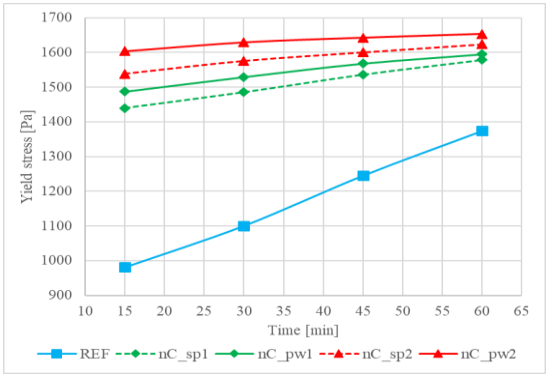

Figure 7. Trend of yield stress with time for different mortar mixture containing nanoclay.

A good correlation is observed between flow value and yield stress value with coefficient of determination being 0.98 (R^2 = 0.98). This correlation is obtained for all mortar mixtures with values measured at 15 min interval for 1 hour with different amounts of nanoclay tested in this experiment. This implies that the behaviour of nanoclay is consistent during measurement of yield stress and flow value.

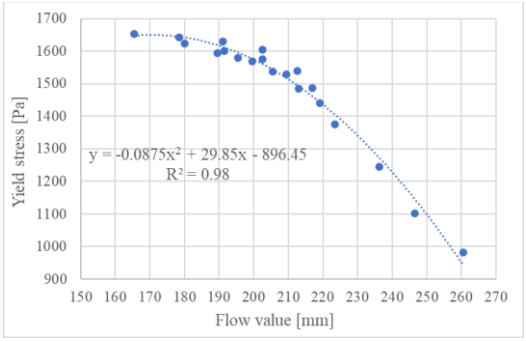

Figure 8. Correlation between flow value and yield stress for different mortar mixture containing nanoclay.

The initial yield stress value for the ‘Ref’ mix is not significantly high for maintaining shape stability of mortar after printing. The higher the initial yield stress the better it is for maintaining the shape stability of printed components. However, it is important to note that at high yield stress value the process of extrusion becomes difficult as the mortar becomes less flowable and therefore occurrence of cracks at the surface of printed components is a common phenomenon. The printed components for mortar mix ‘nC_pw2’ and ‘nC_sp2’ are shown in picture below. The print quality between these two mixes is almost same except for ‘nC_pw2’ the cracks on the surface have started occurring at 60 minutes after mixing commenced. The shape of printed components using ‘nC_pw2’ and ‘nC_sp2’ can be seen improving when compared ‘Ref’ mix. Printed components are shown for different mortar mixtures at approximately 15 minutes and 60 minutes in Figure 9 below.

Figure 9. Printing component of ‘Ref’, ‘nC_sp2’ and ‘nC_pw2’ mixes at 15 minutes and 60 minutes respectively.

3.2 Density of mortar

As the concentration of nanoclay in the mortar is increased, the density of the mortar increases. This is due to the presence of nanoclay, which generates an increased packing density. It is observed that both 'nC_pw1' and 'nC_pw2' mixes have a higher density than 'nC_sp1' and 'nC_sp2'. The density of the 'Ref' mixture has not been as high as that of the nanoclay mixtures, because flocculation is not happening as fast as the other mixture with nanoclay. Kawashima et al. [13] studied and discovered that loss of water in the mixture is not the governing stiffening mechanism rather it is the flocculation which causes water to get entrapped in particles resulting in a change in solid volume fraction. So, adsorption of water is not the principal cause of improving packing density, but flocculation is. Mixtures containing higher amount of nanoclay, therefore, have increased degree of flocculation and have larger floc size, allowing them to fill voids and increase the packing density of the mortar at the same water content. This effect is somewhat stronger with mixtures containing powder nanoclay (nC_pw1 & nC_pw2), which may be due to increased water entrapment. The slight decrease in the density of mortar towards the end of measurement shows the end of highly flocculated stage and

beginning of dispersed state when the mortar has reached a stable matrix.

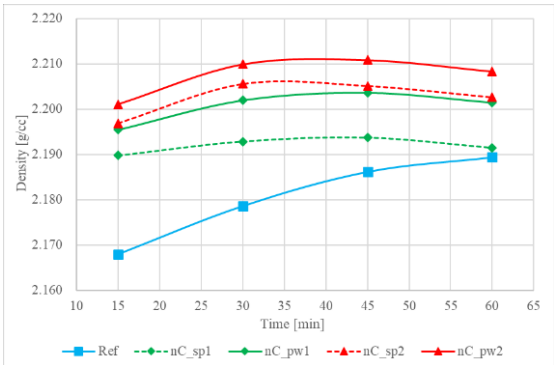

Figure 10. Trend showing changing value of density of mortar with time.

Printed components were easily extruded, and the shape of these components improved with the use of nanoclay. Some surface cracks were observed in the extruded mortar mixture (nC_pw2) having maximum dose of powder nanoclay due to loss of flowability at 60 minutes but no such cracks were observed for mortar mix with nanoclay suspension, nC_sp2.

4 CONCLUSION

The effect of nanoclay in both powder and suspension form on fresh properties of mortar was determined from the mortar mixtures investigated in this paper. The density and yield stress values for mortar containing powder nanoclay remained high, while the flow value remained low throughout the experiment. The degree of flocculation caused by the presence of nanoclay may alter the fresh properties, while water adsorption due to high specific surface area also played an important role in altering the rheology of mortar containing nanoclay. When nanoclay is used in powder form in the mixture, it has a better rheology modifying ability. When mortar is blended with nanoclay in powder form, it has a higher density compared to mortar blended with nanoclay in suspension form.

The mortar with nanoclay suspension can be extruded easily for longer periods because of higher flowability values than mortars with powder nanoclay. Mortar with nanoclay in the form of suspension were extruded for a period longer than 60 minutes without any surface cracks. Except for 'Ref' mix, all mortars have reasonably high static yield stress for adequate buildability and shape stability. Therefore, considering both extrudability and buildability requirements, mortar with nanoclay in suspension form seems more suited for 3DCP.

The availability of free water in the mixture and utilisation of this water through dispersion of nanoclay plays a significant role in achieving desired extrudability and buildability for 3DCP. The impact of free water present on the surface of each layer on interlayer bond behaviour is being studied as part of my future research on nanoclay.

REFERENCES

[1] T. T. Le, S. A. Austin, S. Lim, R. A. Buswell, A. G. F. Gibb, and T. Thorpe, "Mix design and fresh properties for high-performance printing concrete," *Mater. Struct. Constr.*, vol. 45, no. 8, pp. 1221–1232, 2012, doi: 10.1617/s11527-012-9828-z.

[2] T. Wangler *et al.*, "Digital Concrete: Opportunities and Challenges," *RILEM Tech. Lett.*, vol. 1, p. 67, 2016, doi: 10.21809/rilemtechlett.2016.16.

[3] V. Mechtcherine, V. N. Nerella, F. Will, M. Näther, J. Otto, and M. Krause, "Large-scale digital concrete construction – CONPrint3D concept for on-site, monolithic 3D-printing," *Autom. Constr.*, vol. 107, no. August, p. 102933, 2019, doi: 10.1016/j.autcon.2019.102933.

[4] K. G. Kuder and S. P. Shah, "Rheology of extruded cement-based materials," *ACI Mater. J.*, vol. 104, no. 3, pp. 283–290, 2007, doi: 10.14359/18674.

[5] T. Wangler, R. Pileggi, S. Gürel, and R. J. Flatt, "A chemical process engineering look at digital concrete processes: critical step design, inline mixing, and scaleup," *Cem. Concr. Res.*, vol. 155, p. 106782, 2022, doi: https://doi.org/10.1016/j.cemconres.2022.106782.

[6] L. Reiter, T. Wangler, N. Roussel, and R. J. Flatt, "The role of early age structural build-up in digital fabrication with concrete," *Cem. Concr. Res.*, vol. 112, no. November 2017, pp. 86–95, 2018, doi: 10.1016/j.cemconres.2018.05.011.

[7] N. Roussel, "Rheological requirements for printable concretes," *Cem. Concr. Res.*, vol. 112, no. April, pp. 76–85, 2018, doi: 10.1016/j.cemconres.2018.04.005.

[8] R. J. M. Wolfs, F. P. Bos, and T. A. M. Salet, "Early age mechanical behaviour of 3D printed concrete: Numerical modelling and experimental testing," *Cem. Concr. Res.*, vol. 106, no. February, pp. 103–116, 2018, doi: 10.1016/j.cemconres.2018.02.001.

[9] N. A. Tregger, M. E. Pakula, and S. P. Shah, "Influence of clays on the rheology of cement pastes," *Cem. Concr. Res.*, vol. 40, no. 3, pp. 384–391, 2010, doi: https://doi.org/10.1016/j.cemconres.2009.11.001.

[10] N. Tregger, H. Knai, and S. P. Shah, "Flocculation behavior of cement pastes containing clays and fly ash," *Spec. Publ.*, vol. 259, pp. 139–150, 2009.

[11] Y. Qian, S. Ma, S. Kawashima, and G. De Schutter, "Rheological characterization of the viscoelastic solid-like properties of fresh cement pastes with nanoclay addition," *Theor. Appl. Fract. Mech.*, vol. 103, no. April, p. 102262, 2019, doi: 10.1016/j.tafmec.2019.102262.

[12] A. Douba, S. Ma, and S. Kawashima, "Rheology of fresh cement pastes modified with nanoclay-coated cements," *Cem. Concr. Compos.*, vol. 125, no. March 2021, p. 104301, 2021, doi: 10.1016/j.cemconcomp.2021.104301.

[13] S. Kawashima, J. H. Kim, D. J. Corr, and S. P. Shah, "Study of the mechanisms underlying the fresh-state response of cementitious materials modified with nanoclays," *Constr. Build. Mater.*, vol. 36, pp. 749–757, 2012, doi: 10.1016/j.conbuildmat.2012.06.057.

[14] L. Senff, J. A. Labrincha, V. M. Ferreira, D. Hotza, and W. L. Repette, "Effect of nano-silica on rheology and fresh properties of cement pastes and mortars," *Constr. Build. Mater.*, vol. 23, no. 7, pp. 2487–2491, 2009, doi: 10.1016/j.conbuildmat.2009.02.005.

[15] British Standard Institution BSI, "BS EN 197-1:2011 Cement Part 1: Composition, specifications and conformity criteria for common cements." BSI Standards Publication, p. 50, 2011.

[16] British Standard Institution BSI, "BS EN 450-1:2012 Fly ash for concrete Part 1: Definition, specifications and conformity criteria." BSI Standards Publication, p. 30, 2012.

[17] "ACTI-GEL® PURIFIED MAGNESIUM ALUMINOSILICATE," *Active Minerals International, LLC*, 2021. https://activeminerals.com/products/acti-gel-208/ (accessed Oct. 28, 2021).

[18] "Cimgel 2080®MAGNESIUM ALUMINIUM SILICATE," *Faber&VanderEnde BV*. 2021, Accessed: Nov. 30, 2021. [Online]. Available: https://www.fabervanderende.com/inorganic-thickeners/.

[19] N. Roussel and P. Coussot, "'Fifty-cent rheometer' for yield stress measurements: From slump to spreading flow," *J. Rheol. (N. Y. N. Y).*, vol. 49, no. 3, pp. 705–718, 2005, doi: 10.1122/1.1879041.

[20] V. Mechtcherine *et al.*, "Extrusion-based additive manufacturing with cement-based materials – Production steps, processes, and their underlying physics: A review," *Cem. Concr. Res.*, vol. 132, no. December 2019, p. 106037, 2020, doi: 10.1016/j.cemconres.2020.106037.

[21] T. Wangler, N. Roussel, F. P. Bos, T. A. M. Salet, and R. J. Flatt, "Digital Concrete: A Review," *Cem. Concr. Res.*, vol. 123, no. March, 2019, doi: 10.1016/j.cemconres.2019.105780.

[22] N. Roussel, G. Ovarlez, S. Garrault, and C. Brumaud, "The origins of thixotropy of fresh cement pastes," *Cem. Concr. Res.*, vol. 42, no. 1, pp. 148–157, 2012, doi: 10.1016/j.cemconres.2011.09.004.

Alkali-activated cements and concretes – where have we come from, and where might we be going?

John L. Provis[1], Susan A. Bernal[2]
[1]Department of Materials Science and Engineering, University of Sheffield, Mappin St, Sheffield S1 3JD, UK
[2]School of Civil Engineering, University of Leeds, Woodhouse Lane, Leeds LS2 9JT, UK

email: j.provis@sheffield.ac.uk, s.a.bernallopez@leeds.ac.uk

ABSTRACT: This paper provides a brief overview of some of the key milestones in the history of alkali-activated cements and concretes that have brought us to the point where these materials are now considered a credible option for use in practical civil engineering projects. Some commentary on likely (and possible) future directions for research and development activities on this topic is also included. The key focus of the discussion is to highlight the multi-decade processes and efforts, motivated for very different reasons. These efforts have built the evidence base for the technical performance of this class of materials and brought the technology of alkali-activation to market-readiness in response to environmental and commercial drivers that have arisen more recently.

KEY WORDS: Alkali-activated cements, alkali-activated concretes, milestones in materials development, drivers for innovation

1 INTRODUCTION

A number of detailed reviews of the various aspects of the technical properties and engineering applications of alkali-activated materials have been published recently, including [1-7]. Rather than repeating or recapitulating the information presented in those papers, here we focus on revisiting several historical milestone publications (from the past 80 years of work on alkali-activated material) and use these as a framework to better understand how these materials have been developed, analysed and used. This historical view must necessarily underpin future developments in the area, because of the multi-decade timescales over which civil engineering materials must be designed to serve. It is also useful to consider the factors that have historically driven different research and development activities, to understand why past scale-up efforts have not always been successful and to avoid similar frustrations in future. This paper is to some extent an update to, and extension of, the authors' previous milestone-based analysis of alkali-activation [8], but also provides some additional insight into commercialisation pathways and drivers based on events that have taken place in the 7 years since that paper was published.

The earliest accessible publication related to alkali-activated binders (to the knowledge of the authors) is an 1895 patent by the US-based researcher Jasper Whiting [9][1], who described a process where blast furnace slag was water-granulated, dried, and mixed with slaked lime and caustic soda, then finely ground for use as a cement. At that time, Whiting considered blast furnace slag to be "*practically inexhaustible in supply*" – and considering his role as a senior technical staff member of the Illinois Steel Company, this may have been an accurate statement from his own perspective, even if it is not true in general in Europe in the 2020s. Questions of material availability will be revisited later in this paper, but it is interesting to note that this has long been an important consideration in discussions of alkali-activated cements.

Turning to consideration of the earliest clay-based alkali-activated products, the earliest study we have identified which described the reaction of a calcined kaolinitic clay with an alkali source (sodium silicate, in this instance) to produce a binding material was published in 1920 by Homer Staley of the U.S. National Bureau of Standards [10]. As part of a study of many attempted high-temperature adhesive binders for engine spark plug production, it was noted that "*When brought into contact with a strongly alkaline substance such as sodium silicate, calcined kaolin reacts quite rapidly to form a friable, porous mass*", but with "*little strength"* [10]. Despite this rather unpromising initial starting point, the development of materials based on alkali-activation of calcined kaolinitic clay did not stop at this rather unpromising beginning (and the desired strength and heat resistance have been demonstrated numerous times through optimisation of alkali-activated binder formulae and production routes) [11]. Usage of calcined clay-based alkali-activated adhesives in spark plugs was eventually enabled by the use of organic additives (e.g. [12]), while other early (pre-1970) applications for similar materials included waterproof wallboards [13], and granular coatings for the protection of bitumen-based roofing components [14].

The alkali-activation of slags was given major impetus by the work of Arthur O. Purdon, a British chemist working in Belgium between World Wars 1 and 2. Purdon filed a patent covering various types of alkali-activated slag cements and concretes in 1934 [15], and then published a detailed investigation of the chemical activation of several blast furnace slags of varying compositions and finenesses in 1940 [16]; this paper will be discussed in more detail below as a key milestone

[1] Much of the literature takes a 1908 patent of Kühl (U.S. Patent 900,939, "Slag cement and process of making the same") as the earliest available reference for alkali-activation; the authors thank Dr Neil Milestone for making us aware of the Whiting patent which predates Kühl's work by more than a decade

in the field. After World War 2, Purdon brought these materials into limited-scale commercial production under the name 'Purdocement' (or 'Le Purdociment'). Several of the structures in Belgium that were produced using Purdocement in the 1950s are still standing, and have been studied and discussed in some detail by Buchwald et al. [17] as well as in the Masters degree thesis of Vanooteghem [18]. However, Purdocement production was never extended to a full commercial-scale operation, and the company was put into liquidation in 1957 [17].

From the 1950s-1980s, the main research and scale-up advancements related to alkali-activation were centred in Kyiv, as the institute initially led by Viktor Glukhovsky [19] (and later named in his honour), and then afterwards under the leadership of Pavel Krivenko [20], developed and produced cementitious binders containing alkalis in combination with a very wide range of natural, synthetic, and waste-derived precursors. These binding systems have been used at large scale in Ukraine, Russia, and several central Asian nations in structural, non-structural and niche applications (e.g. oil-well cementing and nuclear waste immobilisation) [21], with successful performance reported in terms of material handling, engineering properties, and durability [22].

In the 1970s, Joseph Davidovits commenced a long-running series of applied research and development activities based on combining calcined clays (particularly metakaolin, calcined kaolinite clay) with alkaline solutions; in 1979 he began to more broadly promote these materials under the name 'geopolymers' [23]. Broader research and development activities in alkali activation (often, but not always, using the name geopolymer) grew very significantly from the 1990s onwards. In a seminal 1991 paper which has now attracted more than 3900 citations, Davidovits [24] described many aspects of the chemistry and technology of geopolymers (defined specifically in that work as alkali aluminosilicate binders), and essentially defined this class of materials as a field of research in its own right for the international English-speaking academic community in a way that had not been done previously.

The early work of Davidovits focused on the use of the reaction between alkalis and calcined clays to produce low-cost, thermally-resistant materials, as well as some applications of those materials in the immobilisation of hazardous wastes. Commercialisation activities related to alkali-activation have since tended to shift to focus on higher-volume applications in concrete production, which has been driven by the need to secure deep and rapid CO_2 emissions savings in the construction sector [25]. It is interesting to mention that the need for such emissions cuts in the production of cement and concrete was foreshadowed by Davidovits in his 1991 paper [24], published long before emissions control and sustainability issues became a major focus of research and development, and investment, across the global cement and concrete community. There has also continued to be a great deal of academic interest in these materials for both refractory and hazardous waste immobilisation applications, and some continuing industrial interest in both aspects, but these topics are both dwarfed in scale and potential global impact by the question of whether low-carbon materials may become available for use in concrete construction.

This paper therefore draws on more than 100 years of developments in alkali-activation, reassessing some of the strengths and weaknesses that were identified in key milestone publication in the past, and providing commentary regarding which drivers are likely to motivate the use (or disuse) of this class of binders in the coming decades.

2 DISCUSSION – REVISITING SOME MILESTONES

2.1 The work of Purdon revisited

The first major journal publication on alkali-activated cementitious materials was authored by Purdon (as mentioned above) and published in 1940 [16]. Purdon's key finding was that adding NaOH into a cement based primarily on blast furnace slag increases both early and later strength, and that this was more effective than the alternative modes of slag activation that were under discussion at the time, which involved Portland cement clinker, CaO, or $CaSO_4$. Identified disadvantages of the alkali-activation approach included the hygroscopicity of the solid NaOH, which caused problems when attempting to intergrind the activator with the slag to produce a one-part cement, and also a tendency toward inconveniently rapid carbonation of the activator. He indicated that for precasting or ready-mixed operations in particular, the addition of the NaOH as an aqueous solution at the point of concrete mixing offered advantages in mitigating these disadvantages. The technical characteristics of the slag-based binders described in [16] were outlined in very positive terms: low water permeability, moderate shrinkage, and low heat of hydration.

To further attempt to avoid difficulties related to the direct use of NaOH as an activator, Purdon also tested a variety of alternative and multicomponent activators. The compressive strength data for concretes produced using $Ca(OH)_2$ and additional constituents as blended activators are summarised in Figure 1. The key conclusion of this part of the work of Purdon [16] was a recommendation that it is worthwhile to generate NaOH in-situ by reacting $Ca(OH)_2$ with Na_2CO_3 or Na_2SO_4; this process has been adopted by many researchers since its initial description (e.g. the studies summarised in [21] and many others), and has indeed proven to be effective. Purdon also noted that there was little influence on strength development from pre-mixing the activator constituents externally, or conducting the NaOH generation reactions in-situ [16], indicating that the content of NaOH was more important in defining alkali-activation performance rather than its specific formation mechanism.

It is maybe notable that Purdon did not consider (or at least did not discuss) the possibility of alkali silicate activators in this publication [16], although sodium silicate was mentioned as a potential binder constituent in his earlier patent [26]. The ideas and fundamental science of silicate activation were explored in much more detail by Glukhovsky [19], and many lines of investigation and commercialisation of alkali-activated cementitious materials have since been based on sodium silicate as an activator due to its ability to provide generally high strength and good concrete durability characteristics. The work of Purdon [16] did provide some discussion of durability-related aspects such as permeability, but mainly with comparisons of selected mixes against then-current Portland cement concretes rather than extensively across the range of

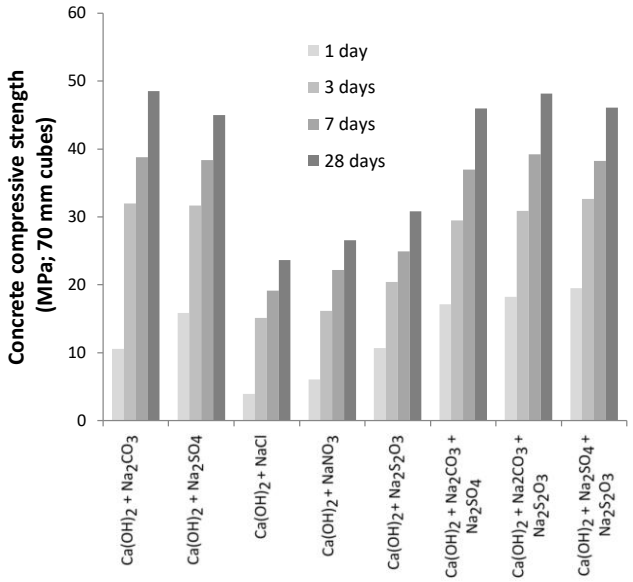

Figure 1. Compressive strengths of alkali-activated slag concretes produced using various combinations of activator compounds, dosed to give the equivalent of 6% NaOH in the mix water assuming that all Na added is converted to NaOH. Data from [16]; presentation adapted from [8].

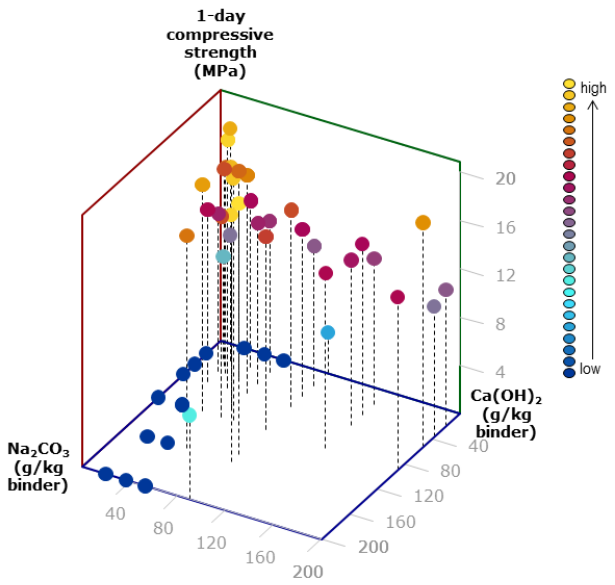

Figure 2. Compressive strengths of concretes based on blast furnace slag with different contents of Na2CO3 and Ca(OH)2 as activators, at 400 kg/m3 binder content. Legend shows the colour-coding of strength data, which are taken from [16]. Graphic reproduced from [8].

alkali-activated formulations investigated.

Figure 2 also shows data from the study of Purdon [16], relating 1-day concrete strengths to the quantities of Na_2CO_3 and $Ca(OH)_2$ added into the alkali-activated concrete mixes. This graphical presentation of the data shows a clear optimum in strength at relatively modest doses of both activator constituents, with the strength decreasing significantly once the optimum is exceeded for one or both alkaline components. The fact that the performance of alkali-activated concretes, in both the fresh and hardened states, tends to be quite sensitive to details of the formulation (i.e. is less robust than Portland cement to variations in mix constituents), remains a challenge in the scale-up of these materials [26]. Based on these and other findings, Purdon [16] indicated that these alkali-activated slag materials may not be so suitable for '*small undertakings in which the proportioning of the concrete is often done in a haphazard fashion*', but that precasting or ready-mixed production offer important opportunities for commercial deployment. Research since that time has supported these findings, particularly considering the sensitivity of alkali-activated concretes to differences in curing conditions [27-29] as well as chemical factors related to the mix design [30, 31].

2.2 Issues highlighted by Talling & Brandstetr in 1989

After several decades in which alkali-activation was largely described in national and local publications in eastern Europe with only sporadic coverage outside that region, Talling and Brandstetr in 1989 published a review summarising and outlining much of this work, in the proceedings of an ACI conference in Trondheim [32]. Much of the information provided in that paper was thus presented in the English language for the first time, which is of value to the international audience. However, maybe more importantly in terms of this review, Talling and Brandstetr also provided some insightful and forward-looking commentary, which will be briefly revisited here. Brandstetr and Talling, who had each been intimately involved in research and development of alkali-activated materials in the eastern parts of Europe up to (and since) the publication of that paper, provided suggestions regarding potential advantages of alkali-activation as an alternative route to large-scale concrete production, and concluded by providing a list of technical issues which they believed to merit further attention from the research and development community. The entries on this list are summarised below in italics, accompanied by commentary (with the benefit of some hindsight) regarding the relevance of these topics some 33 years later.

The possibility of altering the composition and properties of the slags

This point does not appear to have been taken up at scale, due largely to the difficulty associated with cementitious material producers requesting that metallurgical furnace operators alter their process plant or conditions in any way to manipulate slag formation, which could have possible impacts on the operational cost and/or purity of their primary (metal) products. Nonetheless, it remains a point of potential interest if these practical issues can be resolved. Alkali-activated products based on synthetic slags and other similar purpose-formulated glasses have been developed [33, 34], in addition to a large volume of work on alkali-activation of waste glasses, and small-scale scientific studies using laboratory-synthesised vitreous precursors.

The characteristics of different kinds of slags

A large part of the academic literature remains focused on alkali-activation of blast furnace slags, but the influence of slag chemistry (within the usual slag compositional range of blast

furnace operations) on binder properties is becoming better understood [35-40]. Work on non-blast furnace slags is growing rapidly as the global supply of blast furnace slags is becoming more constrained, with particular interest in copper, phosphorus, and steelmaking slags [41-45], among others [46].

Newly formed hydration compounds and their quantification

The subject of which precise binding phases are formed via alkali-activation processes was mentioned by Talling and Brandstetr [32] as needing further attention, and was also mentioned in the review of Wang et al. [47] in 1995 as being subject to '*considerable confusion*'. However, dramatic advances have been made since that time [1, 3], including descriptions and predictions of the thermodynamic stability of both the major and ancillary binder phases which can form in alkali-activation of various types of precursors [48-52], and the inclusion of many of the phases relevant to alkali-activation in major cement thermodynamics databases [53]. However, further work is still needed in defining and characterising gel stability, gel coexistence, and metastability in alkali-activated binder systems. It remains challenging – and somewhat contentious – to quantify the extent of reaction of solid precursor materials (at the bulk or particle levels) in alkali-activation via various analytical techniques; this difficulty is also experienced in analysis of Portland cement blends with slag, fly ash, or calcined clays [54], and receives ongoing research attention in that context also.

Identification of minor components in the raw material which may have a deleterious effect

Potentially hazardous elements are often found in low concentrations in fly ashes and metallurgical slags, and these need to be considered with care via leaching tests [55, 56] applied to both the precursors and the hardened cementitious products. These considerations are equally true whether the materials are being used in alkali-activation or in blends with Portland cement, although there is an added emphasis on understanding potentially hazardous constituents in alkali-activated materials because of (a) the higher percentage of these precursors as a fraction of the overall material, (b) the elevated activator pH and overall binder chemistry design yielding a greater degree of reaction of the precursor grains than is often the case in a blend with Portland cement, and (c) the use of a broader range of industrial by-products in alkali-activation research and development activities than is generally the case in commercial Portland cement blends. There have also more recently been investigations of naturally occurring radioactive constituents [57, 58], which may become important in some applications depending on the precise nature of the precursors used. With increasing emphasis on whole-life-cycle environmental impacts, including recyclability and toxic element release at end of life, the need to understand and describe this aspect of alkali-activated binder (and, for that matter, Portland cement-based binder) chemistry is receiving increasing attention.

Simple and effective testing procedures; Standardisation and codes of practice

Points related to standardisation will be discussed in more detail below but remain a key point of activity. Durability and other testing protocols are also under discussion and development through standards agencies in various jurisdictions worldwide, and the work of RILEM Technical Committee 247-DTA on this topic [59-61] has laid some important initial steps in the assessment of testing methods, but much more work is still evidently needed. Continuing efforts include RILEM Technical Committees 283-CAM specialising in chloride ingress testing, and 294-MPA addressing mechanical properties, both focused on alkali-activated materials. These questions remain of critical importance to engineers and specifiers who seek to ensure the safety and serviceability of structures and must underpin standardisation (as discussed below).

2.3 Revisiting the 2007 'State of the Art' [62] [2]

Another major milestone in the field of alkali activation is the 2007 review paper of Duxson *et al.* [62], published as part of a Special Issue of *Journal of Materials Science* focused on geopolymer technology. This paper was a collaboration between the Australian and Spanish research groups that were at the time at the forefront of international developments, particularly in investigation lower-calcium alkali-activated binders which are the main focus of the literature examined. This paper has been cited more than 3800 times in the Google Scholar database, and as such is the second-most cited paper in this research field behind the 1991 paper of Davidovits [24]. Many of these citations – which are still accruing at a rate of several hundred per year –use this paper as a reference point describing the state of the art in the field; this is inaccurate, as the field of alkali-activation has developed very significantly in the past 15 years and numerous other review papers have been published which better represent the current state of understanding. Nonetheless, as a detailed review of the state of the art at the time it does represent an important landmark, and also raised issues relevant at the time which are worthy of discussion in a retrospective sense. These include the following topics:

Reaction path modelling

Duxson *et al.* [62] presented a widely-reproduced illustration that schematically described the chemical reaction sequences involved with the reaction, formation and hardening processes of low-calcium alkali-activated binders, developed from the concepts proposed by Glukhovsky [19]. This conceptual formulation has also provided the basis for various reaction kinetic descriptions of the alkali-activation process. The description of phase formation and evolution was later extended to additionally describe the formation of Ca-rich and Mg-rich hydrates that are important in alkali-activated slag binders [1], which were not presented in the 2007 version with its focus on low-calcium binders. The conceptualisation of alkali-activation as a multi-stage chemical reaction process, mediated by aqueous chemical reactions and requiring the dissolution of a solid precursor and later nucleation and growth of solid products, has proven to be helpful in enabling different

[2] Note that the lead author of this paper was a co-author of the 2007 Duxson et al. paper; it is hoped that this does not prevent us from presenting an unbiased view of its role in the past and present literature discussion of alkali-activation.

aspects of the alkali-activation reaction sequence to be controlled and manipulated, and is therefore a very useful aspect of the fundamental literature in this field.

Engineering properties and applications

One of the main conclusions of the assessment of Duxson *et al.* [62] was that concretes based on alkali-activated fly ash appeared to have significant potential for commercialisation and full-scale deployment, but still needed further (and longer-term) investigation of the durability properties of the binder. The discussion of durability in [62] was focused mainly on the binder itself rather than interactions with steel reinforcement; since that time, a lot of focus has shifted to the study of the ability of alkali-activated binders to protect steel reinforcement from corrosion, which was not a main topic of discussion in the assessment conducted in 2007. Results related to steel protection (particularly passivation and resistance to chloride attack) have been rather mixed [63], with the potential for excellent protection of steel identified both in highly alkaline pore fluids [64, 65] and in the presence of high concentrations of reduced sulfur [66]. Overall it seems that a more calcium-rich binding system offers the opportunity for better protection of steel reinforcing elements due to the ability to close down the pore network of the binder and restrict ingress of external aggressive species [60]; these aspects were not considered in detail in the 2007 assessment of Duxson *et al.* [62], but since that time have become a major focus of both technical analysis and commercial developments.

2.4 A standardisation milestone – BSI PAS 8820:2016

It is important also to mention the British Standards Institute Publicly Available Specification (BSI PAS) 8820:2016 [67] as a notable milestone in the history of alkali-activation. In this specification, a performance basis for the testing and validation of alkali-activated binders was defined for the first time by a major national standardisation body. Performance-based concrete specification is seen as a very important step in introducing opportunities for innovation in material design for technical attributes and for sustainability [68, 69], and this BSI PAS document provides a framework by which this can be achieved within the UK regulatory system. Although uptake and usage of this specification in actual industrial practice remains rather limited to date, its existence and availability provide a useful signposting effect for other international standardisation efforts which may be able to benefit from (and improve upon) the ideas and testing protocols described therein.

3 ALKALI-ACTIVATION AND THE PATHWAY TO NET ZERO

It is also worthwhile to consider the potential future of alkali-activated materials in a highly carbon-constrained world as net-zero targets are emphasised by policymakers and broader society [7]. It is clear that the supply of conventional coal fly ash and blast furnace slag will become more restricted as these processes are replaced by other, less carbon-intensive methods of production of electricity and iron respectively. Calcined clays have been identified, among the portfolio of available alternative cementitious constituents, to offer probably the greatest scope for use on a gigatonne per annum scale [70]; their use in Portland cement blends (with or without added limestone) will obviously add value in the global built environment if clay calcination can be sufficiently scaled-up, but the use of alkali-activated clay-based cements is also of strong interest in areas where the necessary resources are available [7, 71-73]. There is open and ongoing debate about whether the best pathway to utilisation of slag, ash and clay resources is to use them in alkali-activation or in blends with Portland cement, and there are numerous national and global roadmaps available which describe potential pathways for the cement and/or concrete sectors to approach net zero emissions. Some of these roadmaps place a high emphasis on the use of alternative binders such as alkali-activated materials, while others more or less discard the possibility of any non-Portland binders playing a significant role in a net-zero future.

Without providing a detailed critique of the reasons for either including or excluding alkali-activation from the future cements technology portfolio, the position presented here is fairly straightforward: it is essential that the toolkit of available materials, techniques, and creative solutions to technical problems is kept as broad and inclusive as possible, to enable the most suitable possible approach to be selected for each and every local situation, need and application. It would be short-sighted and potentially self-sabotaging for the global cements sector to place full reliance on one technology, or even a small number of technologies, to the exclusion of all others.

The heart of sustainable development is intrinsically about fit-for-purpose materials and solutions that take full advantage of local opportunities in material resources (by-products and/or geological), climate, sustainable energy sources (e.g. decarbonised electricity or waste heat). It is extremely unlikely that alkali-activation will be the sole necessary answer to cement supply questions in a net-zero scenario [74] – but it can, and should, at least be considered a valid and potentially valuable attribute of the future cements toolkit with which the industry addresses its responsibility to decarbonise while meeting the infrastructure materials needs of a developing global society.

ACKNOWLEDGEMENTS

The authors are grateful for very enlightening discussions with many experts in alkali activation and the broader field of concrete technology, particularly through a succession of RILEM Technical Committees that have been active in this area. S.A. Bernal is grateful for the EPSRC Early Career Fellowship EP/R001642/1.

REFERENCES

[1] J. L. Provis and S. A. Bernal, "Geopolymers and related alkali-activated materials," *Annual Review of Materials Research*, vol. 44, no. 1, pp. 299-327, 2014.

[2] J. L. Provis and J. S. J. van Deventer, Eds. *Alkali-Activated Materials: State-of-the-Art Report, RILEM TC 224-AAM*. Dordrecht: Springer/RILEM, 2014.

[3] C. Shi, B. Qu, and J. L. Provis, "Recent progress in low-carbon binders," *Cement and Concrete Research*, vol. 122, pp. 227-250, 2019.

[4] K. Arbi, M. Nedeljković, Y. Zuo, and G. Ye, "A review on the durability of alkali-activated fly ash/slag systems: Advances, issues, and perspectives," *Industrial & Engineering Chemistry Research*, vol. 55, no. 19, pp. 5439-5453, 2016.

[5] N. Li, C. Shi, Z. Zhang, H. Wang, and Y. Liu, "A review on mixture design methods for geopolymer concrete," *Composites Part B: Engineering*, vol. 178, p. 107490, 2019.

[6] T. Luukkonen, Z. Abdollahnejad, J. Yliniemi, P. Kinnunen, and M. Illikainen, "One-part alkali-activated materials: A review," *Cement and Concrete Research*, vol. 103, pp. 21-34, 2018.

[7] J. L. Provis, "Alkali-activated materials," *Cement and Concrete Research*, vol. 114, pp. 40-48, 2018.

[8] J. L. Provis and S. A. Bernal, "Milestones in the analysis of alkali-activated binders," *Journal of Sustainable Cement-Based Materials*, vol. 4, no. 2, pp. 74-84, 2015.

[9] J. Whiting, "Manufacture of cement," U.S. Patent 544,706, U.S. Patent Office, 1895.

[10] H. F. Staley, "Cements for Spark-Plug Electrodes (Technologic Papers of the National Bureau of Standards, #155)," U.S. Department of Commerce, Washington DC, 1920.

[11] A. Z. Khalifa, Ö. Cizer, Y. Pontikes, A. Heath, P. Patureau, S. A. Bernal, and A. T. M. Marsh, "Advances in alkali-activation of clay minerals," *Cement and Concrete Research*, vol. 132, #106050, 2020.

[12] K. Schwartzwalder and C. D. Ortman, "Sodium silicate type cement", U.S. Patent Office 2,793,956, USA, 1957.

[13] R. E. Parry, "Structural unit and method of manufacture", U.S. Patent 2,549,516, U.S. Patent Office, 1946.

[14] G. W. Morrow and N. B. Sackrison, "Mineral surfacing granules containing calcined clay", U.S. Patent 3,169,075, U.S. Patent Office, 1965.

[15] J. Davidovits, "Properties of geopolymer cements," in *Proceedings of the First International Conference on Alkaline Cements and Concretes*, Kiev, Ukraine, P. V. Krivenko, Ed., 1994, vol. 1: VIPOL Stock Company, pp. 131-149.

[16] A. O. Purdon, "The action of alkalis on blast-furnace slag," *Journal of the Society of Chemical Industry - Transactions and Communications*, vol. 59, pp. 191-202, 1940.

[17] A. Buchwald, M. Vanooteghem, E. Gruyaert, H. Hilbig, and N. Belie, "Purdocement: application of alkali-activated slag cement in Belgium in the 1950s," *Materials and Structures*, vol. 48, no. 1-2, pp. 501-511, 2015.

[18] M. Vanooteghem, "Duurzaamheid van beton met alkali-geactiveerde slak uit de jaren 50 - Het Purdocement," M.Ing. thesis, Faculteit Ingenieurswetenschappen en Architectuur, Universiteit Gent, Ghent, Belgium, 2011.

[19] V. D. Glukhovsky, *Gruntosilikaty (Soil Silicates)*. Kiev: Gosstroyizdat, 1959, 154 pp.

[20] P. V. Krivenko, "Alkaline cements," in *Proceedings of the First International Conference on Alkaline Cements and Concretes*, Kiev, Ukraine, P. V. Krivenko, Ed., 1994, vol. 1: VIPOL Stock Company, pp. 11-129.

[21] C. Shi, P. V. Krivenko, and D. M. Roy, *Alkali-Activated Cements and Concretes*. Abingdon, UK: Taylor & Francis, 2006, 376 pp.

[22] H. Xu, J. L. Provis, J. S. J. van Deventer, and P. V. Krivenko, "Characterization of aged slag concretes," *ACI Materials Journal*, vol. 105, no. 2, pp. 131-139, 2008.

[23] J. Davidovits, *Geopolymer Chemistry and Applications*. Saint-Quentin, France: Institut Géopolymère, 2008, 592 pp.

[24] J. Davidovits, "Geopolymers - Inorganic polymeric new materials," *Journal of Thermal Analysis*, vol. 37, no. 8, pp. 1633-1656, 1991.

[25] G. Habert, S. A. Miller, V. M. John, J. L. Provis, A. Favier, A. Horvath, and K. L. Scrivener, "Environmental impacts and decarbonization strategies in the cement and concrete industries," *Nature Reviews Earth & Environment*, vol. 1, pp. 559-573, 2020.

[26] A. O. Purdon, "Improvements in processes of manufacturing cement, mortars and concretes," British Patent GB427227A, 1934.

[27] A. Cwirzen, R. Engblom, J. Punkki, and K. Habermehl-Cwirzen, "Effects of curing: comparison of optimised alkali-activated PC-FA-BFS and PC concretes," *Magazine of Concrete Research*, vol. 66, no. 6, pp. 315-323, 2014.

[28] G. Kovalchuk, A. Fernández-Jiménez, and A. Palomo, "Alkali-activated fly ash: Effect of thermal curing conditions on mechanical and microstructural development – Part II," *Fuel*, vol. 86, no. 3, pp. 315-322, 2007.

[29] J. Małolepszy and J. Deja, "The influence of curing conditions on the mechanical properties of alkali-activated slag binders," *Silicates Industriels*, vol. 53, no. 11-12, pp. 179-186, 1988.

[30] P. C. Hewlett and M. Liska (eds.), *Lea's Chemistry of Cement and Concrete, 5th Ed.* Oxford, UK: Butterworth Heinemann, 2019, 858 pp.

[31] S. D. Wang, K. L. Scrivener, and P. L. Pratt, "Factors affecting the strength of alkali-activated slag," *Cement and Concrete Research*, vol. 24, no. 6, pp. 1033-1043, 1994.

[32] B. Talling and J. Brandstetr, "Present state and future of alkali-activated slag concretes," in *3rd International Conference on Fly Ash, Silica Fume, Slag and Natural Pozzolans in Concrete, ACI SP114*, Trondheim, Norway, V. M. Malhotra, Ed., 1989, vol. 2: American Concrete Institute, pp. 1519-1546.

[33] A. Buchwald and J. Wierckx, "ASCEM cement technology - Alkali-activated cement based on synthetic slag made from fly ash," in *First International Conference on Advances in Chemically-Activated Materials*, Jinan, China, C. Shi and X. Shen, Eds., 2010: RILEM, pp. 15-21.

[34] M. I. M. Alzeer, H. Nguyen, C. Cheeseman, and P. Kinnunen, "Alkali-activation of synthetic aluminosilicate glass with basaltic composition," *Frontiers in Chemistry*, vol. 9, #715052, 2021.

[35] M. Ben Haha, B. Lothenbach, G. Le Saout, and F. Winnefeld, "Influence of slag chemistry on the hydration of alkali-activated blast-furnace slag -- Part I: Effect of MgO," *Cement and Concrete Research*, vol. 41, no. 9, pp. 955-963, 2011.

[36] M. Ben Haha, B. Lothenbach, G. Le Saout, and F. Winnefeld, "Influence of slag chemistry on the hydration of alkali-activated blast-furnace slag -- Part II: Effect of Al_2O_3," *Cement and Concrete Research*, vol. 42, no. 1, pp. 74-83, 2012.

[37] S. A. Bernal, R. San Nicolas, R. J. Myers, R. Mejía de Gutiérrez, F. Puertas, J. S. J. van Deventer, and J. L. Provis, "MgO content of slag controls phase evolution and structural changes induced by accelerated carbonation in alkali-activated binders," *Cement and Concrete Research*, vol. 57, pp. 33-43, 2014.

[38] M. Criado, S. A. Bernal, P. Garcia-Triñanes, and J. L. Provis, "Influence of slag composition on the stability of steel in alkali-activated cementitious materials," *Journal of Materials Science*, vol. 53, no. 7, pp. 5016-5035, 2018.

[39] M. Criado, B. Walkley, X. Ke, J. L. Provis, and S. A. Bernal, "Slag and activator chemistry control the reaction kinetics of sodium metasilicate-activated slag cements," *Sustainability*, vol. 10, #4709, 2018.

[40] R. Tänzer, A. Buchwald, and D. Stephan, "Effect of slag chemistry on the hydration of alkali-activated blast-furnace slag," *Materials and Structures*, vol. 48, no. 3, pp. 629-641, 2015.

[41] S. Onisei, A. P. Douvalis, A. Malfliet, A. Peys, and Y. Pontikes, "Inorganic polymers made of fayalite slag: On the microstructure and behavior of Fe," *Journal of the American Ceramic Society*, vol. 101, no. 6, pp. 2245-2257, 2018.

[42] Y. Pontikes, L. Machiels, S. Onisei, L. Pandelaers, D. Geysen, P. T. Jones, and B. Blanpain, "Slags with a high Al and Fe content as precursors for inorganic polymers," *Applied Clay Science*, vol. 73, pp. 93-102, 2013.

[43] H. Mehdizadeh, E. Najafi Kani, A. Palomo Sanchez, and A. Fernandez-Jimenez, "Rheology of activated phosphorus slag with lime and alkaline salts," *Cement and Concrete Research*, vol. 113, pp. 121-129, 2018.

[44] C. Shi and Y. Li, "Investigation on some factors affecting the characteristics of alkali-phosphorus slag cement," *Cement and Concrete Research*, vol. 19, no. 4, pp. 527-533, 1989.

[45] P. L. Lopez Gonzalez, R. M. Novais, J. Labrincha, B. Blanpain, and Y. Pontikes, "Modifications of basic-oxygen-furnace slag microstructure and their effect on the rheology and the strength of alkali-activated binders," *Cement and Concrete Composites*, vol. 97, pp. 143-153, 2019.

[46] M. Criado, X. Ke, J. L. Provis, and S. A. Bernal, "Alternative inorganic binders based on alkali-activated metallurgical slags," in

Sustainable and Nonconventional Construction Materials using Inorganic Bonded Fiber Composites, H. Savastano Jr, J. Fiorelli, and S. F. dos Santos, Eds. Duxford, UK: Woodhead, 2017, pp. 185-220.

[47] S.-D. Wang, X.-C. Pu, K. L. Scrivener, and P. L. Pratt, "Alkali-activated slag cement and concrete: a review of properties and problems," *Advances in Cement Research*, vol. 7, no. 27, pp. 93-102, 1995.

[48] R. J. Myers, S. A. Bernal, R. San Nicolas, and J. L. Provis, "Generalized structural description of calcium-sodium aluminosilicate hydrate gels: The crosslinked substituted tobermorite model," *Langmuir*, vol. 29, no. 17, pp. 5294-5306, 2013.

[49] R. J. Myers, B. Lothenbach, S. A. Bernal, and J. L. Provis, "Thermodynamic modelling of alkali-activated slag cements," *Applied Geochemistry*, vol. 61, pp. 233-247, 2015.

[50] R. J. Myers, S. A. Bernal, and J. L. Provis, "Phase diagrams for alkali-activated slag binders," *Cement and Concrete Research*, vol. 95, pp. 30-38, 2017.

[51] B. Lothenbach and A. Gruskovnjak, "Hydration of alkali-activated slag: Thermodynamic modelling," *Advances in Cement Research*, vol. 19, no. 2, pp. 81-92, 2007.

[52] B. Walkley, X. Ke, O. Hussein, and J. L. Provis, "Thermodynamic properties of sodium aluminosilicate hydrate (N–A–S–H)," *Dalton Transactions*, vol. 50, no. 39, pp. 13968-13984, 2021.

[53] B. Lothenbach, D. A. Kulik, T. Matschei, M. Balonis, L. Baquerizo, B. Dilnesa, G. D. Miron, and R. J. Myers, "Cemdata18: A chemical thermodynamic database for hydrated Portland cements and alkali-activated materials," *Cement and Concrete Research*, vol. 115, pp. 472-506, 2019.

[54] P. T. Durdziński, M. Ben Haha, S. A. Bernal, N. De Belie, E. Gruyaert, B. Lothenbach, E. Menéndez Méndez, J. L. Provis, A. Schöler, C. Stabler, Z. Tan, Y. Villagrán Zaccardi, A. Vollpracht, F. Winnefeld, M. Zając, and K. L. Scrivener, "Outcomes of the RILEM round robin on degree of reaction of slag and fly ash in blended cements," *Materials and Structures*, vol. 50, no. 2, #135, 2017.

[55] M. Izquierdo, X. Querol, J. Davidovits, D. Antenucci, H. Nugteren, and C. Fernández-Pereira, "Coal fly ash-slag-based geopolymers: Microstructure and metal leaching," *Journal of Hazardous Materials*, vol. 166, no. 1, pp. 561-566, 2009.

[56] H. A. van der Sloot, D. S. Kosson, N. Impens, N. Vanhoudt, T. Almahayni, H. Vandenhove, L. Sweeck, R. Wiegers, J. L. Provis, C. Gascó, and W. Schroeyers, "8 - Leaching assessment as a component of environmental safety and durability analyses for NORM containing building materials," in *Naturally Occurring Radioactive Materials in Construction*, W. Schroeyers Ed. Duxford, UK: Woodhead Publishing, 2017, pp. 253-288.

[57] J. Labrincha, F. Puertas, W. Schroeyers, K. Kovler, Y. Pontikes, C. Nuccetelli, P. Krivenko, O. Kovalchuk, O. Petropavlovsky, M. Komljenovic, E. Fidanchevski, R. Wiegers, E. Volceanov, E. Gunay, M. A. Sanjuán, V. Ducman, B. Angjusheva, D. Bajare, T. Kovacs, G. Bator, S. Schreurs, J. Aguiar, and J. L. Provis, "7 - From NORM by-products to building materials," in *Naturally Occurring Radioactive Materials in Construction*, W. Schroeyers Ed. Duxford, UK: Woodhead Publishing, 2017, pp. 183-252.

[58] P. Krivenko, O. Kovalchuk, A. Pasko, T. Croymans, M. Hult, G. Lutter, N. Vandevenne, S. Schreurs, and W. Schroeyers, "Development of alkali activated cements and concrete mixture design with high volumes of red mud," *Construction and Building Materials*, vol. 151, pp. 819-826, 2017.

[59] J. L. Provis, K. Arbi, S. A. Bernal, D. Bondar, A. Buchwald, A. Castel, S. Chithiraputhiran, M. Cyr, A. Dehghan, K. Dombrowski-Daube, A. Dubey, V. Ducman, A. Dunster, G. J. G. Gluth, S. Nanukuttan, K. Peterson, F. Puertas, A. van Riessen, M. Torres-Carrasco, G. Ye, and Y. Zuo, "RILEM TC 247-DTA Round Robin Test: Mix design and reproducibility of compressive strength of alkali-activated concretes," *Materials and Structures*, vol. 52, #99, 2019.

[60] G. J. G. Gluth, K. Arbi, S. A. Bernal, D. Bondar, A. Castel, S. Chithiraputhiran, A. Dehghan, K. Dombrowski-Daube, A. Dubey, V. Ducman, K. Peterson, P. Pipilikaki, S. L. A. Valcke, G. Ye, Y. Zuo, and J. L. Provis, "RILEM TC 247-DTA round robin test: carbonation and chloride penetration testing of alkali-activated concretes," *Materials and Structures*, vol. 53, no. 1, #21, 2020.

[61] F. Winnefeld, G. J. G. Gluth, S. A. Bernal, M. C. Bignozzi, L. Carabba, S. Chithiraputhiran, A. Dehghan, S. Dolenec, K. Dombrowski-Daube, A. Dubey, V. Ducman, Y. Jin, K. Peterson, D. Stephan, and J. L. Provis, "RILEM TC 247-DTA round robin test: sulfate resistance, alkali-silica reaction and freeze–thaw resistance of alkali-activated concretes," *Materials and Structures*, vol. 53, no. 6, #140, 2020.

[62] P. Duxson, A. Fernández-Jiménez, J. L. Provis, G. C. Lukey, A. Palomo, and J. S. J. van Deventer, "Geopolymer technology: The current state of the art," *Journal of Materials Science*, vol. 42, no. 9, pp. 2917-2933, 2007.

[63] S. Mundra, S. A. Bernal, M. Criado, P. Hlaváček, G. Ebell, S. Reinemann, G. J. G. Gluth, and J. L. Provis, "Steel corrosion in reinforced alkali-activated materials," *RILEM Technical Letters*, vol. 2, pp. 33-39, 2017.

[64] S. Mundra, M. Criado, S. A. Bernal, and J. L. Provis, "Chloride-induced corrosion of steel rebars in simulated pore solutions of alkali-activated concretes," *Cement and Concrete Research*, vol. 100, pp. 385-397, 2017.

[65] R. Pouhet and M. Cyr, "Carbonation in the pore solution of metakaolin-based geopolymer," *Cement and Concrete Research*, vol. 88, pp. 227-235, 2016.

[66] S. Mundra and J. L. Provis, "Mechanisms of passivation and chloride-induced corrosion of mild steel in sulfide-containing alkaline solutions," *Journal of Materials Science*, vol. 56, no. 26, pp. 14783-14802, 2021.

[67] *BSI PAS 8820:2016, Construction materials – Alkali-activated cementitious material and concrete – Specification*, British Standards Institute, London, UK, 2016.

[68] M. G. Alexander and G. Nganga, "Reinforced concrete durability: some recent developments in performance-based approaches," *Journal of Sustainable Cement-Based Materials*, vol. 3, no. 1, pp. 1-12, 2014.

[69] R. D. Hooton, "Current developments and future needs in standards for cementitious materials," *Cement and Concrete Research*, vol. 78, no. A, pp. 165-177, 2015.

[70] K. L. Scrivener, "Options for the future of cement," *Indian Concrete Journal*, vol. 88, no. 7, pp. 11-21, 2014.

[71] S. E. M. Lawther, J. A. McIntosh, S. Nanukuttan, J. L. Provis, M. N. Soutsos, and D. Jose, "Understanding the microstructure of alternative binder systems – banahCEM, a metakaolin based geopolymer," in *Civil Engineering Research in Ireland 2016*, Galway, J. Goggins, Ed., 2016: Civil Engineering Research Association of Ireland. [Online]. Available: https://ceri2016.exordo.com/files/papers/164/final_draft/164.pdf.

[72] J. Kwasny, T. A. Aiken, M. N. Soutsos, J. A. McIntosh, and D. J. Cleland, "Sulfate and acid resistance of lithomarge-based geopolymer mortars," *Construction and Building Materials*, vol. 166, pp. 537-553, 2018.

[73] R. Pouhet and M. Cyr, "Formulation and performance of flash metakaolin geopolymer concretes," *Construction and Building Materials*, vol. 120, pp. 150-160, 2016.

[74] J. L. Provis, "Innovation in cements - can we meet future construction needs sustainably?," in *Proceedings of the 6th International Conference on Geotechnics, Civil Engineering and Structures (CIGOS21) (Lecture Notes in Civil Engineering vol. 203)*, Ha Long, Vietnam, H.-M. Cuong, A. M. Tang, T. Q. Bui, X. H. Vu, and D. V. K. Huynh, Eds., 2021: Springer Singapore, pp. 29-36.

Review of fly-ash as a supplementary cementitious material

Nikki Maria Shaji[1], Niall Holmes[1,2], Mark Tyrer[1,2]
[1]School of Civil & Structural Engineering, Technological University Dublin, Dublin 1, Ireland
[2]Institute of Advanced Study, Collegium Basilea, Basel, Switzerland

email: C17399161@mytudublin.ie, niall.holmes@tudublin.ie, m.tyrer@mtyrer.net

ABSTRACT: This paper presents a review of fly-ash as a Supplementary Cementitious Material (SCM) in concrete in terms of its effects on hydration and durability. The climate change agenda has focused the cement and concrete industry on using low embodied CO_2 materials and much effort has been made on incorporating industrial by-products into cement as SCMs. With worldwide cement production (circa 4 billion tonnes) currently accounting for approximately 8% of global CO_2 emissions and 7% of industry energy use, the use of suitable SCMs to partially replace cement in concrete is extremely important. However, while coal-fired power stations are in the decline, due to the need for more sustainable energy generation, there remains stockpiles of fly-ash for potential use as an SCM. This creates opportunities for ashes not previously used in concrete to be studied both in terms of its behaviour during hydration and durability performance in harsh environments. However, these new fly-ash sources need to be studied carefully due to uncertainties about their physical and chemical constituents, reactivity, long term stability and phase relationships and minor elements distribution due to the variability in the source of coal. The work presented includes a review of fly-ash in terms of its effects during cement hydration and contribution to concretes performance in harsh environments from the literature.

KEY WORDS: Cement; Fly ash; Concrete; Cement Hydration; SCM.

1 INTRODUCTION

Concrete is one of the leading construction materials in the world today with approximately 14 billion cubic meters of concrete cast each year, according to the Global Cement and Concrete Association (GCCA) [1]. In Ireland, the consumption of concrete is approximately 15 million cubic meters per annum and according to Aecom, there was a 15% growth in the Irish construction industry in 2021 [2].

However, concrete has a problem [3]. Due to its usage, cement production now contributes to 5-10% of global CO_2 emissions. With the GCCA 2050: Concrete Future introduced, methods to producing carbon neutral construction is set in motion [1]. This policy encourages construction industries and researchers to innovate towards producing low carbon structures. One such action that will accelerate the CO_2 reduction is increasing the clinker substitutions in concrete. Various Supplementary Cementitious Materials (SCMs) such as fly ash, calcined clays, ground granulated blast-furnace slag, and ground limestone can be used to replace the heavy CO_2 emitters [1]. The use of these SCMs, with no additional clinkering process involved, can lead to significant reduction in the CO_2 emissions produced for as less cement will be used in concrete.

One material commonly used to replace cement is Pulverised Fuel Ash (PFA), also known as fly ash (in the USA). Generally considered as a waste material, it is a by-product formed by the combustion of coal. Fly-ash particles tends to be spherical in shape (see Figure 1), ranging in micrometre particle sizes with a relatively high reactivity depending on the chemical composition of the individual particles [4,5]. Fly ash has been used as a SCM in concrete for some time in the UK, Europe, USA and Asia due to the improvements it offers in durability, workability, and higher compressive strengths compared to plain Ordinary Portland Cement (OPC) concretes. According to ASTM standard [6], the three classifications of fly ash,

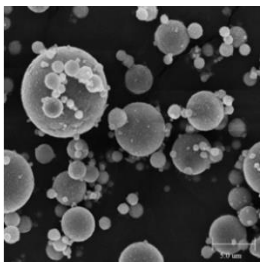

Figure 1. Fly Ash at Low Magnification. [4]

Class C, Class F and Class N which differ through their chemical compositions [6,7]. However, due to its pozzolanic properties, Class C and Class F fly ash are mostly used as cement substitutes with the main difference between them is the Calcium (Ca) content (Class C has a higher Ca content than Class F). Also, Class F has a higher Silica (Si), Alumina (Al) and Iron (Fe) content [8].

This paper will present a short review of the influence fly-ash has as a SCM during cement hydration and in concrete.

2 FLY ASH IN CEMENT

2.1 Material Properties of Fly Ash

Multiple tests and research have been conducted over the years to obtain the desired amount of fly ash that could be added to concrete to achieve a greater strength than with OPC. The nature and origin of the used coal along with the furnace design and operation contributes to the physical properties of the fly ash produced. The cooling time of the burned material contribute to the crystallization of the fly ash particles. Rapid cooling of the ash attributes to the formation of higher proportions of glassy phases. Tests such as X-ray diffraction (XRD), X-ray fluorescence (XRF) and scanning electron microscopy (SEM) have been used to compile the crystalline

phases of fly ash [9]. Minerals such as magnetite, quartz, hematite, mullite and calcite are the most common minerals found in fly ash from bituminous coal.

The chemical aspects of the fly-ash however are characterized by the lower Ca content than plain OPC, which influences the type and volume of solid hydrates formed during hydration, which influence the long-term strength and durability of the concrete. Blending fly ash with OPC decreases the amount of portlandite in the hydrated mixture while increasing the amount of low Ca/Si content C-S-H. In addition, the volume of alumina, ferric oxide, monosulfate (AFm) phases is increased due to the high quantities of Al_2O_3 present in the ash. Addition of further gypsum ($CaSO_4$) can increase the amount of ettringite formed giving a higher total volume of hydrates. When high quantities of Al-rich fly ash are blended with OPC, strätlingite is formed as shown in Figure 2. According to Hanehara *et al*. [10], with a substitution of 60% fly ash, the volume of portlandite becomes so low, self-neutralization may occur. During this phenomenon, the alkalinity of the hardened cement and concrete is lowered due to the calcium hydroxide being excessively consumed by the pozzolanic reaction. Studies [10,11] have shown that after a hydration period of 1 year and longer, the complete depletion of the portlandite was observed, along with a significant decrease in the amount of ettringite precipitated and an increase in the AFm phases with increasing fly ash reaction.

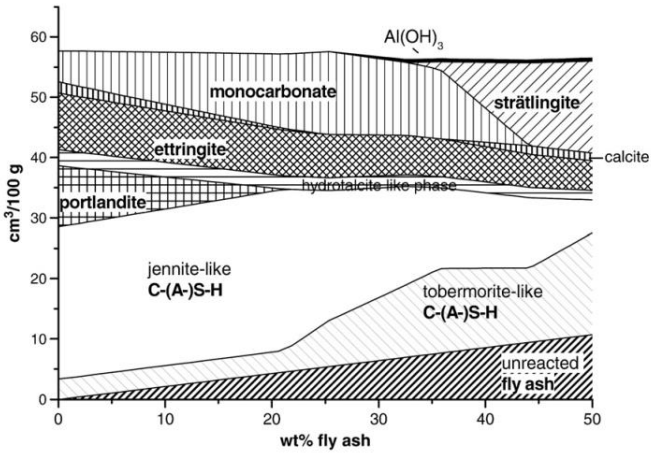

Figure 2. Phase assemblage of hydrated Portland cement upon blending with fly ash [11]

2.2 Heat of Hydration / Cement Hydration

Heat of hydration in cement refers to the exothermic reaction when cement is mixed with water. This production of heat during the curing of concrete has correlation to the composition and fineness of the cement powder, the water to cement (w/c) ratio and cement type. The cement hydration process can be distinguished by five stages as shown in Figure 3a [12].

With the addition of fly ash as a replacement to cement, the time taken for the heat of hydration to reach its maximum peak is less compared to plain OPC due to the fineness of the fly ash particles. This is a result of the lower specific surface area and reduced solubility of the aluminosilicate in the fly ash. Figures 3b and 3c illustrates the heat evolution of different types of fly ashes, Classified fly ash (CFA), Run-of-station fly ash (RFA)

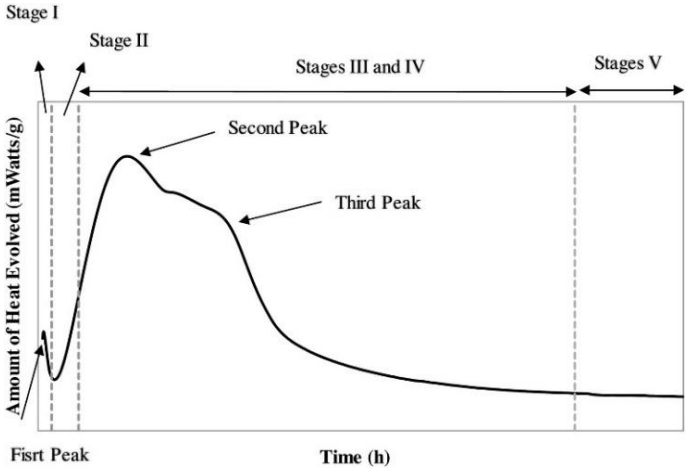

(a)

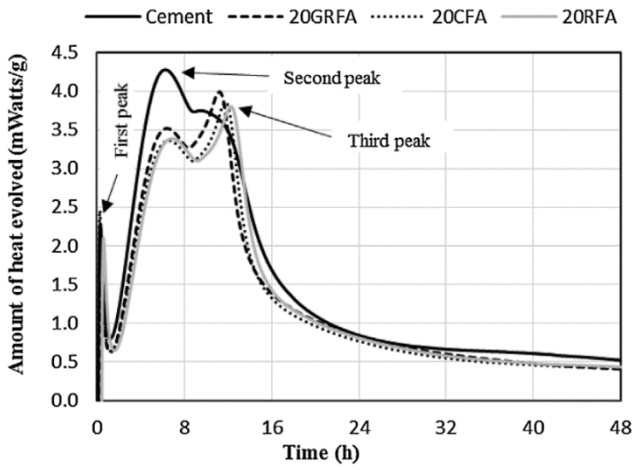

(b)

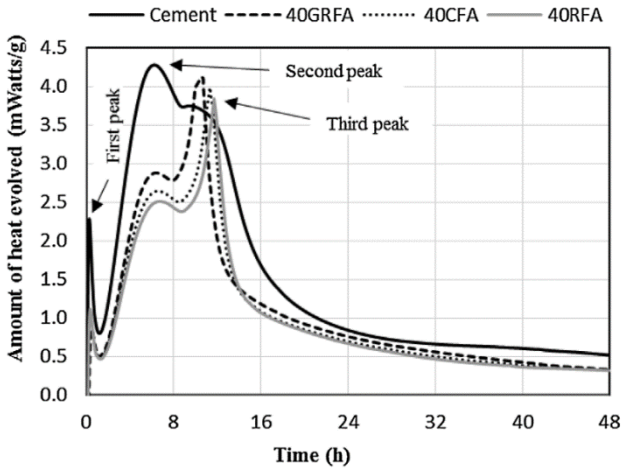

(c)

Figure 3. Heat Evolution Curve (a) cement hydration heat evolution curve (b) heat evolution curve for 20% fly ash blended cement paste (c) heat evolution curve for 40% fly ash blended cement paste [13].

and Grounded run-of-station fly ash (GRFA), with a substitution level of 20% and 40% in the blended cement paste. Studies have shown [14] that the fineness of the fly ash has a correlation with the peak intensities for the heat of hydration of blended cement.

It has been observed in the literature [15,16] that in blended cements, the intensity of the second peak decreases due to the dilution effect, which occurs when the cement content is reduced as the portion of fly ash increases (Figure 3(b) & (c)). This low pozzolanic activity could also be attributed to the lower solubility of the fly ash in the pore solution. Finally, the third peak was recorded to be more evident for the fly ash blended cement compared to plain OPC. This enhancement of the reaction was found to be due to the fly ash providing more nucleation sites for the calcium aluminates to precipitate, known as the filler effect, thereby increasing the reaction of tricalcium aluminate (C_3A) with the gypsum present in the cement and the conversion of ettringite to monosulfate [15,16].

3 FLY ASH IN CONCRETE

When fly ash is added to concrete as a cement replacement, it has been reported in the literature that its performance compared to plain mixes is improved. This section looks at how the addition of fly-ash improves the performance of concrete in different harsh environments.

3.1 Compressive Strength

The compressive strength of OPC increases rapidly during the early stages. Figure 4 displays the compressive strength of concrete with varying amount of fly ash at 3, 7, 28 and 90 days. As can be seen, the compressive strength of those concretes with fly ash is more gradually increasing over time compared to the plain OPC mixes. At 3 days, all fly ash concretes were found to have a lower compressive strength than the plain cement mixture. As the percentage of fly ash increased, the initial hydration rate of cement is reduced and therefore a mixture with 25% fly ash had the lowest compressive strength compared to others. This can be attributed to the dilution effect of the fly ash, which lowers the relative proportion of cement and dilutes the active component in the blended cement pastes due to the lower pozzolanic activity of the ash early on.

However, as shown in Figure 4, the strength of the fly ash mixture increases over time. Notably, the mixture with 10% and 15% fly ash content were found to acquire a higher strength than the plain cement mixture and the fly ash mixture of 20% and 25% after 90 days of curing with the mixture of 15% attaining the maximum compressive strength at 79.5MPa. From the provided data, it could be seen that all fly ash mixtures had a higher compressive strength compared to plain OPC after 90 days of curing. This development of compressive strength at a later stage is due to the increasing pozzolanic effect over time, set in motion by the calcium hydroxide (CH) formed during the cement hydration. However, with a 20% fly ash content, the compressive strength has notably decreased due to the portlandite in the PFA cement being dissolved at the 20% substitution level. When fly-ash is present, large amounts of C-(A)-S-H gel are formed when the amorphous SiO_2 and Al_2O_3 released during the reaction react with the CH, creating a denser microstructure, improving the compressive strength of fly ash concrete significantly [17,18].

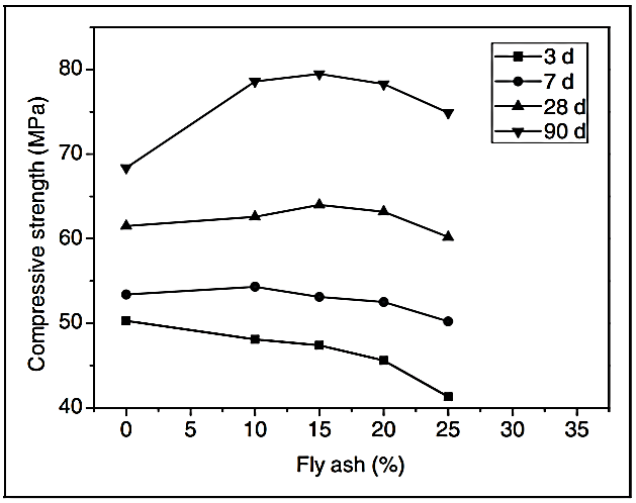

Figure 4. Compressive Strength of Concrete with Varying Fly Ash Content [17].

3.2 Flexural Strength

The flexural strength of concrete has been shown to have a similar strength development. An initial lower flexural strength compared to OPC slowly increases over time, as shown in Figure 5. However, unlike the compressive strength, the sample with 20% substitution of fly ash is shown to have a flexural strength higher than that of OPC. This is also shown in Table 1 [19]. This increase in the flexural strength is due to the fineness of the fly ash and the morphology of the particles as the fine particles fill the pores during the hydration process, producing a denser microstructure.

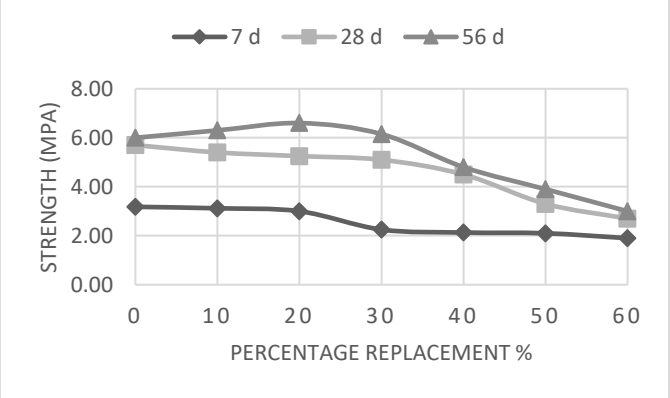

Figure 5. Flexural Strength of Concrete [19].

Table 1. Chemical Properties of Fly Ash and OPC

Beam Designation	Fly Ash %	Flexural Strength (Mpa)		
		7 d	28 d	56 d
B1	0	3.18	5.70	6.00
B2	10	3.12	5.40	6.30
B3	20	3.00	5.25	6.60
B4	30	2.25	5.10	6.15
B5	40	2.13	4.50	4.80
B6	50	2.10	3.30	3.90
B7	60	1.90	2.70	3.00

3.3 Effect of fly ash on fresh concrete

3.3.1 Workability

The degree of fineness of fly ash can contribute to the workable properties of fresh concrete. The increased fineness of the fly ash particles increases the lubricant effect in compared to cement particles which improves the workability of the blended cement paste. Figure 6 displays the flow of fly ash blended pastes assessed using the mortar flow test according to ASTM C1437 [20] with cement replacement levels of 20% and 40%. It can be seen that the workability of the blended fly ash cement mixture has an increased flow compared to OPC. This is due to the ball bearing effect of the blended cement mixture which is improved because of the spherical shape of the fly ash particles. The glassy and smooth surface of the fly ash reduces their water absorption capacity compared to plain cement particles help to improve the flow of the mixture [15].

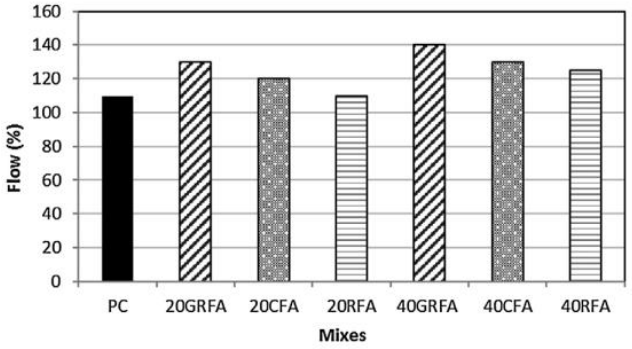

Figure 6. Flow rate of fly ash cement with varying fineness and cement replacement levels [15].

Slump tests by Mahajan *et al* [21] noted that the round spherical shape of the fly ash improves the workability. Concrete produced with fly ash has been shown to have improved workability compared to OPC concrete due to the improved cohesiveness of the fly ash mixture [22]. Figure 7 shows with increasing fly ash content, the concrete slump also increases, thereby reducing the water demand of the blended concrete paste for workability purposes [23].

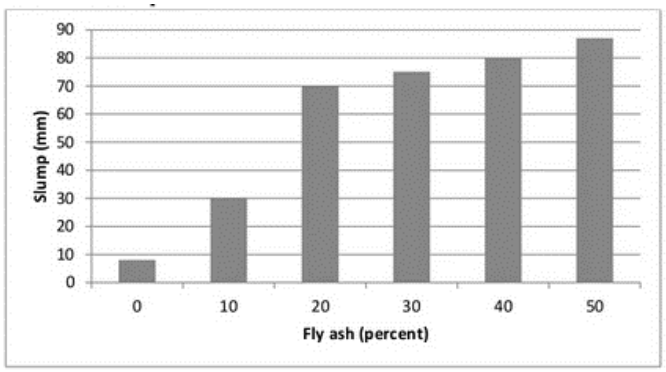

Figure 7. Slump for various fly ash replacement levels in concrete mix [23].

3.3.2 Bleeding

Fly ash in concrete has less bleeding and segregation compared to OPC due to the reduced water demand during hydration. High fly ash content in concrete with low water content can reduce the effect of bleeding on concrete to a point of practically eliminating it. Gebler *et al* [24] noted reduced bleeding was a result of the lower water requirement of fly ash mortar. Therefore, during the production of concrete containing PFA, the water usage in the paste can be reduced according to the rate of replacement of cement to fly ash [22,24,25].

3.3.3 Setting time

The use of fly ash in the concrete mixture can retard the setting time of freshly poured concrete, depending on (1) cement type and content, (2) w/c ratio, (3) the type and amount of chemical admixtures, (4) temperature and (5) the quantity and composition of the fly ash. The setting time of PFA concrete is controlled by the chemical reactions occurring between the cement compounds. Silicates and aluminates present in reacted PFA cement mixture tends to dominate during the early stages of hydration which contributes to the setting and early strength development. This is due to the silicates and aluminates being the predominant component responsible for the formation of the principal product of hydration, C-A-S-H.

The climate of the region affects the setting time of the concrete as hot climate regions experience a reduced retardation which allows more time to place and complete the pouring of the concrete. However, during cold weather, the use of fly ash can lead to significant delays, especially with high levels of replacement. Due to this delay, practical consideration could lead to a limited use of fly ash in the concrete mixture to reduce the difficulties with regards to finishing operations. The use of admixtures can partially or wholly decrease the setting time. Ref [25] found that Class C fly ash generally delays the setting time compared to Class F and concluded that the increased hydraulic reactivity of the fly ash, as well as the calcium content, was the main reason why [22,26,27].

3.4 Durability

3.4.1 Sulfate resistance

Sulfate attack, a common cause of deterioration, can occur when concrete is located in environments with high ionic strengths, as found in some soils, groundwater and seawater. Sulfate attack tends to soften the concrete and may lead to expansion, cracking and loss of strength due to the re-formation of gypsum, ettringite and thaumasite at high sulfate concentrations through the reactions with calcium hydroxide and calcium aluminate hydrate (Figure 8) [28,29].

Following a number of studies conducted on Class C and Class F fly ashes, it was demonstrated that sufficient use of low-calcium Class F fly ash contributed to the increased resistance of concrete to sulfate attack and high-calcium Class C fly ashes were found not as effective. Indeed, Class C may have a tendency to increase the rate and extent of the sulfate attack.

3.4.2 Carbonation

The process where CO_2 from the air penetrates into the concrete which reacts with calcium hydroxide, calcium silicate

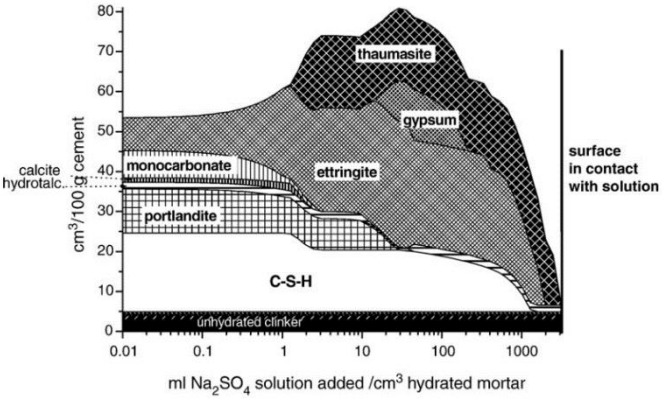

Figure 8. Calculated phase assemblage of a mortar sample immersed a Na_2SO_4 solution [30].

and aluminates, to form carbonates is known as carbonation of concrete. Carbonation reduces the alkalinity of the mixture, which leads to the corrosion of the embedded steels [25]. As the pH falls below ~10/9, hydration of the CO_2 occurs resulting in the formation of carbonic acid (H_2CO_3) which speciates into the HCO_3^- and CO_3^{2-} ions formed by the rapid dissolution of the CO_2 into the alkaline pore solution, leading to the corrosion of concrete [31]. Fly ash helps to decrease the permeability of the concrete thereby increasing its ability to resist cracking. It has been documented through various studies by multiple researchers [31,32,33,34] that fly-ash blended concrete exhibited a reduced likelihood of carbonation than of OPC mixes.

3.4.3 Chloride Resistance

Fly ash reduces the penetration of chlorides and cations due to the changes in the pore structure and the chloride binding capacity of the cement paste [35]. The chloride ions present in the concrete attacks the protective oxide film formed around the reinforcement steel in the initial high alkaline chemical environment. Fly ash reduces the chloride-ion ingress through the binding and immobilization of the chloride ions which is achieved due to the much higher quantities of active alumina present in the fly ash compared to OPC. [35]

3.5 Precast Concrete

The use of fly ash as an SCM in precast concrete helps to improve the quality as well as the durability of the material. The addition of fly ash helps improve the workability of the mixture with reduced amount of water, which in turn contributes to the improved strength of concrete. However, the use of fly ash in precast concrete can reduce the early strength gain and slow the setting time. Having less reactive particles than OPC, the time taken for heat of hydration can extend for six months and longer. With the use of accelerators, plasticizers and or small amounts of additional condensed silica fume (CSF) can help to diminish the problem, providing high ultimate strength, high-performance concrete [36].

4 RESEARCH

Research is ongoing by the authors to determine the optimum cement replacement level of conditioned pulverised fuel ash in concrete using the current stockpile deposited at the ESB Moneypoint power station in Co. Clare. This work will include a comprehensive thermodynamic cement hydration study using state of the art models and experimental techniques, assess the improved durability performance in concretes containing PFA by undertaking a suite of non-destructive tests in three exposure environments and confirm the environmental benefits of it as a SCM.

5 CONCLUSIONS

The use of fly ash as SCMs with OPC enhances the properties of plain concrete along with reducing the CO_2 emissions of cementitious materials through the avoidance of the clinkering process while utilizing the by-product formed by industrial manufacturing process. The optimum level of fly ash for the blended mixture varies on (1) the chemical and physical properties of the fly ash, (2) the proportion of fly ash along with the other materials such as aggregates present in the concrete mixture, (3) the conditions during placing and (4) the exposure conditions subjected to the fly ash concrete. The use of fly ash as a cement replacement substitute increases the overall strength, workability and durability of concrete.

ACKNOWLEDGMENTS

The authors acknowledge the financial support for the research through a TU Dublin Business Partner award.

REFERENCES

[1] Global Cement and Concrete Association. 2021. The GCCA 2050 Cement and Concrete Industry Roadmap for Net Zero Concrete. [online] Available at: <https://gccassociation.org/concretefuture/wp-content/uploads/2021/10/GCCA-Concrete-Future-Roadmap-Document-AW.pdf>.

[2] Gleeson, C., 2021. Construction 'to grow by 15%' in 2021 despite Covid and Brexit. [online] The Irish Times. Available at: <https://www.irishtimes.com/business/construction/construction-to-grow-by-15-in-2021-despite-covid-and-brexit-1.4462147> [Accessed 27 February 2022].

[3] Crow, J.M. (2008) The Concrete Conundrum. Chemistry World, 62. http://www.rsc.org/images/Construction_tcm18-114530.Pdf https://doi.org/10.1201/b12851-5

[4] Feng, J., Sun, J. and Yan, P. (2018). The Influence of Ground Fly Ash on Cement Hydration and Mechanical Property of Mortar. Advances in Civil Engineering, pp.1-7.

[5] Aboustait, M., Kim, T., Ley, M. T., and Davis, J. M. (2016). Physical and chemical characteristics of fly ash using automated scanning electron microscopy, Construction and Building Materials, 106, pp.1–10

[6] ASTM Standard ASTM C618:(2003)

[7] Wardhono, A. (2018). Comparison Study of Class F and Class C Fly Ashes as Cement Replacement Material on Strength Development of Non-Cement Mortar. IOP Conference Series: Materials Science and Engineering, 288, pp.012-019.

[8] Gamage, N., Liyanage, K., Fragomeni, S. and Setunge, S. (2011). Overview of different type of fly ash and their use as a building and construction material. International Conference of Structural Engineering, Construction and Management.

[9] Wesche K. Fly Ash in Concrete: Properties and Performance / Editor, K. Wesche. First edition. (Wesche K, ed.). CRC Press; 2014. doi:10.1201/9781482267051

[10] S. Hanehara, F. Tomosawa, M. Kobayakawa, K.R. Hwang, Effects of water/powder ratio, mixing ratio of fly ash, and curing temperature on

pozzolanic reaction of fly ash in cement paste, Cement and Concrete Research 31 (1) (2001) 31-19.
[11] Lothenbach, B., Scrivener, K. and Hooton, R., 2011. Supplementary cementitious materials. Cement and Concrete Research, 41(12), pp.1244-1256.
[12] Bullard, J., Jennings, H., Livingston, R., Nonat, A., Scherer, G., Schweitzer, J., Scrivener, K. and Thomas, J. (2011). Mechanisms of cement hydration. Cement and Concrete Research, 41(12), pp.1208-1223.
[13] Brueggen, B., Kang, T. and Ramseyer, C. (2010). Experimental and SEM Analyses of Ground Fly Ash in Concrete. International Journal of Concrete Structures and Materials, 4(1), pp.51-54.
[14] V. Rahhal, R. Talero, Influence of two different fly ashes on the hydration of portland cements, J. Therm. Anal. Calorim. 78 (1) (2004) 191–205
[15] Moghaddam, F., Sirivivatnanon, V. and Vessalas, K., 2019. The effect of fly ash fineness on heat of hydration, microstructure, flow and compressive strength of blended cement pastes. Case Studies in Construction Materials, 10, p.e00218.
[16] Snelson, D., Wild, S. and O'Farrell, M., 2008. Heat of hydration of Portland Cement–Metakaolin–Fly ash (PC–MK–PFA) blends. Cement and Concrete Research, 38(6), pp.832-840.
[17] Zhang, P., Li, Q. and Zhang, H. (2011). Combined effect of polypropylene fiber and silica fume on mechanical properties of concrete composite containing fly ash. Journal of Reinforced Plastics and Composites, 30(16), pp.1349-1358.
[18] Sun, J., Shen, X., Tan, G. and Tanner, J., 2018. Compressive strength and hydration characteristics of high-volume fly ash concrete prepared from fly ash. Journal of Thermal Analysis and Calorimetry, 136(2), pp.565-580.
[19] Upadhyay, R., Srivastava, V., Herbert, A. and Mehta, P. (2014). Effect of Fly Ash on Flexural Strength of Portland Pozzolona Cement Concrete. Journal of Academia and Industrial Research (JAIR), 3, pp.218-220.
[20] ASTM International, ASTM C1437 Standard Test Method for Flow of Hydraulic Cement Mortar, (2015).
[21] Mahajan, L., Mahadik, S. and Bhagat, S. (2020). Investigation of Fly Ash Concrete by Slump Cone and Compaction Factor Test. IOP Conference Series: Materials Science and Engineering, 970(1), pp.012011.
[22] Thomas, M. (2007). Optimizing the Use of Fly Ash in Concrete. Portland Cement Association.
[23] Rkein, M., 2015. Study of utilization of fly ash as a replacement of cement and fine aggregates in concrete. Bachelor of Engineering. Charles Darwin University.
[24] Gebler, S. H., and Klieger, P., Effect of Fly Ash on Some of the Physical Properties of Concrete (RD089.O IT), Portland Cement Association, 1985. Preprint of Proceedings, Second International Conference on the Use of Fly Ash, Silica Fume, Slag, and Other Mineral By-Products in Concrete, April 21-25, 1986, Madrid, Spain (American Concrete Institute publication SP-9 1).
[25] Kosmatka, S., Kerkhoff, B. and Panarese, W. (2002). Design and Control of Concrete Mixtures. Portland Cement Association, pp.57-72.
[26] Roberts, L.R. and Taylor, P.C. (2007). Understanding Cement-SCMAdmixture Interaction Issues: Staying Out of the Safety Zone. Concrete International, pp. 33-41.
[27] Wang, H., Qi, C., Farzam, H. and Turici, J. (2006). Interaction of Materials Used in Concrete: Effects of Fly Ash and Chemical Admixtures on Portland Cement Performance. Concrete International, pp.47-52.
[28] Breysse, D. (2010). Non-Destructive Evaluation of Reinforced Concrete Structures, 3 - Deterioration processes in reinforced concrete: an overview. Woodhead Publishing, pp.28-56
[29] Panesar, D. (2019). Developments in the Formulation and Reinforcement of Concrete, 3 - Supplementary cementing materials. 2nd ed. Woodhead Publishing, pp.55-85.
[30] Thomas Schmidt, Barbara Lothenbach, Michael Romer, Jürg Neuenschwander, Karen Scrivener, Physical and microstructural aspects of sulfate attack on ordinary and limestone blended Portland cements, Cement and Concrete Research 39 (2009) 1111–1121
[31] von Greve-Dierfeld, S., Lothenbach, B., Vollpracht, A., Wu, B., Huet, B., Andrade, C., Medina, C., Thiel, C., Gruyaert, E., Vanoutrive, H., Saéz del Bosque, I., Ignjatovic, I., Elsen, J., Provis, J., Scrivener, K., Thienel, K., Sideris, K., Zajac, M., Alderete, N., Cizer, Ö., Van den Heede, P., Hooton, R., Kamali-Bernard, S., Bernal, S., Zhao, Z., Shi, Z. and De Belie, N., 2020. Understanding the carbonation of concrete with supplementary cementitious materials: a critical review by RILEM TC 281-CCC. Materials and Structures, 53(6).
[32] Glinicki, M., Jóźwiak-Niedźwiedzka, D., Gibas, K. and Dąbrowski, M., 2016. Influence of Blended Cements with Calcareous Fly Ash on Chloride Ion Migration and Carbonation Resistance of Concrete for Durable Structures. Materials, 9(1), p.18.
[33] Bargaheiser, Keith & Butalia, Tarunjit. (2007). Prevention of Corrosion in Concrete Using Fly Ash Concrete Mixes.
[34] Zhang, D., Cai, X. and Shao, Y., 2016. Carbonation Curing of Precast Fly Ash Concrete. Journal of Materials in Civil Engineering, 28(11), p.04016127.
[35] Dhir, R. and Jones, M., 1999. Development of chloride-resisting concrete using fly ash. Fuel, 78(2), pp.137-142.
[36] Rosenberg, A., 2022. *Using Fly Ash in Concrete*. [online] Precast.org. Available at: <https://precast.org/2010/05/using-fly-ash-in-concrete/> [Accessed 5 July 2022].

Use of low grade kaolinitic clays in development of a pozzolan-cement binder system

Kwabena Boakye[1*], Morteza Khorami[1], Eshmaiel Ganjian[2], Ahmad Ehsani[3], Andrew Dunster[4], Messaoud Saidani[1], Mark Tyrer[5] and Xiang Zhang[1]
[1]Faculty of Engineering, Environment & Computing, Coventry University, UK
[2]Concrete Corrosion Tech Ltd., UK
[3]Indo-UK Centre for Environmental Research & Innovation, University of Greenwich, UK
[4]Andrew Dunster, BRE, UK
[5]Consulting Scientist, Geomaterials, Geochemistry
email: boakyek4@uni.coventry.ac.uk; aa8186@coventry.ac.uk; eganjian@yahoo.co.uk; a.ehsani@greenwich.ac.uk andrew.dunster@bregroup.com; cbx086@coventry.ac.uk; m.tyrer@mtyrer.net; ab8295@coventry.ac.uk

ABSTRACT: The use of calcined, kaolinite-rich clays as pozzolanic components in blended cements has gained a great deal of attention in recent years. This reflects its impact on reducing the total embedded carbon dioxide associated with concrete made from such binders. Reduction of CO_2 is two-fold: the clays are calcined at a lower temperature than Portland cement and also replace some of the clinker in the binder phase. Pure kaolinite clay is relatively expensive however, as it is used in other industrial applications.
This work studies the potential utilization of low-grade (less pure) kaolinitic clay as a supplementary cementitious material in mortar formulations. Examination by XRD revealed the presence of kaolinite, illite and quartz as the main clay minerals present in the materials. The clay samples were dried and calcined at 600 °C and the effect of heat treatment on the physical, mineralogical and microstructural properties studied.
The calcined clay was uniformly blended with ordinary Portland cement at replacement levels of 10%, 20% and 30% by weight and their mechanical properties determined after 7 and 28 days. Blended cements containing 10 wt.% and 20 wt.% calcined clay were seen to have compressive strength results comparable to the reference cement at 28 days.

KEY WORDS: Pozzolan; Kaolinitic clays; Microstructural properties; Calcined clay; Compressive strength; Portland cement.

1 INTRODUCTION

The incorporation of supplementary cementitious materials (SCMs) as a partial replacement of Portland cement for construction applications has been reported as the most effective approach towards the reduction of greenhouse gases from the construction industry [1].

Industrial and agricultural by-products such as pulverised fly ash, ground granulated blast-furnace slag (GGBS), silica fume and rice husk ashes are the most common SCMs. Aside their contribution to the mitigation of solid waste management problems, SCMs also present several technical advantages in concrete including improved compressive strength, durability and impermeability [2].

Notwithstanding these benefits, the accessibility of conventional SCMs from industrial and agricultural sources has its own challenges due to the over dependence on the few industries for a worldwide supply [3]. Again, most of the waste generated by these industries, which can be used as SCMs are of low quality compared to the standard [4]. It has become therefore essential to explore other materials, which possess the quality and are available in quantities that can meet the construction industry's demand.

Kaolinitic clays have been described as the most suitable alternative to replace fly ash and other industrial by-products due to their properties and availability. Clays in their natural form may not have the desired reactivity because of their crystalline structure. However, after heat-treatment, their crystalline structures are transformed into amorphous, thereby improving their pozzolanic reactivity [4]. Furthermore, the temperatures required for clay calcination (usually between 600-900 °C) are much lower than that of Portland cement [5]. This, in a way, decreases the amount of energy and carbon footprints related to the concrete industry. Even so, clays containing high levels of kaolinite are most preferable because of their appreciable reactivity. High-grade kaolinitic clays are, however, not easily accessible since they are found in only specific places and can also be expensive due to their use in the paper and ceramic industries [6].

Several researchers [7] have extensively studied the use of pure calcined kaolinitic clays for concrete applications and reported improved mechanical and durability properties due to its high reactivity. This research studies the influence of low-grade kaolinitic clay, calcined at 600 °C, on the thermal, mineralogical and mechanical properties of mortar.

2 MATERIALS AND METHODS

Portland cement (CEM I 52.5 N), manufactured by Hanson, was used as the main binder in this research. Brick clay was obtained from a local brick manufacturer in Bellingdon, England. The raw clay was dried in an oven at a temperature of 120 °C.

The clay was crushed, pulverized using a hammer mill and oven-dried at 50 °C for 24 hours. It was then calcined in a Nabertherm Muffle Furnace at a temperature of 600 °C at a heating rate of 10 °C/min. The calcined clay, after cooling on a laboratory bench, was milled into fine powder.

Chemical composition of the raw samples were determined by XRF using Panalytical Axios mAX WDXRF spectrometer. XRD analysis of the powders were also carried out using a 3rd generation Malvern Panalytical Empyrean XRD Diffractometer. TG/DSC analysis was also conducted with the Perkin Elmer DSC 7 analyser. Particle size analysis was

performed using the Laser Diffraction method with the Malvern Mastersizer 2000 analyser.

CEM-I cement was partially replaced with the calcined clay in weight percentages of 10 wt.%, 20 wt.% and 30 wt.% to form Portland-calcined clay blended cements. 50 × 50 × 50 mm mortar cubes were prepared according to methods specified by BS EN 196-1:2016, using a cement to sand ratio of 1:3 and water/binder ratio of 0.4. The mortar cubes were cured under water and their respective compressive strengths determined after 7 and 28 days. Setting times and water demand was also determined using the Vicat apparatus as described in BS EN 196-3:2016.

Figure 1. Raw clay

Figure 2. Calcined clay

3 RESULTS AND DISCUSSION

The particle size distributions of the clay, calcined clay and CEM-1 cement are presented in Figure 3. Other physical properties are also shown in Table 1. Specific gravity is observed to decrease with increasing calcined clay content in the mortar. Water needed to form a workable paste, on the other hand, increased with increase in the calcined clay content. The smaller particle size of the calcined clay, possibly increased the surface area of blended cement and therefore required more water [8]. There was also a progressive increase in both initial and final setting times as the pozzolan content increased.

Table 1. Some properties of the reference cement , calcined clay and blended cements

Property	CEM I	CC	10%CC	20%CC	30%CC
Specific gravity	3.15	2.62	3.05	2.96	2.82
water demand, %	28.2	–	32.4	33.3	39
Initial set, min	162	–	180	190	200
Final set, min	250	–	280	295	320

CC – Calcined clay

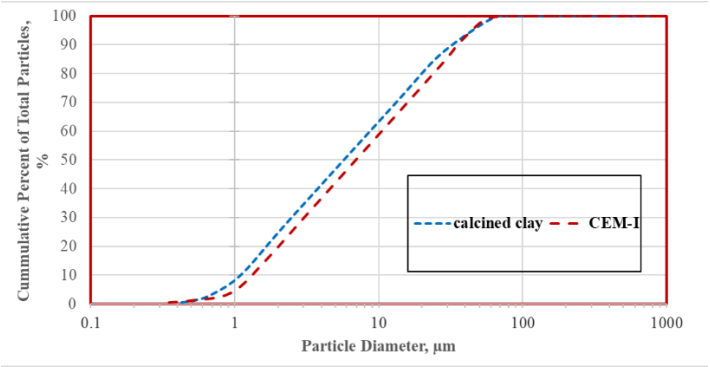

Figure 3. Particle size distribution of calcined clay and the reference cement.

The XRF analysis of the calcined clay and the reference cement are shown in Table 2. The chemical compositions of the raw materials were generally within acceptable limits. The calcined clay contains 40.54% SiO_2, which passes the ASTM C618 minimum requirement of 25% for pozzolans. Also, the sum SiO_2, Al_2O_3 and Fe_2O_3 is higher than the minimum 70% prescribed by ASTM C618 but must, however, be interpreted with caution.

Table 2. Chemical composition of calcined clay and the reference cement.

Material	Chemical composition, %								
	SiO_2	Al_2O_3	Fe_2O_3	MgO	CaO	Na_2O	K_2O	SO_3	Cl
CC	40.54	28.75	25.42	1.40	0.25	0.20	1.07	0.19	0.01
CEM-1	21.0	4.4	2.7	1.6	66.7	0.6	1.99	2.27	≤0.1

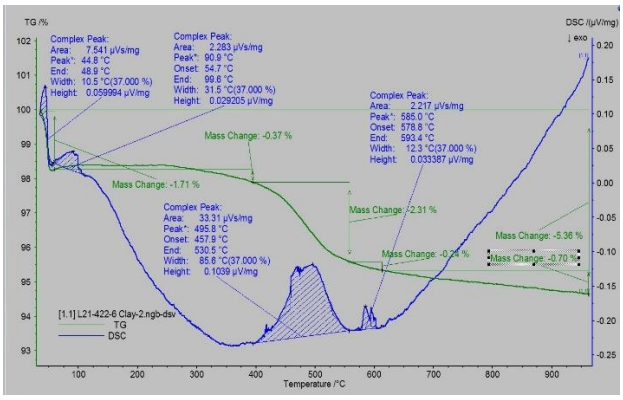

Figure 4. TGA/DSC of the clay.

The XRD patterns of the raw clay, as shown in Figure 5 is generally made up of quartz, kaolinite, illite and other

associated minerals. The presence of illite can be associated with K_2O and Na_2O/MgO [13] as seen in the XRF data in Table 2.

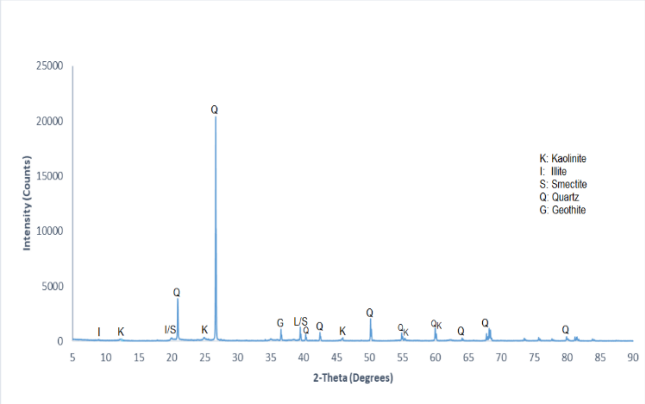

Figure 5. XRD of clay

The 7 and 28 day compressive strength results of the reference and blended cements are presented in Figure 6. The control sample recorded 7 and 28 day strength of 36.6 MPa and 58.5 MPa respectively. These strength values consistently reduced as the calcined clay replacement increased from 10 wt.% to 30 wt.%. The addition of 10% metakaolin decreased strengths to 34.5 MPa and 55.5 MPa respectively, but still satisfied EN 197-1 [17] standard. Considering the percentage reductions, 20 wt.% appears to be the optimum replacement level.

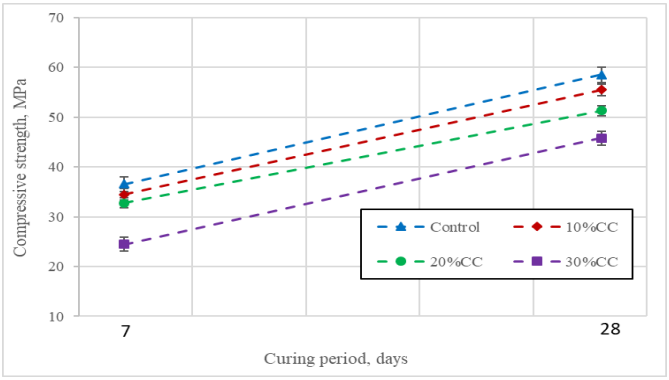

Figure 6. Compressive strength of calcined clay mortar.

4 CONCLUSION

This paper has studied the potential of calcined low-grade kaolinitic clay, calcined at 600 ºC, as cement replacement in mortar formulations. The chemical compositions of the reference cement and calcined clay contained all the relevant oxides and were within acceptable limits. TGA/DSC analysis revealed a complete dehydroxylation of kaolinite to form metakaolinite at 600 ºC. XRD analysis showed that the clay largely made up of quartz, kaolinite, illite and other associated minerals. The partial replacement of CEM I with the calcined clay caused a decrease in both early and later strengths. At this stage, 20 wt.% is recommended as the optimum replacement, pending further investigations.

REFERENCES

[1] Juenger MCG, Siddique R. Recent advances in understanding the role of supplementary cementitious materials in concrete. Cem Concr Res 2015;78:71-80.

[2] Nehdi ML. Clay in cement-based materials: Critical overview of state-of-the-art. Constr Build Mater 2014;51:372-82.

[3] Li C, Zhu H, Wu M, Wu K, Jiang Z. Pozzolanic reaction of fly ash modified by fluidized bed reactor-vapor deposition. Cem Concr Res 2017;92:98-109.

[4] Zhao D, Khoshnazar R. Microstructure of cement paste incorporating high volume of low-grade metakaolin. Cement and Concrete Composites 2020;106:103453.

[5] Sabir BB, Wild S, Bai J. Metakaolin and calcined clays as pozzolans for concrete: a review. Cement and Concrete Composites 2001;23:441-54.

[6] Scrivener K, Martirena F, Bishnoi S, Maity S. Calcined clay limestone cements (LC3). Cem Concr Res 2018;114:49-56.

[7] Hu L, He Z. A fresh perspective on effect of metakaolin and limestone powder on sulfate resistance of cement-based materials. Constr Build Mater 2020;262:119847.

[8] Schulze SE, Rickert J. Suitability of natural calcined clays as supplementary cementitious material. Cement and Concrete Composites 2019;95:92-7.

[9] Fernandez R, Martirena F, Scrivener KL. The origin of the pozzolanic activity of calcined clay minerals: A comparison between kaolinite, illite and montmorillonite. Cem Concr Res 2011;41:113-22.

[10] Taylor-Lange SC, Lamon EL, Riding KA, Juenger MCG. Calcined kaolinite–bentonite clay blends as supplementary cementitious materials. Appl Clay Sci 2015;108:84-93.

[11] Yanguatin H, Ramírez JH, Tironi A, Tobón JI. Effect of thermal treatment on pozzolanic activity of excavated waste clays. Constr Build Mater 2019;211:814-23.

[12] Fabbri B, Gualtieri S, Leonardi C. Modifications induced by the thermal treatment of kaolin and determination of reactivity of metakaolin. Appl Clay Sci 2013;73:2-10.

[13] Dixit A, Du H, Pang SD. Marine clay in ultra-high performance concrete for filler substitution. Constr Build Mater 2020;263:120250.

An insight into graphene as an additive for the use in concrete

Tahreer M. Fayyad[1*], Ahmed F. Abdalqader[1], Mohammed Sonebi[2]
[1]Tracey Concrete Ltd, Sligo Road, Enniskillen, BT74 7LF, Northern Ireland
[2]Queen's University Belfast, Stranmillis Rd, Belfast BT9 5AG, Northern Ireland
Email* : fayyadt@gmail.com

ABSTRACT: The upshot of COP 26 highlighted the urgent need for an accelerated reaction within the construction industry to the calls for adaption to climate change and towards the zero-carbon future. Where cement and concrete industries are responsible for no less than 5-10% of human-made CO_2 emissions, the development and application of low carbon concrete on a global scale is ever more urgent. Graphene is one of the most recent technologies that has promising characteristics that promote sustainable solutions in various applications. Graphene is a single layer of tightly bound carbon atoms where it is the thinnest and the strongest compound known to mankind making it a potential eco-friendly and sustainable solution. It positively impacts the concrete industry as the use of graphene would reduce the amount of Portland cement (PC) in concrete mixes, thereby contributing to the decarbonisation vision by reducing the use of PC and saving carbon emissions. Over the last decade there has been intense research for the deployment of graphene in concrete mixes and there are recent trials for commercial adaption as well. The current paper reviews the latest scientific and technical information on graphene for the use in concrete. The up-to-date findings of the usage of graphene in concrete mixes will be presented. Then, the combination of graphene with other technologies or solutions will be highlighted in the context of enhancing the concrete properties as well as the carbon footprint. This paper will discuss the applicability and the viability of using graphene in concrete in the context of precast concrete industry.

KEY WORDS: Graphene; Precast concrete; Carbon footprint; Construction materials.

1 INTRODUCTION

The growing climate crisis is the most urgent matter of our time. All communities and industries are in a race to accelerate the transition to more sustainable and environmentally friendly practices. The construction industry is no exception and faces greater pressure to speed up the adoption of cleaner and greener materials and processes. Concrete is the most widely used construction material worldwide and is responsible for extremely large emissions. Cement, the main binding material in concrete, is the source of about 8% of the world's carbon dioxide (CO_2) emissions [1], [2]. Therefore, the cement and concrete manufacturers as well as the construction industry have been working hard to decarbonise the sector as much as possible. Some countries set approaches and propose plans to reach net zero carbon and beyond such as Ireland and the UK [3], [4].

To achieve this target, a set of strategies and tools is required. One strategy is to develop new and innovative technologies such as the use of graphene in concrete [3]. Graphene is a carbon-based nanomaterial with a two dimensional (2D) structure [5]. Graphene has high aspect ratios (i.e., ratios of planar dimension to thickness), thermal conductivity, Young's modulus, stiffness and fracture strength [6]. There are four forms of graphene products, namely; graphene, graphene oxide (GO), reduced graphene oxide (rGO) and graphene nanoplatelets (GNP) [7] as shown in Figure 1.

Since the discovery of graphene, several researchers have examined the addition of graphene on the properties of cement-based materials [5], [8]. The distinct characteristics of graphene strongly favour their effects on the mechanical and durability performance of cement-based composites [9]–[11]. Moreover, it is claimed that graphene can contribute to the sustainability of concrete as some researchers reported that the inclusion of graphene in concrete can result in a decrease by 50% of the required concrete material without compromising the structural safety. Such cut in materials was estimated to reduce 446 kg per tonne of the carbon emissions by the cement manufacturing [9].

This review aims to give a brief overview on the properties of graphene-enhanced concrete and to shed a light on the challenges and issues related to the use of graphene in concrete from the perspective of precast industry.

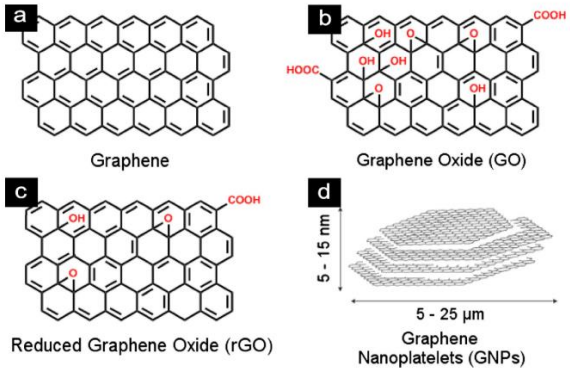

Figure 1. Representation of (a) graphene, (b) graphene oxide (GO), (c) reduced graphene oxide (rGO) and (d) graphene nanoplatelets (GNPs) [7].

2 PRECAST CONCRETE

Over 90 million tonnes of concrete, both ready mix and precast, is manufactured every year in the UK [12]. Precast concrete is

an important part of construction products industry. In the UK, more than 35 million tonnes of precast concrete products are manufactured yearly [13]. The UK Precast Sector reported an annual turnover of £1.3 billion and is estimated to employ around 13,000 people in the UK [14]. Precast concrete offers an economic advantage due to the multiple use of the same mould for one element, a better quality of workmanship and faster operations on site due to pre-production [15]. This is associated with lower carbon footprint and better health and safety.

Precast concrete industry should commit to decarbonising its industry by adopting the latest available technology; developing lower carbon cements and concretes; and switching from traditional fossil fuels such as coal and petcoke to the use of waste, waste biomass and waste part biomass fuels [12]. The use of graphene will help the industry to fulfil its commitment. It is believed that starting the scale up of using graphene into concrete in precast concrete can be a promising option where production quality control is higher than ready mix concrete. In the following sections, the effect of graphene on concrete properties will be highlighted in the context of precast concrete requirements.

3 EFFECT OF GRAPHENE ON CONCRETE PROPERTIES

Most of the work on graphene in cementitious composites have been conducted on cement paste or mortar and only few studies focused on the use of graphene in concrete. This paper primarily reviews the work on concrete and readers are referred to other review papers on paste and mortar [7], [8], [11]. This section will discuss the effect of graphene on concrete workability, mechanical strength and durability.

3.1 Effect on mechanical properties

A distinctive feature of graphene and nano materials is that they can significantly improve the mechanical behaviour and ductility of concrete. The improvement in mechanical properties is attributed to nucleation effect and filling effect. The graphene sheets provides additional nucleation sites for the C-S-H crystals, thereby promoting the hydration reactions and increasing the strength [5]. Moreover, adding graphene into cementitious matrix can fill the nano voids and lead to finer and denser microstructure, thus reducing the porosity and improving the strength [16].

It was demonstrated that concrete containing graphene exhibited a remarkable increase of up to 146% in the compressive strength (Figure 2) and up to 79.5% in the flexural strength as well as a significant reduction in the maximum displacement due to compressive loading by 78% [9]. Similarly, graphite nanoplatelets (GNPs, up to 0.3 wt.%) was found to increase the tensile and flexural strengths of ultra-high performance concrete (UHPC) by 40-45% and 39-59%, respectively depending on the type of GNPs [17]. It was reported that incorporating graphene improved the flexural and compressive strengths of UHPC, with the increase in flexural strength more than that of compressive strength. Particularly, the compressive strength of UHPC incorporating 0.01% by weight of cement graphene after curing for 28 days increased by 7.82% than that of UHPC without graphene (117.34 MPa) [18].

A lesser degree of improvement was reported by Chen et al. [19] who added graphene nano particles into concrete mix in a range of 0.02 wt.% to 0.4 wt.% and tested the compressive strength. They found that the concrete compressive strength improved by adding graphene up to 0.3%, with the addition of 0.05% led to the highest improvement. Similarly, another study reported an increase of 12% and 14% in compressive and flexural strength, respectively was reported for a mixture with 0.045 vol% graphene and 0.6 vol% PVA fibres [20]. In agreement with this, Jiang et al. [21] reported that the compressive strength of concrete improved at low dosages of graphene (0.025% and 0.05%) as this dosage can eliminate the weak cement hydration crystals with tight cross-linking structures. However, higher ratios of graphene led to a decrease in the compressive strength, which might be attributed to the weak zone in the concrete matrix created by agglomeration of graphene. They also found no effect of graphene on flexural strength and explained that due to the small size and aspect ratio of graphene sheet.

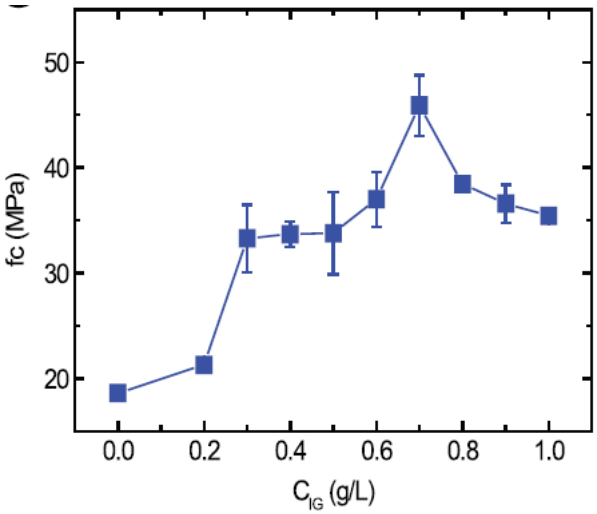

Figure 2 Compressive strengths of concrete incorporating graphene at 7 d [9]

Although the effect of graphene on the early strength of the concrete has not been thoroughly explored yet, the distinct improvement in the strength gives an indication regarding a possible early strength enhancement. The improvement in the early strength of concrete is vital in the precast concrete as it will decrease the open time and accelerate productivity, thus reducing the cost. Therefore, more studies are necessary to explore the potential of adding graphene on accelerating the striking time.

3.2 Effect on workability

Workability is an important factor in the adoption of any new admixture into any concrete. This becomes even more important in precast concrete practices, where it is important to place fresh concrete in forms as quick as possible. Graphene would decrease the workability of concrete. This reduction can be attributed to various mechanism such as the flocculation between cement grains and graphene by electrostatic interactions, which entraps large amount of free water [22], the large surface area and hydrophilicity of graphene nanosheets,

which thus absorbs the available water in fresh mix to wet their surface [10], and the formation of graphene agglomerates because of the chemical reaction between graphene and the hydration products [23].

It was reported that the slump values of concrete mixes containing up to 0.4 wt.% graphene decreased with the increase in graphene content, with values ranging between 70 and 57 mm [19]. Likewise, the fluidity of UHPC decreased with the increasing addition of graphene oxide nanosheets [18]. However, at volume fractions of up to 0.07%, graphene did not change the workability of high performance concrete [20].

To improve the workability of graphene-incorporated cementitious mixtures, different approaches have been recently proposed. It was found that the addition of fly ash can interrupt the flocculation of graphene with cement, releasing the entrapped water and increasing the fluidity [24]. Similarly, the use of silica fume and graphene showed better workability due to the synergetic effect of the surface activity of graphene and the shape effect of silica fume [25]. A recently developed polyether amine functionalized-graphene contributed to the improvement of workability resulted from the steric hindrance of the hydrophilic polyether amine chains [26].

These possible solutions for the decrease of workability should be applied and investigated thoroughly for graphene to be employed in precast concrete industry.

3.3 Effect on durability

It is believed that graphene can contribute to the enhancement of concrete resistance to aggressive liquids. This is because graphene is impermeable and would enable graphene-based materials to act as barriers to prevent ions diffusion. In addition, graphene can densify the microstructure and block interconnected pores [27]. However, up to date, research on using graphene to improve the durability of concrete is still limited. Dimov et al. [9] found that graphene enhanced the water permeability by 400% and the heat capacity by 88% compared to the standard concrete. Another study found that the graphene considerably improves the moisture sorption resistance [20].

It was reported that concrete containing graphene showed better performance after 200 freezing and thawing cycles, evident by lower mass and compressive strength loss and fewer damages on the sample's surfaces [19]. The resistance of concrete to chloride ingress was improved by using an optimal dosage of 1.5% of graphene, which reduced the water permeability (Figure 3), chloride diffusion coefficient, and chloride migration coefficient by 80%, 80%, and 40%, respectively [27]. In another aspect, the loss of mechanical strength of concrete after exposure to 800 °C can be reduced from 70% to 35% by addition of graphene [28].

4 CHALLENGES AND FUTURE PROSPECTS

Despite of the substantial progress achieved in research of graphene-based cementitious composites, the transition to industrial/commercial scale, either in ready mix concrete or precast concrete, is still challenging. Some of these challenges are technical and some are related to production and quality as will be discussed in the following sections.

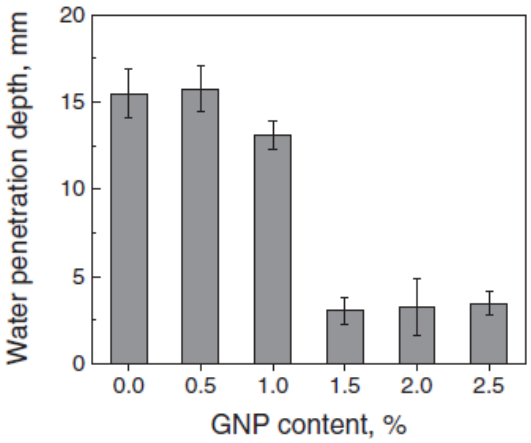

Figure 3 Water penetration depth of GNP infused concrete

4.1 Production consistency

Production of graphene occurs through different methods such as vapor deposition, chemical exfoliation and liquid phase exfoliation [9]. However, these methods produce different graphene products [29]. In addition, many challenges are associated with the production of these products. The properties of synthesised graphene are strongly dependent on the production method as to get perfect graphene sheet, bottom-up methods are recommended. However, these are costly and cannot produce large quantities. Therefore, bulk quantities with reducing graphene oxide can be obtained but this could result in a significant number of defects on the graphene's surface, leading to lower electrical conductivity and mechanical strength [30].

The current large scale techniques of producing graphene oxide shows large variability in surface functionality and sheet size, leading to different hydration rates, dispersibility and interfacial interaction issues between cement and graphene [29]. A recent survey into the properties of commercially available graphene found high variabilities in manufacturing methods, lateral size, thickness and defects [31], [32]. It was concluded that most companies produce graphite micro platelet with poor qualities, so called "flake graphene". However, it is believed that new technologies such as liquid phase exfoliation made by using high-shear blending has remarkably enhanced the quality of graphene and the volume–time dependency of exfoliating graphene in water, allowing for production of large quantities of defect-free graphene solution [9]. The recent development of modified Hummers method would result in safer, cheaper, more sustainable and scalable production of GNS, thereby making the production sufficiently large and reproducible for the construction industry [29].

4.2 Cost

Producing graphene with controllable quality at low cost on an industrial scale is a big challenge. The current cost of producing 1 kg of GNPs ranges from US $65 to $400 [21]. However, it is believed that the growth in industrial production and applications of graphene will lead to sharp decrease in their cost. It is also believed that any additional cost of using graphene would be offset by the reduction in material to deliver

an overall saving of graphene-based concrete over standard concrete.

4.3 Dispersion

A uniform dispersion of nanomaterials, e.g. graphene, in the cement/concrete matrix is vital to achieve a higher strength and a more durable composite. Failing to achieve such dispersion could potentially have an adverse effect on concrete properties due to the formation of agglomerates and weak pockets [22]. The reason of this behaviour can be explained by high surface energy, strong Van der Waals interactions and high hydrophobicity of some forms of graphene [25]. Most of work done on incorporating graphene in concrete found it is a challenging to attain a proper and uniform distribution of graphene in the matrix, thus hindering its widespread incorporation [5].

To overcome this problem, many researchers have employed different methods based on physical action such as ultrasonication, high shear mixing, and ball milling or based on chemical actions such as covalent and noncovalent functionalisation [21]. The noncovalent functionalisation method, for instance, can be achieved through the use of surfactants. A combination of physical and chemical methods can also be used to improve the dispersion.

The use of silica fume and silica sand was used to increase the dispersion of graphene in mortar [33]. A traditional surfactant such as Methylcellulose (MC) was employed with ultrasonic to disperse graphene nanoparticles in water and then cement was added [34]. Commercial superplasticisers based on polycarboxylate-ether (PCE) and naphthalene sulfonate enhanced the dispersion of graphene in cement-based composites [7], [35]. Findings in the use of SPs as a dispersion agent suggest that PCE outperformed ligno- or naphthalene-based SPs as well as air entrainer and Gum Arabic in dispersing graphene [36].

Jiang et al. [21] studied the effect of dispersion techniques on the properties of graphene-reinforced concrete and found that using high shear mixing or high shear mixing combined with ultrasonication in the presence of polycarboxylate-based superplasticiser in both cases promoted better dispersion performance in water. However, the effectiveness of this method in concrete is still required, taking into account the alkaline nature of the matrix. It was suggested that using chemical vapour deposition (CVD) to form the nanosheets on the surface of cement grains or admixtures is worthy to be explored to solve the dispersion problem [30]. Most recently, a new technology was proposed by Nationwide Engineering and the University of Manchester's Graphene Engineering Innovation Centre, involving adding graphene into concrete as a liquid admixture with a trade name of *Concretene*. They claim that this admixture provides an optimised liquid admixture added to concrete at source and disperses evenly, creating stronger, cheaper and more durable concrete [37].

Although these methods were found effective in dispersion of graphene in aqueous solutions and cement-based composites, their capacity to disperse high doses of graphene is still questioned. Therefore, more investigations into dispersing high dosage of graphene in concrete are necessary to ensure full utilisation of its benefits.

4.4 Technical challenges

As presented in Section 3, there are different effects of adding graphene to concrete on the concrete properties such as strength and workability. Further research is still needed regarding the early strength of concrete in order to be applied in precast concrete manufacturing. Also, precast industry requires workable and consistent concrete especially when self-compacting concrete (SCC) is used. Various research results show that the addition of graphene to cement-based mixtures has an adverse effect on the workability. This reduction in workability increases the difficulty of handling, placing and compacting concrete in the forms, leading to severe defects in concrete such as voids and honeycombing. In order to take graphene-enhanced concrete forward into application in precast concrete industry, the workability issue should be addressed and the methods that is believed to mitigate this issue and were presented in Section 3.2 should be investigated and developed.

4.5 Sustainability, Health and safety

It is claimed that the incorporation of graphene in concrete can offer substantial savings in carbon footprint, assisting the industry to achieve construction CO_2 reduction targets.

Papanikolaou et al. [38] conducted a life cycle assessment (LCA) of graphene-based concrete and they mentioned that graphene does not show a negative environmental impact. They reported that the production of 1 kg of G2NanPaste (GNPs product) is found to result in 0.17 $kgCO_2$ equivalent units. They suggested that graphene can be used as additive nano-reinforcement material in the cement composites to reduce the greenhouse gas emission. The improvement of sustainability credentials of graphene-based concrete is attributed to the fact that graphene will assist in reducing maintenance, in using less material, particularly cement, and in lengthening the whole life cycle of structures.

Health and safety in construction is the responsibility of everyone. Thus, the use of any new material should be assessed carefully to mitigate any risk and eliminate its hazards. Nanomaterial such as graphene could be harmful to the human body, if inhaled or ingested into the human body. This is because they might cause troubles for lungs and cardiovascular system. Therefore, it is necessary to investigate the effect of graphene particles on human health. Moreover, graphene oxide can be potentially hazardous material because it can cause explosion under certain conditions. For instance, slow heating of graphene oxide under inert gas to around 140 °C could lead to explosion [39]. Similarly, heating graphene oxide in air to approximately 300 °C could cause explosion [40].

Moreover, it has been reported that powdered graphene oxide is not stable at ambient conditions, resulting in change in their chemical properties during storage in a short span of time ranging between 5 to 30 weeks [41], [42]. However, graphene oxide can be more stable in solutions in the absence of NaOH [43]. Long-term assessment of the stability of graphene products should thoroughly investigated as this aspect has clear implications on industrial production and the uptake of graphene products into the construction market.

4.6 Future Prospect

It is obvious that the climate crisis and the United Nation sustainable development goals UN SDGs are main strategic

trends that affecting civil engineering and construction industry where net zero and sustainability are becoming central to project outcome. The Low Carbon Concrete Routemap that was published in April 2022 by the Institution of Civil Engineers (ICE) sets out recommendations and actions towards zero carbon in the concrete industry. As per the routemap, the next steps in the decarbonisation of concrete include the use of graphene in concrete to enable reductions in volume of concrete and/or cement content starting from 2024. For this to happen within the coming two years, more research is required for the formulation of practical graphene-based concrete for both ready mix concrete and precast concrete. More detailed investigations need to proceed to overcome the challenges that are associated with the production of graphene-enhanced concrete. This always should happen with a parallel sustainability analysis in order to achieve the goal of zero carbon in the construction industry.

5 CONCLUSION

This paper gives a brief overview on the properties of graphene-enhanced concrete and highlights the challenges and issues related to the use of graphene in concrete from the perspective of precast industry.

The paper showed that small dosages of graphene can enhance the mechanical and durability performance of cement-based composites. However, this comes at the expense of loss in workability of mortar/concrete. Improving the workability of graphene-based concrete is pivotal for precast concrete and is possible, though, by different methods such as increasing the SP dosage and using SCMs.

Potential challenges to the use of graphene products in the construction industry were identified and should be first addressed in order to establish a feasible and consistent utilisation of graphene in concrete industry, particularly precast concrete. These challenges compose the production consistency, cost of graphene-based additions, dispersion of graphene in concrete, workability and flowability of graphene-based concrete, sustainability and issues related to health and safety.

Although there has been a substantial progress in addressing these challenges, some important concerns remain and more systematic and thorough work is still required.

REFERENCES

[1] J. de Brito and R. Kurda, "The past and future of sustainable concrete: A critical review and new strategies on cement-based materials," *J. Clean. Prod.*, vol. 281, p. 123558, 2021, doi: 10.1016/j.jclepro.2020.123558.

[2] T. M. Fayyad and A. F. Abdalqader, "Demountable reinforced concrete structures: A review and future directions," in *Civil Engineering Research in Ireland 2020*, 2020, pp. 218–222.

[3] Low Carbon Concrete Group (LCCG), "Low Carbon Concrete Routemap," 2022.

[4] Irish Green Building Council (IGBC), "Net Zero Whole Life Carbon Roadmap for the Built Environment in Ireland," 2022.

[5] Y. Lin and H. Du, "Graphene reinforced cement composites: A review," *Constr. Build. Mater.*, vol. 265, p. 120312, 2020, doi: 10.1016/j.conbuildmat.2020.120312.

[6] U. Sajjad, M. N. Sheikh, and M. N. S. Hadi, "Incorporation of graphene in slag-fly ash-based alkali-activated concrete," *Constr. Build. Mater.*, vol. 322, no. January, p. 126417, 2022, doi: 10.1016/j.conbuildmat.2022.126417.

[7] E. Shamsaei, F. B. de Souza, X. Yao, E. Benhelal, A. Akbari, and W. Duan, "Graphene-based nanosheets for stronger and more durable concrete: A review," *Constr. Build. Mater.*, vol. 183, pp. 642–660, 2018, doi: 10.1016/j.conbuildmat.2018.06.201.

[8] S. Chuah, Z. Pan, J. G. Sanjayan, C. M. Wang, and W. H. Duan, "Nano reinforced cement and concrete composites and new perspective from graphene oxide," *Constr. Build. Mater.*, vol. 73, pp. 113–124, 2014, doi: 10.1016/j.conbuildmat.2014.09.040.

[9] D. Dimov *et al.*, "Ultrahigh Performance Nanoengineered Graphene–Concrete Composites for Multifunctional Applications," *Adv. Funct. Mater.*, vol. 28, no. 23, 2018, doi: 10.1002/adfm.201705183.

[10] Z. Pan *et al.*, "Mechanical properties and microstructure of a graphene oxide-cement composite," *Cem. Concr. Compos.*, vol. 58, pp. 140–147, 2015, doi: 10.1016/j.cemconcomp.2015.02.001.

[11] S. Wu, T. Qureshi, and G. Wang, "Application of graphene in fiber-reinforced cementitious composites: A review," *Energies*, vol. 14, no. 15, 2021, doi: 10.3390/en14154614.

[12] MPA, "UK Concrete and Cement Industry Roadmap to Beyond Net Zero," 2020.

[13] I. Holton, J. Glass, and A. D. F. Price, "Managing for sustainability: findings from four company case studies in the UK precast concrete industry," *J. Clean. Prod.*, vol. 18, no. 2, pp. 152–160, 2010, doi: 10.1016/j.jclepro.2009.09.016.

[14] British Precast, "WHY BUY BRITISH Reasons to Buy British Precast," 2017.

[15] H. Bachmann and A. Steinle, *Precast Concrete Structures*. 2012.

[16] M. li Cao, H. xia Zhang, and C. Zhang, "Effect of graphene on mechanical properties of cement mortars," *J. Cent. South Univ.*, vol. 23, no. 4, pp. 919–925, 2016, doi: 10.1007/s11771-016-3139-4.

[17] W. Meng and K. H. Khayat, "Mechanical properties of ultra-high-performance concrete enhanced with graphite nanoplatelets and carbon nanofibers," *Compos. Part B Eng.*, vol. 107, pp. 113–122, 2016, doi: 10.1016/j.compositesb.2016.09.069.

[18] L. Lu and D. Ouyang, "Properties of cement mortar and ultra-high strength concrete incorporating graphene oxide nanosheets," *Nanomaterials*, vol. 7, no. 7, pp. 1–14, 2017, doi: 10.3390/nano7070187.

[19] G. Chen, M. Yang, L. Xu, Y. Zhang, and Y. Wang, "Graphene nanoplatelets impact on concrete in improving freeze-thaw resistance," *Appl. Sci.*, vol. 9, no. 17, 2019, doi: 10.3390/app9173582.

[20] A. Peyvandi, P. Soroushian, N. Farhadi, and A. M. Balachandra, "Evaluation of the Reinforcement Efficiency of Low-Cost Graphite Nanomaterials in

High-Performance Concrete," *KSCE J. Civ. Eng.*, vol. 22, no. 10, pp. 3875–3882, 2018, doi: 10.1007/s12205-018-0168-6.

[21] Z. Jiang, O. Sevim, and O. E. Ozbulut, "Mechanical properties of graphene nanoplatelets-reinforced concrete prepared with different dispersion techniques," *Constr. Build. Mater.*, vol. 303, no. January, p. 124472, 2021, doi: 10.1016/j.conbuildmat.2021.124472.

[22] M. Wang, R. Wang, H. Yao, Z. Wang, and S. Zheng, "Adsorption characteristics of graphene oxide nanosheets on cement," *RSC Adv.*, vol. 6, no. 68, pp. 63365–63372, 2016, doi: 10.1039/c6ra10902k.

[23] X. Li *et al.*, "Effects of graphene oxide agglomerates on workability, hydration, microstructure and compressive strength of cement paste," *Constr. Build. Mater.*, vol. 145, pp. 402–410, 2017, doi: 10.1016/j.conbuildmat.2017.04.058.

[24] Q. Wang, X. Cui, J. Wang, S. Li, C. Lv, and Y. Dong, "Effect of fly ash on rheological properties of graphene oxide cement paste," *Constr. Build. Mater.*, vol. 138, pp. 35–44, 2017, doi: 10.1016/j.conbuildmat.2017.01.126.

[25] Y. Shang, D. Zhang, C. Yang, Y. Liu, and Y. Liu, "Effect of graphene oxide on the rheological properties of cement pastes," *Constr. Build. Mater.*, vol. 96, pp. 20–28, 2015, doi: 10.1016/j.conbuildmat.2015.07.181.

[26] M. Wang, H. Yao, R. Wang, and S. Zheng, "Chemically functionalized graphene oxide as the additive for cement–matrix composite with enhanced fluidity and toughness," *Constr. Build. Mater.*, vol. 150, pp. 150–156, 2017, doi: 10.1016/j.conbuildmat.2017.05.217.

[27] H. Du, H. J. Gao, and S. D. Pang, "Improvement in concrete resistance against water and chloride ingress by adding graphene nanoplatelet," *Cem. Concr. Res.*, vol. 83, pp. 114–123, 2016, doi: 10.1016/j.cemconres.2016.02.005.

[28] A. Mohammed, J. G. Sanjayan, A. Nazari, and N. T. K. Al-Saadi, "Effects of graphene oxide in enhancing the performance of concrete exposed to high-temperature," *Aust. J. Civ. Eng.*, vol. 15, no. 1, pp. 61–71, 2017, doi: 10.1080/14488353.2017.1372849.

[29] S. E. Lowe and Y. L. Zhong, "Challenges of Industrial-Scale Graphene Oxide Production," *Graphene Oxide Fundam. Appl.*, no. November 2017, pp. 410–431, 2016, doi: 10.1002/9781119069447.ch13.

[30] S. Park and R. S. Ruoff, "Chemical methods for the production of graphenes," *Nat. Nanotechnol.*, vol. 4, no. 4, pp. 217–224, 2009, doi: 10.1038/nnano.2009.58.

[31] A. P. Kauling *et al.*, "The Worldwide Graphene Flake Production," *Adv. Mater.*, vol. 30, no. 44, pp. 1–6, 2018, doi: 10.1002/adma.201803784.

[32] P. Bøggild, "The war on fake graphene," *Nature*, vol. 562, no. 7728, pp. 502–503, 2018, doi: 10.1038/d41586-018-06939-4.

[33] X. Li *et al.*, "Incorporation of graphene oxide and silica fume into cement paste: A study of dispersion and compressive strength," *Constr. Build. Mater.*, vol. 123, pp. 327–335, 2016, doi: 10.1016/j.conbuildmat.2016.07.022.

[34] B. Wang, R. Jiang, and Z. Wu, "Investigation of the mechanical properties and microstructure of graphene nanoplatelet-cement composite," *Nanomaterials*, vol. 6, no. 11, 2016, doi: 10.3390/nano6110200.

[35] Z. S. Metaxa, "Polycarboxylate Based Superplasticizers as Dispersant Agents for Exfoliated Graphene Nanoplatelets Reinforcing Cement Based Materials," *J. Eng. Sci. Technol. Rev.*, vol. 8, no. 5, pp. 1–5, 2015.

[36] S. Chuah, W. Li, S. J. Chen, J. G. Sanjayan, and W. H. Duan, "Investigation on dispersion of graphene oxide in cement composite using different surfactant treatments," *Constr. Build. Mater.*, vol. 161, pp. 519–527, 2018, doi: 10.1016/j.conbuildmat.2017.11.154.

[37] Nationwide Enginering, "Stronger Cheaper Greener Concrete." p. 20, 2021.

[38] I. Papanikolaou, N. Arena, and A. Al-Tabbaa, "Graphene nanoplatelet reinforced concrete for self-sensing structures – A lifecycle assessment perspective," *J. Clean. Prod.*, vol. 240, no. 2019, p. 118202, 2019, doi: 10.1016/j.jclepro.2019.118202.

[39] Y. Qiu, F. Guo, R. Hurt, and I. Külaots, "Explosive thermal reduction of graphene oxide-based materials: Mechanism and safety implications," *Carbon N. Y.*, vol. 72, pp. 215–223, 2014, doi: 10.1016/j.carbon.2014.02.005.

[40] D. Krishnan *et al.*, "Energetic graphene oxide: Challenges and opportunities," *Nano Today*, vol. 7, no. 2, pp. 137–152, 2012, doi: 10.1016/j.nantod.2012.02.003.

[41] S. Kim *et al.*, "Room-temperature metastability of multilayer graphene oxide films," *Nat. Mater.*, vol. 11, no. 6, pp. 544–549, 2012, doi: 10.1038/nmat3316.

[42] C. K. Chua and M. Pumera, "Light and Atmosphere Affect the Quasi-equilibrium States of Graphite Oxide and Graphene Oxide Powders," *Small*, vol. 11, no. 11, pp. 1266–1272, 2015, doi: 10.1002/smll.201400154.

[43] S. Eigler, S. Grimm, F. Hof, and A. Hirsch, "Graphene oxide: A stable carbon framework for functionalization," *J. Mater. Chem. A*, vol. 1, no. 38, pp. 11559–11562, 2013, doi: 10.1039/c3ta12975f.

Sensor-based decision making in precast concrete production

Sree Nanukuttan[1], Gareth Conway[1], Odhran Cummings[1,2], Ruben Correia[2], Sean Toal[2], William Doherty[2]
[1]Faculty of Engineering and Physical Sciences, Queen's University Belfast, Northern Ireland
[2]Creagh Concrete Products Limited, Toomebridge, Northern Ireland
email: s.nanukuttan@qub.ac.uk, g.conway@qub.ac.uk, rcorreia@creaghconcrete.com, seantoal@creaghconcrete.com, wdoherty@creaghconcrete.com

ABSTRACT: Creagh concrete required a digital solution to reduce the factory occupation time, enable smart storage/retrieval, faster inventory, and efficient product tracking at site. Working with Queen's University Belfast, the team developed a four-part solution for this problem. A wireless in-concrete sensor that provides temperature and location tracking, a receiver (node) that can connect to several of these sensors and have environmental sensing capability, a wired receiver (family) that integrate several nodes and a LoRa gateway mounted at altitude to integrate all family and cover the entire production yard. This article outlines the features of the digital solution, curing duration and influence of the ambient environment, benefits to the production and challenges that lay ahead.

KEY WORDS: Sensors; Wireless network; Concrete, Maturity, Location tracking, Optimised curing

1 NEED FOR DIGITALISATION

Precast concrete sector relies on large volume of production to reduce overheads. For Creagh concrete as the demand for their flagship product Rapidres™ increased, they needed better integration and coordination between different departments within Creagh and the supply chain. Rapidres is a fast track offsite crosswall build system typically used for multi-storey apartments, student accommodation, hotels and social housing. For a typical 26 storey apartment, inception to completion can be 74 weeks with only 50 weeks of site occupation. A sensor system was needed for optimising factory occupation time and also to retrieve the products efficiently. Commercially available systems such as Converge-IO [1] and SmartRock by Giatec [2] are advanced, but are cost prohibitive for the precast sector. Working together the team at Queen's University and Creagh jointly developed a four-part sensor system for the sector. There are several components to this system, the most fundamental of which is an affordable single use wireless sensor. Second is an array of receivers and transmitters designed to get the data onto cloud. Followed by a software. These are outlined below.

2 SINGLE USE WIRELESS SENSOR & ITS FEATURES

Affordability and ruggedness are two must have features for a sensor for precast sector. The team designed a sensor with antenna optimised to work best with the dielectric properties of the concrete. The complex permittivity and permeability of wet concrete was measured using a dielectric probe and these values were used in an electro-magnetic simulation environment to create an appropriate antenna design. An optimum impedance match was achieved for both wet and dry concrete. The sensor transmits at its peak efficiency when buried in concrete, typically mounted near the lifting hooks (Figures 1-2). For example, the simulated radiation efficiency is 69% when transmitting through a 50 mm coverage of dry concrete, meaning 31% energy will be lost in transmission. A thermistor was inserted onto the sensor module to capture concrete temperature and has a range of -30 to 80˚C with an accuracy of ±0.5˚C @ 25˚C. Sensor is given a unique ID (Figure 3) and is designed to start measurement when it gets in contact with wet concrete and has a typical life span of up to 5 years when sending data every 10 minutes. Overall dimensions of the sensor are 46 x 34 x 11.6 mm. Sensor has a communication range of up to 25m with a clear in line of sight, when buried in 50mm of wet concrete.

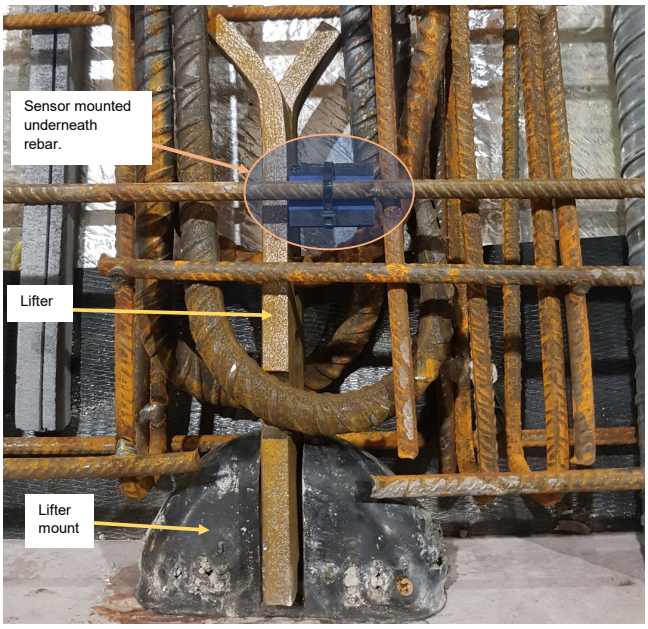

Figure 1 Sensor fixed to the reinforcement bar near lifter.

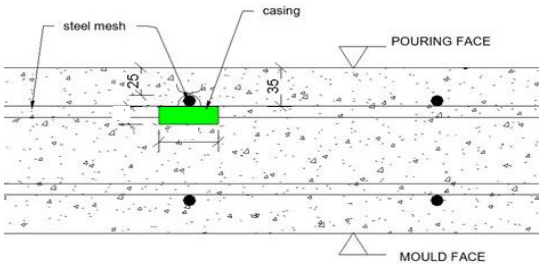

Figure 2 Sketch showing the location of sensor (in green) in the cross-section of the concrete panel.

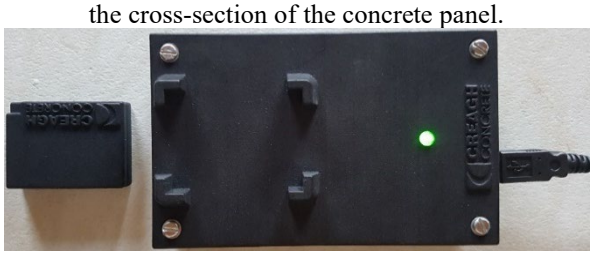

Figure 3 A typical sensor and the electronic module used for giving a unique ID.

3 ALLIED INFRASTRUCTURE

The network of infrastructure that seamlessly send data from sensor to a cloud-based storage point is shown in Figure 4. Sensor data and signal strength (power) is received by a dual-polarised 2.4 GHz receiver, termed as node (Figure 5). It can receive data from multiple sensors in its range. The signal strength received by the node from the embedded sensors will allow for relative location tracking of concrete panel. Node also measures ambient temperature and humidity and communicates all this data along with the power through a wired connection to a backhaul transmitter, termed as family (Figure 6), which also provides power to the node. Family is a repeater device which transmits data using the LoRa protocol on the 868 MHz ISM band. Data send by the family is received by the LoRa gateway (Figure 7), forwarded to the LoRa server which then sends it over internet to the cloud. Family can support up to 4 nodes as shown in Figure 8. The Family communicates over a half-duplex wireless channel, allowing downlink packets to control traffic lights for autonomous visual communication to the factory floor. For this project a network arrangement of one node and a traffic light per bed (5m x 16m) was chosen, as shown in Figure 8. Traffic light concept is further explained in the next session.

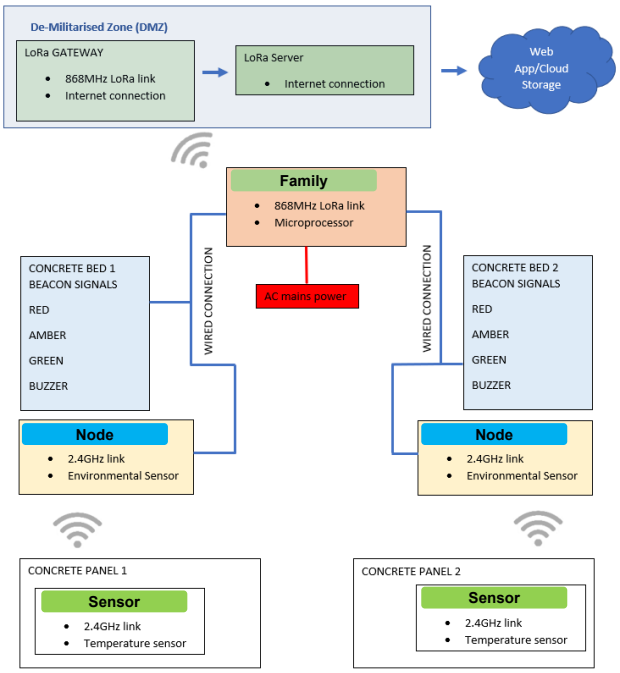

Figure 4 Sensor infrastructure showing the features and communication hierarchy.

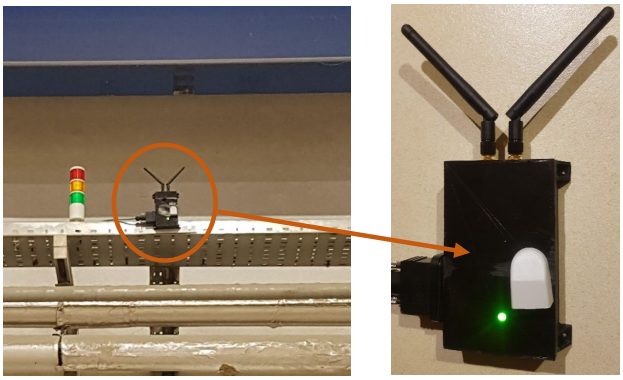

Figure 5 Close up of a **node**, a dual-polarised wireless receiver installed near the top gantry crane.

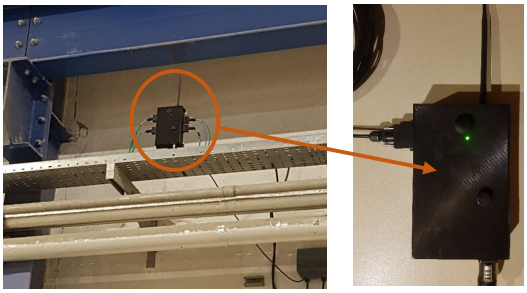

Figure 6 A family module installed near gantry crane for transmitting data from nodes to LoRa gateway. Family unit is mains powered.

Figure 7 LoRa gateway installed at 50m altitude.

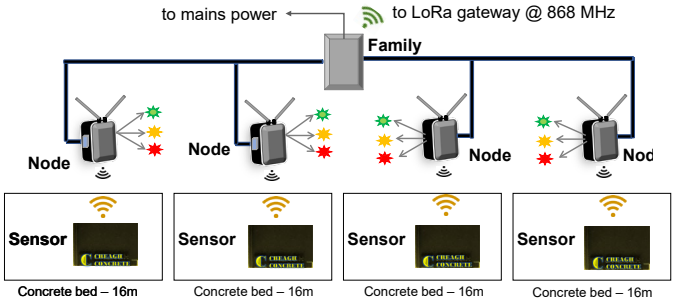

Figure 8 A typical network unit for precast factory building, consisting of one family and four nodes that covers four number of 16m wide concrete beds.

A sensor was placed in the reinforcement cage of the concrete panel before casting, and the node will start receiving data once wet concrete touches the sensor. The node will transmit data higher up in the network until the product leaves the digitised area.

4 PROPRIETARY SOFTWARE

LoRa server forwards all network data to an end-point. This can be a cloud provider or a custom software. In this project, a proprietary software was used that allowed all data to be viewed by workers for analysis. The software had an automated back-end which uses the temperature history provided by sensors to predict the real-time strength of precast panels using typical Concrete Maturity equations. The software has a feature to trigger the traffic light beacons in the factory floor based on certain threshold strength being achieved. For example, an amber light warning is produced when the concrete strength (predicted) near the lifting hook reaches 15 MPa. Intense data collection from the sensors and ambient environment allows for the software to further learn and handle reliability and errors. This allows staff to optimise the curing duration and organise lifting of panel, safely and efficiently.

5 DATA ANALYSIS

The first phase of the work was held during summer of 2020. Sensor data correlated very well to the data from thermocouples for all scenarios. Concrete cubes cast during the production of the panels were cured at 20˚C, 25˚C and also in temperature match cured tanks. A thermocouple inserted next to the sensor controlled the water temperature in the match curing tank. The concrete cured in this bath can be perceived as cured similarly to the concrete panels. For further information on the design and working of the match curing tanks refer to [3].

Maturity methods - A linear [3] and logarithmic estimation [4] of strength (i.e., Maturity method) were studied. Three parameter equation [5] was also studied, but the absolute error was slightly higher than that for other methods and therefore was discontinued. Arrhenius method [6] was not considered as it required the estimation of apparent activation energy through analytical techniques.

Linear estimation of strength:

$$Strength = aM + b \quad (1)$$

Logarithmic estimation of strength:

$$Strength = aln(M) + b \quad (2)$$

Where, Strength has the units of MPa, a and b are constants, b will assume the unit of strength (MPa). M is the maturity coefficient estimated from the area under the temperature time curve [5], in ˚C.hours.

The relationship between strength and maturity can be considered as linear or non-linear during the early phase of the curing as shown in Figure 9. For the data shown in Figure 9, the R^2 value does not change, if a logarithmic or linear best fit is considered. The graphs widely reported in literature shows a linear portion for the early age, especially 1 day [7]. As the focus of those studies are on days of curing as compared to hours, a different approach may need taken for precast sector that relies of first 15-20 hours of curing.

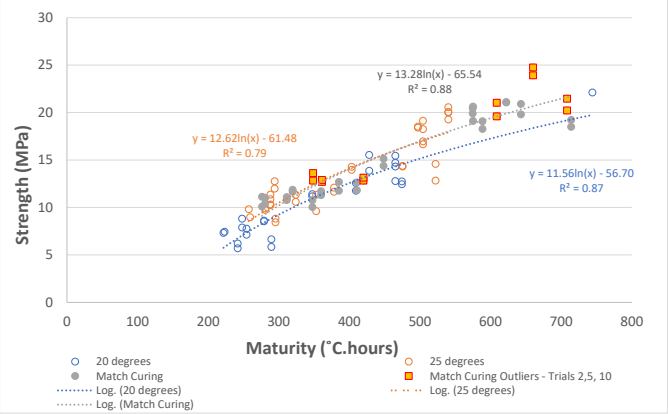

Figure 9 Strength maturity relationship for the three curing regimes during the early phase of curing, first 24 hours.

Cube compressive strength was determined for specimens stored in 20˚C, 25˚C and match curing tanks. Cubes form the match curing tank is considered to be representative of the *in situ* strength as the panel temperature (obtained via the sensor) was controlling the water temperature in the match curing tank. Therefore, this was considered as the reference strength.

Based on maturity in ˚C.hours, the strength of concrete was predicted using both equation 1 and 2. The difference between the reference strength and predicted strength was computed for all 11 trials (21 data points - typically at 8 hrs and at 15 hrs), the average of the difference is reported in Table 1 as absolute error. Table 1 also shows the values for a, b and correlation of regression.

Table 1. Variables obtained by best fitting equations 1 and 2 to the data.

	Linear Estimation			
	a	**b**	R^2	Abs. error
Ref - 20˚C	0.94	-0.21	0.9	1.77
Ref - 25˚C	1.18	0.58	0.81	1.17
Match curing	1.35	-0.21	0.91	1.41
	Logarithmic Estimation			
	a	**b**	R^2	Abs. error
Ref - 20˚C	11.56	-17	0.87	1.87
Ref - 25˚C	12.62	-16.26	0.79	1.26
Match curing	14.67	-20.02	0.88	1.28

One would estimate that the absolute error from match curing will be 0, but this is not the case. For such an occurrence, maturity prediction should be an absolute science, which it is not. So the absolute error of 1.41 or 1.28, seems acceptable for an experimental investigation and empirical maturity relationship (or model). From other data in Table 1, it is clear that predicting real strength of concrete (panels) using cubes cured at a 20˚C reference tank will result in larger error (1.77 and 1.87) compared to using match curing tanks or 25˚C tanks. 25˚C tanks however provide a more or less similar estimate of strength as that of cubes from the match curing tank. Linear or Logarithmic estimation would be considered appropriate for predicting strength for such an early age.

Duration of curing: The focus of this investigation was to determine the optimum duration of curing, required for achieving 15 MPa strength. The desired value of strength is depended on the type of products, lifting mechanism, handling methods, etc. So please note that 15 MPa is very specific to the type of panels studied in this project.

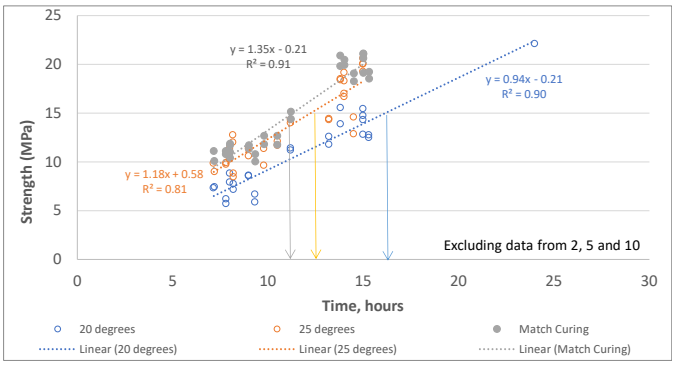

Figure 10 Real and predicted strength vs curing duration – Linear method of prediction.

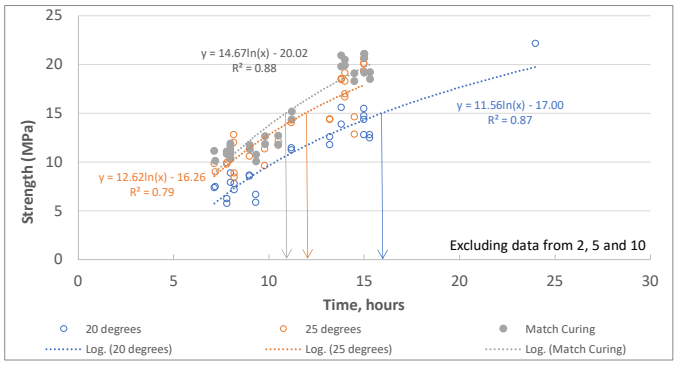

Figure 11 Real and predicted strength vs curing duration – Logarithmic method of prediction.

Based on Figure 10 and 11, approximately 11 hours of curing is required for concrete strength to reach the 15 MPa threshold. 11.3 hours for linear estimation (Figure 10) and 10.9 hours if based on logarithmic estimation (Figure 11). The method of prediction does not seem to create a significant difference as we explored in Table 1 using absolute errors.

Common practice in the industry is to cure cubes in water tanks kept at either 20˚C or 25˚C. The cubes cured in 25˚C tanks (highlighted in Orange data points/trendline) provide a more closer estimation of curing duration to those in match curing tanks, however, approximately 1 hour more. Samples cured at 20˚C required 16 hours approximately to reach similar strength. This is to be expected as the higher curing temperature will elevate the kinetic energy of molecules and encourage faster hydration reaction [6]. This observation that the 25˚C curing tanks are a better representation might not be the case for winter when the ambient temperature is a lot lower.

Influence of the ambient: Panels were of different size, thickness, and design but they all had the same concrete mix design. Concrete was cured at ambient conditions and was covered with a dense plastic sheet. Concrete beds were maintained at 20˚C, but this is unlikely to influence the curing due to the insulation in the panels. The spread of data for a curing duration (i.e., vertical spread – for all three curing regimes – Figures 10 or 11) indicates the natural variability caused by the differences in concrete, design features and ambient environmental condition. To study this further, cumulative concrete temperature (obtained from the sensor) and ambient temperature (obtained from the node on the factory wall) over the curing duration was determined (˚C.hrs) and this data was normalised by dividing with the duration (hrs). The resultant which will be in ˚C, was plotted against the strength gain in concrete up to that time (strength/duration). Data is presented in Figure 12.

Figure 12 shows the difference in concrete temperature and ambient and its effect on strength gain per hour. If the difference is low, strength gain will be reduced indicating the low rate of exothermic hydration reactions. For a shorter curing duration (ie faster lifting), the difference should be higher. For example if the difference in temperature is 10˚C, the panel will gain strength at the rate of 1.35 MPa/hour. Indicating that 15 MPa can be achieved in a little over 11 hours. Surface effects

can be ruled out as the sensors are buried 40mm from the concrete surface. Such a simplification will allow for adopting appropriate corrective measures, much early on the curing duration, if the difference in temperature is lower. Simple message is that for a strength gain of 1.3 MPa/hr (which equates to >15MPa at 12 hrs), a temperature difference of 8˚C is required (averaged across the curing duration).
The second phase which is ongoing targeted winter months as curing duration is likely to be longer in winter. Data from this phase is yet to be finalised.

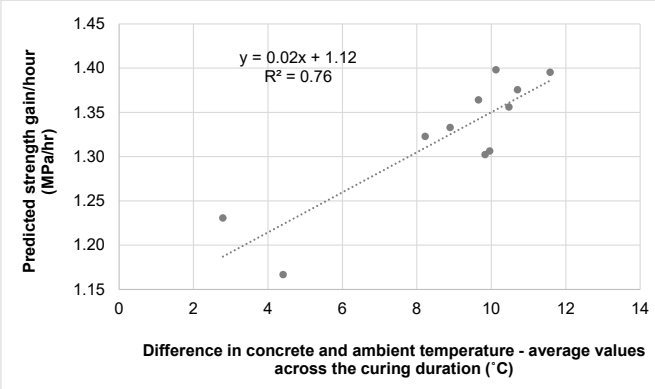

Figure 12 Concrete compressive strength of cubes in match curing tank/the panel obtained from cubes cured at various temperature regimes.

6 PROVING THE TAG AND TRACK CONCEPT

Concrete panels are produced in TF1 and once curing is completed, the panels are lifted and transported on to TF4 for processing and remedial works. Panels are further moved to TF13 before despatched. A birdseye view of the production facilities is provided in Figure 13. Sensor networks were installed in these factory units to track the time spent and progress of each panel. Unlike TF1, both TF4 and TF13 had only limited receivers, sufficient to capture panel entering and leaving the facility. The 25m communication reach of the sensor and received signal strength helps to further clarify the location of the panel.
A typical tracking data is overlayed on to Figure 11. It reveals that the panel was cured for 16.2 hrs before lifting it to a new location in TF1, where it spends further 4.8hrs. The panel then is moved to TF4 for processing where it remains for further 2 hours. Panel is moved on to non-digitised storage yard for which there are no data. Panel reappears at TF13 after 90 hours.

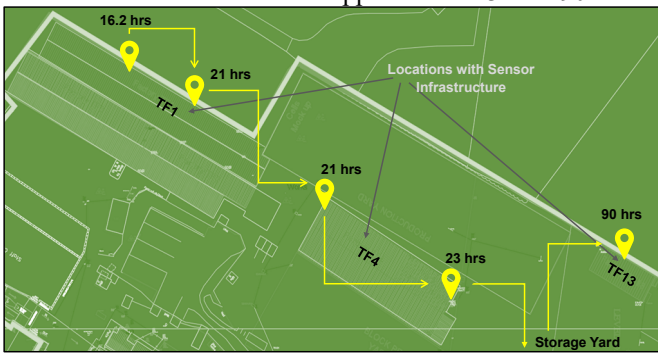

Figure 13. Birdseye view of one of Creagh's production yard, showing key locations that have the sensor infrastructure such as TF1, TF4 and TF13. Time stamp equating to when the panel left the node location is shown in hours. Direction of travel is shown by arrows.

7 CONCLUSIONS & CHALLENGES AHEAD

A robust sensor system was developed that can wirelessly transmit temperature and identity to receivers located in the factory or elsewhere. A four-part system, consisting of sensor, receivers and transmitter were successfully developed and demonstrated in practice. Tag and track concept was demonstrated by tracking one panel across the various production facilities.

Sensor based strength estimation, using either a linear or logarithmic prediction method provided reliable values that can be used to determine the lifting time. Approximately 11 hours of curing was deemed necessary to achieve a 15 MPa strength. The absolute error for this prediction was between 1.17 to 1.87 MPa. Over the summer production, 25˚C curing tanks provided more reliable estimation of concrete strength than 20˚C curing tanks. To consider the influence of the ambient conditions, a simplistic model is proposed that looks at the strength gain/hour vs difference in strength between concrete and ambient. Based on this approach, if a 8˚C temperature difference (over the curing duration) will achieve 1.3MPa strength gain per hour.

Challenges: During the trial period only handful of panels were instrumented. As the production gets further digitised, there is a high chance of overcrowding of data on nodes, especially due to the 25m reach length of the sensor. A large frequency of measurement might help to avoid data crowding. When the sensor communicates through obstacles, it will also affect the signal strength, which can be misinterpreted as a distance effect. Increasing the number of nodes/family is one way to mitigate this problem, but that will result in greater financial investment.

ACKNOWLEDGMENTS

Funding for this work was obtained via Knowledge Transfer Partnership (ref. 511602 - https://gtr.ukri.org/) through UKRI/Innovate UK. Sincere gratitude to the (1) Wireless research facilities at Institute of Electronics Communications and Information Technology (ECIT) at Queen's University Belfast and (2) Materials Characterisation facilities at School of Natural and Built Environment. Sincere thanks to Prof. Marios Soutsos for guidance on Maturity methods and mathematical models.

REFERENCES

[1] Converge, Concrete DNA and Signal system, Coverge, London EC4V 3DB, www.converge.io
[2] Giatec, SmartRock for concrete maturity measurements, Giatec Scientific Inc. Ontario, Canada. www.giatecscientific.com
[3] Soutsos, M., Vollpracht, A. and Kanavaris, F., Applicability of fib model code's maturity function for estimating the strength development of

GGBS concretes, *Journal of Construction and Building Materials*, 264, 2020, pp. 120-157, doi.org/10.1016/j.conbuildmat.2020.120157
[4] Plowman, J. M., 1956, "Maturity and the Strength of Concrete," Magazine of Concrete Research, Vol. 8, No. 22, March, pp. 13-22.
[5] Freiesleben Hansen, P. and Pedersen, J., 1985, "Curing of Concrete Structures," CEB Information Bulletin 166, May, 42 p
[6] Brown, T.L. and LeMay, H.E., 1988, Chemistry: The Central Science, 4th Ed., Prentice Hall, Englewood Cliffs, NJ, pp. 494-498.
[7] Carino, N.J., and Lew, H.S. (2001), 'The maturity method: From theory to application', Proceedings of the 2001 Structures Congress & Exposition, May 21-23, 2001, Washington, D.C., American Society of Civil Engineers, Reston, Virginia, Peter C. Chang, Editor, 2001, 19 p.

Comparative study of soft computing techniques for the prediction of concrete strength containing waste material

Ayaz Ahmad [1,2], William Finnegan[1,2], Yadong Jiang[1,2], Jamie Goggins[1,2,3]

[1] Civil Engineering, School of Engineering, College of Science & Engineering, National University of Ireland Galway, University Road, Galway, Ireland.
[2] MaREI Centre, Ryan Institute, National University of Ireland Galway, University Road, Galway, Ireland.
[3] ERBE Centre for Doctoral Training, National University of Ireland Galway, University Road, Galway, Ireland.

Email : a.ahmad8@nuigalway.ie ; william.finnegan@nuigalway.ie; yadong.jiang@nuigalway.ie; jamie.goggins@nuigalway.ie;

ABSTRACT: The application of artificial intelligence algorithms to anticipate the strength properties of various types of concrete is increasing in prominence. This study describes the use of two artificial intelligence algorithms, such as decision tree (DT) and bagging algorithm (BA), to anticipate the compressive strength of concrete containing fly ash. Python instructions were executed on the appropriate models using the anaconda navigator software. The models were conducted with seven input variables (cement, water, fly ash, superplasticizers, coarse aggregate, fine aggregate, and age) and one output parameter (i.e. compressive strength). Results show that the precision level of the BA towards the prediction of concrete's strength is high compared to the DT model. The said accuracy is indicated by the coefficient of determination value, which equals 0.93 for the BA and 0.86 for the DT model. The statistical checks also verified the accuracy level of the employed algorithms. The low values of the mean absolute error and root mean square error also confirm high accuracy for BA compared to DT.

KEYWORDS: concrete, fly ash, decision tree, bagging, modelling.

1. INTRODUCTION

Globally, demand for construction materials is expanding tremendously as infrastructure develops at a breakneck pace [1]. However, in the current context of sustainable development, the durability of building materials is not the only factor to consider. Additionally, economic and environmental considerations are becoming increasingly relevant. Portland cement, a commonly used construction material, is well-known for its high energy consumption [2], [3]. Numerous international initiatives and conferences aimed at reducing greenhouse gas emissions have spurred the adoption of supplementary cement-based materials (SCMs) as binders in place of ordinary cement [4], [5]. The application of fly ash in concrete as a partial replacement for cement is gaining popularity since it not only reduces the emission of carbon dioxide from the production and use of cement but also satisfies the strength requirements of concrete [6], [7]. Mehta et al. [8] used two types of waste materials (ground granulated blast furnace slag and fly ash) in concrete to investigate the numerous properties. A 52% increase in compressive strength was reported during the experimental program. The study of Stolz et al. [9] was also based on the several properties of activated fly ash (cellular alkali) concrete. Significant changes have been reported with various mixes.

The use of machine learning (ML) approaches in the civil engineering field is one of the popular trends in investigating and predicting the performance of materials [10], [11], [12]. This is especially true when predicting the mechanical properties of concrete since it takes time for concrete to reach the desired strength [13], [14], [15], [16]. The number of ML algorithms to resolve the regression and classification problems that are commonly used to anticipate the strength of concrete [17], [18]. Shahmansouri et al. [19] introduced the GEP model to investigate the CS of the concrete material, which shows an appreciable result in terms of prediction. Akande et al. [20] employed the neuron-based model (ANN) and SVM to anticipate and compare the compressive strength (CS) of selected concrete. The result shows that the SVM performed better than the ANN technique in the prediction of the required result.

This research explains the application of two ML algorithms, decision tree (DT) and bagging regressor (BR), to foretell the same property of the concrete having waste material (fly ash). A comparative study of the individual (DT) and ensemble (BR) ML approaches was conducted to investigate their performance. The accuracy level of the BR was better than the DT, as illustrated by the coefficient of determination (R^2) value. The R^2 value for BR was reported as 0.92, while DT gave the value of 0.86. This research aims to apply and compare the various ML approaches to forecast the strength of concrete. The study's main objective is to compare and recommend the highly precise ML algorithm that can be successfully employed to predict the mechanical properties of any type of concrete.

2. DATA DESCRIPTION

The Anaconda navigator software utilises Python codding to run the appropriate models. The database having input parameters and required output was used in the software for predicting the outcome. A total of 570 data points were retrieved from the literature with seven inputs (cement, water, superplasticizers, fly ash, fine aggregate, coarse aggregate, and a number of days) and one output (strength) parameter. The statistical descriptive explanation (analysis) for all variables is shown in table 1.

Table 1: Input variables used in the present study that were retrieved from the literature (cement, water, superplasticizers, fly ash, fine aggregate, coarse aggregate, and number of days)

Statistics	Cement (kg/m^3)	Fly ash (kg/m^3)	Water (kg/m^3)	SP*	CA*	FA*	Age (days)
Mean values	288.31	73.14	181.33	5.24	1003.73	793.41	45.42
Standard Error result	4.06	2.66	0.76	0.23	3.09	2.93	2.56
Median data	275.00	98.80	185.70	5.50	1006	792.50	28
Mode values	213.50	0.00	192	0.00	968	613.00	28
Standard Deviation	96.86	63.54	18.06	5.42	73.69	69.85	61.04
Sample Variance	9381.53	4037.84	326.29	29.39	5430.84	4878.38	3726.0
Variable's range	405.30	200.10	88.00	28.20	324	351.00	364.0
Low values	134.70	0.00	140.00	0.00	801	594.00	1.0
High values	540.0	200.1	228.0	28.2	1125	945	365
Total result	164047.4	41618.3	103177.2	2982.7	571123.9	451449.4	25845.0
Count	569.00	569.00	569.00	569.00	569.00	569.00	569.00

Superplasticizers (kg/m^3); *CA = Coarse aggregate (kg/m^3); *FA = Fine aggregate (kg/m^3).

3. METHODOLOGY

Both the ensemble and individual model strategies are introduced to anticipate the properties of materials in a short period of time. The R^2 value (which varies from 0–0.99) is commonly used to determine the amount of accuracy between the actual and predicted levels. A high R^2 value suggests that the chosen technique produces satisfactory results. The CS of concrete containing waste material is predicted by employing two types of ML approaches in the study.

3.1. DECISION TREE ALGORITHM

This approach is a supervised technique of learning that is normally introduced for classification plus problems related to regression [21]. This method uses a classifier with a tree structure, whose inner nodes describe the database properties. The conclusion rules are described by the branches, while the outcome is shown by each leaf node. The essential decision-making nodes are a decision node and a leaf node. Decision nodes have a number of branches and can make any tentative decision, whereas leaf nodes operate without branching and are regarded as the output of the decisions. It's known as a DT because it looks like a tree whose root starts from a node and grows into a bunch of branches [22]. At each location, the program identifies the variation between the actual and anticipated value. At each splatted point, the errors are evaluated, and the parameter with the lowest fitness function result is selected as the split point. The process is then repeated.

3.2. BAGGING ALGORITHM

The ensemble technique is an artificial intelligence (AI) paradigm that uses a similar learning algorithm to train several models [23]. Many algorithms, called multi-classifiers, are used in the ensemble. Thousands of learners are brought together with a single goal in mind to solve the problem. Bagging is an alternative ensemble approach that generates additional data during the training phase to explain the prediction model's variance. This is a result of sampling with irregularity. This includes data substitutions from the genuine set. Some of the values can be repeated in an additional training data set by making samples with replacement. All the components have the same opportunity for representation in the other dataset when bagging. Increasing the size of the training set will not increase the predictive power. With the fine-tuning of the prediction to an expected outcome, the variation can be minimized even further. All these sources of data are typically utilized to train many models. The approximate average of all the forecasts from the number of models is used in this ensemble of models. In regression, the prediction can be the mean or average of the forecasts from several models. [24].

4. K-FOLD CROSS-VALIDATION (C-V) AND STATISTICAL MEASURES

K-fold C-V is employed to check the model's performance in terms of bias and variance. The data is separated into ten stratified groups, each of which is randomly assigned to a training and test set. As shown in Figure 5, this procedure divides the total data into two halves, one for the test data and the other for the training data. The precision and efficiency of the selected model are then verified via C-V by averaging 10 rounds of varying mistakes. Likewise, statistical indicators are employed to assess the model [25]. In our current study, we use two different sorts of indicators, which are given below, mean absolute error (MAE) and root mean square error (RMSE). (Equation 1-2)

$$\mathrm{MAE} = \frac{1}{n}\sum_{i=1}^{n} |x_i - x| \qquad 1$$

$$\mathrm{RMSE} = \sqrt{\sum \frac{\left(y_{pred} - y_{ref}\right)^2}{n}} \qquad 2$$

5. RESULT AND DISCUSSION

5.1. DECISION TREE

The DT model gives a strong relationship between the experimental result and the result obtained from the model. The better result can be observed from the coefficient of determination (R^2) values equalling 0.86 as depicted in Figure 1. However, the dispersals of the error results for the DT model

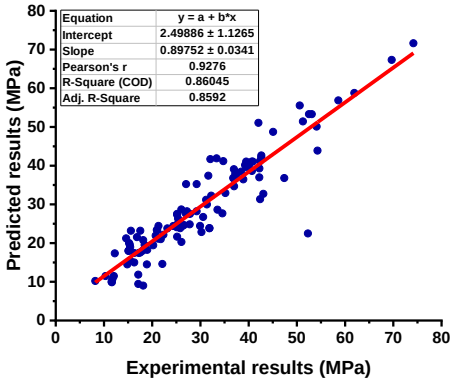

Figure 1. A comparison of experimental and anticipated DT model output.

are shown in Figure 2. The variation for DT models gives a maximum value of 29.81 MPa, and the average value is equal to 3.17 MPa. It was also noted that the 34.21 % of the error's data were lie between 0 to 1 MPa, and 42.10 % of the data were lie between 1 and 5 MPa. However, 23.68% of the error data was located above 5 MPa.

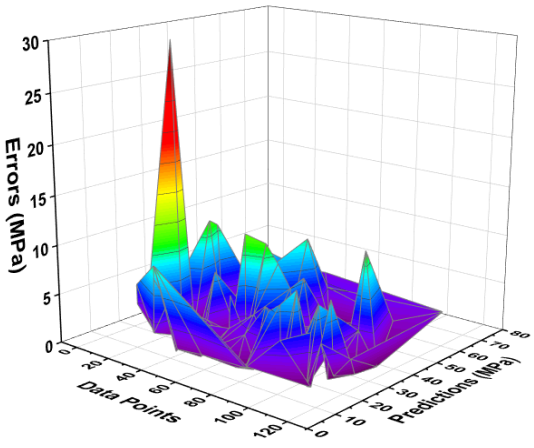

Figure 2. Representation of error's distribution for DT model

5.2. BAGGING ALGORITHM

The bagging model was reported to be more accurate as opposed to the DT model while investigating the CS of the selected concrete. The better performance of the said model was indicated by the better relationship between the actual and forecasted output, as depicted in Figure 3, while the dispersion of its errors is shown in Figure 4. The distribution gives the high, lower, and average values of 14.93 MPa, 0.0015 MPa, and 2.60 MPa, respectively. 32.45% of the error data lies between 0 MPa and 1 MPa, and 56.14% of the data lies between 1 MPa and 5 MPa. However, only 11.40% of the error's data were lying above 5 MPa 1 MPa, and 5 MPa. However, only 11.40% of the error's data were lie above 5 MPa.

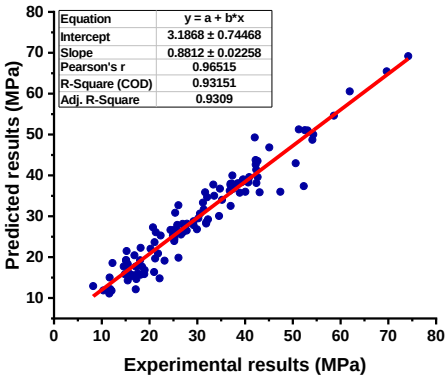

Figure 3. A comparison of experimental and anticipated bagging model output

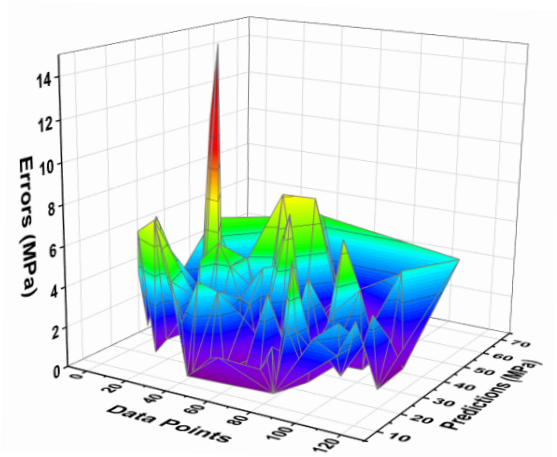

Representation of error's distribution for bagging model

6. CONCLUSIONS

The implementation of machine learning algorithms to predict the CS of concrete, including waste material, is described in this research. The two ML techniques (DT and bagging algorithm) were introduced for forecasting the CS of flay ash-based concrete. The performance comparison was carried out on the precision level of both the employed models. The following conclusion can be drawn from the study:

The bagging model shows a better relationship between the actual and predicted outcome and shows an impressive result as indicated by the coefficient of determination value equal to 0.92.The DT model predicted result for CS of fly ash-based concrete was also in the acceptable range by giving an R^2 value of 0.86.

To summarize, both the employed show a significant effect on the predicted result. To achieve more accuracy, it is necessary to enhance the data set through experiments. However, other ensemble ML approaches like boosting, Adaboost, and random forest can also give better results in terms of prediction. Moreover, it is clear that the ML approaches can be successfully employed for predicting different types of strength properties such as compressive strength, flexural strength, and splitting tensile strength. This successful adoption will not only reduces the physical effort on the experimental work in the

laboratory but also minimize the cost and time of the construction project.

ACKNOWLEDGMENTS

The authors would like to acknowledge the support of Science Foundation Ireland (SFI) through the MaREI Research Centre for Energy, Climate and Marine (Grant no. 12/RC/2302_2) and the Sustainable Energy Authority of Ireland (SEAI) through the WindLEDeRR Project (Grant no. 21/RDD/601).

REFERENCES

[1] G.J. Parra-Montesinos, High-performance fiber-reinforced cement composites: an alternative for seismic design of structures, ACI Structural Journal 102(5) (2005) 668.
[2] C. Shi, A.F. Jiménez, A. Palomo, c. research, New cements for the 21st century: The pursuit of an alternative to Portland cement, Cement 41(7) (2011) 750-763.
[3] C. Dow, F.P. Glasser, Calcium carbonate efflorescence on Portland cement and building materials, Cement Concrete Research 33(1) (2003) 147-154.
[4] U. Environment, K.L. Scrivener, V.M. John, E.M. Gartner, Eco-efficient cements: Potential economically viable solutions for a low-CO2 cement-based materials industry, Cement Concrete Research 114 (2018) 2-26.
[5] Á. Fernández, J.G. Calvo, M.C. Alonso, Ordinary Portland Cement composition for the optimization of the synergies of supplementary cementitious materials of ternary binders in hydration processes, Cement Concrete Composites 89 (2018) 238-250.
[6] G.N.K. Reddy, G.H. Vardhan, S.V.B. Reddy, Partial replacement of cement in concrete with sugarcane bagasse ash and its behaviour in aggressive environments, IOSR Journal of Mechanical Civil Engineering e-ISSN: 1684 (2016).
[7] F.A. Olutoge, O.M. Okeyinka, O.S. Olaniyan, Assessment of the suitability of periwinkle shell ash (PSA) as partial replacement for ordinary Portland cement (OPC) in concrete, International Journal of Research Reviews in Applied Sciences 10(3) (2012) 428-434.
[8] A. Mehta, R. Siddique, T. Ozbakkaloglu, F.U.A. Shaikh, R. Belarbi, Fly ash and ground granulated blast furnace slag-based alkali-activated concrete: Mechanical, transport and microstructural properties, Construction Building Materials 257 (2020) 119548.
[9] J. Stolz, Y. Boluk, V. Bindiganavile, Mechanical, thermal and acoustic properties of cellular alkali activated fly ash concrete, Cement Concrete Composites 94 (2018) 24-32.
[10] S.-C. Lee, Prediction of concrete strength using artificial neural networks, Engineering structures 25(7) (2003) 849-857.
[11] A. Ahmad, K. Chaiyasarn, F. Farooq, W. Ahmad, S. Suparp, F. Aslam, Compressive strength prediction via gene expression programming (GEP) and artificial neural network (ANN) for concrete containing RCA, Buildings 11(8) (2021) 324.
[12] M. Shariati, M.S. Mafipour, P. Mehrabi, M. Ahmadi, K. Wakil, N.T. Trung, A. Toghroli, Prediction of concrete strength in presence of furnace slag and fly ash using Hybrid ANN-GA (Artificial Neural Network-Genetic Algorithm), Smart Structures Systems 25(2) (2020) 183-195.
[13] Z. Keshavarz, H. Torkian, Application of ANN and ANFIS models in determining compressive strength of concrete, Journal of Soft Computing in Civil Engineering 2(1) (2018) 62-70.
[14] H. Naderpour, A.H. Rafiean, P. Fakharian, Compressive strength prediction of environmentally friendly concrete using artificial neural networks, Journal of Building Engineering 16 (2018) 213-219.
[15] J.-S. Chou, C.-F. Tsai, A.-D. Pham, Y.-H. Lu, Machine learning in concrete strength simulations: Multi-nation data analytics, Construction Building Materials 73 (2014) 771-780.
[16] W.Z. Taffese, E. Sistonen, Machine learning for durability and service-life assessment of reinforced concrete structures: Recent advances and future directions, Automation in Construction 77 (2017) 1-14.
[17] P. Chopra, R.K. Sharma, M. Kumar, T. Chopra, Comparison of machine learning techniques for the prediction of compressive strength of concrete, Advances in Civil Engineering 2018 (2018).
[18] F. Farooq, M. Nasir Amin, K. Khan, M. Rehan Sadiq, M. Faisal Javed, F. Aslam, R. Alyousef, A comparative study of random forest and genetic engineering programming for the prediction of compressive strength of high strength concrete (HSC), Applied Sciences 10(20) (2020) 7330.
[19] A.A. Shahmansouri, H.A. Bengar, E. Jahani, Predicting compressive strength and electrical resistivity of eco-friendly concrete containing natural zeolite via GEP algorithm, Construction Building Materials 229 (2019) 116883.
[20] K.O. Akande, T.O. Owolabi, S. Twaha, S.O. Olatunji, Performance comparison of SVM and ANN in predicting compressive strength of concrete, IOSR Journal of Computer Engineering 16(5) (2014) 88-94.
[21] A. Karbassi, B. Mohebi, S. Rezaee, P. Lestuzzi, Damage prediction for regular reinforced concrete buildings using the decision tree algorithm, Computers Structures 130 (2014) 46-56.
[22] W.B. Chaabene, M. Flah, M.L. Nehdi, Machine learning prediction of mechanical properties of concrete: Critical review, Construction Building Materials 260 (2020) 119889.
[23] M.H.D.M. Ribeiro, L. dos Santos Coelho, Ensemble approach based on bagging, boosting and stacking for short-term prediction in agribusiness time series, Applied Soft Computing 86 (2020) 105837.
[24] J. Dou, A.P. Yunus, D.T. Bui, A. Merghadi, M. Sahana, Z. Zhu, C.-W. Chen, Z. Han, B.T. Pham, Improved landslide assessment using support vector machine with bagging, boosting, and stacking ensemble machine learning framework in a mountainous watershed, Japan, Landslides 17(3) (2020) 641-658.
[25] F. Aslam, F. Farooq, M.N. Amin, K. Khan, A. Waheed, A. Akbar, M.F. Javed, R. Alyousef, H. Alabdulijabbar, Applications of gene expression programming for estimating compressive strength of high-strength concrete, Advances in Civil Engineering 2020 (2020).

Automated quality inspection in precast concrete production using stereoscopic computer vision

Paul Ross McWhirter[1,2], Gareth Robinson[1], Muddasar Anwar[1], Su Taylor[2], Gerard Hamill[2], Darragh Lydon[2]
[1]FP McCann Precast Office, 16-18 Quarry Road, Knockloughrim, Magherafelt, BT45 8NR, Northern Ireland
[2]School of Natural and Built Environment, Queen's University Belfast, David Keir Building, Stranmillis Road, Belfast, BT9 5AG, Northern Ireland
email: RMcWhirter@fpmccann.co.uk, GRobinson@fpmccann.co.uk, MAnwar@fpmccann.co.uk, S.E.Taylor@qub.ac.uk, G.A.Hamill@qub.ac.uk, D.Lydon@qub.ac.uk

ABSTRACT: The quality inspection process in precast concrete production remains a primarily manually driven process leaving it error prone and time intensive. The automation of quality inspection allows for real-time identification of faults using computer models built using the combined expertise of highly skilled individuals. Through the exploitation of modern computer vision methods, an image collection and processing data pipeline has been established to inspect precast concrete drainage products at an in-factory inspection line and record detected faults to a central database. A stereoscopic camera image acquisition system has been designed to provide 3D images of the drainage products which are annotated into a dataset to train machine learning models. A fully convolutional neural network model has been designed to identify surface features from the interior of cylindrical drainage products by performing a perspective transformation on the 3D images achieving 70% to 77% detection rates on important fault codes with a <1% false positive rate. The detection of defects is not a trivial problem as the surface of good-quality precast concrete remains visually highly variable. Additionally, the 3D images are used to measure geometric properties of individual products to ensure that they conform to the tolerances of the design specifications with an uncertainty of <5mm. The continuous collection of this data will also provide information on the day-to-day status of the health of the production line. The installation of these automated systems is a critical component to the realisation of modern smart factory operations in the precast concrete industry.

KEY WORDS: Precast Concrete; Quality Assurance; Automation; Computer Vision; Stereoscopic Vision.

1 INTRODUCTION

A comprehensive study of precast concrete manufacturing combining a large literature review and visits to factories in Germany and Austria describes the current practice of automation in precast concrete production [1]. This study demonstrates that the introduction of computer-controlled manufacturing of moulds and concrete pours has accelerated the production of precast concrete products whilst minimising the potential for error and subsequent wastage. It also indicates that this progress has not been extended into the quality inspection process for the resulting precast concrete products. This process remains a primarily manual effort involving technicians utilising various measuring devices to identify manufacturing flaws such as geometry defects and cracking or blistering on the surface finish.

Several academic groups have created methods to automatically detect faults on a variety of products, but few have been deployed full-time in the factory environment. Much of this research field has been focused on using sensors designed to create 3D representations of products which are directly compared to the Building Information Modelling (BIM) design models of these products. The sensor devices used during these processes included Terrestrial Laser Scanners (TLS) [2-4] and Light Detection and Ranging (LiDAR) [5].

The TLSs were utilised to create a framework for identifying geometric defects and surface level details on rectangular precast elements although this research was limited to specimens in a laboratory [2]. This team extended their method for the analysis of planar precast elements and successfully field tested the system at a precast concrete company achieving measurement uncertainties of around 3mm [3]. They further improved their method for a more complex 3D geometry in the form of concrete bridge deck panels however they were still dependent on the regularity of certain features on the surface of this product [4].

Other research deployed a LiDAR on a drone to inspect completed buildings using precast components and comparing the final 3D representation to the BIM model. This approach has a greater focus on inspecting the combined assembly of the precast components compared to inspecting the individual components prior to delivery [5]. Improvements to the generation of the 3D representations have also been presented designed to minimise uncertainty and improve the comparison to the BIM models [6].

These approaches have demonstrated the capability of 3D sensors for the inspection of both geometric defects and surface quality issues. The methods have been applied to precast concrete products well-suited to an assembly line such as planar walls and slabs with regular surface features. This paper describes and demonstrates a computer vision system designed to incorporate 3D information and perform real-time quality assurance on drainage products on an operating precast concrete production line. An accurate detection of cracking on the interior and spigots of precast 2.5m length drainage pipes is performed in addition to geometric measurements of interior and spigot dimensions with uncertainties of under 5mm by aggregating multiple frames. This is accomplished utilising stereoscopic camera products, specifically Intel RealSense d435i cameras [7], with a price of less than a tenth of LiDARs and TLSs.

The throughput of precast concrete production lines allows for a large quantity of data to be collected and analysed on these

products. This rapid production cycle makes it is an ideal place to deploy a system to minimise waste reducing the carbon utilised in a batch. This technology is being implemented in a real-time monitor system in select precast concrete factories.

2 BACKGROUND

2.1 Precast Concrete Drainage Pipes

An important set of products from the precast production line is a range of drainage products for water transport, sewage, and storm-drain projects. A single dry-cast machine can produce over a hundred drainage pipes a day. Each of these pipes must be quality tested to confirm that they meet casting (surface quality) standards, geometric tolerances and are watertight. The geometric tolerances are required as the pipes have a spigot end and a socket end and are connected by the spigot of one pipe positioned into the socket of another pipe. Deformations of the spigot or socket can prevent a watertight seal between pipes. In this paper, two types of drainage pipes are discussed: a full-length pipe of 2.5m in length and a shorter butt pipe of length 600mm. The pipe products are identified according to their diameter with five products considered in this paper: full-length pipes with diameters of 300mm (Ø300), 375mm (Ø375), 450mm (Ø450) and 525mm (Ø525) and a butt pipe with a diameter of 300mm (Ø300).

2.2 Stereoscopic Computer Vision

Computer Vision is the field of research and development involving the production of algorithms and methods to allow computer systems to automatically interpret image data. For example, a typical image is usually stored as a 2D array of 8-bit integers containing values between 0 to 255 representing the intensity of pixels. Colour images incorporate three of these 2D arrays called 'channels' with each channel corresponding to the red, green, and blue (RGB) colours. A pixel located at (x,y) in the 2D arrays would have a colour based on the intensity of the RGB arrays. For example, if the pixel has a red and green value of 255 and a blue value of 0, it is coloured yellow.

For standard images, this is the limit of information available. Algorithms can be used to interpret edges and colours of the image to identify objects and their associated boundaries. Traditional edge-detection methods have now been replaced with machine learning driven approaches. It is extremely difficult to implicitly create a set of rules to identify properties of a specific object such as a concrete pipe which operates reliably across the variability of concrete pipes and changing lighting levels. Machine learning allows the input of a large dataset of example images of a given set of classes to teach a computer vision model to probabilistically identify never-before-seen images of those classes based on their similarity to the example dataset.

There are multiple machine learning architectures with some better suited to computer vision tasks. In 2012, AlexNet [8], the first family of high-performing image classification models were produced using deep convolutional neural networks (CNNs). These networks mirror the traditional computer vision approach of kernels. Kernels are small 3x3 or 5x5 matrices which when convolved with an image can be used to detect specific features such as horizontal or vertical lines. A convolutional neural network utilises machine learning to build customised kernels optimised for the specific task. Groups of learned kernels are then combined into feature maps as the network combines simple shapes into more complex forms. This approach can be further accelerated using transfer learning, a method of utilising a pre-trained model on a larger set of generalised image data which has already learned the lower-level features. This is known as the 'backbone' of the neural network. This allows the set of training data for a specific task to be much smaller in volume as it is only required to 'fine-tune' the model for the desired purpose often referred to as the 'head' of the neural network. Multiple new CNN backbone architectures have been introduced in the last decade such as ResNet [9], DenseNet [10], InceptionNet [11] and EfficientNet [12] adding new operations to the network layers.

Stereoscopic cameras introduce another level of complexity to image data by providing a 4th channel of data corresponding to the depth of the pixel, the distance of the object represented by that pixel from the camera plane. This depth value can be combined with the (x,y) coordinates from the RGB channels to determine the location of the pixel in the 3D camera reference frame allowing 3D representations to be constructed of the objects within the camera field of view. This is accomplished using a similar technique utilised by the brain to grant animals with two eyes depth perception. The stereoscopic cameras have two imaging sensors separated by a baseline. Images from each camera vary due to their differing perspectives. A feature detection algorithm is used to detect the same features in the two images and the pixel-wise distances between the features are computed in a process named disparity. Pixels with a greater disparity are closer to the camera as their position changes more between the two images. Using the calibrated intrinsic parameters of the stereoscopic camera, this disparity is transformed into a depth value.

Stereoscopic Computer Vision combines Stereoscopic vision with computer vision to create algorithms which operate on the 4-channel RGB-Depth (RGB-D) image data to automatically detect, classify, and compute the spatial locations and dimensions of objects in the coloured 3D space. Figure 1 shows the RGB frame of a full-length pipe in the factory. The view is of the interior of the pipe as imaged by the camera located at the spigot end of the pipe with the socket end occluded.

Figure 1. Full-length drainage pipe in the factory.

3 METHODS

3.1 Surface Quality Estimation using Computer Vision

Imperfection in the surface quality of concrete drainage pipes are indicators that the product may not be watertight.

Additionally, defects which may not inhibit the performance of the product could be evidence of a deterioration in the manufacturing machine or a flaw with the current mix. Identifying defects is therefore important in both ensuring the quality of products and minimising wastage from future manufacturing from degraded materials or equipment.

The method proposed in this paper utilises a Fully Convolutional Neural Network (FCN) [13], an architecture designed for semantic segmentation with object localisation capability but trained using simple image classification labels. During training, the network aggregates predictions from across the image to determine a final class prediction and learn to automatically localise the defective regions. This approach requires substantially less labelling effort although the localisation is relatively low-resolution resulting in defects being centralised in extended detection regions.

The method requires a pre-processing operation where the drainage pipe is detected, localised, and extracted from the image data. This is accomplished by combining the RGB and depth data from the stereoscopic camera frames. Two circles indicating the near and far end of the pipe are detected using the RGB and depth data. These circles are used to mask the background pixels of the RGB image. Then a linear polar transformation is used to 'unwrap' the cylindrical interior of the pipe into a flat surface. Finally, the masked pixels are used to correct unevenness in the polar image due to misalignment with the camera with the pipe's central axis.

This processed linear polar image reorients features as if they were aligned with the camera frame and represents the physical area of features independent of their distance from the camera in the 3D space. The limitation is that features located more distantly in the pipe are more blurred as they are represented by a lower number of pixels in the RGB-D frame. Figure 2 shows the linear polar transformation of the interior of a full-length drainage pipe.

Figure 2. Linear Polar transformation of the interior pixels of a full-length drainage pipe. The far end of the pipe is to the left and the near end, including the spigot, is to the right.

These linear polar images are then classified using an FCN model pre-trained on ImageNet [14] then trained on 122 hours of data collected from the factory production line of 2.5m drainage pipes of all four diameters.

During training the linear polar images are resized to a resolution of 300x360 for input into this classifier. The model outputs *N* 2D arrays containing the predicted probability that the *N* fault codes are present in the polar image. Each element of the 2D arrays localise the fault codes within the linear polar images. To compute the performance of the model, these predicted arrays must be aggregated to a single probability per class to be compared to the training labels. This is accomplished by identifying the maximum predicted probability across all localisations for each fault code class and forwarding them as the probability vector for the image. More specific details on the training of the FCN model are given in section 4.2.

This model is then able to run inference on unknown quality drainage pipes by performing the linear polar pre-processing, resizing the linear polar image to 300x360, and using the model to return the 2D arrays of localised class predictions. Contours are fit to regions of high probability and the coordinates of these contours are transformed back into the image frame to identify defective sections of the drainage pipes and assign appropriate fault codes. These results are then uploaded into a database to monitor the overall health of the production line.

3.2 Geometry Estimation using Calibrated Point Clouds

In addition to surface defects such as cracks and blisters, the precise dimensions of the drainage products are of great importance. As these products are designed to interconnect, the dimensions must be precise to produce a watertight seal. For drainage pipes, the socket contains a seal which can compensate for minimal deviations defining the tolerance in which the pipes can still function.

The utilisation of stereoscopic data presents an opportunity to inspect the 3D geometry of products. This is accomplished by constructing point clouds of the target product. A point cloud is a 3D distribution of data pixels in a spatial coordinate frame – the length, width and depth dimensions are all in units of distance such as millimetres. This transformation can be performed from the RGB-D data using the 2D location of the RGB image pixels and the depth value of the depth frame aligned to the RGB frame. This alignment ensures that for a given (x,y) coordinate of a pixel in the RGB frame, the (x,y) coordinate of the depth frame is the associated distance of the RGB pixel. Equation 1 demonstrates the computation of the X coordinate in the 3D space, equation 2 computes the Y coordinate and equation 3 the Z coordinate.

$$X = D(x - p_x)/f_x \quad (1)$$

$$Y = D(y - p_y)/f_y \quad (2)$$

$$Z = D \quad (3)$$

In these equations, D represents the depth frame, a 2D array of pixel distance values. The values x and y represent 2D arrays containing the x and y coordinates respectively of the pixels in the RGB image. Finally, the variables p_x, p_y, f_x, and f_y are scalar intrinsic parameters of the stereoscopic camera. The variables p_x and p_y are the (x,y) pixel coordinates of the centre of the 3D space (X, Y = 0mm) and then f_x and f_y are the focal lengths of the stereoscopic RGB camera (as the depth

frames are aligned to the RGB image) in units of pixels. The 2D X, Y, and Z arrays are then flattened into 1D vectors. Figure 3 demonstrates the point cloud of a 2.5m drainage pipe imaged by an Intel RealSense d435i camera.

Figure 3. Point cloud of the spigot and interior of a Ø525 full-length drainage pipe as viewed from the spigot-end of the pipe. The socket (far) end of the pipe is poorly defined as much of the socket is occluded from the camera viewpoint.

As the point cloud of only the target drainage product is desired, the inner and outer circles utilised in the previous section are reused and converted into the 3D point cloud space. They are then used to filter points external to the target.

The objective of producing this point cloud is to measure Euclidean distances between points associated with pipe features to determine geometric quantities such as the diameters of the interior, spigot and socket ends of the drainage pipes, the pipe length and any ovality to the spigot and socket as this can prevent a successful interconnection. The point cloud also provides for the computation of the geometric angles between the pipe interior, the ends of the pipe and relative to the stereoscopic camera. The position of the pipes on the production line can vary by a few tens of millimetres and the angle of the pipe to the camera can vary by up to 5°. Fortunately, all these quantities can be determined using a set of trigonometric operations on the point cloud.

The first requirement is to determine the 3D angles of the pipe centre axis to the camera to rotate the point cloud, centring on the pipe independent of the pipe's real-world placement. A subset of points representing the interior of the drainage pipe is selected. These points are binned into 4mm groups by distance and for each bin a circle is fit to the coordinates (X, Y) projected along the Z direction. The centroids of these circles in the X and Y are paired with the midpoint Z coordinate of each bin and used to compute a linear centre axis for the drainage pipe using linear regression. The Euler angles (α, β, γ) of the pipe centre axis relative to the camera coordinate frame are computed using equations 4, 5, and 6.

$$\alpha = \tan^{-1}(m_y) \quad (4)$$

$$\beta = \tan^{-1}(m_x) \quad (5)$$

$$\gamma = \tan^{-1}(m_y/m_x) \quad (6)$$

In these equations, $\tan^{-1}$ is the inverse tangent operation, m_x is the gradient of the pipe centre axis in the X dimension and m_y is the gradient in the Y dimension. The Euler angles are then used to rotate the point cloud so that the pipe centre axis is fixed on the (X, Y = 0mm) axis.

This rotation allows the projection of the point cloud onto the (X, Y) plane where the interior points should now produce a circular shape. An ellipse is fitted to this projection determining the diameter of the major d_{maj} and minor d_{min} axes of the interior of the pipe which is then used to compute the ovality o of the pipe interior as defined in equation 7.

$$o = \frac{d_{maj} - d_{min}}{d_{maj}} \quad (7)$$

The dimensions of the near end of the pipe are computed next. The initial camera reference frame point cloud is processed to isolate the pixels associated with the near end of the pipe by binning the pixels according to their Z distance.

This point cloud contains drainage pipe pixels associated with the near end of the pipe. The pixels are placed into 4x4 pixel bins in the (X, Y) plane and the minimum Z value in each bin is retained to remove outliers. The remaining points are a 3D representation of the near end of the pipe in the camera reference space. Singular Value Decomposition (SVD) is utilised to fit a plane to the 3D coordinates of the pipe-end point cloud. This fit provides the normal vector out of the plane for the end of the pipe. This normal vector indicates the angle of the plane of the pipe near end to the camera. The distance of the centroid coordinate of the plane fit is also an improved estimation of the distance to the near end of the pipe, z_{nend}. This is combined with the diameter of the outer circle d_{pix} from the previous section to determine the outer diameter of the end of the pipe d_{out} using equation 8.

$$d_{out} = \frac{d_{pix} z_{nend}}{f_y} \quad (8)$$

Finally, the near end point cloud is used to compute the ovality of the near end of the pipe using a similar method to the method applied to the interior of the pipe. The Euler angles of the near end of the pipe are computed using the normal vector and the point cloud is rotated so that the normal vector lies on the new (X, Y = 0mm) axis. The point cloud is projected onto the (X, Y) plane and an ellipse model is fit to the points to compute the major diameter, the minor diameter and the ovality of the end of the pipe. The returned diameters are for a midpoint between the interior diameter of the pipe and the exterior diameter of the near end of the pipe, either spigot or socket. Finally, the length of the pipe may be calculated by combining the distance to the spigot and socket from cameras at both ends of the pipe. Combined with a well-calibrated separation between the cameras, the length is computed.

4 EXPERIMENTS

4.1 Hardware Setup

The experimental setup utilises an Intel RealSense d435i stereoscopic camera. This device consists of two near-Infrared (nIR) cameras positioned with a horizontal separation of 50mm, an RGB camera and a nIR laser dot projector. The nIR

laser dot projector is designed to actively illuminate the scene with nIR laser dots to assist in the disparity calculation on surfaces with little to no texture.

The Intel RealSense d435i camera is a development unit and therefore requires a connection to a control computer for the issuing of commands and the download of image frames. A Raspberry Pi 4 (RPi4) with 64GB of storage is utilised for this task. The setup is deployed on a tripod with custom 3D-printed containers to support the RPi4 and sensor devices.

4.2 Surface quality inspection at a factory production line

In this experiment the performance of the surface quality inspection machine learned classification model is investigated. The device described in section 4.1 was deployed within the FP McCann precast concrete factory at Knockloughrim to monitor drainage pipes on a leak-testing quality control line. The camera was placed at the spigot end of the drainage pipes as they move on a conveyor and a bright light was placed at the socket to illuminate the interior of the pipes. In total, 88,282 frames were collected over 122 hours containing images of 1667 individual 2.5m drainage pipe products of all four possible diameters. Each pipe has been labelled to identify the presence of one or more fault codes:

- Poor quality spigot: not sufficient to fail the product but a key feature of required maintenance.
- Broken spigot: Significant cracks or missing segments of the spigot preventing a watertight seal.
- Cracked or broken interior: Significant cracks in the interior. Also includes pipes formed from dry mixes as they suffer from global cracking.

Of the 1667 monitored pipes, 149 exhibited poor-quality spigots, 16 had broken spigots, 17 showed significant interior cracking mostly due to a dry mix during production with 5 containing water from a leak. The images for the individual pipes are split into a training set and a validation set using stratified sampling to maintain a similar proportion of the fault codes in each dataset. Despite not containing fault codes, the normal-quality pipes are still utilised in the datasets to assist in the modelling of the wide variation in the surface appearance of normal concrete.

ResNet-18 was chosen as the neural network backbone. The ResNet backbone has associated hyperparameters which define how the images are processed. These hyperparameters must be optimised to obtain superior performance. This is accomplished using a brute-force grid search on kernel size, stride and average pool size. Consult the ResNet paper for more information on the meaning of these hyperparameters [9].

Figure 4 demonstrates the Receiver Operating Characteristic (ROC) curves for each fault type. The ROC curve demonstrates the true positive rate, the rate at which faulty pipes are correctly identified against the false positive rate, the rate at which good-quality pipes are incorrectly identified as faulty.

The poor spigot is the worst performing class. The features of a poor spigot have a small area in the polar images. This makes it difficult for the neural network to detect the features and learn their relation to this class. To correctly classify half of the faulty pipes, a tenth of the good-quality pipes are misclassified. The broken spigot and broken interior classes perform much better by comparison. The model successfully recovers 70% of the broken spigot pipes whilst maintaining <1% false positives. The performance is even better for the broken interior pipes as 77% of the faulty pipes are correctly classified whilst maintaining <1% false positives. These fault codes cover a greater surface area of the pipes and are more easily detected.

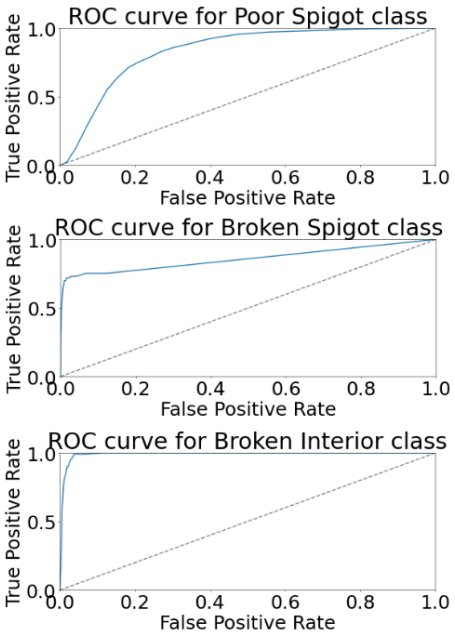

Figure 4. ROC curves for the three fault code classes. The dashed line represents the ROC curve of a model with performance no better than random chance.

4.3 Geometry Estimation of a control Butt Pipe

This experiment has been designed to verify the precision of the geometry estimation with the Intel RealSense d435i camera. A Ø300 butt pipe with known dimensions was selected as a control pipe. Table 1 contains the manually measured dimensions of this pipe which act as the ground truth values for this experiment with measurement uncertainties as shown. The pipe has been positioned on a platform at a test location within the R&D facility at the Knockloughrim site.

Table 1. Ground truth dimensions of the control butt pipe.

Geometry Item	Measured Value
Length	596 mm ± 0.5 mm
Interior major	297 mm ± 0.5 mm
Interior minor	295 mm ± 0.5 mm
Spigot major	372 mm ± 0.5 mm
Spigot minor	370 mm ± 0.5 mm
Spigot-to-pipe angle	0.39° ± 0.10°

The setup as described in section 4.1 was deployed at the spigot end of the test butt pipe. Real-time observations were taken with a cadence of 5 seconds with a total of 412 observations collected of the control butt pipe. Of these observations, the data from 4 frames failed to produce viable 3D solutions due to sparse point clouds and are discarded leaving 408 frames with full measurements.

Five geometric measurements are extracted from these 408 frames plus a measurement of the distance between the spigot and the camera. This distance is included as it linearly influences the uncertainty on the other measurements. Figure 5

shows the histograms and fit Gaussian functions to these six measurements. The mean value of the observations is used to estimate the geometric values and two standard-deviations mark the uncertainty range within which 97% of the observations are expected to lie.

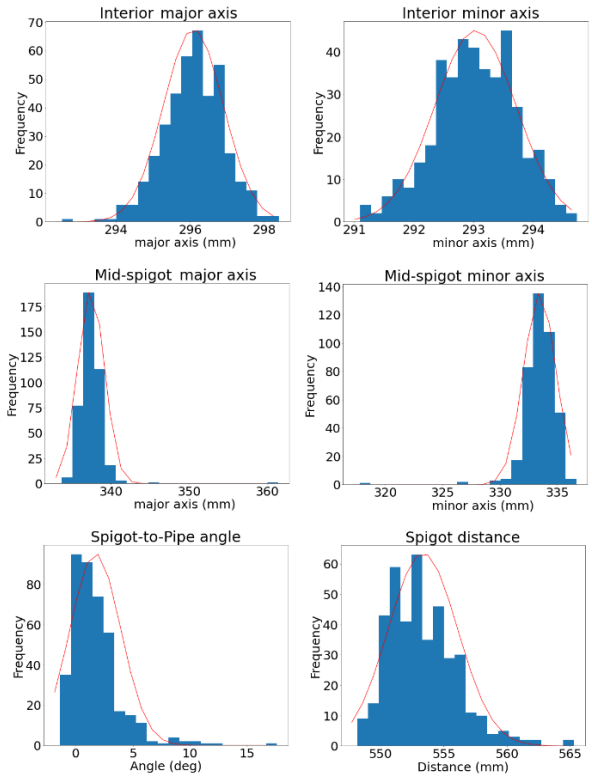

Figure 5. Histograms of 5 geometric measurements of the butt pipe and the distance from the camera using the 408 frames. The line is a Gaussian function fit to the measured values.

The interior major and minor axes have estimated values of 296mm and 293mm respectively. The uncertainties are 1.6mm and 1.4mm indicating the estimated major distance is consistent with the ground truth value and the estimated minor distance is slightly below the expected ground truth value.

The mid-spigot values are calculated from a midpoint between the outer spigot distance and the interior distance. Using the ground truth of these values, the expected values are 334.5mm and 332.5mm for the major and minor distances respectively. The estimated values of these distances from the data are 337.5mm and 333.5mm. The uncertainties are 3.4mm and 2.8mm respectively and are therefore consistent with the ground truth values.

The spigot-to-pipe angle estimated from the data is 1.7° with an uncertainty of 4.5°. This value is highly influenced by the depth noise of the camera creating outlier values but pipes with an angle >2° should be reliably detected. A similar conclusion is reached for the spigot distance estimation which has an uncertainty of 5mm due to outliers from 8% of the frames.

5 CONCLUSION

This paper demonstrates techniques to extract geometric measurements and to detect surface quality issues on cylindrical precast concrete drainage pipes.

The machine learned FCN model successfully identified features associated with three potential faults with the full-length drainage pipes. Fault codes which produce larger deformations in the drainage pipes have a higher detection performance due to their surface area in the unwrapped linear polar image. This network can be improved by providing it with the capability to investigate smaller scale features. In addition, the training dataset can be augmented with more examples of faults which can have a wide variety of appearances.

The geometry estimation performed well with the stereoscopic cameras capable of uncertainties of under 5mm when measuring pipe dimensions. Given the manufacturing tolerances of these products, this approach has the precision to identify products which deviate from these tolerances. Some of the pipe dimensions cannot be measured from one camera due to occlusion requiring additional devices. The extension of this technology to multiple product lines marks the next innovation towards fully realised precast concrete smart factories.

REFERENCES

[1] Reichenbach, S. and Kromoser, B. (2021), 'State of practice of automation in precast concrete production', *Journal of building engineering*, 43, 102527.

[2] Kim, M.-K., Cheng, J.C.P., Sohn, H. and Chang, C.-C. (2015), 'A framework for dimensional and surface quality assessment of precast concrete elements using BIM and 3D laser scanning', *Automation in Construction*, 49, 225-238.

[3] Kim, M.-K., Wang, Q., Park, J.-W., Cheng, J.C.P. and Sohn, C.-C. (2016), 'Automated dimensional quality assurance of full-scale precast concrete elements using laser scanning and BIM', *Automation in Construction*, 72, 102-114.

[4] Wang, Q., Kim, M.-K., Cheng, J.C.P. and Sohn, H. (2016), 'Automated quality assessment of precast concrete elements with geometry irregularities using terrestrial laser scanning', *Automation in Construction*, 68, 170-182

[5] Wang, J., Sun, W., Shou, W., Wang, X., Wu, C., Chong, H.-Y., Liu, Y. and Sun, C. (2015), 'Integrating BIM and LiDAR for Real-Time Construction Quality Control', *Journal of Intelligent & Robotic Systems*, 79, 417-432

[6] Rebolj, D., Pucko, Z., Babic, N.C., Bizjak, M. and Mongus, D. (2017), 'Point cloud quality requirements for Scan-vs-BIM based automated construction progress monitoring', *Automation in Construction*, 84, 323-334

[7] Intelrealsense.com. (2022), 'Intel RealSense Product Family D400 Series Datasheet', [online] Available at: <https://www.intelrealsense.com/wp-content/uploads/2022/03/Intel-RealSense-D400-Series-Datasheet-March-2022.pdf> [Accessed 3 May 2022].

[8] Krizhevsky, A., Sutskever, I. and Hinton, G.E. (2012), 'ImageNet Classification with Deep Convolutional Neural Networks', *Advances in Neural Information Processing systems*, 25.

[9] He, K., Zhang, X., Ren, S. and Sun, J. (2016), 'Deep Residual Learning for Image Recognition', *2016 IEEE Conference on Computer Vision and Pattern Recognition (CVPR)*, 770-778.

[10] Huang, G., Liu, Z., Van Der Maaten, L. and Weinberger, K.Q. (2017), 'Densely Connected Convolutional Networks', *2017 IEEE Conference on Computer Vision and Pattern Recognition (CVPR)*, 2261-2269.

[11] Szegedy, C., Liu, W., Jia, Y., Sermanet, P., Reed, S., Anguelov, D., Erhan, D., Vanhoucke, V. and Rabinovich, A. (2015), 'Going deeper with convolutions', *2015 IEEE Conference on Computer Vision and Pattern Recognition (CVPR)*, 1-9.

[12] Tan, M. and Le, Q. (2019), 'EfficientNet: Rethinking Model Scaling for Convolutional Neural Networks', *Proceedings of the 2019 International Conference on Machine Learning (ICML)*, Long Beach, CA, USA.

[13] Long, J., Shelhamer, E. and Darrell, T. (2014), 'Fully convolutional networks for semantic segmentation', *2015 IEEE Conference on Computer Vision and Pattern Recognition (CVPR)*, 3431-3440.

[14] Deng, J., Dong, W., Socher, R., Li, L.-J., Li, K., & Fei-Fei, L. (2009), 'Imagenet: A large-scale hierarchical image database', *2009 IEEE Conference on Computer Vision and Pattern Recognition (CVPR)*, 248-255.

Bridges

THE PURSIT OF TOTAL DESIGN OF BRIDGES IN THE ERA OF CLIMATE CHANGE

Marcos Sanchez[1]
[1]ARUP Ireland. Director of Bridges and Civil Structures. Global Bridges and Civil Structures Skills Leader.
e-mail: marcos.sanchez@arup.com

ABSTRACT: Structural engineers involved in bridge design have a great responsibility: the impact of their job goes beyond the pure functional requirements, from the original Vitruvian principles (*firmitas, utilitas, venustas*), strength, utility and beauty. A bridge spans clearly beyond the strength principle: its appearance cannot be concealed by other elements as it usually happens in buildings. Throughout history, these Vitruvian principles have been expanded adding three additional ones: economy, durability and in the last few years, sustainability. Achieving "Total Design" in bridge engineering where each of these six principles are maximized becomes a real challenge. Bridge designers play a significant role, particularly in the current environment of climate change emergency as the current one, in achieving the best outcome. Conceptual design, inspiration, experience, innovation, and multidisciplinary collaboration all became equally important in delivering successful bridge design in the current context.

KEY WORDS: Bridges, Total Design, Sustainability, Conceptual design, Concrete, Steel, Construction materials

1 THE ROLE OF THE CONSRUCTION INDUSTRY IN CLIMATE CHANGE

With the current focus from all parts of society on reducing carbon footprint significantly by 2030 and a more ambitious goal of achieving Carbon neutrality by 2050 in every country, including Ireland [1], every sector in society is under significant pressure to deliver a significant reduction within their own activity.

The construction industry plays a substantial role in terms of their total share in embedded $C0_2$ with the largest proportion compared to any other activity [2].

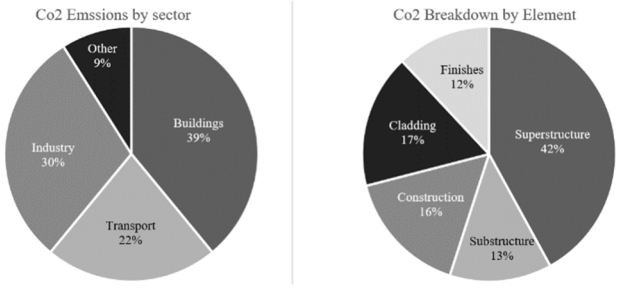

Figure 1. $C0_2$ Emissions by sector and breakdown by Element for Buildings. *Source: World Green Council (left), Keathner and Burridge, The structural Engineer, May 2012 (left).*

While the figures above vary by country and in time and the breakdown by element within the buildings include both bridges and civil structures along with conventional buildings, it is clear that our industry and, in particular civil constructions of which bridges are a large contributor play a key role in the $C0_2$ emissions.

2 THE ROLE OF BRIDGE ENGINEERS IN REDUCING CARBON FOOTPRINT

The current use of carbon at an individual level has different sources, and can be classified in two groups:

- Living activities: Food, Housing (heating/cooling, etc) and Transport (commuting, local and holidays/professional long haul travelling).
- Direct impact of professional activity.

The items in the first point above are common to any other citizen while the second one is associated with the practice of the profession, which in the case of bridge engineers is directly related to embedded carbon of the structures designed as part of our professional activity.

By using average values of well-established metrics [3], it is clear how the impact of our professional activity outweighs any other in terms of carbon footprint. For example, cutting off your meat, dairy and beer intake for a year might save around 2t of C02e; while a Dublin-New York return flight will save around 1t; and making your house carbon neutral in the order of 1t as well, to completely give up your private car and switching your travel to cycling would also have a significant impact, in the order of 2-5tons/year depending on your commuting and driving habits, all the above are significant sacrifices that few of us are prepared to fully implement.

On the other hand, assuming an embedded carbon footprint of 2 tons per m^2 as a safe average (See Figure 2 below,[4]) for a typical short/mid span bridge, a conventional overpass with a length of 60m and a width of 10m has an embedded carbon footprint of 600t, a saving of 10% in quantities in a single overpass will produce a reduction of 60ton, which it's clearly a different order of magnitude to any of the other figures considered above, even combined.

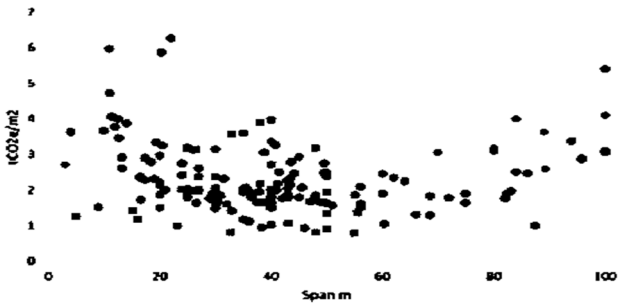

Figure 2. Normalized capital carbon (tonnes C02e/m2). Source D. Collings SEI 2021-2 [4]

The impact on carbon footprint savings that bridge engineers can achieve is increased when it comes to retrofitting and strengthening existing bridges instead of demolishing and building new ones for obvious reasons. Reusing or repurposing existing bridges and ensuring that only the right new bridges for the right use are built clearly produces more savings than new construction.

In conclusion, it is clear that our profession plays a significant role achieving our sustainability goals when it comes to carbon footprint. It is also clear that from the two key strategies, "build less" by reusing and recycling, and "build better" by reducing the carbon footprint of new construction, the former has a larger impact in carbon footprint reduction.

However, with an increasing population projected to be 10 billion in the planet and 6 billion for Ireland by 2050[5], there is a clear limitation on the strategy of "build less". A significant amount of new infrastructure will be required to be built between now and 2050, and therefore "build better" becomes also paramount.

In this context, to "build better bridges" with sustainability playing a central role, but without forgetting the other components of a good design, the Vitruvian principles of "strength", "beauty" and "utility" along with the additional requirements of "economy" and "durability", becomes a formidable challenge.

This challenge can only be met with an approach that will require expertise, inspiration, and innovation from all fields of engineering, from transport planners, material engineers, designers, contractors, policy makers in what could be called "Total Design".

3 TOTAL DESIGN

3.1 *On Total Design*

Arup founder, in its key speech [6] coined the concept of "Total Architecture" as:

"*at all relevant design decisions have been considered together and have been integrated into a whole by a well organised team empowered to fix priorities"*

The term Architecture was used at the time in the context of buildings, but it is easily extended to other activities of Civil Engineering in general and Bridge Engineering in particular becoming "Total Design".

Similar concepts exist in other countries and amongst bridge engineers, Mike Schlaich uses the term "Baukultur"[7] which he defines as:

"Good bridge design creates Baukultur, the culture of building, which has got to do with quality, with consciously creating value. Graspable structures, where materials are properly selected according with their characteristics, let us experience and understand the flow of forces; they are carefully detailed and this leads to beauty."

From the end user point of view, quality is usually focused to two of the six values previously mentioned "utility" and "beauty", which both of which have a subjective component, in particular the second one.

However, it is well known the strong influence of the economic context in the construction industry, which has led in the past to bridge designs that are driven by cost, except for "landmark structures" or "signature bridges", either governed by long span requirements or specific environmental constraints.

These two approaches have been generally conceived as contradictory, with a general perception that "iconic" or "signature" bridges are usually unnecessarily expensive (and by extension, inefficient structurally, and as a direct consequence, "unsustainable" from a materials optimization point of view). While on the other hand, economic, and purely functional bridges are widely seen as aesthetically limited if not directly "ugly".

There are, however, multitude of examples where a true balance of all conditions are met and, in the context of a sustainably driven narrative, Total Design, becomes even more important. There are three components required to achieve total design, Conceptual Design, Inspiration and Multidisciplinary approaches where professionals with different expertise bring value to the final product in the design.

3.2 *The importance of conceptual design*

Bridge Engineers, by nature, are attracted to numbers and calculations, spending much, if not all of their time, on analysis and verification against existing codes. The time that it is usually dedicated to the conceptual design stage is very limited, in many cases, it is avoided or left to others (architects, contractors, transport planners, etc). In the worst cases, conceptual design is limited to a "cut and paste" exercise of replicating similar structural forms with minor tweaks to fulfil the specific requirements (ground conditions, bridge width, span and clearance, etc).

Conceptual design, which should include a holistic approach where each of the six principles of good design are pondered and the trade-offs between them are carefully considered should be fundamental in the bridge engineer's mind, starting from Education in universities to everyday 's practitioners.

It requires a deep understanding of each material's behavior (concrete, reinforced or prestressed, structural steel, or others if used) and choices of structural forms and boundary conditions. It has also strong connections, particularly when the span is significant, with constructability and construction methods. It is not possible do deliver Total Design without a deep knowledge of material behavior and a clear understanding of the optimum construction methods. Bridge design is,

consequently, strongly connected with many other disciplines: Architecture, Transport Engineering, Material Engineering, Ground engineering, Construction engineering, etc, which can only be developed through experience, or inspiration from other engineers in the past and by collaboration with Multidisciplinary teams.

4 INSPIRATION AND EXPERIENCE

There is a common understanding that in general, beauty and user experience are at odds with economy and by extension with efficiency and sustainability.

While this might be the case in some structural forms, there is abundant evidence of the opposite and as part of a "Total Design" approach, it should be central in good bridge design.

The following examples show several cases, both historic that served as inspiration to the Author or directly based on the Author's experience where a successful outcome of Total Design was achieved.

4.1 Salgina Tobel.

Salgina Tobel bridge is well known by bridge engineers as one of the finest designs from Robert Maillart and it has been used in many publications as an example of high-quality aesthetics and landscape integration.

Figure 3. Salgina Tobel Bridge. Robert Maillart. 1929

While the beauty of the bridge is unquestionable, probably the most remarkable aspect of this bridge, and little known, even amongst bridge engineers, is that the primary motivation and selection process at the time was economy. The project was a cost only competition where the cheapest bidder won, with Prader as contractor teaming up with Maillart. The bridge is actually a slightly larger version of a previous bridge with the same structural form, less known, as it was destroyed by a flood in Tavanasa[8] and the winning team adapted their tested idea at the time where concrete forms were being discovered, to a larger and more challenging span as part of natural evolution.

The construction of the bridge, subject to the technological challenges of the beginning of the 20th century and the remote location of the structure was integral with the concept, with an extremely lean timber scaffold spanning the 90m by cantilevering from both sides, which relied in the inverted "pi" section of the arch to be cased in stages and self-supporting the rest of the structure once casted.

Figure 4. Salgina Tobel Construction.

This is a clear example of Total Design and how a concept, initially driven by cost and efficiency can deliver high quality aesthetics and environmental integration when adapted to the site specific constraints.

4.2 Los Tilos Arch

In 2000, I was part of a team that was assigned to value engineer a project of a 250m span arch in the canary island of Palma. Similarly to Salgina, the remoteness of the project (the island is merely 30km high and 15km wide) required to carefully integrate the construction challenges on the design.

Figure 5. Los Tilos Arch (Source. J.J. Sanchez Ramirez)

The original design included a full concrete deck, columns and arch, built using a conventional cable stayed cantilever. The variation included a steel composite deck on which the steel section of the deck was used as top tension tie during construction and with temporary diagonals minimizing the temporary steel and reducing the total weight of the structure by 30% which also allowed to reduce the arch section [9].

Figure 6. Los Tilos Arch during construction

Again, the value engineering was entirely driven by cost at the time but the sustainability benefits in terms of material savings both in the permanent structure and during construction becomes obvious.

4.3 Composite bridges

The natural evolution of concrete and steel structures is to combine them in what is known as composite concrete-steel structures.

Steel composite structures, usually consist of a concrete slab that relies on a set of steel beams with bracing or a steel box. It is a structural solution that has been used for more than 70 years and represents a good use of both concrete and steel. This structural system is efficient to prevent sagging, as the tension is in the bottom of the section and the compression at the top, so concrete and steel are placed efficiently. However, it becomes far less efficient in continuous structures over supports where the bending moment is reversed and the top face is in tension while the bottom face is in compression for which neither concrete and steel are working at their best.

4.4 Double composite action.

Double composite action by, which incorporates concrete in the bottom slab as a composite action in addition to the concrete slab in the top face of the deck has been used in multiple structures and represents a very good refinement of a conventional multi-span steel composite bridge.

This concept is widely used in the continent, and surprisingly has had little impact in Ireland and the UK where very few bridges with double composite action are known by the Author.

4.5 Cortegada.

An exceptionally elegant bridge typology that pushes the boundaries of double composite action by removing the concrete in the side spans and leaving the lighter steel composite section limited to a much larger main span are portal frames with double composite action.

A remarkable case of this type of structure is Cortegada bridge in Galicia, Spain. With a main span of 180m and a portal frame configuration where the central span is a corten steel composite section, it was designed as an alternative, value engineering proposal, focusing on construction cost saving to the original design: a full concrete balanced cantilever with a main span of 130m.

Figure 7. Cortegada Bridge over Mino River (Source: Pondio Ingenieros)

This alternative solution provided several additional advantages, it avoided piers in the river and also avoided the use of any type of form traveller, by delivering a clever construction method consisting on building the concrete parts parallel to the river on a scaffold which was rotated 90 degrees and lifting the central steel part delivered by floating [10]. It represents again, a perfect case of Total Design, where every principle of good design is maximized.

Figure 8. Cortegada construction (Source: Pondio Ingenieros)

4.6 Composite arches

Another step towards the optimal use of the two most common materials in bridges, structural concrete and structural steel, is the use of composite arch sections. Tubular sections are commonly known CFST (Concrete Filled Steel tubes), are widely used in the construction industry to provide higher capacity to steel tubular structures and also used in bridges, although with questionable aesthetic results.

A much better alternative to small diameter CFST trusses, which exploits the optimum behavior of a steel composite arch is the use of two staged construction of large steel sections, either circular in cross section or by folded plates, which are later infilled with self-compacting concrete.

With this approach, the outer steel provides the maximum lever arm for a structural concrete-steel composite section, as it equates to “zero cover”. A two stage construction of the cross section enables the lighter material (steel) to be erected first, and the arch infilled later. This means that the capacity of the section is increased with a much more efficient material in compression and allows for the thickness of the structural steel in the arch to be minimized.

4.6.1 Logrono arch

This solution was used with a circular section arch for the first time in Logrono Arch in 2002, a 140m span bowstring arch [11].

Figure 9. Logrono Arch. Spain (Source: CFCSL)

As in previous cases, the main motivation for this solution, which was not in the original design, was cost motivated, but the sustainability benefits are also obvious.

4.6.2 Vicaria Arch

Following a similar approach, Vicaria Arch was designed using a steel composite arch. In this case, to avoid a large diameter tube, a folded plate section was chosen, which allowed a extremely slender structure, with a span of 160m and steel plates in the arch of merely 12mm thickness.

Figure 10. La Vicaria Arch. Spain (Source L.M. Tereso)

As in previous cases, the main motivation for an efficient use of the materials that led to the development of the steel composite section was cost, which is directly related to the sustainability due to material optimization.

4.6.3 Monastery Road Bridge

Using this technology, here in Ireland, the bridge over Monastery Road in Dublin is also another example of material optimization. The infilled concrete arch section allows the 60m span arch to achieve a slender section without the need of transversal bracing despite the fact that bridge carries a dual carriageway.

Figure 11. Monastery Road Bridge. Dublin.

4.7 An Exceptional Case. Extrados bridges and RFK Bridge over the river Barrow

Most of the examples previously mentioned are successful examples of where a holistic approach, which takes into account the six main conditions of good design, has been achieved. There are however, scenarios for which a compromise on some of these parameters needs to be made, in some cases, due to the importance of the structure, compromising efficiency to achieve an unique structure in terms of environmental integration. The Rose Fitzgerald Kennedy Bridge over the River Barrow is a clear exponent of this case.

Figure 12. RFK Bridge over the river Barrow

While it is obvious that it is not the most efficient solution within the purely functional constraints, and it remains open whether further value engineering without changing fundamental appearance of the structure, its undoubtedly quality has already been recognized internationally. Which is unprecedented for any structure build in Ireland [14],[15] and [16].

5 PEDESTRIAN BRIDGES

Pedestrian bridges deserve a special category in Total Design. Sustainable transport policies will increasingly encourage pedestrian and cycle use of the urban environment. In addition, due to their smaller scale and greater integration with the urban fabric, design considerations such as place making and user experience become even more important for this bridge type.

This leads to increased importance of the fourth component of Total Design in addition to Conceptual Design, Inspiration and Experience which is a Multidisciplinary Approach: Architects, Landscape, Transport and Urban planners play a far more influential role in pedestrian bridges that arguably they may play in Road and Rail Bridges.

An additional parameter to consider for pedestrian bridges is a lightweight approach. While it is clear that a leaner and lighter structure will reduce the material quantities and thus, have a direct impact in sustainability and carbon footprint, this is usually limited in road and rail bridges due to the functional requirements imposed by the loading type. However, pedestrian bridges have a greater scope for more ambitious structural forms and leaner structures to embody the principles of good Total Design.

5.1 Placemaking

Pedestrian and urban bridges can be considered beyond the pure experience of crossing as in many cases they can become places to stay and gather. There are several successful examples on integrating urban pedestrian or shared bridges beyond the primary function.

A good example is Mary Elmes Bridge in Cork , where, in addition to an optimum use of the materials and a strong conceptual design that took into account the site constraints, the architect proposed to provide a bench at midspan, integrated into the spine steel beam. The result is an extended function of the bridge as a popular and successful urban space.

Figure 13. Mary Elmes Bridge (Source Wilkinson Eyre)

Another good example, although unsuccessful in a recent bridge competition, was ARUP-AFA-Aires Mateus for the fourth crossing over the River Mino in Porto. The initial client requirement for a shared bridge for cyclists, pedestrians and metro all situated at the same level did not provide an optimum user experience for the cyclists and pedestrians being confined to a narrow stripe beside a live metro line. The crossing span, over 400m of main span allowed for alternatives that were explored by our team.

Figure 14. Porto Bridge competition. Proposed Structure

Inspired by the successful reuse of rail lines to provide a linear park such as High Lane Park in New York, our team proposed a two-level structure, that given the scale of the bridge, could still provide a slender and visually unobtrusive while delivering a completely different user experience for pedestrians and cyclists than for the train users.

Figure 15.Proposed cross section for the Porto Competition

5.2 Lightweight structures

The lower live load of pedestrian bridges and the differing functional requirements when compared to road and rail bridges, this allows not only to explore new materials as we will see in the following section, but also to push for lighter structural forms such a stress ribbons, suspended and cable stayed structures.

A very interesting structural form in this field are stress ribbon bridges, there are excellent examples of this typology that have been used extensively in mountain paths, as one of its major limitations is the slope that can be achieved comfortably for pedestrians or when accessibility requirements of urban environments limit the slope of the deck.

Probably one of the best examples is the Suransus bridge in Switzerland, by the Swiss architect Jurg Conzett[18].

Figure 16. Pont du Suransuns. J. Conzett

A further development to overcome the limitations of the slope and allowing for further spans is to combine a stress ribbon with an arch structure by the use self-anchored abutments. This typology has been successfully used already by the Czech engineer Jiri Straktski in Svratska bridge [19] and it was proposed for ARUP-Sean Harrington for a bridge competition over the Liffey in Memorial Gardens.

Figure 17. Memorial Gardens Bridge Proposal (ARUP-Sean Harrington)

6 NEW MATERIALS & CONSTRUCTION TECHNIQUES

To achieve the ambitious sustainable goals by 2050, every single component in the construction industry needs to be looked at. In addition to “better design” using traditional materials (structural concrete and steel) it will be necessary to push innovation in new structural materials and construction forms. Good examples range from stone (Suransuns, the bridge described in the previous section has a stone deck) to aluminum as a lighter alternative material to steel, and carbon fibre for tension elements for example. Timber, despite its relatively low structural capacity has significant potential, particularly in pedestrian bridges.

6.1 Timber

Timber has a reduced capacity when compared to concrete and steel. There are however several built examples of excellent timber pedestrian bridges for short and mid spans. Durability and other aspects such a fire resistance remain a challenge, but from a sustainability point of view, the advantages are unquestionable.

An excellent example of good use of timber in bridges is the Neckar crossing designed by Miebach Engineering in Germany, shown below.

Figure 18. Timber pedestrian bridge in Neckartezlingen. Miebach Engieurburo

Hybrid solutions, using concrete or steel and timber in different configurations remain interesting proposals to be developed and tested in the built environment in the near future.

6.2 Carbon fiber

Carbon fiber is extensively used as a repair material, mostly in the form of CFRP, but most recently have been used in both stress ribbons but also as a tension component for the hangers of a 80m main span bowstring arch in Germany as shown in Figure 19 below.

Figure 19.Tram bridge over A8 Motorway. Stuttgart (Source SBP).

6.3 Aluminum

Aluminum is a lighter material than steel, and while it has other disadvantages (flexibility, construction joints, etc), there are several feasibility studies on its use in long span structures. ARUP has recently participated in the feasibility study of a suspension bridge in Langenuen, a 1.2Km main span suspension bridge in Norway, in collaboration with AAS Jacobsen and Staten Vegvesen.

Figure 20. Langenuen bridge concept (Source SV).

An interesting outcome of this study is the large variability of embodied $C0_2$ in aluminum, depending on its sourcing, as part of the study, a market research on different aluminum specifications was taken, showing that the embodied $C0_2$ has a large dispersion depending on the source (see the Figure 21 below).

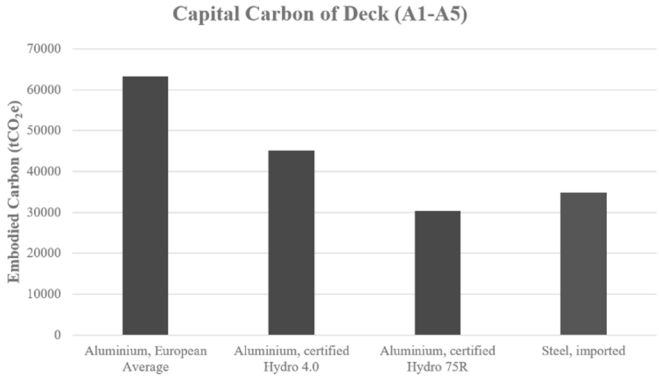

Figure 21. Embodied carbon per ton of aluminium vs steel

This also raises another important topic beyond the scope of this paper in relation to the importance of using transparent metrics in relation to assess accurately the embodied carbon of different materials including the traditional ones (concrete and steel). There is no single accurate figure, even for traditional materials when it comes to $C0_2$ metrics, raw materials, process and transport have an impact in the real, accurate, measurement of carbon footprint.
In the near future, it is very likely that a quick development of "low carbon" concrete and/or steel will emerge, associated with CE marking or industry certifications, as material suppliers are working towards a more sustainable sourcing of materials and processes to reduce their carbon footprint impact.

Another area where future technologies might bring innovative approaches is robotic or automated construction, although it remains to be seen how much impact they may have in producing sustainable outcomes, 3D printing technology, both in concrete and steel is in its infancy but there are already some real life prototypes like the 3D printed bridge recently installed and opened to the public in the Netherlands [20] and Figure 22 below.

Figure 22. 3D Printed bridge in Amsterdam

7 CHALLENGING THE STANDARDS

While this paper has mostly focused on "Total Design" by exploring the importance of Conceptual Design and Inspiration coming from experience along with collaborative work where Bridge Engineers will need to engage more meaningfully with other disciplines to achieve the current ambitious goals in relation to sustainable construction and net zero carbon by 2050, it is also important to highlight the current compromises that are present in the structural standards.

For example, the current design criteria in terms of the lifespan of bridges usually prescribed to 100 years or even 200 years design life, which in many cases requires a greater amount of material quantities (larger cover in concrete structures, sacrificial thickness in steel, etc) have a strong aim in maximizing durability and reducing maintenance on new structures. Their principles have been developed based on "lessons learnt" from previous specifications on structural concrete and steel structure, but the tradeoff when sustainability is introduced as another design constraint is obvious.

A similar concept applies to integral structures when compared to modular bridges for example.

While both examples mentioned above unquestionably maximize durability and minimize long term maintenance, they do have a considerable impact on short term sustainability by increasing the carbon footprint of new construction. This is because they generally involve a greater use of conventional materials to meet the requirements in the code or reduce their potential for future reuse or repurposing by extension or modification of the structure. Unfortunately, integral and monolithic structures are not necessarily aligned with the principles of Circular Economy.

8 CONCLUSIONS

The current paper reflects in the role of Bridge Engineers in the context of the current Climate Crisis, where sustainability principles need to be added to the traditional ones that lead to "good bridge design", Strength, Beauty and Functionality, along with Economy and Durability.

The current targets to achieve net zero carbon by 2050 are extremely ambitious and every profession will need to play a critical role in meeting the current goals. Bridge Engineers, due to their involvement in specifying materials characteristics and their influence in quantities have a huge impact in reducing $C0_2$ emissions.

While reuse and repurposing based on assessment of existing structures will lead to significant savings, combined with an appropriate transport planning, focused on building only when needed and where needed, will play a critical role in achieving the Sustainability Goals: new construction both in Ireland and globally is unavoidable and "build less" and "reuse more" needs to be combined with "build better" strategies.

"Total Design", where a holistic approach that considers every aspect of the project will play a fundamental role in delivering high quality bridges, and Bridge Engineers, by strengthening their skills in Conceptual Design, extensive use of inspiration and experience from existing successful structures and stronger use of Multidisciplinary teams will play a key role in achieving this.

The future remains open, and an ambitious approach to new materials, construction techniques, and innovation are paramount. Challenging every aspect of our profession, including industry standards will be paramount to achieve the ambitious goals we have set up to leave a better Built Environment to future generations.

REFERENCES

[1] Irish Government. Department of the environment, Climate and communications. *Low Carbon development (amendment) Act 2021*. 23 July 2021.

[2] Ian Firth, Keynote Presentation, IAASS2021 Virtual Congress, University of Surrey.

[3] Will Arnold. The structural engineer's responsibility in this climate change emergency. T*he Institution of Structural Engineers*, June 2020.

[4] David Collings. The carbon Footprint of Bridges. *Structural Engineering International*. 2021

[5] The Pensions Commission, Population and Labour Force Projections. Technical Sub-Committee-Working Paper 1. July 2021.

[6] Sir Ove Arup. The Key Speech. 1970.

[7] Mike Schlaich, "Baukultur and Bridge Design". Reflections of the Greatest Bridge Engineers and Architects of the 20th and 21st Centuries. 2017.

[8] David P. Billington. Robert Maillart, Builder, Designer and Artist. Cambridge University Press, 1997.

[9] Fadon P., Beneitez J.E. El Arco de los Tilos en la isla de la Palma (Canarias). Hormigón y Acero. 2005.

[10] Calvo Rodriguez, J.M, Arroyo Marquez, Joaquin. Nova ponte sobre o río Miño (Cortegada). *IV Congreso de la Asociación Científico-Técnica del Hormigón Estructural - Congreso Internacional de Estructuras*, Valencia, 24-27.11.2008.

[11] Gil Gines, M.A, Manterola Armisen, J. Cuarto Puente sobre el Rio Ebro en Logroño, 2002. II Congreso de ACHE.

[12] Pérez-Fadón Martínez, Santiago / Herrero, José Emilio / Martin-Tereso, L. / Sanchez, M. (2007): La Vicaria Arch over La Fuentesanta Reservoir. Presented at: IABSE Symposium: *Improving Infrastructure Worldwide*, Weimar, Germany, 19-21 September 2007, pp. 50-51.

[13] Astiz Suarez M.A, Sanchez M (2022). Rose Fitzgerald Kennedy Bridge over the River Barrow. Design and Construction of a multispan extrados concrete bridge. International Bridge Congress, Pittsburg.

[14] IABSE Outstanding Structure Award 2021

[15] FIB Outstanding Structure award 2022

[16] IStructE Structural Awards 2021.

[17] Sanchez M., Roberts S., Ryan R. Mary Elmes Pedestrian Bridge, from concept to opening. IABSE Congress 2020, Christ Church.

[18] Conzett, J. Landschaft und Kunstbau.Scheidegger & Speiss.2010.

[19] Strasky J. Stress Ribbon & Arch Pedestrian bridges. IBC, 2015

[20] Printing the built environment Arup Journal. Issue 1. 2022.

A 3D computational fluid dynamics validation study for the Queensferry Crossing Bridge with bus models on the deck

Licheng Zhu[1], Daniel McCrum[1], Jennifer Keenahan[1]
[1]School of Civil Engineering, University College Dublin, Belfield, Dublin, Ireland
email: licheng.zhu@ucdconnect.ie, daniel.mccrum@ucd.ie, jennifer.keenahan@ucd.ie

ABSTRACT: In this paper, 3D CFD models of a bridge section of the Queensferry Crossing Bridge including a bus and other secondary structures on the deck are developed in OpenFOAM using the k-ω-SST turbulence model to determine the aerodynamic coefficients. The aerodynamic performance of the bridge deck accounting for several angles of attack with the bus located in various traffic lanes is investigated. The models are then validated with wind tunnel test results and good agreement is found between the 3D CFD models and the wind tunnel tests. The importance of the validated models is that they can be used in the future to study what wind speed should be set as a limit to prevent high-sided vehicles from overturning on the Queensferry Crossing Bridge.

KEY WORDS: Aerodynamic; bridge; CFD; wind tunnel.

1 INTRODUCTION

Wind is one of the pivotal external factors that can adversely affect the safety of long span bridges. The potential hazardous phenomenon induced by wind flow, such as vortex induced vibration (VIV), fluttering and galloping, are significant. Furthermore, the safety of vehicles and pedestrians can be affected as well [1]. Therefore, bridge aerodynamic studies have attracted increasing attention from researchers to improve accuracy and efficiency of assessment methods.

Traditionally, wind tunnel tests have been regarded as the standard assessment method for wind effects on long-span bridges and their results are considered credible to the majority of industries and designers. The wind tunnel test simulates a scaled wind environment with scaled models. The common range of scales used in wind tunnel tests for bridge models is 1/50 to 1/200 [2]. For example, groups of wind tunnel tests were conducted during the construction of the Izmit Bay Bridge to subsequently refine the shape of the deck and to confirm the stability of the bridge [3]. During the design of the Sutong Bridge, wind tunnel tests were used to test the safety of the free-standing pylon and the bridge girder [4].

In recent years, numerical simulations are showing great potential in the field of wind engineering [5]–[7]. The evolution of modern computers provides researchers with sufficient computational power to encourage them to conduct sophisticated CFD simulations, for example. Meanwhile, compared with wind tunnel tests, the advantages of CFD simulations, such as operational convenience and the fact that they are sensors-free, justify futher investigation and development. He et al., [8] investigated the aerodynamic performance of various shapes of box girders with the help of 2D CFD simulations and found out that the wind fairing with a larger angle tends to be more beneficial. Zhu et al., [9] created a 2D deck section model of the Sanchaji Bridge to evaluate the flow field around the bridge deck. The estimated aerodynamic coefficients showed good agreement with wind tunnel results, except for the drag coefficient which deviated significantly from the experimental wind tunnel results. It was suggested that the mesh quality was the reason for the discrepancy. Helgedagsrud et al. [10] investigated the presence of flutter in bridges subjected to strong winds using a 2D bridge deck model. Compared with wind tunnel tests results, it showed that the numerical models can accurately capture the aeroelastic behaviour in terms of aerodynamic stiffness, damping and flutter characteristics. Recently, a few studies applied 3D CFD in the field of aerodynamic studies of long-span bridges. In order to emphasize the necessity of considering the 3D effects, Bai et al., [11] performed a 3D CFD analysis using an extruded 2D bridge section to calculate aerodynamic coefficients. Zhang et al., [12] created 3D models of Rose Fitzgerald Kennedy Bridge and demonstrated detailed procedures of the verification and validation of the applied CFD model.

In this paper, 3D CFD models of the bridge section of the Queensferry Crossing Bridge with a bus and other secondary structures on the deck are developed in OpenFOAM using the k-ω-SST turbulence model to determine the aerodynamic coefficients. The details of the CFD model developed for this work is presented, including geometry of the model, the domain, the mesh, the governing equations and the numerical configuration. Then, the aerodynamic performance of the bridge deck at several angles of attack and with the bus in various traffic lanes are investigated.

2 THE QUEENSFERRY CROSSING BRIDGE

The Queensferry Crossing is a road bridge in Scotland, United Kingdom which opened to traffic in August 2017. It carries the M90 motorway across the firth of Forth between Edinburgh and Fife. The 2.7km long span makes it one of the longest three-tower cable stayed bridges in the world. The 210m bridge tower is the highest bridge tower in the United Kingdom. The balanced cantilevers which extend 322m north and south from the central tower was recorded as the longest free-standing balanced cantilever in the world. Overall, it is the biggest infrastructure project in Scotland for a generation [13].

Figure 1. View of the Queensferry Crossing Bridge [13].

3 THE WIND TUNNEL TESTS

The wind tunnel tests were carried out in Politecnico di Milano Wind Tunnel Boundary Layer test section on a 1:40 scaled section model of the Queensferry Crossing. The wind tunnel is 36m in length, 14m wide and 4m high. The scaled bridge deck was 6m long and 1.042m wide. Figure 3 shows the vehicle lanes selected for investigation. It should be noted that Lane 1 refers to the hard shoulder, which may be used periodically as a traffic lane or a bus lane. These lanes were selected based on the potential effects of southwesterly winds, which are the most common and strongest winds in the United Kingdom. Lane 1 and 2 are the most exposed ones, and Lanes 3 and 4 have vehicles travelling at high speeds into the wind. The bus model was located at each lane, in turn, located at 1.125m along the 6m span.

Figure 2. View of the bridge model in the wind tunnel [14]

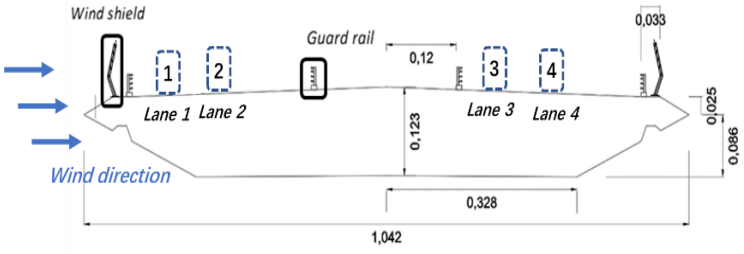

Figure 3. Scaled bridge deck cross section (dimensions in m)

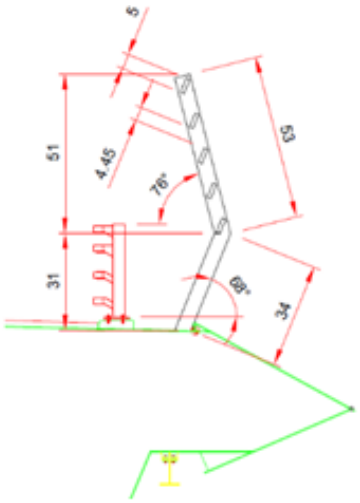

Figure 4. Details of wind shield and guard rail (dimensions in mm)

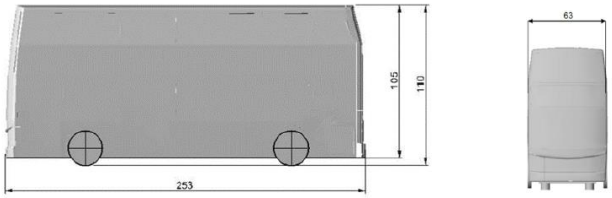

Figure 5. Scaled double deck bus model details (dimensions in mm)

4 CFD MODEL

4.1 Geometry

The CFD geometry has the same dimensions as the model used in the wind tunnel tests, including all the secondary structures. The bridge deck was created using AutoCAD software. by sketching in 2D and then extruding to 3D. The bus model and other secondary structures were created as separate 3D features and then attached onto the deck. As shown in Figure 6(b), the bus model was placed in each of the four lanes. The four lanes are at 200mm, 260mm, 650mm and 700mm away from the windward edge, respectively.

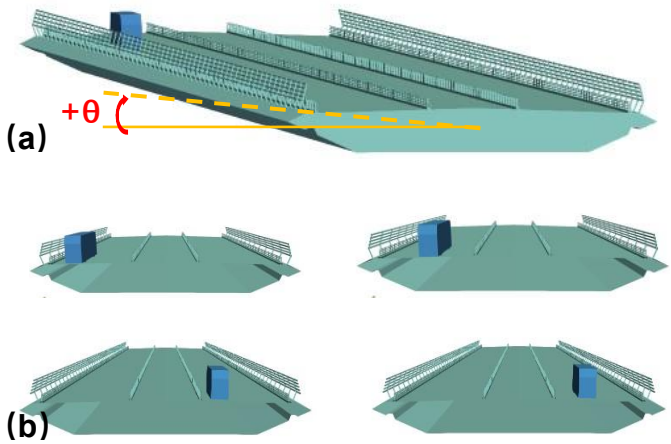

Figure 6. CFD models: (a) overview of the geometry; (b) geometries of the bus on four lanes respectively

4.2 Domain

Based on the domain study from Zhang et al., [12], the size of domain can affect the aerodynamic coefficients when the angle of attack varies between both negative and positive degrees of 5 and 10. For the angle of 0 degrees, the domain size does not significantly affect the simulation results. Thus, for this study, the computational domain is set as 10m long, 5m wide and 2m high. These dimensions are smaller than the size of the wind tunnel to save on computational time and effort. As shown in Figure 7, the blue face is the inlet, the red face is the outlet and the rest of faces are defined as no-slip walls.

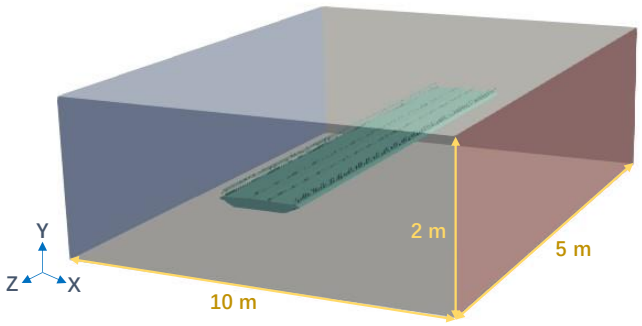

Figure 7. Computational domain used in simulations

4.3 Mesh scheme

The mesh scheme applied in the simulations was created with OpenFOAM. Firstly, the blockMesh utility was used to divide the domain into 12,800 cubic cells of 0.25m width. Then, the snappyHexMesh utility was used to initially create a refinement box near the bridge model area. The refinement level was set as level six which would bring the cell size down to 0.00312m, with seven buffer layers between each level. The area around the bus model was further refined to level seven which is 0.00156m cells. When it came to the bridge surface, seven layers of 0.00004m cells were applied to resolve the viscous sublayer.

The overall mesh quality is deemed to be of very high quality, which is not easily achieved in 3D simulations. The final mesh scheme contained around 102 million cells. There were no distorted cells in the mesh, the average non-orthogonality was approximately 7° and the maximum skewness was below 4. The y+ of the bridge surface, which is a critical value to evaluate mesh quality, was less than 1, as shown in Figure 9. However, it should be mentioned that the average y+ value for the bus model is 5.57 due to few part of the bus surface has y+ higher than 4 (highlighted in Figure.10). Further refinement would require millions more cells and it may affect the balance of current mesh structure, moreover, the total cell number for the current scheme was on the edge of collapsing for post-analysis tools such as Paraview. The authors therefore decided to investigate the performance of the current mesh scheme without any further adjustment.

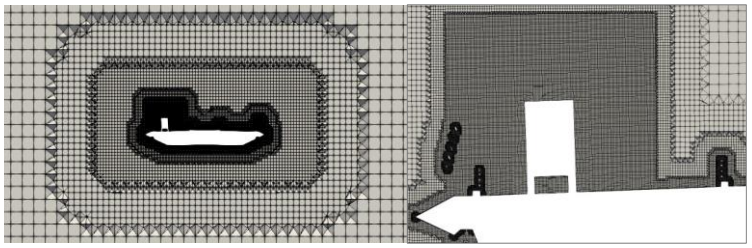

Figure 8. Slice overview of the mesh scheme and the mesh scheme close to the bus model

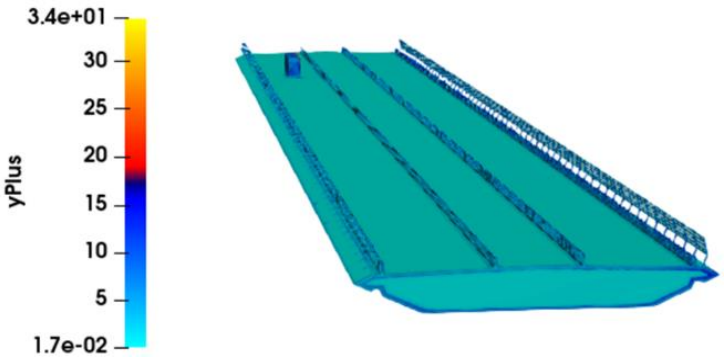

Figure 9. y+ value distribution over the model

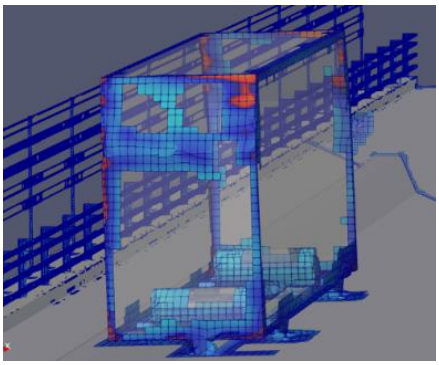

Figure 10. Highlight of y+ > 4 mesh of the bus model

4.4 Numerical configuration

The flow within the computational domain is assumed to be incompressible and statistically steady. The effects of temperature and gravity are neglected as well. The wind flow is simulated by the Reynolds-averaged Navier–Stokes (RANS) equations:

$$\nabla \cdot U = 0 \quad (1)$$

$$\nabla \cdot (UU) = \nabla \cdot [v_{eff}(\nabla U + (\nabla U)^T] - \nabla p \quad (2)$$

where U is the time-averaged velocity, ∇ is a gradient operator, p is the time-averaged kinematic pressure, and v_{eff} is the effective kinematic viscosity, which is the summation of laminar kinematic viscosity ($1.47 \times 10^{-5}\ m^2/s$) and the turbulent kinematic viscosity (calculated with k-ω SST turbulence model).

Based on the information from wind tunnel tests, the wind velocity is set at 4m/s. The turbulence intensity is 5% and the mixing turbulence length is 0.7m. The turbulence kinetic energy (k) and the energy dissipation frequency (ω) are configured with adaptive wall functions built in OpenFOAM, the function can automatically switch between the viscous and logarithmic equation depending on the value of y+.

5 CFD MODEL VALIDATION

Except for the location of the bus model, the mesh scheme and simulation settings for the four CFD models were the same. To assess the accuracy of the CFD modelling, converged simulation results of the aerodynamic coefficients of the bus in the four lanes were compared with the corresponding results from the wind tunnel tests, as shown in Figure 11. The aerodynamic coefficients were calculated from the aerodynamic forces determined in simulations, using the equation below:

$$C_{fi} = \frac{\overline{F_i}}{\bar{q}_H L_j H_j} \quad \text{i} = \text{x, y; j} = \text{B, T} \tag{3}$$

Where, F_x is the drag force, F_y is the lift force, L and H are the characteristic length and height of the model, and $\bar{q}_H$, which is the mean dynamic pressure at 0.04 m above the deck surface.

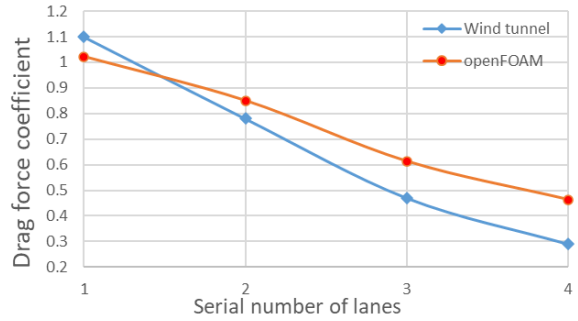

Figure 11. Aerodynamic coefficients of the bus model: (a) drag coefficient; (b) lift coefficient

Figure 11 shows that the drag coefficients of numerical results and wind tunnel results are in good agreement. The lift coefficients show a similar trend and are partially in good agreement. Meanwhile, the results suggest that the numerical simulations tend to overestimate the forces, especially for the lift coefficients. Lift coefficients predicted by the CFD simulations for the bus in Lane 1 and Lane 2 have 71% and 88% relative differences respectively. The maximum difference in results of the drag coefficients is 37%. A potential reason for the overestimation is the highly refined mesh scheme. The cells can be more sensitive than the sensors installed in the wind tunnel, which leads to the accumulation of the over discretization and overstated kinematic energy from each cell.

Moreover, it is interesting to note that the lift coefficient results from both CFD simulations and wind tunnel tests suggest that the lift force would be higher when the vehicle is further away from the windward edge. A potential cause is observed from the CFD simulation wind field. As shown in Figure 11, the wind shield and guard rail provide significant reduction in the on-coming wind speed. When the bus is located in Lane 4, the space between the bus and the guard rail allows the slowed wind flow to generate a small vortex which leads to a re-acceleration of the flow velocity. This phenomenon only occurs when the flow decelerates as a result of the wind shield and the three guard rails. Further research is needed to investigate the trigger range of the wind velocity.

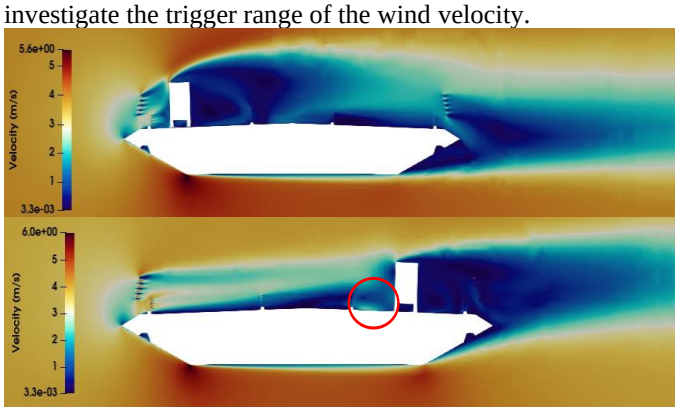

Figure 11. Slice cut view of wind field around the geometries: (a) the bus on the Lane 1; (b) the bus on the Lane 4.

Next, the vehicle model was removed. Based on the wind tunnel tests, the aerodynamic coefficients of the bridge deck were investigated under different angles of attack. As indicated in Figure 6(a), the deck was rotated to three different angles of attack, which were 1.5°, 3° and 5°. Drag coefficients determined by wind tunnel tests were found to be moderately larger than the numerical results. The maximum relative difference was 12% at the angle of attack of 3°. It demonstrates that numerical results can closely match with wind tunnel results in predicting drag coefficients.

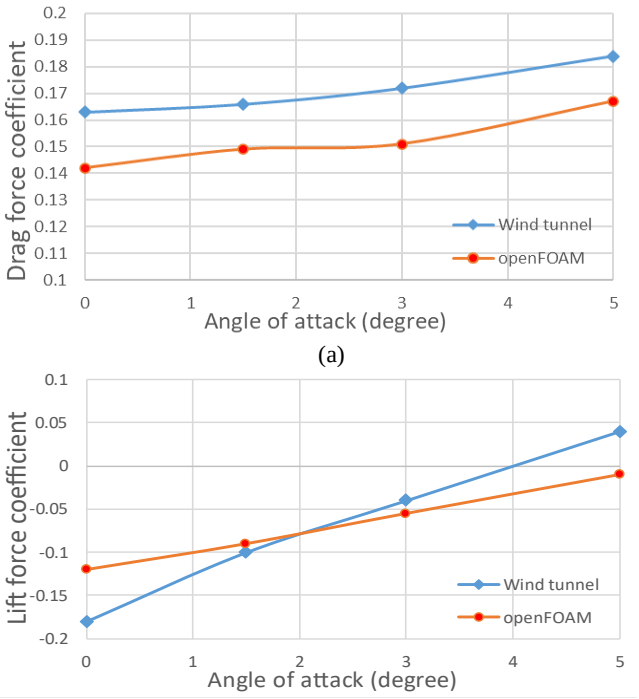

Figure 12. Aerodynamic coefficients of the bridge deck: (a)drag coefficient; (b) lift coefficient

As for the lift coefficients, results from both methods are very close with an angle of attack of 1.5° and 3°. However, wind tunnel results have a more rapidly increasing trend so that the discrepancies between the two would in theory, get larger with increases in angle of attack.

In general, there is a good agreement between the numerical results and the wind tunnel test results of aerodynamic coefficients for the bridge deck models. CFD simulation shows a good ability to predict drag force coefficients, whereas it is slightly conservative in determining lift force coefficients. Additionally, the CFD results suggests that a highly refined mesh scheme may not be necessary since it can lead to overestimation compared with the experimental results. Further study is needed as well to verify the model with different wind velocity and under different range of angle of attacks.

6 CONCLUSIONS

In this paper, 3D CFD models of the bridge section of the Queensferry Crossing Bridge with a bus and other secondary structures on the deck are developed. A highly refined mesh scheme is applied to the models. The simulations used the RANS method with the k-ω-SST turbulence model. Then, the aerodynamic coefficients of the bridge section and the bus on selected lanes are numerically investigated and validated with the wind tunnel results. It has been found that CFD simulations provide a good ability in capturing the aerodynamic coefficients and there is a good agreement between the numerical results and the wind tunnel test results. Moreover, the study indicates that further research may need to find an efficient extent of mesh refinement for the 3D simulations. Meanwhile, further study is required as well to verify the model with different wind velocity and under different range of angle of attacks. The importance of the validated models is that they can be used in the future to study what wind speed should be set as a limit to prevent high-sided vehicles from overturning on the Queensferry Crossing Bridge.

ACKNOWLEDGMENTS

The authors wish to acknowledge the Irish Centre for High-End Computing (ICHEC) for the provision of computational facilities and support and the authors would also like to acknowledge the support given by Transport Scotland and Arup Consulting Engineers to this work. Licheng Zhu acknowledges the scholarship (No.201908300012) received jointly from University College Dublin and the China Scholarship Council.

REFERENCES

[1] Cochran, L. and Derickson, R., "A physical modeler's view of computational wind engineering," *J. Wind Eng. Ind. Aerodyn. Eng*, vol. 99, pp. 139–153, 2011.

[2] Zhang, Y., Cardiff, P. and Keenahan, J, "Wind-Induced Phenomena in Long-Span Cable-Supported Bridges: A Comparative Review of Wind Tunnel Tests and Computational Fluid Dynamics Modelling," *Appl. Sci.*, vol. 11, no. 4, p. 1642, 2021.

[3] Diana, G., Yamasaki, Y., Larsen, A., Rocchi, D., Giappino, S., Argentini, T., Pagani, A., Villani, M., Somaschini, C. and Portentoso, M., "Construction stages of the long span suspension Izmit Bay Bridge: Wind tunnel test assessment.," *J. Wind Eng. Ind. Aerodyn.*, vol. 123, pp. 300–310, 2013.

[4] C. M. Ma, Q. S. Duan, and H. L. Liao, "Experimental investigation on aerodynamic behavior of a long span cable-stayed bridge under construction," *KSCE J. Civ. Eng.*, vol. 22, pp. 2492–2501, 2018.

[5] McGuill, C. and Keenahan, J., "A Parametric Study of Wind Pressure Distribution on Façades Using Computational Fluid Dynamics," *Appl. Sci.*, vol. 10, no. 23, p. 8627, 2020.

[6] Bernardo, P., Réamoinn, R.M., Young, P., Brennan, D., Cardiff, P. and Keenahan, J., "Investigation of the helicopter downwash effect on pedestrian comfort using CFD," *Infrastruct. Asset Manag.*, pp. 1–8, 2019.

[7] Keenahan, J., MacReamoinn, R. and Paduano, C., "Sustainable design using computational fluid dynamics in the built environment–A case study," *J. Sustain. Archit. Civ. Eng.*, vol. 19, no. 2, pp. 92–103, 2017.

[8] L. M. He XH, Li H, Wang HF, Fang DX, "Effects of geometrical parameters on the aerodynamic characteristics of a streamlined flat box girder," *J. Wind Eng. Ind. Aerodyn.*, vol. 170, pp. 56–67, 2017.

[9] Z. W. Zhu, M. Gu, and Z. Q. Chen, "Wind tunnel and CFD study on identification of flutter derivatives of a long-span self-anchored suspension bridge," *Comput. Civ. Infrastruct. Eng.*, vol. 22, no. 8, pp. 541–554, 2007.

[10] T. A. Helgedagsrud, Y. Bazilevs, K. M. Mathisen, and O. A. Øiseth, "Computational and experimental investigation of free vibration and flutter of bridge decks," *Comput. Mech.*, vol. 63, no. 1, pp. 121–136, 2019.

[11] Y. Bai, D. Sun, and J. Lin, "Computers & Fluids Three dimensional numerical simulations of long-span bridge aerodynamics , using block-iterative coupling and DES," *Comput. Fluids*, vol. 39, no. 9, pp. 1549–1561, 2010.

[12] Zhang, Y., Cardiff, P., Cahill, F., Keenahan, J., "Assessing the Capability of Computational Fluid Dynamics Models in Replicating Wind Tunnel Test Results for the Rose Fitzgerald Kennedy Bridge," *CivilEng*, vol. 2, no. 4, pp. 1065–1090, 2021.

[13] "Queensferry Crossing," *THE FORTH BRIDGES*, 2014. [Online]. Available: https://www.theforthbridges.org/queensferry-crossing/.

[14] Politecnico di Milano, "Main Crossing Wind Tunnel Testing - Wind Shield Studies," 2010.

Scour at a drowned FlexiArch bridge

Sachie Prabuddha Sathurusinghe, Gerard Hamill, Su Taylor, Desmond Robinson
Queen's University, Belfast, United Kingdom
sprabuddha01@qub.ac.uk, g.a.hamill@qub.ac.uk, s.e.taylor@qub.ac.uk, des.robinson@qub.ac.uk

ABSTRACT: The research currently being carried out at Queen's University Belfast on scour at a single-span FlexiArch bridge and the resulting structural failure of the bridge is, to the best of the authors' knowledge, the first to study this phenomenon without decoupling the structural response of a scoured bridge from the hydraulics that drives the scour. In these experiments, a 1:10 scale single-span FlexiArch bridge model, seated on a bed of non-cohesive sediment, is subjected to hydraulic loading inside a flume and is load tested at different levels of foundation scour to assess the effect of scouring on its structural characteristics.

This article presents the development and preliminary testing of the experiment. The results presented here demonstrate that the bridge model can be assembled to be structurally similar to the prototype bridge so that it responds to developing scour (i.e., settlement due to loss of support). Moreover, computer vision-based sensors have been tested to be used to 1) measure the geometry of the drained scour hole under the model bridge, and 2) monitor the structural failure of a loaded FlexiArch bridge based on noncontact multi-point displacement monitoring. The results from this research will provide a fundamental understanding of the scour-induced bridge damage as well as vital tools and data to develop a robust real-time Structural Health Monitoring (SHM) platform.

KEY WORDS: FlexiArch, scour, load test, structural health monitoring.

1 INTRODUCTION

1.1 Fluid-structure interactions at bridges

The failure and collapse of a bridge subjected to foundation scour is a complex phenomenon where the geometry of the structure, hydraulics, geotechnical properties of the soil at the bridge supports and structural properties of the bridge interact.

However, prior research into the change in the structural performance of bridges due to the evolution of foundation scour usually modelled the scour with *assumed* states of scour (extent and location of scour). Examples can be found in the finite element (FE) analysis conducted by Zampieri et al. [1], Tubaldi et al. [2] and Scozzese et al. [3] to study the structural response of multi-span arch bridges to developing foundation scour. The states of scour that were employed in the FE models were not based on scour measurements at the actual bridges they modelled, nor were they based on hydraulic tests on scaled models under the hydraulic conditions that exist at the actual bridges.

Moreover, in the field of structural health monitoring (SHM), Kariyawasam et al. [4] carried out research into detecting scour at bridge foundations by monitoring changes in bridge natural frequency. In this study, the progressive scour was simulated by manually removing sand around model piers from the dry bed. In this case also, the states of scour they employed were not based on measurements of realistic scour holes. Likewise, Khan et al. [5] developed a method based on decentralized modal analysis to monitor scour at bridges with multiple spans. The evolution of the scour process was approximated in their physical models by changing the stiffness of springs which modelled shallow foundations under the piers. Here again, the levels of stiffness of the supports were based on assumptions and not calculated based on any measurements of actual scour holes.

The use of assumed conditions of scour at bridge supports may be sufficient in providing means of validating SHM systems that are being developed to detect the level and location of scour. But, in such SHM research, and especially in cases where a particular bridge is being assessed for scour damage, the geometry of the assumed scour holes and their evolution should be carefully evaluated so as not to be *unrealistic*.

It should always be remembered that scour at a bridge site depends on many variables [6, 7]. Therefore, neighbouring bridges in a river may experience different levels of scour during a flood due to differences in bridge geometry, while bridges with the same geometry but in different rivers may experience different scour levels due to different hydraulic conditions that exist at the sites. Also, channel instabilities may cause severe scour concerns to bridges [8] which might not have been identified as having scour concerns before the channel migration. Moreover, the introduction of scour countermeasures would shift the location of the maximum scour [9]. Therefore, the assumed level of scour at a bridge model (even if based on measurements at an existing bridge) may not be what the prototype bridge would be subjected to at the site. Therefore, for a more accurate representation of a bridge's structural response to scour, the scour process should be modelled as accurately as possible. This idea is supported by the conclusion Ettema et al. [10] have drawn from their findings from flume experiments on scour and stability of masonry arch bridges - "*The final failure mechanism of the structure will be*

a complex interaction of hydraulic, geotechnics & structural processes, thus a combined rationale for the management of these key assets is needed".

On the other hand, research on the hydraulics of scour at bridges [9, 11-13] has so far employed bridge models that were ill-representative of the structural properties of real bridges. This is because their fabrication (hollow construction and/or the model being rigidly connected to the flume) would not allow the model to have a realistic structural response to scour (i.e., settle/collapse). Hence, such models would provide an estimation of scour that may not exist at a real bridge site (since a real bridge could fail before the level of scour that these models predict).

Therefore, it is the author's opinion that the study of the structural behaviour of a bridge with scoured supports conducted in combination with the hydraulics that drives the scour would provide more realistic estimates of both these phenomena. In that regard, this paper presents what is believed to be the first holistic research into damage evolution at the novel FlexiArch masonry arch bridge, in which, scour process and the response of the bridge to the scour are explored by conducting hydraulic tests followed by in situ load tests on the scoured bridge model.

1.2 FlexiArch™ bridge system

A novel flexible arch bridge, called the FlexiArch™, has been developed by Queen's University Belfast and Macrete Ireland Ltd. and has been used to strengthen or replace old masonry arches and as a lower-carbon alternative to the box culvert [14, 15]. The system consists of arch rings made up of precast concrete voussoirs that arrive at the site in a flat form (Figure 1a). The rings naturally assume the designed arch shape once lifted and placed on skewbacks (Figure 1b). A polymeric reinforcement that binds the top surfaces of the voussoirs carries the tension that develops in the ring as it is lifted.

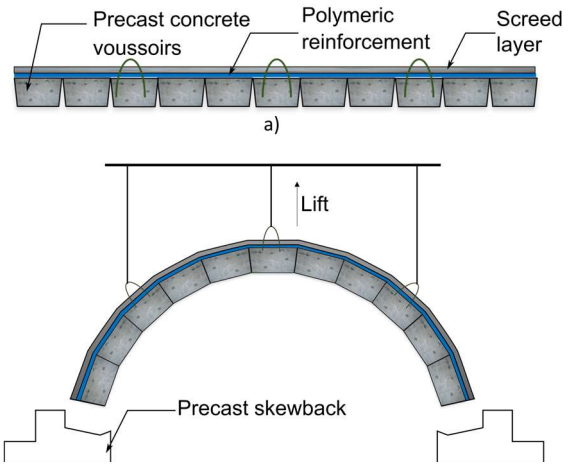

Figure 1. a) Initial flat form of a FlexiArch™ arch ring, b) the ring forming the desired arch shape as it is lifted.

Once the arch rings are seated on the skewbacks, they perform similarly to traditional masonry arches. As the system does not involve any corrodible reinforcement, it would similarly be durable. Therefore, these bridges would not require frequent repair work or premature replacement.

Not only would this save resources directly, but as repairs are usually associated with congestion or long detours, a considerable amount of time, money and energy would be saved from being spent [6, 16]. Therefore, the total life cycle costs of FlexiArch bridges are found to be lesser than reinforced alternatives [14, 17].

The success of the system has led to the deployment of the system in the UK, Ireland and Denmark [15] and the development of double radius [18] and skew FlexiArch bridges [19].

Even though the static load carrying capacity [20-22], dynamic load response [23] and behaviour under seismic loading [24] have been investigated in previous research, the behaviour of the system under scoured conditions has not been carried out yet. Therefore, the research presented here will provide insight into the scour problem at this novel type of bridge, especially in the critical case of scouring when the arch opening is drowned. Arch bridge openings drown easily during high floods and, as the occurrence of high magnitude floods is expected to increase due to climate change, more FlexiArch and traditional masonry arch bridges would be subjected to this type of scour [25].

2 METHODOLOGY

The experiments in the current research are conducted on 1:10 scale FlexiArch models with a span of 500mm, a rise of 200mm and a width of 200mm and are constructed to behave similarly to the structural behaviour of the prototype. The construction details of the components and the setup of the experiment are documented in [26].

Though one major advantage of the prototype scale FlexiArch bridges is that they do not require a centring during construction, the arch rings of the 1:10 scale models require supports during backfilling, as even the forces generated during compacting by hand resulted in large movements of the arch ring.

The 1:10 scale FlexiArch model assembled on a flat sediment bed in the flume is shown in Figure 2. The bridge was perpendicular to the flow direction and was subjected to increasing magnitude of flow, and the velocity field of the flow approaching the bridge opening was visualised using particle image velocimetry (PIV) conducted using a 200 mJ, 532 nm laser at 15 Hz (Dantec Dynamics, Skovlunde, Denmark) illuminating the seeding, and a HiSense Zyla (Dantec Dynamics, Skovlunde, Denmark) camera with a 50mm prime lens observing the approach flow to the bridge from the side.

Figure 2. 1:10 scale FlexiArch model on the sediment bed.

2.1 Measuring the extent of scour under the bridge model

The resulting scour hole was measured using a ZED 2 (Stereolabs Inc., San Francisco, USA) stereo vision 3D camera with a stated accuracy of < 1% up to 3m away from the camera. This was achieved by panning the camera across the initial and scoured sediment bed (Figure 3) and using the spatial mapping capabilities of the camera. The small size of the stereovision camera enables it to be moved close to the bridge and reoriented as necessary to capture the full extent of scour hole under the model. This allowed the model to be kept in its scoured state while the scour hole under it is mapped, thus protecting the scour hole from any disturbance before mapping it.

a)

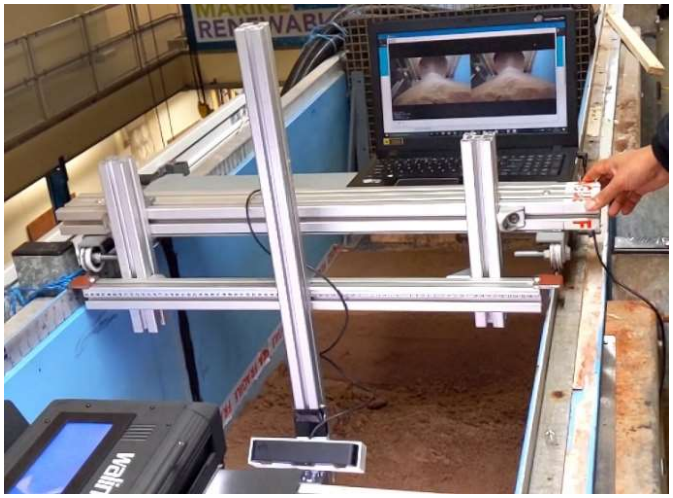

b)

Figure 3. Stereovision-based 3D camera setup. a) The ZED 2 camera, b) panning the camera across the sediment bed.

2.2 Dry load test

To assess the load-carrying capacity of the model when seated on rigid supports, the model was assembled on a rigid steel platform and lateral restraint was provided by steel angles (Figure 4). Then the bridge was loaded at the ⅓ span point by stacking weights (each weighing 22.7 kg).

Total weight of 158.9 kg was stacked on the bridge model. The loading was terminated at this load as this was the maximum weight that could be safely stacked.

The movement of the model during the loading process was recorded using a GoPro Hero 7 camera placed in front of the bridge model and oriented so that the image plane is parallel to the plane of the bridge spandrel. Figure 5a shows a frame from the recorded video.

2.3 Development of a computer vision-based multi-point displacement monitoring system

The basic steps in the computer vision-based displacement measurement method that is employed here are camera calibration, feature extraction and feature tracking [27]. Salient features were detected on the arch ring using the Speeded-Up Robust Features (SURF) [28] feature detector and descriptor and the motion of these points were tracked between the frames using the Lucas-Kanade-Tomasi (LKT) [29] tracking algorithm (Figure 5b and Figure 5c). These algorithms are available in MATLAB Computer Vision Toolbox™ [30] as functions. The displacement of each successfully tracked point was then obtained as the change in the location of each point from the initial position (the yellow lines in Figure 5c indicate the displacements).

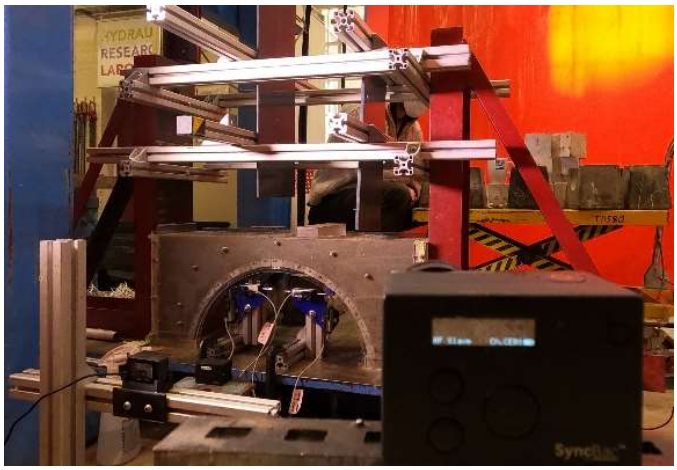

Figure 4. Set up of the bridge model for dry load test

3 RESULTS

3.1 Scour and response of the bridge to the scour under self-weight

Figure 6a shows the model in Figure 2 subjected to a flow test (subcritical, turbulent, flowrate ~30 l/s). The effect of scour on the model is evident in Figure 6b which shows an instance when the scour has undermined the bridge to an extent where the foundation on the right-hand side has settled under self-weight. This is a response of the model to scour that would not have been observed in earlier bridge scour research. This is because the models they employed were not representative of the structural behaviour of prototype bridges.

As can be seen in the image, this collapse occurred during free-flow conditions (at a flowrate ~30 l/s → 14.3 m^3/s at prototype scale from Froude scaling). However, scour at the bridge opening was observed to begin at lower flowrates (~10 l/s).

Figure 6c shows a side view of the bridge after the flow has been terminated and the flume is drained (some water can be seen in the scour hole). The 3D scan of the scour hole taken after the water has been fully drained is shown in Figure 7. A fully mapped scour hole as obtained here provides realistic input to analyse future numerical models of scoured arch bridges.

3.2 Effect of contraction of flow at the bridge opening

The 2-dimensional velocity field of the approach flow, obtained through laser PIV, is shown in Figure 8. Here, the field was obtained for a vertical plane along the arch centreline in the streamwise direction. The flow is from the left to the right of the image. The flow approaching the model had a mean

velocity of ~ 0.25 m/s (yellow) and is accelerated by about 1.8 times in front of the arch inlet as indicated by the region in purple (arch inlet visible in the top right corner).

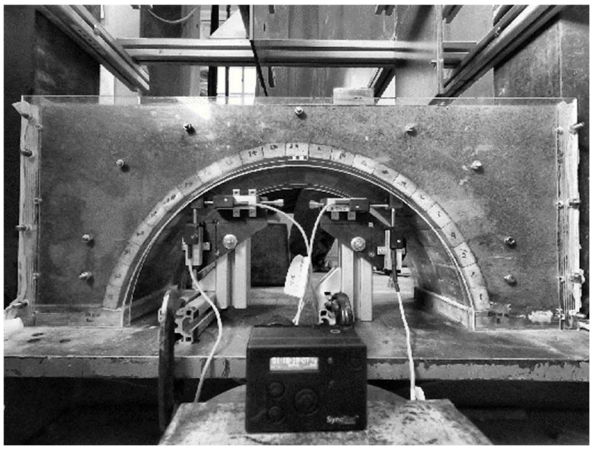

a)

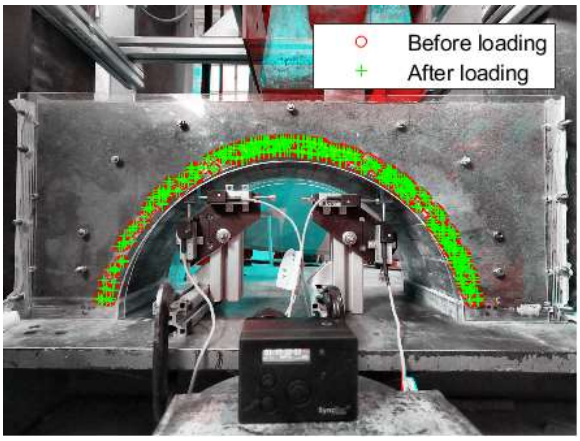

b)

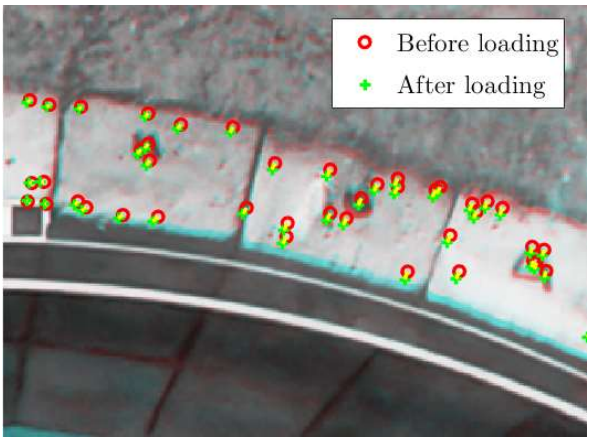

c)

Figure 5. a) A frame extracted from the recording of the load test, b) feature detection on the arch ring (two frames have been superimposed), c) a crop of the frames in b) showing the feature points that have been validly tracked over the two frames (the undeformed bridge is masked in red while the deformed bridge is masked in cyan.)

a)

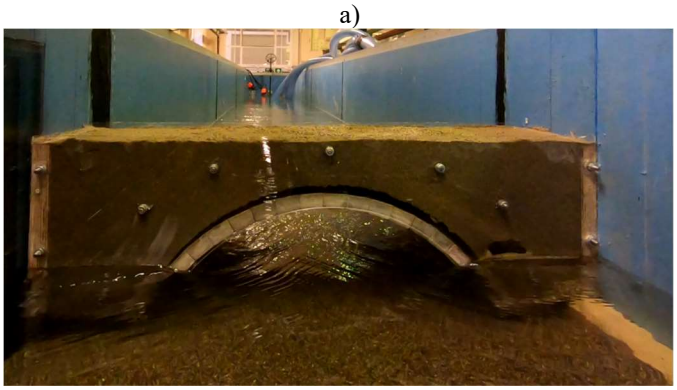

b)

c)

Figure 6. a) The bridge model subjected to free-flow conditions, b) settlement of the arch ring due to scour, c) side view of the scour hole as the water is being drained.

3.3 Identifying the failure mechanism of the bridge model using computer vision techniques

The vectors indicating the displacements of the arch ring at the end of the dry loading test are shown in Figure 9a. These have been filtered to remove spurious vectors using the M-estimator SAmple Consensus (MSAC) algorithm [31]. Inward movement of the ring can be observed directly beneath the loaded ⅓ span point and outward movement can be observed on either side of the region moving inward, i.e., the arch ring is bulging out.

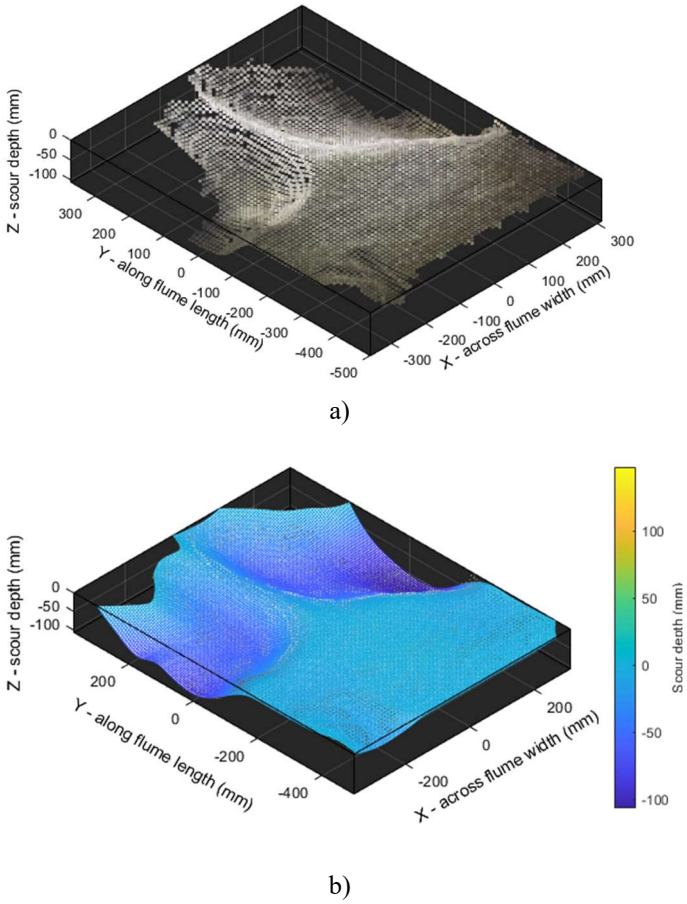

a)

b)

Figure 7. The 3D scan of the scour hole. a) Point cloud obtained from the camera, b) point cloud fitted with a smooth surface.

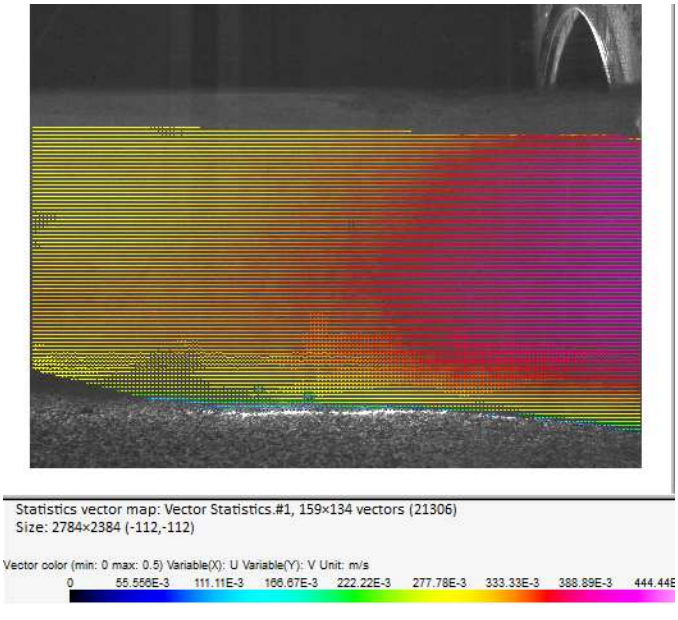

Figure 8. Time-averaged velocity field of the approach flow in a streamwise, vertical plane along the arch centreline.

Two inflection points in the vector orientation can also be observed roughly at the ¼ and ½ span points (Figure 9b). As the image plane of the camera is parallel to the plane of the arch ring and as the arch ring only moves in this plane, these inflection points indicate the region where hinges form, i.e., where the thrust line would not be contained inside the voussoirs, which leads to the collapse of the bridge.

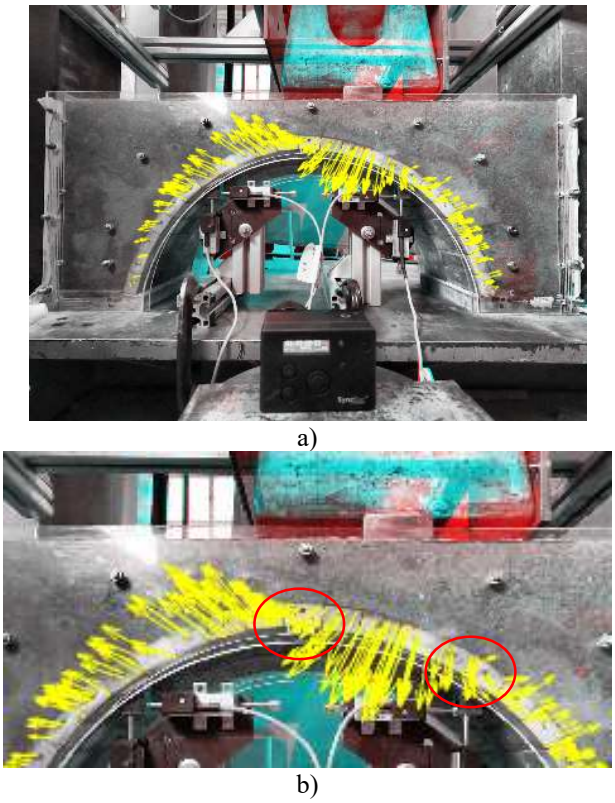

a)

b)

Figure 9: a) Calculated displacement vectors (not to scale), b) close-up of the arch ring and the displacement vectors (not to scale).

4 CONCLUSION

Scour at bridge foundations is a complex fluid-structure interaction. The failure of a bridge is a result of the consequential nature of this interaction. But prior research has studied these two phenomena separately from each other.

The present paper presents ongoing research in which scour, and the consequential structural behaviour of the bridge are studied holistically in a series of flume experiments. Currently, a method to assemble a functional 1:10 scale FlexiArch bridge has been developed and the model has been demonstrated to respond to foundation scour via settlement. Also, a method based on a stereo vision 3D camera to map the full scour hole under the model has been developed. Finally, a computer vision approach has been developed and applied to identify the failure mode of loaded FlexiArch bridges and two hinge formations have been identified near the ½ span ¼ span points when loaded at the ⅓ span point.

It is expected that the results from the current study will help elucidate the dependence of scour on the hydraulic characteristics that exist at a bridge and how the evolving scour will affect the stiffness and the stability of the bridge. This will provide a foundation to develop an SHM platform that is being developed at Queen's University Belfast [32] based on a validated real-time vision-based displacement monitoring

system and a numerical model of the bridge, which will provide bridge managers vital information about scour critical bridges.

ACKNOWLEDGMENTS

The first author acknowledges the funding from the UK's Engineering and Physical Sciences Research Council (EPSRC) and the W.A. Hill Civil Engineering Travel Award awarded by the School of Natural and Built Environment of Queen's University Belfast.

REFERENCES

[1] P. Zampieri, M. A. Zanini, F. Faleschini, L. Hofer, and C. Pellegrino, "Failure analysis of masonry arch bridges subject to local pier scour," *Engineering Failure Analysis,* vol. 79, no. July 2016, pp. 371-384, 2017 2017, doi: 10.1016/j.engfailanal.2017.05.028.

[2] E. Tubaldi, L. Macorini, and B. A. Izzuddin, "Three-dimensional mesoscale modelling of multi-span masonry arch bridges subjected to scour," *Engineering Structures,* vol. 165, pp. 486-500, 2018 2018, doi: 10.1016/j.engstruct.2018.03.031.

[3] F. Scozzese, L. Ragni, E. Tubaldi, and F. Gara, "Modal properties variation and collapse assessment of masonry arch bridges under scour action," *Engineering Structures,* vol. 199, no. March, pp. 1-10, 2019, doi: 10.1016/j.engstruct.2019.109665.

[4] K. D. Kariyawasam, C. R. Middleton, G. Madabhushi, S. K. Haigh, and J. P. Talbot, "Assessment of bridge natural frequency as an indicator of scour using centrifuge modelling," *Journal of Civil Structural Health Monitoring,* vol. 10, no. 5, pp. 861-881, 2020/11/01 2020, doi: 10.1007/s13349-020-00420-5.

[5] M. A. Khan, D. P. McCrum, L. J. Prendergast, E. J. Obrien, P. C. Fitzgerald, and C.-W. Kim, "Laboratory investigation of a bridge scour monitoring method using decentralized modal analysis," *Structural Health Monitoring,* vol. 20, pp. 1-15, 2021, doi: 10.1177/1475921720985122.

[6] A. M. Kirby, M. Roca, A. Kitchen, M. Escarameia, and O. J. Chesterton, *Manual on Scour at Bridges and Other Hydraulic Structures*, 2nd ed. CIRIA, 2015, p. 282.

[7] L. A. Arneson, L. W. Zevenbergen, P. F. Lagasse, and P. E. Clopper, "Evaluating Scour at Bridges," Federal Highway Administration, U.S. Department of Transportation, FHWA-HIF-12-003 HEC-18, 2012.

[8] T. Inoue, J. Mishra, K. Kato, T. Sumner, and Y. Shimizu, "Supplied Sediment Tracking for Bridge Collapse with Large-Scale Channel Migration," *Water,* vol. 12, no. 7, p. 1881, 2020. [Online]. Available: https://www.mdpi.com/2073-4441/12/7/1881.

[9] B. Solan, R. Ettema, D. Ryan, and G. A. Hamill, "Scour Concerns for Short-Span Masonry Arch Bridges," *Journal of Hydraulic Engineering,* vol. 146, no. 2, p. 06019019, 2020, doi: 10.1061/(ASCE)HY.1943-7900.0001675.

[10] R. Ettema, B. Solan, C. Watters, G. Hamill, and R. Donal, "Scour and the stability of short-span, masonry arch bridge: findings from a diagnostic, flume study," presented at the Civil Engineering Research in Ireland 2018, Dublin, 29 - 30 August, 2018.

[11] L. A. Arneson and S. R. Abt, "Vertical Contraction Scour at Bridges with Water Flowing Under Pressure Conditions," *Transportation Research Record,* vol. 1647, no. 1, pp. 10-17, 1998, doi: 10.3141/1647-02.

[12] B. W. Melville, "Pressure-flow scour at bridges," in *Scour and Erosion: Proceedings of the 7th International Conference on Scour and Erosion*, Perth, Australia, L. Cheng, S. Draper, and H. An, Eds., 2-4 December 2014, London: CRC Press, 2015, pp. 449-453.

[13] M. Ebrahimi *et al.*, "Experimental investigation of scour and pressures on a single span arch bridge under inundation," in *Proceedings of the 7th IAHR International Symposium on Hydraulic Structures, ISHS 2018*, Aachen, Germany, D. Bung and B. Tullis, Eds., 15-18 May 2018: Utah State University, 2018, pp. 715-722, doi: 10.15142/T33D25.

[14] A. Long, J. Kirkpatrick, A. Gupta, S. Nanukuttan, and D. M. Polin, "Rapid construction of arch bridges using the innovative FlexiArch," *Proceedings of the Institution of Civil Engineers - Bridge Engineering,* vol. 166, no. 3, pp. 143-153, 2013, doi: 10.1680/bren.11.00036.

[15] Macrete Ireland Ltd. "FlexiArch Projects." http://www.macrete.com/flexiarch-flexiarch-projects/ (accessed 08 May, 2020).

[16] S. G. Aydin, G. Shen, and P. Pulat, "A Retro-Analysis of I-40 Bridge Collapse on Freight Movement in the U.S. Highway Network using GIS and Assignment Models," *International Journal of Transportation Science and Technology,* vol. 1, no. 4, pp. 379-397, 2012/12/01/ 2012, doi: 10.1260/2046-0430.1.4.379.

[17] A. E. Long, P. A. M. Basheer, S. E. Taylor, B. G. I. Rankin, and J. Kirkpatrick, "Sustainable bridge construction through innovative advances," *Proceedings of the Institution of Civil Engineers - Bridge Engineering,* vol. 161, no. 4, pp. 183-188, 2008, doi: 10.1680/bren.2008.161.4.183.

[18] D. Quinn, A. Gupta, D. McPolin, S. Taylor, and A. Long, "Development of a double radius FlexiArch," presented at the BCR10 Bridge & Concrete Research in Ireland, Cork, Ireland, 2-3 September 2010, 2010. [Online]. Available: http://www.cerai.net/download/file/bcri2010_proceedings_v1.pdf.

[19] P. Mc Nulty, "Behaviour and Analysis of a Novel Skew Flexible Concrete Arch Bridge," Queen's University Belfast, 2013.

[20] S. Taylor, D. Robinson, N. Ritchie, K. Mcllwaine, and A. Gupta, "Testing of half-scale model flexible concrete arches," in *Bridge and Infrastructure Research in Ireland: Symposium*, 2006.

[21] S. Taylor, A. Gupta, J. Kirkpatrick, A. Long, and I. Hogg, "Production of novel flexible concrete arch," 2006.

[22] J. Bourke, S. Taylor, D. Robinson, and A. Long, "Modelling of solid and hollow voussoir FlexiArch systems," *Proceedings of the Institution of Civil Engineers - Bridge Engineering,* vol. 167, no. 1, pp. 61-73, 2014-03 2014, doi: 10.1680/bren.11.00015.

[23] M. Lydon, D. Sivakumar, S. Taylor, and D. Robinson, "Monitoring of a novel FlexiArchTM bridge system to investigate soil-structure interaction," presented at the 5th International Conference on Structural Health Monitoring of Intelligent Infrastructure (SHMII-5), Cancun, Mexico, 2011.

[24] C. McCracken, S. Taylor, P. McNulty, M. Lydon, D. McCrum, and D. Robinson, "Seismic Testing and Analysis of the FlexiArch™," presented at the Civil Engineering Research in Ireland Conference (CERAI), Belfast, UK, 28-29 August, 2014.

[25] P. Sathurusinghe, G. Hamill, S. Taylor, and D. Robinson, "Hydraulics of Scour in the Vicinity of a FlexiArch bridge," presented at the Civil Engineering Research in Ireland 2020, Cork, Ireland, 2020. [Online]. Available: https://sword.cit.ie/ceri/2020/3/5/.

[26] S. P. Sathurusinghe, G. A. Hamill, S. E. Taylor, and D. Robinson, "Foundation scour and its effect on the performance of FlexiArch™ modern arch bridge system," presented at the 10th International Conference on Structural Health Monitoring of Intelligent Infrastructure, Porto, Portugal, 30 June - 2 July, 2021.

[27] D. Lydon, M. Lydon, S. Taylor, J. M. Del Rincon, D. Hester, and J. Brownjohn, "Development and field testing of a vision-based displacement system using a low cost wireless action camera," *Mechanical Systems and Signal Processing,* vol. 121, pp. 343-358, 2019, doi: 10.1016/j.ymssp.2018.11.015.

[28] H. Bay, A. Ess, T. Tuytelaars, and L. Van Gool, "Speeded-Up Robust Features (SURF)," *Computer Vision and Image Understanding,* vol. 110, no. 3, pp. 346-359, 2008/06/01/ 2008, doi: https://doi.org/10.1016/j.cviu.2007.09.014.

[29] C. Tomasi and T. Kanade, "Detection and tracking of point," *Int J Comput Vis,* vol. 9, pp. 137-154, 1991.

[30] *Computer Vision Toolbox™*. (2021). [Online]. Available: https://uk.mathworks.com/help/vision/

[31] P. H. S. Torr and A. Zisserman, "MLESAC: A New Robust Estimator with Application to Estimating Image Geometry," *Computer Vision and Image Understanding,* vol. 78, no. 1, pp. 138-156, 2000/04/01/ 2000, doi: https://doi.org/10.1006/cviu.1999.0832.

[32] B. Millar, S. P. Sathurusinghe, G. Hamill, S. Taylor, and D. Robinson, "The development of assessment models for the Flexiarch bridge system experiencing bridge scour, under loading," (forthcoming), SHMII-11: 11th International Conference on Structural Health Monitoring of Intelligent Infrastructure, Montreal, QC, Canada, 8-12 Aug, 2022.

Vulnerability Assessment of Existing Bridges to Scour: An Indirect Monitoring Approach

Sinem Tola[1], Joaquim Tinoco[1], José C. Matos[1], Eugene OBrien[2]
[1] University of Minho, ISISE, Department of Civil Engineering, Av. da Universidade, Guimarães, Portugal
[2] University College Dublin, School of Civil Engineering, Belfield, Dublin 4, Ireland
email: tola.sinem@gmail.com, jtinoco@civil.uminho.pt, jmatos@civil.uminho.pt, eugene.obrien@ucd.ie

ABSTRACT: Detecting scour in railway bridges is possible by locating accelerometers and GPS on carriages of passing trains and processing the resulting signals. This research aims to detect scour based on these drive-by measurements, obtained from an instrumented passing vehicle. Signals from multiple train passages will be collected before and after scour repair to determine the change in bridge behavior. Measurements from a train in the UK passing over the Carlisle Bridge will be provided through In2Track3, an ongoing Horizon 2020 project.

In the first stage of the numerical approach, off-bridge conditions are considered. The carriage vibrational responses to track with different ground conditions – represented by altering the stiffnesses in a Winkler spring model – are calculated. In second stage, the bridge 'apparent profile'(AP), which is made up of the true profile on the bridge plus components of bridge/track deflection, will be computed. The Moving Reference Influence Line, i.e., deflection per unit load at a moving reference point, is found from the measured deflections. Bridge support stiffnesses will be modified to represent the loss of stiffness due to scour. Then, signals from the instrumented in-service train carriage i.e., measured AP, will be processed. Finally, an optimization algorithm will find foundation stiffnesses by minimizing the sum of squared differences between the calculated AP and the corresponding measured AP. The presence of scour will be determined by the difference between the stiffness values in the scoured and repaired cases. The results will help to optimize retrofits or develop mitigation measures to scour.

KEYWORDS: Bridge Scour; Indirect Monitoring, Influence Line; Optimization.

1 INTRODUCTION

The Federal Highway Administration defines scour as a washout or discharge of material stored in the river bed by water flow, over a long period [3]. There are different types of scour seen around a bridge pier: natural, contraction and local scour [4], having different formations and triggered by different mechanisms. Local scour is the most influential and therefore one of the most frequently researched scour types on bridges. When the water flow is obstructed by structures, centred turbulence is induced-which is the main mechanism behind local scour [4].

Scour is a slowly developing destructive process for bridges and one of the major factors in many bridge collapses. For example, researchers have determined that 3 out of 5 bridge failures in the United States between 1960 and 1990 were caused by scour [1]. Moreover, in the United Kingdom, the annual cost of railway bridge scour damage has been evaluated to be more than about £1 million [2]. The situation is exacerbated by the changing climatic conditions (such as rainfall regimes) which, in the bridge's lifetime, are likely to be different from those assumed in the bridge's original design.

This study is aimed at finding the flexural rigidity of an existing railway bridge, which minimizes the sum of squared differences between measured and calculated displacements using optimization methods. This research seeks to identify foundation scour by combining drive-by SHM methods with ML algorithms. An experimental campaign in the UK, a partner of an international project, is providing indirect monitoring data for the study. Measurements will be used from multiple batches of passing train runs. A methodology is being developed to identify scour based on the bridge's response. In the first step, a numerical method that consists of 2 stages will be conducted to find deflections, i.e., the APs. The AP is the profile experienced by the train and consists of the pre-existing profile of the track plus elements of bridge deflection. In the first stage, the off-bridge will be used to consider soil conditions and to calibrate the vehicle. In the second stage, the model will compute the displacements under the instrumented carriage and will use them to find the Influence Line of the bridge, i.e., the deflection due to a unit load. Reductions in support stiffnesses will be used to represent the effects of foundation scour. To inspect the impact of scour, before and after repairing a scoured bridge, signals from various batches of train passes will be acquired. Later, to find the bridge stiffness, ML-based algorithms will be applied to minimize the difference between measured and simulated influence lines. The long-term impact of the study will be developing possible repair or mitigation countermeasures. The flowchart in Figure 1 summarises the study. This paper was mainly focused on the background, methods, case study characterization, and numerical model of the study.

2 BACKGROUND AND METHODS

Structural Health Monitoring (SHM) is one of the methods to detect scour. SHM is a term used to cover a range of electronic techniques for health monitoring, including the scour damage state. It has the major advantage of ensuring improvement in public safety, early risk detection, and minimizing downtime. SHM can be divided into two main categories: direct and indirect monitoring. Direct monitoring involves instrumenting

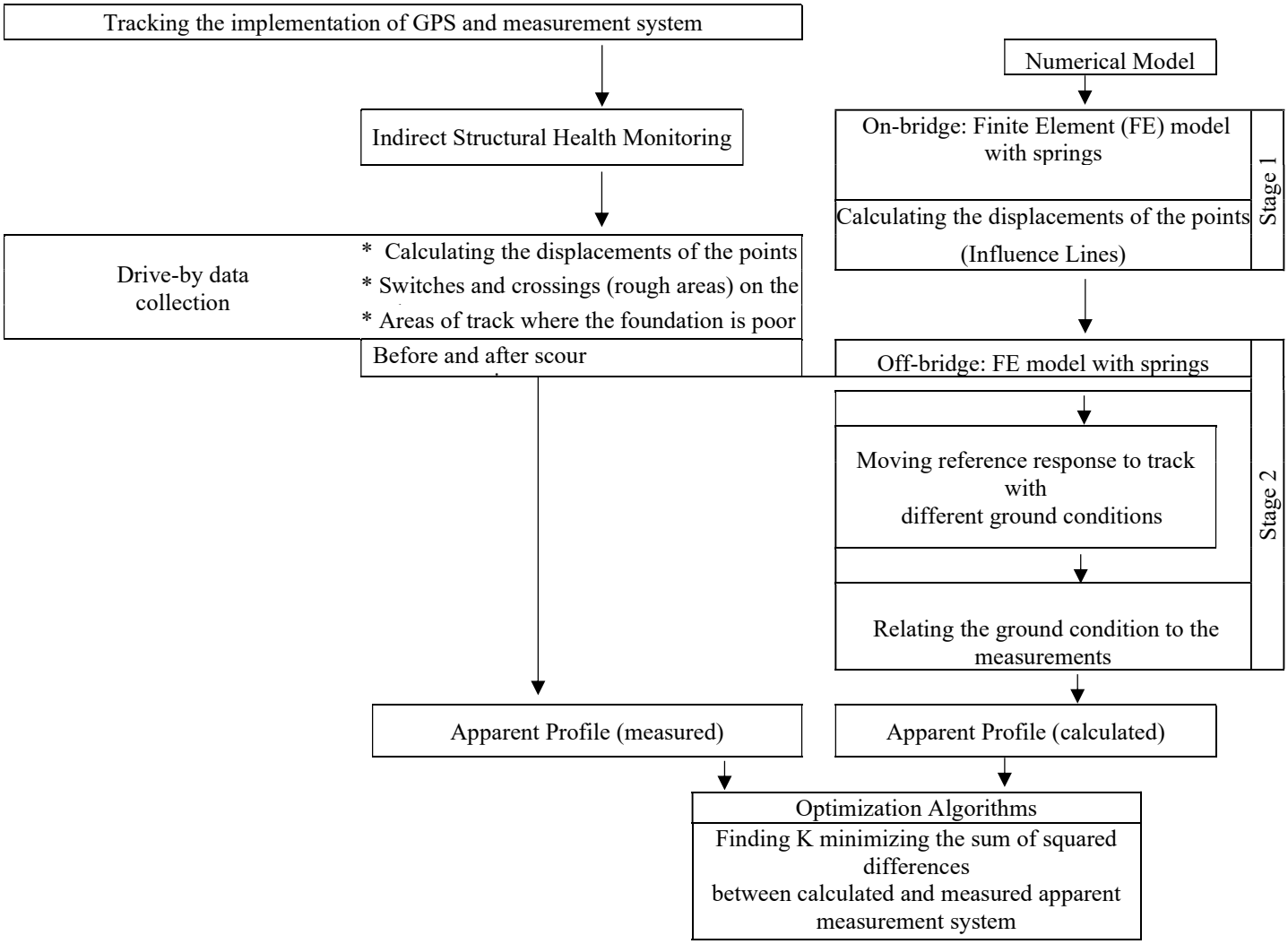

Figure 1. Flowchart of the study.

the bridge with sensors. It has some disadvantages of the total process being costly and requiring periodic maintenance or replacement of sensors [5]. On the other hand, indirect monitoring, i.e., instrumenting a passing vehicle, has the potential to be more economical at the network level, as one vehicle can be used to monitor many bridges. Furthermore, it causes no service disruption and has the potential to provide updated information frequently. It is possible to process collected vehicle data to obtain the bridge's frequencies by numerical techniques and, possibly also mode shapes. Eigen frequency analysis [6] and closed-form mode shape derivation [7] are methods proposed to identify scour in a bridge but further research is required before these methods can be used routinely in the industry. It was possible to identify the presence of scour by applying Continuous Wavelet Transformation to simulated acceleration measurements. The difference in the average CWT coefficients between healthy and scoured bridges from sets of train crossings was the scour indicator [8]. Other researchers have applied Wavelet Transforms to acceleration signals directly [9, 10]. O'Brien & Keenahan propose the AP [11], derived from measured accelerations in passing trains, to detect the presence of scour. The AP is the profile experienced by the train so it consists of any pre-existing profile plus elements of track and bridge deflection.

Machine Learning (ML) algorithms and optimization techniques have also been used in scour detection by taking advantage of its capability to deal with a large number of inputs. For example, Zhang and Zhao [12] by training Convolutional Neural Networks and Dong et al. by utilizing the Multiple Linear Regression method [13] predicted local scour depth around piers better than empirical formulas. Hybrid K-star models [14] were outperformed the scour equations in the literature in the prediction of relative scour depth around abutments. Reduced Error Pruning Tree-Base Classifier [15] predicted local scour depth at complex piers, whereas Extreme Learning Machines [16, 17, 18] predicted pier local scour depth better than frequently used ML algorithms such as Support Vector Machines and Artificial Neural Networks and empirical formulas. A combination of Gradient Tree Boosting with the Group Method of Data Handling technique [19] predicted scour depth around piers with different shapes. Evolutionary Radial Basis Function Neural Network [20] outperformed several algorithms and equations in predicting equilibrium scour depth. Non-dominated Sorting Genetic Algorithm [21] was used for

predicting critical scour depth and studies adopting Gaussian Process-based models [22, 23, 24] performed more accurate predictions of local scour around piers and piles than empirical formulas. The empirical scour depth formulas mentioned above were Hydraulic Engineering Circular No. 18, Melville [25]-Sheppard [26], 65-1, and 65-2 (Chinese).

More recently, heuristic optimization methods have been applied in civil engineering to predict scour depth around a pier [27]. In fact, heuristic optimization algorithms are competent in solving complex, non-linear civil engineering problems. Some of most widely used are genetic algorithm, ant colony algorithm, simulated annealing and particle swarm optimization [28]. The latter one has been adopted in several studies addressing scour depth prediction, being defined as particle swarm optimization method. In this method, when the swarm readjusts itself to the ambient by reappearing in the previously explored areas, the current location of every particle is updated by a vector of velocity, according to the social attitudes of individuals [29]. Particle swarm optimization method was used for updating the FE model of an existing bridge to obtain a more robust one [30], and in another study, for the analysis of a suspension bridge installation [31]. Considering its performance in past studies, it is thought to be an adequate candidate to solve the sum of the squared roots-minimization problem of this study in the latter period.

3 CASE STUDY CHARACTERIZATION

The bridge monitored is the Eden Viaduct, located in Carlisle, United Kingdom, in Figure 2**Error! Reference source not found.** [32]. It is a 7-span simple span bridge, each span 12.7 m in length. It has 5 masonry piers, in-situ a concrete deck, and each span has 8 prestressed concrete beams with a prestressed parapet unit and a reinforced concrete parapet upstand unit on each side. Continuously welded rails rest on concrete sleepers on one end of the structure (to the High Mileage end), while there are timber sleepers at the other end of it (to the Low Mileage end) [33]. There are 2 up and down fast lines with a speed of about 160 km/h [34]. The bedrock was scoured throughout the pier faces, the piers were lifted off the bedrock that surrounds them, and the overhanging foundation courses were identified by underwater examinations [32]. For this reason, between July-October 2015, scour protection was applied to foundations and the masonry piles by implementing permanent sheet piles and concrete backfill [33]. The bridge also experienced a flood in 2015.

Figure 2. Eden Viaduct bridge. [32].

The data collection system is called RILA. It is built for measuring the track's longitudinal level and is located at the back of the train carriage [35, 36]. The traditional way to measure the geometry of a track is through track geometry cars, also called loaded measurement, which has high associated costs, including service disruption. RILA is an alternative, cheaper solution which increases the frequency of measurements. Track geometry monitoring sensors are located further away from the axle. This type of measuring is called unloaded (static) measurement [35]. Although it was proven by the field tests that unloaded measurement resulted in small disparities from loaded measurements, it satisfies all the requirements of the measurement standards [35].

4 NUMERICAL MODEL

To find the pseudo-static bridge response due to the moving train, Moving Reference Influence Lines (MR-IL)s were calculated. A simulation model was generated in the MATLAB environment for this purpose. First, a single span was considered. Then, it was upgraded to the 7-span simple supported case, which is the real condition of the bridge monitored. The bridge was modelled as an Euler-Bernoulli beam [37] and divided into several smaller elements. The Foundation stiffness value was calculated with the FEMA 2000 [38, 39] formula, which includes foundation dimensions as an input:

$$k_f = [G_B/(1-v)][1.55\left(\frac{L}{B}\right)^{0.75} + 0.8] \quad (1)$$

where G is the soil shear modulus, L is foundation length and B is its width. The train carriage is Vehicle 66 and has 6 axles. The location of the measurement point is at a distance x from the start of the bridge and axle loads are behind point x, as illustrated in Figure 3**Error! Reference source not found.Error! Reference source not found.**.

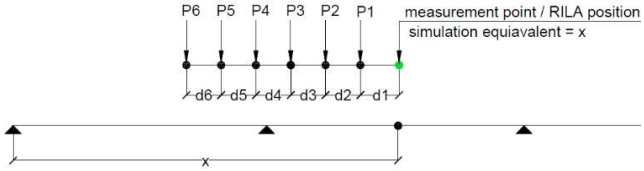

Figure 3. Axle loads and the measurement point.

There are 2 components of δ_x, the first is the bending of the beam, which will be called δ_{x1} and for which the Unit Load Theorem was applied. δ_{x1} is computed with equation 2, where M_R and M_V represent the moment diagrams of the virtual and real systems respectively.

$$\delta_{x1} = \int M_R M_V / EI \quad (2)$$

The second component of δ_x is the support deflection, i.e., δ_{x2}. Both components could be seen in Figure 4**Error! Reference source not found.**, for the single load case. k_{f1} and k_{f2} are spring stiffnesses, computed with equation 6. Total displacement is equal to:

$$J(x, d_i) = \delta_x = \delta_{x1} + \delta_{x2} \quad (3)$$

The moving reference response of the beam is computed as the sum of the contributions due to each axle:

$$\delta_{xR} = \sum_{i=1}^{n} P_i J(x, d_i) \quad (4)$$

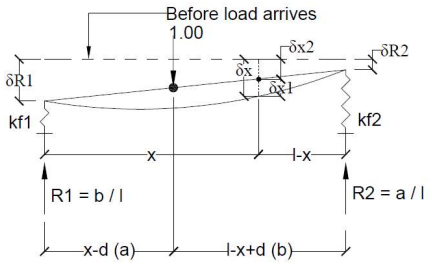

Figure 4. δ_x and components.

4.1 Single span 1-axle case

The model was developed gradually. First, a single-span one-axle case was studied. Figure 5**Error! Reference source not found.** demonstrates the MR-IL of the 1-axle case. The black curve represents the support deflection component (δ_{x2}), while the magenta line belongs to the beam deflection component (δ_{x1}). The moving reference response to the train is illustrated in Figure 6**Error! Reference source not found.**. Both MR-IL and response are zero until load enters the bridge, i.e., x equals to d_1.

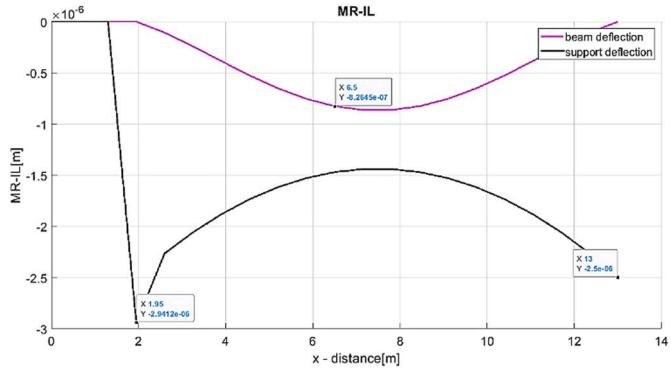

Figure 5. MR-IL for 1-axle single-span case.

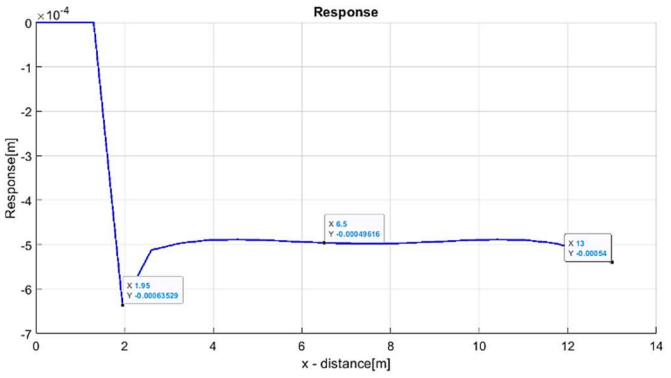

Figure 6. Response for 1-axle single-span case.

5 FINAL REMARKS AND CONCLUSIONS

Results obtained so far through simulation belong to the MR-ILs and responses, representing the calculated APs due to a moving train carriage. The values are verified through hand calculations or the computations performed with the structural analysis program. The shapes of the bending moment and deflection graphs, local maxima points, etc. are compatible with the expectations.

ACKNOWLEDGMENTS

This work was partly financed by FCT / MCTES through national funds (PIDDAC) under the R&D Unit Institute for Sustainability and Innovation in Structural Engineering (ISISE), under reference UIDB / 04029/2020. This work has also been partly financed within the European Horizon 2020 Joint Technology Initiative Shift2Rail through contract no. 101012456 (IN2TRACK3).

REFERENCES

[1] Shirole, A. M., & Holt, R. C. (1991). Planning for a comprehensive bridge safety assurance program. Transportation Research Record, 1290(3950), 290-005.

[2] Safety, R. (2005). Safe Management of Railway Structures Flooding and Scour Risk, *Rail Safety and Standards Board (RSSB)*. https://www.rssb.co.uk/research-catalogue/CatalogueItem/T554

[3] Richardson, E. V., & Davis, S. R. (2001). *Evaluating scour at bridges* (No. FHWA-NHI-01-001). The United States. Federal Highway Administration Office of Bridge Technology.

[4] Pizarro, A., Manfreda, S., & Tubaldi, E. (2020). The science behind scour at bridge foundations: A review. *Water*, 12(2), 374.

[5] Chandrasekaran, S. (2019). *Structural health monitoring with application to offshore structures*. (pp. 1–50). World Scientific Publishing Co. https://doi.org/10.1142/9789811201097_0001

[6] Prendergast, L. J., Hester, D., & Gavin, K. (2016). Determining the presence of scour around bridge foundations using vehicle-induced vibrations. *Journal of Bridge Engineering*, 21(10), 04016065.

[7] Tan, C., Zhao, H., OBrien, E. J., Uddin, N., Fitzgerald, P. C., McGetrick, P. J., & Kim, C. W. (2021). Extracting mode shapes from drive-by measurements to detect global and local damage in bridges. *Structure and Infrastructure Engineering*, 17(11), 1582-1596.

[8] Fitzgerald P. C., Malekjafarian A., Cantero D., OBrien E., Prendergast L. (2019). Drive-by scour monitoring of railway bridges using a wavelet-based approach. *Engineering Structures*, 191, 1-11. DOI: 10.1016/j.engstruct.2019.04.046.

[9] OBrien, E. J., Malekjafarian, A., & Fitzgerald, P. C. (2018, August 29-30). Bridge Scour Detection using Vehicle Acceleration Measurements. In *Civil Engineering Research in Ireland 2018 Conference (CERI 2018)*, Dublin, Ireland.

[10] OBrien, E. J., McCrum, D. P., Khan, M. A., & Prendergast, L. J. (2021). Wavelet-based operating deflection shapes for locating scour-related stiffness losses in multi-span bridges. *Structure and Infrastructure Engineering*, 1-16.

[11] OBrien, E., & Keenahan, J. (2015). Drive-by damage detection in bridges using the apparent profile. *Structural Control & Health Monitoring*, 22, 813-825. DOI: 10.1002/stc.1721.

[12] Zhang, J., & Zhao, H. (2020, August). A Prediction Model for Local Scour Depth around Piers Based on CNN. In *2020 International Conference on Information Science, Parallel and Distributed Systems (ISPDS)* (pp. 318-320). IEEE.

[13] Dong, H., Chen, F., Zhou, H., Guo, C., & Sun, Z. (2020, June). A Prediction Model for Local Scour Depth around Piers Based on Machine Learning. In *IOP Conference Series: Earth and Environmental Science* (Vol. 525, No. 1, p. 012080). IOP Publishing.

[14] Khosravi, K., Khozani, Z. S., & Mao, L. (2021). A comparison between advanced hybrid machine learning algorithms and empirical equations applied to abutment scour depth prediction. *Journal of Hydrology*, 596, 126100.

[15] Tien Bui, D., Shirzadi, A., Amini, A., Shahabi, H., Al-Ansari, N., Hamidi, S., ... & Ghazvinei, P. T. (2020). A hybrid intelligence approach to enhance the prediction accuracy of local scour depth at complex bridge piers. *Sustainability*, 12(3), 1063.

[16] Ebtehaj, I., Bonakdari, H., Moradi, F., Gharabaghi, B., & Khozani, Z. S. (2018). An integrated framework of Extreme Learning Machines for predicting scour at pile groups in clearwater conditions. *Coastal Engineering,* 135, 1-15.

[17] Ebtehaj, I., Bonakdari, H., Zaji, A. H., & Sharafi, H. (2019). Sensitivity analysis of parameters affecting scour depth around bridge piers based on the non-tuned, rapid extreme learning machine method. *Neural Computing and Applications*, 31(12), 9145-9156.

[18] Ebtehaj, I., Sattar, A. M., Bonakdari, H., & Zaji, A. H. (2017). Prediction of scour depth around bridge piers using self-adaptive extreme learning machine. *Journal of Hydroinformatics*, 19(2), 207-224.
[19] Sreedhara, B. M., Patil, A. P., Pushparaj, J., Kuntoji, G., & Naganna, S. R. (2021). Application of gradient tree boosting regressor for the prediction of scour depth around bridge piers. *Journal of Hydroinformatics*, 23(4), 849-863.
[20] Cheng, M. Y., Cao, M. T., & Wu, Y. W. (2015). Predicting equilibrium scour depth at bridge piers using evolutionary radial basis function neural network. *Journal of Computing in Civil Engineering*, 29(5), 04014070.
[21] Kim, I., Fard, M. Y., & Chattopadhyay, A. (2015). Investigation of a bridge pier scour prediction model for safe design and inspection. *Journal of bridge engineering*, 20(6), 04014088.
[22] Pal, M., Singh, N. K., & Tiwari, N. K. (2014). Kernel methods for pier scour modelling using field data. *Journal of Hydroinformatics*, 16(4), 784-796.
[23] Zheng, W., Qian, F., Shen, J., & Xiao, F. (2020). Mitigating effects of temperature variations through probabilistic-based machine learning for vibration-based bridge scour detection. *Journal of Civil Structural Health Monitoring*, 10(5), 957-972.
[24] Maroni, A., Tubaldi, E., Val, D. V., McDonald, H., & Zonta, D. (2020). Using Bayesian networks for the assessment of underwater scour for road and railway bridges. *Structural Health Monitoring*, 1475921720956579.
[25] Melville, B. W., & Coleman, S. E. (2000). *Bridge scour*. Water Resources Publication.
[26] Sheppard, D. M., & Renna, R. (2005). *Bridge scour manual*. Florida Department of Transportation. 605 Suwannee Street. *Tallahassee*. Florida.
[27] Shamshirband, S., Mosavi, A., & Rabczuk, T. (2020). Particle swarm optimization model to predict scour depth around a bridge pier. *Frontiers of Structural and Civil Engineering*, 14(4), 855-866.
[28] Cong, S., Jia, Y., & Deng, K. (2010). Particle Swarm and Ant Colony Algorithms and Their Applications in Chinese Traveling Salesman Problem. In *New Achievements in Evolutionary Computation*. IntechOpen.
[29] Venter, G., & Sobieszczanski-Sobieski, J. (2003). Particle swarm optimization. *AIAA journal*, 41(8), 1583-1589.
[30] Xia, Z., Li, A., Li, J., Shi, H., Duan, M., & Zhou, G. (2020). Model updating of an existing bridge with high-dimensional variables using modified particle swarm optimization and ambient excitation data. *Measurement*, 159, 107754.
[31] Chen, Z., Cao, H., Ye, K., Zhu, H., & Li, S. (2015). Improved particle swarm optimization-based form-finding method for suspension bridge installation analysis. *Journal of Computing in Civil Engineering*, 29(3), 04014047.
[32] NetworkRail, (n.d.) Infrastructure Projects Central: 129038 WCM1/5 1m 0440yds Eden Viaduct.
[33] Network Rail, (May 2020) Eden Viaduct Main Lines Bridge Detailed Examination Report (Underwater Exam) Contract Mileage: 001m 0455yds 20.68chs.
[34] Network Rail. (January 2012). River Eden Viaduct (WCM1/5) Stage 2 Assessment Report.
[35] Wang, H., Berkers, J., van den Hurk, N., & Layegh, N. F. (2021). Study of loaded versus unloaded measurements in railway track inspection. *Measurement*, 169, 108556.
[36] Network Rail. (November 2021). Carlisle Bridge | Utrecht, the Netherlands, Report No. 9221-197241-01 1.0.
[37] Kwon, Y. W., & Bang, H. (2018). The finite element method using MATLAB. CRC press.
[38] McCrum, D., O'Brien, E., & Khan, M. (2013). Bridge Health Monitoring Using an Acceleration-Based Bridge Weigh-in-Motion System. *Key Eng. Mater*, 569, 183-190.
[39] FEMA, P. (2000) 'commentary for the seismic rehabilitation of buildings (FEMA356)', *Washington, DC: Federal Emergency Management Agency*, 7.

Bridge global damage detection using direct acceleration data

Muhammad Arslan Khan[1], Eugene J. OBrien[2], Daniel McCrum [2], Abdollah Malekjafarian[1]
[1]Structural Dynamics and Assessment Laboratory, School of Civil Engineering, University College Dublin, Dublin, Ireland
[2] School of Civil Engineering, University College Dublin, Belfield, Dublin, Ireland
email: muhammad.khan@ucd.ie, eugene.obrien@ucd.ie, daniel.mccrum@ucd.ie, abdollah.malekjafarian@ucd.ie

ABSTRACT: Bridge structures often experience global damage and change in stiffness due to aging, environmental effects, foundation scour, and support deterioration. For this reason, reliable and efficient health monitoring of bridges, along with regular repair and maintenance, is desirable to prevent unplanned closures. This paper focuses on detecting global damage to bridges using directly calculated acceleration data. A novel technique using statistical analysis of data calculated from an acceleration-based modal estimation approach, is used to detect changes in the global stiffness of a bridge. A finite element model of a simply supported beam is used to develop a short-span bridge model. Bridge dynamic analysis using a vehicle-bridge interaction model is carried out to obtain simulated bridge accelerations, and modal parameters are calculated for healthy and damaged bridge conditions. Forced loading using a transient vehicle half-car model, instead of traditional hammer test loading, is used to excite the bridge structure. Direct accelerations are calculated in this paper to test a modal analysis approach that can also decrease the required number of sensors to be installed on the bridge. A statistical modal-based damage indicator is developed to assess bridge condition with damages caused by changing global stiffnesses of the bridge. The proposed approach is shown to give effective results in detecting global change in bridge stiffness using forced direct accelerations with a low number of accelerometers.

KEY WORDS: Damage Detection; Accelerometer; Structural Health Monitoring; Statistical Analysis; VBI; Global Damage.

1 INTRODUCTION

Bridges are amongst the most critical and traffic sensitive components of transport infrastructure. To ensure their useability, these structures are designed for a specific span of life. However, they require continuous monitoring and repairs to protect against local as well as global damage. Traditionally, visual inspections or an array of strain sensors are used to inspect the performance of bridges, which require a significant amount of time and cost. Further, a significant distribution of sensors is required to detect local changes in the bridge condition if that location is not known in advance [1-3]. For the case of any sudden damages, these methods may require unplanned road closures and traffic disruption. For this reason, an efficient and reliable Structure Health Monitoring (SHM) technique would be useful to maintain the performance of bridge structures throughout their lives.

Bridge structures deteriorate over their lifetimes, commonly due to traffic loading, aging, environmental influences, and accidental actions that may cause local or global damage. Local damage consists of cracks or loss of steel section, which are normally visible through cameras or with the human eye. Global damage, on the other hand, is often invisible and hard to detect using visual inspection techniques [4]. Common examples of global damage include bridge bearing seizure and scour at piers for multiple span bridges.

This paper focuses on the detection of bridge global damage using directly installed accelerations. Bridge accelerations tend to show sensitivity to change in bridge stiffness [5]. Accelerations are calculated here in response to a fleet of half-cars traversing the bridge and are statistically analysed to develop novel damage indicators. In this study, numerical simulations are carried out to develop and test the damage detection approach based on the modal estimation of the bridge using a low number of accelerometers that can redeploy and change locations to cover the full length of the bridge. Using this strategy, a lower number of accelerometers are required that decreases the cost of testing. Also, this strategy can be implemented using unmanned aerial vehicles (UAVs), especially in case of remote locations for measurement points, by acquiring bridge data through UAV deployment at various bridge locations (further research is undergoing for the application using UAVs). For the global damage, two damage cases are studied – increased boundary stiffness due to a deteriorated bearing, and reduced foundation stiffness due to scour. Statistically estimated mode shapes are used to illustrate changes in the magnitude due to changing damage percentages.

2 NUMERICAL MODEL

2.1 Vehicle model

In this study, a two-axle half-car is used to model a vehicle that traverses the bridge. Figure 1 shows a schematic of the half-car model. The modelling and simulations are carried out using MATLAB [6, 7]. The half-car model contains 4 degrees of freedom (DOFs) which consist of a body mass translation (*ys*) and pitch (θ), and two axle mass translations (*yu*,*i*). There are

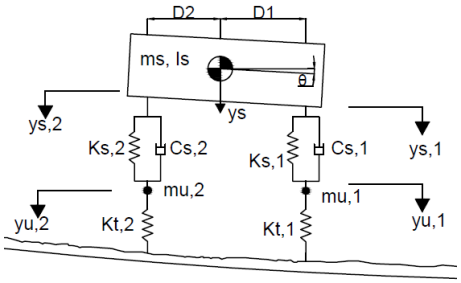

Figure 1 Schematic of a two-axle half car.

two axle masses *mu*,*1* and *mu*,*2*, and springs with linear stiffnesses (*ks*,*i*) and viscous damping coefficients (Cs,i) connecting them to the body mass (*ms*). The vehicle contacts the road surface though tyre springs with linear stiffness (*kt*,*i*).

Vehicle properties are taken from the literature and are presented in Table 1 [7, 8]. The body mass and speed of the traversing vehicle are picked randomly from a data set of real traffic data for each run to ensure realistic representation of the vehicle.

Table 1 Mechanical properties of the half-car model [7].

Half-Car Property	Notation	Value
Unsprung mass, 1	*mu,1*	750 kg
Unsprung mass, 2	*mu,2*	1000 kg
Tyre stiffness, 1	*Kt,1*	1.75×10^6 N/m
Tyre stiffness, 2	*Kt,2*	3.5×10^6 N/m
Suspension Stiffness, 1	*Ks,1*	0.4×10^6 N/m
Suspension Stiffness, 2	*Ks,2*	1×10^6 N/m
Suspension Damping, 1	Cs,1	10^4 Ns/m
Suspension Damping, 2	Cs,2	20×10^3Ns/m

2.2 Two types of bridge model

Two types of bridge are modelled using the 1D Finite Element (FE) of the simply supported beam. Beam is divided into multiple beam elements with 4 DOFs each – vertical translation and rotation at both ends of the element. Table 2 lists the mechanical properties of the FE model. An approach length of 100 m and a rough road profile [9] are added to the model to ensure equilibrium of DOFs, and a realistic representation of a highway bridge, respectively. For the road profile, a class A general profile is used and generated randomly based on the ISO standard [9].

Table 2 Properties of the FE Bridge model

Bridge Property	Notation	Value
Number of elements	*N*	20
Young's Modulus	*E*	3.5×1010 N/m^2
2nd moment of area	*I*	0.75 m^4
Mass per unit length	μ	37500 kg/m
Damping	ξ	3%
Sampling Frequency	*fs*	100 Hz
Approach Length	*Lapp*	100 m

The first bridge model has two additional rotational springs at the support ends to add stiffness representing bearing seizure. Figure 2 shows the bridge model with additional stiffness (K_{rot}) at supports. Here the stiffness K_{rot} represents the condition of the bridge support bearings whose value lies somewhere between 0 (free to rotate) and infinity (fully fixed) and is measured in kNm per unit rotation. The first natural frequency of the bridge is evaluated by the FE analysis as 4.24 Hz.

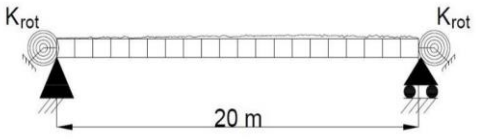

Figure 2 Bridge model with additional rotational support springs

The second bridge model consists of a series of simply supported beams, resting on sprung piers and foundations. This model is developed to assess the effect of scour at piers on the bridge accelerations. A bridge with four 10 m long simply supported beams is chosen, as shown in Figure 3. The ends are resting on undeformable supports, modelled as pins and rollers, whereas the internal three supports are modelled as hinged supports, with single DOF sprung masses (with stiffness $K_{pier,i}$ and $m_{pier,i}$). For the foundation, a shallow foundation is modelled using a spring with stiffness $K_{f,i}$. The properties of the foundation and pier springs are derived to correspond to a 4 m × 2 m shallow pad in contact with a uniform medium dense sand deposit using the details from [10, 11].

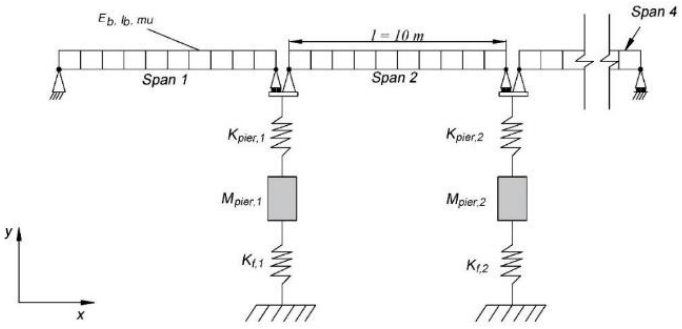

Figure 3 Schematic of the multi-span bridge model

The bridge and vehicle models are coupled together to simulate a traversing vehicle. The interaction between the vehicle and the road profile is implemented using the equations from [7, 12, 13]. For calculating the dynamics of the bridge DOFs, a numerical integration method using Wilson-Theta integration [14] is used to solve the coupled equation of equilibrium.

2.3 Simulation of global damage

In this paper, two types of global damage are analysed for detection using bridge vibrations: (i) Bearing seizure is modelled as an increase in the stiffness of K_{rot} that, in turn, makes it difficult for the supports to rotate. Normally the starting value of K_{rot} is zero, representing ideal healthy conditions, however it increases over time until makes the support fully fixed. (ii) Scour damage is modelled as a reduction in foundation stiffness at one pier. Two percentages – 25% and 45% loss of stiffness at the middle pier are used to assess the efficiency of the proposed approach. These percentage of losses are measured according to the various depth of scour holes undermining a foundation pad and explained in [4] and [15].

3 MODAL ESTIMATION STRATEGY

3.1 Moving sensors strategy for modal estimation

In this paper, a novel strategy of modal estimation is proposed to estimate the first mode shape of the bridge models. A concept of moving sensors is proposed that (i) uses a small number of accelerometers to measure accelerations of a part of a bridge, and (ii) move the accelerometers forward to repeat and cover the rest part of the bridge (given that there is different excitation forces on the bridge at each stage). For excitation forces, vehicles with different masses and speeds are simulated for each run. The forced vibrations of the bridge are calculated at two locations from each run (starting from one end of the bridge). Fifty runs are used for each set of two locations. The sensor at one of these two locations is then moved forward (keeping one location common in order to provide a reference

point). This way, the full bridge can be covered in 4-5 stages. Figure 4 shows the proposed strategy of measurement, where "Ac" represents the accelerometer and $\ddot{y}$ represents the calculated acceleration. The acceleration signals from each set are analysed using the Frequency Domain Decomposition (FDD) algorithm that estimates the mode shape amplitudes from the spectral densities of the accelerations in the frequency domain [16]. Each stage returns a statistic of mode shape amplitude at two locations in a segment. All the segments join together using the common reference points at subsequent stages to form a global mode shape. For each joining process, the segments are normalized using the common point amplitudes to eliminate the effect of different excitation forces in each run. This process results in the formation of a global mode shape for the bridge that is analysed in this paper to detect global damage. The 1st global mode shape of the bridge model is illustrated in Figure 5. It can be seen that the global mode shape matches nearly perfectly with the FE mode shape that is the model theoretical 1st mode shape.

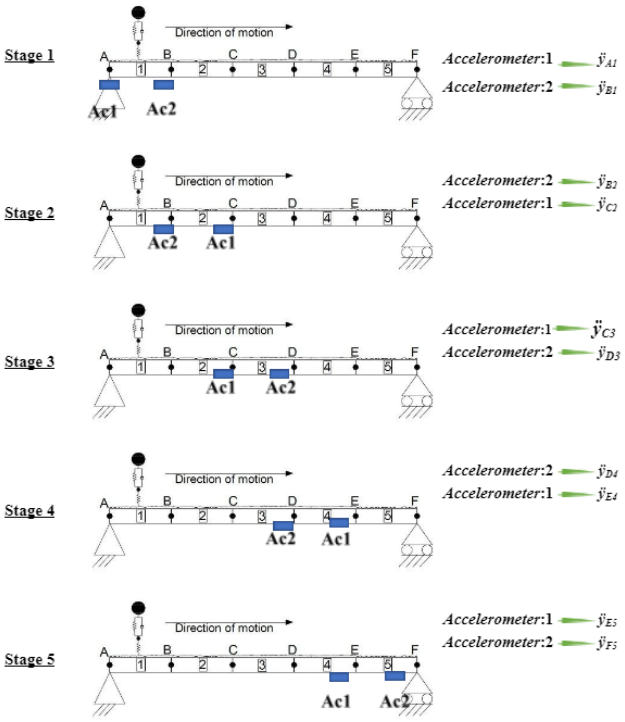

Figure 4 Measurement scheme of the proposed approach.

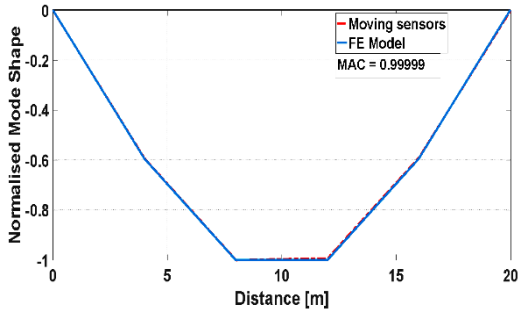

Figure 5 1st global mode shape of first bridge model.

4 DAMAGE INDICATORS

Two damage indicators are used to detect the two types of global damage. The bearing damage condition is analysed using the shape of the first mode shape and its slope. The increase in rotational stiffness at the supports changes the behaviour towards that of a fixed boundary, which can be seen in the slope of the first mode shape near the supports. The impact of the change in the mode shape due to damaged bearing is also tested in the field by [17].Statistics of the shapes are studied in this paper to assess the change due to deteriorating bearing conditions.

For the scour damage, a statistic of the 1st global mode shape is calculated for healthy and scoured pier conditions. Root mean square difference between healthy and scoured mode shapes is calculated and assessed for changing percentage of scour damage. The damage indicator (DI) is represented in Equation 1, where x is the amplitude of the 1st mode shape at the i^{th} location.

$$DI = \sqrt{\sum_{i=1}^{n} x_{i,healthy} - x_{i,damaged})^2} \quad (1)$$

5 RESULTS AND DISCUSSION

For the analysis, each case is simulated 50 times, with different properties of vehicle to assess the repeatability of the approach. For the first damage type, i.e., bearing failure, the single span bridge model is used, and the accelerations are calculated to calculate the 1st global mode shape and its slope. The K_{rot} value is increased until the bridge supports reach fully fixed stage. Figure 6 shows the first global mode shape of the single span bridge model with two K_{rot} values – 10^9 and 10^{13}. Here it can be seen near the support nodes, i.e., 1 and 21, that with higher K_{rot}, the slope of the first mode shape changes.

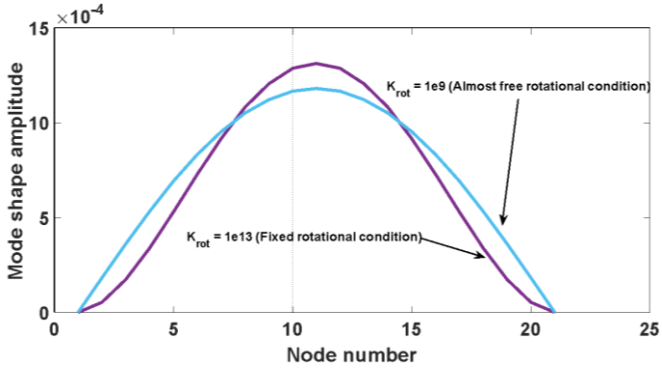

Figure 6 The 1st global mode shape of the single span bridge with different K_{rot} values.

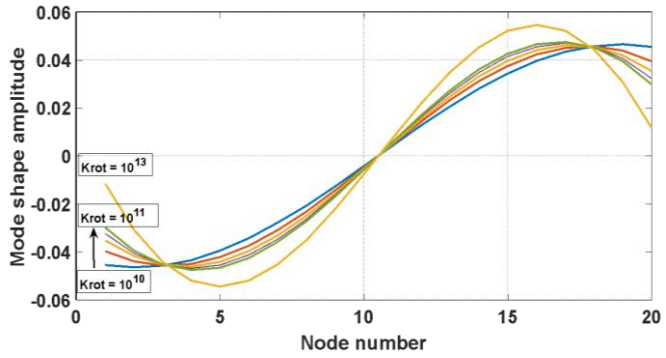

Figure 7 Slopes of the first mode shape with increasing K_{rot} value.

In Figure 7, the slopes of the first mode shape with increasing K_{rot} value are plotted. The damage indicator is considered as the boundary amplitude of the slope of the first mode shape, which is shown to be decreasing with increasing support bearing stiffness. It can be seen in Figure 7 that the first amplitude of the slope is decreasing with increasing K_{rot} value (slope amplitude leading to zero value which represents fully fixed condition). This way the deteriorated bearings can be detected using a visual indicator calculated from the dynamic response.

For the scour damage, two damage cases are simulated – 25% and 45% loss of foundation stiffness at the middle pier of the bridge. The normalised 1st global mode shape of the multi-span bridge is calculated for healthy and scoured cases and shown in Figure 8. For testing the approach, a fleet of 50 vehicles are simulated for each damage case and shown in Figure 8 as mean +/- one standard deviation (shaded region). It can be seen in Figure 8 that at the 50% bridge length (scoured location), the 1st mode shape amplitude reduces with an increase in scour percentage. Hence, the impact of scour damage can be visually assessed using this representation of the 1st mode shape of the bridge.

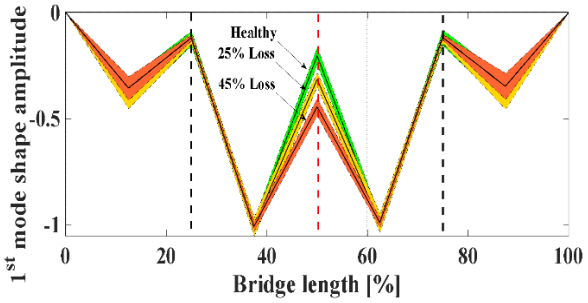

Figure 8 The 1st normalised global mode shape of the multi-span bridge for healthy and scoured conditions.

The damage indicator is calculated statistically for each loss of foundation stiffness case. Figure 9 illustrates the root mean square difference between the healthy and scoured bridge 1st mode shape amplitude. Here, a trend is noted that the DI increases reasonably with an increase in the percentage loss of the foundation stiffness. From Figures 6-9, it is clear that the bridge accelerations can be used, in segments, to measure the 1st mode shape and can detect bridge global damage effectively.

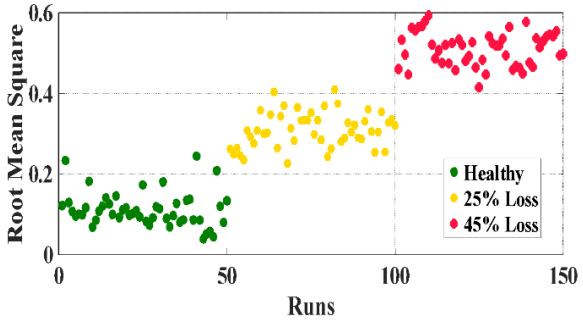

Figure 9 Effect of scour damage on the damage indicator.

6 CONCLUSION

This paper develops a novel strategy of moving sensors that uses bridge forced accelerations to detect global damage and analyses the effectiveness of the approach using statistical analysis of results. Global damages are normally invisible and difficult to detect using traditional visual based inspections. The bridge accelerations, on the other hand, tend to be damage sensitive and therefore, are used in this paper to develop the moving sensors approach. The proposed approach uses a low number of accelerometers to acquire data from a segment of the bridge. After acquiring the data, sensors move forward to the next segment of the bridge, while keeping one point in common for consecutive segments. A vehicle and two bridge models are created numerically and coupled to calculate the system dynamics using an integration technique. The bridge accelerations are used to calculate the 1st bridge mode shape in segments that are stitched together to form the global mode shape. One-span and multi-span bridge models are created to simulate two types of global damage – bearing seizure and scour. A fleet of 50 vehicles is used to measure the bridge accelerations for each bridge condition. Along with a visual damage indicator, a statistical damage indicator based on the root mean square difference between the healthy and scoured 1st mode shape amplitudes is also calculated to assess the efficacy of the approach. The following are the main conclusions from the analysis of the proposed approach:

- The stitched global 1st mode shape of the bridge matches almost perfectly with the FE based theoretical mode shape.
- Increase in the K_{rot} value changes the slope of the 1st mode shape at the supports. With higher K_{rot}, the slope tends to move toward a zero value, which represents the fully fixed boundary condition (full bearing seizure).
- Reduction in the vertical foundation stiffness, i.e., scour, causes a reduction in the 1st mode shape amplitude at the damaged location.
- The statistically based DI shows an incremental trend with increasing scour percentage. This shows the efficacy of the proposed approach.

The proposed approach has provided effective results in detecting two types of global bridge damage using forced bridge accelerations. However, this approach needs to be validated using field tests and experimental studies, including all the external parameters that may impact the bridge accelerations.

ACKNOWLEDGMENTS

This publication has emanated from research conducted with the financial support of Science Foundation Ireland under Grant number 20/FFP-P/8706.

REFERENCES

1. OBrien, E., M.A. Khan, D. McCrum, and A. Žnidarič, *Using Statistical Analysis of an Acceleration-Based Bridge Weigh-In-Motion System for Damage Detection.* Applied Sciences, 2020. **10**(2): 663.
2. Carden, E.P. and P. Fanning, *Vibration based condition monitoring: a review.* Structural health monitoring, 2004. **3**(4): 355-377.
3. Quirk, L., J. Matos, J. Murphy, and V. Pakrashi, *Visual inspection and bridge management.* Structure and Infrastructure Engineering, 2018. **14**(3): 320-332.

4. Khan, M.A., D.P. McCrum, L.J. Prendergast, E.J. OBrien, P.C. Fitzgerald, and C.-W. Kim, *Laboratory investigation of a bridge scour monitoring method using decentralized modal analysis.* Structural Health Monitoring, 2021. **20**(6): 3327-3341.
5. Avci, O., O. Abdeljaber, S. Kiranyaz, M. Hussein, M. Gabbouj, and D.J. Inman, *A review of vibration-based damage detection in civil structures: From traditional methods to Machine Learning and Deep Learning applications.* Mechanical systems and signal processing, 2021. **147**: 107077.
6. Kwon, Y.W. and H. Bang, *The finite element method using MATLAB*. 2018: CRC press.
7. Cantero, D., E.J. O'Brien, and A. González, *Modelling the vehicle in vehicle—infrastructure dynamic interaction studies.* Proceedings of the Institution of Mechanical Engineers, Part K: Journal of Multi-body Dynamics, 2010. **224**(2): 243-248.
8. Keenahan, J., E.J. OBrien, P.J. McGetrick, and A. Gonzalez, *The use of a dynamic truck–trailer drive-by system to monitor bridge damping.* Structural Health Monitoring, 2014. **13**(2): 143-157.
9. ISO, *Mechanical vibration—Road surface profiles—Reporting of measured data*. 1995.
10. Fitzgerald, P.C., A. Malekjafarian, D. Cantero, E.J. OBrien, and L.J. Prendergast, *Drive-by scour monitoring of railway bridges using a wavelet-based approach.* Engineering Structures, 2019. **191**: 1-11.
11. Prendergast, L.J. and K. Gavin, *A comparison of initial stiffness formulations for small-strain soil–pile dynamic Winkler modelling.* Soil Dynamics and Earthquake Engineering, 2016. **81**: 27-41.
12. González, A., *Vehicle-bridge dynamic interaction using finite element modelling*, in *Finite element analysis*, D. Moratal, Editor. 2010, InTechOpen: Rijeka, Croatia. 637-662.
13. Yang, Y.-B. and J.-D. Yau, *Vehicle-bridge interaction element for dynamic analysis.* Journal of Structural Engineering, 1997. **123**(11): 1512-1518.
14. Tedesco, J., W.G. McDougal, and C.A. Ross, *Structural dynamics*. 2000: Pearson Education.
15. OBrien, E.J., D.P. McCrum, M.A. Khan, and L.J. Prendergast, *Wavelet-based operating deflection shapes for locating scour-related stiffness losses in multi-span bridges.* Structure and Infrastructure Engineering, 2021: 1-16.
16. Brincker, R., L. Zhang, and P. Andersen, *Modal identification of output-only systems using frequency domain decomposition.* Smart materials and structures, 2001. **10**(3): 441.
17. Khan, M.A., D.P. McCrum, E.J. OBrien, C. Bowe, D. Hester, P.J. McGetrick, C. O'Higgins, M. Casero, and V. Pakrashi, *Re-deployable sensors for modal estimates of bridges and detection of damage-induced changes in boundary conditions.* Structure and Infrastructure Engineering, 2021: 1-15.

Monitoring the health of bridges using accelerations from a fleet of vehicles

Daniel P. McCrum, Shuo Wang, Eugene J. OBrien,

School of Civil Engineering, University College Dublin, Ireland
Email: shuo.wang@ucdconnect.ie

ABSTRACT: This paper proposes a new indirect structural health monitoring concept which uses acceleration data from a vehicle fleet. When a vehicle passes the bridge, the displacement under its wheels can be inferred from its accelerations. This displacement is named as the 'apparent profile'. It contains two components: bridge profile height and bridge deflection under the wheel. This deflection can be used to find the moving reference influence function (MRIF), defined as the deflection at a (moving) reference point due to a unit load at another point, moving at the same speed. The MRIF can be found when all axle weights are known. In this paper, a new method is proposed to obtain road profile and bridge health condition from the vehicle acceleration, without knowing axle weights. Numerical simulation results show that the inferred bridge profile is different when the bridge condition is different. The difference can be used as an indicator of bridge damage and is illustrated here through an example of bearing damage.

KEY WORDS: Acceleration, bridge, structural health monitoring, damage, moving reference influence function.

1 INTRODUCTION

The concept of structural health monitoring (SHM) has been developed to identify the condition of bridge structures during their service lives. According to the source of measurement, SHM methods can be divided into two groups: direct methods with sensors on the bridge and indirect methods with sensors in a passing vehicle [1]. Direct methods aim to assess the structural condition from signals which are directly measured on the structure itself. Typically, signals can be strain [2], displacement [3], rotation [4] or acceleration [5]. Indirect methods infer the condition of the structure by analysing inertial measurements in vehicles passing over it. The implicit assumption is that the signals measured in the passing vehicle are affected by the bridge and contain bridge condition information. When the vehicle passes the bridge, the vibration of the vehicle will be affected by both vehicle properties (speed, mass, etc.) and bridge properties (stiffness of the bridge material, boundary conditions, etc.). Hence, the bridge condition can be obtained by analysing the signals from the vehicles. Compared with direct methods, indirect methods have the potential to easily monitor a large stock of bridges. Once the measurement system is installed on the vehicle and the system is calibrated, the vehicle can monitor every bridge it crosses. In contrast, direct monitoring requires each bridge of interest to be separately monitored.

From vehicles' vibration signals, many bridge properties can be obtained: natural frequencies, mode shapes and damping ratio. Yang et al. [6] first introduces a method to obtain bridge frequency and successfully identifies 4 key frequencies. Kim et al [7] validate this theory through a laboratory test and Siringoringo and Fujino [8] find the frequency of a bridge being crossed by a train (30 km/h speed) in a field test. In frequency-based methods, the concept is that vehicle vibration contains frequency components which are related to the vehicle frequencies, the bridge frequencies and the profile on the bridge. Unfortunately, the amplitudes of the bridge natural frequencies tend to be relatively small. Particularly when the bridge frequencies are close to the other components, the accuracy of the inferred frequency can be low. In an alternative approach, Malekjafarian and OBrien [9] decompose bridge vibration in the frequency domain to obtain mode shapes but a very low speed is required. McGetrick et al. [10] find the changes in bridge damping when the bridge is damaged using assumed Rayleigh damping. González et al. [11] find the absolute damping ratio through an error minimisation process. However, the damping ratio is difficult to quantify in practice and is not well correlated with structural condition.

The displacement under the wheel of a vehicle is of interest to researchers as it contains components of bridge deflection. When the vehicle passes over the bridge, the displacement under the wheel is the sum of the bridge profile height and the bridge deflection under the wheel. As the location of this bridge deflection is changing as the vehicle passes over the bridge, the bridge deflection under the wheel is termed the moving reference deflection (MRD). In some studies, the displacement under the wheel (when the vehicle passes over the bridge) is called the 'apparent profile' (AP). To infer AP from vehicle vibrations, different approaches have been proposed recently. OBrien and Keenahan [12] use a simulated traffic speed deflectometer to determine AP. They suggest that the differences between AP from two wheels can be used as a damage indicator. However, the measurement accuracy needs to be very high and the concept is sensitive to small differences in axle properties. Yang et al. [13] propose a way to infer AP when both axle accelerations and the bridge influence line is known. Keenahan et al. [14] develop an inverse integration method to obtain AP from vehicle accelerations. As all vehicle properties are required in this study, they also propose a fleet monitoring concept to obtain the road profile and infer vehicle properties from accelerations measured on a fleet of vehicles.

From AP, OBrien et al. [15] determine a moving reference influence function (MRIF) to describe the relationship between MRD and the weights of vehicle axles. The results show that MRIF can be a good indicator of bridge bearing damage. In this paper, a fleet monitoring concept is developed to monitor bridge bearing damage without knowing axle weights. This is more challenging but is necessary if, in an internet-of-things scenario, data is to be utilized from a large number of uncontrolled vehicles in random traffic.

2 OBTAINING BRIDGE PROFILE WITHOUT KNOWING AXLE WEIGHTS

To formulate the relationship between AP and MRD, Eq. (1) is used:

$$R_x^a = R_x^p + \delta_x \tag{1}$$

where R_x^a denotes the AP at location x, R_x^p denotes bridge profile and δ_x denotes the MRD under the measured wheel at that location. In this paper, two quarter-car models are used to represent a 2-axle vehicle from the fleet in which acceleration is measured in the 1st quarter-car. From the literature [15], the relation between MRD and MRIF can be written as:

$$\delta_x = W_1 J_{x,0} + W_2 J_{x,s} \tag{2}$$

where W_1 and W_2 are the weights of the 1st and 2nd axles respectively. The term, $J_{x,0}$ denotes the MRIF for the MRD at x and a unit load zero distance behind that point, i.e., MRD at x due to a unit load at x. The symbol s in $J_{x,s}$ represents the distance between the measured axle and the unit load, i.e., the MRD at x due to a unit load s behind that point. Combining Eqs. (1) and (2) gives,

$$R_x^p = R_x^a - (W_1 J_{x,0} + W_2 J_{x,s}) \tag{3}$$

In Eq. (3), the AP (R_x^a) can be inferred from vehicle accelerations by using a method proposed in the literature [14] and the MRIF for the healthy bridge can be found using basic principles of static mechanics. For each individual vehicle, bridge profile height (R_x^p) can be calculated if axle weights are known. In practice, accurate individual axle weights are hard to obtain. However, the mean value of gross vehicle weight (GVW) at a given site is quite repeatable and can be found. Further, using off-bridge data, the ratios of the two axle weights can be found, i.e., the ratio of each axle weight to GVW. Assuming the mean GVW to be known and the axle weight ratios, a typical distribution of axle weights in the fleet can be randomly generated. For each randomly generated set of vehicle axle weights, R_x^p can be inferred.

As each vehicle axle weight is randomly generated but not true value, the inferred bridge profiles are not equal to each other. To make one bridge profile fit all inferred bridge profiles (R_x^p) as well as possible, an error minimisation process is used. The error function is defined as:

$$E = \sum_{n=1}^{N} (R_{x_k}^{p,best} - R_{x_k,n}^p)^2 \tag{4}$$

Where N is the total number of vehicles in the fleet. $R_{x_k}^{p,best}$ denotes the best fit bridge profile height at scan k and location x_k. $R_{x_k}^{p,best}$ denotes the inferred bridge profile height at scan k for Vehicle n. Taking the partial derivative of E with respect to $R_{x_k}^{p,best}$,

$$\frac{\partial E}{\partial R_{x_k}^{p,best}} = 2N * R_{x_k}^{p,best} - \sum_{n=1}^{N} (2R_{x_k,n}^p) \tag{5}$$

The minimum is found by setting Eq. (5) to 0, giving:

$$R_{x_k}^{p,best} = \frac{\sum_{n=1}^{N} (R_{x_k,n}^p)}{N} \tag{6}$$

3 NUMERICAL SIMULATION AND DAMAGE DETECTION

A finite element beam model interacting dynamically with a rigid body vehicle model, is used to generate vehicle axle accelerations. A 4 m wide simply supported bridge with a 20 m span is assumed to be made up of three Y3 beams, topped by a 210 mm deep slab. The bridge is represented by 10 beam finite elements and 11 nodes. The properties are shown in Table 1.

Table 1. Properties of bridge model

Span	20 m
Number of finite elements	10
Total degrees of freedom	21
Young's Modulus, E	3×10^{10} N/m^2
Cross sectional area	2.09 m^2
Second moment of area, J	0.301 m^4
Damping,	3%

Figure 1 shows the two-quarter-car model and the bridge finite element model. The sprung mass M_s and an unsprung mass M_u are connected through a viscous damper with coefficient, C_s and a spring with stiffness, K_s. The unsprung mass is connected to the bridge through a spring with linear stiffness K_t. In this study, typical vehicle properties, such as speed, axle spacing, gross vehicle weight and axle weight ratio, are taken from the Long-Term Pavement Performance Weigh-in-Motion database [16]. Some of the vehicle properties for the fleet, M_u, C_s, K_s and K_t are generated randomly by Monte Carlo simulation using the population means and standard deviations shown in Table 2, taken from the literature [17].

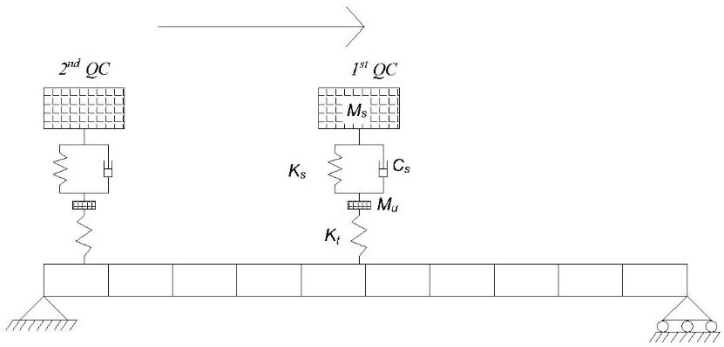

Figure 1. Vehicle and bridge models.

Table 2. Vehicle fleet properties

Property	Symbol/ Units	Mean value	Standard deviation
Unsprung mass	M_u: kg	700	250
Damping	C_s: Ns/m	2×10^4	5×10^3
Unsprung stiffness	K_s: N/m	4×10^5	1×10^5
Tyre stiffness	K_t: N/m	1.75×10^6	5×10^5

To obtain the bridge profile, for the healthy bridge case, a fleet of 100 vehicles are used. Figure 2 shows that the inferred bridge profile and the real bridge profile match well except for the first metre after the vehicle arrives on the bridge. This error is due to the process which fixes the drifting issue in the inferred APs.

When the bridge is damaged, the MRIF is still calculated using the information of the (assumed) healthy bridge. As the vehicle accelerations have changed, the inferred MRIF diverges from the real MRIF. These differences between inferred bridge profiles are used as indicators of bridge damage. In this paper, bridge bearing damage is considered and the bearing damage model is the same as that used in the literature [15]. A rotational stiffness of 10^8 N•m is assumed as the damage, i.e., failure of the bearing is assumed to be equivalent to a rotational spring with this stiffness.

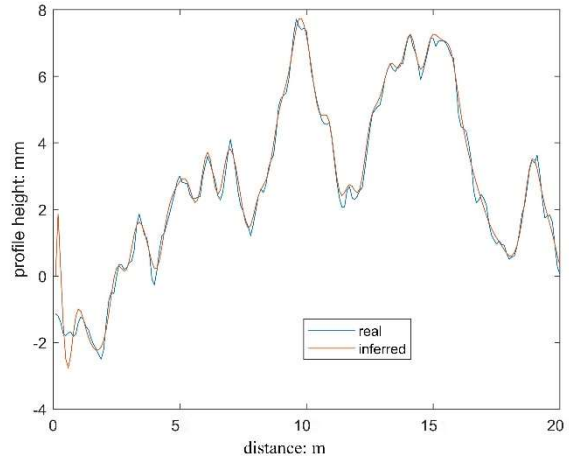

Figure 2. Real bridge profile and inferred bridge profile.

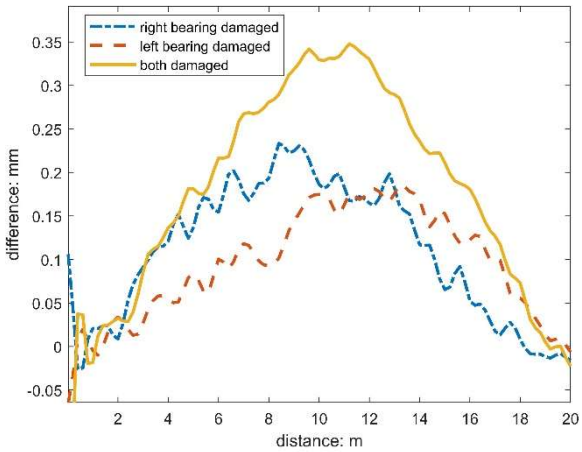

Figure 3. The difference between inferred healthy bridge profile and inferred damaged bridge profile.

Figure 3 shows the differences between the bridge profiles inferred using accelerations on the healthy and damaged bridges (healthy minus damaged). The differences are mostly larger than zero. When the bearing on one side is damaged, the difference tends to skew to the other side. When both bearings are damaged, the magnitude of the difference is greater than when only one is damaged. Further, the peak of difference when both bearings are damaged is located in the middle.

4 CONCLUSION

A new fleet monitoring concept, with partially instrumented vehicles, is proposed in this paper. With prior knowledge of a healthy MRIF for the bridge, the bridge profile can be accurately estimated without knowing each axle weight. A non-zero difference between inferred healthy bridge profile and inferred damaged bridge profile can show when a bridge bearing is damaged and which one (or both) is damaged. Further research is required to quantify the damage level and test different damage types.

ACKNOWLEDGMENTS

The author Wang Shuo wishes to acknowledge the financial support received from University College Dublin and the Chinese Scholarship Council. The authors also gratefully acknowledge the Federal Highway Administration and the Long-Term Pavement Performance Program for access to WIM data.

REFERENCES

[1] Yang, Y.B. and Yang, J.P. (2018) 'State-of-the-art review on modal identification and damage detection of bridges by moving test vehicles.' *International Journal of Structural Stability and Dynamics,* 18(02): 1850025.

[2] Li, Y.Y. (2010) 'Hypersensitivity of strain-based indicators for structural damage identification: A review.' *Mechanical Systems and Signal Processing,* 24(3): 653-664.

[3] Martinez, D., Malekjafarian, A. and OBrien, E.J. (2020) 'Bridge health monitoring using deflection measurements under random traffic.' *Structural Control and Health Monitoring*, 27(9): 2593.

[4] McGeown, C., Huseynov, F., Hester, D., McGetrick, P., OBrien, E.J. and Pakrashi, V. (2021) 'Using measured rotation on a beam to detect changes in its structural condition.' *Journal of Structural Integrity and Maintenance*, 6(3): 159-166.

[5] Carden, E.P. and Fanning, P. (2004) 'Vibration based condition monitoring: a review.' *Structural health monitoring*, 3(4): 355-377.

[6] Yang, Y.B., Lin, C.W. and Yau, J.D. (2004) 'Extracting bridge frequencies from the dynamic response of a passing vehicle.' *Journal of Sound and Vibration*, 272(3-5): 471-493.

[7] Kim C.-W., Isemoto R., Toshinami T., Kawatani M., McGetrick P., OBrien, E.J. (2011) 'Experimental Investigation of Drive-by Bridge Inspection.' *5th International Conference on Structural Health Monitoring of Intelligent Infrastructure (SHMII-5)*. Cancun, Mexico.

[8] Siringoringo, D.M., Fujino Y. (2012) 'Estimating Bridge Fundamental Frequency from Vibration Response of Instrumented Passing Vehicle: Analytical and Experimental Study.' *Advanced Structural Engineering*, 15, 417-33.

[9] Malekjafarian, A. and OBrien, E.J., (2014) 'Application of output-only modal method in monitoring of bridges using an instrumented vehicle.' In *Civil Engineering Research in Ireland,* Belfast, 28-29.

[10] McGetrick, P.J., Gonzalez, A., OBrien, E.J. (2009) 'Theoretical investigation of the use of a moving vehicle to identify bridge dynamic parameters.' *Insight*, 51(8), 433-438.

[11] González, A., OBrien, E.J. and McGetrick, P.J. (2012) 'Identification of damping in a bridge using a moving instrumented vehicle.' *Journal of Sound and Vibra*tion, 331(18): 4115-4131.

[12] OBrien, E.J. and Keenahan, J. (2015) 'Drive- by damage detection in bridges using the apparent profile.' S*tructural Control and Health Monitoring*, 22(5): 813-825.

[13] Yang, Y.B., Wang, B.Q., Wang, Z.L., Shi, K., Xu, H., Zhang, B. and Wu, Y.T. (2020) 'Bridge surface roughness identified from the displacement influence lines of the contact points by two connected vehicles.' *International Journal of Structural Stability and Dynamics*, 20(14): 2043003.

[14] Keenahan, J., Ren, Y. and OBrien, E.J. (2020) 'Determination of road profile using multiple passing vehicle measurements.' *Structure and Infrastructure Engineering*, 16(9): 1262-1275.

[15] OBrien, E.J. McCrum, D.P. and Wang S. (2022) 'Fleet monitoring of bridges using a moving reference influence function.' *Engineering Structures*, under review.

[16] Walker D, Cebon D. (2012) 'The metamorphosis of LTPP traffic data.' *In 6th International Conference on Weigh-In-Motion (ICWIM 6) International Society for Weigh-In-Motion, International Society for Weigh-in-Motion,* Dallas, United States, 272-281.

[17] Keenahan, J., OBrien, E.J., McGetrick, P.J. and Gonzalez, A. (2014) 'The use of a dynamic truck–trailer drive-by system to monitor bridge damping.' *Structural Health Monitoring*, 13(2), 143-157.

Laboratory Verification of Vehicle Contact Point Response for Bridge Condition Monitoring

Robert Corbally[1], Abdollah Malekjafarian[1]
[1]Structural Dynamics and Assessment Laboratory, School of Civil Engineering, University College Dublin, Ireland
email: robert.corbally@ucdconnect.ie, abdollah.malekjafarian@ucd.ie

ABSTRACT: Limited maintenance budgets, coupled with an ageing bridge-stock, mean that there is much appetite for efficient and inexpensive techniques for monitoring and detection of damage in bridges. Drive-by bridge monitoring techniques, which use in-vehicle sensors to monitor changes in bridge condition over time, represent a solution to this challenge. This paper presents the concept of using an inferred acceleration response at the point of contact between the vehicle tyre and the bridge surface as an enhanced method of monitoring the bridge frequency. A novel expression is presented, which allows the contact-point (CP) response to be inferred from the in-vehicle measurements and considers the vehicle suspension system which has been neglected by previous models. A numerical example is initially provided to demonstrate the benefits of using the CP response to identify the bridge frequency. The concept is then tested using a laboratory-scale vehicle-bridge interaction model and it is shown that the CP response provides accurate estimates of the bridge frequency. Two damage cases are also simulated in the laboratory, and it is shown that changes in bridge frequency can be detected, with the CP response being more sensitive to damage than the signals directly measured from the sensors on the vehicle. It is observed that the detected frequency is sensitive to vehicle speed, which is an important consideration when combining the results of multiple vehicle passages. Overall, the results verify that the CP response can enhance drive-by bridge monitoring results.

KEY WORDS: Drive-By; Bridge; Structural Health Monitoring; SHM; Damage Detection; Contact-Point Response; Laboratory; Scale Model; Vehicle-Bridge Interaction.

1 INTRODUCTION

Bridges are critical components for any transportation network and it is essential that they are inspected and maintained appropriately to ensure that vehicles can travel in a safe and efficient manner. However, as transport networks age and the infrastructure deteriorates over time, inspection of large bridge stocks and prioritisation of maintenance budgets towards specific structures becomes more and more challenging. For this reason, there is a clear need for quick and efficient techniques for ongoing monitoring and inspection of bridges.

Drive-by bridge monitoring approaches utilise in-vehicle sensors to monitor bridge condition based on measurements taken as the vehicle traverses the bridge. The drive-by concept was initially proposed by Yang et al. [1] in 2004 where it was theoretically demonstrated that the fundamental frequency of a bridge can be extracted from the vibration of the traversing vehicle. Given that bridge frequency is sensitive to damage, this represented a method of monitoring changes in bridge condition over time, without the need to install sensors on the bridge, or the need for manual visual inspections. Since the concept was initially proposed, there have been numerous developments in the use of drive-by bridge inspection techniques. Different damage mechanisms can affect bridge vibrations in different ways so there have been various efforts to examine how drive-by techniques can be used to identify these changes, e.g. for scour [2], cracking in the deck [3, 4] or changes in boundary conditions [5, 6] amongst others. Drive-by techniques have also been used for different applications, including calculation of bridge damping [7], estimation of vehicle properties and investigation of pavement characteristics [8, 9]. More recently there have been a number of developments where researchers have explored the use of Machine Learning approaches to account for environmental or operational factors which may influence the measured bridge properties during any given vehicle passage [10-12].

One of the primary challenges of using drive-by techniques to measure the dynamic properties of a bridge relates to the fact that the contribution of the bridge vibration to the overall vehicle vibration is usually small, making it difficult to isolate the bridge-related components from the response. Yang et al. [13] developed a formulation which allowed the response at the point of contact between the vehicle and the bridge to be derived from the measured response within the vehicle. The formulation was developed for a single degree of freedom, sprung mass, model. This model represented a specific trailer which was designed to be towed across a bridge. The contact-point (CP) response calculated from the measurements within the vehicle was then used to detect the bridge frequencies. Results from field testing of the approach were promising and demonstrated the ability to extract the bridge frequencies with little interference from the vehicle frequencies.

In order to extend the approach to more commonly used vehicles, the vehicle suspension and vibration of the vehicle body need to be considered. A relationship has been proposed by the authors [14] which utilises a quarter-car representation of a vehicle to derive an expression for the CP response and allows the vehicle suspension and body vibration to be taken into consideration. In this paper, the concept is demonstrated using a numerical example, and then tested using a laboratory scale vehicle-bridge interaction model, where successful detection of bridge frequency is demonstrated along with detection of changes in frequency due to damage.

2 DRIVE-BY BRIDGE MONITORING

The vast majority of drive-by bridge monitoring techniques aim to detect the dynamic properties of a bridge based on vibration measurements taken on a passing vehicle. In this paper, the first natural frequency of the bridge is extracted from the vehicle measurements. This section uses a numerical example to demonstrate the proposed concept and highlights the advantage of using the CP response to detect the bridge frequency rather than trying to extract it directly from the measured signals on the vehicle.

2.1 Numerical Modelling of Vehicle-Bridge Interaction

Figure 1 illustrates a numerical modelling approach which adopts a quarter-car vehicle representation to model a vehicle traversing a finite element model of a bridge. The finite element model uses 20 no. beam elements, 0.75m long, with 2-degrees of freedom per node, representing rotational and vertical displacements. The bridge model represents a 15m long simply supported concrete slab with cross sectional area A = 7.5m^2, second moment of area I = 0.352m^4, material density ρ = 2,500kg/m^3 and Young's modulus E = 35GPa.

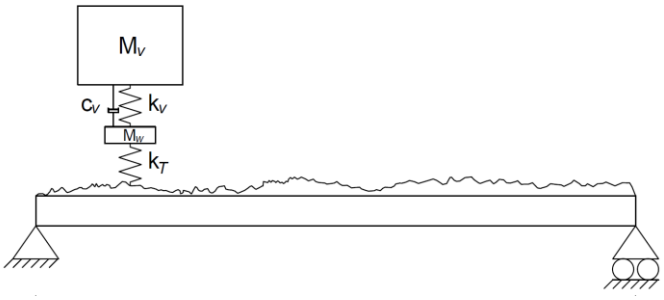

Figure 1. Numerical Vehicle-Bridge Interaction Model.

In order to consider the interaction between the vehicle and the bridge, a quarter-car model was used to represent the vibration of the vehicle. The quarter car model, as shown in Figure 1 & Figure 2, consists of two degrees of freedom, with two lumped masses, representing the vertical motion of the (i) vehicle body and (ii) the axle (including the wheel). The two masses are connected using a spring and dashpot representing the stiffness and damping properties of the vehicle suspension and the axle degree of freedom is connected to the bridge using a spring to represent the tyre stiffness. While the quarter-car is a simplified representation of the actual behaviour of a vehicle, it has been widely adopted to represent the two primary modes of vibration of a vehicle, i.e. 'bounce' of the vehicle body and axle 'hop' [15]. The properties used in the quarter-car model and the natural frequencies of the model are included in Table 1.

2.2 Evaluating the Contact-Point Response

In order to extend the approach proposed by Yang et al. [13] to more commonly used vehicles, the vehicle suspension and vibration of the vehicle body need to be considered when evaluating the CP response. The quarter-car model allows these effects to be considered. As per Figure 2, y_V and y_W represent the displacement of the vehicle body and the wheel/axle respectively and u_{cp} represents the deflection at the contact point between the wheel and the surface of the bridge. The remainder of the vehicle properties are as described in Table 1.

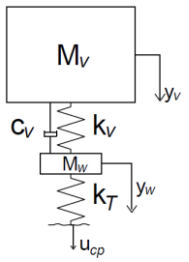

Figure 2. Quarter-Car Vehicle Representation.

Table 1. Properties of Vehicle Model.

Property	Value
Body Mass (M_v)	9,300 kg
Axle Mass (M_w)	700 kg
Suspension Stiffness (k_v)	4x10^5 N/m
Suspension Damping (c_v)	10,000 Ns/m
Tyre Stiffness (k_T)	17.5 x10^5 N/m
First Frequency (body bounce)	0.9 Hz
Second Frequency (axle-hop)	8.8 Hz

Equation 1 shows the formulation of the equations of motion for the quarter-car model, with dot notation used to indicate the time derivatives of variables (i.e. velocity and acceleration).

$$\begin{bmatrix} M_V & 0 \\ 0 & M_W \end{bmatrix} \begin{Bmatrix} \ddot{y}_V \\ \ddot{y}_W \end{Bmatrix} + \begin{bmatrix} c_V & -c_V \\ -c_V & c_V \end{bmatrix} \begin{Bmatrix} \dot{y}_V \\ \dot{y}_W \end{Bmatrix} + \begin{bmatrix} k_V & -k_V \\ -k_V & k_V + k_T \end{bmatrix} \begin{Bmatrix} y_V \\ y_W \end{Bmatrix} = \begin{Bmatrix} 0 \\ k_T u_{cp} \end{Bmatrix} \quad (1)$$

Utilising the axle/wheel equation from Equation 1 and rearranging in terms of the contact-point acceleration, $\ddot{u}_{cp}$, the CP response can be represented by the formulation shown in Equation 2 [14].

$$\ddot{u}_{cp} = \frac{M_W}{k_T}\frac{d^2\ddot{y}_W}{dt^2} + \frac{c_V}{k_T}\left(\frac{d\ddot{y}_W}{dt} - \frac{d\ddot{y}_V}{dt}\right) + \frac{k_V}{k_T}(\ddot{y}_W - \ddot{y}_V) + \ddot{y}_W \quad (2)$$

In Equation 2 the $\frac{d^n\ddot{y}_V}{dt^n}$ notation is used to represent the nth time derivative of the measured acceleration signals on the vehicle. All other parameters are as defined above and in Table 1. This relationship between the measured accelerations in the vehicle, and the acceleration at the contact point, can be used to infer the CP response directly from measurements on the vehicle, once the properties of the vehicle are known.

2.3 Numerical Example

An illustrative numerical example of a low-speed vehicle passage is initially used demonstrate the concept. A 3m/s passage of the vehicle across the bridge, with a 'Class A' pavement roughness (as per with ISO8608 [16]), was simulated in MATLAB. The vertical acceleration signals during the passage were calculated by solving the dynamic equations of motion for the overall vehicle & bridge system and the simulated vibration measurements were used as inputs to Equation 2 to allow the CP response to be evaluated. Figure 3

shows the frequency spectrum of both the axle response and the CP response after applying a Fast Fourier Transform (FFT) to the simulated signals. The first frequency of the bridge is also shown, along with the two vehicle frequencies. It is seen that the axle response has a distinct peak at the axle-hop frequency of the vehicle, and the bridge frequency is much less distinct. However, the CP response displays a clear peak at the bridge frequency and is not governed by the vehicle frequencies.

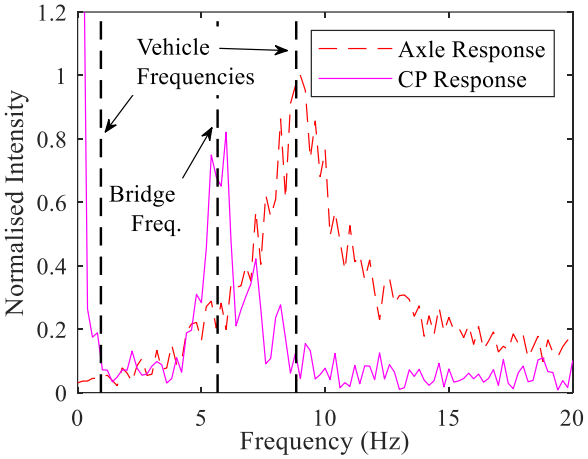

Figure 3. Frequency Spectrum of Axle Response and Contact-Point Response.

This numerical demonstration clearly highlights the potential advantages of using the CP response to isolate the bridge-related vibrations from the measured responses. The subsequent sections extend this approach and aim to verify the concept in the laboratory.

3 LABORATORY MODELLING OF VEHICLE BRIDGE INTERACTION

A scaled vehicle-bridge interaction laboratory model was constructed to test the application of the theory. The laboratory model was developed to replicate, at a reduced scale, the interaction between the vehicle and the bridge in a controlled environment.

3.1 Beam & Slab Bridge Laboratory Model

The bridge model, shown in Figure 4, consists of a 5mm deep, 600mm wide steel plate representing the bridge deck, with 6 no. steel angle beams (20x20x4mm) bolted to the underside of the deck. The bridge deck spans 2m between the supports, which were designed to allow simply-supported rotational behaviour at each end. The supports consist of a steel shaft which spans between two pillow-block bearing units and a 3D printed bearing shelf which surrounds the steel support shaft and provides a plinth to support the beams. The laboratory model was designed to represent the behaviour of a typical concrete beam and slab bridge under vehicular loading and is based on an existing bridge. Due to the complexities of modelling the geometry of the bridge at a reduced scale, various scaling laws were employed to optimise the geometry of the cross section so that the span-deflection ratio under the load of a typical truck would remain constant, and the first natural frequency of the bridge would be in a similar range to that of the full scale bridge (the bridge length is scaled using a factor of 1:12.5). Timber approach spans were provided at either end of the bridge.

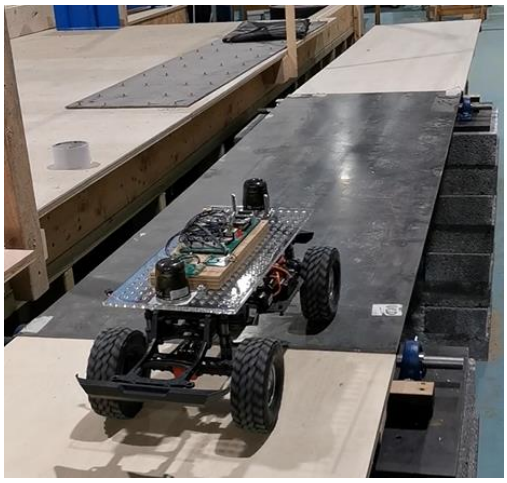

(a)

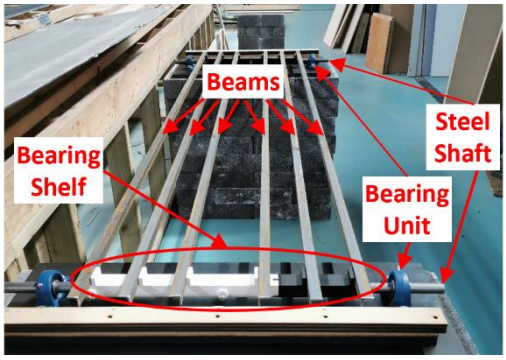

(b)

Figure 4. Photograph of (a) Laboratory Scale Bridge Model (b) Beams & Support Conditions Prior to Adding Deck Plate.

3.2 Laboratory Vehicle Model

The vehicle was modelled using a commercially available remote-controlled vehicle. The Axial SCX10™ III Jeep has three speed settings and allows some customisation of components. The vehicle suspension system uses oil-filled shocks with single coilover springs and tuneable damping. For the purposes of testing, the outer plastic cover of the vehicle was removed, as shown in Figure 5, to allow wireless accelerometers to be attached to the vehicle.

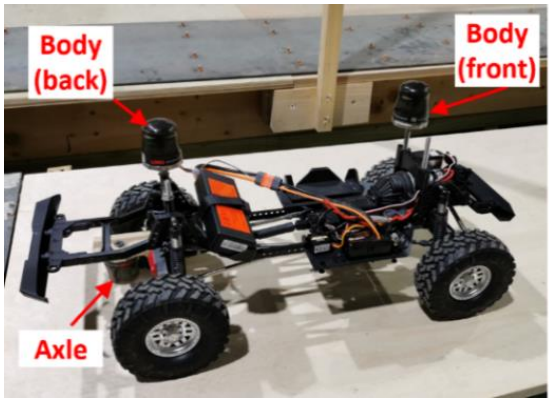

Figure 5. Vehicle Model & Placement of Accelerometers.

Three accelerometers were installed, at the locations depicted in Figure 5, to allow vibrations to be measured on the vehicle body (at the front & back, above the suspension) and on the rear axle of the vehicle.

3.3 Modal Testing of Bridge Frequencies

Prior to commencing drive-by testing, the natural frequencies and mode shapes of the bridge were evaluated using a direct modal analysis of the bridge. Eight accelerometers were installed on the bridge surface, at the locations shown in Figure 6(a) and acceleration data was captured after striking the bridge deck surface at a number of locations. The data from 72 hammer impacts was then analysed in MATLAB and an algorithm was developed to automatically identify the natural frequencies and mode shapes of the bridge using Frequency Domain Decomposition (FDD). The results for the first three frequencies are depicted in Figure 6(b)-(d), where a surface was fitted between sensor locations to visualise the deflected shape of the bridge for each of the modes of vibration. It can be seen that the first and third mode shapes represent the first two global bending modes, with the second mode of vibration representing global torsion of the bridge deck. Measuring the dynamic properties of the bridge directly in this way, allowed the accuracy of the drive-by testing results to be assessed.

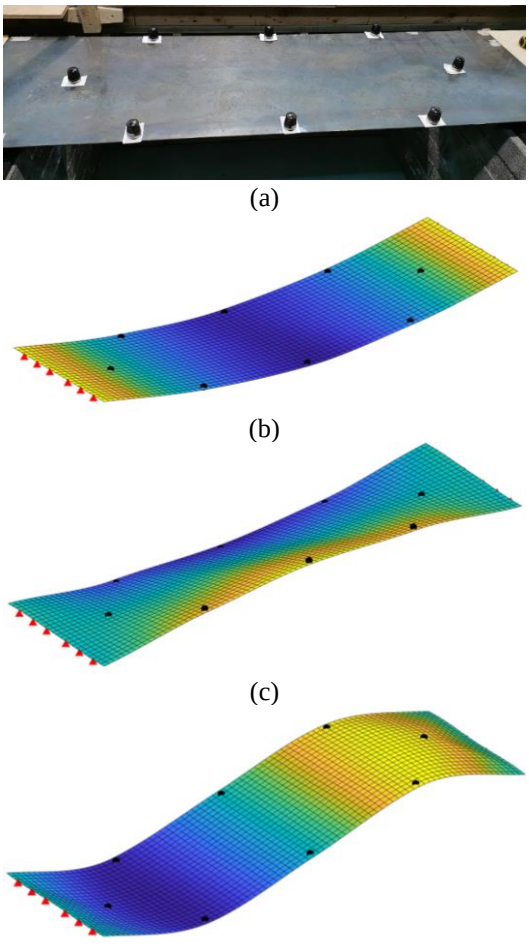

(a) (b) (c) (d)

Figure 6. Results of Modal Testing (a) Sensor Locations (b) Mode 1: 8.8Hz (c) Mode 2: 15.3Hz (d) Mode 3: 29.9Hz.

4 DRIVE-BY BRIDGE FREQUENCY IDENTIFICATION

The remote-controlled vehicle was driven over the bridge a number of times and the vibration data on the vehicle body was collected during each passage. An algorithm was developed to automatically identify the point of entry to and exit from the bridge based on peaks in the signals as it passed over a small gap at each end. The average vehicle speed during each passage was also automatically calculated from the signals. In order to estimate the CP response, Equation 2 was used with the signals from the back axle and the body just above the back axle. The vehicle properties were estimated based on the datasheets for the vehicle, and where parameters were not known, reasonable estimates were used. The authors have previously demonstrated numerically that the accuracy of the CP response is not sensitive to errors in the vehicle properties [14]. Figure 7 shows the measured signals, along with the CP response for a single vehicle crossing at approximately 0.6m/s. It can be seen that the vibrations measured on the vehicle are all of similar magnitude, with the CP response being significantly higher.

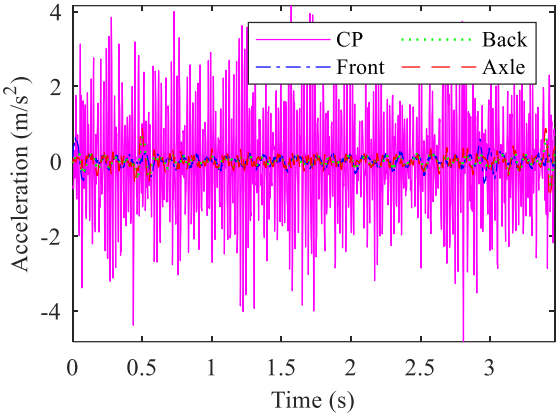

Figure 7. Measured Signals & Calculated Contact-Point Response during a 0.6 m/s Vehicle Crossing.

To estimate the bridge frequency from the drive-by measurements, the portion of the signals during each vehicle passage was extracted and the frequency spectrum of each signal was evaluated by applying an FFT to the data. The results were initially separated to examine the influence of vehicle speed. The vehicle has 3 speed settings, low, medium and high. The average speeds recorded for all of the vehicle crossings in each speed setting are shown in Table 2, and the equivalent speed ranges, in km/h for the full-scale bridge upon which the laboratory model is based, are also shown.

Table 2. Vehicle Speeds.

Speed Setting	Speed Range (m/s)	Avg. Measured Speed (m/s)	Equivalent Full-Scale Speed (km/h)	No. of Crossings
Low	0-0.85	0.73	14-33	20
Med.	0.85-1.25	1.11	22-50	3
High	>1.25	1.52	30-68	3

The equivalent full-scale speed range is based on either scaling up using a factor of 12.5 (geometrical scale factor for the bridge length), or using a more suitable scaling rule which maintains an equivalent relationship between the vehicle speed, the fundamental bridge frequency and the bridge length for the full-scale and reduced scale scenario as described by McGetrick et al. [17]. It should be noted that the speed of 3m/s used for illustrative purposes in the numerical example in Section 2.3 was not subject to scaling laws. The numerical model is a full-scale representation of a different vehicle/bridge and as such, no direct comparison of the results can be made.

The resulting FFTs for all vehicle passages in a given speed range were averaged to give an overall frequency spectrum for each speed setting. The results were normalised before plotting and Figure 8 shows the FFTs for each speed setting. The measured bridge frequency is also shown on the plots (8.8Hz) for comparison, and it can be seen that the signals all contain a localised peak in the vicinity of the bridge frequency, however the peak is slightly shifted depending on the speed setting used, which is not unexpected as previous research has demonstrated that the measured frequency will be influenced by vehicle speed [18]. It should be noted that the medium and high-speed cases are only based on 3 vehicle passages, however the low-speed case is based on 20 passages.

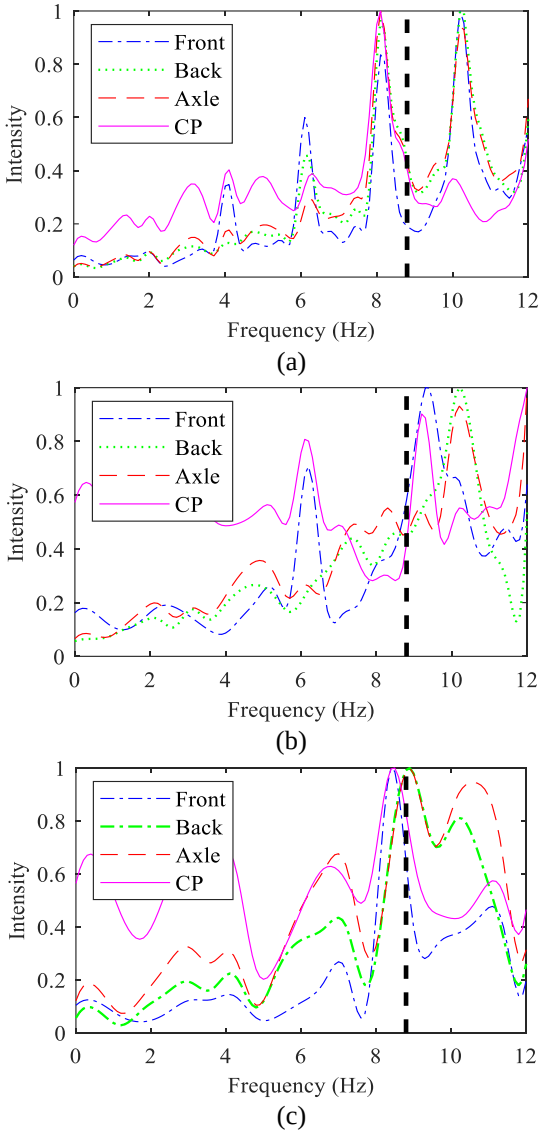

Figure 8. FFT Plots of Measured Signals & Calculated CP Response for (a) Low, (b) Medium, (c) High Speeds.

Examining the results from the low-speed setting in Figure 8(a) it can be seen that all of the measured signals contain multiple peaks, with the peaks associated with the bridge frequency slightly underpredicting it. Most importantly, it can be seen that the CP response exhibits a single distinct peak, just below the bridge frequency, verifying the theory that the CP response is governed by the bridge frequency rather than the vehicle frequencies, making it a better predictor of bridge frequency. The accuracy of the predictions for the high-speed vehicle setting are closer to the actual bridge frequency, but due to the small number of vehicle passages at this speed, the results are less reliable, and the peak is less distinct. However, it can be concluded that the CP response provides improved bridge frequency detection capabilities, but the influence of varying vehicle speed on the detected frequency should be considered if the measured frequency is to be used for condition monitoring.

5 DRIVE-BY DAMAGE DETECTION

To assess the ability of the CP response to detect changes in bridge frequency due to damage, the experiments were repeated, with two 'simulated' damage conditions considered. The effect of damage on the bridge frequency was simulated by clamping masses to at each side of the deck at midspan, to artificially induce a change in frequency. The damage conditions are summarised in Table 3 along with the frequency values measured directly from the bridge.

Table 3. Description of Simulated Damage Conditions.

Damage Case	Bridge Freq. (Hz)	Description
Healthy	8.8	Bridge in healthy condition
Dam1	8.6	1kg each side @ midspan
Dam2	8.1	2kg each side @ midspan

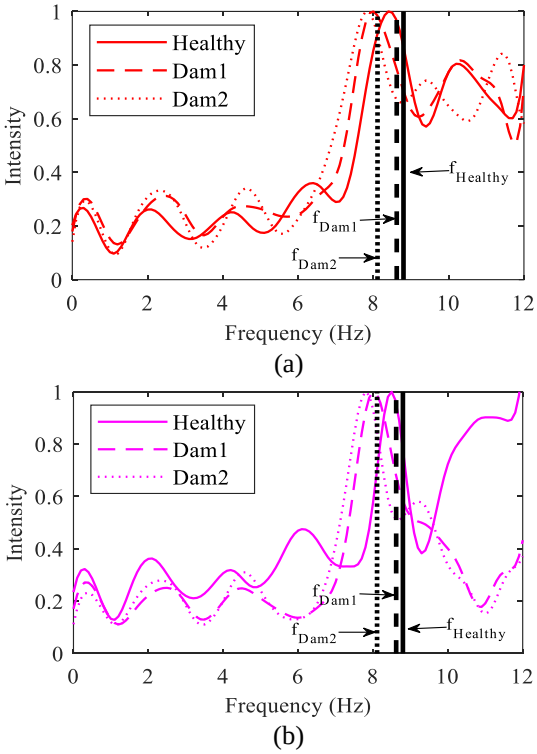

Figure 9. FFT Plots of (a) Axle Response & (b) Contact-Point Response, for the Healthy & 2 Damaged Cases.

The experiments were repeated, this time with 20 vehicle passages at the high-speed setting, for each bridge damage condition. Before each passage, the bridge was manually excited to induce free vibration in the structure, to simulate a situation where other traffic is also crossing the bridge. Figure 9 shows the frequency spectra for the axle response and the CP response for the healthy condition and the two damaged

conditions. The actual bridge frequency, for each case, is also included in the plots, as represented by the three vertical lines. It is clear that the addition of mass at midspan has the effect of reducing the natural frequency of the bridge, and it can also be seen that the peak of the FFT plots, for both the axle and CP response give reasonably accurate measures of bridge frequency, albeit slightly under-predicted for each case. Most importantly, it can clearly be seen that the peak shifts to the left as the level of simulated damage increases, providing confidence that this approach can be used to monitor changes in the bridge frequency. It can be seen once again that the CP response provides a more distinct peak at the bridge frequency than the axle response, although for the healthy case, it is not quite as distinct. It is also clear that manually exciting the bridge has increased the prominence of the peak for the axle response (a similar situation was observed for the sensors on the vehicle body). This shows the benefits of using the CP response when bridge vibrations are lower, as seen in the previous section. In such cases, the vehicle frequencies tend to make it difficult to identify the peak associated with the bridge frequency, particularly as the exact frequency of a real bridge would not be known in advance.

Finally, to assess the sensitivity of the CP response to damage, and compare it to the other signals, the peak values for the FFT plots for the two damaged cases were compared to the peaks identified for the healthy case and the percentage change is shown in Figure 10. It is seen that the change in frequency is most distinct for the CP response, with the axle response being slightly less sensitive and the two body sensors (front and back) provided the exact same results, again, slightly less sensitive. Overall, it is seen that damage can be detected using any of the signals, however the CP response clearly demonstrates the advantage of being more sensitive to damage, but also allowing the bridge frequency to be more easily identified.

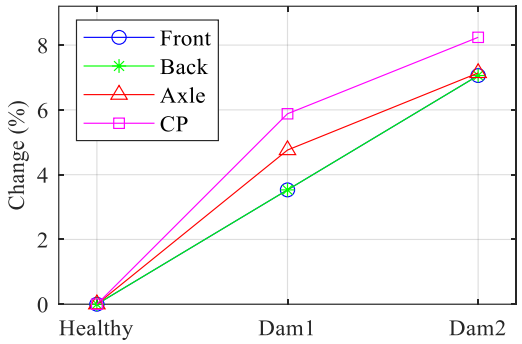

Figure 10. Change in Identified Frequencies for both Damage Cases Compared to those Identified for the Healthy Case.

6 CONCLUSIONS

This paper presents the concept of using the CP response of a passing vehicle to facilitate drive-by bridge condition monitoring. An expression is presented which allows the CP response to be inferred from vibration measurements taken on the vehicle. A numerical example is initially used to demonstrate that the bridge frequency is more easily identified using the CP response compared to the vibration response measured directly on the vehicle. The concept is then tested using a laboratory-scale vehicle-bridge interaction model and the bridge frequency is shown to be visible using the CP response. Experiments are also used to assess the ability of the CP response to monitor changes in bridge frequency which occur when damage is simulated in the bridge. The CP response is shown to be more sensitive to damage than any of the signals measured directly on the vehicle. Results provide confidence in the proposed drive-by bridge monitoring method, however it is noted that the detected bridge frequency is sensitive to vehicle speed, and this must be accounted for when combining information from vehicle passages at different speeds. This is particularly relevant given the significant potential for using this method with crowdsourced vibration data from in-built sensors in existing vehicle fleets where the speeds will vary.

REFERENCES

[1] Yang, Y.B., C.W. Lin, and J.D. Yau. (2004). Extracting bridge frequencies from the dynamic response of a passing vehicle. *Journal of Sound and Vibration*. 272(3-5): p. 471-493.

[2] Fitzgerald, P.C., et al. (2019). Drive-by scour monitoring of railway bridges using a wavelet-based approach. *Engineering Structures*. 191: p. 1-11.

[3] McGetrick, P.J. and C.W. Kim. (2013). A Parametric Study of a Drive by Bridge Inspection System Based on the Morlet Wavelet. *Key Engineering Materials*. 569-570: p. 262-269.

[4] Malekjafarian, A., D. Martinez, and E.J. OBrien. (2018). The Feasibility of Using Laser Doppler Vibrometer Measurements from a Passing Vehicle for Bridge Damage Detection. *Shock and Vibration*. 2018: p. 1-10.

[5] Mei, Q. and M. Gül. (2019). A crowdsourcing-based methodology using smartphones for bridge health monitoring. *Structural Health Monitoring*. 18(5-6): p. 1602-1619.

[6] Cerda, F., Chen, S., Bielak, J., Garrett, J. H., Rizzo, P., & Kovacevic, J. (2014). Indirect structural health monitoring of a simplified laboratory-scale bridge model. *Smart Structures and Systems*. 13(5): p. 849-868.

[7] Keenahan, J., et al. (2014). The use of a dynamic truck–trailer drive-by system to monitor bridge damping. *Structural Health Monitoring: An International Journal*. 13(2): p. 143-157.

[8] McGetrick, P.J., D. Hester, and S.E. Taylor. (2017). Implementation of a drive-by monitoring system for transport infrastructure utilising smartphone technology and GNSS. *Journal of Civil Structural Health Monitoring*. 7(2): p. 175-189.

[9] McGetrick, P.J., et al. (2013). Dynamic Axle Force and Road Profile Identification Using a Moving Vehicle. *International Journal of Architecture, Engineering and Construction*. 2(1): p. 1-16.

[10] Locke, W., et al. (2020). Using drive-by health monitoring to detect bridge damage considering environmental and operational effects. *Journal of Sound and Vibration*. 468.

[11] Malekjafarian, A., et al. (2019). A machine learning approach to bridge-damage detection using responses measured on a passing vehicle. *Sensors*. 19.

[12] Corbally, R. and A. Malekjafarian. (2022). A data-driven approach for drive-by damage detection in bridges considering the influence of temperature change. *Engineering Structures*. 253.

[13] Yang, Y.B., et al. (2020). Measuring bridge frequencies by a test vehicle in non-moving and moving states. *Engineering Structures*. 203.

[14] Corbally, R. and A. Malekjafarian. (2021). Examining changes in bridge frequency due to damage using the contact-point response of a passing vehicle. *Journal of Structural Integrity and Maintenance*. 6(3): p. 148-158.

[15] Jazar, N.R. (2008). *Vehicle Dynamics, Theory and Application*. 2008: Springer.

[16] ISO, I. (2016). *ISO 8608 Mechanical Vibration–Road Surface Profiles–Reporting of Measured Data*, BSI Standards Publication: London, UK.

[17] McGetrick, P.J., et al. (2015). Experimental validation of a drive-by stiffness identification method for bridge monitoring. *Structural Health Monitoring: An International Journal*. 14(4): p. 317-331.

[18] Sitton, J.D., et al. (2020). Frequency Estimation on Two-Span Continuous Bridges Using Dynamic Responses of Passing Vehicles. *Journal of Engineering Mechanics*. 146(1).

Cost-Benefit Analysis of various mitigation measures on bridge and tunnel strike events by oversized vehicles in different socio-economic regions

Ilaria Bernardini[1], Emmanouil Kakouris[1], Mark Tucker[1]
[1]Roughan & O'Donovan Innovative Soutions, Arena House, Arena Road, Sandyford, Dublin 18, Ireland
email: ilaria.bernardini@rod.ie, emmanouil.kakouris@rod.ie, mark.tucker@rod.ie

ABSTRACT: This paper presents the outcome of the Special Project - Bridges and Tunnels Strikes by Oversize Vehicles commissioned by the World Road Associations (PIARC) in 2021. The objective of this study was to examine proven countermeasures, practices, and technologies used to reduce the incidence of oversize vehicles striking bridges and tunnels along with effective processes for accurately reporting and tracking bridge strike occurrences. A Cost Benefit Analysis (CBA) methodology was developed for road administrators to discern the best mitigation practices for a given scenario. Based on the data gathered through a combination of desk-based research, project specific surveys and interviews with key stakeholders, a semi-quantitative CBA was carried out on a typical structure at a global level based on the framework developed. The semi-quantitative CBA led to the subdivision of the mitigation measures analysed into three categories depending on their cost efficiency, allowing recommendations to be drawn for different income countries categories. The key findings of the study are to provide a formalised method of recording data for strikes, to move toward driver-based mitigation practices and that a multi-sectoral panel should be put in place to allow all key actors to work together to provide a coordinated response to strikes.

KEY WORDS: Cost-Benefit Analysis; Bridge; Tunnel; Oversize Vehicle; Strike; High Income Countries (HICs); Lower Middle Income Countries (LMICs).

1 INTRODUCTION

Bridge and tunnel strikes by oversize vehicles are a threat to road user's safety, and the operation of highway and rail infrastructure. These incidents cause significant damage to infrastructure, injuries and fatalities, secondary crashes, traffic delays, emergency response, rerouting of traffic to remove trucks and repair damage, and economic costs related to response, recovery and repair efforts. Bridge strikes are a global issue affecting both Higher Income Countries (HICs) and Lower Middle-Income Countries (LMICs).

The purpose of this study was to examine proven countermeasures, practices, and technologies used to reduce the incidence of oversize vehicles striking bridges and tunnels along with effective processes for accurately reporting and tracking bridge strike occurrences. The developed formal CBA methodology enables road administrators to perform an assessment on their own networks. Its application in this study led to broad recommendations for different socio-economic regions.

The socio-economic impact of damage to bridges and tunnels due to over-height vehicles varies based on geographical location and the economic status of the region in question. Hence, the study considers both HIC and LMIC use cases. It is acknowledged that there is no "one size fits all" solution to address the issue of bridge and tunnel strikes globally. Thus, this study has established a range of potential solutions that will allow an individual stakeholder to determine the correct fit to suit their needs and end-goals. For countries that cannot provide statistics prior to implementing solutions, it is difficult to quantify the effectiveness of a countermeasure in their own region prior to implementing a solution. Therefore, different regions have been clustered based on similar socio-economic backgrounds. Recommendations are then made for the most effective countermeasures for each cluster based on available data within that cluster.

2 METHODOLOGY

The overarching methodology consisted of an initial desk study to understand the causes, consequences and mitigation measures for bridge and tunnel strikes. A gap analysis from the desk study was then carried out to inform the first project specific survey, which acted as an initial data gathering phase and allowed identification of key stakeholders for the second survey which consisted of a more focused approach to obtain cost, consequence and mitigation effectiveness data. The information gathered during the desk study was then discussed with stakeholders in one-to-one interviews and then used to perform a semi-quantitative CBA to make recommendations to the World Road Association (PIARC) and road administrators on addressing the bridge and tunnel strike problem. The stakeholders engaged consisted of a mix of road hauliers, contractors, and infrastructure owners. Stakeholders were obtained from Roughan & O'Donovan's extensive list of industry contacts in consultation with PIARC.

3 MITIGATION MEASURES

3.1 Overview

Various prevention systems have been proposed in the past to eliminate bridge / tunnel strikes. These can be categorised into passive, sacrificial, and active systems as described in [1]. Other proposed systems are detection systems, and driver-based countermeasures to reduce the number of strikes.

Passive systems are currently considered the most cost-effective systems, readily available in terms of supply chain, simple installation and low maintenance requirements. They can include static signage, Variable Message Signs (VMS) [2], beacons [3], bridge markings [4], flashing beacons and lights [5]. These systems use static or variable measures which inform the oncoming driver about the danger or possible alternative routes. Globally, passive systems are considered the primary and most widely used countermeasure against bridge and tunnel strikes. Although these systems are inexpensive, they rely on driver education and attention and are typically used in conjunction with other preventative methods.

Sacrificial systems involve physical contact with the upcoming vehicle, being installed close-by the structure to dissipate the energy from the vehicle impact or at a moderate distance before the structure to warn the driver of the forthcoming danger and ultimately protect the structure itself. Examples of sacrificial prevention systems include crash beams, hanging chains or bells and road narrowing techniques e.g. speed bumps and rumble strips ([6], [7], [8]). While these systems will alert a driver prior to striking a bridge, they may still cause damage to the vehicle itself, and associated disruptions to road traffic. Although, crash beams are very effective in preventing a bridge strike, they are costly and they only act as a protective rather than a preventative measure, with additional costs associated with the strike.

Active prevention systems can be Intelligent Transportation Systems (ITS) which include Early Warning Detection Systems (EWDS), computer vision systems, infrared dual beam arrays ([1], [9]), LaRa-OHVD systems [10], radar systems [11] and laser vision [12]. Alternative and less expensive systems to detect over-height vehicles have been proposed by [13] and [14] based on cameras and computer vision techniques.

Detection systems are mainly structural health monitoring tools [15] such as accelerometers, piezoelectric, and fibre optic cables that are used to record the case of a bridge or tunnel strike and effectively transit warning messages to the corresponding authorities to shut down the transportation services around the incident. These sensors measure the dynamic displacement of structures due to a strike and are key to addressing a different aspect of the bridge / tunnel strike problem – unreported strikes.

Driver-based systems reduce the number of bridge / tunnel strikes through increased fines and surveillance and / or better driver education [16]. Infrastructure owners have attempted to reduce the number of bridge / tunnel strike incidents by implementing permits, axle load restrictions, fines, driver education and awareness programs, good practise manuals and protocols. These can have a positive impact with a reasonably low cost and can be easily applied in LMICs. An alternative but more expensive prevention system is also the Geographical Positioning Systems (GPS) which helps optimising the route and identifying low clearance bridges. Modern trends seem to be drifting toward these types of methods as opposed to infrastructure mitigation systems / technology, in an effort to reduce the impact of the problem at source.

3.2 Costs and effectiveness

Valuable qualitative data was obtained from the desk study and first survey for which bridge and tunnel strikes have been recognised as one of the main issues by organisations, especially for infrastructure owners, and one of the main hazards impacting cost and safety of bridges and tunnels.

The second survey aimed to collect quantitative data on strike and countermeasure costs and countermeasure effectiveness. The effectiveness of mitigation measures relates to the percentage reduction in bridge / tunnel strikes due to the implementation of a mitigation measure. For example, presuming static warning signs reduce the number of bridge strikes on average per year from 10 to 8, we would state that static warning signs are 20% effective. A significant amount of information was requested in the surveys to achieve a more effective CBA. However, this proved challenging for stakeholders to retrieve and provide the data requested. It was clear from the stakeholder comments and following stakeholder interviews that the main reason for this was the lack of data storage or the lack of standardisation making it difficult to recover information. This highlights the need for a formalised approach for gathering and processing strike data.

From the data collected in the second survey it was noticed that the quantitative data can vary considerably based on the country and organisation. Additionally, the strike cost breakdown showed that there is not a typical cost breakdown, but that different countries and different types of organisations are subject to unique costs. These considerations lead to the obvious conclusion that average cost and effectiveness values are difficult to calculate and that considering the variability of the data being analysed, each value should be obtained on a case-by-case basis. However, given certain project constraints, average values of costs and effectiveness were calculated to demonstrate the application of the CBA framework. The data obtained from both surveys and the desk study was analysed to obtain an average value for strike cost and strike cost breakdown based on the strike type, and also mitigation measure costs and mitigation measure effectiveness. Strike types were categorised in this study into small, medium and large based on the vehicle and infrastructure damage. Detailed data values obtained from the desk study and surveys are available in the project final report [17].

4 COST-BENEFIT ANALYSIS

4.1 Proposed methodology

The proposed Cost-Benefit Analysis framework gives guidance to road administrators and owners to perform an assessment on their own networks. This methodology has been developed from the point of view of road administrators and aims to compare different mitigation measure scenarios. Different requirements, objectives or data availability might require the framework to be adapted accordingly. The developed methodology allows the road administrator to include, remove or modify the cost and benefit categories considered to suit the particular case analysed.

Figure 1. Cost-Benefit Analysis methodology.

The proposed methodology is subdivided in five different steps (Figure 1): definition of the objective, identification of different scenarios, identification of cost and benefit categories, calculation of costs and benefits, comparison of costs and benefits through their difference or ratio.

Defining the CBA objective from the outset is critical as this will influence the inputs and final outcome.

When multiple scenarios are being considered and need to be compared, it is important to clearly identify the scenarios. The CBA can be performed to determine if a scenario is beneficial or not, and to identify the best option. In this study, several countermeasure scenarios are analysed to provide recommendations on the most suitable mitigation methods. Each scenario is compared to a do-nothing scenario, which assumes that no mitigation measures have been installed and the bridge or tunnel status is unchanged. For this study, these scenarios were analysed for both HICs and LMICs.

Costs and benefits are disaggregated into their constituent parts, which will facilitate the calculation of their values in the later steps. In this study, the do-nothing scenario acts as a reference scenario where costs and benefits have the same overall value, so that their difference and ratio have a predetermined value equal to 0 and 1, respectively. The mitigation measure scenario includes different cost and benefit categories. The cost of a strike is included in the mitigation measure scenario as benefits, interpreted as saved cost due to the reduction in number of strikes after installation of countermeasure selected.

The costs categories identified in this study are:

- Purchase cost [€]: initial cost of purchase of the countermeasure
- Installation cost [€]: installation cost of the countermeasure, including the cost of the labour and the traffic disruption due to its installation
- Maintenance cost [€/year]: annual maintenance cost of the countermeasure, including occasional repairs due to malfunctions, cost of labour and traffic disruption due to its maintenance
- Repair cost due to strike [€/year]: annual repair cost of the countermeasure due to strikes; it includes the cost of the labour, and the traffic disruption costs due to the repair.

The benefit categories identified in this study are:

- Saved cost for infrastructure repair [€/year] due to strikes
- Saved cost for vehicle repair [€/year] due to strikes
- Saved cost for increased infrastructure maintenance [€/year]: cost saved of additional maintenance required after strikes
- Saved cost for emergency services [€/year] in the event of a strike
- Saved cost for fines applied to driver [€/year] in the event of strikes
- Saved cost for traffic disruption [€/year] due to strikes
- Saved cost for loss of business [€/year]: cost saved associated with loss of future business for infrastructure owners in the event of a strike, due to a change in public perception etc
- Saved cost for injuries & fatalities [€/year] in the event of strikes
- Saved environmental costs [€/year] due to strikes.

Cost and benefit values for each category can be estimated from historical data, available data, or data obtained through surveys and interviews. If data is missing, alternative valuation methods need to be adopted, such as theoretical and experimental formulas [18].

It is important to consider costs and benefits across a reasonable length of time, to take both the short- and long-term effects into consideration as costs and benefits will evolve over time. As such a CBA should consider inflation, interest rates, and the net present value (*NPV*) of money. The concept of present value states that a unit of money in the present day is worth more than receiving that amount in the future since today's money could be invested and earn income. Saying that a unit today is worth more than a unit next year is equivalent to saying that a unit next year is worth less than a unit this year. In other words, the future unit has to be discounted to make it comparable to a current unit. An amount of money m in n years, will have a net present value today of:

$$NPV = \frac{m}{(1+r)^n} \quad (1)$$

where r is the discount rate, expressed in %. The *NPV* of a series of benefits or costs $\mathcal{CB}$ from next year (t = 1) to the end of the project ($t = T$) can therefore be summarised as:

$$NPV = \sum_{t=1}^{t=T} \frac{CB}{(1+r)^t} \quad (2)$$

The discount rate r varies based on the country / region, usually being higher for developing countries (8%-15%) than developed ones (3%-7%) [19]. Some of the considered cost / benefit categories are present costs / benefits, referring to the starting time of the project (year 0) and being a one-time rate. Others are future rates, referring to one or multiple years, recurring annually or periodically and applied to the whole length of the project or to only some years.

The total cost of a mitigation measure scenario is defined as C_{tot} and is equal to:

$$C_{tot} = C_p + C_i + C_m + C_r \quad (3)$$

where:

- C_p is the mitigation measure purchase cost. C_p is a present cost paid in year 0;

$$C_p = C_{p,0} \quad (4)$$

- C_i is the mitigation measure installation cost, which includes the labour C_{il} and the traffic disruption costs due to the installation, C_{it}. C_i is a present cost paid in year 0;

$$C_i = C_{il,0} + C_{it,0} \quad (5)$$

- C_m is the mitigation measure maintenance cost including occasional repair costs due to malfunctions, which includes labour (C_{ml}) and traffic disruption (C_{mt}) costs due to maintenance. C_m is an annual cost which must consider a discount rate r from year 0 to n;

$$C_m = \sum_{t=0}^{t=n} \frac{(C_{ml,t} + C_{mt,t})}{(1+r)^t} \quad (6)$$

- C_r is the mitigation measure repair cost due to strike damage, which includes labour (C_{rl}) and traffic disruption (C_{rt}) costs due to repair. C_r can be assumed as an annual or a sporadic cost: in the first case costs and discount rates r are considered for each year from 0 to n, whereas in the second case costs and discount rate are considered only for relevant years. The repair cost depends on the average number of strikes per year $N_{s,av}$ after the mitigation measure installation, which can be defined as

$$N_{s,av} = N_s \cdot (100\% - E_{MM}) \quad (7)$$

where N_s is the average number of strikes per year before the mitigation measure installation, and E_{MM} is the countermeasure effectiveness. Additionally, the repair cost depends on the probability of required repair due to strike ($\%_{repair}$): for example, a sacrificial beam has a higher probability of required repair after a strike than road markings, whose probability of repair can be assumed to be 0%. If the $\%_{repair}$ value is equal to 0%, the C_r value is automatically zero since no cost would be required for the repair. In formula (8) only costs of relevant years should be considered, assuming a cost of 0 for the excluded years.

$$C_r = N_{s,av} \cdot \%_{repair} \cdot \sum_{t=0}^{t=n} \frac{(C_{rl,t} + C_{rt,t})}{(1+r)^t} \quad (8)$$

The total benefit of a mitigation measure scenario is defined as B_{tot} and is equal to:

$$B_{tot} = E_{MM} \cdot S_{MM} \cdot C_{s,tot} \quad (9)$$

where:

- E_{MM} is the mitigation measure effectiveness
- S_{MM} is the mitigation measure suitability, expressed in %, defined as the appropriateness of a mitigation measure to be adopted in a specific socio-economic region or country. This variable aims to consider that a countermeasure might not be the most suitable for a country, for example due to its advanced technology. In a low-income country, basic methods might be preferred
- $C_{s,tot}$ is the total cost due to strikes to be borne by the road administrator for n years. $C_{s,tot}$ is an annual cost that needs to consider a discount rate r from year 0 to n. It depends on N_s which is the number of strikes per year without mitigation, C_s which is the cost for a single strike and $\%_{recover}$ which is the percentage of money recovered by the road administrator for example through insurance or from the vehicle owner / manager

$$C_{s,tot} = N_s \cdot (100\% - \%_{recover}) \cdot \sum_{t=0}^{t=n} \frac{C_{s,t}}{(1+r)^t} \quad (10)$$

C_s represents the cost of a single strike, which can be defined as the sum of:

- C_{sri} is the infrastructure repair cost due to a strike, including labour and traffic disruption / delay
- C_{srv} is the struck vehicle repair cost
- C_{sm} is the increased infrastructure maintenance cost due to a strike
- C_{ses} is the emergency services cost
- C_{sf} is the cost of fines applied to the driver
- C_{st} is the cost of traffic disruption & delays due to the strike
- C_{sb} is the cost of loss of business for infrastructure owners in the event of a strike
- C_{sc} is the cost of fatalities and injuries in the event of a strike
- C_{sen} is the environmental cost caused by a strike.

There must be a reasonable amount of flexibility in how these costs are considered. Owners may wish to apply percentages of recovery to the individual categories of C_s, where one category may be more likely to have cost recovery than others. Only costs which are of interest to the organisation carrying out CBA should be considered, and particular attention should be paid to certain cost categories that may overlap and that might be double counted.

Specific factors and costs described above might be subject to variation based on the socio-economic region and on the type of strike. If sufficient data is available, category values could also be calculated for different strike types, where costs and benefits could be defined as follows:

$$C_{tot} = C_{tot,small} + C_{tot,medium} + C_{tot,large} \quad (11)$$

$$B_{tot} = B_{tot,small} + B_{tot,medium} + B_{tot,large} \quad (12)$$

The outcome of a CBA is a comparison of the benefits and costs of the project and can be expressed as:

- economic efficiency, difference between benefits B and costs C *(B-C)*
- benefit-cost ratio, ratio between benefits B and costs C *(B/C)*.

In both cases, the aim is to maximise the difference or ratio between benefits and costs. CBAs with positive economic efficiency and / or benefit-cost ratio higher than 1 can be considered as economically advantageous. When different scenarios are compared, the option with higher economic efficiency and / or benefit-cost ratio is the most profitable. Both economic efficiency and benefit-cost ratio provide relevant information on the case being analysed, but it is important to use reason in the result interpretation. The economic efficiency represents the net profit of the project and the additional resources available, whereas the benefit-cost ratio represents the overall relationship between the relative costs and benefits.

4.2 Application of CBA framework

A semi-quantitative CBA has been carried out on a typical structure with the aim to make broad recommendations at global level on the best mitigation measures for a given socio-economic region, based on road administrators' and owners' point of view. These recommendations aim to inform different socio-economic regions on the mitigation measures that may most commonly be applied, but should not prevent the individual region from considering and evaluating the use of other measures at certain sites. It is indeed suggested that a CBA is carried out on a case by case basis to better take into consideration the unique factors characterising the analysed site. The data being used in the CBA was collected from the first and second surveys or obtained from the desk study.

Average values of strike costs, strike cost breakdown, mitigation measure costs and mitigation measure effectiveness were calculated and the probability of a mitigation measure repair due to a strike and the related mitigation measure repair cost have been assumed based on survey data, desk study and engineering judgement [17].

The CBA was carried out with averages representing typical situations for a typical structure strike in HICs. Recommendations for both HICs and LMICs are based on the outcome of the CBA. The CBA has considered a time study of 10 years, assuming a total number of strikes per structure per year of 0.12, where 60% are small type strikes, 30% medium type strikes and 10% large type strikes. The discount rate has been assumed as 5% for HICs based on available literature. A discount rate of 12% is suggested for LMICs. The mitigation measure suitability has been assumed as 100% for all mitigation measures in HICs, but a lower value is suggested for more advanced mitigation measures in LMICs.

Analysing the results obtained from the CBA, the mitigation measures can be subdivided into three categories based on the benefit-cost ratio:

- Low benefit-cost ratio: benefit-cost ratio is below 0.2
- Medium benefit-cost ratio: benefit-cost ratio is between 0.2 to 1
- High benefit-cost ratio: benefit-cost ratio is higher than 1.

Mitigation measures found to be in the low benefit-cost ratio category are listed in Table 1.

Table 1. Low benefit-cost ratio mitigation measures category in HICs.

Mitigation Measure	B/C ratio
Increased structure vertical clearance	0.02
Laser vision	0.03
Variable message signs (VMS)	0.04
Road narrowing techniques	0.06
Hanging chains or bells	0.10

Hanging chains or bells are relatively expensive and have a relatively low effectiveness since they do not avoid the strike but only warn a driver of the danger ahead. If used in combination with other countermeasures however, hanging chains or bells could be cost-effective for particular scenarios. The other mitigation measures listed are relatively expensive, and even though their effectiveness is high, the CBA suggests these measures not to be cost-effective. However, it must be noted that the CBA carried out in this section refers to a typical structure. These latter types of mitigation measures are recognised to be best suited for more important and critical nodes on the network and are also normally only appropriate for sites that are prone to strikes and severe damage, as evidenced by prior occurrences. In these scenarios a customised CBA would be likely to show cost-effectiveness.

The mitigation measures which were found to be in the medium benefit-cost ratio category are listed in Table 2. In general, these mitigation measures can be more expensive, less effective or require more maintenance and repair. For example, crash sacrificial beams are very effective in avoiding the infrastructure being struck, but are not effective in avoiding the occurrence of strike events, which have additional costs and disruptions. A combination of some of these mitigation measures may prove beneficial to have a higher effectiveness and reduce installation, maintenance and repair costs by simultaneously carrying out these works.

Table 2. Medium benefit-cost ratio mitigation measures category in HICs.

Mitigation Measure	B/C ratio
Crash sacrificial beams	0.22
Cameras and computer vision techniques	0.23
Accelerometers, piezoelectric sensors and fibre optic cables	0.49
Infrared dual beam arrays LaRa-OHVD systems	0.55
Bridge markings	0.57
Rumble strips	0.99
Speed bumps	0.99

The mitigation measures which were found to be in the high benefit-cost ratio category are listed in Table 3.

Table 3. High benefit-cost ratio mitigation measures category in HICs.

Mitigation Measure	B/C ratio
Static signage	1.39
Clear heights signage and obstacles related to dimensional loads	1.48
Beacons	1.55
Flashing beacons and / or lights	2.12
Vehicle redirection in case of excessive dimensions	2.12

These mitigation measures have low purchase, installation and maintenance costs and are often mandatory measures at a low height structure location. It is not then surprising that these measures are strongly recommended solutions to prevent and reduce the bridge and tunnel strike issue.

Finally, consideration should be given to the prominent driver-based mitigation measures including media campaigns, increased fines and surveillance, heavy vehicle goods licence test, better driver education, good practice manuals, pre-routed maps, and increased restrictions on vehicle dimensions. These mitigation measures were not included in the CBA results since they are not implemented for a single structure, but for an entire network. The benefit-cost ratio for these categories is very high since the purchase and installation costs are diluted for the whole network, resulting an extremely cost-effective solution.

It should be noted that in applying the framework, assumptions and generalisations were made. A typical structure was considered as representative of the whole network, inevitably excluding more critical structures. Equally, each mitigation measure was considered to be individually applied to the structure, while in reality a combination of countermeasures is often used. Notwithstanding this fact, the proposed CBA methodology serves as a useful tool to undertake an initial comparative assessment of a particular measure and / or measures. Furthermore, it is recommended to

carry out a CBA on a case by case basis, to better represent the system analysed.

5 CONCLUSIONS

This study examined proven countermeasures, practices, and technologies used to reduce the incidence of oversize vehicles striking bridges and tunnels. A desk study, two detailed surveys and stakeholder interviews provided the information and data to develop a detailed CBA methodology and apply it on a typical structure at a global level to identify the relative appropriateness of various countermeasures and make recommendations.

The stakeholder engagement highlighted that although many organisations have data available, the data is not stored in a coordinated way which can limit the effectiveness of a CBA. It is recommended that a formalised method of recording data strikes should be developed.

The CBA performed for HICs showed that lower cost systems, (Table 3), appear to be the most universally recommended physical solutions for mitigation. Although a number of mitigation systems were found to be in a low benefit-cost ratio category (Table 1), this is due mainly to the global nature of the analysis performed and may not be considered a realistic interpretation of the value of these high cost systems. Although it is beyond the scope of this paper, it should be noted that sample CBAs at a site-specific level were carried out in the project adopting a combination of mitigation measures in the different benefit-cost ratio categories. These showed that the adoption of an appropriate combination of mitigation measures at a problem site can be extremely cost-effective and emphasise the need to carry out site specific CBAs.

It is recommended that HICs continue to ensure adequate basic mitigation measures in the high and medium benefit-cost ratio categories and more advanced technology in certain high-profile sites. For LMICs the most beneficial mitigation measures are those in the high benefit-cost ratio category. While LMICs already install overheight clearance signage at structures, this signage is often outdated, obscured or damaged. Hence, it is recommended that further efforts be made to ensure signage is maintained and legible, particularly at high-risk structures. Adoption of a CBA methodology is recommended to road administrators similar to that presented herein, even in a simplified form and particularly for critical nodes that have experienced previous strikes of high severity damage. The development of a multi-sectoral panel to address and share / disseminate knowledge on the issue is recommended to road administrators and governments in both HICs for the short term and LMIs for the long term. Involvement from road administrators, hauliers, government, and police in a collaborative way is essential. The primary goal of the panel would be to provide better driver education, advertising of the consequences and informing legislation in relation to the bridge / tunnel strike problem. Adoption of mitigation measures is still essential and required in vulnerable sites.

Finally, while drivers' education, advertising and engagement are essential to address the issue, enhancements to vehicle technologies are required considering that in the majority of strike cases, the driver appears to be at fault. Future technologies were found to have significant promise in tackling the bridge / tunnel strike problem. For this reason, for HICs it is recommended in the long term, more research is required to demonstrate the effectiveness and enhance the TRL of these systems.

ACKNOWLEDGMENTS

The presented work was funded by the World Road Association (PIARC) under the "Bridge and Tunnel Strikes by Oversized Vehicles" Special Project. This project was defined in the PIARC Strategic Plan 2020–2023 and approved by the Council of the World Road Association.

REFERENCES

[1] B. Nguyen and I. Brilakis, "Understanding the Problem of Bridge and Tunnel Strikes Caused by Over-Height Vehicles," *6th Transport Research Arena*, vol. 14, pp. 3915-3924, 2016.

[2] M. D. Fontaine, "Engineering and Technology Measures to Improve Large Truck," Virginia Transportation Research Council, Charlottesville, Virginia , 2003.

[3] S. Mattingly, "Mitigating overheight vehicle crashes into infrastucture: a state of practice.," in *Proceedings of the 82 nd Annual Meeting of the Transportation Research Board*, Washington, D.C., 2003.

[4] T. Horberry, M. Halliday and A. G. Gale, "Bridge strike reduction: optimising the design of markings," *Accident Analysis & Prevention*, vol. 34, no. 5, pp. 581-588, 2002.

[5] M. Kumar, S. Albert and D. Deeter, "A Summary of Rural Intelligent transportation systems (ITS) benefits as applied to ODOT region 1," Oregon Department of Transportation Region 1, 2005.

[6] A. Byrne, "Special Topics Report - Railway Bridges in Ireland & Bridge Strike Trends," Railway Safety Commission, Dublin, Ireland, 2009.

[7] B. Nguyen, *Vision-Based Over-Height Vehicle Detection for Warning Drivers*, Doctoral dissertation, University of Cambridge, 2018.

[8] Transport Asset Standards Authority, "Bridge Impact Protection," Transport Asset Standards Authority, New South Wales, 2020.

[9] TRIGG Industries International, *Overheight vehicle detection and warning systems*, TRIGG Industries International, 2015.

[10] A. Singhal, *LaRa-OHVD: An Innovative Over-Height Vehicle Detection System to Protect our Bridges to Prosperity*, New York: A student essay submitted for ITS-NY 2015 Best Student Essay Competition at 2015 Intelligent Transportation Society of New York 22nd Annual Meeting, 2005.

[11] I. Urazghildiiev, R. Ragnarsson, P. Ridderstrom, A. Rydberd, E. Ojefors, K. Wallin, P. Enochsson, M. Ericson and G. Lofqvist, "Vehicle classification based on the radar measurement of height profiles," *IEEE Transactions on intelligent transportation systems*, vol. 8, no. 2, pp. 245-253, 2007.

[12] Laservision, "SOFTSTOP™ Barrier System, Australia," Laservision, [Online]. Available: https://www.laservision.com.au/portfolio/softstop/. [Accessed 26 July 2021].

[13] M.-W. Park, F. Dai, M. J. Sandidge and I. Brilakis, "Vision-based approach for Measuring On-Road Truck Heights," *Creative Construction Conference*, pp. 587-596, 2013.

[14] F. Dai, M.-W. Park, M. Sandidge and I. Brilakis, "A vision-based method for on-road truck height measurement in proactive prevention of collision with overpasses and tunnels," *Automation in Construction*, vol. 50, pp. 29-39, 2015.

[15] P. K. Patil and S. Patil, "Structural health monitoring system using WSN for bridges," *2017 International conference on intelligent computing and control systems (ICICCS)*, pp. 371-375, 2017.

[16] M. Wheel, *Bridge Strikes - Risk, Consequences and Costs*, Network Rail, 2020.

[17] L. Connolly, I. Bernardini and E. Kakouris, "Bridge and Tunnel STrikes by Oversized Vehicles," World Road Association (PIARC), 2021.

[18] R. J. Brent, Applied Cost-Benefit Analysis, Edward Elgar Publishing, 2006.

[19] Asian Development Bank, Cost-Benefit Analysis for Development: A Practical Guide, Asian Development Bank, 2013.

Finite element modelling of the Loopline Bridge and model validation using ground-based radar interferometry

Conor Flannery[1], Paraic Quirke[2], Cathal Bowe[3], Abdollah Malekjafarian[4]
[1]AECOM, One Trinity Gardens, Broad Chare, Newcastle upon Tyne, NE1 2HF, United Kingdom
[2]Murphy Geospatial, Global House Business Campus, Kilcullen, Co. Kildare, R56 K376, Ireland
[3]Iarnród Éireann Irish Rail, Technical Department, Engineering & New Works, Inchicore, Dublin 8, D01V6V6, Ireland
[4]School of Civil Engineering, Newstead, University College Dublin, Dublin 4, Ireland
email: conor.flannery@aecom.com, pquirke@murphysurveys.ie, cathal.bowe@irishrail.ie, abdollah.malekjafarian@ucd.ie

ABSTRACT: This research investigates the procedure of using ground-based radar interferometry to develop and validate a finite element model of the Loopline Bridge in Dublin, Ireland. A description of the bridge is outlined and a three-dimensional finite element model was developed using RFEM, a commercial software package. The modelling approach was first validated against known theoretical solutions. The bridge model was then verified with section property calculations, experimental studies in the literature and deflection tests. The dynamic deflection at midspan of the Loopline Bridge was measured for two train crossing events using ground-based radar interferometry. A single train crossing event showed the deflection of the loaded side of the span with respect to the unloaded side. Additionally, a dual train crossing event demonstrated the twist in the deck from the train loads travelling in opposite directions on separate sides of the bridge. The same loading conditions were simulated in the finite element model and the resulting deflections were extracted. A comparison between both sets of deflection data was carried out and their correlation validated that the model accurately captures the behaviour of the real Loopline Bridge structure for both train loading scenarios.

KEY WORDS: Bridge; Finite Element Model; Model Validation; Radar Interferometry; Deflection;

1 INTRODUCTION

Bridges are among the most complex and important structures in modern transportation systems and crucially require maintenance and monitoring for both safety and economic reasons. Finite element (FE) models are regularly used in modern engineering for the structural analysis of bridges. FE models cannot solely predict the actual behaviour of such structures. The accuracy of FE modelling strongly depends on the experimental validation of the numerical results [1]. Therefore, a validation process is required which introduces the actual condition of the structure under observation, to synchronise the FE model and increase its accuracy [2]. This research aims to investigate the procedure of using ground-based radar interferometry to develop and validate a finite element (FE) model of the Loopline Bridge in Dublin.

Ground-based radar interferometry is a newly established, non-destructive, powerful remote sensing technique that can measure the vertical and horizontal deflection of several points on a structure to a sub-millimetre accuracy, within a 500 m range [3].This method of measurement has several advantages compared to conventional sensors; including its high accuracy, being remote and non-intrusive, and its ability to be carried out from a great distance over a short period of time [4],[5]. Disadvantages include the effects of the environment on its accuracy, only 1D imaging capability, and the high cost of the device which typically results in rental of the equipment for any research or use. For this technique, the radar instrument generates and transmits electromagnetic waves from its antennas with a high frequency. The system then measures the radial displacement of specific target objects by comparing the phase differences between the emitted and reflected electromagnetic signals from an object, at different moments in time [6]. The vertical displacement is then computed using simple trigonometry, typically processed by the built-in software of the device on site. Figure 1 illustrates this process.

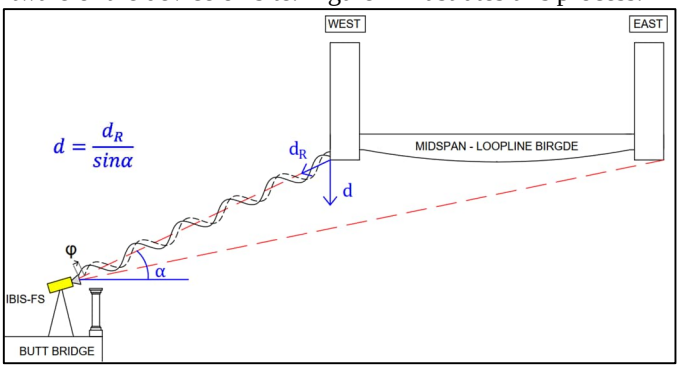

Figure 1. Radar interferometry working principle on Loopline Bridge; phase difference (φ) of radar waves to find radial displacement (dR) to determine vertical displacement (d).

The Loopline Bridge, originally constructed between 1889 and 1891, is a wrought iron lattice truss girder bridge in the centre of Dublin City. The five span viaduct structure carries two curved ballasted tracks of the active Dublin loop line over the River Liffey in addition to several roads and streets. Restoration works were carried out to the structure between 1958 and 1960 which comprised the replacement of the trough deck with welded steel stringer beams to a flat deck plate, and the replacement or reconditioning of several cross girders. The 36 m single-span section of the bridge over the River Liffey will be considered and focused on for the purpose of this paper, shown in Figure 2. Detailed drawings for the construction and refurbishment of the bridge, and specific railway vehicle information was provided and utilised for this research courtesy of Iarnród Éireann Irish Rail.

Figure 2. The Loopline Bridge span over the River Liffey.

The dynamic deflections of the Loopline Bridge under operational conditions were measured using a ground-based radar interferometer, carried out by Murphy Geospatial. Two train loading events of interest were analysed – a single and dual train crossing event.

An FE model is developed and the modelling approach is analysed with comparisons to known theoretical solutions for a simply supported beam with various loads applied. A two-dimensional model was first formed and verified before the development of the three-dimensional model. The FE model is verified with cross-sectional property calculation checks, simple deflection loading tests and experimental truss deflection tests from the literature. Lastly, the final model is validated with the real deflection measurements of the bridge obtained using the ground-based radar interferometry device.

It was found that the developed FE model accurately imitates the behaviour of the Loopline Bridge for both train crossing events. The deflections of the FE model are shown to correlate with those measured on the real bridge using the ground-based radar interferometric device. The limitations of the research include the secondary sourced experimental data and the assumptions made in the FE modelling due to the unknowns associated with the bridge structure and train loading.

2 DEFLECTION MEASUREMENTS USING RADAR INTERFEROMETRY

2.1 Experimental setting

The dynamic deflections of the Loopline Bridge under operational conditions were measured in an experiment by Murphy Geospatial on 30th January 2018, using a commercial IBIS-FS interferometric radar, photographed in Figure 3. The device was set up on the adjacent Butt Bridge (see Figure 1) which provided the best line of sight for the radar to measure the midspan deflection of the structure at both sides. Other impactful characteristics such as weather conditions, proximity and visibility of the structure were favourable.

Figure 3. Interferometric radar set up at the Loopline Bridge.

2.2 Experimental crossing events and loading

The dynamic bridge responses of two train crossing events are focused on for the purpose of this paper. It should be noted that the deflection measurements obtained by the interferometer are with reference to the unloaded, static deflection of the bridge due to its self-weight.

Crossing event No. 1 lasts for 31 seconds and consists of a southbound DMU (Diesel Multiple Unit) arriving first onto the east side of the span before a northbound EMU (Electrical Multiple Unit) DART (Dublin Area Rapid Transit) arrives shortly after, travelling in the opposite direction on the west side of the bridge. The DMU exits the bridge span first, before the EMU exits, causing both sides of the span to be individually and simultaneously loaded at different stages of the crossing event.

Crossing Event No. 2 lasts for 60 seconds and features a northbound EMU arriving onto the west side of the span for the full duration of the event leaving the east side unloaded throughout.

The railway vehicles that crossed the bridge during the crossing events, were identified through observation. The specific vehicle classes were estimated and considered to be a four-axle 29000 class DMU and a four-axle 8200 class EMU, due to their median wheel loads. Figure 4 illustrates the axle and wheel loads of for these vehicles. It should be noted that an expected variation in loading during the day due to passengers or luggage was unknown and therefore not considered.

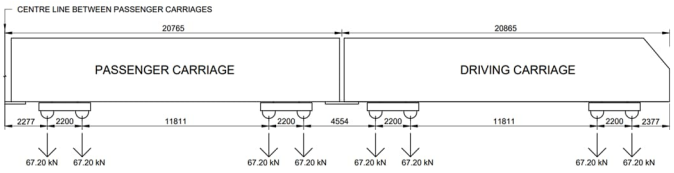

a) 29000 Class DMU (all dimensions in mm).

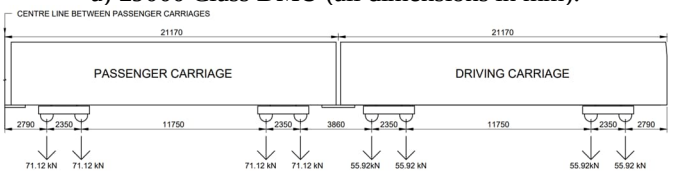

b) 8200 Class EMU (all dimensions in mm).

Figure 4. Typical axle spacing and loading of Iarnród Éireann railway vehicles DMU (a) and EMU (b).

2.3 Ground-based radar interferometry measurements

The midspan vertical deflections of both edges of the bridge were captured and analysed. The dual train crossing event demonstrated the twist in the deck from the train loads travelling at different times, in opposite directions and on separate sides of the bridge. The single train crossing event showed the deflection of the loaded side of the span with respect to the unloaded side. The displacements over time graphs for both train crossing events are shown in Figure 5 and Figure 6. The timing for each event is considered to have started when the first train enters onto the span of the bridge.

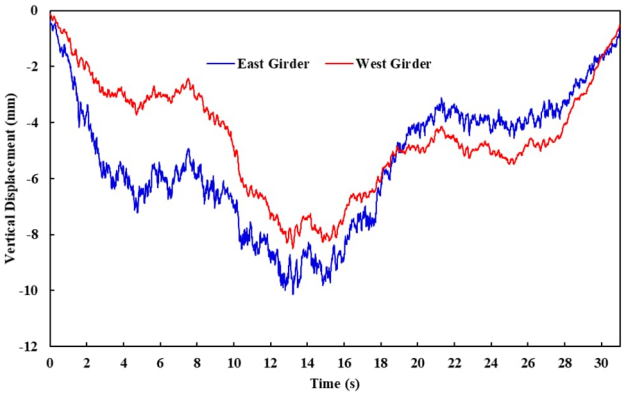

Figure 5. Crossing event No. 1 measured midspan deflections.

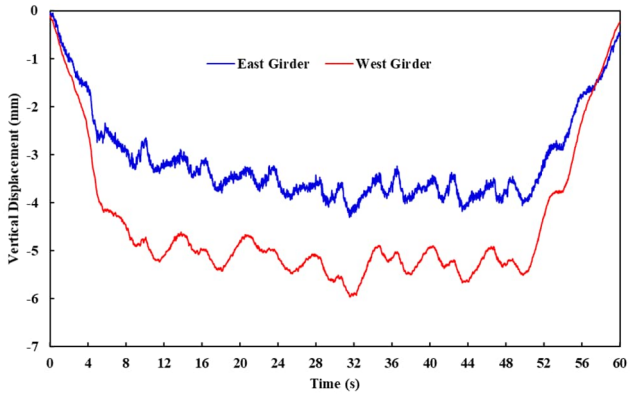

Figure 6. Crossing event No. 2 measured midspan deflections

3 FINITE ELEMENT MODEL

3.1 Modelling method

An FE model of the Loopline Bridge was developed using RFEM, a commercial software package. Typically, it is advised to simplify FE models down to one or two-dimensional structure models, however a three-dimensional model was chosen for the purpose of this study with the objective to model the twist of the deck caused by the two, oppositely moving loads from the dual train crossing event No. 1.

The FE model has been developed using nodes and lines in a three-dimensional plane. Relevant member cross sections were created and assigned to the model lines using beam elements. The FE modelling approach was first validated against known theoretical solutions. A simply supported beam was modelled and analysed with various load cases applied, with the expected deflections calculated theoretically for comparison. The FE beam model gave identical results to the theoretical solutions, hence validating the modelling approach.

3.2 Loopline Bridge model

For all associated models; structure arrangement, section properties and both global and local element support conditions were input to reflect that of the as-built structure.

Material properties for the model elements were adopted from known steel characteristics in the 1960s period, from when the structure underwent reconditioning, and the wrought iron was inevitably replaced by steel [7]. Steel S355 was therefore considered for all structural materials within the model. No self-weights were active in the model to allow for the deflection results to be only due to the live loading, and comparable with those measured by the radar interferometer.

A simplified two-dimensional FE model of the bridge consisting of one truss girder was first created to ensure the model behaved as expected. The model was created using nodes and lines to which element members were assigned, see Figure 7. Loading of a single typical railway vehicle was idealised and applied to the bottom chord elements of the model. Satisfactory midspan deflection results were observed in the model when compared to the measured maximum deflection from crossing event no. 2. This model represents half of the structure and experienced the load of one railway vehicle - half of the crossing event's loading.

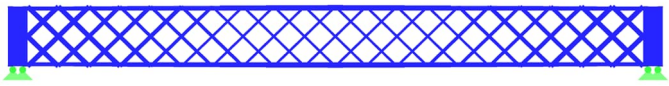

Figure 7. Two-dimensional truss girder FE model.

After the 2D model gave satisfactory deflection results, a three-dimensional FE model was developed in the same manner, shown in Figure 8. The supports at one end were fully fixed while the supports at the other were fixed but allowed longitudinal translation, in line with the details of the real-life structure.

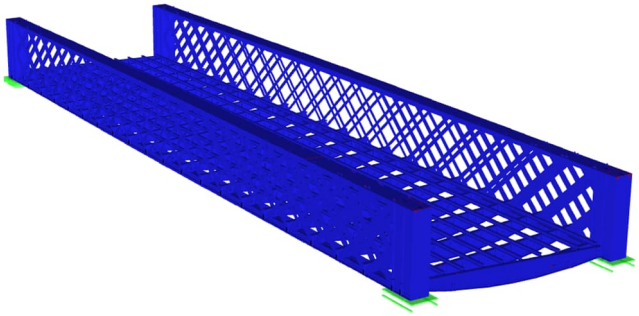

Figure 8. 3D Loopline Bridge FE model.

The 3D model accurately represents the articulation of the superstructure; two truss girders supporting twenty-two transverse cross girders from the bottom chords. Longitudinal steel stringer beams were modelled, supported by the cross girders, to allow for the application of moving loads to the FE model. Furthermore, the steel stringers assisted with the application of moving loads in addition to the longitudinal distribution of loads, Load distribution helped to prevent localised deflections, and partially provided the structural role of the bridge deck which was unknown and out of the modelling scope.

3.3 Model verification

FE modelling is only an approximation and is not completely robust so requires a model verification process to identify any small errors that could impact the results. The 3D FE model was first verified in terms of the element cross-sectional properties. The automatically calculated section properties from RFEM were comparable to those obtained using equations from First Principles. Secondly, simple deflection tests were carried out on the model to assure it deflected appropriately and expectantly. Point loads were applied to the midspan of the cross girders at central and quarter span of the truss girders, and separately to the truss girders at midspan and quarter span. Deflections were extracted at points where loads were applied. The deflection results from a 50kN point load applied to the central two cross girder at midspan are shown in Figure 9.

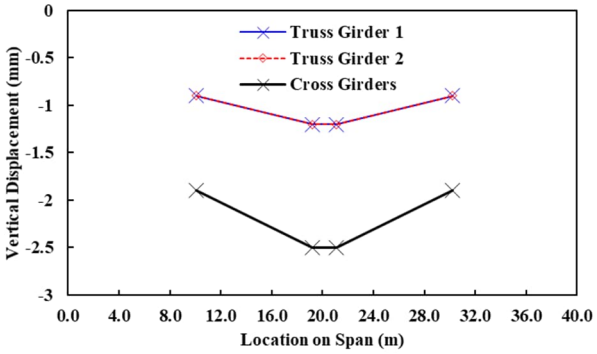

Figure 9. Model deflections due to loads on cross girders.

Lastly, deflections observed by the model were validated against three experimental truss structure deflection tests found in the literature. One of these studies considered a 4 kN/m^2 load applied to the centre third of a 48.8 m steel truss pedestrian footbridge [8]. To compare with the results from the literature, the self-weight of the model was active and representative loads were applied along the FE model's cross girders to replicate uniform loading on a deck. The deflections of the model were measured at the same locations with respect to the span as those from the experiment – quarter and mid span. The deflection curve comparison is shown in Figure 10.

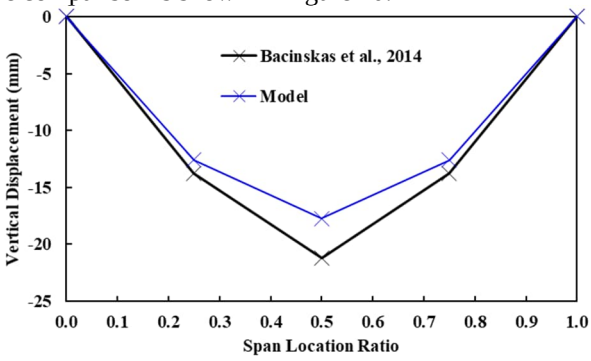

Figure 10. Deflection curve comparison with literature.

Removing these variables (loads and measurement location) allowed for a stronger comparison in the deflections. However, several variables were still present; span, width, build and material, and so the purpose of this test was not to compare deflection magnitudes but the deflection curves themselves.

3.4 Model validation with ground-based interferometry measurements

As previously discussed, every FE model should be verified based on experimental data or a mathematical approach to conform to reality. Simplification is inevitable in computer-aided modelling approaches which may cause some disparity between the real and modelled case. In this paper, the ground-based radar interferometric measurements are used to calibrate the behaviour of the model.

Identical loading conditions to those illustrated in Figure 4 were introduced into the RFEM model. These loads are treated as static loads with a moving step of 1.5 m. Specific loading details were not precisely recorded during the experimental crossing events which resulted in several additional unknown factors. Firstly, the exact times for each train entering the span for crossing event No.1 were unknown. Estimates of these critical times were made through analysing the radar interferometry deflection measurements (Figure 5). The timing for the single vehicle crossing event No. 2 was easily obtained from available video footage.

While the number of carriages and therefore axle loads present during crossing event No. 2 was easily obtained from the video footage, this was unknown for crossing event No. 1. To estimate the number of carriages, an iterative approach was employed to align modelled loading and resulting deflections with the measured deflections of the radar interferometer. Static deflections were measured in the model with point loads, representing the axle weights of the vehicles, moving along the structure in steps of 1.5 m. This step count was used consistently for all modelled vehicle loads with only the number of carriages being adjusted. It was determined that the EMU had eight carriages for both events and the DMU had six carriages for crossing event No. 1. These carriage numbers are within the standard Iarnród Éireann fleet carriage ranges and therefore conform to reality and to the likely loading.

To compare the model deflections with those measured, the number of static load cases required to have the loads move over the bridge was translated into the time taken for the actual crossing events to occur. The final velocities for all railway vehicle loads in the model for both crossing events was approximately 32 km/h, aligning with the low-speed restrictions of the line at this location.

4 RESULTS & DISCUSSION

Deflections were extracted from the model at the midspan of both truss girders for the two crossing event loading cases. These points of interest correspond with the points on the bridge measured by the ground-based radar interferometer and so can be compared accordingly. An example of the deformed three-dimensional FE model for a typical load case during the moving simulation of the first crossing event is portrayed in Figure 11. Each wheel load is assumed to distribute equally to two longitudinal steel stringers, therefore each axle is represented by four point loads, each applied to one steel stringer.

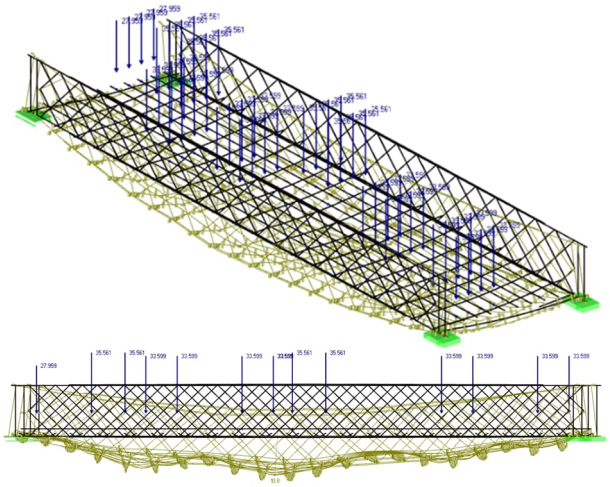

Figure 11. Final 3D FE bridge model deflection results: 3D projection (above) and elevation (below) (300 scale factor).

The deflection results extracted from the model for the simulation of both crossing events are presented in Figure 12 and Figure 13 accordingly.

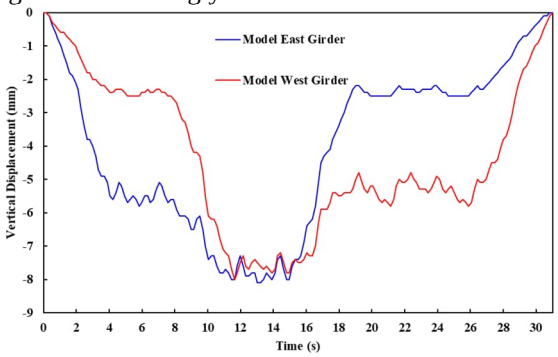

Figure 12. 3D FE bridge model deflection results for crossing event No.1

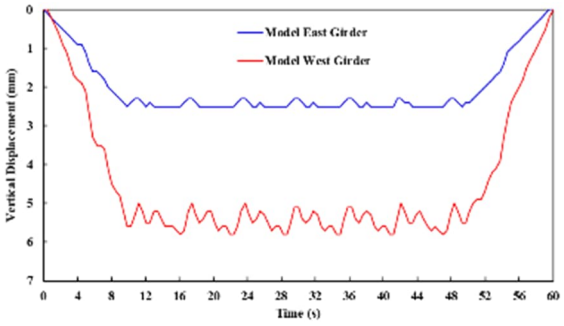

Figure 13. 3D FE bride model deflection results for crossing event No.2

4.1 Verification of model

The objective of this research was to develop a three-dimensional FE model of the Loopline Bridge and validate it with the measured midspan deflections obtained using ground-based radar interferometry. Midspan deflection from the FE model have been analysed and compared with the actual measured deflections of the span for both railway vehicle crossing events. Both sets of data demonstrate strong correlation between the performance of the model and the real deflections experienced by the bridge.

The model verification process, most noticeably checking the cross-sectional properties against theoretical calculated values, was deemed effective. This verification check identified several issues which were initially causing the model to show extremely localised deflections. Additionally, the global deflections of the model were verified with simple loading tests and were comparable to experimental truss deflections found in the literature.

4.2 Modelled and measured deflections

The measured dynamic deflections from the ground-based radar interferometer and the FE modelled static deflections for both crossing events were analysed. As the exact loading on the bridge is unknown, it is difficult to comment specifically on the accuracy of the results, however, the results will be compared and discussed holistically.

The modelled and measured deflections for the dual train crossing event No.1 are portrayed in Figure 14.

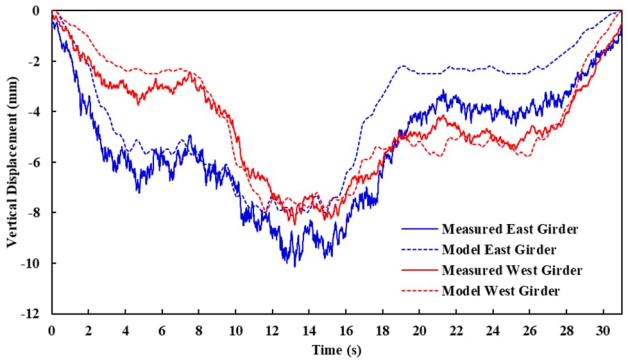

Figure 14. Deflection comparison for crossing event No.1.

As the DMU railway vehicle first loads the east side of the span, the measured deflections for both girders are marginally greater than the modelled deflections, until they get closer as the EMU enters from the opposite side after 7.5 seconds. Both sets of deflections are then relatively equal for a short period of time until the east girder begins showing a 1.5mm difference in magnitude. A strong correlation in the timing of changes in deflections is seen throughout for both girders. The results show the model effectively simulates the torsion or 'twisting' of the bridge deck due to different sides of the span being loaded at different times. This is shown with the alteration of span side with maximum deflection, changing from the east girder to the west.

Additionally at the start of the event, the deflection of the loaded (east) side is twice as large in magnitude as the unloaded (west) side in both the model and the bridge indicating an accurate simulation of the degree in twist of the deck. The model repeats this same degree of twist with the west girder loaded at the end of the event, however this does not align with the bridge itself.

The measured and modelled deflection for the single EMU railway vehicle crossing event No. 2 is presented in Figure 15.

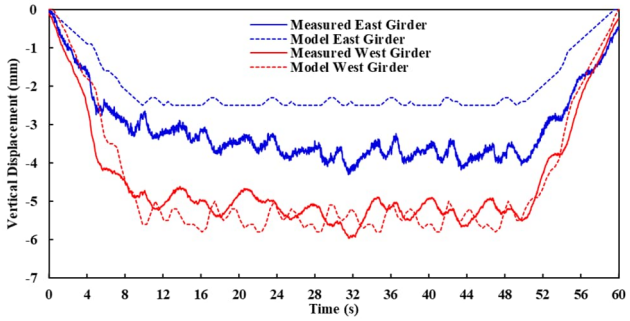

Figure 15. Deflection comparison for crossing event No.2.

The deflection of the model for this crossing event shows similar correlation with the measured deflection, notably for the loaded west side and girder. The deflection of the unloaded side is less comparable. The deflections for both girders are seen to fluctuate within a similar range and at equal occurrences, with the modelled east girder fluctuating in opposite directions to the measured.

Results from both crossing events for the model show strong association with the interferometry measured data. However, a consistent discrepancy is seen for the comparison of deflections for both crossing events when the west girder is solely loaded.

Both sides of the FE model are expected to behave relatively equally when either side of the span is individually loaded with loads of similar magnitude. Despite the skew, the approach in geometry of the bridge is identical for both vehicle directions on each side of the span. Therefore, it is likely that the inconsistency of the real bridge is due to unsymmetrical structural behaviour due to factors not accounted for in the model such as bearing issues, defects or construction errors.

4.3 Limitations and recommendations for future work

Several limitations have influenced the accuracy of these results both in the reliability of the experimental data and some unknown variables in the development of the FE model. Firstly, the measured bridge deflections are a secondary source of data, carried out prior to this research. Additionally, dynamic displacement measurements are compared to static deflections of the model, creating a source of error due to the influence from the dynamic amplification phenomenon. Applying dynamic loads to the model was not within the scope of this research. Lastly, the rail vehicle classes and crossing event timings required estimations, and the inevitably present additional loading due to passengers or luggage was unknown and therefore not accounted for.

It is recommended that further work is carried out to improve the accuracy of the research results. More known and controlled dynamic loading should be applied in the model for improved accuracy. Additional parameters such as transverse or longitudinal deflections, vibrations, and natural frequencies of the bridge could also be incorporated into further studies for a more precise model validation. Ground-based radar interferometry can be used to measure vibrations of the structure, however, it is recommended that further research should be first carried out on its accuracy through a comparative analysis with other conventional sensory systems.

5 CONCLUSION

This paper focused on the procedure of using ground-based radar interferometry to develop and validate a FE model of the Loopline Bridge in Dublin, Ireland. Ground-based radar interferometry is a newly researched, powerful, remote sensing technique that accurately and rapidly measures the deflection of structures under live loads. By analysing the measured dynamic deflections of the Loopline Bridge and showing a correlation with the deflection of the FE model, this study validates the accuracy of the developed model in relation to the ground-based radar interferometry measurements. Several assumptions made in the modelling process were defined with reference to their limitations on the outcome of the research. The final, validated model was found to represent the behaviour of the real Loopline Bridge structure which was confirmed through a comparison of the real and modelled deflections. Recommendations for future work is given to improve the accuracy of the research and reduce the limitations.

Ground-based radar interferometry is an invaluable remote sensing technique for structure asset owners like Iarnród Éireann, who have used the process frequently on structures after the success of these experimental measurements. Despite the equipment's high cost, benefits from economies of scale could be made if the methodology and equipment were more accessible, making the process more cost-effective.

ACKNOWLEDGMENTS

The authors acknowledge the support from Murphy Geospatial for carrying out and providing the experimental data, and to Iarnród Éireann Irish Rail for providing relative information on the Loopline Bridge and railway vehicles. The authors would also like to thank the management of AECOM Newcastle upon Tyne for supporting the publication of this paper.

REFERENCES

[1] D. Ribeiro, R. Calçada, R. Delgado, M. Brehm, and V. Zabel, "Finite element model updating of a bowstring-arch railway bridge based on experimental modal parameters," Engineering Structures, vol. 40, pp. 413-435, 2012.

[2] A. M. Alani, M. Aboutalebi, and G. Kilic, "Use of non-contact sensors (IBIS-S) and finite element methods in the assessment of bridge deck structures," Structural Concrete, vol. 15, no. 2, pp. 240-247, 2014.

[3] IDS GeoRadar, "IBIS-FS - An innovative sensor for remote monitoring of structural movements and deformations," ed. Pisa, 2017.

[4] P. Quirke and A. Barrias, "Validation Of Finite Element Light Rail Bridge Model Using Dynamic Bridge Deflection Measurement," 2020.

[5] S. Rödelsperger, G. Läufer, C. Gerstenecker, and M. Becker, "Monitoring of displacements with ground-based microwave interferometry: IBIS-S and IBIS-L," vol. 4, no. 1, pp. 41-54, 2010.

[6] M. Sofi, E. Lumantarna, P. Mendis, C. Duffield, and A. Rajabifard, "Assessment of a pedestrian bridge dynamics using interferometric radar system IBIS-FS," Procedia engineering, vol. 188, pp. 33-40, 2017.

[7] W. Bates, Historical Structural Steelwork Handbook. London: The British Constructional Steelwork Association Limited, 1984.

[8] D. Bacinskas et al., "Field load testing and structural evaluation of steel truss footbridge," presented at the Environmental Engineering. Proceedings of the International Conference on Environmental Engineering. ICEE, 2014.

Structural monitoring of N80-S1 River Slaney bridge

António Barrias, Jorge Martínez García, Pat Moore
Bridges and Civil Structures, Arup, 50 Ringsend Road D04 T6X0 Dublin, Ireland
email: antonio.barrias@arup.com, jorge.martinez@arup.com, pat.moore@arup.com

ABSTRACT: During the construction phase of the N80-S1 River Slaney bridge, deformations in the web plates of the main steel girders were identified. As part of the detailed structural assessment following the detection of these deformations, it was decided to conduct structural monitoring and collection of data to demonstrate that the bridge was not susceptible to web breathing or other fatigue damage during its service life. For this reason, a vehicle load test followed by a daily continuous displacement monitoring at two web panels for a period of four months was envisioned and conducted. This was done with displacement sensors set up in two 7x7 grids instrumented at previously identified critical web panels. In this paper, the activities associated with the monitoring are presented, including the installation of the displacement sensors on the structure, its data capture/extraction and post-processing, the continuous daily measurements, and the interpretation of the monitoring results leading to the structural assessment conclusions.

KEY WORDS: Composite bridge; Daily structural monitoring; Load test, Displacement monitoring.

1 INTRODUCTION

1.1 Context

The N80-S1 River Slaney bridge is a steel composite structure with a 70-meter central span in County Wexford, Ireland, completed in 2019 within the M11 Gorey to Enniscorthy PPP Scheme. During its construction, different aspects relating to structural deformations were identified for further consideration. More specifically, there was visual evidence of deformations in the web plate of its steel girders along its full length. This phenomenon is commonly known as "web breathing" [1] and was most apparent over the central portion of the main span, see Figure 1.

Figure 1. Observed deformations in the web plate of the N80-S1 River Slaney bridge girders

By July 2019 an inspection and technical assessment was undertaken to assess this issue in more detail. The main conclusion was that the bridge had been designed in accordance with the applicable standards. Moreover, the undertaken inspections and tests also confirmed that there were no structural concerns, performance issues or other technical reasons that would prevent its opening and normal use.

Nevertheless, by August 2019, the structure's owner TII (Transport Infrastructure Ireland) issued a Notice of Authority Operation Variation (AOV No.1), in order to perform further testing, monitoring, and reporting of results on this structure's girders to the Operations Contractor and Authority. In the aftermath of this, discussions were conducted with all relevant parties to determine the most appropriate and desired monitoring methods. Henceforth, it was then agreed that the first step would be to perform a continuous displacement monitoring at two representative web panels for a minimum period of four months to establish whether there was evidence of web breathing happening.

In this way, in August 2020, after the installation of the displacement sensors by James Fisher Testing Services Limited (JFTS), it was agreed by all parties to conduct a load test to both validate the correct functioning of these sensors and to calibrate the finite element (FE) analytical local model of the web panels to be used in the assessment.

1.2 Goals

There are various studies and works that have referred the relevance and necessity of assessing and controlling fatigue damage in composite bridges such as the N80-S1 River Slaney bridge due to the slenderness of the girders [2]–[4]. In this way, the final goal of this monitoring, was to study the possible fatigue damage related to the potential web breathing deformations at the main girders of this bridge structure. Nevertheless, in this document, the activities related with the sensor installation, conducted load test results and daily continuous measurements are described and its results presented, while the actual fatigue assessment is outside its scope and documented in a different paper [5].

The main goal in the study described in this document is to characterize the observed displacements in the monitored web girders, assess the evolution of these throughout a continuous monitoring period and communicate the lessons learned in this application especially regarding the obstacles and challenges that are faced when conducting these types of applications in real world conditions.

2 SENSOR SETUP

The N80-S1 Slaney River is a three-span bridge with a 42.85 x 70 x 42 m configuration. The reinforced concrete deck slab has circa 250 mm thickness and is characterized by four pairs of 2 m deep braced steel I-girders, Figure 2. It should be noted that in the permanent situation, all the girders have a similar order of structural utilisation. In the initial assessment conducted in July 2019, it was concluded that due to the position of the haul road and its permitted construction traffic, girder G was the most heavily loaded girder in the temporary situation. In this way, girder G was considered as an appropriate location to conduct the envisioned out-of-plane web displacement.

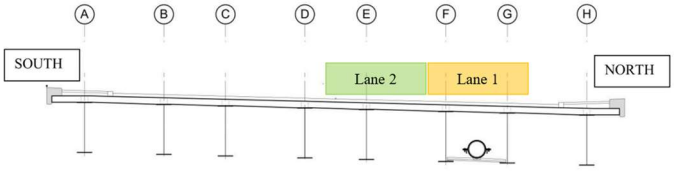

Figure 2. Bridge cross section and its girders naming convention

The system was then deployed to monitor web deflections at two different sections along the inside face of girder G (between girder G and F), hereafter referred as positions B and C.

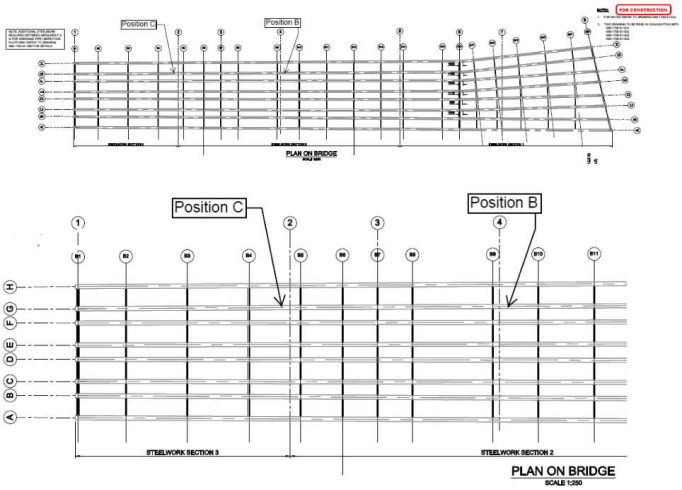

Figure 3. Monitoring positions in plan

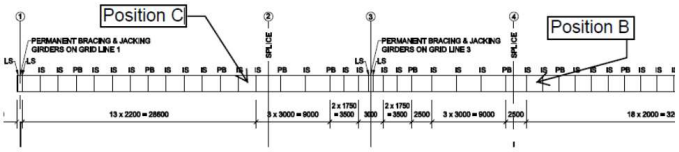

Figure 4. Monitoring positions in elevation

Monitoring Position B was installed on Girder G, around 17.5 m from the west pier at the web adjacent to splice location on central main span on a 1910 mm height x 2000 mm width panel. Monitoring Position C was installed on the same girder, 12.5 m from the west pier, i.e., at the web adjacent to splice location on West end span, on a 1910 mm height x 2200 mm width panel.

At each location, a grid of 7x7 allowing for the use of 49 displacement sensors was deployed, as per Figure 5.

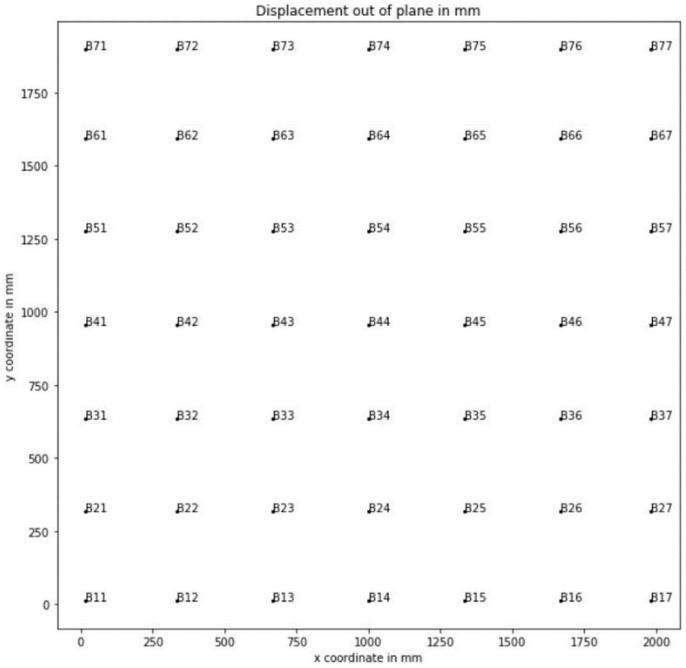

Figure 5. Sensors naming and spacing adopted in Position B

Nevertheless, due to space constraints two sensors in the bottom left of Position C could not be installed, C_{11} and C_{12}. In this way, a total of 96 displacement sensors and 4 temperature sensors were deployed in this assessment, Figure 6.

Figure 6. Displacement potentiometer and PT100 temperature sensor

A temporary frame was installed to securely mount and position the sensors. These measured the change in position of the web panel relative to the initial installed position of the sensor mainly due to short term loading from traffic. The displacement sensors deployed in this application were of the potentiometer type and had the following specifications, Table 1.

Table 1. Displacement Sensor Specifications

Name	Strainsense MS-94SR Linear Potentiometer
Supply Voltage	1-30 V DC (used 10V)
Stroke Range	12.5 mm (set at mid-stroke +/- 6.25 mm)
Electrical and mechanical life	>25 million cycles
Sealing	IP65
Resolution	Infinite (stated); 0.01 realistic resolution with observed SNR

3 LOAD TEST

3.1 Description

As referred above, after the sensor's installation, a load test was carried during one day on the beginning of September 2020 to both validate the correct functioning of these and to calibrate the FE local model of the monitored webs.

A total of twelve runs were performed using different load positions, configurations (half and fully laden trucks) and travel speeds with four five-axle truck vehicles, as per Table 2.

Table 2. Load test runs description

Run	Load weight [tons]	Position	Speed
1	17.84	Lane 1	5 km/h
2	17.84	Lane 1	80 km/h
3	17.84	Lane 2	5 km/h
4	17.84	Lane 2	80 km/h
5	36.26	Lane 1	5 km/h
6	36.26	Lane 1	80 km/h
7	36.26	Lane 2	5 km/h
8	36.26	Lane 2	80 km/h
9	35.82, 36.00	Lanes 1 & 2	5 km/h
10	35.82, 36.00	Lanes 1 & 2	80 km/h
11	35.84, 36.26, 36.00, 35.82	Lanes 1 & 2	5 km/h
12	35.84, 36.26, 36.00, 35.82	Lanes 1 & 2	80 km/h

In all runs, the vehicles were required to be positioned in the centre of its corresponding lane and drive at a constant velocity throughout the passage of the entire length of the bridge deck.

3.2 Measurements

The sensors obtained data throughout the entire conduction of the test and were outputted in CSV files with the displacement readings in mm. The sampling acquisition frequency was of 50 Hz for the voltage channels (displacement sensors) and 1 Hz for the temperature channels.

It was observed some global variance of the measurements due to ambient conditions during the test, i.e., changes in temperature. In this way, each run was postprocessed by resetting its values to the measurements occurring one minute before the passing of the vehicle. Note that the test specifications instructed this time window without traffic on the bridge before and after each run, Figure 7.

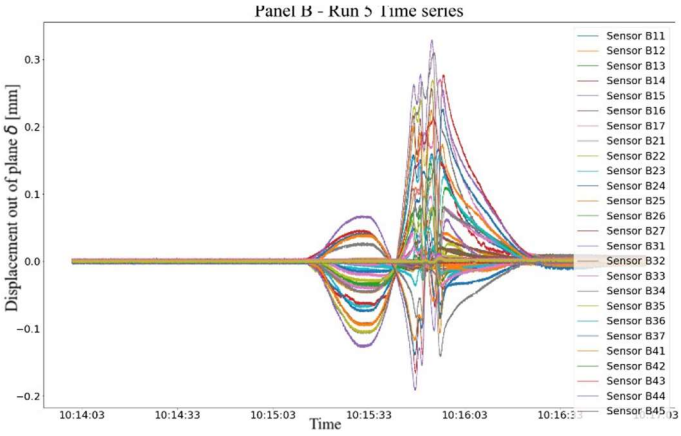

Figure 7. Position B Run 5 time series of all sensors

Moreover, it was soon observed that three sensors in Position C, namely C_{15}, C_{16} and C_{54} were providing faulty readings. Therefore, it was decided to remove these from the post-processing assessment and reducing the number of sensors in Position C to 44.

Due to the configuration of the sensor setup, the obtained measurements were also possible to be assessed in 2D and 3D contour plots for every timestep as seen in Figure 8.

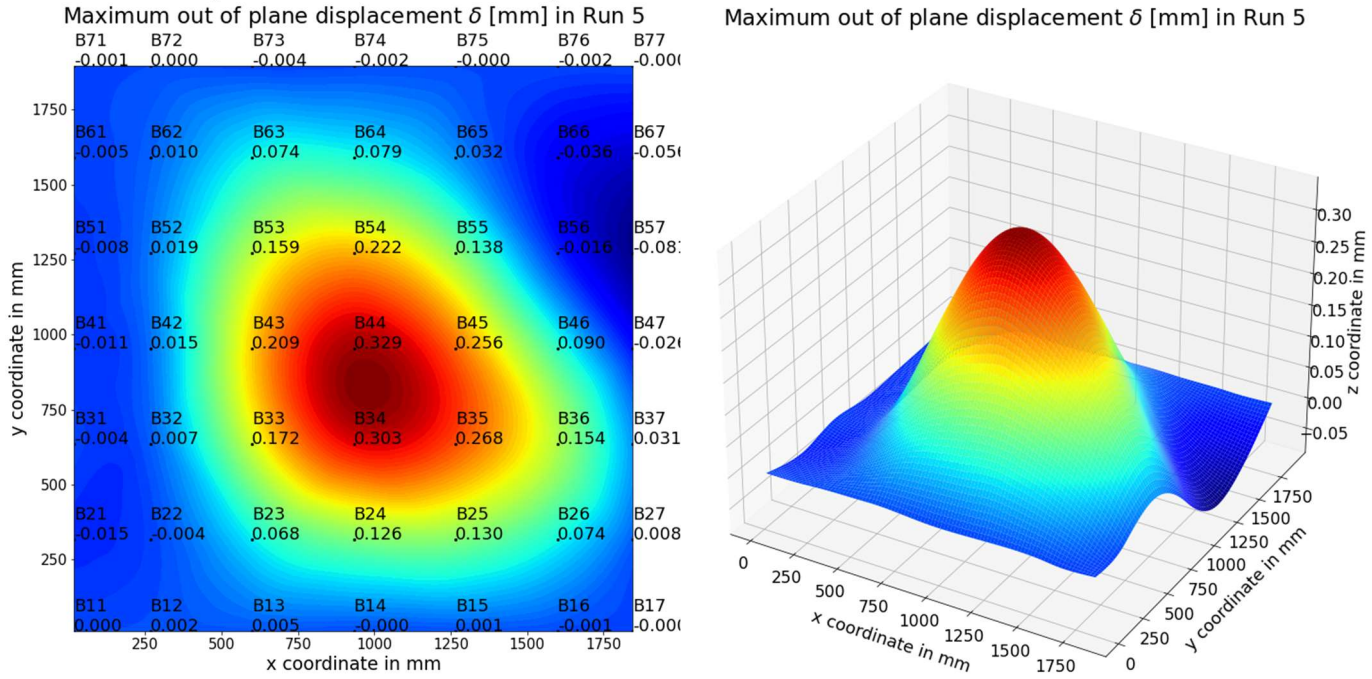

Figure 8. Panel in Position B in the instant of maximum variation displacement in Run 5: (left) 2D change in shape; (right) 3D change in shape

From Figure 7 it is observed how depending on the location of the sensor within the monitored web panel, due to the passage of the vehicle, the web is deflected initially in one out of plane direction changing quickly to the opposite direction.

For all runs, the maximum (positive) and minimum (negative) displacements, and their respective timestamps were obtained. These are described in Table 3 and Table 4.

Table 3. Max and min out-of-plane displacements measure for web panel in Position B

Run	Sensor	Max [mm]	Time max	Min [mm]	Time min
1	B44	0.16	09:00:40	-0.05	09:00:19
2	B44	0.15	09:23:29	-0.07	09:23:28
3	B34	0.37	09:30:36	-0.13	09:30:34
4	B44	0.13	09:41:33	-0.06	09:41:31
5	B44	0.33	10:15:53	-0.13	10:15:30
6	B44	0.32	10:27:26	-0.14	10:27:24
7	B34	0.15	10:38:46	-0.08	10:38:23
8	B34	0.18	10:50:58	-0.08	10:50:57
9	B34	0.46	11:17:58	-0.18	11:17:29
10	B34	0.46	11:27:58	-0.20	11:27:56
11	B34	0.56	11:46:30	-0.22	11:45:49
12	B34	0.50	11:58:29	-0.20	11:58:25

Table 4. Max. and min. out-of-plane displacements measure for web panel in Position C

Run	Sensor	Max [mm]	Time max	Min [mm]	Time min
1	C44	0.03	09:00:22	-0.02	09:00:53
2	C44	0.04	09:23:28	-0.02	09:23:30
3	C33	0.06	09:32:29	-0.01	09:33:33
4	C33	0.06	09:42:48	-0.01	09:42:49
5	C44	0.08	10:15:32	-0.06	10:15:56
6	C44	0.08	10:27:24	-0.05	10:27:26
7	C33	0.12	10:38:25	-0.03	10:38:48
8	C33	0.12	10:50:57	-0.03	10:50:59
9	C33	0.17	11:17:32	-0.09	11:18:01
10	C33	0.17	11:27:56	-0.09	11:27:59
11	C33	0.19	11:45:44	-0.16	11:46:34
12	C33	0.17	11:58:26	-0.13	11:58:29

A more selective look at the graphs provides additional information. Having this in mind, the individual results of sensor B44 (identified as measuring the highest displacement) in run 5 are shown in Figure 9. Here it is observed the outward deformation produced while the truck passes across the first span and the inward deformation while the truck passes across the middle span, where panel B is located. The local peaks that each axle or group of axles produces can also be appreciated in the figure: first, there are two relative peaks which correspond to the two front axles, and later, another peak which corresponds to the group of the three rear axles, and which is higher due to the total load of these axles group being also higher.

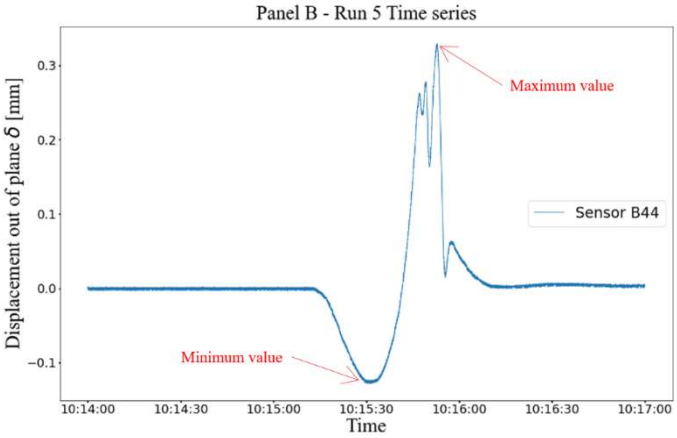

Figure 9. Maximum (positive) and minimum (negative) displacement variation of panel B sensor that measured the highest peak of run 5 (B_{44})

In this way, from this load test, it was concluded that the maximum displacement in Position B and C, were 0.56 mm and 0.19 mm respectively, occurring both during run 11 (4 fully laden vehicles) as expected. Moreover, the runs with vehicles crossing Lane 1 measured around twice the displacement than the corresponding runs in Lane 2. The use of different velocities when crossing the structure did not imply significant effects in the displacement. Finally, as the sensors measured normal traffic between the trucks crossing, it was observed that the maximum measured displacement for general traffic on this day was around 0.3 mm.

4 DAILY CONTINUOUS MEASUREMENTS

Following the conduction of the load test in September 2020, the sensors kept obtaining data until the end of December 2020.

Due to the large amount of data being collected in this period and in order to ease the analysis of the daily data being measured, a daily peak ranking process was devised in order to dynamically filter this data. The goal of this process was to output the daily ten highest peaks. For this, an automated process was implemented that analysed all sensors and found the top 10-second periods for each sensor.

At the same time, the data was dynamically baselined for each sensor on a daily basis by calculating the average recording between 1am and 3am and calculate the absolute difference between that baseline and the maximum value of each 10-second periods. This difference was then appended to a dictionary of 10 s start times, along with one or more mean differences (depending on how many sensors had a top-10 value occurring). Each period then read the 20 s to either side of the interval adding to a total of 50 s period.

In this way, for each ten 50 s periods the obtained information was categorized in five columns: sensor id reading the maximum (positive) displacement variation; value of this displacement; timestamp for this measurement; minimum (negative) displacement measured by this sensor; timestamp of this measurement.

This was of vital importance as in this study only the daily short-term mechanical displacements produced by the crossing of the normal traffic in this structure were of interest. This post

processing filtered out, both the global displacements produced by changes in the surrounding environment (mainly due to the overall decrease of temperature from the September to the December readings) and the daily variations from night and day temperatures.

This was obtained and processed for everyday of the monitoring period and for both instrumented positions. Table 5 shows an example of the result of this procedure for a given day.

Table 5. Position B peaks summary for 19/10/2020. Values are shown in chronological order

Sensor	Max [mm]	Time max	Min [mm]	Time min
B44	0.46	07:49:42	-0.20	07:49:41
B44	0.46	13:29:07	-0.18	13:29:05
B44	0.42	14:10:25	-0.18	14:10:24
B44	0.45	14:11:41	-0.20	14:11:39
B34	0.42	14:26:42	-0.16	14:26:41
B44	0.48	15:01:05	-0.23	15:01:03
B44	0.40	15:10:12	-0.19	15:10:10
B44	0.41	15:33:01	-0.16	15:33:00
B34	0.44	15:47:54	-0.16	15:47:52
B44	0.38	16:15:10	-0.17	16:15:08

However, it should be noted that initially a different ranking process had been deployed. This process was found to present several drawbacks including still presenting data for the previously identified unusable channels corresponding to sensors C_{11}, C_{12}, C_{15}, C_{16} and C_{54} which were significantly skewing this ranking. Only after a thorough coordination between Arup and JFTS, the ranking process described at the beginning of this section was agreed. This was corrected from October 18th onwards. This process was applied retroactively to the measured data before that date, although with some caveats. In this way, the impact of this change of ranking process is ultimately observed in the overall results of this monitoring.

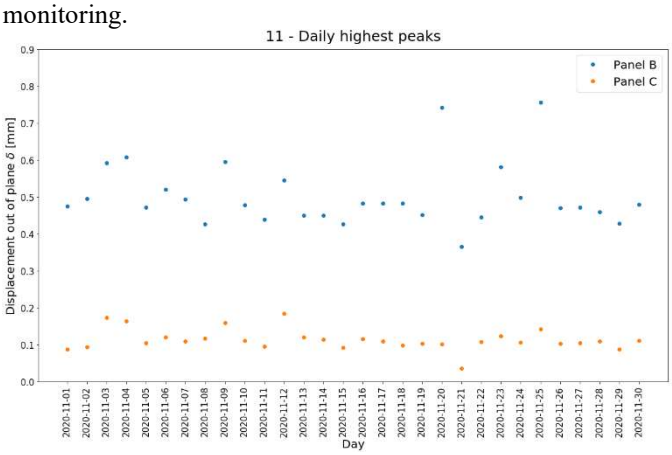

Figure 10. Daily highest displacements [mm] measured in November 2020

The variation of the maximum daily peaks for each position panel during this monitoring period was then assessed. An example of this is depicted in Figure 10 for the month of November. In this image it is seen how in November, the daily measured maximum variation in displacement was varying from 0.4 mm to 0.75 mm at the panel in Position B, and from 0.1 mm to 0.2 mm at the panel in Position C. This was a trend that was seen throughout the four months of the monitoring period as seen in Figure 11.

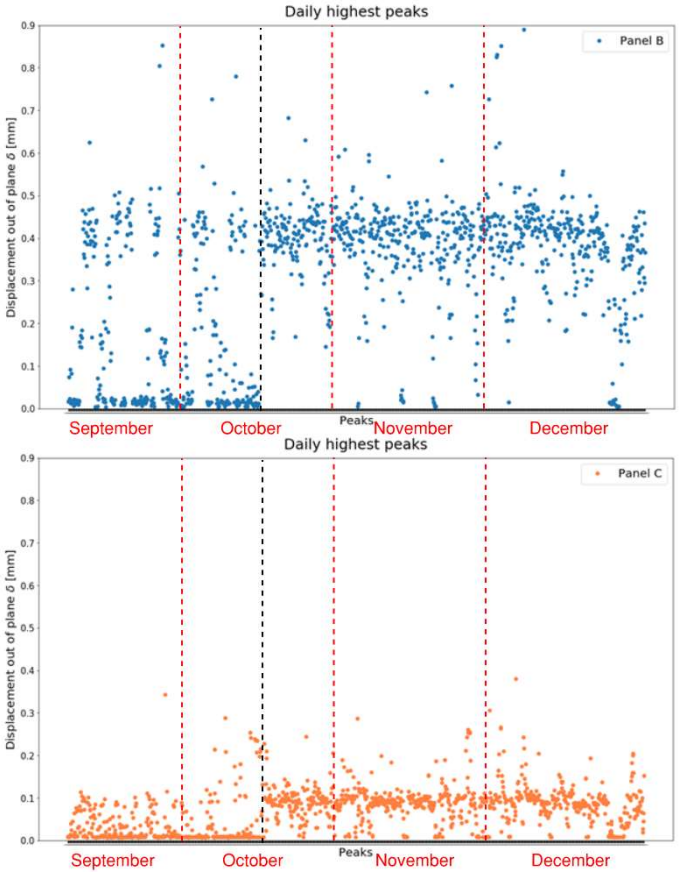

Figure 11. Chronological depiction of all analysed peaks for the four months monitoring period in Position B (above) and C (below). Black dashed line depicts date of changing of ranking process. Red dashed lines depict month delimitations

Exceptions to this range of values are particularly observed for a few days at the end of September and beginning of December where the maximum displacements measured at the panel in Position B were above 0.8 mm. The same happening for Position C, where displacements above 0.3 mm were captured in a couple of days in the beginning of December.

Additionally, the changes introduced in October in the post-processing procedure were concluded to have a positive impact on the data, removing the close-to-zero values that were obtained before, and which were not among the real highest peaks of their day. In Figure 11, a clear change is observed in the measurements taken before and after October 18th.

Moreover, it is seen how the mean value for the measured peaks is similar throughout the entire monitoring period and at the same time, being of the same order of magnitude of the highest measured displacement during the previously conducted load test. Nevertheless, it is seen how the highest measured peaks are greater than the ones verified in the load test.

The distribution of the daily highest peaks was also assessed for each month and monitored panel position. This is depicted in Figure 12, with its values for the month of December as an example.

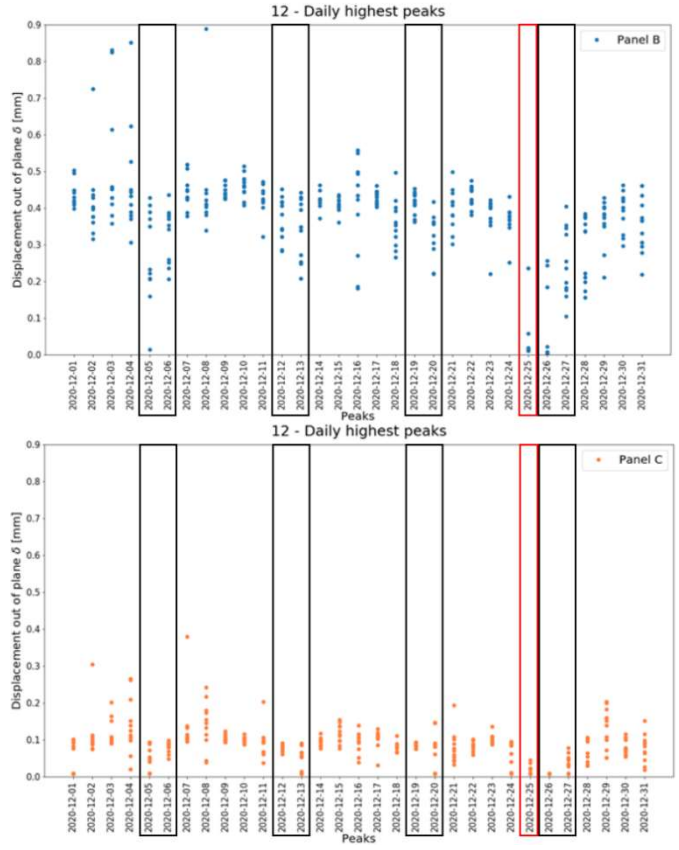

Figure 12. December peaks distribution by days. Weekends are marked in black. Christmas day is marked in red

From this, it is seen that the range of the measured peaks are quite varied. There are days presenting the ten highest peaks with very similar values, while other days where the highest peak and the 10th peak of the day are quite away from each other. Moreover, it is observed how the highest peaks are generally lower at the weekends and bank holidays, being this expected due to the lower and lighter traffic on these days. Unfortunately, there was no traffic monitoring system (e.g., WIM) close to this structure that could be used to compare with the displacement readings.

Notwithstanding, the information collected during this period allowed the verification that the measured displacements were not following an upward trend and were generally constant throughout the monitoring process.

This data also allowed for the definition of boundary conditions of a local FE model of the web plates used to further assess the fatigue behaviour and capacity of these elements. This study is available in [5] to any interested reader.

5 CONCLUSIONS

During the construction phase of the N80-S1 River Slaney bridge, visual evidence of deformations in the web plates of the girders were observed. The purpose of the monitoring task was to assess the characteristics of these displacements and evolution throughout a four-month period.

In this process it was seen how the challenges of structural monitoring when faced with real world conditions are quite significant and needed to be taken into consideration when devising the monitoring system to be in place. For instance, the choice of using displacement sensors instead of strain gauges which was related to the preference of minimizing the intrusiveness of the procedure as the use of the later sensors would require the preparation of the surface where deployed and repainting after its removal.

Moreover, it was observed how some of the deployed sensors did not provide useful data and how this had to be overcome and incorporated in the post-processing of the measurements to obtain reliable and representative conclusions from the measured values. In the authors' opinion, some of these observed challenges were related with the use of electrical based and local sensors. As more type of sensing technologies, such as fiber optics and remote sensors, make way for a more mature and systematic use in these types of applications, it is envisioned that these challenges can be mitigated in certain scenarios in the near future.

Furthermore, and in this line, when dealing with continuous monitoring over a period of time that reached from the end of summer until well within winter, it was seen how the peak ranking process deployed and its adjustments were of extreme importance to obtain data that was reporting actual short-term mechanical displacements produced by the traffic crossing the structure during that period. As it is inherent in this type of procedures the amount of data collected was immense, so the decision and setup of the filtering post processing methodology was of great importance and had to be carefully examined at the scoping/planning stage as it influences the type of both the hardware and software required as well as the type of communications used to transfer the measured data.

Finally, this information was of extreme value in order to conduct a more detailed and further analysis on the fatigue behavior and capacity of the monitored web panels and in this way satisfy all involved authorities, and ultimately its users, in the safety and reliability of this structure.

REFERENCES

[1] M. M. Jalali, J. D. Marshall, and J. S. Davidson, "Buckling and distortion induced fatigue of curved steel plate girders with slender web," 2020.

[2] K. Rykaluk, K. Marcinczak, and S. Rowiński, "Fatigue hazards in welded plate crane runway girders–Locations, causes and calculations," *Arch. Civ. Mech. Eng.*, vol. 18, no. 1, pp. 69–82, 2018.

[3] E. Maiorana, C. D. Tetougueni, P. Zampieri, and C. Pellegrino, "Experimental and numerical investigations on slender panels with holes under symmetrical localised loads," *Eng. Struct.*, vol. 228, p. 111323, 2021.

[4] M. Yaghoubshahi, M. M. Alinia, and A. S. Milani, "Master SN curve approach to fatigue prediction of breathing web panels," *J. Constr. Steel Res.*, vol. 128, pp. 789–799, 2017.

[5] A. Barrias, J. Martínez García, and P. Moore, "N80-S1 River Slaney bridge monitoring and fatigue assessment," 11th International Conference on Bridge Maintenance, Safety and Management, IABMAS, Barcelona, Spain. July 2022.

A numerical study on the sheltering effects of the central wind barriers on the Rose Fitzgerald Kennedy Bridge

Yuxiang Zhang[1], Philip Cardiff[2], Conor Sweeney[3], Fergal Cahill[4], Jennifer Keenahan[1]
[1]School of Civil Engineering, University College Dublin, Belfield, Dublin 4, Dublin, Ireland
[2]School of Mechanical and Materials Engineering, University College Dublin, Belfield, Dublin 4, Dublin, Ireland
[3]School of Mathematics and Statistics, University College Dublin, Belfield, Dublin 4, Dublin, Ireland
[4]Transport Infrastructure Ireland, Parkgate Business Centre, Dublin, Ireland
email: yuxiang.zhang1@ucdconnect.ie, philip.cardiff@ucd.ie, conor.sweeney@ucd.ie, fergal.cahill@tii.ie, jennifer.keenahan@ucd.ie

ABSTRACT: This study aims to examine the sheltering effects of central wind barriers installed near the pylons of the Rose Fitzgerald Kennedy Bridge. A full-scale Computational Fluid Dynamics (CFD) model is developed, which includes high-precision geometries of the bridge and the terrain. Simulations using this model are performed at realistic wind conditions as boundary conditions are mapped from mesoscale Weather Research and Forecasting (WRF) simulations. Wind velocities at multiple locations on the bridge predicted by the CFD simulations are compared with field measurement data where a good agreement is reached. The validated model is then applied with bridge geometries with and without the central wind barriers at high wind conditions. Comparisons between these two groups of simulations show that the wind barriers can effectively reduce wind velocities on traffic lanes near the pylon, which validates the current design of the barriers on the bridge.

KEY WORDS: Wind effects; Bridge aerodynamics; Computational Fluid Dynamics simulations; Weather Research and Forecasting model; Field measurement; OpenFOAM.

1 INTRODUCTION

Wind is an invisible yet powerful force of nature. Its potential destructive influence on bridges has been observed historically. In December 1879, the Tay Bridge in Dundee, Scotland, collapsed during a storm, leading to a death toll of over 60 people, where the underestimation of the wind pressure was believed to be one of the main causes of this disaster [1]. This incident was the first wind-induced bridge failure that had been systematically investigated and archived, which urged the bridge engineers at that time to re-examine their designs against wind loads [2]. However, history has proven that human understanding of wind at that time was far from sufficient. In 1940, the Tacoma Narrows Bridge collapsed during a moderate wind of approximately 17.9 m/s [3], which is believed to be the result of a self-excited aeroelastic phenomenon, flutter [4]. Although the bridge was closed to traffic when the accident occurred, it has remained one of the most significant bridge collapses due to its size. Lessons learned from the collapse of the Tacoma Narrows Bridge urged bridge engineers to consider wind effects as one of the critical factors during the design of long-span bridges which are more vulnerable to complex wind conditions due to their relatively lower stiffness when compared to small bridges and culverts.

While the inclusion of analysis of wind effects in bridge design has largely prevented bridge collapses due to wind, wind-induced problems have not been eliminated and have strongly affected the serviceability of numerous long-span bridges. For instance, vortex-induced vibrations are witnessed on long-span bridges around the world, such as the Kessock Bridge in Scotland [5], the Rio-Niterói bridge in Rio de Janeiro [6], the Storebælt Bridge in Denmark [7], and most recently the Humen Pearl Bridge in China [8]. Besides, wind effects can also cause safety issues to traffic on the bridge. One of these problems is the cross-wind effects on vehicles when they are passing through regions of bridge pylons. Nowadays, the most commonly adopted countermeasure for such effects is installing central wind barriers at the bottom of the bridge pylon [9-11]. However, Argentini et al. [12] conducted wind tunnel tests at a scale of 1:40 on a bridge-vehicle model and found that the installation of central wind shield near bridge pylons might not always help reduce the cross-wind effects on vehicles. Salati et al. [13] performed CFD simulations on a bridge-vehicle model at a scale of 1:30 to study the cross-wind effects on vehicles near the bridge pylon. Although their bridge geometry was a simplified one that did not include any wind barriers, their study demonstrated the feasibility to apply CFD simulations in this type of study. Whether applying CFD simulations or wind tunnel tests, existing studies in this area applied simplified wind conditions that can be substantially different from the realistic wind conditions at the bridge site. This might limit the applicability of their findings in bridge design practice, especially when high wind conditions are of concern.

During the design of the Rose Fitzgerald Kennedy Bridge in New Ross, Ireland, there is a concern that cross-wind effects might severely influence traffic on the bridge near the pylons. To reduce such effects, central wind barriers are installed at the three main pylons of the bridge. This study offers numerical investigations on the sheltering effects of these central wind barriers. A full bridge CFD model is developed at full scale using the open-source software OpenFOAM v9 [14]. This model includes geometries of the bridge and a terrain model with a precision level of 3 m provided by Ordnance Survey Ireland [15], where the boundary conditions are mapped from mesoscale simulations results using the Weather Research and Forecasting (WRF) model [16]. The inclusion of this mapped boundary conditions from WRF simulations can help create realistic wind conditions in this study. Two-dimensional (2D) sonic anemometers were installed on the Rose Fitzgerald Kennedy Bridge which provide examples of high wind

conditions. The field measurement data is also used in the validation of the CFD simulations. Through these CFD simulations, this study aims to provide evaluations of the performance of the wind barriers on the Rose Fitzgerald Kennedy Bridge under high wind conditions. This study is also expected to contribute to the validations of the use of CFD simulations within bridge aerodynamic studies.

2 METHODOLOGY

2.1 Field measurement

As part of the Structural Health Monitoring (SHM) system, RM Young 8600 ultrasonic 2D anemometers are installed at four locations on the Rose Fitzgerald Kennedy Bridge, which offer a sampling frequency of 10 Hz, a wind speed accuracy of ± 0.1 m/s, and a wind direction accuracy of ±2 degrees. Compared to propeller type anemometers, ultrasonic anemometers will have less interference with the flow as there are no moving parts, and so can provide more reliable results. Since April 2020, after 2 months of calibrations, these sensors have been recording wind data including the magnitude of wind velocity and wind directions. Figure 1 shows the locations of these four sensors on the bridge.

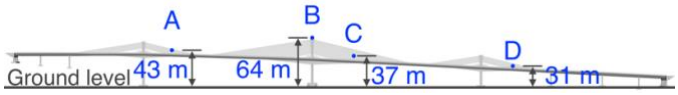

Figure 1. Locations of the sensors on the bridge.

Figure 2 shows the wind data of two days collected by Sensor B during which the magnitude of wind velocity reaches to the maximum value of year 2020. The reason for using data from Sensor B to select the period of interest is that this sensor is the far from the bridge deck and so the interference from traffic on wind velocities can be neglected.

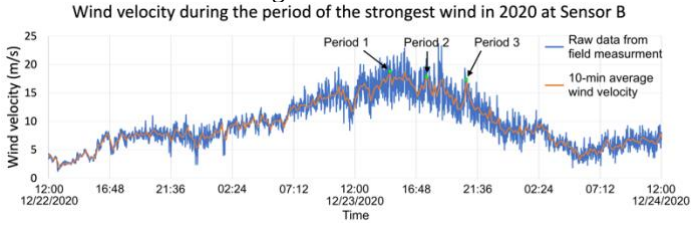

Figure 2. Wind velocity at Sensor B.

In Figure 2, both the 1-minute raw data and the 10-minute averaged data are presented. Based on such data, three periods of ten minutes from 15:00 to 15:10 (Period 1), from 17:30 to 17:40 (Period 2), and from 18:40 to 18:50 (Period 3) on December 23rd, 2020 are selected as periods of interest in this study as they are representative on high wind conditions in 12 months.

2.2 CFD modelling

In this study, a full-scale CFD model is developed using open-source software OpenFOAM v9 [14]. This model includes geometries of the Rose Fitzgerald Kennedy Bridge and the terrain at its site. The full-bridge geometry is created based on construction drawings. To examine the sheltering effects of the central wind barriers, two full-bridge geometries are prepared, as shown in Figure 3, where Figure 3a shows the full-bridge geometry with the central wind barriers and Figure 3b shows the full-bridge geometry that neglects the central wind barriers. Beside the difference in central wind barriers, these two geometries are identical to each other.

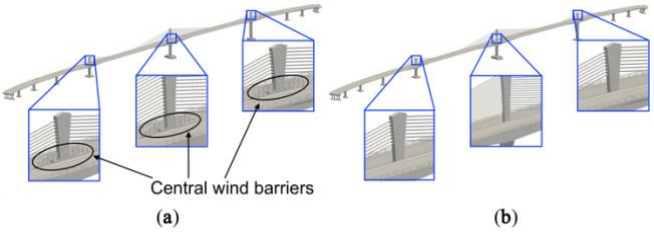

Figure 3. Full-bridge geometries of the Rose Fitzgerald Kennedy Bridge.

The terrain model is generated using contour data provided by Ordnance Survey Ireland [15] which has a precision level of 3 m. Figure 4 shows the combination of the bridge geometry and the terrain model.

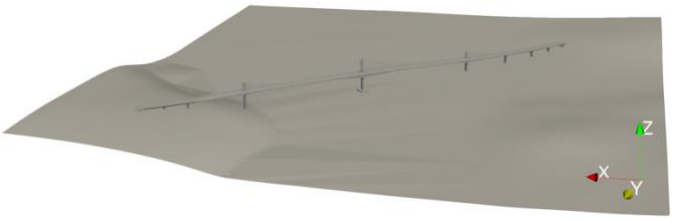

Figure 4. Full-bridge geometry sitting on the terrain model.

According to field measurement data, the wind direction to the main span of the bridge is of 46.4 degrees at the three chosen periods. Hence the bridge geometry is not placed perpendicular to the mean wind direction, where the alignment is shown in Figure 5 with reference to the North.

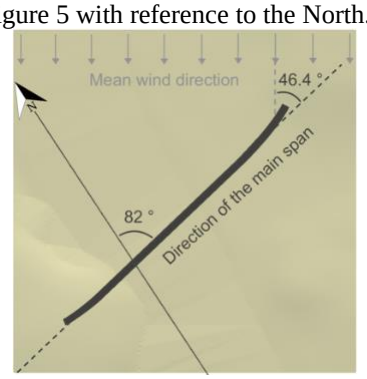

Figure 5. Alignment of the bridge.

The CFD model here aims to simulate the global wind environment around the bridge in full scale. The flow within the testing domain is assumed to be incompressible, Newtonian, and statistically steady, with temperature and gravity effects neglected. Hence, the flow is governed by the Reynolds-Averaged Navier-Stokes (RANS) equations:

$$\nabla \cdot \mathbf{U} = 0 \tag{1}$$

$$\nabla \cdot (\mathbf{UU}) = \nabla \cdot [\nu_{\text{eff}}(\nabla \mathbf{U} + (\nabla \mathbf{U})^{\mathbf{T}})] - \nabla \mathrm{p} \tag{2}$$

where $\mathbf{U}$ is the mean wind velocity, p is the kinematic pressure, ν_{eff} is the effective viscosity of the air which is the summation of the laminar kinematic viscosity and the turbulent kinematic viscosity of the air. The laminar kinematic viscosity is 1.338×10^{-5} m^2/s, while the turbulent kinematic viscosity is resolved by using the standard k-ε turbulence model [17].

Figure 6 shows the computational domains used in this study, where the computational domain of the CFD simulations is significantly smaller than that used in the WRF simulation.

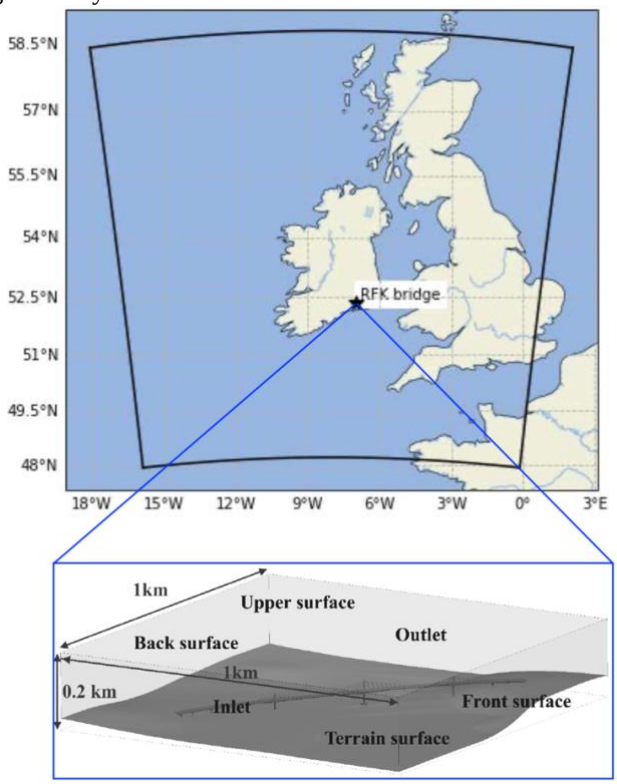

Figure 6. Computational domains used in this study.

The WRF simulations were performed at the chosen three periods of interest, results of which are then used to provide estimations of initial conditions of the velocity and pressure fields at the inlet surface of the computational domain of the CFD simulations. This mapping procedures that initialises the CFD simulations is conducted by applying a built-in boundary condition in OpenFOAM v9, *timeVaryingMappedFixedValue*, on the surfaces of the computational domain. A list of boundary conditions used in the CFD simulations are shown in Table 1.

Table 1.Boundary conditions of the CFD simulations.

Boundary	Parameter	Type
Inlet	**U**	Dirichlet
	p	Neumann
	k	Dirichlet
	ε	Dirichlet
Outlet	**U**	Neumann
	p	Dirichlet
	k	Neumann
	ε	Neumann
Bridge & terrain	**U**	no-slip
	p	Neumann
	k	wall function
	ε	wall function
Upper, front and back surfaces	**U**	slip
	p	Neumann
	k	Symmetry
	ε	Symmetry

In this study, the computational mesh is developed using the *blockMesh* and the *snappyHexMesh* utilities in OpenFOAM v9. Firstly, the structured background mesh is generated using *blockMesh* where every cell within the mesh is equal in size and has a dimension of 20 m × 20 m × 20 m. Then, the background mesh is refined using snappyHexMesh where regional refinement strategy is applied. The cell size is controlled over the distance to the surface of geometries, which is shown in Table 2.

Table 2. Regional refinement controlled by distances

Distance to the bridge surface (m)	Size of the cell (m)
16	1.25
8	0.625
4	0.3125
2	0.15625
1	0.078125

Figure 7 shows a cross-section of the final mesh of the simulations that apply the full-bridge geometry with the central wind barriers.

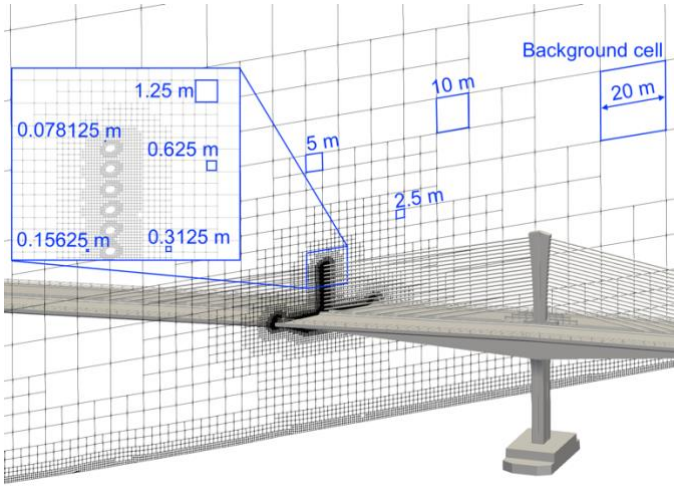

Figure 7. Computational mesh used in this study.

The final mesh of the case with the central wind barriers contain 64,865,217 cells, 57,331,928 of which are hexahedrons. The total cell count of the final mesh of the case without the central wind barriers is 64,773,593, where 57,254,105 of them are hexahedrons.

In this study, the SIMPLE algorithm [18] is adopted to conduct the pressure-velocity coupling. The governing equations are discretised using the nominally second-order finite volume method [19]. The discretised equations are solved using two linear solvers, the Preconditioned Conjugate Gradient solver [20] for symmetric matrices, and the Preconditioned Bi-Conjugate Gradient solver [21] for asymmetric matrices. Since the total cell count is over a million, it is not practical to conduct these computations in serial. The SCOTCH library is used to decomposing the whole computational domain into 128 partitions and then computations are performed using 128 CPU cores. An average finishing time for each simulation (of 5000 iterations) is around 4 hours.

2.3 *Comparisons of CFD results and the field data*

Wind velocities at the four sensors (in Figure 1) were determined by the CFD simulations that include the central wind barriers. To validate the CFD modelling in this study, results of these wind velocities during the three periods of interest are shown in Figure 8, where they are compared with the 10-minute averaged field measurement data.

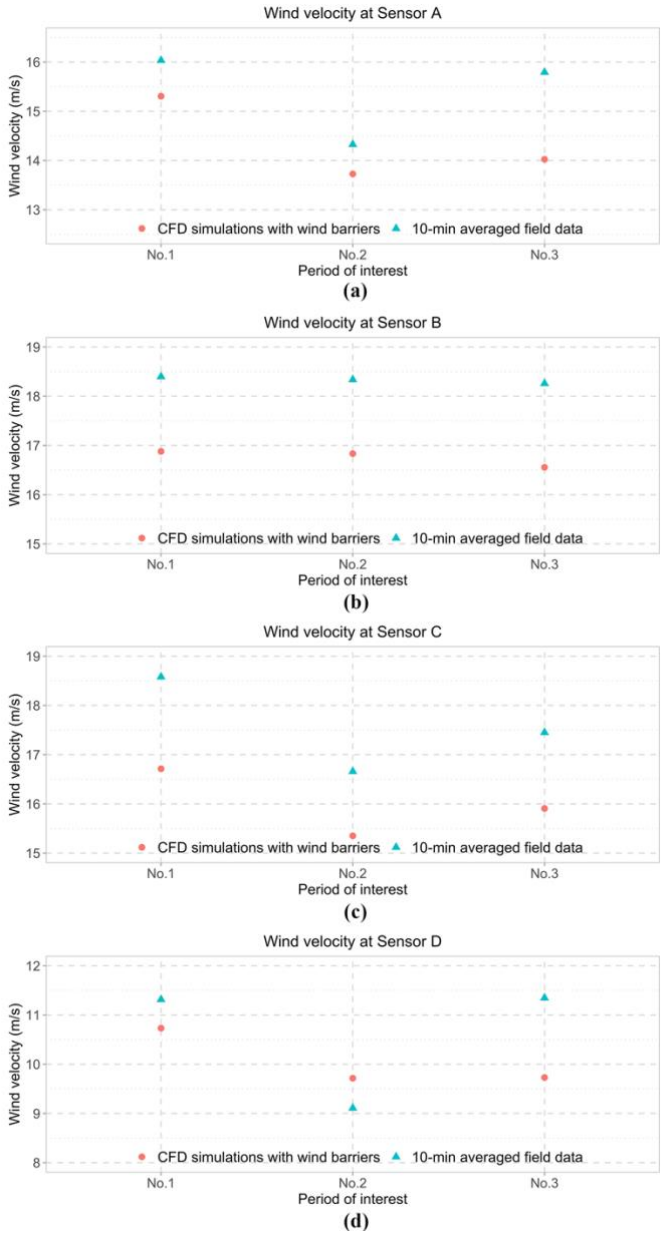

Figure 8. Comparisons of wind velocities at sensor locations.

Overall, wind velocities predicted by CFD simulations are lower than those recorded by sensors. This might be the results of the use of RANS formulations, which might over-simplify the turbulent effects on the flow field [22]. However, the maximum relative differences between wind velocities predicted by CFD simulations and the field measurement data are approximately 11.2%, 9.3%, 10%, and 14.3% in Figures 8a to 8d, respectively. Therefore, it is deemed that the CFD modelling developed in this study is validated in terms of predicting wind velocities at multiple locations on the bridge.

2.4 *Sheltering effects of the central wind barriers*

There are currently three sets of wind barriers installed on the Rose Fitzgerald Kennedy Bridge. In this study, the sheltering effects of the largest wind barrier are examined by comparing results of velocity fields from simulations that have wind barriers and those that neglect the barriers.

To demonstrate the differences between the two groups of simulations, three cross-sections are selected near within the region near the pylon. Locations of the three cross-sections are shown in Figure 9.

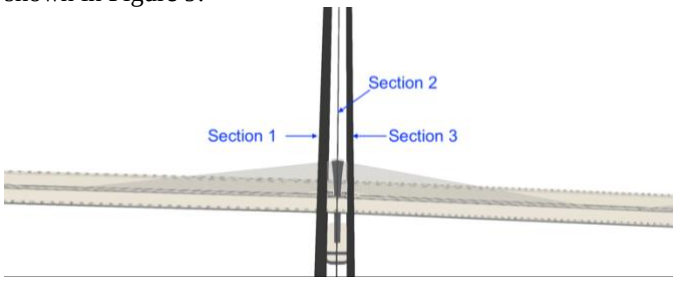

Figure 9. Locations of the cross-sections for analysis.

Wind velocity fields of the three cross-sections (in Figure 9) determined from simulations with and without the central wind barrier are shown and compared in Figures 10 to 12.

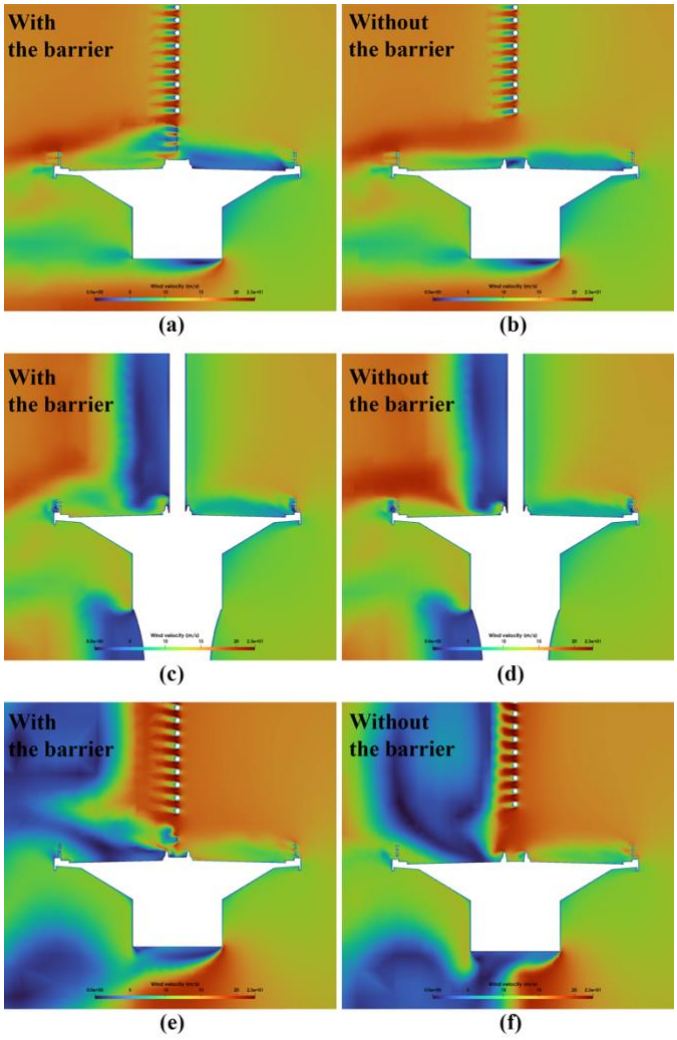

Figure 10. Wind velocity fields at period of interest No.1.

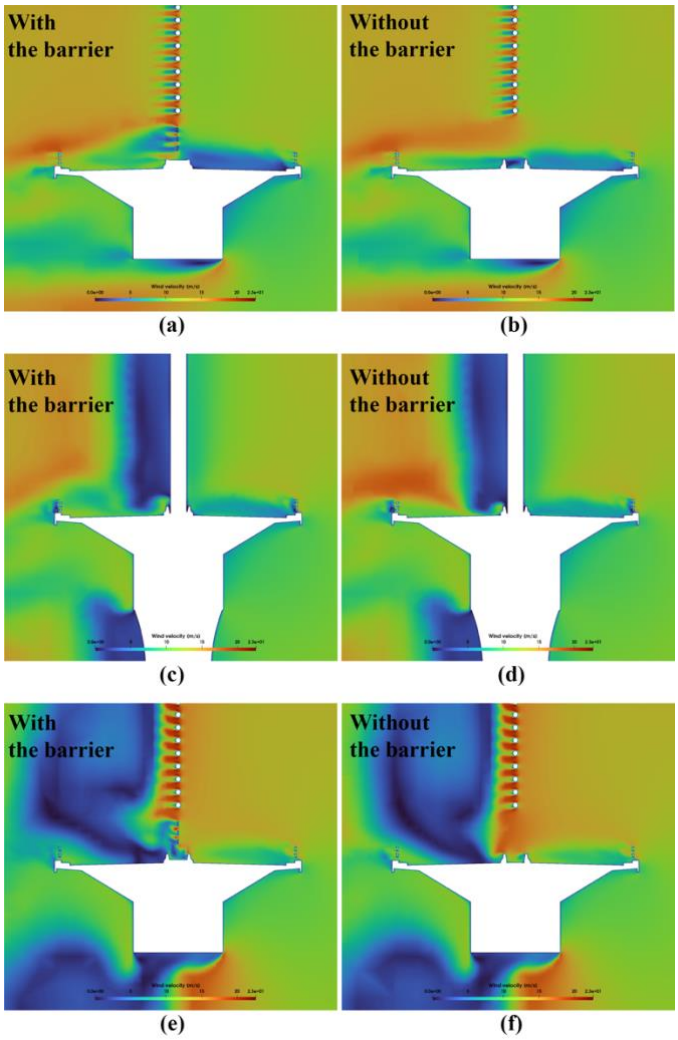

Figure 11. Wind velocity fields at period of interest No.2.

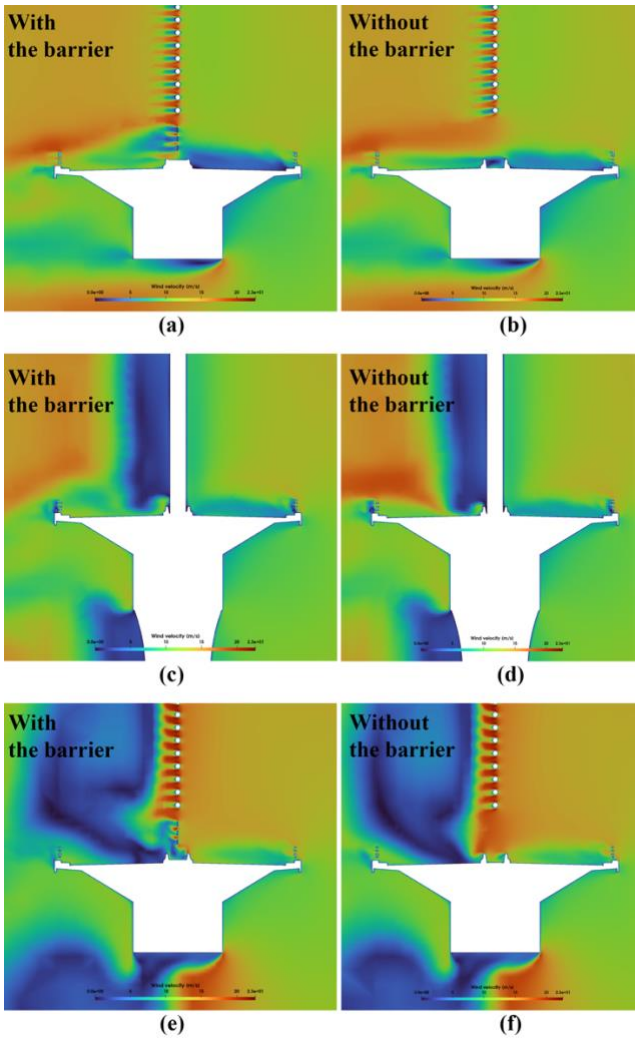

Figure 12. Wind velocity fields at period of interest No.3.

Results in Figure 10 represent the highest wind condition at the Rose Fitzgerald Kennedy Bridge, while results in Figures 11 and 12 have the second and third strongest wind in 2020. It is found that the installation of the central wind barrier can significantly reduce the wind velocity in the traffic lanes near the pylon. Such sheltering effects are most evident within comparisons of wind velocities at section 1, shown in Figures 10a and 10b, Figure 11a and 11b, and Figures 12a and 12b. In these figures, the presence of the wind barriers can reduce the wind velocity in the near-pylon by 50% to that in the results of the simulation without the wind barrier, indicating the good performance of the current design under strong wind conditions.

3 CONCLUSION

In this study, a full-bridge CFD model is developed at full scale, which includes the full-bridge geometry of the Rose Fitzgerald Kennedy Bridge and a high-precision terrain model of the bridge site. This CFD model also maps its boundary conditions from mesoscale WRF simulations, which help create realistic wind conditions at the bridge site. Wind velocities predicted by simulations using this CFD model are compared with field measurement data where a good agreement is achieved. This validates the CFD model and demonstrates the capacity of CFD simulations performed at full scale. Furthermore, this study investigates the sheltering effects of the central wind barriers installed at regions close to bridge pylons on the Rose Fitzgerald Kennedy Bridge. It is found that these wind barriers can effectively reduce wind velocities on the traffic lanes near the pylon at high wind conditions. This validates the design of such structures and offers insights into the future design of similar wind barriers.

ACKNOWLEDGMENTS

The authors wish to acknowledge the Irish Centre for High-End Computing (ICHEC) for the provision of computational facilities and support. The authors also wish to acknowledge Transport Infrastructure Ireland (TII) for the provision of the

field measurement data. Additionally, Yuxiang Zhang acknowledges the scholarship received jointly from University College Dublin and the China Scholarship Council.

REFERENCES

[1] H. C. Rothery, *Tay Bridge Disaster: Report of the Court of Inquiry, and Report of Mr. Rothery, Upon the Circumstances Attending the Fall of a Portion of the Tay Bridge on the 28th December 1879*. George Edward Eyre and William Spottiswoode, 1880.

[2] P. M. R. Lewis and K. Reynolds, "Forensic engineering: a reappraisal of the Tay Bridge disaster," *Interdisciplinary Science Reviews*, vol. 27, no. 4, pp. 287-298, 2002.

[3] O. H. Amman, T. von Kármán, and G. B. Woodruff, "The failure of the Tacoma Narrows bridge," 1941.

[4] K. Y. Billah and R. H. Scanlan, "Resonance, Tacoma Narrows bridge failure, and undergraduate physics textbooks," *American Journal of Physics*, vol. 59, no. 2, pp. 118-124, 1991.

[5] J. Owen, A. Vann, J. Davies, and A. Blakeborough, "The prototype testing of Kessock Bridge: response to vortex shedding," *Journal of Wind Engineering and Industrial Aerodynamics*, vol. 60, pp. 91-108, 1996.

[6] R. C. Battista and M. Pfeil, "Control of wind oscillations of Rio-Niterói bridge, Brazil," *Proceedings of the Institution of Civil Engineers-Structures and Buildings*, vol. 163, no. 2, pp. 87-96, 2010.

[7] A. Larsen, S. Esdahl, J. E. Andersen, and T. Vejrum, "Storebælt suspension bridge–vortex shedding excitation and mitigation by guide vanes," *Journal of Wind Engineering and Industrial Aerodynamics*, vol. 88, no. 2-3, pp. 283-296, 2000.

[8] Xinhua, "Traffic resumes on South China sea bridge," in *China Daily*, ed. China, 2020.

[9] D. Wang, Y. Zhang, M. Sun, and A. Chen, "Characteristics of the wind environment above bridge deck near the pylon zone and wind barrier arrangement criteria," *Applied Sciences*, vol. 10, no. 4, p. 1437, 2020.

[10] W. Da-lei, C. Ai-rong, and M. Ru-jin, "Influence of wind barrier on aerodynamic characteristics of automobiles on bridge girder near pylon," *Engineering Mechanics (in Chinese)*, vol. 30, no. 10, pp. 244-250, 2013.

[11] N. Chen, Y. Li, B. Wang, Y. Su, and H. Xiang, "Effects of wind barrier on the safety of vehicles driven on bridges," *Journal of Wind Engineering and Industrial Aerodynamics*, vol. 143, pp. 113-127, 2015.

[12] T. Argentini, E. Ozkan, D. Rocchi, L. Rosa, and A. Zasso, "Cross-wind effects on a vehicle crossing the wake of a bridge pylon," *Journal of wind engineering and industrial aerodynamics*, vol. 99, no. 6-7, pp. 734-740, 2011.

[13] L. Salati, P. Schito, D. Rocchi, and E. Sabbioni, "Aerodynamic study on a heavy truck passing by a bridge pylon under crosswinds using CFD," *Journal of Bridge Engineering*, vol. 23, no. 9, p. 04018065, 2018.

[14] OpenFOAM, "OpenFOAM user guide version 9," vol. 3, O. F. Ltd, Ed., ed, 2021, p. 47.

[15] OSI. *Terrain data of the Rose Fitzgerald Kennedy Bridge site*, 23 March 2021.

[16] W. C. Skamarock *et al.*, "A description of the advanced research WRF model version 4," *National Center for Atmospheric Research: Boulder, CO, USA*, vol. 145, p. 145, 2019.

[17] B. E. Launder and D. B. Spalding, "The numerical computation of turbulent flows," *Computer Methods in Applied Mechanics and Engineering*, vol. 3, no. 2, pp. 269-289, 1974/03/01/ 1974, doi: https://doi.org/10.1016/0045-7825(74)90029-2.

[18] J. P. Van Doormaal and G. D. Raithby, "Enhancements of the SIMPLE method for predicting incompressible fluid flows," *Numerical heat transfer*, vol. 7, no. 2, pp. 147-163, 1984.

[19] H. Jasak, "Error analysis and estimation for the finite volume method with applications to fluid flows," 1996.

[20] R. Barrett *et al.*, *Templates for the solution of linear systems: building blocks for iterative methods*. SIAM, 1994.

[21] H. A. Van der Vorst, "Bi-CGSTAB: A fast and smoothly converging variant of Bi-CG for the solution of nonsymmetric linear systems," *SIAM Journal on scientific and Statistical Computing*, vol. 13, no. 2, pp. 631-644, 1992.

[22] J. D. Holmes, *Wind loading of structures*. CRC press, 2007.

Structures

50 Years of Pultruded FRP Materials in Structural Engineering

Lawrence C. Bank
School of Architecture, Georgia Institute of Technology, North Av NW, Atlanta, Georgia 30332, USA
email: lbank3@gatech.edu

ABSTRACT: Fiber reinforced polymer (FRP) standard profile shapes and other custom profile sections have been produced by the pultrusion processing method for use in structural engineering since the 1970s. In the past 50 years numerous attempts have been made by the industry and by the academic community to further develop these products for more widespread use by structural engineers. However, this has met with only limited success. This paper discusses the types of pultruded products developed for use by licensed professional structural engineers for use in structures over the past 50 years and provides an assessment of the current State-of-the Art. The paper does not discuss pultruded products used for architectural and industrial applications where a structural engineering professional is not required by the authorities to certify the design, nor does it discuss the use of pultruded materials as reinforcing bars or strengthening strips. The paper discusses topics related to Codes and Specifications, Standard Profiles, Building Systems, Bridges and Walkways, Poles and Powerline Parts, and Piles.

KEY WORDS: Buildings; Bridges; Codes; Infrastructure; Profiles; Pultrusion; State-of-the-Art; Structural Engineering

1 INTRODUCTION

Pultruded shapes and other profiles have been produced since the 1970s for use in structural engineering by licensed structural engineers. The first patents were issues in the 1950s [1] and a number of the larger pultrusion companies, first in the United States (e.g., Strongwell, Creative Composites Group, Bedford Reinforced Plastics), then in the UK and Europe (e.g., Pultrex, Fiberline, Exel) and more recently in China (e.g., Jiangsu Amer New Material Co) produce these items. Industry organizations include the Pultrusion Industry Council (PIC) of the American Composites Manufacturers Association (ACMA), the European Pultrusion Technology Association (EPTA), the European Composites Industry Association (EuCIA), and the International Institute for FRP in Construction (IIFC). The global pultrusion market is valued at approximately 2.5 billion USD with a compound annual growth rate (CAGR) of about 4-5% to the year 2028. The ASCE Journal of Composites for Construction [2], as well as other academic journals, publish current research in the field. A comprehensive database of publications related to pultruded structures is maintained by Professor Toby Mottram at Warwick University [3].

Over the last 50 years the major pultrusion companies, often led by the industry associations, have developed and produced numerous unique products for use by structural engineers in buildings, bridges and other infrastructure. Most of this work occurred in the 1980s to the 2000s when the industry embarked on efforts, often encouraged by government funding (e.g., US NSF, US DOT, EUROCORE), to introduce fiber composite materials, in general, and pultruded products, in particular, into civil infrastructure. A review of the State-of-the-Art up to the 2000s can be found in [4, 5]. In [4] the authors laid out the then challenges for the "Future for Pultruded Structural Shapes" as follows: "The increased acceptance of pultruded structural shapes for mainstream building and bridge superstructure applications will depend on three key developments. The first is the development of an internationally accepted material specification for pultruded materials ... the second is the development of a design code for pultruded structures … and the third … will be to reduce the cost of pultruded shapes …"

2 PULTRUDED MATERIALS FOR STRUCTURES

In the light of the three challenges presented above the pultruded products that have been developed and their successes and failures to penetrate the civil engineering profession and the construction industry are discussed by application area: Codes and Specifications, Standard Profiles, Building Systems, Bridges and Walkways, Poles and Powerline Parts, and Piles.

2.1 Design Codes and Specifications

In the early 1990s efforts began to develop design codes and specifications for use of pultruded FRP composites in structural engineering [6]. Most large manufacturers of pultruded profiles (e.g., Strongwell, Creative Composites Group, Bedford Reinforced Plastics, Fiberline) publish in-house design guides and material property specifications for use by structural engineers. These documents are manufacturer specific and are not approved by any code making authority. Today, in the absence of approved codes and specifications structural engineers who certify pultruded structures rely on these documents and other sources in the literature.

Since 1997 the American Society of Civil Engineers (ASCE) has been in the process of developing a standard for 'Load and Resistance Factor (LRFD) Design for Pultruded Fiber Reinforced Polymer (FRP) Structures.' Publication is expected in 2023-2024 [7]. In Europe, development of a Eurocode for 'Fibre-Polymer Composite Structures' is underway. Publication is expected in 2027-2028. [8]. A CEN specification for pultruded materials was published in 2002 [9]. Two grades,

E23 and E17 of pultruded materials are specified having minimum longitudinal tensile moduli of 23 GPa and 17 GPa, and tensile strengths of 240 and 170 MPa, respectively. Transverse, bearing and shear properties as well as full section properties of profiles are also specified. In comparison the specification for pultruded FRP reinforcing bar for concrete construction requires a minimum longitudinal tensile modulus of 39.3 GPa for all bars and a minimum guaranteed tensile strength of 690 MPa (13 mm diameter) and 550 MPa (25 diameter mm) glass reinforced FRP bar (strength is bar size dependent) [10]. As can be seen these are significantly higher than those specified for pultruded profiles. The very modest minimum properties specified in the CEN standard [9] for pultruded profiles means that there is no incentive for manufacturers to produce products with higher properties that would make pultruded profiles more competitive with conventional materials. With the properties specified in the CEN standard pultruded profiles have difficulty competing with solid lumber sections (i.e., they have the same flexural stiffnesses (EI) in the longitudinal fiber direction).

The concern that the author has with all these code and specification efforts is that they do not sufficiently exploit the advantages of pultruded composites such as anisotropy and inhomogeneity [11]. In many cases the guidance provided by the design documents listed above assume uniform mechanical properties in the profile elements (e.g., flanges and webs) or the properties specified are too low to enable meaningful designs for civil engineering structures, as noted above. Consequently, this author does not expect these new standards to encourage more structural engineers to design with pultruded materials. A more rigorous model specification that allows for different fiber layups and properties in a section is needed.

2.2 Standard Profiles

Common-sized I, H, and tubular profile shapes are made by many pultruders. Most to these shapes are based on those first developed in the 1970s by MMFG (now Strongwell). These shapes are not formally standardized according to any specification and each manufacturer produces slightly different geometries and properties for use with their design guides. Glass fiber reinforced profiles with polyester and vinylester resins are typically available but inventories are not large and large quantities (typically a minimum of 1000m in total length) need to pre-ordered with a six to eight week lead time if needed. Typical shapes are shown in Figure 1. The largest standard I beams are only 360 mm deep and have limited spanning capability due to their low depth and low stiffness [5]. Fiberline in Denmark developed their own shapes in the 1990s that have different geometries from those produced elsewhere but their load carrying capacities are similar.

Figure 1. Typical profiles shapes (National Grating)

Due to the small sizes available such shapes can only be used for small structures such as stairs, walkways and small trusses. In the early 1980s it was hoped that pultruded shapes having large multicellular sections would be produced that would allow for large multistory structures. This has not happened due to a variety of factors, but most likely because of cost relative to other structural materials. Pultruded profiles sell for about 4-6 €/kg and have a density of about 1.8 g/cm^3. In the opinion of this author the cost of pultruded material has been the most significant impediment to market penetration in civil engineering and not the absence of codes and specifications.

2.3 Building Systems

Early one-of-a-kind single-story gable-frame warehouse type buildings were constructed from custom and standard pultruded profiles in the 1970s to take advantage of their electromagnetic transparency. In the late 1980s Maunsell in the UK developed a building system based on multicellular panels and custom connectors [12]. One small building was built as a demonstration. A number of bridges, including the Aberfeldy footbridge in Scotland [5,12], were built using the system in the 1990s. A demonstration building called the eyecatcher was built in Switzerland in the late 1990s using Fiberline profiles. [5,12]. Exel composites in collaboration with Warwick University developed the Starlink Lightweight Building System in 2009-2012 [12], however, the system has only used in a demonstration project to-date. The light-weight non-corrosive advantages of these systems for housing or manufacturing were never realized due to the lack of customers. As with many pultruded products produced over the years these products are now dormant – meaning that they are no longer produced but that the pultrusion dies still exist and the shapes can readily be pultruded again if the demand picks-up. Images of these dormant products are not shown in this paper so as not to perpetuate the myth that these products are still being used by structural engineers.

The only building-type systems that are commonly constructed these days are those for specialized non-habitable HVAC cooling towers. Both ‘stick-built’ using balloon-frame light tubular pultruded profiles with FRP cladding and ‘beam-and-column frame’ systems with cladding are produced as seen in Figure 2. Pultruded profiles for cooling towers exploit the corrosion resistance of the FRP composites in the hot-wet environments of cooling towers and are a major part of this market. The structures are typically designed by in-house or consulting licensed structural engineers.

Figure 2. Stick-built (under construction) and Frame-type Cooling Towers. (Strongwell, Creative Composites Group/Tower Tech)

2.4 Bridges and Walkways

A detailed review of applications of pultruded materials in highway bridge decks and pedestrian bridges built in the US in the 1980s and early 1990s is presented in [13]. In the 1990s there was significant effort and funding devoted to developing pultruded bridge deck panels for corrosion resistance and ease of construction due to their light weight (approx. 100 kg/m^2) and prefabrication. This included Superdeck (Creative Composites Group) and DuraSpan (Martin Marietta Composites). Over 50 bridges were constructed in the US in the 1990s and early 2000s using primarily the DuraSpan system [14]. In Europe the ASSET Eurocore project also developed an FRP bridge deck in the late 1990s are used it in a small number of bridges [15]. In Korea a deck system called Delta deck was developed and marketed in the early 2000s [16]. A number of other pultruded multicellular geometries have been attempted. However, all of these products are now dormant and there is no longer an application of FRP decks in highway bridges. The primary impediment to the use of FRP decks has been installed cost (around \$800/m^2) and to some extent the inability of the bridge construction industry to integrate the products into their work processes and skill sets that typically use reinforced concrete decks that are easily finished with crowns and cross-slopes to the elevations needed.

Lighter weight and less bulky FRP planks are becoming quite popular for pedestrian bridge decking and for boardwalks as seen in Figure. 3 One specialty application where FRP plank decks exploit the light weight and corrosion resistance of pultruded materials is in case where pedestrian walkways and cycleways are added to existing bridges. Such structures are typically cantilevered off the original structure as seen in Figure 3.

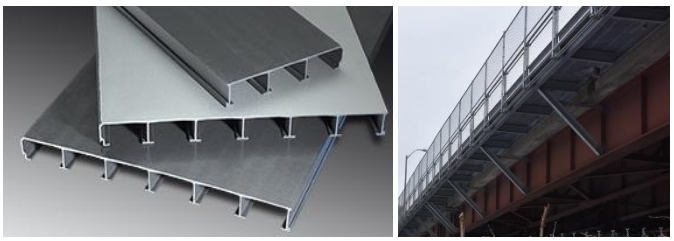

Figure 3. Pultruded Planks and Cantilevered Bridge Walkway (Strongwell and Creative Composites Group)

Small square and rectangular FRP pultruded profiles have been very successfully used in pedestrian or cycle or trail truss bridges over the past 30 years. Pioneering work by ET Techtonics (now part of Creative Composites Group) starting in the 1980s has led to FRP pultruded profiles being used in hundreds of relatively short span (10-30 m) through-truss bridges such as those shown in Figure 4. These bridges typically have a timber plank decking, however, FRP planks have also been used in some cases. They can be assembled on-site using standard steel (typically stainless steel) hardware or prefabricated and delivered to a site.

Figure 4. Pultruded Pedestrian Bridges (Creative Composites Group and Bedford Reinforced Plastics)

The success of FRP pedestrian bridges is due to the fact that they are cost-competitive with conventional welded steel truss bridges and more durable than timber bridges. In addition, they are significantly lighter and easier to deliver and install in inaccessible locations (hiking trails etc.). They resemble timber truss-bridges and blend in well with the natural environment. The bridges are typically designed by in-house structural engineers.

Similar to pedestrian bridges pultruded materials have been successful in the industrial and transportation fields where stairs, walkways, safety railings, and platforms are needed due to their ease of assembly, light-weight and corrosion resistance. Pultruded gratings are typically used for the decking as seen in Figure 5.

Figure 5. Pultruded Stairways and Platforms (Strongwell and Creative Composites Group)

2.5 Poles and Powerline Products

Pultruded constant cross-section poles and tapered poles constructed from pultruded plates are produced for street lighting and for powerlines. The lighting poles are typically standard pultruded round tubes that are fitted with hardware for attachments and foundations. Larger pultruded utility poles are available for a number of pultrusion companies. Pultruded cross-arms (seen in Figure 6), guy strain insulators, and insulators are marketed by a number of specialty companies (e.g., Hughes Brothers). Advantages include light weight for transportation and erection and resistance to the elements and animals. Many other FRP poles are produced by other processes such as filament winding and centrifugal casting that have the advantage of being able to produce tapered poles that are often desired. Poles and other transmission structures (e.g. substations) are typically designed by licensed structural

Figure 6. Round pultruded pole and pultruded cross-arm attachment (Creative Composites Group and PUPI Inc).

engineers at specialty powerline design consultants. The authors believes that more opportunities will be available in this market with the rapid expansion of wind power.

2.6 Piles

Round pipe piles and interlocking sheet piles produced by the pultrusion process have been under development for at least the past 25 years [17]. Examples are shown in Figure 7. They are now available from a number of suppliers and are typically designed by specialty firms. Most applications involved marine or waterfront locations that take advantage of the corrosion resistance of the FRP material.

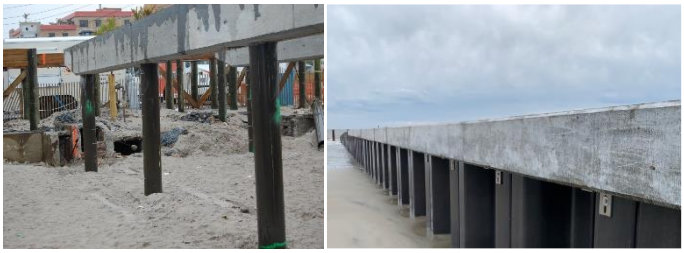

Figure 7. Pipe pile and sheet pile installations (Creative Composites Group and CMI/Strongwell).

3 CONCLUSIONS

Pultruded FRP materials that are currently available for design of civil structures by licensed structural engineers have been discussed in this paper. The assessment of the author is that the ambitious goals for the widespread use of pultruded FRP composites in civil infrastructure set by academic researchers, industry groups and government funding agencies in the 1980s and 1990s have unfortunately not been met. The three elements of the "Holy Grail" noted in the introduction – design codes, meaningful specifications, and lower costs have not yet been realized.

The development of codes and specifications was intended to allow non-FRP-expert structural engineering professionals engaged in the design of steel, concrete and timber structures on a routine basis to be able to similarly design with FRP pultruded profiles. However, today most FRP structures are still designed by in-house licensed structural engineers or specialty consultants using proprietary products. The very slow pace of code and specification development has contributed to this, but costs still are the most important impediment to widespread use of pultruded FRP in civil infrastructure, even in corrosive environments. There is still some hope that the now dormant FRP pultruded products may yet have their day in the sun.

The industry appears to have retreated to its original roots of producing commodity parts such as ladder rail, and other small-sized pultruded profiles for specialized industrial applications. The industry growth appears to be mostly in these areas and not in the large pultruded profiles needed for civil infrastructure. Promising areas for the widespread use of FRP pultruded profiles in civil infrastructure at this time appear to be in HVAC cooling towers and pedestrian footbridges. Marine and coastal applications have potential but the cost of FRP pultruded products relative to conventional alternatives remains a challenge, even when life-cycle costs are taken into account.

A future challenge for pultruded products and all FRP composites in infrastructure is also emerging – how to dispose of or recycle these non-biodegradable products at their end-of-life. Even though more durable than existing construction materials they will eventually need to be replaced, possibly due to functional obsolescence rather than material degradation or structural deficiencies.

ACKNOWLEDGMENTS

The many colleagues and students who have worked with me over the past 35+ years on FRP pultruded structures are sincerely thanked for their contributions. Special thanks are extended to Prof. Russell Gentry at Georgia Tech and Prof. Toby Mottram at Warwick University. Funding for the work over the years was provided primarily by the US National Science Foundation and the US Department of Transportation. Generous donations of pultruded materials from Creative Composites Group and Strongwell (originally MMFG) over the years are also appreciated.

REFERENCES

[1] Goldsworthy, W. B., and Landgraf, F. (1959), 'Apparatus for producing elongated articles from fiber-reinforced plastic material,' U.S. patent 2,871,911.

[2] Journal of Composites for Construction, (1997-), American Society of Civil Engineers (ASCE), Reston, VA.

[3] Mottram, J.T., (current), 'Reference and Bibliography Database on Research and Development with Pultruded Fibre Reinforced Polymer Shapes and Systems database,' https://warwick.ac.uk/fac/sci/eng/people/toby_mottram/hp-contents/pfrp_latest.pdf (Accessed 6 July 2022)

[4] Bakis et al, (2002), 'Fiber-Reinforced Polymer Composites for Construction - State-of-the-Art Review,' ASCE J. of Comp. for Const., Vol. 6, No. 2, pp. 73-87.

[5] Bank, L.C., (2006), Composites for Construction: Structural Design with FRP Materials, John Wiley & Sons, ISBN: 0-471-68126-1, 551 pages. pgs. 18-23; 359-363.

[6] Bank, L.C., (1995), 'How Standards will Develop Markets in Building Construction,' in the proceedings of the 50th Annual SPI Conference, Composites Institute, Society for the Plastics Industry, Cincinnati, OH, January 28 - February 1, 1995.

[7] Chambers, R. (1997), 'ASCE Design Standard for Pultruded Fiber-Reinforced-Plastic (FRP) Structures,' ASCE J. of Comp. for Const. Vol. 1, No. 1

[8] Eurocode (2022), 'Toward a Eurocode for Fiber-Polymer Composite Structures,' https://eucia.eu/news/new-brochure-on-eurocodes/ (Accessed 6 July 2022)
[9] EN 13706:2002 'Reinforced plastics composites - Specifications for pultruded profiles, Parts 1,2 and 3' CEN European Committee for Standardization, Brussels, BELGUIM.
[10] ACI SPEC-440.6M-08(17)(22) (2022), Specification for Carbon & Glass Fiber-Reinforced Polymer Bar Materials for Conc Reinforcement (Metric) (Reapproved 2022).
[11] Bank, L.C., Yin, J. Nadipelli, M. (1995), "Local Buckling of Pultruded Beams - Nonlinearity, Anisotropy and Inhomogeneity," Construction and Building Materials, Vol. 9, No. 6, pp. 325-331.
[12] Evernden, M., Mottram, J. (2009) 'A Case for Houses in the UK to be constructed of Fibre Reinforced Polymer Components,' 11th International Conference on Non-conventional Materials and Technologies, NOCMAT 2009, Bath, UK.
[13] Bank, L.C. (2006), 'Application of FRP Composites to Bridges in the USA,' Proceedings of the International Colloquium on Application of FRP to Bridges, Japan Society of Civil Engineers (JSCE), pp. 9-16.
[14] Triandafilou L, O'Connor J. (2009), 'FRP Composites for Bridge Decks and Superstructures: State of the Practice in the U.S.' Proceedings of International Conference on Fiber Reinforced Polymer (FRP) Composites for Infrastructure Applications, University of the Pacific, Stockton, CA, 2009.
[15] Luke, S. Canning, L. Collins, S., Knudsen, E., Brown, P., Taljsten, B., and Olofsson, I, (2002) 'Advanced Composite Bridge Decking System—Project ASSET', Structural Engineering International, 12:2, 76-79.
[16] Lee, S-W., Hong, K-J., and Park, S-Z., (2012) 'FRP Composite Decks for Bridges and Walkway/Bikeway Expansions in Korea,' International Workshop on Applications of FRP Composites in Civil Engineering 2012 IWAFRPCCE Taipei, Taiwan, 5-6 November, 2012.
[17] Zyka, K., Mohajerani, A., (2016) 'Composite piles: A review,' Construction and Building Materials, Vol. 107, pp. 394-410.

Optimising existing digital workflow for structural engineering organisations through the partnering of BIM and Lean processes.

John McLaughlin[1] and Barry McAuley[2]
[1&2] School of Surveying and Construction Innovation, Technological University Dublin, City Campus Dublin 1, Ireland.
email: jmclaughlin@jbbarry.ie, Barry.Mcauley@TUDublin.ie

ABSTRACT: Building Information Modelling (BIM) is now seen as one of the leading transformative processes within the Architectural, Engineering and Construction (AEC) sector and has the potential to assist in streamlining the structural design process. However, its practical implementation can often add another layer to the existing workflow and can result, to its detriment, in the primary objective of optimising structural workflows being hindered. This can lead to structural organisations producing 3D models in tandem with traditional drawings, a lack of human intervention regarding software interoperability, and a reluctance to move away from conventional work methods. This paper will explore how a lean approach to BIM adoption can optimise the digital structural workflow, thereby enhancing BIM adoption. Although much research has been conducted on BIM as an enabler of Lean, there remains a gap regarding the synergies in how Lean tools can advance BIM adoption within the structural discipline. The closing of this knowledge gap will be advanced by comparing existing digital workflows within a structural organisation against a proposed integrated BIM workflow underpinned through Lean. The findings highlight that while BIM and Lean offer enhanced digital solutions to modernise structural design office workflows, the true capability of these tools will not be realised without a cultural change.

KEYWORDS: Building Information Modelling; BIM and Lean; Robot; RC; Value Stream Mapping.

1 INTRODUCTION

Engineering is constantly evolving and, through its very nature, embraces innovation. An innovation currently shaping the construction industry's future is Building Information Modelling (BIM). BIM can be viewed as a disruptive innovation; it requires a fundamental shift from traditional work practices. It is not a software but a process underpinned by technology and collaboration, requiring cultural change within organisations to leverage its benefits fully. BIM adds value to the construction design process, but that is dependent on human interaction with it.

The authors' anecdotal experience within the structural engineering sector suggests that BIM is used primarily due to project or client requirements. The organisational structure, in many cases, is set up to react to this requirement, not embrace it. BIM can often be viewed as a draughting software and when introduced alongside traditional work practices can sometimes add to existing workflows and create a more inefficient structural design process. BIM in isolation has not resulted in a complete cultural change within the sector; a shift in mindset is also required to facilitate this. Lean thinking, a philosophy driven by eliminating waste and creating better value, helps accelerate this cultural change.

This paper highlights how lean thinking can aid effective BIM implementation within the structural engineering sector, removing wastes, adding value, and optimising design office workflows.

2 LITERATURE REVIEW

Structural engineering is a sub-discipline of civil engineering that deals primarily with analysing, designing, and constructing structures. Structural engineers apply the laws of mathematics, physics, and empirical knowledge to safely design the internal skeleton and foundation of a structure [1]. The field has advanced by necessity to support the growing size and complexity of buildings and other structures through the ages. As human knowledge has progressed, it has introduced new ideas and technologies that continue to evolve the industry, such as the use of cast iron and cement in built structures and the introduction of AutoCAD, one of the most widely utilised CAD programs in the structural engineering sector today [2]. One of the more recent advances with the potential to transform the industry is Lean construction, a philosophy based on lean manufacturing concepts.

2.1 Lean

Toyota developed the 'Lean' manufacturing process in its car manufacturing plants in Japan in the decades after the Second World War, which at its core was eradicating waste and non-value-adding methods [3]. Toyota achieved this by developing the 5S (sort, set in order, sweep, standardise, sustain) process and empowering employees [4].

The success of Toyota's lean approach led to the realisation that the same principles, extrapolated from the specific environment of car manufacturing, have the potential for a universal application in other areas of manufacture and production. Adopting Lean principles such as defining value; mapping the value stream; creating flow; using a pull system, and pursuing perfection would significantly reduce waste from the supply chain. Many studies have explored its context within the construction industry, where adopting this new philosophy would create a paradigm shift within the sector [5,6].

Lean implementation is mainly focused on eliminating Muda (waste) in the process. Lean tools, including Value Stream Mapping (VSM), Last Planner, and Just-in-Time, help identify these wastes, allowing the sector to improve efficiency, and enabling lean thinking to be applied in practice [5].

Despite increased awareness and the clear advantages offered by implementing Lean thinking, tools, and principles in the

construction sector, the actual implementation of Lean construction practices has been anything but universal in the industry. Many structural and cultural factors feed into the failure to embrace Lean construction principles fully, including:-

- Traditional management structures within the sector that do not allow for the 'flattening of the management structure' and 'closing the loop';
- The existing disconnection between design and design implementation leads to costly conflicts;
- The adoption of Lean-thinking principles from the manufacturing industry without the necessary modification for the construction sector;
- A lack of knowledge or understanding of the fundamental concepts and application of Lean;
- The disparate and fragmented nature of the construction industry;
- The financial cost of providing the necessary education, skills, and resources required to implement Lean [6].

This has seen the argument for the partnering of Lean and BIM due to their substantial synergies as a potential vehicle to advance the sector.

2.2 BIM

Traditional non-BIM methodologies see professionals develop their design in silos before exchanging information with the rest of the project team. As a result, this data may have already become obsolete by the time it is shared. In contrast, BIM, which can be defined as using a shared digital representation of a built asset to facilitate design, construction, and operation processes to form a reliable basis for decisions, can enable a more integrated approach [7,9].

The information produced through the BIM model can be shared with partners through a common data environment (CDE), which encourages collaboration and enables the structural engineer to connect with the workflows and data of all project team members, offering a real-time view of the design development [11].

BIM is becoming an integral part of the structural engineering workflow. The interoperability of programs within BIM allows for a quicker and more accurate structural design. The structural engineer's ability to collect a vast amount of information from these data-rich models has resulted in a more precise assessment of developments allowing them to incorporate as lean and as sustainable a design as possible [8].

If BIM implementation is successful, companies need to ensure that their adoption processes result in a leaner and more efficient workflow [9]. Suppose BIM is operated in tandem with traditional methods. In that case, the company does not benefit from BIM's potential for streamlining the construction process, enhancing efficiency, and waste reduction, but it can add to workflows and costs. This, in turn, can lead to a negative view of new technologies and a reluctance to introduce them into the sector [10].

2.3 Lean and BIM

BIM facilitates lean measures through design to construction to occupancy and, at the same time, contributes directly to lean goals of waste reduction, improved flow, reduction in overall time, and improved quality by utilising clash detection, visualisation, and collaborative planning [15]. According to Sacks *et al.,* there are 56 synergies between BIM and Lean construction. A survey of experimental and practical literature found that 48 of the 56 interactions were seen as beneficial in optimising the flow of information and materials [11].

The Construction Industry Research and Information Association (CIRA) put forward four main mechanisms for how Lean and BIM interact. These mechanisms include;

- *BIM contributes directly to Lean goals* - BIM offers the ability to visualise the project and analyse the building design, greatly benefiting the client, designers, and contractors. This results in reduced variations at the planning and design stage.
- *BIM contributes indirectly to Lean goals by enabling Lean processes* - Utilising BIM tools such as 4D planning to simulate and demonstrate how a task can be best-performed offers a much greater understanding than the traditional methods at the planning stage.
- *The auxiliary information systems of the design team can, when enabled by BIM, contribute directly and indirectly to Lean goals* - The analysis model for the structural engineer is an example of this, whereby the interoperability of BIM programs has enabled a smoother iteration between the design and analysis programs than more traditional methods.
- *Lean processes facilitate the introduction of BIM* - Lean construction's emphasis not only on collaboration, predictability, and discipline but also on experimentation facilitates BIM implementation [12].

Team working skills, critical thinking, leadership, communication skills, work ethics, knowledge, and positive attitudes help enable lean and provide the foundation to facilitate the full potential of BIM within the sector [13]. A willingness to transition from traditional working methods and embrace Lean thinking and new technologies could positively impact structural engineering organisations. An example of this is in modelling reinforced concrete (RC) components in structural concrete models. RC can account for up to 15% of an overall construction build, so a significant opportunity exists to leverage BIM for RC design within the sector to minimise waste and visualise complicated junctions to solve clashes before they reach the site, ultimately saving considerable time and money on a project [14].

3 METHODOLOGY

This paper aims to understand to what extent Lean thinking and its culture can enhance BIM processes and facilitate its adoption within a structural engineering organisation. Focusing on an existing BIM project, an action research study is applied to discover and compare the current workflow used on BIM projects against a leaner BIM workflow. The subject of the action research study is a large mixed-use development spread over multiple blocks comprising of apartments, commercial and amenity spaces. Due to the scale of the development, the fact that it is still under construction, and the time constraints of this study, the authors focused solely on one aspect of the structural design office workflow, namely the current RC element of the project, from the initial design to publishing the drawings and schedules on the project's CDE. The potential

benefits of utilising the interoperability of the company's analysis software and integrating project reinforcement elements into the BIM environment will be explored.

Design engineers built the initial analysis model, and a survey was issued to help gather an accurate indication of the data for this element. The results found that the engineers did not complete an overall analysis model containing the complete design analysis for the development; instead, a series of individual models were built up based on the most urgent RC requirement on site. The process involved in building these models, how long it took, and the advantages and disadvantages of this method were investigated. The information gathered helped to assign a time to this research element.

To provide data for building the proposed future state analysis model, the authors used the structural model to set up the analytical model in Revit before using the bi-directional link to send this information to Robot. The design engineers then checked the model to ensure it was fit for purpose. The time taken to undertake this process was recorded.

The time constraints of this study meant it was not possible to re-do the entire reinforcement drawings and schedules for the project in 3D. Instead, the authors completed an area within the BIM environment utilising CADS RC3D, and the time taken to undertake this task was recorded.

The Lean tool Value Stream Mapping (VSM) was chosen to provide a structured visualisation of the critical steps and associated data to help understand and optimise the entire process. VSM, one of the most widely adopted Lean tools for construction, is designed to eliminate waste and all activities that do not add value throughout the construction processes, thereby providing a clear view of the best way to maximise customer value.

4 PRIMARY RESEARCH

4.1 The current workflow for reinforcement on BIM projects

To evaluate if Lean and BIM synergies could enhance RC workflows within the structural engineering sector, it is essential to understand the organisation's current process. The action research was conducted on a BIM project set to ISO 19650 standards. The concrete elements were modelled within the BIM environment; however, the reinforcement input sat unconnected alongside this process. As discussed earlier in this paper, BIM is not widely leveraged by structural engineering organisations for reinforcement design, a more traditional workflow is often used.

Revit and Robot Structural Analysis Professional software was used to create draughting and analysis models on structural projects within the organisation. Revit supports the BIM process by providing a physical model for documentation and an associated analytical model for structural analysis and design. The bidirectional link between these programs enables users to send a model directly from Revit to Robot for structural analysis and design.

Similar to traditional non-BIM methodologies, software-dependent silos developed within the organisation, as illustrated in Figure 1. Each professional developed the design before exchanging this information with the rest of the structural team. As a result, this data can become obsolete by the time it is shared.

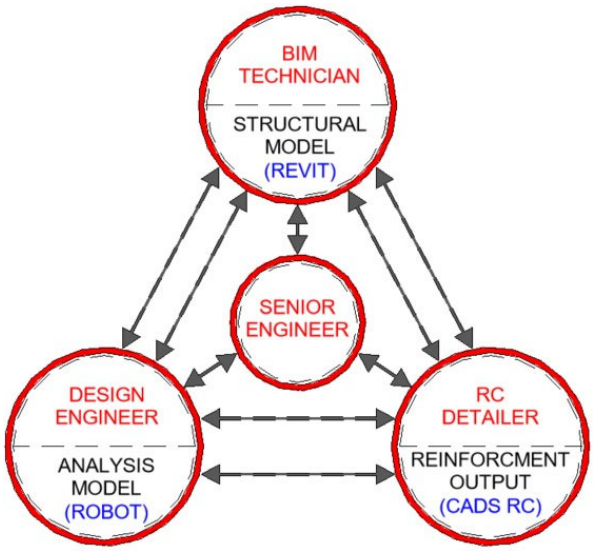

Figure 1. Current RC Workflow

The current organisational workflow for project reinforcement design and the production of RC construction documentation is detailed below:

- A structural model is created from the existing architectural information;
- 2D dwg format plans are extracted from the model by the BIM technician and sent to the design engineer;
- The design engineer inputs connection point locations into these drawings and links this information into Robot Structural Analysis;
- The design engineer creates an initial independent analysis model from 2D information;
- The design engineer runs calculations within Robot and informs the BIM technician of the required changes;
- As neither model is linked, the BIM technician updates the Revit model accordingly, i.e., incorporate beam loads and changes, column or foundation sizes, etc.;
- Multiple plans, sections, and elevation sheets are created and cut from the Structural model by the BIM technician, providing this information to the RC detailer;
- After extraction to dwg format, this information is deleted from the model to ensure no reinforcement-specific section marks, plans, or elevations are shown on the general arrangement (GA) drawing sheets within the model;
- In AutoCAD, the extracted sheets are cleaned up by the RC detailer to align with all company draughting standards, including line type and text styles;
- The RC detailer undertakes the reinforcement in CADS RC 2D; and
- The RC detailer then publishes the reinforcement drawings and schedules to the project CDE.

As the project design develops, the structural and analysis models and reinforcement drawings are updated independently, requiring the above steps to be repeated after every design change.

4.2 VSM – The Current State

A value stream map was created to help record and reflect on this workflow. Each step was mapped, with a data box included in each process containing information on the cycle time (C/T) or person-hours to undertake the task.

As illustrated in Figure 2, the information flows left to right across the page from the project CDE before being pushed back into the CDE once the design and analysis processes are completed. Due to the siloed nature of the current workflow, mapping of three independent design engineers, BIM technicians, and RC detailer workflows was required, placed from top to bottom respectively, on the diagram. Points, where these workflows interact, were added before two timelines were created, one for the reinforcement design and the second for the drawing and schedule production process. The timelines have two levels of information taken from the data boxes. On the top are the value-added processes' times, and on the bottom, the non-value-added actions or lead times. Added together, this provides the total C/T to complete each workflow.

The current state had excessive waste in the process, with considerable time, effort, and re-work expelled on the project. A significant finding of the mapping exercise was that the total contribution of the BIM technician to the current RC workflow consisted solely of waste or necessary non-value-adding activity. In essence, the current way of working with reinforcement was not only outside the BIM workflow but it also required much additional work to extract information.

4.3 Embedding reinforcement drawings and schedules within the BIM workflow

Mapping the current process enabled the authors to identify the areas of overproduction and waste, and this information was used as the basis for the future state map. The authors identified some typical lean opportunities within this design environment to eliminate this waste to improve efficiency and the overall quality of the process. One of these opportunities involved leveraging the power of the software packages and utilising the interoperability of the organisation's structural design and analysis software to reduce the person-hours within the workflow.

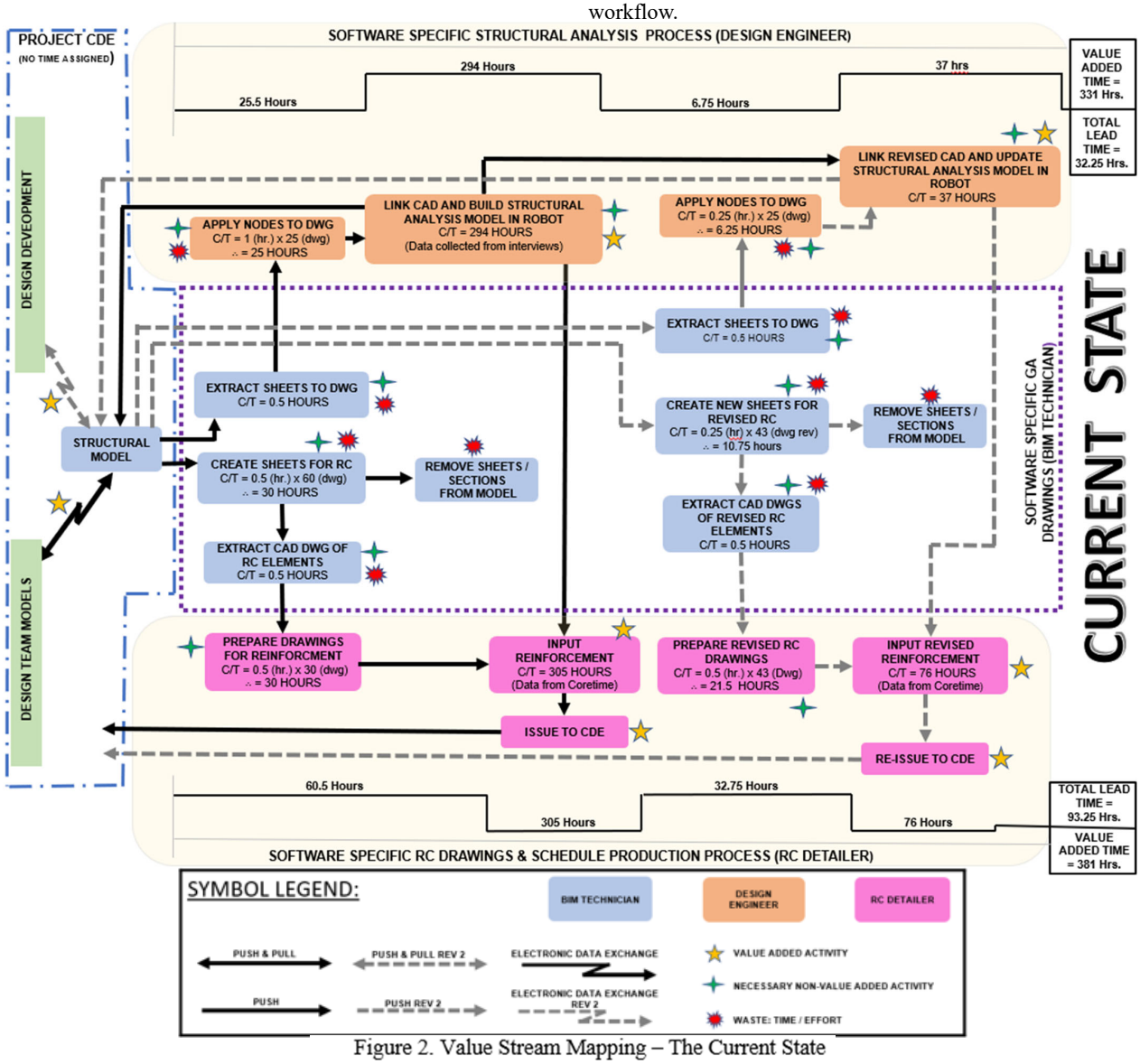

Figure 2. Value Stream Mapping – The Current State

The current software used to detail reinforced concrete within the organisation is CADS RC2D. In recent years a Revit add-on CADS RC3D., has been developed to enhance reinforcement detailing and scheduling within Revit. This has made the transition from 2D detailing more straightforward, offering increased productivity through its enhanced functionality. The authors explored the functionality of this software by detailing sections of the project previously completed in 2D and testing the viability of introducing it into the company's reinforcement workflow.

There were significant advantages that contributed to lean goals. The ability to produce the reinforcement within the structural model provided the opportunity to streamline the office workflow significantly by removing the excessive non-value added activities. In addition, as the design develops, less re-work is required. Initial parameters, such as reinforcement cover and centres of bars, are set, and Revit retains this information. If a pile cap, column, or beam size, for example, is changed, then the reinforcement for these elements will automatically update. The detailing process is also enhanced by visualising this information in 3D. A complete view of complicated areas is provided, ensuring all factors are considered and offering greater clarity.

The reinforcement now embedded in the BIM workflow enables the project team to utilise clash detection tools. The entire project team can track the progress of this clash resolution, ultimately eliminating the risk of costly errors and re-work on site.

4.4 VSM – The Future State

A VSM was created to focus on what the workflow ideally looks like after the process improvements outlined in the previous sections of this paper have taken place in the value stream. This future state workflow, illustrated in Figure 3, shows considerably less waste in the process. The fragmented nature of the current workflow is replaced by a more collaborative approach achieved through integrating the RC deliverables into the BIM workflow. The ability to push and pull information electronically from the structural and analysis model, as illustrated in Figure 4, enriching the central structural model hosted on the project CDE helps avoid potential errors resulting from manual coordination of construction documentation. The structural model is enriched with the RC analysis and draughting information, ensuring that the organisation's design team, the project design team, and all other professionals involved in the project have access to the most up-to-date and reliable information.

While the data illustrated demonstrates the considerable gains in design efficiency in bringing the development to its current stage on-site utilising this workflow, it also indicates the potential of exponential advantages as the project develops. Design changes naturally occur on projects; the dashed arrows shown on the future state map represent such changes undertaken on the project to date. With the link already created between the RC elements and the structural model, the time

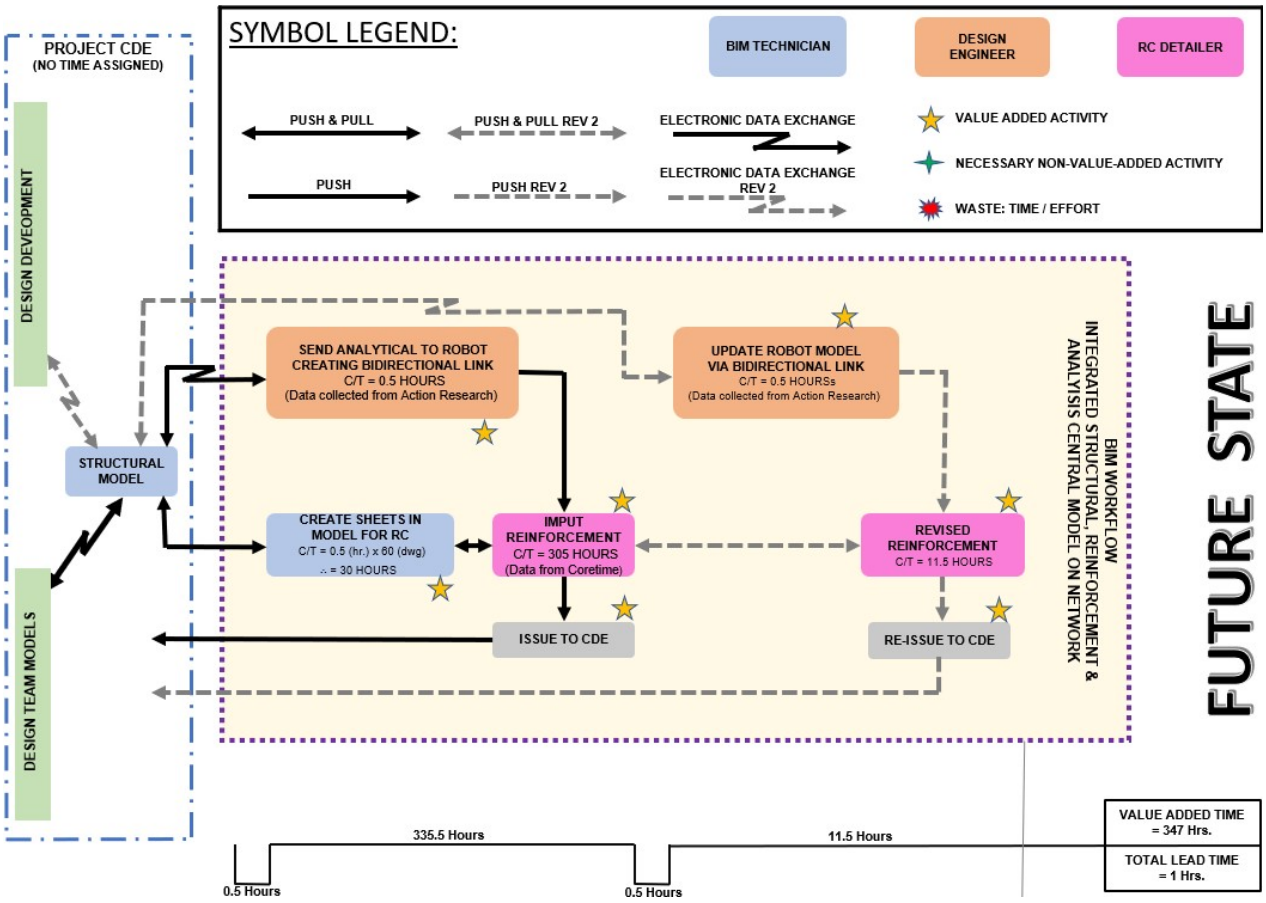

Figure 3. Value Stream Mapping – The Future State

required to undertake these revisions would be reduced up to the project completion stage.

From conducting the VSM exercise on both the current and future state workflows, the importance of integrating the reinforcement elements of projects into the BIM environment is evident.

4.5 Enhanced BIM and Lean workflow

Throughout their research on the project, the authors found that embedding the reinforcement design and draughting processes can bring the whole structural design team together, offering a more collaborative workflow that eliminates non-value-added activity.

The central model stored on the organisation's network, hosting the integrated structural, reinforcement and analysis models, essentially acts as a CDE for the project. Creating local files from this data-rich central model, which serves as `the single source of truth` for the structural information, allows each collaborator to proceed with their specific design or detailing before syncing this information back to the central model and updating it. The enhanced workflow, illustrated in Figure 4, removes the current design silos, ensuring that the most up-to-date information is accessible to all stakeholders within the process.

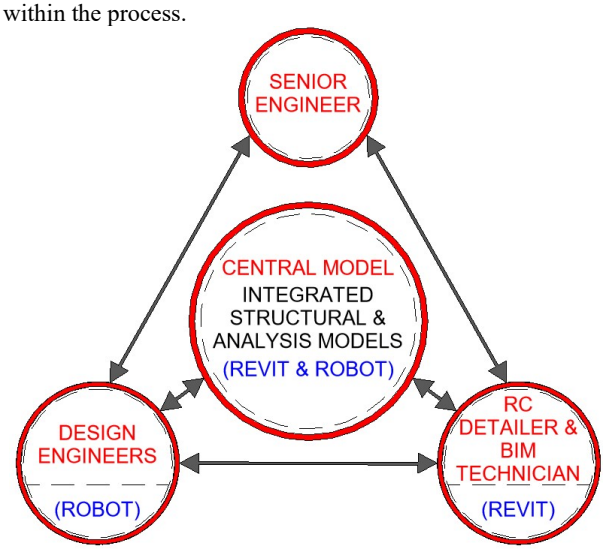

Figure 4. Enhanced RC BIM Workflow

The findings of the mapping exercise highlighted a marked increase in efficiency, with the future state workflow reducing cycle times by 60%, as shown in Table 1.

Table 1: Cycle Time Reduction

	Current State (hrs)	**Future State (hrs)**
Value Added Time	712	347
Lead Time	168.25	1
Cycle Time	880.25	348
Percentage Improvement in Process Time = (Future State–Current State)/Current State x 100%		
∴ (348-880.25) / 880.25 x 100% ∴-532.25 / 880.25 x 100% ∴ = -60.46%		

5 CONCLUSIONS

One of the most significant obstacles to the advancement of BIM within structural engineering organisations is that it is often presented as a stand-alone initiative. As highlighted in this paper, BIM can be applied without Lean; however, the efficiencies inherent in BIM are not often realised when implemented in this way. Introduced in this manner, BIM can, in many cases, add another layer to the traditional structural design workflows without the proper organisational structure in place. Thus, the successful alignment of BIM with work processes is critical for successful BIM adoption. Lean thinking fosters a culture of continuous improvement, enabling organisations to adapt and embrace this new way of working. The synergies between Lean and BIM mean combining both achieves more significant benefits than introducing BIM in isolation.

REFERENCES

[1] D. M. El-Mogy and N. Moscovitch, "Ultimate Guide to Structural Engineering Basics!," ed. https://structuralengineeringbasics.com/, 2019.

[2] E. Lockatong, "A Brief History of Structural Engineering," ed. https://www.lockatong.com/a-brief-history-of-structural-engineering, 2019.

[3] J. P. Womack, D. T. Jones, and D. Roos, "The machine that changed the world: the story of lean production -- Toyota's secret weapon in the global car wars that is revolutionising world industry," Simon and Schuster, 1990.

[4] L. Koskela, "Application of the New Production Philosophy to Construction," Stanford University, 1992.

[5] G. A. Howell, "What Is Lean Construction - 1999," in *7th Annual Conference of the International Group for Lean Construction*, Berkeley, California, USA, 1999/07/26 1999, Berkeley, California, USA. [Online]. Available: http://iglc.net/Papers/Details/74

[6] S. Sarhan and A. Fox, "Barriers to Implementing Lean Construction in the UK Construction Industry," *The Built & Human Environment Review,* vol. Volume 6, pp. pages 1-17, 01/01 2013.

[7] R. Sacks, C. Eastman, G. Lee, and P. Teicholz, *BIM Handbook - A Guide to Building Information Modeling for Owners, Designers, Engineers, Contractors, and Facility Managers*, Third Edition ed. John Wiley & Sons, Inc., Hoboken, New Jersey, 2018.

[8] P. Bynum, R. R. A. Issa, and S. Olbina, "Building Information Modeling in Support of Sustainable Design and Construction," *Journal of Construction Engineering and Management,* vol. 139, no. 1, pp. 24-34, 2013, doi: 10.1061/(ASCE)CO.1943-7862.0000560.

[9] R. Sacks, L. Koskela, B. A. Dave, and R. Owen, "Interaction of Lean and Building Information Modeling in Construction," *Journal of Construction Engineering and Management,* vol. 136, no. 9, pp. 968-980, 2010, doi:10.1061/(ASCE)CO.1943-7862.0000203.

[10] R. Montague. "No more `pseudo BIM` please." NBS. https://www.thenbs.com/knowledge/comment-no-more-pseudo-bim-please (accessed 11/11/2021, 2021).

[11] R. Sacks, B. Dave, L. Koskela, and R. L. Owen, "Analysis framework for the interaction between lean construction and Building Information Modelling," *Proceedings of IGLC17: 17th Annual Conference of the International Group for Lean Construction,* 01/01 2009.

[12] B. Dave, L. Koskela, A. Kiviniemi, P. Tzortzopoulos, and R. Owen, *Implementing lean in construction: lean construction and BIM*. 2013.

[13] K. A. T. O. Ranadewa, Y. G. S. Y.G. Sandanayake, and M. Siriwardena, "Enabling lean through human capacity building: an investigation of small and medium contractors," *Built Environment Project and Asset Management,* vol. 11, no. 4, pp. 594-610, 2021, doi: 10.1108/BEPAM-03-2020-0045.

[14] S. Kumar and J. Trivedi, "BIM for reinforcement detailing in RCC frame structures," International Journal of Research in Engineering and Technology, vol. 05, no. 32, pp. 307–313, 2016.

An advanced binary slime mould algorithm for feature subset selection in structural health monitoring data

Ramin Ghiasi[1], Abdollah Malekjafarian[1]
[1]Structural Dynamics and Assessment Laboratory, School of Civil Engineering, University College Dublin, D04V1W8 Dublin, Ireland
email: rghiasi.s@gmail.com, abdollah.malekjafarian@ucd.ie

ABSTRACT: Feature selection is an important task for data analysis, pattern classification systems, and data mining applications. In this paper, an advanced version of binary slime mould algorithm (ABSMA) is introduced for feature subset selection to enhance the capability of the original SMA for processing of measured data collected from monitoring sensors installed on structures. In the first step, structural response signals under ambient vibration are pre-processed according to statistical characteristics for feature extraction. In the second step, extracted features of a structure are reduced using an optimization algorithm to find a minimal subset of salient features by removing noisy, irrelevant and redundant data. Finally, the optimized feature vectors are used as inputs to the surrogate models based on radial basis function neural network (RBFNN). A benchmark dataset of a wooden bridge model is considered as a test example. The results indicate that the proposed ABSMA shows better performance and convergence rate in comparison with four well-known metaheuristic optimizations. Furthermore, it can be concluded that the proposed feature subset selection method has the capability of more than 80% data reduction.

KEY WORDS: Feature selection; Binary slime mould algorithm; Surrogate model, Data reduction.

1 INTRODUCTION

Vibration-based structural health monitoring has been widely explored over the past decades. Avci et al. [1] and Das et al. [2] presented a comprehensive review of various vibration-based damage detection methods and their applications to civil structures and infrastructures. Recently, with the fast development in sensing technologies [3], [4], signal processing techniques [5], [6], and machine learning [7], [8], a number of advanced methods have been proposed [10,11]. Gharehbaghi al. [9] recently reviewed the new development of structural health monitoring for civil engineering structures.

In vibration-based SHM, damage identification is performed from vibration signals measured simultaneously at different locations of the structure [10]. Damage detection can be performed in the time domain from the raw sensor data or in the feature domain, in which damage-sensitive features are first extracted from the time series, This process is referred to as feature extraction [11].

Another importing step in extracting the useful information and signal processing is Feature Selection (FS) [12], [13]. FS is generally used in machine learning, especially when the learning task involves high-dimensional datasets. The primary purpose of feature selection is to choose a subset of available features, by eliminating features with little or no predictive information and also redundant features that are strongly correlated [12]–[14]. The availability of large amounts of data represents a challenge to classification analysis. For example, the use of many features may require the estimation of a considerable number of parameters during the classification process. Ideally, each feature used in the classification process should add an independent set of information. Often, however, features are highly correlated, and this can suggest a degree of redundancy in the available information which may have a negative impact on classification accuracy [12]. Thus, the FS approaches is needed to tackle these problems.

For a large number of features, evaluating all states is computationally non-feasible and therefore metaheuristic search methods are required. Due to the inefficiency of traditional search approaches in solving complex combinatorial optimization problems various metaheuristics have been proposed, such as Particle Swarm Optimization (PSO)[15], Genetic Algorithm (GA)-based attribute reduction [16], Gravitational Search Algorithm (GSA) [17].

The metaheuristic algorithms above-mentioned strengths motivated us to present a metaheuristic-based method for FS in SHM. Slime mould algorithm (SMA) [18] is a novel and robust metaheuristic algorithm proposed to solve continuous problem and it's inspired by the propagation and foraging of the slime mould and includes a unique mathematical model. However, considering that the FS is a combinatorial optimization problem, a binary version of SMA is used [19], and its performance is improved by incorporating two new operators in algorithm: mutation and crossover.

The main focus of this research is facilitating the processing of large data set in SHM [20]. Accordingly, the integrated system consists of three blocks is used in this paper. Firstly, statistical characteristics of structural response signals under ambient vibration are extracted, and feature vectors are obtained. Subsequently, the best feature subset is selected by the ABSMA algorithm based on desirability index using F-score [21]. In the final step, selected feature is employed for training the surrogate model based on radial basis function neural network (RBFNN).

The proposed method's performance is evaluated statistically on benchmark dataset of wooden bridge model [22]. Furthermore, the efficacy of using ABSMA as the main algorithm for feature selection is compared to Binary Particle

Swarm Optimization (BPSO) [15], binary Harris hawks optimization(BHHO) [23], binary whale optimization algorithm (BWOA) [24] and binary farmland fertility optimization algorithm (BFFA) [25]. Moreover, the impact of various transfer functions on accuracy of ABSMA is also accessed

2 DAMAGE DETECTION PROCEDURE BASED ON THE PROPOSED ALGORITHM

Fig. 1 presents a summary of the method employed in this paper for an optimal feature subset selection and health monitoring of structures. The method consists of three main blocks:
(A) The Feature Extraction Block, (B) The Feature Selection Block and (C) The Feature Classification Block.

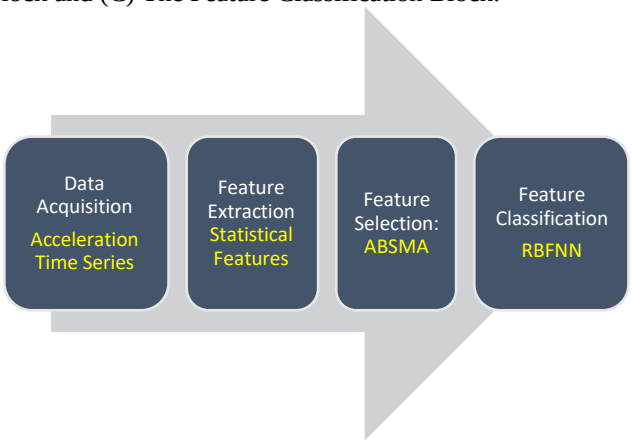

Figure 1. Summary of damage detection approach

2.1 Feature Extraction block: Statistical Features (SF)

Time-domain vibrational signals collected from sensors can be pre-processed to form feature vectors using the functions shown in Table 1. The features of each sensor are: root mean square, variance, skewness, kurtosis, crest factor, the maximum and range of acceleration response signal of each sensor [26].

Table 1 Time-domain features

Feature	Function
Root mean square	$rms = \sqrt{\frac{\sum_{n=1}^{N}(x(n))^2}{N}}$
Variance	$var = \sigma^2 = \frac{\sum_{n=1}^{N}(x(n) - mean(x))^2}{(N-1)}$
Skewness	$skewness = \frac{\sum_{n=1}^{N}(x(n) - mean(x))^3}{(N-1)\sigma^3}$
Kurtosis	$kurtosis = \frac{\sum_{n=1}^{N}(x(n) - mean(x))^4}{(N-1)\sigma^4}$
Crest factor	$crest = \frac{\max\ \lvert x(n)\rvert}{rms}$
Maximum value	$max = \max\ \lvert x(n)\rvert$
Range	$range = \max\lvert x(n)\rvert - \min\lvert x(n)\rvert$

These features represent the energy, the vibration amplitude and the time series distribution of the signal in time-domain [26].

2.2 Feature Selection Block: Slime mould algorithm

In second block, the best subset of extracted features will be selected using ABSMA based on the objective function that will describe in next subsection.Slime mould algorithm (SMA) is proposed by [18] based on the oscillation mode of slime mould in nature. The proposed SMA has several features with a unique mathematical model that uses adaptive weights to simulate the process of producing positive and negative feedback of the propagation wave of slime mould based on bio-oscillator and to form the optimal path for connecting food with excellent exploratory ability and exploitation propensity. For complete details, please refer to main paper by Li et al. [18]. The logic of SMA is shown in Fig. 2.

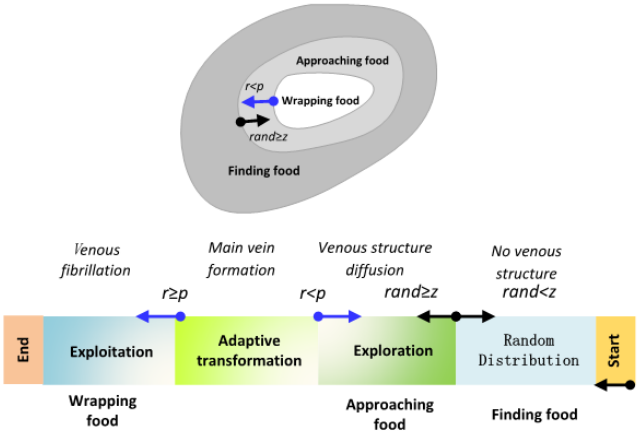

Figure 2. The overall steps of SMA [18].

2.2.1 Binary Slime mould algorithm

All meta-heuristics start with the initialization step to spread the solutions within the search space of the optimization problem. Accordingly, the proposed algorithm is initialized by creating a population of n moulds. Each mould which represents a solution to the optimization process that has d dimensions equal to the number of features in the used dataset. The FS problem is considered a discrete problem as it is based on choosing a number of features that provides the machine learning methods with better classification accuracy. Therefore, for each dimension, the proposed algorithm is randomly initialized with a value of 1 for the accepted feature or 0 as the rejected one as shown in Fig. 3. This provides the representation of an initial solution for the FS. Then, at the end of each iteration, each mould has a solution in the form of a binary vector with the same length as the number of the features, where 1 means selecting and 0 means deselecting the corresponding feature. This process continues for all iterations and at last, the best feature subset with the least classification error of the classifier is suggested as the best result.

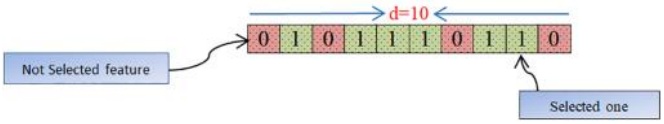

Figure 3. An initial solution to the FS.

It should be noted that, the values generated by the standard SMA are continuous, but the features in FS problems are binary: 0 (selected feature) and 1 (not selected) values. Therefore, a wide range of transfer functions belonging to the family of the V-Shaped and S-Shaped functions [19] has been supposed to convert continuous values into binary.
Selected V-Shaped and S-shaped transfer functions are listed in Table 2. A transfer function receives a real value from the standard SMA as an input and then normalizes this value between 0 and 1 using one of the formulas in Table 2. The normalized value is then converted to a binary value using Eq. (2) [19] .

$$S_{binary} = f(x)\begin{cases}1, & if\ S(a) > 0.5\\ 0, & otherwise\end{cases} \quad (1)$$

Table 2: V-Shaped and S-shaped transfer function.

V-Shaped	S-Shaped
V1,$F(a) = \left\lvert \frac{2}{\pi}\tan^{-1}(\frac{\pi}{2}a)\right\rvert$	S1, $F(a) = \frac{1}{1+e^{-a}}$
V2,$F(a) = \lvert\tanh(a)\rvert$	S2, $F(a) = \frac{1}{1+e^{-2a}}$
V3,$F(a) = \left\lvert \frac{a}{\sqrt{1+a^2}}\right\rvert$	S3, $F(a) = \frac{1}{1+e^{-\frac{a}{2}}}$
V4,$F(a) = \left\lvert \mathrm{erf}(\frac{\sqrt{\pi}}{2}a)\right\rvert$	S4, $F(a) = \frac{1}{1+e^{-\frac{a}{3}}}$

2.2.2 Fitness Function

The fitness function (FF) is an important factor for the speed and the efficiency of ABSMA algorithm. In this study, the fitness function of ABSMA is developed based on the surrogate model accuracy and the efficiency of selected subset of features. The surrogate model (RBFNN) accuracy is obtained by the evaluation of the test data classification using the trained model. In addition, efficiency of the selected subset of features are evaluated using the F-score to measure desirability of the features. ABSMA selects the vector with the smallest fitness value when the completion conditions are satisfied. The fitness function of ABSMA is formed as follows:

$$FF = 1 - \left[W \times (Classification\ Accuracy) + (1-W) \times \left(\frac{1}{\mathrm{n}}\sum_{i=1}^{n} F_{score_i}\right)\right] \quad (2)$$

where W is weighting factor between 0 to 1 and n is the total number of features.

2.2.3 Measure the desirability of features: F-score

A desirability value, for each feature generally represents the attractiveness of the features, and can be any subset evaluation function like an entropy-based measure or rough set dependency measure [27]. In this paper, F-score will be used as index for measuring the desirability of the features. The F-score is a measurement to evaluate the discrimination ability of the feature $\boldsymbol{i}$. Eq. (3) defines the F-score of the $\boldsymbol{i^{th}}$ feature. The numerator specifies the discrimination among the categories of the target variable, and the denominator indicates the discrimination within each category. A larger F-score implies to a greater likelihood that this feature is discriminative [21].

$$F_{score_i} = \frac{\sum_{k=1}^{c}\left(\bar{x}_i^k - \bar{x}_i\right)^2}{\sum_{k=1}^{c}\left[\frac{1}{N_i^k - 1}\sum_{j=1}^{N_i^k}\left(x_{ij}^k - \bar{x}_i^k\right)^2\right]} \quad (3)$$

where c is the number of classes and **n** is the number of features; N_i^k is the number of samples of the feature i in class k, ($\boldsymbol{k} = \boldsymbol{1, 2, \dots, c}$; $\boldsymbol{i} = \boldsymbol{1, 2, \dots, n}$), x_{ij}^k is the $\boldsymbol{j}$-th training sample for the feature $\boldsymbol{i}$ in class k, ($j = 1,2, \dots, \boldsymbol{N_i^k}$), $\boldsymbol{x_i}$ is the mean value of feature $\boldsymbol{i}$ of all classes and x_{ik} is the mean value of feature $\boldsymbol{i}$ of the samples in class $\boldsymbol{k}$ [21].

It should be mentioned that the features selected by the proposed algorithms are evaluated with the well-known metrics precision, recall, accuracy, F1- score and Feature-Reduction index (F_r). In this paper, the classification accuracy (CA) is used to define the quality function of a solution, which is the percentage of samples correctly classified and evaluated as Eq. (4):

$$Accuracy = \frac{Number\ of\ samples\ correctly\ classified}{Total\ number\ of\ samples\ taken\ for\ exprimentation} \quad (4)$$

Another parameter which is used for comparison is the average feature reduction F_r, to investigate the rate of feature reduction:

$$F_r = \frac{n-p}{n} \quad (5)$$

where n is the total number of features and p is the number of selected features by the FS algorithm F_r is the average feature reduction. The more it is close to 1, the more features are reduced, and the classifier complexity is less.

2.2.4 Advanced version of binary slime mould algorithm

In the proposed BSMA, two ideas from genetic algorithm [28] are implement on the BSMA to enhances its capability for the FS and solve low population diversity. The new solutions in GA are created by the two operators: crossover and mutation. In the crossover operator, two solution sets are selected randomly and some portions are exchanged, thereby creating two new solutions. In the mutation operator, a randomly selected bit of a particular solution is mutated; means the 1 is changed to 0 and 0 is changed to 1. Therefore, in the first step of proposed method, a random solution is generated, and then a crossover operation is applied to the randomly generated solution and the best solution. Next, the solution obtained from the crossover operation is given as inputs to the mutation operation. The main intention of these operations is increase population diversity and escapes from local optimal points and improve solutions' quality.

2.3 Feature Classification Block: radial basis function neural network

In the final block of the employed framework, a well-trained surrogate model is applied to classify various condition of the structure. In these models, the input matrix will include the selected features and the outputs are the corresponding damage conditions. In recent years, many neural network models have been proposed or employed for various components of structural health monitoring in order to perform pattern classification, function approximation, and regression [29],

[30]. Among them, the RBF network is a type of feed forward neural networks that learns using a supervised training technique. Lowe and Broomhead [31] were the first researchers that exploited the use of the RBF for designing neural networks. Radial functions are a type of function in which the response reduces or grows monotonically with the distance from the center point. It has been shown that the RBF networks are able to approximate any reasonable continuous function mapping with a satisfactory level of accuracy [32].

3 EXPRIMENTAL RESULTS

In this section, a benchmark data set is used to show the effectiveness of the proposed feature selection algorithm. The data set collected in the laboratory of Helsinki Polytechnic Stadia [22], [33] is employed in this paper. The structure was a timber bridge model as shown in Fig. 4. In order to excite the lowest modes, a random excitation was generated with an electrodynamic shaker to activate the vertical, transverse, and torsional modes. The response was measured at three different longitudinal positions by 15 accelerometers. The frequency of sampling was 256 Hz and the measurement period was 32 s. The data were filtered below 64 Hz and re-sampled for sufficient redundancy. The measurements were repeated several times and it was noticed that the dynamic properties of the structure vary due to the environmental changes. The main influencing factors were assumed to be the changes in the temperature and humidity.

In the SHM community, there are various schemes for modelling of damage scenarios, mainly damage modelled as decreasing in the module of elasticity or in the stiffness parameter of elements [8]. Moreover, some researchers used additional mass as an indicator of damage [34]. In this benchmark data set, five artificial damage scenarios were then introduced by adding small point masses of different size on the structure. The mass sizes were 23.5, 47.0, 70.5, 123.2 and 193.7 gr. The point masses were attached on the top flange, 600 mm left from the midspan (Fig. 4). The added masses were relatively small compared to the total mass of the bridge (36 kg), where the highest mass increase was only 0.5 %.

The total number of experiments were carried out on the structure was 273. The 190 measurements were selected as the training data. The test data consisted of both healthy and abnormal systems measurements. It is worth mentioning that the total number of extracted features for each experiment based on Table 1 is: 15 sensors ×7 features=105 features.

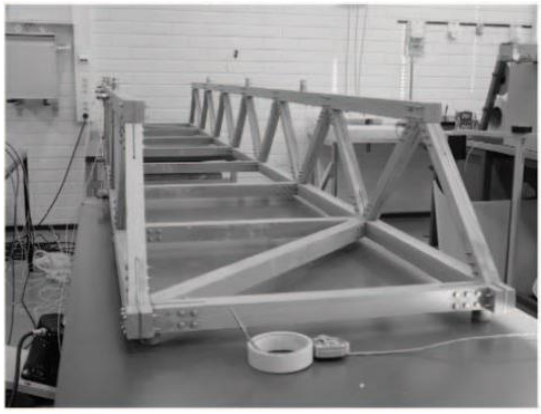

(a) Wooden bridge model

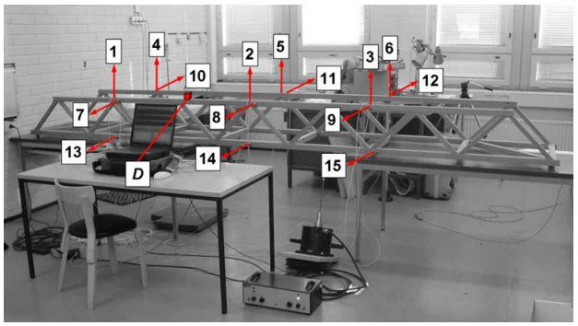

(b) Wooden bridge with the locations of sensors and damage (D) are indicated [22].

Figure 4. Wooden bridge

3.1 *Impact of transfer functions on the ABSMA*

In this subsection, the impact of the transfer functions on the ABSMA's performance is investigated. For providing the stochastic behaviour of metaheuristic algorithms, the performance of the algorithms is compared using the best, worst, average and standard deviation (SD) of the obtained fitness values over 20 independent runs in Table 3. Columns BSMAS1, BSMAS2, BSMAS3, BSMAS4, BSMAV1, BSMAV2, BSMAV3, and BSMAV4 gives the results of the transfer functions S1, S2, S3, S4, V1, V2, V3, and V4, respectively. According to the results of Table 3, the ABSMA algorithm has performed the best using V2. Moreover, according to the SD, the best performance is related to BSMAV2. Therefore, V2 is selected as the transfer function in this study.

Table 3: The best fitness values under eight different transfer functions

	ABSMA-V1	ABSMA-V2	ABSMA-V3	ABSMA-V4
Best	0.07	0.04	0.09	0.1
Avg	0.11	0.07	0.11	0.13
Worst	0.14	0.12	0.13	0.15
SD	0.02	0.02	0.01	0.02
	ABSMA-S1	ABSMA-S2	ABSMA-S3	ABSMA-S4
Best	0.11	0.1	0.07	0.05
Avg	0.13	0.12	0.09	0.07
Worst	0.14	0.14	0.11	0.1
SD	0.01	0.01	0.01	0.01

3.2 *Classification accuracy of metaheuristic optimization algorithms*

In this section, the accuracy and effectiveness of the proposed framework for feature extraction/selection in SHM domain is evaluated. Furthermore, the results obtained by the proposed ABSMA algorithm are compared to BPSO [15], BHHO [23], BWOA [24], and BFFA [25] which are reported to be good algorithms in FS [19]. The parameters need to be set in these algorithms are set to the best values are reported in the original papers. The population size for all the algorithms is 50 and the maximum iterations is set to be 200. The weighting factor W in the fitness function is varied from 0.6 to 0.9 to get the different sets of features. The results are averaged over 20 independent runs in each data set and by every algorithm.

Table 4 gives the mean of the CA, best, worst, average and SD of the results for each algorithm. The number in the brackets in each table slot shows the ranking of each algorithm. A comparison of the average precision, recall, F1 score and the amount of F_r for other algorithms are given in Table 5. It can concluded from these tables that the proposed ABSMA algorithm can obtain, in most of cases, better classification accuracy using a smaller feature set, compared to other algorithms

Table 4: Classification accuracy of each algorithm for the tested datasets of Wooden bridge

	ABSMA	BHHO	BPSO	BWOA	BFFA
Mean of CA (Rank)	**0.94** (1)	0.87 (2)	0.81 (4)	0.86 (3)	0.8 (5)
Best	0.04	0.09	0.12	0.09	0.13
Avg	0.07	0.13	0.17	0.13	0.19
Worst	0.12	0.16	0.22	0.16	0.23
SD	0.02	0.02	0.03	0.02	0.03

Table 5: Comparison of the performance (precision, recall, F1-score and Fr) of the algorithms on Wooden bridge

Metrics	ABSMA	BHHO	BPSO	BWOA	BFFA
Precision	0.94	0.88	0.83	0.87	0.81
Recall	0.96	0.92	0.87	0.91	0.86
F1-score	0.95	0.90	0.85	0.89	0.83
Fr	0.81	0.714	0.667	0.743	0.619

The extended results are also shown in Figures 5-6. From these figures, one may admit that ABSMA not only finds smaller feature subsets than the other algorithms, but also the number of selected features also decreases much faster.

It can be concluded that the ABSMA provides a higher degree of exploration than the other algorithms, which enables it to explore the search space to find a solution that selects a smaller number of features and better performance.

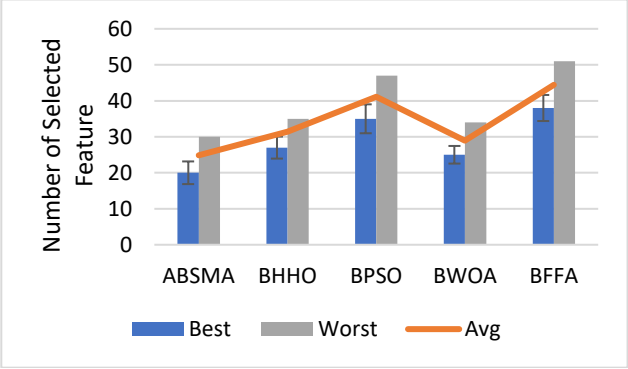

Fig. 5 Number of selected features of each optimization algorithms

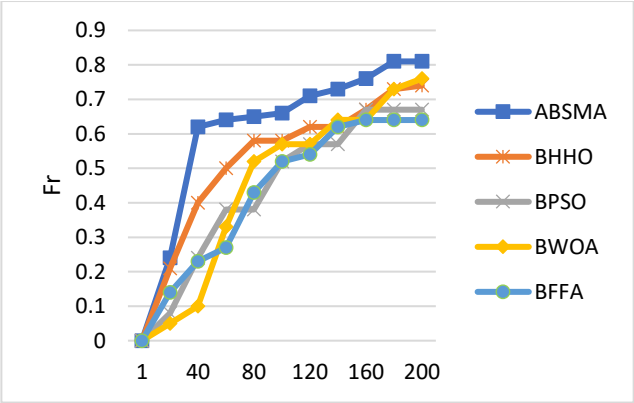

Fig. 6 Average of Fr for each optimization algorithms with respect to number of iteration

It is worth to note that, the FS method proposed in this study is a supervised wrapper-based feature selection method [13]. Generally, in comparison with the filter model, the wrapper model could achieve a higher classification accuracy and tend to have a smaller subset size; however, it has high time complexity [12].

Finally, according to the results shown, adding desirability index, mutation and crossover operators to the BSMA increases the exploration of the search and guide the algorithm to more salient features.

4 CONCLUSIONS

In this paper, a new framework is presented for the feature selection for SHM problems. Furthermore, an ABSMA is presented for enhance capability of SMA in this domain. The mutation and crossover operators are employed in the original BSMA to the proposed ABSMA which could increase diversity and prevent excessive convergence during the optimization process, and local optimal trap escape. A data set collected from a timber bridge is employed in this paper. The ABSMA is initially evaluated using eight transfer functions that convert continuous solutions to binary ones, in which the best transfer function (transfer function V2) is selected. The results obtained from the proposed algorithm were compared with 4 state-of-the-art metaheuristic-based algorithms including BHHO, BPSO, BWOA and BFFA. The results of the experiments indicate that a significant improvement in the proposed algorithm compared to other ones. Moreover, the proposed framework can remove the irrelevant and redundant information by choosing useful features as the input of the surrogate model. It is shown that the proposed FS approach based on the ABSMA optimization algorithm reaches a better feature set in terms of classification accuracy and the number of selected features.

5 ACKNOWLEDGEMENT

This publication has emanated from research conducted with the financial support of Science Foundation Ireland under Grant number 20/FFP-P/8706.

REFERENCES

[1] O. Avci, O. Abdeljaber, S. Kiranyaz, M. Hussein, M. Gabbouj, and D. J. Inman, "A review of vibration-based damage detection in civil structures: From traditional methods to Machine Learning and Deep Learning applications," *Mech. Syst. Signal Process.*, vol. 147, p. 107077, 2021.

[2] S. Das, P. Saha, and S. K. Patro, "Vibration-based damage detection techniques used for health monitoring of structures: a review," *J. Civ. Struct. Heal. Monit.*, pp. 1–31, 2016.

[3] A. Malekjafarian, E. J. Obrien, P. Quirke, and D. Cantero, "Railway Track Loss-of-Stiffness Detection Using Bogie Filtered Displacement Data Measured on a Passing Train," *Infrastructures*, vol. 6, no. 93, pp. 1–17, 2021.

[4] R. Corbally and A. Malekjafarian, "A data-driven approach for drive-by damage detection in bridges considering the influence of temperature change," *Eng. Struct.*, vol. 253, no. December 2021, p. 113783, 2022.

[5] A. Silik, M. Noori, W. A. Altabey, and R. Ghiasi, "Selecting optimum levels of wavelet multi-resolution analysis for time-varying signals in structural health monitoring," *Struct. Control Heal. Monit.*, vol. 28, no. 8, 2021.

[6] A. Silik, M. Noori, W. A. Altabey, J. Dang, R. Ghiasi, and Z. Wu, "Optimum wavelet selection for nonparametric analysis toward structural health monitoring for processing big data from sensor network: A comparative study," *Struct. Heal. Monit.*, 2021.

[7] A. Malekjafarian, F. Golpayegani, C. Moloney, and S. Clarke, "A Machine Learning Approach to Bridge-Damage Detection Using Responses Measured on a Passing Vehicle," *Sensors*, vol. 19, no. 4035, 2019.

[8] R. Ghiasi, P. Torkzadeh, and M. Noori, "A machine-learning approach for structural damage detection using least square support vector machine based on a new combinational kernel function," *Struct. Heal. Monit.* , vol. 15, no. 3, pp. 302–316, May 2016.

[9] V. R. Gharehbaghi *et al.*, "A Critical Review on Structural Health Monitoring: Definitions, Methods, and Perspectives," *Arch. Comput. Methods Eng.*, pp. 1–27, 2021.

[10] G. F. Gomes, Y. A. D. Mendez, P. da S. L. Alexandrino, S. S. da Cunha, and A. C. Ancelotti, "A review of vibration based inverse methods for damage detection and identification in mechanical structures using optimization algorithms and ANN," *Arch. Comput. Methods Eng.*, pp. 1–15, 2018.

[11] L. Zhong, H. Song, and B. Han, "Extracting structural damage features: Comparison between PCA and ICA," in *Intelligent Computing in Signal Processing and Pattern Recognition*, Springer, 2006, pp. 840–845.

[12] S. Kashef and H. Nezamabadi-pour, "An advanced ACO algorithm for feature subset selection," *Neurocomputing*, vol. 147, pp. 271–279, 2015.

[13] S. Kashef, H. Nezamabadi-pour, and B. Nikpour, "Multilabel feature selection: A comprehensive review and guiding experiments," *Wiley Interdiscip. Rev. Data Min. Knowl. Discov.*, vol. 8, no. 2, p. e1240, 2018.

[14] H. Liu and L. Yu, "Toward integrating feature selection algorithms for classification and clustering," *IEEE Trans. Knowl. Data Eng.*, no. 4, pp. 491–502, 2005.

[15] L.-Y. Chuang, C.-H. Yang, and J.-C. Li, "Chaotic maps based on binary particle swarm optimization for feature selection," *Appl. Soft Comput.*, vol. 11, no. 1, pp. 239–248, 2011.

[16] I.-S. Oh, J.-S. Lee, and B.-R. Moon, "Hybrid genetic algorithms for feature selection," *IEEE Trans. Pattern Anal. Mach. Intell.*, vol. 26, no. 11, pp. 1424–1437, 2004.

[17] E. Rashedi and H. Nezamabadi-pour, "Feature subset selection using improved binary gravitational search algorithm," *J. Intell. Fuzzy Syst.*, vol. 26, no. 3, pp. 1211–1221, 2014.

[18] S. Li, H. Chen, M. Wang, A. Asghar, and S. Mirjalili, "Slime mould algorithm : A new method for stochastic optimization," *Futur. Gener. Comput. Syst.*, vol. 111, pp. 300–323, 2020.

[19] B. Abdollahzadeh, S. Barshandeh, H. Javadi, and N. Epicoco, "An enhanced binary slime mould algorithm for solving the 0 – 1 knapsack problem," *Eng. Comput.*, no. 0123456789, 2021.

[20] C. Cremona and J. Santos, "Structural Health Monitoring as a Big-Data Problem," *Struct. Eng. Int.*, vol. 28, no. 3, pp. 243–254, 2018.

[21] C.-L. Huang, "ACO-based hybrid classification system with feature subset selection and model parameters optimization," *Neurocomputing*, vol. 73, no. 1–3, pp. 438–448, 2009.

[22] J. Kullaa, "Distinguishing between sensor fault, structural damage, and environmental or operational effects in structural health monitoring," *Mech. Syst. Signal Process.*, vol. 25, no. 8, pp. 2976–2989, 2011.

[23] A. A. Heidari, S. Mirjalili, H. Faris, I. Aljarah, M. Mafarja, and H. Chen, "Harris hawks optimization: Algorithm and applications," *Futur. Gener. Comput. Syst.*, vol. 97, pp. 849–872, 2019.

[24] S. Mirjalili and A. Lewis, "The whale optimization algorithm," *Adv. Eng. Softw.*, vol. 95, pp. 51–67, 2016.

[25] H. Shayanfar and F. S. Gharehchopogh, "Farmland fertility: A new metaheuristic algorithm for solving continuous optimization problems," *Appl. Soft Comput.*, vol. 71, pp. 728–746, 2018.

[26] A. Widodo, B.-S. Yang, and T. Han, "Combination of independent component analysis and support vector machines for intelligent faults diagnosis of induction motors," *Expert Syst. Appl.*, vol. 32, no. 2, pp. 299–312, Feb. 2007.

[27] R. Jensen, "Combining rough and fuzzy sets for feature selection." Citeseer, 2005.

[28] M. Melanie, *An Introduction to Genetic Algorithms*. The MIT Press, 1999.

[29] W. A. Altabey, M. Noori, T. Wang, R. Ghiasi, S.-C. Kuok, and Z. Wu, "Deep learning-based crack identification for steel pipelines by extracting features from 3d shadow modeling," *Appl. Sci.*, vol. 11, no. 13, 2021.

[30] A. Malekloo, E. Ozer, M. Alhamaydeh, and M. Girolami, "Machine learning and structural health monitoring overview with emerging technology and high-dimensional data source highlights," *Struct. Heal. Monit.*, vol. 0, no. 0, pp. 1–50, 2021.

[31] D. Lowe and D. Broomhead, "Multivariable functional interpolation and adaptive networks," *Complex Syst.*, vol. 2, pp. 321–355, 1988.

[32] J. Park and I. W. Sandberg, "Universal approximation using radial-basis-function networks," *Neural Comput.*, vol. 3, no. 2, pp. 246–257, 1991.

[33] J. Kullaa, "Eliminating environmental or operational influences in structural health monitoring using the missing data analysis," *J. Intell. Mater. Syst. Struct.*, vol. 20, no. 11, pp. 1381–1390, 2009.

[34] E. Papatheou, G. Manson, R. J. Barthorpe, and K. Worden, "The use of pseudo-faults for damage location in SHM : An experimental investigation on a Piper Tomahawk aircraft wing," *J. Sound Vib.*, pp. 1–20, 2013.

Nonlinear finite element modelling and analysis of a novel self-centring steel structure under cyclic lateral loading

Yadong Jiang[1,2,3], Suhaib Salawdeh[4], Gerard J. O'Reilly[5], Hatim Alwahsh[1,2,3], Jamie Goggins[1,2,3]
[1]School of Engineering, National University of Ireland, Galway, University Road, Galway, Ireland
[2]Ryan Institute, National University of Ireland, Galway, University Road, Galway, Ireland
[3]SFI MaREI Centre for Energy, Climate and Marine, National University of Ireland Galway, Ireland
[4]Department of Building and Civil Engineering, Atlantic Technological University, Dublin Road, Galway, Ireland
[5]Scuola Universitaria Superiore IUSS di Pavia, Palazzo del Broletto, Piazza della Vittoria, Pavia, Italy
email: yadong.jiang@nuigalway.ie, suhaib.salawdeh@gmit.ie, gerard.oreilly@iusspavia.it, h.alwahsh1@nuigalway.ie, jamie.goggins@nuigalway.ie

ABSTRACT: After a major earthquake event, it can be problematic for building retrofitting due to the residual deformations developed under seismic excitation. To minimise this structure deformation after seismic events, a novel self-centring concentrically braced frame (SC-CBF) is developed by combining the advantages of conventional concentrically braced frames (CBFs) and self-centring structures. The self-centring behaviour of the SC-CBF is achieved by employing a horizontal post-tensioning (PT) system. Under seismic excitation, the PT system can prevent the beams and columns from developing plastic hinges at connections. This ensures the concentrically braced members are the only energy-dissipation components of the frame. At the end of an earthquake event, the PT system can position the structure back to straight. Hence, the residual deformation is eliminated.

This research focuses on developing a finite element model for predicting the seismic behaviour of an SC-CBF. To capture the rocking mechanism, the beam-column connection is modelled as a combination of multipoint constraint elements. Shell elements are utilised to model the brace to capture the plastic deformation during energy dissipation. Considering the other members, namely the beams and columns, remain elastic under loading, they are modelled as 2D beam-column elements. The accuracy of the proposed finite element model is validated against experimental test data. The elastic stiffness and the flag-shaped hysteresis loops are captured by the finite element model, demonstrating the feasibility of using the finite element model for further analysis of the SC-CBF.

KEY WORDS: Concentrically braced frame; Self-centring; Energy dissipation; Pushover loads; Test specimens; Lateral deformation.

1 INTRODUCTION

Nowadays, 2.7 billion people are living in seismically active regions, contributing to one-third of the global population [1]. Earthquake protective technology is proposed for building design in order to reduce the threats posed by the seismic activities on life and economic activities in high seismic zone. Concentrically braced frames (CBFs), a type of energy-dissipation system, are increasingly applied in seismic regions. According to the earthquake events, failures of many historic buildings are found to be caused by lateral deformations [3]. It indicates that the structural damage is directly related to the structural lateral deformation. Therefore, in modern seismic design codes, restrictions are placed to control the structure drifts under serviceable limit state conditions. In recent years, many research works, including experimental testing and numerical analysis, are carried out to characterise the seismic performance of CBF structures [2]-[13]. The CBFs are proved to be efficient in limiting the peak inter-storey drift of a structure under seismic events. Besides the ultimate structure drift, the building is likely to develop residual deformations after a medium or severe earthquake due to the plastic deformation. These residual displacements may introduce additional costs to the retrofitting of a structure. Despite the fact of several buildings experienced low damage ratios the Canterbury earthquakes of 2011 and 2012, they were demolished due to excessive residual deformations [14]. Self-centring systems can be a solution to control residual deformations and limit damage to structures. PREcast Seismic Structural Systems (PRESSS), a self-centring structure, was proposed in a US-Japan research programme. The PRESSS utilises a post-tensioning system at connections to provide moment resistance and a self-centring force taking the structure back to its vertical positions [15]. As with other self-centring structural systems, the SC-CBF was developed as an extension of the unbonded, post-tensioned precast concrete wall concept that was introduced in the early 1990s. The SC-CBF system is comprised of beams, columns, and braces dissipation elements. For different SC-CBF configurations, a separate lateral load resisting system is provided through additional gravity columns. Roke et al. [16] and Sause et al. [17] developed a SC-CBF system that incorporated a vertical uplift rocking mechanism through vertical post-tensioned strands and used additional components for energy dissipation in order to provide sufficient self-centring capability. In this configuration, self-centring provides a flag-shaped hysteresis loop behaviour.

Over the last few years, a self-centring concentrically braced frame (SC-CBF), which combines the advantages of self-centring structures and conventional CBFs, was proposed as a novel energy-dissipation system based on horizontal orientation post-tensioned strands [18]-[23]. Similar to the PRESSS structure, the SC-CBF system employs a post-tensioning system to develop self-centring behaviour. This system works based on a rocking mechanism which opens at joints between beams and columns. This configuration avoids the potential beam and column damage caused by earthquakes.

The post-tensioning system can provide forces to bring the structure back to its vertical position. In order to dissipate earthquake energy through plastic deformation, the bracing members are installed concentrically. A series of experimental studies, including static pushover tests [18]-[21] and shake table tests [22]-[23], have been performed to investigate the seismic behaviour of SC-CBF systems. The self-centring behaviour and energy-dissipation mechanism are verified through the testing events. However, limited to the testing facilities, these experimental tests only focused on the responses of single-storey SC-CBF. To extend the research to multi-storey SC-CBF systems, an accurate and efficient numerical model should be derived. Hence, this paper describes a simplified finite element model developed for SC-CBFs. The cyclic pushover tests, aiming to evaluate the seismic performance of a full-scale SC-CBF system, are utilised to verify the accuracy of the model.

2 METHODOLOGY

2.1 Concept

The schematic shown in Figure 1 illustrates the concept of an SC-CBF system. The components are similar to that of conventional CBFs. However, in SC-CBF, gusset plates are connected to beam flanges only. The main difference between the conventional CBFs and SC-CBFs is the connections. The beams and columns are connected using rocking connections (Figure 2). The beams are connected to the column via two bolts. When the system develops a lateral displacement, the bolts can slide along the slots, allowing the beams to rock against the column flange. In this way, no moment is developed at connections, preventing the beams and columns from plastic deformations. However, by utilising the rocking connections, extra flexibilities are introduced to the structure. To solve this problem, post-tensioning strands are placed horizontally along the beams. The post-tensioning strands introduce self-centring forces to the frame to help the rocking connections return to its initial positions. Therefore, with a proper post-tensioning forces configured, the residual displacements can be eliminated after earthquake events. By employing the post-tensioning system, the beams and columns are protected and the self-centring behaviour is developed. To dissipate the earthquake energy, the bracing members, which are connected to the frame via gusset plates, are used. The braces are designed to deform plastically during the rocking of the post-tensioning system. Hence, the earthquake energy is dissipated. It should be noted that the braces are the only energy-dissipation members of the SC-CBF. After the earthquake events, only the bracing members are the components to be replaced.

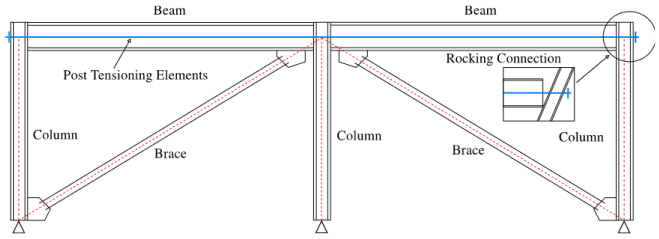

Figure 1. Concept of SC-CBF (adapted from O'Reilly and Goggins [21]).

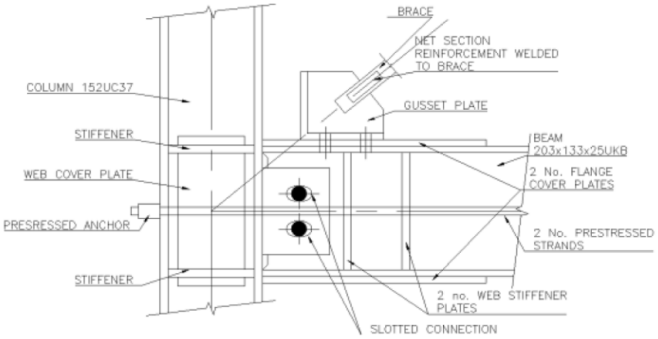

Figure 2. Details of the rocking connection (adapted from O'Reilly and Goggins [21]).

2.2 Experimental testing

To validate the feasibility of the SC-CBF system, a testing frame was designed and tested in the Large Structures Laboratory of National University of Ireland, Galway [20]-[21]. Figure 3 shows the tested structure, which is a two-bay frame. The bracing members were connected to the upper and lower beams through the gusset plates. Post-tensioning strands were located along with the beams. The post-tensioning force was applied with 80 kN, which is selected based on the BS 5896:1980 BSI [24], aiming to be sufficient to develop the flag shape hysteretic loops for the four specimens. An actuator, which is mounted to the steel reaction frame, was utilised to apply lateral cyclic displacements to the top of the middle column. The frame was fixed to the reinforced concrete floor using steel bolts. It should be noted that the middle column was pinned connected to the supporting component while the two side columns were fixed using sliders. This is because the quasi-static lateral force is only applied to the middle column. Benefiting from these boundary conditions, the symmetric lateral force, which is detailed in the following subsections, induced by the actuator was transferred to the strong floor only through the pinned connection of the middle column.

Figure 3. SC-CBF was designed for pushover testing (adapted from O'Reilly and Goggins [21]).

The beams and columns were connected through the rocking connections, with the details shown in Figure 2. The beam was connected to the column flange via a slotted plate. This allows the beam to have the flexibility to rotate. The post-tensioning strands were used to introduce the self-centring forces to the structure. When the beam started to rock against the column, the post-tensioning strands were elongated and the tensile force closed the gap opening of the rocking connection. Hence, with a proper post-tensioning strands and forces selected, the frame can be positioned back to its vertical positions. The bracing members are connected to the beam through gusset plates. The braces, which are the energy-dissipation component, deform under the development of the rocking mechanism. To avoid local failures, the ends of the braces, beams and columns were strengthened with cover plates and stiffeners.

There were four bracing members considered as the energy-dissipation components in the tests. Table 1 summarises the geometry of each specimen. Hot-rolled square hollow section (SHS) members with a steel grade of S235 were selected as the testing specimens. Similar to the conventional CBF structures, the lateral resistance of the bracing member was mainly provided by the tensile strength, due to their relatively high slenderness. Hence, most of the energy was dissipated through the plastic deformation of the bracing members. Coupon tests were carried out to characterise the mechanical properties of the steel, with slenderness ratio, λ, Young's modulus, E, yield stress, f_y, and ultimate stress, f_u, listed in Table 1 (O'Reilly and Goggins [21]).

Table 1. Mechanical properties of the bracing members.

ID	Section	L [mm]	λ	E [GPa]	f_y [MPa]	f_u [MPa]
B1	SHS 20×20×2.0	1438	2.21	231	433	437
B2	SHS 25×25×2.5	1435	1.70	217	469	494
B3	SHS 30×30×2.5	1433	1.39	215	449	470
B4	SHS 40×40×4	1395	1.03	163	411	429

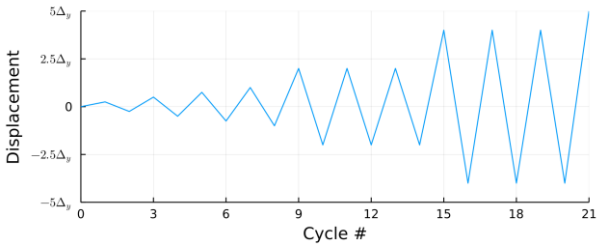

Figure 4. ECCS loading protocol

The frame is loaded laterally with a 750 kN actuator mounted on the steel reaction frame. To investigate the seismic performance of the SC-CBF system, a cyclic loading, proposed by ECCS [25], is selected as the loading protocol, as shown in Figure 4. The applied displacement pattern depends on the yield displacement, Δ_y, of the system. To monitor the performance of the post-tensioning system, displacement transducers were used to record the gap opening of the rocking connections. The post-tensioning strands were anchored with load cells at the ends to observe the force increasing caused by elongations. Strain gauges were installed on the upper and lower flanges of the beams and columns to ensure these components are protected from plastic deformation. The lateral load and displacement were internally recorded by the actuator.

2.3 Finite element modelling

The main objective of this research is to develop a numerical model for predicting the seismic responses of SC-CBF structures accurately. One of the main challenges of analysing this self-centring structure is to simulate the complex rocking mechanism of the post-tensioning system. In the research works of O'Reilly [20], a finite element model has been proposed. This model utilised a combination of different types of spring and beam-column elements to simulate the mechanism of the post-tensioning system. However, solving the numerical model can be time-consuming. Hence, a simplified finite element model is developed in this research to reduce the complexity of the model while keeping the prediction accuracy.

The numerical model is constructed by finite element software Ansys® Academic Research Mechanical, Release 17.1 [26]. Based on the energy-dissipation method of the SC-CBF system, the frame can be modelled as two parts, namely the elastic and the inelastic parts. The elastic part, contains the beams, columns, rocking connections, and post-tensioning strands, behaves elastically throughout the analysis. This part is critical for simulating the self-centring behaviour. Benefiting from the rocking connection, the beams are allowed to rock against the column. Therefore, the rocking connections are simplified as pinned connections with friction forces neglected, as shown in Figure 5. However, this simplification cannot mimic the gap opening of the rocking connection. Consequently, the elongation of the post-tensioning strand is not captured, and the self-centring behaviour cannot be developed. To solve this issue, a multi-linear spring is added to the top of the frame. This spring should provide the lateral reaction force which is equivalent to the responses of the post-tensioning system. As discussed in O'Reilly and Goggins [21], the responses of the post-tensioning system can be simplified as a bi-linear curve. The data assigned to the multi-linear spring is from the analytical model in O'Reilly [20].

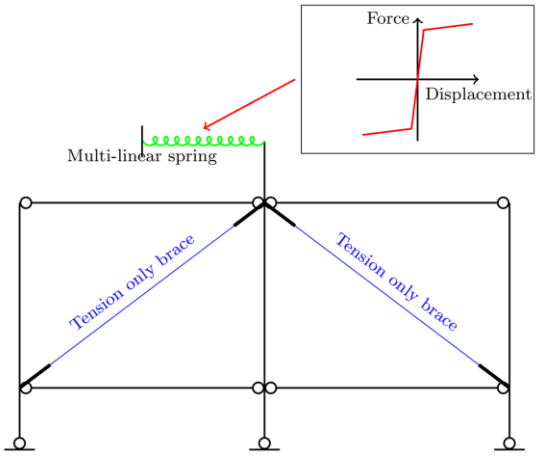

Figure 5. Finite element model of the SC-CBF

The two bracing members are the only energy-dissipation components of the SC-CBF. Bi-linear kinematic material is assigned to the braces according to the coupon test results. The beam-column element combined with the fibre section is used

to model the bracing members. The imposed energy is dissipated through the plastic deformation of the braces. Under large lateral deformations, the braces will experience both global buckling and local buckling in the mid-span, which massively reduces the compressive strength of the braces. However, this local buckling phenomenon cannot be captured by the fibre section used by the beam-column element. The brace member size is relatively small compared to the beams and columns. Due to the development of the local buckling under compression deformation, the compressive resistances of these members can be considered to be neglectable compared to their tensile capacity. Hence, braces are configured as tension-only members. Since the tension-only members are used, it is not necessary to model the initial imperfection of the braces and the gusset plates are neglected in the numerical model. Instead of that, the braces are jointed to beams with rigid elements.

3 RESULTS AND DISCUSSION

During testing, all the bracing members were observed to experience significant plastic deformation. As shown in Figure 6, local buckling due to large compressive deformation developed at the middle of the braces B4, the strongest members out of the four specimens. No damage was observed to the beams, columns and post-tensioning strands. Therefore, the rocking mechanism is developed. It proves that the energy is only dissipated by the bracing members, which is in line with the design. The rocking mechanism was demonstrated to occur at the rocking connections with gap opening recorded under the lateral loading. The load cells showed that the post-tensioning strands were elongated and provided the self-centring forces.

Figure 6. Deformation of the bracing members after testing (B4B specimens)

The lateral force versus drift ratio plots is shown in Figure 7, where the lateral force is given by the actuator and the drift ratio is defined as the ratio between the lateral displacement and the column length. The flag-shaped hysteretic loops were achieved under the cyclic pushover loading. It demonstrates that the lateral force decreases to zero when the frame returns to its vertical position, demonstrating that the self-centring behaviour is developed. The energy-dissipation capacity of the SC-CBF increases with the increase in the brace sizes. B1

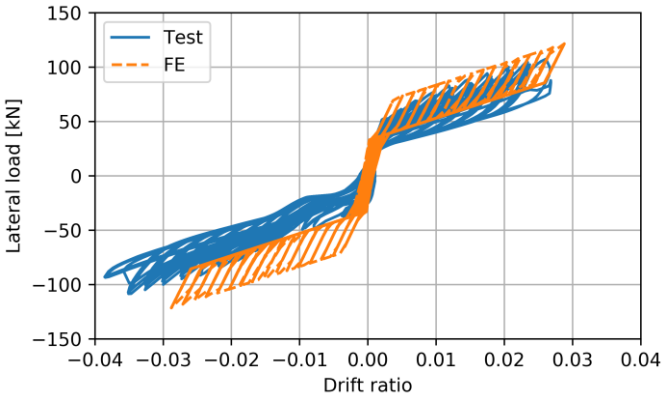

(a) B2

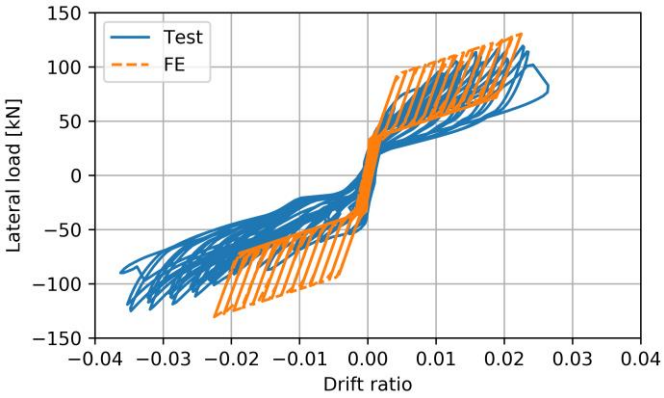

(b) B3

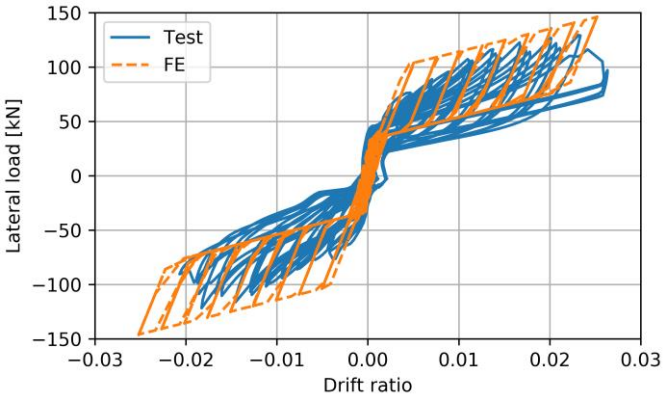

(c) B4

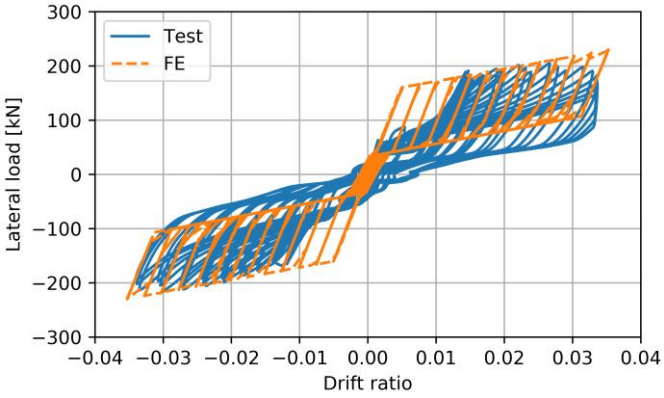

Figure 7. Force versus drift ratio plot comparisons between the testing data and the numerical predictions

It should be noted that the hysteretic loops of the tests are not symmetric. This is mainly due to the flexibility introduced by

the rocking connections. The looseness in various parts of the frame can delay the compression and tension of the braces, which not only causes the asymmetric responses of the loops but also reduced the stiffness of the system. Further details about the push over test results can be found in O'Reilly and Goggins [21].

The testing procedures were simulated by the proposed finite element model and the results are compared with the experimental data to validate the accuracy of the model. The predicted lateral force versus drift ratio data is plotted against the test results in Figure 7. The initial elastic stiffness of the frames with the four different bracing members is well captured. Regarding the inelastic behaviour, the flag-shaped hysteretic loops can also be seized by the finite element model. The experimental and predicted ultimate laterals forces are compared in Table 2. The ultimate strength of tests B2 and B4 agree well with the prediction while B1 and B3 tests are slightly overestimated. However, there are some noticeable differences between the numerical and experimental results. The tangent stiffness predicted by the model is larger than the testing data. The lower bounds of the flag-shaped hysteretic loops are overestimated by the model and the asymmetry existing in the experimental results is not replicated. These differences are mainly due to the flexibility of the testing frame, due to the looseness of the rocking connections, which cannot be measured, and hence, are considered during modelling.

Table 2. Ultimate lateral force comparisons (in unit kN)

ID	Section	Test	FE	Difference
B1	SHS 20×20×2.0	108	122	12.0%
B2	SHS 25×25×2.5	125	131	4.4%
B3	SHS 30×30×2.5	129	146	13.0%
B4	SHS 40×40×4	216	230	6.7%

4 CONCLUSIONS

In this paper, the performance of a novel self-centring moment-resisting frame under cyclic pushover loading was examined. A system combining the rocking connections and post-tensioning strands was employed to develop the self-centring behaviour. Therefore, the concentrical braced members were selected to dissipate the energy through plastic deformation. By carrying out the pushover testing, the post-tensioning system was verified to work with the bracing members buckled under cyclic loading while the other structural members (beams, columns, rocking connections and post-tensioning strands) were protected. The flag-shaped hysteretic loops demonstrated that self-centring behaviour was successfully developed. Based on the test configuration, a simplified finite element model was proposed for predicting the behaviour of the SC-CBF building. By comparing the analytical results with the experimental data, the elastic stiffness, ultimate strength, and flag-shaped hysteretic loops were well captured, proving finite element model is suitable for analysing the behaviour of the SC-CBF structure. However, the flexibility of the structure, caused by the looseness existing between the components, cannot be simulated. Hence, the asymmetry and the tangent stiffness observed in the tests are not well captured. In the future, the model will be used to simulate the recently performed shake table tests [22]-[23] to further validate the model's accuracy. The model will be used for designing the multi-storey SC-CBF buildings in future research works.

ACKNOWLEDGMENTS

This research was funded by the SERA - Seismology and Earthquake Engineering Research Infrastructure Alliance for Europe (SERA-H2020-INFRAIA-2016-2017/H2020-INFRAIA-2016-1) under grant agreement No. 730900 for the project 'Investigation of Seismic Deformation Demand, Capacity and Control in a Novel Self-Centring Steel Braced Frame (SC-CBF)'. The first author would like to acknowledge the support of the Marine Institute Postdoc Fellowship (PDOC/21/03/01). The last author would like to acknowledge the support of Science Foundation Ireland through the Career Development Award programme (Grant No. 13/CDA/2200) and the MaREI Centre (Grant No. 12/RC/2302_2). Additional thanks are given to the technical staff at IZIIS, Skopje, North Macedonia.

REFERENCES

[1] CRED, Retrieved from Centre for Research on the Epidemiology of Disasters. https://www.cred.be
[2] Goggins, J. (2004). *Earthquake resistant hollow and filled steel braces*. PhD thesis, University of Dublin, Trinity College, Dublin, Ireland.
[3] Uriz, P., and Mahin, S. A., *Toward Earthquake-Resistant Design of Concentrically Braced Steel-Frame Structures*. Berkeley: Pacific Earthquake Engineering Research Center, 2008.
[4] Goggins, J., Broderick, B.M., Elghazouli, A.Y. and Lucas, A.S. (2005), 'Behaviour of tubular steel members under cyclic axial loading', *Journal of Constructional Steel Research*, 62 (1-2), 121–131.
[5] Goggins, J., Broderick, B.M., Elghazouli, A.Y. and Lucas, A.S (2005), 'Experimental cyclic response of cold-formed hollow steel bracing members', *Engineering Structures*, 27, 977–989.
[6] Elghazouli, A.Y., Broderick, B.M., Goggins, J., Mouzakis, H., Carydis, P., Bouwkamp, J. and Plumier, A. (2005), 'Shake table testing of tubular steel bracing members', *Institute of Civil Engineers: Structures and Buildings*, 158, 229–241.
[7] Goggins, J. and Salawdeh, S. (2012), 'Validation of nonlinear time history analysis models for single-storey concentrically braced frames using full-scale shake table tests', *Earthquake Engineering & Structural Dynamics*, 42, 1151–1170.
[8] Salawdeh, S. and Goggins, J. (2013), 'Numerical simulation for steel brace members incorporating a fatigue model', *Engineering Structures*, 46, 332–349.
[9] Salawdeh, S. and Goggins, J. (2016), 'Performance based design approach for multi-storey concentrically braced steel frames', *Steel and Composite Structures*, 20, 749–776.
[10] Salawdeh, S. and Goggins, J. (2016), 'Direct displacement based seismic design for single storey steel concentrically braced frames', *Earthquakes and Structures*, 10, 1125–1141.
[11] Salawdeh, S., English, J., Goggins, J., Elghazouli, A.Y., Hunt, A. and Broderick, B.M. (2017), 'Shake table assessment of gusset plate connection behaviour in concentrically braced frames', *Journal of Constructional Steel Research*, 138, 432–448.
[12] Goggins, J., Broderick, B.M., Elghazouli, A.Y., Salawdeh, S., Hunt, A., Mongabure, P. and English, J. (2018), 'Shake table testing of concentrically braced steel structures with realistic connection details subjected to earthquakes', *Structures*, 12, 102–118.
[13] Salawdeh, S., Ryan, T., Broderick, B.M. and Goggins. J. (2019), 'DDBD assessment of steel CBFs using full scale shake table tests with realistic connections', *Journal of Constructional Steel Research*, 154, 14–26.
[14] Elwood, K., Marquis, F., Kim, J.H, 'Post-Earthquake Assessment and Repairability of RC Buildings: Lessons from Canterbury and Emerging Challenges', *Australian Earthquake Engineering Society (AEES)*, 2015.

[15] Henry, R.S. (2011), *Self-centering precast concrete walls for buildings in regions with low to high seismicity*, PhD thesis, University of Auckland, Auckland.
[16] Roke, D., Sause, R., Ricles, J.M., and Gonner N. (2008), 'Design concepts for damage-free seismic resistant self-centering steel concentrically-braced frames', *14th World Conference on Earthquake Engineering*, Beijing, China.
[17] Sause, R., Ricles, J.M., Garlock, M.M., VanMarcke, E., Peh, L.S., and Liu, J. (2005), 'Self-centering seismic-resistant steel frame systems: Overview of past and current research'. *U.S.A Taiwan Workshop on Self-Centering Structural Systems*, NCREE., Taiwan.
[18] O'Reilly, G.J., Goggins, J. and Mahin, S.A. (2012), 'Behaviour and design of a self-centering concentrically braced steel frame system', *15th World Conference on Earthquake Engineering*, Lisbon, Portugal.
[19] O'Reilly, G.J., Goggins, J. and Mahin, S.A. (2012), 'Performance-based design of a self-centering concentrically braced frame using the direct displacement-based design procedure', *15th World Conference on Earthquake Engineering*, Lisbon, Portugal.
[20] O'Reilly, G. (2013), *Development of a Novel Self-Centering Concentrically Braced Steel Frame System*, PhD Thesis, National University of Ireland, Galway.
[21] O'Reilly, G. and Goggins J. (2021), 'Experimental testing of a self-centring concentrically braced steel frame', *Engineering Structures*, 238, 111521.
[22] Goggins J., Jiang Y., Broderick, B., Salawdeh, S., O'Reilly, G., Bogdanovic, A., Rakicevic, Z., Gjorgjiev, I., Poposka, A. and Petreski, B. (2020), 'Experimental testing of a novel self-centring steel braced frame on the shake table in DYNLAB-IZIIS', *Proceeding of Conference: 17th World Conference on Earthquake Engineering*, Japan, 65-72.
[23] Goggins J., Jiang Y., Broderick, B., Salawdeh, S., O'Reilly, G., Elghazouli, AY., Bogdanovic, A., Rakicevic, Z., Gjorgjiev, I., Poposka, A., Petreski, B. and Markovski, L. (2020), 'Shake Table Testing of Self-Centring Concentrically Braced Frames', *ce/papers*, 4, 2-4.
[24] British Standard BS 5896:1980. *Specification for: High tensile steel wire and strand for the prestressing of concrete*. BSI, London, England, 1980.
[25] European Convention for Constructional Steelwork, *Recommended testing procedure for assessing the behaviour of structural steel elements under cyclic loads, Technical Committee 1, Structural Safety and Loadings. Technical Working Group 1.3, Seismic Design*, ECCS General Secretariat, Brussels, Belgium, 1986.
[26] Ansys® Academic Research Mechanical, Release 17.1 (2016), *Help System, Mechanical APDL*. ANSYS, Inc.

Model Validation for the Wind Response of Modular High-Rise Buildings through Full Scale Monitoring

Hollie Moore[1], Brian Broderick[1], Breiffni Fitzgerald[1], Vincent Barrett[2], Shane Linehan[2]
[1]Department of Civil, Structural and Environmental Engineering, Trinity College Dublin, Dublin 2, Ireland
[2]Barrett Mahony Consulting Engineers, Dublin 2, Ireland
email: : mooreho@tcd.ie , Brian.Broderick@tcd.ie , Breiffni.Fitzgerald@tcd.ie, Vincent.Barrett@bmceuk.com, Shane.Linehan@bmceuk.com

ABSTRACT: For many tall building forms, habitability requirements associated with excessive acceleration response become a governing design criterion as building heights increase. This study considers the wind-induced acceleration response of tall modular buildings and validates computational model predictions using recorded acceleration responses obtained from full-scale monitoring of high-rise buildings. The modelled mechanical behaviour of these steel framed module and RC core buildings and their predicted acceleration response, natural frequency and damping ratio are compared to the actual measured responses.
The acceleration response of a full-scale tall modular building experiencing ambient wind excitation is obtained through a monitoring campaign employing two triaxial accelerometers located at the top of the structure, a data acquisition system and a data storage system; wind speed and direction are also recorded. The acceleration response is processed using modal identification techniques to obtain the natural frequency and damping ratio of the completed structure. The acceleration response, natural frequencies and damping ratios are then compared to the outputs from a previously developed ETABS model of the structure.
The comparison between the model and the full-scale monitoring campaign provides insight into model accuracy and identifies opportunities for further refinement of the modelling of tall modular buildings to reduce model size, run time and computational expense, without loss of accuracy in wind-induced response prediction. The validation of the model supports structural optimisation analyses and the numerical investigations required to include vibration response mitigation measures in future designs.

KEY WORDS: Modular Construction, Tall Buildings, Wind-Induced Vibration, Structural Modelling, Natural Frequency

1 INTRODUCTION

In recent years modular buildings have experienced increased interest due to their reduced environmental impact, improved quality and accuracy, and speed of construction [1-4]. Volumetric modular construction typically involves the off-site manufacture of individual modules in a controlled factory environment. The modules are then transported to site where they are constructed around an in-situ lateral stability element, such as a reinforced concrete core, to complete a finished building. The construction of the modules in a factory results in a significant saving in on site construction time, less labour being required, and more accuracy, less injuries and less waste in the construction process [5]. Whilst modular construction is predominantly used in low to medium rise construction projects such as multi-unit residential accommodation, it is a relatively new concept for taller buildings [1, 5, 6]. Modular construction continues to increase in height due to economic drivers, with building heights of over 130m now realised [7, 8]. However, as with other structural forms, habitability requirements associated with excessive acceleration response become the governing design criterion as building heights increase. Hence, it is crucial for the further development of modular construction that modelling techniques used to identify inherent properties are validated and that the limits of this form of construction are better understood and characterised.

As the construction of modular buildings to new heights continues, issues with applying traditional modelling techniques to these structures are becoming apparent. It has been found that current modelling techniques do not cater for the variety of elements and connections seen in modular buildings and they do not capture the dynamic behaviour of modular buildings sufficiently [9, 10]. There is a significant lack of standards for modular buildings; both in the case of design and applications of BIM [11-13]. Design of modular buildings is currently completed using traditional, non-specific design codes and there are no standards for the modelling of modular buildings resulting in traditional BIM techniques being applied [9,11]. Using practices which were not created for this type of construction leads to inefficiency in design and modelling processes, impeding the progression of this form of construction [9,11].

A significant issue with using current modelling practices arises from the nature of volumetric modular construction. A typical modular building has a double member at every external beam and column and results in the doubling of double member, resulting in quadruple members, in place of every internal beam and column and doubles of all bracing members. This is due to each module being a separate structural system with a full set of members of its own. The stacking and aligning of modules next to each other to complete the finished structure results in duplicates of every member. There is also a significant increase in the number and complexity of the connections throughout a modular structure and replicating the connections with current finite element software can prove difficult-. Whilst using current techniques to model a modular building, in which every element is modelled individually, may

be possible for smaller modular structures, modelling of each element in tall modular buildings with over 40 storeys becomes problematic. The number of elements needed to be modelled becomes considerably large and requires significant computational power and run time to analyse the model, to the point where the practicality of modelling every element becomes questionable. A PC with 32 GB of RAM and an 8 core Intel i9 processor takes approximately 180 minutes to run eigen modal analysis on such a model, and up to ten hours to produce the tables of results. The accuracy this type of model provides is not noteworthy with regards to global dynamic behaviour especially when the significant time producing and running the model are considered. Whilst a global model of a modular structure with every element modelled individually is useful for checking capacities, stresses and the localised behaviour of members, it is worth exploring whether such an extensive model is necessary to represent the properties of a modular structure for the specific purpose of ensuring that habitability requirements are satisfied. This is important because the computational demands associated with the dynamic analysis of the response of buildings to wind loading can be much greater than those required for static analysis of gravity load response. On the other hand, the low amplitude vibrations associated with habitability requirements imply small displacement, elastic response that can be well represented by modal properties, suggesting considerable scope for computational efficiency.

Given the nature of modular buildings as repeatable units stacked around a lateral stability system, there is considerable capacity for efficient modelling techniques to be employed [9]. The purpose of this paper is to consider one such technique in which a macro 'module' element is created and used in the ETABS model of a 135m tall modular building. The modal properties of the model are identified and the model validated using acceleration responses from the in situ 135m tall modular structure. Validation of this modelling technique creates a more accessible method for the dynamic modelling of modular structures and identification of modal properties in the design stage.

2 METHODOLOGY

2.1 Description of In-Situ Structure

The full-scale in-situ structure which is used for validation is a 44 storey, 135m tall modular building. The structure consists of a slip formed concrete core, transfer slab at level 4 and two adjoined towers of 37 and 44 stories that consist of volumetric corner post modules stacked around and connected to two concrete cores. The concrete cores are approximately 8 x 8 m in plan and have walls which vary in thickness between 300mm to 450mm. The landing slabs within the core are 300mm thick. For design purposes, the concrete core is assumed to act as the primary element for lateral load resistance.

The modules are typically 2.875m tall, are limited in length and width to 13m and 6m respectively due to transportation, and have a typical self-weight of 7kN/m. The structure has an overall slenderness ratio (Height/Breadth) of 8. The contribution of the modules to the overall stiffness of the structure, and hence, the lateral load resistance of the modules is so far unknown and is a topic of current research by the authors.

Monitoring of the structure was undertaken over a two month period, beginning in late August 2019 and ending in late October 2019. Two three-axis accelerometers and tilt sensors were directly mounted on a rigid support at approximately 1.84m height from the floor slab at level 43. One accelerometer was located at the center of the concrete core and the other at the edge of the core so as torsional modes were captured. The sampling rate for the accelerometers was 20 Hz; given the height and slenderness of the structure and initial modal analysis, low natural frequencies were expected.

On the roof of the core, a weather station was installed to record 10-minute averaging wind speed and direction, maximum/minimum wind speed and direction within each 10-minute window, temperature, humidity, atmospheric pressure, rain and its duration. A 3G router was also installed to allow for remote access to all data. Data from the weather station was continuously monitored.

In total acceleration time history data was recorded for ten periods of 12 hours in which the structure's acceleration due to ambient white noise excitation from the wind exceeded a threshold value. Each of these acceleration time histories have been assessed using the Bayesian Fast Fourier Transform (BFFT) and Random Decrement Technique (RDT) in order to identify the natural frequency and damping ratio of the structure. The BFFT was applied as described by Au, 2012 [14], and the RDT was applied as described by Wang, 2013 [15]. The estimated natural frequency and damping ratio in the first mode of the structure in both the x and y horizontal directions were identified and verified using these two methods. The estimated values obtained as the average value from the ten 12 hour monitoring periods are listed in Table 1.

Table 1. Modal properties of in-situ structure

	X-X Direction	Y-Y Direction
Natural Frequency	0.316 Hz	0.326 Hz
Damping Ratio	1.1 %	1.28 %

2.2 Macro Module Element

The macro module element is not an existing element within ETABs software and was created within ETABs from replicating properties from a full ETABs model of a typical individual module. The size, mass, stiffness and natural frequency of the typical module were replicated in the macro module element. The mass of the macro module was extracted from an ETABS analysis of a model of a typical module by considering the base reactions under dead loading. This mass is representative of the mass of the module including the self-weight of non-structural elements as each module arrives to site fully fitted out. The stiffness of the module was found by applying a 100 kN force to the top of the model and recording the deflection; the stiffness could then be calculated using Equation 1.

$$k = \frac{F}{\delta} \quad (1)$$

Where k is the stiffness in N/m, F is the applied lateral force, in this case 100 kN and δ is the lateral deflection in mm.

A modal analysis was run using ETABs in order to obtain the natural frequency of the individual module. The stiffness, mass and natural circular frequency of the module were verified using Equation 2.

$$k = {\omega_n}^2 m \quad (2)$$

Where ω_n is the natural circular frequency in rad/sec, k is the stiffness of the module in N/m and m is the total mass of the module in kg.

Once the stiffness was found, the Modulus of Elasticity, E, of the macro module was found using Equation 3.

$$E = \frac{k\,L}{I} \quad (3)$$

Where E is the Modulus of Elasticity in MPa, L is the length of the module in m and I is the Second Moment of Area of the module in m^4 is calculated using Equation 3.

$$I = \frac{b\,d^3}{12} \quad (4)$$

Where b is the total breadth of the module (m) and d is the total depth of the module (m).

The properties derived from the detailed model of the individual module and adopted for use in the macro module element are shown in Table 2.

Table 2 - Properties of a typical module

Property	Value
Length, L	8.887 m
Breadth, b	3.472 m
Depth, d	2.875 m
Second Moment of Area, I	6.876 m^4
Mass, m	16,927 kg
Stiffness, k	89134223 N/m
Natural Frequency, ω_n	72.5652 rad/sec
Modulus of Elasticity, E	115 MPa

Figure 1 shows the model of a typical individual module whilst Figure 2 shows the macro module element. There are a total of 19 beam, column and shell elements in the detailed model of a typical module, whereas the macro module element consists of only one shell element representing the entire module. When this is considered over the entire scale of the structure, with 1,248 modules in total, this implies a difference of over 22,000 beam, column and shell elements. This does not account for joint and connection elements which are also greatly reduced when the macro module element approach is employed.

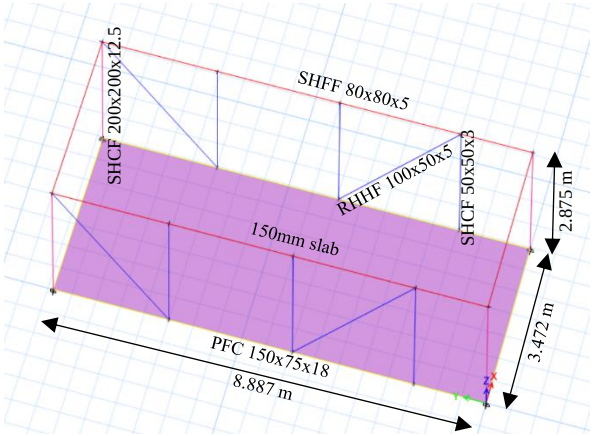

Figure 1. Model of Typical Module

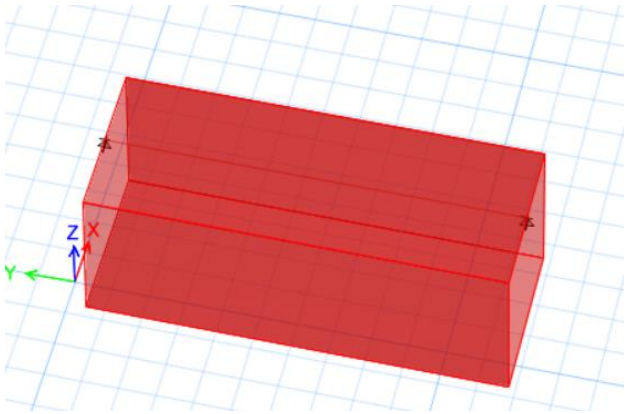

Figure 2. Macro Module Element

2.3 ETABS Model

An ETABS model of the concrete cores was built to replicate the actual as built concrete cores of the in-situ building. The model of the concrete cores is shown in Figure 3. In place of a detailed model of each module, one macro module element is used. Single bar elements of steel plates 150mm x 5mm were used to connect the module elements to one another and back to the core. These bar elements represent a simplification of the actual connection between modules. The use of the macro module element reduced the number of elements in the model from over 260,000 to just over 60,000 when compared to using a detailed model with each member of each module being modelled. The run time for eigen value computation reduces from over 180 minutes to 10 minutes. A typical floor plan from a previously developed full model including all module elements is seen in Figure 4. This is in stark contrast to the typical floor plan when macro module elements are used, as shown in

Figure 5. A side-by-side comparison of both models can be seen in **Error! Reference source not found.**.

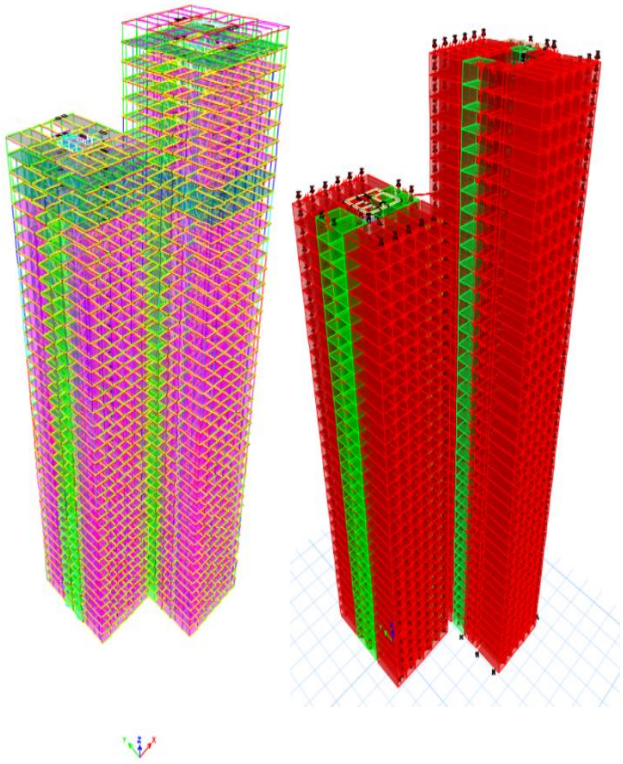

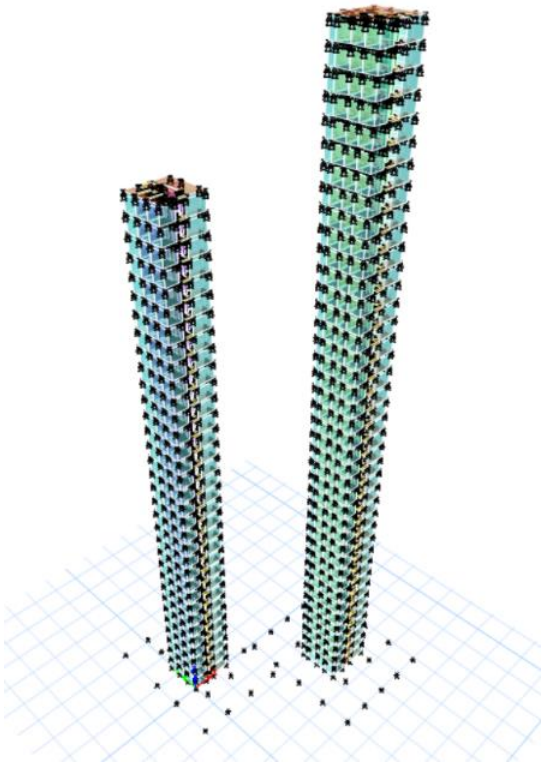

Figure 3. Model of Concrete Cores

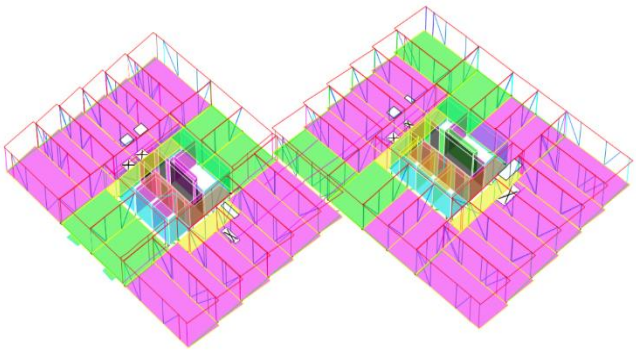

Figure 4. Typical floor plan from full model including all module elements

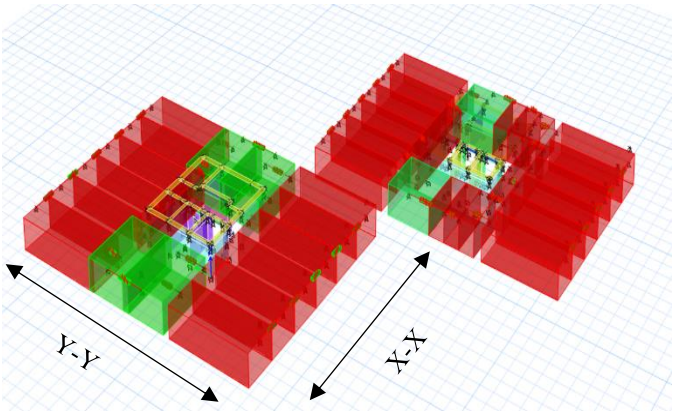

Figure 5. Typical floor plan from model employing macro elements

3. RESULTS

3.1 Validation of Full Module Model

Prior to verifying the macro module element and the full-scale model including the macro module element, the full scale detailed model including all the individual module elements that the macro module element was created to replace must be validated. To this end, the natural frequencies in the first mode in both the x and y directions of the full model were obtained by completing a modal analysis in ETABs. These values are then compared to the actual measured natural frequencies in the x and y direction of the in situ building obtained by performing modal identification techniques on its recorded acceleration response, as described in Section 2.1.

Table 3 compares the natural frequencies estimated from the measured in situ response and the ETABs model.

Table 3. Natural frequencies obtained from in-situ data and from full scale model

	X-X Direction	Y-Y Direction
Natural Frequency from modal identification of in-situ acceleration response	0.316 Hz	0.326 Hz
Natural Frequency from modal analysis of full scale model including all module elements	0.29 Hz	0.31 Hz

It is clear that the modal properties of the full-scale model are in good agreement with the observed dynamic response of the in-situ structure. The natural frequencies obtained from the model are slightly lower than the actual natural frequencies. The actual structure is likely to be somewhat stiffer than is accounted for in the model. The complexity of the connection types used in the construction of the modular building is difficult to represent in an ETABs model and instead a single steel flat plate is used to represent connections. The steel plate is assigned an estimated stiffness value close to what the actual stiffness of the connection is thought to be. There is the potential to tune the modal properties of the model by adjusting this estimated value.

Whilst the natural frequencies estimated from the full ETABs model are slightly lower, it remains an accurate representation of the dynamic behavior of the actual structure. It can be concluded that the detailed model of the module including each member is an accurate representation of the dynamic behavior of an individual model and this is sufficient for use in creation of a macro module element.

3.2 Validation of the Macro Module Element

ETABS modal analyses were performed to identify the first lateral modes on both a model of an individual module with each element modelled and a model consisting of a single macro module element. The results are shown in Table 4.

Table 4. Natural frequencies of alternative module models

	X-X Direction	Y-Y Direction
Full module model with each element modelled	16.95 Hz	12.34 Hz
Macro module element	16.99 Hz	12.36 Hz

It is clear that the natural frequencies obtained from both models lie close in value with very little error. Although the properties of the macro module element were set to reflect the full module model, there is still a slight error in the natural frequency of the macro element. This is likely due to the lumped mass of the macro module element and negligible rounding of values. It is evident that the macro module element can be a suitable substitute for a full model of a single module, indicating that there is significant scope for the macro module element to replace full models of individual modules in a full-scale model of the structure.

3.3 Validation of Macro Module Element Model

The validation of a full model including the macro module element is ongoing. This process involves validation of the full model including the macro element at different stages of construction.

In total, in-situ data was recorded for 10 periods of 12 hours when the structure's acceleration exceeded a threshold value. When the threshold value for acceleration was exceeded, 6 hours of data from before and after the exceedance was used for analysis. The structure was still under construction while a number of these acceleration responses were being recorded and not all modules were installed. The dates in which each 12 hour period began recording and the number of modules installed at this date can be seen in Table 5.

A natural frequency in the first mode in x and y directions was obtained for each of the twelve-hour periods and it is seen to decrease as more stories of modules are installed. ETABS models of the modular structure using macro module elements for each set of conditions in Table 5 are being assessed in order to validate the model, and hence the macro module element at each stage of construction. The verification of the macro module element in each of these conditions will provide more confidence in its effectiveness for a wider variety of structures.

Table 5. Dates in-situ data was recorded and the number of floors of modules installed

Date	Number of Modules Installed	
	Tower A	Tower B
31/08/2019	32	32
02/09/2019	33	32
06/09/2019	34	34
09/09/2019	35	34
11/09/2019	36	34
27/09/2019	41	34
29/09/2019	42	34
11/10/2019	44	37
13/10/2019	44	37
26/10/2019	44	37

4. CONCLUSIONS

A macro module element has been created using properties and modal analysis results from a full model of an individual module employed in high-rise volumetric modular construction. The macro module element has been used to replace the intricate module in full scale modelling of a modular structure. By using the macro module element in the full scale model, the number of elements reduces from approximately 260,000 to 60,000. This yields a significant reduction in model complexity and run time.

Modal analysis was performed on a full scale ETABs model of a 44-storey modular building to obtain the natural frequency in the first mode of the structure in the x and y directions. These natural frequencies were compared to natural frequencies obtained through performing modal identification on acceleration responses from the actual in situ modular structure. It was found that the natural frequencies of the model were quite close to the actual values. Hence, this verified the intricate model of the individual module.

The macro module element was verified by performing modal analysis on both the ETABs intricate model of a single module and the ETABs model of a single macro module element. It was found that the natural frequencies were in good agreement, hence validating the macro module element.

Work is continuing on validating full scale ETABS models of the in-situ modular structure at different stages of construction. The acceleration responses of the in-situ structure at these stages are being used to compare the natural frequencies and acceleration responses of the models with the macro elements.

It is evident that the use of a macro module element greatly improves the efficiency of modelling a modular structure. It has been shown that a macro module element can accurately represent the global dynamic behavior of a typical module. The use of macro module elements in full models of modular buildings will lead to easier assessment of the dynamic behavior of modular structures and their ability to meet habitability requirements.

ACKNOWLEDGMENTS

The Funding for this research was provided by the Irish Government through the Irish Research Council and by Barrett Mahony Consulting Engineers.

Information and data collection for this research was facilitated and supplied by Tide construction.

The authors are thankful for the support received through data acquisition and financial funding.

REFERENCES

1. Hough, M.J. and R.M. Lawson. *Design and construction of high-rise modular buildings based on recent projects*. in *Proceedings of the Institution of Civil Engineers-Civil Engineering*. 2019. Thomas Telford Ltd.
2. Gunawardena, T., et al., *Innovative Flexible Structural System Using Prefabricated Modules.* Journal of Architectural Engineering, 2016. **22**(4): p. 05016003.
3. Lacey, A.W., et al., *Structural response of modular buildings – An overview.* Journal of Building Engineering, 2018. **16**: p. 45-56.
4. Lawson, R.M., R.G. Ogden, and R. Bergin, *Application of modular construction in high-rise buildings.* Journal of Architectural Engineering, 2012. **18**(2): p. 148-154.
5. Ferdous, W., et al., *New advancements, challenges and opportunities of multi-storey modular buildings – A state-of-the-art review.* Engineering Structures, 2019. **183**: p. 883-893.
6. Lawson, M., R. Ogden, and C. Goodier, *Design in modular construction*. 2014: CRC Press.
7. Lane, T., *The sky's the limit: See the world's tallest modular tower in Croydon.* Building, 2019.
8. Thai, H.-T., T. Ngo, and B. Uy, *A review on modular construction for high-rise buildings.* Structures, 2020. **28**: p. 1265-1290.
9. Ramaji, I.J. and A.M. Memari, *Extending the current model view definition standards to support multi-storey modular building projects.* Architectural Engineering and Design Management, 2018. **14**(1-2): p. 158-176.
10. Chua, Y.S., J.Y.R. Liew, and S.D. Pang, *Modelling of connections and lateral behavior of high-rise modular steel buildings.* Journal of Constructional Steel Research, 2020. **166**: p. 105901.
11. Sun, Y., et al., *Constraints Hindering the Development of High-Rise Modular Buildings.* Applied Sciences, 2020. **10**(20).
12. Wang, Z. and K.D. Tsavdaridis, *Optimality criteria-based minimum-weight design method for modular building systems subjected to generalised stiffness constraints: A comparative study.* Engineering Structures, 2022. **251**: p. 113472.
13. Ye, Z., et al., *State-of-the-art review and investigation of structural stability in multi-story modular buildings.* Journal of Building Engineering, 2021. **33**: p. 101844.
14. Au, S.-K. and F.-L. Zhang, *Ambient modal identification of a primary–secondary structure by Fast Bayesian FFT method.* Mechanical Systems and Signal Processing, 2012. **28**: p. 280-296.
15. Wang, Z.-C. and G.-D. Chen, *Analytical mode decomposition of time series with decaying amplitudes and overlapping instantaneous frequencies.* Smart materials and structures, 2013. **22**(9): p. 095003.

A systematic approach for the preliminary design of stadium roofs

Clíodhna Duggan[1], Rui Teixeira[1], Antonio Barrias[2]
[1]Department of Civil Engineering, University College Dublin, Belfield, Dublin 4, Ireland
[2]Arup, 50 Ringsend Road D04 T6X0 Dublin, Ireland
email: cliodhna.nidhugain@ucdconnect.ie

ABSTRACT: Stadiums are iconic landmarks and historically significant structures. From an engineering standpoint they are large-scale, geometrically complex and test the limits of material, requiring sophisticated design techniques. Their construction is also a major contributor to total global emissions. Structural integrity, economic design and sustainability are important design considerations from an early stage. In the preliminary design stages, requirements for strength, stiffness and stability need to ensure structural safety and to minimise resource consumption. Design decisions made in this stage have the greatest potential to improve the costs, environmental impact and benefits attained with a structural form. In practice, several design alternatives must be assessed to arrive at an ideal or optimised solution, which makes traditional design techniques highly effort-consuming. In preliminary design, efficient design solutions can be created with the help of parametric modelling. However, parametric tools are typically applied to well-developed design problems rather than early conceptual design problems. In the present work a systematic parametric modelling approach to support the design and optimization of open stadium roofs is proposed. It focuses on the structural typology and material usage of several stadium roofs. The need for a progressive approach to conceptual parametric design where complexity is progressively introduced in the parametric model is emphasized. This approach is studied in the parametric design of a radial stadium where variations of structural mass can occur when deciding between preliminary design parameters and comparing parametric solutions within a feasible empirical parametric space. Parametric design is shown to have large potential in significantly improving current design outcomes and enabling fully optimal automated stadium roof designs.

KEYWORDS: Preliminary Design, Optimization, Parametric Modelling, Stadium Roof, Automated Design.

1 INTRODUCTION

Preliminary design is an iterative process at the beginning of a project where ideas are generated, evaluated and tested for rejection or further refinement [1]. This involves gathering design requirements, constraints and establishing several various design solutions that satisfy these requirements. The design steps of this procedure as defined by Okudan, Gul E. and Tauhid, S, are divergent idea generation followed by convergent idea assessment, prior to selection. The process of preliminary design involves much creativity and iteration of the many possible structural forms. It is noted that the emphasis of preliminary design is not on structural analysis but on requirements for strength, stiffness, stability, structural safety, to minimise resource consumption and to outline a structures form and function. Traditional methods of preliminary design involve hand sketches, and approximate hand calculations to test several ideas and to quickly arrive at an acceptable preliminary design solution. However, due to a series of factors, such as effort and cost, among others, only a small number of design solutions can be created using these methods [3]. As concerns over climate change, population increase and resource exhaustion becomes more urgent, the need for the design of structures to evolve, to understand structural efficiency and the objectives of future sustainable design, is paramount. With 25% of total global emissions now coming from the construction sector [4], engineers have an increased responsibility of making the most of the resources available to them and arbitrary decision making (or decision making based on "rules of thumb") is not sufficient anymore.

In this context, more efficient design alternatives and solutions can be created with the help of computational design, (parametric modelling in particular). Computational Design is the application of strategies such as computer algorithms to a design process [5]. In most situations computational design is applied to well-developed design proposals where the majority of the design parameters are known or have been already determined by the design team [6]. This is because of the detailed nature and amount of input required to describe a computational model. Computational design software needs a large number of design parameters such as geometry inputs, structural member sizes and material strength grades early on to produce a model with an acceptable structural design solution. Such data very early in the design acts to interrupt the process of iterative decision-making and forces the designer to prematurely make decisions, frequently in an arbitrary manner. A detailed discussion on the different benefits that such computational implementation can promote in the design of structures is presented in [7]. In the practices of design, there is a separation between the act of design and the act of analysis [1]. This results in the preliminary design stages confined within the domain of so-called expertise, hand calculations, sketches, and some less complex forms of analysis to validate decisions.

One of the main challenges of stadium-roof design in its early-stages is to develop a holistic understanding of the degree of complexity in structural systems that may suffice an adequate structural form.

The present work discusses computational parametric modelling as a technique for preliminary design and investigates the extent to which it can influence design outcomes in the preliminary stages. It emphasises the importance of computational design techniques to be incorporated into the design process from the beginning. The ultimate goal of this discussion is to foment discussion on a rationale that can be used in a systematic form and enable automated preliminary brainstorming of structural forms, quantified by their efficiency in relation to some form of performance measure.

2 COMPUTER-AIDED PARAMETRIC DESIGN AND OPTIMISATION

Computer-aided parametric design provides a promising solution to deal with the sheer number of unknown parameters limiting the use of more detailed design alternatives. In it, a model can be built with very little knowledge of the design space and variables can be changed using parametric relationships. Its usage can decrease an engineer's workload significantly by performing several repetitive processes with varying inputs to optimise and greatly increase the efficiency of a design. It allows the design to change and reorder even in the late stages of the design process with little consequence. It is known that several design alternatives must be assessed to arrive at the ideal and optimised solution [8]. This is difficult and time consuming when carried out without the support of computational tools that allow a systemic implementation.

2.1.1 Types of Parametric Design and Tools

Parametric design is a process based on algorithmic thinking that enables the expression of parameters and rules that together define, encode and clarify the relationship between design intent and design response. Three main types can be highlighted:

- Interactive design focuses on the user's experience of hardware and programmable systems. It consists of six main components, user control, responsiveness, real-time interactions, connectedness, personalization, and playfulness. It provides interactivity by focussing on the capabilities and constraints of human cognitive processing [9].
- Generative design is a design exploration process with design goals that generates design alternatives with rapid performance feedback [10].
- Algorithmic design creates large design spaces, highly complex geometries and performance simulations which allows the designer to explore a wider range of possibilities rapidly and with little effort [11].

Different tools are available for parametric design. A common approach is to use a visual script (a flowchart with parameters interconnected). This is advantageous for visual design particularly in the conceptual stages because the designer can control and visualise the design and its process. Grasshopper is one of the alternatives that uses a scripting software and graphical algorithm. This operates within Rhinoceros and produces powerful generative and parametric modelling that incorporates parameter control, programming functions, generative and randomness capabilities. It is the tool applied in the present implementation.

2.1.2 Design Processes and Decision-Making Techniques

Future design practices according to [12, 13] includes iterating the following three steps: parametric modelling (step 1), as an enabler of the generation of numerous design alternatives; performance simulation (step 2) to imitate real world conditions and produce values for quantitative parameters that can be used to assess a structures performance; and design optimization (step 3) to create design solutions that satisfy multiple, potentially conflicting, performance criteria.

Design optimisation, in particular, will play a major role in the achievement of highly efficient design solutions in the preliminary phases of design. Optimization in this context includes Single Objective Optimization (SOO), Multi Objective Optimization (MOO) and Multi-Disciplinary Objective Optimization (MDOO) [14]. If correctly used these have the potential to improve current conceptual workflows by generating high performance designs at any stage of the design procedure.

3 PARAMETRIC APPROACHES IN STADIUM ROOF DESIGN

Designing stadium roofs parametrically has been used before, however only in a limited form for early-stage design and prototyping different schemes.

There has been research carried out for generating variable seating bowls using parametric modelling [9]; associating seating bowls with specific roof structures [15]; optimizing structural [16], energy [16], wind and solar [17] performances based on specific types of geometry; focusing on architectural design variables; studying the structural performance of large indoor arenas and full coverage roof structures using parametric modelling [14]. [9] explores a flexible parametric model composed of the stadium's pitch, bowl, and roof structure; where the roof structure focuses on three structural types (grid-shell, spaceframe, and truss beam). [16] focus on the structural efficiency, operational energy efficiency and architectural expression of long span design. They use multi-objective optimization for the generation and selection of high performing long span structural solutions for structural typologies that are not purely rectangular or regular geometric shapes. The paper concludes that future work should build on the optimization model in terms of structural systems and understanding trade-offs between design objectives. [13] present a computational method for the design of sports buildings in the early stages of design using performance simulation tools and multi objective algorithmic optimization. Design variables include the roof geometry (curvature and dimensions), the position of skylights, building rotation and the properties of the construction materials. The optimization algorithms used Self-Organizing Maps and Hierarchical Clustering on an interactive dashboard to convey the various interacting objectives in the design space and to search for high performance solutions. The research also included multi-disciplinary optimization during the conceptual stages of the design process. This simultaneously considered the performance criteria and design requirements needed for different disciplines leading to an optimal solution. The paper discusses the complexity of sports building roofs and concludes with the explanation of ongoing future work, including additional testing of case studies and further integration of computational methods.

4 SYSTEMATIC APPROACH TO PARAMETRICALLY MODELLING STADIUM ROOFS

For parametric design in stadium roofs to be realistic for the designer, they must not require a large amount of knowledge of the design space to create an efficient workflow. Ideally the number of inputs required in the model should be the minimum number that carries approximately all the information about the problem in-hand. Although no design process is ever simple,

parametric design, digital workflows, and decision-making techniques such as optimization, aim to automate these processes to make the overall design process efficient. The objective of the present work is to create a standardized way for decision making, or a methodology (systematic framework) for the preliminary design of stadium roofs using parametric modelling. The following 8 steps are proposed to initiate a framework that automates the parametric design in the preliminary stages. These are to some extent self-explanatory of the steps that a designer needs to follow to set-up a parametric model with several degrees of freedom. In practice, preliminary design starts from a full parametric space where all degrees of freedom are available. Then the designer progresses from the system of systems to component level locking different degrees of freedom. (S)He uses *a priori* knowledge to perform this procedure. If an automated procedure is aimed at systematically applying this process, then it should be able to, in a structured way, follow the same line of thought and be able to iterate through it.

STEP 1: Parametric Design Modelling Program and Design Process. This initial self-explanatory step will frame the computational support layout required for a parametric approach to preliminary design. It is not part of the iterative procedure and the layout defined should take the software's parametric design abilities into account and their synergies with the stadium problem in-hand (ease in which parameters can be set and changed). It should also include design types, design processes and decision-making techniques. For example, as stadiums are expected to be multi objective, the optimization process should be able to support this.

STEP 2: Stadium Function(s) and Location(s) – Inner-Outer Boundaries. In this step, the capacity of the stadium, the bowl shape, the roof coverage requirements (e.g., indoor, outdoor), the sporting event (pitch shape) and the functionality of the space being designed needs to be considered. These elements will establish the inner and outer boundaries of the parametric model. In this step, within the parametric space, there is a fully-free experimental design. Any structural systems are feasible, and any discrete connection of points within the parametric boundaries is a solution. Several different bowl shapes and sizes can be used.

STEP 3: Design Outcomes(s) and Objective(s). Once step two is complete, the designer must decide what design outcomes are important in the project such as efficiency in terms of environmental impact and cost. The design objectives associated with this outcome included minimizing the self-weight of the structure and optimizing the cross sections of the elements. Other relevant quantitative design objectives could include layout optimization, structural typology efficiency, minimizing operational energy, optimizing construction sequence and fabrication, acoustic atmosphere, and natural lighting. More objectives can be added if required.

STEP 4: Stadium Structural System(s) – Systems. Once the stadium function, location and design objective(s) have been decided, the structural systems that are best suited for the implementation are selected, considering the appropriate load paths and any spectra of existing knowledge. This step reduces the fully-free parametric space to a combination of structural systems, within the inner and outer boundaries. A subset of structural systems from a wider range of available systems constrains the preliminary design. Parametric variables that are related to the system of systems are identified in this phase too (e.g., spacing between structural system).

STEP 5: Stadium Structural System(s) - Component(s). Once the structural system(s) are decided on, the variables that each structure have in common must be examined. These variables will establish the parametric relationships in the model. This includes the identification of degrees of freedom that exist in each structural system, as a system of components. It also includes the identification of any model dependencies for each (e.g., how the individual component variables in the parametric model, can be altered, and what type of impact each will have on the structural system). In this phase the experimental design for the preliminary design is further reduced to combinations of parametric systems.

STEP 6: Initial Parametric Model. With the parametric components established in steps 2-5, the geometry of the various structures can be created.. Each structural system can be designed using lines and parametric relationships corresponding to each variable. After the parametric script is set-up, changes between structural systems and system variables are expected to require virtually zero design efforts.

STEP 7: Structural analysis – Establish feasible domains. Once step 6 has been completed, the structural analysis suitable for the design decisions can be implemented into the parametric model. With the design standards, limits and checks established the model can be analysed. It is here that structural engineering knowledge and expertise is applied for the model to be realistic and ensure structural stability and safety for the preliminary design. The preliminary analysis can take load bearing capacities, buckling, vibration and deflection limits into account. If designer input is considered, limits must include rules of thumb for ranges of variables. All will constrain the parametric space to a space of feasible parametric solutions.

Step 6a & 7a: Rolled Parametric Design (Update/ Augment the parametric model). With the design variables, geometry, parametric relationships and analysis modelled, the designer can revisit the design, objectives, parameters, functions, and additional systems in the model. An initial parametric model is established that can be updated or further parameterised if required. Step 6a and 7a involve looping through the previous steps 2-6 if required.

STEP 8: Parametric Decision-Making. Using the decision-making technique enabled in Step 1, the design objectives from Step 3 and the system components from Step 4-5; the parametric evaluation of the model, built in Step 6 and constrained in Step 7, can take place. If parametric optimization is applied, results can be visualised and various solutions examined.

Step 8a: Re-evaluation. The decision-making should follow an iterative design process. In this step a decision should be made regarding whether to return to **step 6a** or **7a** and update/ augment the parametric model; or accept the current parametric solution. Useful decision criteria should include any variables that converged to the boundary of the design space. This means that there is an interest for an augmented spaced to be rolled back to the previous steps (that is, an increased parametric range). Any new ranges should be re-evaluated, to give new parametric solutions, and if any new solution does not improve the previous outcome, the previous outcome can be accepted.

If scope is identified in augmenting the parametric variables, not only in range but in characterisation, then these should be added in **step 7a**. If new client requirements or inputs external to the parametric model are added, they should also be included in augmented models. Figure 1 gives an overview of the structure discussed above.

5 IMPLEMENTATION OF A PARAMETRIC MODEL IN PRELIMINARY DESIGN

Following the approach described in section 4, a progressive parametric preliminary design model was generated to illustrate the benefit of thinking systematically in parametric design and the potential it has to improve the outcomes of design. It combines the software Rhino with Grasshopper along with several plug-ins. The Grasshopper model consists of four sections including input parameters, geometry, a structural analysis, and an optimization. By examining the information extracted from literature and using design requirements, each design decision was made with the idea that it could be changed, re-analysed or increased in complexity in the future, i.e. being progressive in nature. Figure 2 presents the structure of the parametric script developed. It describes a stadium roof with parametric radial trusses. The interested reader is directed to [7] for a detailed explanation of the model.

5.1 Input Parameters

To begin the modelling process several key starting points, optimization parameters, user defined parameters and fixed parameters were established. These included 6 parameters; capacity, material, truss internal spacing, angle (referred to as height above the pitch), truss depth and number of truss bays. An initial radial system was considered, but the model indicated how additional structural systems might be incorporated into the script.

5.2 Geometry and Check

The model incorporated five rounded polygonal curves which defined its geometry based on the capacity, pitch outline, sightlines, viewing angles, rows of seats and the grandstand structure below. These curves constrained the geometry of the stadium to a specific boundary. The curves were split into sections and all structural elements. An example of the stadium roof model is presented in Figure 3.

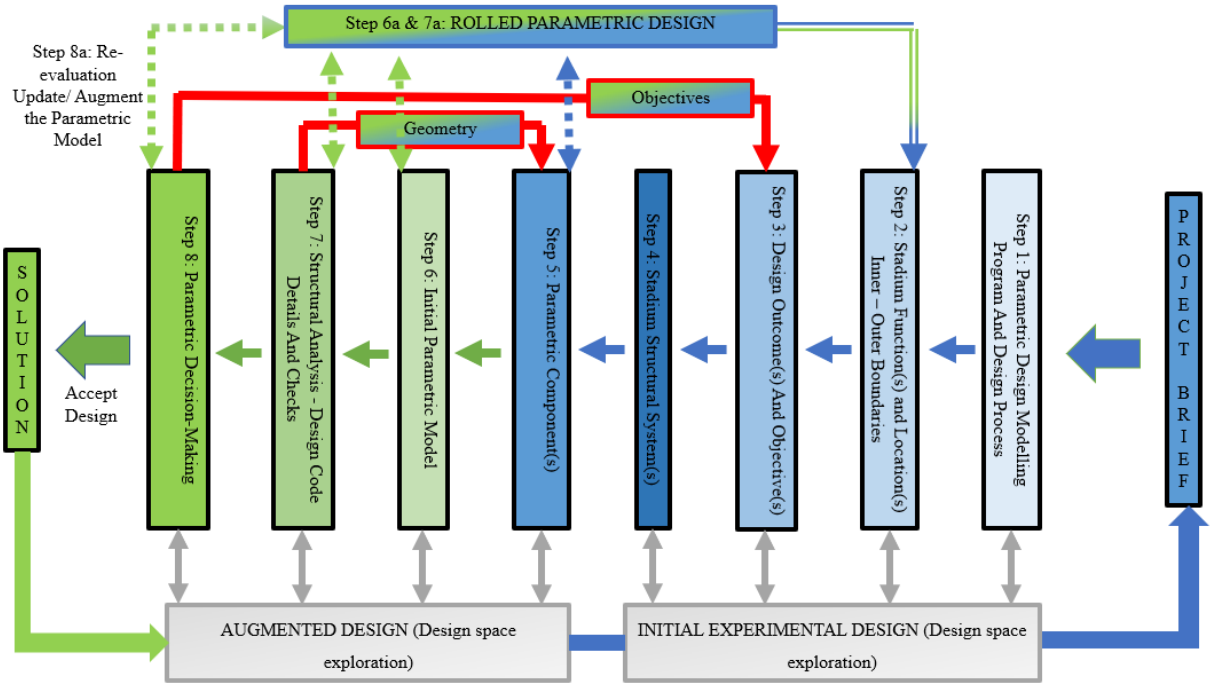

Figure 1. Example of the systematic structured procedure for preliminary progressive parametric design.

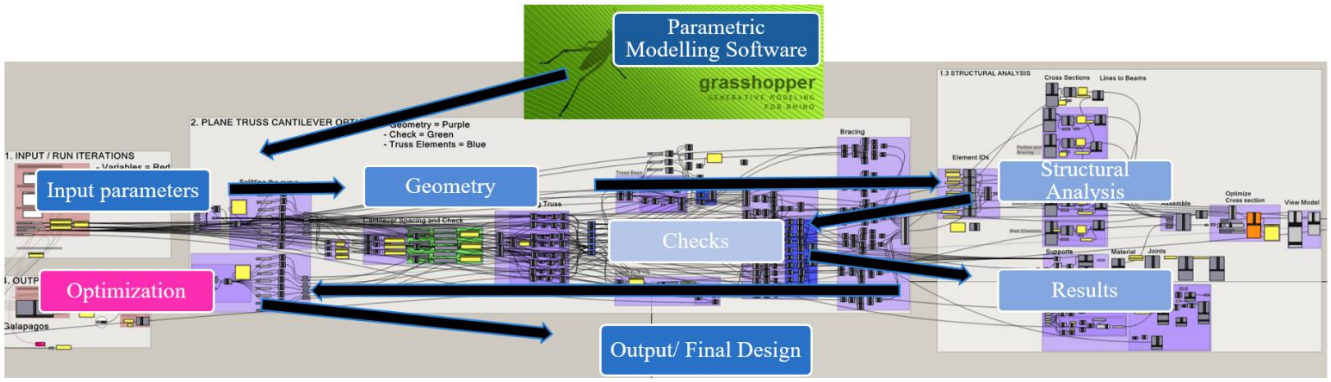

Figure 2. Structure of the model of the radial based truss system, parametric stadium roof developed.

5.3 Preliminary Structural Analysis

A simplified finite element code (Karamba3D), suitable for calculation in the preliminary design stages, was used to conduct the structural evaluation of the parametric solutions. In this code, design decisions for the analysis included the application of cantilever steel trusses with UC sections as top and bottom chords with purlins and bracing as square or rectangular hollow sections with simple connections.
The supports used in the model were the two bottom nodes and the first top node. Each roof truss had a uniformly distributed load along the top chord to represent the weight of the cladding, services, and wind. Ultimate (ULS) and Service (SLS) limit states load combinations were considered. Utilisation ratios and deflection limits also constrained the parametric space.

5.4 Optimization and decision criterion

The goal of the analysis was to merge optimisation with preliminary design so that the full benefit of parametric modelling in preliminary design could be attained. In the present example one objective (the mass) was considered. The the optimisation was run using 4 parameters (no. of truss internal spaces, angle, truss depth, and number of truss bays). A Genetic Algorithm (GA) was applied to solve the optimisation. GAs are well-suited to be applied with parametric models, in bi-level approaches [18].

5.5 Results

An optimisation run on the 4 parameters mentioned above ran in approximately 10 minutes. Figure 3 presents a feasible solution of the parametric space. Results for different feasible parametric solutions are presented in Figure 4.

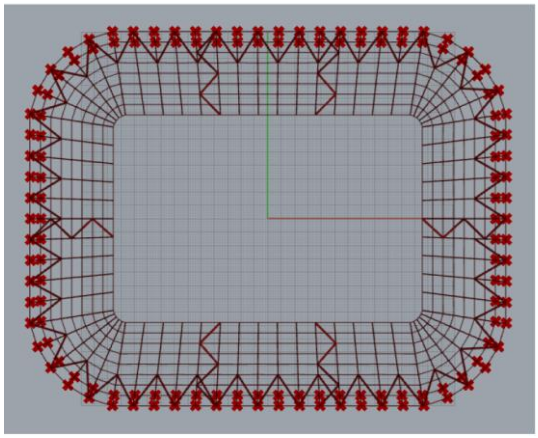

Figure 3. Example of a feasible parametric solutions for the roof stadium. It is noted that each radial line is a truss system.

The ranges of values for each variable are represented by vertical axes (increasing in value from bottom to top) and each line represents a different design solution. The point where each line intersects the vertical axes represents the value of a corresponding design variable for a particular design. The red line in Figure 4 represents the design with the minimum mass. The variable values include 12 spaces (9.5m spacing), 12m height above pitch, 9 truss bays and 4.5m in depth. These variables correspond to 4500 tonnes of steel. This equals 11,025,000 kgCO^2e of embodied carbon, according to the EPD of British steel. A total cost of €55,125,000 and a social environmental impact cost of €661,500.

It is possible to infer that simple parametric changes can lead to a high variation in the weight of the structure. Structural mass can change in up to 25% of the minimum mass attained within the parametric ranges considered. In this cantilever structure for 25,000 capacity if 15 spaces (7.5m spacing), 12m height above pitch, 8 truss bays and 4.5m in depth, a final mass of 6000 tonnes is attained. This is a 1500 tonne increase in mass with a relatively minor change in the design parameters, which is a significant representation of how simple arbitrary decisions that can be made in preliminary design can lead to significant changes in the design outcomes.

The parametric outcomes allow designers to study also the influence of the design variables, where the spacing between radial trusses and height of the cantilever can be quickly identified as range variables to augment in further iterations. This is of interest if an automated construction of space is sought, where results can inform the roll-back of the parametric design, as highlighted in steps 6a, 7a and 8a in the framework proposed. With such consideration a learning approach can be used to inform new parametric design exploration in the preliminary stages where all the degrees of freedom are still available for the designer, regardless of this learning being done in a supervised or unsupervised approach.

6 CONCLUSIONS

6.1 Current state of the work

The present work studied parametric design as a tool for the preliminary design of roof stadiums. It showed that a systematic approach to parametrically designing stadium roofs rapidly produces and analyses design alternatives, integrates a variety of tools into one environment and can customize optimization and decision-making strategies to produce suitable designs. The results show that the ability to define and modify the geometric and non-geometric parameters of a design in a flexible and user-friendly environment without significant effort to regenerate geometry and re-assign attributes can be attained using parametric modelling. Parameterization of the design significantly increases the complexity of the design task since in it there is a need to not only model the structure but also make it one that has as many parametric relationships as possible. Nonetheless, once this work has been completed, the design is automated which significantly reduces the time required to change and re-analyse outcomes. A systematic approach for parametric progressive

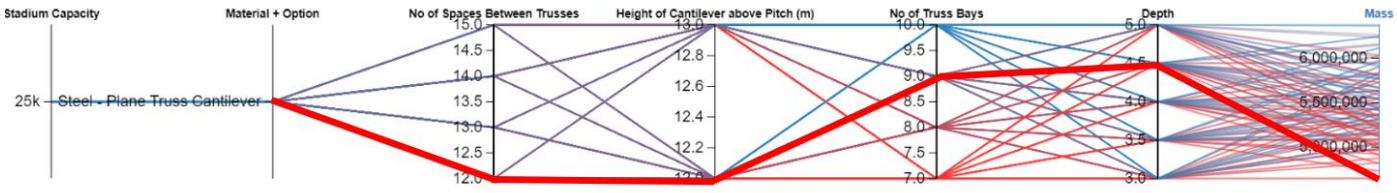

Figure 4. Example of feasible space and parametric optimal solution. The optimal solution is represented by the (red) bold line.

preliminary design was also proposed. Its foundation is in the assumption that, despite preliminary design being highly explorative by nature, it still consists in a series of systematic steps. It has large reliance on the experience of the designer to take decisions, therefore, if a large enough spectrum of projects already exists, then there is scope to automate the task. The approach proposed here consisted of structuring the different steps that are taken in preliminary and parametric design. Finally, a representative implementation of a parametric stadium was developed to research the benefits of using a parametric implementation in the preliminary stages of design. With a limited CPU time it was possible to achieve an optimal parametric solution for the implementation. Moreover, it was shown that up to 25% of variations in mass could occur due to simple parametric changes (in the present work 4 parameters were used for reference). It was shown that empirical decisions are not adequate to achieve efficient solutions. For reference, a simple increase in the number of spaces of vertical truss members from 12 to 15, even with a decrease of other variables, increased the mass in the overall system approximately 25%.

Several recommendations for future work are presented below, nonetheless, the results obtained are representative of the untapped potential that exists in parametric design, in particular in preliminary design where decisions made will lock up many of the degrees of freedom in the design.

6.2 Future work

Potential avenues for the future include developing an augmented design approach, design coordination and developing artificially intelligent designers.

Future work could address the need to progressively increase the complexity of the model by augmenting the design space, developing additional components or by offering new strategies altogether. There is scope to use as many variables as possible in the parametric script, which can all be implemented in an iterative procedure until a convergence criterion is achieved. The design alternatives explored in this work were limited and topological variations were not fully explored. Increasing the number of structural systems analysed in the model and making the script produce solutions more quickly are also potential avenues for future research. Results in the model could also be improved by adding additional analyses or load combinations.

Further research could also address the need to examine optimization methods that can tackle larger and more complicated design spaces. This could result in further developing the systematic framework proposed in the present work and examining the potential it has to automate design. This could involve building an "artificially intelligent designer" (that uses a spectrum of completed examples to inform the parametric learning). It could use only the inner-outer boundaries to set-up a parametric model, and eventually an optimal structural system form for a stadium roof. This is something that is of interest to stadiums, but also for any other type of structure. Additionally, a parametric model in the future could incorporate the entire stadium structure as well as a detailed structural analysis. The benefits of such a model could include coordinating communication between various designers for example, a design team could generate and improve a design, a contractor could use it in a similar way and the client could visualise the outputs.

ACKNOWLEDGMENTS

The authors thank Agnes Lindblom and Matilda Svensson for their assistance in the development, as well as Tim Finlay, for providing essential information for completion, of this work.

REFERENCES

[1] - Marsh, A.J., 1997. Performance analysis and conceptual design.

[2] - Okudan, Gul E., Tauhid, S., (2008). Concept selection methods - a literature review from 1980 to 2008, International Journal of Design Engineering 1 (3), pp. 243–277. DOI: 10.1504/IJDE.2008.023764

[3] - Turrin, M. 2014, Performance Assessment Strategy: a computational framework for conceptual design of large roofs. PhD. Delft University of Technology

[4] - IEA, 2021. Emissions by sector – Greenhouse Gas Emissions from Energy: Overview – Analysis - IEA. [online] IEA. Available at: <https://www.iea.org/reports/greenhouse-gas-emissions-from-energy-overview/emissions-by-sector> [Accessed 31 October 2021].

[5] - Debney, P. and Brohn, D., 2021. Computational engineering. London: The Institution of Electrical Engineers.

[6] - Marsh, A. and Haghparast, F., 2004, September. The optimization of stadium roof glazing for cost and solar access using built form generation based on performance optimised solutions to tightly defined design problems. In 21st International conference on Passive and Low Energy Architecture, Eindhoven (pp. 19-22).

[7] – Clíodhna Duggan. 2022. MEng thesis. A systematic approach for the preliminary design of stadium roofs.

[8] - Pan, W., 2021. Computational Design of Indoor Arenas (CDIA): Integrating multi-functional spaces and long-span roof structures. A+ BE| Architecture and the Built Environment, (10), pp.1-296.

[9] - Saffer, D., 2010. Designing for interaction: creating innovative applications and devices. New Riders.

[10] - Autodesk.com. Available at: <https://www.autodesk.com/solutions/generative-design> [Accessed 31 October 2021].

[11] - ADA, 2021. ADA. [online] Algorithmicdesign.github.io. Available at: <https://algorithmicdesign.github.io/> [Accessed 31 October 2021].

[12] - Aish, R., Fisher, A., Joyce, S. and Marsh, A., 2012. Progress towards multi-criteria design optimisation using DesignScript with SMART form, robot structural analysis and Ecotect building performance analysis.

[13] - Turrin, M., Yang, D., D'Aquilio, A., Sileryte, R. and Sun, Y., 2016. Computational design for sport buildings. Procedia engineering, 147, pp.878-883.

[14] - Pan, W., Sun, Y., Turrin, M., Sariyildiz, S. and Paulb, J., 2016, September. A Parametric Modelling Process for the Integration of Architecture and Structure in Large Multi-functional Sports Hall Design: A Case Study. In Proceedings of IASS Annual Symposia (Vol. 2016, No. 10, pp. 1-10). International Association for Shell and Spatial Structures (IASS).

[15] - Lewis, C. and King, M., 2014. Designing the world's largest dome: the National Stadium roof of Singapore Sports Hub. The IES Journal Part A: Civil & Structural Engineering, 7(3), pp.127-150.

[16] - Brown, N., De Oliveira, J.I.F., Ochsendorf, J. and Mueller, C., 2016, July. Early-stage integration of architectural and structural performance in a parametric multi-objective design tool. In International conference on structures and architecture.

[17] - Marsh, A. and Haghparast, F., 2004, September. The optimization of stadium roof glazing for cost and solar access using built form generation based on performance optimized solutions to tightly defined design problems. In 21st International conference on Passive and Low Energy Architecture, Eindhoven (pp. 19-22).

[18] – Teixeira, R., Martinez-Pastor, B., Nogal, M., & O'Connor, A. 2022. Metamodel-based metaheuristics in optimal responsive adaptation and recovery of traffic networks. Sustainable and Resilient Infrastructure, 1-19.

Developments in the Manufacture of Powder Epoxy Fibre Reinforced Polymer Composite Structures

M. Flanagan[1,3,4], J. Goggins[1,3,4] , T. Flanagan[2], W.Finnegan[1,3,4]

[1]Civil Engineering, NUI Galway, Ireland
[2] ÉireComposites Teo, Indreabhán, Galway, Ireland
[3] Centre for Marine and Renewable Energy (MaREI), Galway, Ireland
[4] Ryan Institute, Galway, NUI Galway, Ireland
email: m.flanagan@nuigalway.ie

ABSTRACT: Fibre reinforced polymer composite materials are used in the aerospace, automotive and renewable energy sectors due to their low weight, high-strength and relatively low cost. Powder epoxy is a form of epoxy which is suitable for use in the manufacture of fibre reinforced polymer composite structures. Manufacturing composites using powder epoxy has several advantages over traditional epoxy matrices in that it offers increased toughness and better design flexibility when compared to traditional epoxy materials. Due to these advantages, along with its corrosive resistant properties, powder epoxy has recently been used in several marine renewable energy devices. This paper presents a review of research and commercial work carried out to date on the development of powder epoxy. Key properties of powder epoxy, including mechanical properties, manufacturability and processability, are presented and discussed. The cure kinetics of powder epoxy are also presented and an alternative cure cycle, which would reduce the cost of manufacturing powder epoxy, are discussed. The superior properties of powder epoxy make it an excellent material for use in the renewable energy sector and its implementation in the sector would contribute to reducing the levelised cost of energy, which is essential for the transition from fossil fuels to renewable sources of energy.

KEY WORDS: Polymer composites; Glass fibre; One shot process.

1 INTRODUCTION

Renewable energy devices such as wind and tidal turbine convert the mechanical energy of the fluid into electrical energy. For both tidal and wind energy devices large blades use aerodynamic lift to convert wind energy into rotational motion which in turn is converted to electrical energy via a generator. These blades are commonly made from fibre reinforced polymer composite material including glass fibre epoxy and carbon fibre epoxy. Wind turbine blades are manufactured from thermoset materials using methods such as vacuum assisted resin transfer or wet layup. The most common approach is to manufacture sub components and bond them together using adhesives [1].

Eirecomposites, Inverin Galway, have developed a vacuum forming process using Glass Fibre (GF) polypropelyne (PP) which they have applied to blades up to 4m long [2]. These blades are formed under vacuum pressure at 180ºC in a single step using no adhesive and the material is more suitable to recycling than traditional thermoset materials. Forming a blade in a single step can be referred to as a "one shot" process or "co-curing" in some instances. In this paper the term "one shot" is used to refer to a process where a composite part is manufactured in one piece. The one shot process eliminates glue and associated steps such as surface preparation, assembly, shimming and unlike glue, it results in a blade which can have continuous fibres running along the load paths. This can result in a reduction in cost, production time and weight [1][3]. These advantages make it an excellent manufacturing method for any load bearing composite structure. Large scale one shot processes are being developed in aerospace and renewable sectors [3], [4]. One of the challenges in manufacturing parts in one shot is forming the shape of the final part, including all internal structures, during curing or thermally welding the part. The term thermal welding refers to aligning several thermoplastic components and applying heat and pressure so that they bond together without the use of glue. Traditional un-cured thermoset composite materials are not rigid and they must be supported by complex tooling to create a high quality final structure. For thermoplastics, which are generally rigid at room temperature, solid sub components can be assembled at room temperature, vacuum bagged and thermally welded in one part. The ability to assemble rigid thermoplastic structures and then thermally weld them, under vacuum bag only, reduces or may even eliminate the need for the complex tooling that is required during thermoset one shot manufacture.

Heat activated powder epoxy is a material which behaves like a thermoplastic prior to cure. The material has low viscosity at high temperatures, which allows it to fully impregnate or "wet out" fibres, however it is a solid at room temperature. The material can be formed into a net shape solid composite part, which is consolidated but not polymerised. These parts can be assembled at room temperature and cured in a one shot process. During this process the epoxy viscosity drops significantly allowing the sub components to form glueless joint lines in a process that is similar to thermal welding. Figure 1 shows the sub components that are used in the manufacture of a 13 m wind turbine blade using power epoxy and Figure 2 shows the final commercial blade manufactured using the one shot process.

In this paper recent work on the cure cycle of powder epoxy is reviewed in order to better understand the factors that influence the quality and cost of parts manufactured using powder epoxy.

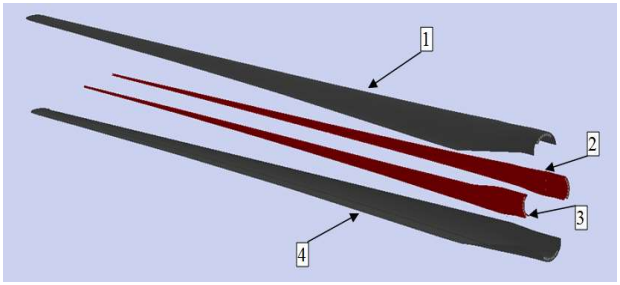

Figure 1 Sub components of a one shot Vestas V-27 wind turbine blade, showing (i) the top skin, top root anchors, inserts, and top spar (part 1) in grey, (ii) the leading edge root anchors, inserts and leading edge web (part 2) in red, (iii) the trailing edge root anchors, inserts and trailing edge web (part 3) in red, and (iv) the bottom skin, bottom root anchors, inserts and bottom spar (part 4) in dark grey[1].

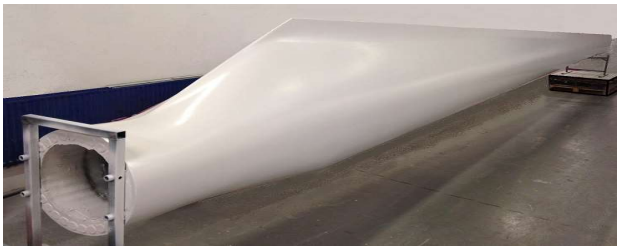

Figure 2 13 metre commercial wind turbine blade manufactured using an out of autoclave one shot process [1].

2 MATERIALS AND METHODS

2.1 Aim and objectives

The overarching aim of this paper is to identify a pathway to reduce cost while maintaining the quality of powder epoxy composite structures.

In order to achieve this aim, this study has the following objectives :

- Carry out a literature review on the powder epoxy material.
- Identify areas that show potential for process improvement.
- Create a research plan to investigate the proposed process improvement.

2.2 Material overview

Powdered thermosetting polymers are the most economical and environmentally friendly metal coating and, as such, they are used widely in the coatings industry [5]. These materials are designed to have excellent strength, toughness, adhesion and chemical resistance. Thermosetting powders change phase from a brittle solid powder, to a low viscosity liquid, and finally to a tough solid when the catalyst in the resin is heated. The powder epoxy considered in the current paper is one such powdered thermosetting material. At room temperature powder epoxy can be a powder or a brittle solid. Because it requires heat to cure, it does not need to be stored in refrigerated conditions and it has excellent shelf life. Once the material is heated the material melts into a low viscosity which allows excellent fibre wet out. The compressive and tensile strength and moduli of powder epoxy with 50% volume fraction of glass fibre are given in Table 1.

Table 1 Mechanical properties of glass fibre powder epoxy laminates.

Fibre type	E Glass
0º Tensile modulus GPa	40[6]
0º Tensile strength MPa	782[6]
0º Compression modulus GPa	38[6]
0º Compression strength MPa	643[6]

Powder epoxy can be used as the matrix in fibre reinforced polymer composites. Powder epoxy composites can be created by either manually adding powder to the composite fabric prior to cure or melting the powder into the fabric prior to cure to create a pre-impregnated material. The process results in a composite with low void content, no dry fibres and good mechanical properties.

Figure 3 shows a typical cure cycle for a thick powder epoxy laminate consisting of a drying stage, an impregnation stage and a cure stage. The purpose of the drying stage is to ensure that all moisture is removed from the powder prior to impregnation and cure. The impregnation stage allows the epoxy to fully penetrate the fibres and allows any gas to leave the composite, as such this stage is key to manufacturing void free composites. The cure stage ensures the epoxy is fully polymerised. This cure cycle has been shown to result in fully cured laminates with low void contents and excellent material properties.

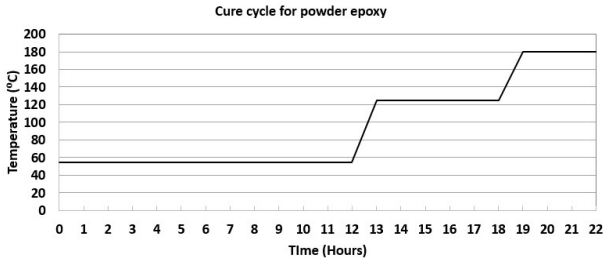

Figure 3 Cure cycle for powder epoxy laminates consisting of a drying cycle at 55ºC, an impregnation stage at 120ºC and a cure stage at 185ºC, adapted from , adapted from [7]

3 LITERATURE REVIEW

NASA conducted extensive research into carbon fibre powder epoxy composites in the 1980's and 1990's [8]–[12]. The purpose of the work was to develop a suitable matrix material for manufacture of textile, tow placement and filament winding. Powder epoxy impregnated tows were produced using several powder epoxies, and process development and material characterisation work was carried out. Press and autoclave fabrication demonstrators were manufactured and the authors stated that initial work on advanced tow placement and filament winding was carried out, although results of this work were not published [8]. NASA showed that for the powder epoxies considered, the powder coated tows could be woven braided and pultruded without the use of solvents and that they could be stored at room temperature indefinitely. One noted disadvantage of the powder epoxy material is that it had a high

'bulk factor' meaning that tows impregnated with powder epoxy were thicker than equivalent prepreg tows. It was noted that debulking without cure could be carried out intermittently to reduce the size of the layup. NASA coated individual tows prior to braiding to create a co-mingled towpreg. NASA set up a tow powder coating line, manufactured test samples and made several demonstrators, however no publications could be found that indicate that the work progressed beyond NASA TRL 4.

Recently there has been renewed interest in powder epoxy materials with academic research in the topic in the University of Edinburgh, Queens University Belfast and the National University of Ireland Galway. Companies such as Eirecomposites (Galway Ireland) and Swiss CMT AG (Sieben Switzerland) are also using powder epoxy composites for commercial products.

Several commercial products and technology demonstrators have been manufactured by Eirecomposites and tested in static and fatigue loading. [13], [14] give details of modelling and testing of a 13 metre commercial wind turbine blade, shown in Figure 1, manufactured by Eirecomposites from GF powder epoxy. The results showed that the structure, manufactured using a one shot process was capable of reaching the design loads without any indications of failure. [15] gives details of testing of a Carbon Fibre (CF) one shot tidal energy foil manufacture by Eirecomposites using the one shot process. [16] tested an 8 metre tidal turbine blade manufactured by Eirecomposites using GF powder epoxy in a one shot process. The results showed that the blade was capable of reaching the maximum design loads and also the fatigue loading for the lifetime of the blade. This work is the largest tidal blade to undergo a full lifetime fatigue loading and it is also the highest mechanical load ever reported to have been applied to a tidal blade. This structure was up to 130 mm thick at the root and as such this demonstrated the manufacturability of large thick sections with the powder epoxy material. [17], [18] tested hybrid GF CF carbon wind blade demonstrators including a 6m structure and again showed that the structure reached the design loads without any indication of failure. Several studies have also looked at the addition of novel erosion protection systems for powder epoxy structures [19]–[22].

Maguire et al [23], [24] carried out an investigation into the cure kinetics of two powder epoxy systems using Differential Scanning Calorimetry (DCS), Thermo-Gravimetric Analysis (TGA) and parallel plate rheology. The DSC showed that powder epoxy material exotherms at a rate of 138-184 J/g, whereas traditional epoxies typically produce greater than 400 J/g. This relatively low exotherm means that powder epoxy is less susceptible to thermal runaway than tradition liquid epoxies. This makes thermal control during the manufacture of thick sections easier and hence makes the process safer and easier to control. The degree of cure was also calculated isothermally for temperatures at 150, 160, 179 and 180ºC. The results showed that it took under 10 minutes to reach 80% degree of cure at 180ºC compared to circa 100 minutes at 150ºC. It is interesting to note that although a typical cure cycle including drying and impregnation is circa 16 hours, the majority of the cure takes place over 10 minutes. This indicates that the powder epoxy cure cycle could be optimised to reduce the cure cycle duration or temperature. The viscosity was measured using parallel plate rheology at a temperature increase of 5ºC per minute and it was shown that the viscosity is less than 10 Pa-s above 130ºC.

The work also indicated that the powder transforms to its liquid stage between 40ºC and 60ºC but the low viscosity required for full wetting out of the fibres is not reached until above 100ºC. The epoxy exhibits a low viscosity over a wide range of temperatures and as such it has a wide processing window from a point of view of both time and temperature. When held isothermally at 121ºC powder epoxy maintains a viscosity below 100 Pa-s for 300 minutes and has a gel time of 8 hours. This processing window is wider than comparable out of autoclave prepregs (Cycom 5320-1, ACG MTM45-1) but lower than autoclave resin (hexply 8552). The wide processing window results in a fully consolidated, low defect part, even if different sections of a laminate are exposed to different thermal profiles.

The fact that the parts are consolidated and fully impregnated at 121ºC and can even be cured past the gel point at this temperature indicates that this step is the most critical part of the manufacturing process from a point of view of laminate quality. This information also raises the possibility of curing past the gel point at a relatively low temperature and then carrying out a free standing post cure at elevated temperature to fully cure the part.

After the initial characterisation work Maguire et al used the material properties to model the manufacture of thick laminates and validated the models by manufacturing several 100mm thick laminates [7], [25]. The models looked at the cure kinetics and thermal profile through the thickness of the laminate in order to verify experimentally that the wide process window identified in the initial characterisation study would translate into a wide processing window in a thick laminate. The work showed that the powder epoxy prepreg undergoes sintering and a reduction in thickness of 50 % between 50ºC and 60ºC. The results of dynamic vapour sorption also showed that sintering negatively influences the desorption of the powder and it is hypothesised by the authors that a drying cycle below the sintering temperature could reduce the overall cycle time. This area is highlighted as an area for potential cycle time improvement. The results showed that the 100 ply laminate was de-compacting for the entire time that the laminate was in the impregnation phase (about three hours), this suggests that an impregnation time shorter than this would result in a laminate that was not fully impregnated. Note this laminate was created with no de-bulk phases. Despite the long impregnation phase there were a lot of defects in the laminate at the fibre tow centres. The reason for the defects is unknown but the lack of a debulks during the manufacturing may have contributed to this.

Maguire [7], [25] also looked at manufacturing GF powder epoxy from prepreg and from manual addition of the powder to glass. The prepreg material resulted in lower void content in the final laminate. The prepreg laminate also had increased thermal conductivity prior to melting and as such its temperature increased more quickly, relative to the manual created material, during the drying phase. It was noted that due to the temperature gradients in the laminate it was possible that significant thermal stress could form in the laminate. A cure cycle with an extended dwell at 135ºC was modelled and the results were shown to minimise the temperature gradient as the laminate reached its gel temperature which would reduce

thermal stress. The current paper has found no evidence that indicates that residual thermal stress is a problem in the manufacture of powder epoxy composites, but it is certainly possible that it has a negative influence on the material properties of the final structure.

Carbon fibre is more sensitive to wrinkling during infusion, which results in poor mechanical performance and the use of carbon fibre with traditional blade manufacturing processes has resulted in blade failures [26]. Despite this, the availability of pultruded elements which reduce wrinkling, a better understanding of CF's manufacturing sensitivities, and the need for materials with high specific strength, are likely to lead to an increase in the use of CF in wind applications in large wind turbine blades [26]. Pultrusion of composites is a high throughput, continuous automated process which involves pulling fibres and resin through a heated die which simultaneously cures and consolidates the composite. The process results in composites with excellent material properties due to a combination of reasons such as the high fibre volumes achievable, the low void content and the high fibre straightness. Typical wind turbine blades are beams in bending, as such they experience high compression and tensile stresses. Continuous fibre based composites are generally weaker in compression than in tension and this means that the compression strength of the base material is often the most important factor in the material selection process [26]. Fibre straightness has been shown to increase the compression strength of composites and as such the increased fibre straightness in pultrusion processes may be particularly advantageous in systems such as cantilevered wind and tidal turbine blades. Pultruded rods and planks, designed for incorporation into large composite structures including wind turbines, with mechanical properties superior to Vacuum Bag Only (VBO) prepreg materials, are commercially available [27]. While the pultruded elements have excellent material properties, incorporating them into the structure offers many technical challenges as the pultruded sections must be formed into the shape and integrated into the final structure. This will likely negate some of the advantages of the pultruded systems.

[28], [29] investigated the influence on fibre straightness and fibre sizing type and amount on the properties of carbon fibre powder epoxy laminates. As fibre straightness is one of the key differences between pultruded composites and VBO, this study provides a valuable insight into why pultrusion can result in superior properties to VBO manufacturing techniques. CF epoxy laminates were manufactured using a standard VBO process and a novel process which held the laminates under tension during a VBO process. Applying tension during infusion was also used by [26] in order to compare test results with pultruded samples. All laminates were well consolidated with few defects. Tensile test results showed that the addition of tension during the manufacturing process led to an increase in modulus and failure strength. The modulus for samples manufactured under tension approached the theoretical modulus based on the rule of mixtures and the strength was in line with the datasheet values (these results are very impressive, given that datasheet values usually represent autoclave laminates). The work also showed that the glass transition temperature, TG, of the composite material was in the range of 105ºC to 110ºC and that the fibre sizing influenced the strength of the laminates with the 50c fibre sizing giving the best results.

[30] compared the compressive and tensile strengths and modulus of two Uni-Directional (UD) carbon fibre types manufactured using powder epoxy. T700S UD 24k fibres were manufactured under tension using vacuum bag only. Zoltec PX 35 50k fibres with a polyester tricot stitching pattern were manufactured without tension using vacuum bag only. Both systems resulted in high quality laminates and optical microscopy showed full fibre tow impregnation in both the 50k and 24k fibre bungles. For both systems there was little difference in modulus but tension strength was over twice the compression strength for both fibre types with the T700 performing better overall. The T700 fibre is stronger than the PX 35, it did not contain stitching and it was manufactured under tension, so it was expected to have better results than the PX 35 fibres.

[31] investigated the joining powder epoxy GF using secondary gluing with traditional adhesives, secondary gluing using neat powder epoxy as an adhesive, co-curing and co-curing in combination with z pinning. Secondary gluing is bonding two fully cured composites and co-curing is bonding partially cured or uncured composites. The results of the lap shear testing are shown in Figure 4. The results show that the powder can be used as a high temperature adhesive, and that co-curing and co-curing in combination with z pinning results in excellent lap shear strength results.

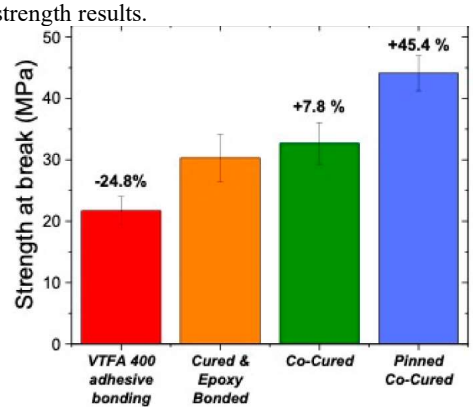

Figure 4 Lap shear results for powder epoxy joined using four separate methods [31].

[32] developed a machine for manufacturing tows which were impregnated with powder epoxy, manufactured laminates under tension and mechanically tested samples before and after hygrothermal aging. Powder epoxy coated tows were successfully manufactured and these tows were layed up to create high quality laminates. The mechanical testing resulted in excellent tensile properties but compression properties (presented for basalt fibres only) were below those of similar materials from literature.

[33] investigated the mechanical properties of powder epoxy GF and CF laminates including the mixed mode interlaminar fracture toughness. The tensile and compression properties, given in Table 1, indicated that these properties were comparable to standard epoxy composites. The mixed mode fracture toughness results were far superior to other epoxy composite systems and the authors stated that no epoxy (including toughened epoxy) could be found in the literature

which showed a higher fracture toughness than the powder epoxy system. The authors stated that the powder epoxy matrix is a very good material choice for composite structures, where delamination is a major risk.
[34] investigated the influence of hygrothermal aging on the flexural and toughness of UD GF epoxy laminates. The results showed that moisture uptake of circa 1% mass occurred. This resulted in a significant decrease in toughness, flexural strength, and glass transition temperature. [35] investigated the moisture uptake of GF powder epoxy, CF powder epoxy, GF ampreg epoxy and GF polyetheretherkeytone. The results showed that all powder epoxy laminates were well manufactured with no voids detectable via CT scanning, and that the moisture uptake of the powder epoxy material was in line with the conventional ampreg epoxy system.

4 DISCUSSIONS

The literature review, presented in Section 3, indicates that the powder epoxy material is comparable to traditional epoxy materials but that it has advantages in the areas of manufacturability and toughness. Several areas were identified that could further improve the powder epoxy system:

- Investigate the influence of reduced drying cycles on the material properties. The literature indicates that drying the material in a powder state instead of a sintered state would be more efficient. The current cure cycle, including drying, and impregnation is circa 22 hours, the actual time to cure for the resin, is in the order of 10 minutes. This suggests that there is room for improvement in the overall cure time. To investigate this several laminates will be manufactured with different drying cycles and the mechanical properties of the laminates will be measured and compared to the original cure.
- Investigate the influence of a free standing post cure on the material properties of the laminates. The literature indicates that the material reaches a degree of cure of 80% after 100 minutes at 150ºC. This indicates that the material could be cured past its gel point at 150ºC in its tooling. The part could then be removed from its tooling and post cured at 180ºC to fully cure. This would mean that tooling with a maximum temperature of 150ºC, rather than 180ºC could be used. This cure would also reduce thermal stress in the part. To investigate this several laminates will be cured to the gel point under vacuum. They will then be removed from the tooling and the vacuum and post cured at 180ºC. Finally the mechanical properties of the laminates will be measured.
- Investigate the influence of residual thermal stress on powder epoxy composites. To date no studies have been carried out on the influence of thermal stress on powder epoxy laminates. Thermal stress can result in reduced material properties, particularly in compression, hence it may be worthwhile investigating the influence of thermal stress on powder epoxy laminates. The influence of residual thermal stress can be difficult to isolate. One approach would be to manufacture laminates on metal tooling and also on composite tooling with a matched coefficient of thermal expansion. While this may be of academic interest it may not be relevant in a broader context as thermal stress is not known to be an issue in the manufacture of powder epoxy.
- Investigate the possibility of using powder epoxy in conjunction with pultrusion to increase material properties. The literature shows that the fibre straightness of CF powder epoxy results in improved material properties. Pultruding the powder epoxy to a part cured state and then co-curing the rods into the final shape could result in a composite structure with excellent material properties. This investigation would require a significant investment and is not feasible in the current study.

5 CONCLUSION

This paper has presented the results of a literature review on the powder epoxy material and areas for improving the technology have been discussed. Powder epoxy composites are currently being used in renewable energy applications. The work identified here could result in reduced cycle time and energy, reduced tooling cost, and improved material properties. This in turn would result in an overall reduction in cost for the end user.

AKNOWLEDGMENTS

This research was funded in part by Science Foundation Ireland (SFI) through the MaREI Research Centre for Energy, Climate and Marine (Grant no. 12/RC/2302_2).

REFERENCES

[1] M. H. Flanagan *et al.*, “Large Scale Structural Testing of Wind Turbine Blades Manufactured Using a One-Shot Out-Of-Autoclave Process,” *Proceedings of the Civil Engineering Research Ireland Conference, Galway, Ireland*, 2016.

[2] Eirecomposites, “Eirecomposites Blades Manufactured,” *https://www.eirecomposites.com/renewables/*, Apr. 2022.

[3] M. Damiano, A. Russo, A. Sellitto, E. Vecchio, T. Stellato, and A. Riccio, “Design of a composite wind turbine blade manufactured with the ONE SHOT BLADE® technology,” *Materials Today: Proceedings*, vol. 34, pp. 103–105, Jan. 2021, doi: 10.1016/J.MATPR.2020.01.366.

[4] T. Margraf, D. McCarville, J. C. Guzman, A. Dillon, and R. Tidwell, “Smart Tooling™ for fluted core composite cryotank and dry structure manufacture,” *CAMX 2015 - Composites and Advanced Materials Expo*, 2015.

[5] T. A. Misev and R. van der Linde, “Powder coatings technology: new developments at the turn of the century,” *Progress in Organic Coatings*, vol. 34, no. 1–4, pp. 160–168, 1998.

[6] Eirecomposites, “EC1921-003-01 Technical Datasheet Glass Fibre Powder Epoxy Composites.”

[7] J. M. Maguire, K. Nayak, and C. M. Ó. Brádaigh, “Novel epoxy powder for manufacturing thick-section composite parts under vacuum-bag-only conditions. Part II: Experimental validation and process investigations,” *Composites Part A: Applied Science and Manufacturing*, vol. 136, p. 105970, 2020.

[8] J. T. Hartness, T. L. Greene, and L. E. Taske, “Characterisation and Development of Materials for Advanced Textile Composites,” *Composite Technology Conference*, 1993.

[9] T. D. Bayha *et al.*, "Processing, properties and applications of composites using powder-coated epoxy towpreg technology," *Advanced Composite Technology Conference*, 1993.

[10] N. J. Johnston, R. J. Cano, J. M. Marchello, and D. A. Sandusky, "Powder-coated towpreg: Avenues to near net shape fabrication of high performance composites," *Proceedings of ICCM10*, pp. 407–415, 1995.

[11] J. T. Hartness and T. Greene, "An evaluation of composites fabricated from powder epoxy towpreg," *Conference on Advanced Engineering Fibers and Textile Structures for Composites*, 1992.

[12] J. G. Davis Jr and H. L. Bohon, "Third NASA Advanced Composites Technology Conference, volume 1, part 1," 1993.

[13] E. M. Fagan, M. Flanagan, S. B. Leen, T. Flanagan, A. Doyle, and J. Goggins, "Physical experimental static testing and structural design optimisation for a composite wind turbine blade," *Composite Structures*, vol. 164, 2017, doi: 10.1016/j.compstruct.2016.12.037.

[14] W. Finnegan, Y. Jiang, N. Dumergue, P. Davies, and J. Goggins, "Investigation and validation of numerical models for composite wind turbine blades," *Journal of Marine Science and Engineering*, vol. 9, no. 5, 2021, doi: 10.3390/jmse9050525.

[15] P. Meier *et al.*, "Static and Fatigue Testing of A Full Scale Helical River Turbine Foil," *Civil Engineering Research in Ireland 2020*, 2020.

[16] W. Finnegan, E. Fagan, T. Flanagan, A. Doyle, and J. Goggins, "Operational fatigue loading on tidal turbine blades using computational fluid dynamics," *Renewable Energy*, vol. 152, 2020, doi: 10.1016/j.renene.2019.12.154.

[17] C. Floreani *et al.*, "Testing of a 6m Hybrid Glass/Carbon Fibre Powder Epoxy Composite Wind Blade Demonstrator," *SAMPE Journal*, p. 6, 2021.

[18] E. J. Pappa *et al.*, "Fatigue life analysis of hybrid E-glass/carbon fibre powder epoxy materials for wind turbine blades," *ECCM 2018 - 18th European Conference on Composite Materials*, 2019.

[19] W. Finnegan *et al.*, "A novel solution for preventing leading edge erosion in wind turbine blades," *Journal of Structural Integrity and Maintenance*, vol. 6, no. 3, 2021, doi: 10.1080/24705314.2021.1906091.

[20] W. Finnegan, T. Flanagan, and J. Goggins, "Development of a Novel Solution for Leading Edge Erosion on Offshore Wind Turbine Blades," in *Lecture Notes in Mechanical Engineering*, 2020, pp. 517–528. doi: 10.1007/978-981-13-8331-1_38.

[21] W. Finnegan, P. D. Keeryadath, R. Coistealbha, T. Flanagan, M. Flanagan, and J. Goggins, "Development of a numerical model of a novel leading edge protection component for wind turbine blades," *Wind Energy Science*, vol. 5, no. 4, 2020, doi: 10.5194/wes-5-1567-2020.

[22] E. Hassan *et al.*, "Erosion mapping of through-thickness toughened powder epoxy gradient glass-fiber-reinforced polymer (GFRP) plates for tidal turbine blades," *Lubricants*, vol. 9, no. 3, p. 22, 2021.

[23] J. M. Maguire, K. Nayak, and C. M. Ó. Brádaigh, "Characterisation of epoxy powders for processing thick-section composite structures," *Materials & Design*, vol. 139, pp. 112–121, 2018.

[24] J. Maguire, A. Roy, D. Doyle, M. Logan, and Conchur O Bradaigh, "Resin Characterisation for Numerical Modelling of Through-Thickness Resin Flow During OOA Processing of Thick Section Wind or Tidal Turbine Blades," *International Conference on Composite Materials*, 2015.

[25] J. M. Maguire, P. Simacek, S. G. Advani, and C. M. Ó. Brádaigh, "Novel epoxy powder for manufacturing thick-section composite parts under vacuum-bag-only conditions. Part I: Through-thickness process modelling," *Composites Part A: Applied Science and Manufacturing*, vol. 136, p. 105969, 2020.

[26] B. L. Ennis *et al.*, "Optimized Carbon Fiber Composites in Wind Turbine Blade Design.," *Sandia Report SAND2019 14179*, 2019.

[27] Zoltec, "Technical Datasheet Zoltec PX35 pultruded profiles."

[28] D. Mamalis, T. Flanagan, and C. M. Ó. Brádaigh, "Effect of fibre straightness and sizing in carbon fibre reinforced powder epoxy composites," *Composites Part A: Applied Science and Manufacturing*, vol. 110, pp. 93–105, 2018.

[29] D. Mamalis *et al.*, "Novel carbon-fibre powder-epoxy composites: Interface phenomena and interlaminar fracture behaviour," *Composites Part B: Engineering*, vol. 174, p. 107012, 2019.

[30] J. J. Murray *et al.*, "Characterisation of carbon fibre reinforced powder epoxy composites for wind energy blades," *ECCM 2018 - 18th European Conference on Composite Materials*, 2020.

[31] T. Noble *et al.*, "Powder Epoxy for One-Shot Cure, Out-of-Autoclave Applications: Lap Shear Strength and Z-Pinning Study," *Journal of Composites Science*, vol. 5, no. 9, p. 225, 2021.

[32] C. Robert, T. Pecur, J. M. Maguire, A. D. Lafferty, E. D. McCarthy, and C. M. Ó. Brádaigh, "A novel powder-epoxy towpregging line for wind and tidal turbine blades," *Composites Part B: Engineering*, vol. 203, p. 108443, 2020.

[33] C. Floreani, C. Robert, P. Alam, P. Davies, and C. M. Ó Brádaigh, "Mixed-Mode Interlaminar Fracture Toughness of Glass and Carbon Fibre Powder Epoxy Composites—For Design of Wind and Tidal Turbine Blades," *Materials*, vol. 14, no. 9, p. 2103, 2021.

[34] D. Mamalis, C. Floreani, and C. M. Ó Brádaigh, "Influence of hygrothermal ageing on the mechanical properties of unidirectional carbon fibre reinforced powder epoxy composites," *Composites Part B: Engineering*, vol. 225, p. 109281, 2021, doi: https://doi.org/10.1016/j.compositesb.2021.109281.

[35] D. M. Grogan *et al.*, "Influence of microstructural defects and hydrostatic pressure on water absorption in composite materials for tidal energy," *Journal of Composite Materials*, vol. 52, no. 21, pp. 2899–2917, 2018.

Robustness of Square Hollow Column Sections in Open-sided Corner-supported Modular Steel Buildings

Si Hwa Heng[1,2], Daniel McCrum[1], David Hyland[2], Michael Hough[2]
[1]School of Civil Engineering, University College Dublin, Belfield, Dublin 4, Ireland
[2]MJH Structural Engineers, 3, Anglesea House, 63 Carysfort Ave, Blackrock, Co. Dublin, Ireland
Email: heng.si-hwa@ucdconnect.ie, daniel.mccrum@ucd.ie, david.hyland@mjhse.com, michael.hough@mjhse.com

ABSTRACT: This paper investigates the performance of the commonly used and computationally efficient one-dimensional finite element line elements in capturing the nonlinear buckling response of a hot-finished steel column with global geometric imperfection as well as the bending and axial load response of a welded tubular T-joint connection. Frequently, the robustness assessments of corner-supported modular steel buildings (MSBs) have been based on perfectly straight columns which do not represent the actual profile of the columns due to imperfections in the steel fabrication process. Also, the assumption of fully rigid beam-to-column connections in numerical models with welded tubular joints may not be appropriate due to the flexibility of hollow sections' wall which is susceptible to local deformation. In the analysis in this paper, a column with the global geometric imperfection of $L_{eff}/1000$ modelled using line elements was found to perform similarly to experimental results in terms of capturing global buckling response. For the welded T-joint, a 3D solid element model was investigated to capture the failure behaviours. The assignment of the joint behaviours, obtained from the results of a 3D solid element model, in the spring element connecting the beam and column (line element) reproduces a joint response similar to that in the 3D solid model. The practical application of this study is that a high-fidelity phenomenological model of corner-supported MSBs can be produced for use in the robustness analysis of an entire MSB.

KEY WORDS: Robustness, Modular Steel Buildings, Corner-supported, Simplified Line Element Model, Hollow Sections

1 INTRODUCTION

To keep up with the ever-rising housing demand in major cities around the world, modular construction is becoming a key player in meeting supply targets with the benefits of not only its speed of construction but also the solution to several highly concerning issues today. To name a few, modular construction reduces the overall carbon footprint of a building with less wastage, reduces the number of site-related accidents by limiting on-site personnel and offers better quality products with a stringent factory setting [1]. Despite the significant benefits the modular industry offers, the uptake of modular construction practice is still far behind its traditional counterpart. One of the reasons is the lack of proper understanding of this relatively new construction technique (in both normal and extreme loading scenarios) and the lack of modular-specific design guidelines [1], [2]. Considering the deficiency in modular building-related structural design knowledge, especially its performance under progressive collapse loading conditions, the industry has been slow to publish its knowledge. However, this is starting to change. Alembagheri et al., [3] investigated the role of inter-module connections in corner-supported MSBs in redistributing gravitational load under multiple module loss scenarios. In order to focus specifically on the inter-module connections, Alembagheri et al. [3] have modelled the modular unit (or module) as a solid block (i.e. macro model) and subsequently analysed the notional removal of a combination of these blocks. Although the results have demonstrated that inter-module connections are capable of resisting progressive collapse with the removal of two modules simultaneously, the ability of the structural elements within the modules to fail before the inter-module connections has not been accounted for. A study by Luo et al., [4] highlighted the importance of modelling the structural elements within a module as column buckling was identified numerically as the primary cause the structure lost its stability and collapsed progressively. Chua et al., [5] investigated the robustness of a high-rise 40-storey corner-supported MSB stabilised laterally by a central concrete core. Despite progressive collapse not occurring after the removal of a corner column in the numerical model, the assumption of rigid beam-to-column connections within the modules could have underestimated the actual vertical displacement and second-order effects. Recently, Chua et al., [6] studied the progressive collapse behaviour of a laterally braced MSB under various column removal scenarios and found that a dynamic amplification factor of two overestimated the inertia effect in nonlinear static analysis and caused the column to buckle. The observation could again be in part due to the use of fully-rigid beam-to-column connections which attracts a greater bending moment than actually would exist in the column. It should be noted that the assumption of rigid beam-to-column connections would be more appropriate for moment connections between I or H sections in traditional hot-finished steel framed buildings but not necessarily for that in corner-supported MSBs. This is because corner-supported MSBs often use hot-finished steel hollow sections in the shape of rectangles or squares as columns with the floor beam welded to the face of the hollow section columns [1] as shown in Figure 1. Therefore, local deformation at the face of the hollow section columns essentially causes a welded joint to behave more like a semi-rigid joint than a full-rigid. In light of the aforementioned, this paper aims to produce a high-fidelity phenomenological finite

element model for use in the robustness/progressive collapse analysis of open-sided corner-supported MSBs made of hot-finished steel hollow sections. To achieve this, a geometric and material nonlinear analysis with imperfection was conducted to assess the accuracy of 1D line elements (also known as beam elements) in capturing the nonlinear buckling response of a geometrically imperfect column. In addition, the response of a welded tubular T-joint under bending and axial load (considered separately) was investigated in a detailed 3D solid model. The 3D model is validated against published (not by these authors) experimental results and then used as a comparison for the 1D line element model. Later, the identified joint response was assigned in the connector/spring element of the equivalent 1D line element model of the welded tubular T-joint to assess the performance of the simplified model.

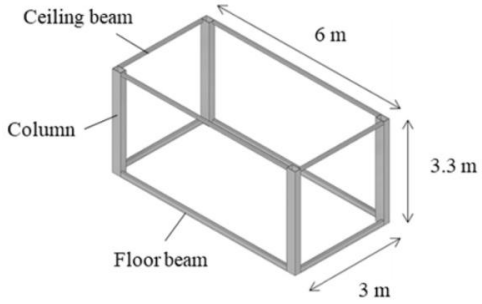

Figure 1. Typical open-sided corner-supported module frame [6].

2 NUMERICAL SIMULATIONS

2.1 Model descriptions

2.1.1 Column

A geometric and material nonlinear analysis with imperfection was performed to study the nonlinear buckling behaviour of a 120x120x6.3mm hot-finished square hollow section (HFSHS) in S770 steel using ABAQUS [7]. To account for global geometric imperfection and ensure global buckling can occur in the static nonlinear buckling analysis, the column was superimposed with the profile of a half-sine wave with the amplitude of $L_{eff}/1000$ in the beginning of the analysis, where L_{eff} is the effective length of the column depending on its boundary conditions. In this analysis, L_{eff} was the distance between the two supports due to pin-ended boundary conditions with an effective length factor of 1. Based on Meng & Gardner [8] experiment, the distance between the supports was 2550mm, calculated as the height of the column (i.e. 2400mm) plus two 75mm supports offset at both ends of the column which gives an imperfection of 2.55mm at the mid-height of the column. For the experimental set-up, mechanical and geometric properties of the column, please refer to [8]. The adopted imperfection of $L_{eff}/1000$ was assumed to include only the global imperfections due to the initial out-of-straightness of the column. Eccentricity in axial load due to misalignment during module positioning was not included in the model. Although the adopted imperfection was used in the formulation of the European buckling curves following extensive experiments conducted by [9] and deemed sufficient to also include the eccentricity due to misalignment in conventional steel buildings construction, this appeared to be inadequate for modular construction as the misalignment due to inaccuracy in module positioning could be higher. This is because the inaccuracy associated with module positioning is highly dependent on the type of vertical inter-module connecting system employed, which can be different across different modular building providers. Therefore, this led to difficulty in quantifying and specifying an exact tolerance due to the lack of consistent connection and practice as in traditional steel building constructions.

To model the initial global bow imperfection in the column, ABAQUS Eigenvalue Buckling Analysis was first conducted to identify the critical buckling mode (fundamental mode shape) that has the least buckling load. The fundamental mode shape obtained, in the shape of a half-sine wave, has a peak displacement of 1mm at the mid-height and zero at both ends of the column. The fundamental mode shape was then factored by 2.55 ($L_{eff}/1000$) to achieve a 2.55mm amplitude half-sine-like curve and served as the initial global bow imperfection profile for the nonlinear column buckling analysis. The same steps were used to pre-process the imperfect shape of the column in the line element model.

2.1.2 Beam-to-column connection

A welded T-joint made of 2 HFSHSs was investigated numerically to study the bending and axial load (considered separately) responses of the commonly used welded T-joint in corner-supported MSBs [6], [10]. The column and beam sections considered in the analysis were 150x150x8mm HFSHS and 100x100x8mm HFSHS, respectively. The perimeter of the beam was welded centrally to the face of the column at mid-height to form a T-joint using an 8.48mm fillet weld (FW) (i.e. 6mm throat). The contacts between the FW and sections were modelled using ABAQUS tie constraint. Both sections were 700mm long and have a steel grade of S420. Two analyses were conducted to study the: 1) moment-rotation (M-θ) relationship and 2) axial load-displacement (P-δ) relationship of the welded tubular T-joint.

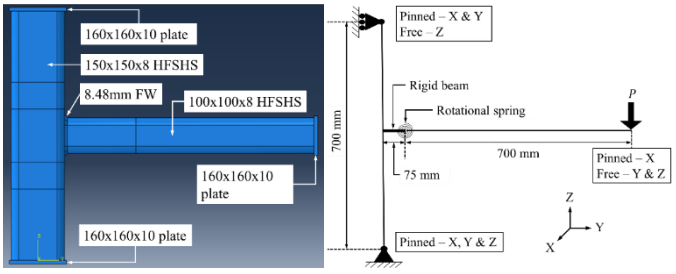

Figure 2. Welded tubular T-joint in; (a) 3D solid model and; (b) 1D line element model.

For other details regarding the experimental set-up, mechanical and geometric properties of the T-joint please refer to [11]. Figure 2(a) shows the configuration of the solid model in ABAQUS while Figure 2(b) illustrates the line element model. As can be seen in Figure 2(b), the load was applied at the free end of the beam. A rigid beam was modelled to account for the eccentricity between the welded joint and the centre of the column in the line model. The analysis was conducted using a

dynamic implicit solver for the solid model and a static general solver for the line model.

2.1.3 Modelling programme

The column was first modelled using ABAQUS 2D shell element S4R (4-noded shell element with linear shape function, reduced integration and hourglass control) for validation purposes and later compared with the results of the same column modelled using 1D line element B23 (2-noded line element with cubic shape function). Shell element was chosen to ensure local buckling is captured in the section, if any. For the welded T-joint, the analysis was first performed using ABAQUS 3D solid element (C3D8R) to failure (Figure 2(a)) and followed by 1D line element (B22) to investigate the reliability of the simplified line element model (Figure 2(b)). C3D8R is a 3D solid 8-noded element with linear shape function, reduced integration and hourglass control function. Solid element was chosen rather than shell element to model the weld with full contact area. B22 is a 3-noded line element with a quadratic shape function which is suitable for short sections where shear deformation is dominant.

2.2 Solid/shell element numerical model validation

2.2.1 Column

Nonlinear buckling analysis of 120x120x6.3mm HFSHS was conducted using ABAQUS. Displacement-controlled approach was adopted in the analysis for better convergence in highly unstable and nonlinear buckling analysis. A series of mesh refinement analyses have been performed to identify an economical yet accurate density of mesh for the column and was summarised in Table 1. To ensure buckling response can be captured accurately, the column was evenly partitioned into 3 equal segments with the middle one-third segment having double the mesh elements compared to the remaining ends. For the corners of the section, a fixed number of 6 elements was considered as shown in Figure 3.

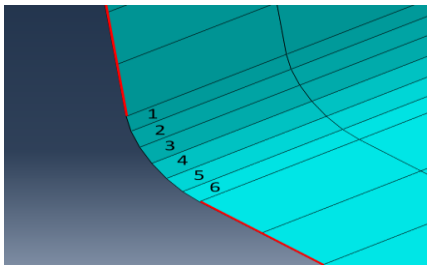

Figure 3. Six mesh elements around the corner of HFSHS.

Table 1. Global buckling load for column of different meshes.

	Mesh Size			
	Centre 1/3 (mm)	Remaining ends (mm)	Buckling load (kN)	Difference to [8]
Meng & Gardner [8]	8	16	1549	N/A
Mesh 1	32	64	1565	1.0%
Mesh 2	24	48	1575	1.7%
Mesh 3	16	32	1581	2.1%
Mesh 4	8	16	1582	2.1%

The results, in Table 1 indicate that all the meshes of different densities performed similarly and have a peak buckling load within a maximum of 2.1% difference from that identified in the test results [8].

To better observe for any discrepancies, the mesh refinement analysis results were plotted against the experimental results from [8] and summarised in Figure 4(a). From the graph, a consistent primary mode of failure (i.e. global buckling) was observed between the experiment and numerical analyses. However, a slight discrepancy was observed in the lateral displacement at which the local buckling occurred between the analysis and experiment. In the analyses, local buckling occurred later than that in the experiment as local geometric imperfection was not considered in the numerical model. As shown in Figure 4(b), for sections with slender cross-sections, the mesh density becomes important to capture local buckling accurately. The section investigated herein has a local buckling slenderness ratio, c/t of 29ε which is Class 1 under section classification as per [12] and therefore, only buckled locally after substantial plastic rotation. Other than that, the numerically simulated nonlinear buckling response of the column was in good agreement with the experimental results.

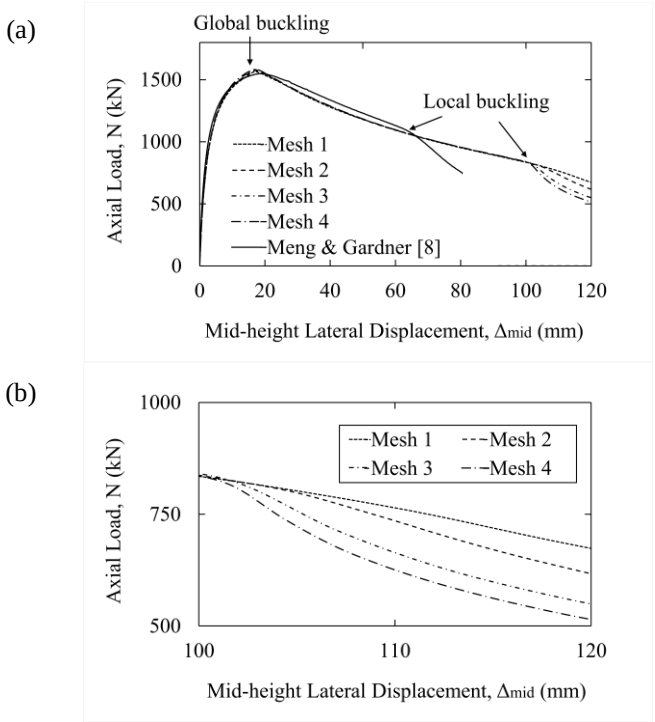

Figure 4. (a) Nonlinear buckling response of shell element column and; (b) close-up view of different meshes at local buckling loading level.

2.2.2 Beam-to-column connection

The M-θ relationship of the T-joint (both solid and line element models) was analysed by loading at the cantilever end of the 100x100x8mm HFSHS using displacement-controlled analysis. The material properties of the steel were identified in the coupon test provided by Havula et al., [11]. Figure 5 shows the M-θ relationship obtained in the numerical analysis and plotted against the actual experiment conducted by [11]. Figure 5 shows accurate model results, with some minor difference when the joint rotation reaches approximately 0.2 rad rotation

where the stiffness in the analysis model starts to reduce due to the initiation of material failure in the tension zone. The experiment attained a peak moment of 34.6 kNm while that observed in the numerical analysis was 5.8 % lower at 32.6 kNm. The observed failure was shear tearing at the face of the column in the extreme tension zone and quickly propagated through the cross-section of the joint as the rotation increased further. Similar failure was observed in the experiment by [11]. The overall response of the welded T-joint was in close agreement with that from the experiment up to the peak. To identify an approximate yield point of the joint, two lines tangential to the elastic and hardening portion of the M-θ curve were drawn, as shown in Figure 5. The point where the two tangential lines cross signifies the yield point of the T-joint. This method was suggested by [13] to approximate the yield characteristics in joints without distinct yield points (i.e. joints exhibit ductile yielding). The approximated rotation at which yielding occurs was then used in the line element model to simulate the onset of the plastic phase and the results will be discussed in the next section.

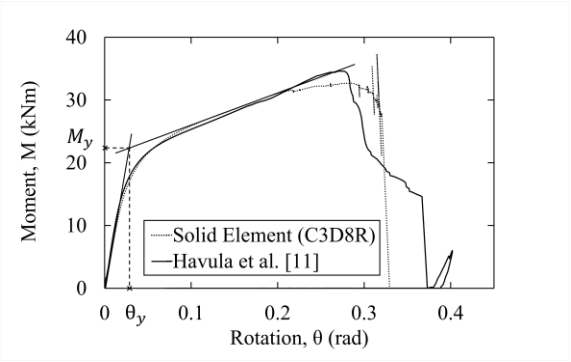

Figure 5. M-θ relationship of T-joint in solid element model and experimental results.

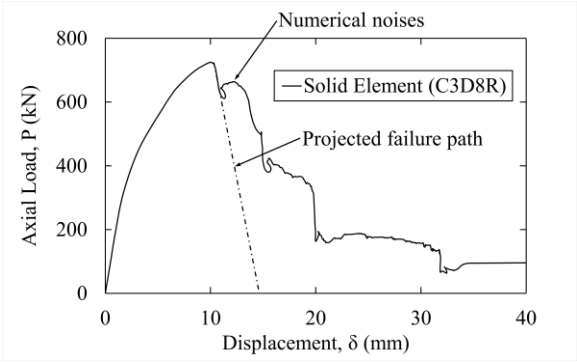

Figure 6. P-δ relationship of T-joint in solid element model.

The next part assessed the response of the T-joint under axial load by using the validated solid model and loaded the beam axially to failure. The axial load in the beam would replicate catenary action in a progressive collapse loading scenario and is an important behaviour to capture. Figure 6 shows the axial load-displacement (P-δ) plot obtained in the analysis. Axial load was calculated by summing the reaction forces at both ends of the column that were pinned in place while displacement was measured from the local deformation of the column face under axial loading. The peak load attained before failure was 724.9 kN at approximately 10mm displacement. After that, rapid degradation in the material strength was observed with the drop in axial load as displacement increased. As more mesh elements started to fail, the analysis suffered convergence issues in the post-peak response, which is a general trend in the results. Despite significant numerical convergence issues as the displacement increased, a conservative failure path can be estimated by projecting a line, tangent to the softening branch short after attaining the peak load, to intersect the displacement axis.

2.3 Simplified numerical model validation

2.3.1 Column

For comparison purposes, the same column (120x120x6.3mm HFSHS in S770) used for validation was modelled using ABAQUS line elements (B23) with the same magnitude of geometric imperfection (2.55mm) located at the mid-height of the column as shown in Figure 7. The pre-processing procedure to obtain an initially imperfect column is similar to that mentioned in Section 2.1.1. The column was discretised into a different number of elements namely, 2, 4, 6, and 8 elements to identify the appropriate number of elements required to capture the global buckling behaviour. Meshes with an even number of elements were considered to ensure imperfection is the highest at the mid-height of the column and consistent across the column of different meshes. Since the number of elements discretising the column is rather low, the initial profile of the imperfect column ranges from a triangular shape, for the column discretised with 2 elements, to a smoother half-sine curve as the number of elements increases. Figure 7 shows the initial profile of the column discretised with a different number of elements.

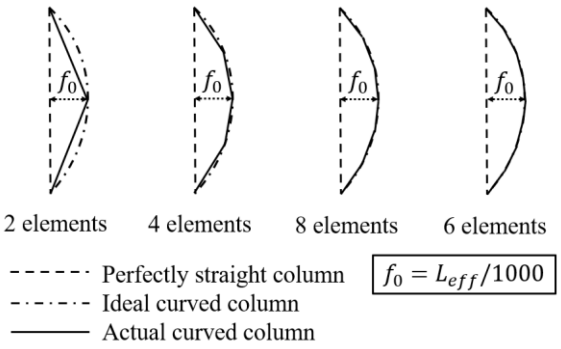

Figure 7. Column discretised with a different number of elements.

Table 2 summarised the peak global buckling load attained by the column with different meshes and the percentage difference compared to that from the experiment by [8]. It can be seen that all the meshes have a peak buckling load higher than [8] with the largest difference being 6.8%. Part of the reason for observing a higher buckling load in the numerical analyses was that ABAQUS does not allow the corner radius of the column to be explicitly defined. Therefore, the column in the line model has a 90° corner which caused the column to be slightly stiffer than the actual. The second reason was the local geometric imperfection in the column was not considered in the line model.

Figure 8(a) shows the load-displacement curve of the column with different meshes versus that from [8]. The buckling loads of the column with Mesh 2 to 4 were almost identical while that for Mesh 1 was slightly lower and smoother over the peak. This was due to the bending stress being concentrated at the only available mid-height node which resulted in a more thorough penetration of yield stress across the cross-section of the column. Therefore, the global buckling load in Mesh 1 was governed by yielding and plastic rotation at the mid-height node which resulted in a rounder peak compared to the other meshes. Whereas for the column with Mesh 2 to 4, stability seems to have governed the failure as the global buckling occurred abruptly after attaining the peak buckling load. However, all meshes showed no sign of local buckling after substantial plastic hinge rotation due to the intrinsic limitation of line element formulation. Hence, for columns that are susceptible to local buckling, the material yield strength and Young's modulus (E) could be reduced to ensure the column can buckle prematurely to indirectly capture local buckling. Also, the fact that ABAQUS does not allow the corner profile of the section to be explicitly defined in line element has resulted in a stiffer section (due to the slight difference between the actual and modelled geometry) with a higher buckling load compared to that obtained from the experiment. Figure 8(b) shows the nonlinear buckling response of the column with its Young's modulus proportionally reduced based on the difference in the second moment of area between the actual section and that defined in ABAQUS. After the reduction, the buckling load in Mesh 1 became 1535 kN (i.e. a reduction of 62 kN from the original 1597 kN) which is approximately 1% less than the experimental buckling load. Apart from that, the column modelled with line elements using as few as two elements across its full height was observed to be sufficient to produce results close to the actual behaviour of global buckling.

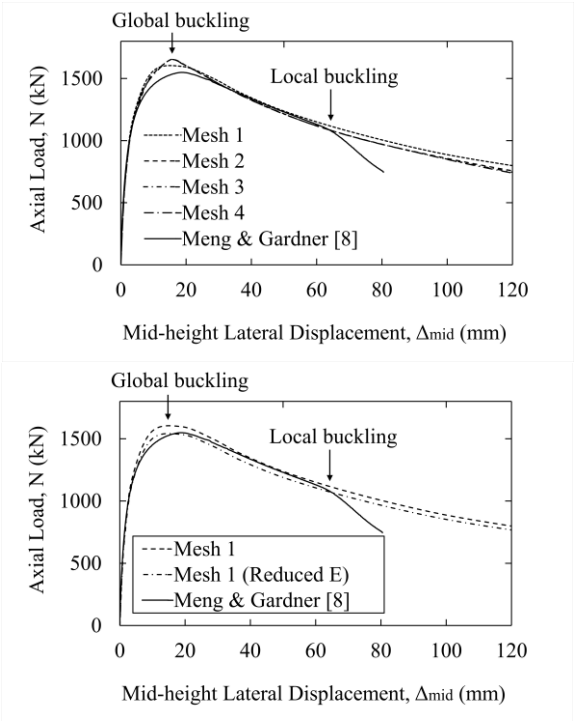

Figure 8. Nonlinear buckling response of line element column (a) with different meshes and (b) with a reduced E.

Table 2. Mesh refinement analysis for line elements column.

Analysis	No. of Elements	Peak Load (kN)	Difference Compared to [8]
Meng & Gardner [8]	-	1549	N/A
Mesh 1	2	1597	3.1%
Mesh 2	4	1649	6.5%
Mesh 3	6	1655	6.8%
Mesh 4	8	1652	6.7%

2.3.2 Beam-to-column connection

The same configuration of T-joint was modelled using ABAQUS 1D line element (B22) to assess its ability in capturing the response to local bending and axial load (considered separately). A schematic of the line element model was shown in Figure 2(b). In the line model, the rotational stiffness of the welded T joint was modelled using ABAQUS connector element with the M-θ relationship and approximated yield point obtained in Section 2.2.2 assigned. Damage characteristics of the joint were also included to allow the connector element to fail after significant rotation. The damage criteria and material properties were based on the steel coupon test performed by [11]. When assigning the stiffness to the connector element, only the rotational stiffness to resist the applied load was assigned while the stiffnesses in the other directions were all assumed to be fully rigid. In Figure 9, the M-θ relationship obtained in the analysis was plotted against that from the solid model and [11] for comparison. As shown in Figure 9, a close agreement was observed at the transition phase between the elastic and hardening phase, in the line model, using the approximated yield point suggested by [13]. At approximately 0.3 rad of rotation, a linear softening of the joint was observed due to the evolution of damage in the connector element. The rotation at which the joint failed completely was assigned so that the area under the M-θ curve (which corresponds to total work done) for line and solid element were approximately the same. As a result, the slope of the softening branch in the line model is slightly gentler compared to that in the solid model.

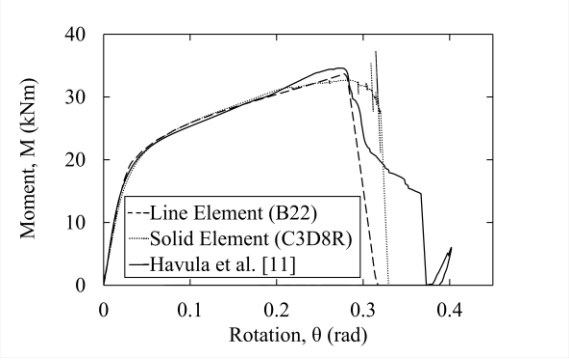

Figure 9. M-θ curves from [11], solid and line element model.

A final analysis was conducted to examine the ability of the line element model in capturing the response of the T-joint under axial load in the beam. Instead of having rotational stiffness in the connector element as before, the P-δ relationship identified

in the solid model was assigned to the connector element. The beam was then loaded axially to failure in the same manner as in the solid model. The P-δ curve of the line element model was plotted against that for the solid model and shown in Figure 10. In the figure, it can be seen that the line model performed similarly to the solid model and has a peak load of 724.8 kN, which is 0.01% below that of the solid model. Due to the accumulation of numerical convergence error in the highly unstable softening branch, the failure path in the solid model diverged from its initial path. This was resolved in the line model by choosing a slope for the softening branch of the P-δ curve so that it is parallel to the initial downtrend observed in the solid model. Overall, a close agreement was observed in the P-δ curve between the solid and line element model up to the peak.

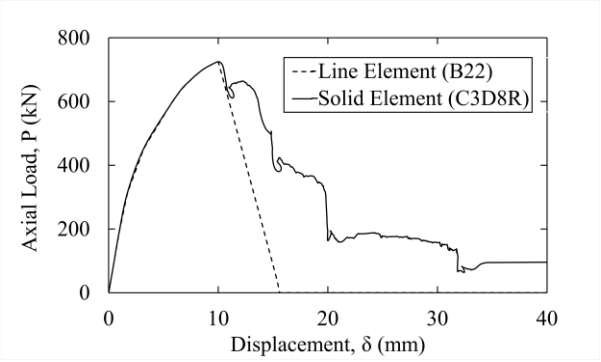

Figure 10. P-δ curves from solid and line element model.

3 CONCLUSIONS

This study has produced a high-fidelity phenomenological numerical model for use in the robustness/progressive collapse analysis of open-sided corner-supported MSBs made of hot-finished hollow steel sections. In particular, the global buckling response of the square hollow section columns and moment-rotation behaviour of a T-joint beam-to-column connection typically used in open-sided corner-supported MSBs were modelled and compared to experimental results. The first modelling approach was a 3D solid finite element modelling, as this would explicitly model all geometries and potentially capture local buckling behaviour. However, due to the large number of structural elements in a typical MSB, it would be impractical and time-consuming to analyse an entire MSB with this approach. Therefore, a second modelling approach was proposed to generate a simple yet accurate model that closely represents the structural behaviour of an open-sided corner-supported MSB. Below is a summary of the key findings of the numerical analyses conducted in this paper.

- The global buckling response of columns with Class 1 cross-section classification as per EN 1993-1-1 and global geometric imperfection in the shape of a half-sine wave with an amplitude of $L_{eff}/1000$ can be captured with sufficient accuracy using as little as two line elements across its full height.
- For columns with limited plastic rotation capacity or prone to local buckling before reaching the yield point (i.e. Class 2 to 4 cross-sections), modification to the stress-strain curve may be required to allow the column to buckle prematurely by reducing the stiffness and yield strength of the section.
- Welded tubular T-joints modelled using line elements and connected using connector/spring elements accurately captured the moment-rotation and axial load-displacement response provided the corresponding response identified in a solid element model (micro-model) is assigned to the connector/spring element.

ACKNOWLEDGMENTS

The first author gratefully acknowledges the financial support provided by Irish Research Council under the Employment-based PhD programme (IRC-EBP) [Grant No: EBPPG/2021/24] and the technical support provided by colleagues in MJH Structural Engineers.

REFERENCES

[1] M. Lawson, R. Ogden, and C. Goodier, *Design in Modular Construction*. Boca Raton: CRC Press, 2014.

[2] W. Ferdous, Y. Bai, T. D. Ngo, A. Manalo, and P. Mendis, "New advancements, challenges and opportunities of multi-storey modular buildings – A state-of-the-art review," *Eng Struct*, vol. 183, pp. 883–893, 2019.

[3] M. Alembagheri, P. Sharafi, R. Hajirezaei, and B. Samali, "Collapse capacity of modular steel buildings subject to module loss scenarios: The role of inter-module connections," *Eng Struct*, vol. 210, p. 110373, 2020.

[4] F. J. Luo, Y. Bai, J. Hou, and Y. Huang, "Progressive collapse analysis and structural robustness of steel-framed modular buildings," *Eng Fail Anal*, vol. 104, pp. 643–656, 2019.

[5] Y. S. Chua, J. Y. R. Liew, and S. D. Pang, "Robustness of Prefabricated Prefinished Volumetric Construction (PPVC) High-rise Building," *Proc 12th Int Conf Adv Steel-concrete Compos Struct - Asccs 2018*, 2017.

[6] Y. S. Chua, S. D. Pang, J. Y. R. Liew, and Z. Dai, "Robustness of inter-module connections and steel modular buildings under column loss scenarios," *J Build Eng*, vol. 47, p. 103888, 2022.

[7] M. Smith, *ABAQUS/Standard User's Manual, Version 6.9*. Providence, RI: Dassault Systèmes Simulia Corp, 2009.

[8] X. Meng and L. Gardner, "Behavior and Design of Normal- and High-Strength Steel SHS and RHS Columns," *J Struct Eng*, vol. 146, no. 11, p. 04020227, 2020.

[9] ECCS, "Manual on Stability of Steel Structures," European Convention for Constructional Steelwork (ECCS), 1976.

[10] X.-H.-C. He, T.-M. Chan, and K.-F. Chung, "Effect of inter-module connections on progressive collapse behaviour of MiC structures," *J Constr Steel Res*, vol. 185, p. 106823, 2021.

[11] J. Havula, M. Garifullin, M. Heinisuo, K. Mela, and S. Pajunen, "Moment-rotation behavior of welded tubular high strength steel T joint," *Eng Struct*, vol. 172, pp. 523–537, 2018.

[12] BSI, "BS EN 1993-1-1:2005 Eurocode 3: Design of steel structures - Part 1-1: General rules and rules for buildings," British Standards Institution, 2005.

[13] D. Grotmann and G. Sedlacek, "Rotational stiffness of welded RHS beam-to-column joints. Final Report No. 5BB–8/98," RWTH-Aachen: Institute of Steel Construction, Aachen, 1998.

The Effectiveness of Non-Destructive Testing for Decision Making in Structural Assessments – A Case Study using Impulse Response Method

Shahnur Alam Sourav[1], Thomas Callanan[1], Desmond McNair[1]
[1]Infrastruct Asset Management Limited, Cloncannon Lower, Mountmellick, Co. Laois, Ireland
email: shahnur@infrastruct.ie, tom@infrastruct.ie, des@infrastruct.ie.

ABSTRACT: Infrastructures around the world are aging. To ensure continued safe use of the aging infrastructures, there is an on-going need to actively manage the structural condition, undertake repairs, and/or strengthening. As part of these processes, Engineers are required to carry-out inspections, structural testing and investigations, and structural assessments. The use of Non-Destructive Techniques (NDTs) along with minimal destructive testing can enable efficient evaluation of the structural condition, and target deteriorated areas for repairs, rehabilitation, and strengthening. There are many types of NDT systems available within the Civil Engineering industry, from simple devices to highly advanced systems. The selection of the right system leads to a better match between the information needed by the Engineers for their assessments and the information collected on-site. The collection of appropriate data when testing leads to more effective decision-making in structural assessments. This paper presents a brief overview of certain NDTs. A case study is presented where the impulse response method was successfully used in assessing multiple composite slabs in a larger floor. Based on the comparative analysis of the NDT results, a limited number of slabs (poorest performing slabs in terms of certain NDT parameters) were further evaluated by static load testing. The case study shows that the use of a NDT technique led to a cost-effective evaluation of the in-situ slabs. This paper thus provides an example of the use of NDT methods for better decision-making in structural assessments for the practicing engineers and relevant personnel.

KEY WORDS: Existing building, structural assessment, cost-effective evaluation, non-destructive testing, impulse response method.

1 INTRODUCTION

Civil engineering infrastructures around the world are aging. To ensure continued safe use, there is an on-going need to actively manage these old infrastructures. Moreover, with high environmental and economic impact of new construction, the choice to reuse and extend the life service has become more desirable and efficient. In fact, more than half of the all construction activities in recent years relate to the existing buildings, bridges, and other civil engineering works [1]. Assessment of structural condition is important before carrying out any repair or maintenance work. If the defects or damage in a structure can be identified properly, an efficient repair strategy can be applied and hence, the cost of repair will be reduced. Non-destructive testing (NDT) can greatly help assessing the performance of the structures or identifying the damage within the structures [2]. NDTs are usually non-invasive indirect techniques that provide information on the physical or other mechanical properties of the structural elements. During NDT assessment, the condition of the concrete is inferred from the measured response to some stimulus, such as impact or electromagnetic radiation. The use of NDT helps reduce the extent of destructive or invasive investigation of the structure. Once the reliability of the NDT method is established, the assessment of the structure can be done economically [3].

NDT technologies are improving and with the advancement of technological aspects and quick data processing capability allows for investigating larger areas of a structure at a faster rate. There are several NDT methods available for investigation different types of defects or damage within the structures. A comprehensive review of the NDT methods with their principles and field of applications is documented in the literature [2,4,5].

NDT methods can offer the advantages by providing information related to the in-situ properties of hardened concrete, such as, elastic properties, density, resistivity, moisture content, penetrability characteristics, etc. Also, NDTs offer information regarding the in-situ quality of concrete i.e., delamination, presence of voiding, honeycombing. Location and size of reinforcement, corrosion activity of reinforcement can also be estimated using NDTs.

Selection of NDTs to be used for structural investigation is a choice by the Engineers. Proper choice of NDT will lead to a better match between the information needed and the information collected on-site. The appropriate selection of NDT, thus, will lead to more effective decision-making in structural assessments.

This paper presents such a practical application of NDTs where the performance of an existing structure was evaluated in a cost-effective way. The paper also provides a brief overview of commonly used NDT systems and their applications. The paper focuses on the application of Impulse Response (IR) test in a comparative evaluation of the structural performance of multiple slabs in an existing floor structure. The IR test was used as a fast-screening method where the anomalous areas of the floor were differentiated from relatively sound areas. The selected areas of the floor based on the IR test were further investigated to finally assess the overall capacity of the slabs. Since the invention, the IR test has been reported

to be applied for locating voids, delamination, honeycombing, and/or poor supporting condition in concrete structures as well as for pile integrity assessment.

2 BRIEF OF OVERVIEW OF NDT METHODS

Different types of NDTs are used for different purposes during the condition evaluation of existing structures. Many of the methods are completely non-destructive, while certain methods require localised intrusion on the surface. NDTs can be grouped into few different categories depending on the purpose of use on-site. A brief overview on the possible applications of several methods is provided here.

2.1 NDTs for mechanical properties of concrete

For the assessment of in-situ compressive strength of concrete, NDTs such as rebound hammer, Ultrasonic Pulse Velocity (UPV) and Cut And Pull Out (CAPO), penetration resistance test are frequently used both in industry and research. Combination of two or more NDTs, especially rebound hammer and UPV (i.e., SonReb) are popular. ACI 228.1R [6], RILEM TC249-ISC [7] and EN 13791 [8] provide detailed guidelines on the use of the NDTs, interpretation of results in evaluating the in-situ compressive strength of concrete.

2.2 NDTs for relative quality assessment of concrete

NDTs used for assessing mechanical properties of concrete can provide useful information in evaluating variation in the apparent properties of concrete within the structure. Ultrasonic pulse echo is cable of locating delamination and voids in relatively thin elements [9,10]. Sounding technique is an efficient tool to locate delaminated areas. Infrared thermography is a newly adopted technology in the industry in evaluating delamination, cracked areas in concrete [11].

Impact echo can help locating defects within the concrete elements such as delamination, voids, honeycombing or measure element thickness [12]. Impulse response provides information regarding the relative quality of concrete in an area of a structure [13].

2.3 NDTs for structural make-up in concrete

Low frequency alternating magnetic field (commercially known as covermeter) can locate the embedded steel reinforcement, measure depth of cover, and estimate diameter of reinforcement [5]. Ground Penetrating Radar (GPR) is useful in locating metal embedment, pipes, voids, regions of high moisture and thickness of different layers (if present) and members [14]. Ultrasonic pulse echo can measure element thickness in relatively thin elements [9].

2.4 NDTs for durability related issues

Half-cell potential can identify the regions in a structure with high probability of corrosion [5]. Polarisation methods determine the instantaneous corrosion rate of the reinforcement located below the test point [5]. Electrical resistivity can be used for the performance-based evaluation of concrete as resistivity is directly linked to the chloride penetration into concrete [15]. Penetrability methods indicate penetrability characteristics of concrete which in turn can provide an indication of concrete resistance against aggressive ions [16].

3 IMPULSE RESPONSE (IR) TEST METHOD – A CASE STUDY

This paper presents a case study where the IR technique was applied to assess the performance of multiple composite metal deck slabs in an existing structure. The concrete slabs exhibited cracking at different locations. Previous investigations where cores were removed indicated low to moderate compressive strength. Out of 40no. slabs in the floor, 30no. slabs were determined to have compressive strength below 30 MPa. There was a concern that the slab would not be suitable for the design load of 3 kPa. To ensure the performance of the floor, full-scale static load testing was initially proposed. A full-scale load test would be a time-consuming operation involving higher costs and operational disruption in the building. Instead of full-scale load testing on all the suspected slabs, a cost-effective and rapid assessment using the IR technique was proposed. Thus, IR testing was performed on 31no. slabs including one reference slab in order to identify the poorest performing slabs in the floor. The reference slab was selected based on the in-situ compressive strength of concrete in the slab and design performance of the slab. Based on the data obtained by the IR testing, the 3no. poorest performing slabs were identified and assessed by static load testing for the selected design criteria.

3.1 Theoretical background of IR test method

The IR test was developed as a steady state vibration test for investigating pile shafts in the early 1970s [17]. In the 1980s, especially with the advancement of portable computers, data acquisition system, increased data storage facilities and data processing, the test has developed to investigate other concrete structures such as concrete slab on ground, pavements, bridge decks, walls, particularly plate-like structures, etc. ASTM C1740-10 “Standard Practice for Evaluating the Condition of Concrete Plates Using the Impulse-Response Method” provides the procedure and technical aspects for using the IR test method to evaluate the condition of the concrete structures rapidly [13].

The test is a low strain, elastic stress wave propagation method. The test involves the use of mechanical impact to cause transient vibration of a concrete test element, the use of a velocity transducer placed on the test element adjacent to the impact point to measure the response, and the use of signal processing to obtain the mobility spectrum of the test element [13]. Figure 1 shows the schematic of the test set-up and apparatus of the IR test.

A load cell is incorporated within the hammer to measure the transient impact force and a velocity transducer is used to measure the resulting response of the test object. The impact mainly results in flexural vibration of the tested element. Force time history from the load cell and velocity time history from the velocity transducer are converted to the frequency domain and mobility spectrum, a basic output of the test, is computed using FFT (Fast Fourier Transformation) algorithm. This mobility plot is later used to analyse and obtain parameters representing the element’s response to the impact. These parameters are then used to locate the areas of anomaly within the tested element [18]. Figure 2 shows an example of a mobility plot obtained from the IR test of a plate-like concrete element.

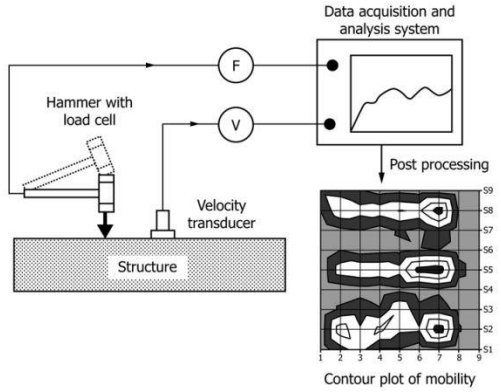

Figure 1: Schematic of the test set up and apparatus (taken from [13])

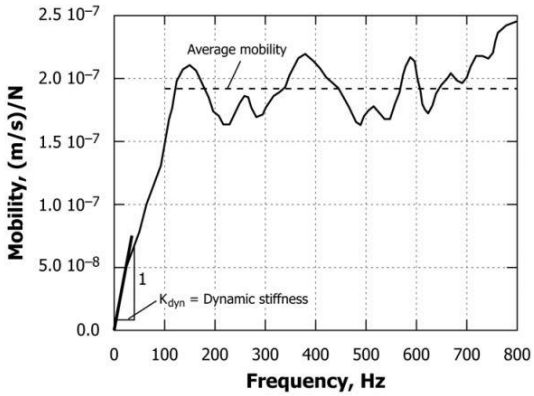

Figure 2: Typical Mobility (taken from [13])

3.2 Application of IR Test and Its Limitations

The IR test method is used for the condition assessment of concrete slabs, pavements, bridge decks, walls, or other plate like concrete structures. The method is also applicable to overlay structures such as asphalt or portland cement overlays on the bridge decks. Review of the application of the method suggests various successful application for identifying the potential poor areas within concrete [19,20]. A range of applications for the test method includes investigation on delamination/spalling/debonding [21,22], honeycombing and poorly consolidated concrete [23], cracking [24,25], assessing wall thickness variability [24], quality of support condition [18], etc.

The test can be used for rapid screening of the structures to identify potential locations of anomalous conditions that require more detailed investigation. Destructive or invasion testing such drilling holes or cores or chipping away concrete can be used to confirm the IR test results.

The following are parameters used for evaluation of concrete structures:

- **Average mobility:** It is defined as the ratio of the velocity amplitude at the test point to the force amplitude at a given frequency. The mean value of the mobility within the frequency range of 100-800 Hz is taken as the average mobility, see Figure 2. It is an indication of the relative flexibility and directly related to the density, support condition, and thickness of the structure as well as the concrete elastic modulus. A comparatively higher value in an apparently homogenous area may indicate reduced thickness, delamination, or voiding within the concrete.
- **Dynamic stiffness:** It is the inverse of the initial slope of the mobility plot from 0 to 40 Hz, see Figure 2, where the initial slope defines the dynamic compliance or flexibility at the test point. An indication of the stiffness of the structure at the test point and can be a function of relative quality of concrete, element thickness and support condition.
- **Mobility slope:** It is the slope of a best – fit line to fit the mobility curve between 100 and 800 Hz. This parameter is used to find poorly consolidated areas of concrete. A higher slope or non – stable mobility plot can be correlated with the areas of honeycombed or poorly consolidated concrete.
- **Peak-mean mobility ratio or void index:** It is the ratio of the peak mobility value between 0-800 Hz to the average mobility as defined above. This is an indication of the support condition or potential void within the concrete. A higher value indicates loss of support or voids beneath concrete slab bearing on ground.

The method is an empirical based method and uses a comparative assessment. The test does not provide any indication of the depth and size of the defects within the concrete. Lack of understanding of the response of the plate-like structures and no prior knowledge of the boundary conditions of the structure may lead to misinterpretation of the data. The results may be influenced by noise from traffic movement or low frequency structural movement. Heavy loads on suspended structures may alter the frequencies and shape of different modes of vibration and hence may affect the test results [13].

3.3 Proposed Methodology

As discussed, previous application of IR method successfully identified the problematic areas within concrete and later confirmed by other NDTs and/or invasive methods. Unlike other studies (where single area of concrete was the target for investigation), 31no. areas of slab were targeted to determine the poorest performing slabs on a comparative basis based on the results of the IR test. The structural system for all the slabs is similar; 160 mm concrete on the metal deck with 60 mm trapezoidal rib profile, primary beams between columns, columns being at 9m centres, and secondary beams at 3m centres along one direction. One of the 31no. slabs was taken to be the reference slab for comparative assessment of the other slabs. The locations of the slab area for the investigation are shown in Figure 3. It is to be noted that the floor surface had a polished finishing on top. Cracking was observed on the surface of the slab. In some slabs, there was evidence of repair works.

For the assessment of the slab, *s'MASH* Impulse Response system, a system developed by Germann Instruments, was used. Each slab was marked with a grid of 500 mm x 500 mm, thus providing 289no. of test points per slab area. In areas where the test slab had reduced accessibility, the number of test points varied. The evaluation of each test point on the top surface of the concrete surface was completed using the software provided by Germann Instruments. The data was

analysed, and the parameters associated with the test such as, the Average Mobility, Stiffness, Mobility Slope, Void Index, and the Mobility multiplied by Slope were calculated.
The test results were further analysed using statistical software to evaluate the condition of the slab with respect to the reference slab. The data obtained from individual slabs were analysed and compared with reference slab using first order statistics, pattern of distribution of the data, box-plot representations, tables, and graphs. In addition, Analysis of Variance (ANOVA), t-test and multiple comparison post-hoc tests were performed. Also, normalised contour plot data for all the slabs were visually assessed to evaluate the findings of the statistical analysis. This helped to identify the slab locations for further load testing for capacity evaluation. All mathematical computations were performed using Microsoft Excel Package and IBM SPSS Statistics (Version 27).

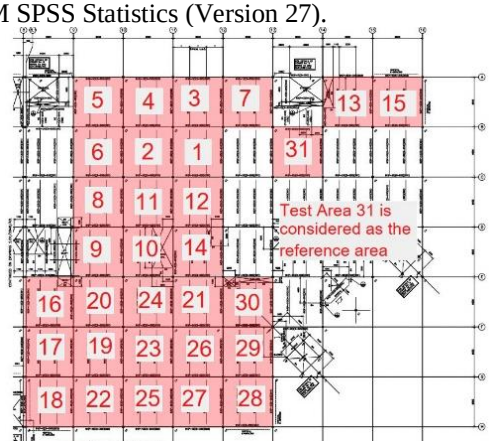

Figure 3: Individual slab locations in the floor during the assessment of composite metal deck slabs using the IR test.

3.4 Results of the IR test method

s'MASH Impulse Response testing provides four outputs (often referred to as parameters), namely the average mobility, dynamic stiffness, mobility slope, and void index. Each output is sensitive to different slab conditions and therefore indicating different properties associated with the slab. After the testing was done and data assembled and analysed on-site for each slab, a visual inspection of the slab was carried out to identify any anomaly present on the slab. As mentioned before, the slabs had severe cracking in certain areas and had repair patches in a few locations. Figure 4 shows the typical contour plots of different parameters, i.e., average mobility, dynamic stiffness, and void index. All the slabs had similar structural system. Hence, the parameters of the impulse response test would not be influenced by the structural system, rather depend on the inherent properties of the slab, such as, relative quality of concrete, elastic modulus, cracked and delamination areas, quality of concrete bond with the metal deck, etc. Assessment of average mobility parameter provided an indication of the poor, heavily cracks areas on the slab, see Figure 4(a). The locations of the secondary beams in the slab were clearly identified by assessing dynamic stiffness parameter, shown in Figure 4(b). Assessment of concrete based on the void index would indicate loss of support or voids beneath concrete slab bearing on ground. As all the slabs were supported on primary and secondary beams at fixed locations, the void index value confirmed the voiding under the slab and also the locations of the beams under the slab. Mobility slope is correlated with the areas of honeycombed or poorly consolidated concrete. Due to the thin section of the slab, no clear conclusion was made from the mobility slope data.

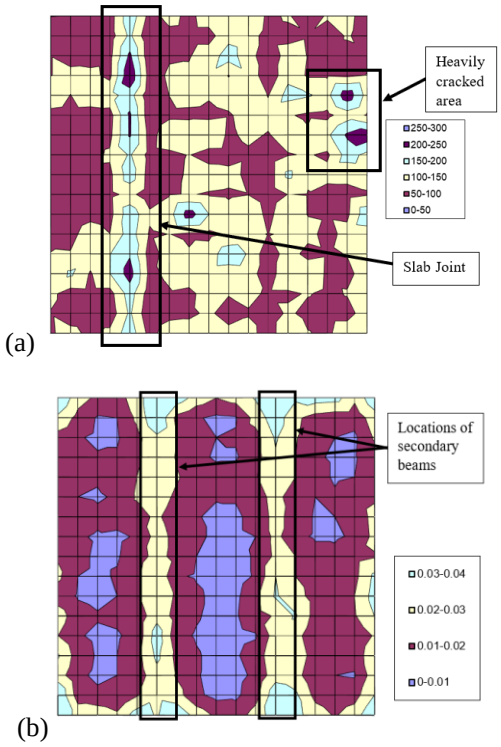

Figure 4: Contour plots of different parameters of the IR test; (a) average mobility for slab 31 (Reference Slab), and (b) dynamic stiffness for slab 6.

3.5 Analysis of the IR test results

Each parameter of the s'MASH Impulse Response test is sensitive to different slab conditions and therefore indicating different properties associated with the slab. Analysis of the output parameters will provide information on the changes of the properties within the slab and thus the poor/weak performing areas can be identified and assessed for further investigation. In order to identify the poorest performing slabs against the reference slab, a series of statistical analyses were performed, and the results were evaluated in a step-by-step procedure.
As indicated by Levene's Test for homogeneity of variance, null hypotheses of equal variance are rejected for all the datasets for a significance level of 95%. In this case, Welch's test (assuming normally distributed data with unequal variance) and Kruskall-Wallis H test (assuming equal variance and non-normally distributed data) were both performed. In both cases, p-value being less than 0.05 for a significance level of 95%, the analyses suggested that there are significant differences between the slabs for each type of datasets.

As in all cases, the null hypotheses of normally distributed data are rejected for a significance level of 95%. For this reason, both parametric and non-parametric tests were performed in the analysis. It is to be note that for sufficient number of data, ANOVA test can provide robust performance against non-normally distributed dataset. Mann-Whitney U test (with the assumption of normally distributed

data is violated for t-test) was also performed to compare the performance of the slabs with the reference slab. Based on the p-value and other statistical parameters using appropriate post-hoc tests (such as highest absolute mean difference using ANOVA, highest absolute Z value using the Mann-Whitney test), the slabs were ranked and studied for the poorest possible performance as indicated by the test parameters.

Also, mean and median plots were studied to assess the performance of the slabs with respect to the reference slab. Mean plots with standard deviation as error bar are shown in Figure 5 for average mobility data. Based on the highest absolute difference from the mean value and associated standard deviation, the slabs were ranked and studied for the poorest possible performance as indicated by the test parameters relative to the reference slab. Similar studies were performed for other sets of data, such as, dynamic stiffness, mobility slope, void index, and mobility x slope. Due to limitation of space, the plots are not shown in the paper.

A summary of the statistical analysis of test data is provided in Table 1. Table 1 only provides information of the average mobility and stiffness parameters. The slabs indicating maximum deviation from reference slab in terms of average mobility and stiffness parameters are only shown in the table.

4 DISCUSSION

The structural system for all the slabs on each floor of the multistorey building were found to be identical in nature. Each of the IR test parameters is related to the properties of the slab. When all the slabs have a similar structural system, the mobility was highly influenced by the elastic modulus of the concrete and internal defects. A higher mobility indicates problematic areas within the concrete. Statistical analyses showed differences in the performance of the slabs in terms of average mobility as indicated in Table 1. When assessing the data, Slabs 6, 16, 19, 20, and 24 provided the poorest possible performance with respect to the other slabs and reference slab. Except Slab 6, the rest of the slabs are clustered together. Slab 7 also indicated a high deviation from the reference (see Table 1), the lower mobility in the slab compared to the reference slab indicated a better performance of the slab in terms of average mobility parameter.

Dynamic stiffness can be an indicator of relative quality of the concrete, thickness, and support conditions. Others being constant, a relative quality of concrete can be assessed using this parameter. As indicated by Table 1, Slabs 19, 20, and 24 showed the lowest dynamic stiffness. These locations are the same cluster of slabs having poor average mobility results. Slabs 7, 13, and 14 showed higher stiffness values than the reference slab. The higher stiffness indicated a better performance of these slabs in terms of dynamic stiffness parameter compared to reference slab.

Similar conclusions on the Slabs 6, 16, 19, 20, and 24 were made based on the analysis of the mobility slope data.

As all slabs are supported by the beams and columns at fixed locations, the area underneath the slabs can be regarded as void when testing with the IR test method. This was indicated by the statistical analyses as the performance of all the slabs in terms of void ratio were found to be similar with no significant difference.

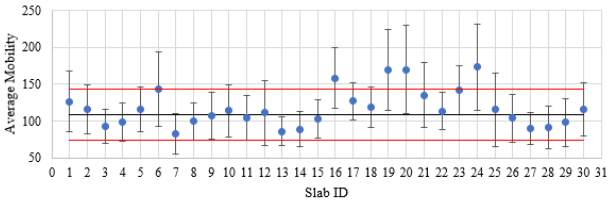

Figure 5: Mean plot representation with standard deviation as error bar. The black solid line represents the mean value obtained in the reference slab; and the upper and lower red solid line represents the mean plus standard deviation and mean minus standard deviation for the reference slab, respectively.

From the discussion of the results, it can be confirmed that Slabs 6, 16, 19, 20, and 24 provided the poorest performance compared to the reference slab and were selected for further investigation (e.g., static load testing). The tested Slabs 16, 19, 20, and 24 were noted to form a cluster within the same region indicating possible poor construction quality in the region during the concrete placement. The Slabs for static load testing were selected in such a way that they not only indicated the poor performance in terms of NDT parameter, but also, they represent different regions. Therefore, Slabs 6, 19 and 24 were selected for static load testing to establish the performance of the slabs under the proof load.

The design load of the composite slab was 3.0 kN/m^2. The slab was investigated for a proof load of 1.5 times the design load for a period of 24 hours. The maximum allowable deflection for the static load was set to 28mm. The Slabs 6 and 19 resulted in the similar performance providing maximum deflection of 14.5mm. The maximum deflection of 4.8mm was obtained in Slab 24. Further investigation revealed a load bearing wall hidden under the Slab 24, which restricted the movement of the wall during the static load testing. The crack width measurement at certain locations before and after the static load test indicated no change in width. Based on the acceptance criteria for maximum deflection and deflection recovery, the slabs were considered to be adequate for the design load.

5 CONCLUSION

Assessment of existing structure is of paramount importance to ensure the safe performance of structures. NDTs play an important role in condition and structural assessment of existing structures. The proper selection of NDT methods will influence the overall structural assessment and the quality of assessment with a cost-effective solution in the process.

In this regard, this paper presents a case study where a NDT method was used in the decision-making process for structural evaluation of composite slabs in an existing building. The impulse response test method was performed and based on the statistical analysis of the data; the poorly performing slabs of the floor were identified for further investigation. Though the method is empirical, uses comparative assessment and while the test does not provide any indication of the depth and size of the defects within the concrete, the method was successfully used to target the poor performing areas in the floor. Instead of carrying out a full-scale load testing on each slab at significant cost, the identified slabs were subjected to static load testing for

capacity evaluation based on the design criteria and the overall structural capacity of the slabs was evaluated in a cost-effective way.

The paper intends to highlight the gap between the use of NDT methods and the need for information in the decision-making process during an industrial application. The purpose of testing is not the test itself, but to gather information that can be used as a decision-making tool in the efficient evaluation of the existing structures.

REFERENCES

[1] M. Holicky, C. Viljoen, J. V. Retief, Assessment of existing structures, 2019. https://doi.org/10.1201/9780429426506-363.

[2] J.H. Bungey, S.G. Millard, M.G. Grantham, Testing of concrete in structures, 4th ed., Taylor & Francis, London & New York, 2006.

[3] American Concrete Institute (ACI), ACI 211.2-98, Standard Practice for Selecting Proportions for Structural Lightweight Concrete, Michigan, United States, 1998.

[4] C. Maierhofer, H.W. Reinhardt, G. Dobmann, Non-Destructive Evaluation of Reinforced Concrete Structures: Non-Destructive Testing Methods, CRC Press, Boca Raton, USA, 2010.

[5] V.M. Malhotra, Carino N. J., Handbook on Non Destructive Testing of Concrete, 2nd ed., CRC Press, Boca Raton, USA, 2004.

[6] American Concrete Institute (ACI), ACI 228.1R-03, In-Place Methods to Estimate Concrete Strength, Michigan, United States, 2003.

[7] D. Breysse, J.P. Balayssac, S. Biondi, D. Corbett, A. Goncalves, M. Grantham, V.A.M. Luprano, A. Masi, A.V. Monteiro, Z.M. Sbartai, Recommendation of RILEM TC249-ISC on non destructive in situ strength assessment of concrete, Mater. Struct. Constr. 52 (2019) 1–21. https://doi.org/10.1617/s11527-019-1369-2.

[8] National Standards Authority of Ireland (NSAI), I.S. EN 13791:2019, Assessment of in-situ compressive strength in structures and precast concrete components, Dublin, Ireland, 2019.

[9] A.O. De La Haza, A.A. Samokrutov, P.A. Samokrutov, Assessment of concrete structures using the Mira and Eyecon ultrasonic shear wave devices and the SAFT-C image reconstruction technique, Constr. Build. Mater. 38 (2013) 1276–1291.

[10] W.A. Zatar, H.D. Nguyen, H.M. Nghiem, Ultrasonic pitch and catch technique for non-destructive testing of reinforced concrete slabs, J. Infrastruct. Preserv. Resil. 1 (2020) 1–14.

[11] American Society for Testing and Materials (ASTM), ASTM D4788-03, Standard Test Method for Detecting Delaminations in Bridge Decks Using Infrared, n.d.

[12] American Society for Testing and Materials (ASTM), ASTM C 1383 - 98a Standard Test Method for Measuring the P-Wave Speed and the Thickness of Concrete Plates Using the Impact-Echo Method, 2013.

[13] ASTM C1740-10, Standard Practice for Evaluating the Condition of Concrete Plates Using the Impulse-Response Method, 2010.

[14] M.K. Lim, H. Cao, Combining multiple NDT methods to improve testing effectiveness, Constr. Build. Mater. 38 (2013) 1310–1315. https://doi.org/10.1016/j.conbuildmat.2011.01.011.

[15] American Society for Testing and Materials (ASTM), Standard Test Method for Bulk Electrical Conductivity of Hardened Concrete, 2019. https://doi.org/10.1520/C1760-12.2.

[16] The Concrete Society, Technical Report No. 31 Permeability Testing of Site Concrete, 2008.

[17] A.G. Davis, C.S. Dunn, From Theory To Field Experience With the Non-Destructive Vibration Testing of Piles., Proc Inst Civ Eng. 57 (1974) 571–593. https://doi.org/10.1680/iicep.1974.3895.

[18] J.S. Clausen, A. Knudsen, Nondestructive testing of bridge decks and tunnel linings using impulse-response, Am. Concr. Institute, ACI Spec. Publ. (2009) 263–275.

[19] A.G. Davis, The nondestructive impulse response test in North America : 1985 – 2001, 36 (2003) 185–193.

[20] S. Sajid, L. Chouinard, Impulse response test for condition assessment of concrete: A review, Constr. Build. Mater. 211 (2019) 317–328. https://doi.org/10.1016/j.conbuildmat.2019.03.174.

[21] A.G. Davis, B.H. Hertlein, Nondestructive testing of concrete chimneys and other structures, in: Nondestruct. Eval. Aging Struct. Dams, 1995: pp. 129–136.

[22] G. Rapaport, Condition Evaluation of Bridge Deck Surface Structure by Using State of the Art NDT- Techniques, in: Int. Symp. Non-Destructive Test. Civ. Eng. (NDT-CE), Berlin, Ger., 2015.

[23] A. Davis, B. Hertlein, M. Lim, K. Michols, Impact-Echo and Impulse Response stress wave methods: Advantages and limitations for the evaluation ofhighway pavement concrete overlays. Allen Davis1, Bemhardt Hertlein2, Malcolm Lim3 and Kevin Michols3, 2946 (n.d.) 88–96.

[24] N. Zoidis, E. Tatsis, C. Vlachopoulos, A. Gotzamanis, J. Stærke, D.G. Aggelis, T.E. Matikas, Inspection , evaluation and repair monitoring of cracked concrete floor using NDT methods, Constr. Build. Mater. 48 (2013) 1302–1308.

[25] T. Gorzelanczyk, J. Hola, Ł. Sadowski, Krzysztof Schabowicz, Methodology of nondestructive identification of defective concrete zones in unilaterally accessible massive members, J. Civ. Eng. Manag. 19 (2013) 775–786.

Table 1. Summary of the statistical analysis of Impulse Response Test results

Parameters	Slab ID	Mean	Median	Std	CoV (%)	Comments	Statistical Evaluation+
Average Mobility	6	143.1746	135.0726	50.42834	35.2223	Higher mobility	Mean difference from ANOVA = -34.59651315; Z value =-10.011
	7	82.86924	77.37344	27.63006	33.34176	Lower Mobility**	Mean difference from ANOVA = 25.705874 Z value from t-test=-11.153
	16	158.5077	148.1644	41.55093	26.21382	Higher mobility	Mean difference from ANOVA=-49.42654657; Z value =-14.647
	19	169.2088	155.0531	55.41131	32.74729	Higher mobility	Mean difference from ANOVA=-60.63370123; Z value =-14.771
	20	169.4528	158.2815	59.95746	35.38298	Higher mobility	Mean difference from ANOVA=-60.87771802; Z value = -14.468
	24	173.3087	160.5005	58.74972	33.89889	Higher mobility	Mean difference from ANOVA=-64.73354800; Z value = -15.698
Stiffness	7	0.027007	0.025	0.009424	34.89353	Higher Stiffness**	Mean difference from ANOVA=-.00802422; Z value = -10.666
	13	0.024853	0.024	0.007662	30.82746	Higher Stiffness**	Mean difference from ANOVA=-.00587036; Z value = -9.094
	14	0.02586	0.023	0.011208	43.3411	Higher Stiffness**	Mean difference from ANOVA=-.00687766; Z value = -7.637
	19	0.013685	0.012	0.005948	43.46172	Lower Stiffness	Mean difference from ANOVA=.00529758; Z value = -9.619
	20	0.014377	0.012	0.007706	53.60163	Lower Stiffness	Mean difference from ANOVA=.00460554; Z value from t-test= -9.279
	24	0.014176	0.013	0.006263	44.18109	Lower Stiffness	Mean difference from ANOVA=.00480623; Z value from t-test= -8.925

*Based on Median, rest is based on both median and mean

**Better performance of the slab compared to Reference Slab

+Mean different calculated assuming unequal variance of the data, and Z-value based on Mann-Whitney test (non-parametric test) for comparing two sets of data.

An integrated dynamic analysis of a 5MW monopile-supported offshore wind turbine under environmental loads

Satish Jawalageri[1,2*], Soroosh Jalilvand[2], Abdollah Malekjafarian[1]
[1]Structural Dynamics and Assessment Laboratory, School of Civil Engineering, University College Dublin, Dublin, Ireland.
[2]Gavin and Doherty Geosolutions, Dublin, Ireland.
* Corresponding author, Email address: satish.jawalageri@ucdconnect.ie

ABSTRACT: This paper investigates the dynamic behaviour of an offshore wind turbine (OWT) supported on medium dense sand using an integrated load assessment. An integrated modelling approach is introduced to allow for considering aerodynamic and hydrodynamic loading and also soil-structure interaction. A numerical model of the NREL 5MW monopile-supported OWT is initially developed in OpenFAST software. The foundation of the structure is modelled using SESAM software where soil-structure interaction is adopted using API curves and integrated to the OpenFAST model using the stiffness values at mudline level. The integrated model provides a better understanding of the structural behaviour of OWT under various environmental conditions.

KEY WORDS: Offshore wind turbines, Waves, Wind, Load assessment, Integrated model, Monopile, Soil-structure interaction.

1 INTRODUCTION

A large amount of carbon dioxide is emitted from non-renewable energy resources such as fossil fuels. Renewable energy resources like wind energy and solar energy play a significant role in addressing carbon footprint. Among these resources, wind energy is one of the most widely used resources and it is proven to be one of the most efficient and reliable [1].

Offshore wind turbines (OWTs) are more effective than onshore wind turbines because the speed of the wind and its direction are consistent, so fewer turbines are required to produce the same amount of electricity as offshore turbines generate. The foundations of offshore wind turbines contribute up to 20-25% of total cost of the structure [2]. This leads to the need to optimise both the design and installation of the structure. The majority of offshore foundations across the world are monopile based foundations [3]. In general, monopile foundations may have a diameter of 8-10 m [4] and embedment lengths depend on the water depth, soil properties and turbine size.

Due to the advancement of technology in offshore industry, OWTs are becoming taller with relatively deeper foundations in order to produce more energy. OWTs are unique structures due to their operational conditions where they are working under harsh environmental conditions [5]. In general, they are subjected to various environmental loads such as wind, wave and current. Further, the interaction of foundation structure with soil along with external loads make it complicated to design and analyse the OWT structure. The natural frequencies of the structure are close to the rotor frequency during operational condition and wave frequencies which may result in fatigue damage of the structure [6]. Therefore, it is important to understand the dynamic response of the OWT subjected to external loads considering soil-structure interaction (SSI) under different loading conditions in which OWTs operate.

In this study, an integrated approach for modelling OWTs considering SSI is introduced. An NREL 5MW monopile supported OWT is used as a reference model. The environmental loads including wind, wave and current are modelled using OpenFAST software. The foundation and SSI are modelled in a software called SESAM. The SSI is then integrated to the OpenFAST model using the mudline stiffness matrix which is extracted from SESAM model. The integrated model is used to analyse dynamic behaviour of the OWT under external loading conditions.

2 EXTERNAL LOADS

This section introduces various external loads acting on the OWTs. Primarily, there are two types of loading that OWTs experience i.e., aerodynamic loads and hydrodynamic loads. These are the governing loads that should be considered during the design of offshore wind structure. Figure 1 shows the components of the OWT and various loads experienced by the wind turbine during the service time of the structure.

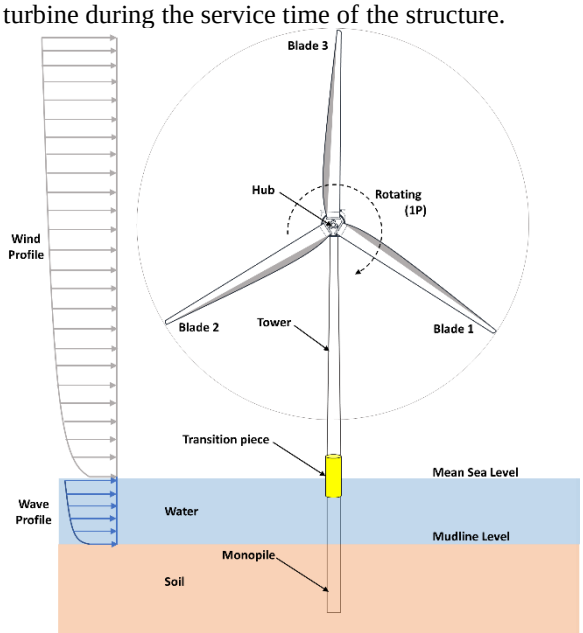

Figure 1. Components and loads on OWT.

2.1 Aerodynamic Loads

The wind loads acting on the structure are the dominant load during the operation of OWTs. The turbine tower and blades are subjected to the wind loads acting on the wind turbines. OpenFAST uses the blade element momentum (BEM) theory [7] to calculate the aerodynamic loadings along the blades. BEM theory is the combination of blade element theory (or propeller theory) and momentum theory. Blade element theory calculates the forces by dividing the blade into a number of segments along the length and then the force is calculated on each segment. Momentum theory calculates the reduction in velocity when wind passes through the rotor. BEM uses these two concepts to find the axial forces and torques acting on the rotor blades.

In addition to this, power law is used to calculate the wind load along the turbine tower as wind speed along the vertical height changes [8]:

$$V(z) = V_{hub}\left(\frac{z}{z_{hub}}\right)^{\beta} \quad (1)$$

where $V(z)$ and V_{hub} are the mean wind speeds at the height z above the MSL and hub height, z_{hub}, respectively, and the power law coefficient, β of 0.143 has been considered in this study [9].

2.2 Hydrodynamic Loads

These are the loads caused due to the action of waves on the structure submerged below the water. Hydrodyn is a module in the OpenFAST which is used to calculate the hydrodynamic loads. Regular waves have been considered for the calculation of hydrodynamic loads on the structure in this study. The hydrodynamic loads on the structure are calculated based on strip theory using Morison's equation [10]. In this study, Morison coefficients (C_d and C_m) are calculated by considering the marine growth thickness of 100mm and diameter of pile as 6m with wave height of 6m and wave period of 10sec. C_d and C_m are obtained as 0.64 and 2, respectively ([8] and [11]). Morison's equation is a function of water particle velocity and acceleration along the depth and the force per unit length along the cylinder is given by,

$$dF_h = 0.5\,\rho_w\,C_d\,D\,dz\,|v_r|v_r + C_m\,\rho_w\,A(z)dz\,a_r \quad (2)$$

where ρ_w represents the density of water, Ddz is the area of the strip with diameter (D) of 6m and Adz is the displaced volume, v_r is the relative water velocity with respect to velocity of the body and a_r represents the relative fluid acceleration.

A surface current velocity of 1.5m/s has been considered where OpenFAST calculates the current velocity along the depth using the power law [12].

3 INTEGRATED APPROACH

This section introduces the integrated model in order to understand the behaviour of OWTs considering soil-structure interaction. In this study, an NREL 5MW turbine is considered as the reference model.

OpenFAST software is used for structural analysis including the external loads. The software currently does not support the foundation modelling which creates a limitation for scour modelling. However, the dynamic contribution of soil properties below the mudline can be simplified using a stiffness matrix which represents soil-structure interaction. To overcome this drawback, the scour process and soil-structure interaction are modelled accurately in a software called SESAM. Figure 2 shows the integration of the two software - SESAM and OpenFAST. The following modelling approach is used to integrate the SESAM and OpenFAST,

Step 1: Initially, the maximum interface load among the time series from the OpenFAST with a rigid connection at the bottom are calculated for each load scenario.

Step 2: The above obtained loads are used as inputs in SESAM where the soil model and wave loads are incorporated to enable soil structure interaction to be considered.

SESAM considers the pile below the mudline by subdividing it into a number of elements that are rigidly interconnected at nodal points and each node has six degrees of freedom. Further, the soil profile in the SESAM is modelled by multiple sublayers in order to capture the pile soil interaction at each node. The soil spring stiffness at the mudline level is obtained.

Step 3: The mudline spring stiffness 6x6 matrix is obtained for each load condition as the output of SESAM. These spring stiffness values are then integrated in OpenFAST for a medium dense soil profile.

The integrated model is then used to analyse the behaviour of the structure for which acceleration data at nine different levels are extracted along the tower of the OWT (Figure 3). Power Spectral Density (PSD) is then applied to these acceleration data to extract the global natural frequencies for a soil profile.

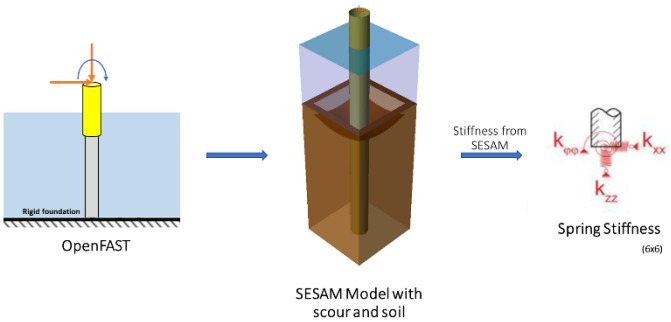

Figure 2. Modelling Approach

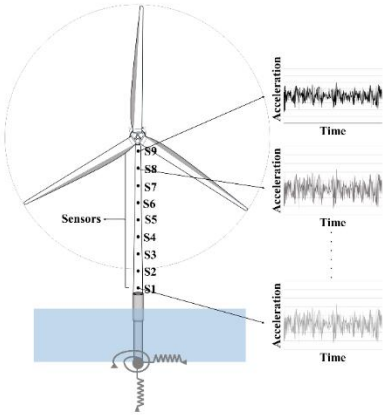

Figure 3: Sensor locations in the simulations

4 RESULTS

In this study, medium dense sand with unit weight, angle of internal friction and initial modulus of subgrade reaction of 19 kN/m^3, 35 deg and 22000 kN/m^3, respectively, are considered [13]. Figure 4 shows the power spectral density of an OWT supported on medium dense sand. PSD peaks correspond to the harmonics of the system (3P, 6P and wave harmonics) and the natural frequencies. The presence of these frequencies makes it difficult to identify the system natural frequencies. The first two natural frequencies of the system are detected at 0.244 and 1.419 Hz.

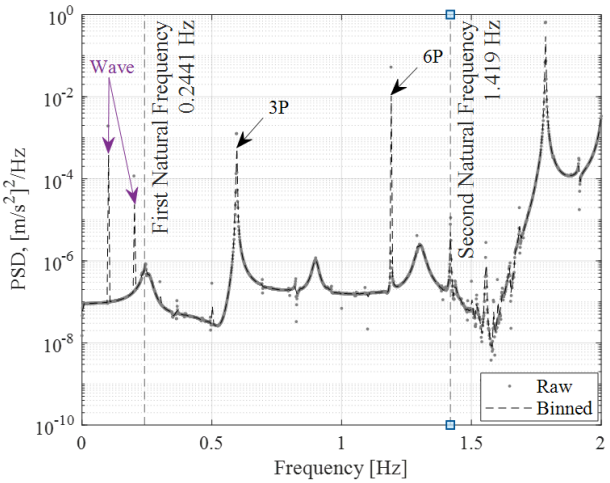

Figure 4. Power spectral density of structure

5 CONCLUSION

The paper introduces an integrated approach to the analysis of OWTs in order to understand the response of the structure to external loads such as aerodynamic and hydrodynamic loads, taking account of soil-structure interaction at foundation level. An NREL 5MW turbine is considered as the reference model where OpenFAST is used for structural analysis and SESAM is used to model the foundation part of the OWT. This model enhances the understanding of the structural response of OWTs founded on medium dense sand under environmental loads.

ACKNOWLEDGMENTS

The authors wish to express their gratitude for the financial support received from the Irish Research Council (IRC) EBPPG/2020/259.

REFERENCES

[1] K. A. Abhinav and N. Saha, "Dynamic analysis of monopile supported offshore wind turbines," *Proceedings of the Institution of Civil Engineers - Geotechnical Engineering*, vol. 170, no. 5, pp. 428-444, 2017, doi: 10.1680/jgeen.16.00022.

[2] W. Carswell *et al.*, "Foundation damping and the dynamics of offshore wind turbine monopiles," *Renewable Energy*, vol. 80, pp. 724-736, 2015, doi: 10.1016/j.renene.2015.02.058.

[3] WindEurope, "Offshore Wind in Europe," in "Key trends and statistics 2020," 2021.

[4] C. Reale, J. Tott-Buswell, and L. J. Prendergast, "Impact of Geotechnical Uncertainty on the Preliminary Design of Monopiles Supporting Offshore Wind Turbines," *ASCE-ASME J Risk and Uncert in Engrg Sys Part B Mech Engrg*, vol. 7, no. 4, 2021, doi: 10.1115/1.4051418.

[5] I. B. Løken and A. M. Kaynia, "Effect of foundation type and modelling on dynamic response and fatigue of offshore wind turbines," *Wind Energy*, vol. 22, no. 12, pp. 1667-1683, 2019, doi: 10.1002/we.2394.

[6] L. J. Prendergast, K. Gavin, and P. Doherty, "An investigation into the effect of scour on the natural frequency of an offshore wind turbine," *Ocean Engineering*, vol. 101, pp. 1-11, 2015, doi: 10.1016/j.oceaneng.2015.04.017.

[7] P. J. Moriarty and A. C. Hansen, "AeroDyn Theory Manual," in "NREL/TP-500-36881," National Renewable Energy Laboratory, 2005.

[8] *DNV-RP-C205 Environmental Conditions and Environmental Loads*, DNVGL, 2014.

[9] S. Bhattacharya, *Design of Foundations for Offshore Wind Turbines*. John Wiley & Sons Ltd, 2019.

[10] J. R. Morison, J. W. Johnson, and S. A. Schaaf, "The force exerted by surface waves on piles," *Journal of Petroleum Technology*, no. 2, pp. 149-154, 1950. [Online]. Available: https://doi.org/10.2118/950149-G.

[11] *IEC 61400-3-1:2019&A11:2020 Wind energy generation systems - Part 3- 1: Design requirements for fixed offshore wind turbines*, IEC, 2020.

[12] J. Jonkman and B. Jonkman, "OpenFAST Manual," National Renewable Energy Laboratory, 2020.

[13] L. J. Prendergast and K. Gavin, "A comparison of initial stiffness formulations for small-strain soil–pile dynamic Winkler modelling," *Soil Dynamics and Earthquake Engineering*, vol. 81, pp. 27-41, 2016, doi: 10.1016/j.soildyn.2015.11.006.

Understanding mould growth causes and solutions for A-rated homes

Orlaith Murphy[1], Roger P. West[1], Eoin Kelly[1] , Niti Saini[1]
[1]Department of Civil Structural and Environmental Engineering, Trinity College, College Green, Dublin 2.

Email : murphyo6@tcd.ie, rwest@tcd.ie, kellye46@tcd.ie, sainin@tcd.ie

ABSTRACT: In recent years it has emerged that with the enhanced air-tightness of A-rated homes, brought about in the pursuit of improved thermal performance, the potential for mould growth has increased. The ventilation in A-rated homes by design or by occupant actions is often proving to be inadequate in maintaining a suitable indoor air quality environment. It has been found that the air in A-rated homes can have very high humidity and carbon dioxide levels for prolonged periods since natural ventilation is often minimal due to their airtight design. These high humidity levels enhance the risk of mould growth occurring such that it can create a health hazard for the occupants. This paper will review recent research that has been conducted to examine further the main causes of mould growth. New laboratory experimentation into the factors affecting the extent and rapidity of mould growth will be conducted. Experimental evidence of the conditions which promote mould growth will be identified from which guidance will be given for home owners to help identify the potential for mould growth at an early stage. Aspects such as the substrate type, temperature and humidity levels were investigated through experimentation to determine the main triggers of mould growth. From this research, solutions are suggested as to how to prevent mould growth from occurring through guidance on modifying occupant behaviour and ventilation design in A-rated homes.

KEY WORDS: Mould growth; A-rated homes; Ventilation.

1 INTRODUCTION

It is estimated that approximately 83% of the homes in Ireland have some form of mould growth [1]. It would initially be assumed that all of this mould growth occurs in old, damp and badly insulated homes, however recent studies [2] have shown that some new airtight and energy-efficient homes are starting to show signs of significant mould growth at an early age. In recent years there has been an increase in the number of new homes being built and old homes being retrofitted to a high standard of airtightness. This standard has been implemented because the airtight design reduces the amount of heat escaping from the home which increases its energy efficiency. However, these standards are being implemented sometimes without a full awareness of the effects extreme airtightness has on the functionality of the home and the comfort and health of the occupants, particularly when occupier interventions override the design assumptions. There is a risk that without adequate ventilation insufficient air changes and low air quality in these airtight homes may increase the chance of toxic mould growth occurring [3]. This fact, coupled with the growing use of organic building materials that support microbial growth, has increased the probability of mould growth in these homes. It is well known that mould growth in the home can have many adverse health effects, such as worsening asthma and allergies [4] and it can cause insomnia and lethargy problems [5].

This problem has been identified in recently built A-rated homes [2] and is of great concern to the construction industry because the current regulations require new buildings to be A-rated and yet have safe environments with adequate occupant comfort. There are also government incentives for older homes with low building energy ratings to be retrofitted and sealed to the A-rated standard to reduce their carbon footprints, also potentially leading to unsightly mould growth. This is a highly frustrating problem since mould growth can be avoided, and homeowners have not always been made aware of their increased risks when they modify the installed ventilation systems provided in their A-rated home. The risks associated with these homes are somewhat unquantified due to these new designs not being tested yet over long periods before implementation or in service.

The problems of mould growth must be thoroughly understood so that, where necessary, design and operational changes can be made to these A-rated homes to prevent mould growth in the future. This study was designed to establish why this mould growth is occurring in these homes and what solutions can be put in place to prevent it. Changes may need to be made to both the building standards and the habits of the occupants of these homes to prevent this mould growth.

2 METHODOLOGY

Initial laboratory experiments were conducted to determine the conditions where mould growth begins to occur and what factors affect the rate and severity of mould growth the most. The factors of humidity, temperature and substrate type were varied to examine how they affected the rate of mould growth. Selected samples (initially in equilibrium at ambient relative humidity, approximately 60%) of known vulnerable substrates, namely wallpaper, untreated timber and plasterboard of defined thickness, were attached to the underside of the lid of airtight containers inside which varying humidity levels were created and then exposed to differing temperatures (see Figure 1). Initially, a test at each humidity level, from 75 to 100% relative humidity and at 15°C and 25°C was conducted with bread as the substrate. This substrate sample was used as a means of comparison since bread is guaranteed to suffer from mould growth even when conditions are relatively mild. The bread experiments were only conducted over a 3-week period whereas the remaining experiments were conducted over a 9-week period each.

Figure 1. Typical laboratory experiment set-up.

In each container, a sensor was attached to the underside of the lid to record the temperature and humidity levels in the box over the experimental period. The higher temperature was controlled in a room with a sensor and the specimens at the lower temperature were left in a room with an average ambient temperature of approximately 15°C.

The humidity levels were controlled with the use of saturated salt solutions. The humidity was controlled at levels of 75%, 80%, 85% and 100%. Past studies [6] showed that saturated salt solutions can control the humidity level to a certain accuracy, as shown in Table 1. The salts that were used are sodium chloride, ammonium chloride and potassium chloride. Past literature used different amounts of salts needed for the solution [6, 7] so experiments were conducted to determine which levels worked best for this experiment. This was achieved by placing a varying amount of salt into three different containers with the same amount of distilled water, enough to cover the base of the containers. A sensor/logger with a USB interface was attached to the underside of each lid which took readings of temperature and humidity at ten minutes intervals and had a six month battery life.

Calibration experiments on each solution were left for 3 weeks and it was determined that a solution of 40g of salt and 70mL of distilled kept a constant humidity level over the three week period (Table 1). The individual mould growth experiments were then set up and the results were analysed on a weekly based with progress photographs and descriptions being recorded.

Table 1. Saturated salt solution humidity levels.

		Humidity (%)	
Temp. °C	Sodium Chloride	Ammonium Chloride	Potassium Chloride
15°C	75.61 ± 0.18%	79.89 ± 0.59%	85.92 ± 0.33%
25°C	75.29 ± 0.12%	78.57 ± 0.40%	85.06 ± 0.38%

The limitations of these experiments are recognised, where particularly it is noted that the saturated salt solutions did not provide a perfectly consistent humidity level. If the experiment was conducted over a longer period the results could change slightly which is relevant as mould growth is often a long-term phenomenon.

A very extensive set of experiments were conducted as part of the AMBER (Assessment Methodology of Building Energy Ratings) project which was carried out by Trinity College Dublin with partners IES to investigate the presence of mould growth in A-rated homes that were constructed as recently as 2018 [2]. These dwellings included both semi-detached and terraced homes that were all rated with an A2 Building Energy Rating (BER). Humidity sensors were placed in five rooms in the forty-four homes tested as part of this aspect of the project. These rooms were the kitchen, living room, second bedroom, master bedroom and ensuite. Data were collected over a six month period and this information was analysed to produce findings on the humidity levels recorded and the incidences of mould growth that had occurred. These findings and results were analysed to determine why mould growth was occurring in these homes.

Results from data taken as part of the AMBER research found that the highest humidity levels are usually found in the master bedroom especially when an ensuite is present (Figure 2). In order to determine what type of ventilation is most effective in these types of rooms, an experiment was conducted testing different ventilation practices and these will be reported on in this paper.

Figure 2: Typical RH data from a main bedroom (black) and ensuite bathroom (red) showing background values and peaks during showers.

3 RESULTS AND DISCUSSION

3.1 Laboratory Experiments

The aim of the main mould growth laboratory experiments was to examine the effects of different humidity and temperature levels on several substrate types. It was found from the data taken from the sensors that the humidity level was kept relatively constant with the use of the aforementioned saturated salt solutions, so the results of the experiment were reliable.

3.1.1 Humidity changes

At 75% RH: It was found that changing the humidity level had a significant effect on the rate of mould growth and the possibility of mould growth occurring. The high indoor temperature created an average humidity of 77.7% in the sealed containers, while the lower indoor temperature resulted in an average humidity level of 72.2% (Figure 3). At these humidity levels, on all the substrates tested, it was found that no mould growth occurred over the 9 week testing period (see Figure 4). Interestingly, the bread substrate tested at this same humidity level also did not develop any mould growth. However, the bread did turn “dry” after a few days. Although these findings

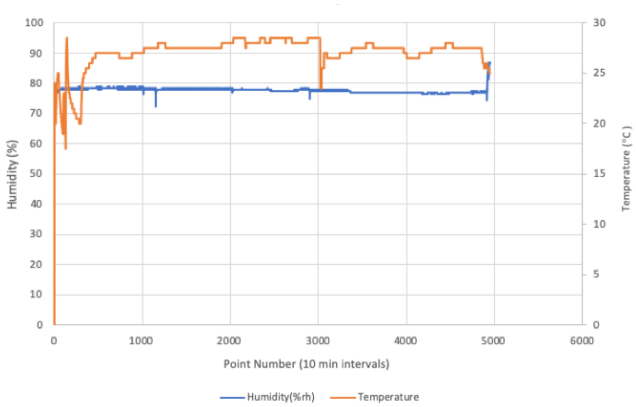

Figure 3: Humidity regime under Sodium Chloride solution at the higher temperature

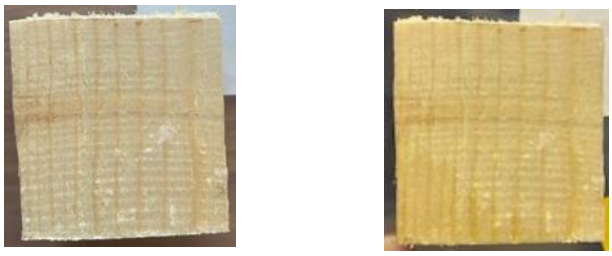

Day 1 Week 9

Figure 4. Untreated timber at 75% humidity and 25°C.

indicate that 75% humidity is insufficient to cause mould growth over this time period, it is recognised that it is possible that mould growth could eventually occur on these samples.

At 80% RH: Ammonium chloride was used to keep a constant humidity of approximately 80% at both temperature levels. The data shows that at high (25 ºC) and low (15 ºC) indoor temperatures the humidity averages were 80.4% and 78.8% respectively. It was also found that the humidity level for the experiments at the low indoor temperature fluctuated more since the area where the experiments were located was not kept at a constant temperature level. It was found in this experiment that mould growth did occur at a humidity level of 80%, but only on the untreated and hygroscopic timber samples. This mould growth was small and was just about visible to the naked eye and was difficult to show through photographs. Over the 9 week testing period no mould growth occurred on the plasterboard or wallpaper samples. This is most likely due to wallpaper and plasterboard being more processed substrates than timber and are made from inorganic materials that can more effectively resist mould growth. It was also found that at the higher temperature level mould growth began to be evident in week 3 but did not occur until week 5 in specimens exposed to 15°C. This result shows the effect temperature can have on the rate of mould growth. The experiment performed on the bread sample yielded similar results, where, surprisingly, after three weeks there had been no mould growth evident on the sample. By week three, the sample had begun to get hard as it dried to the equilibrium humidity, although not as much as the sample tested at 75% humidity. This suggests that the natural moisture content of bread is likely close to 80% and could with more time develop mould growth.

At 85% RH: The substrates tested with the saturated salt solution using Potassium Chloride had an average humidity level of 84.5% at 25°C and 86.7% at 15°C. At a level of approximately 85% humidity, small amounts of mould growth were visible on some of the substrate samples at 15°C and 25°C. Mould growth first occurred on the timber sample which was to be expected given that timber is a natural hygroscopic material that had not been treated with anti-mould chemicals. At the high indoor temperature level, a small quantity of mould had formed on the sample by week 2. This mould growth is difficult to see because on this sample most of the mould has formed on the side of the sample and it is very light in colour. No mould growth occurred on the wallpaper and plasterboard which is a similar result to the other humidity levels. Surprisingly at the low indoor temperature level mould growth began to appear in the same week, week 2 and this mould growth continued to develop over the next few weeks. Mould growth on the bread sample was visible after 2 weeks. This result confirms that 85% humidity is a sufficient humidity level for mould growth to occur at a modest rate within the experimental time period.

At 100% RH: 100% humidity was achieved by placing distilled water into the container. It was expected that mould growth would occur at this humidity level but the effect of substrate type and temperature difference could be analysed more closely in this portion of the experiment. Mould growth began to form in week 1 on the untreated timber substrate (see Figures 5 and 6). A thin layer of mould growth began to form and by week 3 the growth had clustered on the surface of the sample into significant growths. Plasterboard, as demonstrated in the previous experiments, is significantly more resistant to mould growth than untreated timber, in a given temperature/humidity environment due to its surface sorptivity, material and thickness. Mould development did, however, occur at both temperature levels at 100% humidity at 25°C by week 4, with a large quantity of growth by week 9 (see Figure 7). Plasterboard reacted variably depending on the temperature; at 15°C mould development did not begin until week 5 and was quite small. It was visible by week 9 but it was still small in comparison with the 25°C experiment (see Figure 8). Furthermore, in contrast to other humidity levels mould growth did occur on the wallpaper substrates at both temperature levels at this humidity level. At 15°C obvious mould growth started in week 2 and at 25°C it began in week 1. However, the mould growth spores at 15°C were more visible in their traditional circular shape than they were at 25°C (see Figures 9 and 10). At the higher temperature level, the wallpaper sample was affected by a large amount of condensation present on the lid of the container. Mould started to form along the sample's edges and the spores were moist and easy to remove. As expected the bread substrate at 100% humidity produced a significant amount of mould growth after 1 week. A tile sample was also tested at this 100% humidity level and it was found that after a few weeks of testing no mould growth occurred on the sample. This result shows the substrate type is a defining factor in the probability of mould growth occurring. Any non-

hygroscopic materials such as a glazed non-organic tile will not grow mould under any conditions.

3.1.2 Temperature changes

Temperature is also an important aspect of the factors that affect mould growth. Therefore two common household temperatures were tested as part of this experiment. The specimens at 25°C were placed in a room that was controlled by a sensor that kept the room temperature constant. However, the temperature in the majority of the containers had an average of 28°C. Small fluctuations in the temperature can also be noticed in the graphs (Figure 3) which are caused by the opening of the test room door for short periods of time. The opening of the container to allow progress photographs to be taken also impacted the humidity and temperature levels in the containers due to its temporary ventilation. The experiment at the low indoor temperature level was not conducted in a temperature-controlled environment but rather in a room with an average temperature close to 15°C. However, it was found that the containers in this room had an average temperature that was closer to 18°C but this was still acceptable for the experiment since it was a considerably lower temperature than the higher indoor temperature level being used.

Figure 5. Untreated timber at 100% RH, 15°C in week 5.

Figure 6. Untreated timber at 100% RH, 25°C in week 5.

Day 1 Week 9

Figure 7. Plasterboard at 100% humidity and 15°C.

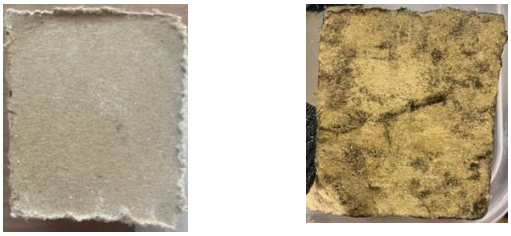

Day 1 Week 9

Figure 8. Plasterboard at100% humidity and 25°C.

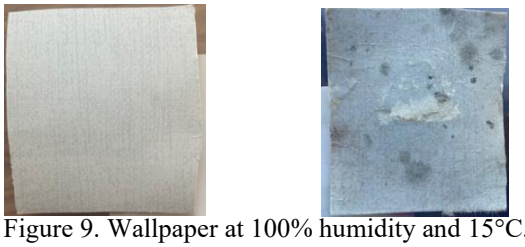

Figure 9. Wallpaper at 100% humidity and 15°C.

Day 1 Week 9

Figure 10. Wallpaper at 100% humidity and 25°C.

Overall from the results from each humidity test as described above, it can be determined that temperature does not play a major role in the rate of mould growth. These findings combined with previous research conclude that a sufficient temperature is necessary but how high this temperature is does not determine if mould growth will occur, although by 80% humidity the temperature did affect the rate of growth, that is mould growth occurred in week 3 at the higher temperature and week 5 at the lower temperature. However, it is a known fact that warm air has the capacity to holds more moisture which can increase the absolute humidity levels within a home if a moisture source exists. Therefore, room temperature must be at a comfortable level but not elevated so that the higher temperature does not encourage higher moisture vapour levels in the air.

3.2 A-rated housing development study

It was found [2] that in Ireland in A-rated homes the average bedroom temperatures are expected to be between 17°C and 19°C in Winter and between 23°C and 25°C in Summer. From the previous laboratory experiment it was shown that with a suitable humidity level and substrate type these temperatures will facilitate mould growth. The study of the data from the A-rated home development showed that humidity levels are highest in the ensuite followed by the master bedroom and kitchen. The goal of analysing the data from the forty-four A-rated homes tested as part of this study was to develop a list of the homes most likely at risk to mould growth and then determine if mould growth did in fact occur in these homes.

Previous experiments have shown that a home that reaches 80% humidity or more in an area with hygroscopic materials is likely to have mould growth occuring. In the majority of the homes studied it was found that the ensuite spent an average of 2% to 5% of the time over 80% humidity (Figure 2). However, in this room, non-hygroscopic materials will prevent the majority of mould from forming but if the window is left closed condensation may occur and could drip onto the surrounding walls and window sill. Most ensuites had

a humidity level of 60% for 60 to 100% of the time. Although experimentation has shown that mould growth is unlikely at 60% humidity, over a long period it is possible that mould growth may eventually occur. It was also found that in homes that had a high humidity level in the ensuite, the humidity level in the master bedroom was also elevated. From these findings, a list of the homes most likely to form mould growth was drafted and their occupants were contacted to establish if indeed mould growth was present.

Mould growth occurred in the master bedroom of house labelled A, where this home was marked as the home with the highest risk of mould growth. House A has the highest average time spent above 80% humidity in all rooms based on the highest monthly values. However, mould growth did not occur in the ensuite of house A, even though the humidity recorded was over 80% for 53% of the time. This lack of mould growth in the ensuite is likely due to the use of non-hygroscopic materials, principally tiles being used in the bathroom. Inspections carried out by the maintenance team as part of this study found that in some of the homes the trickle vents has been closed by the occupants and this may have been a factor that increased the temperature and humidity levels in the homes. Another home marked at a moderate risk of mould growth reported growth in the master bedroom and in the upstairs landing. It was reported that condensation regularly occurs in the master bedroom particularly around the reveal of the window which indicates that it may be caused by the condensation. The presence of condensation also implies that there may be a thermal bridge problem with the window where temperatures are at a low level.

This study shows that high humidity levels in A-rated homes do result in mould growth especially in the bedroom adjoining the ensuite. Also, these studies confirmed the suspicions from previous literature that trickle vents in these homes were being blocked due to draughts affecting thermal comfort levels, stopping the designed circulation of fresh air and allowing the humidity and temperature levels to rise to higher levels that can result in mould growth.

3.3 Ventilation experiment

The humidity levels were tested in the ensuite bathroom, the adjoining master bedroom and the landing outside the bedroom of a randomly selected house with mould growth as part the AMBER project. A sensor was placed in the ensuite, two in the master bedroom, in two different locations and one in the hallway. In order to raise the humidity level, the shower in the ensuite was left running for five minutes at a high temperature. A record was also kept of the times at which the heating turned on in the home to account for any spikes in temperature. The different ventilation methods investigated on separate occasions included:

- No form of ventilation
- Fan in the ensuite on for a ten-minute period
- Fan in the ensuite on for a long period
- Fan in the ensuite on for a long period and the ensuite door open
- Just the ensuite door being open
- Bedroom window open and ensuite door open
- Just bathroom window ventilation
- Both doors open in the bedroom and ensuite
- Ensuite window open and both bedroom and ensuite doors open
- Fan in the ensuite on for a long period, ensuite door and bedroom window open
- Every form of ventilation (Both doors open, both windows open and the fan on for a long period)

The time it took for the humidity level to drop to a normal humidity range was analysed and graphed to determine which form of ventilation is most efficient and which were ineffective. After the shower was run for a period of 5 minutes, in each experiment, the peak humidity reached at the end of this period was in the range of 90-95%. By graphing the dissipation of the humidity level under the different ventilation conditions outlined in the above list, observations can be made regarding the performance of each ventilation method.

Figure 11 shows the graph that displays the humidity levels over time during the different ventilation conditions. It can clearly be seen from the graph that, not surprisingly, no ventilation had the highest humidity level and every form of ventilation had the lowest humidity level. The no ventilation result showed that after 8 hours the humidity level still remained around 90%. Only using the fan for ten minutes had a similar result but the final humidity level was slightly lower. The use of the fan for a long period of time had a similar humidity level after 4 hours to the ensuite door being open. However, the drop in humidity level was much quicker with the door open than with the fan. This is easily explained since the door being open can remove a much larger amount of moisture through diffusion than the fan can but its ability to reduce the relative humidity is the same. Having the fan on for long periods with the ensuite door open and having the bedroom window open with the ensuite door open also produced similar results. It is likely these results are similar since having the bedroom window open would not be as effective as having the ensuite window open. More effective ventilation conditions were just window ventilation and having the doors open and the windows open.

The results clearly show that the more forms of ventilation put in place the faster the humidity was reduced and

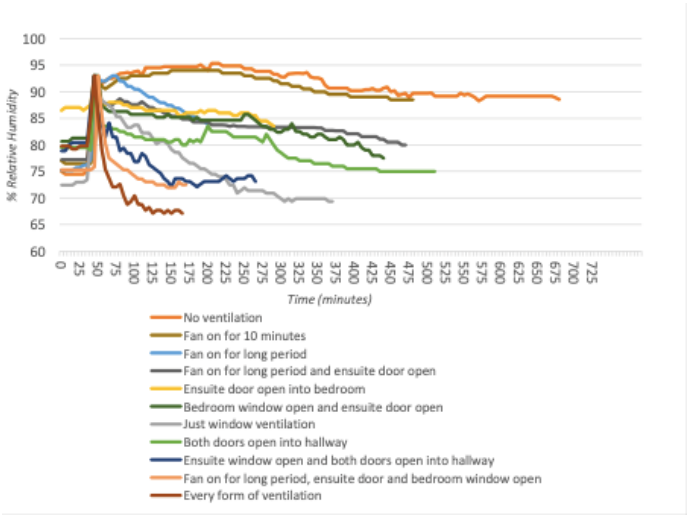

Figure 11. Humidity data from ensuite bathroom.

the level it was reduced to was lower. It was also found that just using the fan for a short period was not an effective form of ventilation to reduce humidity. Also opening the doors without opening a window was not effective since it did not remove any humidity, the humidity was just dispersed over a larger area, so the level reduces slightly. Opening the ensuite window for a lengthy period can be concluded as the single most effective ventilation form. Window ventilation as a whole can be stated as the single most effective form of ventilation as it contributes to the top three ranked methods tested as part of this experiment, but it has seriously adverse effect on thermal efficiency. In contrast, the three lowest methods rely on the extractor fan and it is seen to be very inefficient, so it can be concluded that unless the extractor fan is left on permanently it is ineffective at removing humidity.

3.4 Guidance to Home Owners

In summarising all of these strands, guidance must be given to homeowners on moving in as to how to operate their ventilation to maintain a healthy indoor air quality. To this end two flow charts were developed (one for treated surfaces, one for non-treated surfaces, Figure 12) which show what factors encourage mould growth and, therefore, what regimes should be avoided to prevent mould growth in the medium to long term.

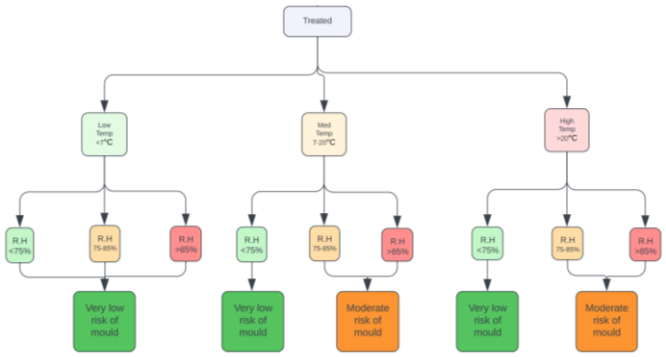

(a)

(b)

Figure 12. Flow chart to assess causes of mould growth in (a) treated and (b) non-treated surfaces in homes

4 CONCLUSIONS

This paper has provided further evidence to help understand mould growth so that the conditions that support this growth can be avoided as a solution to preventing mould growth in A-rated homes. Laboratory experiments have shown that the most important factor encouraging mould growth is the substrate type. Avoiding having hygroscopic materials in areas of high humidity is critical in the design of A-rated homes. On any suitable substrate once the threshold of humidity is reached the risk of mould growth is high. Through experimentation, this threshold level was found to be 80% and humidity levels in A-rated homes should be kept below this level to considerably reduce the risk of mould growth.

A study conducted on the indoor conditions in forty-four A-rated homes found evidence that supported the laboratory findings. It was found that homes that consistently reached a level of humidity over 80% had experienced mould growth. Also, homes that had ensuites with constant high humidity levels experienced mould growth in the master bedroom. In some of these homes, it was also found that trickle vents were blocked by the occupiers which was compounding the increase in humidity and elevated temperature levels. This shows a lack of awareness of the importance of using the ventilation as designed, especially in A-rated homes. Occupants should be informed upon arrival in an A-rated home that any vents should not be blocked to prevent mould growth and reactive mechanical ventilation should not be switched off.

The effectiveness of ventilation in reducing humidity levels was seen in the ventilation experiment. In this experiment, window ventilation was found to be far superior to intermittent extractor fan ventilation, but at a cost to thermal efficiency. It was also found that the window in the ensuite being open was often the most effective form of ventilation.

The information described in this paper is the type of information that should be provided to occupants of A-rated homes so that they clearly understand what actions increase their risk of mould growth. A-rated construction is the future of the construction sector and ventilation is an important element that needs to be carefully designed and understood so that mould growth and its associated deleterious health effects can be prevented in the future.

REFERENCES

[1] Wilson, J., (2021). "Residents living with mould and damp campaign for fast-track regeneration". The Irish Times. Irishtimes.com Accessed 1/12/21

[2] Saini, N., West, R.P. and Shiel, P. (2018). "Analysis of the effectiveness of mechanical ventilation in controlling humidity in sealed dwellings". *Proc Civil Engineering Research in Ireland conference*, UCD, Dublin (2018).

[3] Brambilla, A. and A. Sangiorgio (2020). "Mould growth in energy-efficient buildings: Causes, health implications and strategies to mitigate the risk". Renewable and Sustainable Energy Reviews **132**: 110093

[4] Lu, C., et al. (2020). "Common cold among young adults in China without a history of asthma or allergic rhinitis – associations with warmer climate zone, dampness and mould at home and outdoor PM10 and PM2.5." Science of The Total Environment: 108583

[5] Wang, J., et al. (2020). "Dampness and mould at home and work and onset of insomnia symptoms, snoring and excessive daytime sleepiness." Environment International **139**: 105692

[6] Greenspan, L. (1977). "Humidity Fixed Points of Binary Saturated Aqueous Solutions." Journal of Research of the National Bureau of Standards. Section A, Physics and Chemistry **81A**(1): 89-96.

[7] Naphade, C., Han, I., Lukubira, S., Ogale, A., Rieck, J. and Dawson, P. (2015). "Prediction of mold spoilage for soy/polyethylene composite fibers." International Journal of Polymer, vol.2015: 176826.

Effect of protective cladding on the fire performance of vertically loaded cross-laminated timber (CLT) wall panels

Muhammad Yasir[1,a], Andrew Macilwraith[1], Kieran Ruane[1]
[1]Department of Civil, Structural, and Enviromental Engineering, Munster Technological University, Ireland
[a] email : muhammad.yasir@mycit.ie

ABSTRACT: Cross-laminated timber (CLT) is a sustainable and cost-effective product for modern multi-storey timber buildings, particularly suited to residential use. The fire behaviour of sustainable materials such as timber is often a concern to both regulators, designers, and builders. In this paper, experimental fire testing of CLT panels was performed. The main aim was to analyse the fire performance of CLT wall panels made of Irish Spruce. The experimental testing was performed using the fire testing kilns in the Structural Engineering Laboratory of Munster Technological University, Cork (MTU). This series of tests consisted of four vertically loaded CLT wall panels which were tested under Standard ISO 834 Fire Testing curves. To improve the fire performance of CLT panels, different types of protective claddings were used. The effectiveness of each system of protection has been stated particularly in terms of the delay in the start of charring of the CLT panels. The location of joints in the protective cladding was also analysed and was found to be a key factor in the fall-off time of the protective claddings. The results show that protective claddings made with Gypsum Fireline plasterboard and a combination of plywood and Gypsum Fireline plasterboard delayed the charring of CLT panels by as much as 30 and 45 min respectively. This paper further analyses the detailed results of experimental fire testing, as well as measuring the charring rate and temperature distribution across the panels using thermocouples, and comparisons then being made between each tested panel.

KEYWORDS: Cross-laminated timber (CLT), fire analysis, charring rate, protective cladding.

1 INTRODUCTION

1.1 Background

Cross-laminated timber (CLT) is a multi-layer engineered timber product that has recently gained popularity as a structural member including load-bearing floor and wall panels. CLT consists of an odd number of plies with a minimum of 3 plies that are bonded together using adhesives. In cross-laminated timber, the adjacent plies are oriented orthogonally, which provides structural stability in both directions, as shown in Figure 1. CLT was developed with the idea to decrease the effect of the anisotropic behaviour of timber as well as reduce the influence of knots compared to solid timber [1].

Due to the combustible nature of timber, the study of fire performance of CLT at elevated temperatures is required to design safe, cost-effective, and resilient timber buildings. EN 1995-1-2:2004 [2] specifically focuses on the design of timber structures in fire and provides a one-dimensional design char rate of 0.65 mm/min for softwood with a density of more than 290 kg/m^3. However, the behaviour of CLT under fire can be different from solid timber and hasn't been discussed in the current version of Eurocodes. Both small and large-scale experimental tests [3–8] were performed in recent years to study the behaviour of CLT specimens in a fire. A short description and the key conclusions of these fire tests on the CLT panels are provided here. Fire tests were conducted to understand the behaviour of CLT panels and comparison were made with solid timber panels [4]. The charring rate of homogenous timber panels was found to be less than the 3-layered timber panels. Moreover, thin-layered CLT panels showed a higher charring rate compared to thicker-layered CLT panels, which confirms that the thickness and number of layers affect the fire behaviour and the char rate. No fall-off of charred layers was observed in the fire tests on CLT wall panels and hence showed good agreement with the one-dimensional charring rate for solid timber panels as well as showing better fire behaviour than floor panels [4].

Further experimental testing was conducted by Frangi et al. [5] to understand the performance of adhesive as well as the effect of thickness and number of layers on the fire resistance under the standard fire curve [6]. CLT panels were made using melamine-urea-formaldehyde (MUF), and different types of polyurethane adhesive (PUR) with different layer sizes and having an overall thickness of 60 mm. It was found that the adhesive used in the glue line between the panels affects the fire performance of CLT panels. CLT panels made with MUF adhesives show a uniform charring rate which was even less than the one-dimensional charring rate as defined in EN1995-1-2 for solid timber. All PUR glued CLT panels showed a char rate of 0.85 mm/min and 1 mm/min for 3 and 5 layered CLT panels respectively, which showed that thickness and number of layers influence the charring rate of the panel [5].

Small-scale testing was performed on lap shear test specimens to examine the delamination and the bond strength of wood adhesives at elevated temperatures in CLT [7]. It was observed that polyurethane group adhesives show a higher reduction in strength when compared to other adhesives including phenol-resorcinol formaldehyde (PRF), melamine-formaldehyde (MF), and emulsion polymer isocyanate (EPI) at elevated temperatures [7]. Three full-scale CLT floor assemblies were tested in the US with adhesives being used were PUR and MF.

A two-hour fire rating while loading was achieved. The authors found falling off of char in the assemblies bonded with PUR adhesive [8].

The charring rate of CLT samples was investigated under different heating conditions and it was found that the charring rates are dependent on the test set-up, rate of heating, orientation, and size of the sample[9]. Furthermore, it was found that the charring rate fell to a lower, quasi-steady value after it reached a peak value at the beginning which occurred in the first half-hour of the test [9]. The fire performance of CLT beams was studied by exposing them to standard fire conditions from three sides [10]. The authors concluded that the zero-strength layer from test results shows a higher value than the value given in Eurocode 5 which can be non-conservative [10]. A new charring model was developed for CLT based on different fire tests and according to the EN 1995-1-2 which was then compared with the results obtained from the fire tests [11]. The results showed that when measuring the charring depth, this model gives conservative results by approximately 5 mm [11] when compared to the Eurocode values.

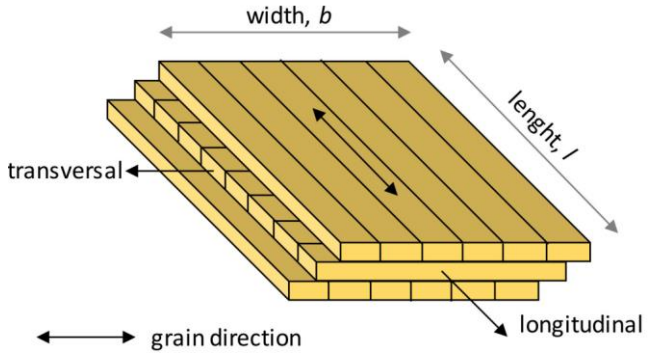

Figure 1. A three-layer CLT panel [12]

1.2 Objectives

In recent years extensive experimental testing has been performed on the fire behaviour of CLT panels in Europe and North America. However, the current research is still lagging on the fire analysis of CLT panels from Irish timber. The main aim of this research is to perform fire testing on Irish Sitka Spruce CLT wall panels. This research also focuses on the use of different types of cladding to protect the CLT panels from direct exposure to fire. The performance of different types of cladding is measured based on the time delay of charring of the CLT panel for each type of protection. Furthermore, this research also focuses on the significance of joints in the cladding, as they can be a significant factor in the fall-off of the cladding during a fire.

2 TEST METHODOLOGY

2.1 Materials

Boards of C16 Irish Sitka spruce with individual plank sizes of 150 mm wide and 40 mm thick were used to produce wall panels that were 1200 mm long and 900 mm high with an overall thickness of 120 mm. The boards used in the preparation of CLT wall panels were first stored in a conditioning room at room temperature with a relative humidity of 65 ± 5% for 8 weeks before the preparation of the specimens. One-component PUR adhesive was used with a spread rate of 160 microns/m^2 in the preparation of the CLT panels. The panels were pressed with a pressure of 600 kN/m^2 using steel plates for 2 hours. Before experimental testing, the CLT panels were placed in a conditioning room for at least 4 weeks.

2.2 Test Specimens

Overall, four three-layered CLT wall panels of Irish Spruce boards were tested, each having a moisture content of 12-13% before testing. The details of the tested wall panels are provided in Table 1. One CLT wall panel was directly exposed to fire on one side while the rest of the three panels were protected with claddings having different joint distribution. In Specimen W-15FP the exposed side of the CLT panel was protected with a 15mm Fireline gypsum plasterboard that had no joint. Similarly, specimen W-15FPJ was protected with a 15 mm fireline gypsum plasterboard but with joints along the perimeter of the panel that is exposed to fire. In specimen W-12.5FP25PW, the CLT panel was protected with a 12.5 mm Fireline plasterboard which was then protected with 25 mm of plywood. Joints were provided in both the gypsum plasterboard as well as in the plywood. Vertical and horizontal joints were placed at the centre of the gypsum plasterboard and plywood respectively. While joints were also placed at 50 mm and 30 mm along the perimeter towards the exposed side of the gypsum plasterboard and plywood respectively. The main idea of these joints was to make the protective claddings free fall during an event of a fire. These different types of CLT panels are illustrated in Figures 2 to 4. In all the test panels, the surface that is directly exposed to fire is 1000 mm * 600 mm which is represented in Figure 2.

2.3 Test setup

The wall panel was placed up against the front of the fire testing kiln, with its door open to one side. The CLT test panel was supported with steel members on the unexposed side of the panel as shown in Figures 5 to 6. The load cell on the top of the panel recorded the applied constant vertical load of 85 kN throughout the test. This load was calculated based on the assumption of a five-storey building. The load was applied using a spreader beam along the top of the panel. A strain gauge at the mid-span of the panel was placed to measure the horizontal displacement throughout the testing. The kiln was also equipped with a propane gas burner which was manually controlled to ensure the ISO-834 curve [6] was followed for heating conditions in the kiln.

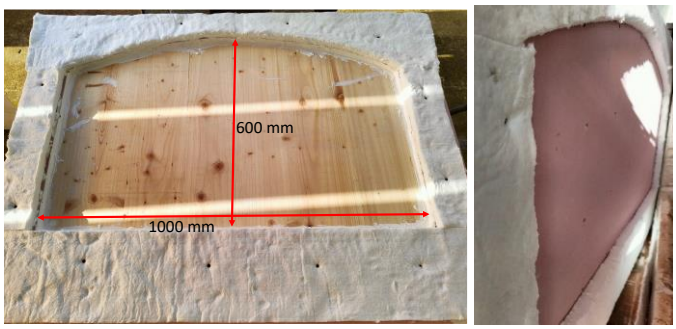

Figure 2. Left: Unprotected CLT panel (W-1), Right: CLT panel protected with 15 mm gypsum Fireline plasterboard without a joint (W-15FP)

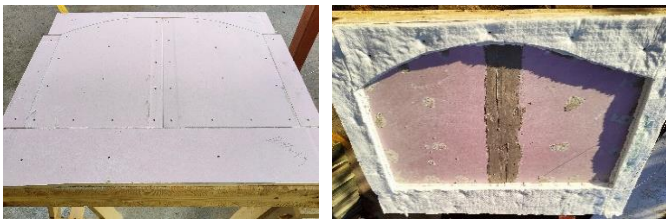

Figure 3. CLT panel protected with 15mm Fireline plasterboard with a vertical joint and a joint around the perimeter (W-15FPJ), Left: Joints are visible, Right: Joints are sealed and the panel is ready to be placed in the kiln for test

Figure 4. W-12.5FP25PW: 12.5mm gypsum fireline plasterboard placed between the CLT panel and the outer plywood layer (Left), Exposed 25mm plywood layer (Right)

Table 1. Tested CLT wall panels

Specimen Designation	Protection on the exposed side
W-1	No
W-15FP	15 mm FireLine gypsum plasterboard with no joints
W-15FPJ	15 mm FireLine gypsum plasterboard with joints
W-12.5FP25PW	12.5 mm FireLine gypsum plasterboard and 25 mm plywood with joints in both

2.4 Location of thermocouples

A plate thermocouple was used to record the temperature in the kiln during the test. Type K thermocouples were inserted from the unexposed side of the panels at different depths in drilled holes each of 2 mm diameter, to record the internal temperature distribution and the progression of the char line during fire tests. A set of three K-type thermocouples were placed at similar depths but at different locations to ascertain any variation in temperature throughout the test. The details of the thermocouple tip locations and their depths from the exposed surface are shown in Table 2.

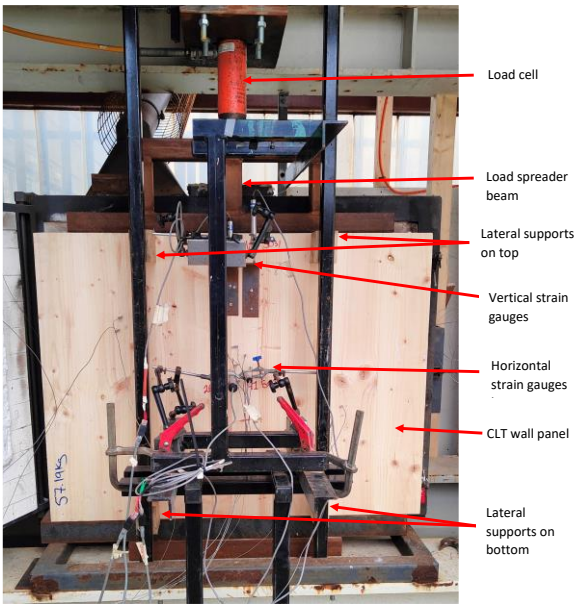

Figure 5. A test panel up against the kiln opening showing the side of the panel not exposed to fire

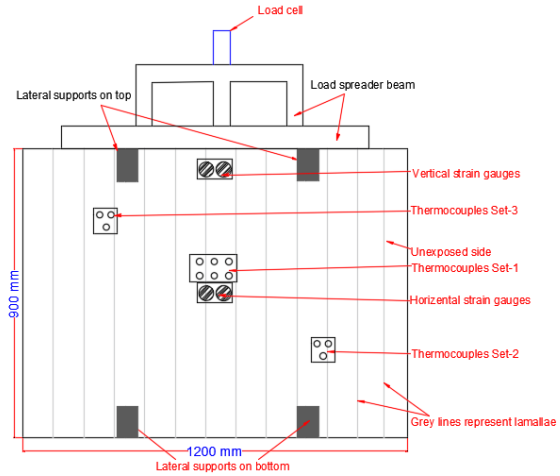

Figure 6. Drawing of the CLT panel set-up up against the kiln

3. Results

The kiln temperature recorded by the plate thermocouple and the temperatures measured at different K-thermocouples installed at various depths is shown in Figure 7. After the test was completed, the burner was stopped, and the panel was unloaded and then removed from the kiln. The panel was then cooled down using water. The overall charring rates based on the actual measurement of the charred depth and total test time of all the test panels are shown in Table 3.

Table 2. Positioning of thermocouples

Specimens	Depth of thermocouples from the exposed surface of CLT panel (mm)									
	(Set-1)				(Set-2)			(Set-3)		
	0	20	40	60	20	40	60	20	40	60
W-1	T0	T1	T2	T3	T4	T5	T6	T7	T8	T9
W-15FP	T0	T1	T2	T3	T4	T5	T6	T7	T8	T9
W-15FPJ	T0	T1	T2	T3	T4	T5	T6	T7	T8	T9
W-12.5FP25PW	T0	T1	T2	T3	T4	T5	T6	T7	T8	T9

Table 3. Measured charred depth

Specimen	Charred depth (mm)	Total test time (mins)	Charring rate (mm/min)
W-1	91	137.5	0.66
W-12.5FP	80	210	0.45
W-12.5FPJ	80	200	0.46
W-12.5FP25PW	75	156	0.67

3.1 Charring rate

The charring rate from TC-TC installed at different depths of unprotected and protected wall panels is shown in Table 4. The charring rate of the unprotected wall panel was in the range of 0.63 mm/min which is slightly lower than the one-dimensional charring rate by Eurocode 5 [2]. The application of protective cladding delayed the charring of CLT panels as well as reduced the overall charring rate. The protective cladding in W-15FP delayed the charring of the CLT panel by 30 mins. While, in W-15FPJ, the charring of the CLT panel was delayed by 25 mins. The overall delay in charring of the CLT panel was 44 mins in W-12.5FP25PW. The temperature behind the plywood reached 300˚C in 28 minutes, which shows that the 25mm plywood layer can delay the charring of the CLT panel by 28 minutes if used alone as a protective cladding.

3.2 Effect of joint location on fire performance

The effect of the joint location of protective cladding on the fire performance of the CLT panel was studied. The W-15FP panel, which had no joint in the plasterboard remained in contact with the CLT panel throughout the test. The temperature measured and recorded by the thermocouple placed between the CLT panel and plasterboard showed a lower temperature than the kiln temperature throughout the test. Thus the direct contact between the plasterboard and the CLT panel gave extra protection to the panel and consequently resulted in the lower char depth. Specimen W-15FPJ, in which the joint in the gypsum fireline plasterboard was placed at the perimeter of the exposed surface of the CLT panel and a vertical joint at the centre of the plasterboard, gave closer results to the specimen W-15FP. In the specimen W-15FPJ, the gypsum fireline plasterboard was in contact with the CLT panel throughout the test as shown in Figure 8, and thus resulted in a lower charred depth. In W-12.5FP25PW, which was protected with 12.5 mm gypsum fireline plasterboard and 25 mm plywood with joints that are exposed directly to fire, resulted in the fall off of claddings during the test. Due to the fall off of the claddings, the temperature recorded by a thermocouple placed between the plasterboard and CLT panel reached the kiln temperature resulting in a faster charring rate due to the direct exposure of the CLT panel to fire. The temperature-time curves recorded by the thermocouples which are installed between the CLT panel and the gypsum fireline plasterboard are shown in Figure 9. It can be seen from Figure 9, that in specimen W-15FP the temperature between the plasterboard and the CLT panel was less than the temperature recorded by thermocouples in W-15FPJ and W-12.5FP25PW. In specimen W-15FPJ, the temperature recorded between the plasterboard was slightly higher than the W-15FP panel at the first 2.5 hours of the test. In the W-12.5FP25P specimen, thermocouples T0A and T0B were placed either side of the plasterboard vertical joint between the plywood and the CLT panel layers and similar temperatures were recorded in these thermocouples throughout the test. However, a sharp increase in the temperature between the plasterboard and CLT panel was observed at around 120 minutes into the test and consequently, the temperature between the plasterboard and CLT panel reached to the kiln

Table 4. Charring rate of unprotected wall panels

Specimen	Charring rate delayed (min) T0, T0a, T0b		Depth of Thermocouples from the exposed surface of the CLT panels (mm)								
			Thermocouples (Set-1)			Thermocouples (Set-2)			Thermocouples (Set-3)		
			20	**40**	**60**	**20**	**40**	**60**	**20**	**40**	**60**
			T1	**T2**	**T3**	**T4**	**T5**	**T6**	**T7**	**T8**	**T9**
W-1	0	$t_{300°C}$ (min)	32	73.5	95	32	-	92.5	28.5	68	93.5
		B_{TC-TC} (mm/min)	0.63	0.48	0.93	0.63	-	0.66	0.70	0.51	0.78
		β_{panel} (mm/min)	0.63	0.54	**0.63**	0.63	-	0.65	0.70	0.59	0.64
W-15FP	30	$t_{300°C}$ (min)	91	151.5	203	105	157	-	97.5	166	209.5
		B_{TC-TC} (mm/min)	0.33	0.33	0.39	0.27	0.38	-	0.30	0.29	0.46
		β_{panel} (mm/min)	0.33	0.33	**0.35**	0.27	0.31	-	0.30	0.29	0.33
W-15FPJ	25	$t_{300°C}$ (min)	102	133	-	97	159.5	-	98.5	151	-
		B_{TC-TC} (mm/min)	0.26	0.65	-	0.28	0.32	-	0.27	0.38	-
		β_{panel} (mm/min)	0.26	**0.37**	-	0.28	0.25	-	0.27	0.32	-
W-12.5FP25P	44	$t_{300°C}$ (min)	88.5	131	150.5	99.5	139.5	-	92.5	-	-
		B_{TC-TC} (mm/min)	0.44	0.47	1.03	0.36	0.5	-	0.41	-	-
		β_{panel} (mm/min)	0.44	0.46	**0.56**	0.36	0.42	-	0.41	-	-

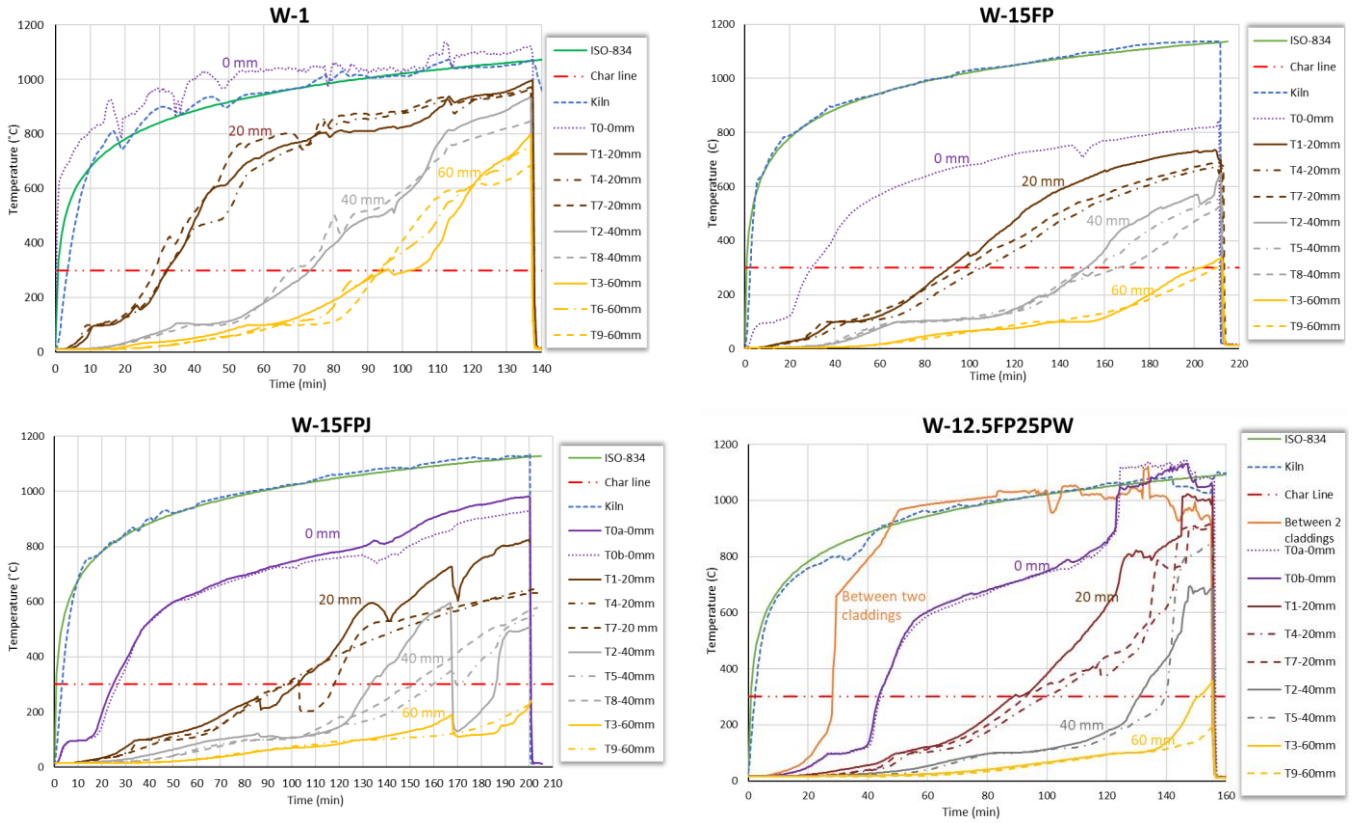

Figure 7. Temperature-time curves of test specimens at different depths

temperature which shows that the fall-off of the plasterboard occurred approximately 2 hours into the test.

The charred depth was measured in two ways. The first technique was the installation of thermocouples at the mid-depth of each layer and along the surfaces of the layers. The charring of the panel at a specific depth was considered when the temperature of the thermocouples reached 300˚C. The second method was to remove the panel from the kiln after the test has finished, cool down the specimen with water and then measure the charred depth, as shown in Figure 10. For specimen W-1, the charred rate calculated using thermocouples installed is 0.63 mm/min while the charring rate calculated after measuring the charring depth was 0.66 mm/min. For specimens W-15FP, W-15FPJ, and W-12.5FP25P, the charring depth calculated from the installed thermocouples were 0.35, 0.37, and 0.56 mm/min respectively. While the charring rate calculated after the actual measurement of charred depth was 0.44, 0.46 and 0.67 mm/min. The actual charred depth is slightly higher than the charring depth calculated from the data recorded by thermocouples due for the following reasons:

- The removal of the panel from the kiln and cooling it down takes approximately 12-15 minutes, which would give an additional charred depth.
- The actual charred depth calculation was considered at the location with the maximum char and not an average charred depth at different points.

Figure 8. Gypsum Fireline plasterboard is intact with the specimen W-15FPJ

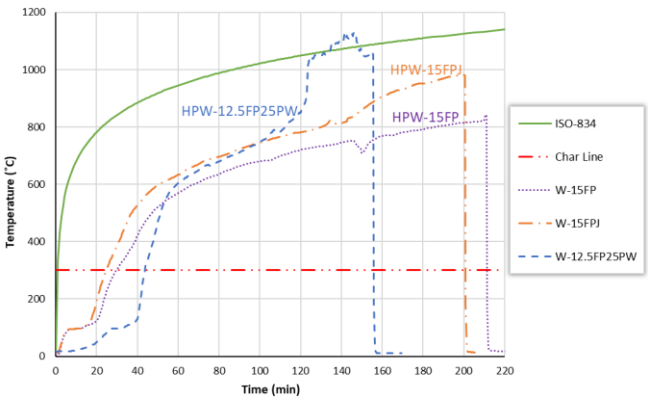

Figure 9. Temperature variation between the plasterboard and CLT panels

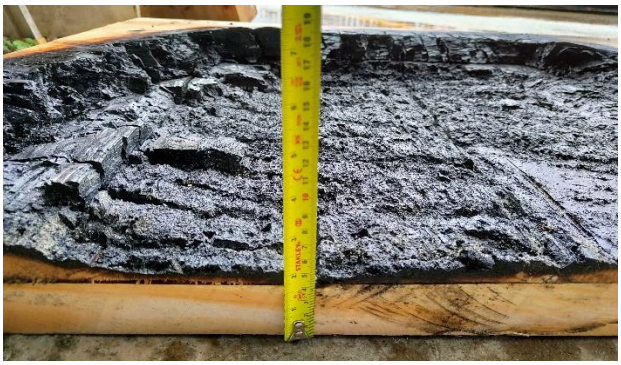

Figure 10. Measurement of uncharred depth

4. CONCLUSIONS

The following are concluded from the experimental fire testing of CLT wall panels under standard fire curve testing conditions:

- The average charring rate of the Irish-grown Sitka spruce CLT wall panel is between 0.63 and 0.65 mm/min, which closely matches the one-dimensional charring rate of 0.65 mm/min in the Eurocode 5 [2]. Thus, these one-dimensional charring rates can be used for Irish Spruce CLT panels in fire design.
- The protective cladding of 15mm gypsum Fireline plasterboard without joints delayed the charring of the CLT panel by 30 minutes, while the 15 mm gypsum Fireline plasterboard with a vertical joint in the middle and a joint along the perimeter of the exposed surface of the panel delayed the charring of CLT panel by 25 minutes. Furthermore, a total charred depth of approximately 80 mm was measured for a test duration of 200 minutes and 210 minutes for a CLT panel with joints and without joints in the gypsum Fireline plasterboard respectively.
- The CLT wall panel which was protected with a combination of 12.5 mm Fireline plasterboard and 25 mm plywood delayed the charring of the CLT panel by 45 minutes. However, in this test, both joints in the protective cladding layers were exposed to fire causing these claddings to fall off during the test. Due to the fall off of protective claddings, the overall charring rate of the CLT panel at the end of the test was 0.67 mm/min which is higher than the other two protected CLT panels.
- The experimental testing in this paper shows that joints in the protective cladding system reduce the fire performance of CLT wall panels. Joints in the protective claddings need to be avoided at the location of significant importance such as in the vicinity of columns and beams, or any other load-bearing components.

ACKNOWLEDGMENTS

The MODCONS Project is a joint project between the Timber Engineering Research Group at the National University of Ireland Galway and Munster Technological University focused on increasing the knowledge and use of timber in modular construction. The MODCONS Project is funded by the Department of Agriculture, Food and the Marine Competitive Research Funding Programmes (Project Ref: 2019R471).

REFERENCES

[1] P. Mestek and H. Kreuzinger, ‘Design of Cross Laminated Timber (CLT)’, p. 8.

[2] ‘European Committee for Standardisation (CEN). Eurocode 5. Design of timber structures. Part 1-2: General – Structural fire design; EN1995-1-2. Brussels, Belgium, 2004.’

[3] J. Schmid, J. Konig, and J. Kohler, ‘Fire-exposed cross-laminated timber-modelling and tests’. World Conference on Timber Engineering, 2010.

[4] A. Frangi, M. Fontana, M. Knobloch, and G. Bochicchio, ‘Fire behaviour of cross-laminated solid timber panels’, *Fire Saf. Sci.*, vol. 9, pp. 1279–1290, 2008, doi: 10.3801/IAFSS.FSS.9-1279.

[5] A. Frangi, M. Fontana, E. Hugi, and R. Jübstl, ‘Experimental analysis of cross-laminated timber panels in fire’, *Fire Safety Journal*, vol. 44, no. 8, pp. 1078–1087, Nov. 2009, doi: 10.1016/j.firesaf.2009.07.007.

[6] ISO 834 (1999). Fire-resistance tests. Elements of building construction. Part 1: General requirements. International Organization for Standardization, Geneva, Switzerland.

[7] B. Miyamoto, N. J. Bechle, D. R. Rammer, and S. L. Zelinka, ‘A Small-Scale Test to Examine Heat Delamination in Cross Laminated Timber (CLT)’, *Forests*, vol. 12, no. 2, p. 232, Feb. 2021, doi: 10.3390/f12020232.

[8] Muszyński, L., Gupta, R., Hong, S. H., Osborn, N., & Pickett, B. (2019). Fire resistance of unprotected cross-laminated timber (CLT) floor assemblies produced in the USA. Fire Safety Journal, 107, 126–136. https://doi.org/10.1016/j.firesaf.2018.12.008

[9] L. Bisby, ‘Analysis of Cross-Laminated Timber Charring Rates upon Exposure to Non-standard Heating Conditions’, p. 16.

[10] R. Dârmon and O. Lalu, ‘The fire performance of Cross Laminated Timber beams’, *Procedia Manufacturing*, vol. 32, pp. 121–128, 2019, doi: 10.1016/j.promfg.2019.02.192.

[11] M. Klippel and J. Schmid, ‘Design of Cross-Laminated Timber in Fire’, Structural Engineering International, vol. 27, no. 2, pp. 224–230, May 2017, doi: 10.2749/101686617X14881932436096.

[12] Sandoli, A.; D’Ambra, C.; Ceraldi, C.; Calderoni, B.; Prota, A. Sustainable Cross-Laminated Timber Structures in a Seismic Area: Overview and Future Trends. Appl. Sci. 2021, 11, 2078. https://doi.org/10.3390/app11052078

Dowel Laminated Timber Elements Manufactured using Compressed Wood Dowels

Conan O'Ceallaigh[1], Annette M. Harte[1], Patrick J. McGetrick[1]
[1]College of Science and Engineering & Ryan Institute, National University of Ireland Galway, University Road, Galway, Ireland
Email; conan.oceallaigh@nuigalway.ie, annette.harte@nuigalway.ie, patrick.mcgetrick@nuigalway.ie

ABSTRACT: In recent years, there has been an increased focus on the environmental impacts of construction and a movement towards more sustainable construction products. The use of timber as a structural material has grown and it has been deemed to be one of the leading materials of choice in the future as a sustainable construction product that not only has a low carbon footprint but also acts as a carbon store for the lifetime of the structural component. To further improve the environmental performance of timber construction, it is beneficial to reduce the use of adhesives, particularly when manufacturing laminated engineered wood products. This study numerically investigates the structural behaviour of dowel laminated timber (DLT) elements which are laminated with compressed wood dowels instead of adhesives. A parametric study is carried out to examine the influence of dowel diameter and spacing on the stiffness and maximum load capacity of the DLT members. The numerical model incorporates orthotropic, linear elastic materials in tension and linear elastic-plastic materials in compression. Furthermore, damage initiation criteria in the respective material directions are utilised to determine the failure behaviour of the structural elements. The results show that the dowel diameter and spacing have a significant influence on the maximum load capacity and stiffness of the DLT members. The predicted failure behaviour of the numerical model comprises a combination of dowel bending, dowel-timber embedment and tensile fracture of the bottom tensile laminate. The numerical model will allow for an optimised dowel arrangement to be manufactured and experimentally tested.

KEYWORDS: Compressed wood dowels; Dowel Laminated Timber (DLT); Engineered Wood Products; Numerical modelling; Parametric study.

1 INTRODUCTION

The construction industry has seen an increased focus in recent years on global warming and the impact of human activities on the built environment. This has mobilised the industry to achieve new standards in environmental performance for our buildings as the construction industry aims to reduce its carbon footprint. It is not surprising that a considerable body of research into the development of timber structures as a sustainable alternative to steel and concrete has occurred in recent years. Many studies have investigated different technologies and materials to develop highly engineered timber products or engineered wood products (EWPs) that can achieve significant load-bearing capacity and stiffness allowing timber buildings to achieve new heights [1,2].

Timber is one of the oldest building materials and is naturally renewable when sustainably grown. As a result, timber is set to be the leading material of choice in the future as a sustainable construction product that not only has a low carbon footprint but also acts as a carbon store for the lifetime of the structural component. One of the significant advances in engineered wood technology has been glued laminating technology to form products such as glulam and cross-laminated timber (CLT), which comprises adhesively bonded timber boards to form a robust, reliable engineered wood panel product that can be used in floor, roof and wall applications [2–6]. The purpose of this research is to investigate the use of dowel laminating technology to form connections between adjacent timber laminations. The process typically involves the use of hardwood dowels positioned within drilled holes to form a tight fit connection between adjacent laminations as shown in Figure 1-1 The use of such technology has been successfully utilised to form dowel laminated timber (DLT) panels and beams using a variety of different species [7–10]. The use of such technology ultimately reduces the use of adhesives in EWPs and further improves the environmental credentials. The efficiency of the connection is reduced when compared to adhesively bonded EWPs and as such, it is important to understand the parameters that affect the strength and stiffness of such connections and the ultimate strength and stiffness of the developed DLT product.

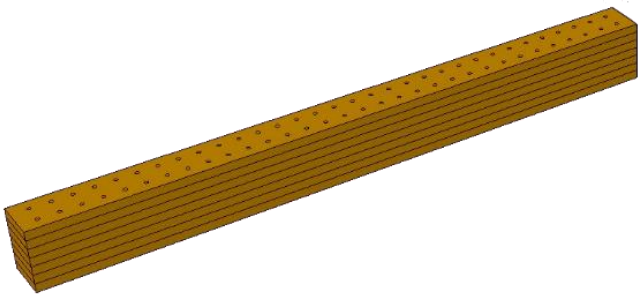

Figure 1-1. Typical dowel laminated timber (DLT) beam connected with hardwood timber dowels.

In this study, the use of compressed timber dowels is explored as a potential alternative to hardwood dowels. Compressed wood (CW) dowels are made from softwoods, which are compressed under heat and pressure to enhance their structural properties, and have been shown to have excellent properties when used in timber connections [11–14]. A finite element (FE) model is developed to predict the structural behaviour of DLT beams utilising CW dowels. The numerical model is developed in Abaqus software and utilises a UMAT

subroutine based on the Hashin damage model to determine the damage initiation criteria within the timber boards and the CW dowels. The model has been formulated to consider damage in the longitudinal direction or along the grain of the timber and in the perpendicular to the grain direction separately. Additionally, the failure criteria under tension and compression are treated differently to accurately model the behaviour of timber under such loading modes and to determine the failure behaviour of the simulated EWPs.

2 DOWEL LAMINATED TIMBER

2.1 Introduction

The use of dowel laminated technology has been the subject of a number of studies in recent years as an alternative to glued laminating technology to further improve the environmental performance of EWPs [7–10,15–19]. There have been significant advances in this technology and a number of commercial products are available and in use in several large timber structures across the world [7,20].

In this study, Sitka spruce timber grown in Ireland is used as the primary structural material and the influence of a series of design parameters, namely, dowel diameter and dowel spacing, on the structural behaviour of a DLT beam is investigated.

Three dowel diameters, 10 mm, 15 mm and 20 mm and three dowel spacing distances of 50 mm, 75 mm and 100 mm will be examined using a numerical model to determine the structural behaviour. The naming convention of each specimen is presented in Table 1.

Table 1. Numerical models and design parameters

Numerical model Specimen	Dowel Diameter (mm)	Dowel Spacing (mm)
DLT-D10-S50	10	50
DLT-D15-S50	15	50
DLT-D20-S50	20	50
DLT-D10-S75	10	75
DLT-D15-S75	15	75
DLT-D20-S75	20	75
DLT-D10-S100	10	100
DLT-D15-S100	15	100
DLT-D20-S100	20	100

2.2 Beam geometry

The beam geometry under investigation in this study is presented in Figure 2-1. The beam comprises three timber laminations measuring 1140 mm in length and a cross-section of 20 mm x 60 mm. The three timber laminations are combined to form a final cross-section of 60 mm x 60 mm and a length of 1140 mm with the dowel diameter and spacing varying as presented in Table 1. The specimen geometry was chosen based on the criteria for the bending test specified in EN 408 [21]. This test standard specifies four-point bending over a test span of 18 times the specimen depth. As a result, the test specimen is supported over a test span of 1080 mm with point loads at 360 mm from each support. Steel plates (60 mm x 30 mm x 10 mm) are positioned at the support points and load points as specified by EN 408 [21]. As seen in Figure 2-1, the midspan of each beam is represented by a red dotted line. It is at this location that the global vertical displacement of the beam is determined for a given load until failure occurs.

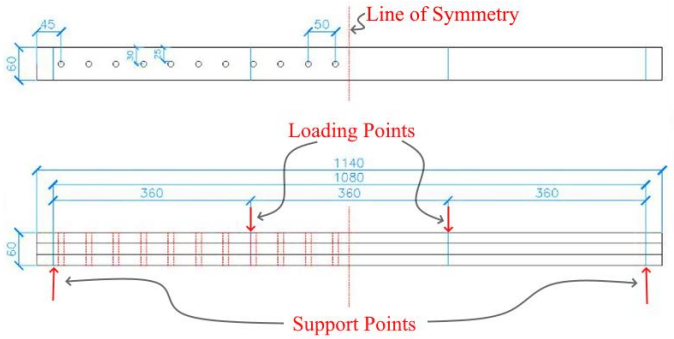

Figure 2-1. DLT geometry for the 10mm diameter dowels and the dowel spacing of 50mm (DLT-D10-S50). Dimensions in mm.

2.3 Timber

For the purpose of this study, Sitka spruce, grown in Ireland, is the primary material under investigation. The timber material is modelled as an orthotropic elastic material in Abaqus FEA software. The Sitka spruce material tested experimentally by O'Ceallaigh et al. [22–24] was graded to strength class C16. The standard EN 338 [25] provides a mean value of 8000 MPa for the elastic modulus of C16 timber in the longitudinal direction; however, it was experimentally determined by O'Ceallaigh et al. [22–24] that a longitudinal elastic modulus of 9200 N/mm^2 is more representative of the actual elastic properties. For simplicity, the radial and tangential properties were assumed to be equal and the tangential value has been selected for the material properties perpendicular to the grain. The tangential elastic moduli (radial and tangential) directions were not measured experimentally; however, Bodig & Jayne [26] expressed a general relationship between the elastic modulus, E and shear modulus, G in the three material directions. Although these ratios are not without their inaccuracies, they are widely accepted for modelling the orthotropic properties of timber.

2.4 Compressed wood dowels

Typically, hardwood dowels have been used in the manufacture of DLT products, however, in this study, compressed wood dowels are used. CW is a type of modified wood material that has been shown to have superior structural properties to natural timber and has proved to be an environmentally friendly alternative to metallic fasteners in timber connections [12,14,27–29]. The compressed wood used in this study was produced by a process of thermo-mechanical compression of softwood timber to increase its density, strength, stiffness, hardness and to reduce its porosity [30,31].

Compressed wood in the form of dowels showed good properties when tested in shear and when compared with other standard hardwood dowels and their use in DLT elements is of interest to the industry [31]. The modification process involves a simultaneous increase in temperature and the application of pressure. As the temperature increases, the timber may be easily compressed reducing the void space between the cell walls, increasing the density significantly and improving many structural properties of the timber. As the density of the timber is increased, a proportional improvement in stiffness, yield load and maximum load is expected. However, in contrast, the plastic modulus has been shown to decrease in some species

[32]. The compressed wood, with enhanced structural properties compared to standard hardwood dowel, also has a spring-back or shape-recovery property that means it will expand over time resulting in a tight fit connection that may be a beneficial characteristic in many structural timber engineering applications, particularly DLT beams and panels [33].

3 NUMERICAL MODELING

3.1 Finite element formulation

In this section, the constitutive model used to simulate the failure behaviour of Sitka spruce DLT members fastened with CW dowels is presented. A three-dimensional finite element model is developed, incorporating a UMAT subroutine to determine the total strain and associated damage experienced in timber elements when subjected to external loading. The elastic component of the timber, CW dowels and steel plates follows the generalised Hooke's law. The material behaviour of the timber and CW dowels are assumed to be orthotropic with a stronger and stiffer response along the fibre direction and reduced properties perpendicular to the grain. The material properties for both the timber and CW are presented in Table 2. For simplicity, the radial and tangential directions of the timber are considered equal in this model. The subscript '*L*' and '*T*' represent the longitudinal and transverse materials directions for timber. E_L and E_T represent the elastic modulus in the longitudinal or parallel to the grain direction and the transverse or perpendicular to the grain direction, respectively. G_{LT} and G_{TT} are the shear moduli and v_{LT} and v_{TT} are the Poisson's ratios.

Similar to the elastic properties, the strength characteristics are also assumed to be orthotropic. The values are presented in Table 2 with superscripts '*t*' and '*c*' which refer to the tension and compression, respectively. For example, $\sigma_L{}^t$ represents the value of the longitudinal failure stress when loaded in tension. The shear failure stress, τ_{LT} is also presented. G_T and G_L represent the fracture energies in the transverse and longitudinal directions, respectively and to improve convergence, a viscosity parameter, η is utilised in the user subroutine to regularise the damage variables and control the rate of damage.

$$f_L = \sqrt{\frac{\varepsilon_{11}^t}{\varepsilon_{11}^c}(\varepsilon_{11})^2 + \left(\varepsilon_{11}^t - \frac{(\varepsilon_{11}^t)^2}{\varepsilon_{11}^c}\right)\varepsilon_{11}} > \varepsilon_{11}^t \quad (1)$$

where

$$\varepsilon_{11}^t = {\sigma_L^t}/{C_{11}};\ \varepsilon_{11}^c = {\sigma_L^c}/{C_{11}} \quad (2)$$

where *Cij* are the components of the elastic matrix in the undamaged state. When Eq. (1) is satisfied, the damage variable d_L is determined according to Eq. (3).

$$d_L = 1 - \frac{\varepsilon_{11}^t}{f_L} e^{(-C_{11}\varepsilon_{11}^t(f_L - \varepsilon_{11}^t)L_c/G_L)} \quad (3)$$

where L_C and G_L are the characteristic element length and the fracture energy, respectively.

The corresponding equations for the perpendicular to the grain direction are produced similarly in Eqs. (4), (5) and (6),

$$f_T = \sqrt{\frac{\varepsilon_{22}^t}{\varepsilon_{22}^c}(\varepsilon_{22})^2 + \left(\varepsilon_{22}^t - \frac{(\varepsilon_{22}^t)^2}{\varepsilon_{22}^c}\right)\varepsilon_{22} + \left(\frac{\varepsilon_{22}^t}{\varepsilon_{12}^\tau}\right)^2(\varepsilon_{12})^2} > \varepsilon_{22}^t \quad (4)$$

where

$$\varepsilon_{22}^t = {\sigma_T^t}/{C_{22}};\quad \varepsilon_{22}^c = {\sigma_T^c}/{C_{22}};\quad \varepsilon_{12}^\tau = {\tau_{LT}^t}/{C_{44}} \quad (5)$$

When Eq. (4) is satisfied, the damage variable d_T is determined according to Eq. (6).

$$d_T = 1 - \frac{\varepsilon_{22}^t}{f_T} e^{(-C_{22}\varepsilon_{22}^t(f_T - \varepsilon_{22}^t)L_c/G_T)} \quad (6)$$

The occurrence of damage is established when the elastic matrix is updated to form an effective elasticity matrix (C_d) which has terms reduced by including the two damage variables d_L and d_T as shown in Eq. (7).

$$C_d = \begin{bmatrix} (1-d_L)C_{11} & (1-d_L)(1-d_T)C_{12} & (1-d_L)C_{13} & 0 & 0 & 0 \\ & (1-d_T)C_{22} & (1-d_T)C_{23} & 0 & 0 & 0 \\ & & C_{33} & 0 & 0 & 0 \\ & Symmetric & & (1-d_L)(1-d_T)C_{44} & 0 & 0 \\ & & & & C55 & 0 \\ & & & & & C66 \end{bmatrix} \quad (7)$$

The damage initiation criteria utilised in this model are based on the Hashin damage model which has been utilised in a series of studies to determine the failure behaviour of timber elements [34–38]. The damage initiation criteria are expressed in terms of strains and are treated differently for tension and compression strains however, one affects the other and if the strains are significant and cause partial or full damage (damage variable greater than zero) both tensile and compressive responses are affected. For example, damage in the longitudinal direction is initiated when the following criterion is achieved.

In the user subroutine, the stresses are then updated according to Eq. (8)

$$\sigma = C_d : \varepsilon \quad (8)$$

The differentiation of the above equation is used to determine the Jacobian matrix as presented in Eq. (9).

$$\frac{\partial \sigma}{\delta \varepsilon} = C_d + \frac{\delta C_d}{\delta \varepsilon} : \varepsilon$$

$$= C_d + \left(\frac{\delta C_d}{\delta d_T} : \varepsilon\right)\left(\frac{\delta d_T}{\delta f_T}\frac{\delta f_T}{\delta \varepsilon}\right) + \left(\frac{\delta C_d}{\delta d_L} : \varepsilon\right)\left(\frac{\delta d_L}{\delta f_L}\frac{\delta f_L}{\delta \varepsilon}\right) \quad (9)$$

Furthermore, to improve the convergence, a viscosity parameter, η is utilised in the user subroutine to regularise the damage variables and control the rate of damage using the following Eqs (10) and (11).

$$\dot{d}_L^r = \frac{1}{\eta}(d_L - d_L^r) \quad (10)$$

$$\dot{d}_T^r = \frac{1}{\eta}(d_T - d_T^r) \quad (11)$$

where all parameters are as presented before but the superscript 'r' indicates regularised and the accent '˙' indicates rate. The regularised damage variable is updated for each time step in the analysis.

4 FINITE ELEMENT MODEL

This section presents the development of the model in Abaqus FEA software.

4.1 Model Geometry

The geometry of the DLT members, which are subjected to four-point bending in accordance with EN 408 [21], has been modelled in Abaqus FE software. As presented in Figure 4-1, the model utilises half symmetry to reduce the number of elements and computational time to solve the model. A symmetric boundary condition (BC) at the midspan is used to achieve this. The DLT member is supported on a steel plate (60 mm x 30 mm x 10 mm) at one end to represent the support condition. As this end support is simply supported, the plate is free to rotate about its central axis. A similar steel plate is also used to apply the vertical load on the top surface of the DLT beam. In relation to the steel-timber interaction, hard contact is defined between the surface of the beam and the steel plates with a tangential friction coefficient of 0.4. Each DLT member in this study comprises three laminations, each of which are assigned material properties in an orthotropic coordinate system. In relation to the timber-timber interaction between each timber lamination, again, hard contact is defined with a tangential friction coefficient of 0.4.

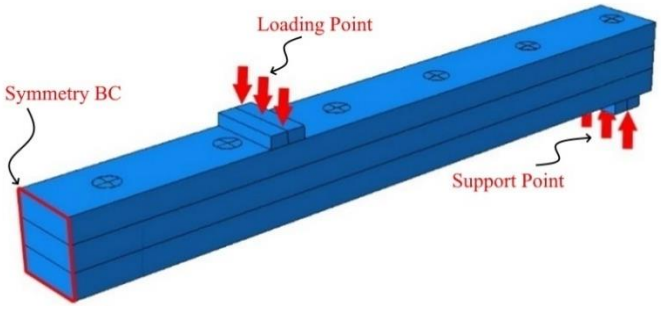

Figure 4-1. Numerical model geometry subjected to four-point bending utilising half symmetry (DLT-D20-S100).

The only differences in the developed models are the dowel diameter and spacing. DLT-D20-S100 is presented in Figure 4-1 and has a dowel diameter of 20 mm and a dowel spacing of 100 mm. The CW dowel-timber interaction is assumed to be similar to the timber-timber interaction, which is a conservative assumption in the absence of more experimental data.

The models were subjected to a mesh sensitivity study prior to performing the parametric study to provide accurate results in a reasonable time frame. All components in the model were meshed with 8-noded C3D8 elements.

4.2 Material data

The material data used in this model for the timber and the CW dowels are presented in Table 2. The steel plates are modelled as linear elastic material with an elastic modulus of 210 GPa and a Poisson's ratio of 0.3. The timber material properties presented in Table 2 are based on a study by O'Ceallaigh et al. [22–24] and the material properties of the CW dowel material are based on findings by O'Ceallaigh et al. [13,30].

Table 2. FEM UMAT Material properties

Property	Timber	CW Dowels	Unit
E_L	9222	28000	MPa
E_T	663	2240	MPa
G_{LT}	659	2000	MPa
G_{TT}	66	200	MPa
ν_{LT}	0.038	0.48	-
ν_{TT}	0.558	0.35	-
σ_L^t	24	130	MPa
σ_L^c	36	130	MPa
σ_T^t	3	80	MPa
σ_T^c	6.3	80	MPa
τ_{LT}	6.9	6.9	MPa
G_T	30	30	N/mm
G_L	60	60	N/mm
η	0.0001	0.0001	-

The definition of the symbols and the notation has been presented in Section 3.1.

5 NUMERICAL RESULTS

In this section, the results of the numerical simulation of the DLT specimens are presented. The load-displacement behaviour simulated by the numerical model is presented along with the maximum load (F_{max}) from each model, the displacement at maximum load and the elastic modulus. The elastic modulus is determined on the linear proportion of the graph between 10% and 40% of the maximum load. These results are presented in Table 3.

Table 3. Numerical model results

Numerical Model Specimen	F_{max} (N)	Displacement (mm)	Elastic modulus (N/mm^2)
DLT-D10-S50	6829	52.2	4517
DLT-D15-S50	6818	57.2	4662
DLT-D20-S50	6245	57.4	4233
DLT-D10-S75	6234	50.3	4120
DLT-D15-S75	6262	46.6	4277
DLT-D20-S75	6058	47.9	4227
DLT-D10-S100	5870	47.2	3910
DLT-D15-S100	6130	48.8	4222
DLT-D20-S100	5943	47.9	4187

The numerical model simulated the load-displacement curves with failure modes comprising a combination of dowel bending, dowel-timber embedment and tensile fracture of the

bottom tensile laminate. The results are graphically presented in Figure 5-1, Figure 5-2 and Figure 5-3 for the dowel diameter of 10 mm, 15 mm and 20 mm, respectively. In each figure, a line indicated as 'Glulam' represents the theoretical stiffness of a glued beam with an elastic modulus of 9200 N/mm^2 to allow for comparison with the stiffness of the DLT members. In Figure 5-1, it is clear that decreasing the spacing between the 10 mm dowels has a positive impact on strength and stiffness. Reducing the spacing from 100 mm to 50 mm results in an increase in strength and stiffness of 16% and 15% respectively.

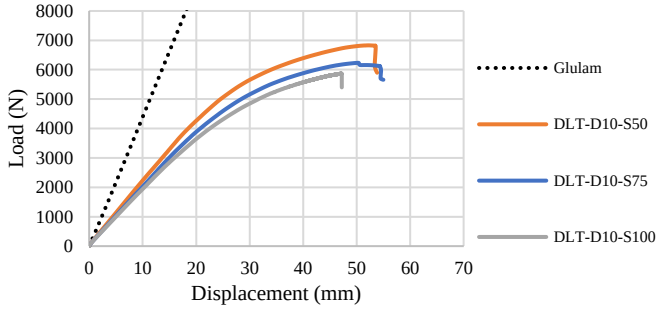

Figure 5-1. Numerical load-displacement curves for specimens with 10 mm diameter dowels (D-10 Series).

When the dowel diameter is increased to 15 mm, as seen in Figure 5-2, an improvement in strength and stiffness was observed for each dowel spacing studied. The influence of dowel spacing was not as significant as was observed for the 10 mm dowels with increases of 11% and 10% in strength and stiffness, respectively.

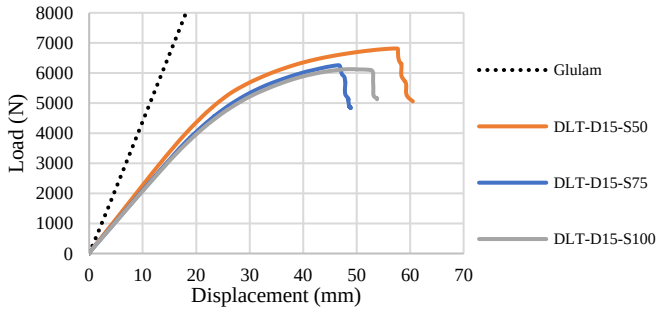

Figure 5-2. Numerical load-displacement curves for specimens with 15 mm diameter dowels (D-15 Series).

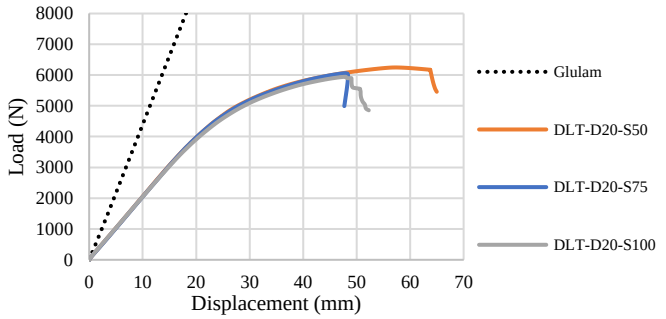

Figure 5-3. Numerical simulated load-displacement curves for specimens with 20 mm diameter dowels (D-20 Series).

Finally, for the 20 mm dowels, presented in Figure 5-3, very consistent load-displacement behaviour was observed. However, increasing the dowel diameter to 20 mm has a negative influence on the strength and stiffness. The results indicate that load-displacement behaviour is governed by the timber substrate and further studies should examine the effect for larger cross-sections.

5.1 Influence of dowel diameter and spacing

The influence of dowel spacing for all specimens studied can be seen in Figure 5-4 and Figure 5-5. In Figure 5-4, it can be seen that the 50 mm spacing provided the highest loads for the 10mm and 15 mm dowel diameters but this reduced for the 20 mm dowels. This may be an issue with reduced edge distances and may not be the case for larger cross-sections.

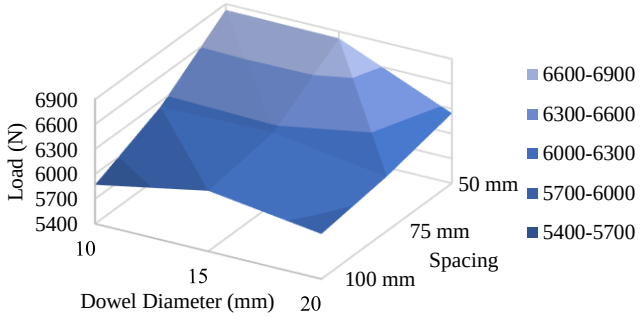

Figure 5-4. The influence of dowel diameter and dowel spacing on maximum load (F_{max}).

In Figure 5-5, the influence of dowel diameter and spacing on the observed elastic modulus for all specimens studied can be seen. It is clear that as the dowel diameter is increased from 10 mm to 15 mm, there was a positive influence on elastic modulus and associated stiffness of the DLT beam. The maximum stiffness was observed for the 15 mm CW dowels with a spacing of 50 mm.

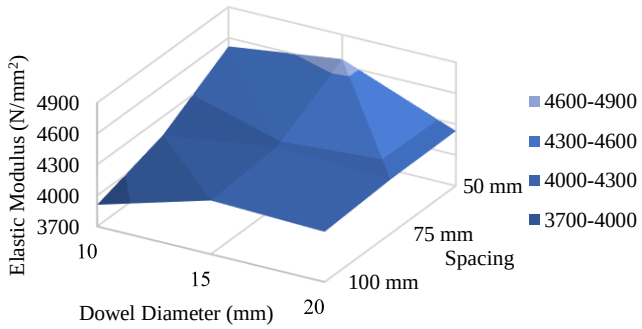

Figure 5-5. The influence of dowel diameter and dowel spacing on elastic modulus.

6 CONCLUSION

The numerical model results for DLT members connected using CW dowels have been presented for dowel diameters of 10 mm, 15 mm, and 20 mm with spacings arrangements of 50 mm, 75 mm and 100 mm.

Typically, increasing the dowel diameter and reducing the dowel spacing have a positive influence on strength and stiffness. This was true for the 10 mm and 15 mm dowel diameters. However, the 20 mm dowels appear to have very consistent behaviour for all spacing arrangements examined, their strength and stiffness values were less than those of the 15 mm dowels. Further studies should examine the effect of larger cross-sections and the influence of edge spacing and end distances on such members.

When examining the load-displacement behaviour, in all cases, it was clear that the spacing had less of an effect on the strength and stiffness as the dowel diameter increased. Further work is required to compare the numerical model to experimental results and utilise the model to further optimise the design of DLT members from Irish grown Sitka spruce and CW dowels.

ACKNOWLEDGEMENTS

The authors would like to acknowledge the support and funding of the Department of Agriculture, Food and the Marine's Competitive Research Funding Programmes, Project Ref: 2019R471 (MODCONS).

REFERENCES

[1] Harte AM. Mass timber – the emergence of a modern construction material. J Struct Integr Maint 2017;2:121–32. doi:10.1080/24705314.2017.1354156.

[2] Brandner R, Flatscher G, Ringhofer A, Schickhofer G, Thiel A. Cross laminated timber (CLT): overview and development. Eur J Wood Wood Prod 2016;74:331–51. doi:10.1007/s00107-015-0999-5.

[3] O'Ceallaigh C, Sikora K, Harte AM. The Influence of Panel Lay-Up on the Characteristic Bending and Rolling Shear Strength of CLT. Buildings 2018;8:15. doi:10.3390/buildings8090114.

[4] Schickhofer G, Brandner R, Bauer H. Introduction to CLT - Product Properties, Strength Classes. Stockholm, Sweden: 2016.

[5] Harte A, McPolin D, Sikora K, O'Neill C, O'Ceallaigh C. Irish Timber – Characterisation, Potential and Innovation. Proc. Civ. Eng. Res. Irel., Belfast, 28-29 August, 2014: 2014, p. 63–8.

[6] Harris R, Ringhofer A, Schickhofer G. Focus Solid Timber Solutions - European Conference on Cross Laminated Timber (CLT). The University of Bath, Bath: The University of Bath; 2013.

[7] StructureCraft. Dowel Laminated Timber (DLT) - Design and Profile Guide. USA: StructureCraft; 2019.

[8] Thoma A, Jenny D, Helmreich M, Gandia A, Gramazio F, Kohler M. Cooperative Robotic Fabrication of Timber Dowel Assemblies. Res. Cult. Archit., Berlin, Boston: Birkhäuser; 2019, p. 77–88. doi:10.1515/9783035620238-008.

[9] El-Houjeyri I, Thi VD, Oudjene M, Khelifa M, Rogaume Y, Sotayo A, et al. Experimental investigations on adhesive free laminated oak timber beams and timber-to-timber joints assembled using thermo-mechanically compressed wood dowels. Constr Build Mater 2019;222:288–99.

[10] O'Loinsigh C, Oudjene M, Ait-Aider H, Fanning P, Pizzi A, Shotton E, et al. Experimental study of timber-to-timber composite beam using welded-through wood dowels. Constr Build Mater 2012;36:245–50. doi:10.1016/j.conbuildmat.2012.04.118.

[11] Mehra S, O'Ceallaigh C, Hamid-Lakzaeian F, Guan Z, Harte AM. Evaluation of the structural behaviour of beam-beam connection systems using compressed wood dowels and plates. In. Proc. WCTE 2018 - World Conf. Timber Eng., Seoul, Rep. of Korea, August 20-23, 2018: 2018.

[12] Mehra S, Mohseni I, O'Ceallaigh C, Guan Z, Sotayo A, Harte AM. Moment-rotation behaviour of beam-column connections fastened using compressed wood connectors. SWST 62 nd Int. Conv. Renew. Mater. Wood-based Bioeconomy, 2019, p. 2019.

[13] O'Ceallaigh C, McGetrick P, Harte AM. The Structural Behaviour of Compressed Wood Manufactured using Fast-grown Sitka Spruce. WCTE 2021 - World Conf. Timber Eng., Santiago, Chile: 2021.

[14] Mehra S, O'Ceallaigh C, Sotayo A, Guan Z, Harte AM. Experimental investigation of the moment-rotation behaviour of beam-column connections produced using compressed wood connectors. Constr Build Mater 2022;331:127327. doi:10.1016/j.conbuildmat.2022.127327.

[15] Plowas W, Bell T, Hairstans R, Williamson JB. Understanding the compatibility of UK resource for dowel laminated timber construction. TH Build Constr 2015:1–12.

[16] O'Loinsigh C, Oudjene M, Shotton E, Pizzi A, Fanning P. Mechanical behaviour and 3D stress analysis of multi-layered wooden beams made with welded-through wood dowels. Compos Struct 2012;94:313–21. doi:10.1016/j.compstruct.2011.08.029.

[17] Sotayo A, Bradley D, Bather M, Sareh P, Oudjene M, El-Houjeyri I, et al. Review of state of the art of dowel laminated timber members and densified wood materials as sustainable engineered wood products for construction and building applications. Dev Built Environ 2020;1:100004. doi:10.1016/j.dibe.2019.100004.

[18] Oudjene M, Khelifa M, Segovia C, Pizzi A. Application of numerical modelling to dowel-welded wood joints. J Adhes Sci Technol 2010;24:359–70. doi:10.1163/016942409X12541266699473.

[19] Guan Z, Sotayo A, Oudjene M, Houjeyri I El, Harte A, Mehra S, et al. Development of Adhesive Free Engineered Wood Products – Towards Adhesive Free Timber Buildings. Proc. WCTE 2018 World Conf. Timber Eng. Seoul, Rep. Korea, August 20-23, 2018, 2018.

[20] ETA-13/0785. European Technical Approval. Solid wood slab element - element of dowel jointed timber boards to be used as a structural elements in buildings. ETA-Denmark, Nordhavn, Denmark: 2013.

[21] CEN. EN 408. Timber structures - Structural timber and glued laminated timber - Determination of some physical and mechanical properties. Comité Européen de Normalisation, Brussels, Belgium: 2012.

[22] O'Ceallaigh C, Sikora K, McPolin D, Harte AM. An investigation of the viscoelastic creep behaviour of basalt fibre reinforced timber elements. Constr Build Mater 2018;187:220–30. doi:10.1016/j.conbuildmat.2018.07.193.

[23] O'Ceallaigh C, Sikora K, McPolin D, Harte AM. Modelling the hygro-mechanical creep behaviour of FRP reinforced timber elements. Constr Build Mater 2020;259. doi:10.1016/j.conbuildmat.2020.119899.

[24] O'Ceallaigh C. An Investigation of the Viscoelastic and Mechano-sorptive Creep Behaviour of Reinforced Timber Elements. PhD Thesis, National University of Ireland Galway, 2016.

[25] CEN. EN 338. Structural timber - Strength classes. Comité Européen de Normalisation, Brussels, Belgium; 2016.

[26] Bodig J, Jayne BA. Mechanics of Wood Composites. Reprinted edition. Von Nostrand Reinhold Company, New York, Cincinnati, Toronto 1993.

[27] Conway M, O'Ceallaigh C, Mehra S, Harte AM. Reinforcement of Timber Elements in Compression Perpendicular to the Grain using Compressed Wood Dowels. Civ. Eng. Res. Ireland, CERI 2020. Cork Inst. Technol. 27-28 August, 2020, p. 319–24. doi:https://doi.org/10.13025/sbeg-3p91.

[28] O'Ceallaigh C, Conway M, Mehra S, Harte AM. Numerical Investigation of Reinforcement of Timber Elements in Compression Perpendicular to the Grain using Densified Wood Dowels. Constr Build Mater 2021;288. doi:10.1016/j.conbuildmat.2021.122990.

[29] Conway M, Harte AM, Mehra S, O'Ceallaigh C. Densified Wood Dowel Reinforcement of Timber Perpendicular to the Grain: A Pilot Study. J Struct Integr Maint 2021;6:177–86. doi:10.1080/24705314.2021.1906090.

[30] O'Ceallaigh C, Mohseni I, Mehra S, Harte AM. Numerical Investigation of the Structural Behaviour of Adhesive Free Connections Utilising Modified Wood. WCTE 2021- World Conf. Timber Eng., Chile: 2021.

[31] Namari S, Drosky L, Pudlitz B, Haller P, Sotayo A, Bradley D, et al. Mechanical properties of compressed wood. Constr Build Mater 2021;301. doi:10.1016/j.conbuildmat.2021.124269.

[32] Jung K, Kitamori A, Komatsu K. Evaluation on structural performance of compressed wood as shear dowel. Holzforschung 2008;62:461–7. doi:10.1515/HF.2008.073.

[33] Mehra S, Harte AM, Sotayo A, Guan Z, O'Ceallaigh C. Experimental investigation on the effect of accelerated ageing conditions on the pull-out capacity of compressed wood and hardwood dowel type fasteners. Holzforschung 2021.

[34] Valipour H, Khorsandnia N, Crews K, Palermo A. Numerical modelling of timber/timber-concrete composite frames with ductile jointed connection. Adv Struct Eng 2016. doi:10.1177/1369433215624600.

[35] Kawecki B, Podgórski J. Numerical analysis and its laboratory verification in bending test of glue laminated timber pre-cracked beam. Materials (Basel) 2019;16:1–15. doi:10.3390/ma12060955.

[36] Portioli F, Marmo R, Ceraldi C, Landolfo R. Numerical modeling of connections with timber pegs. 11th World Conf. Timber Eng. 2010, WCTE 2010, vol. 3, 2010, p. 1881–6.

[37] Khorsandnia N, Valipour HR, Crews K. Nonlinear finite element analysis of timber beams and joints using the layered approach and hypoelastic constitutive law. Eng Struct 2013;46:606–14. doi:10.1016/j.engstruct.2012.08.017.

[38] Chybiński M, Polus Ł. Experimental and numerical investigations of aluminium-timber composite beams with bolted connections. Structures 2021;34:1942–60. doi:10.1016/j.istruc.2021.08.111.

Developing a Model for the Load Response of Open Metal Web Timber Joists

N. Kenneally[1], John J. Murphy[1],
[1]Department of Civil, Structural and Environmental Engineering, Munster Technological University, Bishopstown, Cork, Ireland
email: niall.kenneally@mycit.ie, johnjustin.murphy@mtu.ie

ABSTRACT: One of the major developments in the construction industry of late has been the increased use of engineered timber components in building structures. One such product has been the 'Open Metal Web Joist'. These joists, (more commonly known as "Spacejoists") are increasingly being used to replace traditional solid section timber joists for intermediate span floor and roof structures. Aside from the host of practical benefits, combining the lightness of timber flanges with the strength of steel webs has demonstrated larger spanning capabilities than other types of engineered joists. Like most flexural elements in habitable structures, serviceability limit state criteria govern their design, namely, deflection and vibration. As such, a universally functional design model is necessary to model their load response in this range. In this study, both theoretical and experimental investigations are conducted into the behaviour of Spacejoists, and specifically the load-slip phenomenon at their composite connections. Through a combination of physical and computational testing, characteristic joint slip moduli are established for the three most common Spacejoist sizes. A technique is trialled for extracting these values under an assumption of linear and compatible joint slip deformation. Re-incorporating slip modulus values into FEA models, the software models exhibit load-displacement consistent with that of physical Spacejoist specimens. There now exists a legitimate design aid to predict the deflection of Spacejoists, catering for of any span, loading, and support conditions within serviceability limit state bounds.

.

1 BACKGROUND AND INCEPTION

The advent of the light gauge steel nail plate in the 1950s brought a minor revolution to the manufacturing of structural timber components such as trusses and frames. The introduction of pressed metal plate fasteners meant the size of timber members was no longer controlled by the size of the joint. These fasteners are steel plates with integral nails or teeth, punched out to one side and projecting at right angles to the plane of the plate. They are used as splice plates to connect the members of framed timber structural components such as trusses at any angle within the same plane. A variety of these connector plates is depicted in Figure 1. Joints which utilise these connectors are prefabricated under factory conditions, where heavy press or roller equipment is used to embed the projected nails into the timber. In general, these types of connections exhibit excellent strength and stiffness properties in comparison to other forms of joint.

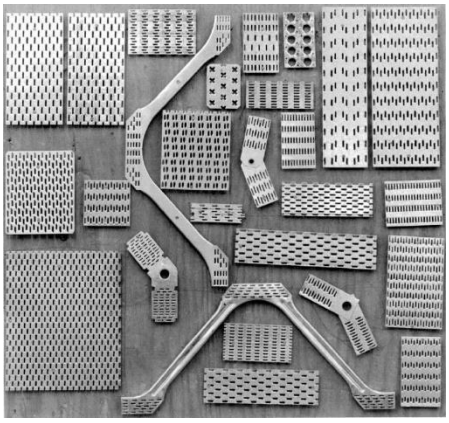

Figure 1: Common Metal Connector Plates used in Trussed Timber Structures (itw.com, 2019)

Open metal web joists (or Spacejoists) are an evolution of traditional solid timber floor joists, which profit from the strength and stiffness properties of metal plate connections. Spacejoist metal web beams and columns are shallow parallel chord trusses in which solid timber flanges are connected to each other by a system of triangulation provided by thin gauge steel webs.

Open Metal Web Joists have been used to form floors, pitched roof and flat roof structures for some time. In Ireland, I.S. EN 1995-1-1 (NSAI, 2014) is used for their design, which comprises ultimate and serviceability limit state design criteria. The latter tends to govern the design of Spacejoists, specifically deflection and vibrational criteria. Accurate prediction of load-deformation becomes critical to the efficiency of designs, and as such, the overall viability of the product.

2 EUROCODE SPACEJOIST DESIGN

A European Technical Assessment (ETA) provides technical certification for Spacejoists. ETA's are commonplace in the absence of a harmonised technical specification for a construction product. They outline the methods and criteria for assessing a product's performance in relation to these essential characteristics. Spacejoist metal web beams are modelled and designed in current software packages using a first order linear elastic plane frame analysis applied to the simplified structural models as illustrated in Figure 2. In the model, flanges are continuous and subject to combined axial and bending. Webs-ends are pinned to flanges and therefore subject to axial forces only. Web strengths (which include various anchorage and web-leg failure modes) are derived from load tests in conjunction with the simplified model.

They are characterised as axial strengths for use in the structural model in ultimate limit state design. The critical thing to recognize, however, is that this same simplified

model must be used to both analyse test results and design the end product. Any attempt to design Spacejoists using test values but not the simplified model would be unacceptable and would contravene the terms of the European Technical Assessment for the product.

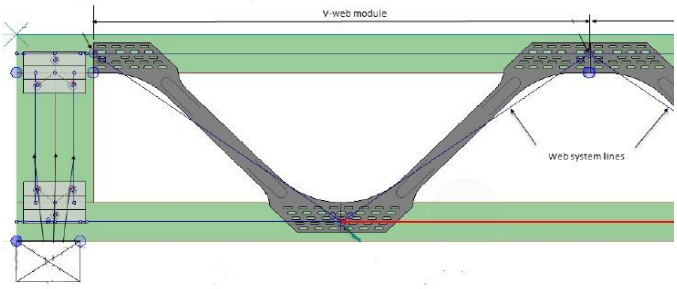

(a)

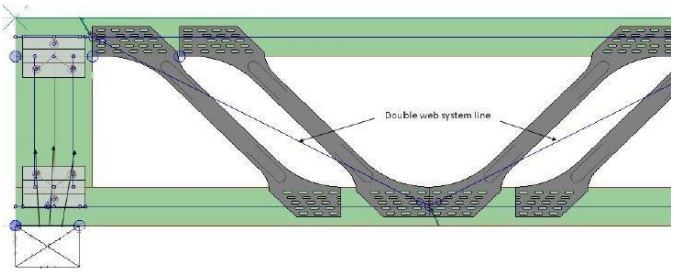

(b)

Figure 2: Structural Model for Metal Web Beams & Columns with (a) Single Webs and (b) Double Webs (EOTA, 2013)

3 APPROACH TO MODELLING LOAD-DEFORMATION

3.1 Test Arrangement and Apparatus

Spacejoists are inherently indeterminate structures due to the continuity of the flange members through the truss nodes, and the rotational stiffness of metal plate connections. Therefore, a global stiffness matrix (or model) is required to solve for all deformations and force distributions. However, all boundary conditions (supports), structure geometry, member end-releases, material properties (strength and stiffness) and loadings are required to solve the global system of equations. The first components to consider are the timber flanges, which are subject to axial loads, bending and shear. The material properties, geometry and support conditions for these members are known, so these elements can be modelled. All axial, bending and shear deformations can theoretically be calculated. The steel webs comprise the profiled 'leg' of the web, and the nail plates (or punched metal fasteners) at web ends. The material properties and geometry of steel legs are also known for different web sizes. The web legs are subject to primarily axial loads and all resulting strain deformations can be calculated. This leaves the final physical component of Spacejoists, the nail plate connections, recurrent at every flange-web joint.

Unfortunately, it is hard to define either physical geometry or material properties for these joints. These joints are the unknown quantities in the stiffness matrix. They are the missing link in the chain, and as such, an accurate structural analysis cannot be performed without their input. What is known however, is that overall deflection of metal web joists is composed of three components:

- Deformations of the timber flanges, which can be evaluated using conventional engineering methods based on a known modulus of elasticity;
- Axial deformation of the steel webs, which can be evaluated using conventional engineering methods based on a known modulus of elasticity;
- Some unknown contribution to overall joist deflection based on the slip characteristics of the multiple web-flange nail plate connections.

The behaviour of metal plate connections is complex and dependent on a wide range of variables. However, the load response of these connections is the single unknown in the model, and it is possible to take their complex behaviour and encapsulate the effects in a single Spacejoist model parameter. If physical load-displacement tests are undertaken on Spacejoists, any displacement additional to the linear elastic response of members can be attributed to the web-flange connections. Figure 3 shows the idealised load-displacement behaviour of a Spacejoist. The red line represents the linear elastic member strains (flanges and web legs) and as such can be characterised by a straight line with a governing slope (M_e). Assuming a linear elastic connection load response (within the serviceability limit state range), the blue line represents the total load-displacement behaviour of the system, characterised by a straight line with a governing slope (M_o). The grey area signifies the additional joint displacements, or 'slips'.

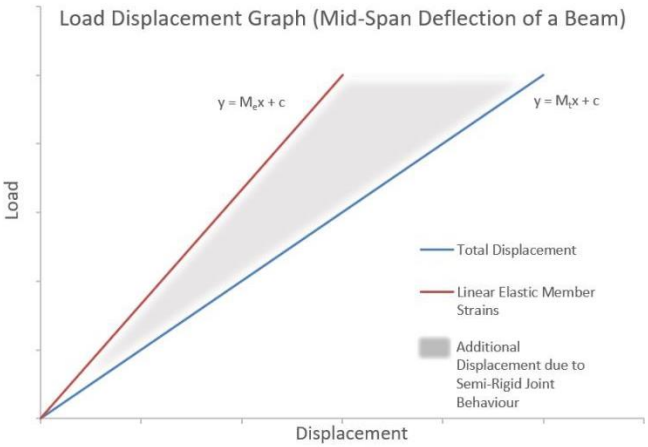

Figure 3: Idealised Spacejoist Load-Displacement Graphs

From a linear elastic model, the 'red line' model can be easily plotted, using fully pinned web-flange joints, i.e. no joint distortions. The 'blue line' can be constructed by plotting 'real life' load-displacement (say midspan deflection) data for a Spacejoist. The additional displacement (grey area) should become apparent. The modulus for midspan deflection due to slip in a Spacejoist can be found using the formula in Equation (1).

$$\frac{1}{M_t} - \frac{1}{M_e} = \frac{1}{M_s} \quad (1)$$

where:

M_s = System Slip Modulus,

M_e = Constant of 'Member Strain Only' Displacement,
M_t = Constant of Total Displacement.

This System Slip Modulus (M_s) defines the 'slip-owing' deflection contribution of that specific Spacejoist truss system. This System Slip Modulus could be described as the slip constant governing deflection of a specific Spacejoist.
With the contribution of joint slip to overall deflection now defined, the next step is to incorporate this load-slip phenomenon into a Spacejoist model. The level and nature of joint slip in a Spacejoist remains the unknown and cannot be derived from first principles. Physical testing is necessary to initially establish slip-defining characteristic values of some nature that can be then incorporated into the design model.

4 PHYSICAL TESTING

Experimental load tests were conducted on the premises of ITW Construction Products, located in Glenrothes, Fife, Scotland. The end goal was to calculate local joint slip moduli for each web size, but to do that, firstly global joist deformation needed to be assessed, i.e. the joint slip had to be evaluated as the joint performed within a Spacejoist, and not, say as a single-joint test. Hence the global joist stiffness first needed measuring, so that local joint stiffnesses could be isolated and extracted from results.

4.1 Test Rig

The test rig consisted of an Instron 5984 universal testing machine, with a maximum capacity of 150kN as shown in Figure 4.

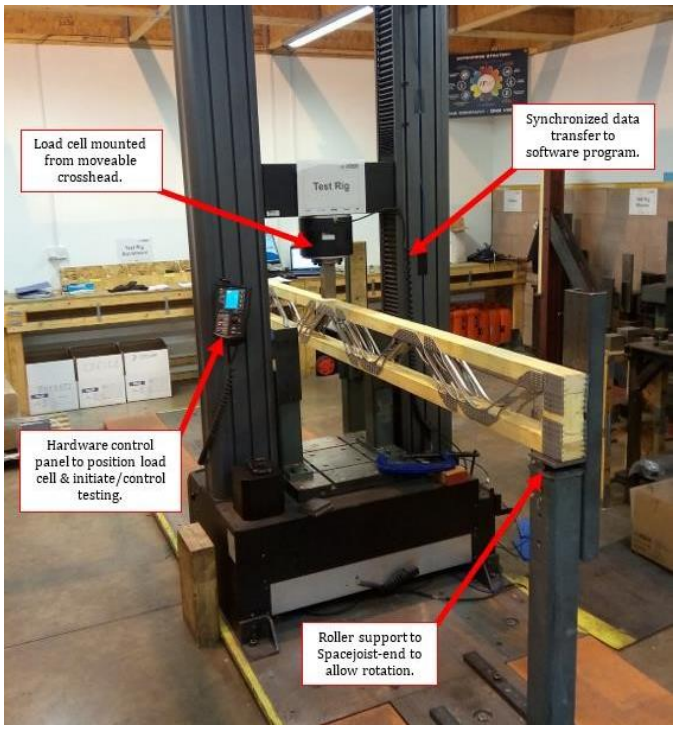

Figure 4: Test Rig for Spacejoist Load Testing

The controller controls the frame and ancillary equipment connected to the testing system. It contains all connectors for load cells, extensometers and other sensors required for testing. Control of the testing system is carried out via the Instron software. The test rig had moveable steel stanchions on which Spacejoist specimens were simply supported during load tests.

4.2 Test Set-Up

All web sizes being tested, SJ9, SJ10 and SJ12's have a V-web length of 605.5mm. This restricts the number of joint span possibilities to multiples of this web length. All joists were made 3773mm in total length, the result of six full V-webs with standard 35mm double end-block details. It was considered that applying multiple point loads was the most accurate method of replicating and measuring a UDL on the joists. Figure 5 shows the loading set-up for the testing regime, where "**P**" is the total load on the joist. The point loads are distributed equally and evenly along the span, and critically, located at node points of the 'shallow truss' to avoid premature local failure in the joist.

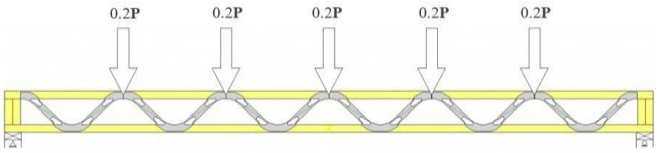

Figure 5: Test Set-Up for Loading Regime (CUAP, 2012)

The test machine had a single load cell, yet it was required to consistently split the load in five equal points for the duration of a test. To achieve this, a transfer structure was employed to distribute the oncoming cell load evenly to the five transfer points on a joist. Hence the load string consisted of the load cell, a square-hollow-section steel with connecting grips, and two steel packer blocks sandwiching a steel roller at every load point as shown in Figure 6.

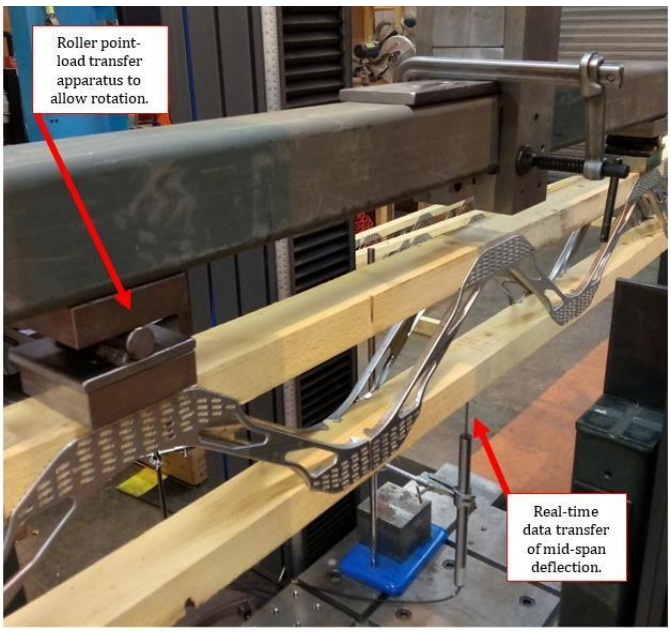

Figure 6: Technique for Applying Multiple Point Loads

The block-roller-block combination transfers the point load but does not inhibit rotation of the top chord as the Spacejoist flexes. The exact distribution of the load onto the Spacejoist is a function of the relative stiffnesses of the spreader beam and the Spacejoist. In the absence of measurements, the load is taken to be evenly distributed. The electronic beam deflection

apparatus was connected to the system controller for synchronised data acquisition throughout the test procedure.

4.3 Loading Procedure

I.S. EN 26891 (NSAI, 2001) contains the general principles for the determination of strength and deformation characteristics of timber-structure joints made with mechanical fasteners. The Spacejoist specimen were tested using the loading procedure in Clause 8 of I.S. EN 26891. This loading procedure is shown in Figure 7. The test specimens are loaded to 40% of the estimated maximum load, F_{est}. This load is maintained for 30 seconds and is then unloaded to $0.1F_{est}$, where it is again maintained for 30 seconds. Thereafter the load is increased until the ultimate load is reached. Deflection measurements in the range $0.1 – 0.4F_{est}$ in the second load cycle were used for the consideration of joint slip moduli values in software modelling.

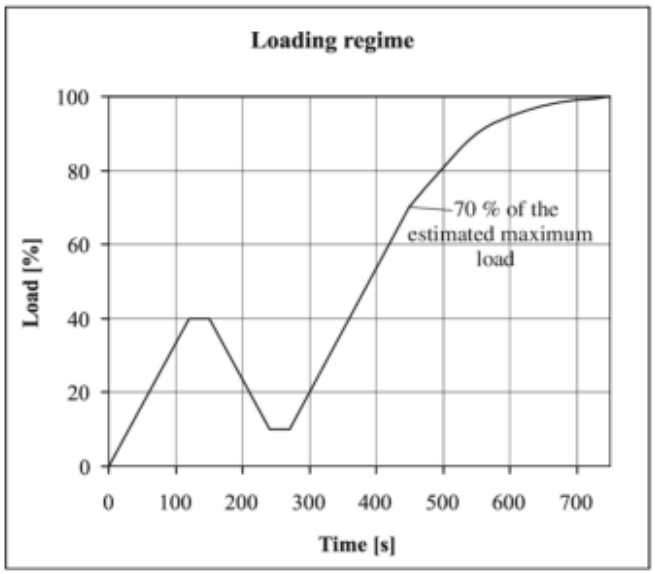

Figure 7: Load Testing Regime for Spacejoists (NSAI, 1991)

4.4 Test Results

Control of the testing system was carried out via the Instron software. Setting test parameters, operating the system, and collecting test data were performed through the software program. The sophistication of the system allowed for synchronised data acquisition as the loading regime was implemented for each test. The mid-span deflection (measured from underside of bottom chord) and corresponding load '**P**' on the Spacejoist were logged at 0.5s intervals as the I.S. EN 26891 loading procedure was executed.

4.5 Raw Data

The load-displacement curves of vertical midspan displacements were plotted for all specimens. There are two distinct phases to the load-displacement behaviour. Throughout the first, and much of the second load cycle of the I.S. EN 26891 loading procedure, there is an apparent linear relationship between load and displacement. The load-displacement curve rises steeply with displacements remaining relatively small. Approaching the maximum load (F_{ult}), there is a levelling out of the curve. The load-displacement curve of a typical SJ9 test specimen is displayed in Figure 8.

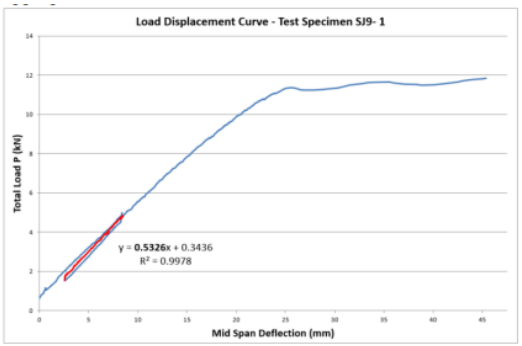

Figure 8: Load Displacement Curve for a Typical Test Specimen

All test specimens behaved similarly during the testing phases. The only difference was that the ultimate failure mode of SJ9 specimens was 'tension-anchorage', whereas 'web buckling' proved the case for all SJ10 and SJ12 specimens. This is not altogether surprising as the increased web length in the deeper Spacejoists sizes leave compression webs more susceptible to this ultimate failure., which does not need to be considered since the subject of this research paper relates to the serviceability limit state. The goal of physical testing is to establish slip-defining characteristic values of some nature that can be then incorporated into a future design model. This information must be extracted from the portion of the curve within the serviceability limit range. For this range, I.S. EN 26891 defines the slip modulus value (K_{ser}) as the 'secant' (average slope) at $0.4\ F_{est}$, where F_{est} represents an estimation of the ultimate failure force. Also deemed suitable is obtaining a slip modulus based on a linear regression analysis of the load-slip response between $0.1F_{est}$ and $0.4F_{est}$.

The ultimate load is defined as either the force at which the sample reaches failure/destruction, or the force at which the slip reaches a value of 15mm. This limit pertains to individual joints in mechanically fastened timber structures. The Spacejoist specimens in this study comprise multiple joints acting (or displacing) simultaneously under the applied load. While the global Spacejoist deflection indeed exceeds 15mm, no individual joint is remotely near this limit, hence why tests continued to web buckling and anchorage failure modes.

It is important to recognise that any "constant" calculated from this data is the "Constant of Total Displacement" described in Equation (1), and not the slip-modulus for either the system or any individual joint. Figure 8 illustrates the linear regression executed between $0.1F_{est}$ and $0.4F_{est}$ for a typical test specimen. Table 1 contains a summary of all test results across the three Spacejoist groups. The average slope of linear regressions for each group is highlighted and the corresponding deflection at 40% of the estimated ultimate load (F_{est}) is also displayed. Slight misestimates of F_{ult} do not have a significant bearing on the calculation of the regression line slopes (M_{test}). There is undoubtedly enough overlap between $0.1\text{-}0.4F_{est}$ and $0.1\text{-}0.4F_{ult}$ to negate any concern over the accuracy of the M_{test} calculations.

Table 1: Summary of Load-Displacement Test Results

STIFFNESS/SLIP RESULTS - ALL JOISTS											
				Recorded Flange Properties							
				Top		Bottom					
Joist Reference	Beam Length (mm)	Span Between Rollers (mm)	Joist Depth (mm)	Width (mm)	Depth (mm)	Width (mm)	Depth (mm)	Estimated Ultimate Load F_{est} (kN)	M_{test} Slope of Linear Regression $0.1F_{est}$ - $0.4F_{est}$ (kN/mm)	F_{ult} Ultimate Failure Load (kN)	Deflection @ 40% F_{est} Based on Average Regression (mm)
SJ9 219mm											
SJ9 219 -1	3774	3710	217	70.93	46.65	71.00	46.15	12.0	0.5326	11.67	
SJ9 219 -2	3774	3710	219	70.92	46.26	71.59	47.81	12.0	0.5200	11.56	
SJ9 219 -3	3774	3710	219	71.50	47.98	71.35	46.40	12.0	0.5077	11.87	
SJ9 219 -4	3774	3710	219	71.45	45.91	71.52	46.30	12.0	0.5493	11.51	
SJ9 219 -5	3773	3710	217	70.94	46.37	72.44	46.50	12.0	0.5069	11.77	
SJ9 219 Average								12.0	0.5233		9.17
SJ10 254mm											
SJ10 254-1	3775	3724	256	72.05	46.80	72.79	46.57	13.0	0.6920	14.65	
SJ10 254-2	3776	3724	255	72.35	48.32	71.91	47.10	14.0	0.6853	14.81	
SJ10 254-3	3776	3724	254	70.34	46.47	71.93	47.46	14.0	0.6986	14.27	
SJ10 254-4	3777	3724	255	70.78	48.23	72.16	47.43	14.0	0.7251	13.96	
SJ10 254-5	3776	3724	253	71.82	47.57	72.80	47.27	14.0	0.7179	14.88	
SJ10 254 Average								14.0	0.7038		7.96
SJ12 304mm											
SJ12 304-1	3778	3710	304	71.75	47.20	70.57	46.36	16.0	0.8780	12.55	
SJ12 304-2	3774	3710	303	71.54	46.28	71.28	46.80	15.0	0.8066	14.18	
SJ12 304-3	3776	3710	304	71.34	46.18	71.45	46.76	15.0	0.8602	14.36	
SJ12 304-4	3777	3710	303	71.67	46.55	70.95	47.21	15.0	0.8022	12.88	
SJ12 304-5	3776	3710	304	71.55	46.48	70.95	46.52	14.0	0.8650	14.00	
SJ12 304 Average								15.0	0.8424		7.12

5 COMPUTER MODELLING AND RESULTS

Physical testing is necessary to establish some slip defining data. Load-displacement curves measure the extrinsic properties of an individual specimen. The main observations are stiffness, ultimate load and displacement. The stiffness defining characteristic extracted from testing was the 'Constant of Total Displacement' (M_t) for a Spacejoist. This constant governs mid-span deflection of a specific Spacejoist design. It incorporates the combination of elastic deformation and slip deformation of that specific truss system. By modelling an equivalent pin-jointed Spacejoist and using Equation (1), the 'System Slip Constant' can be isolated. However, this figure is specific to an individual joist design, and as such, its value is limited. An eventual 'Joint Property Assignment' to a plane frame software model is the universal model parameter that could replicate the joint's load-slip behaviour. Once established, this single characteristic value for each Spacejoist web size caters for the design of all Spacejoist spans, loads and support conditions. These values cannot be derived from first principles and must be established from the empirical test data and results in Section 4. However, it is first necessary to model and quantify the 'non-joint slip' component of total deformation before any joint properties can be established. This allows the 'Constant of Member-Strain-Only Displacement' (M_e) be calculated.

5.1 Structural Model

A plane frame model is adequate to initially model the 'pinjointed truss' Spacejoist. During its design life an individual joist performs within a floor system, where it is laterally braced and continually restrained along its compression chord. Spacejoists are highly indeterminate structures due to the continuity of flange members and the partial stiffnesses of their joints. The structural analysis must be performed by establishing and solving a global stiffness matrix for the structure. Within the plane frame model, each member requires a 3x3 member stiffness matrix to evaluate the axial, shear and rotational displacements of member end joints. The software program chosen needs to not solely to solve for joint displacements, but to enable individual members to be split into discrete subsections, separated by nodes. Should an adequate number of nodes be integrated to permit a comfortable degree of accuracy, the displacement of some key mid-member nodes can be extracted as the key measurement of deflection for the structure.

The Spacejoists were modelled using FEA software 'LUSAS'. For flanges, a line mesh with 10 divisions was defined using '2D thick beam' structural elements. For Spacejoist webs, a line mesh with four elements was defined. The next step was to execute the 'joint property assignment' which was selected as the most sensible approach to modelling joint slip. Section 3 outlined and explained the initial modelling assumptions. One assumption was that of translational joint slip (or displacement) in the model. It is desirable to have the web-flange interface in a shared joint remain like a pin (have zero rotational stiffness) yet have that pin displace (or slip) along web system lines. Given these criteria, it follows that this joint modification should be a translational stiffness assignment coincident with web element lines. Furthermore, there should be two translational stiffness assignments in a typical internal joint since there are two web system lines. LUSAS contains 'Joint Elements', which may be inserted between pairs of corresponding nodes and are used to connect two or more nodes with springs. They enable translational and/or rotational stiffness, i.e. they facilitate F_x, F_y, and M_z spring forces, leading to ε_x, ε_y, and γ_z spring strains in local directions. The suitable LUSAS 2D joint element chosen is a JPH3 element. The joint element has no applicable geometric properties as it essentially exists on the model joint intersection only and has no physical length to begin with. It is therefore classified as a material property that must be applied to the extremity of a model (line) feature. The web line mesh was modified to "include joint" so that the joint property could be "assigned to both line ends", and not assigned to the entire joint. The timber flanges are continuous in nature (no end releases), therefore no additional stiffnesses are required between flange line meshes. A typical internal web-flange joint should contain two joint elements and three nodes; the original model node, common to both member system lines, and now two more joint element nodes, one from each web system line-end. This is portrayed conceptually in Figure 9.

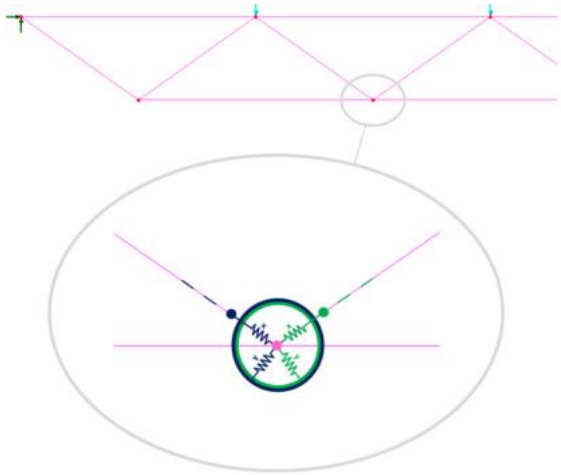

Figure 9: Visualisation of Additional Springs added to Typical Joint in LUSAS Models

All three nodes share the same coordinates in an unloaded state. Local *x* and *y* translational spring stiffnesses are shown for both joint elements. The JPH3 joint elements were

incorporated into all LUSAS models across the different Spacejoist depths. The software prompts three stiffness values to be input since the JPH3 element connects its two nodes by two springs in the local *x* and *y*-directions and one spring about the local *z* direction, but the key attribute here is the spring stiffness in the local *x*-direction of the joint element since the web forces in the model are exclusively axial, This value may be called the slip modulus.

5.2 Establishment of Characteristic Mean Slip Moduli

The premise of all modelling to date has been the linear elastic behaviour of Spacejoists in the SLS range, and therefore all model deformation (including joint deformation) is assumed to occur in the same fashion. For any load in this range, the mid-span deflection owing solely to axial member strains is known. This can be read from the 'pinned web-joint' model graph plots. The web ends in these models have zero rotational restraint, but complete translational restraint at the shared joint. In Spacejoists, it is known that translations (or slips) do occur at this plate-flange interface, and their cumulative effect represents the difference between 'member strain only' and 'total' deflection. If an arbitrary slip modulus is assigned to joints, the resulting mid-span load-displacement line can be plotted for that nominal slip modulus value. Furthermore, if plotted alongside the 'member strain only' plot and the linear regression of 'actual' (test) displacement, a characteristic slip modulus value required to produce the linear regression can be interpolated, using the ratio between the displacements (for any load value) as the ratio between joint stiffness values. In other words, the joint stiffness values are proportional to the amount of'slip-owing' displacement. The proposed idea is represented in Figure 10.

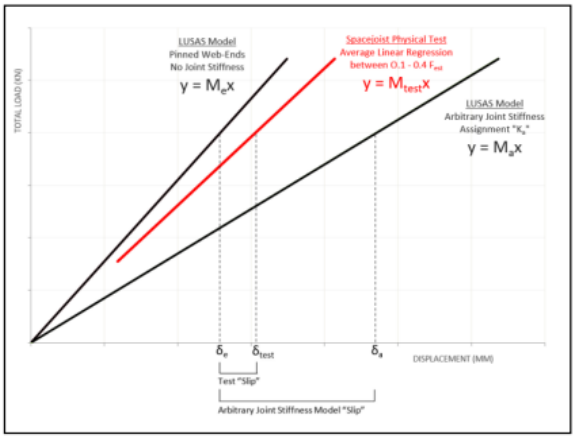

Figure 10: Concept of Characteristic Slip Modulus Determination

Using this approach, the equation representing the characteristic joint slip modulus for any Spacejoist web size can be expressed as per Equation (2).

$$K_{ser} = K_a \left[\frac{\delta_a - \delta_e}{\delta_{test} - \delta_e}\right] \quad (2)$$

As stiffness from the physical testing is defined by the slope of the regression line, the joint slip modulus can also be written as per Equation (3).

$$K_{ser} = K_a \left[\frac{\frac{1}{M_a} - \frac{1}{M_e}}{\frac{1}{M_{test}} - \frac{1}{M_e}}\right] \quad (3)$$

where:

K_{ser} is the slip modulus for the relevant Spacejoist web size,
K_a is the arbitrary slip modulus chosen to facilitate the calculation,
M_e is the slope of the 'member strain only' model,
M_a is the slope of the 'arbitrary slip modulus' model
M_{test} is the slope of the linear regression from physical testing.

Using Equation (3), characteristic slip moduli for Spacejoist groups were determined as **44.2**, **39.6** and **20.8** kN/mm for SJ9, SJ10 and SJ12 webs respectively.

6 CONCLUSION

After a qualitive analysis, it was concluded that 'joint property assignment' is the most appropriate approach to modelling Spacejoist deformation, and specifically, the joint-slip phenomenon at web-flange connections. Physical testing of specimens demonstrates effectively linear elastic deformation of Spacejoists in the serviceability limit state range and linear elastic load-slip behaviour at the metal plate connections.

Through a combination of physical and computational testing, characteristic joint slip moduli were established for the three most common Spacejoist sizes. Calculated values were re-assigned to FEA models, which exhibit load-displacement consistent with that of physical Spacejoist specimens. Using these slip modulus values for future Spacejoist models, there now exists a legitimate model to predict the deflection of Spacejoists.

ACKNOWLEDGMENTS

The research reported in this paper was conducted as part of the taught MEng (Structural Engineering) programme at Munster Technological University

REFERENCES

NSAI, 2014. I.S. EN 1995-1-1:2004 & A1 (2008) & A2 (2014) Eurocode 5: Design of Timber Structures - General Common Rules & Rules for Buildings. National Standards Authority of Ireland, 2014.

CUAP, 2012. Common Understanding of Assessment Procedure - Metal-Web Beams and Columns ETA request No 03.04/30, 2012 & 2018. BM TRADA Certification.

EOTA, 2013. European Technical Assessment ETA-08/0370 Metal Web Beams & Columns for Structural Purposes., 04/06/13. European Organisation for Technical Approvals.

NSAI, 1991. I.S. EN 26891:1991 Timber Structures - Joints Made with Mechanical Fasteners - General Principles for the Determination of Strength and Deformation Characteristics. National Standards Authority of Ireland, 1991.

NSAI, 1991. I.S. EN 28970:1991 Timber structures – Testing of joints made with mechanical fasteners. Requirements for wood density. National Standards Authority of Ireland, 1991.

Geotechnics

The Gjerdrum, Norway quick clay slide of 30 Dec. 2020 and Irish peat slides 2020 – some parallels

Mike Long[1]
[1]School of Civil Engineering, University College Dublin (UCD), Newstead Building, Belfield, Dublin 4, Ireland
email: Mike.Long@ucd.ie

ABSTRACT: This paper contrasts the devastating quick clay slide at Gjerdrum in Norway in 2020 and the three large peat slides which occurred in Ireland in the same year. At first glance these events have similar features with significant retrogressive sliding mechanisms and long run-out of the spoil. The geotechnical properties of the materials are considered as are newer in situ tools which can help in soil characterisation. Geophysical techniques can be especially useful and these methods are explored in the context of the slides. Finally triggering mechanisms and causal forcers of the two sets of slides are discussed.

KEY WORDS: peat; quick clay; landslides; geotechnical properties; geophysics.

1 INTRODUCTION

A devastating landslide in quick clay struck the community of Gjerdrum in Southern Norway at just before 4 am on Wednesday 30th December 2020, leaving 11 people dead. After some "quiet" years with respect to landslides in peat there were several significant slides in Ireland in 2020, most notably those at Shass Mountain, Drumkerrin, Co. Leitrim, Meenbog, Co. Donegal and Mount Eagle Co. Kerry in 2020. The purpose of this paper is to describe the events and the unusual "non-textbook" geomaterials which are at play. The paper will seek links between the events in terms of the nature of the failures, the triggering mechanisms, the use of modern exploration tools to characterise the materials and to the application of geophysics to study the slides and mitigate against the risk of future slides.

2 GJERDRUM SLIDE

2.1 Location

The landslide occurred in the community of Gjerdrum in Southern Norway at about 4am on 30th December 2020. Gjerdrum is located some 30 km north-west of Central Oslo and about 15 km south of Oslo airport at Gardermoen.

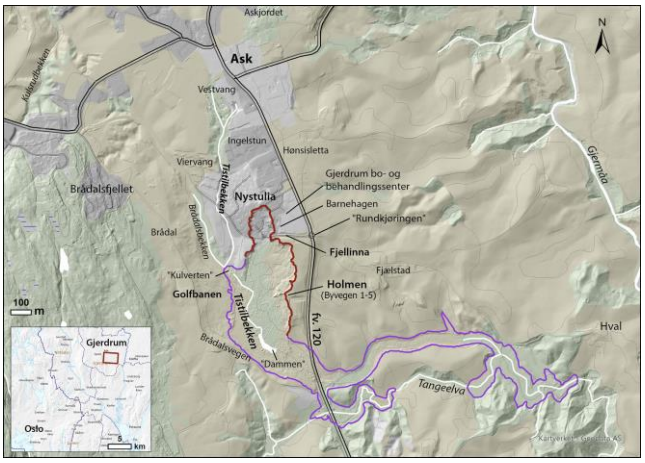

Figure 1. Location and outline of Gjerdrum quick clay slide [1]

The location and layout of the slide are shown on Figures 1 and 2. Unfortunately the slide directly impacted a number of homes. The star shaped building just to the north-west of the slide is the Gjerdrum sykhjem (nursing home).

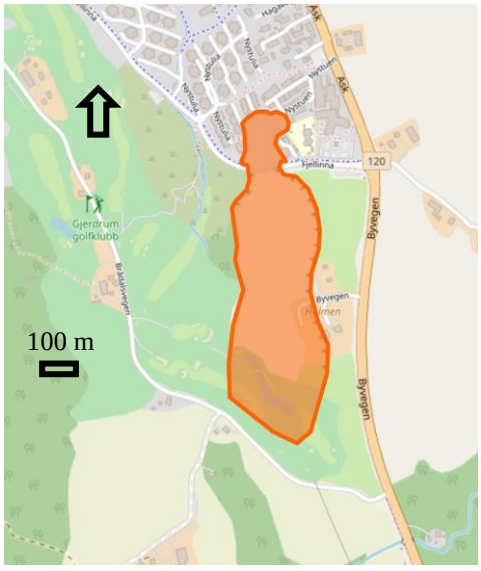

Figure 2. Location and outline of Gjerdrum quick clay slide (www.vg.no and www.nrk.no)

Figure 3. Early image of Gjerdrum slide

The location of the farm Holmen and the creek Tistilbekken are also noted.

2.2 Immediate aftermath of slide

A very early image of the slide taken in the early hours of the next morning is shown on Figure 3. It must be remembered that at this time of the year daylight hours in Norway are relatively short. This image and those following are taken from the Norwegian newspapers Aftenposten (www.aftenposten.no) and VG (www.vg.no) , from the Norwegian Public Broadcaster NRK (www.nrk.no) and from a very useful landslide blog produced by Professor Dave Petley in the UK (https://blogs.agu.org/landslideblog).

The high resolution SkySat satellite images shown on Figure 4 was produced by PlanetLabs https://www.planet.com/. Figure 4 shows the crown of the landslide where the losses occurred. There appears to be a large main source area, and a smaller area to the north that has affected the houses with such catastrophic consequences. This is likely to be due to retrogression from the main landslide bowl.

The whole area affected by the landslide is shown on Figures 1 and 5. The main source appears to be on the western side. The main slide moved roughly towards the south, and then followed a small creek / channel towards the east.

Figure 4. High resolution SkySat satellite image with focus on slide crown from PlanetLabs https://www.planet.com/

Mobility was high – the landslide moved over 2.2 km. In one location the slide bifurcated. There was a very substantial amount of debris deposited at the toe of the landslide.

General images of the slide area are shown on Figures 6 and 7. There were 11 fatalities including an unborn child, 31 homes lost and about 1,600 people had to be evacuated immediately after the slide. There was of course major material damage. The ongoing covid 19 epidemic added to the complexity of this operation.

Figure 5. Overall view of Gjerdrum slide

Figure 6. View at north-east corner of Gjerdrum slide area

Figure 7. View of east side of Gjerdrum slide area

Figure 8. General view of terrain in area with relatively gentle slopes

The general view of the area near the slide (Figure 8) shows undulating terrain with relatively gentle slopes.

2.3 Post slide investigation and causes of failure

A comprehensive post slide investigation and analysis was undertaken [1]. This involved an experienced panel of experts. Physical evidence, witness observations as well geotechnical and hydrological surveys and calculations were carried out and studied. The committee investigated whether various construction measures in the area could have contributed to the causes of the landslide and the course of the landslide. They also assessed the spatial planning, construction case processing and implementation of some of the measures.

The committee found that the landslide started on the slope between the farm Holmen (Figures 1 and 2) and the creek Tistilbekken. Calculations showed that the stability in this slope was marginal. There were large amounts of quick clay present but this was not sufficient to explain why the landslide occurred in December 2020, since the slope had been in this condition for a long time. The slope was robust enough to tolerate both the seasonal variation in precipitation and periods of heavy and prolonged precipitation, e.g. significant precipitation in the year 2000.

Much of the investigation focused on the erosion along the creek. It was found that erosion caused the stream to be lowered up to 2.5 meters. In addition there had been some fill material placed in the vicinity of Holmen farm in order to increase the size of the farmyard (Figure 9). The creek had been piped in places. In some places additional inflows were channelled into the creek. Also locally the creek had broken out of damaged pipes further exacerbating the erosion situation.

Nevertheless the experts agreed that the slopes may have still survived except for the fact that there was a particularly wet autumn and early winter in the area. There had been unusually mild weather, which meant that the beneficial effect of a frozen and stiff terrain crust did not occur.

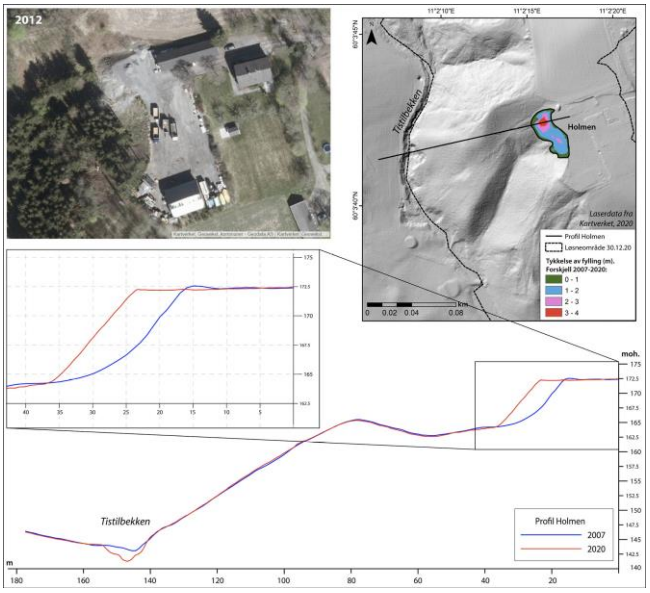

Figure 9. Erosion and terrain alteration near Holmen farm [1]

It was estimated that the saturation in the ground was between 90 and 100 percent in the days before the landslide. There was a particularly heavy rainfall in the period 26 to 29 December 2020. The committee felt that this was most likely the direct trigger for the landslide and that it started with one or more small slides along the east side of Tistilbekken, on the slope below Holmen. The reason this did not happen in the wet period in 2000 was a result of the fact that erosion had, in the intervening period, decreased the stability of the slope and the margin against landslides.

These small slides allowed the overall landslide to develop rapidly in a number of retrogressive steps. The committee were able to develop a clear picture of this action involving ten separate stages.

2.4 Remedial work

Remedial work is still ongoing at the site. It involves erosion protection measures (e.g. see Figure 10), regrading of slopes, construction of stabilising berms and lime / cement stabilisation of the clay masses amongst other actions.

Figure 10. Erosion protection near to Esp quick clay landslide near Trondheim [2]

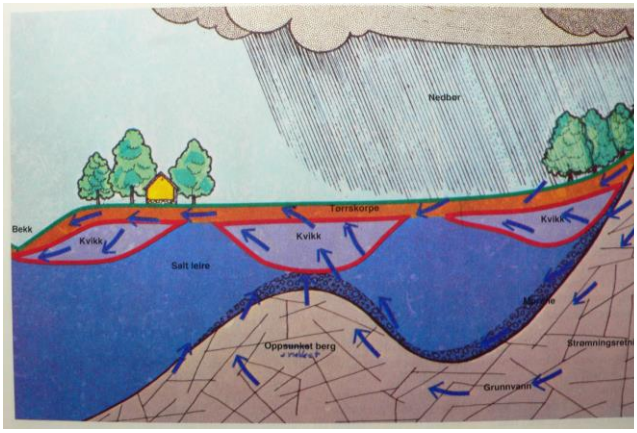

Figure 11. Formation of quick clays. Image courtesy Tor Løken, Norwegian Geotechnical Institute (NGI)

3 QUICK CLAY

3.1 Origin and formation

Sensitive glacio-marine clays, so called quick clays, are typically found in Norway, Sweden and Canada (there often referred to as Leda or Champlain Sea clays) are characterised by a remoulded undrained shear strength (c_{ur}) which is considerably lower than the intact undisturbed shear strength (c_u). In geotechnical engineering the presence of sensitive clays poses a major challenge.

The Scandinavian post-glacial marine clays were deposited in a marine environment during and after the last ice age some 10,000 years ago, entrapping pore water of high salt content in the voids. Following isostatic uplift, starting at the end of the last ice age some 10,000 years ago, these marine clays were exposed to rain and to groundwater movement Leaching of the pore water by rain and groundwater flow has diluted the pore water salinity in some clays removing the salt (Na^+) from the clay (Figure 11). The thickness of the diffuse double layer around the clay particles increases and the repulsive forces between the particles rise. The clay structure can then easily collapse and the clay becomes quick.

In its undisturbed state quick clay is strong and competent (Figure 12).

Figure 12. Undisturbed quick clay can take considerable load. Image courtesy Kjell Karlsrud, NGI

Figure 13. After disturbance / remoulding quick clay can behave like a liquid. Images show Hobøl landslide (2014) and also lab remoulding of quick clay. Images courtesy Rolf Sandven , Multiconsult and Kjell Karlsrud, NGI

However following disturbance and remoulding the clay can behave like a liquid as can be seen in the field and lab images on Figure 13.

Addition of salt to the remoulded / liquid like material can restore its strength, see Figure 14. Unfortunately the situation is dynamic and the ongoing process of introduction of Mg^{2+} and Ca^{2+} replacing the Na^+ ions can ultimately change the behaviour from quick to non-quick [3]. These processes mean that it can be very difficult to locate quick clays in ground investigations.

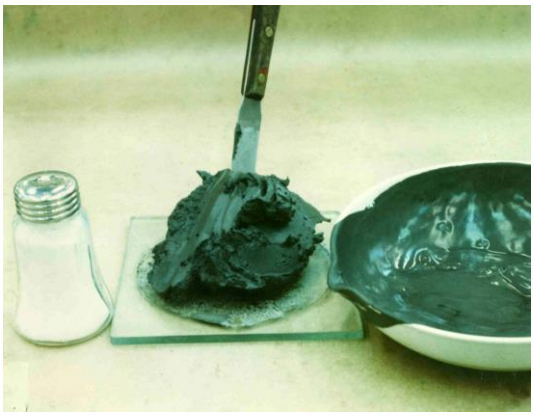

Figure 14. Adding salt can restore strength of disturbed quick clay. Image courtesy Kjell Karlsrud, NGI

Quick clays have been studied for many years and their properties are relatively well understood. The reader is referred to the works of Rosenqvist [4] or Pusch [5] or Torrance [6] or Bjerrum [7] for further details.

3.2 Geotechnical engineering properties of quick clays

According to the Norwegian definition quick clay is one in which c_{ur} is less than 0.5 kPa [8]. The most reliable method to confirm quick clay is sampling and index testing in the laboratory to measure c_{ur} and sensitivity ($S_t = c_u/c_{ur}$). However these tests are costly for systematic quick clay hazard zonation.

A typical geotechnical profile BH2020-7 from the post-slide investigations at Gjerdrum is shown on Figure 15. This borehole was located some 75 m due north of the slide pit. Note that the results of all these investigations were made public immediately, e.g. on the website of the Norwegian Geotechnical Institute (NGI).

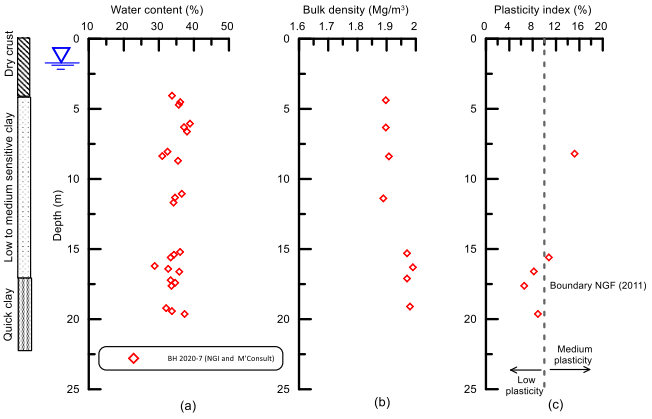

Figure 15. Basic index properties from Gjerdrum BH2020-7, (a) water content, (b) bulk density and (c) plasticity index. Data from www.ngi.no.

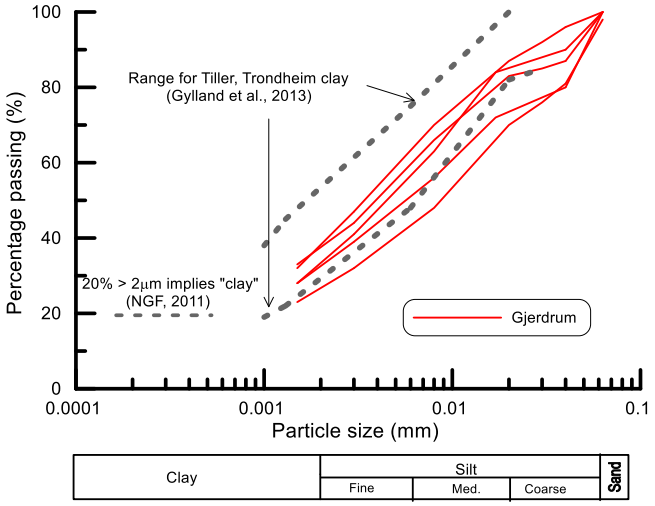

Figure 16. Particle size distribution test results for Gjerdrum BH2020-7. Data from www.ngi.no

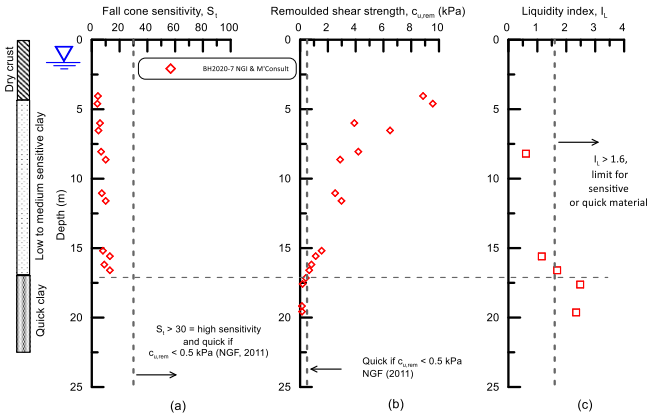

Figure 17. (a) sensitivity, (b) remoulded shear strength and (c) liquidity index from Gjerdrum BH2020-7. Data from www.ngi.no

The properties are typical for Norwegian clays with a water content of some 30% to 25%, a bulk density of 1.9 Mg/m^3 to 2.0 Mg/m^3 and a plasticity index of some 10% indicating the soil is of low to medium plasticity. Some particle size distribution tests are also shown on 16. The material is again typical for Norwegian clays [9] and is classified as a "clay" according to Norwegian practice [8] but the materials does have a high silt content.

Most geotechnical engineers would consider this material to be competent, certainly in its undisturbed sate.

Inspection of the fall cone data on Figure 17 show that below a depth of about 17 m the material has very low remoulded shear strength and high liquidly index and would be classified as "quick".

4 IRISH PEAT SLIDES

4.1 Historical context

Landslides in peat in Ireland are not a new phenomenon. These have been recorded from as far back as the 1400's [10]. In the "Annals of the Four Master" from 1488 a description is given of a "fairy wind" which may have been connected with a bog burst. Presumably this was due to gasses escaping from the bog. In the 1800's mentions of peat slides can be found in the literature. For example in Thomas Beggs "Rathlin a Descriptive Poem" (1820), the poet says:

"Lands o'erwhelmed with watery peat, from Black Knock-laida's bursting breast"

The catastrophic burst of Poulevard or Castlegarde bog in Limerick in 1708 swallowed up three houses, claiming 21 lives. Eight people lost their lives in the Knocknageeha bog burst near Killarney in 1896. The famous polymath Robert Lloyd Praeger was sent to investigate the slide. He reported [11], [12]:

"It was dark cold weather, the Reeks were white with snow, The district a rather desolated one, and I well remember that feeling of depression with which we gazed at that black slimy mass stretching down the valley, somewhere in which lay entoumbed the bodies of Cornelius Donnelly, his wife and six children…."

"Unwise turn cutting, by producing a high face without preliminary draining has frequently been the cause of these accidents. Such was so in the fatal Kerry case."

Lloyd Praeger's analysis was absolutely correct. He was clearly a man ahead of his time. Some memorials have been erected in the area to commemorate the lives lost for both the 100th and 125th anniversary of the landslide, see Figure 18

Figure 18. Memorial to the lives lost in the peat landslide at Knochnageeha, 1896. Photo taken in the Old Chapel Cemetery, Rathmore Co. Kerry.

4.2 Landslides of 2003

Public interest in peat slides in Ireland was again heightened in 2003 by two large events at Derrybrien and Pollatomish. The Pollatomish landslides occurred in the evening of 19 September 2003 (Figure 19) during an exceptional rainfall event [13], [14]. It was determined that 80 mm of rain fell in 2 hours. It was estimated that there were some 40 failures over a 5 km area and about 40 families were evacuated. The structural damage was estimated to be of the order of €3 million. The same storm caused peat slides in Shetland Islands later the same evening [15].

Figure 19. Some of the landslides at Pollatomish / Dooncarton Mountain, September 2003

In October 2003 a large landslide occurred during the construction of the Derrybrien Wind Farm in Co. Galway (Figure 20). It has been widely speculated that the slide was initiated by uncontrolled fill placements during the windfarm access road construction [16], [Irish Times 22/10/2004].

Figure 20. An image of the Derrybrien landslide. Photograph courtesy Koen Verbruggen, GSI

4.3 GSI database

The events in 2003 motived the creation of the Landslide Working Group by Geological Survey Ireland [17] and the development of a landslide database. This database is currently managed by Charise McKeon at GSI and is a very useful resource for all interested in this topic.

The most recent version of the database is from 28 October 2021. It records 2813 "events". Of these 1534 were in peat, i.e. some 55% of the total, supporting the idea that peat slides in Ireland are relatively commonplace. It should be noted that the exact date and details of these slides is not always known.

The number of peat landslides in the GSI database per century is shown on Figure 21a. It would seem that number of slides has increased with time. However the fact there has been much increased reporting over this time probably leads to this outcome. The number of slides per decade since 1900 is shown on Figure 21b. There is no clear pattern to be seen albeit for a relatively large number of slides between 2000 and 2009.

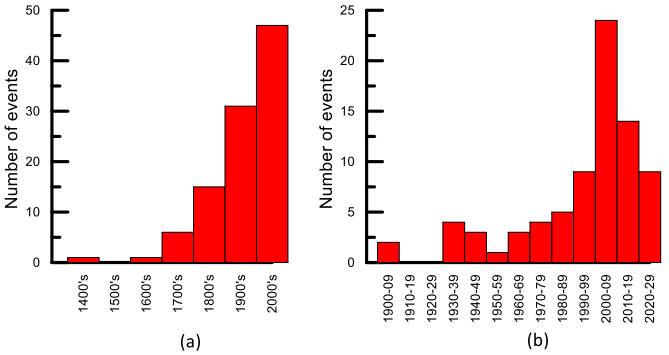

Figure 21. No of peat slides in GSI data base by (a) century and (b) decade

The annual number of slides since 1991 is shown on Figure 22. The pattern is not clear. There have been some very "quiet" years with no slides being recorded in 2011, 13, 15 and 19. In 2020 and 2021 there were six and three events recorded respectively.

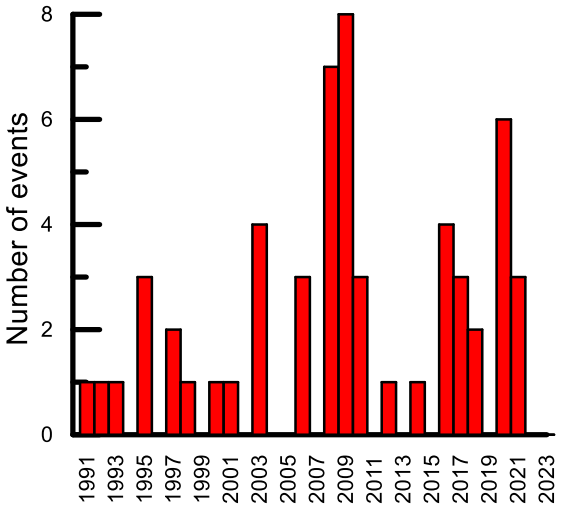

Figure 22. No. of peat slides in GSI database per annum 1991 to 2022

5 THREE IRISH PEAT SLIDES OF 2020

The descriptions which follow come largely from the accounts given on the landslide blog of Dave Petley (see earlier), a paper by Dr. Alan Dykes of Kingston University in the UK [18] and from onsite observations by the author. The Dykes paper is interesting in that it was written during the covid 19 pandemic and aimed to show how much data could be gleaned from online and other sources without actually visiting the sites in question.

5.1 Dawn of Hope Bridge / Shass Mountain, Drumkerrin, Co. Leitrim 28/6/20

Some images of the slide, taken from the YouTube drone imagery posted by John Flynn are shown on Figures 23 and 24 (https://www.youtube.com/watch?v=ttJsyGSBPcc).

The peatland in the area is of good quality. A hypothesis to explain the failure might be that the extreme rainfall in the period leading up to the failure, aided by water flow in piping in the peat, resulted in localised high porewater pressures. These caused an initial failure most likely towards the southern end of the slide area which rapidly progressed up the gentle slope retrogressively. The retrogressive nature of the failure is evidenced by the extensional landforms generated around the perimeter of the slide mass.

Figure 23. Drumkerrin peat slide – looking south towards Lough Allen (Photo John Flynn)

Figure 24. Drumkerrin peat slide – looking north (Photo John Flynn)

Large drains in the forestry adjacent to the slide area would have influenced surface and ground water flow in the area. The failure propagated up a natural drainage channel. A remarkable feature of the slide is the line of trees on small rafts following the drainage line. These trees are Sitka spruce and have root systems that is "shallow and platelike" (USDA Forest Service). Thus root grafting can occur and explains the rafting.

5.2 Meenbog, Co. Donegal, 13/11/20

Some images of this slide are shown on Figures 25 and 26. Again they come from two videos containing aerial drone imagery posted on YouTube (https://www.youtube.com/watch?v=xbQe55YnW5g and https://www.youtube.com/watch?v=rf6S9Uz2Zrw)

Figure 25. Meenbog peat slide (https:// www.youtube.com/watch?v= xbQe5 5YnW5g)

Figure 26. Meenbog peat slide (https:// www. youtube.com/watch?v= xbQe5 5YnW5g)

The landslide is similar in many ways to that at Drumkerrin and developed in an upslope retrogressive type manner. Again the extensional features are evidence of this. The landslide occurred in an area where a windfarm construct was underway and a large drain and access road crosses the slope at the lower end of the landslide, probably where failure was initiated. Similar to Drumkerrin the failure resulted in small rafts with upright trees sliding along the low angled slope. The landslide had a long runout to a major watercourse resulting in a fish kill.

5.3 Mount Eagle, Co. Kerry, mid-November 2020

Again some very interesting internet posts can be viewed on this slide, e.g. the Twitter posts of Save Kerry (https://mobile.twitter.com/savekerry/status/1328059773825257475?lang=en GB and https://twitt er. com/savekerry/status/1328342795795492866? lang= en). An example is shown on Figure 27. The image shown on Figure 28 was produced by PlanetLabs and is taken from Dave Petley's landslide blog.

Figure 27. Mount Eagle peat slide (Save Kerry Twitter post, see above)

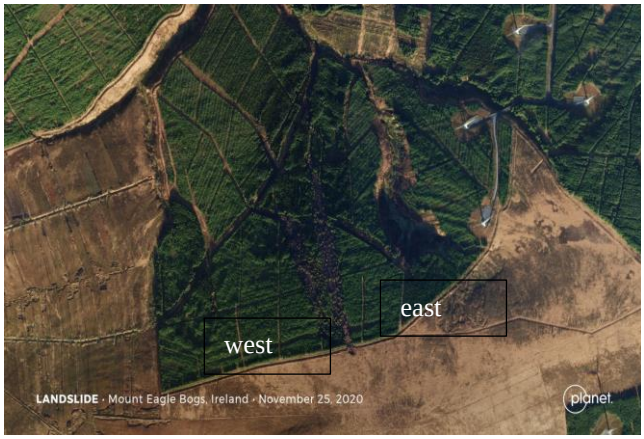

Figure 28. Mount Eagle peat slide – high resolution satellite imagery produced by PlanetLabs

In Figure 28, the high ground is located to the south with a slope down to the north. There are some wind turbines east of the slide area but these were apparently not a factor in the landslide. The image shows two peat slides. That to the west is an older failure and that to the east is the November 2020 failure. The two head scarps are located very close together. The gully further east is probably an older slide. The blocks in the open mountain have travelled only a few metres evidence that they developed late in the evolution of the landslide. The large drains in the open mountain area also likely played a role in feeding water into the slide area.

Figure 27 suggests that the deformation was chaotic without ordered structure as was seen at Drumkerrin and Meenbog. It is possible that the failure occurred towards middle of plantation. Again this is a Sitka spruce area and there was movement with rafts and upright trees and no clear retrogression. Downstream of the slide area there was a transition into channelised flow with long runout.

6 CHARACTERISTICS OF PEAT AT DRUMKERRIN

A limited investigation of the characteristics of the peat at the Drumkerrin site has been undertaken. The data are shown here as they are characteristic of many Irish peats. Samples were taken using a Jowsey auger [19] which produces 0.5 m long 50 mm diameter hemispherical samples of the peat, Figure 29.

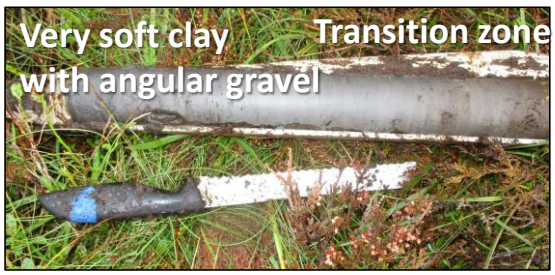

Figure 29. Jowsey peat auger and image of base of borehole showing transition between peat and underlying mineral soils

The log shown on Figure 30 is from just east of the slide area. It shows the peat has a water content of some 1200% near the surface gradually reducing with depth to the interface with the mineral soil. The upper 2.5 m of the sequence contains some sphagnum. The loss on ignition is close to 100% indicating the material is almost entirely organic. Beneath the peat is a very soft clay with some angular gravel. The gravelly layer would also have played some role in the pore pressures in the peat during the failure.

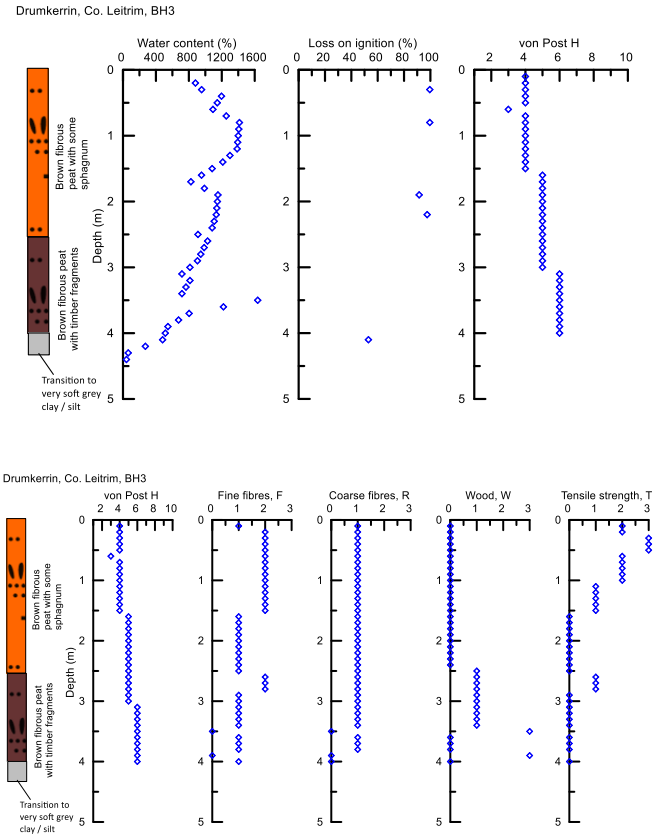

Figure 30. Log of BH3 Drumkerrin

Peat is often logged using the von Post scale [20]. This involves assigning a degree of decomposition to the peat ranging between 1 (fresh peat) to 10 (fully decomposed). Here the peat shows a gradual increase in decomposition from 4 near the surface to 6 with depth. However the von Post log is incomplete without a log of fine fibres (F), coarse fibres (R), wood fraction (W) and tensile strength (T), see Figure 30. All of these factors are assigned a rating between 0 and 3. Here the F value reduce with depth but the W value increases. Perhaps a significant feature is a decrease in the T value from 3 near the surface to zero with depth, indicating the decomposed peat towards the base of the sequence is very weak.

7 MODERN PROFILING TOOLS

7.1 CPTU testing at Gjerdrum

In Norway much use is made of the piezocone (cone penetration test with pore water pressure measurements – CPTU) for profiling soft clay areas [21]. A typical CPTU profile at the same location as the borehole shown on Figures 15 to 17 is given on Figure 31. It shows measurements of corrected cone end resistance (q_t), sleeve friction (f_s) and pore water pressure (u_2) with depth, see also figure 32. Both q_t and f_s are relatively high in the upper dry crust but then drop to low values (especially f_s) in the soft quick clay.

The pore wate pressure parameter (B_q) is often used as a possible indicator of quick clay. Here the values of B_q exceeds 1.0 in the quick clay zone a finding consistent with other Norwegian experience [22].

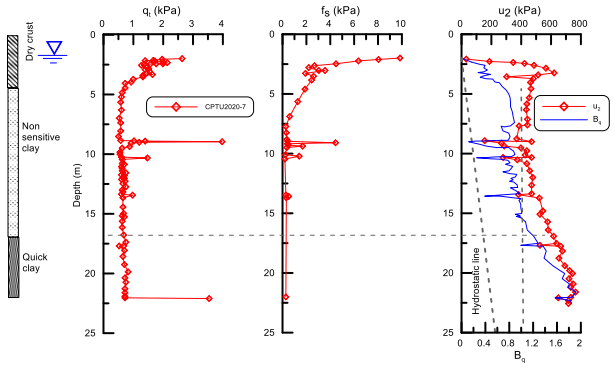

Figure 31. CPTU profile CPTU2020-7 from Gjerdrum (data from www.ngi.no)

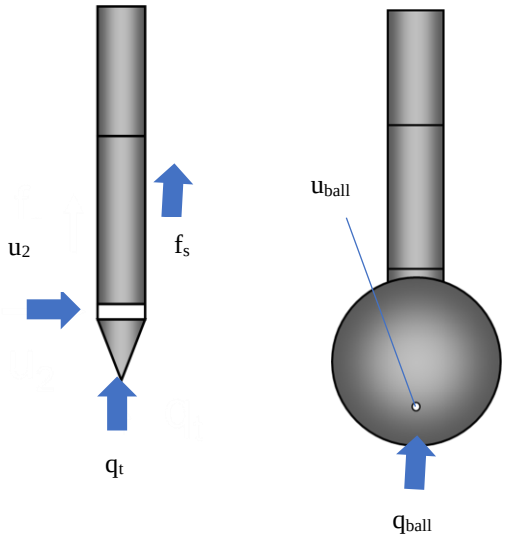

Figure 32. Standard 10 cm^2 CPTU and 100 cm^2 piezoball

7.2 *Piezoball testing in peat*

A criticism of the CPTU in peat is the possible dominant role of the fibres. Hence in Ireland [23] and the Netherlands [24] use is being made of the piezoball, see Figure 32. The idea is that the much greater bearing area is much less susceptible to fibres and the tool gives a better representation of global strength. The greater bearing area also means that the piezoball gives more accurate readings in these very soft deposits.

Some CPTU and piezoball profiles for peat at a windfarm site in Co. Tyrone are shown on Figure 33. The ball gives a much smoother profile than the CPTU. Note also the partially drained behaviour as the tools penetrate the peat.

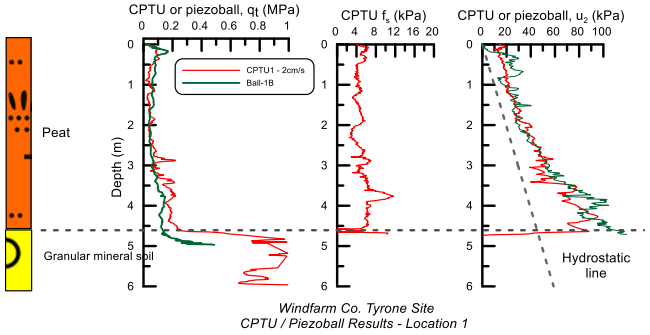

Figure 33. CPTU and piezoball profiles for windfarm site in Co. Tyrone

8 USE OF GEOPHYSICS

Geophysical techniques are becoming more commonly used in geotechnical engineering and can be very useful investigating quick clay and peat areas. For example in quick clay areas Ground Penetrating Radar (GPR), seismic refraction and seismic reflection techniques are used to determine soil stratigraphy, the depth to bedrock and the location of the water table. Shear wave velocity (V_s) profiles are used to determine detailed soil parameters [25] and resistivity can be used to check for possible quick clay.

In peat, resistivity and the seismic techniques can be used for general soil profiling, V_s is being used for estimates of peat undrained shear strength [26] and GPR can be used to estimate peat thickness and study internal structures in the peat [27]. Some examples of these applications follow.

8.1 *Resistivity profiling in quick clay areas*

In Norway resistivity is generally measured either using standard electrical resistivity tomography (ERT), using a resistivity probe (RCPTU), which is essentially a CPTU with an extra module added. For large liner projects (e.g highways) air borne electromagnetics is also being used [28]. These techniques are of different scale ranging from cm to many metres so care needs to be taken when comparing the data.

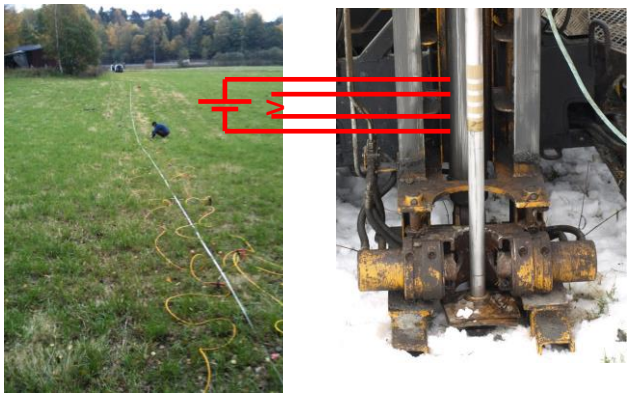

Figure 34. ERT and RCPTU measurements

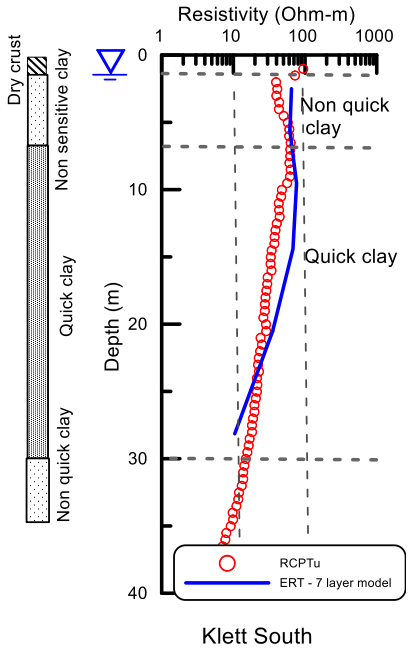

Figure 35. ERT and RCPTU profiles for the Klett South site, Trondheim [29]

Some ERT and RCPTU profiles for the Klett South site in Trondheim are shown on Figure 35. Both techniques give similar results. Use of resistivity to check for the possible presence of quick clay is based on the idea that in leached clays (like quick clays), the salt content will be very low and therefore the resistivity will be high. In non-leached clays the salt content will be high and the resistivity low, see Figure 36.

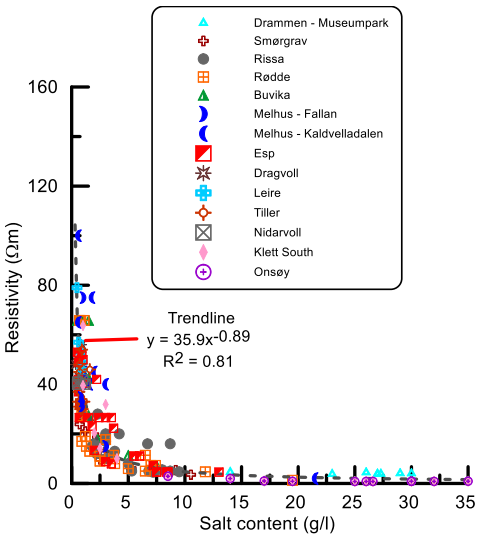

Figure 36. Salt content versus resistivity [30]

Guidelines have been produced linking resistivity to the site conditions similar to those in Table 1.

Table 1. Use of resistivity to assess possibility of quick clay [2]

Material	Resistivity range (Ωm)
Unleached marine clay	1 - 10
Leached, possible quick clay	10 – 80 / 100
Dry crust clay, slide deposits, coarser material line sand, gravel and bedrock	> 100

For the Klett South site (Figure 35), the non-quick clay below 30 m is clearly identified by the RCPTU profile. However the resistivity measurements indicate incorrectly that the upper 7 m are quick. This is because the continued leaching process as described in Section 3.1 above has progressively made the clay quick and then later non-quick. Therefore resistivity will indicate reliably if the soil is non-quick. It will also define whether a site is leached or not but on its own it cannot tell whether a site is quick. Resistivity can be used to screen for possible quick clay areas. Sampling or some other form of in situ testing is also required.

8.2 Use of GPR in peatlands

In upland peat areas GPR is being used to determine peat thickness and to study internal structures in the peat. Given the nature of the terrain the GPR units often needs to be man hauled across the area, see Figure 37.

Figure 37. Man-hauling 100 MHz GPR antenna across an upland peat area (Picture shows Andy Trafford iCRAG / UCD and Ian Sharkey APEX Geophysics)

The electromagnetic waves emitted and received by the unit will be reflected off boundaries such as bedrock or some internal structures in the peat, e.g. timber pieces. An example for the Drumkerrin site at the location of BH3 (Figure 30) is shown on Figure 38.

The bright reflector is the top of the bedrock which is clearly identified. The data shown is for a 100 MHz antenna. Higher frequency antennae were also used. These give more detail on the internal structures in the peat (higher frequency means shorter wavelength).

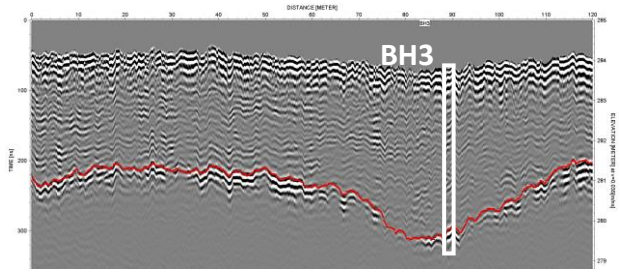

Figure 38. GPR trace near BH3 Drumkerrin. Data is for 100 MHz antenna. v assumed to be 0.036 m/ns

Data such as that shown on Figure 38 can then be used to develop maps of the peat thickness and the bedrock morphology, information which is vital to any landslide study. Ideally these data should be used with lidar imagery or digital surface models to develop three dimensional views of the study area.

9 CAUSAL FACTORS / TRIGGERING MECHANISM

9.1 Quick clay slides

As pointed out earlier quick clay is generally very competent unless disturbed. Some examples of the triggering mechanisms for quick clay slides are small local fillings, blasting or stream erosion. The landslide at Rissa in 1978 [31] is perhaps the most famous quick clay slide as the sliding action was captured on movie camera, see Figure 39. It was caused by a local filling at the edge of a lake, with spoil material from an extension to a barn.

The Kattmarka slide, near Namsos (Figure 40) is thought to have been triggered by rock blasting for a road cutting [32].

Although other factors were also at play, as have been described earlier, erosion is thought to be a primary factor in triggering the failure at Gjerdrum. Stream erosion was also considered to be the main triggering factor in the slide at Esp, near Trondheim in January 2012 [2].

Figure 39. Rissa quick clay slide. Image courtesy Lars Grande, NTNU

Figure 40. Kattmarka quick clay slide. Photo courtesy Anders Gylland, Multiconsult

9.2 Peat slides

Causal factors for peat slides can be sub-divided into external and internal factors as follows [33].

External factors
- High intensity rainfall*
- Long period of dry weather (cracks)
- Excavation in the peat e.g. turf cutting / sausage cutting
- Construction excavation / filling / sudden loading
- Historical land use (drainage, grazing, burning etc.)

* Occurs in many cases but there is often a secondary factor involved

Internal factors
- Slope inclination
- Peat thickness (NB local depressions)
- Slope morphology
- Break in slope
- Impermeable material below peat
- Interface
- Hydrogeology (e.g. peat pipes)

Slides in peat seem to be independent of bedrock type, slope aspect or the time of the year.

Arguments have also been put forward that peat slides are part of a natural cycle and that they occur when peat thickness reaches a critical value. The failure is akin to a “safety valve” being open to restore equilibrium

10 ONGOING AND FUTURE WORK

To the authors knowledge there are at least two ongoing efforts into understanding the recent Irish peat slides. An interdisciplinary group involving researchers from iCRAG (the Irish Centre for Research in Applied Geoscience), the National Centre for Geocomputation, Maynooth University, the School of Computer Science, Maynooth University, the Schools of Geography, Botany and Civil Engineering, Trinity College Dublin, the Schools of Civil Engineering and Earth Science, UCD and the consulting company RPS have been looking into the Drumkerrin slide.

In parallel the National Parks and Wildlife Service (NPWS) and GSI have appointed Fehily Timoney to examine the slides at Drumkerrin, Meenbog and Mount Eagle.

11 SOME CONCLUDING THOUGHTS

In the Irish context, it is considered that these events are complicated and that – cross disciplinary work is essential. Nature is moving the "goal posts" via climate change and other factors so developing an understanding of the factors at play is very important. Bog slides are part of our heritage and as such need to be treated with respect.

Given the impact of the slides it is clear that further research is needed especially in the areas of:

- the role of water (internally in the peat via body flow or via peat pipes and on the surface of the peat),
- the role of historical land use,
- the likely impact of future low frequency / high intensity rainfall events,
- geotechnical properties of peat (strength and permeability),
- the nature of the failure surface in peat slides,
- more use of remote sensing.
- further use of geophysical tools.

Finally, is it possible that we have quick clay in Ireland? Some geotechnical data from the site of the Athlone Relief Road (M6) are shown on Figure 41 [34]. It can be seen that in several places the sensitivity is very high and the remoulded undrained shear strength is less than 0.5 kPa suggesting "quick conditions exist. Söderblom [35] showed that the introduction of organic dispersing agents can produce "quick" conditions and he found that this was the cause of the development of quick clay in 62 of 1848 cases in Sweden. It is likely that this is also the main factor at play here.

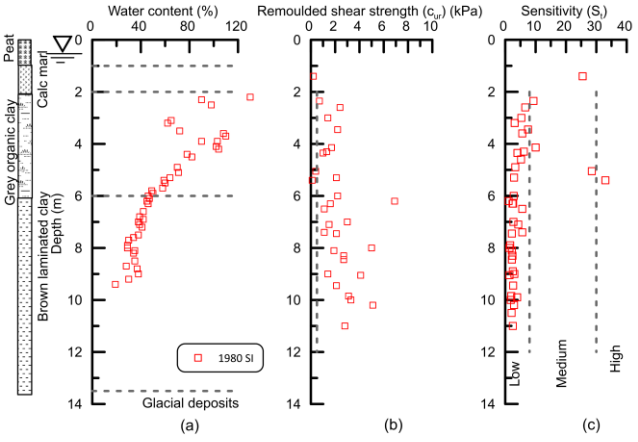

Figure 41. Some geotechnical properties at the site of the Athlone Relief Road

ACKNOWLEDGMENTS

The author is grateful to his many colleagues in Ireland and Norway for their contributions to this work. Many of them have been quoted in the references.

REFERENCES

[1] I. Ryan and H. Riekeles, "Årsakene til kvikkleireskredet i Gjerdrum 2020 - Rapport fra ekspertutvalg (In Norwegian). Available on www.regjeringen.no," 2021.

[2] I. L. Solberg, M. Long, V. C. Baranwal, A. S. Gylland, and J. S. Rønning, "Geophysical and geotechnical studies of geology and sediment properties at a quick-clay landslide site at Esp, Trondheim, Norway," *Engineering Geology (Elsevier)*, vol. 208, pp. 214 - 230, 2016.

[3] T. E. Helle, P. Aagaard, and S. Nordal, "In situ improvement of highly sensitive clays by potassium chloride migration," *Journal of Geotechnical and Geoenvironmental Engineering ASCE*, vol. 143, no. 10, pp. 04017074-1 to 2017.

[4] I. T. Rosenqvist, "Norwegian research into the properties of quick clay: a review," *Engineering Geology*, vol. 1, no. 6, pp. 445 - 450, 1966.

[5] R. Pusch, "Quick-Clay Microstructure," *Engineering Geology*, vol. 1, no. 6, pp. 433-443, 1966.

[6] J. K. Torrance, "Towards a general model of quick clay development," *Sedimentology*, vol. 30, pp. 547 - 555, 1983.

[7] L. Bjerrum, "Engineering geology of Norwegian normally consolidated marine clays as related to settlement of buildings," *Géotechnique*, vol. 17, no. 2, pp. 81-118, 1967.

[8] *Veilding for symboler og definisjoner i geoteknikk - identifisering og klassifisering av jord - Melding Nr. 2, Revidert 2011*, 2011.

[9] A. Gylland, M. Long, A. Emdal, and R. Sandven, "Characterisation and engineering properties of Tiller clay," *Engineering Geology (Elsevier)*, vol. 164, pp. 86 - 100, 2013.

[10] J. Feehan and G. O'Donovan, *The bogs of Ireland – An Introduction to the Natural, Cultural and Industrial Heritage of Irish Peatands*. UCD Environmental Institute, 1996.

[11] R. L. Praeger, "Bog bursts, with special reference to the recent disaster in Co. Kerry," *Irish Naturalist*, vol. 6, pp. 141-162, 1897.

[12] R. L. Praeger, *The way that I went*. Dublin, Ireland: Figgis, 1969.

[13] A. P. Dykes and J. Warburton, "Failure of peat covered hillslopes at Pollatomish, Co. Mayo, Ireland: analysis of topographic and geotechnical influences " *Catena*, vol. 72, pp. 129-145, 2008.

[14] M. Long and P. Jennings, "Analysis of the peat slide at Pollatomish, Co. Mayo, Ireland," *Landslides*, vol. 3, no. 1, pp. 51-61, 2006.

[15] A. P. Dykes and J. Warburton, "Characteristics of the Shetland Islands (UK) peat slides of 19 September 2003," *Landslides*. doi: 10.1007/s10346-008-0114-7

[16] R. Lindsay and O. Bragg, "Wind farms and blanket peat - a report on the Derrybrien bog slide (2nd Edition). Derrybrien Development Cooperative Ltd., Gort, Co Galway. Available at: https://repository.uel.ac.uk/," 2005.

[17] R. Creighton, "Landslides in Ireland." Geological Survey of Ireland, 2006, p.^pp. Pages.

[18] A. P. Dykes, "Landslide investigations during pandemic restrictions: initial assessment of recent peat landslides in Ireland," *Landslides*, 2021.

[19] P. C. Jowsey, "An improved peat sampler," *New Phytologist*, vol. 65, no. 2, pp. 245-248, 1966.

[20] L. von Post and E. Granlund, "Peat resources in southern Sweden," *Sveriges geologiska undersökning, Yearbook*, vol. 335, no. 19.2 Series C, pp. 1 – 127, 1926.

[21] T. Lunne, P. K. Robertson, and J. J. M. Powell, *Cone Penetration Testing in Geotechnical Practice*. Blackie Academic and Professional, London, 1997.

[22] R. Sandven, A. Gylland, A. Montafia, K. Kåsin, A. Pfaffhuber, and M. Long, "In situ detection of sensitive clays – Part II: Results," presented at the 17th Nordic Geotechnical Meeting (NGM), May, Reykjavik, Iceland, 2016.

[23] M. Long and N. Boylan, "In situ testing of peat – a review and update on recent developments," *Geotechnical Engineering Journal of the SEAGS & AGSSEA*, vol. 43, no. No. 4, December, pp. 41 - 55, 2012.

[24] C. Zwanenburg and G. Erkens, "Uitdam, the Netherlands, test site for soft fibrous peat," *AIMS Geosciences*, vol. 5, no. 4, pp. 804 - 830, 2019.

[25] J.-S. L'Heureux and M. Long, "Relationship between shear wave velocity and geotechnical parameters for Norwegian clays," *Journal of Geotechnical and Geoenvironmental Engineering ASCE*, pp. 04017013-1 – 04017013-20, 2017.

[26] A. Trafford and M. Long, "Relationship between shear wave velocity and undrained shear strength of peat " *ASCE Journal of Geotechnical and Geoenvironmental Engineering*, vol. 146, no. 7, pp. 04020057-1 - 04020057-10, 2020.

[27] A. Trafford and M. Long, "Some recent developments on geophysical testing of peat," presented at the 17th Nordic Geotechnical Meeting (NGM), Reykjavik, Iceland, May 2016, 2016.

[28] E. J. Harrison *et al.*, "AEM in Norway: A Review of the Coverage, Applications and the State of Technology," *Remote Sensing MDPI*, vol. 13, p. 4687, 2021.

[29] M. Long *et al.*, "Site characterisation and some examples from large scale testing at the Klett quick clay research site," *AIMS Geosciences*, vol. 5, no. 3, pp. 344 - 389, 2019.

[30] M. Long, A. A. Pfaffhuber, S. Bazin, K. Kåsin, A. Gylland, and A. Montaflia, "Glacio-marine clay resistivity as a proxy for remoulded shear strength: correlations and limitations," *Quarterly Journal of Engineering Geology and Hydrogeology (QJEGH)*, vol. 51, pp. 63 - 78, 2017.

[31] O. Gregersen, "The quick clay landslide at Rissa, Norway," *Norwegian Geotechnical Institute Publication* vol. 135, pp. 1 - 6, 1981.

[32] J. Johansson, F. Løvholt, K. H. Andersen, and C. Madshus, "Impact of blast vibrations on the release of quick clay slides," presented at the 18th International Conference on Soil Mechanics and Geotechnical Engineering (ICSMGE), Paris, France, 2013.

[33] N. Boylan, P. Jennings, and M. Long, "Peat slope failure in Ireland " *Quarterly Journal of Engineering Geology and Hydrogeology*, vol. 41, no. 1, pp. 93-108, 2008.

[34] M. Long and N. J. O'Riordan, "Field behaviour of very soft clays at the Athlone embankments," *Géotechnique*, vol. 51, no. 4, pp. 293 - 309, 2001.

[35] R. Söderblom, "Organic matter in Swedish clays and its importance for quick clay formation," *Swedish Geotechnical Institute, Proceedings*, vol. 26, 1974.

Implementation of PISA numerical framework for offshore wind foundation design

Louis-Marin LAPASTOURE[1,2], David IGOE[1]
[1]Department of Civil, Structural and Environmental Engineering, Trinity College Dublin, College Green, Dublin 2, Ireland
[2]Gavin and Doherty Geosolutions, Unit A2, Nutgrove Office Park, Dublin 14, Ireland
email: lapastol@tcd.ie, igoed@tcd.ie

ABSTRACT: Monopiles are the most common foundation type for offshore wind turbines representing about 80% of the offshore wind turbine installations to date. The recently completed PISA project developed state of the art design practices to model the pile soil interactions for monopiles. The PISA rule-based approach provides equations, referred to as 'depth variation functions', to generate monopile soil reaction curves which can be used in a non-linear beam-spring analysis. These depth variation functions were calibrated to match the results of Finite Element models which were validated against large scale pile tests in Cowden TILL and Dunkirk SAND. The PISA numerical based approach sets out a framework to calibrate site specific depth variation functions based on the results of bespoke 3D finite element modelling. The approach is quite complex requiring extraction of soil reaction curves, curve fitting and multi-variate optimisation. PLAXIS Monopile Designer (previously MoDeTo) is the first commercial implementation of the PISA framework. The software is very user friendly but is lacking a component, referred to as 2nd stage calibration. The 2nd stage calibration is essential to fine tune the depth variation functions in order to obtain best match with pile response. This paper presents key considerations and challenges for the implementation of the PISA numerical framework. Significant improvements are proposed, including the definition of new more time efficient cost function. It is shown that the proposed implementation provides more accurate results than PLAXIS Monopile Designer for a given design example.

KEY WORDS: Offshore Wind; Monopile; Geotechnical Engineering; PISA.

1 INTRODUCTION

In Ireland, no offshore wind farms have been built since the 24 MW Arklow Bank Wind Park Phase 1 in 2004. The offshore wind industry is now gaining momentum with the Climate Action Plan 2021 targeting 5 GW of offshore wind to be commissioned by 2030 [1], the launch of the new Marine Area Consent regime [2] and the release of draft terms and conditions of the first offshore subsidy [3].

Monopiles are the most common foundation type supporting offshore wind turbines, representing about 80% of the installation to date [4]. Monopiles are large diameter (6 – 10 m) open ended piles driven into the seabed. The popularity of monopiles is due to their simple design which allows for quick fabrication and installation. Traditional industry practices for monopile design were based on the American Petroleum Institute (API) standards [5] developed from a limited number of long and flexible pile field tests. It is now widely recognized as being unsuitable for short and rigid monopile design [6].

Due to the shortcomings of the API 'p-y' approach, the PISA project was formed in 2013 with the aim of developing new design methods specifically for the offshore wind industry. The new PISA design method represents the state-of-the-art design methodology for monopiles [7] and is now used globally for monopile design. Parts of the PISA design method have been implemented into the commercial software PLAXIS Monopile Designer [8]. Although the approach is quite complex, the software interface is very simple to use, making state-of-the-art research available for day-to-day engineering. However, the software is lacking an essential component to ensure the best results: the so-called '2nd stage calibration' [9]. Hence, this paper presents key considerations and challenges for the implementation of the PISA numerical framework. The proposed implementation, with a new more time efficient cost function, is also compared to PLAXIS Monopile Designer.

2 PISA FRAMEWORK

2.1 General principle

In the traditional API method for analysing laterally loaded piles, a 1D Finite Element (FE) analysis is used where the pile is modelled as a linear elastic beam and the soil lateral reaction is modelled using decoupled non-linear 'p-y' springs. One of the key differences between the PISA framework and the traditional API 'p-y' approach is the addition of three other soil reaction components to the distributed lateral load: the distributed moment, the base shear and the base moment (see Figure 1). The soil reaction curves can be constructed from a set of equations referred to as 'depth variation functions' following the PISA rule-based approach or using site specific advanced three-dimensional finite-element analysis following the PISA numerical-based approach.

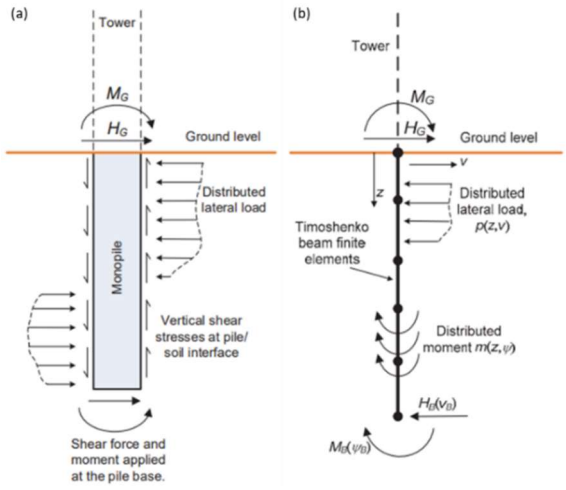

Figure 1. PISA design model: (a) soil reaction components acting on the pile; (b) implementation in 1D FE [10].

2.2 PISA rule-based approach

In the PISA framework the soil reaction curves are normalised by the pile outside diameter (D) and by local stiffness and strength soil parameters: small-strain shear modulus (G_0), initial vertical effective stress (σ'_v) in sand and undrained shear strength (s_u) in clay. The formulae are presented in Table 1 for both sand [11] and clay [12].

One may notice the coupling between distributed moment and distributed lateral load in sand. This coupling requires special attention when implementing the approach. Indeed, the distributed moment is a function of both the lateral displacement and the cross-section rotation.

Table 1. Soil reaction curves normalisation [11,12].

Normalised Variable	Dimensionless form	
	in SAND	in CLAY
Lateral displacement, $\bar{v}$	$\frac{vG_0}{D\sigma'_v}$	$\frac{vG_0}{Ds_u}$
Pile cross-section rotation, $\bar{\psi}$	$\frac{\psi G_0}{\sigma'_v}$	$\frac{\psi G_0}{s_u}$
Distributed lateral load, $\bar{p}$	$\frac{p}{D\sigma'_v}$	$\frac{p}{Ds_u}$
Distributed moment, $\bar{m}$	$\frac{m}{D\lvert p\rvert}$	$\frac{m}{D^2 s_u}$
Base horizontal load, $\bar{H}_B$	$\frac{H_B}{D^2\sigma'_V}$	$\frac{H_B}{D^2 s_u}$
Base moment, $\bar{M}_B$	$\frac{M_B}{D^3\sigma'_v}$	$\frac{M_B}{D^3 s_u}$

In the PISA framework, each soil reaction curve is described using a four-parameter conic function. In both sand and clay, any normalised soil reaction ($\bar{y}$) can be determined explicitly from the corresponding normalised displacement or rotation ($\bar{x}$) as per equation (1).

$$\bar{y} = \begin{cases} \bar{y}_u \dfrac{2c}{-b+\sqrt{b^2-4ac}} & \text{for } \bar{x} < \bar{x}_u \\ \bar{y}_u & \text{for } \bar{x} \geq \bar{x}_u \end{cases} \quad (1)$$

Where a, b and c are computed as per below:

$$a = 1 - 2n \quad (2)$$

$$b = 2n\frac{\bar{x}}{\bar{x}_u} - (1-n)\left(1+\frac{\bar{x}k}{\bar{y}_u}\right) \quad (3)$$

$$c = \frac{\bar{x}k}{\bar{y}_u}(1-n) - n\left(\frac{\bar{x}}{\bar{x}_u}\right)^2 \quad (4)$$

Each of the four parameters employed in the conic function have a clear physical meaning (see Figure 2):

- $\bar{y}_u$ is the ultimate normalised reaction. The reaction is any of the 4 soil reaction components ($\bar{p}$, $\bar{m}$, $\bar{H}_B$ or $\bar{M}_B$).
- $\bar{x}_u$ is the corresponding ultimate displacement or rotation at which the ultimate reaction is reached.
- k is the initial stiffness of the normalised reaction curve.
- n is a curvature parameter ranging from 0 to 1. The curved conic function is simplified to a bi-linear form when $n = 0$ or $n = 1$.

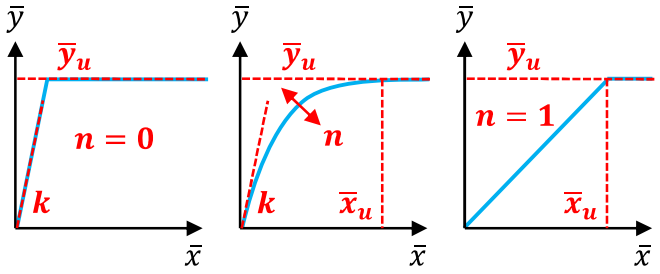

Figure 2. Signification of the four shape parameters.

The variations with depth of the 4 parameters ($\bar{x}_u$, k, n and $\bar{y}_u$) describing the shape of the 4 soil reaction components (distributed lateral load, distributed moment, base moment and base shear) are captured by the depth variation functions (DVF). The 16 DVFs are defined by 24 parameters in sand and 28 in clay (see Table 2). While some parameters remain constant with depth (z), most of them vary linearly with the normalised depth (z/D) at which the soil reaction curve is considered. In sand, the ultimate distributed lateral load and ultimate distributed moment are a function of z/L instead where L is the pile embedded length. In clay, the ultimate distributed lateral is an exponential function of z/D.

These DVF parameters, s_1 to s_{24} in sand and c_1 to c_{28} in clay, were calibrated using a set of three-dimensional finite-element analyses (11 analyses for each soil profile with D ranging from 5 m to 10 m and L/D ranging from 2 to 6) and are provided in [11] and [12], respectively. The 3D FE models were themselves validated against onshore large scale field tests (pile diameter up to 2 m) in Dunkirk dense marine sand [13] and Cowden stiff glacial clay till [14]. Since the vertical effective stress used in the normalisation process in sand does not adequately capture the soil strength, the DVF parameters are defined as a linear function of the relative density in [11] (validated for D_r ranging from 45% to 90%).

Table 2: Depth variation functions [11,12].

Soil Reaction Curve	Shape Parameter	Depth Variation Function	
		in SAND	in CLAY
Distributed lateral load, $\bar{p}$-$\bar{v}$	$\bar{x}_u$	s_1	c_1
	k	$s_2 + s_3 z/D$	$c_2 + c_3 z/D$
	n	s_4	$c_4 + c_5 z/D$
	$\bar{y}_u$	$s_5 + s_6 z/L$	$c_6 + c_7 e^{c_8 z/D}$
Distributed moment, $\bar{m}$-$\bar{\psi}$	$\bar{x}_u$	s_7	c_9
	k	s_8	$c_{10} + c_{11} z/D$
	n	s_9	c_{12}
	$\bar{y}_u$	$s_{10} + s_{11} z/L$	$c_{13} + c_{14} z/D$
Base horizontal force, $\bar{H}_B$-$\bar{v}$	$\bar{x}_u$	$s_{12} + s_{13} L/D$	c_{15}
	k	$s_{14} + s_{15} L/D$	$c_{16} + c_{17} L/D$
	n	$s_{16} + s_{17} L/D$	$c_{18} + c_{19} L/D$
	$\bar{y}_u$	$s_{18} + s_{19} L/D$	$c_{20} + c_{21} L/D$
Base moment, $\bar{M}_B$-$\bar{\psi}$	$\bar{x}_u$	s_{20}	c_{22}
	k	s_{21}	$c_{23} + c_{24} L/D$
	n	s_{22}	$c_{25} + c_{26} L/D$
	$\bar{y}_u$	$s_{23} + s_{24} L/D$	$c_{27} + c_{28} L/D$

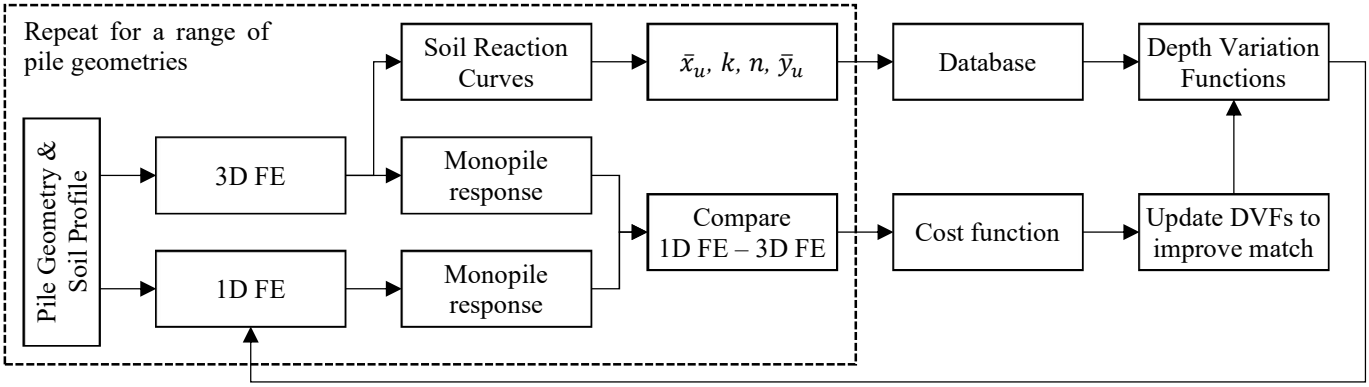

Figure 3. Flowchart of the PISA numerical based approach.

2.3 PISA numerical- based approach

At early stage of design, the PISA rule-based approach offers a simple and quick method to predict monopile responses. However, the predictions may be inaccurate as the soil profiles and pile geometries may be different from those used for calibration original PISA calibration. At later stage of design, when appropriate site investigations have been carried out, the PISA numerical based approach may be more accurate.

Carefully calibrated three-dimensional finite-element analyses are often regarded as the most accurate approach to predict monopile response to lateral loading. However, relying solely on 3D FE would be too time consuming to optimise the foundation design across the entire wind farm. Instead, the PISA numerical based approach offers a good trade-off between 3D FE accuracy and 1D FE computational efficiency. It employs a suite of 3D FE analyses to calibrate site-specific depth variation functions. Those depth variation functions can then be used in 1D FE (similarly to the PISA rule-based approach) to predict monopile response. Pile geometry and load combination can easily be varied in 1D FE at no extra computation cost compared to 3D FE. In addition, the PISA framework was initially only calibrated for a homogeneous soil profile but was later extended to layered soils [15]. Once the DVFs are calibrated for each soil unit, the thickness and arrangement of the different soil layers can be varied to match with the soil profile at different location across the wind farm.

Figure 3 presents the key aspects of the PISA numerical based approach which are detailed below:

- 3D FE analyses for a range of pile geometries are required to calibrate the depth variation functions. The accuracy of the overall approach relies on the accuracy of the 3D FE analyses. Any constitutive model may be considered but it needs to be carefully calibrated to replicate the soil response over the required strain range. The accuracy of the approach is naturally directly affected by the extent and quality of the site investigations.
- Soil reaction curves (distributed lateral load, distributed moment, base shear and base moment) are extracted from each 3D FE model.
- After normalisation, each soil reaction curve is fitted according to the PISA framework presented in section 2.2. A procedure to fit each of the 4 shape parameters for each of the 4 soil reaction components is presented in [11] for sand and [12] for clay.
- The 16 depth variation functions can then be fitted from the database of 3D FE extracted and fitted parameters. This concludes what is described as 'the first stage calibration' [11,12]. However, 1D FE pile response based on those DVFs may not compare exactly with the 3D FE response. Accuracy metrics (defined in Figure 4) as low as 77% were reported in [12] after the first stage calibration.
- A 'second stage calibration' is then required. It consists in fine tuning the DVFs until a good match between 3D FE and 1D FE responses is obtained. It requires the definition of a cost function to define what a good match is. Equation (5) is proposed in [11] and [12]. Then the DVFs can be fine-tuned using standard multi-variate optimisation algorithms available in computing environments such as MATLAB or PYTHON. Accuracy metrics as high as 99% were reported in [12] after the second stage calibration.

$$C = \sqrt{\sum_{i=1}^{N}\left(1-\eta_{ult_i}\right)^2} + \sqrt{\sum_{i=1}^{N}\left(1-\eta_{sd_i}\right)^2} \qquad (5)$$

Where:

- C is the cost function to be minimised
- N is the number of 3D FE calibration models
- η_{ult_i} is the large displacement accuracy metric for model i as defined in Figure 4a.
- η_{sd_i} is the small displacement accuracy metric for model i as defined in Figure 4b.

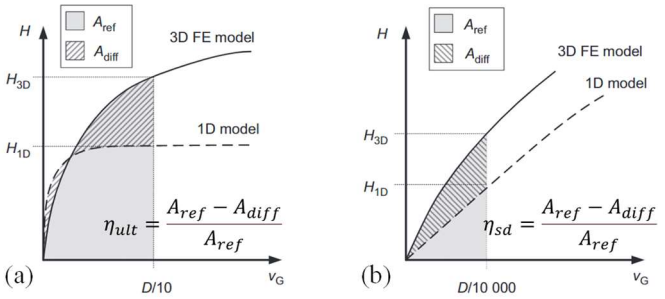

Figure 4. PISA accuracy metrics based on the pile mudline load (H) – displacement (v_g) response for (a) large displacements; (b) small displacements. Modified after [11,12].

3 IMPLEMENTATION OF PISA NUMERICAL-BASED MODELLING APPROACH

Although the PISA numerical based approach is quite complex, its commercial implementation into PLAXIS Monopile Designer offers a very simple user interface, making state-of-the-art research available for day-to-day engineering. However, the software is lacking an essential component to ensure best results: the 2nd stage calibration [8,9].

Hence, the PISA numerical framework has been re-implemented into PYTHON. The following sections presents the key considerations and challenges.

3.1 3-D finite-element modelling

The FE package PLAXIS 3D is commercially available and was selected to model the laterally loaded monopiles due to its popularity in the industry. The monopiles are modelled at full scale and half space (see Figure 5). Being consistent with PLAXIS Monopile Designer [8], the soil is modelled using the NGI-ADP model for clay and Hardening Soil small-strain (HSsmall) model for sand. A fully undrained behaviour is assumed for clay while a fully drained behaviour is considered for sand. The pile structure is modelled using linear-elastic isotropic plate elements with standard steel properties (Young's modulus of 210 GPa and Poisson's ratio of 0.3). The pile is weightless since the focus is on lateral loading. Interfaces at the outside and inside of the pile capture the soil-structure interactions. The undrained NGI-ADP model is replaced by a drained Mohr-Coulomb model at interfaces in clay to allow for tension cut-off. The stiffness parameters are kept the same, but the strength is reduced to 65% of the original value. In sand, the dilation angle is set to 0° and friction angle is reduced to 29° at the interfaces. After the pile is wished-in-place (i.e. no effect of installation), a prescribed displacement is applied in the y-direction at the top of pile until the mudline displacement reaches failure (considered to be 10% of the pile diameter). An additional interface with no strength reduction is added at pile toe to extract soil base reactions. Dummy horizontal surfaces are generated at 1 m intervals along the pile length to facilitate extraction of the soil reaction curves.

The whole process was automated in PYTHON using the PLAXIS API scripting interface. This is to ensure not only minimum computation time but also consistent modelling through all the calibration analyses by avoiding human error.

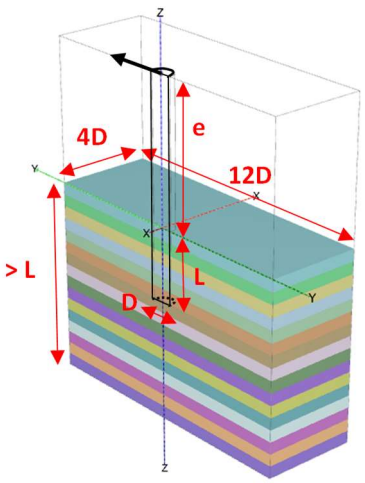

Figure 5. Example monopile model in PLAXIS 3D.

3.2 Extraction of soil reaction curves

It is typical and straight forward to extract mudline load-displacement and moment-rotation curves from laterally loaded pile 3D FE models. However, extraction of soil reaction curves along the pile length is less common and can be more cumbersome. The whole process was also automated in PYTHON using the PLAXIS API scripting interface.

The distributed lateral reaction and moments are extracted from the external vertical interfaces at 1 m intervals ($\Delta Z = 1$ m). Base shear and base moment are only extracted at pile base from the additional horizontal interfaces.

The distributed lateral reaction (p) at any depth (Z) is computed from integration of the interface forces in the y direction, while the distributed moment (m) is computed from integration of forces in the z direction multiplied by the lever arm y. This is presented in equations (6)-(7) and Figure 6a-b.

$$p(Z) = \frac{\int_{Z-\Delta Z/2}^{Z+\Delta Z/2} F_y(z)\,dz}{\Delta Z} \tag{6}$$

$$m(Z) = \frac{\int_{Z-\Delta Z/2}^{Z+\Delta Z/2} y \times F_z(z)\,dz}{\Delta Z} \tag{7}$$

However, in PLAXIS 3D Output, vertical and horizontal forces acting at the interfaces are not accessible. Only stress in local coordinates at either stress points or nodes are accessible. At each stress-point, knowing its coordinates (X, Y), the area of the element (A) and its integration weight (w), the stresses are translated into forces as per equations (8)-(9) and Figure 6c. The same process is applied to base shear and base moment curves.

$$F_y = w\mathrm{A}(\sin\theta\,\sigma_n - \cos\theta\,\tau_2) \tag{8}$$

$$F_z = w\mathrm{A}\tau_1 \tag{9}$$

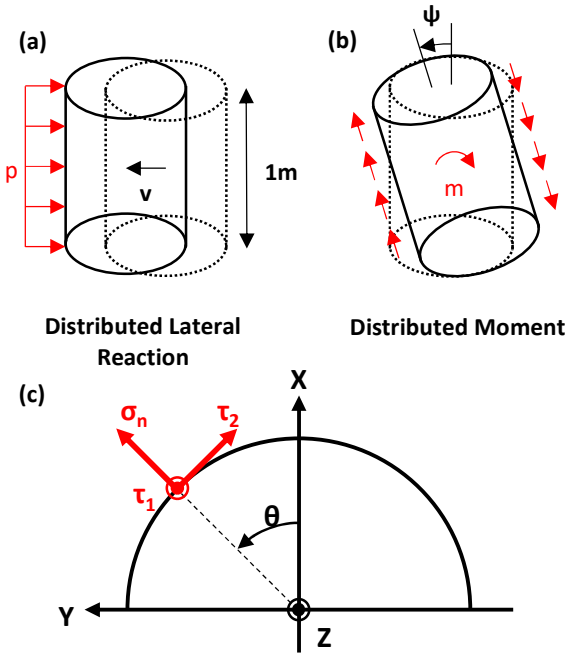

Figure 6. Extraction of soil reaction curves: (a) distributed lateral load; (b) distributed moment; (c) local coordinates system.

3.3 Normalisation and curve fitting

Once extracted, the soil reaction curves are normalized as per Table 1. The normalisation process is straightforward.

However, the curve fitting is more challenging. The ultimate reaction ($\bar{y}_u$) and the ultimate displacement ($\bar{x}_u$) can only be properly fit if sufficient pile displacements are achieved. The left-hand side of Figure 7 shows that, upon lateral loading, very little soil reactions are mobilized along the pile embedded length, even when large displacements are achieved at the mudline. Even the initial stiffness (k) might be problematic close to the point of rotation where no reactions are mobilized at all.

This issue is acknowledged in [11] and [12] where different processes are proposed depending on the soil reaction component (distributed lateral load, distributed moment, base shear or base moment) to be fitted and the soil type (sand or clay). These 8 processes are quite cumbersome to implement and require some user inputs. Hence, a simplified and unique approach is considered as part of this study:

- The initial stiffness, k, is determined by minimizing the root mean square error between the curve extracted from 3D FE and the linear expression $\bar{y} = k\bar{x}$ for the range of data at which the mudline displacement is less than $D/10000$.
- The ultimate reaction, $\bar{y}_u$, is defined as the reaction reached at the end of the analysis (largest displacement or rotation).
- The ultimate displacement or rotation, $\bar{x}_u$, is defined as the displacement or rotation as which $\bar{y}_u$ is reached for the first time.
- The curvature, n, is determined by minimizing root mean square error between the curve extracted from 3D FE and the conic function being fitted.

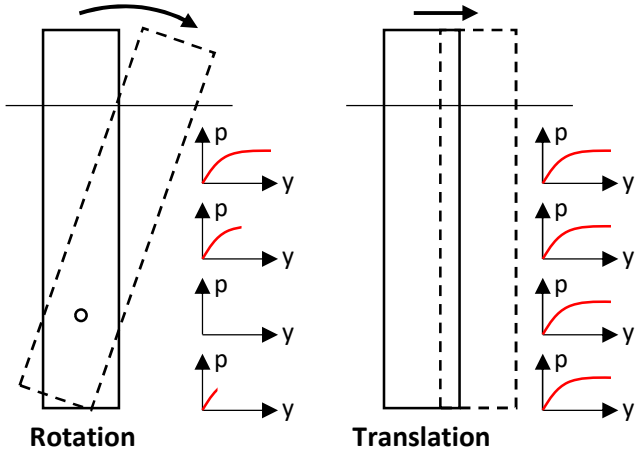

Figure 7. Limitation of the current rotation approach and proposed alternative approach.

3.4 Optimisation of depth variation functions

The so called 'second stage calibration' is a key component of the PISA numerical based approach. As presented previously and in [11] and [12], it consists in optimizing the depth variation functions in order to improve the match between the 3D FE and 1D FE responses. The soil reaction curves extracted from 3D FE, normalized and fitted are only used as a starting point for the optimization procedure. The *minimize* function from the *Scipy.optimise* library in PYTHON is used as part of this study. It allows the definition of bounds and linear constraints to ensure all parameters to be optimized remain in their range of validity. The optimization of 24 to 28 parameters (sand or clay) requires a significant number of iterations and function evaluations (typically more than 1000).

The cost function proposed by [11] and [12] (see equation (5)) was found to be too computationally expensive. The small and large displacement accuracy metrics are based on integration of the differences which may only be accurate if many small increments are summed. Instead, another cost function is implemented as part of this study and presented in equation (10). It only requires 4 loads increment per calibration models, dramatically reducing the computation time. The cost function accounts for both mudline displacement (y) and rotation (θ), minimising the difference between the 1D FE and 3D FE models.

$$C = \sqrt{\sum_{i=1}^{N} C_i(H_{ult}) + C_i\left(\frac{H_{ult}}{3}\right) + C_i\left(\frac{H_{ult}}{10}\right) + C_i\left(\frac{H_{ult}}{100}\right)} \quad (10)$$

Where:

- C is the cost function to be minimised
- N is the number of 3D FE calibration models
- H_{ult} is the ultimate capacity defined for a mudline displacement of D/10.
- $C_i(H)$ is the cost function evaluated for model i under lateral load H computed as per equation (11).

$$C_i(H) = \left(\frac{y_i^{1D}(H) - y_i^{3D}(H)}{y_i^{3D}(H)}\right)^2 + \left(\frac{\theta_i^{1D}(H) - \theta_i^{3D}(H)}{\theta_i^{3D}(H)}\right)^2 \quad (11)$$

4 COMPARISON TO PLAXIS MONOPILE DESIGNER

The implementation of the PISA numerical based approach presented in this paper is compared to PLAXIS Monopile Designer in this section. For the purpose of the comparison, the following inputs are considered:

- Soil profile: homogenous normally consolidated dense sand profile. A CPT based correlation for HSS parameters for monopile modelling was proposed by [16]. The equations were re-arranged to define the parameters assuming $D_r = 80\%$, $\phi'_{cv} = 32°$, $\gamma = 19.5\ \mathrm{kN/m^3}$, $f_s = 0.1q_c$ and $\beta^{CPT} = 185$.
- Loads: Lateral load of 12 MN acting 50 m above mudline.
- Pile geometry: D/t assumed as 110. A total of 9 calibration models were considered (Figure 8), pile diameters ranging from 6 m to 10 m and slenderness ratios (L/D) ranging from 2 to 6 are considered.

The SLS-Geo check [6] requires to limit the permanent (after unloading) mudline rotation accumulated through the cyclic load history to 0.250 degrees. For the sake of simplicity, the cyclic effects are not taken into account here and Figure 9 compares permanent static rotation for pile embedded length ranging from 20 to 50 m, assuming a diameter of 7 m. These piles' geometries fall in the range of validity for which the PLAXIS Monopile Designer and this paper's implementation were calibated.

Additional 3D FE models were run to find out that the design pile embedded length should be 29.5 m. This paper's

implementation compares very well with a design penetration of 29.2 m. However, the PLAXIS Monopile design compares poorly with a required penetration of 26.3 m. This is due to the lack of second stage calibration. See comparison on Figure 9.

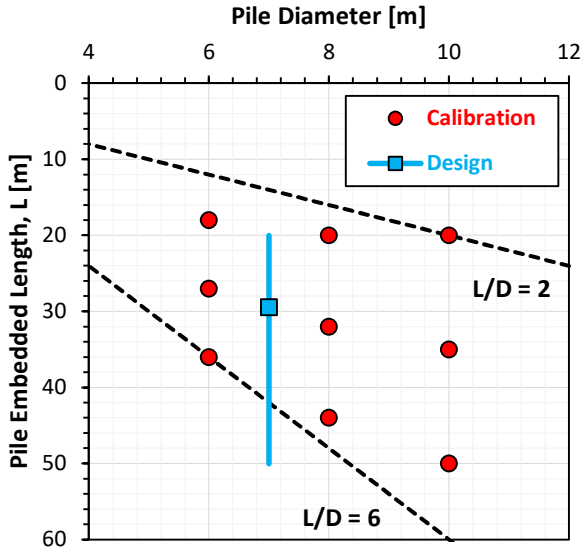

Figure 8. Calibration space and final design.

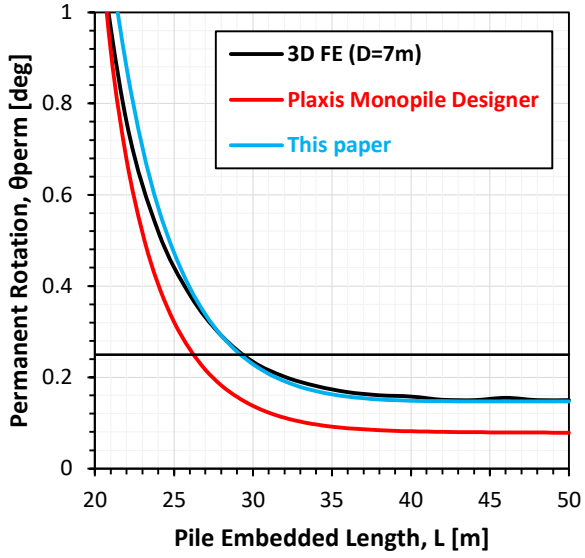

Figure 9. Comparison of PLAXIS Monopile designer results to the PISA numerical-based approach implemented in this paper.

5 DISCUSSION AND CONCLUSION

The PISA framework is the latest state of the art development for monopile design. This paper presented key considerations and challenges for the implementation of the PISA numerical-based approach. For a design example, the poor accuracy of PLAXIS Monopile Designer due to the lack of the 'second stage calibration' is demonstrated. The implementation proposed in this paper, with a new more efficient cost function and simplified curve fitting approach, provides a very satisfactory match with the base case 3D FE models. The implementation could be further improved by considering the following points:

- Fitting the soil reaction curve is challenging because there is little to no soil reaction close to point of rotation. An alternative approach where the pile model in 3D FE would be translated rather than rotated is envisaged (Figure 7 right). This would ensure large mobilization at all depths hence easier and more accurate curve fitting.
- Significant computation efforts are required to extract, normalize and fit the soil reaction curves. However, these curves are only used as a starting point for the second stage calibration. It is also possible to use PISA rule DVFs as a starting point instead, to reduce computation time.
- The cost function only considers mudline displacement and rotation. This ensures best match between the mudline responses in 1D FE and 3D FE. However, it is uncertain how the deflection profiles along the pile embedded length compare. Given that the piles are rigid, it is envisaged to add the toe displacement and rotation into the cost function evaluation to ensure better match of the overall pile response at no extra computation cost.

ACKNOWLEDGEMENT

This research is funded under the IRC employment based postgraduate program (EBPPG/2019/4).

REFERENCES

[1] https://www.gov.ie/en/publication/6223e-climate-action-plan-2021/
[2] https://www.gov.ie/en/press-release/f4c68-ireland-moves-a-step-closer-to-energy-independence/
[3] https://www.gov.ie/en/press-release/f6070-consultation-opens-on-first-auction-to-supply-electricity-from-offshore-wind-under-the-renewable-electricity-support-scheme-oress-1/
[4] Wind Europe (2020). Offshore wind in Europe - key trends and statistics 2020
[5] API (2014). APIRP2GEO Geotechnical and Foundation Design Consideration
[6] DNV (2021). DNV-ST-0126 Support structures for wind turbines.
[7] Byron W. Byrne, Harvey J. Burd, Lidija Zdravković, Ross A. McAdam, David M.G. Taborda, Guy T. Houlsby, Richard J. Jardine, Christopher M. Martin, David M. Potts, Kenneth G. Gavin (2019). PISA: new design methods for offshore wind turbine monopiles. Rev. Fr. Geotech. (158) 3. DOI: 10.1051/geotech/2019009
[8] Plaxis (2022). PLAXIS Monopile Designer CONNECT Edition Version 22 Manual.
[9] Brinkgreve, Ronald, Diego Lisi, Miquel Lahoz, and Stavros Panagoulias. 2020. "Validation and Application of a New Software Tool Implementing the PISA Design Methodology" Journal of Marine Science and Engineering 8, no. 6: 457. https://doi.org/10.3390/jmse8060457
[10] Byrne BW, McAdam RA, Burd HJ, Houlsby GT, Martin CM, Beuckelaers W, Zdravkovic L, Taborda DMG, Potts DM, Jardine RJ, Ushev E, Liu T, Abadias, D, Gavin K, Igoe D, Doherty P, Skov Gretlund J, Pacheco Andrade M, Muir Wood A, Schroeder FC (2017). PISA: New Design Methods for Offshore Wind Turbine Monopiles (Keynote). In: 8th International Conference on Offshore Site Investigations and Geotechnics. DOI: 10.3723/OSIG17.142
[11] Harvey J. Burd, David M. G. Taborda, Lidija Zdravković, Christelle N. Abadie, Byron W. Byrne, Guy T. Houlsby, Kenneth G. Gavin, David J. P. Igoe, Richard J. Jardine, Christopher M. Martin, Ross A. McAdam, Antonio M. G. Pedro, and David M. Potts (2020). PISA design model for monopiles for offshore wind turbines: application to a marine sand. Géotechnique 2020 70:11, 1048-1066. DOI: 10.1680/jgeot.18.P.277
[12] Byron W. Byrne, Guy T. Houlsby, Harvey J. Burd, Kenneth G. Gavin, David J. P. Igoe, Richard J. Jardine, Christopher M. Martin, Ross A. McAdam, David M. Potts, David M. G. Taborda, and Lidija Zdravković (2020). PISA design model for monopiles for offshore wind turbines: application to a stiff glacial clay till. Géotechnique 2020 70:11, 1030-1047. DOI: 10.1680/jgeot.18.P.255
[13] David M. G. Taborda, Lidija Zdravković, David M. Potts, Harvey J. Burd, Byron W. Byrne, Kenneth G. Gavin, Guy T. Houlsby, Richard J. Jardine, Tingfa Liu, Christopher M. Martin, and Ross A. McAdam (2020). Finite-element modelling of laterally loaded piles in a dense marine sand at Dunkirk. Géotechnique 2020 70:11, 1014-1029. DOI: jgeot.18.PISA.006
[14] Lidija Zdravković, David M. G. Taborda, David M. Potts, David Abadias, Harvey J. Burd, Byron W. Byrne, Kenneth G. Gavin, Guy T. Houlsby, Richard J. Jardine, Christopher M. Martin, Ross A. McAdam, and Emil Ushev (2020). Finite-element modelling of laterally loaded piles in a stiff glacial clay till at Cowden. Géotechnique 2020 70:11, 999-1013. DOI: 10.1680/jgeot.18.PISA.005
[15] Harvey J. Burd, Christelle N. Abadie, Byron W. Byrne, Guy T. Houlsby, Christopher M. Martin, Ross A. McAdam, Richard J. Jardine, Antonio M. G. Pedro, David M. Potts, David M. G. Taborda, Lidija Zdravković, and Miguel Pacheco Andrade (2020). Application of the PISA design model to monopiles embedded in layered soils. Géotechnique 2020 70:11, 1067-1082. DOI: jgeot.20.PISA.009
[16] Igoe. D. and Jalilvand, S. (2020). "3D finite element modelling of monopiles in sand validated against large scale field tests." Proceedings to the Fourth International Symposium on Frontiers in Offshore Geotechnics in Houston, USA.

Geotechnical and Drainage Challenges on the N4 Collooney to Castlebaldwin Road Scheme

A.R. Duggan[1], A Wilkins[2], M. Peters[2], S. Fitzsimons[3]
[1]Department of Building and Civil Engineering, Atlantic Technological University, ATU Galway City, Galway, Ireland
[2]ByrneLooby, Galway, Ireland
[3]Clandillon Civil Consulting, Kildare, Ireland
email: alan.duggan@gmit.ie, awilkins@byrnelooby.com, mpeters@byrnelooby.com, sean.fitzsimons@c3.ie

ABSTRACT: The N4 Collooney to Castlebaldwin Road Scheme, the biggest ever infrastructure project in the Northwest of Ireland, opened in August 2021. It comprised 13.8 km of dual carriageway, 0.9 km of single carriageway, and 12 bridge structures. This paper discusses aspects of the geotechnical and drainage challenges on the scheme, concentrating on the engineering solutions, including novel ones developed to overcome these challenges. The risks of soft ground and karst features along the scheme route were of particular concern. The significant thicknesses of peat, marl, and soft alluvial soils at the Castlebaldwin tie-in necessitated excavation of the peat layer and the use of staged construction with band drains. Temporary surcharge fill heights and hold durations were designed to reduce long-term creep settlement, and the embankment was instrumented to monitor stability and settlement performance. Another geotechnical challenge was the high groundwater table levels in some cutting slopes, which required the design of deep counterfort drains and berms. To address hydrological and hydrogeological challenges, two innovative drainage collection systems were developed, which maximise the use of nature-based drainage solutions. Recently completed highway projects in Ireland have predominantly used concrete drainage systems to collect and convey surface water runoff. In addition to being cheaper and having a lower carbon footprint than traditional concrete systems, nature-based drainage solutions can benefit hydrology, hydrogeology, and ecology receptors.

KEY WORDS: Road construction; Counterfort drains; Soft ground; Vertical drains; Nature-based drainage solutions.

1 INTRODUCTION

1.1 Project Description

The N4 Collooney to Castlebaldwin Road Development project was one of the most significant road projects ever built in the Northwest of Ireland. The N4 realignment scheme is 14.5km in length and commences just south of Collooney beginning with a Type 2 Dual Carriageway from the start of the scheme at the N4/N17 Toberbride Roundabout to the Castlebaldwin Roundabout (13.6km). The final section of the route from the Castlebaldwin Roundabout south to its termination point at the tie in location with the existing N4 network is Type 1 Single Carriageway (0.9km). The scheme also includes 8km of side roads and access roads, and 12 primary bridge structures. Following a competitive tender in 2018, the awarded contractor was Roadbridge, with Fehily Timoney, ByrneLooby, and Clandillon Civil Consulting as the Contractor's Designers. The project carried geotechnical risk items such as extensive deposits of extremely weak, highly sensitive and compressible soils in the low-lying areas, and the potential for karst features along the route.

1.2 Site Characterisation

The proposed route traverses typical drumlin topography with elongated hills with low lying soft ground areas, rivers and lakes in between the hills. The soft ground areas generally contain peats, marls and alluvium over glacial till, while the drumlins contain stiff to very stiff glacial till, some of which has been softened by the wet climate in the northwest. The proposed route is predominantly underlain by limestone and shales and is in the vicinity of the largest upland karst in Ireland located between the towns of Sligo, Drumshanbo, Enniskillen and Manorhamilton [1]. Exposures of the limestone are uncommon and blanket bog is widespread.

1.3 Glacial Till Deposits

Glacial till deposits occur throughout the scheme and are broken down into cohesive glacial till and granular glacial till. The results from CU triaxial tests, inferred friction angles (ϕ) from Atterberg Limit Tests [2], and ϕ derived from SPT field data [3], were used to arrive at drained shear strength parameters for the till. A minimum drained friction angle of 33° and a cohesion value of 0 kPa was adopted. This compares well with published work by Farrell [4] who states that boulder clay has a typical friction angle of 34°.

1.4 Marl

Marl was generally encountered below the peat deposits in the low-lying soft ground areas and is described as a very soft to soft white slightly sandy or sandy silt. The Marl has a moisture content of 98% (± 37%) (± one standard deviation). The SPT N values recorded generally ranged from 0 to 2 indicating a very soft to soft soil.

1.5 Soft Alluvial Clays and Silts

The alluvium was found either below the marl or directly below the peat strata in the low-lying soft ground areas and is described as very soft to soft brown or grey slightly sandy/slightly gravelly silt/clay. The alluvium has a moisture content of 49% (± 50%) (± one standard deviation). From the SPT data, shear vane tests, and triaxial tests, the alluvium is a very soft to soft soil.

1.6 Discrepancies in Bedrock Level and Rock Classification

There were discrepancies in the bedrock level in many of the drumlins. The preliminary ground investigation (GI) holes had to be discounted as these were showing that bedrock was relatively shallow between 1.4 and 2.5m bgl near the top of drumlins. The bedrock depth in adjacent holes which were dug as part of the detailed GI, were often 10 to 20m deeper than the preliminary holes but did record high SPTs and refusals. There was uncertainty in the classification of the ground conditions recorded in many of the rotary coreholes dug as part of the preliminary GI. Many of the rotary coreholes recorded very strong/strong limestone rock at depths where the Total Core Recovery is very low, often <25% to 35% and the zones of concentrated core loss were often attributed to cavities or dissolution, which would imply that the rock is highly weathered and karstified. Similar conditions could be recorded in very stiff/dense glacial till with medium to high cobbles and boulder content where the infill material has been washed out by the coring process. It is likely that glacial till with boulders was mistaken as weathered rock.

The detailed GI addressed this uncertainty in some of the deep cut sections by utilizing GeoBore-S rotary coring to maximise core recovery in very stiff/dense glacial till or highly weathered limestone rock where conventional rotary coreholes yielded poor recovery. They also clearly identify the overburden and rock strata and the presence of any karstification in the rock. Where there was a discrepancy between the preliminary and detailed GI, preference was given to the detailed GI in the interpretation of the ground conditions and karst risk on the scheme as these were more accurate and lined up well with the geophysical survey. As a result of the poor descriptions, the contractor in one instance opened a rock borrow pit for Class 1C and 6F capping material only to find the rock to be mudstone/shale rather than the strong limestone which was described in the exploratory hole logs.

2 SPECIAL CUTTING SLOPE DRAINAGE MEASURES

2.1 General

The road cuts through many drumlins with cuttings of more than 10m carried out in several locations within the glacial till deposits. For these cuttings, a side slope of 1 in 2 was considered to be a robust side slope gradient in these materials, with only minor potential for local instability if localised perched water tables and discrete seepages were encountered during construction. However, a major geotechnical challenge was the high groundwater table levels in some cutting slopes, which necessitated designing deep counterfort drains and berms for 1.52km of the road to keep within the CPO boundary and provide safe slope design. Counterfort drains were required at 6 locations ranging from 150m to 440m in chainage length and in depth from 1.5m to 2.8m deep. These cuttings were up to 15m deep. A discussion on these drains is given below.

2.2 Suspicious Groundwater Level Readings

Groundwater readings from the SI data (standpipe and standpipe piezometers) prior to construction indicated some high groundwater levels readings in some of the drumlins, some of which were suspicious due to lower groundwater level readings in other nearby boreholes, the ground topography, and the lack of adjacent groundwater strike records. Groundwater levels were often found a metre or two from the surface, sometimes near the top of the drumlin. It was considered that these instruments were likely reading localised perched water tables within the superficial soils. At one cut location, however, the GSI karst database indicated a spring in this cutting, which was a likely explanation for the groundwater levels in the drumlin that were between 0.2 and 1.88m bgl.

To gain a better understanding of the groundwater level in the cuttings, additional monitoring was undertaken during construction. 1 to 2 rotary coreholes at each cutting were drilled to a depth of 15m bgl behind the crest of the cut slope in question. In the holes, 19mm piezometers were installed with their tips at 15m bgl and a response zone between 14 and 15m bgl. From September to June 2019, readings were taken from each piezometer biweekly. The maximum groundwater level in some of the cuttings showed no obvious trend in the groundwater level reducing since the cuts were finished (3 to 9 months before). The maximum groundwater levels from the additional monitoring were similar to those reported in the original SI, often 1 to 1.5m bgl. Only at one location did the groundwater levels reduce, reducing from March 2019 with groundwater levels in May 2019 decreasing from 1 to 2.8m bgl to below 4 m bgl. Cutting through this drumlin began in early May and it was expected that the groundwater level would further reduce as the cutting progressed.

2.3 Shear box testing

Typically, the generic parameters derived from tests carried out on the glacial till throughout the entire site would be applied in the SLOPE/W analyses for these cutting slopes. However, to reduce the counterfort drain depths, more detailed examinations of the material in these slopes were undertaken to determine site specific frictional behaviour.

Samples were taken from a depth of at least 1.5m below the excavated cutting face ~ halfway way up the cutting slope in question every 100m. 3 No. drained large shear box (300mm sq) tests (direct shear) were carried out on these samples. Shear Box Testing was considered to be the best testing available given the nature and location of the material to be sampled. Material was recompacted in test moulds to as close to in situ density as possible – ideally to achieve a recompacted bulk density of at least 20kN/m^3. Normal stresses of between 50 to 200kPa were applied to the samples. It is noteworthy that the remoulded state of the samples tested in the shear box is probably more conservative than the in-situ conditions. i.e. sample disturbance and recompaction would lead to a lower frictional behaviour being observed in testing. For each of these cuttings, the results were plotted to find the best fit line through the data. Friction angles of between 32.5 to 34° and apparent drained cohesion of 8 to 14 kPa best fitted the data. However, a maximum cohesion value of between 0 and 2 kPa would typically be taken for over-consolidated cohesive materials. To be conservative, the intercept was set a 1 kPa and the best fit line replotted. An angle of between 35.3 to 36° and cohesion value of 1 kPa was the best fit. Based on these analyses, the other SI undertaken and observations on site, an angle of 35° and a cohesion of 1 kPa was adopted specifically for the stiff over-consolidated cohesive material in these particular cuttings.

2.4 Longitudinal spacing of drains

Using the slope drainage design method developed by Hutchinson [5] for counterfort drains which is outlined in the 2008 publication 'Drainage of Earthworks Slopes' [6], the counterfort drains would require significant deep drains every 5m or closer. Using this method, and assuming the water table level to be at surface, a 2m deep drain at 10m spacings has only a drawdown of 0.1m at the midpoint between the drains. This method was considered overconservative and excessive considering the drainage stone volume that would be required.

The availability of software packages such as SEEP/W to determine the drawdown between the counterfort drains means that for significant schemes more sophisticated analyses can now be undertaken using the data specific to the site, for instance, soil permeabilities, drainage boundaries, and groundwater table levels. Steady-state FE seepage analyses were run in SEEP/W to determine the drawdown between the counterfort drains. Analyses were undertaken for 1.5m to 2.5m deep drains, 0.5m wide drains at 10m spacings, with the groundwater level without the drains set at existing ground level. The maximum rise in the GWL between the drains was ~0.4 and 0.63m. Taking a weighted average drawdown level of 2/3 of the rise, this gives a drawdown of 1.23m for 1.5m drains at 10m c/c, 1.67m for 2m drains and 1.87m for 2.5m drains.

Location specific stability analyses of the cuttings were then undertaken in SLOPE/W at the critical sections with the modified depth of drain, for example, the 1.5m deep drains were modelled as 1.23m deep drains. As a result, the over design factors for some of the stability analyses in SLOPE/W were below unity and so had to be increased in depth to account for the rise between drains. To account for the rise between drains in one of the cuttings the 2.5m drains had to be increased to 2.8m in depth. At two locations, a berm made up of unsuitable Class 2C material was built in front of the slope to reduce the drain depths. Piezometers in these cuttings have remained to monitor the long-term groundwater levels. Figure 1 below shows the counterfort drains being constructed.

Figure 1: Counterfort drains

3 EMBANKMENTS ON SOFT GROUND

3.1 Introduction to Castlebaldwin Tie-In

The engineering measures adopted in the embankment designs over soft ground needed to control settlements, and in particular differential settlements, to acceptable limits such that carriageway drainage, pavement durability and vehicle stability were not adversely affected. Significant dig and replace works were carried out at several sections of the scheme where the route traversed through low-lying marshy ground, for example, through Lackagh Fen, Unshin Bog, and parts of the Castlebaldwin Tie-In. The embankments were up to 10.3m high and up to 7.5m of peat and soft compressible deposits such as marl and alluvium had to be excavated.

The N4 carriageway joins with the existing mainline at the Castlebaldwin Tie-In where the embankment is over very soft, compressible soils up to 10m in depth. Whilst capable of supporting the proposed relatively low height embankment, the soil would undergo significant primary and secondary settlement. Given the depth of soft material the proposed strategy was to utilise vertical wick drains from Ch. 13+950 to Ch. 14+145 to accelerate consolidation of the soft ground beneath, and to use temporary surcharge fill heights and hold periods to shorten the period to reach acceptable settlements and to reduce long term creep settlement. The strategy aimed to enable the embankment slopes to be built with an adequate factor of safety against failure and to ensure that primary settlement is substantially complete during construction. Fill surcharging above the final stress level has the effect of reducing the longer-term ground movements due to secondary creep settlements of the marl and alluvial soils. The peat was stripped prior to installation of the drainage blanket.

To confirm the consolidation parameters of the marl and alluvium and the depth of these soil strata, four additional cable percussion boreholes with piston sampling investigated through the drainage blanket to between 7.7 and 10.6m bgl during construction. The laboratory testing consisted of oedometer tests including secondary compression testing and quick undrained triaxial tests. A summary of the engineering properties of the marl and alluvium is given below.

3.2 Undrained Shear Strength c_u

Preference was given to CPT data as it is regarded as a powerful tool in soft soils which gives valuable data and to the supplementary GI data as all the UU tests were carried out on piston samples. With the c_u results from the CPT data, and the additional UU tests, the characteristic value for c_u for the marl and alluvium was taken as 12 kPa to a level of ~6m bgl before increasing linearly with depth to a maximum c_u of 40 kPa at ~10m bgl.

3.3 Consolidation Coefficient c_v and Compression Index C_c

A rate of consolidation, c_v, of 1.0 m^2/yr was adopted from the laboratory consolidation testing undertaken on the piston samples from the marl and alluvium strata, for the stress range representing loading from the initial vertical stress to the predicted maximum embankment loading during construction. The ratio of radial consolidation to vertical consolidation was assumed to be 1:1. It was anticipated that actual field consolidation rates during construction may be faster or slower than this rate. Relationships linking natural moisture content (w_n) with the characteristic settlement parameters, C_c, $C_c/(1+e_0)$ and C_α were developed for the vertical drain area. Figure 2 presents the primary virgin settlement compression ratio, $C_c/(1+e_0)$, derived from the consolidation tests undertaken on samples from the vertical drain area on the marl and alluvium. The trendlines for this GI data in Figure 2 were used to estimate the 'average' primary settlement occurring during construction. The oedometer data collated from the SI compares well to the

empirical relationships derived from testing on the Limerick Tunnel PPP scheme and from soft soils testing by Simons [7].

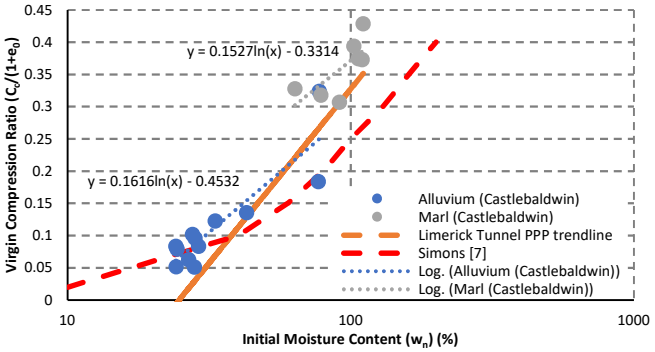

Figure 2: Compression ratio with moisture content for alluvium and marl

3.4 Secondary Compression Index C_α

The secondary compression index C_α was examined following a specialist oedometer testing program carried out on the marl and alluvium. The equation below developed from the additional SI data was used to estimate the average secondary settlement as the empirical relationship derived by Simons and Menzies [8] would overestimate the secondary settlement.

$$C_\alpha = 0.00010 * w_n\ (\%) \qquad (1)$$

3.5 Embankment Design and Staged Construction Analysis

The tight construction programme and the anticipated rate of radial consolidation formed the basis on which the earthwork design, and in particular the wick drain spacing, was developed. The adopted drain spacing was 1.0m c/c on a triangular grid. The ground conditions were extremely variable, and so it was expected that some areas would consolidate slower, or quicker than others, which would lead to an extension of the anticipated construction time and /or surcharge periods. The surcharge fill height was determined by the adjusted amount of surcharge (AAOS) required to reduce the rate of long-term secondary creep settlement to within the settlement limits. For this section, the average fill height to finished road level was generally 1.2m to 3.0m. To reduce the creep settlement rate, the AAOS was between 18% and 48%, the selection of which was balanced with limitations on stability and construction programme. This required that the surcharge fill height was 2.5m.

A staged construction method was used to construct the main embankment. In Stage 1, the embankment is built up to its full height and the additional fill height at a maximum rate of 1.0m depth of fill per week without requiring any hold periods or basal reinforcement to the fill layers. A total of 5 weeks is required to build the full height of embankment including the 2.5m surcharge. The 1st week is spent building the embankment up to existing ground level. On either side of the embankment at certain sections, the ground was filled to 1m above existing ground level with landscape material to help with stability.

3.6 Anticipated Settlement Behaviour

The AAOS provided during embankment construction has been shown to have a beneficial effect on the magnitude of the secondary compression index, C_α'. The relationship postulated by Ladd [9] was used to assess the benefit of surcharge loading but a minimum ratio of $C_\alpha'/C_\alpha'(NC) = 0.1$ was assumed for all values of AAOS greater than 40%. Moisture content profiles and soils strata thicknesses for several locations were used to estimate primary and secondary settlement, considering the beneficial effects of surcharging and vertical wick drains. Embankment primary settlements prior to pavement construction were ~1m for a 3m high embankment. It was calculated that if the surcharge was kept in place for 7.5 months then secondary settlements in the first 3 years of service (defects period) would be of the order of 5 to 20 mm, which would meet the settlement criteria that differential settlement should not be more than 10mm over 10m (0.1% gradient)

3.7 Monitoring/ Instrumentation

Instrumentation was installed and monitored at critical earthwork sections to monitor field behaviour against anticipated design predictions. Instrumentation locations were selected according to the proposed embankment height, and the depth and thickness of soft compressible soils. Settlement plates were installed within the vertical drain section in pairs on the east and west bound carriageways generally every 40m and readings were generally taken every 1-3 days. 3 No. Vibrating Wire (VW) piezometers were installed mid-depth through the soft layers at three locations and readings were recorded hourly. Unfortunately, in March, one of the VW piezometers started recording error readings. It is thought that the cable linking the piezometer to the logger was stretched while upfilling. Attempts were made to salvage it but were unsuccessful. To mitigate the risk of tension cracking in the Class 2C fill during staged construction, additional toe survey monument points were installed every 20m. Readings were taken every second day, and daily where the change in lateral/vertical deformation from prior measurements > 0.1 m.

3.8 Embankment Performance

The surcharge construction was completed on the 30th of March 2020 and by June, primary consolidation had substantially completed. Figure 3, for example, shows the predicted and observed settlement at Ch. 13+950m. 90% primary consolidation was predicted to occur at 234 days after surcharge construction. Comparing the settlement curves, greater than 99% primary consolidation was completed, with the incremental displacements between settlement plate readings reduced to zero for the plates. The field c_v was determined from back calculation and was found to range between 8 and 10 m^2/yr, meaning that 99% consolidation had occurred at between 47 to 59 days (8 to 10 m^2/yr). These values were much higher than the c_v of 1m^2/yr assumed at design stage. It is not unusual for field consolidation rates to exceed laboratory measured rates by 5 to 10 times as the laboratory samples cannot fully evaluate the macro scale deposit structure and composition in the ground and the overlying assumption during design has been that horizontal consolidation rates are the same as vertical consolidation rates. Thin lenses of sand and the slightly sandy nature of the alluvium may also have increased the consolidation rate. In general, the predicted settlements were greater than the observed settlements.

Figure 4 shows the porewater pressure ratio B with time for the VW piezometers. The ratio B is defined as equal to $\Delta u/\Delta\sigma_v$ where Δu is the change in pore water pressure associated with

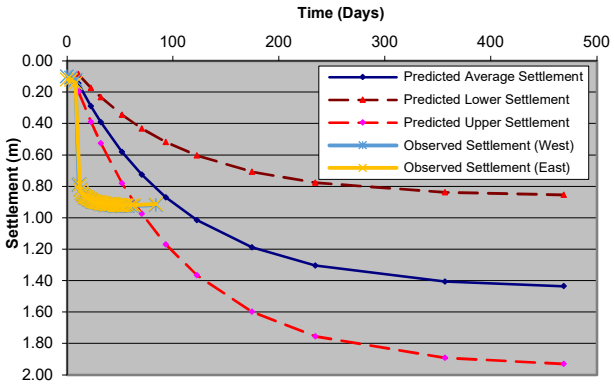

Figure 3: Predicted and observed settlement at Ch. 13+950

an increase in fill thickness and $\Delta\sigma_v$ is the change in total vertical stress. Every upfilling operation led to an increase in excess porewater pressures which corresponds to an increase in the porewater ratio B. This ratio remained less than 0.7 highlighting that the underlying soft marl and alluvial layers were given time to dissipate before the next upfilling occurred. Ratios of <1.0 indicate partially drained conditions and stable conditions. Ratios >1.0 indicate potential instability. By June, the piezometers were recording pore water pressure values similar to those prior to commencement of construction thereby demonstrating that excess pore water pressures had dissipated. This is another indication that primary consolidation is substantially complete.

The amount of primary consolidation settlement remaining under the permanent load following surcharge removal was effectively eliminated. Another benefit from the surcharge derives from a reduction in the secondary creep rate that occurs following surcharge removal, but this only happens if the surcharge is maintained long enough to develop an effective overstress in the foundation soils significantly above that due to the permanent embankment load. Additionally, there is a lag in the onset of secondary creep following surcharge removal. The shorter hold period but higher consolidation degree reached, meant that the secondary settlements were still in the order of 5 to 20 mm, which met the settlement criteria.

4 DRAINAGE DESIGN

4.1 Opportunity and Challenges

In addition to being cheaper than traditional concrete systems, the adoption of nature-based drainage solutions and principles can benefit the local hydrology, hydrogeology and ecology receptors, and the systems have a lower carbon footprint. The Environment Impact Statement (EIS) design for this project consisted of grass surface water channels in cuts and concrete channels on embankments. However, since the EIS was published, the use of lined grass channels, which are sometimes used in areas of groundwater vulnerability and require a departure from Transport Infrastructure Ireland (TII) standards, has decreased. Recently completed highways in Ireland have predominantly used concrete drainage systems to collect and convey surface water runoff. The challenge in this project was to maximise the use of nature-based drainage solutions to accrue the associated cost, constructability and environmental benefits that come with them. To maximise the use of nature-based drainage solutions on the scheme, two innovative drainage collection systems were adopted.

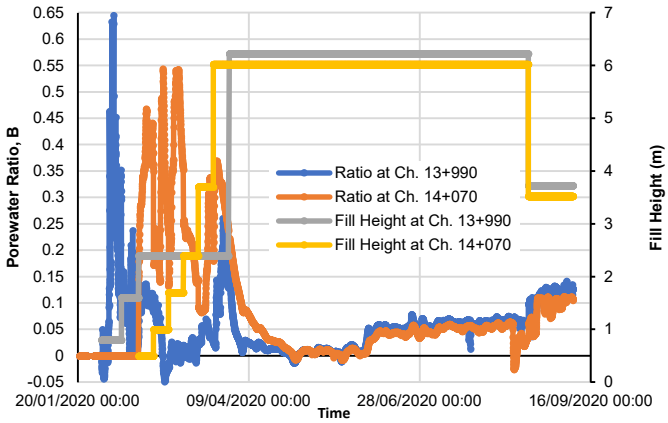

Figure 4: Porewater Ratio B at Ch. 13+990 and Ch. 14+070

4.2 Lined Grass Surface Water Channels

The potential to use standard grass surface water channels, which are considered to be an unsealed system was limited due to concerns in respect of aquifer vulnerability and the risk of karstification. A departure from standard was applied for from TII to adopt a bespoke Lined Grass Surface Water Channel detail developed for the scheme. To address the issue of surface water potentially seeping through or past the system, a construction detail and methodology was developed, which ensured that the impermeable liner associated with the grass channels was sealed to the pavement using a bitumen adhesive. The safety barrier design was also adapted to ensure that barrier posts would not be driven through the liner. To ensure that the system was sealed, where it was intercepted by drainage chambers, the surface water channel outlet areas were concreted, and the liner was carried through into the chamber. Prior to construction, trials were conducted to arrive at the best methodology and the favoured solutions for bonding the liner to the pavement. Non-destructive testing was carried out on the preferred solution, which was ultimately adopted in the works.

4.3 Linear Wetlands

Where the road was on embankment and grass surface water channels could not be used due to restrictions within the design standards, 'over the edge' drainage was typically used. Using this system, road surface water runoff was drained into linear wetlands constructed at the base of embankments. The wetlands are used to collect, convey, treat, and attenuate surface water runoff. The linear wetlands typically followed the gradient of the local topography but incorporated check dams along their length to increase their capacity to attenuate flow. The wetlands were used in areas where it had been envisaged that concrete surface water channels and associated pipe systems, which connected to traditional attenuation ponds, would be required. In areas where it was necessary to provide sealed drainage to mitigate the risk of groundwater contamination or karstification, testing was carried out to ensure that the in-situ permeability of the ground, where the wetlands were placed, was sufficiently low to allow it to be considered to be sealed. The approach adopted avoided the need to excavate out the in-situ impermeable material and

replace it with plastic liners, which have a relatively short life span. One of these linear wetlands is shown in Figure 5.

Figure 5: Example of Linear Wetland

4.4 Positive Impact

The above systems resulted in the removal of 11km of proposed concrete channels, and 9.7km of pipes and associated chambers. Because the linear wetlands follow the local topography there is less 'dead volume' associated with them compared with typical ponds. The systems reduced attenuation related earthworks by 76,000m^3. In addition to the cost and programme savings of these changes, there are potential environmental benefits which go together with the adoption of nature-based drainage solutions but these need to be further researched to understand fully their benefits. Potential environmental benefits include:

- Water – improved water quality [10]; reduction in the rate and volume of storm water runoff at outfalls; and improvements in existing catchment integrity post-construction.
- Ecology – increase in the habitat provision for flora/fauna.
- Climate – Reduction in the carbon footprint associated with concrete channels, pipes, chambers, the provision of drainage stone and all associated transport and construction works.

4.5 Impact on Earthworks

The adoption of the linear wetlands also had a beneficial impact which went beyond the drainage works. The use of linear attenuation systems helped facilitate alignment modifications which were not always possible as there was no space to provide ponds in some locations once alignment changes had been made. The alignment changes allowed structural embankment volumes to be reduced from what was envisaged at the EIS stage.

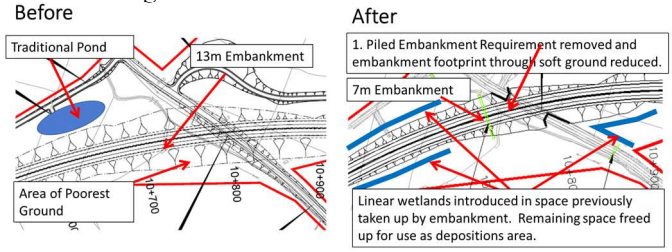

Figure 6: Before and After Comparison of Earthworks and Drainage at Ch. 10+700.

The reduced embankment footprint reduced the requirement for excavate-and-replace of soft materials below ground, removed the requirement for materials to be imported to construct embankments, and afforded some flexibility in respect of the horizontal design, which allowed embankments to be moved away from areas of poor ground. Additionally, the provision of attenuation systems along the embankment base freed up space which had been designated for ponds. This space was used to store unsuitable material generated, which assisted in removing the requirement to export materials. Figure 6 illustrates a location where a number of these measures combined to make significant savings.

5 CONCLUSIONS

Lessons to be learnt on this scheme include the following:

- Careful planning of preliminary SI should be carried out so that bedrock level and classification errors are not made.
- Conservative design options should be taken at the preliminary design stage to ensure sufficient land is available that considers geotechnical risks such as high groundwater table levels and springs in drumlins.
- The rate of consolidation cannot be easily predicted, and as a result is often underestimated, when thin lenses of sand exist in soft compressible material or when the material is slightly sandy in nature. However, there is an upside in producing conservative estimates in the design of a vertically drained embankment solution, should the thin lenses of sand not be representative of the whole footprint.
- The successful use of lined grass surface water channels and linear wetlands within areas that need to be sealed, opens the door to the broader use of nature-based drainage solutions on future projects. This success can be the catalyst for reversing the trend of traditional concrete systems seen on other recently completed projects.

ACKNOWLEDGMENTS

The authors gratefully acknowledge the assistance and support given by many colleagues both during the projects and in the production of this paper. The authors would like to acknowledge Sligo County Council, Roadbridge, Fehily Timoney for their kind permission to publish the data contained within this paper. The views expressed in this paper are the sole views of the authors and do not represent the views of the Sligo County Council, Roadbridge or Fehily Timoney.

REFERENCES

[1] Drew, D., *Karst of Ireland: Landscape Hydrogeology Methods*, Geological Survey Ireland, 2018.
[2] British Standard Institute, *BS 8002: Code of practice for Earth Retaining Structures*, 2015.
[3] Peck, R., Hanson, W., Thornburn, T., *Foundation Engineering,* Wiley, New York, 2nd Edition, 1974.
[4] Farrell, E. R. (2016), 'Geotechnical Properties of Irish Glacial and Interglacial Soils', *1st Hanrahan Lecture.* The Institute of Engineers of Ireland.
[5] Hutchinson, J. N. (1977), 'Assessment of the effectiveness of corrective measures in relation to geological conditions and type of slope movement', *Bulletin IAEG*, 16: 131-155.
[6] Carder, D. R., Watts, G. R. A., Campton, L. and Motley, S., '*PPR 341 - Drainage of earthwork slopes*', IHS, United Kingdom, 2008
[7] Stroud, M. A. (1974), 'The Standard Penetration Test in Insensitive Clays and Soft Rocks', *Proc. Eur. Symp. on Penetration Testing.* 367-375.
[8] Simons, N. and Menzies, B., *A short course in Foundation Engineering*, Thomas Telford, 2nd Edition, 1999.
[9] Ladd, C. C., *Unpublished Class Notes for 1.322, Soil Behaviour,* Cambridge, Massachusetts: Department of Civil and Environmental Engineering, MIT, 1989.
[10] NRA, Drainage Design For National Road Schemes - Sustainable Drainage Options, National Roads Authority, Ireland, 2014

Dredge Sediment Stabilisation Works at Howth Fishery Harbour Centre

Paddy Curran[1], Miron Piwonski[1], Pat Parle[1], Peter Seymour[2] John Farragher[3]
[1]Malachy Walsh and Partners Ltd., Reen Point, Blennerville, Tralee, Co. Kerry
[2]Independent Consultant, Kilkenny, Co. Kilkenny
[3]DAFM, Howth Fishery Harbour Centre, West Pier, Howth, Co. Dublin
email: paddy.curran@mwp.ie, pseymour@iol.ie

ABSTRACT: *This paper provides an overview of the dredge sediment stabilisation works carried out as part of the upgrade of the Middle Pier at Howth Fishery Harbour Centre. Dredging of sediment was carried out to the west of the existing pier to allow access for larger vessels. Approximately 6000m3 of sediments dredged from the western side of the pier was stabilised and used in the widening works on the eastern side of the pier. This process involved constructing a retention berm, placing of dredge material behind the berm and stabilisation of the dredge material with Ordinary Portland Cement (OPC) and Ground Granulated Blast Furnace Slag (GGBS) using a wet mixing process. This process involved setting up a batching plant onsite where water and binder were mixed to create a pumpable slurry of known dosage. This slurry was then pumped to an Allu processor attached to a conventional excavator which mixed the binder slurry in-situ with the dredge sediment. The location, elevation, rate of pumping and rate of movement of the Allu processor were monitored continually to ensure that a homogeneous mix was achieved. This paper includes details of the ground investigation, laboratory trial mixes to determine optimum binder content, leachate testing, the binder-sediment mixing and placement processes, quality control, in-situ testing and monitoring results. Lessons learned from the process are described, as well as advantages and disadvantages of the process*.

KEY WORDS: CERI/ITRN 2022; Dredge Sediment Stabilisation, Harbour Engineering, Geotechnical Engineering, Ground Granulated Blast Furnace Slag (GGBS), Ordinary Portland Cement (OPC)

1 INTRODUCTION

The Department of Agriculture, Food and the Marine commissioned MWP to design an upgrade to the Middle Pier, at Howth Fishery Harbour Centre (FHC), in Co. Dublin. MWPs involvement in the project commenced in 2015 and included provision of planning, environmental, civil, marine, structural and geotechnical services from preplanning stage right through to construction. The main contractor for the scheme was John Sisk & Son Civil & Marine Business Unit. The location of the site is shown in Figure 1.

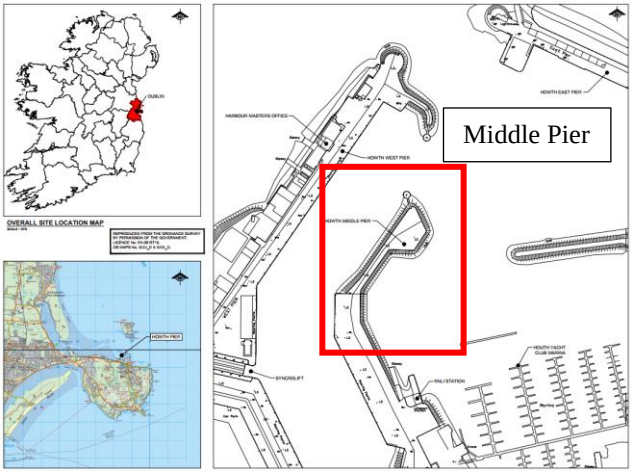

Figure 1 Site Location

The Middle Pier Upgrade project involves the following;

- Provision of 134m long quay wall at the western side of the Middle Pier;
- Realignment of rock revetment at the eastern side of the Middle Pier;
- Associated deck area, road access and hard standing.
- Dredging to -4m below Chart Datum, along the front of the new quay wall for a width of up to 20m out from the proposed quay wall. The dredging involved the removal of approximately 6000m3 of the underlying seabed (including some rock); and
- Land reclamation of an area approximately 0.2 ha on the eastern side of Middle Pier using dredge spoil, imported fill and excavations from the existing rock revetment.

This paper focuses on the engineering associated with the final bullet point above, particularly the dredge sediment stabilisation.

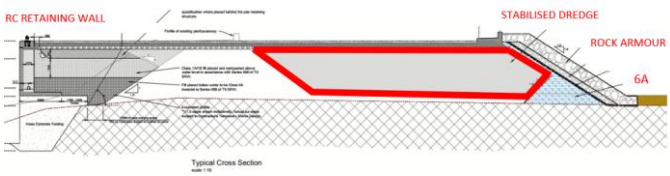

Figure 2 Typical Cross-Section with Stabilised Dredge Sediment Areas Outlined in Red

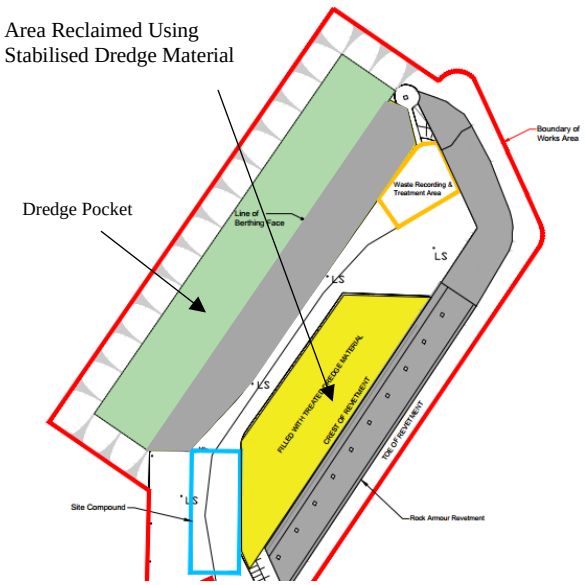

Figure 3 Overview of Proposed Scheme Layout

2 PROJECT BACKGROUND

2.1 Background

The overall project relates to the upgrading of the Middle Pier in Howth FHC. The FHC is owned and managed by the Department of Agriculture, Food and the Marine. A major development was undertaken in the early 1980's by DAFM in relation to the overall harbour. This development left the Middle Pier underdeveloped in terms of its berthage potential. The northern section of the middle pier consisted of a rock armour faced breakwater extending to a circular concrete caisson on which was supported a navigation aid. To provide more berthage and to create an area of hardstanding for use for commercial fishing activities and to move some of the commercial fishing activity away from the existing west pier, DAFM procured engineering and environmental consultancy MWP to develop a design for the Middle Pier that provided an additional 134m of berthage and a 134m by 45m area of hardstanding behind the berth. Part of the brief was to dredge some 6000m3 of silt material from a berthing pocket in front of the proposed new berth. This material contained contaminants making it unsuitable for disposal at sea. Tributylin (TBT) was one of the main contaminants of concern. This chemical was used as a biocide in anti-fouling paint on boats prior to it being band in 1987. The design was to develop a method of treatment so that the dredge spoil could be used in the reclamation of a 0.2ha area to the east of the proposed new berthage and that this area be available for use as a hardstanding.

Earlier work by MWP in the development of Bantry Inner Harbour, Phase 1 for the Port of Cork indicated that it was possible to treat and reuse dredge spoil. In the case of Bantry, the material was utilised to reclaim an area that was subsequently used as an amenity area. This project indicated that it was possible to get the permits regarding the treatment of contaminated (but non – hazardous) dredge spoil and to feasibly treat a large volume of contaminated dredge spoil and successfully use it to reclaim an area from the sea. In the case of Howth, the volume of material is less, requiring a waste facility permit from Fingal County Council instead of a waste licence from the EPA as in Bantry, however, the strength and settlement criteria for Howth are more onerous because of the proposed future use of the area.

Howth Harbour bed comprises a thin layer of silt overlying rock. Ground investigations indicated that in the area to be reclaimed there was approximately 1m thick layer of silt overlying rock. The average level of rock in this area is –2.9mODM. The hard standing level of 3.30mODM comprising a 230mm thick slab on 500mm of imported fill giving approximately 5.5m depth of treated dredge spoil. The maximum allowable total settlement of the slab was 25mm.

Research indicated that adding a binder in the form of a cement/ GGBS mix could achieve the required strengths and settlement characteristics to satisfy functional requirements. In addition, given the silt nature of the sediment, once bound, its permeability would be very low, which, in addition to the ability of the binder to lock in contaminants means that the risk of material escaping into the sea is minimal. The reclaimed area is bounded on the north, west and south sides by the original Middle Pier structure, and, on the east by a new rock armour revetment constructed on a geotextile placed on a graded mound of 6A fill which was used to initially hold the dredge spoil in place prior to treatment.

3 HISTORY OF SEDIMENT STABILISATION TECHNIQUE

Dredged sediment stabilisation using hydraulic binders was developed initially in the Nordic countries, Japan and the US, from the 1960s. Swedish engineers pioneered the use of alternate binders such as GGBS (ground granulated blast furnace slag) in sediment stabilisation. They also pioneered the wet-mixing technique (Process Stabilisation), where the binders are mixed with water and then added to a wet slurry of dredged sediment to provide a homogenous binder/water/sediment mix that is pumped into place, and hardens to a solid mass. This method has been recently used in a major stabilisation project in the Port of Gothenburg where sediments of similar geotechnical and contamination characteristics were identified. A variation on this method is used in Howth, where the binders are first mixed with water and then mixed in-situ with the dredged sediment.

4 SITE INVESTIGATION AND GROUND CONDITIONS

The site investigation at Howth FHC was carried out in a number of phases between 2015 and 2019. The investigations related to a number of ongoing projects and were not solely completed for the middle pier extension. Overall, the investigation consisted of the following:

- 31 No. Surface Sediment Grab Samples
- 32 No. Cable Percussion Boreholes to recover sediment and soil samples
- 40 No. Rotary Core Boreholes recover rock core samples for logging & testing
- A large suite of geotechnical and environmental laboratory testing
- Lab trials to establish the most effective mix design for stabilisation of the dredge sediment

The ground profile at the site was generally found to consist of the following sequence of materials:

- Very soft or soft dark grey or black sandy (occasionally gravelly) CLAY/SILT occasionally with shell fragments present
- Stiff brown or black sandy gravelly CLAY with occasional cobbles and boulders
- Medium to Strong LIMESTONE with some calcite veining partially weathered. Interlaminated with weak to medium strong black fine-grained MUDSTONE

To classify the dredge sediments, a series of laboratory classification tests were carried out. Particle size distribution tests showed that 100% of the material passed the 2mm sieve and 55% of the material passed the 63-micron sieve. The sediment contained between 3.8% and 5.9% organic matter. The liquid limit and plasticity limit were found to be 66% and 34% respectively. The natural moisture content was generally found to be closer to the liquid limit than the plastic limit with an average of approximately 56%.

5 LABORATORY TRIAL MIXES

Samples collected during the ground investigations were taken to commercial laboratories for trialling of various binder mixes to establish the optimum mix design in terms of strength and permeability. The aim was to identify a suitable binder composition and content to create a material akin to a stiff clay with a very low permeability. This would provide a suitable material on which to construct a slab for the pier extension and lock-in contaminants from the dredge sediment. A large series of trial mixes were conducted to establish the optimum mix design for the dredge sediment at this site. The trail mixes were carried out in a number of phases in tandem with the phases of ground investigation.

5.1 Mix Trail 1 – OPC ONLY

Initially, a small set of 12 sediment samples were stabilised with Ordinary Portland Cement only. The test specimens were then prepared such that the sub-sample and binder addition were immediately, upon completion of the mixing, compacted into a 38mm diameter 76mm high (triaxial specimen) split-mould. EuroSoilStab[1] recommended 60mm diameter sample moulds, however a smaller diameter was chosen as a result of the total sample mass available for the trial binder mixes. An initial trial highlighted the difficulty in removing the specimen at an early curing stage from the alloy split-mould. 40mm diameter HDPE moulds were then used which allowed for a more successful removal of the cured specimen. Curing of the specimen took place in a water bath at 20ºC. The results are shown in Figure 4.

The following key findings from the trial were noted:

- Higher binder contents yielded higher strengths. Strengths ranged from 22kPA to 68kPA undrained shear strength after 280 days depending on the content of OPC added.
- No strength gain between the 14 and 280 day test results was noted for the 8% (Approx 190kg/m3) OPC mix
- An approximate strength gain of 50% was noted between 14 and 280 day test results for the 10% (Approx 240kg/m3) OPC mix.
- Negligible strength gain noted between 14 and 280 day test results for the 12% (Approx 290 kg/m3) OPC mix.
- It was concluded that the OPC only mix is unlikely to provide reliable long terms strength gain for stabilised dredge sediments based on these results.

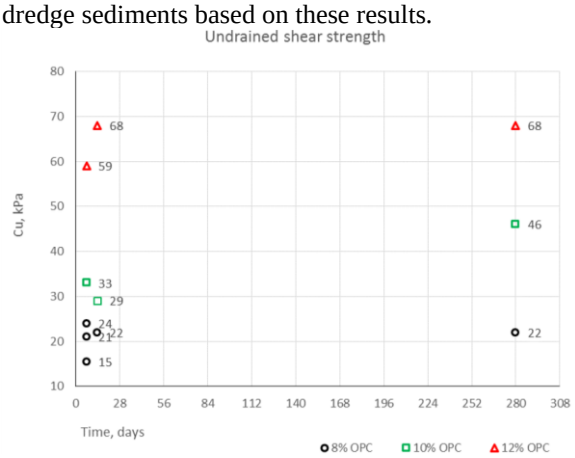

Figure 4 Results from Initial Trial with OPC Only Mix

5.2 Mix Trial 2 - OPC AND GGBS MIX INITIAL TRIAL

A second trial was carried out on samples collected from the dredge pocket to the west of the middle pier. Only limited material was available as the samples were collected during inspection works carried out by a dive team.

The binder used in these tests was a mix of GGBS and OPC. The sample size was also increased to 100mm diameter. Less sample extrusion problems were noted when using the 100mm samples. Samples were cured at 20ºC. A total of 29 samples were tested. A summary of the strength results for the various mix designs is provided in Figure 5. A photograph of one of the UCS test set ups is provided in Figure 6.

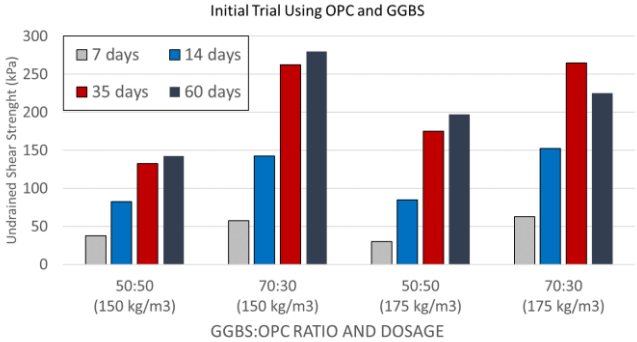

Figure 5 Results from Initial Trial with OPC & GGBS Mix

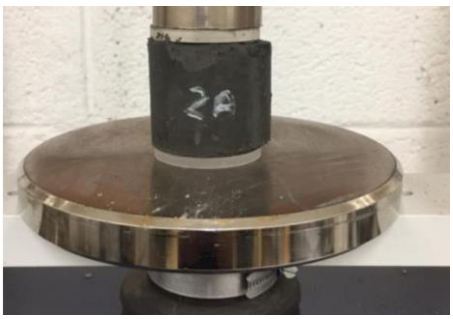

Figure 6 UCS test on a stabilised sediment sample

The following key findings from the trial were noted:

- The strengths from the GGBS:OPC blend out performed all of the OPC only mixes from the previous trial.

- The mixes with a larger portion of GGBS showed better longer term strength gain.
- The 70:30 GGBS:OPC mix appeared to provided better strength results for both binder contents.
- Increasing the binder content from 150kg/m3 to 175kg/m3 for the 70:30 GGBS:OPC mix only appeared to provide marginally different results.

5.3 Mix Trial 3 – OPC AND GGBS MIX DETAILED TRAIL

A larger scale site investigation and trial mix test series was carried out in late 2019 extending into 2020. This involved the testing of 10 different mix designs and a total of 159 UCS tests and 13 permeability tests. The slurries (sediment & binder mix) were poured into cylindrical moulds 50mm diameter x 90mm height and cured at 15^0C for a period of days ranging from 7 to 120 days for UCS testing. The consistency of the slurry and binder mix was developed to give a pumpable liquid with a flow rate of 40secs per litre through a Marsh Funnel. Larger 100mm diameter samples were used for the permeability testing. A summary of the undrained strength tests derived from UCS tests is provided in Figure 7.

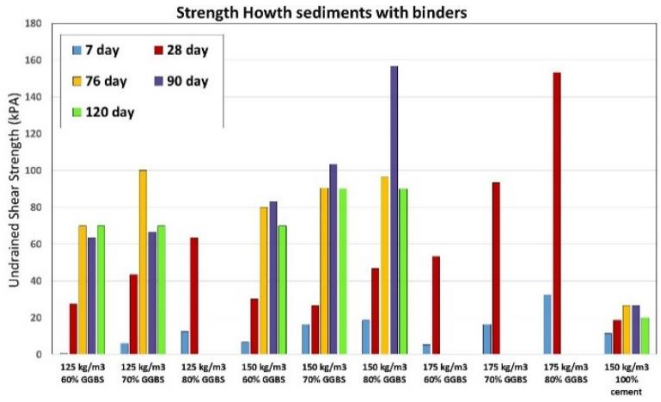

Figure 7 Trial Mix 3 - Results from Sediment Trial Mixes

The following are a number of points to note regarding the results of the dredge sediment trial mixes:

- Mixes containing both GGBS and OPC all demonstrated better longer-term strength gain than the OPC only mix.
- The strength gain between 90 days and 120 days appears to drop for all of the 150kg/m^3 mixes. This is contrary to previous research and literature. This may have been due to the small sediment samples and possible sample disturbance.
- The 175 kg/m^3 mix showed much greater strength gain in the first 28 days compared with the 150 kg/m^3 mix.

5.4 Mix Trial 4 – Higher Strength Mix for Temporary Work

As the contractor's methodology was developed, it became apparent that the in-situ mass stabilisation technique was preferable over the pumping technique due to the scale and site constraints at Howth.

Early strength gain of the mix became the most important criteria to enable heavy plant and machinery to track on the stabilised mass as soon as possible.

Mix trials were carried out on four samples using a 70:30 GGBS:OPC mix with a binder content of 190kg/m3. Tests were carried out on 100x100x100mm cubes. The tests yielded average strengths of 550kPa undrained shear strength after 7 days which allowed for tracking of heavy plant.

5.5 Permeability Test Results

Permeability tests were carried on 13no. 100mm diameter cylinder samples in a triaxial cell. The vertical permeability results ranged from $1.84x10^{-11}$ m/s to $7.7x10^{-11}$ m/s with an average of $5.81x10^{-11}$ m/s. No anisotropic permeability tests were carried out.

6 METHODOLOGY USED AT HOWTH

The Contractors chosen method for dredge sediment stabilisation on this project was in-situ deep soil/sediment mixing, using a mass stabilisation wet mixing technique.

Mass stabilisation involves the mechanical disaggregation of the in-situ soils/sediment using vertical and horizontal movement of rotating mixing tools and the introduction of a wet cement/GGBS or other hydraulic binder, which is homogenised within the soil during the mixing operation. This process produces a cemented soil compound with higher strength and stiffness than the original soils/sediments.

Based on trial mixes a mix consisting of 190 kg of binder (70% GGBS/30% OPC) and 95 litres of water per m3 of stabilised mass was used to give earlier strength gain and more certainty on the final product.

7 CONSTRUCTION STAGE OPERATIONS

Before soil stabilisation works took place the material was dredged from the harbour using long reach excavators and barges. The material was then stored inside two holding cells with a spine wall/road between them. Geosynthetic Clay Liner was used on the seaward face of the holding cells in order to prevent any pollution to the harbour.

The holding cells were later divided into 4m x 4 metre cells (See Figure 8 and Figure 9). These cell details were then uploaded to the machine-controlled GPS to allow the machine operator to identify the extents of each working cell. There was also a minimum overlap of 200mm required between each cell to ensure that there would be no missed areas when moving between cells.

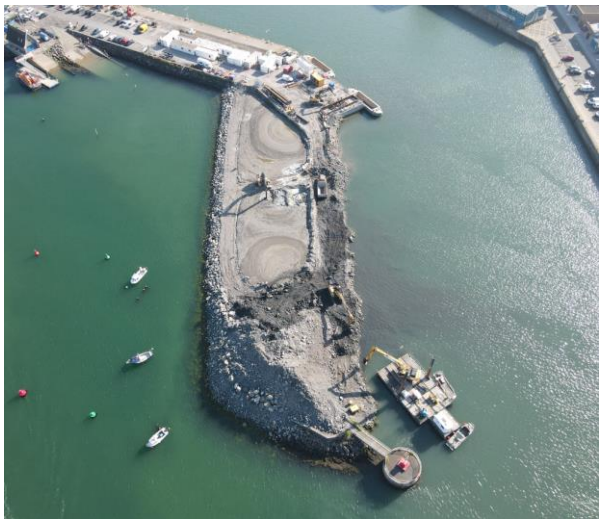

Figure 8 Aerial photograph of the stabilisation cells

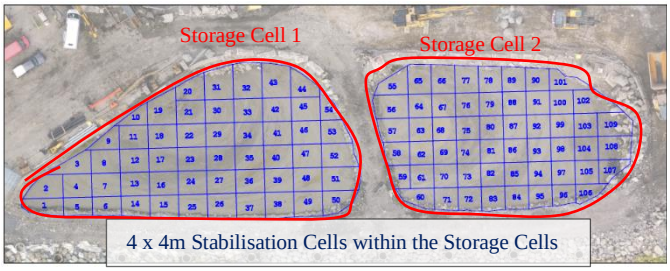

Figure 9 Storage and Stabilisation cells layout in 4m x 4m grids

Prior to addition of the binder mix the machine would mix the sediment within the cells to be worked. There were two main reasons for this, firstly, to homogenise the sediment as much as possible prior to the addition of the cementitious grout, and secondly to allow the machine to probe the extents of the cell i.e., the base level of the cell to be worked. The base level was recorded using a machine GPS system which constantly records the position and elevation of the mixing head, uploading the lowest recorded level to the site office computer. Using this data, a base model was created with volume of soil in each cell calculated. Once volume of each 4m x 4m cell was known, the details were entered into grout plant control panel, at this point the required quality of grout would be produced and stored temporarily in the batching plant's agitator tank.

Figure 10 Mixing head

The grout was later pumped under pressure (30-50 bar) to the mixing head of the machine and mixed with the soils. The quantities of grout pumped to each cell was recorded by the grout batching plant control panel for quality assurance purposes. In order to ensure that the grout is thoroughly mixed through the soils, the machine mixing head moves through the cell horizontally and vertically, starting at the base of the cells and moving up through the cells (Figure 11).

Industry standard for mass soil stabilisation has determined that the optimal mixing duration should be set at 30 seconds/m3. The mixing time required for each cell had been calculated and recorded as part of quality assurance documentation.

The soil stabilisation operation commenced on the perimeter cells of the works area. Once the perimeter cells were treated and sufficient time had elapsed to withstand plant loading, the stabilised cells were used as a temporary working platform for the treatment of the inner cells. Pre-works testing of trial mixes indicated that a period of 5 days post mixing would be required to allow machine loading.

Following completion of the stabilised mass, the area was covered with 100mm of 6F2 aggregate. This was to act as a curing blanket and to give stabilised mass protection from traffic and adverse weather.

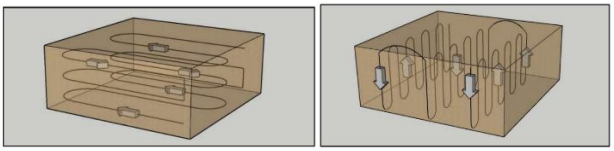

Figure 11 Horizontal and Vertical mixing sequences

8 INSITU TESTING AND MONITORING RESULTS

Following completion of the stabilisation works a series of in-situ testing and monitoring was carried out to verify the performance of the material and provide data for future use.

8.1 CBR from Plate Loads

In-situ plate load testing was carried out 1 month and 2 months after completion of the stabilisation. The results 1 month and 2 months post mixing achieved average CBR results of 23% and >100% respectively. This provides a good indication that material strength gain continues with time and broadly correlates with the laboratory trial mix test results.

8.2 Standard Penetration Tests

Standard Penetration Tests were carried out in two cable percussive completed through the stabilised dredge sediment. One test was carried out in each storage cell. The boreholes were carried out 56 days after completion of the stabilisation.

Both cable percussive holes refused at 1.5m below ground level. An SPT N value of 108 was recorded in both holes at 1m below ground level. The SPT results indicate that the material is of a very high strength and consistent.

8.3 Dynamic Probes

Seven Heavy Dynamic Probes were completed in the deeper areas of each of the storage cells. The results of the dynamic probes were much more variable than the SPT and UCS results. Equivalent SPT values derived from the dynamic probe results range from a minimum of 4 to greater than 50.

The results indicate that there is some variability within the stabilised mass. This may be due to the mixing methodology, consistency of the grout or variability in the dredge material. All settlement monitors showed small amounts of settlement therefore it was concluded that this variability did not have a material impact on the performance of the slab.

8.4 Unconfined Compressive Strength (UCS) Results

Four samples of in-situ mixed material were collected from 13 no. locations and UCS tested at different intervals. See results in Table 1.

In addition, 2 no. grout samples were also collected at each location and the results after 28 days indicated average strength of 42 N/mm2. The results from the grout only tests provided a

useful quality control as consistency of the slurry prior to mixing with the dredge sediment could be checked. The drop in strength between 28 and 56 days could not be categorically explained however in may be due to sample disturbance prior to testing.

Table 1. Undrained Shear Strength (Cu) - Stabilised Sediment

Time Frame	Cu (kPa)	Time Frame	Cu (kPa)
7 Day	550	56 Day	1050
14 Day	600	90 Day	1250
28 Day	1150	-	-

8.5 Temperature Monitoring Results

Temperature monitoring was carried out within the mass of stabilised material to gain information on the temperature at which the material cures. An example plot of the temperature readings is provided in Figure 12. The temperature within the cells ranged from approximately 37.5^{0}C to 50^{0}C. This is much higher than the curing temperatures used in the laboratory trials and may be a factor in the higher strengths achieved onsite.

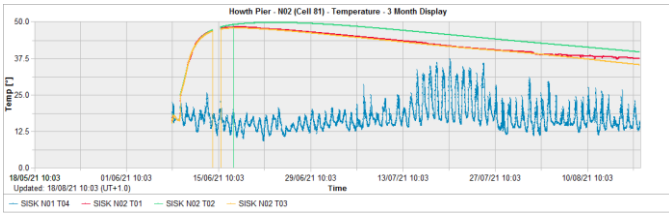

Figure 12 Example of In-Situ Temperature Monitoring

8.6 Settlement Monitoring

Six surface monitoring points were installed on the project to monitor settlement on stabilised soil. The result after five weeks indicated maximum settlement of 6mm.

9 LESSONS LEARNED AND AREAS FOR FUTURE RESEARCH

9.1 Lessons Learned

The main lessons learned from this project are as follows:

The method has proven to be a viable alternative to dumping at sea or removing dredge sediment to landfill

The performance of the binder-stabilised sediment, thus far, has proven suitable for structural slabs on piers.

Obtaining a homogeneous mix is key to the success of the stabilisation. The method used in Howth provided very good results overall, however, some variability was noted in the in-situ testing, particularly the dynamic probe results. Using a wet mixing process that mixes the binders and sediment ex-situ and pumps them into place is likely to improve the homogeneity of the mix.

The methodology of using a wet mix of binders with a wet mix of sediments is demonstrated to be successful - obviating the need to reduce the high moisture content in the sediments before stabilisation.

A combination of OPC and GGBS binder performed better than OPC only. It yields higher strengths and shows better longer-term strength gain.

Samples sizes used for UCS testing in trials should be 100mm cylinders or cubes. Sample extrusion proved difficult in 38mm and 50mm samples. Results from the smaller samples also showed more variability.

The curing temperature used in trial should match the large scale stabilisation. Temperatures between 15^{0}C and 20^{0}C were used in the laboratory trials, however in-situ temperature monitoring showed results between 37.5^{0}C and 50^{0}C

Mix trials should consider temporary works and cater for different construction methodologies. Higher strength mixes should be investigated even if the end-product requirement is surpassed. On this project the programme and methodology required early strength gain and this ultimately dictated the chosen mix design irrespective of the fact that lower binder contents would have yield acceptable performance for the permanent works.

When planning similar projects, sufficient time needs to be allowed for in the overall project programme to carry out sufficient ground investigation and trial mix testing. Sufficient time was available for this particular project and should be the case for future projects which consider this methodology.

9.2 Recommended Future Research

The following areas are recommended to be research on future projects or via academia.

A large database of testing needed to develop correlations for engineering design. The temperature monitoring provides very useful information in understanding the process of stabilising dredged sediments with hydraulic binders, and should be included on any projects of this nature in future.

Establishment of a more standardised testing procedure for this application would be useful as typical concrete and geotechnical procedures don't necessarily work due to the nature of the material.

Alternative binders could be investigated. Further research into the use of higher % of GGBS or use of other potential binders such as lime or Fly Ash as a substitute for OPCs.

Use of stabilised dredge sediments as a structural fill for buildings could be investigated. This could include load testing and settlement assessment under larger and more concentrated loads than those applied at Howth. The feasibility of commercial and residential construction of top of stabilised mass could be assessed.

ACKNOWLEDGMENTS

Department of Agriculture Food and the Marine
John Sisk & Son Civil & Marine Business Unit
Priority Geotechnical Limited
BHP Laboratories
Ground Investigations Ireland
Newton Ground Engineering

REFERENCES

1 EuroSoilStab, Design Guide Soft Soil Stabilisation, CT97-0351, Project No.: BE 96-3177.

2 Port of Gothenburg, Dredging spoils transform into new terminal at the Port of Gothenburg, 11th December 2020, https://www.portofgothenburg.com/news-room/press-releases/dredging-spoils-transform-into-new-terminal-at-the-port-of-gothenburg/ [Accessed on 6th May 2022]

Rock Tunnel Stabilisation Works at Caha Tunnel on the N71

Paddy Curran[1], Jasmin Spoerri[1], Daniel Cagney[1], Seán Regan[1], Liam Duffy[2], Keir Wilson[2]
[1]Malachy Walsh and Partners Limited, Reen Point, Blennerville, Co. Kerry, Ireland
[2]TII, Tunnel Management Building, Little Island, Co. Cork, Ireland
email: Paddy.Curran@mwp.ie, Liam.Duffy@tii.ie

ABSTRACT: *This paper provides an overview of the design and construction of the roof and portal stabilisation works recently completed at Caha Tunnel on the N71 on the Cork/Kerry border. The tunnel is 186m long and one of the four rock hewn tunnels on the National Road Network. This paper describes the geological assessment and interpretation of geophysical surveys carried out to develop an understanding of the rock mechanics and potential failure mechanisms within the rock tunnel. The tunnel was found to consist of alternating bands of sandstones, siltstones and shales with variable orientations and fracture planes. Water ingress was found to be concentrated at certain locations along the tunnel depending on rock type and cover. Each rock type was identified as having a different potential failure mechanism and design load requirements which needed to be accounted for in the detailed design of the stabilisation solution. The preferred stabilisation solution for the roof of the tunnel consisted of rock bolting and meshing. This solution was adapted at various locations within the tunnel to cater for the differing rock types, orientations, and potential failure mechanisms. The mesh type was also varied according to the tunnel geology. The design of the bolting and meshing system is discussed in detail within this paper. The methodologies used during the construction stage and lessons learned from this project are also discussed.*

KEY WORDS: CERI/ITRN 2022; Tunnel Engineering, Geology, Rock Stabilisation, Rock Bolting, Rock Meshing.

1 INTRODUCTION

Caha Tunnel is a rock tunnel located approximately 9km north of Glengarriff, and 18km south of Kenmare, along the N71 on the Cork/Kerry border (Figure 1). The route is the primary link between the towns of Glengarriff and Kenmare and serves as a popular route amongst tourists.

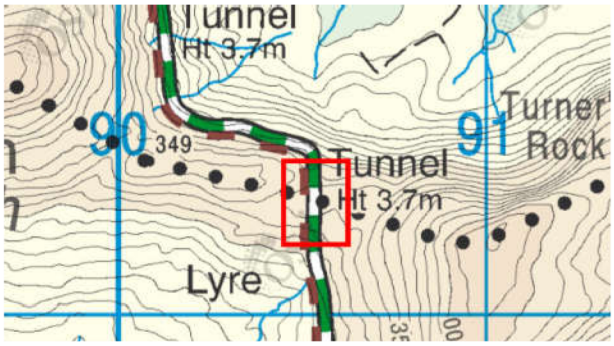

Figure 1: Location of Caha Tunnel

It is a 186m long rock tunnel through siltstone and sandstone formations. The tunnel was formed in the mid-19th century through blasting methods, thus giving it its inhomogeneous cross-sectional shape throughout and exposing the natural face of the rock. The tunnel varies in height and width but is generally approximately 4.0m high and typically 5.0m wide (Figure 2).

As a result of limited headroom and reported rock falls within the tunnel, improvement works to the tunnel were sought by TII. The main aims of these improvement works were to increase the headroom within the tunnel to a minimum head height of 3.85m to cater for large buses and to stabilise areas of the roof of the tunnel which showed signs of potential rockfall.

Figure 2: View of the southern portal. Siltstone.

2 APPROACH TO DEVELOPMENT OF SOLUTION

The approach taken to designing and implementing the preferred stabilisation solutions involved the following steps:

- A desk top review of all the available background information including previous inspection reports and geophysical survey reports.
- A detailed geological assessment and fracture mapping exercise to understand the potential failure mechanisms and volumes of failure within the rock.
- Identification of areas within the tunnel displaying signs of potential failure or signs of persistent water ingress (hence subject to regular freeze thaw).
- Design of a rock bolt and meshing system to cater for a variety of potential failure modes.
- Allowance for additional bolts within the contract to cater for situations where further potential failure zones were identified during the works.

- Continuous onsite support from an Engineering Geologist and Geotechnical Engineer given the nature of works and potential technical changes during the works.

3 THE GEOLOGY OF CAHA TUNNEL

The general geology of the area around the Caha Tunnel is a series of SW-NE trending multilayer folds of alternating bands composed of sandstone, siltstone, and shale. Pre and syn-folding action caused crude axial planar cleavage due to buckling while post-folding action caused tensile jointing to occur later in the system's life.

The two main rock formations in the area are the Slaheny Sandstone Formation and the Caha Mountain Formation. The Caha tunnel lies exclusively within the Slaheny Sandstone Formation and is flanked to the north and south by the Caha Mountain Formation. The junctions between the Slaheny Sandstone Formation and the Caha Mountain Formation are predominantly marked by fault lines, these fault lines run in a Northeast/Southwest direction.

The rocks at Caha experienced ductile deformation in the way of compaction from a N-S direction and caused the system to buckle, producing E-W trending folds.

A detailed geological assessment and fracture mapping of the tunnel was carried out over three days by an Engineering Geologist in February 2020. During these surveys, blocks of potential failure were observed with an average volume of 0.5 - 1m^3, with occasional larger blocks and rock slabs noted at the northern portal.

Sandstone was found between Chainage 40–60m, 90-100m, 130-150m, and 170–186m. Siltstone was found between Chainage 0-40m, 60-90m, 100-130m, and 150–170m. Shale was found at Chainage 150m.

Bedding (S_0), Cleavage (S_1), and Joint (J_1) measurements were recorded with a compass-clinometer and graphed using 'Stereonet 11' software programme [see Figure 3]. Bedding measurements, on average, strike 060-080 and dip between approximately 30°-50°. Poles to bedding show that the orientation of the bedding is within the southern-facing limb of a syncline. Cleavage measurements, on average, strike 060-080 and dip between 50°-90°, and dip direction is distinctly either North or South. Poles to cleavage suggest two distinct orientations within the southern-facing limb of a syncline.

One or more joint sets were identified from measurements obtained from the site investigations and from previous surveys (RPS, 2019). Joint measurements, on average, strike 170 - 220 and dip between 18° - 88°, and dip direction either North or South. Poles to joints suggest more than one joint set within the southern-facing limb of a syncline. The first has an acute to near vertical dip, dipping West. The second is an obtuse dip, dipping East. Dip angles vary across the site due to the degree of folding.

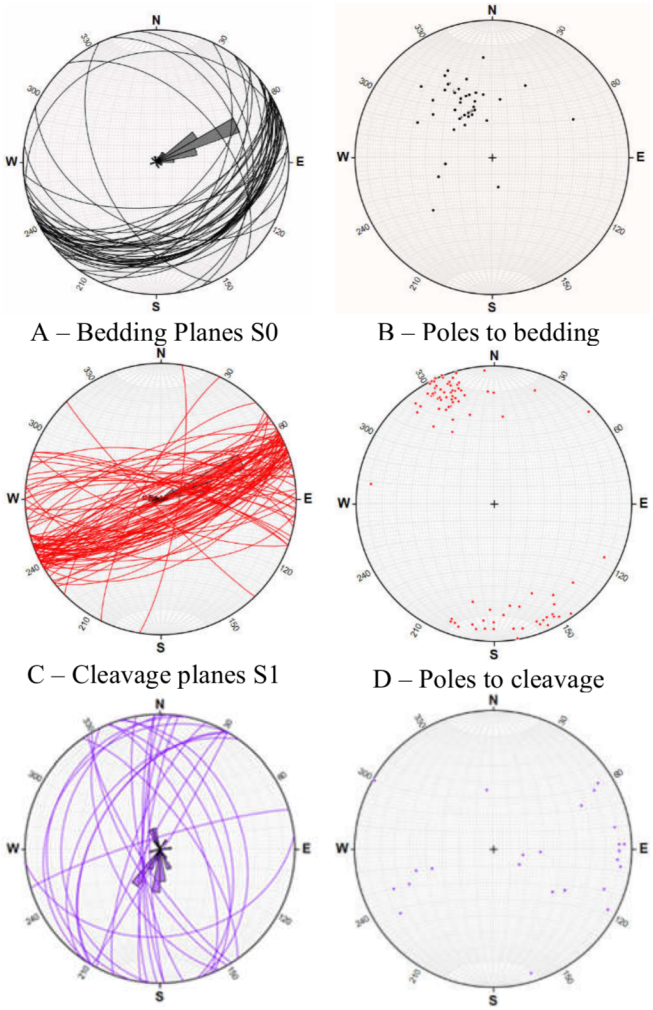

Figure 3: Stereonets for Caha Tunnel

Figure 3(B) shows the poles to bedding and illustrates the form of the fold limb. The limb of this fold is inclined at around 30° reaching as much as 50° towards the southern end, all dipping South - Southwest. An example of this can be found in Figure 4.

The compression-fabric cleavage pattern is best seen in the siltstone and shales. The near-vertical cleavage, a result of horizontal compression, is so well developed that it is often hard to distinguish from bedding. The cleavage poles are parallel to the bedding poles, as seen in Figure 3 (B) and (C). Of the cleavage that was not vertical dipping, many of the cleavage planes dip steeply South. This cleavage developed as the folding continued, in which previous cleavage planes that were at a vertical angle were over-rotated with further buckling and as a result dip North, giving two marginally separate cleavage orientations (Figure 3 (C) & (D)).

There are more than one set of joints that were identified during the survey that were likely created post-folding as a result of a tensile regime (Figure 3 (E) & (F)). The most notable joint set strikes North to South and steeply dips West (Figure 5). The second set also strikes North to South but is less steep and dips East.

Figure 4: View of the northern portal west wall. Fold bedding (S0) intersecting the near-vertical cleavage (S1)

Figure 5: View of the northern portal. Note the size of the potential blocks hanging from the roof entrance and west wall.

3.1 Failure Modes

Block failure (Figure 6 (A)) occurs due to three intersecting discontinuities producing blocks which in turn are acted upon by gravity causing failure. This is presumed to be the most likely mode of failure for the sandstone strata within the Caha Tunnel due to the three intersecting planes of a shallow dipping bedding, steep dipping cleavage (which are parallel to one another) and perpendicular striking jointing (Figure 3 (A)-(F)). An example of this can be seen at the northern portal which is composed of sandstone (Figure 4).

Wedge failure (Figure 6 (B)) occurs due to two intersecting discontinuities producing wedges/elongated blocks which are in turn acted upon by gravity causing failure. This is likely to be the main mode of failure for the siltstone and shale strata within the Caha Tunnel as the bedding plane has been completely overprinted due to the folding deformation. The two intersecting planes are the steep dipping cleavage and the near-vertical joint sets. During site walkovers and fracture mapping, wedge-blocks were noted as averaging in size between 0.1 – 0.35m³.

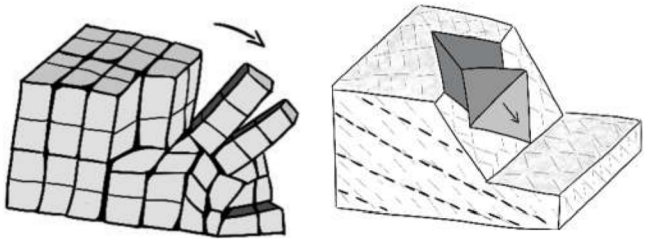
A Toppling Failure B Wedge Failure
Figure 6: Failure Modes.

4 STABILISATION DESIGN

4.1 Optioneering Process

The design process incorporated the extensive site surveys including fracture surveys of the rock conducted by MWP and interpretated the previous studies on the tunnel with the overall goal of achieving a design solution that minimizes the risk to road users in so far as practicable from rockfall from the tunnel onto the carriageway.

The options that were suggested by RPS (2019) were reviewed as part of the process to select the most suitable stabilisation method for the tunnel. These were:

- Fibre Reinforced Sprayed Concrete
- Rock Mesh and Bolting
- Concrete Lining

This optioneering process was driven by the need to ensure the safety of road users without imposing a width or height reduction throughout the tunnel and considered reduction in risk to the road user, cost, programme, practicality to install, environmental impact, ease of maintenance and aesthetics. While the concrete lining would result in the highest reduction in risk to the road user, it was ruled out due to its high cost and impracticalities involved in attempting to install such a measure. The fibre reinforced sprayed concrete option and concrete lining option would result in the reduction of the carriageway geometry unless substantial rock removal occurred. Measures to prevent the ingress of ground water into the tunnel was evaluated but were deemed to be too expensive to implement. It was therefore deemed that rock mesh and bolting would be the most appropriate option in this instance as it provided a measured balance on costs and risks. This option had the added advantage of allowing for the aesthetic exposures of rock to remain visible to the public where feasible. It would permit the rock face to be exposed from road level, insofar as was practicable, which was an important consideration given its uniqueness, ease of inspection, and tourist attraction.

4.2 Bolting and meshing arrangements

Following completion of the detailed geological assessment and fracture mapping as outlined in Section 3, a robust, simple and buildable stabilisation method was developed by utilising two configurations/arrangements of bolts and mesh to suit the variable site conditions as shown in Figure 8. These were named Configuration A (Sandstone) and Configuration B (Siltstone and Shale).

4.2.1 Configuration A

The sandstone sections, which are blocky in nature, were secured by using rock bolts which act to pin the blocks back to competent rock. This was done to secure rocks which are likely to fail as a large mass rather than as small particles.

Configuration A used passive bolts in combination with an 80mm aperture mesh. The design intent was for the bolts to stabilise the larger sandstone blocks and the mesh to intercept smaller blocks of rock which could become detached between the bolt head locations.

Based on the findings of the detailed geological assessment of the tunnel, the design assumed that the depth of block that could fail is approximately 0.55m deep with a density of 25kN/m^3. The rock bolts are assumed to be installed at a maximum inclination to the rockface of 40 degrees on a 2 by 2m grid which equates to a rock volume of 2.24m^3 (56kN).

4.2.2 Configuration B

The areas of siltstones and shales along with areas of interbedding between siltstone and sandstone were assessed as being too sheared, cleaved and thinly laminated for Configuration A to work. Due to the fragmented nature of the rock in these areas, two layers of meshing was placed on the rock face and supported by rock bolts drilled into competent rock. The aim of the meshing was to reduce the likelihood of smaller particles falling onto the carriageway and posing a risk to road users. An 80mm aperture mesh with a finer polypropylene mesh laid inside it was proposed to minimise the risk of smaller particles falling onto the carriageway.

Based on the findings of the detailed geological assessment of the tunnel, the design loading assumed that a thickness of 300mm of this material will fall onto the netting with a density of 25kN/m^3. The rock bolts are assumed to be installed at a maximum inclination to the rockface of 55 degrees on a 2 by 2m grid which equates to a rock volume of 1.2m^3 (30kN).

4.2.3 Provision for variable Rock Behaviour

Provision was included in the tender for additional longer bolts and higher strength steel meshing. This was to account for the inherent uncertainty associated with the complex rock behaviour that would only become apparent during the works. The North Portal was one such area identified as requiring a provision for additional bolts. The rock breaking to increase the tunnel height revealed further areas that required further bolting. A Resident Engineering Geologist onsite throughout the works to identified areas where additional bolting and mesh was required.

4.3 Bolt Design

The rock model assumed for the analysis is shown in Figure 7. The largest fault identified by Apex Surveys (2019) extended 1.3m into the rock face. It was assumed that 1.5m into the rock face was incompetent based on this and to allow for future weathering. The rock deeper than 1.5m from the rock face was assumed to be competent. The minimum fixed length was 2m as advised by BS 8081 for loads under 200kN.

The only loading to the structural solution will be its own self weight (e.g. rock bolts and mesh) and the mass of the rock to be supported by the proposed structural solutions. The aim for this solution was to simplify it as much as possible for ease of construction, reduce complexity, reduce timelines and reduce potential for errors.

The rock bolts/dowels were installed in a grid pattern on the site in a similar manner to the intent sketched in Figure 7.

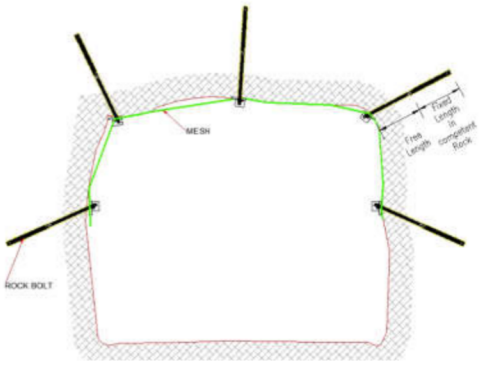

Figure 7: Cross Section of Rock Bolt Arrangement

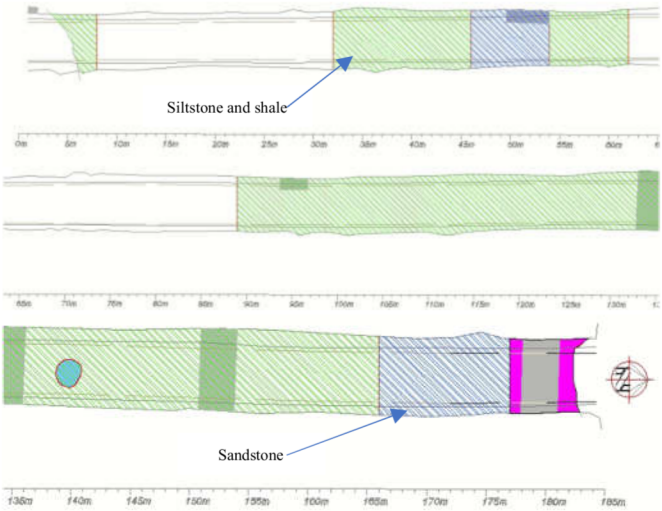

Figure 8: Plan of Tunnel with Geology and Stabilisation Configuration Highlighted

4.3.1 Rockbolts Design

The analysis for this rock bolt and mesh arrangement was completed in accordance with IS EN 1990, IS EN 1997 and BS 8081. The bolting arrangement was designed as a Type A Anchor defined by BS 8081 which is the most common type deployed in rock stabilisation. The bolts were designed to carry the entire design loading in both shear and pull-out to maximise the flexibility of installation angles which simplified the construction process.

Resistance to withdrawal is dependent on the longitudinal shear mobilized at the ground/grout interface. The formula used to determine this is as follows:

$$R_{GG;calc} = \dot{\pi} D L_{fixed} \tau_{ult} \quad (1)$$

$R_{GG;calc}$ = Characteristic ultimate ground/grout interface resistance(kPa)
D = Diameter of the fixed anchor (Minimum bored rock diameter) (m)
L_{fixed} = Fixed Anchor Length (m)
τ_{ult} = ultimate bond or at soil/grout and rock/grout interface (kPa)

The Unconfined Compressive Strength (UCS) of the rock was conservatively assumed to be 3.5MPa based on values from in BS8081 and Look (2007) as well as testing from similar rock on other sites. BS 8081 advises that the shear strength in weathered granular material would be 10% of the UCS value.

The hollow rock bolt used had a characteristic strength of 225kN with an inner and outer diameter of 30/11mm respectively. Centralisers were specified to ensure that there is a consistent cover of grout. The grout was pumped under pressure into the cavity which will ensure that the bar is surrounded with grout.

The maximum ultimate bond (grout-anchor) stress was assumed to be 1MPa based on BS8081 for a clean or plain bar which is conservative as the bar were ribbed in reality. The pull-out cone generated by the proposed anchor was analysed to ensure that sufficient resistance was generated.

4.3.2 Mesh Design

The proposed wire mesh had a nominal punching shear resistance of 65kN which results in a factor of safety of 2.16 when compared to the load of 30kN.

The polypropylene mesh was included to reduce the risk of particles smaller than the aperture of the wire mesh from falling onto the road surface. The wire mesh acts as the primary structural component of the two meshes. Therefore, it was assumed that the polypropylene mesh did not provide any structural capacity.

4.4 Anchor Bolt/ Dowels Corrosion

To ensure that the bolts being specified would achieve a design life of 120 years, calculations were completed on the corrosion that could occur to ensure that a sacrificial thickness was provided. The ground in which the bolt is installed was assumed to behave in a mildly aggressive manner as described within TRL 380. The anchor had a sacrificial thickness to account for corrosion over its envisaged 120 years lifespan. All other metallic elements including anchor plates were specified to be galvanized to Category C5 rating to minimize the risk of failure caused by corrosion to the bolts.

4.5 Miscellaneous Design Aspects

The risk of protruding bolts causing injuries to vulnerable road users such as motorcyclists and cyclists was a concern. This risk was mitigated by detailing the bolts to commence from 2.65m above road level and to overbreak the rock so the bolts did not protrude beyond the original rock face

Over time, it is likely loose material will build up behind the mesh. It will be necessary, in this instance, to remove the base plates and mesh locally and remove the debris before reinstating the mesh. The mesh will likely require re-tensioning to ensure that clearances in the tunnel are not impeded on.

A selection of the anchor bolts installed in the tunnel were acceptance tested in accordance with Method 1of BS EN ISO 22477-5:2018. These verified that the installed works achieved the design resistance. A portion of the boreholes were measured to verify that the required borehole dimensions were achieved. Similar verification tests were conducted on the anchors including measurements of ‘total’ and ‘de-bonded’ lengths as well as visual inspection. Grout cubes were completed throughout the project to insure it met the specified strength prior to anchor testing being performed. Compliance inspections were conducted throughout and after the works to ensure the works were completed to the specification.

5 CONSTRUCTION

Cumnor Construction Ltd. commenced works on site in October 2021 with a 10-week programme. This included the closure of the tunnel to the public with traffic diversions put in place. Phasing of the works was as follows: site set up, scaling of the rock with a hammer tap survey, bolt installation, mesh installation and concluded with ancillary works and demobilisation.

5.1 Methodology

Rock scaling was carried out in areas of the tunnel to remove loose outcrop identified by MWP in advance of bolting the area and to increase clearance in portions of the tunnel for vehicle access and safety. Rock scaling was achieved using a 9T excavator with a hydraulic breaker attachment. Bog mats were placed on the road to protect the road surface. A laser measuring tool was used to accurately measure the height of the tunnel and identify areas with insufficient clearance. Areas requiring rock breaking were physically delineated prior to rock breaking. The hydraulic breaker was orientated at the long axis of the rock to avoid creating further splits in the cleavage discontinuities. Broken rock material was removed using a bucket and transported away in a 6T Dumper.

Rock drilling was carried out using three drilling rig arrangements; a telescopic hydraulic rotary drill rig attached to a 24T excavator, a 10T forklift with a telescopic rotary drill attachment, and a 14T excavator with a telescopic rotary drill attachment. Compressors were used to supply pressurised air and water jets attachments to the plant. Each bolt location was marked out by the Resident Geologist. The drill was aligned to the position with the bolt’s required orientation and bored to the required depth (Figure 9). Once the borehole was complete, it was cleaned using pressured air to remove remaining debris. The bolt was installed into the borehole as a single piece and temporarily supported using stints to ensure accurate installation before being grouted. The grouted borehole was left to cure until sufficient strength had been achieved with the cube test results prior to load testing. A load test was conducted on a selection of bolts for validation. Once the testing was complete, the mesh, plate and washer were installed.

Figure 9: The 24T drilling rig at northern portal.

A template was run through the tunnel to ensure the required geometry of 3.85m high by 3.6m wide was achieved. This was done prior to rock breaking to identify low areas, after rock breaking to ensure sufficient rock was removed, and again after bolting and meshing to ensure none of the installed bolts or mesh encroached on the head room.

Figure 10: Completed Works from Northern Entrance.

5.2 Construction Stage Challenges

The main construction stage challenges are discussed below:

Time pressure / short window for works: The works were completed during the winter of 2021 to coincide with the tourist off-season and low traffic volumes. A diversion of 80km was created for the works to ensure safety of the road user as it was not safe to traverse the tunnel during the works. Thus, as the N71 is a national road, works had to be completed within a short time frame to minimize impact on the public.

Ventilation: Silica dust was created from drilling and rock scaling activities. Diesel fumes were a considerable risk during works. Plant running inside the tunnel and poor air circulation, especially in the centre of the tunnel, caused fumes to build up created confined-space conditions. The restricted nature of the tunnel made ventilation challenging and mitigation measures were employed such as positive passive ventilation, use of P95 masks, dust suppression techniques and carbon monoxide alarms. If dust or fume levels were too high, works ceased until these levels abated.

Rock Hardness: At specific locations, rock hardness was greater than anticipated. Chisels from the rock breaker and drill bits from the drill depleted very quickly. This caused delays during construction due to difficulty sourcing replacements.

Rock instability and prop methods: Due to the nature of the rock along the roof, rock had potential to become unstable during the works such as during the drilling process. If this was seen during prework inspection or during the work itself, work was stopped, and plant moved out of the direct path of a potential fall. A review of stabilisation options and location specific construction methods would then be carried out. If an uncontrolled rock fall was imminent, plant would remove the unstable rock and another inspection would be conducted. If the rock was unstable but integral to the stability of the tunnel, props were erected, and anchor bolts were installed to secure the rock. A subsequent inspection was conducted in advance of the prop removal and works recommencing.

6 "LESSONS LEARNED"

The process of gaining a detailed understanding of the structural geology of the rock hewn tunnel and distilling this complex information into a simple, robust and buildable stabilisation solution was vital for the successful completion of this project within the relatively short timeline available.

These works validated that there is a requirement for extra provisions of bolting and meshing onsite to account for the inherent variability in complex geological conditions.

The use of a full time Resident Geologist was of vital importance to this project to ensure that the complex nature of rock stability was fully understood as the works progressed. It also ensured that the design intent was achieved, a high standard of quality was maintained throughout the works, decisions could be made in an efficient manner and potential for error minimized given the potentially hazardous conditions.

The use of investigation and suitability testing as prescribed in BS EN ISO 22477-5:2018 in advance of the works on future projects is recommended. This would likely lead to cost savings via a reduction in fixed length of anchors and possibly anchor size. This is becoming increasingly important given the inflation in steel cost. The programme would be extended due to extra mobilisation procurement associated with the testing.

Given the variability and complex nature of geological setting, continuous liaison between TII, the Contractor and Designer throughout the design and construction process was vital. This ensured that design requirements were achieved, delays were avoided and operations ran smoothly.

ACKNOWLEDGMENTS

MWP would like to acknowledge TII for their permission to publish this paper. MWP would also like to acknowledge Cumnor Construction Limited for the successful construction of this technically and operationally challenging project.

7 REFERENCES

- Look, B. (2007), Handbook of Geotechnical Investigation and Design Tables, Leiden, The Netherlands: Taylor & Francis/Balkema.
- GSI. (2022), Bedrock Geology 1:100,000 Shapefile.
- http://www.gsi.ie/Mapping.htm
- RPS (2019), N71 Caha Tunnel Rock Improvements Assessment of Geophysical Investigation & Appraisal of Options for Tunnel Stabilisation. RPS Consulting Engineers Ltd., Doc. No.: MCT0758RP0009, October 2019.
- Apex. (2019), 'Report on the Geophysical Investigation at Caha Tunnel, Apex Geophysics Ltd., Doc. No.: AGP18034_01, February 2019'

Numerical analysis of low height piled embankments

S. Ahern[1], P.J. Naughton[2]
[1]Faculty of Engineering & Design, Atlantic Technological University Sligo, Ireland & Cork County Council
[2]Faculty of Engineering & Design, Atlantic Technological University Sligo, Ireland
email: sean.ahern@mail.itsligo.ie, naughton.patrick@itsligo.ie

ABSTRACT: Piled embankments are typically used to support road and rail infrastructure over soft and/or compressible foundation soils. The design of piled embankments is complex and is not yet fully understood. Low height piled embankments, where the height of the embankment is similar to the clear spacing between adjacent pile caps, are particularly difficult to design. The overriding design criteria is the serviceability limit state and, in particular, the need to eliminate differential settlement at the embankment surface. The impact of embankment height to clear spacing between pile caps and the stiffness of the geogrid reinforcement were investigated under plain strain conditions in Plaxis 2D. The Plaxis 2D numerical models were validated against previous physical and numerical modelling reported by Jennings [2]. A parametric study showed that the ratio of embankment height to clear spacing between adjacent pile caps and geogrid stiffness were key parameters in the design of low height embankments. Increasing the geogrid stiffness was found to reduce both the vertical geogrid deformation and vertical embankment surface deformations. The tension in the geogrid was not uniform and generally increased with distance from the embankment centre line to the crest of the embankment, before reducing to zero at the embankment toe. Tension in the geogrid increased with embankment height. Spikes in tension were observed at the edge of the pile caps, which could be 2 – 3 times the mean tension in the geogrid. The strain in the geogrid was also dependent on the geogrid stiffness, with geogrid stiffness greater than 5000kN/m resulting in geogrid strain less than 0.5%. Geogrid with lower stiffness recorded strain up to about 3%. All piles supporting the embankment experienced lateral deformation, with the magnitude dependent on both the embankment height and geogrid stiffness.

KEY WORDS: Piled embankments, low height embankment, numerical modelling, Plaxis.

1 INTRODUCTION

A piled embankment consists of piles, usually in a square grid, driven through the unsuitable foundation soil to a firm-bearing stratum. The piles directly reinforce the soft soil and distribute the embankment load onto the firm stratum. A geosynthetic layer is typically installed over the pile caps at the base of the embankment to further assist in the transfer of load. Piled embankments also rely on arching in the embankment fill to redistribute vertical load at the base of the embankment, increasing the load on the rigid piles and reducing the load on the soft compressible soil between pile caps.

Low height piled embankments arise where the height of the embankment is less than the clear spacing between adjacent pile caps. Full arching may no longer be mobilised in the embankment fill, with a danger that the embankment surface could imitate the ripple effect occurring at the pile level where the geosynthetic deflects downward between the pile caps. BS 8006-1 [1] places restrictions on the design strain in the geogrid reinforcement, with a requirement to have a design strain < 3% where the embankment height is less than 0.7 times the clear spacing between adjacent pile caps.

This paper presents data from a plane strain analysis of piled embankments conducted using Plaxis 2D. The Plaxis models are discussed, together with validation of the models against previous studies. The aim of the study is to better understand the performance of low height piled embankments. The study will also determine the minimum embankment height, pile and pile cap geometry and geosynthetic properties required to minimize deformation at the surface of the embankment.

2 METHODOLOGY

Plane strain numerical modelling using the package Plaxis 2D, Version 20, [2] was used to analyse piled embankment with height, H, ranging from 0.428m to 1.714m. All embankments investigated had 1:2 side slopes. The model examined was symmetric about the embankment centre line, requiring only one side of the centre line to be analysed. The piles had a centre to centre spacing, s, of 1.156m with a pile cap diameter, a, of 0.3m, Figure 1. The depth of the foundation soil was 5m. The pile and pile cap geometry together with the depth of the foundation soil were held constant in all analysis.

The boundary conditions were fixed along the lower horizontal boundary and horizontally fixed along the vertical left and right boundaries. A tolerated error of 5% was adopted in this study.

The Plaxis 2D model was validated against physical and numerical modelling reported by Jennings [3]. A parametric variation examined the impact of embankment height and stiffness of the geogrid placed at the base of the embankment directly over the pile caps on the deformational response of piled embankments.

2.1 Model parameters

The numerical model for both the validation and parametric variation conducted in this study consisted of embankment fill, geogrid reinforcement, foundation soil and pile and pile caps.

In this study the embankment fill was modelled using a Mohr-Coulomb model with the properties given in Table 1. The

foundation soil was modelled using the soft soil model in Plaxis, which is similar to the Cam Clay model, Table 1. The weight density of the foundation soil was 0.39 kN/m^3 and corresponded to the actual value of the material that represented the soft soil in the centrifuge modelling [3].

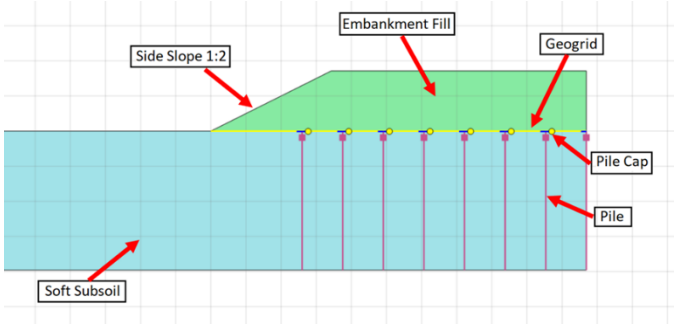

Figure 1. Schematic of model developed in this study.

The geogrid reinforcement was modelled using the geogrid element within Plaxis, which only required the axial stiffness, EA, of the geogrid.

The piles were modelled using Plaxis embedded beam row elements and were fixed at the lower boundary of the model. The pile caps which were fixed at the top of the pile elements were modelled as plate elements. The properties of the pile and pile caps are listed in Table 2.

Table 1. Properties of embankment fill and foundation soil used in this study.

Parameter	Value	
	Embankment fill	Foundation soil
Youngs modulus (MN/m^2)	20	-
Poisson's ratio	0.2	-
Cohesion (kPa)	1.0	3.0
Angle of friction (deg)	30	25
Dilatancy angle (deg)	6.5	0
Weight density (kN/m^3)	15	0.39
Modified compression index	-	0.045
Modified swelling index	-	0.0045

Table 2. Properties of the pile and pile caps used in this study.

Element	Parameter	Value
Pile	Young's modulus (GPa)	1.9
	Weight density (kN/m^3)	25
	Width (m)	0.12
	Centre to centre spacing, out of the plane (m)	1.156
Pile cap	Axial stiffness (GN/m)	3.521
	Flexural rigidity (GNm^2/m)	26.9
	Diameter (m)	0.3

2.2 Model validation

The model developed in this study was validated against plane strain physical modelling in the ATU Sligo geotechnical centrifuge and numerical modelling using Plaxis 2D reported by Jennings [3]. The validation model developed in this study had the material properties listed in Table 1 & 2. The embankment height in the validation model was 1.714m, corresponding to a H/(s-a) ratio of 2.0. The geogrid stiffness, EA, was 282kN/m.

Table 3 presents a comparison of the deformational response of the model developed in this study and values presented by Jennings [3]. Overall good agreement was observed between the predicted values and those reported by Jennings [3]. Based on this data the Plaxis 2D model developed in this study was validated.

Table 3. Comparison of predicted values from this study with data reported by Jennings [3].

Measurement	This study	Jennings [3]	
		Plaxis	Centrifuge
Outermost pile displacement (mm)	66	55	45
Vertical deformation of geogrid near embankment toe (mm)	192	160	180
Average embankment surface deformation (mm)	65	42	75

2.3 Parametric variation

The parametric variation focused on examining the influence of embankment height and geogrid stiffness on the deformational response of piled embankments. The range of geogrid stiffnesses and embankment heights examined are summarised in Table 4.

Table 4. Embankment heights and geogrid stiffness examined in this study.

Parameter	Range
Geogrid stiffness (kN/m)	282 – 15000
Embankment height (m)	0.428 – 1.714
H/(s-a) ratio	0.5 – 2.0

3 RESULTS AND DISCUSSION

The predicted values from the Plaxis analysis are discussed in terms of the geogrid and embankment surface vertical deformations, tension and strain in the geogrid, lateral displacement of the piles and the formation of arches in the embankment fill over the pile caps.

The vertical deformation of the geogrid increased with higher H/(s-a) ratios, Figure 2. In all cases a catenary deflected geogrid shape was observed between adjacent pile caps. The magnitude of vertical displacement was proportional to both H/(s-a) ratio, increasing proportional to the ratio. The vertical displacement near the outer piles were also greater than that predicted closer to the centre line of the embankment. At lower H/(s-a) ratios the vertical displacement of the geogrid was relatively flat over a central portion, indicating that the strength/stiffness of the foundation soil was sufficient to restrict the displacement of the geogrid. At higher H/(s-a) ratios the deflected shape was fully curved, indicating that the support from the foundation soil was exceeded.

The vertical displacement of the geogrid was dependent on both the H/(s-a) ratio and the stiffness of the geogrid, Figure 3. The mean vertical geogrid displacement reduced when the geogrid stiffness was greater than 5000kN/m and at higher H/(s-a) ratios.

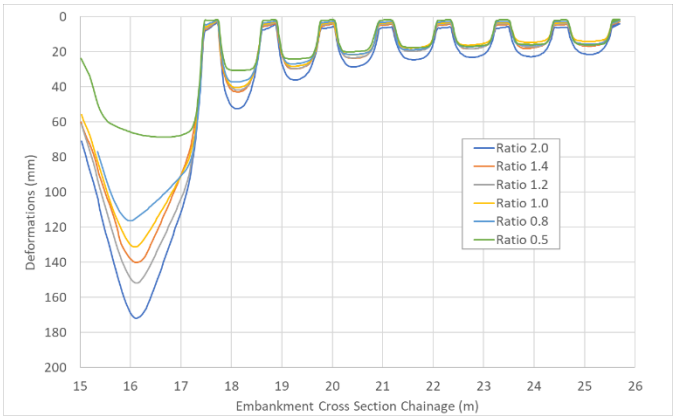

Figure 2. Vertical displacement of geogrid for various H/(s-a) ratios and a geogrid stiffness of 5000kN/m.

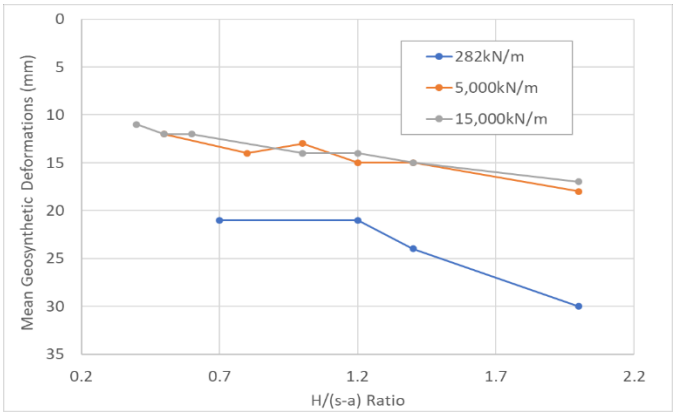

Figure 3. Mean geogrid deflection with H/(s-a) ratio and geogrid stiffness.

The predicted vertical deformation of the embankment surface is presented in Figure 4. All cases examined experienced some vertical deformation. However, for H/(s-a) ratios greater than 1.0, a more uniform deformational response was observed. For lower H/(s-a) ratios, less than 1.0, the surface deformation was more irregular, indicating that at lower embankment heights, the surface deformation may follow that of the geogrid.

The mean surface deformation was found to be inversely proportional to the geogrid stiffness, Figure 5, reducing with increased stiffness, and proportional to the H/(s-a) ratio, increasing as H/(s-a) increased.

The relationship between embankment surface deformation and geogrid deformation is illustrated in Figures 6 & 7, for a geogrid stiffness of 5000kN/m. For a H/(s-a) ratio of 2.0, Figure 7, no relationship between embankment surface and geogrid deformation was observed. However, once H/(s-a) reduced to 0.5, Figure 7, the embankment surface and geogrid deformations aligned, indicating that for low height embankments, approximately H/(s-a) < 1.0, the embankment surface deformation may follow that of the geogrid deformation, resulting in differential settlement at the embankment surface.

The predicted tension in the geogrid is presented in Figure 8. Peak tension occurred at the edge of the pile caps, with magnitudes 2 – 3 that of the mean tension. The tension in the geogrid increased with higher H/(s-a) ratios. Overall, the tension was highest close to the outer most piles, reducing to zero under the embankment side slope and also reducing slightly towards the centre line of the embankment. The predicted tensions were significantly lower than those expected based on a BS 8006-1 [1] design. Including subsoil support to the underside of the geogrid reinforcement in piled embankment applications has been shown to significantly reduce the tension in the reinforcement [4].

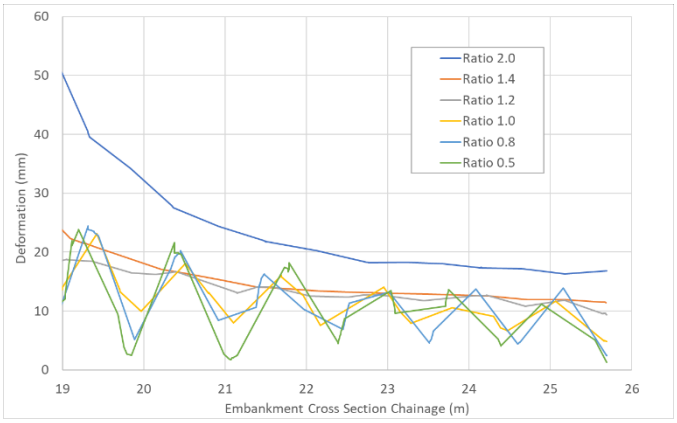

Figure 4. Predicted embankment surface deformations for various H/(s-a) ratios and a geogrid stiffness of 5000kN/m.

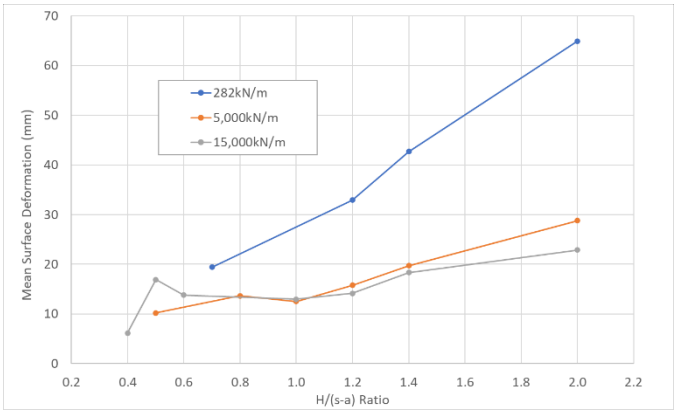

Figure 5. Mean embankment deformation with H/(s-a) and geogrid stiffnesses of 282kN/m, 5000kN/m and 15000kN/m.

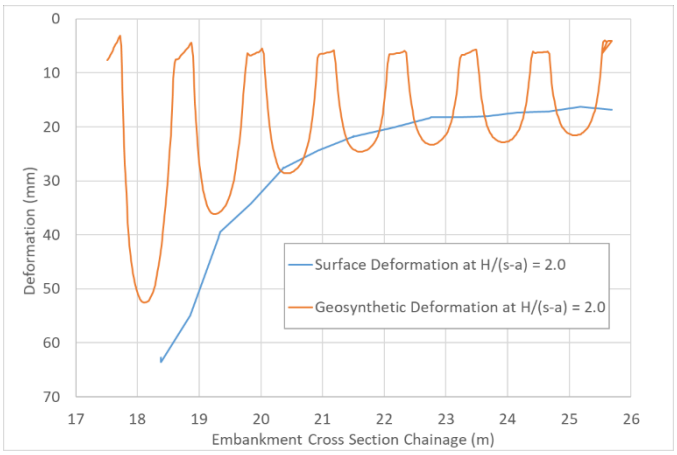

Figure 6. Embankment surface and geogrid deformations for H/(s-a) of 2.0 and a geogrid stiffness was 5000kN/m.

The ratio of peak tension at the pile cap edge to mean tension on the pile cap was found to vary with both geogrid stiffness and H/(s-a) ratio, Figure 9. Furthermore, the mean tension in

the geogrid also varied with H/(s-a) ratio and geogrid stiffness, with geogrid tension increasing with higher geogrid stiffness and higher H/(s-a) ratios, Figure 10.

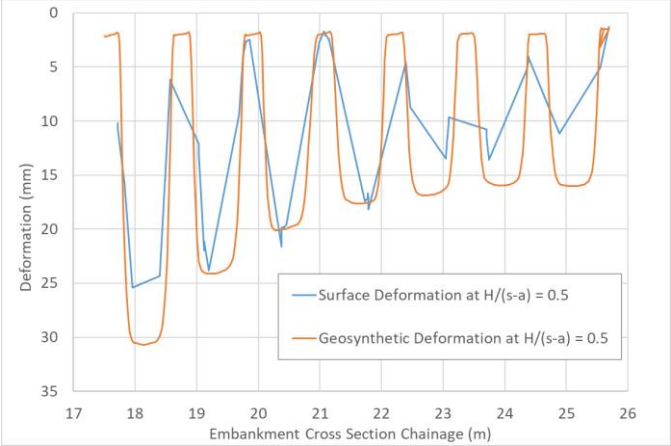

Figure 7. Embankment surface and geogrid deformations for H/(s-a) of 0.5 and a geogrid stiffness of 5000kN/m.

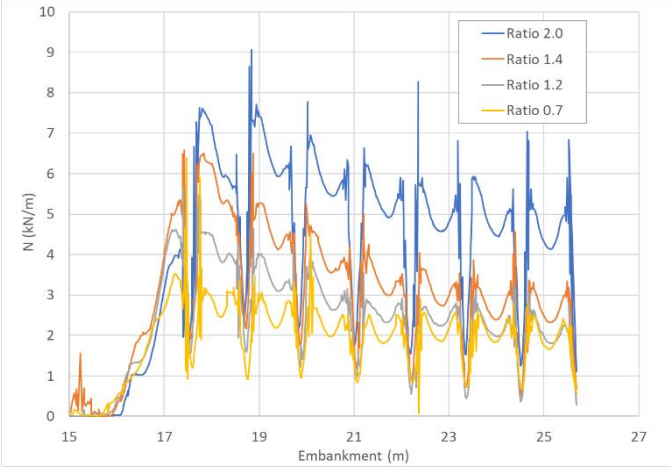

Figure 8. Geogrid tension for various H/(s-a) ratio and a geogrid stiffness of 282kN/m.

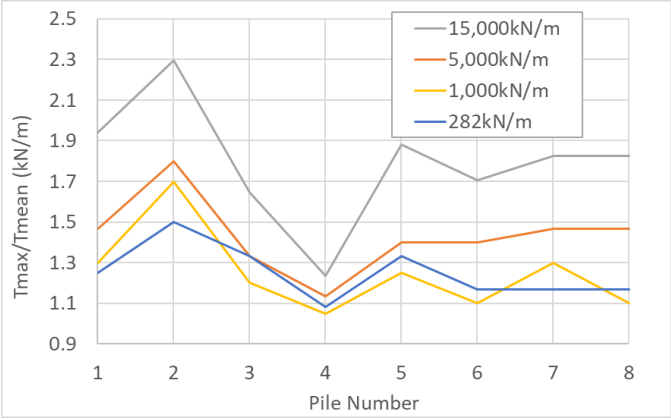

Figure 9. Ratio of maximum tension to mean tension for H/(s-a) ratio of 2.0 and geogrid stiffness between 282kN/m – 15000kN/m.

The strain in the geogrid was found to be dependent on both the embankment height and also the geogrid stiffness, Figure 11. Higher H/(s-a) ratios resulted in higher geogrid strains, while higher geogrid stiffnesses resulted in lower strains. The magnitude of strain varied slightly with location; higher strains were located near the outer most piles (Piles 1 & 2) and reduced towards the centre line of the embankment (Pile 8). Where the stiffness of the geogrid was grater then 5000kN/m the strain in the geogrid was about or less than 0.5%. For a stiffness of 282kN/m the geogrid strain was close to or less than the 3% value recommended in BS 8006-1 [1].

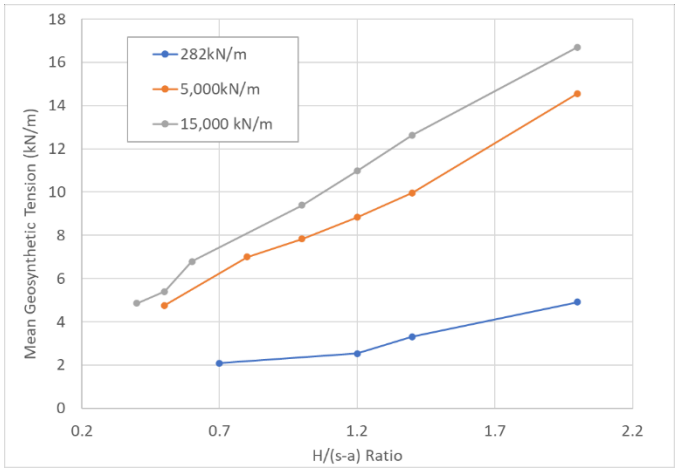

Figure 10. Mean geogrid tension with H/(s-a) ratios between 0.4 – 2.0 and geogrid stiffnesses of 282kN/m, 5000kN/m and 15000kN/m.

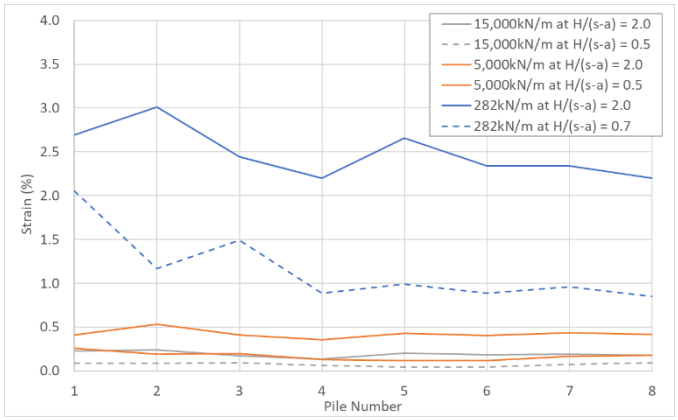

Figure 11. Geogrid strain for H/(s-a) ratios of 0.5, 0.7 & 2.0 and geogrid stresses of 282kN/m, 5000kN/m and 15000kN/m.

The lateral displacement of the piles is presented in Figure 12 for H/(s-a) ratios between 0.5 – 2.0 and with a geogrid stiffness of 10000kN/m. All piles underwent some degree of lateral displacement. The outer most pile (Pile 1) experienced the greatest lateral displacement, with an exponential reduction in lateral displacement in other piles closer to the centre line of the embankment. In the three outer most piles (Piles 1 – 3) the lateral displacement increased with embankment height ratio.

For H/(s-a) = 2.0 the magnitude of lateral deformation was dependent on the geogrid reinforcement stiffness, Figure 13. With low geogrid stiffness, 282kN/m, the lateral deformation was high at over 60mm. Increasing the stiffness to greater than 5000kN/m significantly reduced the lateral displacement to less than 30mm in the outer most piles.

The magnitude of lateral displacement for H/(s-a) = 0.5 was largely independent of geogrid stiffness, with relatively small displacements occurring, typically < 15mm, Figure 14

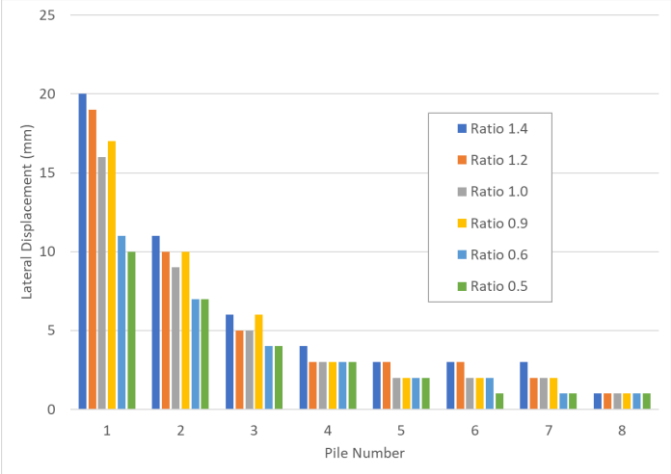

Figure 12. Lateral displacement of piles, geogrid stiffness of 10000kN/m

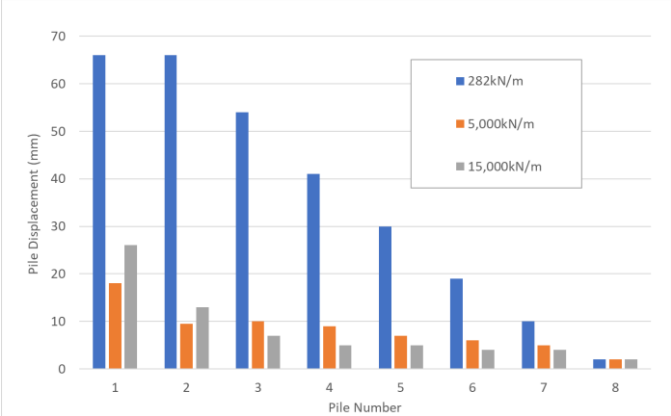

Figure 13. Lateral displacement of piles, for H/(s-a) = 2.0.

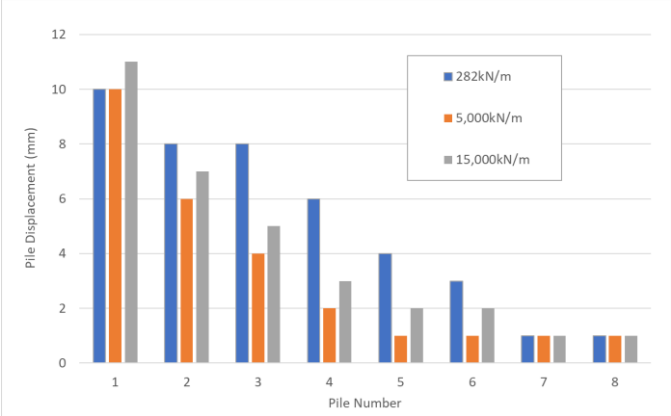

Figure 14. Lateral displacement of piles, for H/(s-a) = 0.5.

The arching occurring in the embankment fill was investigated qualitatively by examining the principal stresses in the embankment fill, Figure 15 and Figure 16. In both cases the arches are clearly visible and span directly between adjacent pile caps. For the low H/(s-a) ratio, Figure 15, the arches extend to the embankment surface, while for the high H/(s-a) ratio, Figure 16, the arching was concentrated in the lower half of the embankment fill.

4 IMPLICATIONS FOR DESIGN

Low height embankments, where the height of the embankment to clear spacing between adjacent pile caps is less than 0.7 can be problematic to design. The overriding criteria is to limit differential settlement at the surface of the low height embankment. BS 8006-1 [1] recommends that the design strain in the geogrid reinforcement should be a maximum of 3%.

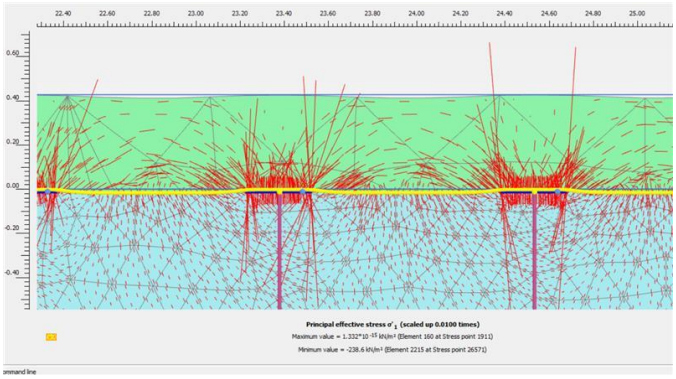

Figure 15. Principal stress in embankment fill for a H/(s-a) ration of 0.5.

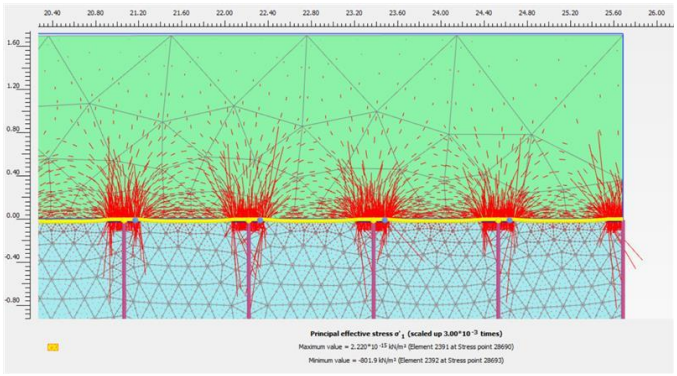

Figure 16. Principal stress in embankment fill for a H/(s-a) ration of 2.0.

The data presented in this paper indicates that both H/(s-a) ratio and geogrid reinforcement stiffness are important factors in the design of low height embankments. Under plane strain conditions limiting the H/(s-a) ratio to a minimum of 1.0 can significantly reduce differential settlement at the surface of the embankment. A H/(s-a) ratio of 1.0 can be achieved by careful selection of pile spacing and pile cap size. In many cases, the size of the pile cap will need to be increased to satisfy this requirement.

Using stiffer geogrid reinforcement will reduce deformation of the geogrid between pile caps, resulting in a reduction in differential settlement at the surface of the embankment. Stiffer geogrid reinforcement will also significantly reduce the strain in the reinforcement to values significantly lower than the 3% maximum value recommended in BS 8006-1 [1].

However, using higher stiffness geogrid reinforcement will increase the ratio of peak to mean tension in the geogrid at the pile cap. Consideration should be given to careful detailing of

the pile cap edge to accommodate this peak tension without damage to the geogrid reinforcement.

All piles will be subject to lateral deformation and should be designed to have adequate bending resistance. While piles near the outer extremity of the embankment are subjected to the largest lateral deformations, all piles, even under the centre line of the embankment, will experience some degree of lateral deformation and bending.

5 CONCLUSIONS

Piled embankments are typically used to support road and rail embankments over soft foundation soils. The design of piled embankments is complex and is not yet fully understood. Low height piled embankments, where the height of the embankment is similar to the clear spacing between adjacent pile caps, are known to be difficult to design. The principal design criterion is the serviceability limit state and the requirement to eliminate the differential settlement at the embankment surface.

The impact of embankment height to clear spacing between pile caps and the stiffness of the geogrid reinforcement were investigated under plain strain conditions in Plaxis 2D. The Plaxis 2D numerical models were validated against previous physical and numerical modelling reported by Jennings [3]. A parametric variation showed that the ratio of embankment height to clear spacing between adjacent pile caps and geogrid stiffness were key parameters in the design of low height embankments. Increasing the geogrid stiffness was found to reduce both the vertical geogrid and vertical embankment surface deformations. Piled embankments with low H/(s-a) ratios appeared to receive support from the subsoil, however this diminished for higher H/(s-a) ratios.

Deformations at embankment surface level were reciprocated of the settlement behaviour that occurred at geogrid level for low H/(s-a) ratios, however, when the H/(s-a) ratio was >1.0, the surface deformations were largely uniform and independent of geogrid deformations.

The tension in the geogrid was not uniform and generally increased with distance from the embankment centre line to the crest of the embankment, before reducing to zero at the embankment toe. Tension in the geogrid increased with embankment height. Isolated peaks in tension were observed at the edge of pile caps, with magnitudes 2 – 3 times the mean tension in the geogrid.

The strain in the geogrid was also dependent on the geogrid stiffness, with geogrid stiffness greater than 5000kN/m resulting in geogrid strain less than 0.5%. Lower stiffness geogrids recorded strain up to approximately 3%. All piles supporting the embankment experienced lateral deformations, with the magnitude dependent on both the embankment height and geogrid stiffness. Maximum lateral deformations occurred at the outermost pile for all models studied and the deformation reduced towards the centre of the embankment. For low H/(s-a) ratios, the lateral deformation was found to be independent of geogrid stiffness, but for high H/(s-a) ratios, the lateral deformation reduced with increased geogrid stiffness.

REFERENCES

[1] BS 8006-1 (2016), *Code of practise for strengthened reinforced soils and other fills,* British Standard Institution, London.

[2] Plaxis 2D (2021), Bentley – Plaxis general information manual. *Delft, Netherlands: Bentley Systems Inc.*.

[3] Jennings, K., (2012), *An investigation of geosynthetic reinforced piled embankments with particular reference to embankment extremities*, PhD Thesis, I.T Sligo.

[4] Russell, D., Naughton, P.J. & Kempton, G. (2003), 'A new design procedure for piled embankments', *Proceedings of the 56th Canadian Geotechnical Conference and 2003 NAGS Conference*, Winnipeg, Canada.

Review of Structural Fills in Irish Practice

Ronan Travers[1], Eoin Wyse[2]
[1,2]Ove Arup & Partners Ireland Ltd., Dublin, Ireland
email: ronan.travers@arup.com[1], eoin.wyse@arup.com[2]

ABSTRACT: Compacted crushed rock is routinely used either beneath concrete floor slabs, against concrete retaining walls or below foundations due to the plentiful supply of good quality quarried rock in Ireland. Its application in construction has resulted in two separate industry "product families" being developed: Transport Infrastructure Ireland (TII) Specification for Roadworks (SRW) Series 600 and 800, and S.R. 21, the Irish national implementation document of I.S. EN 13242 (unbound aggregates). As a result, different aggregates are available on the market which form the family of structural fills available in Ireland, many of which are very similar in nature and application. The materials considered in this paper are TII Class 6N, and S.R. 21 Annex E materials (T0, T1, T2). The proliferation of these materials and their similarity with other aggregate products can lead to confusion for the designer. A review has been undertaken of current Irish industry practice to assist the designer in selecting and specifying the appropriate fill type for its intended end use. Recommendations for possible updates to align the different industry standards and specifications are also presented.

KEY WORDS: Structural Fill, Aggregate Testing, Natural Aggregates, Standards, National Specifications

1 INTRODUCTION

This paper describes the different types of engineered fills in Ireland commonly used either beneath concrete floor slabs, that are typically formed using natural aggregates sourced from quarried rock.

Two separate industry approaches have evolved to cater for the different applications, these are: Transport Infrastructure Ireland (TII) Specification for Roadworks Series 600 [1] and Series 800 [2], and the Irish national implementation document, Special Recommendation (S.R.) 21 [3] for I.S. EN 13242 [4] unbound aggregates. As a result, different aggregates exist that form the suite of structural fills available in Ireland, many of which are very similar in nature and application. This can lead to confusion in specifying these fill types, for the designer.

This paper summarises and compares the fill types and standards to assist the designer in selecting and specifying the appropriate fill type. Recommendations for possible updates to align the different industry standards and specifications are also presented.

2 SOME DEFINITIONS

2.1 Natural aggregate

Natural aggregate is defined as a coarse grained (or granular) material used in construction from mineral sources which have been subjected to nothing more that mechanical processing [4]. In Ireland, this is commonly referred to as hardcore [3], for consistency with the European standard, the term aggregate is preferred.

2.2 Engineered fill

Engineered fill is defined as *'fill which is selected, placed and compacted to an appropriate specification, so it will exhibit the required engineering behaviour'* [5].

2.3 Rockfill

Rockfill is defined as *'A fill produced by blasting or ripping rock strata which may contain large rock fragments'* [5].

2.4 Structural Fill

This is an engineered fill, formed from unbound natural aggregate derived from crushed rock and natural gravels, used beneath concrete floor slabs, against concrete retaining walls or below foundations. TII Series 600 refers to this as either *'fill to structures', 'fill below structures'* [1]. Or *'structural backfill'* in the note for guidance [6]. The term structural fill is preferred and used in this paper.

3 AGGREGATE SOURCE

Most aggregates in Ireland are formed from locally sourced quarried crushed rock due to its plentiful supply.

In the case of highways products, aggregates may be produced on site due to the construction of cut areas, pending confirmation that the site won material will fulfil the requirements of the relevant specification. Typically, this would be the TII SRW Series 600 [1] and Series 800 [2].

Where there is a materials deficit in relation to site won materials, suitable materials produced by third parties, i.e., local quarries may also be imported onto site for use. These materials will also have to fulfil the requirements of the earthwork's specification.

4 BRIEF HISTORY OF AGGREGATES IN IRELAND

A chronology of some key dates is outlined in Table 1, to assist in understanding the evolution and of different aggregates used on infrastructure and building projects in Ireland,

Table 1. Aggregate evolution – key dates

Time	Document/Event	Fill Class
1979 to 2000	Department of the Environment (DoE) Specification for Roadworks	Clause 804 (subbase) and 616 (fill to structures)
1993	Homebond House Building Manual	Use of term hardcore
2000	NRA Specification for Road Works (SRW) Series	Class 6N, Clause 804
2002	European Standard (I.S. EN 13242 [4])	
2004	Standard Recommendation S.R. 21	Referenced NRA SRW
2007	Initial reports relating to problems with Pyrite	
2007	S.R.21:2004+A1:2007	Introduced S_1 requirement in response to pyrite issue
2007	Building Regulations Technical Guidance C [7]	Updated to include use of S.R. 21:2004+A1:2007
2010	NRA Specification for Road Works Series	Subbase type B & C, Clause 808 / 809 introduced
2012	Report on the Pyrite Panel [8]	
2013	TII Specification for Road Works Series, [1, 2]	Class 6N and Type B & C Clause 808 / 809 updated to include oxidisable sulfides
2014	Updated S.R. 21:2014	Significant overhaul of Annex E to include lessons learnt from pyrite
2016	Updated S.R.21:2014+A1:2016 [3], I.S. 888 Code of Practice for Procurement and Use of Unbound Hardcore [9]	Update to SR21 to introduce T0, T1, T2, T3.

Documents relating to structural fill remained relatively constant up until 2004, with products such “hardcore”, 3 inch down (i.e., particle size <100mm), 4 inch down, 4 inch clean, along with clause 804 being ubiquitous both as structural fill and for road make up (subbase and capping) with all considered as quality products.

The introduction of the harmonised EN standards, namely I.S. EN 13242:2002 and the related national implementation document S.R. 21 prompted a review and update of the existing standards to use the terms set out in EN 13242 to describe unbound and hydraulically bound aggregates. S.R. 21:2004 made extensive reference to the NRA Specification for Roadworks at the time.

However, during the summer of 2007, the first cases of pyrite related heave were identified, and this prompted revisions of some of the standards.

S.R. 21 was promptly reviewed and updated, (S.R.21:2004+A1:2007) to include an additional parameter for sub-floor fill, namely a 1% upper limit on total sulfur content.

Parallel to this, Construction Product Regulations (CPR) [10] relating to aggregates were introduced. I.S. EN 13242 [4], came into force in 2009, and this included the requirement for CE marking of manufactured aggregates which are to be placed on the construction market. CE marking would not apply to site won materials, as these materials were incorporated into the works locally and not intended for sale. Therefore, there was (and still is) no reference to I.S. EN 13242 in the TII SRW Series 600.

As the pyrite problem manifested and became more widespread, specifications were updated to reflect the increased understanding of this issue. This included the 2010 revision of the NRA SRW Series 800.

The publication of the Report of the Pyrite Panel in 2012 [8] was a marker point, as this recommended the development of a standard which would allow an assessment of the likely risk of pyrite related heave in aggregates, which led to the development of I.S. 398:2013 [11]. The methods set out in this document were subsequently used as the basis for the assessment of new aggregates for suitability for use and as such, TII Series 800 in 2013 and S.R. 21 in 2014 were published. S.R. 21 was again revisited in 2016 after industry feedback.

The following are the current key standards pertaining to structural fills in Ireland:

1. TII series 600 (2013) earthworks specification
2. European standard for aggregates, I.S. EN 13242 (2007) and the Irish national implementation document S.R 21 (2016)
3. I.S. 888 (2016) code of practice for procurement and use of unbound hardcore

5 STRUCTURAL FILLS

5.1 Purpose

Structural fills should be inert, as physical (e.g., volume change) or chemical changes could impact on the surrounding environment or on other nearby construction materials.

The designer also needs to consider the potential of chemical attack from the underlying ground in addition to the aggregate itself and its durability when selecting an appropriate fill type for use during the construction process and over the design life of the structure.

Structural fills beneath concrete slabs are required to fulfil certain mechanical purposes:

1. The transfer of load from the reinforced concrete (RC) floor slab to the underlying natural ground (sub grade)
2. To provide a level working platform for construction of the RC slab.

The thickness of the structural fill depends on the strength and stiffness of the underlying ground, type and magnitude of

the applied loads and the type of slab finish (in terms level and flatness).

5.2 Types

Table 2 summarises the two suites of structural fill types currently used in Ireland.

Table 2. Irish structural fill types

Fill Class	Typical End Use	Requirement
T0 & T1 STRUC* T2 PERM	Building projects (beneath concrete floor slabs and footpaths)	Irish Building Regulations [7]
6N1 & 6N2	Civil and infrastructure works on building projects (Fill to or below structures)	TII 600 series standard [1]

* For the purpose of this paper T0 STRUC and T1 STRUC are referred to as Class T0 and T1 fills respectively for consistency with TII fill types.

TII Series 600 specification includes numerous other different classes of both granular (coarse grained) and cohesive (fine grained) fill materials, such as capping (Class 6F) for use in road construction. Capping and other Class 6 fill materials are not considered structural fills (see 2.4 for definition) in this paper and therefore not discussed further.

TII Series 800 materials (i.e., Clause 804) were commonly called up as structural fill within the industry prior to 2007. This was due to the perception that this was a material with a robust specification and known handling and compaction requirements, "804" was considered a high quality material.

Technical guidance document [7] on the Building Regulations published in 2008, states that aggregates beneath concrete floors or footpaths should comply with the European standard and the Irish national implementation document, S.R. 21. In addition, a blinding layer should be provided. There is no requirement for fill behind retaining structures to conform to S.R. 21.

It is important to note that Class 6N fills do not comply with the requirements of S.R. 21. They have not been designed to explicitly prevent pyrite heave issues and should not be used on projects where building regulations govern unless modified.

S.R. 21 Annex E aggregates (T0 and T1) are required to be used over the full thickness of build-up beneath a concrete slab. This differs to the approach in TII Series 600 and 800 where protection against concrete attack from aggressive ground conditions is the key requirement, thus requiring fills within 0.5m of concrete slabs to meet higher chemical composition limits.

5.3 Comparison

Table 4 (see end of this paper) summarises the properties and design criteria used for the different structural fills. Both road capping (class 6F) and subbases (Type B, Clause 808) materials are included for reference purposes only, neither of these are considered structural fills.

A comparison has been undertaken to assist the designer in understanding the difference between the fill types, the following is a summary, with a more detailed appraisal included in the sections below:

- It is noted that a fundamental difference exists between the TII SRW Series 600 and S.R. 21 Annex E in that the Series 600 specifications cover both site won and third party produced materials, while S.R. 21 Annex E discusses materials which are purchased from a third-party manufacturer and transported to a site for use.
- Class T0, T1 and Class 6N.
    - S.R. 21 Annex E aggregates have stricter requirements on traceability of the source product and more onerous chemical testing requirements to protect against swelling induced effects from reactive pyrite, see Section 7.
    - The grading limits differ, with Class T0 and T1 broadly falling within the Class 6N envelope, e.g., T0 permits larger particle sizes, see Section 6 for details.
    - Durability requirements (resistance to fragmentation and resistance to freeze thaw) differ with Class 6N having no freeze thaw requirement, see Section 8 for details.
- Class T1 fill and subbase
    - Class T1 fill is based on subbase (Type B, Clause 808) for use beneath concrete road pavements and as such are very similar, with near identical grading curves.
    - T1 allows gravel to be used in addition to crushed rock.
    - Different chemical testing requirements, with subbase designed to protect against chemical attack to concrete.

It is common for quarried rock type to fulfil the requirements of a number of different structural fill types or specifications. Manufacturers typically have a set of known properties for each rock type which they then match to the product being ordered. Rock type inherently influences a number of aggregate properties, and as such there is a consistency of performance with aggregate products manufactured from the same source. It is for this reason that a number of different specifications (and thus fill types) can be fulfilled by materials arising from the same source. For example, if a rock type meets the specification for Class T1, then it could also potentially be sold as a subbase (Type B, Clause 808) or a Class 6N fill.

5.4 Quality control

The harmonized European standard for unbound and hydraulically bound aggregates in civil engineering and road construction, I.S. EN 13242 [4], requires that manufacturers have a factory control system in place to ensure that the aggregate complies with the standard. This includes a requirement to regularly test the source material, to have geological knowledge of the raw material and to ensure that all material delivered to site includes CE marking.

A Declaration of Performance (DoP) is provided by the manufacturer in advance of each project. Some manufactures have made these available through online databases. The quarry deposit is also subject of a geological assessment by a competent professional geologist (PGeo) at least once every three years.

There is a responsibility on the end user to review all documentation to ensure compliance with the project specification. A delivery docket system is required to ensure traceability of the source material, with the onus again on the end user to check for compliance.

There is currently no reference to I.S. EN 13242 in the TII SRW Series 600 specification, should a Series 600 material be prepared and placed on the market, a DoP is required. It is possible to prepare a DoP for such a product, once it complies with the relevant standards.

For S.R. 21 Annex E materials, there are requirements for minimum test frequencies which are carried out as part of required Factory Production Controls (FPC). It is important to note that this testing by the manufacturer is there to demonstrate the consistency and performance of an aggregate to fulfil a certain end use.

To ensure compliance with the project specification, it is key that the designer specifies acceptance testing that is separate to testing undertaken by the manufacturer and should be at a much higher frequency than required for factory production controls. The frequency depends on several factors: fill type, variability of source, volume of fill being placed and progress of works on site. Compliance testing is also required on placed fill to check that the properties selected during design are being achieved on site.

6 GEOMETRICAL PROPERTIES

The geometrical properties of natural aggregates are properties which are controlled and managed through the production process. They are not necessarily an inherent property of the parent rock.

The key geometrical properties of aggregates are particle shape and particle size distribution. These influence the earthworks plant and methods used to achieve the required insitu density of the compacted structural fill and needs careful consideration during design.

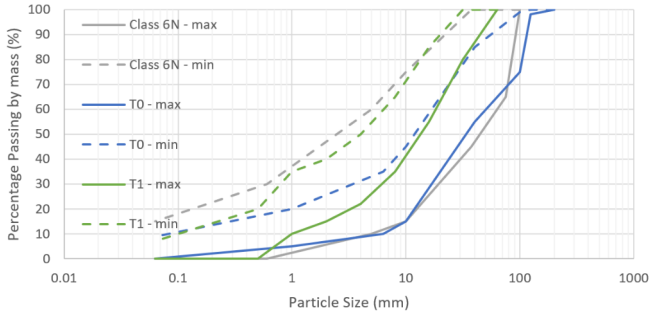

Figure 1. Grading curves of structural fills

Figure 1 presents the grading envelopes for each structural fill and Figure 2 shows the typical build up beneath a concrete slab using S.R. 21 aggregates. The following is noted:

1. Class T1 grading curve in Figure 1 is for crushed rock (natural gravel grading curve is not shown).
2. Grading: Class T0 and T1 broadly fall within the Class 6N grading curve (Figure 2) envelope with Class T0 within the coarser range, while Class T1 is closer to the minimum requirements i.e., finer particle size).
3. A larger percentage of fines (<0.063mm) <15% is permitted in Class 6N than in Class T0 (<9%) and T1 (<7%).
4. Class T0 permits a larger particle size (125mm) than Class 6N (75mm) and with 2% of aggregate particle size permitted between 125 and 200mm.

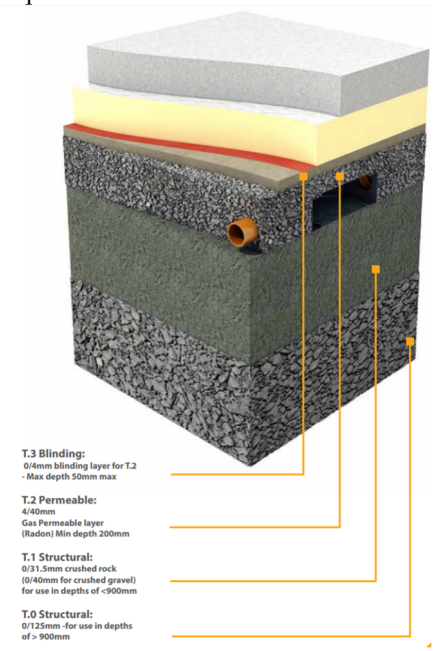

Figure 2. Schematic build up beneath a concrete slab [12]

7 CHEMICAL COMPOSITION

The chemical composition of natural aggregates is an inherent property of the parent rock. It is controlled by the mineralogy of the rock. The limits on chemical properties are required by the specifier depending on its end use and the origin of the aggregate. The following should be considered:

- the risk of concrete attack from aggressive ground conditions; and
- volume change / induced effects due to the presence of deleterious materials / minerals such as pyrite or mica.

Three chemical properties are stated in I.S. EN 13242 [4], for use where required.

- acid soluble sulfate AS
- total sulfur, S
- water soluble sulfate, SS

The Irish national implementation document of this standard, S.R.21, includes additional requirements to protect against the possible presence of pyrite or other sulfides.

The following is a comparison between Class T0, T1 and Class 6N structural fills:

- Clause 601.11 of TII [1] calls up the chemical requirements of materials used within 500mm of concrete, cement bound materials or other cement bound materials.
- S.R 21 has defined chemical limits included in its material specifications. While these initially were specified to minimize the likely presence of sulfides within the aggregate with pyrite related heave in

mind, it also reduces the possibility of sulfate attack on nearby materials or concrete elements.

- The chemical test limits differ in their approach.
    - S.R. 21 sets a pass limit for AS and S of less than 0.2% and 0.1% respectively. In cases where S values lie between 0.1 and 1% a petrographic analysis of the aggregate is required. S values greater than 1% are considered as not suitable for use. Similarly, AS values greater than 0.2% are not considered suitable for use.
    - Class 6N materials have pH, oxidizable sulfides (OS) and SS requirements. Of these only SS is explicitly outlined in the European Standard. However, it is noted that OS is a calculated value based on AS and S values, as shown in Equation (1) below, taken from TII Series 600 Clause 643.
    - For Class 6N materials, SS shall be less than 1.5g/l and OS shall be less than 0.3% SO_4.

It is not possible to directly assess compliance of TII structural fills to S.R.21 materials due to TII setting limits for OS without imposing limits on AS and S. However, it is possible to assess S.R. 21 materials for compliance against Class 6N materials. The calculation for OS is given below.

$$OS = 3S - AS \quad (1)$$

Using this formula and the S.R. 21 limits above, then OS = (3*0.1) – (0.2) = 0.1% SO_4. In addition, other combinations of high S and high AS can still yield values of OS<0.3%. Based on this approach S.R. 21 is considered more onerous because of the need to establish a clear "safe" aggregate. However, materials falling above the lower limits in S.R. 21 require extensive testing and assessment such as petrographic examination and X-ray diffraction analysis to allow their use as T0 or T1 aggregate.

TII series 600 only refers to S.R. 21 as a footnote 8 only of Table 6/1, *'A petrographer's detailed mineralogical description may be required as described under section 3.4.2 of SR 21'*. The use of 'may' indicates a recommendation rather than a requirement.

This footnote is often missed by the specifier and user and has led to misinterpretation in practice. It is recommended that it is removed.

There is additional information presented in the Series TII SRW Notes for Guidance. This covers the assessment of aggregates should the materials exceed the OS limit. The recommended approach considers the nature of the rock from which the aggregate is produced to determine if there is any evidence of an unacceptable risk due to the presence of sulfides using methods and approaches set out in TRL 447 [13].

Regardless, the material requirements of Class 6N fill needs modification to comply with S.R.21.

8 DURABILITY

Durability is another inherent property of the parent rock. This can be influenced by both the mineralogy and the internal structure of the rock. It is influenced by the ability of the source aggregate to resist the temporary loading during the placement and compaction process, along with the long term design loads and climate effects. Two properties which are typically tested for are:

- Resistance to fragmentation
- Resistance to freeze thaw

The following is a comparison between Class T0, T1 and Class 6N structural fills:

- Resistance to fragmentation: Class 6N requires a less onerous Los Angeles Coefficient (LA) limit of 50 and an additional test of slake durability to be measured if argillaceous materials are identified within the aggregates
- Resistance to freeze thaw: limits for magnesium sulphate soundness (MS) and water absorption are required for Class T fills and for subbase (Type B, Clause 808), but these tests are not required for TII Class 6N fills

It should be noted that during research into the pyrite issue, materials susceptible to pyrite related heave were noted to have high water absorption and poor performance in magnesium sulfate soundness tests. As a result, S.R. 21 recommends that durability testing in Ireland is based on magnesium sulfate soundness and water absorption test.

9 COMPACTION

9.1 General

Table 3 summarises the compaction methods used for structural fills in practice.

Table 3. Compaction methods

Fill Class	Method	Typical End Use	Requirement
6N1 & 6N2	End product only		TII 600 series standard [1]
T0, T1, T2	Method Compaction	Small floor slabs	I.S. 888 [13]
	Method and end product	Large floor slabs	

Both standards require a project specification to be produced. In the authors experience this is not always produced in practice. In the absence of this, where S.R. 21 aggregates are used, the default will be for the contractor to place and compact the structural fill using method compaction. However, this may not give the appropriate fill stiffness (E_{PLT}) for all design situations. It is important to note *'provided that the contractor can show that he has followed precisely the method dictated by the engineer or designer in the specification, the responsibility for any subsequent failure usually rests with the engineer'* [14]

The actual choice of compaction method for S.R. 21 aggregates should always be specified by the designer based on their RC slab design and stated in their project earthworks specification.

For large industrial developments that combine extensive site infrastructure and buildings, e.g., for the pharmaceutical or digital industry, it is typical that a single project particular specification linked to the TII specification is used to cover all sitewide earthworks. The challenge for the designer in these situations is producing an earthworks specification that

combines both TII and S.R.21 requirements into one place and avoiding some of the differences (see section 5.3 and the following sections) of having the two types or specifications for structural fill in a single document.

9.2 TII structural fills

The requirements for compaction of TII Class 6N structural fills are set out in clauses 612.11 to 15 and Table 6/1 where end production compaction is specified. Some points to note:

- It is a requirement on the designer to set an acceptable range of water contents, typically as a percentage of the optimum water content in Table 6/1 of the project specification
- Compaction testing of source material is required to determine both optimum water content and maximum dry density in advance of works commencing.
- Field measurements are mandated and are required to achieve ≥95% of maximum dry density, with tests undertaken in accordance with BS 1377 part 9 [15].
- TII clause 601.10 [1], states that 'maximum particle size of any fill material shall be no more than two thirds of the compacted layer thickness'

9.3 S.R.21 Annex E structural fills

The requirements for compaction of S.R.21 Annex E structural fills are set out in the code of practice (CoP), I.S. 888 [9]. For small floor slab construction (e.g., standard residential and commercial), method compaction is specified. This standard directs the contractor to a layer thickness, plant type and number of passes, that if followed will achieve an appropriate level of compaction for these applications. The authors are unaware of any published data on the engineering performance (strength, density and stiffness) of aggregate types placed and compacted to a method for different source materials found in Ireland to understand what is considered an appropriate level of compaction.

For large floor slab construction both method and end product compaction are permitted. The difference between small and large floor slab is not defined, so it is the responsibility of the designer to select the compaction type that provides the appropriate engineering performance of the fill based on their design. In the authors experience, concrete floor slabs for datacentres or sensitive warehouse racking systems typically require more onerous differential settlement criteria that are only achieved through end product specification of structural fill.

Some points to note on I.S. 888:

- On site verification testing must be specified in the project specification.
- Unlike TII there are no detailed clauses provided to support end product compaction requirements. As a result, this needs to be included by the designer in a more comprehensive project specification.
- Method compaction.
    - Is based on TII series 800 table 8/4, and the table is reproduced in the CoP but without the clauses that accompany it. Interestingly, it is broadly similar to TII series 600 table 6/4 method 6, but Table 6/4 allows a thicker layer of 250mm with higher number of passes of compaction plant.
    - For Class T1 fill: minimum layer thickness is 110mm and maximum layer is 225mm
    - For Class T0 fill: minimum layer thickness is 150mm and maximum layer is 250mm. The layer thickness is not consistent with Table B.1 (in I.S. 888) which states a 225mm layer, this is considered an error and will result in lower densities of compacted fill if the thicker layer is used.
    - No requirements to control range of water content of placed aggregate during compaction process.
- All methods of compaction rely on the water content of the material being within an acceptable range of the optimum water content. Aggregates placed too dry of optimum are more difficult to compact and result in lower densities and thus stiffness (E_{PLT}) achieved. When inundated with either surface or ground water it may undergo further settlement. BRE [16] have reported structural issues due to the combination of aggregates placed too dry of optimum and poor compaction procedures on site. Currently this is not required in I.S. 888 where method compaction is used.
- Earthworks industry practice both here in Ireland [1] and the UK [14,17] does not permit a particle size more than two thirds of the layer thickness as it reduces the effectiveness of energy applied during compaction.
- Class T0 fill has a maximum particle size of 125mm and is unsuitable for layer thickness less than 187mm based on above. As a result, a layer thickness of 110 and 150mm on Table B.1 I.S. 888 [9] are not appropriate for T0 fill.

9.4 On site verification

It is important the underlying ground and groundwater conditions are carefully considered during concrete slab design. An appropriate level of testing of the subgrade should be undertaken prior to placement of structural fill.

In addition to a suite of acceptability testing discussed above in Sections 6, 7 and 8, in situ testing is required on the compacted structural fill to demonstrate that it has been laid and compacted in accordance with the project earthworks specification, i.e., it has achieved the required insitu density, water content and stiffness required as part of the slab design.

It is important that testing is undertaken over the full thickness of the fill and not just confined to top of the final layer which is often compacted to refusal as a result, and testing of the final layer only may not be representative of the aggregate at depth.

Nuclear density testing provides a quick way of measuring insitu density but require appropriate calibration. Additional plate load tests are recommended to be undertaken less frequently to provide a direct measure of the load settlement performance. This allows stiffness (E_{PLT}) to be calculated following the approach in Eurocode 7 [18]. BS 1377-9 [15] states that for granular soils the plate diameter should exceed at least five times the size of the nominal size of the coarsest

particle. Therefore, the size of the plate specified needed to be based on the aggregate grading. It is recommended that a minimum diameter of 600mm is used for aggregates.

10 CONCLUSIONS

A detailed review of existing structural fills used in Irish practice has been undertaken to guide the designer in selecting, specifying and verifying structural fill during construction. A brief history of aggregate evolution is included so the user understands the context to their current use. The following is a summary of the key conclusions and recommendations for their use in practice:

- A project earthworks specification is required by the Irish National Standard I.S. 888. Notes on design drawings are not sufficient to adequately specify structural fills.
- The compaction requirements in I.S. 888 are directly taken from TII but without including the accompanying clauses that support the table. As such it is recommended that these missing compaction requirements are covered in the project specification instead, in addition to the acceptability testing requirements and frequency of testing.
- It is considered essential to control water content during placement and compaction of aggregate during method compaction. In the absence of this being included as a requirement in I.S. 888, it is recommended that this is captured in the project specification in the form of setting of water content acceptability limits.
- Advanced earthworks trials should also be considered where demonstration of the end performance of the compacted fill is required and where limited knowledge exists on the source rock type of the aggregates being placed.
- Class 6N fills do not comply with the requirements of S.R. 21 and should not be used use on projects where Building Regulations apply.
- Class 6N has not been explicitly designed for use
    - within a freeze thaw zone. Additional durability testing is required where this needs to be accounted for in design.
    - or where deleterious materials such as pyrite could impair the function of the overlying structure.
- Road capping (Class 6F) and subbase (Type B, Clause 808) should not be used as structural fills (designed in section 2.4). Subbase is designed to for a particular use in relation to a concrete road pavement. Neither Capping (Class 6F) or Sub-base (Clause 808) have been directly designed to prevent pyrite effects.
- The current grading envelope permits Class T0 fills to contain 2% of the aggregate having a particle size between 125 and 200mm. However, large particle sizes reduce the effectiveness of compaction plant and thus the compactive effort achieved. Large quantities of coarser material up to cobble size could also lead to a false positive result from a plate load verification test. The performance of this material should be considered by the designer with these issues in mind.

11 FUTURE WORK AND RECOMMENDATIONS

Both standards have merits, and both clearly have areas which could do with improvement. It is recommended that the two suites of structural fills are more closely aligned, and the number of fill types reduced to simplify the specification, procurement, and manufacture process over the complete lifecycle of its use. This could be achieved as follows:

- Align the Class T0 and T1 aggregates gradings so that they fit more closely with the 6N envelope. Including reducing the maximum particle size below 200mm
- Remove 6N2 and replace with S.R. 21 Class T1 and T0 fills where the grades have been aligned. 6N1 is essentially the same material but for a different application so could also be considered for replacement,
- Include resistance to freeze thaw durability testing as a requirement for 6N fills and thus aligning them with the European standard, TII 800 series fills and Class T fills, thus giving the choice to the designer to specify an appropriate value.
- Remove the minor differences in gradings between Type B Clause 808 and Class T1 fill.
- Align the compaction requirements across all documents, TII series 600, 800 and I.S. 888. Include the requirement to control water content. Ideally, I.S. 888 would refer to the TII document for compaction guidance and we would therefore have a single national source of compaction requirements. Otherwise I.S. 888 requires continuous updating for consistency with TII.
- Simplify the terminology used, e.g., use the term structural fill (see definition in 2.4) instead of structural backfill, use the term aggregate in lieu of hardcore, include the term ‘Class’ for S.R. 21 aggregates thus aligning with the TII approach.

- The number of different national document types should be rationalised, and it is suggested to merge I.S. 888 and S.R.21 documents, with the compaction requirements section referencing the TII series 600 or 800 specification.
- Update TII series 600 to fully align with the European Standard for specifying aggregate properties (I.S. EN 13242) and to also include the S.R. 21 Annex E suite of aggregates.
- Provide clarity on the use of aggregate sourced on site and that manufactured externally in both sets of standards.

It is recommended that more testing data is published by the industry for different source materials. This will allow better understanding of the engineering properties and behaviour of structural fills, thus improving its specification and use within the industry.

While S.R. 21 employs a risk-based approach to examining aggregates, Series 600 has more prescriptive limits. By examining the proposed uses for unbound aggregates in Series

600 and examining the likely risks associated with their placement and use, it may be possible to widen the envelope of use for materials to include those which were previously excluded from use,

ACKNOWLEDGMENTS

The authors would like to thank their colleagues John O'Connor from Arup and Cathal MacMathuna from the Aggregate Panel for providing very helpful comments on this paper.

REFERENCES

[1] *Specification for Road Works Series 600 - Earthworks (including Erratum No. 1, dated June 2013).* CC-SPW-00600, 2013, TII Publications

[2] *Specification for Road Works Series 800 – Road Pavements – Unbound and Cement Bound Mixtures*.CC-SPW-00800, 2013, TII Publications.

[3] *Guidance on the use of I.S. EN 13242:2002+A1:2007 – Aggregates for unbound and hydraulically bound materials for use in civil engineering work and road construction*. Standard Recommendation 21, S.R. 21:2014 + A1:2016, National Standards Authority of Ireland.

[4] *Aggregates for unbound and hydraulically bound materials for use in civil engineering work and road construction*, I.S. EN 13242:2002+A1:2007, National Standards Authority of Ireland.

[5] BRE (2015) Building on Fill: Geotechnical Aspects, BRE FR 75 3rd edition

[6] *Notes for Guidance on the Specification for Road Works Series 600 - Earthworks (including Erratum No. 1, dated June 2013.* CC-GSW-00600, 2013, TII Publications.

[7] *Building Regulations 1997 Technical Guidance Document C, Site Preparation and Resistance to Moisture.* Department of the Environment, Heritage and Local Government, September 2004 Edition

[8] *Report of the Pyrite Panel.* Department of the Environment, Community and Local Government, June 2012

[9] Code of practice for the procurement and use of unbound granular fill hardcore material for use under concrete floors, I.S. 888:2016, National Standards Authority of Ireland.

[10] *Regulation (EU) No 305/2011 of the European Parliament and of the Council of 9 March 2011 laying down harmonised conditions for the marketing of construction products and repealing Council Directive 89/106/EEC,* Eur-Lex, https://eur-lex.europa.eu/legal-content/EN/TXT/?uri=CELEX%3A02011R0305-20210716

[11] *Reactive pyrite in sub-floor hardcore material – part 1: testing and categorization protocol.* I.S. 398-1: 2007, National Standards Authority of Ireland.

[12] Roadstone (2017). S.R.21 – AnnexE:2016. https://www.roadstone.ie/wp-content/uploads/2014/05/SR-21-Brochure-NOV-17.pdf

[13] Reid, J.M., Czerewko , M.A., and Cripps J.C. 2005. Sulfate specification for structural backfills. TRL Report 447, TRL Limited.

[14] Trenter NA (2001). Earthworks a Guide. Thomas Telford Publishing

[15] *Methods of test for soils for civil engineering purposes* – BS 1377 part 9: Insitu tests. British Standards Institution 1990

[16] BRE Digest 522-2 Hardcore for supporting ground floors of buildings Part 2: Placing hardcore and the legacy of problem materials

[17] *Volume I specification for highway works Series 600* Earthworks. Manual of contract documents for highway works. Highways England, 2013

[18] *Eurocode 7 - Geotechnical design: Part 2: Ground investigation and testing. I.S. EN 1997-2:200, National Standards Authority of Ireland*

Table 4: Key specification criteria for fill types

Criteria		6F	6N	T0	T1	T2 Perm	Type B Clause 808
Geometrical requirements	Permitted Constituents	Crushed Rock or Gravel (<50% recycled aggregate, <2% bitumen)	Crushed Rock (excl. argillaceous) Crushed concrete	Crushed Rock or Gravel (<10% sedimentary Mudstone)[1]	Crushed Rock (0/31.5) or Gravel (0/40) (<10% sedimentary Mudstone)[1]	Crushed Rock or Gravel (<10% sedimentary Mudstone)[1]	Crushed Rock
	Mix Designation[2]	(0/75)[3]	(0/75)[3] Max=100mm	(0/125) Max=200mm	(0/31.5) Max=63mm	(4/40)	(0/31.5)
	Fines 63µm (%)	f_{10} 0 to 10%	f_{15} 0 to 15%	f_9 0 to 9%	f_7 0 to 7%	NR	f_7 0 to 7%
	Shape of coarse aggregate - Flakiness Index (FI)	-	-	-	-	-	35
Resistance to fragmentation (Durability)	Los Angeles Coefficient (LA)	50	50	30	30	30	30
	Slake Durability	95% (min)	95% (min)	-	-	-	-
Resistance to freeze thaw (Durability)	Magnesium sulphate soundness (MS)	-	-	MS_{25}	MS_{25}	MS_{25}	MS_{25}
	Water absorption (WA)[4]	-	-	$WA_{24}2$	$WA_{24}2$	$WA_{24}2$	$WA_{24}2$
Chemical requirements	Water Soluble Sulphate (WSS)[3]		1500mg/l SO_4		-		1500mg/l SO_4
	Oxidisable Sulphides (OS)		0.3% SO_4		-		0.3% SO_4
	Acid Soluble Sulfate (ASS)				$AS_{0.2}$		
	Total Sulfur (TS)	1.0%			0.1% (0.1 to 1.0%) require petrographical analysis		
Compaction	Permitted Compaction Method[5]	TII 600 table 6/4 - Method 6	End product (95% max dry density)	In accordance with I.S 888 – based on Table8/4 TII 800 series End production compaction can also be selected.			TII 800 table 8/4 - Method
	Optimum water content	Upper w_{opt} Specified by designer	Specified by designer				-2% of w_{opt} to w_{opt} w_L<20/21%[6]
Test Frequency		Set by designer in Appendix 1/5		Factory control min testing as per I.S. 13242 and S.R. 21 No destination testing (i.e. site testing) included			Set by designer in Appendix 1/5

1. Visual assessment by Professional geologist (S.R. 21 Annex E
2. Lower limiting sieve size (d) and upper limiting size sieve D demoted as d/D
3. Assumed values as TII based different grading limits
4. If water absorption is not greater than 2% then aggregate shall be assumed to be freeze –thaw resistant.
5. Table 8/4 of TII 800 series is similar to table 6/4 of TII series 600 method compaction 6.
6. TII 800series, Clause 804.2, material passing 0.425mm sieve, w_L<20 for limestone and 21% for other rock types and TII 800series, Clause 804.3

The influence of backfill strength and stiffness on the predicted behaviour of Geosynthetic Reinforced Soil – Integrated Bridge Systems (GRS-IBS)

Bahia S El Refai[1] and Dr. Patrick J Naughton[2]
[1]PhD Research Student, School of Engineering & Design, Atlantic Technological University Sligo, Ireland.
[2]School of Engineering & Design, Atlantic Technological University Sligo, Ireland.
email: bahiya.elrifai@mail.itsligo.ie, naughton.patrick@itsligo.ie

ABSTRACT: Geosynthetic Reinforced Soil – Integrated Bridge Systems (GRS-IBS) is an amalgamation of reinforced soil and integral bridge technology with the explicit aim of overcoming several inherent problems with conventional abutment arrangements. Unlike conventional integral abutment systems, GRS-IBS involves the placement of the bridge deck directly onto a reinforced soil structure, which is typically a segmental block wall, without the use of vertical piles or bridge bearings. The aim of this study was to investigate the behaviour of the GRS-IBS using the numerical model code Plaxis 2D. The Plaxis 2D model was validated against field measurements on both self-weight only reinforced soil segmental walls and GRS-IBS abutments reported in the literature. The influence of two properties of the backfill, namely the backfill stiffness and the angle of friction, on the performance of these systems through a parametric variation is presented in this paper. The horizontal deflection of the wall facing was found to be only modestly impacted by a reduction in the backfill stiffness, wall deflection only increased when the backfill stiffness reduced below 40MPa. The wall deflection was sensitive to angle of friction, increasing as the angle of friction reduced. Settlement of the bank seat was sensitive to both the backfill stiffness and angle of friction, increasing as both parameters reduced. The vertical stress under the bank seat remained constant for all values of backfill stiffness examined. However, the peak vertical stress did increase as angle of friction reduced. Reducing the backfill stiffness and angle of friction resulted in a significant increase in geogrid strain.

KEYWORDS: Geosynthetic Reinforced Soil–Integrated Bridge Systems; Backfill Strength; Soil Stiffness; Wall Displacement; Settlement; Strain in the Geogrids; Cyclic Horizontal Load.

1 INTRODUCTION

Geosynthetic Reinforced Soil – Integrated Bridge Systems (GRS-IBS) support a bridge deck directly on top of a reinforced soil structure without the need for piles or bridge bearings. Given the problems with conventional bridges containing joints and bearings, the concept of physically and structurally connecting the superstructure and abutment to create an integral bridge have become very popular, Figure 1(a) [1]. Integral bridges overcome the problems associated with traditional bridges with joints and bearings. However, because of the integral connection between the superstructure and the abutment, the abutments are forced to move away from the soil they retain when the temperature decreases (in winter) and the superstructure contracts and move towards the soil when the temperature rises and the superstructure expands (in summer), Figure 1(b) [2]. As a consequence, the soil behind the abutment is subjected to temperature-induced cyclic loading from the abutment which can generate much higher earth pressures than the structures are designed to take [2, 3].

A new solution evolved as an economical and faster way to construct a system that blends geosynthetic reinforced soil system (GRS) supporting a bridge superstructure without any joints. The Geosynthetic Reinforced Soil – Integral Bridge System, Figure 2, uses alternating layers of compacted granular fill and layers of geogrid reinforcement with a concrete block facing, rather than relying on a conventional bridge support system [4].

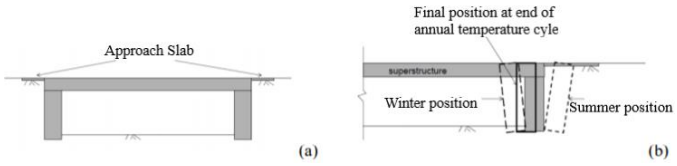

Figure 1. Schematic of (a) integral bridge[1], (b) movement of abutment [1].

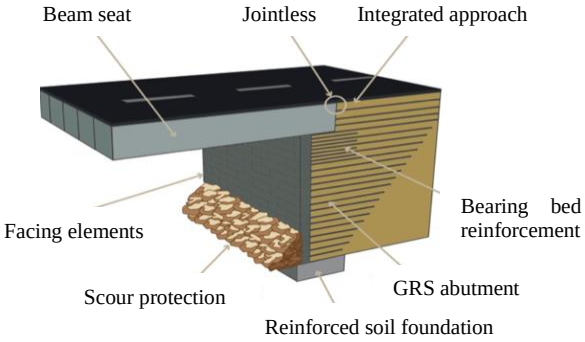

Figure 2. Section view of GRS-IBS abutment.

2 METHODOLOGY

A Plaxis 2D model was used to conduct a parametric study investigating the influence of backfill stiffness and backfill peak angle of friction had on the performance of an GRS-IBS abutment subject to both vertical and alternating horizontal load. The GRS-IBS abutment investigated consisted of a

reinforced soil segmental block wall with a bridge bank seat constructed directly on top.

The Plaxis 2D model was initially validated against data from a full-scale instrumented GRS wall and GRS-IBS abutment reported by Hatami & Bathurst [5] and Abu-Hejleh *et al.* [6] respectively, to ensure that the Plaxis 2D model would adequately capture the deformational response of a GRS-IBS system.

The model selection for the structural backfill, facing block and geosynthetic reinforcement in both the validation and parametric models were identical. The hardening soil model was used to represent the structural backfill, with a linear elastic model representing the concrete facing blocks. The geogrid reinforcement was represented by the geogrid element in Plaxis 2D.

Mesh, interfaces and boundary condition in both models were previously discussed by El Refai & Naughton [8].

2.1 GRS wall validation model and results

The full-scale instrumented GRS wall, consisted of a 3.6m high segmental block wall, with 0.15m high by 0.3m thick concrete facing blocks and a face batter of 8° from the vertical. The geogrid was installed at a vertical spacing of 0.6m (every fourth layer of facing blocks) starting at 0.3m above the base of the wall. In the validation model the geogrid was 2.3m long. The horizontal distance from the rear of the geogrids to the model boundary was nominally 5.8m.

The basic model parameters for the backfill (unit weight γ, plastic straining due to primary deviatoric loading ${E_{50}}^{ref}$, plastic straining due to compression ${E_{oed}}^{ref}$, elastic unloading/reloading ${E_{ur}}^{ref}$, peak angle of friction φ_p, dilatancy ψ and cohesion c) and the facing blocks (unit weight γ, Young's modulus ${E_{50}}^{ref}$, and Poisson's ratio, ν) are presented in Table 1. The structural backfill had a cohesion of 1kPa, to prevent premature soil yielding in locally confining pressure zones, and to take account of any possible apparent cohesion due to moisture in the soil [7, 8].

The geogrid was modelled using the geogrid element in Plaxis 2D, which is a linear elastic-perfect plastic planar element and had a stiffness, EA, of 2000kN/m corresponding to a polyester geogrid with an ultimate strength of approximately 200kN/m.

Table 1. Model parameters for GRS model validation by Hatami & Bathurst [5].

Material	γ (kN/m^3)	${E_{50}}^{ref}$ (MPa)	${E_{oed}}^{ref}$ (MPa)	${E_{ur}}^{ref}$ (MPa)
Backfill	22	50	28	100
Facing block	16	100	-	-

Material	ν	c (kPa)	φ_p (°)	ψ (°)
Backfill	0.15	1	44	11
Facing block	0.15	-	-	-

The predicted horizontal displacement of the wall in the validation model was in good agreement with the values reported by Hatami & Bathurst [5], Figure 3. The displacement started at the base of the wall and increased to a peak value at close to mid-height in the wall, before decreasing again towards the top of the wall.

The predicted axial strain in the reinforcement from this study during construction phase and the absence of any vertical or horizontal loads applied, was also in good agreement with the values reported by Hatami & Bathurst [5], Figure 4. The axial strain was found to reach a maximum value behind the block facing units and to decrease to zero at the end of the reinforcement. Based on the agreements shown between the trend and magnitude of predicted horizontal wall face displacement and axial reinforcement strain and that reported by Hatami & Bathurst [5] it was considered that the Plaxis 2D model was successfully validated.

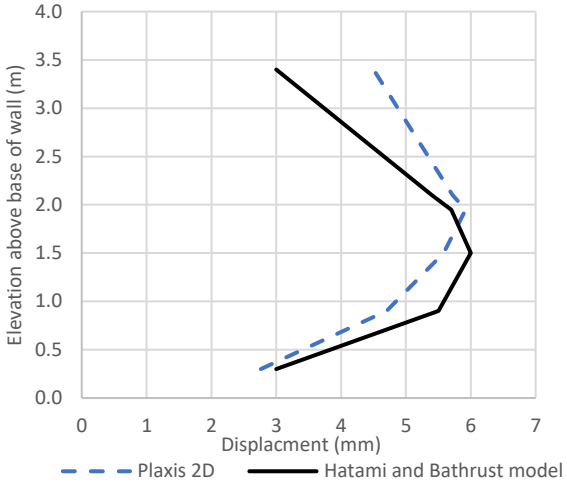

Figure 3. Predicted wall face displacement from this study and Hatami and Bathurst [5].

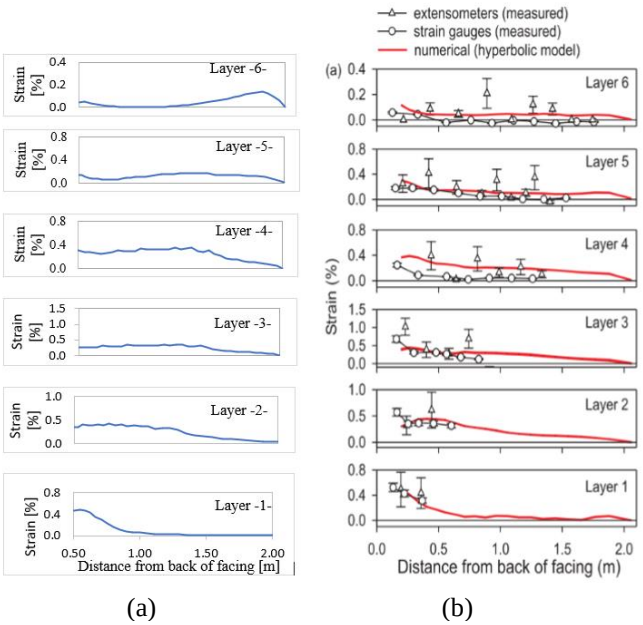

(a) (b)

Figure 4. Predicted axial strain from (a) this study and (b) Hatami and Bathurst [5].

2.2 *Founder/Meadows GRS-IBS abutment validation model and results*

The Founder/Meadows GRS-IBS abutment consisted of a 4.8 m height segmental wall with a face batter of 0° from the vertical. The boundary was located 14.8m from the rear of the geogrids. The vertical and horizontal restraints were applied to provide a limited soil mass to be calculated. The concrete facing blocks were 0.2m in height and 0.2m thick and supported on a steel plate at their base. The concrete facing blocks were represented by a linear–elastic model and the hardening soil model represented the backfill soil, Table 2. The geogrid was modelled using the geogrid element in Plaxis 2D, and had a stiffness, EA, of 2000kN/m.

Figure 6 presents a comparison of the predicted facing displacement from Plaxis 2D with the measured field values reported by Abu-Hejleh *et al.* [6]. The predicted displacement value of the horizontal facing from Plaxis 2D showed good agreement with the reported measured values after the construction of the structure and the placement of the bridge abutment at Section 400 and Section 800, Figure 5.

Based on the agreements shown between the predicted horizontal facing displacement from Plaxis 2D and that reported by Abu-Hejleh *et al.* [6], Figure 5, it was considered that the finite element model was validated.

Table 2. Model parameters for Founder/Meadows bridge validation model [6].

Material	γ (kN/m^3)	E_{50}^{ref} (MPa)	E_{oed}^{ref} (MPa)	E_{ur}^{ref} (MPa)
Backfill	22.1	50	28	100
Facing block	16	20	-	-

Material	ν	c (kPa)	φ_p (˚)	ψ (˚)
Backfill	0.15	1	39.5	6
Facing block	0.2	-	-	-

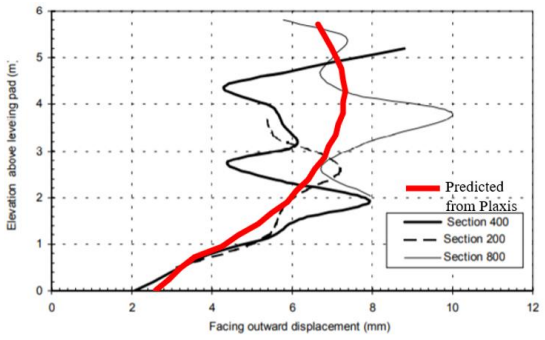

Figure 5. Comparison of facing displacement after the construction of the structure from this study with those reported by Abu-Hejleh *et al.* [6].

2.3 *Parametric study methodology*

The parametric model consisted of an 6m high segmental block wall, Figure 6. The facing blocks were 0.3m wide by 0.3m high and were installed to give a vertical face. The primary geosynthetic reinforcement was 7m long and installed at a vertical spacing of 0.6m (every fourth layer of facing blocks) starting at 0.3m above the base of the wall in addition to two layers of secondary geogrids of 5.8m length located at the top layer of the soil at 0.3m. The use of closer spaced reinforcement near the top of the wall is recommended by the FHWA [9]. The horizontal distance from the rear of the geogrids to the model boundary was nominally 15m. The front face of the abutment bank seat, which was 2m wide by 1.4m high, was located at 1.3m away from the back of the wall facing blocks.

The base line parametric model (Model PS-0) had the same backfill and block material properties as the GRS wall validation model, Table 1. The stiffness, EA, of the geogrid reinforcement was 1500kN/m, corresponding to a polyester geogrid with an ultimate strength of approximately 150kN/m. Four parametric models (Models PS-1 to PS-4) were analysed to assess the impact backfill stiffness and angle of friction had on the performance of GRS-IBS. Table 3 presents the magnitude of backfill stiffness and peak angle of friction used in each model. All other parameters remained constant during the parametric variation.

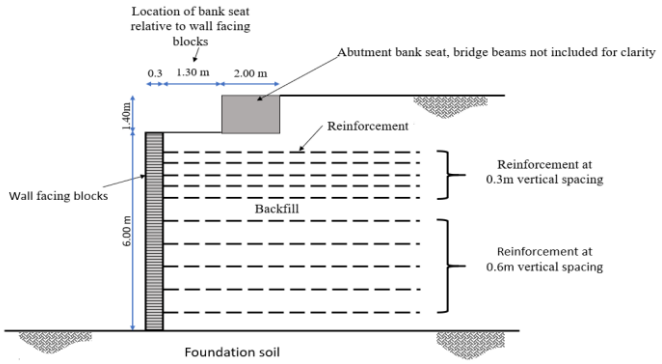

Figure 6. Schematic of GRS-IBS investigated in this study.

Table 3. Parametric variation of backfill stiffness and angle of friction in Models PS-1 to PS-4.

Model	E_{50}^{ref} (MPa)	φ_p (˚)
PS-1	40	44
PS-2	30	44
PS-3	50	36
PS-4	50	30

2.3.1 Construction of model

Each parametric model was constructed in phases within Plaxis 2D, with an analysis undertaken at each stage. The stages used in this study consisted of:

- Phase 1 consisted of modelling the GRS wall only, without the abutment bank seat or bridge loadings.
- Phase 2 added the abutment bank seat and backfill immediately behind the bank seat. The analysis of this stage modelled the impact of the self-weight of the bank seat and bridge beams only.
- Phase 3 applied the vertical self-weight of the bridge structure without any passing traffic to the bank seat.
- Phase 4 applied the horizontal load coming from the shrinkage and creep of concrete, which was applied in the direction towards the bridge abutment.

- Phase 5 applied the horizontal load from the temperature and braking force, both towards (inward) and away (outward) from the bridge abutment.
- Phase 6 applied the vertical and horizontal load from all elements, including the self-weight of the bridge, pavement and imposed dead loads.
- Phase 7 applied the vertical and horizontal load from all applied traffic loads, which was similar to phase 6 in addition to the load of the passing vehicles (LM1).
- Phase 8 and 10: repetition of phase 6.
- Phase 9: repetition of phase 7.

2.3.2 Calculation of the bridge loads

The vertical and horizontal loads used in this analysis are shown in Table 4, and were determined from the analysis of a single lane bridge deck, 15m long, supported on a 2m wide and 1.4m high bank seat and were previously discussed by El Refai & Naughton [8].

Load Model 1 (LM1) - tandem axle and general uniformly distributed case in accordance with the design standard for traffic loads on bridges [10] was used to calculate the vertical traffic loads on the bridge. The shrinkage, creep, temperature and braking force loads were calculated [11] for Irish conditions consisting of a temperature of 25ºC, an ambient temperature of 15ºC and a relative humidity of the ambient environment of 70%.

Table 4. Magnitude of loads used in the analysis.

Load	Self-weight	Variable traffic load	Traffic load LM1	Shrinkage
Vertical (kN)	185.3	31	72	0
Horizontal(kN)	123.4	36.6	10.5	-100
	Creep	Temperature		Braking force
Vertical (kN)	0	0		4.3
Horizontal(kN)	-44.2	±73.5		±23

3 RESULTS AND DISCUSSION OF PARAMETRIC VARIATION

The results from the five parametric models are discussed in the following sections in terms of the total wall face displacement, settlement under the bank seat and the vertical stress distribution under the bank seat. Model PS-4 had a peak angle of friction of 30° which resulted in numerical issues and failure of the model at Phase 6 when the vertical and horizontal load from all applied loads were activated.

3.1 Total wall face displacement

The pattern of total wall displacement during all phases for the five models investigated (PS-0 to PS-4) were similar. Figure 7 presents the total wall face displacement for Model PS-0. The magnitude of predicted total wall displacement changed when changing the soil stiffness parameter and the peak friction angle but the location of the maximum value remained the same in all models, Table 5. Where phase 9 showed the highest deformation at the top of the wall (19mm) and at the mid-height of the wall (31mm) due to the increased load from the traffic passing over the bridge.

No change occurred to the wall displacement when the stiffness of the backfill was reduced from 50MPa to 40MPa (Models PS-0 & PS-1), but an increase in the wall displacement of 3 mm at the mid height of the wall and 2mm at the top of the wall, occurred when the backfill stiffness was reduced from 50MPa to 30MPa (Models PS-0, & PS-2).

Reducing the peak friction angle of the backfill from 44◦ to 36◦ to 30◦ (Models PS-0, PS-3 & PS-4) respectively resulted in a significant increase in wall displacement. Going from a peak angle of friction of 44° to 36° increased the maximum wall displacement by 3mm and the top of the wall by 2mm. Model PS-4, where the peak angle of friction of 30° resulted in numerical issues and failure of the model at Phase 6 when the vertical and horizontal loads were activated.

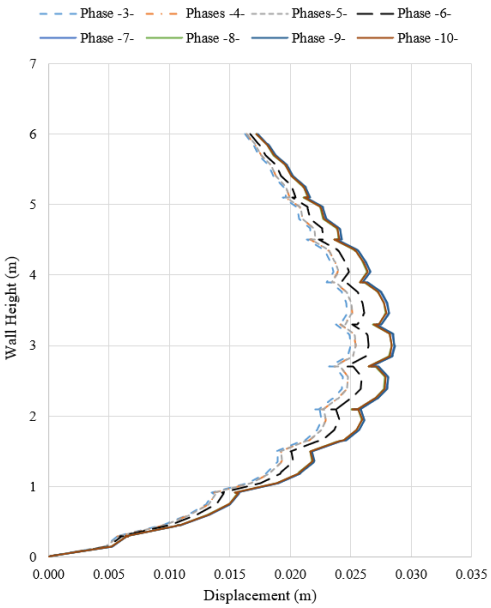

Figure 7. Typical wall displacement shape, Model PS-0.

Table 5. Wall displacement summary.

Model	Max. wall displacement (mm)	Location of max. wall displacement (m)	Top wall displacement (mm)
PS-0	28	3.00	17
PS-1	28	3.00	17
PS-2	31	3.00	19
PS-3	40	3.00	23
PS-4	Failed at Phase 6		

3.2 Settlement of the abutment bank seat

The pattern of the settlement under the bank seat was similar in all models, Models PS-0 to PS-3. Application of the bridge vertical loads to the bank seat, Phase 3, resulted in rotation of the bank seat away from the abutment, resulting in greater vertical settlement at the front of the bank seat (Point B, Figure 8). This rotation was permanent and was not altered by the subsequent application of horizontal loads in later phases, Figure 8.

The magnitude of the predicted settlement under the bank seat changed with soil stiffness, increasing as the soil stiffness reduced, Models PS-0 to PS- 2, and also increased as the peak angle of friction reduced, Models PS-0 & PS-3, Table 6. The

location of the maximum (Point B) and minimum (Point A) settlements remained the same for all models, Table 6. Table 6 showed that the highest settlement of both corners of the bank seat occurred at phase 9, when traffic load was included in the model.

No change in the magnitude of settlement underneath the bank seat was observed when the stiffness of the backfill was reduced from 50MPa to 40MPa (Models PS-0 & PS-1). However, reducing the stiffness from 50 to 30 MPa (Models PS-0 and PS-2) increased the settlement uniformly along the base by 3mm.

Reducing the peak angle of friction from 44˚ to 36˚, Models PS-0 & PS-3 respectively, resulted in a uniform increase of 7mm in the settlement of the bank seat.

3.3 Vertical stress under the abutment bank seat

The pattern of the vertical stress under the bank seat was similar in all models examined. Figure 9 presents the stress distribution directly under the bank seat for Model PS-0 and is representative of all the models examined. A maximum stress was observed at the front bottom corner of the bank seat, Point B, with a lower peak stress under the bottom rear corner of the bank seat, Point A. The minimum stress under the bank seat occurred at approximately the centre line of the bank seat. The highest vertical stresses on both corners reached a maximum during phase 9 where the applied load was higher due to the traffic passing on the bridge, Table 7.

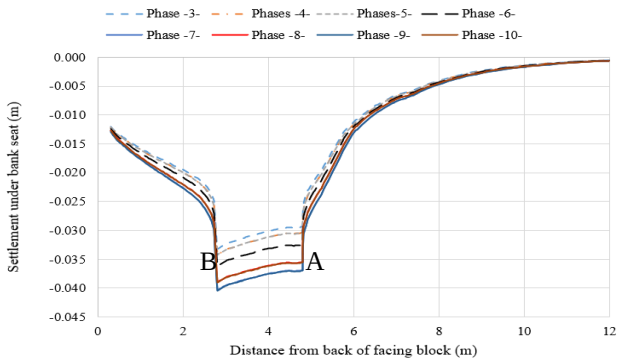

Figure 8. Settlement under the bank seat pattern Model PS-0.

Table 6. Settlement of the abutment bank seat in all models.

Model	Point A, bottom rear corner of bank seat (m)	Point B, bottom front corner of bank seat (m)
PS-0	-0.037	-0.041
PS-1	-0.037	-0.041
PS-2	-0.040	-0.044
PS-3	-0.044	-0.048
PS-4	Failed at Phase 6	

No change occurred in the peak vertical stresses under the bank seat at Points A and B when the stiffness of the backfill was reduced from 50MPa to 40MPa, Models PS-0 & PS-1. A slight change in the peak stress beneath the bank seat of approximately 5% was observed at both Points A and B when the soil stiffness was reduced from 50MPa to 30MPa, Models PS-0 and PS-2.

Reducing the peak friction angle of the backfill from 44˚ to 36˚, Models PS-0 & PS-3 respectively, resulted in a slight increase in the vertical stresses under the rear bottom corner, Point A, and a decrease at the front bottom corner, Point B. While reducing the peak friction angle to 30˚ (PS-4) resulted in a failure of the wall during phase 6.

3.4 Strain in the Geogrids

Figure 10 presents the strain in the geogrid for model PS-0. The tension in the reinforcement was directly related to the strain, through the stiffness of the reinforcement. The line of maximum tension (corresponding to maximum strain in the geogrid) is also shown in Figure 10. In all phases, the line of maximum tension was approximately log spiral in shape and originated, at or close to the bottom-rear corner of the bank seat. It was observed that the strain in the geogrids reached 50% of its peak value after Phase 2, when the abutment bank seat and backfill immediately behind the bank seat were added to the structure.

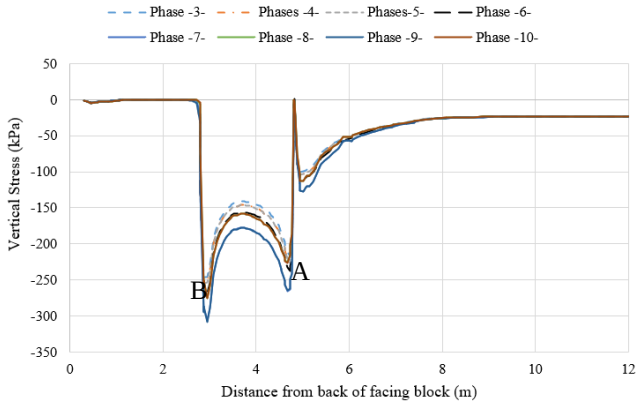

Figure 9. Vertical stress distribution under the bank seat, Model PS-0.

Table 7. Vertical stresses under the bank seat in all models.

Model	A, bottom rear corner of bank seat (kPa)	B, bottom front corner of bank seat (kPa)
PS-0	264.51	307.93
PS-1	265.90	307.93
PS-2	267.51	296.45
PS-3	229.49	323.93
PS-4	Failed at Phase 6	

The double peaks observed in geogrid layers 9 and 10 are associated with the stress distribution on the underside of the bank seat. Peak stresses were observed at the bottom rear and bottom front corners of the bank seat. Double peaks were only observed in the upper most layers as further down the wall the stresses were redistributed through the backfill.

The maximum predicted strain in model PS-0 did not exceed 1% and reached a maximum value in Layer 3 (0.56%) during Phase 9 when the load was the highest. The magnitude of strain varied both along each geogrid layer and its magnitude was also dependent on its location in the structure, Table 8.

Reducing the backfill stiffness from 50MPa to 40MPa (Models PS-0 & PS-1), caused the maximum strain to again occur in Layer 3 during Phase 9. The magnitude of strain increased from 0.56% to 0.76%. Reducing the soil stiffness further to 30MPa (PS-2), also resulted in a further increase in

the strain in the geogrids, reaching a maximum in layer 7 (0.79%) during phase 9, Table 8.

While reducing the peak friction angle of the backfill from 44° to 36°, Models PS-0 & PS-3 respectively, resulted in a significant increase in strain, reaching a maximum in layer 3 of 1.1% during phase 9, Table 8.

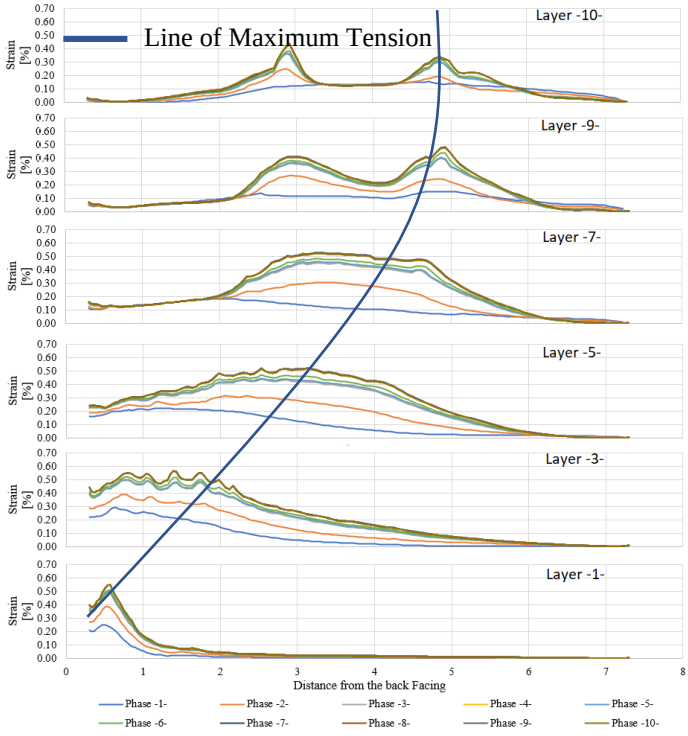

Figure 10. Axial Strain, Model PS-0.

Table 8. Strain in geogrid layers.

Model	Layer -1-	Layer -3-	Layer -5-	Layer -7-	Layer -9-	Layer -10-
PS-0	0.549	0.557	0.513	0.518	0.479	0.434
PS-1	0.680	0.756	0.688	0.705	0.649	0.579
PS-2	0.740	0.747	0.751	0.782	0.654	0.624
PS-3	0.953	1.08	0.993	0.992	0.812	0.868
PS-4	Failed at Phase 6					

4 CONCLUSIONS

Plaxis 2D was used to predict the response of a GRS-IBS abutment under a constant vertical load and cyclic inward and outward horizontal load.

When the soil stiffness was reduced from 50MPa to 40MPa (PS-0 and PS-1) no significant changes occurred, however when reducing the value to 30MPa (PS-2) a very slight increase in the wall deformation occurred. It should be noted that a soil stiffness of 30 MPa is at the lower end of backfill stiffness. However, the presence of geogrid layers in the soil mass will increase the overall stiffness of the reinforced backfill [12]. The stiffness could be measured with laboratory testing using triaxial test or oedometer test.

When the peak friction angle was reduced from 44° to 36° (PS-0 and PS-3) a significant increase in the wall deformation occurred, while reducing the value furthermore to 30° (PS-4) resulted in a failure of the wall at phase 6 where the vertical and horizontal loads were applied to the abutment. It should be noted that the peak angle of friction for such systems would typically be greater or equal to 38° [9].

When the soil stiffness of the backfill was reduced from 50MPa to 40MPa, (Models PS-0 and PS-1), no significant change was observed in the settlement of the bank seat. However, when reducing the stiffness of the backfill further to 30MPa (PS-2) a very slight increase in the settlement occurred. When reducing the peak friction angle from 44° to 36° (Models PS-0 and PS-3), a significant increase in settlement occurred, while reducing the value further to 30° (PS-4), resulted in failure of the wall at Phase 6 where the vertical and horizontal loads were applied to the abutment.

When reducing the soil stiffness from 50MPa to 40MPa and then to 30MPa, (Models PS-0, PS-1 and PS-2) no significant change occurred to the vertical stresses under the front and rear corner of the bank seat, which indicated that changing the soil stiffness does not have any significant impact on the vertical stress under the bank seat.

When reducing the peak friction angle from 44° to 36° (PS-0 and PS-3) a slight increase occurred in the vertical stress under the rear front corner of the bank seat and a significant decrease occurred to the vertical stress under the front bottom corner of the bank seat. Reducing the value of peak friction angle further to 30° (PS-4) resulted in failure of the wall at phase 6 where the vertical and horizontal loads were applied to the abutment at rest.

When reducing the soil stiffness from 50MPa to 40MPa and then to 30MPa, (Models PS-0, PS-1 and PS-2) a significant increase occurred in the predicted geogrid strains.

Reducing the peak friction angle from 44° to 36° (PS-0 and PS-3) resulted in a significant increase in geogrid strain was observed and the maximum strain exceeded 1%.

REFERENCES

[1] D.R. Carder, and G. B. Card, 1997. "Innovative Structural Backfills to Integral Bridge Abutments", Proj. Rpt. 290, Trans. Res. Lab., U.K.

[2] J. S. Horvath, "Integral-abutment bridges: problems and innovative solutions using EPS geofoam and other geosynthetics," Res. Rpt. No. CE/GE-00, vol. 2, 2000.

[3] F. Tatsuoka *et al.*, "Stability of existing bridges improved by structural integration and nailing," *Soils Found.*, vol. 52, no. 3, pp. 430–448, 2012.

[4] M. Adams, J. Nicks, T. Stabile, J. T. H. Wu, W. Schlatter, and J. Hartmann, "Geosynthetic reinforced soil integrated bridge system, synthesis report," United States. Federal Highway Administration, 2011.

[5] K. Hatami and R. J. Bathurst, "Development and verification of a numerical model for the analysis of geosynthethic-reinforced soil segmental walls under working stress conditions," *Can. Geotech. J.*, 2005.

[6] N. Abu-Hejleh., T. Wang, and J.B. Zornberg, 2000. Performance of geosynthetic-reinforced walls supporting bridge and approaching roadway structures. In *Advances in transportation and geoenvironmental systems using geosynthetics* (pp. 218-243).

[7] T. Gouw, "International conference," *J. Soc. Arch.*, vol. 7, no. 5, pp. 341–342, 2018, doi: 10.1080/00379818409514249.

[8] B.S. El Refai and P.J. Naughton, "Numerical modelling of a Geosynthetic Reinforced Soil – Integrated Bridge Systems (GRS-IBS) abutment subject to bridge loads" *Proceeding CERI Conference*, 2020.

[9] M. Adams, J. Nicks, T. Stabile, W. Schlatter, and J. Hartmann, "Geosynthetic reinforced soil integrated bridge system, interim implementation guide," Federal Highway Administration, 2012.

[10] EN 1991-2: (2003) +NA (2009), *Eurocode 1: Actions on structures - Part 2: Traffic loads on bridges*, National Standards Association of Ireland.

[11] EN 1992-2 (2005). *Eurocode 2: Design of concrete structures - Part 2: Concrete bridges - Design and detailing rules*, National Standards Association of Ireland.

[12] P. Vennapusa, D. White, W. Klaiber and S. Wang, 2012. *Geosynthetic reinforced soil for low-volume bridge abutments* (No. IHRB Project TR-621). Iowa State University.

The influence of horizontal load on the predicted behaviour of Geosynthetic Reinforced Soil – Integrated Bridge Systems (GRS-IBS)

D. Naughton[1], P.J. Naughton[2]
[1]Faculty of Engineering & Design, Atlantic Technological University Sligo, Ireland & RPS Consulting Engineers, Galway
[2]Faculty of Engineering & Design, Atlantic Technological University Sligo, Ireland
email: daniel.naughton@rpsgroup.com, naughton.patrick@itsligo.ie

ABSTRACT: Geosynthetic reinforced soil – integral bridge systems (GRS-IBS) are an alternative method for constructing integral bridges. In GRS-IBS the bridge beams are placed directly on top of a reinforced soil structure, typically a segmental block wall. The reinforced soil structure must accommodate the vertical and horizontal loads from the bridge deck. In this study, the results of a numerical analysis using PLAXIS investigating the influence of vertical and horizontal load on the deformational response of a GRS-IBS abutment are presented. A parametric variation of backfill angle of friction and backfill stiffness was also conducted. It was found that the application of the vertical load only resulted in settlement and rotation of the bank seat. Application of a horizontal load, either towards or away from the abutment, only marginally increased the magnitude of settlement and rotation of the bank seat. The face of the GRS-IBS abutment moved outward under the vertical load. Subsequent application of a horizontal load resulted in deformation of the wall face in the direction of the horizontal load. An outward horizontal load increased outward wall deformation, while an inward horizontal load reduced the deformation of the wall. Angle of friction was found to have a significant impact on the deformational response of the wall. Angles of friction of 30o or less resulted in both large settlement and rotation of the bank seat and deformation of the wall face. The stiffness of the backfill, overall, had only a marginal impact on the deformational response of the wall. Settlement and rotation of the bank seat were dominated by the application of the vertical load rather than the horizontal load, while a horizontal load applied away from the abutment significantly increased the outward wall deflection.

KEY WORDS: Integral Bridges; Geosynthetic reinforced soil; GRS-IBS; Geogrid; Horizontal Load; Angle of friction; Backfill stiffness.

1 INTRODUCTION

An integral bridge is a continuous geo-structural system initially developed to overcome some of the problems associated with conventional bridges, that is, bridges with expansion joints and bearings [1]. Conventional bridges require periodic maintenance resulting in increased cost and the possibility of extended road closures [2]. However, although they are cheaper and faster to construct, and require less maintenance, integral bridges come with their own problems [3]. As the structure moves as one unit, temperature fluctuations result in increased earth pressures on the face of the abutment and settlement over time of the soil at the abutment-embankment interface. In winter, when temperatures decrease, the superstructure contracts and moves away from the structure, while in summer, when temperatures increase, the superstructure expands and moves towards the soil. This phenomenon of cyclic temperature induced creep, otherwise known as strain ratchetting, can result in much higher earth pressures than the structure was design to take [4].

An alternative to the traditional integral bridge is the geosynthetic reinforced soil – integral bridge system (GRS-IBS). This system is constructed using alternating layers of compacted granular fill and geosynthetic reinforcement, typically in the form of a geogrid. Many GRS-IBS abutments consist of a segmental modular block wall with the bridge beams resting directly on top of the structure. No bearing or bank seat is required [5].

This research project investigated a GRS-IBS bridge abutment to assess the impact horizontal load and the result strain ratchetting had on the performance of these structures. A parametric variation of backfill angle of friction and backfill stiffness was conducted in PLAXIS. The performance was assessed in terms of the horizontal displacement of the modular block wall and vertical settlement under the bank seat.

2 METHODOLOGY

Plain-strain modelling using PLAXIS software was used to determine the influence backfill angle of friction and backfill stiffness had on the deformational response of a GRS-IBS abutment.

2.1 GRS-IBS abutment validation model and results

Ardah at al. [6, 7] reported monitoring data for the fully instrumented Maree Michel Bridge located on Route LA 91 in Vermilion Parish, Louisiana. The Maree Michel Bridge was the first GRS-IBS to be constructed on footings supported directly by a geosynthetic reinforced soil system [6]. This type of system eliminates the need for deep foundations. The Maree Michel Bridge was a steel girder bridge with a span of 19.8m and a superstructure width of 9.1m. Abutments on the Maree Michel Bridge had a width of 13m and a maximum height of 4.8m from the bottom of the reinforced soil foundation (RSF) to the road pavement. The bridge was instrumented to measure the vertical and horizontal deformations, settlement, the distribution of stress in the GRS-IBS abutments and reinforced

soil foundation, and the strain distribution along the geosynthetic reinforcement [6].

The numerical model developed in this study consisted of 19 segmental blocks forming the abutment wall. The masonry blocks measured 400mm wide x 200mm high.

Geogrid reinforcement was placed between each of the segmental blocks, with secondary reinforcement introduced for the top six blocks, Figure 1. The segmental blocks were set vertically above a reinforced soil foundation, which had a width of 2.83m and was 0.46m deep. Undisturbed foundation soil was present beneath the RSF, with backfill soil extending 9.20m from the back face of the segmental block wall. The water table was not considered during the modelling process.

The soil elements of the PLAXIS model were developed using a plain-strain model with 15-node triangular elements. The model was horizontally fixed in the X-direction, fully fixed in the Y_{min} direction and free in the Y_{max} direction. Additionally, a line displacement was introduced along the lower boundary of the lowest block. This allowed the block to be fixed in place or free to move at the authors discretion. The Hardening Soil Model was used for the backfill soil, the Mohr-Coulomb for the foundation soil and the linear elastic model for the masonry blocks and rip rap at the front of the wall. The model properties are listed in Tables 1 – 3.

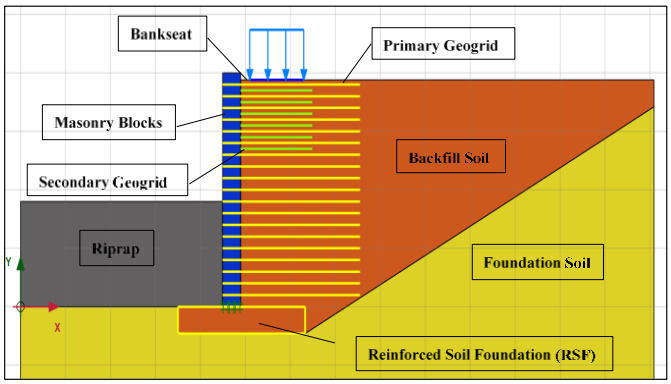

Figure 1. Schematic of validation model used in this study.

Table 1. Backfill model parameters for GRS-IBS validation model [6, 7].

$\gamma_{unsaturated}$ (kN/m^3)	$\gamma_{saturated}$ (kN/m^3)	E_{50}^{ref} (MPa)	E_{oed}^{ref} (MPa)	E_{ur}^{ref} (MPa)	$e_{initial}$
18	19	34	25.59	103.2	0.5
m	ν	c (kPa)	φ_p (°)	ψ (°)	
0.5	0.2	20	51	21	

Geogrid elements with an elastoplastic failure criterion represented the geogrid. The geogrids had an elastic normal stiffness, EA, of 600kN/m and an axial tension, NP, of 80kN/m.

A medium mesh was used for the models in this study. A tolerated error of 1% was used for all the models during the validation process. In contrast to Ardah at al. [6, 7] the wall was wished-in-place.

Figures 2 & 3 show the correlation between the measured wall deformations at the end of abutment construction and end of bridge construction respectively from this study and that reported by Ardah et al. [6, 7]. Overall, reasonable agreement was found between the measured values and those predicted by PLAXIS. During validation it was found that fixing the lowest masonry block in both the x and y directions, greatly improved the overall correlation with the validation model, but did result in an underestimation of the horizontal deformation at the bottom of the wall.

Table 2. Masonry block, foundation soil and rip-rap model parameters for GRS-IBS validation model [6, 7].

Material	$\gamma_{unsaturated}$ (kN/m^3)	$\gamma_{saturated}$ (kN/m^3)	E (MPa)	ν
Masonry blocks	12.5	12.5	30000	0
Foundation soil	15.2	18.65	30	0.2
Rip - rap	22	22	50	0.25
Material	$e_{initial}$	c (kPa)	φ_p (°)	ψ (°)
Masonry blocks	0.5	-	-	-
Foundation soil	0.5	17.7	27	0
Rip - rap	0.5	-	-	-

Table 3. Model interface parameters for GRS-IBS validation model [5, 6].

Interface	c (kPa)	φ_p (◦)	ψ (◦)
Backfill - geogrid	8.6	40.4	0
Masonry block - geogrid	7	34	0

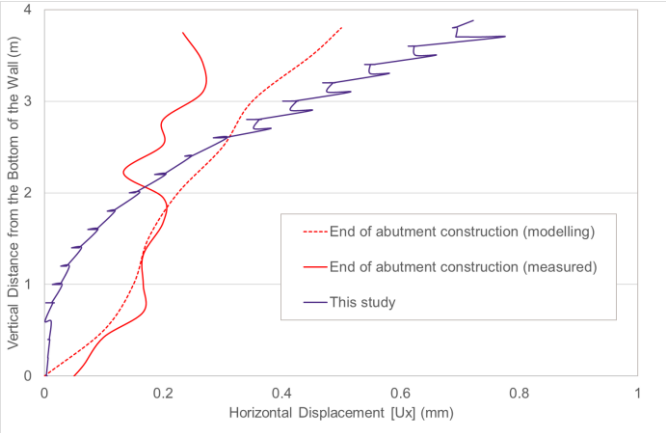

Figure 2. Comparison between measured wall deformations at the end of abutment construction from Ardah et al. [6, 7] and the predicted displacement from this study.

2.2 *Parametric study*

A parametric study was conducted to assess the impact the backfill angle of friction and backfill stiffness had on the deformational response of a GRS-IBS abutment subject to both vertical and horizontal loading.

The geometry of the Maree Michel Bridge [6, 7] used in the validation modelling was used as the baseline model for the parametric variation. The baseline model parameters are those reported in Tables 1 – 3. The range of varied parameters are outlined in Table 4. The bridge load consisted of a vertical component of 100kN/m and a horizontal component of 85kN/m, determined in accordance with IS EN 1991-2 [8] using Load Model 1 (LM1).

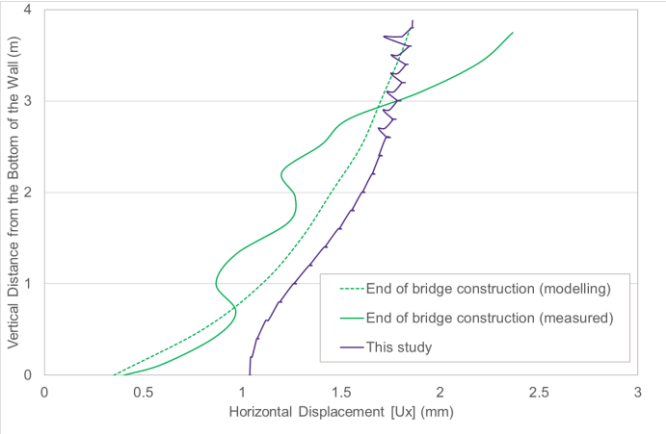

Figure 3. Comparison between measured wall deformation at the end of bridge construction from Ardah et al. [5, 6] and the predicted displacement from this study.

In this study the impact of the direction of the horizontal load was investigated. The horizontal load was first applied in one and then in the opposite direction at the location of the bank seat at the top of the wall. Two cases were examined, applying the load firstly towards the abutment and then away from the abutment, Case A, and secondly the reverse, with the horizontal load first applied away from the abutment and then towards the abutment, Case B. Vertical load was applied simultaneously in each case. Cases A and B represent completing construction of the structure in summer and winter respectively.

Table 4. Range of parametric variation.

Parameter	Values examined
φ_p (°)	27, 30, 35, 40, 45, 55
E_{50}^{ref} (MPa)	50, 75, 100, 125

3 RESULTS AND DISCUSSION

3.1 Impact of angle of friction on deformational response

Figures 4 & 5 present the horizontal displacement of the wall and vertical settlement of the bank seat under the vertical load only. The wall deflected outward with the maximum displacement at the top of the wall for all angles of friction, reducing proportional to elevation to zero at the toe, Figure 4. The magnitude of horizontal displacement was generally consistent for angles of friction greater than 30°, with maximum displacement in a narrow band between 0.8mm and 1.25mm. There was a step change increase in the magnitude of displacement once the angle of friction was 30° or lower, with the maximum displacement of 2.5mm, approximately double that predicted for angle of friction greater than 30°.

The base of the bank seat rotated clockwise, towards the bridge, under the vertical load as a result of the outward movement of the wall, Figure 5. The displacement of the bank seat was again consistent for angles of friction greater than 30°. A step change in the rotation and settlement of the bank seat was again observed once the angle of friction was 30° or lower. For all angles of friction examined, the horizontal outward displacement of the wall was linked to the rotation of the bank seat. For angles of friction less than 30°, the maximum outward movement was accommodated by the greatest rotation of the bank seat, while an angle of friction of 55° had both the small outward displacement and vertical settlement under the bank seat.

Figures 6 & 7 show the deformational response of the abutment for Cases A and B respectively. For Case A when the horizontal load was first applied towards the abutment and then away from the abutment, Figure 6, the greatest displacement of the wall facing was again observed at the top of the wall. With the horizontal load applied towards the abutment, the modular wall moved inwards in the same direction as the applied load, with the higher angles of friction (>30°) backfill experiencing the greatest deformation. When the direction of horizontal load was reversed, significant outward movement of the wall face occurred, with the movement generally inversely proportional to the angle of friction, with higher angles of friction resulting in smaller horizontal deformations. Once again, a step change in deformational response was noted when the angle of friction was 30° or lower.

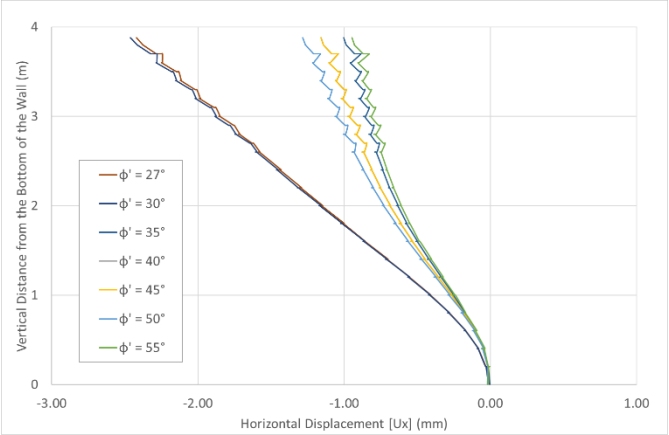

Figure 4. Predicted horizontal deformation under vertical only load.

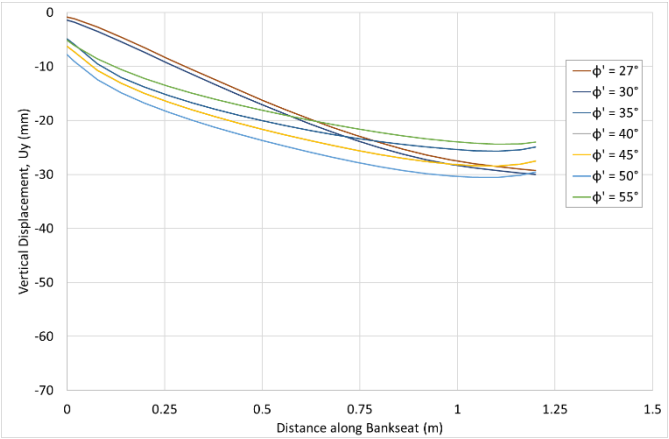

Figure 5. Predicted vertical deformation under vertical only load.

For Case B, Figure 7, when the horizontal load was first applied outward and then inwards towards the abutment, significant outward displacement of the wall was observed, with maximum displacement again occurring at the top of the wall. Reversing the direction of the horizontal load resulted in displacement of the wall towards the abutment. Three responses were noted, for angles of friction less than or equal to 30° the wall did not return to its original vertical position but retained a residual outward

movement. For angles of friction between 30º and 50º the wall almost returned to its original vertical position. For an angle of friction of 55º the wall facing deflected into the abutment.

The application of the vertical load only, Figure 5, resulted in rotation and settlement of the bank seat. Subsequent application of a horizontal load, either Case A or B, resulted in only a further slight increase in settlement and rotation of the bank seat, for angles of friction over 30º, Figure 8. For angles of friction of 30º or less, further significant settlement and rotation of the bank seat was observed. This was in keeping with the large horizontal face displacement observed for this fill.

The deformational response of the wall was dominated by the application of the initial vertical load, Figure 5. This load instigated the initial outward deformation of the wall face and clockwise rotation of the bank seat, Figure 6. Subsequent application of the horizontal load either increased these movements, for outward horizontal load, or reduced them, for inward horizontal load.

For angles of friction of 30º or less, further significant settlement and rotation of the bank seat was observed. This was in keeping with the large horizontal face displacement observed for this fill.

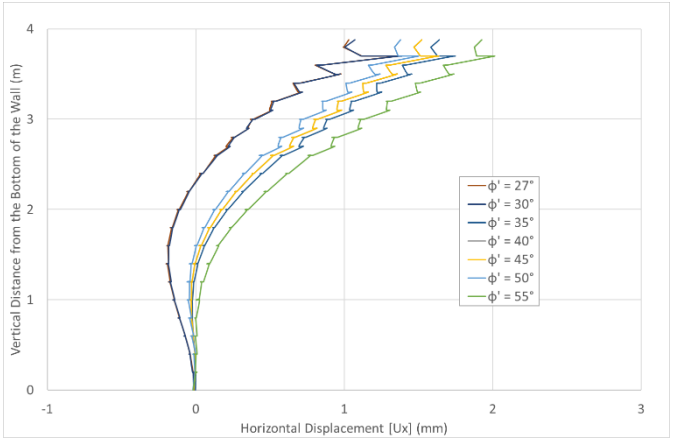

(a)

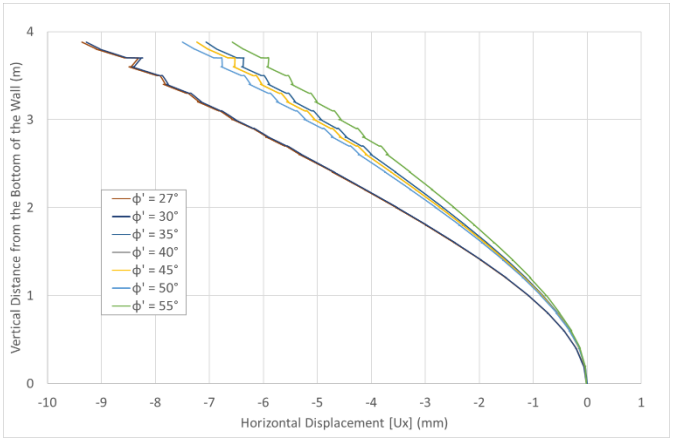

(b)

Figure 6. Predicted horizontal deformation for Case A under vertical load and with the horizontal load applied (a) firstly towards and (b) then away from the abutment.

The direction that the horizontal load was first applied had a marginal impact on the horizontal wall displacement and settlement and rotation of the bank seat. For lower angles of friction, 30º or lower, the impact of horizontal load was significant, with greater wall displacement and rotation and settlement of the bank seat observed. For angles of friction greater then 30º the overall response was similar irrespective of horizontal load application.

Overall, the backfill angle of friction should be greater than 30º to reduce the horizontal deformation of the wall and settlement and rotation of the bank seat.

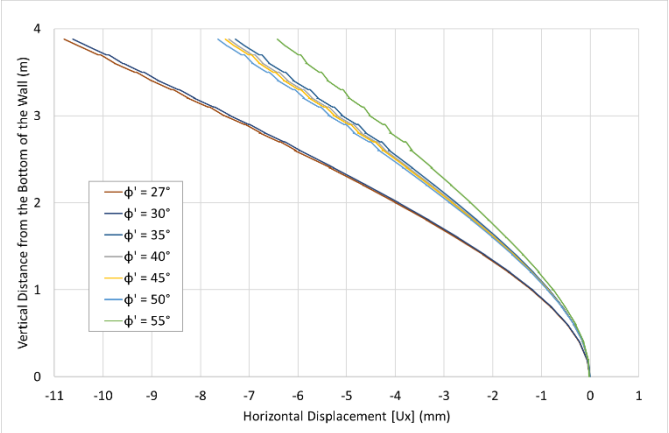

(a)

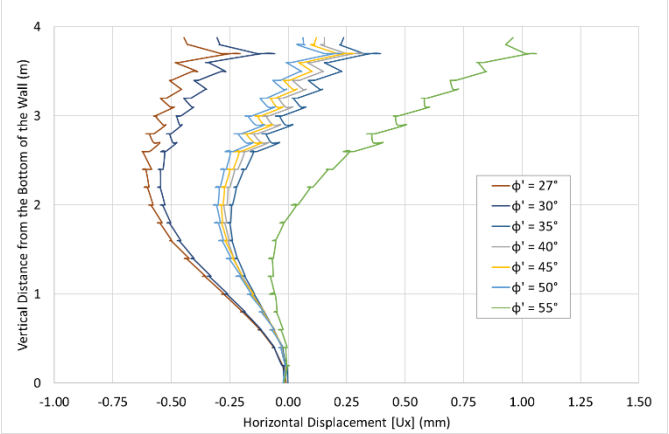

(b)

Figure 7. Predicted horizontal deformation for Case B under vertical load and with the horizontal load applied (a) firstly away and (b) then towards the abutment.

3.2 Impact of backfill stiffness on deformational response

The predicted horizontal deformation of the modular wall under vertical load only, for various backfill stiffness, is shown in Figure 9. The deformational response was nonlinear, with the greatest deformation occurring at the top of the wall. The predicted horizontal deformation increased marginally with increased backfill stiffness, although all predicted values were in a very narrow range, between 0.6mm and 0.8mm. The predicted vertical deformation of the bank seat is presented in Figure 10, with increased vertical deformation as the backfill stiffness reduced. In all cases the bank seat rotated clockwise towards the bridge. The predicted horizontal displacement of

the wall and the settlement of the bank seat were inversely related, as the stiffness of the backfill increased, the outward horizontal displacement of the wall increased, marginally, but the settlement of the bank seat reduced.

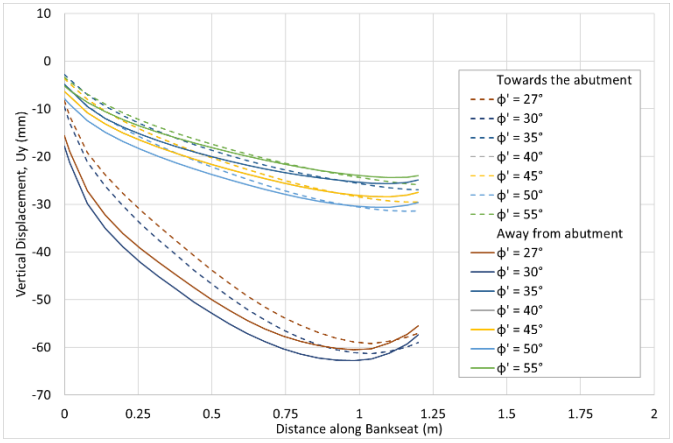

Figure 8. Predicted vertical deformation for Case A when the horizontal load was applied towards the abutment.

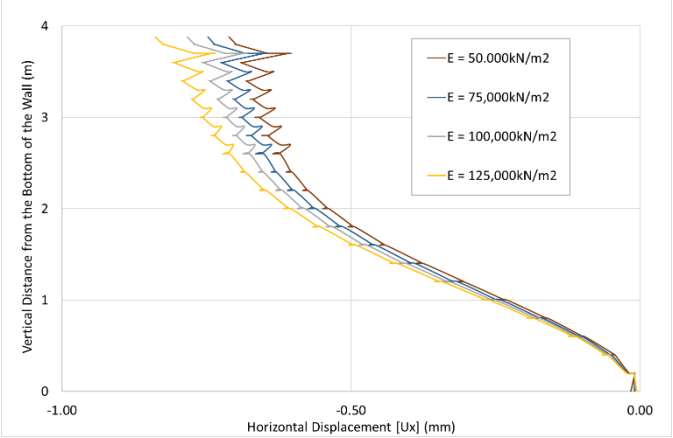

Figure 9. Predicted horizontal deformation under vertical load only.

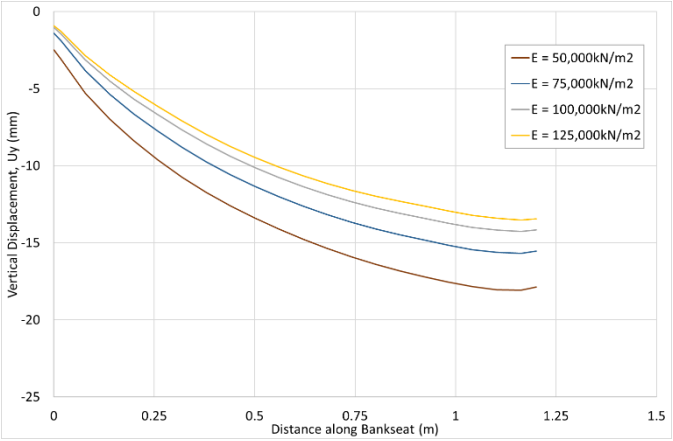

Figure 10. Predicted vertical deformation under vertical load only.

The application of the horizontal load, in both Case A and B resulted in a similar overall deformational response of the wall, with the wall deformation occurring in the direction of the applied horizontal load, Figures 11 & 12. The maximum deformation occurred at the top of the wall.

When the horizontal load was applied away from the abutment in either Case A or B, the deformational response was similar and independent of back fill stiffness, Figure 11(b) & Figure 12(a). In Case A, applying an outward horizontal load, resulted in inward movement of the wall towards the abutment. However, in Case B, when the inward horizontal load was applied after the outward load, the wall did not return to its original position and retained some residual outward movement when E > 100MPa.

Figure 13 presents the vertical settlement under the bank seat for the backfill stiffnesses examined. Once the vertical only load was applied vertical settlement and rotation of the bank seat clockwise towards the bridge was observed. Subsequent application of a horizontal load, either towards or away from the abutment resulted in only small additional settlements and rotation of the bank seat, Figure 13.

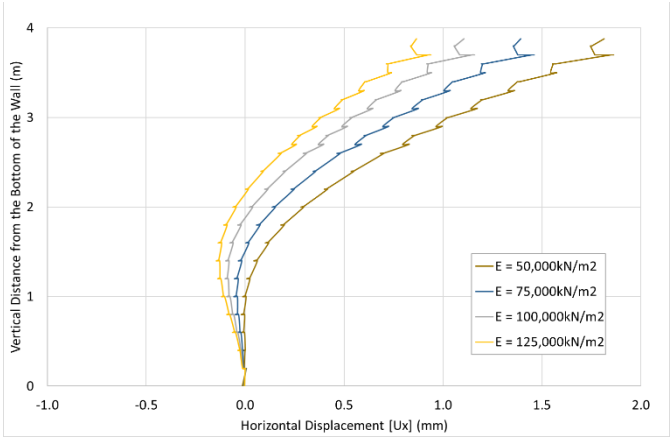

(a)

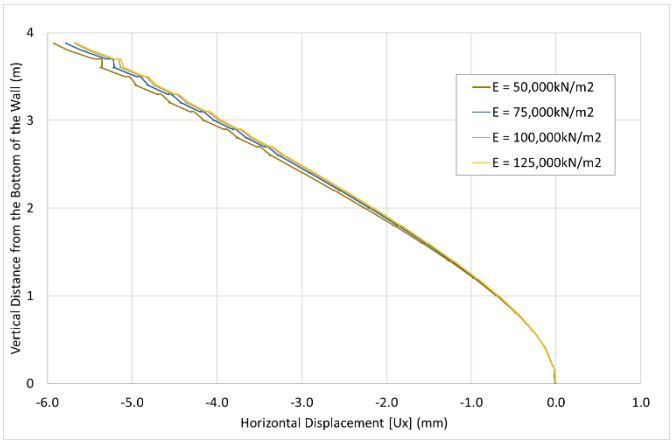

(b)

Figure 11. Predicted horizontal deformation for Case A under vertical load and with the horizontal load applied (a) firstly away and (b) then towards the abutment.

Overall, the stiffness of the backfill had only a slight impact on the outward deformation and settlement and rotation of the bank seat. The greatest impact of the backfill stiffness was on the wall deformation when the horizontal load was applied toward the abutment in both Case A and B. The higher stiffness

backfills reduced the magnitude of overall deformation of the wall towards the abutment.

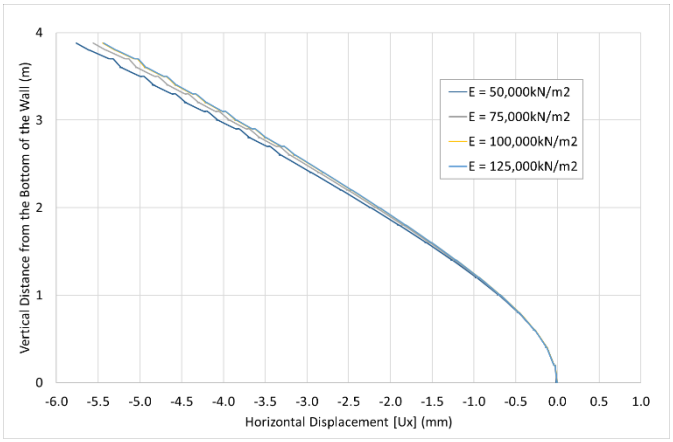

(a)

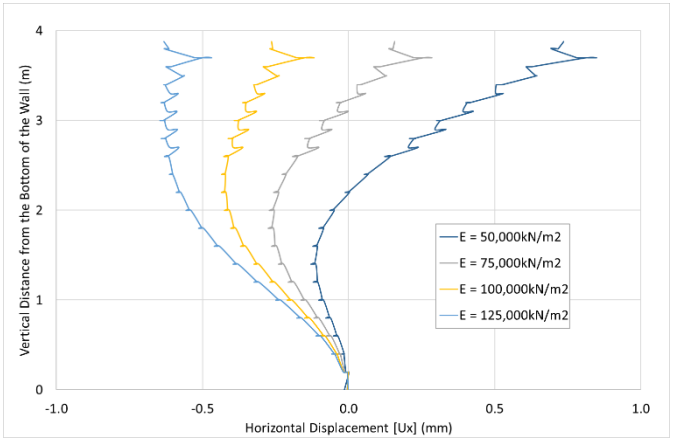

(b)

Figure 12. Predicted horizontal deformation for Case B under vertical load and with the horizontal load applied (a) firstly towards and (b) then away from the abutment.

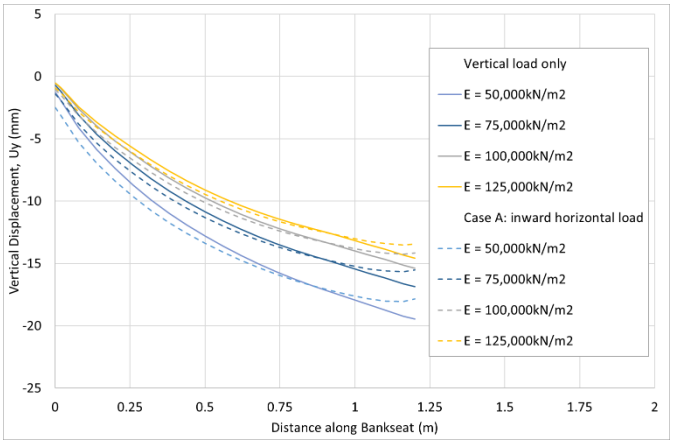

Figure 13. Predicted vertical deformation for vertical load only and for Case A inward horizontal load for different backfill stiffnesses.

4 CONCLUSIONS

A numerical study was presented that assessed the impact angle of friction and backfill stiffness had on the deformational response of a GRS-IBS abutment subject to vertical and horizontal load.

The numerical model developed in this study was validated against an instrumented wall [6, 7] and, overall, the predicted horizontal wall displacement showed reasonable agreement with the measured values.

In the parametric study, applying the vertical load on its own to the top of the wall resulted in outward horizontal displacement of the wall and rotation/settlement of the bank seat. Subsequent application of a horizontal load, in either direction, only marginally increased the magnitude of settlement and rotation of the bank seat.

Applying a horizontal load resulted in deformation of the wall face in the direction of the applied load. An outward horizontal load increased outward wall deformation, while an inward horizontal load reduced the deformation of the wall.

Angle of friction was found to have a significant impact on the deformational response of the wall. Angles of friction of 30^o or less resulted in both large settlement and rotation of the bank seat and deformation of the wall face. Angles of friction greater than 30^o, overall, displayed similar responses and only had marginal impact on the deformational response. The horizontal displacement of the wall and rotation/settlement of the bank seat were linked and general proportional to the angle of friction, lower angles of friction had larger horizontal and larger bank seat settlements and vice versa.

The stiffness of the backfill, overall, also had only a marginal impact on the deformational response of the wall. Settlement and rotation of the bank seat were dominated by the application of the vertical load rather than the horizontal load.

The analysis presented here indicates that fill with an angle of friction greater than 30^o should be used in constructing GRS-IBS structures. The stiffness of the fill was found to have only a marginal impact on the performance of GRS-IBS.

REFERENCES

[1] Dicleli, M., (2000), 'Simplified Model for Computer-Aided Analysis of Integral Bridges'. *Journal of Bridge Engineering*, 5(3).

[2] Springman, S., Norrish, A. & Ng, C., (1996), *TRL Report 146 - Cyclic loading of sand behind integral bridge abutments*, Berkshire: Transport Research Laboratory.

[3] Flener, E. B., (2004), *Soil-Structure Interaction for Integral Bridges and Culverts*, Stockholm: Department of Civil and Architectural Engineering.

[4] J. S. Horvath, "Integral-abutment bridges: problems and innovative solutions using EPS geofoam and other geosynthetics," Res. Rpt. No. CE/GE-00, vol. 2, 2000.

[5] Adams, M. & Nicks, J., (2018), *Design and Construction Guidelines for Geosynthetic Reinforced Soil Abutments and Integrated Bridge Systems*, McLean, VA: Federal Highway Administration.

[6] Ardah, A., Abu-Farsakh, M. & Voyiadjis, G., (2017), 'Numerical evaluation of the performance of a Geosynthetic Reinforced Soil-Integrated Bridge System (GRS-IBS) under different loading conditions', *Geotextiles and Geomembranes 45*, pp. 558-569.

[7] Ardah, A., Abu-Farsakh, M. & Voyiadjis, G., (2021), 'Numerical parametric study of geosynthetic reinforced soil integrated bridge system (GRS-IBS)', *Geotextiles and Geomembranes 49*, pp. 289-303.

[8] EN 1991-2, *Actions on structures - Part 2: Traffic loads on bridges*, European Committee for Standardization, 2006.

Pullout performance of anchored earth systems

K. Nell[1], P.J. Naughton[2]
[11]Faculty of Engineering & Design, Atlantic Technological University Sligo, Ireland & TerraTech Consulting Ltd
[2]Faculty of Engineering & Design, Atlantic Technological University Sligo, Ireland
email: keith.nell@mail.itsligo.ie, naughton.patrick@itsligo.ie

ABSTRACT: Anchored earth is an alternative technology to reinforced soil and involves stabilising a wall using tendons and anchors. In this study the pullout resistance and corresponding displacement of square mild steel anchor plates was investigated. The anchor system was part of a 6.75m high trial wall constructed in Co Offaly. Three anchor sizes, with face dimensions of 100mm x 100mm, 200mm x 200mm and 300mm x 300mm, were investigated. Good repeatability of the pullout resistance – displacement was observed in comparable test series. However, both the peak pullout resistance and corresponding displacement did indicate some scatter. The early stiffness, at displacement less than 10mm, was consistent with the post-peak behaviour and was found to vary from softening, to plastic, to hardening behaviour. The peak pullout resistance was found to increase with area of plate anchor. The smallest plates (100mm x 100mm) reached peak resistance at displacement less than 5mm, while the large plates (200mm x 200mm and 300mm x 300mm) reached peak at similar values between 10 – 30mm. The peak pullout resistance for the 200mm x 200mm and 300mm x 300mm was found to reduce as the insitu vertical stress in the wall increased.

KEY WORDS: Anchored earth, experimental testing, trial wall, pullout testing.

1 INTRODUCTION

Anchored earth technology has been used to construct retaining walls for over 100 years [1]. The system consists of a facing element (nowadays a panel or segmental block system) and a connecting rod or tendon that connects the facing system to an anchor located in the retained fill, Figure 1. Anchored earth systems differ from conventional steel and geosynthetic reinforced wall technologies in that the resistance to outward movement is mobilised, primarily, as passive resistance against the anchor plate, rather than friction along the reinforcement element [1].

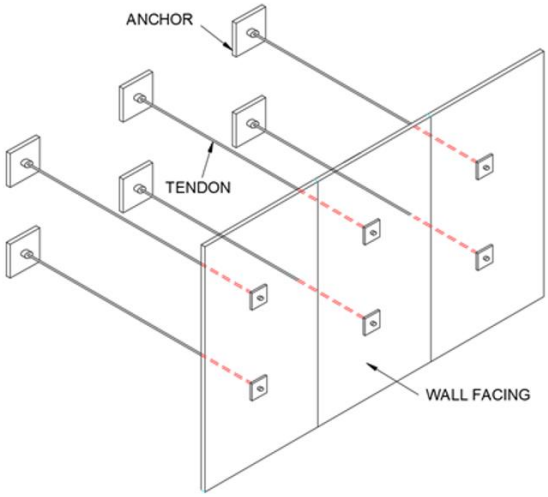

Figure 1. Schematic of an anchored earth structure [1].

Jones [1] reported on early anchored earth technologies, including an array of wooden timber reinforcement units developed in the USA by Munster [2] in 1925. A French engineer also developed a ladder wall in 1932, which consisted of precast concrete facing units, selected stone fill and ties with steel anchor plates [3]. The ladder system allowed the facing units to move relative to each other to accommodate settlement.

The first anchored earth wall in the UK was constructed in 1984 [4]. The wall, which was 6m high and 86m long, formed part of the A660 Otley bypass in West Yorkshire, UK. Different types of anchors, including plate anchors and anchor heads, were utilised on that project.

In this study the pullout behaviour of plate anchors is investigated in a full-scale trial wall. Three plate anchor face dimensions of 100mm x 100mm, 200mm x 200m and 300mm x 300mm were investigated. The data was assessed in terms of peak pullout resistance, stiffness of the pullout response and the impact of both plate size and insitu vertical effective stress on the behaviour of the plate anchors.

2 METHODOLOGY

A full-scale test wall was constructed in Co. Offaly at the Lusmagh Quarry belonging to Banagher Precast Concrete Ltd. The wall had a maximum height of 6.75m, Figure 2, and was faced with 0.14m thick concrete panels. The wall was reinforced with anchors consisting of 4.65m long high tensile steel tendons, 16mm in diameter, connected to steel anchor plates, installed at 0.75m horizontal and vertical centres.

The anchor plates were manufactured from 10mm thick mild steel (S275), of different face dimensions; 100mm x 100m, 200mm x 200mm and 300mm x 300mm. The steel tendons had Lenton treaded tapered ends to hold the anchor plate in place. The plates sizes used at each location are summarised in Table 1. The numbered locations on the front of the wall are shown in Figure 3, with a cross section of the wall shown in Figure 4.

The concrete facing panels were cast with access holes to allow the anchor tendon to protrude at the wall face, allowing ease of access for pullout testing, Figure 5.

Kentledge, in the form of large concrete blocks, was placed on top of the wall to increase the vertical stress in the wall by 20kPa. The backfill consisted of 6I/6J fill compacted in accordance with the Specification for Road Works, Series 600 [5].

While the primary objective of this study was to evaluate the pullout resistance of the anchored earth elements, the face of the wall was also instrumented with Moiré tell-tales and survey targets, Figure 6. The tell-tales would indicate closure of the joints between adjacent panels, while the survey targets would indicate movement of the wall panels.

Figure 2. Image of test wall.

Table 1. Plate sizes at different locations in the wall.

Plate size	Location number
100mm x 100mm	1, 2, 9, 10
200mm x 200mm	5 – 8, 11 – 18, 23 – 26
300mm x 300mm	19 – 22, 27 – 32

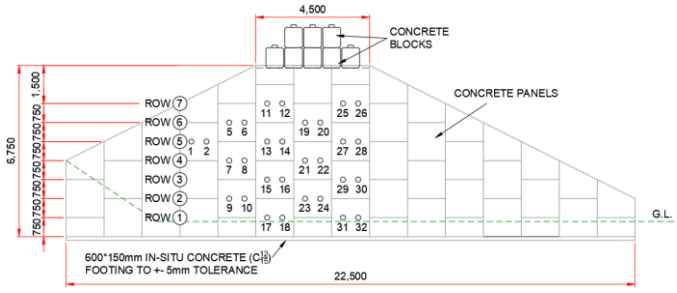

Figure 3. Front elevation of test wall.

2.1 Backfill properties

The Class 6I backfill [5] was produced from locally sourced crushed limestone rock.

Compaction testing in accordance with BS 1377-2 [6] determined the dry weight – moisture content relationship shown in Figure 7. The optimum moisture content was determined as 6.5%, with a maximum dry weight density of 22.3kN/m^3. The insitu moisture content during construction of the wall was about 3.7%, corresponding to a dry weight density of 20.5kN/m^3.

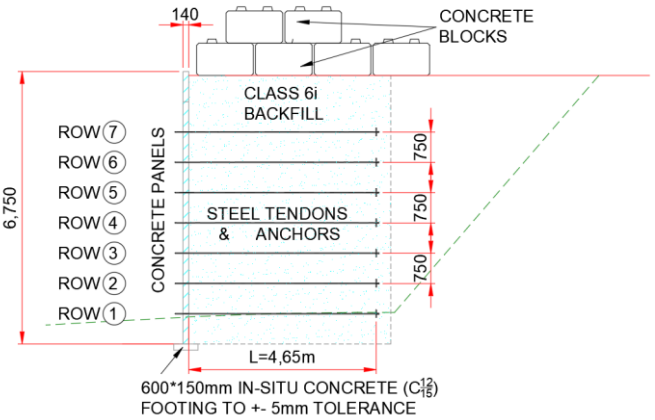

Figure 4. Cross section through the test wall.

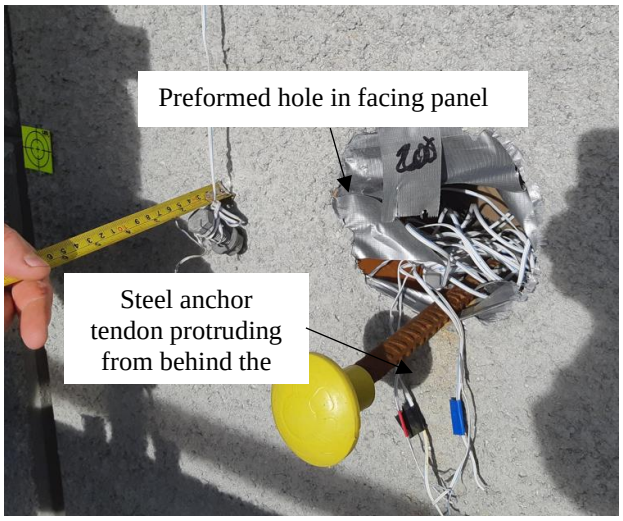

Figure 5. Anchor tendon protruding at face of wall through preformed hole in facing panel.

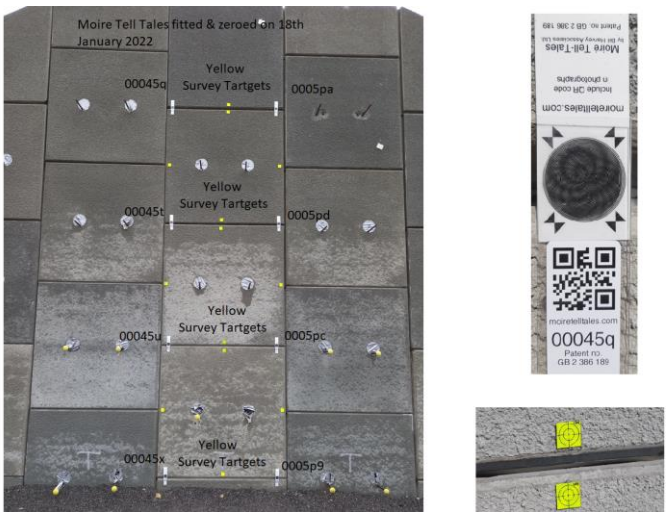

Figure 6. Location of Moiré tell-tales and survey target on front elevation of wall.

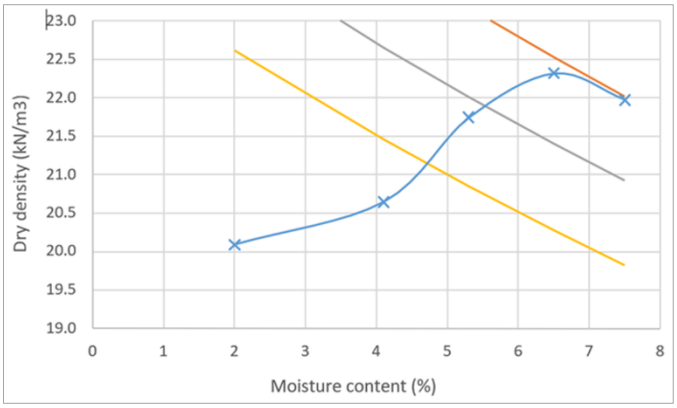

Figure 7. Dry-weigh moisture content relationship for the Class 6I fill used in this study.

Large (300mm x 300mm) shear box testing was conducted in accordance with BS 1377-7 [7]. The samples were prepared by removing all particle sizes greater than 20mm. The fill was compacted in the shear box using standard compaction (2.5kg rammer) at a moisture content of 4.5%, giving a dry weight density of 19.6kN/m^3, corresponding to 88% of maximum dry weight. Normal stresses of 50kPa, 100kPa and 200kPa were used in the shear box testing. The peak angle of friction was measured as 47.8^o with an apparent cohesion of 8kPa.

2.2 Construction of the wall

The wall was constructed in accordance with EN 14475 [8]. The facing panels were stood vertical, and fill placed and compacted in 150mm layers, using Method 2 of Series 600 [5], until the location of the first layer of anchors was reached. The anchors were then installed, Figure 8, and the process repeated until the wall reached its full height.

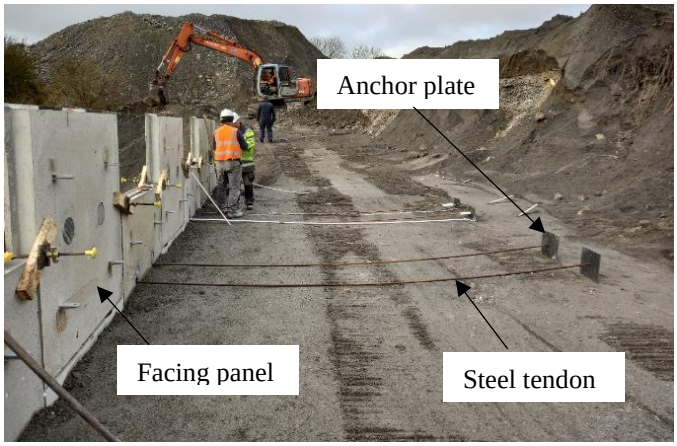

Figure 8. Construction of wall, including installation of anchors.

2.3 Pullout testing

Pullout testing of the anchors was conducted approximately 4 months after construction of the wall. Before testing occurred, the kentledge was placed on top of the wall to increase the vertical stress in the backfill.

A jack with a 20 tonne capacity was used to pull out the anchors. The tendons and threaded bars from the jack were connected using bespoke steel 'H' connectors, manufactured from 50mm wide x 10mm thick S275 steel. The 'H' section had a slotted profile to provide sufficient welding to ensure adequate tensile capacity between the tendon & the 15mm diameter threaded bar, Figure 9. The threaded bar, which was connected to the other end of the 'H' connector, passed through the hole in the centre of the jack and was locked off with a loading plate and wing nut.

The displacement of the jack during pullout was measured using a long-stroke linear voltage displacement transducer (LVDT) with a maximum displacement of 125.4mm. The experimental setup during a test is shown in Figure 10.

A preload of 0.5kN, corresponding to 1% of the tensile strength of the test tendon, was then applied. Pullout testing was conducted at 2mm/minute with pullout resistance and displacement recorded at 1-minute intervals. The horizontal displacements and loads were automatically logged by a Hydrotechnic Multi System 5060 data logger.

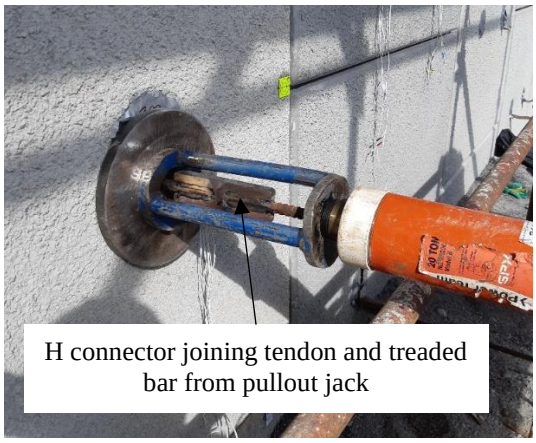

Figure 9. Connection between jack and anchor tendon during a test

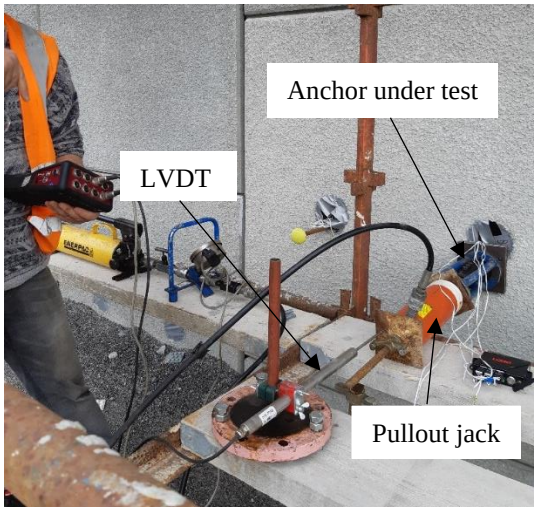

Figure 10. Experimental setup for conducting pullout testing.

3 RESULTS & DISCUSSION

In total 30 pullout tests were conducted. Figure 11 presents four pullout test results, where pullout force is plotted against displacement, for the anchors on Row 7, Anchors 11, 12, 25 and 26. These anchors were all 200mm x 200mm. Good repeatability was observed in the four test results. The early stiffness, up to a displacement of 10mm, observed during

pullout was consistent between all tests. This could be attributed to elastic deformation of the steel tendon, but further study of this is required. There was, however, some scatter in the observed peak pullout resistance, with peak resistance varying between 65 – 85kN and displacement corresponding to peak resistance varying from 20 – 37mm.

The experimental data is discussed in terms of the impact of anchor plate size and vertical stress on the anchors.

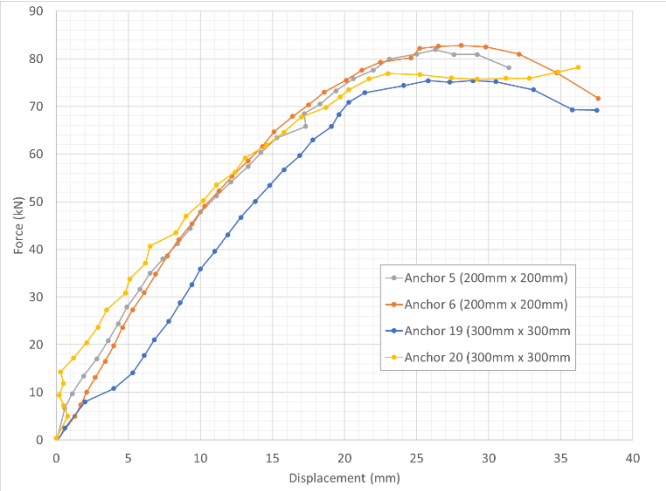

Figure 11. Pullout test results for Row 6 of wall.

3.1 Impact of plate size on pullout resistance

In this study three plate sizes were evaluated, 100mm x 100mm, 200mm x 200mm and 300mm x 300mm.

Figure 12 shows the pullout resistance – displacement relationship for 100mm x 100mm (Anchors 9 & 10) and 200mm x 200mm (Anchors 23 & 24) anchors at Row 2 in the wall. Good repeatability in comparable data was again observed. The 100mm x 100mm anchors appear to have a slightly stiffer response at small displacement than the larger 200mm x 200mm anchors. The smaller anchors also display a definite peak pullout, with the post peak behaviour displaying a plastic response or some softening in post peak behaviour. The 200mm x 200mm plates in contrast do not have a definite peak value and the force – displacement curve hardens at higher displacement. The peak pullout resistance was determined using intersecting lines representing best fit lines to the early and later linear portion of the data sets.

Figure 13 presents the pullout resistance – displacement data for Row 3, where Anchors 15 & 16 were 200mm x 200mm plates and Anchors 29 & 30 were 300mm x 300mm plates. Again, good repeatability is found between comparable data. The stiffness of all anchors on Row 3 was similar for small displacements. The smaller plate, Anchors 15 & 16, did not display a peak value, which was again estimated using intersecting lines.

The peak pullout resistance and corresponding displacement for each anchor is summarized in Table 2. In Row 2 the 200mm x 200mm plates had a higher peak pullout force at a slightly larger displacement compared with the 100mm x 100mm plates. However, the increase in peak pullout force was not proportional to the increase in the cross-sectional area of the plate. Similarly, for Row 3, the larger 300mm x 300mm plate had a higher peak pullout resistance than the 200mm x 200mm plates, but again the increase in resistance was not proportional to the increase in plate area.

The smaller 100mm x 100mm plates reached peak resistance at a much lower displacement than the 200mm x 200mm at the same elevation in the wall. In Row 3, both plate sizes, 200mm x 200m and 300mm x 300mm, had comparable displacements at peak pullout resistance.

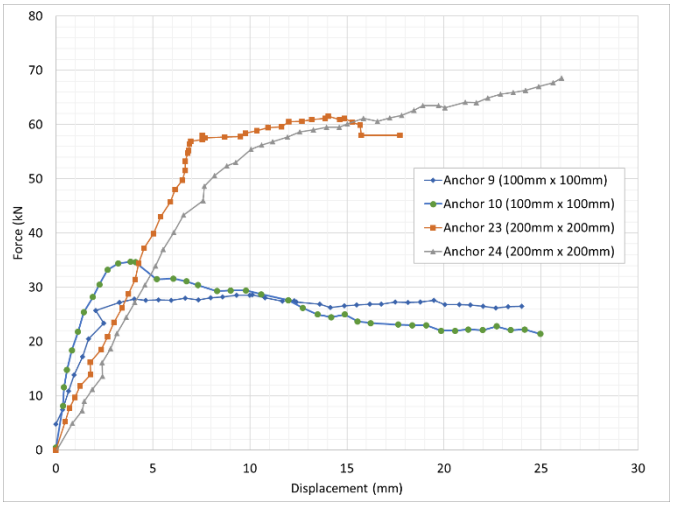

Figure 12. Pullout data for Row 2, Anchors 9 & 10 (both 100mm x 100mm) and 23 & 24 (both 200mm x 200mm).

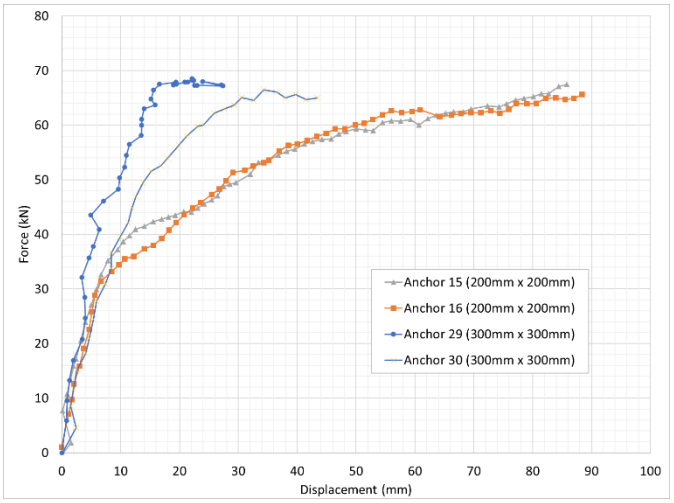

Figure 13. Pullout data for Row 3, Anchors 15 & 16 (both 200mm x 200mm) and 29 & 30 (both 300mm x 300mm).

3.2 Impact of vertical stress on pullout resistance

The impact of vertical stress on pullout resistance was assessed by comparing the pullout resistance of similar sized plates located at different elevations in the wall. The vertical stress was determined using the estimated insitu weight density of the fill, 20.5kN/m^3, taking into account the 20kPa surcharge stress at the top of the wall.

Figure 14 & Figure 15 shows the pullout resistance – displacement relation for the 200mm x 200m plates located in Rows 1 – 7 inclusive and 300mm x 300mm plates located in Rows 3 – 6 inclusive respectively. Both plate sizes displayed a linear and similar value of stiffness for a displacement less than 10mm.

Figure 16 presents the relationship between peak pullout resistance and insitu vertical effective stress. Overall, and irrespective of plate size, a reduction in peak pullout resistance with increased insitu vertical effective stress was observed. The reduction in pullout resistance with increased vertical stress, while counterintuitive, was not unexpected. Pullout testing [9, 10] on inextensible steel reinforcement had found enhanced interaction between the reinforcement elements and the surrounding soil at low normal stress, which is attributed to dilation in the well compacted granular fill near the top of the wall [10]. Typically, the interaction between the soil and inextensible reduces vertical stress to a depth of 6m and then remains relatively constant [9].

Table 2. Summary of peak pullout resistance and corresponding displacement for anchors on Rows 2 & 3.

Row	Anchor No	Plate size (mm x mm)	Peak pullout force (kN)	Displacement at peak pullout force (mm)
2	9	100 x 100	28	4
	10	100 x 100	45	4
	23	200 x 200	58	7
	24	200 x 200	54	9
3	15	200 x 200	48	15
	16	200 x 200	54	24
	29	300 x 300	68	18
	30	300 x 300	76	16

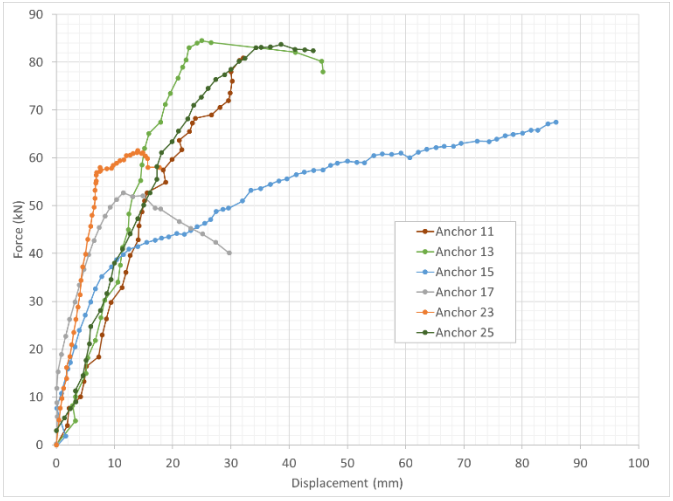

Figure 14. Pullout resistance – displacement relationships for 200mm x 200mm plates.

3.3 *Moiré Tell Tales*

The Moiré Tell Tales were used to measure the vertical panel displacement after the installation of the kentledge on top of the wall. No significant movement of the panels occurred, Table 3.

3.4 *Anchor post-construction excavation and inspection*

The backfill behind the top three rows (Rows 5, 6 & 7) of buried anchor plates was excavated. This action provided the opportunity to inspect the physical state and environment around the anchor plates. The granular backfill was very well compacted, cemented, and difficult to excavate with a spade.

The plates were intact and located in a vertical position, well embedded into the granular backfill. It was difficult to envisage the anchor plates moving through the granular backfill, Figure 17.

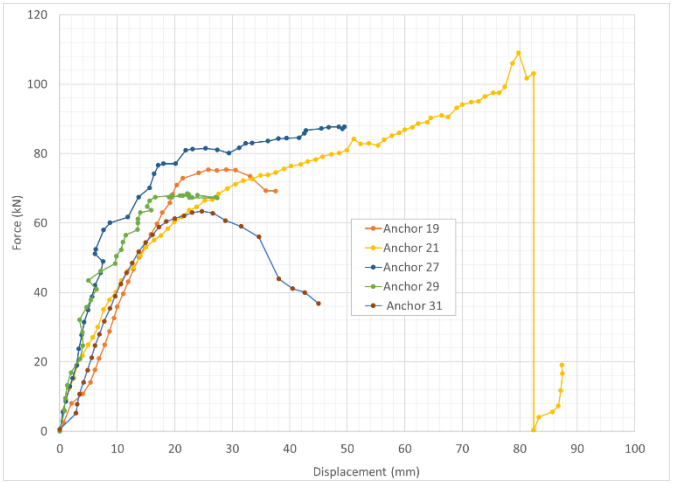

Figure 15. Pullout resistance – displacement relationships for 300mm x 300mm plates.

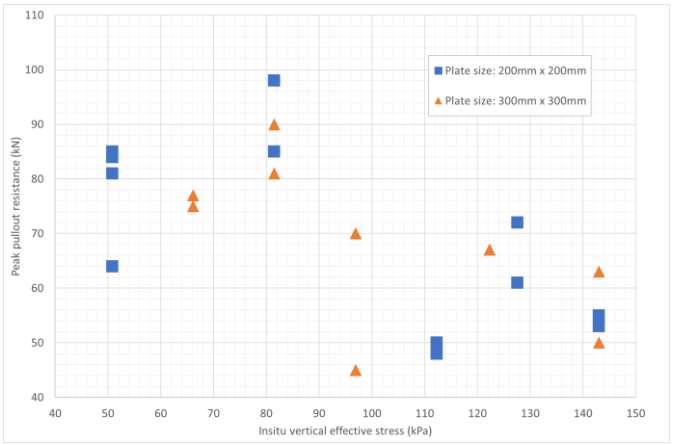

Figure 16. Relationship between pullout resistance and insitu vertical effective stress for 200mm x 200mm and 300mm x 300mm plates.

Table 3. Moiré tell-tales vertical displacement

Moiré Tell Tale no.	Settlement
0005pc	0.1mm
0005p9	0.1mm
00045x	0.3mm
00045u	0.4mm
0005pa	0.4mm
00045q	0.5mm
00045t	0.3mm
0005pb	0.3mm

Row 5 contained all plate sizes, 100mm x 100mm, 200mm x 200mm & 300 x 300mm. The 100mm x100mm plates (Anchors 1 & 2) when exhumed had rotated by approximately 45 degrees from the vertical. The 200mm x 200mm (Anchor 13) & the 300mm x 300mm plates (Anchors 27 & 28) displayed evidence of slight deformation. However, Anchor 14 (200mm x 200mm) was the only plate that displayed any noticeable bending or

deflection - approximately 12mm at the centre of the plate, Figure 18.

In this study, geotechnical considerations were found to be secondary to the mechanical characteristics of the reinforcing tendon and anchor plates.

Figure 17. Exhumed Anchor 28.

Figure 18. Deformed Anchor 14 following exhumation

3.5 Implications for design

The design of plate anchors is detailed in BS 8006-1 [11]. The length of the tendon is dictated by both internal and external stability considerations. BS 8006-1 [11] suggests minimum lengths for reinforcing elements, typically 0.7 x the height of the structure. No guidance is given on the allowable operational deformation of the wall. BS 8006-1 [11] does suggest that the construction tolerances are limited to ± 25mm over a 4m length.

Adopting a displacement limit of 10 – 20mm in the anchor system would reduce the long-term capacity of the anchors to the range of 30 – 60kN depending on anchor size.

The data presented from this study indicates that peak resistance is not likely to be the controlling factor in design. To ensure that the facing is compliant with the displacement survivability limit state, the facing deflection should be not greater than 20mm.

4 CONCLUSION

This study presents pullout testing on a 6.75m high trial anchored earth wall constructed in Co Offaly. The wall was reinforced with three different size plate anchors, which were connected to the concrete facing units by high tensile steel tendons. The wall had concrete facing panels and the backfill was Class 6I/6J high quality granular material. Kentledge was used to apply a 20kPa surcharge load to the top of the wall.

Good repeatability of the pullout resistance – displacement curves, particularly at displacement less than 10mm, was observed in all tests conducted. However, there was significant scatter in the peak pullout resistance and corresponding displacement. The post peak behaviour was also found to vary, with softening, plastic displacement and hardening all observed. The smaller 100mm x 100mm plate failed at small displacements, less than 5mm, while the displacement at peak resistance for the 200mm x 200mm and 300mm x 300m plates were largely consistent and were in the range 10 – 30mm.

The peak pullout resistance was found to be proportional to the anchor plate size, increasing as the area of the anchor plate increased. The peak pullout resistance also varied with insitu vertical stress, reducing as the vertical stress increased. This response is in keeping with pullout testing on inextensible steel reinforcement reported in the literature [9, 10].

The measured displacement of the anchor may be attributed to elastic deflection of the tendon & anchor plate. However, further analysis of the data is required. The passive resistance of the backfill was secondary to the mechanical properties of the tendons and anchor plates used in this study when high quality granular backfill was used.

When the horizontal deflection was limited to 10 – 20mm, the horizontal force that the anchor can resist was 30 – 60kN, depending on the anchor size. The working resistance of the anchor is considered the best approach to take in analyzing pullout data.

REFERENCES

[1] C.J.F.P.J. Jones, *Earth reinforcement and soil structures*, Thomas Telford, UK, third edition 2010.

[2] Munster, A., United States Patent Specification No 1762343.

[3] Coyne, M.A., (1945), Murs de soutenement et murs de quai à echelle. *Le Genie Civil*, May.

[4] Snowdon, R.A., Darley, P. & Barratt, D.A., (1986), 'An anchored earth retaining wall on the Otley bypass: construction and early performance', *Transport and Road research Laboratory, Research report 62, UK*.

[5] Anonymous, *Specification for road works, Series 600*, CC-SPW-00600, Transport Infrastructure Ireland, March 2013.

[6] BS 1377-2, *Methods of test for soils for civil engineering purposes Classification tests and determination of geotechnical properties*, British Standards Institution, 2022.

[7] BS 1377-7, *Methods of Test for Soils for Civil Engineering Purposes Part 7: Shear Strength Tests (Total Stress)*, British Standards Institution, 2015.

[8] EN 14475, *Execution of special geotechnical works - Reinforced fill*, European Committee for Standardization, 2006.

[9] FHWA-NHI-10-024, *Design of Mechanically Stabilized Earth Walls and Reinforced Soil Slopes – Volume 1*, Federal Highways Administration, 2009.

[10] Weldu, M.T., Han, J., Rahmaninezhad, M.S., Parsons, R.L. & Kakrasul, J.I., 'Pullout resistance of mechanically stabilized earth wall steel strip reinforcement in Uniform Aggregate', Report No K-TRAN: KU-14-7, University of Kansas, 2015.

[11] BS 8006-1, *Code of practise for strengthened/reinforced soils and other fills*, British Standards Institution, 2016.

ANN-based bubble tracking algorithm for clay slurries containing large gas bubbles using X-ray CT

Shuoshuo Xu[1], Jinxing Lai[1], Brendan C. O'Kelly[2], Budi Zhao[3]
[1] Chang'an University, School of Highway, Xian, 710064, China
[2] Trinity College Dublin, Department of Civil, Structural and Environmental Engineering, Dublin, D02 PN40, Ireland
[3] University College Dublin, School of Civil Engineering, Dublin, Ireland
email: xushuoshuo@chd.edu.cn, laijinxing@chd.edu.cn, bokelly@tcd.ie, budi.zhao@ucd.ie

ABSTRACT: Gassy clay is a widely-distributed natural composite material consisting of a saturated clay matrix incorporating large gas bubbles. This study aims to develop a novel method to non-destructively monitor the strain field evolution of drying kaolinite slurry samples, with entrained gas bubbles, using X-ray computed tomography (CT). During the drying process, the kaolinite sample is scanned several times at decreasing water content (reducing soil volume. Individual bubbles are identified within the kaolinite sample and their morphology and location are measured via image processing. A bubble-tracking algorithm links associated bubbles between different scans using bubble location and morphology information. The morphology of individual bubbles changes as the soil volume reduces under increased suction during the drying process. Therefore, an artificial neural network (ANN) is adopted to enhance the bubble-tracking algorithm. This method shows great accuracy based on verification with manually linked bubbles. Hence, the three-dimensional (3D) displacement field of bubbles was determined within the soil sample. Finally, the evolution of the 3D displacement field is discussed, both before and after desiccation crack formation.

KEY WORDS: Desiccation crack; Fine-grained soil; Strain field; X-ray computed tomography.

1 INTRODUCTION

The formation of desiccation cracks in drying clay slurries dramatically alters their mechanical and hydraulic properties and leads to engineering problems for geotechnical and agricultural structures, such as dams, roads, landfills, agricultural irrigation, etc. [1-3]. Desiccation cracks with polygonal network are also observed in various geological features [4]. Laboratory experiments and numerical simulations have been employed to characterise the mechanism of desiccation cracks [5-7]. Desiccation cracks tend to nucleate at large surface pores, where capillary pressure generates stress concentration, and the cracks propagate with the further invasion of air into the locally enlarged pores [5]. Previous experimental studies mainly adopted digital cameras to monitor the deformation and crack formation, based on the 2D characterisation of the drying soil surface. However, limited information exists about the 3D deformation within drying soils.

X-ray computed tomography (CT) has been widely applied to coarse-grained materials, e.g., to non-destructively monitor the internal fabric evolution in sand samples [8-9]. Various particle-tracking techniques were developed to monitor the kinematic information with time-lapse scanning [10]. The quantification of particle movement provides new insights on shear band formation [11-12], particle breakage, etc. [13]. Recently, X-ray CT has been applied to monitor the 3D deformation of fine-grained soils under 1D compression [14] and triaxial shearing [15] conditions. The 3D measurements reveal non-uniform and localised deformation.

The tracking techniques can be primarily classified into two groups: (i) digital image correlation (DIC) calculates the cross-correlation between neighbouring monitor windows [16]; (ii) marker-based tracking (MBT) methods link individual markers based on their morphology and location information [11-12]. Both approaches have been widely used to calculate the deformation in geomaterials. The DIC method, relying on the texture of grey-scale images, does not work if textures are too small to identify, whereas the produced strain fields have a low resolution if the texture is too large. For sand samples, MBT provides valuable kinematic information of individual particles [17]. Different MBT methods have been proposed based on particle shape parameters and positions [11-12, 18]. Recently, a similar method was introduced to track the mica particles within a kaolinite matrix [14]. However, the markers tracked in MBT methods are typically the solid particles, such that their morphology remains constant throughout the testing.

In this paper, a novel MBT approach is developed for the internal bubbles entrained in a kaolinite matrix during the drying process. The morphology and location of individual bubbles within a kaolinite sample are extracted from a series of X-ray CT images obtained at different (progressively reducing) water content. An artificial neural network (ANN) algorithm was trained to determine the correlation factors between bubbles within different scans. The suitability of various bubble parameter groupings is examined for the bubble tracking algorithm. Then, 3D displacement fields are obtained from tracked bubbles to characterise the deformation and desiccation-crack formation process for the drying kaolinite sample. The novel technique can help better understand the sample's internal evolution that occurs during desiccation cracking.

2 METHODS

2.1 Soil tested and scanning procedure

Kaolinite slurry was prepared at a water content of 151% (about 3 times greater than its liquid limit). The slurry material was poured into a plastic container, with 32.7-mm inner diameter, for performing a drying test at ambient laboratory temperature.

During the drying process, a series of five X-ray CT scans was collected using the TESCAN CoreTOM apparatus (voltage at 160 keV). In other words, the X-ray scanning of the drying kaolinite sample was performed for progressively reducing water contents of S1 = 48.4%, S2 = 35.3%, S3 = 26.5%, S4 = 23.2%, and S5 = 13.9%. The sample's wet mass (and hence its water content) at each scan was determined by a precision scale. The reconstructed X-ray images have a resolution of 20 μm along three orthogonal directions.

2.2 Image processing and bubbles tracking

The grey values in the reconstructed X-ray images reflect the X-ray attenuation of different materials present. As shown in Figure 1(a), a high contrast exists between air, plastic (of the container side-wall), and kaolinite. A series of image processing steps were conducted to extract individual air bubbles (entrained in the kaolinite matrix) from the grey-scale images, as follows. First, a median filter was used to reduce image noise. Next, the threshold values between air, plastic and kaolinite were determined from grey-value histogram. Then individual air bubbles were identified, each labelled with different IDs. In Figure 1(b), individual gas bubbles with varying size (volume and surface area) and shape are represented with different colours, and the bubbles seem to be evenly distributed in the kaolinite sample.

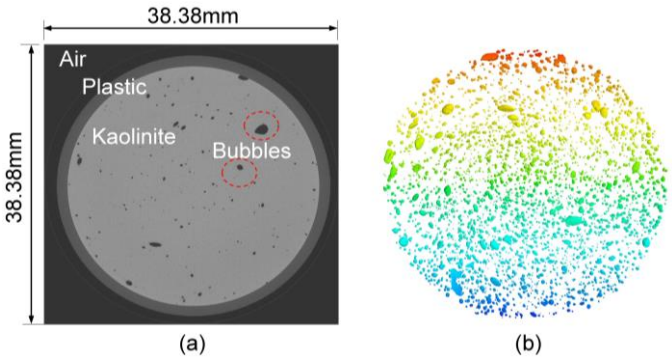

Figure 1. (a) Horizontal slice of grey-scale image; (b) 3D visualisation of internal air bubbles.

The extracted 3D bubble surfaces were analysed to obtain their location and morphology information. The locations (*x*, *y*, and *z* coordinates) of the bubble centroids were determined. Bubble morphology was quantified in terms of volume, surface area, sphericity (SP), aspect ratio (AR), and convexity (CON). SP compares the surface area of a bubble and its volume-equivalent sphere. AR compares three principal dimensions, i.e., maximum, intermedia and minimum. CON compares the bubble volume and the volume of its convex hull. Detailed descriptions of the image processing and shape analysing can be obtained in [19].

The procedure of the bubble tracking algorithm starts with the morphology and location information of individual bubbles and involves the following steps. Firstly, a small portion of the bubbles have unusual shape parameters (e.g., SP>1, which is mainly caused by low bubble-to-pixel size ratio), such that they were excluded from further analysis. Next, the coordinate system was unified between different scans, and then 145 bubbles were manually linked between scans for ANN model training and validation. Finally, the trained ANN model was used to compare all possible links between bubbles in sequential scans.

The coordination system was not consistent between scans due to the movement of the drying kaolinite sample. Thus, a unique coordination system was defined for all scans, using the sample container base (contact surface), and considering a unique bubble, as follows. First, the centre and perpendicular vector of the container base were determined; these being chosen as the origin and the *z*-axis of the unified coordination system. Then, a unique bubble was selected across scans to define the *y*-axis. All bubbles aligned well between different scans after the coordination system update.

Figure 2 shows the architecture of the ANN model with a three-layer structure. The location and morphology parameters of two bubbles in sequential scans were compared to identify if they were correlated. The difference of parameters (ΔX_i) were imported into the ANN model to estimate a correlation factor ($Y \in [0,1]$) between two bubbles in sequential scans. A ranking system was developed to uniquely link bubbles, such that bubbles with the highest correlation factor Y were linked first. For this purpose, 145 bubbles were manually linked between scans S1 and S2 for the training and verification of the ANN tracking algorithm. In other words, the weight of the neural unit (w_n) was obtained using 100 manually linked bubbles between S1 and S2, with the other 45 manually linked bubbles used for verification purposes.

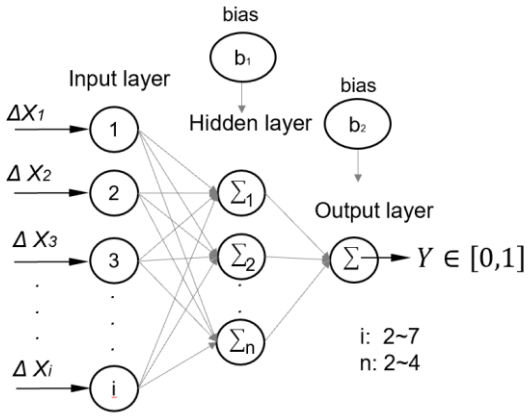

Figure 2. Neuron model for ANN.

3 RESULTS AND DISCUSSION

3.1 Bubble morphology analysis

The sizes and shapes of individual bubbles change during the drying process, such that bubble tracking based on morphology information could be problematic. As shown in Figure 3, a bubble in different scans was extracted, its size

(volume and surface area) decreasing almost proportionally during the sample drying/shrinkage process. However, changes in the shape (i.e., SP, AR, and CON) of the bubble were unpredictable. This could pose a threat to the efficacy of the presented bubble-tracking algorithm.

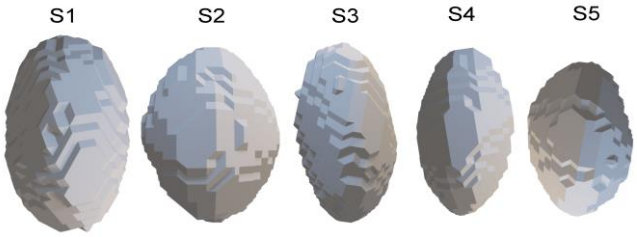

Figure 3. Changing morphology of specific bubble in five scans (for reducing water content of kaolinite sample).

3.2 ANN tracking model optimisation

Eight parameters (i.e., *x*, *y*, *z* coordinates and the volume, surface area, SP, AR, and CON) were extracted from each bubble. The feasibility of applying different parameter combinations for bubble tracking should be examined. For this purpose, various groupings of parameters were adopted in the ANN model. Figure 4 shows the cumulative probability of correlation factors for 2830 bubbles between scans S1 and S2 for nine different parameter combinations investigated.

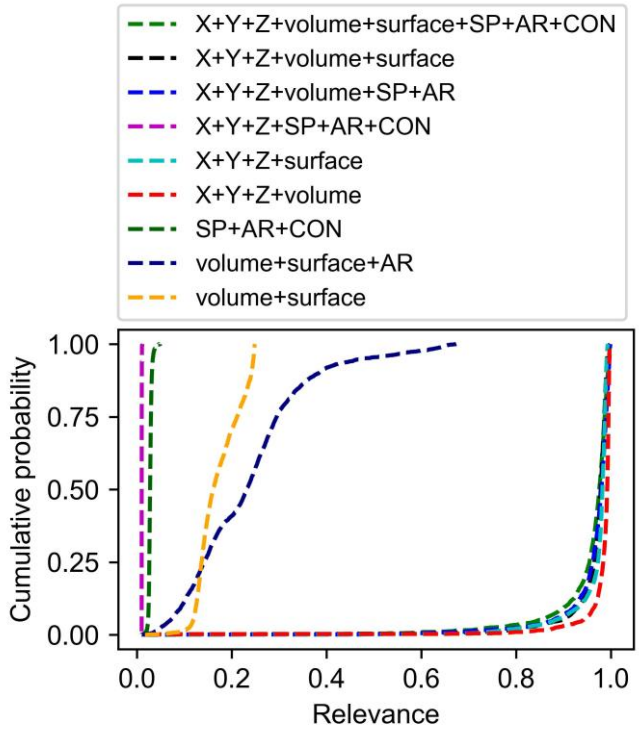

Figure 4. Relevance of all linked bubbles for various bubble parameter groupings investigated. Note: SP, sphericity; AR, aspect ratio; CON convexity.

As evident from Figure 4, parameter groups including location (*x*, *y*, *z*) and volume show the best performance. Whereas the parameter group with SP, AR, and CON shows the worst performance, since these parameters change randomly during the shrinkage process. In other words, these shape parameters will reduce the tracking accuracy if combined with bubble location and size parameters. Further calculations show that the bubble parameter group selected (i.e., *x*, *y*, *z* coordinates and volume) has 100% accuracy for the 45 sets of manually selected bubble validations, and the highest relevance mean, and small standard deviation.

3.3 Displacement field

3D displacement fields were calculated based on the linked bubbles between scans. Figure 5 shows the displacement field obtained between scans S1 and S2 (for reducing water content from 48.4% to 35.3%). The three colours (green, blue, and red) represent the displacement of the upper, middle, and lower sample depth/zones. The bubbles mainly move downwards, with little horizontal displacement occurring at these relatively high water contents, as compared to the air-entry value. As expected, bubbles nearer the top surface of the sample undergo more significant downward vertical movement, with a maximum displacement of 0.82 mm, whereas the minimum displacement of 0.004 mm occurred for bubbles located close to the container base.

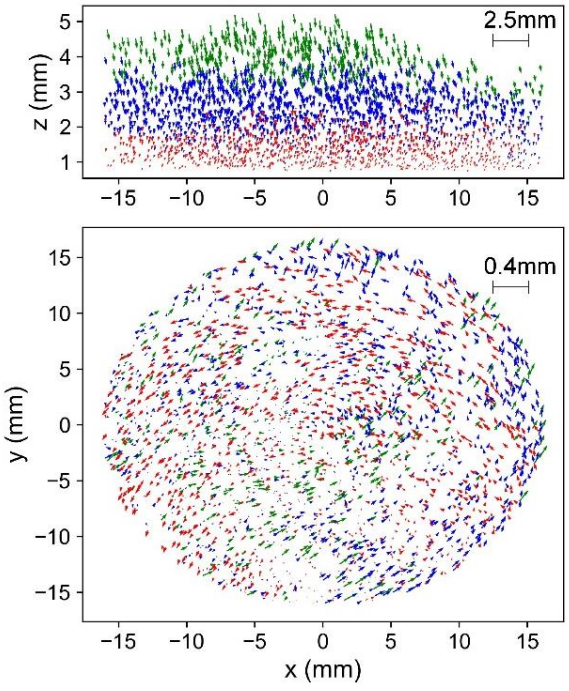

Figure 5. Displacement field of S1-S2 (water content reducing from 48.4% to 35.3%).

The kaolinite sample, of thickness 5.02 mm for S1, was separated into 261 layers. Bubbles were associated with individual layers based on their centroid locations. The averaged vertical displacements of all bubbles in each layer, occurring between scans S1 and S2, are shown in Figure 6. The linear relationship between mean vertical displacement and layer depth indicates a uniform vertical strain occurred over the sample thickness between S1 and S2.

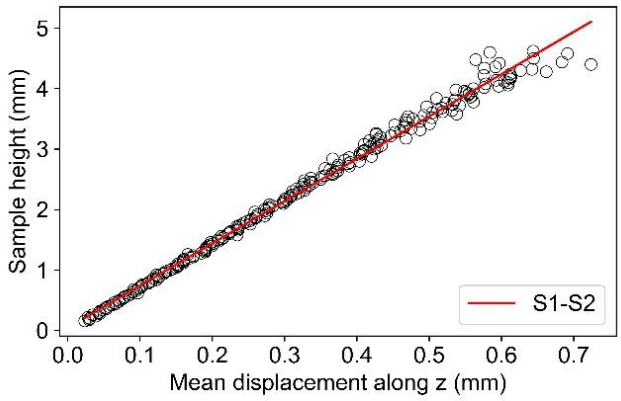

Figure 6. Average displacement in sample depth direction between scans S1 and S2.

Figure 7 shows the displacement fields between scans S4 and S5, with the kaolinite sample having a water content below the air-entry value, and desiccation crack formation. The horizontal displacement of the sample became more prominent than the vertical displacement, mainly caused by crack formation occurring close to the container side-wall. The distribution of the horizontal shrinkage was relatively uniform across the sample depth, and the displacement of bubbles close to the container side-wall was significantly greater than the bubble displacement occurring near the centre of the container base, with maximum and minimum horizontal displacements of 0.59 and 0 mm, respectively.

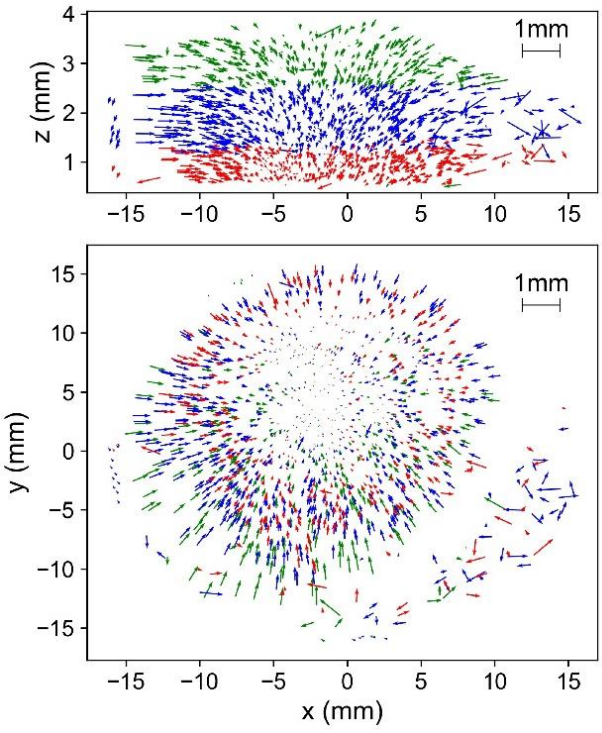

Figure 7. Displacement field of S4-S5 (water content reducing from 23.2% to 13.9%).

4 CONCLUSION

A series of X-ray CT scans were performed on a drying kaolinite sample. A novel MBT approach, enhanced by an ANN algorithm, was developed to monitor the 3D deformation response of the drying sample with entrained gas bubbles.

A series of image processing techniques was adopted to extract individual bubbles, and their location and morphology information. The bubble size (volume and surface area) was found to reduce almost proportionally during the drying process, whereas bubble shape parameters (e.g., AR, SP, and CON) changed randomly.

The ANN model was trained and validated with manually linked bubbles between successive scans of the drying kaolinite sample. Among different bubble parameter groupings investigated, the combination of bubble location and volume shows the best tracking performance. However, shape parameters (AR, SP, and CON) are not suitable for bubble tracking, since they change randomly during drying.

For drying at higher water content, the entrained bubbles experience primarily vertical displacement, bubbles located nearer the top surface of the sample undergoing a higher downward vertical displacement. Furthermore, the linear relationship between vertical displacement and depth in the sample indicates a uniform vertical strain distribution occurred over the sample thickness. Horizontal displacement became more prominent at lower water content, caused by crack formation close to the container side-wall.

REFERENCES

[1] Vallejo, L. E. (2009) Fractal analysis of temperature-induced cracking in clays and rocks. *Géotechnique*, 59(3): 283–286, https://doi.org/10.1680/geot.2009.59.3.283

[2] Corte, A. and Higashi, A. (1964) Experimental research on desiccation cracks in soil (No. CRREL-RR-66 Final Rpt.).

[3] Sinnathamby, G., Pasky, A., Phillips, D. H. H. and Sivakumar, V. (2014) Landfill cap models under simulated climate change precipitation: impacts of cracks and root growth. *Géotechnique*, 64(2): 95–107, https://doi.org/10.1680/geot.12.P.140

[4] Zeng, H., Tang, C. S., Cheng, Q., Inyang, H. I., Rong, D. Z., Lin, L. and Shi, B. (2019) Coupling effects of interfacial friction and layer thickness on soil desiccation cracking behavior. *Engineering Geology*, 260: 105220, https://doi.org/10.1016/j.enggeo.2019.105220

[5] Shin, H. and Santamarina, J. C. (2011) Desiccation cracks in saturated fine-grained soils: particle-level phenomena and effective-stress analysis. *Géotechnique*, 61(11): 961–972, https://doi.org/10.1680/geot.8.P.012

[6] Cordero, J. A., Useche, G., Prat, P. C., Ledesma, A. and Santamarina, J. C. (2017) Soil desiccation cracks as a suction–contraction process. *Géotechnique Letters*, 7(4): 279–285, https://doi.org/10.1680/jgele.17.00070

[7] Lakshmikantha, M. R., Prat, P. C. and Ledesma, A. (2012) Experimental evidence of size effect in soil cracking. *Canadian Geotechnical Journal*, 49(3): 264–284, https://doi.org/10.1139/t11-102

[8] Nielsen, S. F., Poulsen, H. F., Beckmann, F., Thorning, C. and Wert, J. A. (2003) Measurements of plastic displacement gradient components in three dimensions using marker particles and synchrotron X-ray absorption microtomography. *Acta Materialia*, 51(8): 2407–2415, https://doi.org/10.1016/S1359-6454(03)00053-3

[9] Chen, Y., Ma, G., Zhou, W., Wei, D., Zhao, Q. I., Zou, Y. and Grasselli, G. (2021) An enhanced tool for probing the microscopic behavior of granular materials based on X-ray micro-CT and FDEM. *Computers and Geotechnics*, 132: 103974, https://doi.org/10.1016/j.compgeo.2020.103974

[10] Watanabe, Y., Lenoir, N., Otani, J. and Nakai, T. (2012) Displacement in sand under triaxial compression by tracking soil particles on X-ray CT data. *Soils and Foundations*, 52(2): 312–320, https://doi.org/10.1016/j.sandf.2012.02.008

[11] Zhou, B., Wang, J. and Wang, H. (2018) A novel particle tracking method for granular sands based on spherical harmonic rotational invariants. *Géotechnique*, 68(12): 1116–1123, https://doi.org/10.1680/jgeot.17.T.040

[12] Cheng, Z. and Wang, J. (2018) A particle-tracking method for experimental investigation of kinematics of sand particles under triaxial compression. *Powder Technology*, 328: 436-451, https://doi.org/10.1016/j.powtec.2017.12.071
[13] Peng, Y., Ding, X. M., Xiao, Y., Chu, J. and Deng, W. T. (2019) Study of particle breakage behaviour of calcareous sand by dyeing tracking and particle image segmentation method. *Rock and Soil Mechanics*, 40(7): 2663–2672, https://doi.org/10.16285/j.rsm.2018.0689
[14] Ibeh, C. U., Pedrotti, M., Tarantino, A. and Lunn, R. J. (2021) PLATYMATCH — A particle-matching algorithm for the analysis of platy particle kinematics using X-ray computed tomography. *Computers and Geotechnics* 138: 104367, https://doi.org/10.1016/j.compgeo.2021.104367
[15] Birmpilis, G., Andò, E., Stamati, O., Hall, S. A., Gerolymatou, E. and Dijkstra, J. (2022) Experimental quantification of 3D deformations in sensitive clay during stress-probing. *Géotechnique*, (In Press) https://doi.org/10.1680/jgeot.21.00114
[16] Schreier, H. W. and Sutton, M. A. (2002) Systematic errors in digital image correlation due to undermatched subset shape functions. *Experimental Mechanics*, 42(3): 303–310, https://doi.org/10.1007/BF02410987
[17] Ando, E., Hall, S. A., Viggiani, G., Desrues, J. and Besuelle, P. (2012) Grain-scale experimental investigation of localised deformation in sand: a discrete particle tracking approach. *Acta Geotechnica*, 7(1): 1–13, https://doi.org/10.1007/s11440-011-0151-6
[18] Yang, J., Yin, Y., Landauer, A. K., Buyuktozturk, S., Zhang, J., Summey, L., ... and Franck, C. (2022) *SerialTrack: ScalE and Rotation Invariant Augmented Lagrangian Particle Tracking*. arXiv preprint https://doi.org/10.48550/arXiv.2203.12573
[19] Zhao, B. and Wang, J. (2016) 3D quantitative shape analysis on form, roundness, and compactness with μCT. *Powder Technology*, 291: 262–275, https://doi.org/10.1016/j.powtec.2015.12.029

Correlations between dynamic probe blow count and undrained shear strength for peat at a well-characterised raised bog in Ireland

David McHugh[1], Ciaran Reilly[2,3], Juan Pablo Osorio[2]
[1]Tobin Consulting Engineers, Fairgreen House, Fairgreen Road, Co. Galway, Ireland
[2]School of Civil and Structural Engineering, Technological University Dublin, City Campus, Bolton Street, Dublin 1, Ireland
[3]Ciaran Reilly and Associates, Consulting Engineers, Maynooth, Co. Kildare, Ireland.
email: david.mchugh@tobin.ie, ciaran@ciaranreilly.ie, juan.osorio@tudublin.ie

ABSTRACT: Peat deposits are generally heterogeneous, with large variations over small areas. Peat has an extremely high water content, high compressibility and low shear strength. This presents a major issue in studying the geomechanical behavior of peat. For this study, field and laboratory tests were conducted to establish the undrained shear strength (s_u) of peat at a cutover industrial peatland in Ireland which had been extensively characterized in the past. The new field work included TRL-type Dynamic Cone Penetrometer, Mackintosh probe and field vane shear tests. A correlation was developed between the Mackintosh probe "M-value" blow count and the undrained shear strength of peat. The correlation can be expressed as $s_u=16.54M^{0.373}$. Unconsolidated undrained triaxial tests and laboratory vane tests were carried out on samples retrieved from the field. The shear strength results thus derived were lower than the field test results, but consistent with each other. The suggested reason for the reduced undrained shear strength measured in the lab is sample disturbance during extraction, transport and storage prior to testing.

KEY WORDS: peat; shear strength; field vane test; dynamic probing; dynamic cone penetrometer.

1 INTRODUCTION

Peat deposits have an extremely high water content, low bulk density, high compressibility, creep behavior and low shear strength. Peat is a highly heterogeneous and anisotropic material, and its geotechnical properties are generally extremely variable over small distances since peat is formed from different plant species and the decay process is not uniform throughout the bog mass. However, the geotechnical properties of peat are generally closely interrelated [1]. Due to these inherent characteristics, peat is considered to be one of the most problematic types of materials for geotechnical engineers [2], [3]. Furthermore, different forms of anthropic intervention can also significantly alter the geotechnical properties of peat [4]. All these factors present major issues when studying the geomechanical behavior of peat.

The strength and stiffness of peat are dependent on a number of factors, the predominant one being the presence of organic fibers [5]. These fibers are mainly in a horizontal direction, which has been attributed to the large vertical strains associated with one-dimensional consolidation during natural formation of the peat. These fibers readily come apart in the vertical direction but provide tensile strength in the horizontal direction [6].

This research examines the validity of using a field vane testing apparatus in conjunction with a TRL-type dynamic cone penetrometer and Mackintosh probe as a quick and reliable method of testing the in-situ shear strength of organic peat soils was investigated. The results from the in-situ testing were then compared with laboratory-based experiments on samples taken from the same site.

The field vane apparatus is used to measure the undrained shear strength of silt and soft clay deposits. However, it has shortcomings when used to measure the shear strength of peat. This is due to the fibrous nature of peat. According to Radford [9], the effect of the fibers on the shear vane generally decreases with increases in the size of the vane.

The Mackintosh probe is a probing tool which provides a quick and economical method for determining the depth of soft deposits, and it provides a profile of penetration resistance with depth [10]. The driving point has a diameter of 27mm, and the drive hammer has a total weight of 4kg. The connecting rods are 1.2m in length and 12mm in diameter. The hammer is dropped at full drop height, which drives the driving point and connecting rods into the ground. The number of blows for each 100mm of penetration is then recorded as the M-value.

Dynamic cone penetrometer (DCP) tests are usually carried out in clays, silts, sands and gravels down to a maximum depth of one meter and mainly used for pavement design. However, for this research, it was proposed to extend the maximum depth of the test to three metres. The additional depth was provided by using two additional adapter shafts joined using couplers. The aim of this was to establish whether the DCP test could be used to approximate the undrained shear strength of peat using a correlation between shear vane results and the n-value recorded. The test results were reported in terms of the n-value, the number of blows for each 100mm of penetration.

2 TEST SITE DESCRIPTION

Ballydermot Bog was selected as a suitable location for carrying out field testing. This raised bog is situated approximately 2.7 km north of Rathangan, Co. Kildare and 12

km south of Edenderry, Co. Offaly, in the Irish Midlands (Figure 1). The bog was harvested for milled peat.

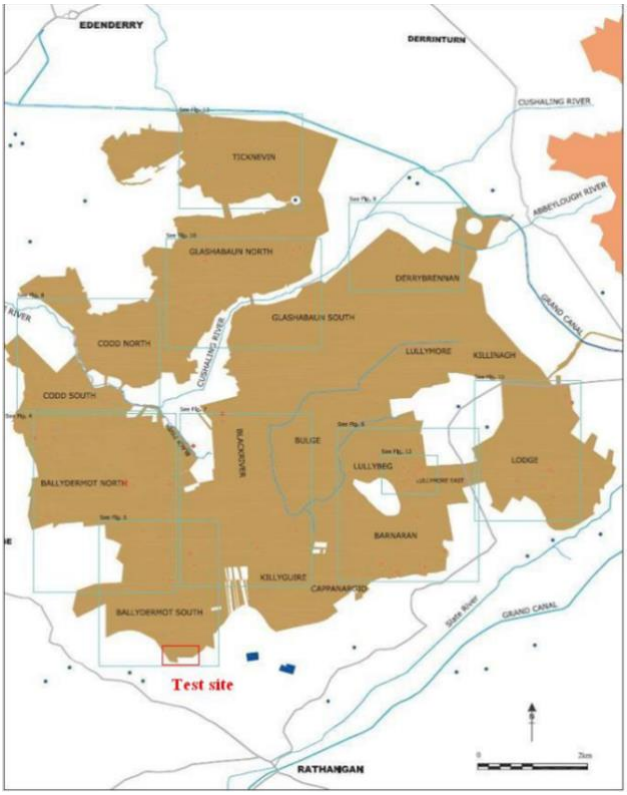

Figure 1. Ballydermot-Lullymore Bog Complex [11].

Authors such as Hanrahan [13], [14], Hanrahan and Rogers [15], Cuddy [16], Hebib [17], O'Loughlin [18], Osorio et al. [19] and Osorio-Salas [20] have conducted multiple research projects into the compressibility behavior and shear strength of peat at Ballydermot bog, producing a detailed characterization of the bog profile.

Figure 2 presents an approximated soil profile, based on the field investigation and soils classification conducted by Osorio-Salas [20]. As it can be seen, the profile is mainly composed of three layers (i) a 0.8 m thick man-made fill, (ii) a 3.2 m pseudo-fibrous peat layer, and (iii) a 1.9 m gravel layer with very high contents of fines and sand, reducing with depth.

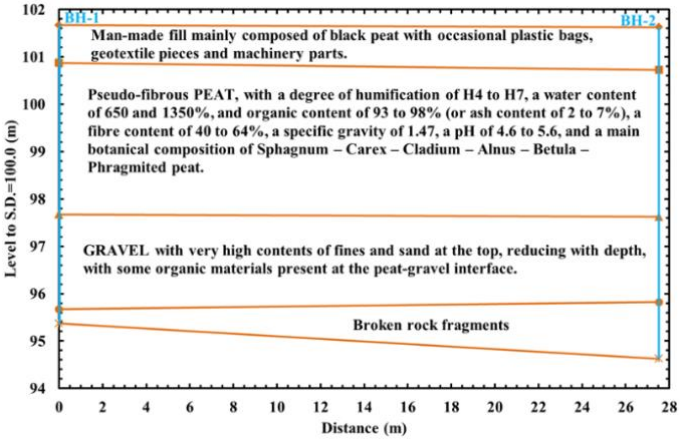

Figure 2. Approximated soil profile at Ballydermot bog [20].

Using the extended von Post system by Hobbs [21] the peat layer classifies as:

$$SCWPh\ H_{4\text{-}7}\ B_{3\text{-}4}\ F_2\ R_2\ W_1\ N_5\ A_0\ pHL$$

According to the ASTM 4427–18 [22], Ballydermot peat can be then classified as: Fibric to Hemic, Low to Medium Ash, Moderately Acidic, Sphagnum – Carex – Cladium – Alnus – Betula – Phragmited peat.

3 RESEARCH METHODOLOGY

The research work carried out was broken into three phases: (i) field testing and sampling, (ii) laboratory testing and (iii) data analysis.

Field testing consisted of the execution of field vane, Mackintosh probe and DCP tests at three selected locations on the Ballydermot Bog site. At each location, the tests were performed near one another. All three tests were carried out at depths ranging from ground level to 3.0m below ground level. Continuous profiles were obtained where possible so that the results from the tests could be compared at similar incremental depths. The general arrangement of the tests carried out is shown schematically in Figure 3.

Peat samples were retrieved from test locations 1 and 2 for laboratory testing. The samples were taken at depths of 0.3m and 1.0m. This allowed a direct comparison between the measurements from the field tests and the laboratory tests. A mechanical excavator was used to dig down to the required sample depths; U100 sampling tubes were then driven into the exposed peat to carefully obtain undisturbed samples of peat at 0.3m and 1.0m below ground level. The samples were extracted and immediately wrapped in plastic wrap to reduce moisture loss, and they were placed in cardboard boxes for transportation to the laboratory.

Four main laboratory tests were carried out on the samples; these included classifying the peat on the von Post scale, measurement of water content, undrained unconsolidated (UU) triaxial testing and laboratory vane testing.

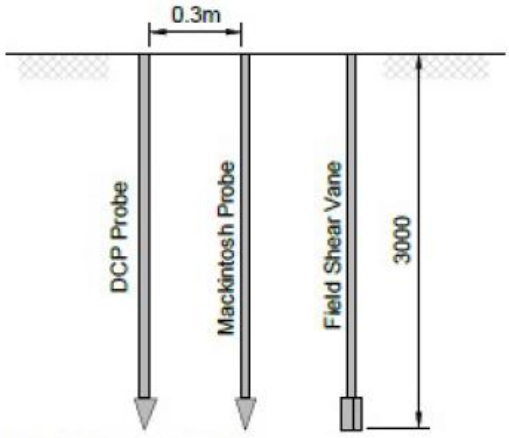

Figure 3. Close proximity of DCP, Mackintosh probe and field vane tests

4 RESULTS AND DISCUSSION

4.1 Field vane tests

Field vane tests were carried out using a Geonor H-60 device. Tests were carried out using the medium and large vanes supplied with the device. The test results are shown graphically in Figure 4.

It is evident from these results that the medium vane gave higher shear strength values than the large vane. This is in keeping with the findings of Radford [9], that the effect of the fibers on the shear strength measured by a field vane generally decreases with increases in the size of the vane. Therefore, the shear strength values measured by the large vane are preferred for data analysis.

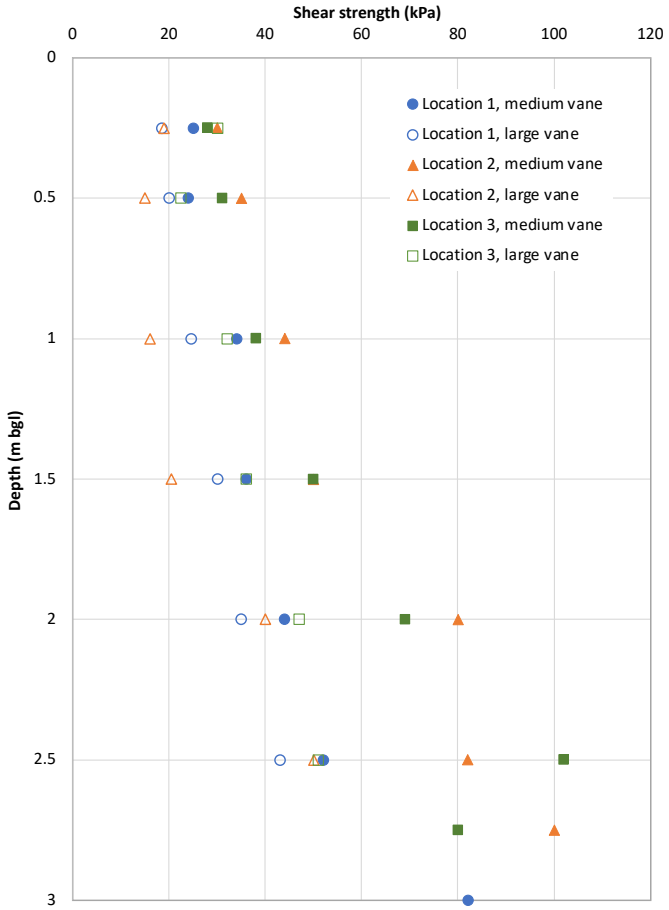

Figure 4. Field vane test results

4.2 Dynamic cone penetrometer test

The DPC tests results gave very low n-values (blows/100mm) for each of the two tests conducted on site (Figure 5). The first single blows resulted in the probe being driven to depths of 630 and 820mm. It was established from the results that the peat layer extended from ground level down to depths of approximately 2.5 to 2.75m at both locations. The n-value at both test locations increased to a maximum of 5, indicating the probe had passed into a stiff clay with an undrained shear strength (s_u) ranging between 50 and 100 kPa [23].

4.3 Mackintosh probe test

The results from the Mackintosh probe tests are shown graphically in Figure 6. The results show similar M-value results, with corresponding probe depths. Similarly to the DCP tests, stiff clay was encountered at depths between 2.4 and 2.75m, resulting in increased M-values.

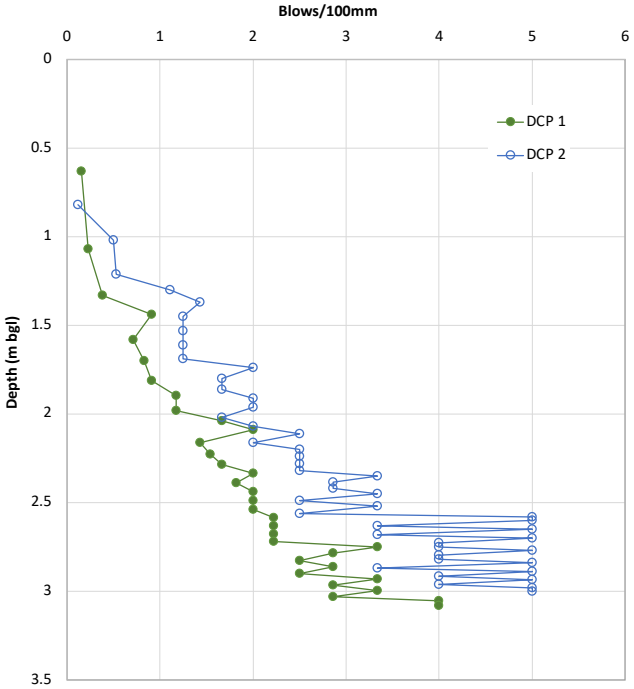

Figure 5. Dynamic Cone Penetrometer Results

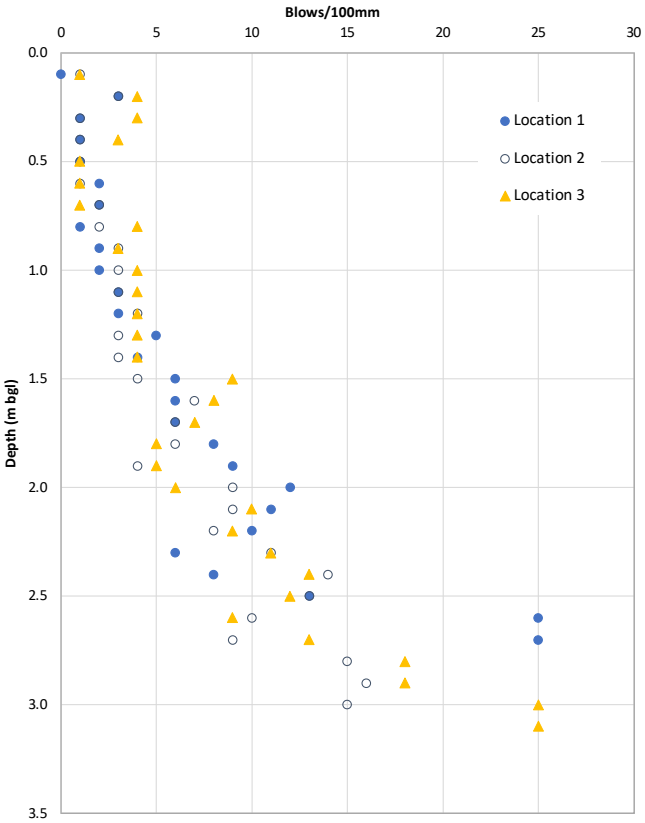

Figure 6. Mackintosh Probe Test Results

It is evident from the Mackintosh probe and the DCP tests that the M-value for peat is higher than the n-value obtained from the DCP test. This suggests that the M-value is more sensitive than n-values to variations in soft soil properties and that the Mackintosh Probe is a more appropriate test to use in

very soft soils such as peat. A correlation between the Mackintosh Probe M-value and the undrained shear strength of peat was established.

4.4 Correlation between s_u and M-value

To develop a correlation between undrained shear strength (s_u) and M-value, the field vane and Mackintosh Probe Tests were conducted on site. The Mackintosh Probe test was carried out at three locations to a maximum depth of three meters. The field vane tests were conducted in close proximity to obtain a good correlation. The M-value, which represents the number of blows taken for every 100mm of penetration of the Mackintosh Probe, was recorded down to a depth of three meters. The shear vane test was performed repeatedly for every increase of 0.5m in depth. A total of 90 data points were obtained from the Macintosh Probe and a total of 18 from the large shear vane tests. A graph of the uncorrected undrained shear strength measured using the field vane (s_u) versus the number of blows (M) was developed to establish the correlation (Figure 7). The resulting power correlation developed is as follows:

$$s_u = 16.54M^{0.373} \quad (1)$$

The resulting coefficient of determination for the proposed correlation equation is 0.765, which is classified as a strong positive correlation.

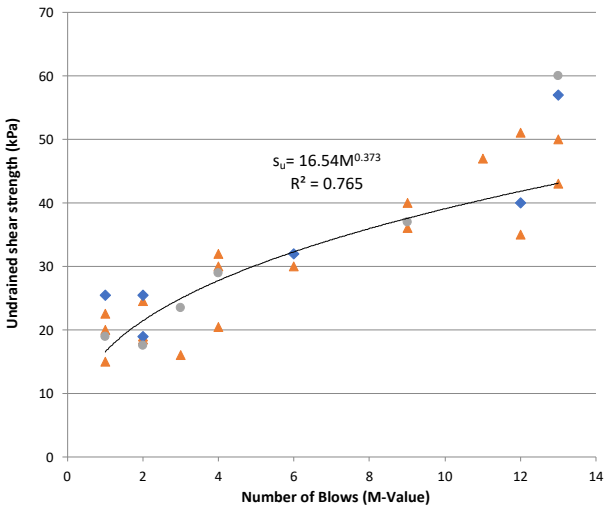

Figure 7. Correlation between s_u and M-value

The results from the proposed correlation between M and s_u were then plotted against the results recorded from the field shear vane tests for each of the three test locations on site (Figure 8, Figure 9 and Figure 10). This undrained shear strength was normalized by total stress (dimensionless). It can be observed from the graphs that the correlation between M and s_u produces results that closely match the uncorrected results of the field vane tests.

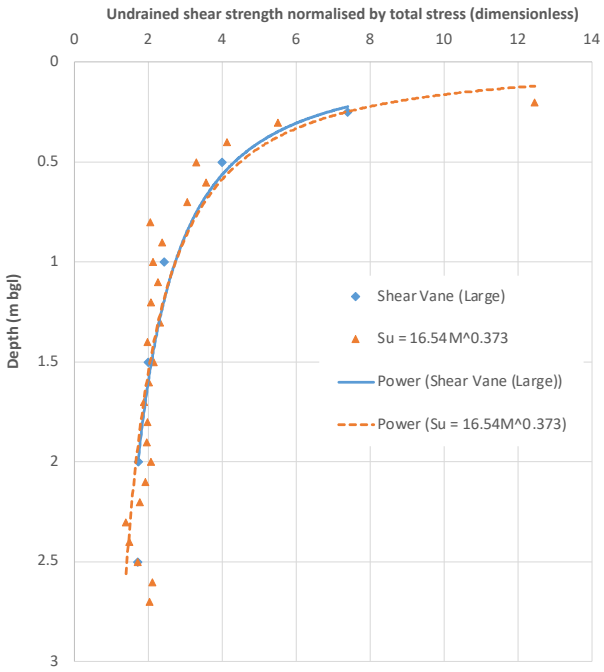

Figure 8. Correlation of M-value and Shear Vane, location 1

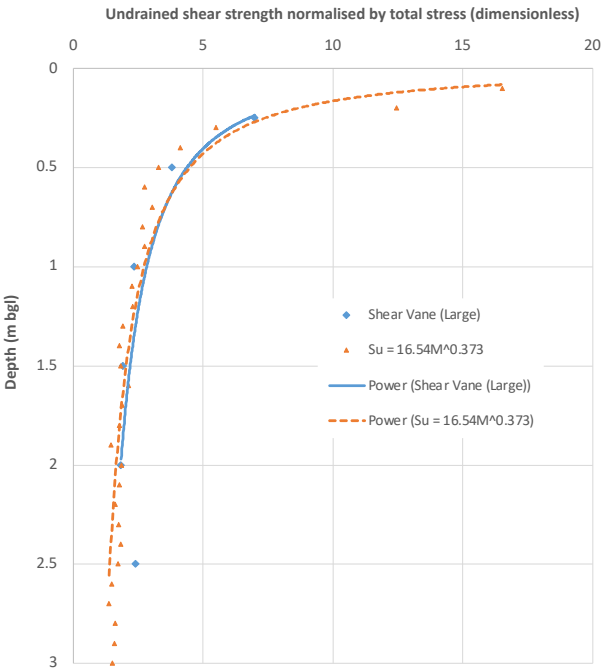

Figure 9. Correlation of M-value and Shear Vane, location 2

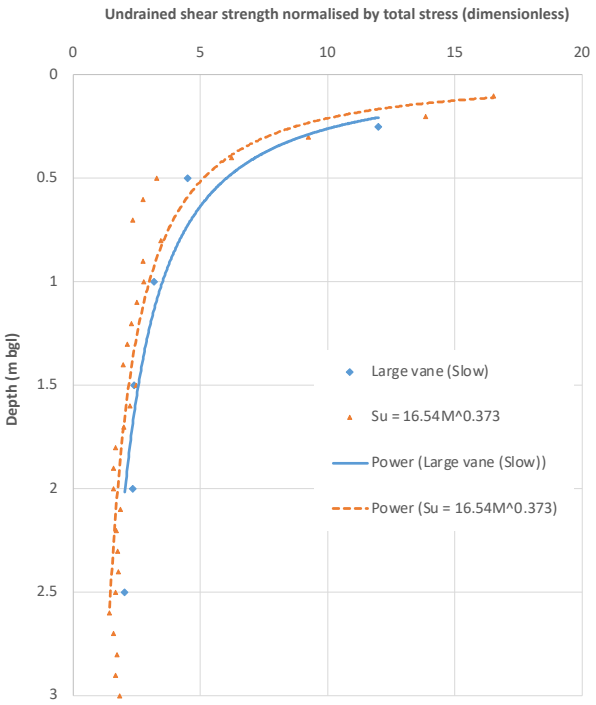

Figure 10. Correlation of M-value and Shear Vane, location 3

4.5 Laboratory testing

Samples of peat were taken at Locations 1 and 2 on site and carefully transported to the TU Dublin soil mechanics laboratory for testing. The samples were taken at depths of 0.3m and 1.0m. This allowed a direct comparison between the measurements from the field tests and the laboratory tests.

4.5.1 Water content

The water content test was conducted on six samples in total using a low-heat oven; three were taken at a depth of 0.3m and three were taken at a depth of 1.0m. The water content for the samples taken at 0.3m ranged between 765-814%; while for samples from 1.0m it ranged between 913-964%.

4.5.2 Von Post classification

The degree of humification of the peat was determined using the von Post system as described by Head [24]. The results of the test indicated that the peat sample could be classified as H3 on the scale, which is in relatively good agreement with what was described in Section 2.

4.5.3 Laboratory vane

Like the water content tests, the laboratory vane tests were conducted on six samples in total; three were from a depth of 0.3m and three from a depth of 1.0m as shown in Table 2. The results indicated an average shear strength of 13.7 kPa at a depth of 0.3m and average shear strength of 8.1 kPa at a depth of 1.0m.

It can be observed from Figure 11 that the laboratory vane test results were consistently lower than the results recorded from field vane tests at similar depths. The suggested reason for this is sample disturbance during extraction and transport, along with possible slight decay of the sample during the short storage in the lab prior to testing. In addition, uncorrected field vane strengths were used, and it is known that the field vane tends to overestimate peat strength [25].

Table 1. Laboratory vane results

Sample Number	Depth (m)	Undrained shear strength (kPa)
1	0.3	14.4
2	0.3	14.5
3	0.3	12.2
Average for depth of 0.3m		**13.7**
4	1.0	9.5
5	1.0	7.0
6	1.0	7.8
Average for depth of 1.0m		**8.1**

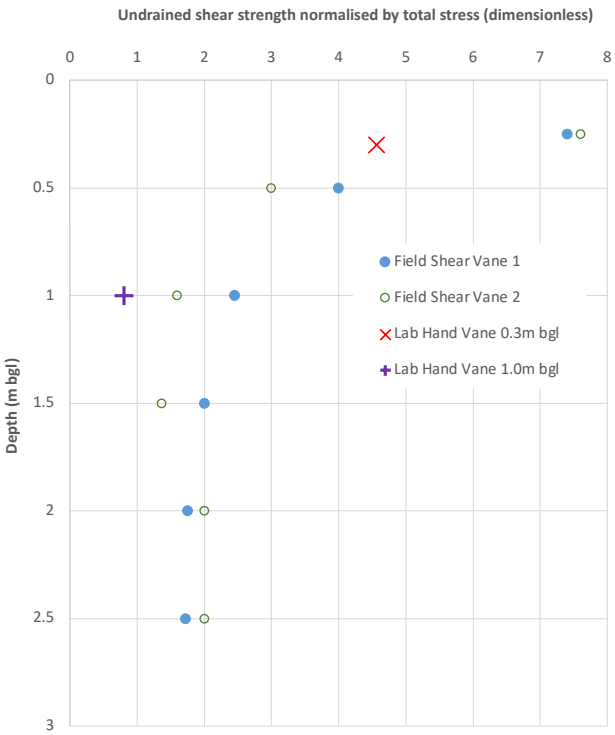

Figure 11. Lab shear vane vs. field shear vane

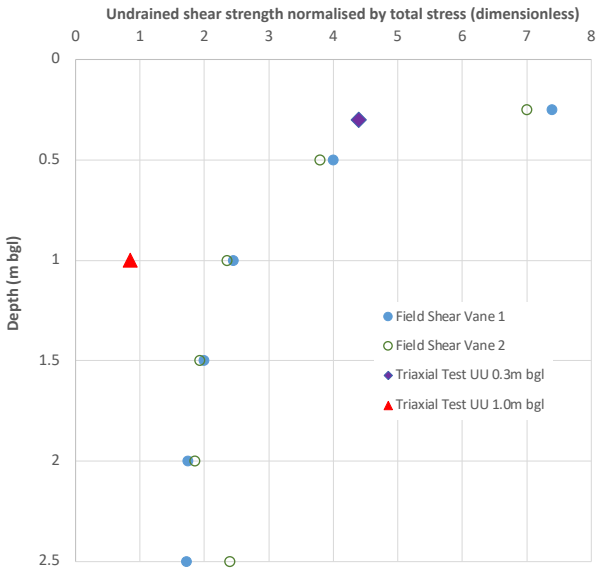

Figure 12. UU triaxial tests vs. field shear vane

4.5.4 Unconsolidated undrained triaxial tests

Unconsolidated undrained (UU) triaxial tests were conducted on six samples in total: three taken at a depth of 0.3m, and three taken at a depth of 1.0m, as indicated in Figure 12. The results recorded from the UU triaxial tests indicated average shear strength of 13.2 kPa at a depth of 0.3m and average shear strength of 8.5 kPa at a depth of 1.0m. It can be observed from Figure 12 that the triaxial test results are lower that the results recorded from field shear vane tests. The results from the triaxial test are very similar to those of the lab shear vane test and follow a similar trend of reducing shear strength with increasing depth. This further strengthens the suggestion that the reason for this is sample disturbance during extraction, transport, and storage in the lab prior to testing.

5 CONCLUSIONS

A program of field and laboratory tests were carried out to investigate the relationship between the undrained shear strength of peat as measured in the field using the field vane and two types of dynamic probe and in the laboratory using the triaxial test and the laboratory vane test. The following conclusions are drawn from the work carried out:

1. From the field vane tests conducted on site, it is evident that the shear strength results from the medium vane are consistently higher than the large vane at each of the three test locations. This suggests that the fibrous nature of peat has a larger effect on the medium vane test results and that the effect of the fibers on the shear vane generally decreases with an increase in the size of the vane.
2. It is evident from the Mackintosh probe and the DCP tests that the M-value for peat is higher than the n-value obtained from the DCP test. This suggests that the M-value is more sensitive than the n-value to variations in soft soil properties and that the Mackintosh probe is a more appropriate test to use in very soft soils such as peat.
3. A correlation between the Mackintosh probe M-value and the uncorrected undrained shear strength as measured by the field vane test was established for peat. This equation is expressed as: $s_u = 16.54M^{0.373}$. This allows the Mackintosh probe to be used as a quick and efficient tool to both profile the depth and assess the undrained shear strength of peat. The Mackintosh probe could also be used to interpolate soil properties between boreholes, reducing the cost of ground investigations.
4. The shear strengths measured by the UU triaxial tests and laboratory vane were consistently lower than the field test results. The results from the triaxial test were very similar to those of the laboratory vane test and also followed a similar trend of reducing shear strength with increasing depth. The reason suggested for the reduced undrained shear strength is sample disturbance during extraction, transport and storage prior to testing.

ACKNOWLEDGMENTS

The authors would like to acknowledge the assistance provided by Mr Conor Keaney (TU Dublin), Mr Ronan Killeen (Irish Drilling Ltd.), Mr Keith Nell (Terratech Consulting), and the staff at Bord na Móna Ballydermot.

REFERENCES

[1] J. P. Osorio, E. R. Farrell, B. C. O'Kelly, and T. Casey, "Rampart Roads in the peat lands of Ireland: Genesis, Development and current Performance," in *Advances in Transportation Geotechnics*, E. Ellis, H.-S. Yu, G. McDowell, A. R. Dawson, and N. Thom, Eds. Nottingham: CRC Press, 2008, pp. 227–233.

[2] E. R. Farrell, "Organic/peat soils," in *ICE Manual of Geotechnical Engineering Volume 1: Geotechnical Engineering Principles, Problematic Soils and Site Investigation*, J. Burland, T. Chapman, H. Skinner, and M. Brown, Eds. London: Institution of Civil Engineers, 2012, pp. 463–479.

[3] F. Celik and H. Canakci, "An Investigation of the Effect of Sand Content on Geotechnical Properties of Fibrous Peat," *Arab. J. Sci. Eng.*, vol. 39, no. 10, pp. 6943–6948, 2014.

[4] J. P. Osorio, "Propiedades Geotécnicas de la Turba Intervenida Antrópicamente," in *Memorias XV Congreso Colombiano de Geología2*, 2015, pp. 673–680.

[5] M. Hendry, "The geomechanical behaviour of peat foundations below rail-track structures," University of Saskatchewan, 2011.

[6] A. O. Landva, P. E. Pheeney, P. La Rochelle, and J. L. Briaud, "Structures on peatland – geotechnical investigations," in *Proceedings of the Advances in Peatlands Engineering Conference*, 1986.

[7] H. Yamaguchi, Y. Ohira, K. Kogure, and S. Mori, "Deformation and strength properties of peat," in *Proceedings of the 11th International Conference on Soil Mechanics and Foundation Engineering*, 1985, pp. 2461–2464.

[8] M. Long, P. Jennings, and R. Carroll, "Irish peat slides 2006-2010," *Landslides*, vol. 8, no. 3, pp. 391–401, 2011.

[9] J. R. Radforth, "Preliminary Engineering Investigations," in *Muskeg Engineering Handbook*, I. C. MacFarlane, Ed. University of Toronto Press, 1969, pp. 127–149.

[10] C. R. I. Clayton, M. C. Matthews, and N. E. Simons, *Site investigation*, 2nd ed. London, U.K.: Blackwell Science, 1995.

[11] J. Whitaker, "Peatland survey 2004: Derrygreenagh bogs, Counties Offaly & Kildae," Department of the Environment, Heritage and Local Goverment, Dublin, 2004.

[12] R. F. Hammond, "Studies into the peat stratigraphy and underlying mineral 'soils' of a raised bog in Ireland," Trinity College Dublin, Dublin, 1969.

[13] E. T. Hanrahan, "An investigation of some physical properties of peat," *Géotechnique*, vol. 4, no. 3, pp. 108–123, 1954.

[14] E. T. Hanrahan, "A Road failure on peat," *Géotechnique*, vol. 14, no. 3, pp. 185–202, 1964.

[15] E. T. Hanrahan and M. G. Rogers, "Road on peat: observations and design," *Am. Soc. Civ. Eng. J. Geotech. Eng. Div.*, vol. 107, no. 10, pp. 1403–1415, 1981.

[16] T. Cuddy, "The behaviour of bog road pavements," Trinity College Dublin, Dublin, 1988.

[17] S. Hebib, "Experimental Investigation on the Stabilization of Irish Peat," Trinity College Dublin, Dublin, 2001.

[18] C. O'Loughlin, "The one-dimensional compression of fibrous peat and other organic soils," Trinity College Dublin, Dublin, 2001.

[19] J. P. Osorio, E. R. Farrell, and B. C. O'Kelly, "Peat improvement under vacuum preloading: a novel approach for bog roads in Ireland," in *Joint Symposium Proceedings, Bridge & Infrastructure Research Ireland and Concrete Research Ireland*, 2010, pp. 255–262.

[20] J. P. Osorio-Salas, "Vacuum consolidation field test on a pseudo-fibrous peat," Trinity College Dublin, 2012.

[21] N. B. Hobbs, "Mire morphology and the properties and behaviour of some British and foreign peats," *Q. J. Eng. Geol.*, vol. 19, no. 1, pp. 7–80, 1986.

[22] American Society for Testing Materials - ASTM, "ASTM D4427-18, Standard Classification of Peat Samples by Laboratory Testing." ASTM International, West Conshohocken, PA, 2018.

[23] B. Look, *Handbook of geotechnical investigation and design tables*. London, U.K.: Taylor & Francis, 2007.

[24] K. H. Head, *Manual of soil laboratory testing - Volume 1: Soil classification and compaction tests*, 3rd ed. Dunbeath: Whittles Publishing, 2006.

[25] A. O. Landva, "Vane testing in peat." *Canadian Geotechnical Journal*, vol. 17, no. 1), pp. 1-19, 1980.

Appraisal of novel power-based extrusion methodology for consistency limits determinations of fine-grained soils

Brendan C. O'Kelly[1]
[1] Department of Civil, Structural and Environmental Engineering, Trinity College Dublin, Dublin D02 PN40, Ireland
email: bokelly@tcd.ie

ABSTRACT: The consistency limits (liquid limit LL and plastic limit PL) are among the most commonly performed tests in geotechnical engineering practice, being used for classification of fine-grained soils and in deducing other parameters (e.g., shear strength, permeability, compressibility), necessary for preliminary design/assessments, via numerous correlations built up over the decades. Depending on geographic region and/or referenced standard, the LL testing is performed using either the fall-cone or Casagrande (percussion-cup) approaches, while Atterberg's PL is universally determined using the thread-rolling method. Because of its dependence on operator judgement regarding the crumbling condition during the rolling-out procedure, the accuracy of the PL test has been called into question by some researchers. This has prompted various alternative proposals, including undrained strength-based fall cone and extrusion approaches, but these are not appropriate for the determination of Atterberg's PL which defines the water content at the plastic–brittle transition point (i.e., not strength-based). This paper presents the culmination of a two-year research project performed at Trinity College Dublin on the investigation and development of a novel power-based extrusion methodology for determination of the consistency limits of fine-grained soils.

KEY WORDS: Atterberg limits; cohesive soil; extrusion; strength; workability.

1 INTRODUCTION

Plasticity of fine-grained soils is considered a function of the liquid limit (LL) and plastic limit (PL), these consistency limit parameters having wide importance for civil/geotechnical engineering and agronomic applications, and in the ceramic industry and brick manufacturing process. The LL, notionally understood as the water content below which fine-grained soil ceases to flow as a liquid, is invariably determined using the fall-cone or Casagrande (percussion-cup) approach. The PL (i.e., the water content at the plastic–brittle transition point) — originally proposed by Atterberg (1911) — identifies a genuine observable transition in soil behaviour, as conventionally determined by rolling-out on a glass plate of soil threads for the standard PL test. Various alternative experimental approaches have been proposed, particularly for PL determination, typically involving variants of the fall-cone approach, but also investigating the extrusion method (see the review papers by O'Kelly (2019, 2021b) and O'Kelly et al. (2018)). Proposed fall-cone approaches define a 'plastic strength limit' PSL (term coined by Haigh et al. (2013)) water content, typically associated with a remoulded undrained shear strength (s_{ur}) value of 100-fold greater than that mobilised at the fall-cone LL (i.e., LL_{FC}) water content. It must be emphasised that the PSL and Atterberg's PL are fundamentally different parameters (Haigh et al., 2013; O'Kelly, 2013; Sivakumar et al., 2016).

Extrusion involves the reduction in cross-sectional area of a billet (fine-grained soil test-specimen for the purposes of this investigation) by forcing it to flow through a die orifice under the action of an extrusion pressure. There are two approaches, direct extrusion and reverse extrusion (see Figure 1); the latter generally being preferred for soil mechanics' applications, since the friction component (mobilised between the test-specimen and the chamber side-wall) associated with direct extrusion does not arise for the reverse extrusion approach.

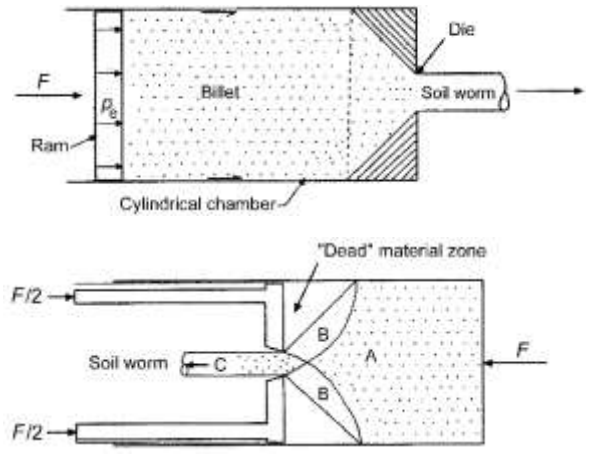

Figure 1. Schematic diagram of typical experimental set-up for (a) direct extrusion, and (b) reverse extrusion (after O'Kelly, 2019).

The first attempts at using the direct and reverse extrusion methods for consistency limits determinations of fine-grained soils were reported by Timár (1974) and Whyte (1982), respectively. Several testing parameters affect the extrusion force F_e (extrusion pressure p_e), such as the cylindrical chamber's geometry/dimensions and extrusion ratio R, the ram displacement rate (velocity), ram–chamber side-wall friction, and (for direct extrusion) the soil specimen–side-wall friction. Note: $p_e = F_e/A_o$ and $R = A_o/A_f$, where A_o is the bore cross-sectional area of the cylindrical chamber and A_f is the die orifice area. The principal material parameter affecting the extrusion

force for testing of fine soil is its undrained shear strength (s_u) (which is dependent on the water content) (O'Kelly, 2019).

Recent research and findings suggest that the conventional extrusion approach, as presently applied, is not suitable (does not provide accurate/reliable experimental results) for consistency limits determinations or s_u measurement of fine-grained soils (O'Kelly, 2019, 2021a). Advocates of the soil extrusion approach argue that these shortcomings can be attributed to limitations of the conventional testing methods for consistency limits and s_u determinations. However, current uncertainties about the conventional extrusion approach for testing of fine-grained soils appear to be far greater (O'Kelly, 2019), including the question of the soil billet's assumed undrained condition, in that, depending on the soil mineralogy and gradation, localised billet consolidation could occur for the combination of slow extrusion (displacement) rates employed and high p_e values required, particularly for stiffer test soils (O'Kelly, 2019). Another important point is that compared to conventional s_u tests (e.g., direct shear (shearbox), undrained triaxial compression), the mechanics of the extrusion method are significantly different, with the process of soil extruding via the die orifice(s) resembling a material 'flow' test (O'Kelly, 2019) — the significant material parameter being the material flow stress. The test soil yields when it enters the shear zone (fan), and it is difficult to see how the material flow stress is not directly related to the s_{ur} parameter. However, based on a reassessment of extensive reverse-extrusion datasets for many hundreds of different fine-grained soils reported in the existing literature, O'Kelly (2019) found that for a given extrusion apparatus and die orifice combination, the p_e magnitudes corresponding to the Casagrande-cup LL, LL_{FC} and Atterberg PL states are not unique, rather the experimental p_e magnitude associated with each of these state parameters can vary over a wide range when considering different test soils, seemingly being dependent on the soil plasticity (plasticity index).

As described in Barnes' PhD dissertation (Barnes, 2013b), various context-specific definitions/criteria of workability exist in different disciplines. For instance, workability is of importance in the ceramics industry (e.g., for assessment of clays used in white-ware production), in the brick manufacturing industry, and in an agricultural context with respect to the efficiency of machinery in ploughing and tilling a clay soil. Workability is also a term associated with freshly made concrete — being assessed using the slump tests (i.e., the ease with which the fresh concrete flows, as evaluated from the stability of the concrete cone). In Soil Mechanics, toughness and workability are interchangeable terms used to explain the resistance to deformation of a soil, being applied to cohesive soils, and mainly clays (Barnes, 2013b; O'Kelly et al., 2022).

2 PROPOSAL OF POWER-BASED EXTRUSION TESTING APPROACH FOR CONSISTENCY LIMITS

Starting from mechanics definitions of work done (W = force × distance; that is, $F\,\Delta x$) and power ($P = W/\Delta t$, where Δt is the time period of soil deformation), it is proposed to investigate the concept of power, in the context of soil extrusion, when developing an alternative approach for consistency limit determinations of fine-grained soils. In other words, the methodology — originally proposed in the MSc research dissertation by Manafighorabaei (2017), and which was supervised by the Author — is that for a particular experimental setup (i.e., extrusion apparatus and die-orifice combination), specific values of power [J/s] could be required to cause extrusion of fine-grained soils to occur at their consistency limits. That is, the particular power values assigned for LL and PL (i.e., $P_{(LL)}$ and $P_{(PL)}$, being obtained from calibration of the extrusion apparatus) could be considered as corresponding to the 'workability' of fine-grained soils at these limit states.

The extrusion apparatus, as a soil deformation system, simply provides the experimental setup for quantification of the billet's resistance to deformation for a given water content w (or liquidity index, I_L) value, with I_L = 0 and 1 for PL and LL, respectively. So, in terms of the definition, power $P = F_e\,\bar{v} = p_e\,A_o\,\bar{v}$, with the average ram velocity $\bar{v} = \Delta x/\Delta t$; Δx being the ram displacement occurring for the extrusion period, Δt. For a given fine-grained soil, the magnitude of F_e increases with decreasing water content w (or I_L) of the soil billet (test specimen). The resistance offered is also dependent on the extrusion ratio, considering the number and combined area of the die orifices through which the soil billet is extruded.

For apparatus calibration, a series of extrusion tests are performed, ideally investigating a range of water contents about each of the conventionally determined LL and PL states. However, from various practicalities of performing the extrusion testing, the investigated water content range may be confined to within the plastic range, and often limited to I_L = 0 to 0.5 (e.g., Kayabali et al. (2015)). From the obtained P–w relationship, the power magnitudes associated with the consistency limit states are established, which may involve extrapolation using linear regression. Based on these calibrated power values, the hypothesis is that, based on the extrusion method, the consistency limit states of a general fine-grained soil could then be established, as follows. Analogous to the semi-logarithmic $s_{ur} - w$ (or I_L) relationship commonly adopted for strength interpolations, the water contents corresponding to the consistency limit states of the test soil could potentially be interpolated from its semi-logarithmic experimental P–w (or I_L) relationship. In the present paper, the 'power' hypothesis is first demonstrated using a purpose-build extrusion apparatus in testing the fine fraction of a Dublin Brown Boulder Clay sample. The veracity of the hypothesis and obtained results are then scrutinised in the context of the conventional consistency limit states (LL and Atterberg PL).

3 TCD EXTRUSION APPARATUS AND POWER-BASED TESTING APPROACH FOR CONSISTENCY LIMITS

This section presents an overview of the purpose-build extrusion apparatus developed in the Department of Civil, Structural and Environmental Engineering, Trinity College Dublin (TCD), over the period March 2015 to February 2017. Full details on the development, proposed testing method and calibration (from testing of 10 fine-grained soils) of the TCD extrusion apparatus are presented in the MSc research dissertation by Manafighorabaei (2017). The purpose of the prototype apparatus (overall 57-cm high × 16-cm square in plan dimensions, as shown in Figure 2) was to experimentally demonstrate the proposed methodology. The direct extrusion method was adopted for its simplicity [the reverse extrusion approach (which negates the soil specimen–side-wall friction effect) could be the subject of investigation in future studies].

Referring to Figure 2, the load (stress) controlled loading (due to the self-weight of the moving ram assembly) applies a constant vertical force F_e (extrusion pressure p_e), via the ram, to the soil billet (remoulded soil paste) contained in the cylindrical chamber, causing downwards extrusion (i.e., direct extrusion) of the soil to occur through the die orifices in the chamber base. A loading hanger and lever arrangement (acting on the ram assembly) may be used to apply greater extrusion force for specimens tested at higher s_{ur}. The vertical movement of the ram is guided by four linear bearings moving along vertical guide rods (see Figures 2 and 3).

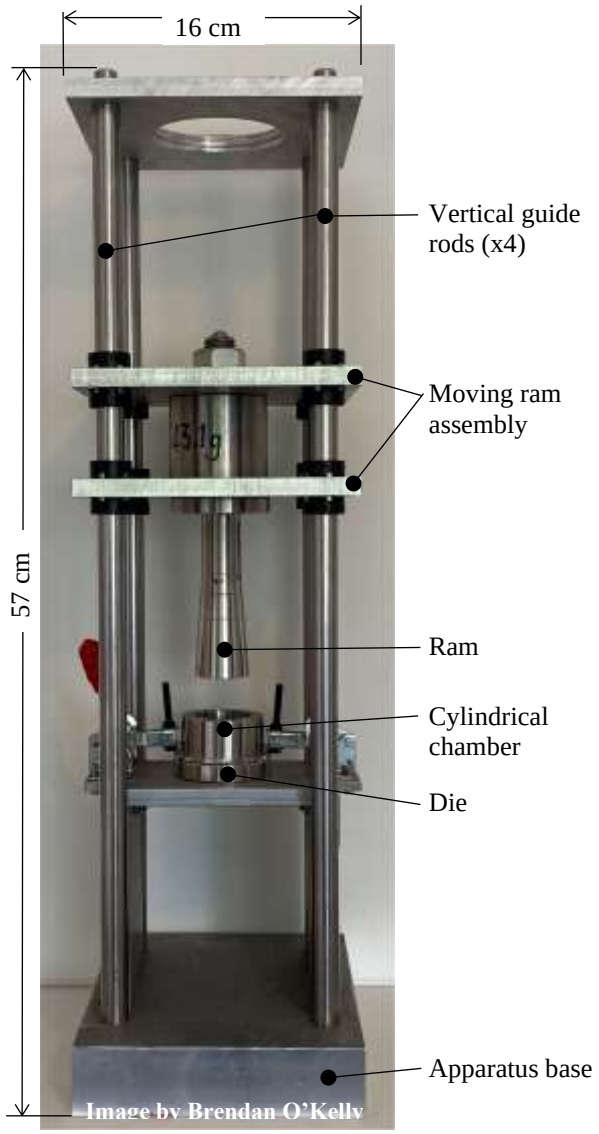

Figure 2. TCD direct-extrusion apparatus for testing fine-grained soils

Referring to Figure 4, the cylindrical chamber has inner diameter and depth dimensions of D = 35 mm and L = 50 mm, respectively; i.e., the short test-specimen length (reducing from 50 mm initially, to zero for full extrusion) means that the billet–side-wall friction effect could be considered negligible. Various die-orifice configurations (i.e., producing different R values) were trialled (full details are presented in Manafighorabaei (2017)) to arrive at suitable experimental set-ups, with consideration of the system's loading capacity and the soil consistency (s_{ur}) range tested when performing extrusion at various water contents, including about the consistency limit states. The configurations finally adopted for investigating the LL and PL states using the TCD extrusion apparatus were seven distributed die orifices, each of 5-mm and 10-mm in diameter, respectively (i.e., producing extrusion ratios of R = 7.0 and 1.75, respectively). Figure 4 shows the cylindrical chamber and die combination employed for LL testing.

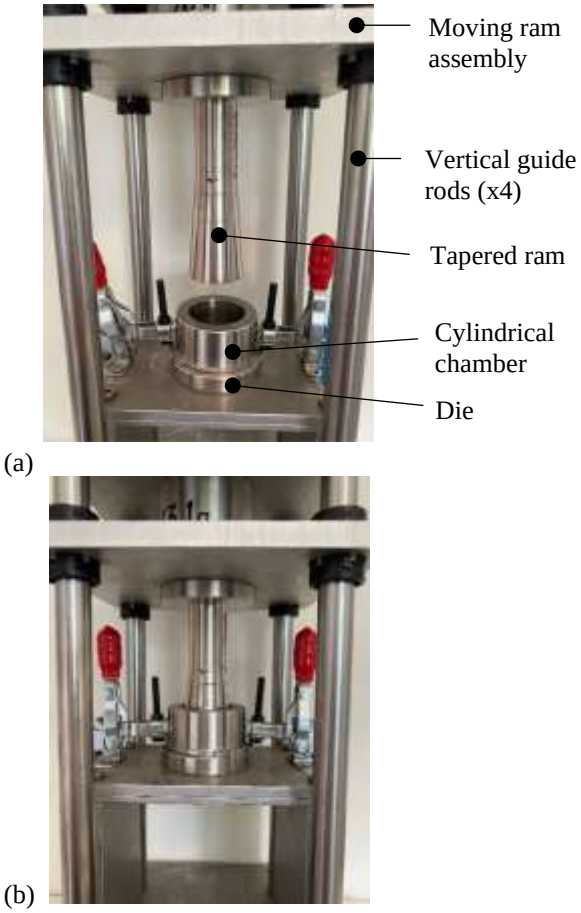

Figure 3. Photographs of TCD extrusion apparatus showing: (a) ram located above cylindrical chamber; (b) ram at full penetration of chamber.

Figure 5 shows the placement of the chamber–die combination in the extrusion apparatus. A small clearance (gap) between the chamber's inner wall surface and penetrating ram prevents friction developing between them. The ram is also tapered (reducing in diameter along its length) for this purpose.

Based on testing of ten fine-grained soils, as reported in Manafighorabaei (2017), the calibration procedure for the TCD extrusion apparatus, with presented die orifice combinations, resulted in $P_{(LL)}$ = 0.171 J/s and $P_{(PL)}$ = 0.749 J/s being tentatively assigned for the LL_{FC} (i.e., 30°–80 g cone) and PL. Furthermore, extrusion pressures of $p_{e(LL)}$ = 35.6 kPa and $p_{e(PL)}$ = 495.4 kPa, as described in Manafighorabaei (2017), were tentatively assigned for the LL_{FC} and PL, respectively.

In performing the extrusion testing, the cylindrical chamber is completely filled with the remoulded fine-grained soil sample under investigation (i.e., initially L = 50 mm). The deformation work is given by the area under the experimental p_e vs. Δx curve, with the p_e magnitude (applied as maintained

load F_e) remaining approximately constant throughout the extrusion test. In applying the proposed power-based extrusion approach for consistency limits determinations, taking LL_{FC} for demonstration purposes; with P = 0.171 J/s, $p_{e(LL)}$ = 35.6 kPa, and A_o = 962 mm^2, the average ram velocity can be calculated as $\bar{v} = P/p_e\ A_o$ = 5.0 mm/s. Similarly, the average ram velocity for the PL would be calculated as $\bar{v}$ = 1.67 mm/s. It is emphasised that these values of P and $\bar{v}$ specifically relate to the TCD extrusion apparatus and die-orifice combinations employed in the present study (different configurations would require separate calibration and will have different P and $\bar{v}$ value combinations associated with the consistency limits). Note the methodology presented in Manafighorabaei (2017), and implemented in the present paper, has been modified to produce a larger and more complex soil-extrusion device (with pneumatic-actuator loading system) and 'workability' methodology, as presented in the paper by Manafi et al. (2022).

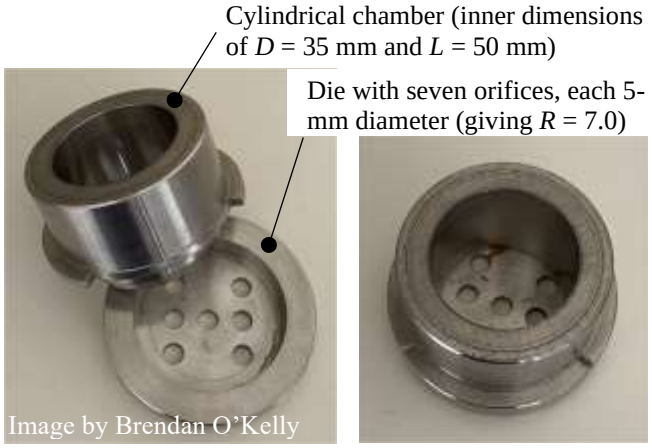

Figure 4. Chamber and die combination for LL testing in TCD extrusion apparatus: disassembled (left); assembled (right).

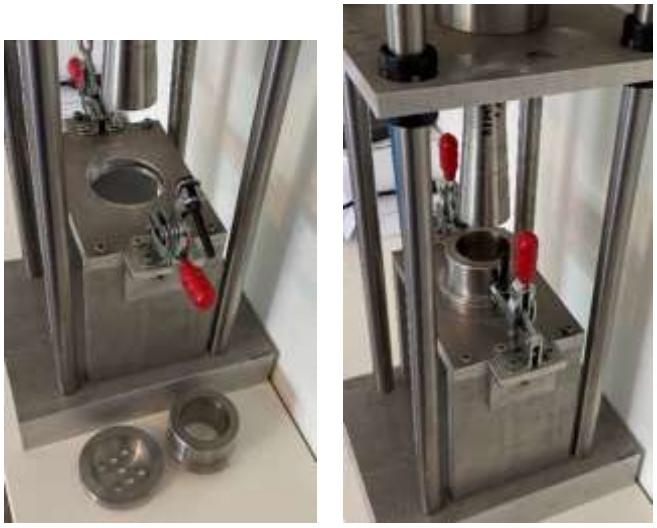

Figure 5. Placement of chamber and LL die combination in TCD extrusion apparatus: unassembled (left); assembled (right).

Hence, in essence, adopting a ram displacement of Δx = 50 mm (i.e., the ram penetrates to the full depth of the cylindrical chamber) for both consistency limits, the operator performs separate extrusion experiments for various (typically 4) water contents about the investigated consistency limit (LL or PL), with the associated extrusion time (Δt) for each water content measured using a stopwatch. Note, because of difficulties in filling the cylindrical chamber to produce a saturated soil specimen for testing at water contents around the PL on account of the material's stiff consistency, it is common practice to perform the testing over a range of higher water contents and then to use extrapolation for interpolation of values associated with lower (in this case the PL) water content (see the review papers by O'Kelly (2013, 2021b) and O'Kelly et al. (2018)).

Hence, the presented power-based extrusion methodology determines that, for the TCD extrusion apparatus and die-orifice combinations, the values of the LL_{FC} and PL could be determined as the water contents corresponding to Δt (= $\Delta x/\bar{v}$) of 10 and 30 s, respectively, as established from interpolation (or extrapolation) of the best-fit regression lines fitted to the experimental data points in a Log Δt vs. water content plot.

4 DEMONSTRATION OF CONSISTENCY LIMITS DETERMINATIONS USING PROPOSED POWER-BASED EXTRUSION APPROACH

Figure 6 presents experimental data from testing of the fine fraction of a Dublin Brown Boulder Clay sample that demonstrates the implementation of the proposed power-based extrusion methodology for consistency limits determinations. The soil investigated had an LL_{FC} of 34.6% (30°–80 g cone) and Atterberg PL of 18.9%, determined in accordance with BS EN ISO 17892-12:2018+A1:2021 (2021), from which the soil is classified as clay of low plasticity (CL). All the presented testing was performed by an independent experienced operator. Some noise (evident in the experimental data) can be attributed to apparatus friction due to fabrication limitations. Unlike in Figure 6(a), where the LL is within the range of the four measurements, the soil was not tested in the range where the PL was found (owing to the soil's stiff consistency that made it difficult to prepare a saturated test specimen); thus, the associated value was extrapolated using linear regression (see Figure 6(b)).

Overall, it could appear that for this particular test soil, good agreement is found between the standard consistency limits and those derived using the proposed power-based extrusion methodology, especially for the LL parameter. While this could be expected for LL_{FC} determination, as explained in the next section, this generally would not be the case for Atterberg PL when investigating a range of different fine-grained soils.

5 DISCUSSION: CRITICAL ASSESSMENT OF POWER-BASED EXTRUSION METHODOLOGY FOR CONSISTENCY LIMITS DETERMINATIONS

The hypothesis is that for a given extrusion apparatus and die-orifice combination, specific values of power [J/s] can be assigned to the consistency limits of fine-grained soils. With the deformation work given by the area under the p_e vs. Δx curve, and for the p_e (F_e) magnitude remaining approximately constant throughout the extrusion process, the proposed power-based extrusion approach is essentially a strength-based method, as explained previously in the paper by O'Kelly (2019). Hence, the power-based methodology can be expected to produce good experimental agreement with (i.e., comparable

results as obtained by) the LL_{FC}, since the latter is also a strength-based parameter (O'Kelly et al., 2018). However, this would generally not be expected for Atterberg's PL, since different fine-grained soils invariably mobilise different s_{ur} at their Atterberg PL water contents (Haigh et al., 2013; O'Kelly, 2013; O'Kelly et al., 2018, 2022), and hence different p_e ($= s_{ur}/A_o$), and also different p_e/s_{ur} (O'Kelly, 2019, 2021a) at their Atterberg PL water contents. Furthermore, different fine-grained soils invariably have different toughness at their Atterberg PL water contents (Barnes, 2009, 2013a, 2013b; Moreno-Maroto and Alonso-Azcárate, 2018; O'Kelly, 2019; O'Kelly et al. 2022). Typically, at (just above) Atterberg's PL, silty and sandy soils have slight toughness, whereas low to medium plasticity soils (e.g., silty clays) have medium toughness, and high plasticity clay soils have high toughness. For instance, employing a thread-rolling device developed to measure soil toughness, Barnes (2013a) presented results for many different cohesive soils that showed the toughness at their Atterberg PL water contents can vary over a wide range.

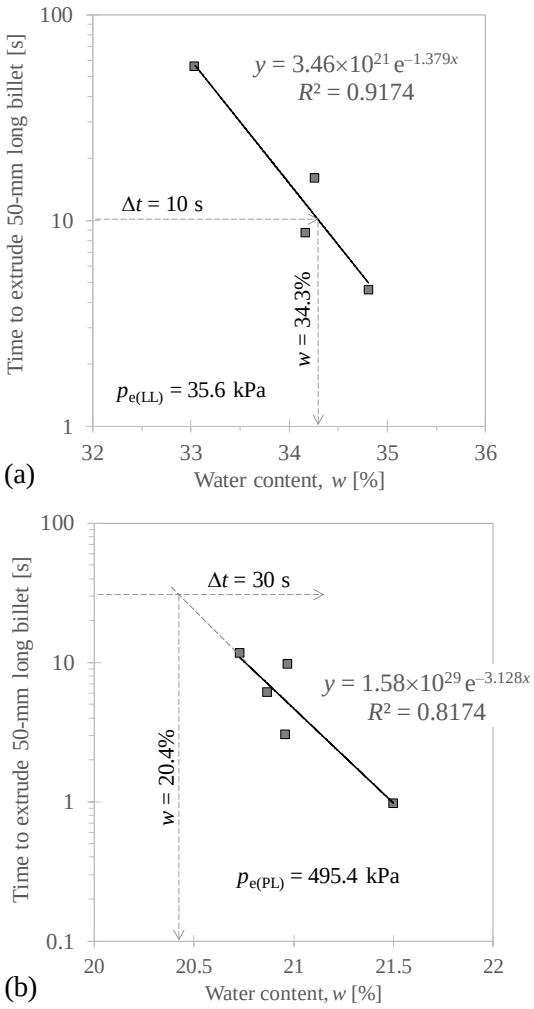

Figure 6. Consistency limits determinations for fine fraction of Dublin Brown Boulder Clay (LL_{FC} = 34.6% and Atterberg's PL = 18.9%) using proposed power-based approach and TCD extrusion apparatus: (a) liquid limit; (b) plastic limit.

Since Atterberg's PL (i.e., the water content at which soil becomes brittle, as determined using the standard thread-rolling method) does not relate to a defined s_{ur} magnitude (Haigh et al., 2013; O'Kelly et al., 2018, 2022; O'Kelly, 2021b), the power-based extrusion methodology is clearly not appropriate for defining the Atterberg PL condition (O'Kelly et al., 2022). However, as a strength-based method, the proposed power-based methodology would be suited for determination of a PSL parameter. Using equation (1), after Johnson (1957), the s_{ur} magnitude for soil direct-extruded using the TCD extrusion apparatus and methodology can be related to the steady-state extrusion force F_e (ignoring rate effects). Considering the presented TCD extrusion apparatus and power-based approach for consistency limits determinations, undrained strengths of s_{ur} = 3.5 kPa (F_e of ~34.2 N) and 151 kPa (F_e of ~476.6 N) can be associated with the LL_{FC} and deduced PSL, respectively. It is noted that the s_{ur} of 151 kPa (for the PSL defined in the present study) fits nicely with the average s_{ur} of 152 kPa (standard deviation of 89 kPa) deduced by Haigh et al. (2013) in analysing data of s_{ur} at the Atterberg PL water contents for 71 different fine-grained soils.

$$s_{ur} = \frac{2\,F_e}{\pi D^2\left[a + b\,\ln R + \frac{L}{D}\right]} \quad (1)$$

where R = extrusion ratio; D and L = cylindrical chamber's inner diameter and depth, respectively; a and b = empirical coefficients dependent on the die angle (for 90° die angle of the TCD cylindrical chamber, a = 0.8 and b = 1.5 (Johnson, 1957)).

6 CONCLUSIONS AND RECOMMENDATIONS

This paper presented the TCD extrusion apparatus and proposed power-based methodology for determination of the consistency limits of fine-grained soils. The methodology was demonstrated for testing of one soil, and involved an extrapolation of the results (at PL). It was explained that the methodology can essentially be viewed as strength-based, and would be appropriate for determination of the LL (i.e., LL_{FC}) and a PSL; the latter based on a mobilised s_{ur} of ~151 kPa. However, as it is strength-based, the proposed approach cannot be used to determine Atterberg's PL (i.e., the water content at the plastic–brittle transition point), which is definitively established using the standard thread-rolling test (Haigh et al., 2013; O'Kelly et al., 2018, 2022). Considering the presented prototype, various recommendations are made for developing an improved extrusion apparatus, as follows:

- For the power calculations, it would be better to consider a ram displacement Δx that does not involve the ram entering the 'dead' material zone of the cylindrical chamber.
- While the s_{ur} of 3.5 kPa at LL_{FC} could be deemed acceptable, the extrusion apparatus and method can be refined to achieve an s_{ur} of ~ 1.7 kPa, this value being generally associated with the (30°–80 g cone) LL_{FC} water content (O'Kelly et al., 2018; O'Kelly, 2021b).
- There might be scope to adjust the extrusion apparatus and pressures to allow a relatively small range of extrusion velocities ($\bar{v}$) for testing at water contents close to the consistency limits (LL_{FC}).

Finally, it is hypothesised that the power-based extrusion methodology could potentially serve as an alternative means of classifying fine-grained soils (based on the power magnitudes

required to cause extrusion at their Atterberg PL water contents). Further research is merited on this aspect.

ACKNOWLEDGEMENTS

Eoin Dunne performed the extrusion (results presented in Figure 6) and consistency limits testing for the Dublin Boulder Clay. Seyedmasoud Manafighorabaei (M.S.G. Manafi) was in receipt of a Postgraduate Research Scholarship award from Trinity College Dublin (2015–2017) during the period of his MSc research.

ABBREVIATIONS

LL	Liquid limit
PL	Plastic limit
PSL	Plastic strength limit

NOTATION

a	Empirical extrusion coefficient
A_f	Die orifice area
A_o	Bore cross-sectional area of cylindrical chamber
b	Empirical extrusion coefficient
D	Inner diameter of cylindrical chamber
F_e	Extrusion force
I_L	Liquidity index
L	Inner depth of cylindrical chamber
LL_{FC}	Liquid limit determined by fall-cone test
p_e	Extrusion pressure
$p_{e(LL)}$	Extrusion pressure for liquid-limit water content
$p_{e(PL)}$	Extrusion pressure for the plastic strength limit
P	Power ($= W/\Delta t$)
$P_{(LL)}$	Power value assigned for liquid-limit water content
$P_{(PL)}$	Power value assigned for plastic strength limit
PL_x	Plastic strength limit defined by x-fold increase in undrained strength from fall-cone liquid limit water content
R	Extrusion ratio ($= A_o/A_f$)
s_u	Undrained shear strength
s_{ur}	Remoulded undrained shear strength
$\bar{v}$	Average ram velocity ($= \Delta x/\Delta t$)
W	Work done ($= F\,\Delta x$)
Δt	Time period of extrusion
Δx	Ram displacement

REFERENCES

[1] Atterberg A (1911) Die plastizität der tone. *Internationale Mitteilungen der Bodenkunde* 1: 4–37. (In German)

[2] Barnes GE (2009) An apparatus for the plastic limit and workability of soils. *Proceedings of the Institution of Civil Engineers – Geotechnical Engineering* 162(3): 175–185, https://doi.org/10.1680/geng.2009.162.3.175

[3] Barnes GE (2013a) An apparatus for the determination of the workability and plastic limit of clays. *Applied Clay Science* 80–81: 281–290, https://doi.org/10.1016/j.clay.2013.04.014

[4] Barnes GE (2013b) *The Plastic Limit and Workability of Soils*. PhD thesis, University of Manchester, Manchester, UK.

[5] BS EN ISO 17892-12:2018+A1:2021 (2021) *Geotechnical investigation and testing. Laboratory testing of soil. Determination of liquid and plastic limits*. BSI, London, UK.

[6] Haigh SK, Vardanega PJ and Bolton MD (2013) *The plastic limit of clays*. Géotechnique 63(6): 435–440, https://doi.org/10.1680/geot.11.P.123

[7] Johnson W (1957) The pressure for the cold extrusion of lubricated rod through square dies of moderate reduction at slow speeds. *Journal of the Institute of Metals* 85: 403–408.

[8] Kayabali K, Akturk O, Fener M, Dikmen O and Harputlugil FH (2015) Revisiting the Bjerrum's correction factor: use of the liquidity index for assessing the effect of soil plasticity on undrained shear strength. *Journal of Rock Mechanics and Geotechnical Engineering* 7(6): 716–721, https://doi.org/10.1016/j.jrmge.2015.07.003

[9] Manafighorabaei S (2017) *Soil Plasticity Determination Using Manafi Method and Apparatus*. MSc thesis, University of Dublin, Trinity College Dublin, Dublin, Ireland, http://hdl.handle.net/2262/81676

[10] Manafi MSG, Deng A, Taheri A, Jaksa MB and HB N (2022) Determining soil plasticity utilizing Manafi method and apparatus. *Geotechnical Testing Journal* 45(4): 797–818, https://doi.org/10.1520/GTJ20210235

[11] Moreno-Maroto JM and Alonso-Azćarate J (2018) What is clay? A new definition of "clay" based on plasticity and its impact on the most widespread soil classification systems. *Applied Clay Science* 161: 57–63, https://doi.org/10.1016/j.clay.2018.04.011

[12] O'Kelly BC (2013) Atterberg limits and remolded shear strength–water content relationships. *Geotechnical Testing Journal* 36(6): 939–947, https://doi.org/10.1520/GTJ20130012

[13] O'Kelly BC (2019) Reappraisal of soil extrusion for geomechanical characterisation. *Geotechnical Research* 6(4): 265–287, https://doi.org/10.1680/jgere.19.00006

[14] O'Kelly BC (2021a) Discussion of "Strength and consolidation characteristics for cement stabilized cohesive soil considering consistency index" by Ahmed F. Zidan, published in Geotechnical and Geological Engineering, https://doi.org/10.1007/s10706-020-01367-6. *Geotechnical and Geological Engineering* 39(6): 4659–4662, https://doi.org/10.1007/s10706-021-01763-6

[15] O'Kelly BC (2021b) Review of recent developments and understanding of Atterberg limits determinations. *Geotechnics* 1: 59–75, https://doi.org/10.3390/geotechnics1010004

[16] O'Kelly BC, Vardanega PJ and Haigh SK (2018) Use of fall cones to determine Atterberg limits: a review. *Géotechnique* 68(10): 843–856, https://doi.org/10.1680/jgeot.17.R.039

[17] O'Kelly BC, Moreno-Maroto JM and Alonso-Azćarate J (2022) Discussion of "Determining soil plasticity utilizing Manafi method and apparatus" by Masoud S. G. Manafi, An Deng, Abbas Taheri, Mark B. Jaksa, and Nagaraj HB. *Geotechnical Testing Journal* (In Press).

[18] O'Kelly BC, Vardanega PJ and Haigh SK (2022) Discussion of "Mohajerani method: tool for determining the liquid limit of soils using fall cone test results with strong correlation with the Casagrande test" by E. Hrubesova, B. Lunackova and M. Mohyla [Engineering Geology 278 (2020) 105852]. *Engineering Geology* 302: 106623, https://doi.org/10.1016/j.enggeo.2022.106623

[19] Sivakumar V, O'Kelly BC, Henderson L, Moorhead C, Chow SH and Barnes GE (2016). Discussion: Measuring the plastic limit of fine soils: an experimental study. *Proceedings of the Institution of Civil Engineers – Geotechnical Engineering* 169(1): 83–85, https://doi.org/10.1680/jgeen.15.00068

[20] Timár A (1974) Testing the plastic properties of cohesive- and intermediate-type soils by extrusion. *Acta Technica Academiae Scientiarum Hungaricae* 76(3–4): 355–370.

[21] Whyte IL (1982) Soil plasticity and strength — a new approach using extrusion. *Ground Engineering* 15(1): 16–24.

AUTHOR BIOGRAPHY

Dr. Brendan O'Kelly has worked in academia and geotechnical engineering practice since graduating as a civil engineer from UCD in 1992. In 2001, he joined the Department of Civil, Structural and Environmental Engineering, Trinity College Dublin, where he is presently an Associate Professor and Fellow of Trinity College Dublin (FTCD, 2010). His main research interests are soil consistency limits, ground improvement, geotechnics of water- and wastewater-treatment sludges, and the geomechanical behaviour/properties of peat and other highly organic soils, on which he has authored more than 120 refereed journal papers. He is an Associate Editor for the journals *Environmental Geotechnics* (ICE) and *Geotechnics* (MDPI), and is a serving council member of the International Society of Environmental Geotechnology.

The C2C project and geotechnical characterisation of carbonate-bearing soil ahead of biomineralisation treatment.

Maria Judge[1], Mike Long[2], Shane Donohue[3], Frank McDermott[4].
[1,2,3] School of Civil Engineering, University College Dublin, Newstead Belfield, Dublin 4.
[4] School of Earth Sciences, University College Dublin, Science Centre Belfield, Dublin 4.
email: maria.judge1@ucdconnect.ie, mike.long@ucd.ie

ABSTRACT:

The C2C project is a collaboration between the Irish Centre for Research in Applied Geoscience (iCRAG), the American Centre for Bio-mediated and Bio-inspired Geotechnics (CBBG), and Northern Ireland's Energy Efficient Materials Research Centre (EEM). Entitled 'Multi-scale investigation of bio-based mineral precipitation in carbonate-bearing granular soils and construction related waste', the project will further the study of biomineralisation treatments previously trialled primarily using silica sands. Biomineralisation works by speeding up the natural processes of calcium carbonate precipitation performed by uratolytic bacteria. The resulting mineral growth ultimately forms bonds between soil particles, thus improving the engineering characteristics of problematic soils by reducing permeability and increasing shear strength and stiffness.
Carbonate-bearing granular soil obtained from a quarry at Blessington, Co Wicklow in 2020 and 2021 has been analysed to determine the suitability of this material for biomineralisation treatment. This soil is a dense over-consolidated silty fine sand. It comprises lithic fragments of carbonates derived from the local limestones and granitic minerals from the Leinster Granite.
This presentation sets out to describe the project in detail and discuss the types of biomineralisation that will be trialled on Irish-type glacially deposited carbonate-bearing soils. It will also outline the key geotechnical parameters of the Blessington soil obtained ahead of biomineralisation treatment. Both miso and macro scale biomineralisation treatments using MICP and EICP are planned to take place once geotechnical characterisation is complete.

KEY WORDS: Geotechnical engineering; Soil characterisation; Carbonate-bearing soil; Biomineralisation; Bio-mediated; Bio-inspired; Soil remediation; Ground improvement; Microbial induced calcite precipitation; Enzyme induced calcite precipitation.

1 INTRODUCTION

Interdisciplinary research in the fields of microbiology, geochemistry and civil engineering are facilitating exploration into bio-mediated and bio-inspired soil improvement [1]. Microbial Induced Calcite Precipitation (MICP), which is bio-mediated, and Enzyme Induced Calcite Precipitation (EICP), which is bio-inspired, are innovative soil remediation techniques that fuse soil particles together by growth of calcite. Using biomineralisation processes that occur in nature, both MICP and EICP rely on the hydrolysis of urea in a calcium-rich environment to produce NH_4^+ and $CO^2{}_3^+$. MICP treatment is aided by the addition or stimulation of urolithic bacteria in the soil that in turn produce urease enzyme, whereas in EICP treatment, the urease enzyme is obtained from plants. During both treatment processes, carbonate ions in the presence of calcium ions, precipitate calcite on the surface of sand particles, thus forming bonds between the particles that strengthen the soil's engineering properties [1-6].

To date, research into MICP and EICP has primarily been conducted on silica sand. Some research has focused on two MICP treatment types and the resulting calcium carbonate bonds between individual soil particles for both silica and carbonate sands [7]. Inspired by problems with pile instillation in calcareous marine sand deposits, studies have also investigated aspects of the MICP process on calcareous marine sand [8-12].

The C2C project is novel in its endeavour to extend the domain of MICP and EICP as a ground improvement technology. Material currently under investigation include silica and calcareous sands. C2C aims to trial MICP and EICP techniques on both carbonate soils derived from Limestone found in terrestrial Quaternary deposits and ubiquitous carbonate-bearing construction waste.

Carbonate-bearing soil presents a challenge in Ireland where much of the country is covered by weak unlithified glacial and fluvio-glacial Quaternary sediments. Thus a test site was established at Blessington, where a large Quaternary glacio-lacustrine sand deposit is under excavation. As a prelude to multiscale investigation of bio-based mineral precipitation treatment of this carbonate-bearing soil, a suite of geotechnical studies were carried out to establish key engineering parameters. Geological and geochemical properties of the soil were also investigated. A summary of the results are presented here with an outline of future work.

2 PROJECT OVERVIEW

2.1 *The C2C project*

C2C stands for Centre To Centre, the C2C project brings three centres of research together: The NSF-funded Centre for Bio-mediated and Bio-inspired Geotechnics (CBBG) based in the United States, the SFI-funded Irish Centre for Research in Applied Geoscience (iCRAG) based in Ireland, and Queen's

University Belfast Energy Efficient Materials Research Centre (EEM) based in Northern Ireland. One of the project's goals is to transfer knowledge and technology for bio-based ground improvement technologies from CBBG to iCRAG and EEM. Together the group endeavour to develop and optimise approaches for the characterisation of MICP and EICP treated deposits in carbonate-bearing soils. It is hoped this joint research will accelerate the development and industry adoption of MICP and EICP as a cost effective and sustainable technique for improving the engineering properties of carbonate bearing soils and waste materials, while reducing Portland cement usage.

2.2 *Site and soil selection*

A site comprising suitable material was identified at the Blessington Quarry as the testbed for the project. This is a sand quarry site on the outskirts of Blessington village, 25 km southwest of Dublin City. Summaries of the geological background and geotechnical characteristics of the site indicate the suitability of the carbonate bearing fine sand here [13-18]. The site has been used by researchers for testing various foundation systems and geotechnical site investigation tools.

Glacial action and the recent removal by quarrying of the upper 15 m of overburden material has resulted in the sand being in a heavily over-consolidated state, with a relative density of the sand close to 100% [19]. Particle size distribution analyses indicate grading of the material varies from that of silty sand (mean grain size, D_{50} = 0.10 mm) to that of coarse sand (D_{50} = 0.32 mm). The sand has a fines content (percentage of clay and silt particles) between 4 and 13% [14-16]. At the main "upper" test area, the water table is approximately 13 m below ground level [15].

Field observations at Blessington and at other sites close to Dublin where limestone clast-bearing glacio-lacustrine and fluvio-glacial sands and gravels are extracted for aggregates, reveal that partial cementation of the gravels by calcium carbonate is a natural phenomenon, locally producing near total occlusion of the pore space and partial lithification. These observations indicate that the biogeochemical conditions favourable for MICP and EICP occur at least locally at shallow depths (upper few metres) within these limestone-bearing deposits.

A site investigation was initiated in 2020 to ascertain ground conditions at alternative locations within the quarry than those previously studied. This is in order to understand the varied soil conditions within the quarry area in which testing is permitted, so as to target optimum soil for testing and treatment. Geophysical site investigations included Ground Penetrating Radar GPR, Electrical Resistivity Tomography (ERT) and Multichannel Analysis of Surface Waves (MASW) profiles. Cone Penetration Tests CPT and Seismic Cone Penetration Testing (sCPTu) were conducted. Two boreholes were drilled and a standpipe fitted. Optimum material for treatment was identified in an operational part of the quarry. This soil is similar in geotechnical characteristics to soil previously studied. Samples were machine excavated, recovered and returned to the laboratory at the School of Civil Engineering at University College Dublin for further analysis. Batches of the material were also sent to project partners at UC Davis, Georgia Institute of Technology and Arizona State University for comparative analysis.

3 SOIL ANALYSIS

The granular carbonate bearing soil retrieved from the Blessington quarry was originally deposited in a subaqueous environment in which soil particles settled in interlaminated and cross-laminated sedimentary beds of particle sizes ranging from clay to fine sand [17, 18]. The individual sedimentary beds record variations in current strength during deposition. By the process of sample extraction the soil was disturbed and was retrieved unintentionally homogenised.

Geotechnical soil fabric, soil stress state, hydraulic conductivity and particle characteristics were ascertained by conducting laboratory analysis at University College Dublin's School of Civil Engineering soils laboratory. Some results are summarised below in Section 3.1 and Table 1.

Geological laboratory analysis designed to establish the soil mineralogy, provenance and particle surface textures were conducted in UCD's School of Earth Sciences. Geological analysis include microscope analysis, optical petrography, Scanning Electron Microscopy (SEM) and Energy-dispersive X-ray spectrometer (EDS) Spectrometry.

3.1 *Geotechnical soil analysis and properties*

To date, only a few studies have focused on improving the engineering properties of carbonate soil by MICP or EICP treatments. The primary objective of this work was to study the geotechnical characteristics of a natural carbonate bearing soil, in order to have an understanding for the baseline soil properties that can be used to instruct the style of treatment. These can also be used as information against which to compare the effectivness of treartment both during and post treatment when the mechanical properties have been altered. Several parameters were studied that relate to the engineering properties of the untreated soil.

Field excavation of the in-situ Blessington sand records a density of 1.91 Mg/m^3. The in-situ water content averages at 15.4%. Particle size analysis was conducted using the wet sieve technique and the hydrometer test based on Stoke's law, results are shown in Figure 1. These tests were conducted in the UCD soil lab, they indicate a fines content of 35%, a D_{60}= 0.11 and effective size D_{10} of 0.02. Falling head permeability measurements suggested hydraulic conductivity ranging from $8.8x10^{-6}$ to $6.59x10^{-5}$ m/s, whereas constant head permeability tests show results of $9.4x10^{-4}$ m/s.

Laboratory soil compaction tests were conducted using two approaches, the British Standard light compaction test followed by a heavy compaction test. Both tests were conducted by firstly adjusting the soils moisture content to the desired starting value. The tests were repeated an additional 4 times with increasing water content. For the light compaction test, equivalent to the standard Proctor test, material was compacted into a 1L cylindrical compaction mould in three layers. Each of the three layers were compacted with a 2.5kg hammer, twenty-seven blows per layer were administered in a concentric fashion. The hammer was dropped from a height of 300mm for each of the twenty-seven blows, these blows were evenly distributed on the surface of the material.

In order to achieve higher compacted densities, a variation on the British Standard heavy compaction test was designed to increase the compactive energy applied to the soil mass. During this test five equal layers of the material were compacted with a hammer weighing 4.5kg. The hammer was dropped from a height of 450mm, eighty-one blows were administered per layer.

As visualised in Figure 2, the maximum dry density and optimum moisture content (OMC) for light compaction, are found to be 1.69 Mg/m^3 and 15.7% respectively. Results obtained during heavy compaction tests show the maximum dry density increased to 1.75Mg/m^3 and optimum moisture content is 12.8% (Figure1).

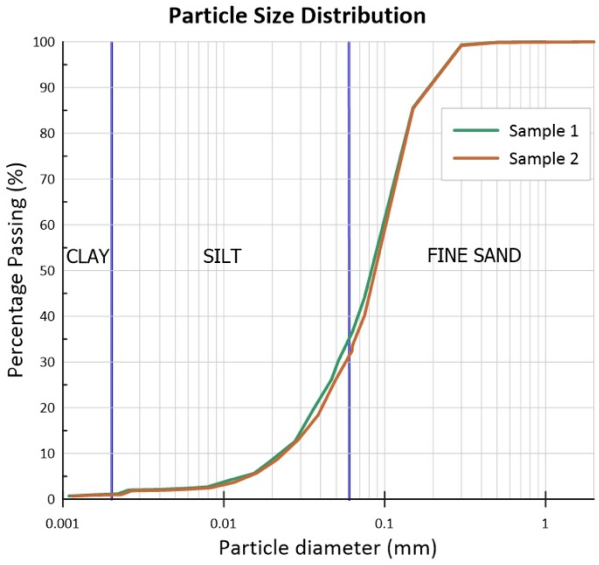

Figure 1. Particle size distribution curve for two samples. Showing the results of wet sieving and hydrometer analysis.

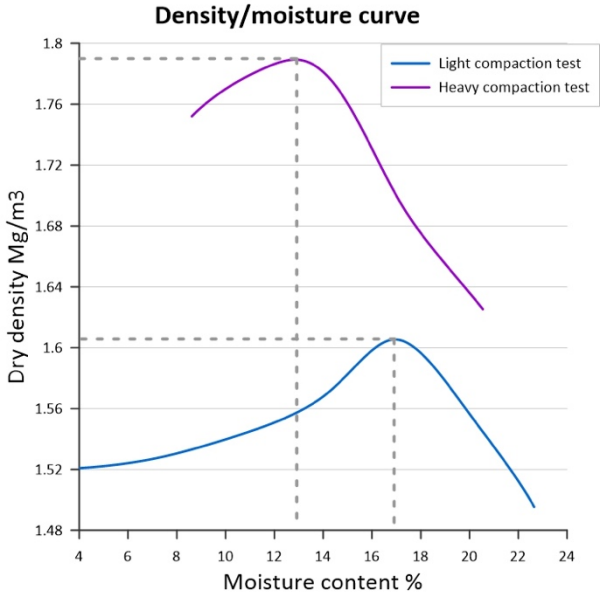

Figure 2. Density moisture curves for light compaction test and heavy compaction test.

Table 1. Summary of geotechnical soil properties.

Blessington quarry material		
	Specific gravity, Mg/m^3	2.75
Grain size distribution	Coefficient of curvature C_c	1.07
	Uniformity coefficient C_u	4.55
	Fines content (< 63µm), %	35
	Clay content (< 2 µm), %	1.1
Compaction	Maximum void ratio	1.09
	Minimum void ratio	0.53
	Maximum dry density (Proctor test) P_{Dmax} Mg/m^3	1.61
	Optimum water content, %	17
Hydraulic conductivity	Falling head, m/s.	6.59x10^{-5}
	Constant head, m/s	9.4x10^{-4}

3.2 *Geological soil analysis*

Studies have shown that the surface texture of individual grains or microtopography does affect the binding strength of bacterial adhesion [20]. Carbonate sand particles provide a relatively rough surface for attachment [21]. It has been predicted that the chemical affinity between the carbonate surface of lithic fragments and the excreted bonding material would result in the formation of strong chemical bonds [7]. Prior studies of an oligotrophic and eutrophic treatment carried out on a carbonate soil show the precipitation of calcium carbonate was more widespread in carbonate sand that silica sands [7].

In order to understand the mineralogical composition and surface textures of the Blessington quarry sample material, a number of geological analysis techniques were carried out. Hand samples were viewed with hand lens and microscope initially. Thin sections were then prepared for petrographic and Scanning Electron Microscope analysis. Visual inspection techniques, photographs and photomicrographs were used for determining the grain angularity and surface textures. Technical qualitative and initial quantitative mineralogical analysis was carried out using an energy-dispersive X-ray spectrometer (EDS), which is connected to the SEM.

3.2.1 *Optical Petrographic analysis*

Optical petrographic analysis was carried out using a binocular Nikon Eclipse LV100POL with a Nikon DS-Fi1 camera. The thin sections were prepared and analysed using this polarising microscope under both plain polarised light and cross polarised light [22]. The soil was impregnated in transparent resin and cut to a thickness of 30µ. The petrographic microscope was used to visualise diagnostic properties of lithic fragments so as to assess the mineralogical composition of the grains. The angularity of the grains was also assessed.

Thin sections analysis show that lithic fragments comprise an assortment of angular to sub-rounded sand grains, in a groundmass of finer rock dust fragments. These sand grains are lithic fragments eroded from local bedrock during the Quaternary glaciation and deposited into a paleo-lake at

Blessington, at the site of the current Blessington quarry. The dominant grain type are quarts fragments. Two types of quartz fragments are identified, whole angular to sub-angular crystal fragments and sub-angular to sub-rounded vuggy microcrystalline fragments. The second most abundant mineral type are angular to sub-rounded carbonates. Two types of carbonate fragments have been positively identified, calcite and dolomite. Both originate in the Carboniferous limestones of the Dublin Basin. Microcrystalline calcite cementations of rock flour are quite common. Fragments of angular to sub-rounded micas including both muscovite and biotite are evident. Subordinate minerals include sub-angular feldspar fragments of both plagioclase and k-feldspar types. Some angular opaque minerals are also present. The opaque minerals are presumed to be magnetite and/or ilmenite. Along with some of the quartz, all of the muscovite, feldspars the iron minerals are thought to have derived from a local granite source. The angularity of the sand grains show little erosion synonymous with a locally sourced material.

3.2.2 *Scanning Electron Microscope (SEM).*

A Scanning Electron Microscope Hitachi TM3030Plus was used to analyse the surface texture, angularity and composition of grains at all grain sizes, see Table 2 for summary. Figure 3 and Figure 4 shows an example of the photomicrographs achieved, illustrating the varied composition and characteristics of the individual lithic fragments.

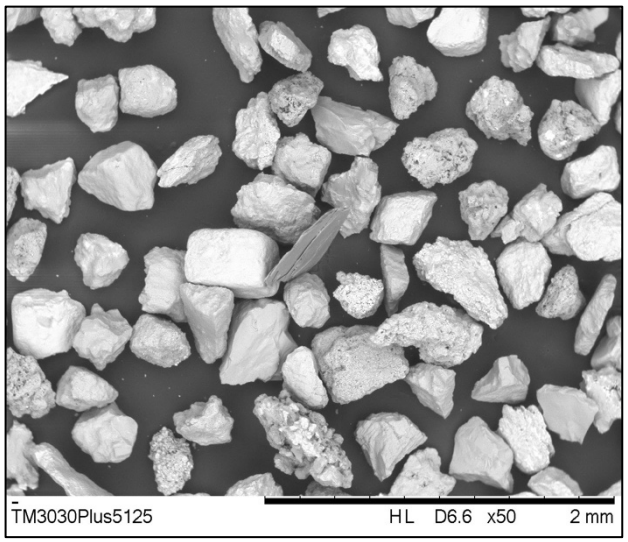

Figure 3. A washed and sieved sample showing sand sized fragments from 0.25 to 0.5 mm. Imaged using the SEM.

The image illustrates angular to sub-angular particles with vary varied surface texture topographies. The grains shown here are comprised both types of quartz and carbonate lithic fragments with a mica in the centre field of view.

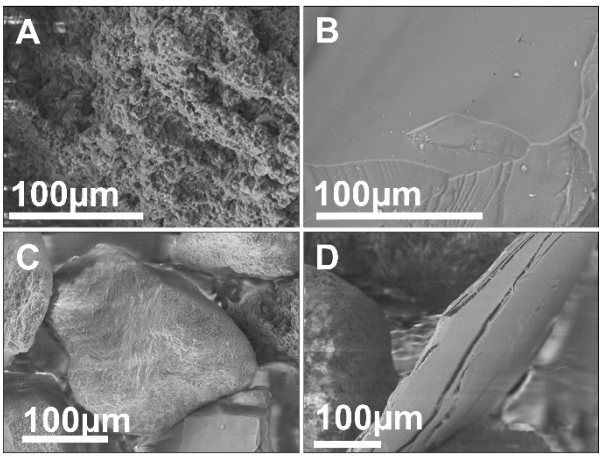

Figure 4. Photomicrographs of surface textures A: vuggy microcristalline quartz fragment. B: smooth quartz C: flaky carbonate D: platy mica.

Table 2. Summary of the lithic fragment types, their shape and surface texture.

Lithic fragment types	Shape	Surface texture
Quartz	Angular	Smooth
Microcrystalline silicate	Sub-angular to sub-rounded	Vuggy
Carbonates	Sub-angular to sub-rounded	Flaky
Mica	Angular	Platy
Feldspar	Sub-angular	Flaky

3.2.1 *Energy-dispersive X-ray spectrometer (EDS)*

A SwiftED-TM energy-dispersive X-ray spectrometer (EDS) was used to identify the elemental composition of fragment types. It works on the principle that the spectrum of energy emitted by specific elements are known and recorded on a spectra. Once the sample is in place, a beam of high-energy electron particles are focused onto a sample, the energy emitted is plotted onto the established spectrum by the EDS. The peaks of emitted energy will be related to specific electrons. A number of spectra were taken from representative sand grains. The elements present were recorded in weight %.

The EDS shows a significant Calcium (Ca) component. This directly corelates with the carbonates derived from limestone fragments. The dolomite grains contain over 14 molar % magnesium (Mg). Subordinate minerals including muscovite and biotite that contain aluminium and potassium (Al, K), plagioclase show the presence of sodium and minor calcium (Na, Ca) whereas for microcline type feldspar the presence of potassium (K) is also recorded. Oxides like magnetite record iron (Fe) values whereas ilmenite shows the presence of titanium and Iron (Ti) (Fe).

At approximately 65%, the silica content of the material is high and reflects the most abundant mineral type. Two type of silica bearing fragments were found. Pure silica, or quartz

grains are angular in shape and are thought to originate from the local Leinster granite and its associated vein quarts or pegmatites. The surface texture is smooth. The second silica type grains are highly textured sub-angular to sub-rounded in shape, these are microcrystalline silica fragments. Likely a shale. Shales are sedimentary rocks comprising clay and silt sized particles. The nearby Quinagh, Ferbane and Cloghan formations consist of interlaminated siltstones, sandstones mudstones and shales, all possible original sources.

The material is highly reactive to dilute hydrochloric acid, which suggests a high carbonate content. Two types of carbonates exist, calcite and dolomite. Under the SEM carbonate grains appears to be sub-angular and occasionally sub-rounded in shape. Both dolomite and calcite have a slightly textured or flaky surface. They would both have emanated from the local Dublin Limestone.

EDS studies of the elemental composition shows the range of calcium recorded in all samples studied which represent the bulk material is between 24 and 31%. Roughly 5% of this material has a high Mg content and is likely high-Mg calcite or dolomite. These figures are based on the molar ration of calcium and Mg in the sample. The majority of calcium originates in the carbonate fragments, a tiny percentage may be present in some feldspar fragments. Studies at partner institutes using different methodologies including a rapid carbonate analyser show the average of carbonate content in samples is 28%.

The muscovite & biotite are angular to sub angular fragments with smooth surface texture. The local Leinster Granite is a two type mica granite, both muscovite and biotite in this material emanate from the Leinster granite. The overall mica content is estimated at 5%.

Few feldspars are found in the material. Both plagioclase feldspars and potassium feldspars are evident. These feldspars are also a feature of the local Leinster granite. Evidence shows these feldspars are generally sub-angular in shape and some are slightly altered. The feldspar content is estimated at 1%. There is less than <1% magnetite/ilmenite.

Considering the shape and composition of the smallest particles the fines appear to be rock flour broken off the larger particles. Petrographic, EDS and SEM analysis suggest that these lithic fragments are calcium based or pure silica deriving from limestone and quarts respectively.

4 CONCLUSION

Previously MICP treatment has focused on quartz sands and calcareous marine sands. Though containing carbonate, this beach sand is a very different material to the terrestrial carbonate bearing sand deposits found in Ireland and much of Northern Europe. While beach sand is generally porous, rounded and has a high degree of pore space these soils differ to terrestrial soil bearing carbonates deposits.

The soil retrieved from the Blessington quarry is a dense over consolidated soil. Though a fines content of no more than 13% was expected the material has a fines content of 35%. Most of the fines are in the silt range. Though material with a high degree of fines and associated low permeability is challenging to work with, it will be possible to treat this material with equipment and methodology currently in use.

The soil fragments in these terrestrial deposits comprises a combination of material eroded from local sources that include lithic fragments of quarts, limestone, mica, feldspars and iron oxides. The material has an average carbonate content of 28%. Carbonate is present at all particle sizes.

No kaolinite or other clay minerals were detected, all the fines are rock flour broken off from the parent material. Petrographic studies show most fines comprise primarily carbonate and quartz.

Soil properties such as the roundness, roughness, and surface textures of each lithic fragment type are varied. Though in general the lithic fragments display a high degree of angularity and textured surfaces. Both these microtopographic attributes will likely favour the binding strength of bacterial adhesion.

Further soil analysis will continue and include laboratory Shear Wave Velocity measurements at a variety of soil densities. These data will be used as baseline information from which to assess the success of biomineralization treatment.

Initially column scale MICP and EICP treatments will be conducted at UCD and our partner institutions. Following this large scale tank tests will be developed at UCD. The tanks will be instrumented with pressure cells as well as seismic source and receiver tubes and a permanent ERT array to allow monitoring of the cementation process. Once procedures have been refined in the lab the project aims to undertake field scale testing.

The application of MICP to carbonate-bearing sediments has profound potential implications for infrastructure resilience and sustainability in many parts of the world. Especially in Ireland where much of the country is covered by weak unlithified glacial and fluvio-glacial sediments.

ACKNOWLEDGMENTS

This work has emanated from research supported in part by a research grant from Science Foundation Ireland (SFI) under Grant Number 19/US-C2C/3606. It is funded under the US – Ireland Research Scheme. The authors are grateful to our research partners in Georgia Tech, Arizona State University, UC Davis and Queens Universtiy, Belfast. The authors also recognise the invaluable assistance of laboratory technicians David Morgan and John Ryan. Thanks to Roadstone Ltd for the use of the Quarry at Blessington and Carnegie Ltd for facilitating work on site.

REFERENCES

[1] J. T. DeJong, B. M. Mortensen, B. C. Martinez, and D. C. Nelson, "Bio-mediated soil improvement," *Ecological Engineering,* vol. 36, no. 2, pp. 197-210, 2010/02/01/ 2010, doi: https://doi.org/10.1016/j.ecoleng.2008.12.029.

[2] V. S. Whiffin, L. A. Van Paassen, and M. P. Harkes, "Microbial carbonate precipitation as a soil improvement technique," *Geomicrobiology Journal,* vol. 24, no. 5, pp. 417-423, 2007.

[3] S. Stocks-Fischer, J. K. Galinat, and S. S. Bang, "Microbiological precipitation of CaCO3," *Soil Biology and Biochemistry,* vol. 31, no. 11, pp. 1563-1571, 1999.

[4] J. Chu, V. Stabnikov, and V. Ivanov, "Microbially Induced Calcium Carbonate Precipitation on Surface or in the Bulk of Soil," *Geomicrobiology Journal,* vol. 29, no. 6, pp. 544-549, 2012/08/01 2012, doi: 10.1080/01490451.2011.592929.

[5] E. Kavazanjian Jr and I. Karatas, "Microbiological improvement of the physical properties of soil," 2008.

[6] J. T. DeJong, M. B. Fritzges, and K. Nüsslein, "Microbially induced cementation to control sand response to undrained shear," *Journal of*

Geotechnical and Geoenvironmental Engineering, vol. 132, no. 11, pp. 1381-1392, 2006.

[7] M. Dyer and M. Viganotti, "Oligotrophic and eutrophic MICP treatment for silica and carbonate sands," *Bioinspired, Biomimetic and Nanobiomaterials,* vol. 6, no. 3, pp. 168-183, 2016.

[8] X. Fang, Y. Yang, Z. Chen, H. Liu, Y. Xiao, and C. Shen, "Influence of fiber content and length on engineering properties of MICP-treated coral sand," *Geomicrobiology Journal,* vol. 37, no. 6, pp. 582-594, 2020.

[9] X. Lei, S. Lin, Q. Meng, X. Liao, and J. Xu, "Influence of different fiber types on properties of biocemented calcareous sand," *Arabian Journal of Geosciences,* vol. 13, no. 8, pp. 1-9, 2020.

[10] Y. Li, Z. Guo, L. Wang, Y. Li, and Z. Liu, "Shear resistance of MICP cementing material at the interface between calcareous sand and steel," *Materials Letters,* vol. 274, p. 128009, 2020.

[11] Y. Li, Z. Guo, L. Wang, Z. Ye, C. Shen, and W. Zhou, "Interface shear behavior between MICP-treated calcareous sand and steel," *Journal of Materials in Civil Engineering,* vol. 33, no. 2, p. 04020455, 2021.

[12] L. Liu, H. Liu, A. W. Stuedlein, T. M. Evans, and Y. Xiao, "Strength, stiffness, and microstructure characteristics of biocemented calcareous sand," *Canadian Geotechnical Journal,* vol. 56, no. 10, pp. 1502-1513, 2019.

[13] I. U. Chattah, "Investigation of installation effects and cyclic loading on piles in sand," MEngSc thesis. University College Dublin, 2006.

[14] P. K. Doherty, Lisa; Gavin, Kenneth; Igoe, David; Tyrrell, Shane; Ward, Darren; O'Kelly, Brendan C., "Soil properties at the UCD geotechnical research site at Blessington," In Bridge and Concrete Research in Ireland 2012, Dublin, Ireland, 6-7 September, 2012..

[15] D. Igoe and K. Gavin, "Characterization of the Blessington sand geotechnical test site," *AIMS Geosciences,* vol. 5, no. 2, pp. 145-162, 2019, doi: 10.3934/geosci.2019.2.145.

[16] L. Kirwan, "Investigation into ageing mechanisms for axially loaded piles driven in sand," PhD thesis. *School of Civil, Structural and Environmental Engineering. Dublin, University College Dublin. Doctoral degree,* 2015.

[17] M. E. Philcox, *Glacial Lake Blessington: Deposits, Deformation, Outflow Features*. Irish Quaternary Association, 2019.

[18] M. E. Philcox, *The glacio-lacustrine delta complex at Blessington, Co. Wicklow and related outflow features* (IAS Dublin 2000, Field Trip Guidebook). Geology Dept., Trinity College, Dublin.: International Association of Sedimentologists, 2000.

[19] A. Tolooiyan and K. Gavin, "Modelling the cone penetration test in sand using cavity expansion and arbitrary Lagrangian Eulerian finite element methods," *Computers and Geotechnics,* vol. 38, no. 4, pp. 482-490, 2011.

[20] K. J. Edwards and A. D. Rutenberg, "Microbial response to surface microtopography: the role of metabolism in localized mineral dissolution," *Chemical Geology,* vol. 180, no. 1, pp. 19-32, 2001/10/01/ 2001, doi: https://doi.org/10.1016/S0009-2541(01)00303-5.

[21] M. A. Scholl, A. L. Mills, J. S. Herman, and G. M. Hornberger, "The influence of mineralogy and solution chemistry on the attachment of bacteria to representative aquifer materials," *Journal of Contaminant Hydrology,* vol. 6, no. 4, pp. 321-336, 1990.

[22] W. S. MacKenzie, A. E. Adams, and K. H. Brodie, *Rocks and minerals in thin section: A colour atlas*. CRC Press, 2017.

Correlation between Uniaxial Compression Strength and Point Load Index for Irish Caledonian granites

Bryan A. McCabe[1], Kevin N. Flynn[2], Sadhbh Baxter[3]
[1]Civil Engineering, School of Engineering, NUI Galway, Galway, Ireland
[2]AGL Consulting, Sandyford, Co. Dublin, Ireland
[3]Earth and Ocean Sciences, School of Natural Sciences, NUI Galway, Galway, Ireland

e-mail: bryan.mccabe@nuigalway.ie, kevin.flynn@agl.ie, sadhbh.baxter@nuigalway.ie

ABSTRACT: While the Uniaxial Compression Strength (UCS) test is the gold standard for determining the UCS of rock for geotechnical and mining applications, empirical correlations between UCS and other test measurements are useful in situations where intact cores are difficult to retrieve and/or the scope of UCS testing is constrained by budget. UCS is most commonly correlated with the cheaper and more accessible Point Load Index (PLI) measurement. In ASTM D5731-16 (2016), it is recommended that site-specific correlations are developed between UCS and $I_{s(50)}$, the point load index adjusted to a specimen diameter of 50 mm, as a means of estimating UCS indirectly. However, in the absence of site-specific data, a UCS/$I_{s(50)}$ ratio in the range 18 to 24.5 (dependent on core diameter) may be used. In this paper, the relationship between UCS and $I_{s(50)}$ is explored for Caledonian granites from three regions in Ireland. The effects of variables such as the direction of point load application (diametral versus axial), UCS core diameter and aspect ratio and Rock Quality Designation are also considered. These data supplement the very limited information on UCS-PLI relationships published for granite internationally, while complementing a similar study recently conducted for Calp Limestone in the greater Dublin area.

KEY WORDS: geotechnical engineering, granite, mining, Point Load Index (PLI), rock, Uniaxial Compression Strength (UCS).

1 INTRODUCTION

The design of geotechnical and mining infrastructure such as building and bridge foundations, excavations, shafts and tunnels in rock are heavily dependent on reliable values of the rock's Uniaxial Compression Strength (UCS). While direct UCS measurements are preferable, difficulties in retrieving intact rock cores and budget limitations often compel engineers to resort to empirical correlations between UCS and other rock test parameters, which are simpler to perform and less expensive. It has been shown that UCS is most successfully correlated with $I_{s(50)}$, the Point Load Index (PLI) test result corrected to a specimen diameter of 50 mm [1,2]. ASTM D5731-16 [3] advises that UCS predictions should be based on site-specific UCS/$I_{s(50)}$ correlations, in the absence of which 'generalised' UCS/$I_{s(50)}$ values may be used; these vary in the range 18 (for a core diameter 21.5 mm) to 24.5 (core diameter 60 mm). In practice, UCS/$I_{s(50)}$=24, originally proposed by Broch and Franklin [4], is in widespread use. Neither of these empiricisms advocate any dependence on rock type.

The ASTM D5731-16 [3] preference for site-specific correlations is justified by the wide UCS/$I_{s(50)}$ variations observed in the literature; UCS/$I_{s(50)}$=3.1 for Arabian-Persian Gulf calcarenites [5] and UCS/$I_{s(50)}$=31 for Calp Limestone in Dublin, Ireland [6], for example. Moreover, some of the linear correlations proposed in the literature have a UCS intercept (i.e. a non-zero UCS corresponding to $I_{s(50)}$=0), and others are non-linear. In addition, many are based on scant data and/or scatterplots offering poor statistical reliability, and most studies do not explore factors on which UCS/$I_{s(50)}$ may depend.

The aforementioned Casey and Fleming [6] paper provided the first UCS-PLI study for an Irish rock formation (Calp limestone), relevant to construction in the greater Dublin area of Ireland. UCS-$I_{s(50)}$ relationships for Irish Caledonian granites are explored in this paper; granite is also commonly encountered in the vicinity of Dublin and at other locations in Ireland. The effects of variables such as the direction of point load application (i.e. axial versus diametral), UCS core diameter and aspect ratio and Rock Quality Designation are also considered. These data supplement the relatively limited information on UCS-PLI relationships published for granite internationally, which is summarised in Section 2 as context.

2 REVIEW OF UCS-PLI CORRELATIONS IN GRANITE

A literature review of UCS-PLI relationships for granitoid rocks has yielded the following findings, ordered by year:

- A best fit of UCS/$I_{s(50)}$ = 12.5 (coefficient of regression R = 0.73) was reported by Chau and Wong [7] for Hong Kong granite and tuff, with weathering grades from fresh to moderately decomposed (n=21). The PLI tests were performed in the axial direction.
- Kahraman and Gunaydin [8] presented the following correlation for Turkish igneous rocks: UCS = 8.2$I_{s(50)}$+ 36.43 (R^2 = 0.68), covering a range of UCS values from 50 MPa to 200 MPa approx. However, only eight of the 17 points in the correlation pertain to granite. The PLI tests were diametral.
- Based on data (n = 19) from Malanjkhand, India, Mishra and Basu [9] proposed the following relationship for granite: UCS = 10.9$I_{s(50)}$+ 49.3 (R^2 = 0.8). UCS values typically fell in the range 100-200 MPa; the direction of PLI tests was axial.
- Tandon and Gupta [10] proposed the following expression for Himalayan granitoid rocks (n=9): UCS = 5.602I_s+ 4.38 (R^2 = 0.94), although it is unclear whether

the I_s value is $I_{s(50)}$. The UCS values range to 100 MPa approx., with the PLI tests conducted on irregular lumps.

- Armaghani et al. [11] conducted UCS and PLI tests on granite (n = 71) from the PSRWT tunnel site in Malaysia, yielding the following power relationship: UCS = $49.337I_{s(50)}^{0.713}$ ($R^2 = 0.711$), representing UCS values up to 200 MPa. The PLI test version was not specified.
- Yin *et al.* [12] conducted 53 diametral, 54 axial and 547 irregular lump PLI tests on Hong Kong granite. A size correction factor was proposed for the irregular lumps. A correlation of $UCS/I_{s(50)} \approx 22$ (R^2 in the range 0.73-0.82) was proposed, essentially independent of whether the PLI tests were diametral, axial or on irregular lumps.

Other authors have incorporated granitoid rocks in their databases, but ultimately the correlations are based on multiple rock categories/types, which is not particularly helpful.

The correlations presented above, which almost exclusively relate to Asia, vary very widely, and although R or R^2 values are reasonable, the datasets are extremely small for the most part. The correlations with a UCS intercept may be difficult to justify if they are to be applied to weak rocks. The UCS range represented is limited in some cases, and important details of the UCS and PLI testing regimes are often missing. Some of these shortcomings are addressed for the study in this paper.

3 IRISH GRANITES

3.1 General

The distribution of granitic rocks on the island of Ireland is shown in Figure 1, after Chew and Stillman [13]. The granites can be divided into two main subgroups: Caledonian granites (Galway, Ox Mountains, Donegal, Newry and Leinster) and Palaeogene granites (Mourne Mountains, Slieve Gullion and Carlingford, all in NE Ireland; shown as uncoloured (white) areas to the east of the Newry granite on Figure 1).

The Caledonian orogeny relates to events that took place from the Ordovician to Early Devonian, 490-390 million years ago (Ma). Caledonian granites are associated with post-orogenic collapse and with the major SW-NE trending faults that were undergoing left-lateral movement at the end of that period. In stark contrast to the post-orogenic origins of the Caledonian granites, the Palaeogene granites owe their origin to the opening of the North Atlantic circa 60 Ma. The UCS/PLI data presented in this paper pertain to Caledonian granites only.

3.2 Irish Caledonian granites

At 1500 km^2, the Leinster batholith (417-405 Ma) is the largest in the UK or Ireland and comprises five plutons. Its chemistry and mineralogy differs from other Irish Caledonian granites in containing both biotite and muscovite mica, reflecting the origin of the magma (possibly related to its position on the south side of the Iapetus Suture, see Figure 1). While magma generation is believed in all cases to be due to decompression melting as a subducted slab detached under the Caledonian orogenic belt, the source rocks for the Leinster granite would appear to be the aluminium-rich schists and other meta-sedimentary rocks that now host the granite.

In contrast, the other Irish batholiths were generated from melting of igneous rocks, and show more evidence of the involvement of mafic magmas in their generation, as evidenced by the presence of mafic enclaves, the lack of muscovite (therefore lower in aluminium) and the presence of hornblende and titanite. The Galway batholith (410-380 Ma) is ~900 km^2 in area, but extends under Galway Bay, so it is likely to be twice that size in areal extent. It comprises multiple, varied, individual plutons, generally granodioritic in nature (i.e. lower quartz content than true granite). The 'main' body is distinctly porphyritic, with large (up to 10cm long) pink K-feldspar phenocrysts in a coarse groundmass. Biotite, hornblende and titanite are common. A key feature is a (presumed axial) band circa 4 km wide of intense magma mixing and mingling between granites and more mafic rocks. Geobarometry suggests intrusion depths of between 18 km and 4 km for the plutons of this batholith.

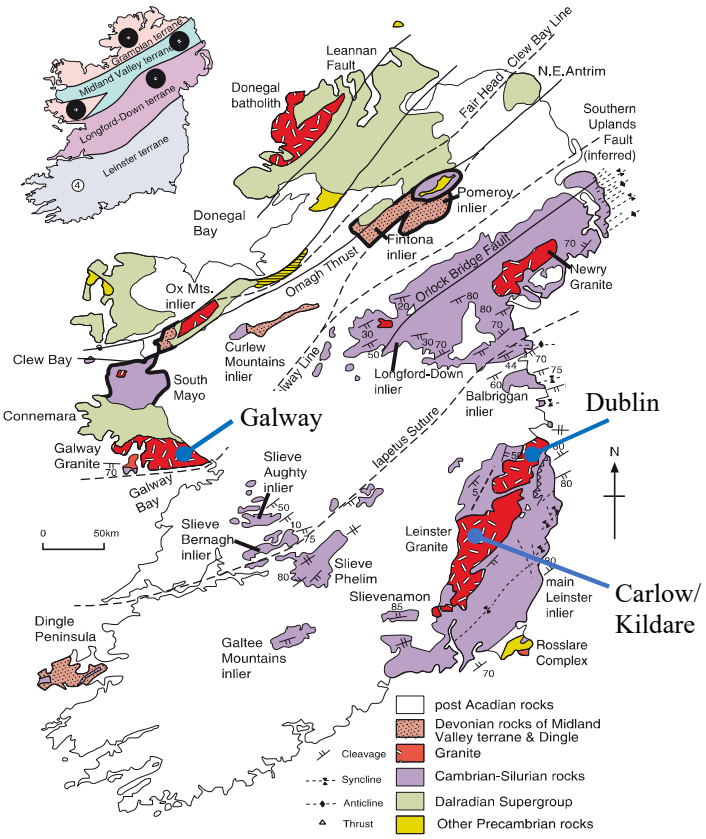

Figure 1. Distribution of granite in Ireland [13]

4 UCS-PLI DATABASE

The UCS-PLI database was compiled from historical ground investigation (GI) reports in the files of AGL Consulting, and some publicly available from the Geological Survey of Ireland (GSI). These reports date from 1996 to 2021 and are attributable to nine separate GI contractors. The database incorporates the following information, where available:

- UCS tests: specimen depth, height, diameter, bulk density, UCS value.
- PLI tests: specimen depth, height, diameter, width, whether tests were diametral, axial, on blocks or irregular lumps, direction of testing (parallel or perpendicular to planes of weakness, unknown/random), $I_{s(50)}$ value.
- The geological formation/unit name, according to the GSI 100k series mapping.

- Description of granite strength, grain size, mineralogy, bedding and weathering.
- Quantification of Discontinuity Spacing, Fracture Spacing, Fracture Intensity (FI), Total Core Recovery (TCR), Solid Core Recovery (SCR) and Rock Quality Designation (RQD).

The main database comprises a total of n=244 UCS-PLI pairs, with UCS and PLI specimen depths within 0.5 m in almost all cases, and the $I_{s(50)}$ measurement based on diametral results. Diametral PLI data dominated the database, and are generally preferred over axial PLI data for geometric sensitivity reasons [4]. The dataset can be attributed regionally as follows: Dublin (n=141) and Carlow/Kildare (n=50) (both from the Leinster batholith) and Galway (n=53). A secondary (and largely separate) dataset of PLI data for Dublin (n = 728) was developed for the purpose of comparing axial and diametral $I_{s(50)}$ values only. Most of these data do not have the comparative UCS tests necessary for inclusion in the main database. For the small number that do, only the diametral ones are included, for reasons already described, and given that the association of a single UCS value with two different $I_{s(50)}$ values would be statistically inappropriate.

5 UCS-PLI CORRELATIONS

5.1 UCS and $I_{s(50)}$ distributions

Statistical data for UCS, $I_{s(50)}$ and bulk density are shown in Figure 2 in the form of *box and whisker* plots (illustrating minimum, lower quartile, median, upper quartile, maximum values and outliers, in the standard way) for the entire database and differentiated by region. The mean value is also included (marked ×). A wide range of UCS values (up to ~240 MPa) and $I_{s(50)}$ values (up to ~13 MPa) is represented overall, in contrast to the more limited ranges on which some of the correlations in Section 2 are based.

It is apparent from Figure 2 that the overall database is somewhat skewed by regional variations. While the mean UCS for the Dublin data follows the overall mean fairly closely (0.88 of the overall mean), the mean UCS values for the Galway and Carlow/Kildare data are 1.83 and 0.44 times the overall mean respectively. Corresponding ratios for $I_{s(50)}$ means are 0.96 (Dublin), 1.64 (Galway) and 0.43 (Carlow/Kildare). Single factor analysis of variance (ANOVA) suggests that these regional differences in UCS and $I_{s(50)}$ are statistically significant in all three cases. The (also statistically significant) higher bulk densities for Galway granite (Figure 2c) are likely to have influenced the higher UCS and $I_{s(50)}$ values. Such differences are probably a reflection of the chemical and mineralogical differences between the Galway and Leinster batholiths discussed in Section 3. However, the differences in UCS and $I_{s(50)}$ between Dublin and Carlow/ Kildare granites, both within the Leinster batholith, are not explained by bulk density (i.e. differences in bulk density not statistically significant) and requires further investigation.

5.2 UCS-PLI linear relationships

A plot of UCS against $I_{s(50)}$ for the entire database is provided in Figure 3, with the Broch and Franklin [4] correlation and the granite correlations presented in Section 2 superimposed. The data in Figure 4 incorporate scatter typical of large rock measurement datasets; the Chau and Wong [7] relationship appears to represent the data best on average. The Broch and Franklin [4] correlation grossly over-predicts UCS for the majority of cases. Also, given that most of UCS cores included in database are 60 mm in diameter or greater, ASTM D5731-16 [3] also overpredicts UCS (very similar to the Broch and Franklin [4] line, so not shown in Figure 3 for clarity). None of the other correlations represent the data well either, although the Armaghani et al. [11] and Tandon and Gupta [10] offer reasonable upper and lower bounds respectively. It is worth noting that while correlations such as those in Figure 3 aspire to produce mean trends (for the purposes of foundation design, for example), upper bounds/over-predictions of UCS can be useful where rock excavatability predictions are sought, such as for shaft and tunnel construction [14].

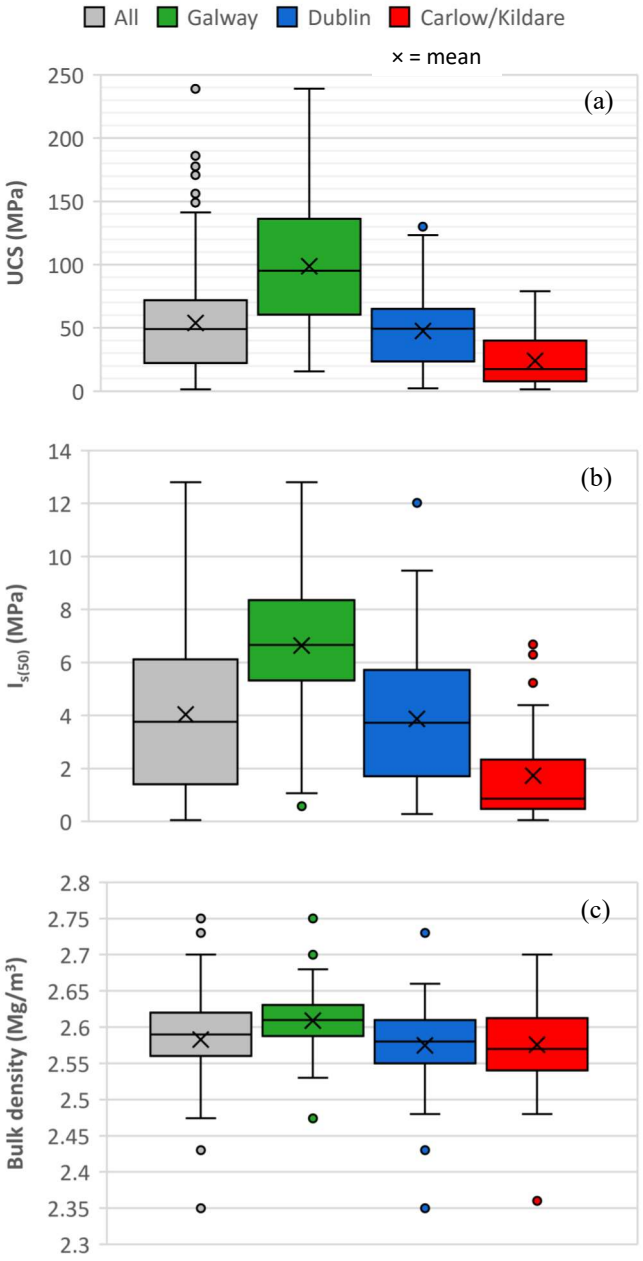

Figure 2: Box and whisker plots for (a) UCS (b) $I_{s(50)}$ and (c) bulk density for entire database and differentiated by region

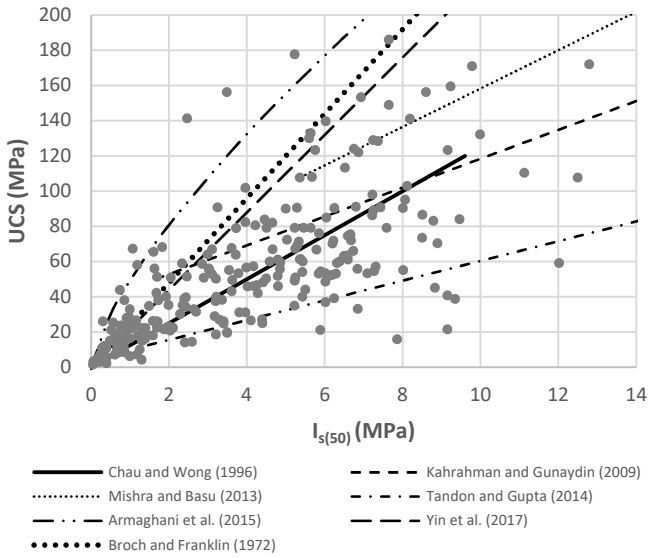

Figure 3: UCS against $(I_s)_{50}$ for the entire granite database (n=244) with correlations from the literature superimposed.

Separate plots of UCS against $I_{s(50)}$ are presented in Figure 4 for the three regions: (a) Galway, (b) Dublin and (c) Carlow/Kildare. Initially, simple linear correlations (zero UCS intercept) were investigated. The best fit for the entire database was found to be $UCS/I_{s(50)}$= 12.3 (R^2=0.45), with $UCS/I_{s(50)}$ values of 13.6 (R^2=-0.17), 11.1 (R^2=0.42) and 11.4 (R^2=0.60) for Galway, Dublin and Carlow/Kildare respectively.

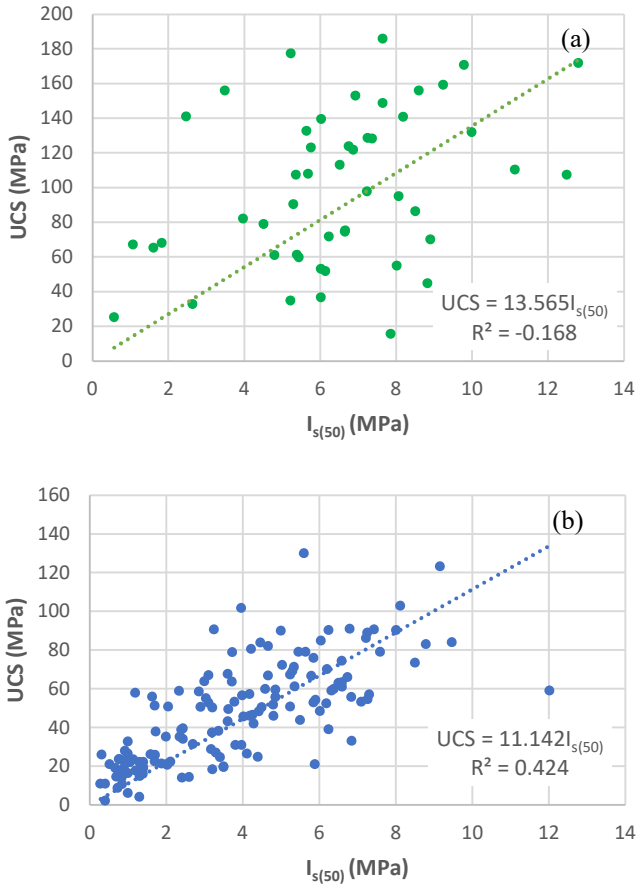

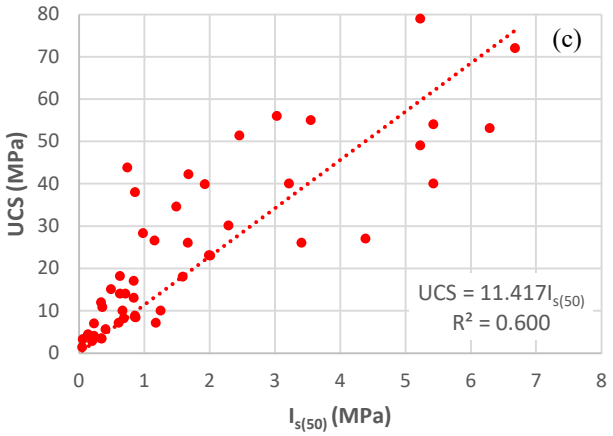

Figure 4: Individual UCS-$I_{s(50)}$ relationships for (a) Galway, (b) Dublin and (c) Carlow/Kildare granites

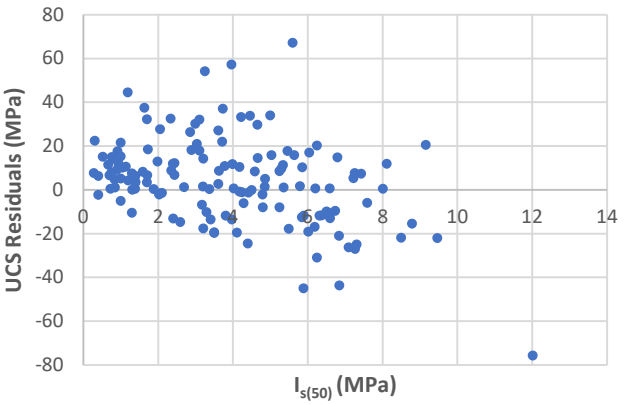

Figure 5: UCS residuals plotted against $I_{s(50)}$ data for Dublin: linear relationship

Individually, these ratios are relatively similar (the Galway value is slightly higher) and broadly in keeping with $UCS/I_{s(50)}$ = 12.5 (for axial PLI specimens) in Hong Kong granite/tuff [7]. However, the negative R^2 for the Galway data implies that the increasing relationship shown in Figure 4(a) does not embody the trend of the data, and therefore its use is not advised until the reason for the spread is better understood.

The UCS residuals (the difference between predicted and observed UCS values in a regression analysis) corresponding to the linear relationships presented in Figure 4 were plotted against $I_{s(50)}$; an example for Dublin granite is shown in Figure 5. These residual plots revealed that the data are not well represented by the linear relationships at lower UCS and $I_{s(50)}$ values; the residuals are predominantly positive up to $I_{s(50)}$ of at least 3 MPa in both Dublin and Carlow/Kildare granites. On this basis, bi-linear relationships were considered for both sets of data, in order to capture the lower strength realm better. However, these were not particularly successful and have the potential to be misused in practice.

5.3 UCS-PLI non-linear relationships

Non-linear (polynomial and power) relationships between UCS and $I_{s(50)}$ were explored for the Dublin and Carlow/Kildare granite data. The following power relationships, similar in

general form to that of Armaghani et al. [11] (i.e. UCS = $AI_{s(50)}^{B}$, where A and B are constants), were ultimately preferred:

Dublin: $UCS = 19.06\ I_{s(50)}^{0.66}$ ($R^2 = 0.55$) (1)
Carlow/Kildare: $UCS = 16.12\ I_{s(50)}^{0.75}$ ($R^2 = 0.71$) (2)

Equations (1) and (2) are displayed in context of the underlying data in Figures 6a and 6b respectively. The corresponding residual plots illustrate that these non-linear correlations model the data more appropriately than the linear ones; the example for Dublin granite in Figure 7 clearly depicts a more equitable spread about the zero residual axis than in Figure 5. A power relationship was not explored for the Galway granite given the poor R^2 value in the linear correlation.

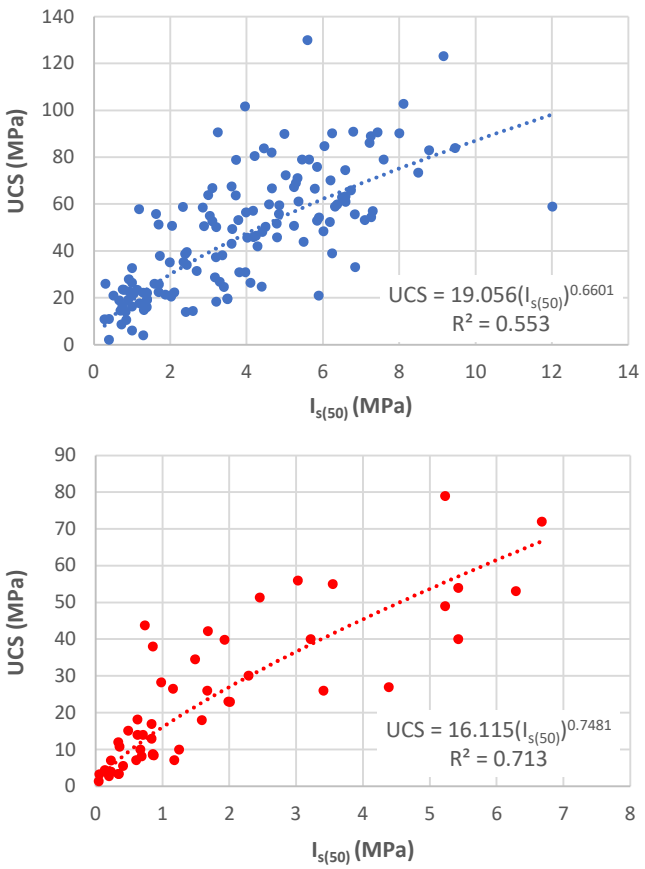

Figure 6: Non-linear UCS-$I_{s(50)}$ relationships for (a) Dublin, (b) Carlow/Kildare granites

5.4 $I_{s(50)}$ values: axial versus diametral

In the aforementioned study, Yin *et al.* [12] conducted 53 diametral and 54 axial PLI tests on Hong Kong granite. Their correlation of $UCS/I_{s(50)} = 22$ was found to be independent of whether diametral or axial tests were considered.

Axial $I_{s(50)}$ values are plotted against diametral $I_{s(50)}$ values (n =752) for Dublin granite in Figure 8, where both measurements correspond to the same depth within the same core. The slope of the best fit line is virtually unity, suggesting, despite the scatter (R^2=0.49), a general equivalence between $I_{s(50)}$ measurements from the two loading directions, in keeping with previous findings [12]. The $I_{s(50),axial}/I_{s(50),diametral}$ ratio appears to be related to anisotropy of the rock; with igneous rocks more likely to yield a 1:1 ratio than sedimentary rocks incorporating bedding planes. For instance, $I_{s(50),axial}/I_{s(50),diametral}$ ratios of 2 to 2.5 were reported for a Western Australian shale, and 1 to 2.5 for a banded-iron formation, with higher ratios reflecting greater weathering in the latter case [15].

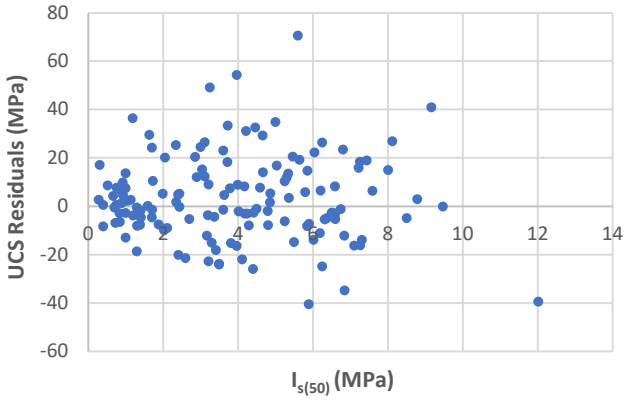

Figure 7: UCS residuals plotted against $I_{s(50)}$ for Dublin: power relationship

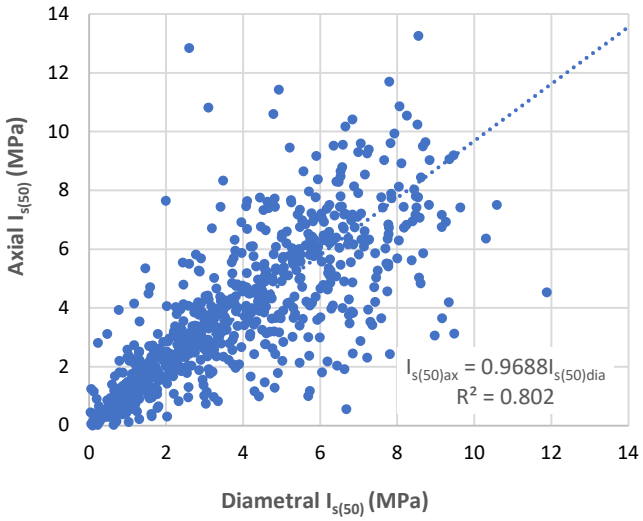

Figure 8: Axial $I_{s(50)}$ plotted against diametral $I_{s(50)}$ for Dublin granite (n=752)

5.5 Other variables

Thuro *et al.* [16] found no significant dependence of UCS on (i) core diameter, in the range 45-80 mm for limestone samples and 50-117 mm for granite samples, and (ii) aspect ratio, in the range 1 to 3 for (igneous) kersantite samples. Notwithstanding the bias in the data due to the much higher UCS for the Galway specimens, no relationship between UCS and core diameter (in the range 34-93 mm) or aspect ratio (mostly the recommended 2-3 range) was evident in this database either. Such comparisons could be considered more broadly with an enhanced dataset, without the requirement of proximal UCS and $I_{s(50)}$ values.

The significant dependence of $UCS/I_{s(50)}$ on core diameter implied in ASTM D5731-16 (2016) relates to core diameters in

the range 21.5 mm to 60 mm. However, no relationship was apparent between UCS/$I_{s(50)}$ and either diameter or aspect ratio (over the ranges quoted above) for the Irish granites considered.

RQD, defined as the percentage of intact drill core pieces longer than 10 cm recovered during a single core run, is a measure of jointing or fracture in a rock mass. Some studies (e.g. [17] in sandstone) have indicated a positive correlation between UCS and RQD. Despite a wide range of RQD values in the database (8%-100%), UCS or UCS/$I_{s(50)}$ for the granites appeared to be insensitive to RQD, perhaps in part due to differences in individual drilling styles across multiple GI companies.

6 CONCLUSIONS

A new UCS-PLI database for Irish Caledonian granites (n=244, i.e. more data than most other granite studies reviewed) has indicated that the commonly-quoted correlation UCS=24$I_{s(50)}$ is likely to overpredict the UCS of these granites by a factor of two on average. Despite the fact that much higher UCS values (and $I_{s(50)}$ values) were encountered in Galway granite than in Leinster granites, probably attributable to significant chemical and mineralogical differences, the best-fit UCS/$I_{s(50)}$ ratio was only slightly higher for Galway data, but with the important caveat of only moderate R^2 values (and very poor in the case of Galway).

A statistical examination of residual UCS values has led the authors to prefer a non-linear (power) relationship between UCS and $I_{s(50)}$ to the more common linear ones. The usual caution is advised in applying these correlations. This research also highlights the danger of applying correlations from other granites worldwide to Irish conditions; only one of the published correlations considered compared favourably to those developed in this paper.

A separate Dublin granite database (n=728) has suggested that the axial and diametral PLI test results are statistically equivalent, in theory rendering either version suitable for the development of local UCS/$I_{s(50)}$ correlations in granite.

There was no apparent effect of other variables such as core diameter, aspect ratio and RQD on UCS and UCS/$I_{s(50)}$ values in the database (although a larger UCS-only database may be more informative in this regard). There is scope to consider geological unit, rock grain size, weathering state and other variables in a further development of this work. In addition, granite UCS-PLI data from other regions (both Caledonian and Palaoegene) will be considered.

ACKNOWLEDGEMENTS

The authors would like to thank Advanced Geotechnics Limited (AGL), Sandyford, Dublin, for access to the historical site investigation reports used in compiling this paper.

REFERENCES

[1] Basu, A. & Aydin, A. (2006) Predicting uniaxial compressive strength by point load tests: significance of cone penetration. *Rock Mechanics and Rock Engineering*, 39, 483-490.

[2] Aledejare, A.E. (2020) Evaluation of empirical estimation of uniaxial compression strength of rock using measurements from index and physical tests. *Journal of Rock Mechanics and Geotechnical Engineering*, 12, 256-268.

[3] ASTM D5731-16 (2016) Standard test method for determination of the point load strength index of rock and application to rock strength classifications.

[4] Broch, E. and Franklin, J.A. (1972) The point-load strength test. *International Journal of Rock Mechanics and Mining Sciences*, 9, 669-697.

[5] Puech, A., Beuce, J.P. & Colliat, J.L. (1988) Advances in the design of piles driven into non-cemented to weakly cemented carbonate formations, *Proceedings of the International Conference on Carbonate Sediments,* Perth, Australia, 1, 305-312.

[6] Casey, P. & Fleming, M. (2015) An investigation of the accuracy of the use of point load index test results to predict the unconfined compressive strength of Calp limestone in Ireland. *Proceedings of the 16th European Conference in Soil Mechanics and Geotechnical Engineering,* 3123-3127.

[7] Chau, K.T. & Wong, R.H.C (1996) Uniaxial compression strength and point load tests in rocks. *International Journal or Rock Mechanics and Mining Sciences and Geomechanics Abstracts,* Vol. 33, No. 2, 183-188.

[8] Kahrahman, S. & Gunaydin, O. (2009) The effect of rock classes on the relation between uniaxial compressive strength and point load index, *Bulletin and Engineering Geology and the Environment*, 68, 345-353.

[9] Mishra, D.A. & Basu, A. (2013) Estimation of uniaxial compressive strength of rock materails by index tests using regression analysis and fuzzy inference system, *Engineering Geology*, 160, 54-68.

[10] Tandon, R.S. & Gupta, V. (2015) Estimation of strength characteristics and different Himalayan rocks from Schmidt hammer rebound, point load index and compressional wave velocity, *Bulletin and Engineering Geology and the Environment* 74, 2, 521-533.

[11] Armaghani, D.J., Mohamad, E.T., Momeni, E., Monjezi, M. & Narayanasamy, M.S. (2015) Prediction of the strength and elasticity modulus of granite through an expert artificial network, *Arabian Journal of Geosciences*, 9, 48.

[12] Yin, J.H., Wong, R.H.C, Chau, K.T.M, Lai, D.T.W. & Zhao, G.S. (2017) Point load strength index of granitic irregular lumps: size correction and correlation with uniaxial compression strength, *Tunnelling and Underground Space Technology*, 70, 388-399.

[13] Chew, D.M. & Stillman, C.J. (2009) Late Caledonian Orogeny and magmatism, In: The Geology of Ireland (pages 143-173), 2nd Ed., Dunedin Academic Press.

[14] Sheil, B.B., Curran, B.G. & McCabe, B.A. (2016) Experiences of utility microtunnelling in Irish limestone, mudstone and sandstone rock, *Tunnelling and Underground Space Technology*, 51, 326-337.

[15] Gao, X. (2020) The effect of anisotropy orientation on the sedimentary rock strength estimated by point load testing strength, Pilbara, Australia, *Slope Stability 2020 Conference*, Australian Centre for Geomechanics, 657-666.

[16] Thuro, K., Plinninger, R.J., Zah, S. & Schutz, S. (2001) Scale effects in rock strength properties. Part 1: Unconfined compressive test and Brazilian tests, *Proceedings of EUROCK 2001: Rock Mechanics A Challenge for Society*, Espoo, Finland, 169-174.

[17] Mahmoud, M.A.A.N. (2003) Correlation of sandstone rock properties obtained from field and laboratory tests. *International Journal of Civil and Structural Engineering,* 4, 1, 1-11.

Relation between Unconfined Compression Strength and Point Load Index applied to Irish rocks

Maxime Delaye[1] and David Igoe[2]

[1]Department of Energy and Environmental Engineering, INSA Lyon, Avenue Albert Einstein, Villeurbanne, France
[2]Department of Civil, Structural & Environmental Engineering, Trinity College Dublin, the University of Dublin, College Green, Dublin 2, Ireland

Email: maxime.delaye@insa-lyon.fr, igoed@tcd.ie

ABSTRACT: The Uniaxial Compressive Strength (UCS) is the most common parameter used to evaluate the strength of rock materials for geotechnical projects. Preparation of samples for Unconfined Compression Testing can be time consuming, and therefore the Point Load Test (PLT) is often used as a quicker and simpler indirect alternative to determine the UCS using empirical correlations. The aim of this paper is to investigate such correlations to determine the properties of Irish rocks. Regression analysis was used to find relationships between UCS and $Is_{(50)}$ index depending on each rock type. The coefficient of determination was not satisfied for every rock, but significant results were found for Irish mudstone, granite and sandstone.

KEY WORDS: Unconfined compression strength; Point load index; Mudstone; Granite; Sandstone

1 INTRODUCTION

The strength of a rock material is a major parameter for geoengineering, for example in civil, mining and offshore projects. Unconfined Compression Strength, also known as Uniaxial Compressive Strength (UCS) is a parameter that represents the maximum axial stress that can be applied to a cylindrical rock sample before failing. The Unconfined Compression Test (UCT) is one of the most commonly used laboratory tests to investigate mechanical properties of rocks, because it is a direct and reliable method to estimate the UCS and therefore rock strength [12]. The Point Load Test (PLT) consists of testing a sample compression between two conical steel plates until failure to determine the corrected Point Load Index ($Is_{(50)}$). The Point Load Test is less expensive and time consuming than the Unconfined Compression Test, and it can be performed on cylindrical, rectangular or even irregular specimens, provided that they comply with some geometric regulations [11]. Many correlations have been proposed in the literature to relate the Point Load Index and the rock UCS. Linear relationships with factors between 21 and 24 are commonly used to predict the UCS value from the $I_{s(50)}$ [6]. A value of 31 was suggested for the Dublin Calp formation [6]. This paper aims to investigate similar correlations for other Irish rock types.

2 GIS INDEXATION

The data used for this statistical study results from tests performed by the Trinity College Dublin in collaboration with the Ground Investigation Ireland (GII) company. The database is composed of 1928 Point Load Tests and 721 Unconfined Compression Tests performed on 115 different locations all around Ireland between 2013 and 2021 (Figure 1). These tests are part of 161 different civil engineering projects. The UCTs and PLTs were undertaken on 60 different rock types gathered according to their lithology: limestone, mudstone, shale, gneiss, granite, slate, sandstone, siltstone, schist, polymict, pelite, calp and quartzite.

The database includes the location and the results of the tests. The data was indexed on a map using the Geographical Information System software QGIS. OpenStreetMap [16] and Geological Survey Ireland (GSI) bedrock data [9] were used to determine each sample rock type according to its locality. For each sample, the following details were included: the name and the date of the testing project, the borehole number, the depth, the length and the diameter of the sample. The maximum load before failure, the Point Load Index (Is) and the corrected Point Load Index ($Is_{(50)}$) are also specified. The locality, the elevation and the specific rock type (GSI specifications [9]) were determined by the authors from the previous attributes. The data selected in this study is based on the PLT and UCS from the same boreholes at similar depths. Thus 657 pairs of $Is_{(50)}$ and UCS were retained. For this data, complementary attributes were added: the lithology, the rock class and the depth gap between both tests (i.e. vertical distance between samples tested).

The GIS database includes some qualitative attributes, which were developed to filter uncertain values. The *Location Confidence Index* translates the fact that the database was not always complete enough to determine the exact borehole locations (Table 1). In the case where multiple PLT were performed on the same sample, the mean value of the $Is_{(50)}$ was used for the statistical work.

Table 1. Location confidence Index interpretation

Location confidence Index	Meaning
0	Unknown location
1	Location not precise enough to determine the rock nature
2	Approximate location known
3	Precisely determined location

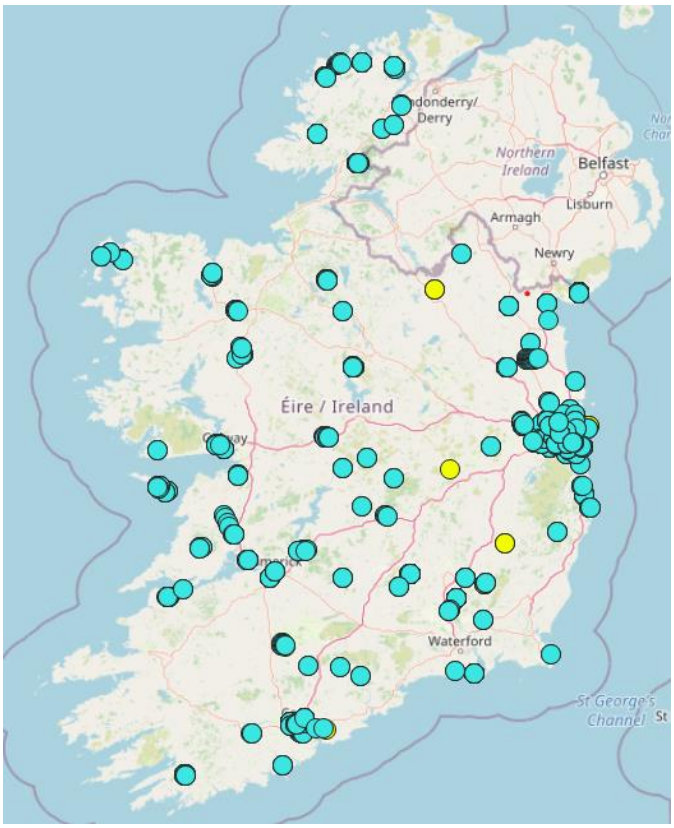

Figure 1. Tests localisations

3 METHODOLOGY

3.1 Unconfined Compression Test

The Unconfined Compression Test is a laboratory test used to determine the UCS. The rock core preparation is time consuming because it must comply with strict specifications [12]. The end surfaces of the sample must be completely flat and parallel to insure an even load distribution. The apparatus must be able to provide a continuous load between steel platens at a constant rate until the sample failure. The failure load, P_u, divided by the specimen cross section area A is used to calculate the UCS Index, see Eq. (1). The length to diameter ratio (h/d) must be between 2 and 3, if not a corrected UCS* value should be calculated as per Eq. (2)

$$UCS = \frac{P_u}{A} \tag{1}$$

$$UCS^* = \frac{UCS}{0.88 + (\frac{0.24\ d}{h})} \tag{2}$$

3.2 Point Load Test

The Point Load Test (PLT) can be performed quickly to determine the strength of a rock material without sophisticated equipment [11]. The Schmidt Hammer Rebound test can be used to determine similar rock properties but it is commonly acknowledged that the PLT is a more precise and reliable test. The apparatus consists in a rigid loading frame and a loading measuring system. The apparatus is portable thus it allows onsite tests. A load is applied between two conical steel platens until the sample failure. The compression can be applied diametrically or axially, and even on irregular samples. In this study only single diametral penetration was performed on the specimens. The failure load, P_u, and the core diameter, D_e, are used to calculate the Point Load Index Is, see Eq. (3). The $I_{s(50)}$ is a corrected index calculated from the Is to take in account the sample size influence on the maximum applied load, see Eq.(4).

$$Is = \frac{P_u}{D_e^2} \tag{3}$$

$$Is_{(50)} = (\frac{D_e}{50})^{0.45} \times Is \tag{4}$$

4 STATISTICAL ANALYSIS

Corresponding pairs of UCTs and PLTs from the same borehole were compared at similar depths. The depth gap between the UCT and the PLT was used as a filter to select the most relevant points to find the correlations. A larger depth gap between the two tests would result in larger variability as the rock strength will vary with depth.

A software code was developed in Visual Basic to allow a quick comparison between different rock types and to determine the various correlations. The following parameters were tested: the location, the project, the specific rock type (GSI specifications [9]), the lithology (e.g. limestone, mudstone, shale etc.), the rock class (e.g. sedimentary, metamorphic, igneous), the depth gap between the PLT and the UCT, the elevation, the $I_{s(50)}$ range and the UCS index range.

Exponential, linear, polynomial, logarithmic and power curve fitting approximations were tried. The one with the highest coefficient of determination (R^2 value) was selected.

The coefficient of determination is not enough to judge from the validity of the model, i.e. to check if the chosen parameters are appropriate. A Fisher-Snedecor test (F-Test) [17] was performed on the coefficients of determination R^2 as a complementary validation of the correlations. All the correlations presented here were validated with this F-Test under a risk of 2.5%.

A 95% prediction interval was also calculated for each rock type. The idea is to obtain a confidence interval on the calculated UCS value depending on the $Is_{(50)}$ value used in the correlation. For a given $Is_{(50)}$ value, there are 95% chance that the predicted UCS value is within the prediction range. The correlation is more precise if the prediction interval is narrow than if this interval is wide.

The absolute value of the difference between the UCS value and the predicted UCS was determined. The average of this value has been chosen as a complementary parameter to judge the distance of the experimental points around the correlation.

The distribution of the $Is_{(50)}$ and the UCS was studied. The number of bins used in the histograms was determined using Sturge's formula, derived from binomial distribution and depending on the number of data [19]. The histograms were compared with the normal, lognormal and gamma distributions. In every case the normal distribution was found to be the best fitting distribution.

5 RESULTS

After sorting the database according to each available parameter, it was concluded that the most relevant parameters were the rock type and the depth gap between the samples used in the UCT and the PLT. These parameters lead to high coefficient of determination with a satisfying number of samples involved in the correlation. The Location Confidence Index was also used to filter the uncertain data.

5.1 Granite Results

54 data points were used to determine the correlations for granite rocks (Figure 4). The average absolute difference to the predicted value is 12.67MPa. The maximum depth gap allowed between the UCS and the PLT was 1m. The mean depth gap was 0.36m. The retained $Is_{(50)}$ values range from less than 1MPa to more than 9MPa with an average of 2.5MPa (Figure 2). The granite UCS values range from less than 10MPa to more than 160MPa with an average of 48MPa (Figure 3). The best fit linear relationship is given in equation (5) below:

$$UCS = 16.7 \times I_{s(50)}$$
$$R^2 = 0.89 \quad n = 54 \qquad (5)$$

This is broadly in agreement with the linear correlation factor of 16 found in multiple literature papers [3][10] .

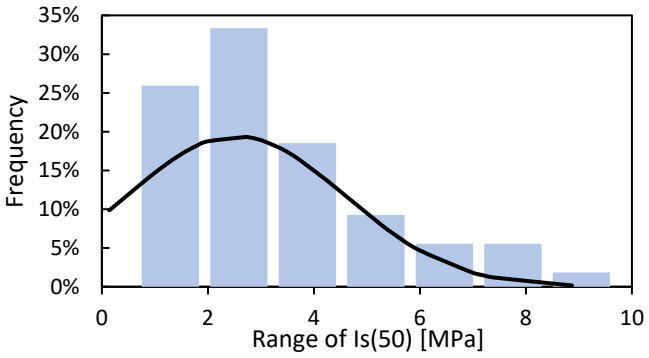

Figure 2. Granite $Is_{(50)}$ histogram

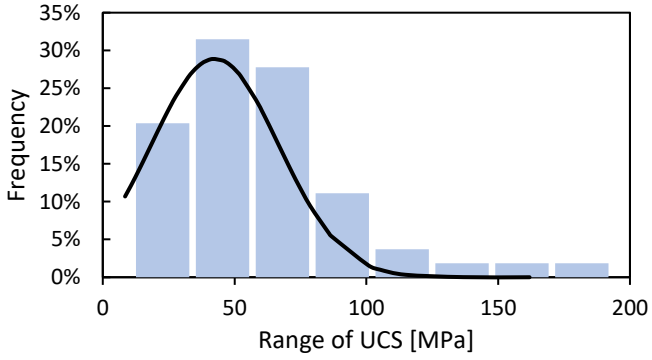

Figure 3. Granite UCS histogram

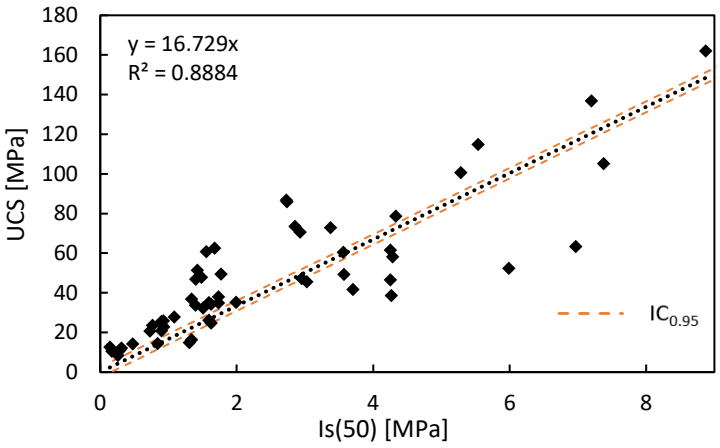

Figure 4. Granite rocks correlation

5.2 Mudstone Results

For mudstone rocks, the best fitting approximation was a linear relationship. The equation of the curve forced to pass through the origin is presented on the graph (Figure 7). With a max depth gap of 1m (an average depth gap of 0.49m), 13 datapoints were available resulting in equation (6) an R-squared value of 0.91, indicating relatively good fit.

The $Is_{(50)}$ values ranged from less than 2 MPa to 13MPa, with an average of 5.2MPa (Figure 5). The UCS range from 8MPa to 188MPa, with an average of 88 MPa (Figure 6).

$$UCS = 16.0 \times I_{s(50)}$$
$$R^2 = 0.91 \quad n = 13 \qquad (6)$$

Rusnak and Mark suggested that for sedimentary rocks like shale and mudstones the linear correlation factor could be less than 16 [18]. No correlations were found by the authors in the literature for mudstone only. However, the shale rock correlations can be considered as a comparison point. Indeed, mudstone consists in parallel layers of minerals, and shale is part of this layers. Das [4] and Vallejo et al [20] both suggested a correlation ratio of 12.6 for shale. .

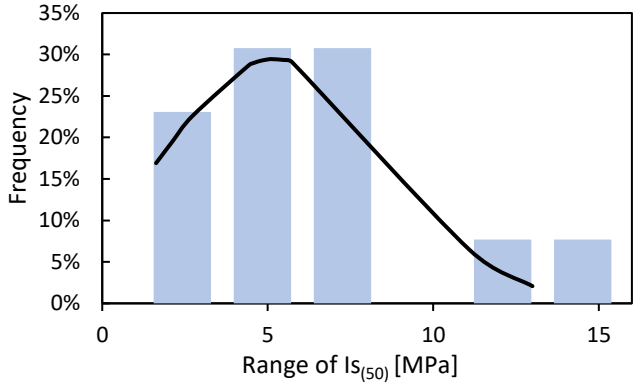

Figure 5. Mudstone $Is_{(50)}$ histogram

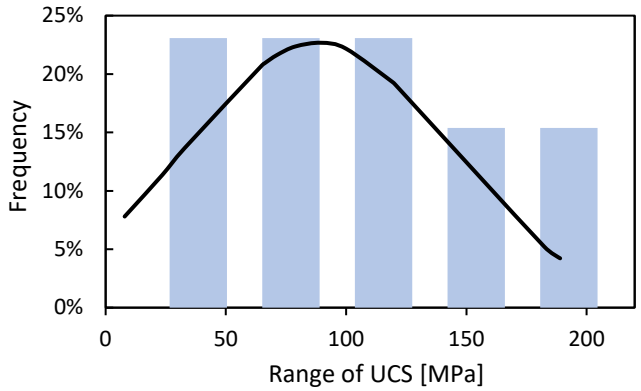

Figure 6. Mudstone UCS histogram

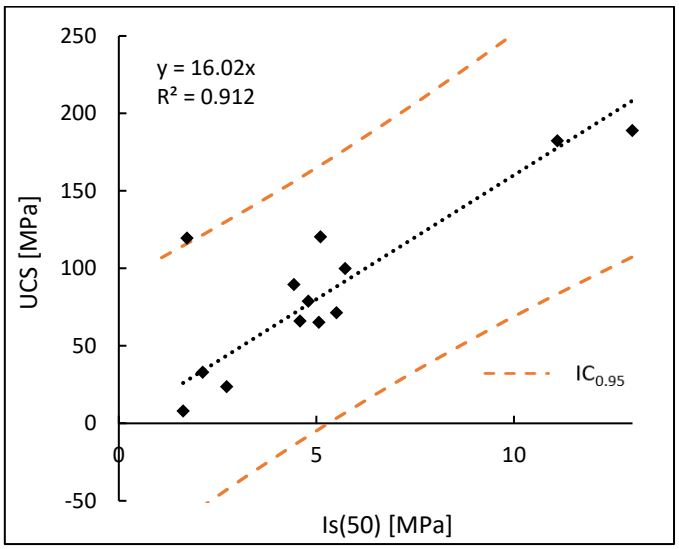

Figure 7. Mudstone rocks correlations

5.3 *Sandstone Results*

A linear relationship was also found for sandstone rocks. The relationship (7) was obtained by selecting a maximum depth gap of 3m between the UCS and the PLT. 27 points are involved in the calculation of the trend line and the average depth gap is 0.97 m. More than 30 sandstone points from the database have a Location confidence Index between 1 and 2: these points were not retained in the correlation calculation because of their uncertain rock type. The sandstone $I_{s(50)}$ range from less than 1MPa to more than 8MPa, with an average value of 2.2MPa (Figure 8). The UCS range from 5MPa to 150MPa with an average value of 42.6MPa (Figure 9).

$$UCS = 16.9 \times I_{s(50)} \qquad (7)$$
$$R^2 = 0.90 \quad n = 27$$

Many different correlations were investigated for sandstone rocks in the literature (Table 2). The wide range between the different literature relationship ratios can be noticed, highlighting the importance to develop local correlations between UCS and $I_{s(50)}$. The sandstone correlation factor found in this report is close to the ones investigated by Bieniawski [2] and Hawkins et al [13].

Table 2: Proposed correlations for sandstone rocks [1]

Author(s)	Suggested sandstone correlation equation
Bieniawski [2]	$UCS = 23.9 \times I_{s(50)}$
Das [4]	$UCS = 18 \times I_{s(50)}$
Hawkins and Olver [13]	$UCS = 24.8 \times I_{s(50)}$
Vallejo et al [20]	$UCS = 17.4 \times I_{s(50)}$

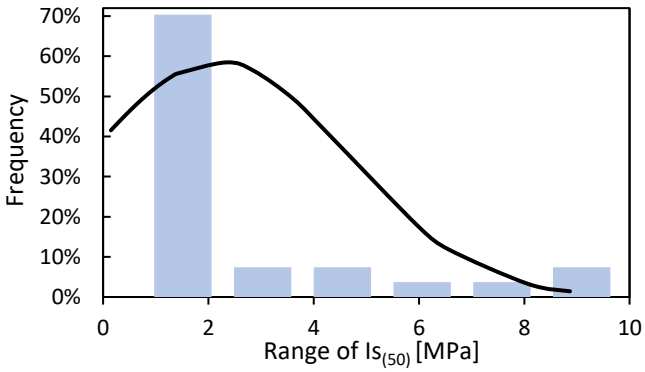

Figure 8. Sandstone $Is_{(50)}$ histogram

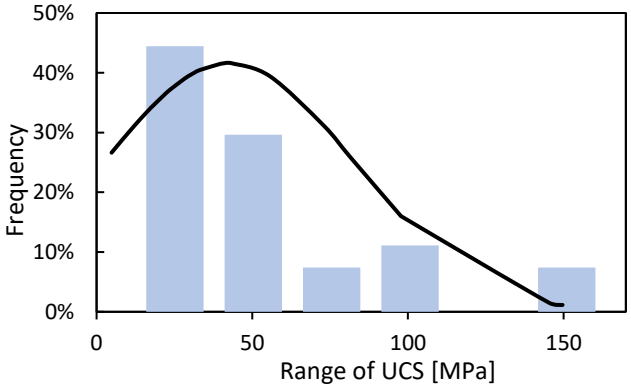

Figure 9. Sandstone UCS histogram

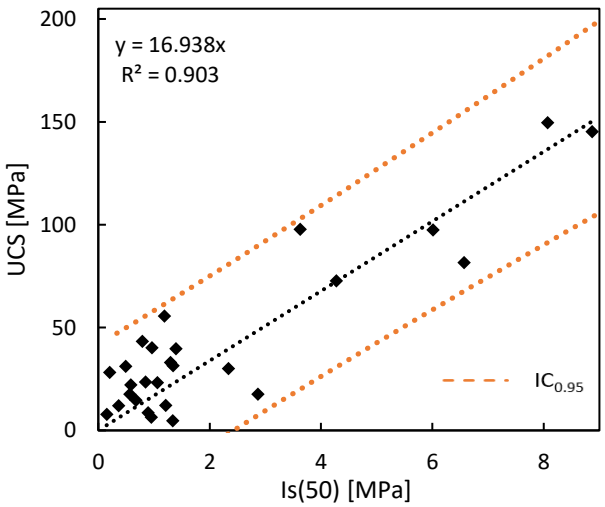

Figure 10. Sandstone rocks correlation

6 DISCUSSION

It has been considered in this paper that a coefficient of determination R-squared value around 0.9 is satisfactory for a geotechnical study because of the heterogeneity of rock materials. The results need to be carefully interpreted and used because they could lead to a consequent difference between the theoretical UCS and the experimental value.

It has been observed that the depth gap between the UCS and the PLT is an important parameter to determine the correlations. When the depth gap between UCT and PLT samples is too large, this can result in lower coefficient of determination (Figure 11). Thus, the correlations need to be used to determine the properties of the soil from similar depth.

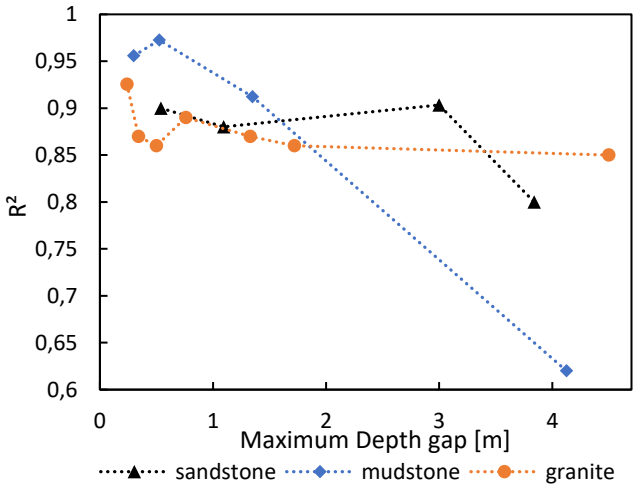

Figure 11. Influence of the depth gap for zero intercept correlations

Satisfactory linear correlations between UCS and $I_{s(50)}$ were determined for granite, mudstone and sandstone. No correlations with satisfying coefficient of determination were found for the other types of Irish rocks. For some rocks, not enough tests were available in the database to observe a correlation. For other rock types, such as those from the Calp formation, enough points were available, but the data is highly scattered. The scattered results of the Calp formation are shown in Figure 12 and could be explained by the significant difference between correlations factors of mudstone and limestone [7]. Another possible reason for the scatter may be the water content of the rock which was not measured and therefore not taken in account in the calculations. According to the literature it can have an important impact on the UCT and PLT results [8]. The coefficients of determination could be higher if the result's uncertainty was reduced by following the ISRM recommendation. The UCS index should be calculated from the mean value of a least 5 samples [11]. In the same way, at least 10 samples should be used to determine the $Is_{(50)}$ [12].

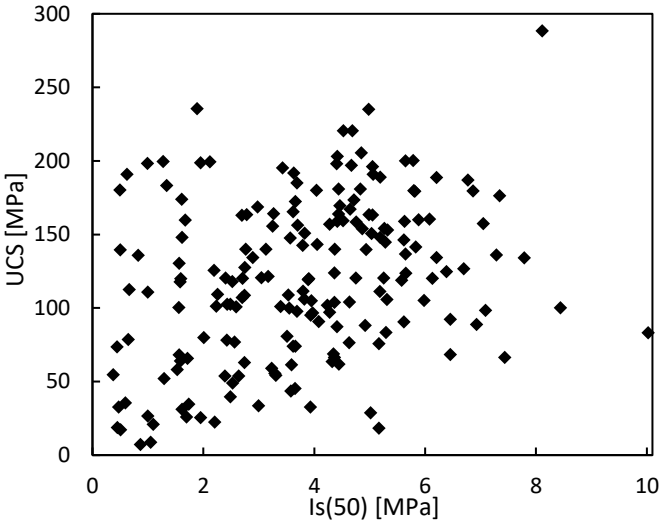

Figure 12. Dublin Calp formation

7 CONCLUSION

A new database of UCT and PLT data has been collated and input into GIS, which is now publically available. The analysed dataset showed that correlations can be used to determine the UCS index from the $Is_{(50)}$ for the Irish granite, mudstone and sandstone rocks. It has been demonstrated that the depth gap between the UCS and the PLT can have an effect on the coefficient of determination between the two indexes. This gap should be as small as possible to observe a satisfying correlation. Further studies could focus on the water content and try to study the impact of the variability in the proportion of limestone and mudstone from the Calp formation. The data is available on the Trinity Access to Research Archive (TARA) by using the following link http://hdl.handle.net/2262/100118.

ACKNOWLEDGMENTS

The authors would like to acknowledge TCD chief technical officer Eoin Dunne, and Conor Finnerty and Craig Bowes of Ground Investigation Ireland for their help in collating the test database.

REFERENCES

[1] Alitalesh, M., Mollaali, M. and Yazdani, M. (2016) 'Correlation between Uniaxial Strength and Point Load Index of rocks', Japanese Geotechnical Society Special Publication, 2(12), pp. 504–507. doi: 10.3208/jgssp.IRN-08

[2] Bieniawski, Z. T. (1975) 'Point load test in geotechnical practice', Engineering Geology, 9(1), pp. 1-11. doi: 10.1016/0013-7952(75)90024-1

[3] D'andrea, D. V., Fisher, R. I. and Fogelson, D. E. (1965) 'Prediction of compressive strength of rock from other rock properties', U.S. Bureau of Mines, Report of Investigation, 5702.

[4] Das, B. M. (1985) 'Evaluation of the point load strength for soft rock classification', Fourth international conference ground control in mining, Morgantown, pp. 220-226.

[5] 'DNV-RP-C207: Statistical Representation of Soil Data' (2012)

[6] Fleming, M., Casey P. (2015) 'An investigation of the accuracy of the use of point load index test results to predict the Unconfined Compressive Strength of Calp Limestone in Ireland', Institution of Civil Engineers, pp. 3123-3127. doi: 10.1680/ecsmge.60678

[7] Fleming, M., Casey P. (2014) 'A systematic review of common correlations between Unconfined Compressive Strength and Point Load Index for Dublin Calp Limestone.', pp 409-414

[8] Galván, M., Preciado, J. and Serón, J. (2014) 'Correlation between the Point Load Index (Is(50)) and the resistance to Unconfined Compression in limestone from the Comunidad Valenciana, Spain', Acta Geotechnica Slovenica, 2014/2, pp. 35-45.
[9] Geotechnical Survey Ireland, 'Irish Public Sector Data (Geological Survey Ireland) - Bedrock Geology 100k'. Available under a Creative Commons Attribution 4.0 International (CC BY 4.0) licence from: https://dcenr.maps.arcgis.com/apps/MapSeries/index.html?appid=a30af518e87a4c0ab2fbde2aaac3c228
[10] Ghosh, D.K., Srivastava, M. (1991) 'Point-load strength: An index for classification of rock material.' Bulletin of the International Association of Engineering Geology 44, pp. 27–33. doi: 10.1007/BF02602707
[11] ISRM (1985) 'Suggested method for determining Point Load strength.' International Journal of Rock Mechanics and Mining Sciences and Geomechanical Abstract, 22(2), pp. 51-60.
[12] ISRM, (1979) 'Suggested methods for determining the Uniaxial Compressive Strength and Deformability of rock materials'. International Journal of Rock Mechanics and Mining Sciences & Geomechanics Abstracts. 16, 2.
[13] Hawkins, A. B. and Olver, J. A. G. (1986) 'Point load tests: correlation factor and contractual use. An example from the Corallian at Weymouth.', In: Hawkins, A.B. (Ed.), 'Site Investigation Practice: Assessing BS 5930', Geological Society, London, pp. 269-271.
[14] Kahraman, S. and Gunaydin, O. (2009) 'The effect of rock classes on the relation between Uniaxial Compressive Strength and point load index', Bulletin of Engineering Geology and the Environment, 68(3), pp. 345–353. doi: 10.1007/s10064-009-0195-0.
[15] McNamee, R. (2021) 'The relevance of laboratory strength testing on stabilised or improved soil', PhD thesis.
[16] OpenStreetMap contributors (2021), 'Map data', OpenStreetMap Foundation: Cambridge. Available under the Open Database Licence from: https://openstreetmap.org
[17] Rousset, F. (2020) 'Cours de Statistique', GEN-3-Stat, Institut National des Sciences Appliquées (INSA) de Lyon.
[18] Rusnak, J. and Mark, C. (2000) 'Using the Point Load Test to determine the Uniaxial Compressive Strength of coal measure rock', International Conference on Ground Control in Mining.
[19] Sturges, H. A. (1926) 'The choice of a class interval'. Journal of the American Statistical Association. 21 (153): pp 65–66. doi:10.1080/01621459.1926.10502161. JSTOR 2965501
[20] Vallejo, L. E., Welsh, R. A. and Robinson, M. K. (1989) 'Correlation between unconfined compressive and point load strength for Appalachian rocks', Proceeding of 30th US Symposium on Rock Mechanics, Morgantown, pp. 461-468.

Transport

Recycling of Plastic Waste in Road Construction

Michael O'Shea[1], Marinel Popa[1]
[1]Department of Built Environment, Technological University of The Shannon, Moylish Park, Limerick, Ireland
email: Michael.OShea@tus.ie, Marinel.Popa@lit.ie

ABSTRACT: Plastic waste is a global problem, as is the unsustainable use of finite resources in construction. Use of recycled plastic in road construction has the potential to help with both - an example of regenerative design. This practice has already been employed in India, Malaysia, Scotland and other countries. However, research to support this approach is still at a relatively early stage. This paper presents a literature review of published research to-date, as well as an update on progress being made on research in this area at the Technological University of the Shannon (TUS). The literature review looks at characteristics of the current plastic waste stream and plastic recycling processes and how these impact options for incorporation of the waste in road construction, including the suitability of different types of plastic based on their physical properties. Two different processes currently employed for incorporation of waste plastic in bituminous road mixes are discussed, as are issues that have arisen in tests, trials and applications to-date, and areas where further research is ongoing and required.

KEY WORDS: CERI/ITRN 2022; Pollution; plastic waste; pavement; recycling; sustainable; binder.

1 INTRODUCTION

Plastic waste management and pollution are global issues. Global plastics production was 311 million tonnes in 2014; this is expected to double over the next 20 years [1]. Plastic packaging accounts for over 25% of this production, with only 14% of the resulting 78 million tonnes being collected for recycling. It is estimated that at least 8 million tonnes of the remaining waste is going into the world's oceans every year [1].

Waste generation is increasing, and Ireland is one of the highest per capita generators of plastic packaging in Europe. The EU average is 33kg per person; the figure in Ireland is 59kg per person [2]. Packaging waste generated in Ireland in 2018 was over 1 million tonnes; 25% of this was plastic, with only 31% of this plastic waste then recycled [2].

It is clear then that there is a need to increase the amount of plastic waste being recycled, to help address the plastic waste management and pollution issues. Finding alternative avenues for recycling plastic waste can form an important part of this effort.

One such avenue, that has been developing slowly, in certain parts of the world, over the last 20 years, is the use of recycled plastic waste in road construction – primarily in flexible pavements.

This paper presents a summary of the literature reviewed to-date on this topic. It also discusses the research currently being undertaken in this area at TUS.

2 PLASTICS & PLASTIC RECYCLING

2.1 Plastics and polymers

The words plastics and polymers are often used interchangeably and there are no strict definitions to differentiate them that are widely accepted. However, plastics commonly refer to commercial materials containing not only polymer molecules but also additives such as colourants, stabilisers and other chemicals required to make stable materials with properties suitable for commercial application [3].

Polymers are large molecules containing hundreds or thousands of atoms formed by combining one or two (typically) types of small molecule caller monomers – into chain or network structures [4].

Plastics have wide application throughout manufacturing and engineering.

There are numerous types of polymers which have a spread of engineering properties. Many types have relatively low elastic moduli and high permissible strains [4]. There are also many ways in which polymers/plastics can be categorised.

One of the principal categorisations relates to how the materials respond to heating – see Figure 1 below:

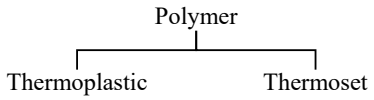

Figure 1. A categorisation of polymers.

Thermoplastics, composed of independent linear polymer chains, melt to form viscous liquids. Melting and solidification occur reversibly, according to temperature. Most thermoplastics melt at temperatures in the range 100-250°C [4].

In contrast, cross-linked polymers cannot melt once formed. These polymers are known as *thermosets*. [4]

2.2 Plastic waste

If total plastics production is broken down it is found that the largest single application of plastic is in packaging, currently

accounting for 25% or more of the total plastic produced [1], [2]. To put this in the context of other uses of plastic see Figure 2 below.

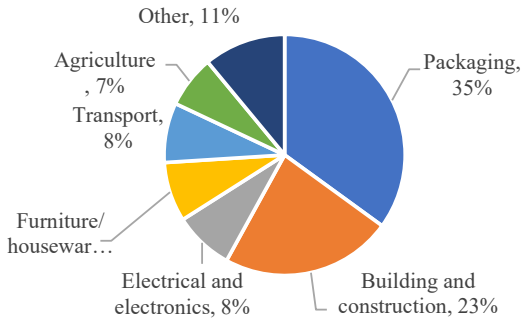

Figure 2. Breakdown of plastic use in UK, after [5].

However, due to the short lifetime of packaging the proportion of plastic waste made up from packaging is even higher – e.g. see Figure 3 below.

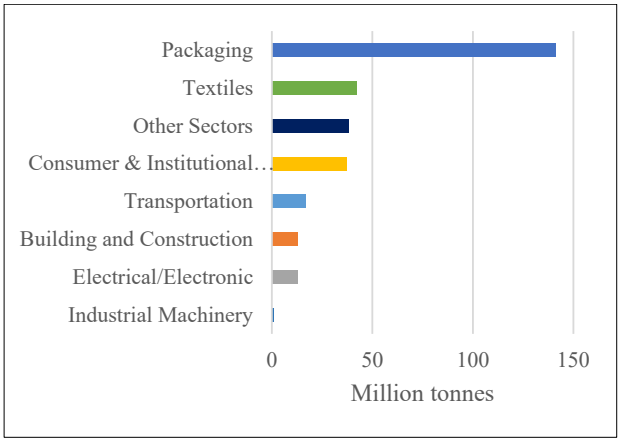

Figure 3. Global plastic waste generation by sector (2015), after [6].

It is also worth looking at the breakdown of plastic waste by type of plastic, as some plastics are more amenable to recycling than others – see Figure 4 below, where the colour of the bars provides an indication of the recyclability of the plastic, as follows:

- Green = Widely recycled
- Orange = Sometimes recycled
- Red = Rarely recycled

The abbreviations for the plastics, used in Figure 4, are explained in Table 1 below.

Table 1 provides a summary of the Resin Identification Code (RIC) system for identifying the types of plastic used in products and packaging. This system was originally developed by the Society of Plastic Industry (SPI) in the US in 1988, to assist waste recovery facilities in the sorting of plastics products prior to recycling – the intention being that all plastic products and packaging would be physically marked in accordance with the coding system. The system is now part of an ASTM international standard, ASTM D7611 [7] [8].

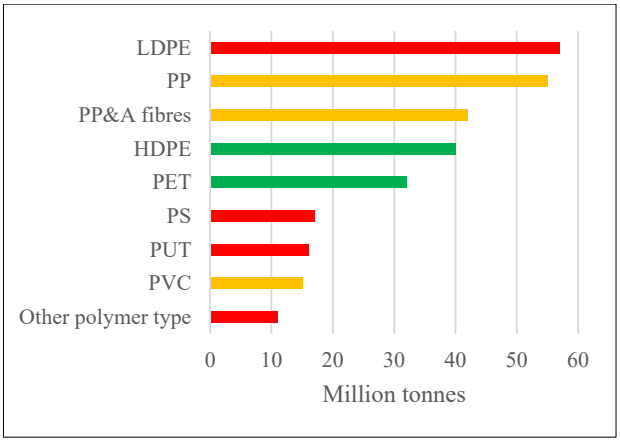

Figure 4. Global plastic waste by polymer (2015), after [6].

Table 1. ASTM D7611 RIC system (summary).

Resin Identification Number	Resin	Abbreviations	
		Option A	Option B
1	Poly(ethylene terephthalate)	PETE	PET
2	High density polyethylene	HDPE	PE-HD
3	Poly(vinyl chloride)	V	PVC
4	Low density polyethylene	LDPE	PE-LD
5	Polypropylene	PP	PP
6	Polystyrene	PS	PS
7	Other resins	OTHER	O

2.3 Plastic recycling

It is noteworthy that all of the resins listed in Table 1 above are thermoplastics. Their property of being able to be heated and softened a number of times without their structure being significantly changed [9] makes them more amenable to recycling than thermosets.

Processing of thermoplastics, to manufacture plastic products, consists of three stages:

- Melting
- Forming
- Solidifying

Similarly, re-processing involves the same stages. The 'feed stock' for thermoplastic manufacturing processes is usually plastic pellets; for these materials to be re-processed they will usually have to undergo a process to return them to this or a similar form.

It is important to note also that plastics undergo some degradation from processing/re-processing (due to heat and shear) and also in service, due to environmental influences. As a result, waste plastics will have degraded to some degree relative to their 'virgin' condition.

Figure 5 below illustrates a typical process required to recycle plastic waste, taking it from a mixed waste stream (including non-plastic materials) to clean, sorted (by plastic

type) granulated plastic ready for re-processing [5] [10]. This is an indication of the process.

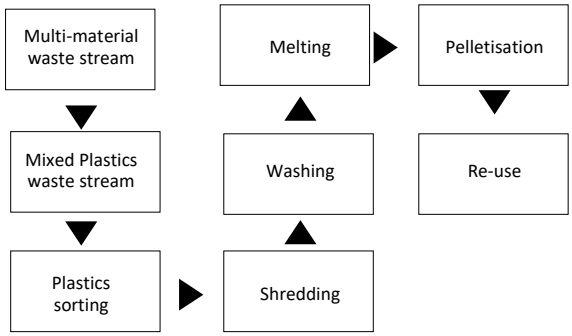

Figure 5. Typical process for recycling plastic waste.

The following provides further explanation on some of the activities in Figure 5.

- *Waste stream*. Typically, in Ireland the recyclable waste stream is mixed (i.e. contains a mixture of materials) and part of the processing of the waste is to separate this waste – either manually or mechanically. This results in a separate stream of plastic waste. At this stage this is made up of various types of plastic.
- *Plastic sorting*. It is necessary to sort the plastic waste stream into the various types of plastic, according to resin type. The reasons for this include (a) polymers do not mix well with each other [5], and (b) different plastics have different melting points – this has implications for reprocessing the material. Methods for sorting include flotation and optical (e.g. x-ray) methods.
- *Size reduction (e.g. by shredding and/or pelletising).* It is generally necessary to reduce the size of the plastic waste, to make it amenable to reprocessing.
- *Washing*. Washing is carried out to remove contaminants and residues – e.g. labels, glue, food residue etc.

3 VIRGIN PLASTICS IN ROAD CONSTRUCTION

The use of virgin plastics/polymers in flexible road construction is largely confined to polymer-modified binders (PMBs) – where polymers may be added to the binder mix to modify (improve) its properties in some way. Examples of polymers commonly used in PMBs are Ethylene Vinyl Acetate (EVA) and Styrene-Butadiene-Styrene (SBS).

PMBs are used in Ireland in a wide range of applications [11].

4 RECYCLED PLASTIC IN ROAD CONSTRUCTION

4.1 History

The earliest reference to the use of waste plastic in road construction found in the literature was a study conducted in Banaglore, India, in 1997 [12]. The first road constructed using this technology also appears to be in India – in Chennai in 2002, and indications are that there is now in excess of 33,000 km of road incorporating plastic waste in India, mostly rural roads [10]. Much of the literature to-date in this area originates in India.

Since then, the technology has been trialled and/or used in many other parts of the world.

The City of Vancouver in Canada commenced using asphalt incorporating plastic waste in 2012 [10].

Research began in 2014 in New Zealand, followed by trials, including one at Christchurch Airport's fire station [10].

In the UK, Cumbria County Council constructed a trial section of road incorporating a proprietary plastic waste product in 2017 [10]. The technology has since been used in Kent and other counties [13].

In Australia, Brisbane City Council performed a trial in 2018. Since then, trials have been conducted in other parts of Australia, including Melbourne and Victoria, and ongoing research is being undertaken at the University of the Sunshine Coast, Queensland [10].

It is also reported than many other countries, including the USA, South Africa, the Netherlands, Indonesia, Thailand, Saudi Arabia and Ghana have trialled and/or used recycled plastic in their roads [10] [13].

4.2 Application

Plastic waste has been incorporated in several ways in road construction – including prefabricated recycled plastic modular units for a bicycle path in the Netherlands [10] and as an ingredient in a cementitious grout for semi-flexible pavement. However, the most widespread application has been the use of recycled plastic waste in flexible road construction, and this is the focus of the current research at TUS.

The recycled plastic waste (RPW) can be incorporated into the bituminous mix for a flexible pavement in two ways:

- *Dry* process, or
- *Wet* process

4.2.1 Dry process

In this process the RPW, generally in the form of pellets or flakes (from shredding of plastic waste), is added to the heated aggregate, prior to mixing of the aggregate with the binder. The RPW and aggregate are mixed, with the intention of melting the RPW and obtaining an aggregate coated with RPW – a recycled plastic coated aggregate (RPCA).

It is reported [14] that in a conventional batching plant the aggregate leaves the dryer at a temperature in the range 120 to 200°C (with a temperature drop of 10 to 20°C between dryer and mixer). This temperature is important for a number of reasons:

i. The RPW will only melt and coat the aggregate if it is heated above its melting point. This melting point varies depending on the type of plastic (e.g. see Table 2 below).
ii. At higher temperatures, fuming, and eventually heat degradation of the plastic may occur. If fuming occurs this may have health and safety and/or environmental implications.

4.2.2 Wet process

In this process the RPW is hot-mixed with the bitumen binder. The result is a binder either extended or modified by the addition of the recycled plastic – i.e. a recycled plastic modified binder (RPMB). The distinction between whether the binder is modified or just extended depends on whether the addition

modifies the properties of the binder; in both cases the addition reduces the amount of bitumen required. The same abbreviation (RPMB) will be used to cover both cases.

Again, the mixing temperature is important here. Hot mixing is indicated [14], [16] to be carried out at temperatures in the range 135 to 170°C.

The RPMB is subsequently mixed with aggregate to form the bituminous mix.

Figure 6 below illustrates the options for incorporation of RPW into the mix, in summary.

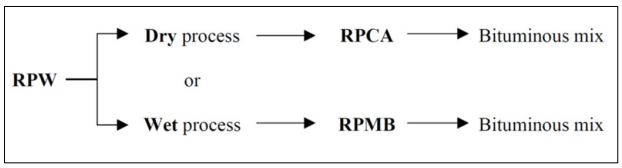

Figure 6. Options for incorporation of RPW in mix.

Table 2. Melting points of common thermoplastics.

Plastic	Melting point (°C)	Source
PET	245	[5]
HDPE	130	[5]
PVC	103-230	[17]
LDPE	115	[5]
PP	170	[5]
PS	275	[17]

4.2.3 Suitable types of recycled plastic waste (RPW)

In both the wet and dry processes described above it is necessary to melt the plastic waste. Thus, only thermoplastics are suitable for such processes (it not being possible to melt thermoset plastics after initial production). Thermoplastics constitute the vast majority of plastic entering the waste stream (see Figure 4 above).

It can also be seen that the melting points of both PET and PS are significantly higher than the normal process temperatures for making bituminous mixtures. This was also found to be the case with PVC in previous research carried out in Ireland [11]. In fact, it is reported [14] that bitumen can ignite instantaneously if temperatures above 230°C are reached so it would not appear to be feasible even to increase the mixing temperatures to allow incorporation of these types of plastic, for safety reasons.

The melting point for PP is at the extreme upper end of the process temperatures for mixing bituminous road materials, indicating potential issues with 'digestion' of this material into the bituminous mixes also. The previous Irish research [11] referred to above found issues with incorporation of PP into bituminous mixes – namely inconsistency in the softening point of the resulting PMB, and storage instability (the PP separating from the binder mix on cooling).

It would appear then that the list of suitable waste thermoplastics suitable for incorporation in bituminous mixes for flexible road construction reduces to LDPE and HDPE. The previous Irish research [11] referred to also found that these were the plastics with most potential for recycled polymer modified binders. Based on Figure 4 above, LDPE and HDPE combined account for about one-third of total global plastic waste. These plastics are widely used for the manufacture of plastic bags and plastic bottles.

Use of waste plastics with melting points above the processing temperatures for bituminous mixes – as an aggregate extender (i.e. replacing some of the stone aggregate) – is mentioned in the literature [10] [13]. However, there are indications of poor bonding of the binder to the plastic fraction of the aggregate [10].

4.2.4 Form and grading of RPW

As noted previously, the recycling process for thermoplastics will typically result in either plastic flakes/shreddings or plastic pellets suitable for reprocessing.

There is somewhat limited information in the literature regarding gradings of the RPW used in bituminous mixes. However, the particle size ranges quoted [18] [15] [19] extend from 1.18mm to 4.36mm.

A report prepared at the University of Birmingham [19] indicates a preferred particle size range of 2 to 3mm for the dry process, based on guidance from authorities in India [20], and indicates that the plastic waste should be in powder form for the wet process.

4.2.5 Dosage rates of RPW

Dosage rates quoted in the literature vary from 1% to 25%, generally quoted as being percentages of the mass of bitumen in the mix. However, most of the literature quoted rates in the range 2 to 10%. Furthermore, Sasidharan et al [19] indicate a narrower range of 5 to 10% for the dry process, based on their literature review, with 8% recommended as the optimum percentage for the dry process and 6 to 8% quoted for the wet process. Casey et al [11], in their research on the use of RPMBs in stone mastic asphalt (SMA) found that a dosage rate of 4% showed the most promise, with storage stability starting to become a significant issue at concentrations of 5%.

4.2.6 Characteristics of the resulting product

The intention with PMBs, using either virgin or recycled polymers, is that a relatively homogeneous, stable, modified binder is produced, where the internal structure of the original bitumen is modified [14], by the polymer, to improve its properties in some way. Thus, a relatively homogeneous, 2-phase (ignoring air voids) matrix, of binder and aggregate is formed when the modified binder and aggregate are mixed. This is what would be expected of a mix produced using the wet process.

With the dry process, however, research by Vasudevan et al [18] suggests a 4-phase matrix is obtained, as illustrated in Figure 7 below. Phase 1 is the aggregate; phase 2 is a plastic coating on the aggregate; phase 4 is the binder; phase 3 is a mixture of plastic and binder.

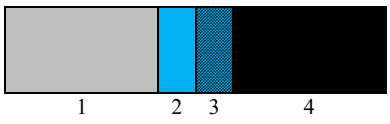

Figure 7. 4-phase matrix of mix from dry process.

The same research reports improved stripping resistance obtained with the dry process mix compared to a control mix

with no recycled plastic. This contrasts with adhesion problems reported in tests using plastic as a partial aggregate replacement, as noted above. However, in that case the plastics used had higher melting points (than the mixing temperature etc). Vasudevan et al postulate that the bitumen binds to the aggregate by diffusion through the plastic layer. However, this does not appear to tally with the multi-phase structure that they propose; if that structure is accurate, it seems more likely that the plastic bonds to the aggregate and that the bitumen bonds to the plastic. Confirmation of the structure obtained from a mix using the dry process seems worthy of further research.

4.3 Test data

There is a reasonable amount of test data available in the literature, for testing conducted on bituminous mixes made with RPW, using both wet and dry mixing processes. Generally, testing on these mixes was compared to the results of testing on a reference mix containing no RPW.

This data is still being analysed and synthesised by the authors. However, based on the review of the literature, including summary reports by Austroads, an Australasian transport agency (which appears to be similar in remit to the Transport Research Laboratory, TRL, in the UK), and by the Institute of Development Studies (UK), it can be concluded that incorporation of RPW in the mix generally results in improved properties. Please see the following sections for further details.

4.3.1 Aggregates

Results reported [12] [21] for aggregate testing on recycled polymer coated aggregate (dry process) indicate improved properties for all properties tested – namely reduced water absorption and improved abrasion and impact resistance. PSV value testing appears notably missing in literature reviewed to date and worthy of further investigation. Shape and grading would not be expected to be significantly affected by the addition of a thin coating of plastic to the aggregate particles.

4.3.2 Binder

Test results reported for modified binders indicate improved stripping resistance [15] [21], increased viscosity and hardness [11] [12] [15], and increased softening point [11] [12].

The increased viscosity values measured [11] were still well within what would be considered the suitable range for laying.

Although the softening point was increased by the modification of the binder using the recycled plastic, indicating improved resistance to deformation at higher temperatures, Casey et al reported that, to comply with Irish requirements for PMBs, that a phosphoric acid (PPA) additive had to be added to their mix (to achieve a value greater than the required minimum of 60°C).

4.3.3 Bituminous mix

Test results reported for the bituminous mix indicated improved Marshall test results (greater stability [12] [19] and reduced flow [19]).

The test results also indicated improved resistance to rutting, generally measured using the Wheel-tracking test, in mixes incorporating RPW, relative to tests on control mixes [12] [13] [19]. It was also found [11] [13] that rutting resistance was not enhanced to the same degree as mixes using binders modified with virgin polymers.

4.4 Performance data

There is not a lot of performance data reported in the literature on roads that have been constructed with flexible pavements incorporating RPW in the mixes. This is in part because it is relatively new technology. It also appears to be in part due to commercial interests – with companies like Dow Chemicals and Petronas conducting research with a view to developing proprietary products in this area.

Lack of performance data is cited by Austroads in their report on a review of this technology [10]. They do, however, conclude that the overall results are positive in the data that is available – while also citing a need for (presumably independent) 3rd party assessment

Vasudevan et al report [21] on performance studies conducted in 2008 on 5 roads constructed in India between 2002 and 2006 which incorporated RPW. The results of these studies reported satisfactory performance in all cases.

4.5 Concerns

The main concerns raised in the literature in relation to this technology are:

- Potential health and safety issues
- Fuming
- Environmental
- Recylability
- Regulation/governance

Health and safety issues raised relate mainly to potential risks to workers working with bituminous mixes containing RPW, including the potential for 'fuming' – where harmful gases may be emitted on heating of the RPW.

Other environmental concerns relate mainly to the potential for leaching of microplastics from the pavement.

Recycling of flexible pavement materials is increasing and the question of how incorporation of RPW in the mixes may affect this in the future has been raised.

Finally, there is currently a lack of technical guidance, regulations, and governance frameworks in place for the use of RPW in flexible pavements.

5 RESEARCH AT TUS

Research to date at TUS has primarily comprised an extensive literature review and preliminary discussions with plastic recycling companies and companies batching bituminous mixes for road construction.

Planned further research at TUS includes further progress on these activities as well as laboratory testing on samples of bituminous mixes made with RPW (as well as control mixes, for reference/comparison) and seeking sponsorship for construction of a trial road pavement incorporating such mixes, for assessment of constructability and performance. It is also planned to seek partners, within TUS or beyond, for investigation into some of the concerns raised (e.g. fuming) that are more related to plastic chemistry and technology than the civil engineering application of the technology.

In relation to a framework for more detailed assessment of the potential of the technology, the TRL report [22] on the use of Shell Thiopave as a sulphur asphalt extender/modifier provides a good structure for similar technology.

6 CONCLUSIONS

A review of the research published to date on the use of recycled plastic waste in flexible road construction indicates great potential for this technology.

The environmental benefits are obvious, in terms of providing a new means of recycling certain plastic waste (LDPE and HDPE) which forms a major component of the plastic waste stream.

To get a measure of the potential impact, in terms of recycling plastic waste, let us consider a kilometre of all-purpose single carriageway road – 8m wide, say, with a thickness of bound pavement of 200mm. Assuming a percentage, by weight, of 5% of binder, and a dosage rate of 8% of RPW (by weight of binder) the amount of plastic weight recycled would be:

$$Weight\ of\ bound\ road\ construction = (1000 \times 8 \times 0.2) \times 2.3 = 3680\ tonnes/km$$

$$Weight\ of\ recycled\ plastic = 3680 \times 5\% \times 8\% = \mathbf{15\ tonnes/km}$$

The benefits are twofold:

i. The environmental benefits of finding another means of recycling plastic waste and diverting it from potential landfilling, and
ii. The use of the RPW reduces the quantity of bitumen required in the mix – a material derived from the world's oil resources, and one that requires energy input to derive it from crude oil.

In addition, testing and performance studies to-date indicate improved properties and performance of the road construction, although much additional testing and performance data is required to provide a higher degree of confidence in this.

Concerns raised in previous research and reviews, regarding potential health and safety and environmental issues, also require further research.

REFERENCES

[1] WEF, "The New Plastics Economy - Rethinking the future of plastics," World Economic Forum, 2016.

[2] EPA, "National Waste Statistics Report," Environmental Protection Agency, Dublin, 2018.

[3] N. Mills, M. Jenkins and S. Kukureka, Plastics - Microstructure and Engineering Applications, Butterworth-Heinemann, 2020.

[4] N. Jackson and D. R, Civil Engineering Materials, Macmillan, 1997.

[5] V. Goodship, "Plastic recycling," *Plastic Progress,* vol. 90, no. 4, pp. 245-268, 2007.

[6] World in Data, "Plastic Pollution," 2022. [Online]. Available: https://ourworldindata.org/plastic-pollution. [Accessed 10 May 2022].

[7] ASTM Technical Committee D20, "ASTM Plastics Committee Releases Major Revisions to Resin Identification Code (RIC) Standard," 2013. [Online]. Available: https://newsroom.astm.org/astm-plastics-committee-releases-major-revisions-resin-identification-code-ric-standard#:~:text=These%20categories%20include%3A%201)%20polyethylene,resin%20from%20categories%201%2D6.. [Accessed 11 May 2022].

[8] American Society for Testing and Materials, *ASTM D7611/D7611M-21 Standard Practice for Coding Plastic Manufactured Articles for Resin Identification,* ASTM, 2021.

[9] S. M. Halliwell, *Plastics recycling in the construction industry,* BRE, 1997.

[10] Austroads, "Viability of Using Recycled Plastics in Asphalt and Sprayed Sealing Applications," Austroads Ltd., Sydney, 2019.

[11] D. Casey, C. McNally, A. Gibney and M. D. Gilchrist, "Development of a recycled polymer modified binder for us in stone mastic asphalt," *Resources, Conservation and Recycling,* vol. 2008, no. 52, pp. 1167-1174, 2008.

[12] R. S. S. a. S. K. Manju, "Use of plastic waste in bituminous pavement," *Int J ChemTech Res,* vol. 10, no. 8, pp. 804-811, 2017.

[13] G. a. H. F. White, "Comparing asphalt modified with recycled plastic polymers to conventional polymer modified asphalt," in *Eleventh International Conference on the Bearing Capacity of Roads, Railways and Airfields, Volume 1*, C. Press, Ed., n.d, CRC Press, 2021, pp. 3-17.

[14] R. N. Hunter, Bituminous mixtures in road construction, ICE Publishing, 1994.

[15] J. G. Speight, Asphalt - Material Science and Technology, Butterworth-Heinemann, 2016.

[16] G. Wypych, Handbook of Polymers, ChemTec, 2016.

[17] Vasudevan R., "Utilisation of plastic for flexible pavements," *Indian High Ways,* vol. 34, no. 7, p. n.d, 2006.

[18] C. S. N. S. C. a. B. A. Raja, "A Review on Use of Plastic in Construction of Roads," *Journal of Advancement in Engineering an Technology,* vol. 7, no. 4, pp. 1-3, 2020.

[19] M. Sasidharan, M. Eskandari Torbaghan and M. P. N. Burrow, "Using waste platics in road construction," UK Institute of Development Studies, Brighton, 2019.

[20] Indian Roads Congress, *Guidelines for the use of waste plastic in hot bituminous mixes (dry process) in wearing courses,* New Delhi: IRC, 2013.

[21] R. Vasudevan, A. Ramalinga Chandra Sekar, B. Sundarakannan and R. Velkennedy, "A technique to dispose waste plastics in an ecofriendly way - Application in construction of flexible pavements," *Construction and Building Materials,* pp. 311-320, 2012.

[22] TRL, "Report TRL672 - Review of Shell Thiopave sulphur-extended asphalt modifier," Transport Research Laboratory, Wokingham, 2009.

Using Machine Learning to Predict the Impact of Incidents on the M50 Motorway in Ireland

Linhao Yang[1], Robert Corbally[1], Abdollah Malekjafarian[1]
[1]Structural Dynamics and Assessment Laboratory, School of Civil Engineering, University College Dublin, Dublin 4, Ireland
email: linhao.yang@ucdconnect.ie, robert.corbally@ucdconnect.ie, abdollah.malekjafarian@ucd.ie

ABSTRACT: Every year thousands of incidents occur on Irish roads. These incidents can be varied in nature and severity, ranging from debris on the road to serious road-traffic-collisions. The management of incidents on motorways is of particular importance, both in terms of road-user safety and maintaining network performance. Incident management encompasses a broad range of activities, with a multi-agency response often required to ensure that an incident is managed safely and efficiently with minimal traffic disruption. When an incident occurs on the motorway network, a dynamic risk assessment must be made by response personnel to estimate the severity of the incident and the potential impact on traffic conditions. A key parameter in this assessment is the duration of the incident, which is often difficult to establish, and likely to change as the incident evolves. Making a judgement on the expected duration of an incident can be difficult, however as traffic management processes become more automated, computer algorithms and historical incident databases can be leveraged to improve real-time predictions of incident duration. This paper analyses incidents that occurred on the M50 motorway in Ireland. By comparing the predictive performance of multiple machine learning methods for different types of incidents, an integrated approach is proposed to utilise the advantages of different methods. The results show that support vector machines perform best in most cases, but in some cases a different method may need to be used. Suggestions are made for further improvements which could improve accuracy and benefit real-time motorway operations response procedures.

KEY WORDS: Traffic incidents; M50 motorway; Duration; Congestion; Machine learning; Regression; Classification.

1 INTRODUCTION

The M50 motorway is the most heavily trafficked road in Ireland with nearly 1400 incidents per year which range from road traffic collisions, breakdowns, and debris on the carriageway to animals on the road or overturned vehicles. To develop efficient incident response procedures for road operators, the ability to predict the impact that an incident will have on traffic flow is of major benefit. The impact of an incident can be quantified as the duration that it affects the traffic. Establishing the expected duration of an incident allows suitable response plans to be put in place, particularly in relation to setting of variable message signs or signals to warn drivers of potential delays or safety issues. As a result of advances in Intelligent Transport Systems (ITS) technology, a large amount of data is available to develop machine learning models. This paper combines incident, traffic flow and weather datasets from Ireland's M50 motorway to predict the incident duration using various machine learning methods, explores the performance of each method and discusses their drawbacks.

The use of machine learning to predict incident duration has been ongoing for over two decades, with different studies demonstrating varying accuracy. In 1999, Ozbay and Kachroo [1] used decision trees to predict incident clearance times in the Northern Virginia region. They built decision trees considering various factors such as road hazards, property damage, personal injuries, disabled truck, vehicle fires, weather, etc. Before constructing the decision trees, the significance of independent variables was tested by analysis of variance (ANOVA). Some types of incidents (such as weather-related incidents) with too little data to be tested are eliminated. The actual data were used for testing and it was found that 60% of the incidents had a prediction error of 10% or less, but some incidents had very large errors.

Chang, Chang [2] analysed 4908 accidents in Taiwan and built a classification trees model containing twenty-seven terminal nodes. Analysis of the distribution of incident durations revealed that although the average incident duration was 36.9 minutes with a standard deviation of 29.9 minutes, it had an extremely right-skewed distribution with a maximum duration of 391 minutes. The model has a classification accuracy of 96.7% for test data with short incident durations, however the classification accuracy for medium and long durations is extremely low (<20%). The authors stated that this was due to the fact that over 72% of incident durations were short duration, resulting in an unbalanced data set, and therefore further research should be conducted on medium and long duration incidents.

Leahy and Lynch [3] similarly used a classification trees approach to 556 accidents on the Dublin M50 from 2014 to 2016. The duration of accidents was classified into three categories (less than ten minutes, ten to sixty minutes and greater than sixty minutes) and classified using the Ensemble Bagged Trees method with an accuracy of 52.7%. Notably, the study found that, similar to previous studies, the classification trees method did not perform well in predicting long durations.

Zong et al. [4] analysed police reported traffic accident records from Jilin Province, China, in 2010. In addition to accident and traffic characteristics, they also collected weather factors and road environment factors. They predicted the severity of accidents using Support Vector Machine (SVM) and

Ordered Probit models and found that the Ordered Probit model was slightly more accurate than the SVM. The results showed that the presence of hazardous materials, the weather and the location of the accident had a significant effect in both models.

Yu et al. [5] compared the performance of Artificial Neural Networks (ANN) and SVM using data from 235 accidents that occurred on a highway in China between 2012 and 2014. The authors noted that both models tended to have low accuracy for longer duration incidents due to the relatively small number of longer duration incidents in the dataset, although the SVM model performed better than the ANN model for medium duration predictions, ANN model has better performance when predicting long duration. The authors also found that there were some outliers due to individual differences in incident management teams responding to incidents, with significant differences between recorded and predicted incident durations.

Valenti et al. [6] compared five machine learning methods (including multiple linear regression, decision trees, ANN, SVM and K-Nearest-Neighbour). The results showed that the proposed model was able to achieve good performance in terms of prediction accuracy for incidents of less than 90 minutes in duration. Similar to previous findings (Yu et al. [5]), linear regression is the best approach for short duration incidents, with Relevance Vector Machine (RVM) models achieving the best prediction in the case of medium and medium to long duration incidents, and ANN being the only model able to predict incidents longer than 90 minutes. For longer duration incidents, the accuracy of all the proposed models is relatively low, partly due to the relatively small number of severe incidents in the dataset.

The studies above demonstrate the potential of combining multiple machine learning methods to improve overall prediction performance for incidents of different types and duration.

2 DATA COLLECTION AND PREPARATIOIN

2.1 Incident data

A database of incidents on the M50 motorway is used in this study. The database was provided by Transport Infrastructure Ireland and contains various details for each incident, including the date, time, location, category, type, travel direction, closed lane count and whether the emergency services were required to attend. It is not considered appropriate to use the latitude, longitude and time of the incident directly in machine learning models, so data pre-processing is necessary.

In some cases, the incident coordinates were not exactly correct, so an estimate of the distance to the nearest junction was calculated by measuring the straight distance from the incident to the adjacent junctions. The extent of the junctions was determined by viewing a satellite map and marking the entry and exit (Figure 1). According to their location, incidents can be classified as before, within or after the junction. Also, for incidents that are not in the middle of the junction, the distance from the incident to the centre of the junction is recorded. Finally, three incident location features are obtained, junction number, location to junctions and distance to junctions, which provide a good representation of the location characteristics of the incidents.

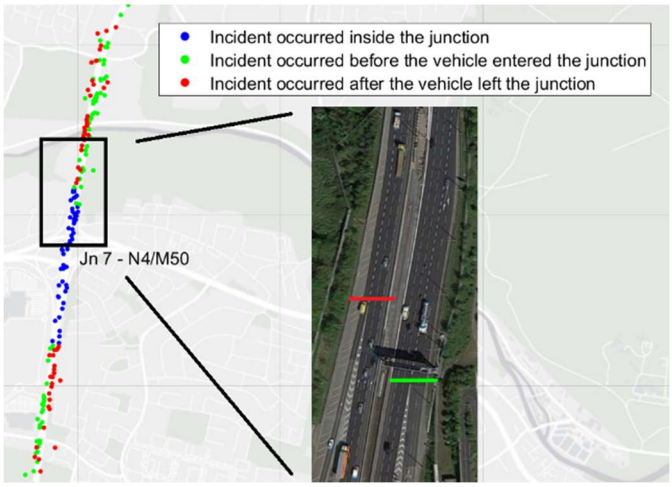

Figure 1. Incident location characteristics at Junction 7.

Road users have different travel patterns on different days, such as commuting to and from their workplace on weekdays, travelling on holidays, etc. Some journeys are regular while others are not, and even on weekdays people do not repeat the same journey every day. The UK Department for Transport [7] divided the dates into 13 types and in addition to each day of the week, they distinguished between different types of holidays and different days within holidays, as described in Table .

Table 1. Definition of Day Types [7]

Day Type	Description	Day Type	Description
0	First working day of normal week	7	First day of week – school holidays, excluding day types 12,13 and 14
1	Normal working Tuesday	9	Middle of week - school holidays, excluding day types 12, 13 and 14
2	Normal working Wednesday	11	Last day of week - school holidays, excluding day types 12, 13 and 14
3	Normal working Thursday	12	Bank Holidays, including Good Friday and excluding day type 14
4	Last working day of normal week	13	Christmas period holidays, days between Christmas Day and New Years Day
5	Saturday	14	Christmas Day/New Years Day
6	Sunday		

The time of day is also an important consideration. Peak periods were defined as 06:30-09:30am and 3:30-6:30pm on weekdays for the morning and evening peak periods, respectively. Figure 1 shows that incidents are more likely to occur and last longer during the peak hours on weekdays.

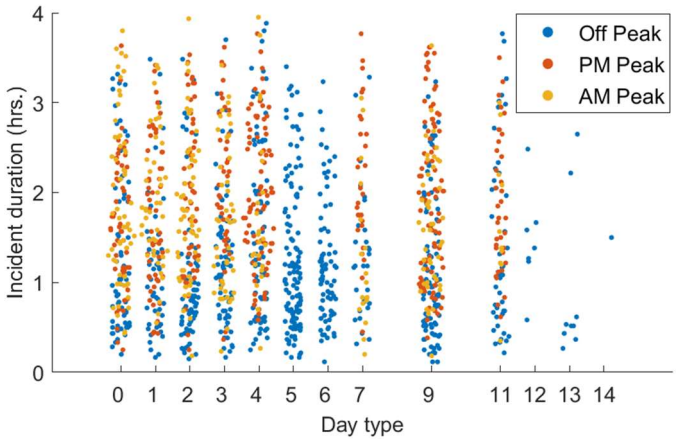

Figure 2. Incident location characteristics vs incident duration.

2.2 Weather data

Weather data is obtained from five weather stations installed along the M50, which record data every 10 minutes. Figure 3 shows the relationship between four different weather factors and the incident duration. Due to the limited measuring range of the visibility sensors, the visibility data is almost entirely capped at 2000m. It should also be noted, that while the water film thickness on the surface of the road is a useful parameter, the localised nature of this measurement will make it difficult to accurately attribute measurements of surface water level to incidents which do not occur directly adjacent to the sensor. As such, rainfall was used instead of water thickness when making predictions. Therefore, when predicting the duration of incidents, this study uses the average of the surface temperature and precipitation intensity over the incident duration.

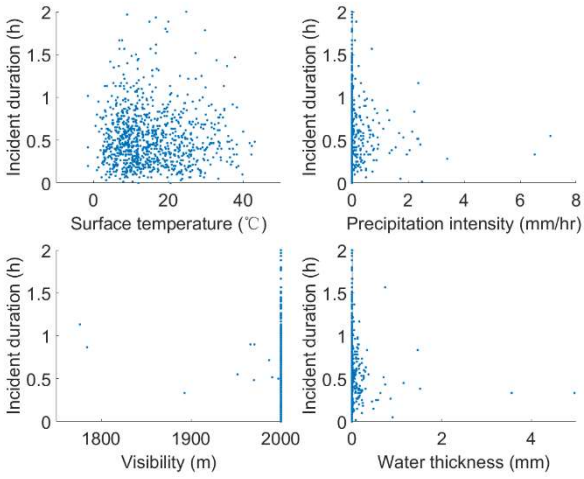

Figure 3. Weather data vs. incident duration.

2.3 Traffic data

TII has installed a large number of ITS devices on the M50, which include double inductance loops spaced every five hundred metres recording the number of vehicles in each lane, average speed, vehicle length and lane occupancy every 20 seconds. As part of the ongoing enhancing Motorway Operations Services (eMOS) programme, Roughan & O'Donovan (ROD) Consulting Engineers, working on behalf of TII, have developed a series of algorithms to determine the time taken for traffic conditions to return to 'normal' following the closure of an incident. A database of these durations was provided by ROD for this study and it was considered more appropriate to use the calculated durations for the purposes of making predictions, rather than the incident durations directly recorded by the control room operators, which may include durations which are not directly related to the impact on traffic flows (e.g. a piece of debris in the grass verge may take a number of hours to be removed, but may not affect traffic flows at all). The downside of using this database is that only incidents with longer durations can be considered, because incidents which have limited impact on traffic typically return to normal traffic conditions before the incident is closed and are disregarded in these calculations.

3 EXPLORATORY ANALYSIS

3.1 Incident duration distribution

The mean incident duration in the dataset is 97.04 minutes, with a median of 85 minutes, a lower quartile value of 52 minutes and an upper quartile value of 135 minutes. Figure 4 shows the distribution of incident durations and it can be seen that the dataset fits the Weibull and Loglogistic distributions well, which is consistent with previous research (Nam and Mannering [8]).

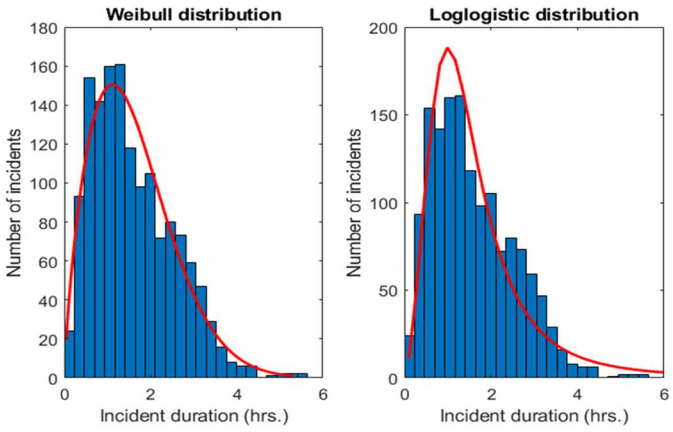

Figure 4. Incidents duration distribution.

3.2 Multiple linear regression

In order to meet the assumption of normal distribution required for the MLR method, the dependent variable is logarithm base 10 of the duration, with a skewness coefficient equal to -0.6. Only features below that are linearly related to the incident duration will be used for prediction.

- X_1: Incident Category
- X_2: Time Period
- X_3: Closed Lane Count
- X_4: Rain
- X_5: Garda Attendance
- X_6: Fire Service or Ambulance Attendance
- X_7: Location to Junction
- X_8: Distance to Junction Entry/Exit

Table 2 shows the results, it can be seen that Closed Lane Count, Location to Junction and Distance to Junction Entry/Exit are not statistically significant, while the other factors are statistically significant. However, with an R^2 of only 0.185, an F-ratio equal to 41.2 and a p-value equal to 0, the

model has a poor explanatory, indicating that the multiple linear regression model cannot accurately capture the incident impact. This is similar to the predictions of Peeta et al. [9] who found an R^2 of 0.234.

Table 2. Coefficients of the MLR model.

	Coefficients (bi)	Std. Error	t-Stat	p-Value
(Intercept)	3.85	0.06861	56.112	0
x1	0.076628	0.02795	2.7413	0.006195
x2	0.46601	0.03412	13.658	4.86E-40
x3	0.004376	0.02160	0.2025	0.83951
x4	0.12767	0.03619	3.5274	0.000433
x5	0.14502	0.03433	4.2232	2.56E-05
x6	0.23743	0.04566	5.1999	2.28E-07
x7	-0.06856	0.04359	-1.5725	0.11605
x8	-0.037	0.03747	-0.9875	0.32356

4 MACHINE LEARNING

The dataset used in this study includes 1,391 incidents that occurred on the M50 motorway between 2017 and 2019 that were validly recorded, and their incident characteristics are mainly shown in Table 3. For both regression and classification analysis, Classification and Regression Trees (CART), SVM and ANN are used.

Table 3. Incidents features used in analysis.

Feature	Notes
Incident Category	1 = Category 1 2 = Category 2 3 = Category 3 4 = Category 4
Primary Incident Type	1 = Collision 2 = Breakdown 3 = Vehicle fire 4 = Debris or Spillage
Peak Hours	0 = Off Peak 1 = PM Peak 2 = AM Peak
Day Type	0 – 7, 9, 11-14
Closed Lane Count	0 – 3
Rain	mm
Surface Temperature	°C
Garda Attendance	1 = true, 0 = false
Fire Service Attendance	1 = true, 0 = false
Ambulance Attendance	1 = true, 0 = false
Junction number	2 – 7, 9 - 17
Location to junction	1 = Before 2 = Middle 3 = After
Distance to junction entry/exit	km

4.1 Regression Analysis

Regression analyses are first performed on all incident data. The SVM using a Gaussian kernel function shows the best prediction performance with a Mean Absolut Error (MAE) of 40.66 minutes and MAE% of 42.2%. Figure 5 indicates that the model it overestimates incident duration for short duration incidents and is unable to predict incidents longer than 150 minutes, which suggests that the SVM may be preferable for predicting incidents of 30 to 120 minutes duration.

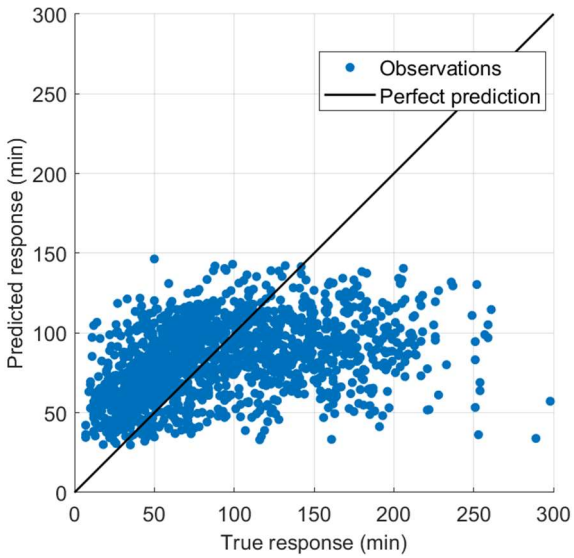

Figure 5. Predicted vs. true values for SVM.

The neural network model with a single hidden layer using ReLU as the activation function also achieves good prediction results. It can be seen from Figure 6 that although the model overestimates incidents of shorter duration and underestimates those of longer duration, it may be more suitable than SVMs for predicting incidents of longer duration.

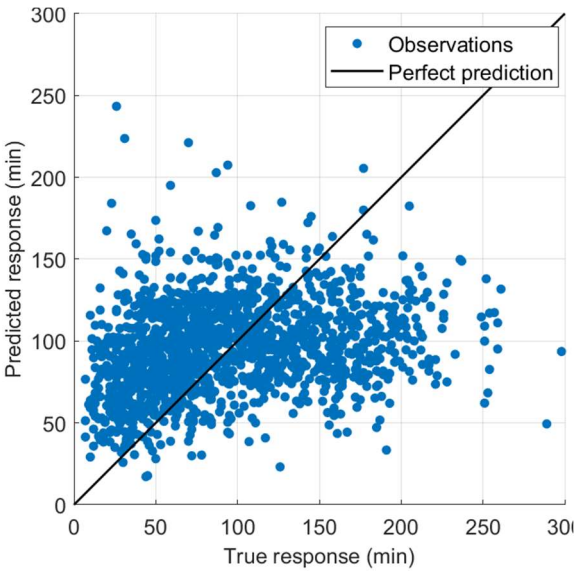

Figure 6. Predicted vs. true values for ANN.

Figure 7 shows the results of the regression analysis for each of the three incident types individually. It can be seen that the SVM model has the best predictive ability for all three incident types, with ANN performing the worst. In particular, SVM demonstrates superior predictive performance for collision

incidents and ANN is not suitable for predicting Debris or Spillage incidents.

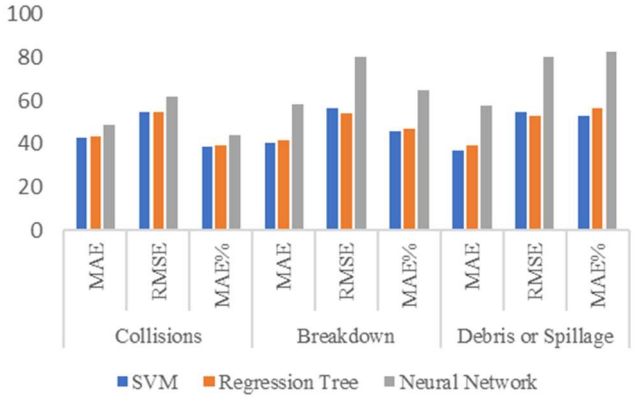

Figure 7. Regression analysis for specific incident types.

4.2 *Classification Analysis*

The dataset is divided as evenly as possible into four parts, depending on incident duration to assess the ability to predict the overall severity of the impact of the incident. Table 4 shows the classification of incidents based on duration.

Table 4. Classification of incident durations.

Incident Duration	Classification	Sample Size
<52 mins	1	347
>=52 & <85 mins	2	346
>=85 & <135 mins	3	348
>=135 mins	4	350

Classification analyses are first performed on all incident data. The SVM using a linear kernel function performs the best prediction performance, with an accuracy of 40.8%. Figure 8 shows its confusion matrix and it can be seen that the model performs better for predicting incidents of less than 52 minutes duration and those lasting longer than 85 minutes. Other methods obtain similar results.

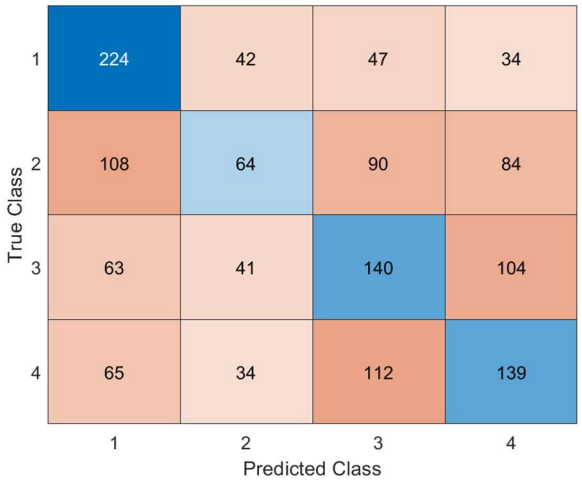

Figure 8. Confusion matrix for SVM classification prediction.

Figure 9 shows the results of the classification analysis for specific incident types and it can be seen that by classifying the incidents, the prediction accuracy for Breakdown and Debris type incidents is improved. The classification trees have the best prediction for Collisions and Breakdown, while ANN has the highest accuracy in predicting the Debris incidents. This is very different from the results where SVM prediction performance is superior when not classified, suggesting that prediction accuracy can be improved by adopting different machine learning methods for different incident types.

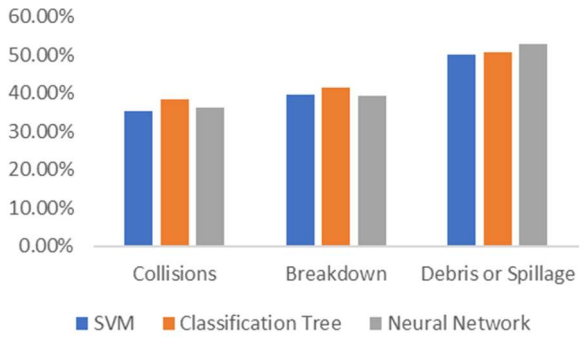

Figure 9. Classification analysis for different incident types.

4.3 *Importance estimates of predictor variables for trees models*

Table 5 presents the importance estimates of the predictor variables after normalization for both Regression trees and Classification trees. They are calculated based on the node risk of each split and vary according to the criteria for splitting, so they are normalized to facilitate comparison, with a value of 1 representing the most important variable. It shows that in the regression trees model, incident type, time period, rainfall, temperature and fire service attendance and location characteristics are considered to be important, while incident category, day type, closed lane count, police cars and ambulances are considered to be unimportant variables. The importance estimates for the classification trees are similar to those of the regression trees model. The main difference is that in the classification trees model, day type is considered to be significant.

Table 5. Importance estimates of predictor variables.

Features	Regression trees	Classification trees
Incident Category	0.0185	0.0370
Incident Type	0.4606	0.5062
Time Period	1	1
Day Type	0.0034	0.4431
Closed Lane Count	0	0.1729
Precipitation	0.2623	0.3557
Surf Temperature	0.2501	0.6191
Police Attendance	0.0241	0.1088
Fire Service	0.2288	0.1876
Ambulance	0	0
Junction number	0.0921	0.3771
Location to junction	0.0334	0.0347
Distance to junction	0.0594	0.2246

4.4 *Discussion*

At an initial glance, the results achieved in this study appear to be less accurate than other research on this topic. For example, the best result achieved by Valenti et al. [6] was an MAE of 16

minutes by ANN model, which is much better than the 40 minute MAE achieved in this study. However, the mean incident duration in the study by Valenti et al. was 45 minutes, whereas in this study the mean incident duration was 97 minutes. Therefore, the percentage error is 40%, which is similar to an 35% error achieved by Valenti et al. Similarly, the study by Leahy and Lynch [3], which also examined incident durations on the M50 motorway in Ireland achieved a MAE of 24.9 minutes, however, the mean incident duration was also significantly lower, making the findings of this paper comparable or better if the results are examined in terms of the percentage error.

Chang, Chang [2] achieved an accuracy of 75.1%, mainly because they classified 72% of the incidents as short duration, 25.7% as medium duration and only 2.2% as long duration. Because its classification is not balanced, it is not surprising that it achieves an accuracy rate of 75%.

This study divides incident durations into four average categories, and the classification accuracy is not skewed towards shorter incidents, which tend to be most common and subject to less error. Overall, the models used in this study, and most other research, are not particularly accurate and would require increased accuracy to represent a truly useful tool for motorway operations. The large prediction errors highlight the varied and unpredictable nature of incidents and the challenges associated with estimating their impact. However, the results do provide some promise that different models could be used to make better predictions depending on the type of incident. Also, if shorter duration incidents were not excluded from the study, it is expected that accuracy levels would be improved.

5 CONCLUSIONS

The aim of this study is to predict the impact of traffic incidents on the M50 motorway using a machine learning approach. This paper combines incident, traffic flow and weather datasets from the M50 to predict the duration of incidents using a variety of machine learning methods. By discussing their prediction performance, it is proposed that the accuracy of regression analysis can be improved by combining SVM and ANN, where SVM is better at predicting short and medium duration incidents and ANN is able to predict long duration incidents. SVM shows the best predictive performance in regression analysis when predicting the duration of a single incident type. In the regression analysis it is found that for different durations, each machine learning method has its own strength and it is possible to use a combination of these three machine learning methods to improve predictive accuracy.

The importance of influential factors is viewed using multiple linear regression and tree models, where both models agree that rainfall, time of day and emergency service attendance have significant influence. The tree models also consider location and incident type to be influential.

Over 60% of the data in the original dataset is removed in this study in order to increase the accuracy of the available data, which results in the dataset used in this study possibly not being a good representation of the original dataset. Compared to other studies, it can be found that the current TII incident dataset could benefit from systematically recording more information such as the number of vehicles involved, or whether trucks are involved. Further research is required to improve prediction accuracy and develop a useful approach which could benefit real time motorway operations response procedures.

ACKNOWLEDGMENTS

The authors would like to acknowledge Transport Infrastructure Ireland (TII) and Roughan & O'Donovan (ROD) Consulting Engineers for the provision of the data sets used in this study.

REFERENCES

[1] K. Ozbay and P. Kachroo, "Incident management in intelligent transportation systems," 1999.

[2] H.-l. Chang and T.-p. Chang, "Prediction of freeway incident duration based on classification tree analysis," *Journal of the Eastern Asia Society for Transportation Studies,* vol. 10, pp. 1964-1977, 2013.

[3] C. Leahy and S. Lynch, "Analysis of Traffic Incidents using Machine Learning," presented at the CERI-ITRN2018, Dublin, Ireland, 2018.

[4] F. Zong, H. Zhang, H. Xu, X. Zhu, and L. Wang, "Predicting severity and duration of road traffic accident," *Mathematical Problems in Engineering,* vol. 2013, 2013.

[5] B. Yu, Y. Wang, J. Yao, and J. Wang, "A comparison of the performance of ANN and SVM for the prediction of traffic accident duration," *Neural Network World,* vol. 26, no. 3, p. 271, 2016.

[6] G. Valenti, M. Lelli, and D. Cucina, "A comparative study of models for the incident duration prediction," *European Transport Research Review,* vol. 2, no. 2, pp. 103-111, 2010.

[7] (2016). *Reliability of Journeys on the Highways Agency's Motorway and "A" Road Network: the On Time Reliability Measure*.

[8] D. Nam and F. Mannering, "An exploratory hazard-based analysis of highway incident duration," *Transportation Research Part A: Policy and Practice,* vol. 34, no. 2, pp. 85-102, 2000.

[9] S. Peeta, J. L. Ramos, and S. Gedela, "Providing real-time traffic advisory and route guidance to manage Borman incidents on-line using the Hoosier helper program," 2000.

Road Drainage Conveyance Systems – Optimum Selection Approach for Road Schemes in Ireland

John Halpin[1,2], Dr. Shane Newell[2]
[1]Barry Transportation, Unit 14C, N5 Business Park, Moneen Rd, Castlebar, Co. Mayo, Ireland
[2]Dept. of Building & Civil Eng., Atlantic Technological University, Galway City, Dublin Road, Galway, Ireland
email: jhalpin@jbbarry.ie, shane.newell@gmit.ie

ABSTRACT: The research presented in this paper outlines an assessment overview of the common road drainage systems adopted on Irish road schemes. Road verge drainage conveyance systems including traditional and Sustainable Drainage Systems (SuDS) were analysed to evaluate if system selection can be enhanced through utilising a scoring/weighted based analysis tool. The tool adopted is the Multi Criteria Analysis (MCA) approach; commonly employed during highway route selection phases. Three criteria – Engineering, Environment, Economics - were used to govern the MCA assessment. The research was conducted against four existing Irish road projects, each offering potential to address common highway drainage works requirements and design constraints. It is envisaged that the MCA technique will assist in scoping out drainage systems during the decision-making phases for road projects.

KEY WORDS: Road drainage, SuDS, Pollution control, Multi Criteria Analysis

1 INTRODUCTION

Current highway research has highlighted that poor drainage techniques are often considered the primary reason in the deterioration and failure of road pavements [1]. An effective road drainage system can be characterised by the conveyance and removal of surface and subsurface highway runoff (Figure 1). A collaborative design approach is essential to ensure all multi-disciplinary highway elements are considered during design delivery. A viable road drainage system must also comply with any environmental, economic and safety requirements in line with current legislative and construction methods.

Figure 1: Surface and subsurface drainage on M17/M18 Gort to Tuam Motorway

In recent times, Ireland has witnessed a significant growth in road improvement and upgrade works due to increased traffic volumes and ageing nature of many of our national roads. Similarly, increased rainfall events have caused strain on existing drainage systems, resulting in prolonged surface water ponding and subsequent pavement erosion.

The composition of highway runoff and its potential adverse impacts on receiving waters is also an important consideration in road drainage system selection. Effective pollution control measures are required to negate the effects of contaminated stormwater discharge. This is commonly achieved through the application of appropriate mitigation measures, i.e., installation of bypass fuel separators. The primary pollution control objective, under the EPA Groundwater Protection Response Assessment [2], is to *"protect/enhance all waters (surface, ground, and coastal waters) - while achieving good status for all waters and manage water bodies based on river basins or catchments"* [3].

Modern road drainage methods are also expected to adopt a Sustainable Drainage Systems (SuDS) approach design approach. SuDS practices have been shown to provide effective means in managing and controlling drainage runoff through application of natural drainage features like filter drains and grass channels. The benefits of SuDS can further be emphasised through its pollution treatment train capabilities [4].

The safety of road users is an important requirement in the delivery of compliant and functional road drainage systems. A reduction in potential high-risk incidents because of surface water ponding is considered a primary safety aim. Furthermore, the associated cost benefits in the provision of safety control measures are likely to reduce highway maintenance costs and enhance the life cycle of a carriageway.

In Ireland, designing a road drainage system involves adhering to a range of highway codes and advice documents administered by Transport Infrastructure Ireland (TII). While these documents offer a comprehensive library to produce compliant drainage systems, the system selection is dependent on other factors bound by project contract and works requirements. This further underlines the importance of a consistent and collaborative decision-making process in all project delivery phases to ensure project time and budget constraints are achieved.

A successful decision-making process is outlined within the TII Project Appraisal Guidelines (PAG) [5]. In Ireland, this

document is commonly employed during highway route selection phases to assess and identify preferable route options. An important aspect of the PAG is the decision-making technique known as Multi-Criteria Analysis (MCA). The MCA tool allows the user to evaluate and determine preferable option(s) by reference to a set of *"explicit set of objectives under established measurable criteria"* [5].

The following research will discuss how a set of road drainage requirements (objectives) can be developed by following a similar approach to the PAG. By application of the MCA tool, potential drainage systems (options) will be identified and evaluated against a set of pre-determined criteria and sub-criteria. The criteria, comprising of Engineering, Environment and Economics, are also important factors within the road drainage decision-making process [6]. It is envisaged that the results (selection) from the assessment will assist the user to identify and select an *optimum* drainage system (Figure 2).

Figure 2: Optimum Selection Approach

It should be noted that although the MCA tool provides a systematic approach to the decision-making process, attainment of all governing objectives forms the foundation of the assessment in determining an optimum solution. The role of the objectives has also been reflected in current UK road drainage design and management methods through a concept known as an integrated design approach (Figure 3).

Similarly, in Ireland, these objectives are set out in accordance with the EU Water Framework Directive [3], governed by the following drainage principles:

- Manage carriageway runoff,
- Manage flood risk,
- Manage pollution risk

These objectives are the cornerstone of all road drainage design measures from an engineering, environmental, financial and safety standpoint.

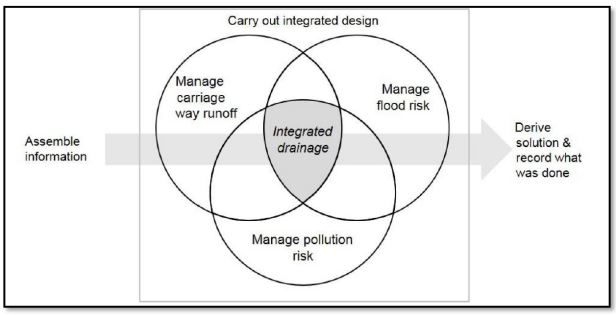

Figure 3: Integrated Design Approach [7]

2 LITERATURE REVIEW

In their comprehensive study on the use of sustainable drainage systems, TII [4] outline the beneficial contributions of SuDS in the effective conveyance, management, and attenuation of road runoff for national road projects in Ireland. A key aspect of this study highlights the importance of early engagement between a multi-disciplinary design team and various environmental bodies i.e. OPW, to ensure compliance with the principles and objectives of the Water Framework and Groundwater Directives (WFGD) [2]. This collaborative mindset encourages stakeholder involvement to derive potential solutions at an early stage which "in turn, lead to the development of a robust drainage design"

While effective SuDS approaches are enlisted to achieve WFGD objectives, enhance biodiversity and quality of place [8], the use of traditional piped drainage systems are still relied upon in the construction industry. The fully sealed assembly of traditional drainage systems offer an advantage over their sustainable counterparts in pollution control. Although, advancements are underway in the application of complete SuDS methods in areas of high groundwater vulnerability, traditional piped sealed drainage and associated fuel separator systems are advised in current standards and guidelines [6] to prevent polluted runoff discharge and preserve underlining aquifers.

The aim in the allocation of any drainage system is to derive a solution so that appropriate design and construction methods are adapted to simultaneously manage carriageway runoff, flooding and prevent pollution risk in line with an integrated design approach [7].

The drainage systems commonly used on Irish roads typically consist of SuDS features like Filter/French drains (Figure 4a), Grass Channels (Figure 4b) and traditional Concrete Channels and Drainage Kerb Systems (Figure 5a and 5b)

In an in-depth analysis on the composition of highway runoff for existing national road schemes, Higgins [9] provides a useful insight into the drainage pollution impacts from SuDS and traditional drainage-based systems. An overview on the advantages and disadvantages of such systems are presented in Table 1 for SuDS (filter drain) versus a conventional (kerb drain) system.

Fig 4(a) Filter (French) Drain; (b) Grass Channel

Fig 5(a) Linear kerb drain; (b) Kerb and gully

Table 1. Filter and Kerb drainage study [9]

Filter Drains		**Kerb and Gullies**	
Advantages	***Disadvantages***	***Advantages***	***Disadvantages***
Simple installation (pipe flexibility)	Localised flooding issues	Assembly of units and direct drainage regime allow access for maintenance purposes	Stagnant water can provide a breeding ground for bacteria and pollutants between storms.
Cost effective	Blockages can result in reduced pipe volume capacity	Not dependent on gradient of road to convey road surface runoff (HD33,TII, 2015)	Maintenance and cleaning considered expensive due to regularity of high storm events in Ireland
Attenuation storage potential	Subsurface drainage performance reduced for inadequate installation	Gully pots shown to remove sediments of particle size greater than 300 microns.	
Good pollution control performance (including sediment and suspended solids removal)	Restricted use along deep embankments (>1.5m (HD33,TII, 2015))		

3 CASE STUDIES

As discussed, many challenges are faced in road drainage system selection. The following section will endeavour to assess and identify why certain drainage regimes were chosen across four highway schemes in Ireland. Through the application of the integrated design approach, an MCA will be adopted to evaluate whether the designated system was the optimum drainage solution for each scheme. The case studies investigated are a selection of completed and ongoing Irish National Road schemes. Each scheme was selected based on their varied nature and provides scope on how the MCA tool can be applied to road improvement schemes and new highway developments. The case studies discussed are:

1. N22 Ballyvourney to Macroom Road Development
2. M17/M18 Gort to Tuam PPP Scheme
3. N63 Abbeyknockmoy to Annagh Hill Road Realignment Scheme
4. N60 Castlebar to Balla Road Improvement Scheme

It is important to note that because of the varied nature of the criteria/option impacts for each scheme, the results of the MCA were assessed holistically across each scheme. This is important so as not to disregard any lower ranked drainage systems options which may provide a viable scheme drainage function i.e., overland flow drainage. This will be particularly evident across the larger M17/M18 and N22 schemes due to varied option impacts along the extents of the 56km and 22km respective developments.

3.1.1 N22 Ballyvourney to Macroom Road Development

The N22 Ballyvourney to Macroom Road Development, currently under construction since 2020, will see the delivery of 22km of Type 2 Dual Carriageway. The main stakeholder objectives of the development include the provision of a strategic high-quality road to reduce capacity deficiencies and journey times, while removing traffic congestion along the existing N22 National Primary Route [13].

With respect to ecology impacts, there are no designated sites directly impacted by the road development. However, the area of the development to the north of the scheme includes a population of the European protected Kerry slug species, with mitigation measures i.e., restricted zones, implemented to preserve the species habitat [13].

Due to the overall negative hydrogeological impacts and potential groundwater contamination, the proposed drainage required the implementation of sealed drainage methods [6]. Concrete channels were selected as the primary carriageway drainage system, accompanied by filter drains in the conveyance of unpolluted runoff from significant embankment cuttings situated along the N22 scheme. Other drainage systems include the use of kerb and gully where appropriate i.e., for structure deck drainage provisions and side road drainage requirements.

3.1.2 M17/M18 Gort to Tuam PPP Scheme

Since its opening in 2018, the M17/M18 Gort to Tuam PPP motorway scheme represents a major route on the Irish road network. The scheme consists of 56km of high-quality motorway and 4.2km of Type 2 dual carriageway that connects a main arterial link in Tuam, County Galway. Due to the extensive size of the M17/M18 scheme, the design and construction of the works were constructed by a joint venture (JV) partnership. This collaborative relationship presented logistical challenges – both in the design and construction of the works, requiring consistent lines of communication and techniques to meet project deliverables in accordance with scheme works requirements.

An example of a collaborative approach included the implementation of sealed drainage methods to minimise and mitigate the impacts from underlying karst features. The sensitivity presented by the underlying limestone aquifer along

with evidence of dissolved limestone rock formations, known as Karstic Features [10], presented many challenges during delivery of the M17/M18 scheme.

3.1.3 N63 Abbeyknockmoy to Annagh Hill Road Realignment Scheme

The N63 road realignment scheme construction coincided with the completion of the M17/M18 project works, tying in with a grade separated junction located at Annagh Hill. The N63 scheme entailed the design and construction of two sections of Type 2 Single Carriageway of 3.2km in total length.

Design challenges faced included the environmental challenges imposed by high groundwater vulnerability levels and presence of shallow bedrock. Flooding events particularly from inadequate existing overland drainage and resultant carriageway ponding were a primary factor in the selection of an upgraded verge drainage system.

The hydrology in terms of road surface water drainage was improved via a sealed drainage system in the form of linear drainage kerb. This enabled the speedy removal of surface water whilst minimising the impact upon the receiving environment. SuDS including filter drains were provided to act as secondary treatment to control and separate groundwater runoff discharge from road cut embankments. Flooding issues were controlled through the application of suitably sized land drainage culverts and attenuation.

3.1.4 N60 Castlebar to Balla Road Improvement Scheme

The N60 Castlebar Balla Road Improvement Scheme at Lagnamuck, located just north of Balla town between Castlebar and Claremorris in County Mayo, was assigned as part of TII national road safety upgrades. The works comprised approximately 1.4km of online upgrade of Type 2 Single Carriageway with associated cycleway and footpaths.

The scheme is situated within a Special Area of Conservation (SAC) known as Balla Turlough [11]. Although the ecological screening report for the N60 indicated "no significant effects to qualifying habitats and species" [12], the sensitive nature of the Turlough habitat required precautionary construction measures to mitigate and preserve the surrounding water quality and environment. With groundwater vulnerability risk classified as low [12], SuDS techniques in the form of grass surface water channels were applied to form the basis of the carriageway drainage conveyance system, while transitioning towards a linear drainage kerb system near Balla town.

The design of the drainage system for the N60 adopts the Highways England integrated design approach [7] concept, while seeking to recognise the rural nature of the scheme and *"reflect broadly the drainage regime on the existing route"* (HB, 2015).

4 MULTI-CRITERIA ANALYSIS (MCA)

As discussed, an effective decision-making framework plays a significant role in achieving the road drainage objectives set by the integrated design approach, while simultaneously fulfilling client and sanctioning authority requirements [5]. The adaptability of the MCA appraisal technique allows the user to examine alternative drainage options by defining potential option impacts under a range of criteria and associated sub-criteria. Following a similar framework to the TII Project Appraisal Guidelines (PAG), *Engineering, Environment* and *Economy* form the main criteria during the option selection assessment. The associated sub-criteria for each designated criterion are then defined based on how they impact upon the drainage design delivery of a road project. Table 2 lists the criteria and related sub-criteria adopted for the drainage MCA assessment.

Table 2. MCA Criteria and Sub-criteria impacts

Engineering
Hydraulics - Surface and subsurface drainage
Earthworks Impacts
Structures Impacts
Alignment impacts
Engineering Sub-Total
Environment
Ecology and Biodiversity impacts
Carbon footprint
Flooding & surcharge prevention
Pollution control
Environment Sub-Total
Economy
Safety and Security of Road Users
Maintenance Impacts
Funding Impacts
Economy Sub-Total

It should be noted that the drainage integrated design approach plays a key role in the selection of each sub-criterion. While option selection should commit to respect all multi-disciplinary elements, the assessment should be considered objectively from a drainage perspective only. This is important to avoid subjective decision making, for example, a client or contractor preference towards a specific type of drainage system may be overlooked if the preferred system does not meet the standards or score favourably in the MCA assessment. This will be determined in the evaluation phase of the MCA, allowing the user/designer to examine, score, and finally rank each option to establish the "optimum" preference.

The MCA appraisal tool adopts a simplified scoring procedure when weighting and ranking the criterion for the designated options. The impact score rating scale (Table 3) follows the procedure set out in the TII Project Appraisal Guidelines with the highest-ranking score at the end of the assessment selected as the preferable or optimum option. While each criterion is weighed equally against each other, further evaluation may be required i.e., through a pairwise comparison, if the final MCA produces equally ranked options.

The following section provides an overview of the MCA appraisal when applied to the road drainage assessment for each case study.

Table 3. MCA impacts scoring system

Impact Level	Score Index
Major or Highly Positive	7
Moderately Positive	6
Minor or Slightly Positive	5
Neutral	4
Minor or Slightly Negative	3
Moderately Negative	2
Major or Highly Negative	1

4.1.1 MCA – N22

The negative groundwater vulnerability impacts throughout the N22 scheme presents challenges in the road drainage system selection approach. Due to this restriction, the use of unsealed SuDS to manage and convey polluted carriageway runoff was effectively ruled out in accordance with the groundwater protection response assessment [2].

The presence of deep embankments and adjacent overland catchments throughout the N22, required the use of SuDS through filter drains, which ultimately scored higher than its sealed drainage counterparts. The filter drain scoring was ultimately enhanced through adopting a hybrid drainage approach i.e., separation of greenfield runoff from contaminated runoff. From drainage viewpoint the benefits not only include preventing the mixing of contaminated runoff but also reducing attenuation pond volumes.

In line with an encouraged SuDS philosophy [8], grass channels scored favourably under ecology and biodiversity. The reduced carbon footprint impacts of the SuDS systems also rank higher against their equivalent conventional drainage systems. Although concrete channels and kerb drainage are known to provide limited sediment control treatment [9], the requirement for additional pollution control measures via fuel/oil separators rank grass channels higher under the Environment criteria.

Due to the limited hard shoulder width and high-speed nature of the N22 Type 2 dual carriageway, several systems received low scores under safety and security of road users' sub criteria. Safety concerns include stone scatter (filter drain), grating defects (kerb and gully) and single wheel vehicle hazards (kerb slot drains). Furthermore, anecdotal evidence of breakages from HGVs reduced the scoring potential of kerbside systems including kerb and gully, kerb slot drains and linear drainage kerbs. Concrete channels received the *optimum* result in the Economy criteria.

Ultimately, concrete channels were selected as the overall preferable system for the N22 scheme, in consideration of the seasonal flood events along southern section near Macroom.

Scoring favourably for all criteria except structures and carbon footprint impacts, concrete channels received the highest preference or optimum ranking for the N22 (score = 54) and the second most favourable option using the MCA was the drainage kerb (score = 50). The least favourable option using the MCA was the filter drain and kerb and gulley (score = 43). This is in keeping with the primary drainage approach for the N22 Ballyvourney to Macroom Road Development.

Table 4. N22 Drainage MCA

N22 - Drainage MCA	Filter Drain	Kerb and Gully	Kerb Slot Drain	Drainage Kerb	Concrete Channel	Grass Channel
Engineering Sub-Total	16	17	20	21	21	14
Environment Sub-Total	17	16	14	16	17	21
Economy Sub-Total	10	10	10	13	16	14
Totals	**43**	**43**	**44**	**50**	**54**	**49**

4.1.2 MCA – M17/M18

The MCA assessment (Table 5) for the M17/M18 Tuam to Gort PPP Scheme presented many similarities to the N22 assessment. However, while consistent sealed drainage requirements were required throughout the N22, the predominant karst features along the southern section allowed for the application of SuDS to manage and convey polluted runoff.

The sealed drainage systems (kerb slot drain, linear drainage kerb and concrete channel) scored equally as the optimum solution under engineering.

Similarly, the results from the MCA assessment under environment defined grass surface water channels as the most optimum system. The overall pollution mitigation potential from grass channels also enhanced filter drains environmental benefits

A joint scoring between concrete and grass channels came out on top for economy with safety concerns reducing filter drain scoring. However, it is noteworthy, that kerb slot drains safety ranking improved by presence of 2.5m wide hard shoulder (as opposed to N22 dual carriageway), which reduced the single wheel safety impacts along the motorway.

As noted, the scope to apply SuDS methods along the M17/M18 identified grass surface water channels as the optimum solution for the scheme. It must be noted that although grass channels have been adopted along sections, the most common road drainage conveyance system used were kerb slot drains and filter drains.

Table 5. M17/18 Drainage MCA

M17/M18 - Drainage MCA	Filter Drain	Kerb and Gully	Kerb Slot Drain	Drainage Kerb	Concrete Channel	Grass Channel
Engineering Sub-Total	18	18	21	21	21	18
Environment Sub-Total	19	16	14	16	17	23
Economy Sub-Total	11	11	14	13	16	15
Totals	**48**	**45**	**49**	**50**	**54**	**56**

4.1.3 MCA – N63

The N63 route is situated within a localised area of high-extreme groundwater vulnerability, requiring a sealed surface water drainage regime to prevent contamination to the underlying aquifer [14]. The ranking results from the engineering assessment indicated that linear drainage kerbs to be the optimum drainage system, corresponding with the upgraded N63 drainage regime. Furthermore, the improved N63 alignment resulted in a primarily level embankment with

minimal overland drainage impacts. Therefore, narrow filter drains combined with the extension of road pavement capping layer adopted for sub-surface drainage and to convey any overland drainage.

In the environmental assessment, drainage mitigation from overland flooding off adjacent agricultural land was improved during installation of culverts and raising of the road vertical alignment. With no apparent ecological impacts, the overall result of the environmental MCA confirmed grass channels as the optimum approach, closely followed by drainage kerbs based on their sealed drainage properties.

Due to rural and reduced design speed constraints, kerb slot drains, and concrete channels were not permitted under [6] requirements. Therefore, the compatibility of the linear drainage was deemed the optimum system to fulfil the economy criterion. Overall, linear, or combined drainage kerbs units were identified as the most preferable drainage system for the N63 MCA assessment.

Table 6. N63 Drainage MCA

N63 - Drainage MCA	Filter Drain	Kerb and Gully	Kerb Slot Drain	Drainage Kerb	Concrete Channel	Grass Channel
Engineering Sub-Total	17	20	15	22	19	17
Environment Sub-Total	17	16	15	18	15	19
Economy Sub-Total	9	10	10	13	13	14
Totals	**43**	**46**	**40**	**53**	**47**	**50**

4.1.4 MCA – N60

The drainage approach for the N60 Balla improvement scheme resembles the N63 scheme in many ways with an identical economy criterion ranking and several similar sub-criteria ranking results including structures, ecology, and flooding.

The viability of a SuDS selection approach was justified through the medium to low groundwater vulnerability impacts [11]. The MCA impacts, therefore scored favourably towards a grass channel system. This can be further emphasised by the positive drainage and environmental impacts that grass channels offer and the suitability to adopt such a system on the N60 project.

Table 7. N60 Drainage MCA

N60 - Drainage MCA	Filter Drain	Kerb and Gully	Kerb Slot Drain	Drainage Kerb	Concrete Channel	Grass Channel
Engineering Sub-Total	20	22	15	22	18	24
Environment Sub-Total	19	15	14	16	14	21
Economy Sub-Total	9	10	10	13	13	14
Totals	**48**	**47**	**39**	**51**	**45**	**59**

5 CONCLUSION

The following conclusions have been drawn from this research study:

- All systems from MCA ranking assessment reflected the systems employed for each case study except the M17/M18 with grass surface channels defined as the optimum system.
- Sealed drainage requirements have a primary influence on the selection criteria of road drainage systems to prevent contamination and preserve underlining aquifers.
- The use of Sustainable Drainage Systems (SuDS) within vulnerable and karstic regions needs to be developed further to expand upon their potential as a sealed drainage method.
- Further research is required to develop pollution control requirements in respect of First Flush Analysis i.e., the initial period of stormwater runoff containing the highest concentration of pollutants, using HAWRAT tool [2].
- Although, not discussed in this paper, the use of alternative hybrid conveyance-attenuation drainage systems could be developed further.
- The MCA tool provides scope to expand option impacts/criteria further to reflect client and stakeholder requirements i.e., Land Use Integration and Amenities.

6 REFERENCES

[1] A. T. S. Matintupa, "Summary of Drainage Analysis in Ireland, Roads N56 and N59," ROADEX, Sweden, 2010.

[2] TII, "Road Drainage and the Water Environment. HD45, Standards," Transport Infrastructure Ireland, Ireland, 2015.

[3] EPA, "Water Framework Directive," 2021. [Online]. Available: https://www.epa.ie/water/watmg/wfd/. [Accessed 21 February 2021].

[4] TII, "Drainage Design for National Road Schemes - Sustainable Drainage Options, Technical Report," Transport Infrastructure Ireland, Ireland, 2014.

[5] TII, "Project Appraisal Guidelines for National Roads Unit 7.0 - Multi Criteria Analysis. PE-PAG-02031, Technical Report," Transport Infrastructure Ireland, 2015.

[6] TII, "Drainage Systems for National Roads. HD33, Standards," Transport Infrastructure Ireland, Ireland, 2015.

[7] Highways England, "CG 501 Design of highway drainage systems (HD 33/16)," Highways England, 2020.

[8] CIRIA, Planning for SUDs C687, London, UK: CIRIA, 2010.

[9] N. M. P. Higgins, "Analysis of Highway Runoff in Ireland," Department of Civil, Structural and Environmental Engineering, Trinity College Dublin, Dublin, 2006.

[10] GCC, "Galway (Rathmorrissy) to Tuam Motorway (Environmental Impact Statement)," Galway County Council, Ireland, 2007.

[11] HB, "N60 Castlebar Balla Road Improvement Scheme at Lagnamuck," Barry Transportation, 2015.

[12] RPS, "N60 Castlebar to Claremorris Road Improvement Scheme - Lagnamuck Section (Ecological Assessment & Appropriate Assessment Screening Report)," RPS Group, Ireland, 2011.

[13] CCC, "N22 Baile Bhuirne-Macroom Environmental Impact Statement Volume 1: Non-Technical Summary," McCarty Hyder Consultants, 2009.

[14] HB, "N63 Environmental Impact Assessment," Halcrow Barry, 2014.

[15] ROADEX, "Why Drainage is Important," 2021b. [Online]. Available: https://www.roadex.org/e-learning/lessons/drainage-of-low-volume-roads/introduction-why-drainage-is-important/. [Accessed 6 April 2021].

[16] ROADEX, "Environmental Issues Related to Road Management," 2021b. [Online]. Available: https://www.roadex.org/e-learning/lessons/environmental-considerations-for-low-volume-roads/environmental-issues-related-to-road-management/. [Accessed 06 April 2021].

[17] TII, "Design of Earthworks Drainage, Network Drainage, Attenuation & Pollution Control. HA33, Standards," Transport Infrastructure Ireland, Ireland, 2015.

Transport in the Northern & Western Region of Ireland – Current Provision & Future Challenges

Steve Bradley[1], Brian McCann[1], Amaya Vega[2]
[1]Atlantic Technological University, Ash Lane, Sligo, F91 YW50, Ireland
[2]Atlantic Technological University, Dublin Road, Galway, H91 T8NW, Ireland.
email: steve.bradley@mail.itsligo.ie, mccann.brian@itsligo.ie, amaya.vega@gmit.ie

ABSTRACT: The Northern and Western Region of Ireland has a population of almost 850,000. It is Ireland's least populated and most rural region, with only one city (Galway – population 79,934 in 2016) and a population density that is less than half the national average (33.2 persons per km^{sq} vs 72 national average). Ireland has set an ambitious target of achieving a 51% reduction in Greenhouse Gas emissions (GHGs) by 2030, and net-zero by 2050. Transportation is the largest energy consuming sector within the State – accounting for 42% of final energy consumption and 20% of total GHGs. The Northern and Western Region's dispersed population and geographic peripherality has resulted in limited public transport networks and a high car dependency – which exacerbates the challenge of transitioning the region towards carbon neutral mobility in an effective and just manner. This paper focuses on the presence and usage of the existing transportation networks within the Northern and Western Region, and points towards the challenges involved and the changes that will be required to assist the region in playing its full part in enabling Ireland to meet its obligations on carbon emissions, modal shift and regional balance as per the Project Ireland 2040 National Development Plan.

KEY WORDS: Sustainable ; Low-carbon ; Transition ; Rural ; Ireland.

1 INTRODUCTION

The Northern and Western Region (NWR) is one of three EU NUTS Level 2 designated regions within Ireland. The region encompasses the province of Connacht (counties Galway, Mayo, Sligo, Roscommon, Leitrim) plus the 3 Ulster counties within the Irish state (Donegal, Cavan, Monaghan). In 2016 the region's population was 847,442 - 17.8% of the Irish State's total [1]. Of the three Irish regions the NWR has the lowest population, lowest population density, and slowest rate of population growth. It also contained the only counties that registered a population decline at the 2016 census [1].

The NWR is a predominantly rural region, with 80% of its population living in small towns, villages or the countryside. It has no settlements of scale and only one city – Galway. Despite being the fourth-largest settlement in the State, Galway City had a population of only 79,934 in 2016 [1]. The NWR's next four largest population centres are all small towns which have faced population decline in recent years. The NWR's eight counties have predominantly rural populations ranging from Leitrim (89% rural) to Sligo (61% rural), compared with a national average of 38% [1].

In 2020 the Northern and Western Region was downgraded by the EU from "more developed" economic status to instead being "in transition" - making it the only Irish region not designated as 'developed'.

2. THE POLICY CONTEXT

2.1 Background

The Irish State is undergoing a period of comparatively high population growth, with the country predicted to contain an additional one million people by 2040 (20% increase) [2]. To manage this growth the State has prepared an over-arching planning and policy framework called Project Ireland 2040 - comprising of a National Development Plan (NDP) and a National Planning Framework (NPF). The NPF was published in 2018 and contains 10 National Strategic Objectives (NSO), which combine to provide a roadmap for the country's spatial development over the next two decades. A number of these NSOs relate specifically to transport, regions and rural areas. The National Development Plan (NDP) outlines the investment plan and spending commitments that aim to deliver those 10 NSOs. These objectives then cascade down (see Figure 1) to Ireland's three Regional Assemblies, which are required to develop a 'Regional Spatial and Economic Strategy' (RSES) to deliver the NSOs in their area. Each county within the three regions is in-turn required to compile its own Development Plan, whilst Ireland's five cities have an additional responsibility to publish a Metropolitan Area Strategic Plan. Finally - the NWR's two Key Growth Centres (Letterkenny and Sligo) must also compile individual Local Transport Plans as part of this policy hierarchy.

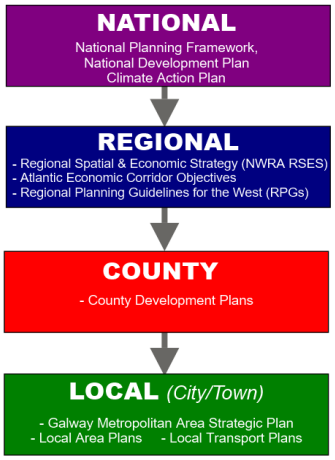

Figure 1. The Hierarchy of Transport Policy in Ireland

In addition to this suite of spatial planning strategies, a specific Climate Action Plan was adopted by Ireland in 2021. Its focus is to deliver the obligations contained within the 2021 Climate Act, by outlining the steps required to reach a

51% reduction in GHG emissions by 2031 and becoming net-zero by 2050 [4]. It includes a focus on measures to discourage private car use – particularly in urban areas – and to promote and facilitate active travel and public transport. It also sets out additional measures to promote complementary transport mitigation measures, such as a switch over to EVs and greater use of renewable fuels for transport.

2.2 Population Targets

P12040 notes that much of the recent spatial growth in Ireland has been characterised by edge-of-town sprawl and one-off rural housing, and acknowledges its negative impact. The document therefore signals a shift in priority towards more compact spatial growth, with a target of ensuring at least 40% of new house building occurs within the existing footprint of towns and cities. To ensure greater regional balance/connectivity and help reduce the over-dominant position of Dublin city, the strategy also mandates that 75% of future population growth should occur beyond the capital - with priority given to ensuring Ireland's four regional cities (including Galway) are developed as larger urban cores. A population increase of 180,000 is proposed for the NWR during the lifespan of the strategy, to take its total to over a million people. PI2040 also identifies the NWR as currently having a weak urban structure overall and lacking significant population centres – though it does acknowledge that Sligo, Letterkenny and neighbouring Athlone fulfil roles within the region that are akin to cities (albeit on a lower scale). The strategy therefore categorises these towns as Key Regional Growth Centres, with population growth targets and a requirement for bespoke development strategies (Table 1).

Table 1. NWR Population Growth by Settlement Type [2]

Settlement Type	**Towns**	**Governing Strategy**	**2040 Population Growth**
City (1)	Galway	Metropolitan Area Strategic Plan ; RSES	+50-55% min.
Regional Growth Centre (2)	Letterkenny, Sligo	Regional Growth Centre Strategic Plan; RSES; Local Transport Plan	+40%
Key Towns (8) *(Pop. 1,500+)*	- Ballina, - Ballinasloe, - Carrick-on-Shannon, - Castlebar, - Cavan, - Monaghan, - Roscommon - Tuam.	RSES	+30%

2.3 Current Transport Sector Emissions

Transportation is the largest energy-consuming sector in Ireland – accounting for 42% of final energy consumption, and 20% of total GHG emissions [4]. Road transport is a significant contributor within that, being responsible for 96% of all transport sector emissions [5]. The limited reduction in emissions during the Covid 19 pandemic (see Section 3.5) illustrate how challenging it will be to secure this level of change within the transport sector in Ireland. This is reflective of the fact that transport and mobility are more intertwined with human behaviour and everyday life than most other sectors [5], making it a particularly difficult area in which to secure behavioural change. O'Riordan et al (2022) identify a further cause for concern in the fact that transport's share of greenhouse gas emissions within Ireland is actually increasing post-Covid, despite government commitments [6]. This points to the scale of the overall challenge for Ireland and its regions.

3 EXISTING TRANSPORT INFRASTRUCTURE

There is a need for the NWR to plan future transport provision to meet both Ireland's emissions reduction commitments and the region's projected population rise. However - the NWR's rural nature, dispersed population and geographic peripherality present a particular challenge in this, as the region has limited public transport provision, a low-capacity road network, and mobility based primarily around private motor vehicles and high car dependency. The Northern and Western Regional Assembly identifies the region as having suffered "a comparatively lower level of investment in enabling infrastructure such as ports, harbours, road, rail and utilities" versus the other regions, and calls for "positive discrimination" to help the region catch up with the rest of the State [7]. The Atlantic Economic Corridor's submission to the National Development Plan also stated that it is "evident that the West of Ireland and, in particular, the northwest has a deficit of infrastructure compared to the east of Ireland" [8]. This is illustrated by the fact that only two of the NWR's 10 largest population centres have both rail and motorway provision (Table 2). This deficit is further exacerbated by an additional infrastructure divide within the region itself - between its five western/Connacht counties and three Border/Ulster ones, with none of the latter having either rail or motorway connectivity.

Table 2. Transport Provision in NWR's 10 Largest Settlements

Settlement	County	Population	Rail ?	Motorway?
1. Galway	Galway	79,934	Y	Y
2. Letterkenny	Donegal	19,274	N	N
3. Sligo Town	Sligo	19,199	Y	N
4. Castlebar	Mayo	12,068	Y	N
5. Ballina	Mayo	10,171	Y	N
6. Tuam	Galway	8,767	N	Y
7. Monaghan	Monaghan	7,678	N	N
8. Buncrana	Donegal	6,785	N	N
9. Ballinasloe	Galway / Roscommon	6,662	Y	Y
10. Westport	Mayo	6,198	Y	N

3.1.1 Rural Travel Patterns

Private car use accounted for 74% of all journeys in Ireland in 2019, with road use responsible for 94% of all transport-based emissions [9]. Dispersed rural settlement patterns mean that this predominance of vehicles is even more pronounced in Ireland's non-urban areas - whilst walking, cycling, rail and bus use are also much less prevalent (Table 3) :

Table 3. Modes of Travel in Ireland, 2019 CSO National Travel Survey [9]

	National	Rural	Urban
Private car	74%	84%	62%
Walking	14%	8%	19%
Cycling	2%	1%	3%
Bus & Rail	7%	2%	12%

3.1.2 Motor Vehicles

In 2021 104,932 new private cars were sold in Ireland – a 19% increase on 2020, but 10.4% down vs 2019 (the last full year unaffected by Covid) [10]. That 2021 increase in sales ended four years of consecutive decline from a market high of 146,602 vehicles in 2016. Car sales in Ireland have tended to mirror the country's economic fortunes, such that the government's 2022 Sustainable Mobility Plan talks about "breaking the link between economic growth and car use" [3].

Diesel vehicles continue to be the most popular format sold in Ireland, though their share of the market has been in notable and consistent decline over the last five years [11]. Electric vehicles have seen relatively strong growth in recent years, but still account for a small segment of the market (Table 4). With almost three-quarters of all new private car registrations in 2021 being powered entirely by fossil fuels, and only 5.3% pure electric [11], the country's fleet has a long way to go in transitioning towards low-carbon fuels. Particularly as the Irish government's Sustainable Mobility Plan aims to secure a 10% reduction in the number of kilometres driven by fossil fuelled cars by 2030 [3], amidst an increasing population.

Table 4. Private Cars Licensed for First Time in Ireland by fuel type, 2021 vs 2017 [11]

Fuel	Market Share 2017	Market Share 2021	Change
Diesel	70.7%	41.7%	-59%
Petrol	25.4%	31.7%	+24%
Hybrid	3.4%	21.1%	+620%
Electric	0.5%	5.3%	+1,060%

Figure 2. Map of Ireland's Road Network, with the Northern and Western Region circled.

3.1.3 Road Network - Region

The Northern and Western Region contains two motorways , both located in Co. Galway (Figure 2). The rest of the region has almost exclusively single carriageway National Roads, with short additional sections of dual carriageway serving Galway, Letterkenny and Sligo. The Regional Assembly has identified a funding disparity facing the NWR's roads, with the region receiving €87,240 per km of National roads in 2008-18 [7] - significantly below the national average of €116,054, and the lowest funding level of the 3 Irish regions.

3.1.4 Road Network – Galway City

Galway is the NWR's only city, with a significant commuter population and travel patterns that indicate a heavy dependence upon car usage [7]. This results in significant peak hours congestion on the city's road network. Galway City was ranked as the worst place in Ireland for traffic congestion in 2015 and 2016 – and was even named 59th worst in the world in 2015 [12]. It has since fallen down that ranking to sit below Dublin and Limerick in the 2021 figures, with an estimated average of 51 hours lost annually by drivers in peak hours congestion. A new orbital route – the N6 Galway City Ring Road – is proposed around the city in the expectation that it will relieve city centre congestion [7]. As Key Regional centres, Letterkenny and Sligo Town are also developing their own Local Transport Plans currently.

3.2 Public Transport

Only 7% of all journeys in Ireland in 2020 were conducted by bus or rail [9]. This is despite a 'Smarter Travel' strategy to increase usage of public transport and active travel having been in place since 2009 (see Section 3.3 below).

3.2.1 Passenger Rail

The NWR contains three mainline rail routes that stretch from Sligo, Ballina/Westport and Galway towards Dublin. An additional rail connection south from Galway to Limerick opened in 2010 as Phase 1 of a restored north-south 'Western Rail Corridor', though proposals for additional phases to extend it onwards to Sligo and Donegal were excluded from PI2040. None of the NWR's three Ulster counties (Donegal, Cavan and Monaghan) are serviced by rail, and the region has no cross-border rail connectivity – despite half of its eight counties bordering Northern Ireland.

The Galway City MASP proposes no additional rail lines or stations/halts for the NWR's largest urban centre – focusing instead on increasing capacity, improving frequency and exploring the possibility of rail freight at Galway Port [13]. The government's Sustainable Mobility Plan commits to investigating the feasibility of light rail for Galway [3].

The RSES is silent on the need or viability of returning rail to the NWR's three Border counties [7]. The document identifies the lack of a multi-purpose transportation point for Letterkenny (the region's second largest population centre) as an issue, but makes no reference to rail within that. The emerging Local Transport Plan for Letterkenny also does not proposes restoration of rail to the town.

3.2.2 Bus

Bus provision within rural Ireland in general, and the NWR in particular, is limited - with the National Transport Authority (NTA) acknowledging that gaps in evening, mid-day and weekend services "can lead to a mismatch between service coverage and customer demand" [14]. The NTA is using 3 strategies to address this and better enable bus provision to

contribute to modal shift. The first is a strategy for rural areas called 'Connecting Ireland' which proposes enhanced regional bus networks that better connect local towns and villages with each other and onto cities and regional centres. This is supported by a second approach based on Demand Responsive Transport, with a network called 'Local Link' providing bookable shared minibus services in rural areas where public transport is particularly limited. Finally, Ireland's 5 key cities are the focus of an urban-based 'Bus Connects' enhancement programme. Within this a new cross-city network of bus services is proposed for Galway to better connect major trip generators, as well as bus corridors on two key arteries within the city and new peripheral Park and Rides linked into the city's bus network [13].

3.3 Active Travel

Over the last decade Ireland has fallen substantially short of its own targets for modal shift and Active Travel. In 2006 just over 50% of all journeys were made by car [15]. By 2019 that figure had climbed to 74% [10], despite a 'Smarter Travel' strategy introduced in 2009 to encourage modal shift [16]. That strategy identified key sustainable transport targets, with a particular focus on modal shift for commuting – seeking to reduce work-related car journeys from 65% to 45% (moving 500,000 commuters onto public transport, cycling or walking). The policy also led to the creation of Ireland's first National Cycle Policy Framework in 2009 [17], which aimed to create a cycling culture and for 10% of all trips to be made by bike by 2020. As Table 4 illustrates, however, the percentage of journeys fulfilled by bike had reached only 2% by 2019. It can therefore be concluded that delivery of the 2009 Smarter Travel strategy fell far short of its stated aims.

One area within the National Cycle Policy Framework where significant progress was made was the objective to "Provide designated rural signed cycle networks, especially for visitors and recreational cycling" [17]. This has been achieved by the creation of a small but growing network of greenway facilities for walking and cycling on former rural railway routes, aimed primarily at tourism and leisure usage. The NWR's 42km Great Western Greenway in Mayo opened in 2011, and was labelled a "huge success" by national tourism authority Failté Ireland. Research by Deenihan et al (2013) estimated that the greenway generates over €1.1m in additional tourism expenditure for the area annually, giving a payback period of 6 years [18]. In 2018 the Government announced a new 'Strategy for the Development of National and Regional Greenways' to expand the network throughout the country. Its focus was again upon tourism and leisure usage of greenways, however, until the 2020 Programme for Government amended it to also include connectivity to towns and villages and a focus on everyday journeys for work and school. A major new greenway is also planned spanning the width of Ireland from Dublin to Galway, and a long-running dispute over whetehr the unopened sections of the Western Rail Corridor should be utilised exclusively as a greenway or for rail [19]

Perhaps mindful of the lack of delivery of previous Active Travel proposals, the current Project Ireland 2040 NDP and NPF includes a new 'Rural Active Travel Investment Programme' announced in 2021 [20]. It is the first major capital programme for active travel designed solely for rural areas, with a budget of over €70m. There is also a requirement for all councils to establish their own Active Travel Units to take forward the commitments in their Development Plans.

At an urban level the Galway MASP includes a Galway City Cycling and Walking Project, which plans for a new cycle network in the city and two greenways to connect it to outlying areas. Improvements to walking, including pedestrianisation schemes and new foot bridges, are also proposed. In 2021 NTA funding of €12m was announced to progress 33 Active Travel projects in the city [21].

3.3.1 Sustainable Mobility

The Government's 2022 Sustainable Mobility Plan highlights the mutual influence that transport and spatial development can have upon each other. It identified linking together the development of transport infrastructure and the development of new housing as an important driver of modal shift (transport-orientated development). The strategy's action plan therefore mandates councils to identify areas within a 1km distance of public transport stops that have the best potential for new housing and population growth [3]. And it also identifies land-use planning as being at the core of the 'Avoid' approach within the 'Avoid-Shift-Improve' principle.

3.4 Freight Transport

Most freight movements within the NWR are undertaken by road, though rail freight also has a growing presence. Ballina (Mayo) is the region's 5th largest town & also a significant rail freight hub by Irish standards, with increasing annual tonnage. It is underpinned by the manufacture and shipment of Coca-Cola concentrate products from the Ballina Beverages plant, which since 2009 has used rail to ship its output globally via Dublin Port (248kms distance). In 2021 a new rail freight service was also introduced between Ballina & Waterford Port in the south-east of the island (318kms distance). There is a proposal to connect Foynes Port on the western seaboard (Co.Limerick) to the rail network, which would offer closer and more direct sea access from the NWR [7].

3.5 Covid 19 Impact

Covid-19 highlighted how it is possible to secure significant change in transport behaviour, and to do so quite suddenly. Statistics showed that the pandemic had a profound impact upon how people in Ireland travelled, when they travelled and their propensity to travel at all [22]. The pandemic had a particular impact upon road traffic levels across the State – falling by 28.1% in 2020 vs 2019, as working from home resulted in a reduction in travel flows to employment centres, but an increased movement to and within local centres [22]. The NWR registered a smaller traffic decline of -27.1% in the Border Region and 24.6% in the West [15]. There was a minimal decline in demand for road freight transportation however, as a fall in distribution to retail outlets was substituted by a significant increase in transport to consumer homes. This resulted in only a 4% year-on-year decline in HGV traffic in 2020 – despite significant periods of restrictions on the construction and retail sectors. Public transport use also fell heavily during the pandemic, whilst walking and cycling increased.

Despite the significant disruption caused by greater remote working practices and severe travel restrictions during

Covid, transport sector emissions in Ireland are estimated to have declined by only 16% in 2020 vs 2019 [22]. This highlights the scale of the challenge involved in transitioning NWR and Ireland towards lower-carbon transport modes.

3.6 Implementation

Previous attempts to tackle Ireland's car dependency and move towards more sustainable transport modes have suffered from a disconnect between strategy and implementation. The 2009 'Smarter Travel' strategy was the State's first significant attempt to promote wholesale transition towards more sustainable mobility. However – it's launch in 2009 coincided with a significant economic and financial crisis in Ireland. As a result the capital funding available for sustainable mobility infrastructure was reduced by 60% between 2009 and 2013, with a consequent impact upon delivery of the strategy. The funding rose again in 2014, but it wasn't until the release of the 2018 NDP that sustained year-on-year increases were restored. The government's 2019 evaluation of the Smarter Travel strategy concluded that substantive progress had been made on only 26% of the document's 49 targets [23]. To ensure a clearer delivery pathway for the strategies within PI2040, the Sustainable Mobility Plan has a detailed action and implementation plan for 2020-25, followed by a mid-term evaluation ahead of publishing the plan for 2026-30.

4. CHALLENGES AND OPPORTUNITIES FOR TRANSITION IN THE NWR

A number of factors will impact, both positively and negatively, the NWR's ability to meet its share of Ireland's carbon-reduction commitments by transitioning towards more sustainable transport.

4.1 The Rural and Peripheral Nature of the NWR.

Research suggests that rural areas have higher per-capita GHG emissions than urban ones - both generally and in terms of transport. A study by the UK Commission for Rural Communities found that rural districts in UK had 8% higher per-capita GHG emissions than urban areas, and 26% higher specifically for transport [24]. This significant variation is believed to reflect both rural travel patterns, which involve significantly longer distances per average trip, and also the lower availability/perceived viability of sustainable transport in non-urban areas. A 2015 study in the US by Perumal and Simmons [25] noted that individuals living in urban cores had lower per-capita transport emissions than those elsewhere, which the researchers considered to be the result of population proximity/density. They also identified this as an inherent trait of urban areas - and that rather than attracting individuals who would be likely to have lower CO2 emissions anyway, urban locations actually mitigated the emissions of people who otherwise would have tended towards higher vehicular emissions. This therefore suggests urban cores can themselves alter the transport behaviour of their residents, such that density has a larger elasticity upon the number of miles driven and emissions generated than was found in earlier research.

Whilst it is helpful to consider how different physical contexts influence travel behaviour patterns, Tønnesen et al (2022) caution against assuming a 'one-size-fits-all' model for encouraging low carbon transport in rural areas [27]. They point out that rural areas lack the sort of key drivers that help nudge behaviour in more urban contexts towards reduced car usage – e.g. congestion, unfavourable conditions for driving and parking in the agglomeration core. They also highlight the fact that rural areas lack the population to support high-quality public transport provision, and assert that they have a different context for policy design and implementation due to their different land-use and transport system characteristics. They therefore conclude that bespoke policy packages are required for rural areas, and recommend doing this through tailored "Rural Policy Packages". These packages combine various place-based policy measures to coordinate the development of land use and transport systems in bespoke ways to reduce car dependency.

There is an additional question regarding the transition of rural areas towards more sustainable transport - and that is whether they are inherently less disposed towards such change in the first place. Research by Weckroth and Ala-Mantila (2022) suggests that rural areas have greater scepticism and lower concern about climate change than urban areas [28]. Phillips and Dickie (2014) researched attitudes towards climate change in a number of rural English villages, which led them to identify a "narrative of stasis" in which respondents believed that significant change wasn't conceivable in their area [29]. Respondents in that research provided arguments for why they and/or others would not change, leading the authors to conclude that "notions of the rural as some antithesis of change were indeed widely enacted in interviews with residents of the case study villages". All of which suggests that there may be a greater and inherent reluctance amongst residents of predominantly rural areas like the NWR to accept the kind of behavioural shift required to significantly reduce GHG emissions.

4.2 Access to Alternatives

The limited availability of public transport within large parts of the NWR is a significant impediment on the ability of its population to shift from car dependency. Section 3 above discusses some of the proposed ways in which this situation is being addressed within the region – particularly for Galway city. The region's population density is such that even after significantly enhanced investment, however, public transport will remain a fringe option for large swathes of the region. For those areas car dependency can at best be partly reduced, rather than removed, so the focus must instead be on transitioning them to zero-emission vehicles. This risks creating or exacerbating issues of transport poverty.

4.3 Transport Poverty & Forced Car Ownership

A 2020 study by Golubchikov and O'Sullivan into 'energy periphery' (places with an inferior physical, economic and political position within the distribution of resources and capabilities) in rural Wales highlighted that those living in places remote from core-urban areas can be doubly disadvantaged - not just by the lack of public transport but also the high cost of fuel for private transport [30]. Mattioli et al (2017) label this as 'Transport Poverty' – defined as a significant proportion of a household's income being consumed by their transport needs [31]. The greatest future energy concern that respondents identified in the study by Phillips and Dickie (2014) was that 'Fuel will become more unaffordable' [29]. Private vehicle usage is therefore viewed

by many as a necessity of rural living - but also one that entails economic stress, either currently or potentially. The NWR's limited public transport, the prevalence of fossil-fuelled vehicles in Ireland and the significant increase in the cost of running a private vehicle (particularly fuel) in recent years are factors which are likely to have increased 'Forced Car Ownership' and car-related economic stress. Carroll et al (2021) define Forced Car Ownership as "...those who may find themselves in circumstances with low transport accessibility and low income, which is intensified by the need to economically participate in society for financial gain" [32]. Chevallier et al (2018) use the term 'Car-related Economic Stress' to describe the negative financial impact that owning a private car can have upon some low-income households - who feel it is essential to have one for access to work and other opportunities, but who struggle to afford it [33]. A barrier to transitioning some of the NWR's rural dwellers to electric vehicles (EVs) will therefore be the significantly higher upfront purchase cost of such vehicles – though the lower running costs of EVs will conversely be of relative economic benefit in rural areas (given greater distance per average journey). Research shows that – whilst securing a switch to non-car modes of transport across the NWR would reduce GHG emissions within a shorter timescale than could be achieved through a switch to EVs alone [34] - the poor availability and connectedness of public transport within the region, combined with the relatively dispersed nature of homes, services, employment etc there and a possible lower propensity to accept the changes required, means that EVs could realistically have a more central role to play in transitioning there than they would in more urbanised environments (Newman et al 2014) [35].

5. CONCLUSION

Since 2009 Ireland has introduced a number of transport policies to reduce GHG emissions, encourage modal shift, decrease car usage and promote active travel. It has so far underperformed in the implementation of these strategies - hampered by issues such as the economic crisis, a lack of clarity over implementation responsibilities, and a failure to more closely link transport strategy and spatial planning. A change in approach was signalled in 2018 with the launch of Project Ireland 2040, which adopts a more holistic approach towards meeting climate commitments and places greater emphasis upon implementation of its proposals. Ireland faces a particular challenge, however, in step-changing transport transition within its Northern and Western Region – the country's most rural and peripheral area, with no population centres of scale and limited public transport provision. This places a particular spotlight upon the potential role that EVs could play in reducing per-capita emissions within the region, which could also help address the related issues there of Forced Car Ownership and Car-Related Economic Stress. To achieve this, however, may necessitate targeted Government assistance within the region to tackle the entry barrier presented by the high purchase cost of EVs.

With Ireland's 2030 target of a 51% reduction in emissions only eight years away, and transportation's progress towards that goal being slow to-date, it is essential that all levels of Government expedite and review existing strategies to encourage modal shift. This will require a strong focus upon implementation - with clear responsibility for delivery, implications for under-performance, and a bespoke approach to the needs of predominantly rural regions like the NWR.

References

[1] Central Statistics Office (2016) : Census Report.
[2] Government of Ireland (2018) : Project Ireland 2040.
[3] Government of Ireland (2022) : Sustainable Mobility Plan
[4] Government of Ireland (2021) : Climate Action Plan.
[5] Van Acker V, Goodwin P & Witlox F 2016 Key research themes on travel behavior, lifestyle, and sustainable urban mobility. International Journal of Sustainable Transport.
[6] O'Riordan V, Rogan F, Ó'Gallachóir B, MacUidhir & Daly H (2022) : 'How and why we travel – Mobility Demand and Emissions from Passenger Transport'. Transportation Research Part D
[7] Northern and Western Regional Assembly 'Regional Spatial and Economic Strategy 2020-2032 (RSES)'.
[8] Atlantic Economic Corridor Submission to National Planning Framework, 2017.
[9] CSO National Travel Survey, 2019.
[10] Society of Irish Motor Industry figures, reported via RTE News - 2021 new car registrations up 19% - SIMI (rte.ie)
[11] CSO (2022): Vehicles licensed for the first time, 2021
[12] INRIX Global Traffic Rankings (2021) : Global Traffic Scorecard
[13] Galway County Council (2022): 'Draft Galway County Development Plan 2022-2028. Galway Metropolitan Area'
[14] National Transport Authority (2022): Connecting Ireland.
[15] Central Statistics Office, Ireland (2006): Census Report.
[16] Government of Ireland (2009) : 'Smarter Travel – A Sustainable Transport Future'
[17] Government of Ireland (2009) : National Cycle Policy Framework.
[18] Deenihan G, Caulfield B and O'Dwyer D (2013): 'Measuring the Success of the Great Western Greenway in Ireland". Tourism Management Perspectives. Vol.7, July 2013.
[19] The Journal, 9th Aug 2021 : Railway, greenway, or disused line? The tangled, uncertain future of the Western Rail Corridor (thejournal.ie)
[20] National Transport Authority (2021): Actice Travel Investment Programme
[21] Galway Daily, 11th Feb 2021 : 'Walking and cycling projects in Galway city get €12m funding boost'.
[22] Sustainable Energy Authority of Ireland (SEAI) (2021) : 'Energy-related CO^2 emissions in Ireland 2020'.
[23] Government of Ireland (2019) : Evaluation of Smarter Travel Areas.
[24] Commission for Rural Communities (2010) : State of the Countryside.
[25] Perumal A, & Timmons D (2015) : 'Contextual Density and US automotive CO^2 emissions across the rural-urban continuum'. International Regional Science Review.
[26] Orru K, Poom A & Nordlund A (2019) : 'Socio-Structural and Psychological Factors Behind Car Use: Comparing Northern and Eastern Europe'. Transportation Research Part A.
[27] Tonneson A, Knapskog M, Rynning M & Groven K (2002): 'Planning for Climate-Friendly Transport in Norwegian Rural Areas'. Transportation Research Part D.
[28] Weckroth M & Ala-Mantila S (2022): 'Socio-economic Geography of Climate Change Views in Europe'. Global Environmental Change, Vol 72
[29] Phillips M & Dickie J (2014): 'Narratives of Transition/Non-Transition Towards Low-Carbon Futures Within English Rural Communities'. Journal of Rural Studies, Vol. 34, April 2014.
[30] Golubchikov O & O'Sullivan K (2020): 'Energy Periphery: Uneven Development and the Precarious Geographies of Low-Carbon Transition'. Energy and Buildings, Vol. 211, March 2020.
[31] Mattioli G, Lucas K & Marsden G (2017): 'Transport Poverty and Fuel Poverty in the UK: From Analogy to Comparison'. Transport Policy.
[32] Carroll P, Benevenuto R & Caulfield B (2021): ' 'Identifying hotspots of transport disadvantage and car dependency in rural Ireland'. Transport Policy Vol. 101, Feb 2021.
[33] Chevallier LB, Motte-Baumvol S, Fol S, & Jouffe Y (2018): 'Coping with the costs of car dependency: A system of expedients used by low-income households on Outskirts of Dijon & Paris'. Transport Policy 65
[34] Hill G, Heidrich O, Creutzig F & Blythe P (2019): 'The role of electric vehicles in near-term mitigation pathways and achieving the UK's carbon budget'. Applied. Energy Vol.251, Oct 2019.
[35] Newman D, Wells P, Donovan C, Nieuwenhuis P & Davies H (2014): 'Urban, sub-urban or rural: Where is the best place for electric vehicles?'. International Journal of Automotive Technology & Management, Vol 14

Development and Application of a Methodology for Pedestrian and Driver Communication Observation to Improve Pedestrian Road Safety

Mr. Peter Dickson[1], Dr. Brian McCann[2]
[1,2] Facility of Engineering and Design, Atlantic Technological University Sligo Campus, Ash Lane, Sligo, F91 YW50, Ireland
email: peter.dickson@mail.itsligo.ie[1], mccann.brian@itsligo.ie[2]

ABSTRACT:

The Road Safety Authority in Ireland state that road fatalities have generally fallen between 2009 - 2018. However, both pedestrian injuries and fatalities have not fallen to the same degree, with pedestrian injuries highest in 2018 and pedestrian fatalities remaining consistent in the same period. As sustainable travel is actively encouraged by the Irish Government in their climate action plan, the priority of pedestrians in urban centres, their safety and communication with other road users warrants further investigation. This study examined a national road in an urban centre with existing collision clusters involving pedestrians and vehicles. Pedestrian-driver interactions and communication were observed to ascertain the suitability of shared space principles to improve pedestrian road safety. Locations selected had limited pedestrian crossing facilities, but high numbers of pedestrian crossing movements combined with high traffic volumes. A draft observation protocol was developed for a pilot study on the N15 in Ballybofey-Stranorlar, testing parameters used in the literature for suitability in Ireland. The pilot field study findings were then used to refine a final observation protocol. Results showed that both implicit and explicit communication and reactions between pedestrians and drivers was common and more regular than that identified in the literature. It was determined these communications and driver actions are needed for effective shared space operation with recommendations made in this study for increased road user integration and the application of shared space principles for two of the three sites examined.

KEY WORDS: Pedestrian road safety; Road user interactions; Road user communication; Shared space; Pedestrian priority.

1 INTRODUCTION

The purpose of this research was to investigate road user interaction and communication in busy urban centres with the aim of improving pedestrian road safety. Road user interaction and communication was studied at locations with existing pedestrian collision clusters. This was achieved by developing, testing and applying a novel pedestrian crossing observation protocol for the Irish Context and then using the findings to assess the potential suitability of shared space principles to improve pedestrian road safety. The urban design approach 'shared space' consists of a section of public road where road users are not regulated by traditional traffic controls, but rather social protocols and human interaction [1].

Historical collision patterns involving pedestrians and vehicles on national roads within town centres were identified which had limited or no pedestrian crossing facilities, but high numbers of pedestrian crossing movements combined with high volumes of traffic. National roads extending through urban centres in Ireland that have not been bypassed tend to be heavily trafficked with a mixture of both local and national strategic traffic and have high pedestrian movements associated with commercial and retail activity. It has been observed from personal experience and research that crossing a busy national road in an urban centre away from a controlled crossing is challenging and requires a combination of assertiveness, coordination and communication with oncoming drivers. It is considered pedestrians in these locations are generally not adequately catered for, especially the timid or those who are mobility, visually or sensory impaired. The Design Manual of Urban Roads and Streets (DMURS) has made great strides toward reprioritising the hierarchy of pedestrian movements over vehicular traffic for new schemes [2]. However, on some legacy routes through urban centres, the needs of pedestrians are yet to be incorporated into the road environment.

2 LITERATURE REVIEW

2.1 Pedestrian Injury and Fatality

The World Health Organisation reports fatalities on the world's roads are increasing, with approximately 1.35 million each year [3], equating to nearly 3,700 fatalities daily. Of these, more than half are vulnerable road users such as pedestrians, cyclists and motorcyclists. Fatalities arising from road collisions are the leading cause of death for people between 5 and 29 years and are the eighth overall leading cause of death for all age groups. Vulnerable road users are significantly affected by poor road safety with 26% of all road fatalities globally either pedestrians or cyclists [3].

The Road Safety Authority (RSA) indicate fatalities in Ireland have generally been falling in the ten-year period from 2009 to 2018. Total fatalities have fallen from 220 in 2009 to 134 in 2018 with small variations as shown in Figure 1 [4]. However, both pedestrian fatalities and injuries have not fallen to the same degree in that ten-year period with pedestrian injuries highest in 2018 and pedestrian fatalities generally remaining consistent with a small drop and rise again in the years 2015 to 2018. Given the lack of a decrease in both pedestrian fatalities and injuries which could be contributed to any number of factors such as economic drivers or increased walking from sustainable travel initiatives, it was considered there was scope for further research into pedestrian road safety in Ireland.

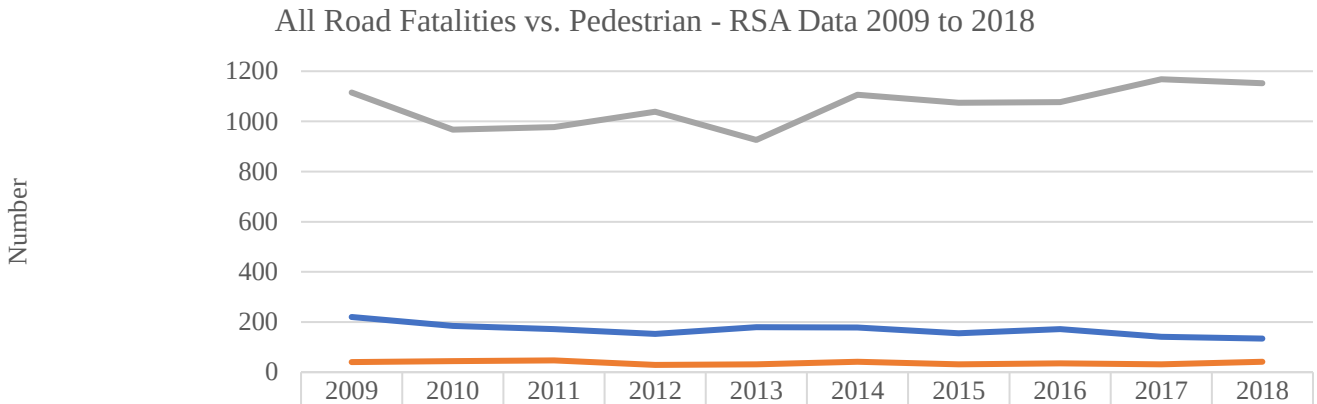

	2009	2010	2011	2012	2013	2014	2015	2016	2017	2018
All Fatalities	220	185	172	152	179	178	155	172	141	134
Pedestrian Fatalities	40	44	47	29	31	41	31	35	31	42
Pedestrian Injuries	1115	967	977	1038	926	1106	1074	1077	1168	1152

Figure 1. All Fatalities vs. Pedestrian - RSA Data from 2009 - 2018 (Source: rsa.ie)

2.2 Pedestrian – Driver Interaction and Observation Protocols

The safety of pedestrians is impacted by a number of factors in urban areas including pedestrian-driver interaction and communication [5]. Uttley et al., [5] indicate that pedestrians misunderstanding the intentions of drivers can result in collisions and significant problems arise when nonverbal communication between pedestrians and drivers suffers due to a lack of shared expectations of the road environment.

Sucha et al., [6] found the factors which influenced a pedestrian's decision making process at a crossing included various signs given by the driver such as physically slowing down, eye-contact, gestures or flashing of the lights [6]. They also found pedestrians attempted to communicate their intention to use the crossing by the way they stood at the waiting point, putting one foot onto the crossing, waving, or making eye contact with the driver. Sucha et al., [6] concluded further research could be undertaken into understanding the balance of pedestrian-driver communication and safety implications. Uttley et al., [5] stated that nonverbal cues play a significant role in pedestrian movements such as eye contact, nodding and hand gestures. They comment that a wide body of work has been undertaken on sections of road with well-defined rules such as controlled crossing points. However pedestrian-driver interactions are likely to be more uncertain in non-formal areas where there are limited road user norms, for example shared spaces [5].

Uttley et al., [5] and Sucha et al., [6] state that studies examining road conflicts as well as historical collision data is helpful in understanding pedestrian and driver behaviour. Kaparias et al., [7] noted that much of the research to date has been concerned with pedestrian-driver interactions using traffic conflict analysis, based on vehicle conflict principles. Research into the behavioural analysis of pedestrian and driver interactions as well as implicit or explicit communication techniques is less common and the lower severity conflicts especially have not been investigated thoroughly [7].

Four recent case studies where an observation protocol was used for the study of pedestrian-driver interaction and communication were examined. The study of Uttley et al. [5] focused on road user interactions in a UK train station carpark where there were no existing pedestrian crossings. They considered this location effectively acted as a shared space and therefore provided a useful baseline for comparison in this study. Anciaes et al. [8] examined the various factors leading to driver yielding behaviour for pedestrians at courtesy crossings. Lee et al. [9] established the level of explicit communication in 701 road user interactions at junctions, pedestrian crossings and road links with no formal crossing point. The case study of Madigan et al. [10] differed slightly as its main focus was to validate a methodology for a systematic observation protocol for pedestrian-driver interactions which could be carried out by both live field observations and video recording from 50 pedestrian-driver interactions at an urban intersection in Leeds, UK.

2.3 Shared Space

Historically in developed countries, safety improvements for vulnerable road users have been enacted by physical separation of road user groups [5]. However, Kaparis et al [7] state in recent decades increased integration of road users on urban roads has been implemented, in the creation of public realm and sense of place. These measures can include the removal of signage, kerb upstands and road markings as well as the provision of more informal crossing points for pedestrians or even no dedicated crossing points at all. As shared space approaches require much more pedestrian-driver interactions and observance of social protocols [1] there is a need for further analysis of the behavioural patterns in pedestrian-driver interactions [5].

The use of shared space requires innovative analysis and design as drivers, cyclists and pedestrians navigate the same road space with limited regulation [1]. Jayakody et al., [11] identify the most important objectives for shared space implementation as pedestrian prominence and priority; distinctive sense of place; inclusive design for all road users; and siting and

connectivity. DMURS [2] stipulate the fundamental design factors in successful shared space as creative use of materials and finishes to indicate to drivers that the carriageway is an extension of the pedestrian domain, avoidance of raised kerbs which may give the impression to drivers that pedestrians are confined to the raised areas and minimising the overall carriageway areas and corner radii to reduce vehicles speeds. Older guidance like 'the Institute of Highway Engineers Home Zone Design Guidelines' recommend vehicle movements of less than 100 per day for shared space application, but this is considered outdated and superseded with newer schemes like the Ashford Ring Road, Kent and Exhibition Road, London [12]. DMURS [12] identify reduced vehicle speeds of around 20km/h being a key objective for designers of shared space through a self-enforcing street design. Shared space examples of a courtesy crossing are shown in Figure 2, Figure 3 and Figure 4.

While shared space can operate best as traffic flows and traffic speeds reduce [13], recent studies state that through implementation of schemes internationally, more heavily trafficked streets have proved suitable for shared space [2]. Where heavily trafficked streets are selected for shared space implementation, there must be significant analysis of its suitability [2]. It is important to note where shared space principles are applied to heavily trafficked streets, the main function of that street does not become pedestrian amenity and dwelling but rather increased pedestrian prominence and priority, allowing pedestrians to cross the carriageway with safety and comfort. Among the examples identified of heavily trafficked shared spaces was the conversion of a signalised cross roads junction into a double roundabout shared space in Poynton, Cheshire, UK with circa 26,000 vehicles per day [14].

Figure 2 - Example of pocket square courtesy crossing in an urban centre [12]

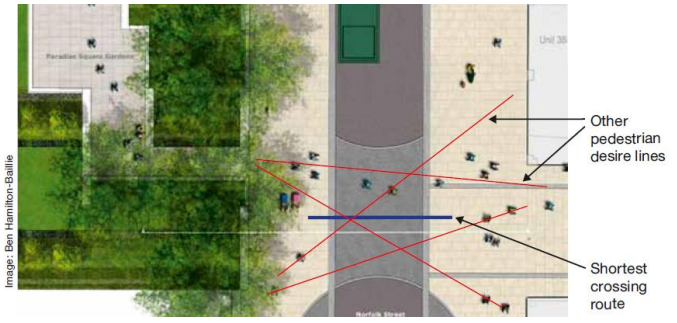

Figure 3 – Potential Shared Space Principles and Design [12]

Figure 4 - Example of courtesy crossing with shared space principles, R132 Clanbrassil Street, Dundalk [12] and Before Image [15]

3 METHODOLOGY

3.1 Site Selection

The study examined the N15 national primary road in Donegal which extends through the busy town centres of the twin towns of Ballybofey and Stranorlar. The locations, vehicle-pedestrian collisions, and images of all three sites are shown in Figure 5 to Figure 9. Sites were selected which met the following criteria:

1. Existing vehicle-pedestrian collision cluster identified from the RSA online collision map (where a cluster equated to over three collisions of a similar collision type in the same area);
2. Busy urban area with an active road edge; and
3. Lack of existing controlled pedestrian crossings.

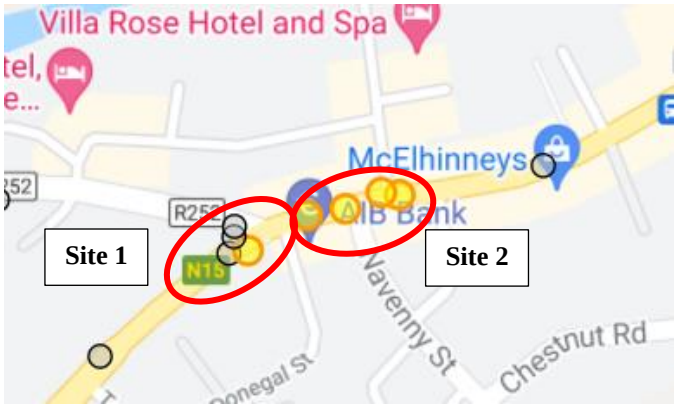

Figure 5 - Site 1 & 2 Location and Pedestrian Collisions [16]

Figure 6 - Site 1 [15]

Figure 7 - Site 2 [15]

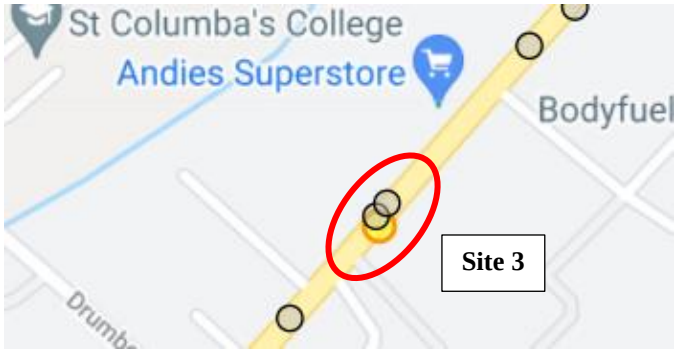

Figure 8 - Site 3 Location and Pedestrian Collisions [16]

Figure 9 - Site 3 [15]

3.2 Observation Protocol

A draft observation protocol for recording pedestrian and driver interactions and communications was developed for the Irish context from examples in the existing literature. This protocol was refined in two pilot studies in December 2021, with a number of amendments made after each pilot study. The finalised observation protocol interface is shown in Table 1 which had 23 different categories.

Field observations with a single observer were undertaken with accompanying video footage for subsequent verification as Madigan et al. (2021) found that field observers were needed to record the human communication both explicit and implicit, whereas video recordings were useful to extract exact sequences of complex manoeuvres and provide verification.

4 RESULTS AND ANALYSIS

Seven field observations were undertaken in February and March 2022 totalling 4.75 hours in duration and 119 pedestrian crossing manoeuvres were observed between the three sites. The number of observations per hour at Site 1, Site 2 and Site 3 were 21, 38 and 1.3 respectively. As the crossing manoeuvres recorded were low for Site 3, no further field studies were undertaken at this site.

Table 1. Sample of the Populated Observation Protocol

Location	7.3 Site 1			
Date / Time	16:35 - 17:20, 25/02/2022, Friday			
No. Cameras	1			
Camera Position(s)	Parking bay SB carriageway			
Observer Position(s)	NB footpath, outside BoI			
	1	**2**	**3**	**4**
	Site 1	**Site 1**	**Site 1**	**Site 1**
Weather	DRY	DRY	DRY	DRY
Visibility	OVERCAST	OVERCAST	OVERCAST	OVERCAST
Time	16:35	16:35	16:37	16:38
Crossing Location	M	M	M	M
At Ped. Crossing?	N	N	N	N
Ped. Age	61	60	60	60,16
Gender	F	M	F,F	M,F
No. of Ped.	1	1	2	2
Mobility Restriction	-	-	-	-
Veh. Type	C,HGV	C	C	C
Veh. Approach L/R/M	M	M	M	L
Traffic Movement Gap/slow/stop/fast	SLOW	STOP	SLOW	FAST
Ped. Approach Stop/Slowed/Sped up/DNS	STOP	DNS	STOP	STOP
Ped. Head Movement Left/Right/Straight/A	A	R	A	A
Ped. Waiting time (Sec)	2	0	1	2
Ped. Wait Position	PB	-	PB	FP
Ped. Communication BEFORE Nod/foot out/wave/look only/go	LOOK,WAVE	LOOK,WAVE	LOOK,WAVE	LOOK
Ped. Communication AFTER Nod/wave	-	-	WAVE	WAVE
Ped. Movement During Crossing Kept pace/sped up	SPED UP	KEPT PACE	KEPT PACE	KEPT PACE
Ped. Stranded at Centreline	-	-	-	Y
Veh. Action Brake/Acc/Slow down	SLOW DOWN	-	SLOW DOWN	BRAKE
Driver Communication Nod/hand gesture/flash/honk	HAND GESTURE	-	NOT OBS	HAND GESTURE
Comments				PEDS WALKED INTO TRAFFIC LANE, GOT STRANDED AT CENTRELINE AND DRIVER HAD TO BRAKE

At all three sites, courtesy crossings were provided although they were poorly defined, not easily identifiable to drivers or located out of the pedestrian desire line and it was found 75% of pedestrians did not use them. Traffic condition recordings found 33 (28%) pedestrians crossed during a gap in traffic, 60 (50%) pedestrians crossed when traffic was moving slow, 18 (15%) pedestrians crossed when traffic was stopped, and 8 (7%) pedestrians crossed when approaching traffic was travelling at a speed.

All pedestrians made attempt at communication with drivers before crossing with 105 (88%) pedestrians looking towards the approaching vehicle or driver and 14 (12%) pedestrians both looking and using a hand gesture (waving) toward the approaching driver. Pedestrian communication with drivers during or after the crossing included 32 (27%) waving and 84 (71%) providing no form of communication.

80 (67%) pedestrians kept pace and 39 (33%) sped up while crossing, six pedestrians were also noted to sprint across the carriageway. 11 (9%) pedestrians got stranded at the centre line after crossing one lane of traffic successfully, these pedestrians either had to wait for a subsequent gap in traffic in the other traffic lane or driver action. The field observer considered these pedestrians did not display signs of unease.

35 (29%) drivers on the N15 braked and came to a direct stop for a pedestrian to cross and 26 (22%) drivers slowed down to allow a pedestrian to cross. In 55 (46%) observations there was no vehicle action required, although there still may have been communication. Drivers used hand gestures in 39 (33%) cases and a hand and horn gesture in 1 (1%) observation. In 14 (12%) observations, it was not possible to observe driver communication due to the position of the observer, position of camera, obscured visibility to the driver or the frequency of the pedestrian movements. This same limitation was noted by Uttley et al. [5] who did not observe 14 of 66 driver's head or hand movements.

5 DISCUSSION

At all sites, 75% of pedestrians did not use the provided courtesy crossings, with no statistical significance found with the likelihood of pedestrians to jaywalk according to demographics or traffic conditions. This indicated the likelihood of pedestrians to jaywalk could have been associated with the road environment or other factors such as pedestrian attitude unmeasurable by the observation protocol, namely courtesy crossings not located within predominant desire line; courtesy crossings of insufficient quality to encourage use; or pedestrians felt that due to the active road edge, the carriageway was equally for the use of pedestrians as well as vehicles.

Evidence of implicit and explicit road user communication was found in this study. More pedestrians looked towards an approaching vehicle before crossing, more pedestrians waved to drivers during or after crossing, more drivers made a vehicle action for crossing pedestrians and more drivers communicated with pedestrians than any of the studies identified in the literature review as summarised in Table 2. Therefore, it was considered that an identifiable trend of implicit and explicit communication between road users was evident at Site 1 and Site 2 which could contribute to an assessment of shared space application.

By comparison, Lee et al. [9] surmised that in the six European cities, pedestrians and drivers exhibited much lower levels of explicit communication to indicate intention.

Table 2. Communication and Interaction Comparison

Communication or Interaction Category	Percentage of Total Observations - N15	Literature Findings
Implicit pedestrian communication - looking toward approaching vehicle before crossing	100%	42% - Uttley et al. [5] 89% - Lee et al. [11] 84% - Sucha et al. [6]
Explicit pedestrian communication – pedestrian hand gesture during/after crossing	27%	17% - Uttley et al. [5] 6% - Lee et al. [11]
Pedestrian acceleration during crossing	33%	7% to 26% - Lee et al. [11]
Vehicle action for pedestrian (braking sharply or slowing down)	57% (jaywalking) 43% (at crossing) Overall vehicle action 54%	Lee et al. [11] - 0% (jaywalking) 45% (at crossing)
Explicit driver communication with pedestrians	34%	12% - Uttley et al. [5] 5% - Lee et al. [11] 5% - Sucha et al. [6]

Uttley et al. [5] concluded that explicit communication between pedestrians and drivers was rare in the carpark. They did note however that hand gestures in their study were more common from pedestrians at 17% compared to the study by Lee et al. [9] and considered that this was because of the shared space nature of the site and the more ambiguous nature of the road environment.

Madigan et al. [10] found explicit communication between pedestrians and drivers was limited, similar to Lee et al. [9] and Uttley et al. [5]. They surmised that road users were able to alter their movements smoothly around one another without the need for explicit communication at the urban junction in Leeds.

The application of this study was to use findings of field observations to consider possible measures to improve pedestrian road safety, accessibility and movement. Traditional remedial measures like controlled crossings have a procedural assessment outlined in TII Publication DN-GEO-03084. However, no similar defined assessment procedure for shared space intervention was identified in the literature. The key objectives of shared space outlined in Section 2.3 by Jayakody et al., [11] are considered the governing criteria when considering shared space. These objectives were suitable for application at Site 1 and Site 2. These objectives rely on road user integration [7] and so communication between road users is critical. The higher levels of explicit and implicit communication observed on the N15 compared to the literature indicated pedestrians and drivers may be well placed to adapt to shared space principles in this location.

Site 1 and Site 2 shared characteristics with successful shared space case studies identified in the literature such as busy urban centres with active street edges, large traffic volumes, issues with pedestrian flow, vehicle dominated carriageways and significant numbers of pedestrians walking within the carriageway. It was considered that Karndacharuk et al., [17] addressed the obvious concern of high traffic volumes being [18] suitable for shared space with a review of numerous shared space case studies. Thus a short length of shared space on the N15 serving both Site 1 and Site 2 located within the observed pedestrians desire lines was recommended as shown in Figure 10, similar to the examples shown in Figure 2, Figure 3 and

Figure 4 previously. It is envisaged that the shared space could effectively act as an enhanced courtesy crossing. In contrast to a traditional controlled crossing, this shared space would need to be self-regulating, alerting drivers to the likelihood of pedestrians crossing the carriageway and not using road markings, signage or traffic signals to do so.

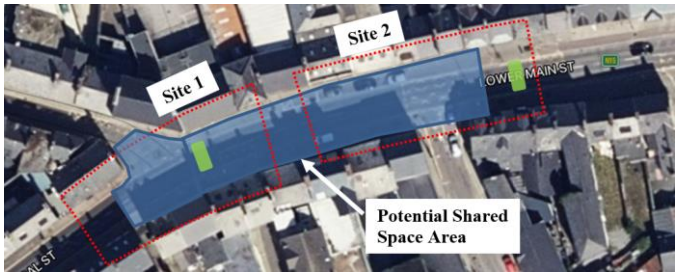

Figure 10 – Potential Shared Space Area [19]

6 CONCLUSIONS AND RECOMMENDATIONS

It was considered the site selection process based on collision cluster identification was robust, given the initial objective to improve pedestrian road safety and understand the cooperative behaviour of road users. To improve site selection, it is recommended that a site visit be undertaken to avoid sites with insufficient pedestrian movement. The developed and tested novel observation protocol was able to record road user implicit and explicit communication. The use of a single field observer limited the data collected and a second or third field observer was considered necessary given increased resources. The recording methodology could also be improved using voice recorders to vocalise interactions, improving accuracy.

Most pedestrians were found to not use the courtesy crossings, possibly due to the road environment or other societal factors unmeasurable by field observations. Pedestrian attitude questionnaires are recommended for verification of conclusions in relation to road user attitudes and preferences.

Explicit and implicit communication and driver actions were found to be more common on the N15 when compared to the studies in the literature. More pedestrians turned to look towards an approaching vehicle before crossing, more pedestrians communicated with drivers during or after the crossing (27%), more drivers made a vehicle action for crossing pedestrians and more drivers communicated with pedestrians (34%) than in the literature. Patterns of road user collaboration and communication were found to be evident on the N15 in this segregated road environment. Therefore, this made a case to provide shared space principles in problem areas to aid pedestrian crossings and ultimately pedestrian road safety.

Further research at selected sites should include questionnaires to verify assumptions made about road user attitudes, feelings and perceptions as recommended by Anciaes et al. [8]. For pedestrians these could be undertaken at the roadside after a pedestrian has undertaken a crossing, similar to the study of Lee et al. [5]. To record driver attitudes, focus groups would be more appropriate with a diverse range of drivers, similar to Sucha et al. [6]. To draw conclusions for the wider Irish context, field observations at other sites should be completed to validate the findings and identify any potential localised societal anomalies with road user behaviour. This could also be done on other road classifications in urban centres such as regional roads and local roads or streets. It was evident that this type of observation protocol into human communication could also be applied in the autonomous vehicle industry, as identified by the four case studies examined in the literature review. Further research into driver reactions to groups of pedestrians should be undertaken. This was not analysed in this study due to the generally small groups of pedestrians at the study sites. Similar to conclusions drawn by Madigan et al. (2021), further research is needed to identify the effects on behaviour of groups of pedestrians crossing in larger towns near centres of employment or education.

7 ACKNOWLEDGEMENTS

With thanks to Dr. Brian McCann for his direction in this part-time research in part fulfilment for the award of Master of Engineering in Road and Transportation Engineering in ATU.

REFERENCES

[1] F. T. Johora and J. P. Müller, “Zone-Specific Interaction Modeling of Pedestrians and Cars in Shared Spaces,” *Transp. Res. Procedia*, vol. 47, pp. 251–258, 2020.
[2] DTTAS, *Design Manual for Urban Roads and Streets*. Ireland, 2019.
[3] WHO, “Global Status Report on Road Safety,” Geneva, 2018.
[4] RSA, “Road Collision Facts Sheet 2013,” Dublin, 2016.
[5] J. Uttley, Y. M. Lee, R. Madigan, and N. Merat, “Road user interactions in a shared space setting: Priority and communication in a UK car park,” *Transp. Res. Part F Traffic Psychol. Behav.*, 2020.
[6] M. Sucha, D. Dostal, and R. Risser, “Pedestrian-driver communication and decision strategies at marked crossings,” *Accid. Anal. Prev.*, vol. 102, pp. 41–50, 2017.
[7] I. Kaparias, M. G. H. Bell, T. Biagioli, L. Bellezza, and B. Mount, “Behavioural analysis of interactions between pedestrians and vehicles in street designs with elements of shared space,” *Transp. Res. Part F Traffic Psychol. Behav.*, 2015.
[8] P. Anciaes, G. Di Guardo, and P. Jones, “Factors explaining driver yielding behaviour towards pedestrians at courtesy crossings,” *Transp. Res. Part F Traffic Psychol. Behav.*, vol. 73, pp. 453–469, 2020.
[9] Y. M. Lee *et al.*, “Road users rarely use explicit communication when interacting in today’s traffic: implications for automated vehicles,” *Cogn. Technol. Work*, vol. 23, no. 2, pp. 367–380, 2020.
[10] R. Madigan, Y. M. Lee, and N. Merat, “Validating a methodology for understanding pedestrian – vehicle interactions: A comparison of video and field observations,” *Transp. Res. Part F Traffic Psychol. Behav.*, vol. 81, pp. 101–114, 2021.
[11] R. R. J. C. Jayakody, K. Keraminiyage, M. Alston, and N. Dias, “Design factors for a successful shared space street (SSS) design,” *Int. J. Strateg. Prop. Manag.*, vol. 22, no. 4, pp. 278–289, 2018.
[12] DMURS, “DMURS Frequently Discussed Issues,” 2022. [Online]. Available: https://www.dmurs.ie/frequently-discussed-issues. [Accessed: 09-Apr-2022].
[13] Department of Transport, “Smarter Travel - Sustainable Transport Future,” 2009.
[14] R. Steuteville, “Shared space applied to high-volume intersection,” *Public Square, An CNU J.*, 2013.
[15] Googlemaps, “google.ie/maps,” 2021. [Online]. Available: www.gogle.ie/maps. [Accessed: 20-Mar-2021].
[16] RSA, “Road Safety Authority Website,” 2020. .
[17] A. Karndacharuk, D. J. Wilson, and R. Dunn, “A Review of the Evolution of Shared (Street) Space Concepts in Urban Environments,” *Transp. Rev.*, vol. 34, no. 2, pp. 190–220, 2014.
[18] RSA, “Our Journey Towards Vision Zero. Ireland’s Government Road Safety Strategy 2021–2030,” 2021.
[19] A. Maps, “Irish grid reference finder,” 2021. [Online]. Available: https://irish.gridreferencefinder.com/. [Accessed: 20-Mar-2021].

Managing Driving Under the Influence of Alcohol using Driver Rehabilitation and Alcohol Ignition Interlock Systems

Ryan, M.[1], O'Neill, D. [1& 2], Carr, R[2]. Abdul Ghani[2], A. Noonan, D.[1]
[1]National Office for Traffic Medicine (RCPI/RSA)
[2]School of Medicine, Trinity College Dublin
email : ryanf1@tcd.ie

ABSTRACT: Alcohol use disorder (AUD) is prevalent in Ireland and consequently, driving under the influence of alcohol (DUI) is a major societal problem. We estimate that over 21,000 alcohol treatment episodes are required for Irish drivers with AUD, however, there is no provision in Irish law for managing DUI using rehabilitative/therapeutic approaches or alcohol interlocks.
Following on from the definitive EU-funded Driving Under the Influence of Drugs and Alcohol study we conducted a literature review and survey-based research with members of the International Commission on Driver Testing (CIECA). Our findings encapsulate 61 relevant articles and responses from 51% of CIECA members. These showed that punitive measures (driving bans, prison sentences, penalty points) are commonly used for DUI offences. Alcohol interlocks are used widely in North America and increasingly in EU states. Issues identified include scheme participant selection and monitoring methodologies. The available evidence shows that interlocks are effective in reducing DUI and its consequences but do not address the underlying cause, which can only be addressed using diagnostic/therapeutic, educational elements. Our findings indicate that state-of-the-art interventions based on the WHO Screening, Brief Interventions and Referral to Treatment model (WHO, 2021) can address the causes of DUI efficiently and effectively.
There is clear evidential support for a multi-component approach for DUI offenders combining diagnostic/therapeutic and educational components and linked to an Alcohol Interlock Intervention Programmes (AIIPs). This requires cross-agency collaboration by the police, courts and the health service for screening and diagnosis of AUD and providing appropriate assessment and treatment of drivers with AUD.

KEY WORDS: Driving Under the Influence of Alcohol, Alcohol Ignition Interlock Systems, Driver Rehabilitation.

1 INTRODUCTION

Driving under the influence of alcohol (DUI) is a major source of death and injury and it is estimated that between 5 – 35% of all road deaths reported globally are alcohol-related [1]. Drivers with a blood-alcohol concentration (BAC) of at least 1.2 g/L have a 20-200 times higher risk of injury in a crash and although this group accounts for just 1% of all alcohol positive drivers in traffic, it includes two-thirds of all alcohol positive seriously and fatally injured drivers [2].

1.1 Driving under the influence of alcohol in Ireland

In Ireland, it is a criminal offence to drive a vehicle with a BAC above a permitted limit. The limit for fully licenced drivers is 50 milligrams of alcohol per 100ml of blood. A lower limit of 20 milligrams of alcohol per 100 ml of blood applies for professional, learner and newly qualified drivers [3]. Penalties for drink-driving offences range from disqualification periods from three months to six years, depending on the classification of the driver (learner, novice or professional), alcohol level detected and whether it is a first or subsequent offence [4].

Alcohol use is a major contributory factor in road deaths in Ireland. The Road Safety Authority (RSA) reported that over one-third (36.5%) of road user fatalities between 2013 and 2017 tested positive for alcohol. This consisted of 135 drivers who were predominantly male (92%) and under 45 years old (82%). The majority of these drivers had a BAC greater than 150mg/ml (69%) i.e., three times over the legal limit [5]. The Medical Bureau for Road Safety (MBRS), which analyses samples taken from drivers who were arrested for DUI reported that almost one-third (32%) of the blood/urine samples and close to a half (45%) of the breath samples analysed in 2019 revealed that these drivers had consumed at least twice the legal limit of alcohol [6].

A recent analysis of data on problem alcohol use in Ireland used data from the National Drug Treatment Reporting System (NDTRS). This showed that 44,079 adults aged 18-64 entered treatment for Alchol Use Disorder (AUD) between 2015 and 2019, indicating that the national rate of treated AUD was 270 cases per 100,000 annually [7]. Estimates suggest that there should be about 690 episodes of treated alcohol dependence per 100,00 per year in Ireland based on population prevalence estimates and ranges of treatment engagement in the international literature [8].

Population estimates calculated by the CSO indicate that there were 3,782,874 people aged 17 years and over in Ireland in 2019 and of these, 3,047,912 (80.6%) held current driving licences. Assuming a need for 690 treatment episodes for every 100,000 drivers, this would suggest a need for 26,102 treatment episodes per year among the population generally. However, data from the NDTRS showed that just 7,546 AUD treatment episodes were provided in 2019 [7]. Furthermore, assuming that AUD is normally distributed in the population, including the driving population, we estimate that 21,031 AUD treatment episodes were needed for this group in 2019.

Legislative approaches for dealing with DUI offending in Ireland are mainly punitive in nature, with little acknowledgement that DUI offending is very often symptomatic of an underlying medical/psychological condition that requires appropriate treatment and remediation to reduce the problem of DUI recidivism. Although Irish law does not provide for use of driver rehabilitation (DR) or alcohol interlocks currently, these options will be considered under the next Government Road Safety Strategy (2021-2030).

1.2 Alcohol Ignition Interlock Systems (AIIS)

Alcohol interlock devices are used to prevent drivers from starting their vehicles if they have consumed alcohol [9]. These alcohol-sensing devices connect to the vehicle ignition system and prevent it from starting if alcohol above a specified limit is detected in the driver's breath [10]. Additionally, interlocks may be equipped with a data recorder that logs each breath test completed by the driver, its results, and all relevant data, e.g., date and time. An advantage of the interlock approach is that it provides offenders and their families with ongoing mobility and thus access to employment, education, and other daily activities [11]. In addition, it is also a potentially important biofeedback mechanism for assisting in recovery from AUDs.

2 DRIVER REHABILITATION (DR) PROGRAMMES

There is a growing consensus that an educative/therapeutic approach is required to affect lasting behavioural change in drivers convicted of DUI. Educational approaches provide information about alcohol use and the risks involved in DUI [11].

The EU-funded study Driving Under the Influence of Drink and Drugs (DRUID) reviewed DR programmes for DUI offenders within Europe, most of which included elements such as discussions and self-reflection covering a wide range of topics such as the negative consequences of alcohol abuse to the risks of drink-driving. DRUID also highlighted considerable variability in the implementation and application of DR in Europe and further afield, noting a strong trend in favour of developing national guidelines covering different aspects of DUI rehabilitation [11].

The aim of the current study was to review developments in the management of DUI offenders using behavioural interventions, including alcohol ignition interlocks and DR programmes in Europe since the publication of the DRUID study in 2008. This will include evidence of effectiveness in terms of recidivism and involvement in subsequent alcohol-related motor vehicle crashes.

3 METHODS

Two complimentary approaches were used when surveying this field: A review of the academic and 'grey' literature and survey of CIECA member countries.

3.1 Search of the academic and grey literature

The literature search was conducted using online databases such as PubMed, ScienceDirect, and Transport Research International Documentation (TRID). Our search strategies involved using terms to describe DUI, in combination with terms to describe DR and/or alcohol interlocks. MeSH terms were used, where possible, to increase the specificity of searches. The search strategy for grey literature involved collecting relevant information from reports and other relevant documents. This included Road Safety Observatory Reports, RSA reports and other documents identified in personal contacts with subject matter experts. Searches were restricted to articles published from 2009 and were completed between 8 – 16 July 2021. The initial search yielded 525 papers/reports and this was reduced to 61 full text documents that form part of the review.

3.2 Survey of CIECA members

The survey was distributed to members of the International Driver Testing Commission (CIECA) who represent 37 countries in Europe, and also include the United Arab Emirates, Australia, and the United States.

4 RESULTS

4.1 Alcohol Interlock Installation Programmes (AIIP)

4.1.1 North America

Alcohol interlocks are used widely to sanction DUI offenders in North America; they are provided in every region in Canada [12] and also in all 50 U.S. states and Washington (DC) [13]. McGinty, Tung[10] assessed the effectiveness of state interlock laws on alcohol-related fatal crashes across 50 U.S. states from 1982 to 2013. This showed that states requiring interlocks for all DUI offenders recorded a 7% decrease in the rate of BAC units >0.08 fatal crashes and an 8% decrease in the rate BAC ≥0.15 crashes, translating into an estimated 1,250 prevented crashes where BACs were >0.08.

4.1.1.a Voluntary versus mandatory installation

Currently, 28 U.S. states have mandatory interlock provisions for all offences. Although voluntary interlock schemes are often used as an alternative to other sanctions, research shows a low uptake on voluntary programmes particularly when licence suspension is offered as an alternative [13]. Some researchers challenge the reliability of findings from studies involving voluntary participation due to the risk of self-selection bias (i.e. there may be a systematic difference between the interlock group and the no-interlock controls) [14]. For instance, a study conducted by Assailly and Cestac [15] involving the French voluntary interlock programme showed that there were twice as many drivers aged 18 – 24years in the control group as in the interlock group. They speculated that the high cost of installing the interlock and the likelihood that younger drivers might not own a car were barriers to participation in voluntary programmes. In line with the review findings [see 16] the recidivism rate for the interlock group increased over time such that it was similar to that of the control group by the end of a five-year period.

Research investigated Washington State's AIIP after mandatory interlocks were introduced in 2004 for first-time DUI offenders with BACs below 0.15 (termed 'simple' DUIs) [17]. This showed that although the proportion of simple DUIs declined in 2004, the proportion of negligent driving convictions (with no interlock requirement) continued an upward trend. Interlock installation rates for 'simple' DUIs increased from 3-5% to 33%. The recidivism rate declined by an estimated 12% and the change in the law was associated with an 8.3% reduction in single-vehicle late-night crash risk.

4.1.1.b Interlocks for first-time offenders

The feasibility and practical utility of providing an interlock programme for first-time DUI offenders is contested [18]. A study of Washington State's mandatory interlock programme highlighted reductions in both DUI recidivism and crashes for first-time offenders [19]. However, the inclusion of such offenders can be contentious because they can contribute to low participation rates and many believe that attention should be

focussed on repeat offenders, who have a greater risk of crashing Robertson and Vanlaar [20].

4.1.2 Alchol Interlock Installation Programmes in Europe

Alcohol interlocks are also used widely in Europe. The European Transport Safety Council (ETSC) Sober Mobility Across Road Transport (SMART) project addressed issues related to alcohol and driving at EU and Member State levels and also summarised progress on reducing drink driving in Europe [21]. The ETSC Alcohol Interlock Barometer indicates that Interlock laws for DUI offenders and/or professional drivers have been introduced in nine of the
27 EU countries including Austria, Belgium, Denmark, Finland, France, Poland and Sweden [22]. Laws are also being considered in Germany, Spain, and Ireland.

A recent review on managing DUI offending by the UK Parliamentary Advisory Council on Transport Safety (PACTS) showed reductions of 60-75% when alcohol interlocks are fitted [23]. The review recommended introducing alcohol interlocks in the UK as part of the regime available to the courts for dealing with DUI offenders.

Finally, a study commissioned by the European Commission's Directorate-General for Mobility and Transport (DG MOVE) concluded that alcohol interlocks offer effective and cost-beneficial improvement to road safety in Europe, particularly for the offender and commercial vehicle populations [24]. Subsequently, EU vehicle safety standards published in 2018 included a proposal that all new vehicles sold in the EU will feature a standardised interface to enable retrofitting of alcohol interlock devices. This would make it simpler and cheaper to fit an interlock when a driver is required to do so by law or when interlock use is part of a rehabilitation programme [25].

4.1.3 Barriers to interlock implementation

The implementation of AIIPs can be challenging. For instance, one review highlighted that the most pronounced barrier is the EU Driving Licence Directive requirement that driver licences cannot be issued or renewed for drivers who are dependent on alcohol or are unable to refrain from drinking and driving. Programme administration is challenging due to the number and range of authorities, agencies, medical and allied professionals, and interlock service providers that need to be involved. Management and coordination across these entities are essential to programme success, so coordinated efforts are needed to strengthen relationships and partnerships to facilitate the smooth running of these schemes. Criminal justice practitioners need to take a leadership role in ensuring that alcohol interlocks are applied regularly for DUI offences. However, concerns exist regarding the cost, workload and levels of knowledge required to operate schemes at this level. Low levels of participation in voluntary programmes also cause concern and this is often because driving bans are time limited. Political and administrative issues may need to be resolved before mandatory interlocks can be introduced. The overall understanding of interlock programmes among frontline practitioners and the general public is often low, and more needs to be done to promote their use. Also, enforcement of interlock restrictions is hampered by cross-country variations in licence restriction codes [20].

Importantly, there is a growing consensus that unless interlock programmes are linked with close psycho-medical follow-up, the recidivism rate will catch up quickly with DUI drivers who did not have interlocks installed [16, 26].

4.2 Driver Rehabilitation (DR) for DUI offenders

4.2.1 Programme design

Three approaches to DR programme design for DUI offenders were identified: diagnostic/therapeutic, educational, and multi-component approaches sometimes including alcohol interlocks.

4.2.1.a Diagnostic/therapeutic approaches

Diagnostic/therapeutic approaches aim to instigate positive cognitive and behavioural change. This review also identified therapeutic components that are used in alcohol rehabilitation including Cognitive behavioural therapy (CBT)/Behavioural counselling; Brief interventions (BIs); and Motivational interviews (MIs).

4.2.1.b Cognitive Behavioural Therapy (CBT)

Some treatment approaches for DUI offenders include counselling and one very interesting study highlighted the value of Cognitive Behavioural Therapy (CBT) in helping offenders control their DUI tendencies [27]. CBT provides individuals with coping and problem-solving skills and uses cognitive restructuring to address how interactions between individuals' thoughts, feelings and actions influence well-being [28]. For example, research found that compared to those receiving 'usual care' (UC) participants receiving CBT had lower odds of driving after drinking at the four- and ten-month follow-ups (odds ratio [OR] = 0.37, p = 0.032, and OR = 0.29, p = 0.065, respectively). This suggests that learning CBT may help offenders reduce or refrain from DUI, at least in the short term [29].

4.2.1.c Screening, Brief Intervention and Referral to Treatment (SBIRT)

Several jurisdictions deliver brief interventions based on the WHO Screening, Brief Intervention and Referral to Treatment (SBIRT) model [30]. This intervention begins with universal screening of DUI offenders using the Alcohol Use Disorder Identification Test (AUDIT) [31]. AUDIT scores are categorised into risk zones that are used to determine the intensity of intervention delivered as part of the SBIRT procedure.

Table 1 AUDIT Test Zones and SBIRT Intervention Types [32]

Intensity Zone	AUDIT Score Range	SBIRT Intervention Type
1	0-7	Alcohol Education
2	8-15	Simple advice focused on reducing hazardous drinking
3	16-19	Brief intervention & continuous monitoring
4	20-40	Brief intervention & referral to a specialist for diagnostic evaluation and treatment

The interventions incorporate behavioural therapies such as the delivery of brief advice or motivational interviewing by a healthcare professional where the objectives include reduction in alcohol use [33].

Randomised trials support the efficacy of SBIRT in minimising alcohol use and alcohol-related consequences including DUI [34]. However, SBIRT also demands resources to deliver four different intensities of intervention in SBIRT: Alcohol education, simple advice, brief counselling and continued monitoring, and brief counselling and referral to a specialist (from least to most intense in terms of delivery time, the skill level of the provider, and personnel resources). However, research from Texas showed that the majority of DUI cases required low-intensity interventions e.g., AUDIT Zones 1&2 [32].

The Swedish DR Programme is called 'SMADIT' and it resembles the SBIRT approach by offering immediate help to suspected DUI drivers which is then provided collaboratively by the Swedish Transport Administration, police organisation and the dependency care and treatment services [35]. A qualitative study conducted by Gustafsson, Nyberg [36] found that this timely intervention enabled offenders to face up to their problems and seek help, and many described this as a turning point in their lives. A one-year follow up showed the focus for offenders had shifted from thinking about personal consequences of their behaviour and displayed greater insight into the harm that they could have done to others when they drove while drunk.

4.2.2 Education courses

The aim of DUI education is to inform offenders about the risks of alcohol use.

The 'Alcohol and Traffic' Course has been delivered in each region in Denmark since 2002. Attendance is mandatory for all DUI offenders who have their licence suspended or have a driving ban. The aim of the course is to develop better habits and a new culture to avoid further DUI behaviours. An evaluation showed that DUI relapses were reduced by 40% following the introduction of these courses [37].

The course for DUI offenders in the Swiss canton of Fribourg starts with an interview with a psychologist, after which drivers are informed about their drinking status and can receive counselling along with education. Three variations of this format were evaluated by Vaucher, Michiels [38]. The standard programme involves seven hours of lectures delivered in one day. A short version is delivered over four hours where the participant is accompanied by a 'proxy'. Alternatively, a two-hour lecture is delivered by a psychologist with educational experience. The teaching objectives remained the same for all three courses. Intriguingly, the findings from this study showed that the risk of DUI recidivism for those taking the seven-hour course was 47% higher compared to a no-intervention control group within two years of a first offence. Conversely, the recidivism rate fell by 28% among those who took the two-hour course compared to the controls. Also, compared with those who took the standard course, those who took the four-hour course with a proxy were 47% less likely to commit a DUI offence and those who took the two-hour course were 25% less likely to recidivate in the two years after an initial conviction. These effects diminished over time, most likely as a result of gaining maturity and changes in social norms around driving.

4.2.3 Multi-component programmes - Education and treatment

The evolution of multi-component programmes involving education and treatment is exemplified by the Driver Education and Evaluation Programme in Maine, USA. Initially this provided a standard care (SC) intervention involving a stand-alone prevention programme and where relevant substance use treatment. In 2001 the Prime for Life (PFL) motivational enhancement programme was implemented. This group-based motivational enhancement programme is delivered over 20 hours. A study comparing the three-year re-arrest rates among drivers who received the SC intervention with those who took the PFL course found that those who took the PFL course had lower rearrest rates (7.4% versus 9.9%, OR=.73, $p<.05$) [45].

4.2.4 DUI courts

Court-mandated programmes are used widely in the US following the introduction of DUI courts [39, 40].

For instance, the DUI court system in Georgia, USA use a multi-component approach for their DR programme [39]. This multi-collaborative intervention involves treatment providers, members of the court, probation officers and community self-help groups (e.g., Alcoholics Anonymous). This programme is divided into five phases and includes key components such as orientation, assessment, active treatment, relapse prevention and continuum of care. DUI offenders are expected to participate in treatment groups, undergo random screening for alcohol and drugs, attend DUI school and meetings with the supervising team (court personnel and probation officers). Programme impact was measured longitudinally by comparing the performance of three groups; DUI court offenders, a matched retrospective comparison group who offended before the DUI courts were established and a contemporary comparison group from counties that did not have DUI courts. The recidivism rate after four years for the DUI court group was 38.2% lower than that for the contemporary comparison group and 65% lower than the retrospective comparison group. These findings provide good support for the DUI court concept as a means of reducing recidivism.

Some limitations and difficulties associated with DUI Courts have been highlighted including costs, the multiplicity of programme requirements which induced scheduling conflicts and distrust of some service providers [40, 41].

4.2.5 Multi-component programmes treatment and alcohol interlock

Multi-component interventions involving alcohol interlocks and education and/or treatment are used widely in North America. A good example is a DR treatment programme that was combined in the existing AIIP programme in Florida. The treatment was required when the offender accumulated three violations (defined as two 'lockouts' within four hours; a lockout occurs when the device prevents a drinking driver from starting the vehicle). Analysis showed that compared to the interlock only group, those who received the additional treatment showed lower recidivism (-32%) after the interlock was removed during the 12 – 48-month period of the study. The researchers estimated that the decline in recidivism would have prevented 41 rearrests, 13 crashes and almost nine injuries in crashes involving 640 offenders during that time [42].

Although previous research supports the efficacy of alcohol ignition interlocks in preventing DUI incidences and in reducing alcohol-related crashes, less is known about the extent to which the beneficial effects persist after the devices are removed, especially in a European context. Nevertheless, a large-scale evaluation of the Dutch AIIP which combines interlock installation with an education programme showed that the recidivism rate was lower in the AIIP group (4%) than it was for the controls (8%) [43].

4.2.6 Voluntary versus mandatory participation

Participation in some DR programmes is a prerequisite for licence reinstatement while others involve incentives such as avoidance of licence revocation alongside maintenance of interlock driving permit and even reduction in the period for licence suspension. For instance, programme participation is required for licence reinstatement in Maine and Florida [42, 44]. Legislation in Florida requires DUI offenders to attend the DR programme while simultaneously participating in the interlock programme. Involvement in DR programmes is also court-mandated in Mississippi and California [29, 45]. A voluntary approach is used in, Maryland where proceedings against the offender are delayed provided they participate in a DR programme. [46].

Both mandatory and voluntary approaches are used across Europe. For instance, a mandatory DR programme is delivered synchronously with the Dutch Alcohol Ignition Interlock Programme (AIIP) [43], allowing offenders to retain driving privileges. Voluntary DR programme participation is a feature of the Swiss [38] and Swedish [36] systems. In Switzerland, programme participation provides a one-month reduction in the period of licence suspension. The SMADIT method used in Sweden relies on voluntary participation, indeed this approach assumes that "the sobriety checks carried out by the police create a crisis situation that increases the likelihood that suspected drink drivers will be receptive to offers of help" [36, p.559.].

DR programmes are established with varying methods of participation across countries and even between states. Mandatory participation is commonly associated with licence reinstatement while most voluntary programmes come with incentives to promote participation. These incentives often include a reduction in the duration of licence suspension. However, a range of factors that affect participation needs to be considered to maximise the uptake of these interventions.

1. Programme duration

It is widely acknowledged that when it comes to educational and therapeutic interventions, quality matters more than quantity. Nevertheless, programme duration remains an important consideration because of the associated costs (financial, time commitment etc.).

For instance, the Swiss study described previously showed that both or the short duration interventions were significantly more effective than the than the standard day-long series of lectures. Some explanations were proffered for these findings for instance, longer lectures may enhance non-acceptance and increase feelings of hopelessness and negative mood that limits attendees' ability to initiate changes Alternatively, longer lectures afforded opportunities to interact with other offenders and thus minimise the impact of preventative messages. Finally, shorter lectures may make it easier to focus on the content and to identify and retain important messages [38].

5 CONCLUSIONS AND RECOMMENDATIONS

This review identified some new approaches that have emerged since the publication of the DRUID study and highlighted a trend towards embedding techniques such as interlocks into structured and universally applied education and rehabilitation programmes for DUI offenders which are coordinated with judicial processes.

It identified that DUI offending is very frequently symptomatic of an underlying alcohol misuse/addiction problem that cannot be addressed by education or Alcohol Ignition Interlock Programmes (AIIPs) alone. This is evidenced by the increasing proliferation of DUI courts in the U.S. and the development of multi-component programmes that include educational and therapeutic elements, sometimes used in tandem with AIIPs. We propose that The WHO Screening, Brief Intervention and Referral to Treatment (SBIRT) model [30] signals the way forward in this area. The strength in multi-component interventions including diagnostic/therapeutic elements is that they can adapt to diverse characteristics and needs of DUI offenders who participate in these programmes.

A vast body of accumulating evidence from North American and European studies shows clearly that AIIPs reduce DUI recidivism, supporting safe mobility for both offenders and the wider community. The evidence also supports mandatory AIIP's to reduce recidivism among high-risk offenders, at least during the time when the devices are fitted. New EU vehicle safety standards mandating the fitment of a standardised interface to enable retrofitting of alcohol interlocks will make it easier and cheaper to fit these devices. However, more needs to be done to reduce costs and to change attitudes to make interlocks more acceptable

In sum, there is clear evidential support for a multi-component approach for DUI offenders combining diagnostic/therapeutic and educational components and linked to an AIIP. This requires cross-agency collaboration by the police, courts and the health service for screening and diagnosis of AUD and providing appropriate assessment and treatment of drivers with AUD.

6 RECOMMENDATIONS

Given that DUI convictions provide "a window of opportunity to encourage behavioural change" [36] we recommend that a framework for developing a joint medico-legal programme should be established based on input from key stakeholders to help DUI recidivists to recognise and manage their drinking behaviours as a means of improving road safety in Ireland.

This programme should be developed by stakeholders in the light of the structures and processes currently in place, the modalities of treatment, and likely development, adaptation of the framework and practices of the contributory services and is likely to require legislative change. This process may be aided by the parallel review of interlock programmes, including the outcome of the cost-benefit analysis, currently underway with the RSA.

7 REFERENCES

1. WHO, *Global status report on road safety 2018*. 2018, World Health Organisation: Geneva.
2. Hels, T., et al., *Driving under the Influence of Drugs, Alcohol and Medicines (DRUID): Risk of injury by driving with alcohol and other drugs*. 2011.
3. RSA. *Alcohol and driving*. 2021 [cited 2021 12/08/2021]; Available from: https://www.rsa.ie/en/RSA/Licensed-Drivers/Driving-in-Ireland/.
4. Citizens Information. *Drink driving offences*. 2021 [cited 2021 11/08/2021]; Available from: https://www.citizensinformation.ie/en/travel_and_recreation/motoring_1/driving_offences/drink_driving_offences_in_ireland.html.
5. RSA, *Road deaths and alcohol*. 2020, Road Safety Authority: Ballina.
6. Medical Bureau of Road Safety, *Annual Report 2019*. 2020, Medical Bureau of Road Safety Dublin.
7. Condron, I., A.M. Carew, and S. Lyons, *National Drug Treatment Resporting System 2013 - 2019 Alcohol Data*. 2020, Health Research Board: Dublin.
8. Carew, A.M., et al., *Estimating need for alcohol treatment in Ireland using national treatment surveillance data.* Ir J Med Sci, 2021.
9. Vanlaar, W.G.M., M. Mainegra Hing, and R.D. Robertson, *An evaluation of Nova Scotia's alcohol ignition interlock program.* Accid Anal Prev, 2017. **100**: p. 44-52.
10. McGinty, E.E., et al., *Ignition Interlock Laws: Effects on Fatal Motor Vehicle Crashes, 1982-2013.* Am J Prev Med, 2017. **52**(4): p. 417-423.
11. Boets, S., et al., *State of the Art on Driver Rehabilitation: Literature Analysis & Provider Survey*. 2008.
12. Canadian Council of Motor Transport Administrators, *Canadian Guidelines for Interlock Programs*. 2018, Canadian Council of Motor Transport Administrators: Ontario.
13. Elder, R.W., et al., *Effectiveness of Ignition Interlocks for Preventing Alcohol-Impaired Driving and Alcohol-Related Crashes: A Community Guide Systematic Review.* American Journal of Preventive Medicine, 2011. **40**(3): p. 362-376.
14. Marques, P., et al., *Evaluation of the New Mexico Ignition Interlock Programme*. 2010, National Highway Safety Administration, U.S. Department of Transportation.
15. Assailly, J.P. and J. Cestac, *Alcohol interlocks and prevention of drunk-driving recidivism.* European Review of Applied Psychology, 2014. **64**(3): p. 141-149.
16. Elder, R.W. *Overview of effectiveness of ignition interlocks: Reflections from the perspective of theories of punishment*. in *Countermeasures to address impaired driving offenders: Towards an integrated model*. 2011. Beckman Conference Centre, Irvine, CA.
17. McCartt, A.T., et al., *Washington State's alcohol ignition interlock law: effects on recidivism among first-time DUI offenders.* Traffic Inj Prev, 2013. **14**(3): p. 215-29.
18. Bailey, T.J., V.L. Lindsay, and J. Royals, *Best practice in alcohol ignition interlock schemes*, in *A Safe System: Road Safety Discussion*. 2013, Australaisian College of Road Safety Conference: Adelaide.
19. McCartt, A.T., W.A. Leaf, and C.M. Farmer, *Effects of Washington State's alcohol ignition interlock laws on DUI recidivism: An update.* Traffic Inj Prev, 2018. **19**(7): p. 665-674.
20. Robertson, R.D. and W. Vanlaar. *Alcohol Interlocks: Opportunities to Improve Traffic Management, Proceedings of the 13th International Alcohol Interlock Symposium*. 2012. Helsinki: Traffic Injury Research Foundation
21. ETSC, *Progress in reducing drink driving and other alcohol-related road deaths in Europe*. 2019, ETSC: Brussels.
22. ETSC. *Alcohol Interlock Barometer*. [cited 2012 22 September]; Available from: https://etsc.eu/issues/drink-driving/alcohol-interlock-barometer/.
23. Norbury, F. and E. Webster, *Locking Out the Drink Driver: Using alcohol interlocks to reduce drink driving in the UK*. 2021, PACTS: London.
24. ECORYS, *Study on the prevention of drink-driving by the use of alcohol interlock devices*. 2014, European Commission, DG for Mobility and Transport: Rotterdam.
25. EU Commission, *Road safety - easy installation of alcohol interlocks in vehicles*, E. Commission, Editor. 2021.
26. Robertson, R.D., E. Holmes, and W. Vanlaar, *Alcohol interlocks in Canada. From resarch to practice*. 2009, Traffic Injury Research Foundation
27. Osilla, K.C., et al., *A pilot study comparing in-person and web-based motivational interviewing among adults with a first-time DUI offense.* Addict Sci Clin Pract, 2015. **10**: p. 18.
28. Dobson, D. and K.S. Dobson, *Evidence-based Practice of Cognitive-Behavioural Therapy*. 2nd ed. 2017, London: The Guilford Press.
29. Osilla, K.C., et al., *Randomized Clinical Trial Examining Cognitive Behavioral Therapy for Individuals With a First-Time DUI Offense.* Alcohol Clin Exp Res, 2019. **43**(10): p. 2222-2231.
30. Office of National Drug Control Policy, *Screening, brief intervention, and referral to treatment (SBIRT)*. 2012, Office of National Drug Control Policy (ONDCP), Substance Abuse and Mental Health Services Administration (SAMHSA): Washington.
31. World Health Organization, *AUDIT: the Alcohol Use Disorders Identification Test : guidelines for use in primary health care / Thomas F. Babor ... [et al.]*. 2001, World Health Organization: Geneva.
32. Mathias, C.W., et al., *Estimating resource utilization demands in implementing statewide screening, brief intervention, and referral to treatment for alcohol-impaired drivers.* Traffic Injury Prevention, 2019. **20**(1): p. 15-22.
33. Barata, I.A., et al., *Effectiveness of SBIRT for Alcohol Use Disorders in the Emergency Department: A Systematic Review.* West J Emerg Med, 2017. **18**(6): p. 1143-1152.
34. Babor, T.F., F. Del Boca, and J.W. Bray, *Screening, Brief Intervention and Referral to Treatment: implications of SAMHSA's SBIRT initiative for substance abuse policy and practice.* Addiction, 2017. **112**(S2): p. 110-117.
35. Forsberg, I. *Rehabilitation of drunk drivers and the SMADIT project: collaboration between the police force, the road administration and the social services.* in *International Conference on Alcohol, Drugs and Traffic Safety*. 2011. Brisbane.
36. Gustafsson, S., J. Nyberg, and R. Hrelja, *The Swedish joint action method against drink driving-a study of suspected drink drivers' own experiences.* Traffic Inj Prev, 2016. **17**(6): p. 558-63.
37. Rasmussen, I.L., *Background of the alcohol and traffic courses in Denmark.* SCHRIFTENREIHE FAHREIGNUNG, 2012: p. pp 80-1.
38. Vaucher, P., et al., *Benefits of short educational programmes in preventing drink-driving recidivism: A ten-year follow-up randomised controlled trial*. Int J Drug Policy, 2016. **32**: p. 70-6.
39. Fell, J.C., A.S. Tippetts, and J.D. Ciccel, *An Evaluation of Three Driving-Under-the-Influence Courts in Georgia*. 2011, Association for the Advancement of Automotive Medicine (AAAM). p. pp 301-312.
40. Fell, J.C., *Approaches for reducing alcohol-impaired driving: Evidence-based legislation, law enforcement strategies, sanctions, and alcohol-control policies.* Forensic Sci Rev, 2019. **31**(2): p. 161-184.
41. Narag, R.E., S.R. Maxwell, and B. Lee, *A Phenomenological Approach to Assessing a DUI/DWI Program.* International Journal of Offender Therapy and Comparative Criminology, 2013. **57**(2): p. 229-250.
42. Voas, R.B., et al., *Mandating Treatment Based on Interlock Performance: Evidence for Effectiveness.* Alcohol Clin Exp Res, 2016. **40**(9): p. 1953-60.
43. Blom, M. and D. Blokdijk, *Long-term effectiveness of the alcohol ignition interlock programme: A retrospective cohort study in the Netherlands.* Accid Anal Prev, 2021. **151**: p. 105888.
44. Beadnell, B., et al., *Operating under the influence: Three year recidivism rates for motivation-enhancing versus standard care programs.* Accid Anal Prev, 2015. **80**: p. 48-56.
45. Robertson, A.A., et al., *The impact of remedial intervention on 3-year recidivism among first-time DUI offenders in Mississippi*. Accident Analysis & Prevention, 2009. **41**(5): p. pp 1080-1086.
46. Ahlin, E.M., et al., *First-time DWI offenders are at risk of recidivating regardless of sanctions imposed.* Journal of Criminal Justice, 2011. **39**(2): p. 137-142.

Evaluating the Impact of Connected and Autonomous Vehicles on Long Span Bridge Loading

Cian Collins[1], Michael Quilligan[2]
[1]Garland, Riverfront. Howley's Quay, Limerick, Ireland
[2]School of Engineering, University of Limerick, Limerick, Ireland
email: cian.collins@garlandconsultancy.com, michael.quilligan@ul.ie

ABSTRACT: Road transport is rapidly evolving and recent technological advancements have brought the era of Connected and Autonomous Vehicles (CAVs) closer to reality. The introduction of CAVs will likely bring significant changes to the driving environment. For long span bridges, the critical traffic loading conditions are when vehicles are closely spaced together during congestion events. CAV technology has the potential to significantly impact such congestion events with changes to inter-vehicle gap distances and lane changing decisions. For this study, the microscopic traffic simulation tool PTV Vissim is used to investigate the potential impact of CAVs on long span bridge structures. A baseline PTV Vissim model is developed and the traffic output is compared to data derived from image data collected using an Unmanned Aerial Vehicle (UAV) at a location of recurring congestion on the N7/M7 national primary route in Ireland. The micosumulation model is extended to introduce CAVs into the traffic flow at various penetration rates. The total load effect on a long span structure with a loaded length of 1000 m during periods of recurring congestion is investigated. The change in driving strategy of the CAVs impacts the propagation and dissolving of the congestion shockwaves. Insights into long span load effect patterns and correlations to spatial densities during recurring congestion are presented for CAV penetration rates of 25, 50 and 100%. For larger penetration rates it is shown that the load effect experienced under recurring congestion is significantly reduced.

KEY WORDS: Congestion; Connected Autonomous Vehicles; CAV; Bridge Loading; Long-span; Unmanned Aerial Vehicle; UAV.

1 INTRODUCTION

Traffic congestion on long span bridges results in a reduction in the gaps between vehicles and the cumulative effect of these closely spaced vehicles causes critical load events [1-3]. This is different to short and medium span bridges where individual heavy vehicles, typically in free flow conditions, produce the maximum load effect. Weigh-in-Motion technology is used in existing load models to account for the variability in weight of Heavy Goods Vehicles (HGVs), however details on the car/HGV mix and distance between vehicles during congested traffic is limited [4-6]. This is due to the fact that traditional loop detectors do not provide accurate traffic data during stop-and-go conditions [7]. As a result of these uncertainties, existing bridges can be subject to unnecessary and expensive interventions when assessed using current load models.

Some recent studies on long span bridge loading have used traffic microsimulation to better represent traffic congestion patterns. Many approaches combine car following and lane changing models [6, 8-11]. The work of O' Brien et al. [12] shows that critical loading on long span structures can result from any one of several types of congestion that may occur on the bridge, i.e. the widely-used full stop condition, which is only one realisation of vehicles on the bridge, is not always critical and the simulation of multiple slow moving congestion events can give rise to more onerous bridge loading events.

An Autonomous Vehicle (AV) can be broadly defined as any vehicle that moves people or freight without the intervention of a human operator. The potential benefits of this technology relate to increased driver productivity, road safety and energy savings [13]. A Connected Autonomous Vehicle (CAV) is similar, but also allows for the continuous communication with other CAVs on the network as well as infrastructure.

State of the art HGV CAV systems will actively seek to take advantage of reduced air resistance at highway speeds caused by platooning [14]. This may result in lighter traffic changing lane and an increased density of HGVs on the road leading to even longer HGV platoons forming. Using microsimulations to represent this behaviour, it has been found that CAVs have the possibility of increasing the load on a long span bridge by 25% [15].

Although CAVs have the potential to increase road capacity, other studies indicate they could also have the potential to reduce the loading on bridges by implementing a behavioural change. This reduction could be achieved by the controlled movement of cars and HGVs from one lane to another. If lane change restrictions are put in place prior to the bridge infrastructure, the likelihood of natural platoons can be reduced [16]. Applications can be considered where certain zones have restrictions on lane changing programmed automatically into CAVs. It has been found that implementing such a restriction has the potential to reduce loading on bridge infrastructure by 20-30% [16].

This paper investigates the use of traffic microsimulation to develop insights into the potential impact of CAVs on the loading of long span bridge structures. The study focuses on recurring congestion, i.e. congestion caused when the capacity of a local road network is exceeded during peak travel periods. The percentage of HGVs in the traffic flow during these periods is low as professional drives plan their routes to avoid regular congestion.

Figure 1. View of lane drop at Naas, Ireland from UAV [17].

A microsimulation model is developed in PTV Vissim and the traffic output is compared to data derived from image data collected using an Unmanned Aerial Vehicle (UAV) at a location of recurring congestion on the N7/M7 national primary route in Ireland. Output from four different microsimulation vehicle parameter sets are compared and a set chosen that best simulates traffic densities and load effects compared to the measured data. The microsimulation model is extended to introduce CAVs into the traffic flow at penetration rates of 25, 50 and 100%. The total load effect on a long span structure with a loaded length of 1000 m during periods of recurring congestion is then investigated.

2 MEASURED TRAFFIC DATA

Quilligan and O' Brien [17] outline a study where recurring traffic congestion at a site on the N7/M7 motorway outside Naas in Co Kildare, Ireland was monitored. The N7/M7 experiences an Annual Average Daily Traffic (AADT) flow of approximately 105,000 vehicles. This high traffic flow, which peaks in the southbound during evening rush hour when commuters exit Dublin, causes significant recurring congestion at Naas as the number of traffic lanes drop from 3 to 2 (Figure 1).

As traditional data collection devices such as loop detectors are ineffective when traffic breaks down [7], an Unmanned Aerial Vehicle (UAV) was used to collect image data of the congested traffic. The UAV was set to hover at a height of 120 m above ground, 30 m back from the edge of the carriageway. At this height approximately 165 m of carriageway could be seen and recorded by the UAV with the camera pointed directly downwards. The ground sampling distance was estimated to be approximately 4.3 cm. For each UAV flight, 20 minutes of traffic footage was typically recorded, with a 5-minute turnaround required to change batteries.

The image data was post processed using a cloud based platform DataFromSky (DFS) [18]. DFS outputs significant information about each vehicle observed, including vehicle position, velocity and acceleration for each timestep. After recent updates the vehicle length is also output. Using data from this study, a plot of spatial density, the percentage of the 165 m length of observed carriageway that is covered by vehicles, versus time for three flights recorded on the 18th October 2018 is illustrated in Figure 3a.

3 SIMULATED TRAFFIC DATA

3.1 Microsimulation

Microsimulation is an analytical process used by traffic engineers which allows for a detailed analysis of a data set by looking at the interaction between individual units. This is advantageous for bridge design engineers looking to estimate the demands of the road infrastructure. PTV Vissim [19] is a stochastic and discrete simulation software based on time steps. This microsimulation package allows for a detailed analysis of a data set by looking at the interaction between individual units. These micro results can be aggregated together to give a macro result of an overall network. The car following models implemented are pyscho-physical models, where equations are used to replicate the human perception and reaction thresholds [20].

3.2 Microsimulation Model of N7/M7 Network

Using an inbuilt feature within PTV Vissim, aerial photography was used as a template to construct a model of the southbound N7/M7 road network in the vicinity of Naas. This is comprised of approximately 7.3 km of three lane carriageway before Naas (N7) and approximately 5 km two lane carriageway after Naas (M7) (Figure 2a). At Naas a diverging exit lane defines the lane drop (Figure 2b).

Three individual lanes were created at the start of the network to allow for a high level of control over the input flow and composition of vehicle types into each lane (Figure 2c). The lanes were then merged to form the N7 carriageway proper.

a) b) c)

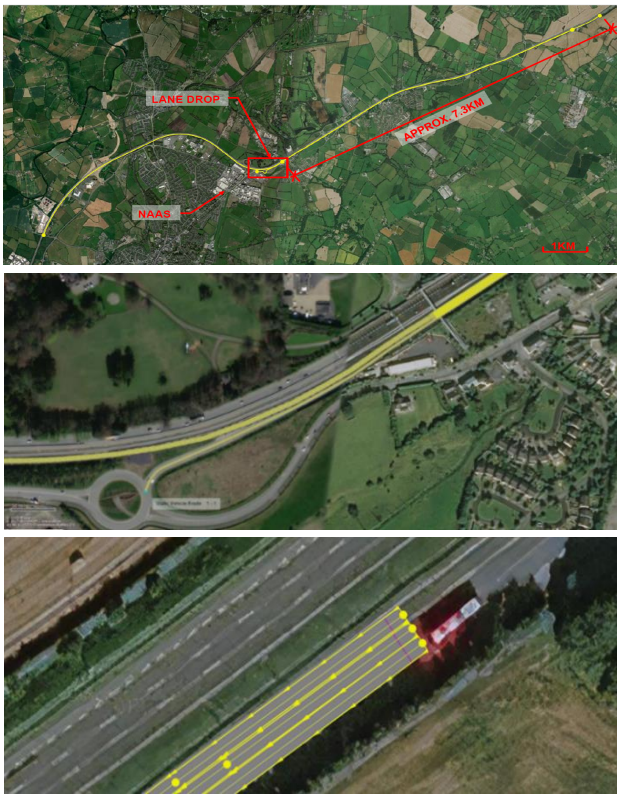

Figure 2. PTV Vissim model view illustrating a) Aerial view of network; b) Diverging exit lane at Naas; c) Individual input lanes at the start of the model.

Table 1. Input traffic flow data for N7/M7 simulation model taken from TII monitoring site (18th October 2018).

Time	Lane 1 (Inside) Equiv. Flow (veh/hr)	Lane 2 Equiv. Flow (veh/hr)	Lane 3 (Overtaking) Equiv. Flow (veh/hr)
16.45	1003	1160	1230
17.00	1041	1597	1989
17.15	1283	1624	1970
17.30	1455	1594	1839
17.45	1455	1436	1713
18.00	1540	1467	1659
18.15	1567	1482	1548
18.30	1459	1386	1444
18.45	1421	1317	1421

The lanes start location was chosen to coincide with a Traffic Infrastructure Ireland (TII) traffic counter site for which traffic flow and classification data is available. Traffic flow data at a fifteen minute interval resolution was used as input into the simulation model (Table 1). For the purpose of this study just two vehicle classifications were used – cars and HGVs. Based on the TII data, the percentages of HGVs in Lanes 1, 2 and 3 (overtaking lane) were 11.0, 7.5 and 2.5 % respectively at the time of the study.

The PTV Vissim 'vehicle attribute decision' feature was used to define the percentage of vehicles leaving the network at the diverging exit lane at Naas. This was estimated to be approximately 20% based on a review of the UAV image data and the TII traffic counter data.

3.3 Vehicle Parameters

Traffic congestion is a complex and varying phenomenon replicated in microsimulation packages using a combination of car following and lane changing models. The stochastic nature of traffic is accounted for in PTV Vissim by implementing two Wiedemann car following models, termed the Wiedemann 74 and Wiedemann 99. The Wiedemann 99 is considered to be the most suitable model for replicating freeway traffic congestion as oscillations in perceived speeds and distances of an operated vehicle are accounted for [21].

Calibration or adjustment of the vehicle input parameters is recommended to suit local site conditions to ensure that the simulated response is representative of measured field conditions [22]. Suggested values and/or ranges for these parameters are described in detail in a number of sources including guides from the State of Wisconsin's Department of Transportation [23] and the German Highway Capacity Manual (HCM) [24].

While a detailed calibration was not undertaken in this study, the lane changing and car following models of the N7/M7 model were varied for four different parameter sets to investigate the effects on the simulated traffic outputs: PTV Vissim default values, Wisconsin DoT maximum suggested values, Wisconsin DoT minimum suggested values and German HCM values.

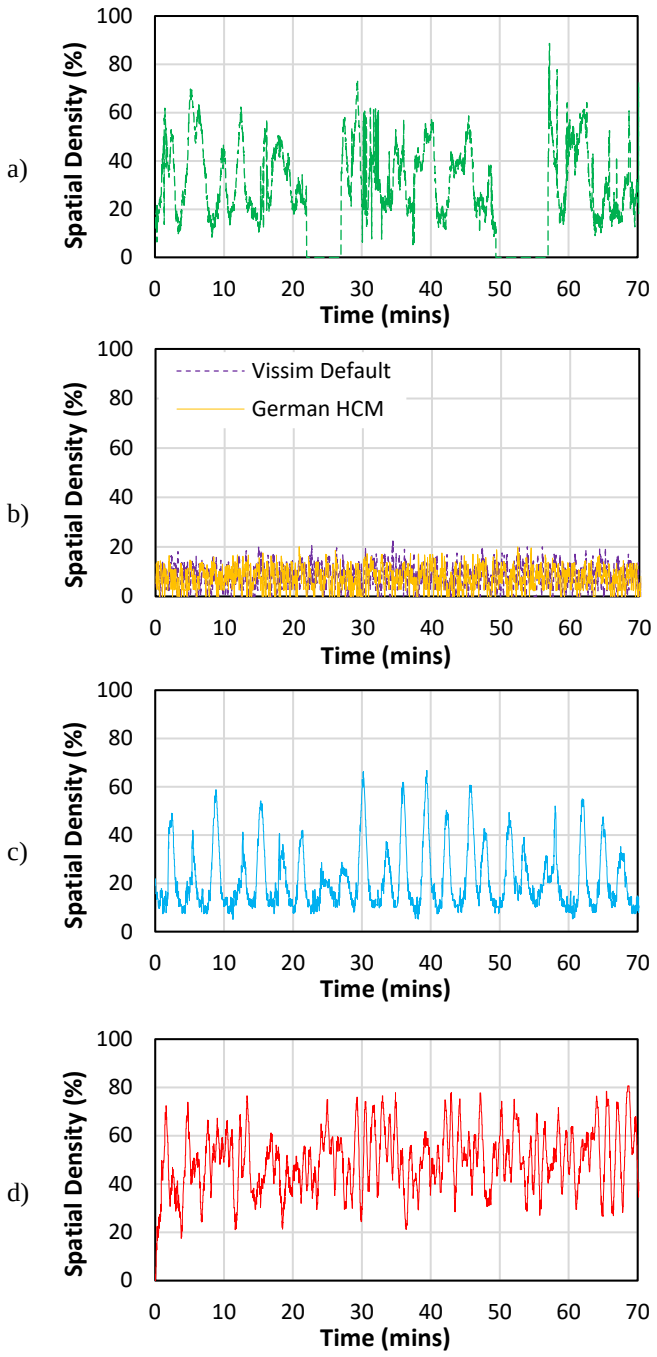

Figure 3. Spatial density vs time plots for a) measured; b) PTV Vissim default & German HCM; c) Wisconsin DoT max; d) Wisconsin DOT min parameter sets.

Figure 3b-d) illustrates the spatial density time plots for Lane 2 at the location of the UAV monitoring site approximately 750m upstream of the lane drop at Naas. This lane is of intertest from a bridge loading perspective as it becomes the inside lane of the M7 and has the highest percentage of HGVs at this location.

It can be seen that the PTV Vissim default and German HCM (Figure 3b) parameter sets simulate no congestion. The Wisconsin DoT maximum values simulate Stop-and-Go Waves (SGW), i.e. a series of localised traffic jams events lasting for approximately one minute with free flowing traffic in between. These waves propagate upstream and are generally observed to

have a high amplitude but no typical wavelength [25]. The Wisconsin DoT minimum values on the other hand simulate Oscillating Congested Traffic (OCT) with waves that are less pronounced and closely spaced with a much higher mean density, in this case, of approximately 51%.

The measured data in Figure 3a shows aspects of both SGW and OCT congestion.

3.4 Bridge Load Effect

In order to investigate the impact of the traffic congestion caused by the different Wisconsin DoT parameter a road section of 1000 m, starting at location of the diverging exit lane, was monitored to represent a notional long span bridge structure. A total load influence line was adopted which is representative of long span loading effects. Constant vehicle Gross Vehicle Weights (GVW) of 300 and 50 kN were applied to all HGVs and cars respectively for the measured and simulated runs using the flow data from Table 1. The simulated parameter sets were run for a duration of approximately one and a half hours to coincide with the duration of the UAV study [17].

Table 2 presents the maximum values of total load recorded during each of the measured and Wisconsin DoT simulated runs. The results of the Wisconsin DoT minimum parameter set provide the best match to the measured load effects, particularly for Flight Numbers 1 and 2.

Table 2. Comparison of maximum total load values for measured and simulated runs.

	Measured	Wisconsin DoT Min		Wisconsin DoT Max	
UAV Flight No.	Total Load (kN)	Total Load (kN)	% Diff from Measured	Total Load (kN)	% Diff from Measured
Flight 1	5544	5100	-8.7%	2660	-70.3%
Flight 2	5086	5640	+9.8%	3980	-24.3%
Flight 3	6405	6420	+0.23%	6500	+1.47%

3.4.1 Parameter Set Selection

From the above comparisons of the N7/M7 model created in PTV Vissim, it can be seen that the Wisconsin DoT minimum parameter set provides representative traffic densities and load effects compared to the measured data. SGW, with some OCT, were the congestion type most commonly observed at the N7 site. While a more detailed calibration of the parameters is required for more detailed study, the Wisconsin DoT minimum parameter set is therefore used herein to replicate the manually operated vehicles while assessing the influence of varying penetration rates of CAVs into the network.

4 CONNECTED AND AUTONOMOUS VEHICLES

The implementation of CAVs into a microsimulation model like PTV Vissim can be achieved through three different methods. The first is an external method whereby external scripting is used to replace the internal driving models [21]. The second is a combination method of internal parameter changes and external coding [20]. The third method, which was chosen for this study is an internal method only whereby the default car following and lane changing models are modified to replicate CAV behaviours and has been shown to be sufficient in delivering feasible results when the network is inspected at a macroscopic level [26].

Modification of the internal Wiedemann 99 and 74 car following and lane changes parameters along with many other functions of speed, time and distributions to replicate the behaviour of CAVs in PTV Vissim is possible. Zeidler et al. [26] collected data from real world autonomous tests and replicated them in PTV Vissim. The study comprised of having two CAVs following a single manually operated vehicle on public roads. Both autonomous behaviours and connected autonomous behaviours were investigated.

A separate study by Atkins [27] for the Department of Transport in the UK provides different parameter sets based on plausible future predictions of the behaviours of CAVs. This study also provides guidance on parameter changes which affect merging behaviours, time gaps and headways. Parameters are provided for each level of autonomous technology based on the Society of Automotive Engineers levels outlined by the National Highway Transportation Safety administration from Level 0 to 5 [28]. Level 3 has also been provided with varying aggression levels, cautious, normal cautious, normal aggressive and aggressive.

Table 3 outlines a comparison of the parameter values, CC0-CC9, for the Wiedemann 99 car following model and lane changing behaviours for these different studies. Note that LC4 refers to minimum clearance or headway (front/rear), LC5 is a safety distance reduction factor, MG1 is a user-defined minimum time-gap and MG2 is a user-defined minimum clearance or headway.

Table 3. Vehicle parameter values for manually operated and CAVs (NC implies no change from PTV Vissim default values).

W99 Parameter	Unit	Vissim Default	Wisconsin DoT Min	Zeidler et al (2019)	Atkins (2016)					
					Level 2	Level 3				Level 4
						Cautious	*Normal Cautious*	*Normal Assertive*	*Assertive*	
CC0	m	1.50	1.22	4.00	1.5	2.5	2.0	1.0	0.5	0.5
CC1	S	0.9	0.9	0.3,0.6,1.0	0.9	1.8	1.2	0.8	0.6	0.6
CC2	m	4.0	3.0	0.0	NC	NC	NC	NC	NC	NC
CC3	s	-8.0	-8.0	-40.0	NC	NC	NC	NC	NC	NC
CC4	m/s	-0.35	-0.35	0.00	NC	NC	NC	NC	NC	NC
CC5	m/s	0.35	0.35	0.00	NC	NC	NC	NC	NC	NC
CC6	1/ms	11.44	11.44	0.00	NC	NC	NC	NC	NC	NC
CC7	m/s^2	0.25	0.25	0.25	0.25	0.10	0.20	0.30	0.40	0.40
CC8	m/s^2	3.50	3.50	3.50	3.50	1.20	1.40	1.60	1.80	1.80
CC9	m/s^2	1.50	1.50	1.50	1.50	1.20	1.40	1.60	1.80	1.80
LC4	m	NC	NC	NC	0.5	0.8	0.6	0.4	0.2	0.2
LC5	%	NC	NC	NC	60	90	70	50	30	30
MG1	(s)	NC	NC	NC	3.0	3.6	3.2	2.8	2.4	2.4
MG2	(m)	NC	NC	NC	5.0	6.5	5.5	4.5	3.5	3.5

For this study the parameter set chosen to replicate CAVs is Level 4 Atkins [27] as Zeidler et al. [26] noted that for SGW the delay times in acceleration are not reproduced and could potentially lead to an overestimation in capacity, therefore not selected for use in this investigation.

a)

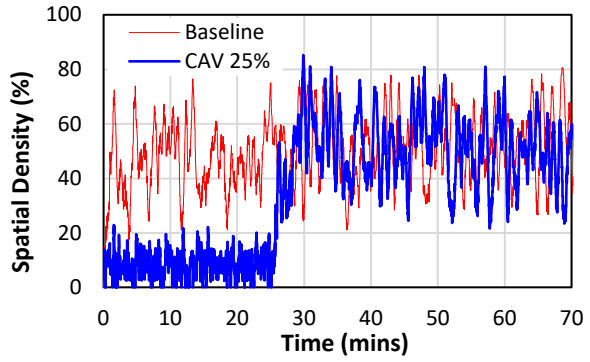

b)

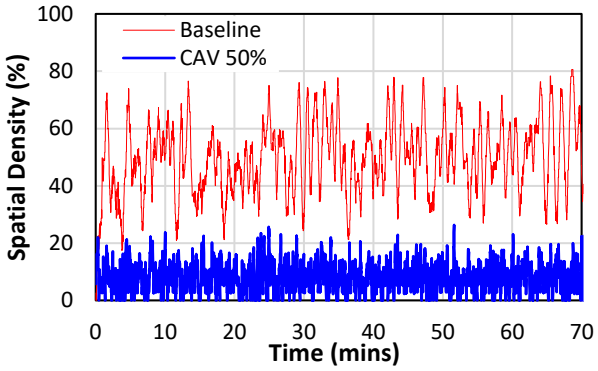

c)

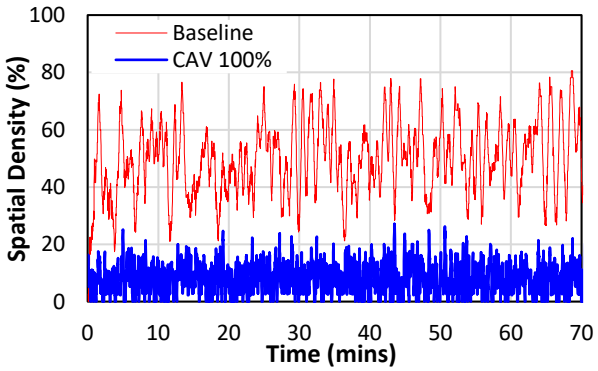

Figure 4. Lane 2 spatial density vs time plots for CAV penetration rates of a) 25%, b) 50% and c) 100%.

4.1 Implementing CAVs in PTV Vissim

Varying levels of CAV penetration rates are implemented into the N7/M7 model. The penetration rates selected for analysis were 25, 50 and 100% which aim cover a wide range of market penetration rates from the present day until 2055 where it is predicted that 90% of all vehicles being sold will be fully autonomous [29]. The current baseline of manually operated vehicles is based on the Wisconsin DoT minimum parameter set as described in Section 3.4 above.

CAVs are entered into PTV Vissim by creating new attributes in the following manner:

1. Create new CAV vehicle class;
2. Create new driving behaviour and change car following and lane changing parameters to Level 4 Atkins;
3. Specify driving behaviour by vehicle class attribute and apply CAV vehicle class and driving behaviour to the freeway link type;
4. Create new CAV Vehicle type by duplication of the desired vehicle type being modified, i.e. HGV;
5. Modify vehicle compositions and relative flows input into the system to implement the penetration rates.

5 RESULTS

Figure 4a-c illustrate the spatial density versus time plots for CAV penetration rates of 25, 50 and 100% compared to the current baseline. The time axis has been modified on these plots for the purposes of presentation, with 0 referring to a time of day of 17.27. For a CAV penetration rate of 25% (Figure 4a) there is a delay in the onset of congestion by approximately 25 minutes, after which time SGW develop in the traffic. For CAV penetration rates of 50 and 100%, no traffic congestion develops.

Figure 5a-c) illustrate the total load versus time plots for CAV penetration rates of 25, 50 and 100% compared to the current baseline. It is evident from the comparison of road densities in Figure 4 and total loads in Figure 5, that a pattern of high spatial densities correlates to a pattern of high levels of

a)

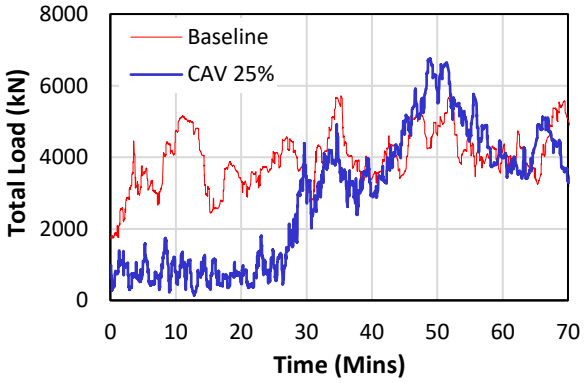

b)

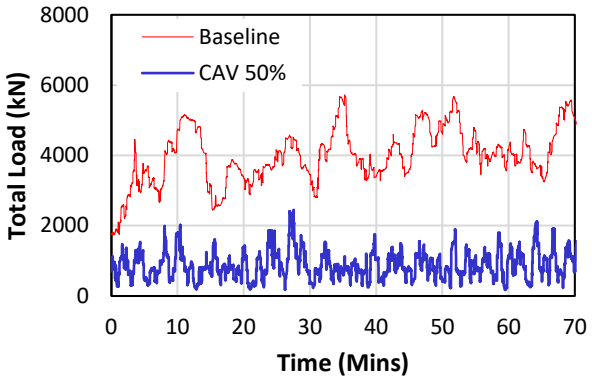

c)

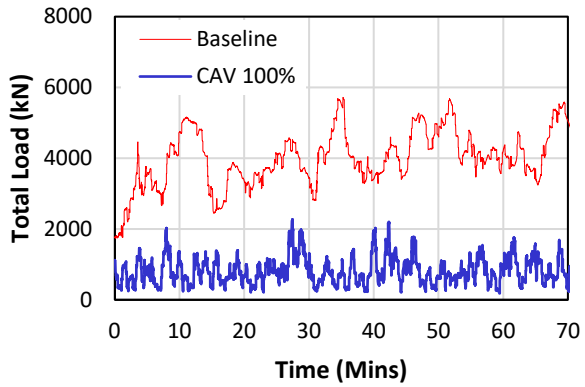

Figure 5. Lane 2 total load vs time for CAV penetration rates of a) 25%, b) 50% and c) 100%.

total loading. For a CAV penetration rate of 25% (Figure 5a) the delay in onset of congestion is mirrored in the total load effect which only begins to rise after approximately 25 minutes.

As peak total loads are dependent on the composition of the traffic, more specifically the presence of HGVs within the traffic flow, the exact timing of a peak load occurrence does not necessarily correlate with time of a peak density. For the example illustrated here the maximum load with 25% CAV penetration is approximately 5% higher than the baseline.

For CAV penetration rates of 50 and 100% the load effect experienced by the notional bridge structure is significantly decreased. This is as a result of CAVs ability to return the network to free flow conditions. This increase in capacity allowed the N7/M7 model to remain in free flow state as shown in Figure 4 and thereby significantly reduce bridge loading events. Maximum total loads for 50 and 100% penetration rates drop to 38 and 35% of their baseline values respectively.

6 CONCLUSIONS

This paper investigates the use of traffic microsimulation to develop insights into the potential impact of CAVs on long span bridge structures.

The default PTV Vissim lane changing and car following parameters were not sufficient in replicating the congested conditions observed on the N7/M7 in Ireland. Measured traffic congestion patterns and the maximum total loads on a notional 1000 m long bridge were better represented by a minimum parameter set from the Wisconsin DoT dataset.

CAV penetrations rates of 25, 50 and 100% were simulated into this baseline traffic. At a CAV penetration of 25% there is a delay in the onset of congestion by approximately 25 minutes, after which time SGW develop in the traffic. For CAV penetration of 50 and 100%, recurring congestion does not occur in the simulated model and there is a corresponding reduction in the severity of long span loading effects to approximately 35-38% of baseline values.

This study provides an insight into the possible ability of CAVs to reduce load effects on long span bridges due to the subsequent reduction recurring congestion. Further work is recommended to fully calibrate the baseline model and extend the number and range of CAV simulations, including situations where HGV platooning may be prevalent.

REFERENCES

[1] Ivy, R., Lin, T., Mitchell, S., Raab, N., Richey, V., and Scheffey, C., *Live loading for long-span highway bridges.* American Society of Civil Engineers Transactions, 1954.

[2] Buckland, P.G., McBryde, J.P., Zidek, J.V., and Navin, F.P.D., *Proposed Vehicle Loading of Long-Span Bridges.* Journal of the Structural Division, 1980. 106(4): p. 915-932.

[3] Flint & Neill Partnership, *Interim design standard: long span bridge loading*. 1986: Crowthorne.

[4] Bruls, A., Calgaro, J.A., Mathieu, H., and Prat, M., ENV1991 – Part 3: *The main models of traffic loads on bridges; background studies*, in IABSE Colloquim. 1996: Delft, The Netherlands. p. 215-228.

[5] Hwang, E.-S. and Kim, D.-Y., *Live Load Model for Long Span Steel Cable Bridges Considering Traffic Congestion Scenarios*. International Journal of Steel Structures, 2019. 19(6): p. 1996-2009.

[6] Caprani, C.C., OBrien, E.J., and Lipari, A., *Long-span bridge traffic loading based on multi-lane traffic micro-simulation*. Engineering Structures, 2016. 115: p. 207-219.

[7] Klein, L., Mills, M., and Gibson, D., *Traffic detector handbook*, 2006, Federal Higway Administration: MacLean, Virginia.

[8] Enright, B., Carey, C., and Caprani, C.C., *Microsimulation evaluation of Eurocode load model for American long-span bridges*. Journal of Bridge Engineering, 2013. 18(12): p. 1252-1260.

[9] Lipari, A., Caprani, C.C., and OBrien, E.J., *A methodology for calculating congested traffic characteristic loading on long-span bridges using site-specific data*. Computers & Structures, 2017. 190: p. 1-12.

[10] Carey, C., Caprani, C.C., and Enright, B., *A pseudo-microsimulation approach for modelling congested traffic loading on long-span bridges*. Structure and Infrastructure Engineering Maintenance, Management, Life-Cycle Design and Performance, 2018. 14(2): p. 163-176.

[11] Zhou, J., Ruan, X., Shi, X., and Caprani, C.C., *An efficient approach for traffic load modelling of long span bridges*. Structure and Infrastructure Engineering, 2019: p. 1-13.

[12] OBrien, E.J., Lipari, A., and Caprani, C.C., *Micro-simulation of single-lane traffic to identify critical loading conditions for long-span bridges*. Engineering Structures, 2015. 94: p. 137-148.

[13] Greenblatt, J.B. and Shaheen, S. *Automated vehicles, on-demand mobility, and environmental impacts*. Current sustainable/renewable energy reports, 2015, 2(3): p.74-81.

[14] Nowakowski, C., Shladover, S.E., Lu, X.Y., Thompson, D. and Kailas, A., *Cooperative adaptive cruise control (CACC) for truck platooning: Operational concept alternatives*. PATH Research Report. 2015.

[15] Enright, B., Carey, C., Caprani, C., C. and OBrien, E., J., *The Effect of Lane Changing on Long-Span Highway Bridge Traffic Loading*. In Bridge Maintenance, Safety, Management, Resilience & Sustainability, Sixth International IABMAS Conference, Stresa, Lake Maggiore, Italy, 8 – 12 July 2012. CRC Press.

[16] Caprani, C., Carey, C. and Enright, B., *Lane changing control to reduce traffic load effect on long-span bridges*', in: International Conference on Bridge Maintenance, Safety and Management, Stresa, Italy. 2012. Taylor and Francis.

[17] Quilligan, M. and O'Brien, E.J., *Loading on Long Span Bridges in Heavily Trafficked Areas*, in Civil Engineering Research in Ireland 2020, Cork Institute of Technology, Ireland, 2020.

[18] Adamec, V., Herman, D., Schullerova, B., and Urbanek, M., *Modelling of Traffic Load by the DataFromSky System in the Smart City Concept, in Smart Governance for Cities: Perspectives and Experiences*, N.V.M. Lopes, Editor. 2020, Springer Nature: Switzerland. p. 135-152.

[19] PTV Group, PTV Vissim & Connected Autonomous Vehicles, 2021.

[20] Motamedidehkordi, N., Margreiter, M. and Benz, T., *Shockwave suppression by vehicle-to-vehicle communication*. Transportation Research Procedia, 2016, 15: p.471-482.

[21] Ahmed, H., Huang, Y. and Lu, P., *A Review of Car-Following Models and Modeling Tools for Human and Autonomous-Ready Driving Behaviors in Micro-Simulation*, Smart Cities, 2021, 4(1): p. 314-335.

[22] Dowling R, Skabardonis A, Halkias J, McHale G, Zammit G. 'Guidelines for Calibration of Microsimulation Models: Framework and Applications', Transportation Research Record, 2004;1876(1):1-9.

[23] Wisconsin Department of Transport, *Traffic Engineering Operations Safety Manual*, 2019.

[24] Leyn, U. and Vortisch, P., *Calibrating VISSIM for the German highway capacity manual*. Transportation Research Record, 2015, 2483(1): p.74-79.

[25] Schönhof, M. and Helbing, D., *Empirical Features of Congested Traffic States and Their Implications for Traffic Modeling*, Transportation Science, 2007, 41(2): p. 135-166.

[26] Zeidler, V., Buck, H.S., Kautzsch, L., Vortisch, P. and Weyland, C.M., *Simulation of autonomous vehicles based on Wiedemann's car following model in PTV Vissim'*, in Proceedings of the 2019 98th Annual Meeting of the Transportation Research Board (TRB), 2019, Washington, DC, USA.

[27] Atkins Ltd., *Research on the Impacts of Connected and Autonomous Vehicles (CAVs) on Traffic Flow, Summary Report*, Department for Transport. (2016) United Kingdom [online] Available at: https://assets.publishing.service.gov.uk/government/uploads/system/uploads/attachment_data/file/530091/impacts-of-connected-and-autonomous-vehicles-on-traffic-flow-summary-report.pdf [Accessed 25 July 2021].

[28] Lutin, J.M., *Not If, but when: autonomous driving and the future of transit*. Journal of Public Transportation, 2018, 21(1): p.10.

[29] IHS Automotive., *Autonomous cars – not if, but when.* Emerging Technologies, 2014.

Investigation into the Viability of Electric Light Commercial Vehicles for Local Authority Applications in Ireland

Jack Houlihan, Dr. Brian McCann
Faculty of Engineering and Design, Sligo Campus, Atlantic Technological University, Ash Lane, Sligo, F91 YW50, Ireland
email: jack.houlihan@mail.itsligo.ie, mccann.brian@itsligo.ie

ABSTRACT: A key objective of Ireland's Climate Action Plan for the transport sector is for 100% of all new cars and vans to be electric vehicles (EV) by 2030. In order to achieve this target, one proposed measure is the conversion of public fleets, including local authority (LA) fleets, to EV. The primary aim of this research is to establish whether electric light commercial vehicles (eLCV) are viable for use in the LA sector, based on current policy, travel demand, technological and infrastructural constraints. Viability was measured in terms of economic viability, fitness for purpose and environmental performance. The methodology included a nationwide survey of LA fleet managers to establish current eLCV uptake and experience in LAs. An assessment of two LAs, urban and rural, was undertaken involving driver surveys, a Total Cost of Ownership (TCO) analysis, and an environmental analysis to establish potential reduction in emissions. It was found that eLCVs are more suited to urban-based LAs than rural-based LAs as they are challenged by EV range limitations and inadequate charger infrastructure. However, it is anticipated eLCVs will become viable for longer range journeys with increased deployment of EV chargers and enhanced battery efficiency. Furthermore, eLCVs will reach cost parity with internal combustion engine vehicles (ICEV) with reduced battery costs and increased fuel costs. Key constraints relating to eLCV viability and their altering factors were identified. It is intended that this research will inform LA fleet managers on the potential of eLCV to compliment or replace their existing fleets.

KEY WORDS: Electric light commercial vehicle; Local authority; Total cost of ownership; Range anxiety; Capacity fade; Worldwide Harmonised Light-Duty Vehicles Test Procedure; Real-world driving; Driver survey; Fleet manager survey.

1 INTRODUCTION

1.1 Background

Ireland's Climate Action Plan for the transport sector aims for 100% of all new cars and vans to be EV by 2030 [1]. In order to achieve this target, one proposed measure is the conversion of public fleets, including LA fleets, to EV. LAs are responsible for providing essential public services and heavily utilise light commercial vehicles (LCV) with a combined total of over 3,700 LCVs nationally [2]. In 2017, LCVs accounted for 10% of transport energy-related non-Energy Trading System CO2 emissions [3]. It is incumbent on LAs to lead by example in the change to a more sustainable and climate neutral society [4]. There is a dearth of literature on the viability of eLCV in the context of their application to LAs. Furthermore, the rapidly evolving technology of EVs gives rise to a continual need for further research. This research aims to close this research gap.

2 LITERATURE REVIEW

2.1 eLCV Applications

Studies have shown eLCVs are suited to urban logistics, however, payload limitations has been noted as a challenge to be overcome to broaden their application [5]. A number of countries in the European Union (EU), including Ireland [6], have increased the gross vehicle weight (GVW) restriction for Category B licences from 3.5t to 4.25t with the purpose of persuading vehicle manufacturers to develop a wider range of eLCV models with larger batteries, hence, increasing drive range [7]. Other studies have shown that construction, health and other services sectors are most appropriate for eLCV use, with the highest proportion of average travel distances less than 100km [7].

2.2 Range Anxiety

'Range anxiety' is a phenomenon generally defined as a fear of running out of battery power during a journey without any means of re-charging [8]. Frank et al. [9] determined that, due to psychological factors, all battery electric vehicles (BEV) have a usable range (referred to as comfortable range) which is less than their technical range. This comfortable range is defined as the range typically used by drivers before range anxiety occurs and is driver specific. The gap between the remaining battery range and a trip's range is termed the 'safety buffer'. A finding of the study was that users reserved a safety buffer of approximately 19km remaining range, below which they would not use the BEV (except in exceptional circumstances). Another finding was that the average users' comfort zone threshold was reached at 73.2km remaining BEV range for a 60km trip. A separate study by Yuan et al. [8] made similar findings.

2.3 Vehicle Type Approval Testing

Since 2018, all vehicles in the EU are tested in accordance with the Worldwide Harmonised Light-Duty Vehicles Test Procedure (WLTP). In the context of EVs, energy consumption (kWh) is determined by measuring the amount of energy used to fully charge the battery following completion of the test cycle. The laboratory test procedure is divided into four parts comprising of different speeds, collectively referred to as the 'combined' cycle. The test is carried out at two defined temperatures; 14°C and 23°C (the former representing the European average). Ireland's average annual temperature is 10.9°C with mean monthly temperatures only exceeding 14°C for 3 months of the year [10]. Therefore, it can be inferred that achievable EV drive

ranges would be inherently less than their WLTP range for much of the year. The vehicle test mass for LCVs accounts for 28% of the maximum payload. Mass (or weight) has a significant bearing on energy consumption in BEVs [11] and, consequently, it can be inferred that eLCVs have a high degree of variance in drive range due to variable payloads which can make up over a third of their overall GVW.

2.4 'Real-World' Driving

It is well recognised that, in practice, EVs generally do not achieve the range stated under standardised test conditions [12][13]. The actual travel range of EVs is impacted by a number of factors including weather conditions (such as temperature, precipitation and wind speed), topography, terrain, driving behaviour and road type [12]. Various studies have shown that the WLTP is not fully representative of 'real-world' driving conditions [14]. Küng et al. [14] found from a study of five vehicles with varying powertrains (including BEV) over a 2-year period, that real-world energy consumption for ICEs and BEVs can be 22% and 25% greater than the WLTP cycle respectively. Fetene et al. [13] undertook a study of 741 BEV drivers extending over a combined 2.3 million km travelled in Denmark and found that there was a 25% reduction in drive range in the winter compared with the summer, with the ideal temperature for energy efficiency being 14°C. Other studies have also concluded that winter conditions reduce the BEV range by 8% and 9% for a small car (1.6 ton) and truck (14.7 ton) respectively [12]. Furthermore, it was found that hilly terrain reduces the BEV range by 7% and 9% respectively [12]. It was also found that the factor with the biggest impact on energy consumption and range was driving behaviour, with aggressive driving styles reducing range by 20% and 17% respectively [12].

2.5 Total Cost of Ownership

TCO analyses are a useful tool to project the total cost of a product over its lifetime. Tsakalidis et al. [15] concluded from TCO analysis of eLCVs compared against conventional LCVs, that small eLCVs were cost competitive, while medium and large eLCVs had a higher TCO, of €1,200 and €2,300 respectively over 5 years. Lebeau et al. [16] developed a TCO model comparing 7 EVs with 8 petrol/diesel alternatives. They demonstrated that eLCVs begin to have a lower TCO than conventional petrol and diesel alternatives where annual travel distances exceed 16,000 km. Babin et al. [17] undertook a study to identify potential improvements that could be made to the TCO of a 3.5t eLCV used for home deliveries in an urban/extra urban environment. They found that the single largest factor affecting the TCO was the battery, for a variety of reasons. Batteries can account for up to 45% of the total purchase price of a 3.5t eLCV, and also account for up to 31% of the total vehicle mass [17]. Due to its mass, the battery can subsequently account for up to 15% of the vehicle's total energy consumption [17]. Another important factor relating to the battery is its lifespan, which is largely affected by temperature and State-of-Charge (SoC). The study showed that the optimal temperature was 22°C, while the optimal SoC range is between 40-70% [17]. Based on the study, the analysed 3.5t eLCV only became more profitable than the thermal engine between the 33rd and 43rd month of ownership for a 25°C temperature (Figure 1) [17]. After the 43rd month, the TCO of the eLCV is severely hampered by the cost of battery replacement.

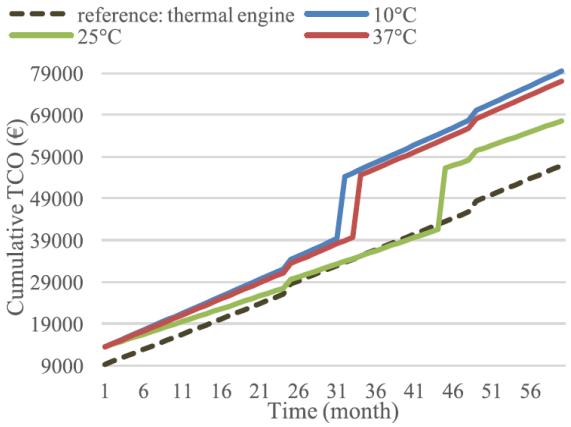

Figure 1. TCO comparison of eLCV and LCV [17]

2.6 Battery Degradation

Batteries experience a phenomenon known as 'capacity fade' whereby their energy storage capacity, known as State-of-Health (SoH), reduces with time [18]. Capacity fade is also dependent on factors such as temperature, driving behaviour, the number of charge cycles, depth of discharge, and SoC [19]. High SoC, between 70-100%, significantly increases the rate of degradation, while the optimal SoC range is between 40-70% (Figure 2) [17].

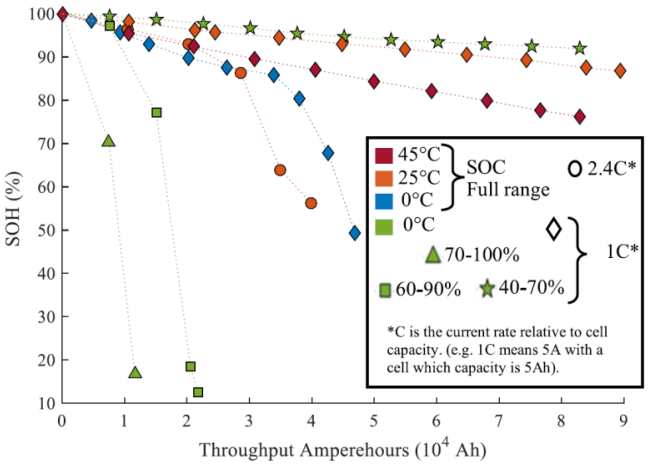

Figure 2. SoH evolution for capacity fade [17]

3 METHODOLOGY

3.1 Overview

The purpose of this research was to establish whether eLCVs are a viable alternative to conventional LCVs used by LAs. For the purposes of this research, viability was defined as follows:

i. **Fitness for Purpose** – is the functional performance of eLCVs in terms of drive range, payload and charge times satisfactory for LA applications?

ii. **Economic viability** – would eLCVs be cheaper or more expensive to run based on their TCO plus the cost of installation of charge infrastructure?
iii. **Environmental performance** – would conversion to eLCVs make a significant impact in reducing CO2 emissions?

The scope of the research was to analyse the driving patterns of LA employees and vehicle functions of existing LCVs in LA fleets, and determine whether electric alternatives could be used instead. eLCVs are shown to be suited to urban rather than rural transit [5]. This is an important factor in the context of LAs, which predominantly comprise county councils covering large geographical areas. Consequently, the research incorporated an analysis of two LAs, one city council and one county council. The research was limited to commercial cars (<2t GVW), small vans (<2.5t GVW), medium (MWB) and long wheel base (LWB) vans (<3t GVW) and pick-up trucks (3.5t GVW).

3.2 Data Collection

LA Fleet Manager Survey - An online questionnaire survey was undertaken with all LA fleet managers in the Republic of Ireland (31 in total) to establish the present status of EV roll-out in LAs, and to receive feedback on their performance so far to date.

Commercial Fleet Manager Interviews - The fleet manager survey highlighted the significant role that the commercial fleet sector plays in the supply of eLCVs to LAs. Consequently, two commercial fleet managers were interviewed. Questioning related to perception and experience with eLCVs, perceived advantages and disadvantages, and perceived challenges to be overcome in order to support eLCV roll-out.

Driver Surveys - Driver specific data (such as work sector, daily maximum incurred drive ranges, travel patterns, parking characteristics and payload and towing requirements) was collected by undertaking questionnaire surveys with individual LA employees. A sample size of 30 participants were included in the study, 7 from Galway City Council and 23 from Galway County Council. This represents 8% and 7% of the total number of drivers in the respective LAs.

Vehicle Manufacturers' Technical Data - Data pertaining to the various eLCVs and LCVs currently available in Ireland was collected from manufacturer websites and main dealers. This data included 'Combined' WLTP range, purchase price, dimensions, GVW, payload, cargo capacity, towing capacity, fuel consumption, CO2 emissions, battery capacity, power output and battery warranty details. In some instances, data was not available from manufacturers' websites and, hence, other non-official sources were used or values were estimated.

3.3 eLCV Technical Assessment

A technical assessment of eLCVs to meet driver needs was carried out by comparing the driver survey data with the vehicle manufacturers' technical data. Range adequacy was assessed over 5-year and 8-year ownership periods (Table 1). WLTP ranges were reduced by 25% to reflect real-world driving and by the conservatively proportionate amount of capacity fade covered under manufacturers' warranties (3-6%/annum). A 5km and 15km safety buffer was also applied to drivers' stated required range depending on the regularity of their driving pattern. The potential for charging events during work, whilst noted, was not taken into account due to difficulties in accurately ascertaining when charge events would take place, the SoC before charging commences and the high variability in charging durations. Similarly, the effects of heavy payloads on range could not be determined and, hence, was ignored.

Table 1. eLCV Real-World Range plus Capacity Fade.

Vehicle Model	Segment	WLTP Range (km)	'Real World' Range after Capacity Fade	
			5 Years	8 Years
Nissan Leaf SV Van	Commercial Car	385	244	228
Renault Zoe R110	Commercial Car	395	233	217
Hyundai Kona Electric 64kWh	Commercial Car	484	295	275
Nissan E-NV200	Small Van	200	127	118
Renault Kangoo Z.E. 33	Small Van	216	113	108
Peugeot e-Partner	Small Van	275	168	156
Citreon e-Dispatch MWB 75kWh	MWB Van	330	201	187
Opel Vivaro-E L1 75kWh	MWB Van	330	201	187
Maxus eDeliver 9 LH 88.55kWh	LWB Van	296	187	175
Ford e-Transit chassis cab 68kwh	Pick-up Truck	240	146	136

3.4 TCO Analysis

A TCO analysis was undertaken, comparing eLCVs with the ICEV models used in LA fleets. The analysis, exploiting the use of Microsoft Excel® spreadsheet software, was carried out for a range of annual mileages, including those of the study sample. The analysis was based on the following data and assumptions:

i. **Purchase cost** – the recommended retail price including taxes and SEAI grant (€3,800) as applicable.
ii. **Charger cost** – home chargers were assumed given the vast majority of drivers use their vehicle to commute to and from work. A cost of €450 was assumed for purchase and installation (including €600 SEAI grant) based on industry quotations.
iii. **Insurance costs** – Insurance quotations were obtained for each vehicle from the AXA Insurance website.
iv. **Motor tax** – The Motor Tax Online website was used to calculate the relevant road tax for each vehicle. All LCVs (including eLCVs) are taxed based on unladen vehicle weight with a tax rate €333/annum applied to 1.5-3ton.
v. **Maintenance costs** – costs of €0.072/km and €0.058/km were adopted for ICEV and BEV respectively, based on research by Propfe et al. [20].
vi. **Fuel costs** – WLTP consumption rates were increased by 22% and 25% for ICEVs and BEVs respectively, based on findings of Kung et al. [14]. Diesel was based on a cost of €1.90/litre. Electricity costs were based on a night unit price of 9.69c/kWh plus a €250 standing charge.
vii. **Depreciation** - an annual rate of 18.57% was chosen for ICEVs, mimicking Lebeau et al. [16] while a rate of 22.28% was chosen for BEVs (20% higher than ICEVs).

3.5 Environmental Analysis

The potential reduction in CO2 tailpipe emissions that could be achieved by converting suitable drivers to eLCV was determined. WLTP emissions values were increased by 22% based on findings of Küng et al. [14].

4 RESULTS

4.1 LA Fleet Manager Survey

The survey found that 19 LAs currently utilise eLCV as part of their fleet, making up a combined 235 units nationally. The small van is the most popular segment for electrification, with a 69% share, followed by the commercial car with a 23% share. eLCVs are predominantly used for short trips in urban environments (typically less than 15km) by 58% of LAs, while 37% use them for a combination of urban and rural trips. 26% of LAs (all urban based) stated that eLCVs drive range more than adequately meet all, or nearly all, travel needs, while 74% stated they have limited applications due to drive range. 68% stated that eLCVs' do not meet their WLTP range with seasonal temperature fluctuations, driving styles, terrain, payload and use of on-board climate control features stated as contributory factors. Interestingly, only 21% of LAs have provided drivers with Eco-driving training. A lack of available capital for eLCV purchase and charger installation was noted by 45% of LAs as the biggest obstacle to eLCV roll-out, while 39% stated inadequate driving range as the biggest issue. Insufficient grant funding and inadequate payload capacity were also noted as significant secondary issues. Other obstacles highlighted by LAs included challenges associated with installing chargers in employees' homes and a lack of eLCV availability within the commercial leasing industry were also noted. Limited variety in the pick-up truck segments, including limited payload and lack of towing capability, was also highlighted as an issue.

4.2 Commercial Fleet Manager Interviews

Opinion on eLCVs was conflicting between fleet managers. One fleet manager, who used eLCVs, noted a positive experience with them becoming a steadily growing market share and having a significantly lower maintenance cost to ICEVs. However, they noted their customers predominantly used eLCVs for urban-based transit or well defined routes. The other fleet manager, whilst having trialled eLCVs, did not own any due to concerns with high purchase cost, range limitations and uncertainty surrounding payback periods and a rapid evolving technology. Both fleet managers shared the opinion that eLCV applications were still limited due to their range capacity. Both also noted that government supports were needed for the commercial sector to support wider eLCV diffusion.

4.3 eLCV Technical Assessment

Nine county council drivers (39%) were concluded to be suitable candidates for eLCV, while all seven city council (100%) drivers were suitable candidates (Table 2). For the commercial car segment, four out of five county council drivers could only be accommodated by the eLCV with the highest range (Hyundai Kona Electric) up to a 5-year ownership period. For the small van segment, three out of eight county council drivers could be accommodated by an eLCV up to an 8-year ownership period. None of the county council drivers could be accommodated by an eLCV for the MWB or LWB segments and only two drivers could be accommodated for the pick-up van segment up to eight years.

Table 2. Driver range and payload requirements.

Driver	Segment Type	Range Requirement (km)	Payload Requirement (kg)	Suitability
Galway County Council				
Technician 1	Car	295	50	Suitable
Technician 2	Car	320	50	Not suitable
Technician 3	Car	295	50	Suitable
Technician 4	Car	205	50	Suitable
Technician 5	Car	295	50	Suitable
Warden 1	Small Van	245	100	Not suitable
Warden 2	Small Van	205	100	Not suitable
Warden 3	Small Van	195	100	Not suitable
Warden 4	Small Van	265	100	Not suitable
Warden 6	Small Van	330	250	Not suitable
General Operative 1	Small Van	70	1000	Suitable
General Operative 2	Small Van	55	1000	Suitable
Foreman	Small Van	120	1000	Suitable
Craftworker 1	MWB Van	225	1000	Not suitable
Craftworker 2	MWB Van	330	200	Not suitable
Craftworker 3	MWB Van	335	1000	Not suitable
Craftworker 4	LWB Van	345	1000	Not suitable
Caretaker 1	LWB Van	230	200	Not suitable
General Operative 3	Pick-up Truck	150	1000	Not suitable
General Operative 4	Pick-up Truck	175	1500	Not suitable
Landscaper	Pick-up Truck	120	1000	Suitable
Refuse Collector	Pick-up Truck	55	1000	Suitable
General Operative 5	Pick-up Truck	170	1000	Not suitable
Galway City Council				
Warden 6	MWB Van	65	100	Suitable
Warden 7	Small Van	50	50	Suitable
Warden 8	Small Van	85	Unknown	Suitable
Warden 9	Small Van	50	Unknown	Suitable
Warden 10	Small Van	165	Unknown	Suitable
Clerk of Works 1	Small Van	65	750	Suitable
Craftworker 5	Small Van	70	250	Suitable

There was low potential identified amongst county council drivers for charging in public places with the majority (70%) never parked in urban areas and the remainder (30%) spending <1 hour/day parked. Conversely, high potential was identified for city council drivers with 55% parked for 2-3 hours/day and 30% parked for 3-5 hours/day parked in urban areas. There was high potential for charging at social houses by county council craftworkers, with durations between 2-5 hours/day.

4.4 TCO Analysis

The TCO analysis yielded that eLCVs had a higher TCO than LCVs over an 8-year period for eight of the nine county council drivers identified in the technical assessment (Table 3). The TCO model also yielded the annual mileage required for eLCVs to start to reach cost parity with their ICEV equivalents (Table 4). The analysis shows that city council drivers would need to drive an average of 46km/ working day

to reach cost parity over 8 years, which is close to some drivers' maximum daily distance travelled. Hypothetically, if a driver had an annual mileage of 20,000km, eLCVs would be more economical in all segments, with cost parity reached as soon as 4 years and 2.4 years in some cases for small and MWB vans respectively (Figures 3 - 6).

4.5 Environmental Analysis

The environmental analysis yielded that 20.1 ton/annum of CO2 tailpipe emissions could be eliminated by converting the nine suitable drivers to eLCV.

Table 3. TCO comparison of eLCV and LCV.

Driver	Vehicle Segment	Annual Mileage (km)	BEV TCO (€)	ICEV TCO (€)
Technician 1	Car	18,787	57,611	47,762
Technician 3	Car	27,334	62,796	60,489
Technician 4	Car	31,973	56,816	67,181
Technician 5	Car	12,594	53,854	39,228
General Operative 1	Small Van	8,359	41,866	34,764
General Operative 2	Small Van	5,310	39,877	30,366
Foreman	Small Van	10,809	43,464	38,298
Landscaper	Pick-up Truck	10,803	71,885	60,219
Refuse Collector	Pick-up Truck	6,967	69,234	52,237

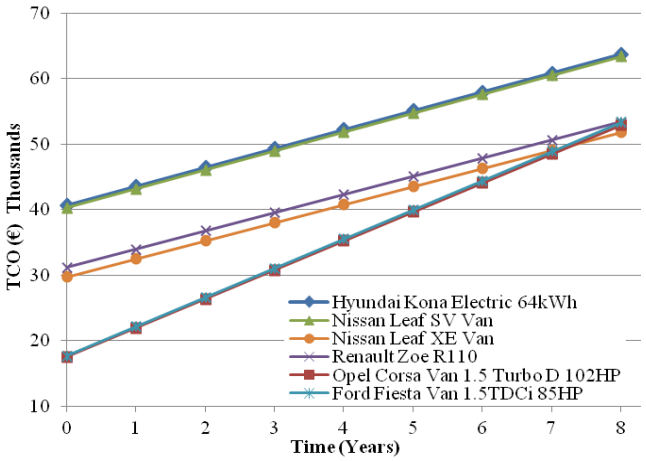

Figure 3. TCO comparison – commercial car.

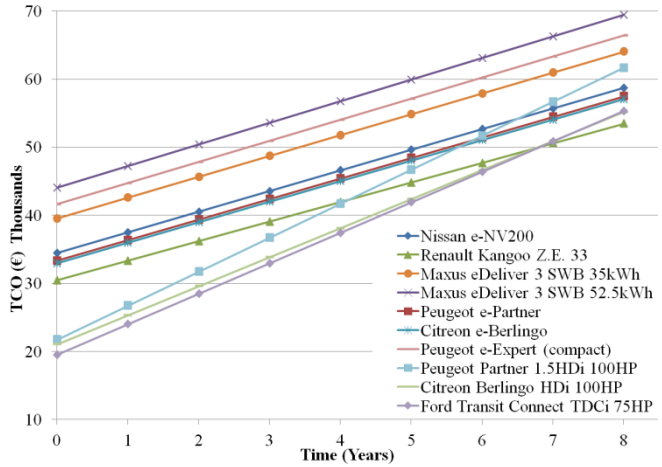

Figure 4. TCO comparison – small van

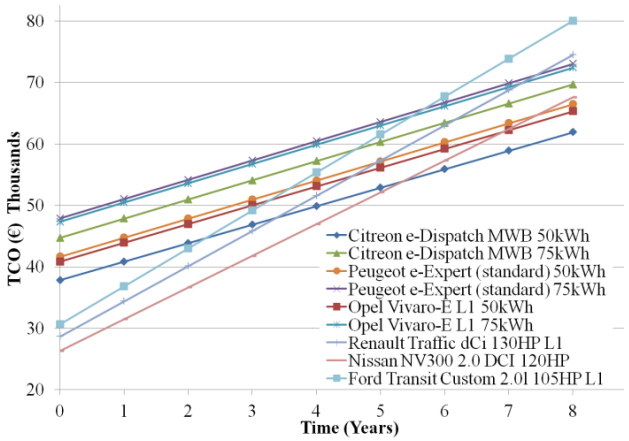

Figure 5. TCO comparison – MWB van

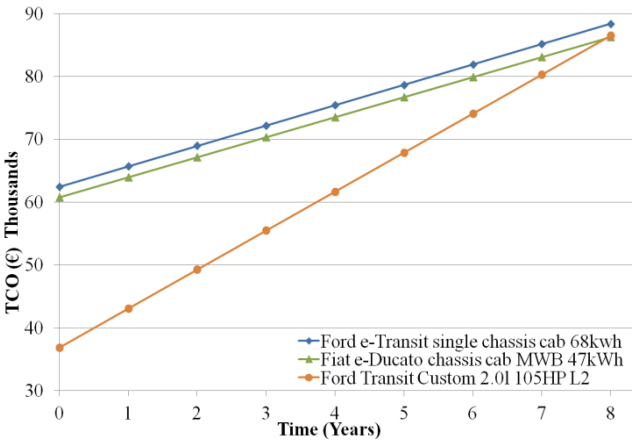

Figure 6. TCO comparison – pick-up truck

Table 4. eLCV breakeven annual mileages.

Vehicle Segment	Vehicle Model	Annual Mileage (km)	
		8-Year Period	5-Year Period
Car	Nissan Leaf XE Van	17,500	23,500
Small Van	Renault Kangoo Z.E. 33	12,000	16,000
MWB Van	Citreon e-Dispatch MWB 50kWh	7,000	10,000
LWB Van	Citreon e-Dispatch LWB 50kWh	7,000	10,000
Pick-up Truck	Fiat e-Ducato chassis cab MWB 47kWh	19,000	25,000

5 DISCUSSION

The technical assessment highlights challenges faced by eLCVs to meet the needs of rural-based LAs, primarily due to range limitations. Payload and towing capability are also problematic for larger segments. This aligns with the findings of fleet manager surveys and interviews. Comparatively, the driving ranges of rural-based LA drivers are significantly greater than those of other work sectors noted in previous studies [7]. A limitation of this study, however, was the proportion of long journeys could not be determined by questionnaire-based methods. GPS tracking or longitudinal surveys would be required to gather this information. eLCVs may, in fact, accommodate a significant proportion of drivers' journeys, but alternatives would be needed for longer ones. Another limitation is that the sample size was relatively small and a larger scale study may yield varying results. The effects of real-world driving and capacity fade are shown to have a significant impact on eLCV ranges. This highlights the

importance of driving behaviour and charging regimes, as outlined in previous literature [12,17]. Eco-driving training may help to mitigate this, however, only 38% of LAs have provided such training. Conservative values for capacity fade were adopted. In reality, fade rates may be less, extending the useable life of an eLCV. However, ultimately Ireland's winter climate plays a big factor in range capacity. All of the rural-based LA drivers surveyed use their vehicles to commute to and from work with little time spent parked on work premises or public spaces. Therefore, home charging would appear to be the optimal charging solution for this group. However, alternative strategies involving overnight charging on work premises may prove effective in some cases where the economic and environmental benefits of eLCVs outweigh the time-cost of additional driving. Due to the short-duration of parking in public areas by rural LA drivers, it is considered this group would gain little benefit from standard public chargers and, instead would rely on fast/rapid charger infrastructure (≥43kW). Conversely, urban-based LA drivers, who spend significant durations parked in public areas, would benefit from standard public chargers (≥7kW). The commercial car segment was shown to be practical but less economical than ICEVs for the majority of drivers. This differs from the findings of other studies which found BEVs to be cost competitive for small LCVs [15]. This is partly due to the ICEV model being from a cheaper car category, owing to the drivers' basic utility needs, and the limited range of BEV commercial car models. Consequently, there is an imbalance in the pricing for this segment at present, with a need for greater variety in small electric vans. The recently launched Peugeot e-208 and Opel e-Corsa may fill this gap. Secondly, the most expensive eLCV happened to be the only suitable model for 4 drivers due to range. It is anticipated falling battery costs and potentially increased fuel costs will close this price gap in the coming years. Similar to the findings of Lebeau et al. [16], this study shows small eLCVs are cost competitive with ICEVs, albeit, with a 2-year shorter ownership period (partly due to different assumptions on vehicle prices). MWB and LWB vans are also shown to be competitive with ICEVs for relatively low annual mileage. This study yielded a longer breakeven period for pick-up trucks (5.5 years) than the study by Babin et al. [17] for a similar annual mileage. Range and energy consumption data was unavailable for pick-up trucks, due to the variety of body configurations available for this segment. Therefore data from equivalent LWB models was assumed. There is a dearth of information relating to the effects of heavy payloads on range and, consequently, a high margin of error exists in the assessment of this segment. This, alongside uncertainties with trailer towing, was noted by fleet managers as an obstacle to utilising this segment. There is also limited uptake of the 4.25t GVW increase with only two models available at present.

6 CONCLUSIONS

This study shows the importance of evaluating the practical, economic and environmental characteristics of eLCVs in determining their overall viability. Driver specific parameters such as driving range, pattern, payload and towing requirements and parking characteristics need to be carefully considered in the planning process. This study shows that eLCVs are more suited to urban-based LAs than rural-based LAs as they are challenged by range limitations. However, it is anticipated eLCVs will become viable for longer range journeys in the near future with increased deployment of EV chargers and enhanced battery efficiency. This research will inform LA fleet managers on the potential of eLCVs to complement their existing fleet or transform them altogether.

REFERENCES

[1] Ireland. DoECC (2019a) *Climate Action Plan*. Dublin: Stationery Office.

[2] Climate Action Regional Offices (2022*) Reimagining Transport in Local Government: Survey Overview*. Kilkenny: CARO

[3] Environmental Protection Agency (2021) *Opportunities to Decarbonise the Irish Transportation Sector*. Wexford: EPA.

[4] Ireland. DoECC (2019b) *Climate Action Charter For Local Authorities and Minister for Communications, Climate Action and Environment on behalf of Government*. Dublin: Stationary Office.

[5] Quak, H., Nesterova, N. and van Rooijen, T. (2016) 'Possibilities and Barriers for Using Electric-powered Vehicles in City Logistics Practice', *Transportation Research Procedia*, [online] 12, pp.157-169.

[6] *Road Traffic (Licensing of Drivers) (Amendment) (No.8) Regulations, 2020* (No. 489) Dublin: Stationery Office.

[7] Christensen, L., Klauenberg, J., Kveiborg, O. And Rudolph, C. (2017) 'Suitability of commercial transport for a shift to electric mobility with Denmark and Germany as use cases'. *Research in Transportation Economics*, 64, pp.48-60.

[8] Yuan, Q., Hao, W., Su, H., Bing, G., Gui, X. and Safikhani, A. (2018) 'Investigation on Range Anxiety and Safety Buffer of Battery Electric Vehicle Drivers'. *Journal of Advanced Transportation*, 2018, pp.1-11.

[9] Franke, T., Neumann, I., Bühler, F., Cocron, P. and Krems, J. (2012) 'Experiencing Range in an Electric Vehicle: Understanding Psychological Barriers'. *Applied Psychology*, 61(3), pp.368-391.

[10] Met Éireann (2012) *Climatological Note no.14: A Summary of Climate Averages for Ireland 1981-2010*. Dublin: Met Éireann.

[11] Ramanujam, Y., Malhotra, I. and Thimmalapura, S. (2019), 'A Study of Parameters Influencing Energy Consumption of an Electric Vehicle', *2019 IEEE Transportation Electrification Conference (ITEC-India)*, 2019, pp. 1-6.

[12] Dollinger, M. and Fischerauer, G. (2021) 'Model-Based Range Prediction for Electric Cars and Trucks under Real-World Conditions'. *Energies*, 14(18), p.5804.

[13] Fetene, G., Kaplan, S., Mabit, S., Jensen, A. and Prato, C. (2017) 'Harnessing big data for estimating the energy consumption and driving range of electric vehicles'. *Transportation Research Part D: Transport and Environment*, 54, pp.1-11.

[14] Küng, L., Bütler, T., Georges, G. and Boulouchos, K. (2019) 'How much energy does a car need on the road?'. *Applied Energy*, 256, p.113948.

[15] Tsakalidis, A., Krause, J., Julea, A., Peduzzi, E., Pisoni, E. and Thiel, C. (2020) 'Electric light commercial vehicles: Are they the sleeping giant of electromobility?', *Transportation Research Part D: Transport and Environment*, 86, p.102421.

[16] Lebeau, P., Macharis, C., Van Mierlo, J. and Kenneth, L. (2015) 'Electrifying light commercial vehicles for city logistics? A total cost of ownership analysis'. *European Journal of Transport and Infrastructure Research*, [online] 15(4), pp.551-569.

[17] Babin, A., Rizoug, N., Mesbahi, T., Boscher, D., Hamdoun, Z. and Larouci, C. (2018) 'Total Cost of Ownership Improvement of Commercial Electric Vehicles Using Battery Sizing and Intelligent Charge Method'. *IEEE Transactions on Industry Applications*, 54(2), pp.1691-1700.

[18] Peterson, S., Apt, J. and Whitacre, J.F. (2010) 'Lithium-ion battery cell degradation resulting from realistic vehicle and vehicle-to-grid utilization', *Journal of Power Sources*, 195(8), pp.2385-2392.

[19] Jafari, M., Gauchia, A., Zhao, S., Zhang, K. and Gauchia, L. (2018) 'Electric Vehicle Battery Cycle Aging Evaluation in Real-World Daily Driving and Vehicle-to-Grid Services'. *IEEE Transactions on Transportation Electrification*, 4(1), pp.122-134.

[20] Propfe, B., Redelbach, M., Santini, D. and Friedrich, H. (2012) 'Cost analysis of Plug-in Hybrid Electric Vehicles including Maintenance & Repair Costs and Resale Values'. *World Electric Vehicle Journal*, 5(4), pp.886-895.

Factors that Influenced the Acceptance or Rejection of Transfers on Dublin's new bus network.

Brendan Meskell
2022 Graduate, MSc Sustainable Mobility and Transport, TU Dublin, Bolton Street, Dublin 1
Email: brendan.meskell@gmail.com

ABSTRACT: This paper is an abridged version of the author's dissertation for the MSc Sustainable Mobility and Transport at TU Dublin (with some minor updates) that was submitted in December 2021. Noting a lack of literature on the introduction of transfers into a bus network, the research sought to ascertain the factors influencing the acceptance or rejection of transfers into Dublin's new 'BusConnects' network. Following a review of literature on the best practice for bus networks, research was undertaken using interviews with stakeholders and a review of anonymised submissions and selected social media posts. It found that the major recurring issues were (i) frequency may impact the acceptance of transferring, (ii) the discomfort or inconvenience of transferring, (iii) the importance of maintaining regional and local links and (iv) the need for a more localised level of consultation at the earliest possible stages of the consultation process.

KEY WORDS: Bus; Public Transport; Transfer; Interchange; Consultation; Frequency.

1.INTRODUCTION

The BusConnects project was launched in 2017 to overhaul Dublin's bus network. It saw the biggest ever public consultation for a transport project in Ireland. The consultation saw resistance in some areas of the city to the earlier drafts' idea of having to make a transfer on a bus journey and the final draft saw many direct routes to the city centre reinstated. In 2021 the author undertook a dissertation as part of a postgraduate degree to explore the reason for this resistance using a case study area approach [1].

This paper provides an abridged version of that research. It will firstly examine literature on bus networks as well as consultation reports on the BusConnects project. It will then outline the methodology used in this research. The findings will be presented and discussed. After a brief update of some recent developments on the BusConnects project, the paper concludes with some suggestions for future research.

2. LITERATURE REVIEW

While some degree of literature exists on network design and attitudes to transferring, in contrast, the literature on *introducing* transfers to a public transport network is relatively sparse [1].

Public transport operators must compete with the 'anywhere to anywhere' convenience provided by the private car [2]. Transfer-based systems provide the best opportunity for something close to the anywhere-to-anywhere scenario as a 'many to one' service is not desirable or feasible [3]. Currie and Loader (2010, p. 8) estimate that transfer-free public transport networks only allow access to 5% of destinations and thus:

> *"Transfers between routes and a network to encourage them are therefore essential features of an effective public transport system"* [4]

Badia et al (2017, p. 84) suggest that while passengers are averse to transfers and want direct routes, a transfer-based system "can better satisfy dispersed mobility patterns" [5].

Various tools are available to planners to improve network connectivity and transfers. A reduction in overall route numbers can yield increased resources for local and orbital services and a simpler design for users – particularly occasional users - to understand [6][7]. This integrated, transfer-based system can lead to a 'network effect' which expands the catchment area for users of the system [2]. This is exemplified in the 'pulse system', used in Zurich's regional area, where a high frequency bus and tram network in the city centre can result in a 'forget the timetable' level of service, and where frequent suburban rail and tram services are timed to connect bus services to less populated areas (see Mees (2009) Chapter 8) [2].

When a transfer-based system has frequent and/or reliable services, passenger usage and satisfaction can increase [5][8]. Studies of the phased introduction of a new transfer-based bus network in Barcelona showed that the network is used as such, not as a combination of separate lines and saw an increase in passenger numbers and transfers compared to the older part of the network [5][9].

While the benefits of a transfer-based network have been outlined above, various studies have demonstrated a reluctance to make a public transport journey involving transfers that create uncertainty in travellers' minds [10]. It is noted that the transfer penalty – the financial or other costs of having to make a transfer – may increase with less frequent services and/or with bus-bus transfers (as opposed to transfers involving rail) [4][7]. Creating a sense of seamlessness for those who use

interchanges is seen as essential and this can be facilitated by improved frequency and reliability as well as fare integration to negate a financial transfer penalty[8][11]. The environment of the interchange location – which can be anything from a central station to two bus stops at a junction - is a significant factor in passenger attitudes [7][8][10]. Citing Scott (2003), Hernandez and Monzon affirm that "urban transport interchanges are therefore key features for the future development of cities" (2016, p. 164) [11]. The literature also highlights some social issues such as transferring being more likely to be done by younger male passengers [4] and concerns about interchanging at night [10].

In postgraduate research, presented as part of the MSc in Sustainable Transport and Mobility at TU Dublin and reproduced here in this paper, Meskell (2021) outlines the evolution of the BusConnects project from its launch in 2017 until just after the second phase of implementation in November 2021[1]. BusConnects aims to expedite an overhaul of Dublin's bus network. There are 9 strands of the BusConnects project, including new livery, newly designed stops and shelters, a revised fare structure, the construction of high-quality bus corridors on major arteries and a redesign of the bus network [12]. This paper is primarily concerned with the network design aspects of the BusConnects project. In 2017, the NTA and Jarrett Walker and Associates (JWA) produced the 'Choices Report' which gave an overview of the issues affecting the existing bus network. The Choices Report invited participation in a survey, which generated 11,000 responses. 81% of respondents thought it reasonable to change buses during their trip if it resulted in quicker journey times [13]. Following a workshop with stakeholders, the first draft of the BusConnects network was drawn up.

There was subsequently a public consultation process, which saw a roadshow engaging with some 15,000 citizens as well as online and social media engagement [13]. There was backlash to the proposals to withdraw some direct services. Some 48,000 petition signatures and submissions were received in an unprecedented response to a transport consultation. 60% of people said the proposed network was "somewhat" or "much" worse than the existing one [13]. A second draft was then drawn up with "nearly all [routes] edited in some way" and new routes added (JWA, 2019, p. 73) [13]. Another round of consultation took place which saw 11,000 submissions to the second draft

The third, and final draft of the BusConnects network was issued in 2020 as well as report into the 2019 Consultation. In all consultations, concerns about capacity, inconvenience (including transferring), and accessibility for the elderly and disabled were recurring themes [14].

In the final iteration of BusConnects, 95% of areas that did not currently require interchange would now retain a direct service, while remaining areas would have peak-time direct buses to the city centre [14]. It was the stated intention that that the operation of the new network…

> *"…will require careful coordination of timetables to manage interchange from higher frequency to lower frequency bus services. This will be carefully managed during the implementation phasing of the project."*
>
> (National Transport Authority, 2020, p. 8) [14]

3. METHODOLOGY

The research aimed to find out why some areas were more receptive to transferring while other areas strongly resisted this. It was decided to focus on three case study areas: Howth in north-east Dublin; Killinarden in south-west Dublin; and the commuter town of Blessington. The case studies present contrasting contexts, Blessington and Howth being affluent areas close to rich amenity, while Killinarden is a residential estate of mostly publicly built housing within the Tallaght area that has high reported levels of social deprivation (Pobal, 2021 cited in [1]). Howth and Killinarden saw proposals to withdraw direct routes to the city centre abandoned after local opposition, whilst Blessington saw the withdrawal of direct routes maintained in subsequent drafts [1].

There were two broad strands of the research. Interviews with seven stakeholders took place in July and August 2021. Representatives from the National Transport Authority and Jarret Walker and Associates were interviewed to gain a better insight into the devising and dissemination of the proposals. Representatives from the Irish Business Employers Corporation (IBEC) and the Dublin Commuter Coalition (DCC) were interviewed as campaign groups who would have been involved in the consultation process. Finally, activists and elected representatives from the three case study areas were also interviewed to gain an insight to the local issues and concerns.

The second plank of research was an analysis (i) of anonymised submissions made to the NTA from case study areas and (ii) of selected social media posts from Cian O'Callaghan TD (for Howth)., from the Tallaght Echo (for Killinarden), and from the Blessington Blog. For both NTA submissions and Tallaght Echo posts, comments referring to the wider Tallaght area were included but those specifically mentioned other areas were excluded. This was due to the very small number of comments explicitly referring to Killinarden.

Using methodology outlined by Cresswell (2009), a coding sheet was used to segment the findings of the interviews into broad themes of transferring, network (local and overall) and consultation [15]. For submissions and social media posts, an excel sheet was used to count the number of times these broad topics occurred. Recurring topics throughout the interviews and data sets were clustered together to formulate some common themes that go toward the findings outlined in the following sections of this report (the actual coding sheet and data sets used for the dissertation are included in the appendices of Meskell (2021)).

4. FINDINGS AND DISCUSSION

Figures 1-5 illustrate the main recurring issues in case study areas in submissions to the NTA and in selected social media posts

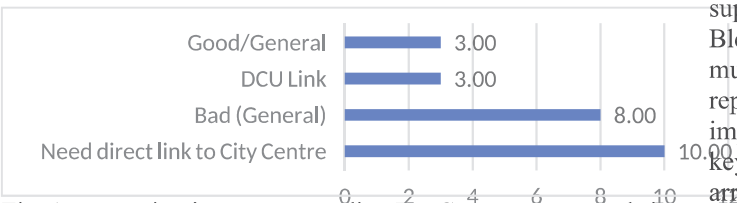

Fig. 1 – recurring issues surrounding BusConnects proposals in Howth as seen on Cian O'Callaghan's Facebook post of 3 July 2018

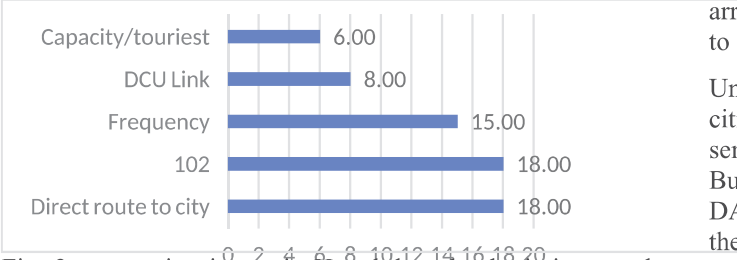

Fig. 2 – recurring issues in Howth-based submissions to the NTA

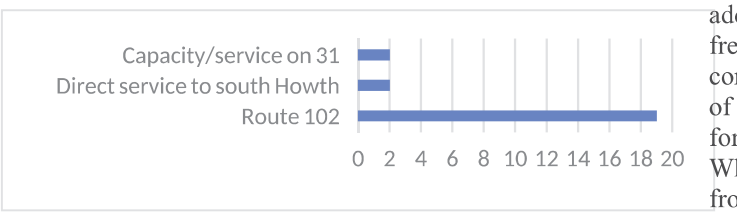

Fig. 3: Recurring issues in comments on Cian O'Callaghan Facebook post re: the second draft of the BusConnects network, 23 October 2019

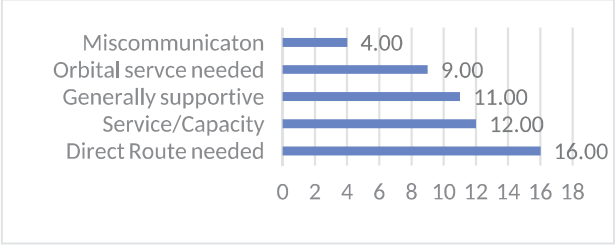

Fig. 4 – recurring issues surrounding BusConnects proposals in Tallaght (including Killinarden) from submissions to the NTA

Fig. 5 – recurring issues surrounding BusConnects proposals in Tallaght as seen on The Echo's Facebook post of 17 August 2018

4.1 *Frequency*

Compared to the other areas, the public reactions to having to make a transfer were more positive in Blessington. Of the comments that could be found on social media, 5 were broadly supportive of the new proposals and 3 were against. While the Blessington representative's recollection was that there was not much public engagement with the issue, the DCC representative and several posts on Facebook indicated that the improved frequency from every two hours to every hour was a key factor in welcoming the proposed changes. Those who arrive at Tallaght from Blessington will have several buses and a Luas service to choose from when they arrive at their interchange. As the Blessington bus service is hourly, it will be crucial to ensure that services are coordinated and that those arriving in Tallaght from the city centre do not have to wait up to an hour for their connecting bus to Blessington.

Under interview, the Howth representative echoed this by citing the need for a coordination between DART and bus services at Howth Station. In the newly rolled-out BusConnects network, there is a lack of coordination between DART arrivals and bus departure times at Howth Station, with the hourly route 6 leaving minutes before the DART has arrived. This lack of timetable coordination belies the connectivity ethos of BusConnects and should perhaps be addressed. Submissions to the NTA cited the lack of improved frequency in the southern end of Howth as a major issue of concern. Clearly, the improved frequency at the northern end of Howth under the first draft's proposed N6 was not sufficient for people to accept the loss of a direct bus to the city centre. While there were concerns about the reduction in frequency from 20-25 minutes to 30 minutes on the direct route, this may have been acceptable in return for the welcomed retention of a direct route to the city. Coupled with several submissions and comments calling for the orbital route 102 to be extended from Sutton to Howth, this may be indicative of a general aversion to transferring in the area.

In Killinarden, the local 240 would have had an improved frequency of every ten minutes – as opposed to approximately every 20 minutes under the existing network. This improvement in frequency did not appear to be sufficient for locals to counteract the loss of a direct route to the city or other areas. The Killinarden and DCC representatives affirmed that the trade-off between higher frequencies and making transfers was not adequately conveyed. The frequency improvements in Howth and Killinarden were thus not seen as a sufficient justification for the withdrawal of direct buses to the city centre and the introduction of transfers.

4.2 *Inconvenience of transferring*

Some of the literature on transfers such as Grisé and El-Geneidy (2019) and Hine and Scott (2000) highlighted the importance of comfort and convenience when making transfers [8][10]. This was a recurring theme in interviews, submissions, and Facebook comments.

The perceived inconvenience of transferring from one bus to another on a journey that currently involves no transferring was frequently cited in submissions and posts as a major issue of concern with the elderly, disabled and child-carrying travellers

being referred to. This was tied into the issue of capacity – including at interchanges. Howth submissions and comments cited their concerns about locals being able to access their bus which is a popular route with tourists. The Killinarden representative and several comments and submissions from Killinarden and Blessington referred to having to transfer onto a very busy bus or Luas at Tallaght. This alludes to the importance of a reliable transport network and the need to provide a service that will meet demand.

In addition to several submissions and social media comments, the NTA representative noted how security at interchanges and travelling at night were subjects of concern. The DCC representative noted how the fact that Tallaght, along with Liffey Valley, Blanchardstown and UCD would be hubs and not merely a collection of bus stops, was not clearly relayed to citizens. This shows another gap in communications but also the need for measures to address a sense of security and for interchange points to be safe and comfortable 'places' as referred to by Hernandez and Monzon (2016) [11].

Some interviewees felt that the benefits of the new network were undersold with the IBEC representative noting how BusConnects was more controversial than the Metro despite being of benefit to more people, including expanding catchment areas for businesses and educational institutions.

4.3 *Regional and local links*

While much of the debate and comment surrounding BusConnects demonstrated the importance of accessing the city centre, the interviews and data sets also highlighted the importance of access to more localised destinations.

While not more important that the city centre, the Blessington representative said that Tallaght was an important location for locals accessing employment, healthcare, and shopping.

In Howth one of the most frequently cited issues was the retention of bus route 102 between Sutton Station, Portmarnock, Malahide and Dublin Airport to access jobs, schools, and amenities in these areas. As cited by the NTA in their consultation report, and as noted by the Killinarden representative, access to the local post office by bus was a major issue of concern in Killinarden [14]. The link between the post office and the rest of Killinarden estate was restored in the final draft, albeit in an hourly service.

Submissions from Tallaght more generally saw comments welcoming the introduction, improvement, or retention of links to areas such as Maynooth, Celbridge, Blanchardstown and Dundrum.

All of the above suggests that even within a radial public transport network such as Dublin's, the need to provide links to employment, education and services in other areas is vital. As noted in USA by Brown & Thompson (2012), a transfer-based network, which links employment and education hubs outside the city centre can generate new ridership [16]. The positive comments in submissions and Facebook posts from Tallaght regarding new orbital routes indicate this may also be the case in Dublin.

4.4 *The importance of communication*

Communication and the design of consultations has turned out to be as important an issue as the design of the network itself.

The DCC representative was particularly critical of the failure to adequately communicate the change in fare structure to allow a free transfer within 90 minutes. This was borne out by several comments on the social media posts which complained about having to pay extra for taking two buses (as was the case at the time) as a reason for their opposition to the proposed changes. While various literature on BusConnects did cite this as an element of the project, it was perhaps not adequately emphasised and led to a certain amount of, what the NTA representative described as, 'fire-fighting'. There should have been greater emphasis and publicity on the free transfer.

The interviewees suggested – and several submissions and social media posts demonstrated – that the presentation of city-wide plans generated some confusion. Several interviewees agreed that a Google Maps-style tool, which would allow users to map out how their regular journeys would work under BusConnects, would be of benefit. This again demonstrates the importance of a locally focused campaign as well as a clear and legible network design.

The data from interviews and social media suggest that many users of buses and other public transport in Dublin do not currently see their public transport service as a network but as a series of separate lines, of which only those they use regularly are important to know.

There was also a discrepancy between the data which informed the Choices Report – based upon 11,000 submissions – and the opposition to the proposals in the Choices Report, which generated up to 50,000 responses. This discrepancy could be remedied by the proposal cited by several interviewees to start with a more locally focused campaign (via letter boxes and on buses) to generate awareness and then to better ascertain the needs and travel patterns of local residents. The fact that additional staff were recruited to process the voluminous submissions suggests that the NTA may have been caught unawares by the extent of the engagement with (and opposition to) BusConnects. There was subsequently an extensive, locally focused, consultation. Future proposals may wish to consider greater adherence to these procedures at an earlier stage of the consultation process. By engaging with local communities before the first draft of the BusConnects network was announced, subsequent controversy and opposition to the proposals may be neutralised.

5. SOME RECENT DEVELOPMENTS

As noted previously, the first phase of BusConnects to be rolled out was the H Spine on the Howth Road in June 2021 [17]. Since this research was completed, the C Spine has been introduced in November operating via Lucan Road and Ringsend in addition to local services in Lucan and north Kildare [18]. In May 2022, two of the northern orbital routes were introduced. An additional facet of the BusConnects project that has been rolled is the free transfer, where passengers have the option of pay the €1.30 "short-hop" fare or

the €2.00 fare that will allow unlimited free transferring for up to 90 minutes after the first tap [19].

There have been some issues with the rollout of the C Spine. The difficulty for passengers in Lucan Village to access citybound buses at peak times has been raised in the Dáil, with the used of empty double decker buses on local routes at the same time being noted [20].

6. CONCLUSION AND SUGGESTIONS FOR FURTHER RESEARCH

Because of time limits, the scope of social media research was limited. A further study could take a wider look at social media accounts or use other methods to ascertain public opinion on the new network including travel surveys. One of the main findings of this research was that the improvement in frequency in Blessington from two to one hours helped generate acceptance of transfers but changing frequency from 20 to 10 minutes did not do so in other areas: a study could examine the time/frequency impact of the transfer penalty within Dublin. Several interviewees cited the failure to communicate the 90-minute fare (free transfer) during the consultation. Following its rollout in late 2021, its impact could be investigated. Finally, of the three case study areas, the affluent suburb of Howth appeared to have the most engaged and organised response to the BusConnects consultation. While other areas of the city (including Killinarden) were also engaged, there could be investigation as to socio-economic background impacts on such levels of engagement.

Some of these issues (particularly in relation to communication) were resolved over the course of the consultation process and in later drafts of the proposed network but other issues such as interchange infrastructure, security, frequency, and capacity will require ongoing attention and collaboration with stakeholders if the BusConnects project is to ultimately be successful. Immediate and ongoing examination will also be needed if a successful future research project into the project is to be carried out. It is hoped that these findings and the information provided in this paper can be of some value to those carrying out such research or designing similar network overhauls in the future.

ACKNOWLEDGEMENTS

Thank you to ITRN for the opportunity to present this paper. I would like to thank my dissertation supervisor David O'Connor, TU Dublin, for his indispensable support and guidance. I am also indebted to those who agreed to be interviewed for this research for their time and insights. Finally, I would like to thank my classmates on the MSc Sustainable Transport and Mobility at TU Dublin and my family for their support.

REFERENCES

[1]. Meskell, B. (2021). *Understanding the Factors that influenced the acceptance or rejection of transfers on Dublin 's new bus network* [TU Dublin]. https://library-cc.tudublin.ie/record=b5406559

[2]. Mees, P. (2009). Transport for suburbia: Beyond the automobile age. In *Transport for Suburbia: Beyond the Automobile Age*. https://doi.org/10.4324/9781849774659

[3]. Walker, J. (2012). Human transit: How clearer thinking about public transit can enrich our communities and our lives. In *Human Transit: How Clearer Thinking About Public Transit can Enrich our Communities and our Lives*. https://doi.org/10.5822/978-1-61091-174-0

[4]. Currie, G., & Loader, C. (2010). Bus network planning for transfers and the network effect in Melbourne, Australia. *Transportation Research Record*, *2145*, 8–17. https://doi.org/10.3141/2145-02

[5]. Badia, H., Argote-Cabanero, J., & Daganzo, C. F. (2017). How network structure can boost and shape the demand for bus transit. *Transportation Research Part A: Policy and Practice*. https://doi.org/10.1016/j.tra.2017.05.030

[6]. Nielsen, G. et al. (2005). *Hi Trans Best Practice Guide 2: Public Transport - Planning the Networks*.

[7]. Nielsen, G., & Lange, T. (2008). NETWORK DESIGN FOR PUBLIC TRANSPORT SUCCESS – THEORY AND EXAMPLES Civitas group of consultants. *Transport* , 30. http://www.ppt.asn.au/pubdocs/thredbo10-themeE-Nielsen-Lange.pdf

[8]. Grisé, E., & El-Geneidy, A. (2019). Transferring Matters: Analysis of the Influence of Transfers on Trip Satisfaction. *Transportation Research Record*, *May*. https://doi.org/10.1177/0361198119844964

[9]. Allen, J., Muñoz, J. C., & Rosell, J. (2019). Effect of a major network reform on bus transit satisfaction. *Transportation Research Part A: Policy and Practice*, *124* (April), 310–333. https://doi.org/10.1016/j.tra.2019.04.002

[10]. Hine, J., & Scott, J. (2000). Seamless, accessible travel: Users' views of the public transport journey and interchange. *Transport Policy*. https://doi.org/10.1016/S0967-070X(00)00022-6

[11]. Hernandez, S., & Monzon, A. (2016). Key factors for defining an efficient urban transport interchange: Users' perceptions. *Cities*. https://doi.org/10.1016/j.cities.2015.09.009

[12]. National Transport Authority. (2022). *BusConnects*. Www.Busconnects.Ie. https://busconnects.ie/ Accessed 28 June 2022

[13]. Jarrett Walker and Associates. (2019). *Dublin Area Bus Network Redesign. Revised Proposal*.

[14]. National Transport Authority. (2020). *Report on BusConnects Consultation 2019*.

[15]. Cresswell, J. W. (2009). *Research Design: Qualitative, Quantitative, and Mixed Methods Approaches* (3rd ed.). Sage.

[16]. Brown, J. R., & Thompson, G. L. (2012). Should transit serve the CBD or a diverse array of destinations? A case study comparison of two transit systems. *Journal of Public Transportation*, *15*(1), 1–18. https://doi.org/10.5038/2375-0901.15.1.1

[17]. Transport for Ireland (2021) 'H Spine'. Available at: https://www.transportforireland.ie/getting-around/by-bus/h-spine/ Accessed 28 June 2022

[18]. Transport for Ireland (2021) 'C Spine'. Available at: https://www.transportforireland.ie/c-spine/ Accessed 28 June 2022

[19]. Transport for Ireland (2022) 'Northern Orbitals'. Available at: https://www.transportforireland.ie/northern-orbitals/ Accessed 28 June 2022

[20]. Brennan, Cianan and McConnell, Daniel (2022) '€2bn revamp of Dublin bus services 'deplorable' TD claims 27 January 2022 https://www.irishexaminer.com/news/politics/arid-40794507.html' Accessed 28 June 2022

Public transport deprivation in County Limerick and the development of an effective rural public transport network

Thomas Bibby[1]
[1]MSc Sustainable Transport and Mobility, School of Transport Engineering, TU Dublin, Bolton Street., Dublin, Ireland
email: thomas@bibby.ie

ABSTRACT: This study examines public transport in Co. Limerick by analysing the quality of public transport service offered in each census settlement in the county to identify any transport deprivation and opportunities for improvement. A number of metrics are proposed to benchmark the level of provision of public transport services in a rural context, and how this provision aligns with car ownership rates. A proposed bus network and timetable is outlined that would give an 'every village, every hour' service to every census settlement in Co. Limerick.

KEY WORDS: CERI/ITRN 2022; Rural Public Transport; Network Design.

1 INTRODUCTION

The availability of public transport in rural areas can have a profound effect on economic participation and quality of life for individuals, as well as impacting the wider issues of sustainability and climate change, yet has received comparatively less attention in the literature compared with urban contexts. To address this lack, this study investigates access to public transport in settlements in Co. Limerick in the Mid-West of Ireland.

The local government area of Limerick city and county has a population of 194,899 (2016 census), with the majority living in Limerick city (population 94,192) in the east of the county. Newcastle West is the largest town (population 6,619), 42 km to the west of the city on the N21. There are 10 towns with populations from 1,000 to 3,000, 13 settlements of 500 to 1000, and 21 settlements with population under 500. Excluding the city, there are 14 settlements where more than 20% of households own no car. There are no rail connections west of the city. The terrain is mostly flat or rolling hills, with most settlements easily accessible by road, with some higher land on the county boundaries. The city and county councils merged in 2014, bringing challenges and opportunities for management of the county as a whole.

The existing public transport is examined and metrics devised and applied to provide a quantitative measure of the level of service of the public transport network. A public transport network for Co. Limerick is proposed that would provide an improved level of service, based on the principles of interchange, serving every settlement, every hour. The proposed network and timetable are evaluated for quality of service.

2 LITERATURE REVIEW

Compared with urban contexts, rural public transport has received comparatively less focus in the international literature. Hansson *et al.* [1] found that there is a lack of focus on regional transport in the literature. In a review of 7,968 public transport research papers published between 2009 and 2013, it was noted that the keywords "regional", "rural" or "interurban" did not appear once in the top 59 keywords, nor did any of those 59 top keywords relate to regional public transport [1].

The challenges of providing good public transport in rural areas has been noted, for example "the question of access to bus services can be most problematical in rural areas where demand density tends to be lowest" [2]. Despite the greater challenge of providing good public transport, there is also evidence that the lack of public transport has a greater effect in rural areas [3].

Petersen [4] outlines how a network planning approach based on pulse timetabling and an integrated approach is implemented in rural areas Switzerland. He notes that "pulse timetable-based approach can deliver a viable, high-quality, fixed public transport network in a region with very low population densities", even in an area with very low population densities and no significant urban settlements such as Lower Engadine.

Both Petersen [4] and Nielsen and Lange [5] acknowledge the contribution of Paul Mees to the development of public transport networks based on interconnection between different services, most memorably described in terms of his "Squaresville" example [6]. In this example he compares the effect of doubling service along unconnected lines with adding the same number of extra services to connect the lines instead, creating a network. While acknowledging that there may be a transfer penalty, Mees models an increase in ridership of 5.5 times with a two times increase in service provision. Although much of his research was focused on suburban areas with medium density, Mees did note that in the highly rural canton of Graubunden in Switzerland, a public transport network based on pulse timetabling and interconnection resulted in higher public transport ridership than most Australian or UK cities.

Although concerned mostly with public transport in urban areas, Walker [7] also notes that many of the challenges facing public transport network design are universal by nature, because they come down to geometry. He notes that whatever the population density of the areas being served, there are still fundamental questions of geometry involved that can only be

effectively answered by the use of connections between services.

Much of the research into rural public transport in Ireland has focused on the significant effect that poor public transport has on people in rural areas. This has been particularly noted for people on low incomes [8], people living with disabilities [9], and elderly people [10]. With reference to network design, it has been noted that the radial design of public transport networks in rural Ireland specifically hinders travel between smaller rural towns [9].

The main policy response to the lack of rural transport in rural areas has been to provide demand-responsive transport (DRT) through the Rural Transport Programme (now Local Link). Although this scheme has been shown to reduce car dependency where it operates [11], it is still the case that there are significant unmet transport needs in rural areas [12] even with the scheme in operation.

The appropriateness of DRT transport systems has been debated in the literature. It has been claimed that the effect of the actions of proponents of DRT is to mount a challenge to "conventional public transport" [4]. It has been noted that the aim of combating social exclusion has led to the fundamental unviability (in terms of ridership as well as operating costs): "By focussing on only providing rural services for minority groups and special groups, we have in fact put those services at a greater risk" [10].

3 METHODOLOGY

3.1 Demographic data

The demographic data of 45 out of 46 census settlements in Limerick (Limerick City was excluded) were examined according to mobility factors, including the percentage of households that do not own a car and mode share for work and education trips. The population of the settlements ranged from 144 (Tournafulla) to 6,619 (Newcastle West). The driving distance and time to Limerick City was calculated for each settlement using Google Maps.

For two census settlements in Co. Limerick, Ballyhahill and Fedamore, the census data was suppressed by the Central Statistics Office (CSO) to protect against disclosure. For these settlements, an estimation was made based on the relevant Small Area statistics surrounding the village.

3.2 Bus network

The existing timetabled bus network was examined. The number of services along each route variation was counted for Saturday, Sunday and Monday–Friday using the timetables published on each operator's website. Each route was mapped according to Google Maps and the distance for each service run was calculated. For routes that also serve settlements in other counties, the distance was calculated to the first settlement outside Co. Limerick. The number of services per week was multiplied by the route distance to calculate the total weekly route kilometres in the network.

3.3 Level of service calculations

For each of the 45 census settlements in Limerick, the timetables of all 33 route variations were used to calculate the average number of services per day, and the journey time by bus to Limerick City. The number of bus services per 1,000 inhabitants was calculated for each settlement to further investigate if any settlements were particularly underserved by public transport. The ratio of bus journey time to driving time by private car was calculated for each settlement as a proxy for the directness of the bus service.

A set of three quality of service metrics were chosen to assess the accessibility provided by the existing public transport services.

3.3.1 Departure time to reach Limerick City by 08:40

The employment accessibility metric chosen was the time of departure to reach Limerick City by 20 minutes before 09:00 to allow onward travel to the suburbs.

3.3.2 Departure time to arrive at a hospital appointment at 14:00

University Hospital Limerick (UHL) is on the western approach to the city. Buses travelling in from the west and south along the N20 (from Cork) and N21 (from Kerry) call directly at the hospital. For other services, although the journey time from Limerick Bus Station by bus is 16 minutes, arrival at the bus station is necessary before 13:25 to make a connecting bus to reach the hospital before 14:00.

This metric was chosen to reflect accessibility of essential services.

3.3.3 Existence of a bus back from Limerick City after 18:00

A test of whether or not a settlement had a return service back from Limerick City was used as a minimal proxy for the accessibility of socialisation and further education opportunities. The only cinemas in Co. Limerick are in the city and out of 40 evening courses listed on the government's fetchcourses.ie website, all of them are in Limerick City, therefore a service out from Limerick City is necessary to access these opportunities.

The results of the above tests were highlighted, and settlements that are particularly poorly served were highlighted by sorting by each metric.

3.4 Selection of services to define the public transport network and rationale

The following services were chosen to define the public transport network:

- Bus Éireann Public Service Obligation (PSO) services
- Bus Éireann commercial Expressway services
- Timetabled Local Link services

The following services were excluded as part of the public transport network:

- Privately owned and operated services
- DRT services operated by Local Link

3.5 The rationale for exclusion of privately owned services

Commercial services were excluded because although they are licensed by the National Transport Authority, they are not under the overall policy direction of the Minister for Transport, as is the case for Bus Éireann and Local Link.

3.6 Development of proposed network: initial steps

A set of criteria was developed to underpin the development of a proposed public transport (bus) network for Co. Limerick:

- It should serve all 45 census settlements.
- While it should focus on Co. Limerick, routes should serve villages and towns in adjacent counties where logical.
- Interchange should be used to increase route efficiency.
- Direct routes should be favoured over indirect routes.
- While the primary objective should be to link all settlements to Limerick City, a secondary objective should be to link smaller settlements to nearby larger ones, especially for settlements at a greater distance from Limerick City.
- The network should be as efficient as possible, where total route km to serve all settlements is the measure of efficiency.
- The network should be scalable to an "every village, every hour" timetable where all services run hourly.

An initial network was sketched out based on the existing public transport network in Co. Limerick, the regional road network and the initial objectives outlined above. Distances between village pairs on the route were calculated using Google Maps and travel times were calculated based on looking up car driving time on Google Maps, applying a 50% increase and rounding up.

3.7 Timetable development

Once the initial network and journey times had been constructed, timetables with a single run in both directions for all routes were developed. The objective of developing the "single run" timetables was to identify and synchronise interchange opportunities where different routes served the same settlement. Synchronisation at this stage of the process was in terms of services arriving and departing at the same "minutes past the hour".

An iterative process of changing departure times to enable interchange was followed: as some single routes interchanged with more than one other route, a large amount of "rechecking" was needed to see how changes in the timing of one route would cascade down to affect interchange in other routes.

Different combinations of radial and orbital routes were experimented with, to improve interchange and journey time on individual routes, as well as reducing the overall route km of the network.

Once a number of iterative network development passes had been carried out, full timetables for all services were written based on the hourly timetable pattern identified, between 06:00 and 22:00, giving 16 services a day.

3.8 Reduced 2-hourly timetable

To assess the potential impact of a less significant increase in route km, the timetable was cut to a 2-hourly service, or eight services a day between 06:00 and 21:00. The reduced timetable was worked through to make sure all previous interchanges between routes were possible, and additional services were added if needed to re-establish interchanges for services to Limerick City. The reduced network was assessed again in terms of 2-hour morning commute and 14:00 hospital appointment time.

4 RESULTS

4.1 Current public transport provision in Co. Limerick

A total of 947 services a week were counted, giving a total of 12,046 km per week or 614,366 km per year. A total of 17 advertised services were analysed (14 Bus Éireann, three timetabled Local Link), with a total of 33 route variations being taken into account.

The analysis of the bus network in Co. Limerick showed that a total of nine settlements (20%) in Co. Limerick are not served by any timetabled public transport whatsoever, and a further nine are served by an average of four or fewer services in any direction per day, defined as a very low level of public transport provision. Table 1 shows the settlements in these categories together with population, percentage of households with no car, and average number of services per day.

Table 1. Settlements with no or very low timetabled public transport.

Settlement	Population	Average services/day	% households no car
Ballingarry	521	0.0	13.8%
Athea	369	0.0	24.0%
Fedamore	329	0.0	9.6%
Broadford	276	0.0	16.5%
Mountcollins	201	0.0	8.5%
Ballyagran	179	0.0	10.0%
Kilteely	171	0.0	18.8%
Ballyhahill	146	0.0	8.9%
Galbally	251	1.4	15.2%
O'Briensbridge–Montpelier	396	1.7	8.9%
Ballylanders	308	2.1	20.2%
Knocklong	256	2.1	18.9%
Doon	516	2.6	21.4%
Bruree	580	2.9	16.7%
Ardagh	266	3.0	18.4%
Kilfinane	789	3.4	18.5%

A further 17 settlements have an average of between four and 11 bus services daily and the final 11 settlements have over 11 bus services on average daily.

For each settlement, three metrics were measured: whether it is possible to depart at 07:00 or later in order to reach Limerick City at 08:40 to facilitate travel to suburban employment areas before 09:00 (less than 2 hours journey time), whether it was possible to depart 3 hours or less before a hospital appointment for UHL at 13:00, and if a service departing Limerick City after 18:00 existed. Table 2 gives the proportion of the 45 settlements in Co. Limerick that meet each of the three criteria.

Table 2. Effectiveness of existing public transport network according to selected criteria.

Metric	Percentage
Work <2 h	60%
Hospital <3 h	29%
Return >18:00	22%

4.2 Network development

The network development started by sketching out in a table the spatial distribution of settlements in Co. Limerick. From this initial draft a grid network was laid out, following the path of regional and significant tertiary roads. The initial network designed consisted of eight radial services and nine orbital services, giving all settlements a connection to Limerick City with at most one interchange. The initial network included adjacent settlements in neighbouring counties where appropriate.

The expected travel time between settlement pairs was calculated with reference to existing bus timetables. For shorter links, the journey time was calculated as 150% of the car journey time, rounded up. For longer links, a time of 10 minutes was added to the journey time by car.

Once the journey times had been calculated, a timetable was constructed for each service in each direction. Once the first route had been timetabled, the timetable for route that intersected with the original route, syncing the time of intersection. This was repeated to build out the timetable for the whole network.

To simplify the task of timetable synchronising, as the network was highly connected, a decision was made to prioritise interchanges that would allow settlements without a direct service to Limerick City to transfer to a service that served Limerick City.

After a number of iterations of shifting timetables to facilitate interchange, a number of interchanges were still not synchronised. The network was then changed to see if a change in network structure could improve interchange at certain points. The iterative process of syncing interchanges was then restarted.

4.3 Final network design and timetable

After a number of passes of timetable syncing and network redesign, a final network was produced as shown in Figures 3 and 4.

Figure 1. Geographical map of proposed network

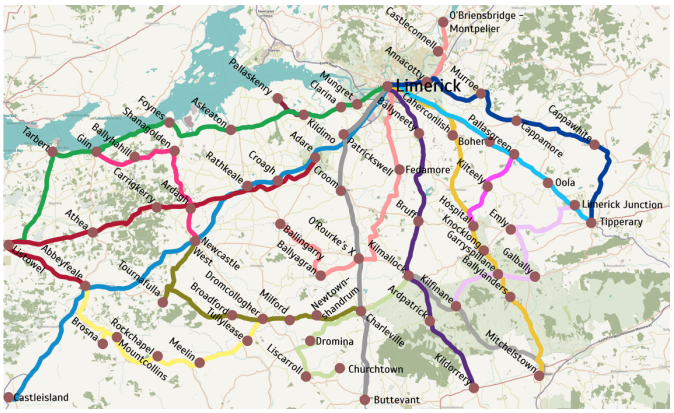

Figure 2. Symbolic map of proposed network

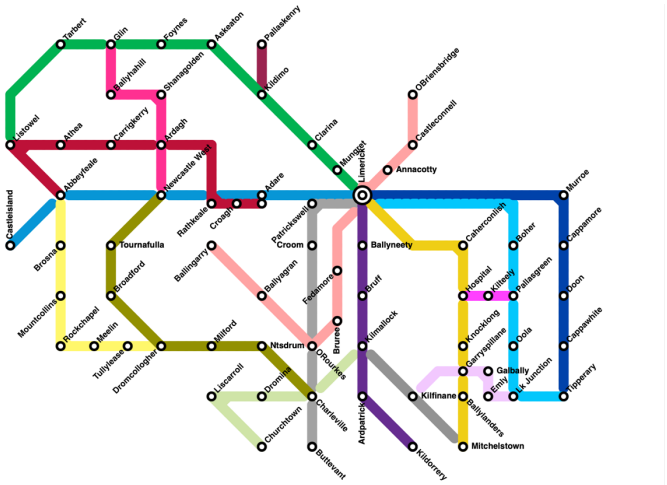

4.4 Hourly timetable and total route km

The new network was then analysed in terms of route km and buses needed. The route km for each hourly "pulse" is 1,156 km for the portion of the network within Co. Limerick. Based on a 7-day hourly service between 06:00 and 22:00 (16 services a day), the total route km of the network would be 129,472 km a week, which is 10.7 times the current route km of 12,046 per week.

4.5 Two-hour timetable

To investigate a less significant increase in route km, a 2-hourly timetable was modelled between 06:00 and 22:00. It was found that the timetable could shift to 2-hourly and all connections to Limerick City could be kept, apart from services on three of the 17 lines. To simplify the interchange modelling, these three services were kept at an hourly frequency and all other services were changed to eight 2-hourly services a day. This would then be 75,040 route km a week, a 6.2 times increase on current service provision.

5 ANALYSIS

5.1 Significant public transport deserts in Co. Limerick

The study identified nine settlements that can be classified as public transport deserts as they are not served by any timetabled public transport service. A particularly notable case is the village of Athea, which has the second highest rate of households without a car in Co. Limerick at 24.0%, behind only Rathkeale. It is also notable that Athea has a higher proportion of households without a car than Limerick City and suburbs. This is a significant case of transport deprivation and it is suggested that Athea be prioritised for any future public transport provision. Overall, the proportion of households with no car in this settlement classification ranged from 8% to 24%.

All of these settlements with the exception of Fedamore are in the West of Co. Limerick and all nine settlements are not on significant roads travelling through the county. While some of these settlements were straightforward to serve in a new network, a few (notably Ballyagran and Ballingarry) were a challenge to incorporate into the network and needed a comparatively circuitous service to serve them.

5.2 Transport deprivation exists in most towns

The nine settlements that had some public transport service could not be said to be well served by public transport, having between one and four services a day in any direction. The rate of households without a car ranged from 8.9% to 18.9%. None of these settlements had a service back from Limerick after 18:00, denying residents without a car the opportunity to socialise or take advantage of night classes. Only three out of the nine settlements in this category are served by a bus service that arrives by 08:40 that would be suitable for accessing many employment opportunities. Bus services to this category of settlement also have the characteristic of having a high journey time by bus compared with the private car: with settlements such as Ardagh (2.7 times) and Doon (2.6 times) particularly poorly served in this regard.

5.3 Overall level of performance provided by the network

The current public transport network in Co. Limerick plays some role in enabling people to access employment on an office timetable, with people in 60% of settlements able to get to Limerick City in time for starting work at 09:00, but it does not facilitate people who do not work 9–5, as the network only allows people in 29% of settlements to travel to a middle of the day hospital appointment within 3 hours, and only 22% of settlements have a service from Limerick City after 18:00.

5.4 Performance of proposed hourly and 2-hourly networks

The developed hourly network has the following qualities:

- All settlements have an hourly service 06:00 to 22:00.
- All settlements can reach Limerick City by 08:40.
- 91% of settlements can reach Limerick City by 08:40 by setting off after 07:00.
- 73% of settlements can reach a hospital appointment for UHL by setting off after 12:00.

Table 3 shows a summary of the effectiveness of both the proposed hourly and the proposed 2-hourly networks, together with the existing network.

Table 3. Comparison of existing and proposed networks under effectiveness metrics.

Evaluation of efficiency	Hourly	2-hourly	Existing
2-hour morning commute	91%	91%	60%
2-hour hospital appointment	73%	11%	29%
3-hour hospital appointment	100%	89%	29%
Service from Limerick after 18:00	100%	100%	22%

5.5 Journey times

The new timetable was compared to the existing timetable to see whether the time of departure for the morning work journey and the afternoon hospital appointment had improved. For the work trip, 65% of journeys enabled a later departure time (including where journeys are not possible in the current timetable). For the hospital trip, 76% of journeys enabled a later departure time. The 35% of work journeys that would be slower is a significant dis-improvement from the current timetable. The reason for this is that the new table is optimised for interchange, which means services may depart and arrive earlier in the hour so their connections with other routes are synchronised.

5.6 Use of interchange

Out of the 45 settlements, 30 are served with direct services to Limerick City in the final network. This is a significant level of interchange in an Irish public transport context but it is much less than in earlier network designs, due to the practicalities of synchronising timetables at interchange points outlined earlier. Of the remaining 15 services requiring a transfer to reach Limerick City, nine of these transfer from and to one line.

Overall, there are 25 interchanges between different pairs of the 17 lines on the network (where three lines intersect, this will result in three line-pairs of an interchange). Of these, 12.5 of the interchanges are timed in at least one direction. That is, two buses will arrive and depart at the same time. The other 12.5 interchanges are not timed.

Because only half of the interchange points are synchronised in the timetable, the network may result in user confusion. This is potentially exacerbated by the use of a London Underground-style network map. A user may expect to be able to transfer between different services at any interchange point without having to wait

Finally, although some extra padding was put into the timetable to facilitate interchange between services, it is possible that the network will not be reliable enough to consistently offer interchange. This is a risk to the viability to the network.

6 SUMMARY AND CONCLUSIONS

Significant transport deprivation was found in Co. Limerick. Many settlements in Limerick have a high proportion (above 15%) of households with no car and some of these settlements are served by no timetabled public transport at all. The current timetabled public transport network does not serve nine census settlements at all.

Three basic metrics were developed to measure the quality of service provided by the network: the departure time to reach Limerick City for 08:40 for transfer on to suburban services for employment for a 09:00 work start time, the departure time for a hospital appointment for UHL at 14:00, and whether a service after 18:00 from Limerick City exists. Under existing timetables, 60% of settlements are served for work with a 2-hour threshold, 29% are served for the hospital trip with a 3-hour threshold, and 22% are served for a service from Limerick City after 18:00.

A public transport network and timetable was developed to serve every census settlement in Co. Limerick with an hourly bus service between 06:00 and 22:00. The network was developed from a comprehensive grid with many orbital services to a network where two thirds of settlements had a direct connection to Limerick City and one third had to make use of interchange.

The proposed network has a weekly route km of 129,472 in Co. Limerick, which is 10.7 times the current route km per week of 12,046. The proposed network would need 53 buses to operate it, not including driver breaks. It would give every census settlement in Limerick an hourly connection to Limerick City.

Using the same criteria as previously, 91% of settlements are served for work with a 2-hour threshold, 91% are served for the hospital trip with a 3-hour threshold (and 73% with a 2-hour threshold), and 100% are served for a service from Limerick City after 18:00.

The 2-hourly route km total in Co. Limerick (with three routes being kept on an hourly timetable to facilitate interchange) would be 75,040, or 6.2 times the current route km, needing 37 buses. 91% of settlements would be served for work with a 2-hour threshold, 11% are served for the hospital trip with a 3-hour threshold (and 89% with a 2-hour threshold), and 100% are served for a service from Limerick City after 18:00.

The proposed network was critically examined and it was noted that although relying on interchange brought some efficiency benefits, there may be barriers to significant modal shift on the network.

ACKNOWLEDGMENTS

This paper is based on research completed for a dissertation completed as part of an MSc. in Sustainable Transport and Mobility at TU Dublin. The assistance and advice of dissertation supervisor Sinead Canny is gratefully acknowledged.

REFERENCES

[1] Hansson, J. *et al.* (2019) "Preferences in regional public transport: a literature review," *European Transport Research Review*, 11, Art. No. 38. doi: 10.1186/s12544-019-0374-4.

[2] Balcombe, R. *et al.* (2004) "The demand for public transport: a practical guide." Transportation Research Laboratory Report (TRL593). Transportation Research Laboratory, London, UK. Available at: https://www.researchgate.net/publication/32885889_The_demand_for_public_transport_A_practical_guide (Accessed May 31, 2021).

[3] Lucas, K. (2012) "Transport and social exclusion: Where are we now?" *Transport Policy*, 20, pp. 105–113. doi: 10.1016/j.tranpol.2012.01.013.

[4] Petersen, T. (2016) "Watching the Swiss: A network approach to rural and exurban public transport," *Transport Policy*, 52, pp. 175–185. doi: 10.1016/j.tranpol.2016.07.012.

[5] Nielsen, G. and Lange, T. (2005) "HiTrans Best Practice Guide No. 2, Public Transport: Planning the Networks," *Interreg IIIB project: HiTrans-Development of principles and strategies for introducing high quality public transport in medium sized cities and regions*. Available at: http://civitas.no/assets/hitrans2publictransportplanningthe-networks.pdf (Accessed: May 31, 2021).

[6] Mees, P. (2009) *Transport for suburbia: Beyond the automobile age*, Routledge, London. doi: 10.4324/9781849774659.

[7] Walker, J. (2012) *Human transit: How clearer thinking about public transit can enrich our communities and our lives*, Island Press, Washington DC. doi: 10.5822/978-1-61091-174-0.

[8] McDonagh, J. (2006) "Transport policy instruments and transport-related social exclusion in rural Republic of Ireland," *Journal of Transport Geography*, 14(5), pp. 355–366. doi: 10.1016/j.jtrangeo.2005.06.005.

[9] Gallagher, B. A. M. *et al.* (2011) "Mobility and access to transport issues as experienced by people with vision impairment living in urban and rural Ireland," *Disability and Rehabilitation*, 33(12), pp. 979–988. doi: 10.3109/09638288.2010.516786.

[10] Ahern, A. and Hine, J. (2012) "Rural transport - Valuing the mobility of older people," *Research in Transportation Economics*, 34(1), pp. 27–34. doi: 10.1016/j.retrec.2011.12.004.

[11] Carroll, P., Benevenuto, R. and Caulfield, B. (2021) "Identifying hotspots of transport disadvantage and car dependency in rural Ireland," *Transport Policy*, 101, pp. 46–56. doi: 10.1016/j.tranpol.2020.11.004.

[12] Rau, H. and Vega, A. (2012) "Spatial (Im)mobility and Accessibility in Ireland: Implications for Transport Policy," *Growth and Change*, 43(4), pp. 667–696. doi: 10.1111/j.1468-2257.2012.00602.x.

Investigate the rural mobility and accessibility challenges of Seniors using the Free Travel Scheme.

Tom Ryan[1]
[1]Technological University Dublin, Bolton Street, Dublin 1, Co Dublin, Ireland.
Email : D19127880@mytudublin.ie

ABSTRACT: This paper investigates the rural mobility and accessibility challenges of a specific target group - Seniors. The target group is those over 66 years of age who are entitled to use the Public Transport (PT) Free Travel Scheme in rural Ireland. The paper explores at a high level some of the projected rural PT challenges and requirements over the next 10-15 years, noting that statistical predictions show that there will be a significant population demographic shift within the Senior's age profile. Using the PESTEL framework, the literature review explored existing research concerning mobility, accessibility challenges, and the opportunities Seniors face.
Twenty-seven qualitative in-depth interviews with stakeholders within the ecosystem were undertaken. The stakeholders included: rural PT customers, Local-Link managers, NTA senior management, a Minister of State, and a European parliament policymaker. Tier 1 interviewee feedback spotlights that the PT network system does not exist for rural patients to access hospital facilities. There was no evidence from the Tier 2 research findings to show that health policymakers and transport planners are working to deliver a national solution to support patients getting access to hospital appointments. Several research interviewees discussed the theme of isolation and the perceived stigma of senior males utilising PT. The findings indicated that MaaS is potentially revolutionary in the PT arena.
Finally, this paper suggests several short-, medium- and long-term recommendations based on the research findings. These recommendations are a potential springboard to ensure that rural PT is suitable for future Irish generations.

KEY WORDS: Accessibility; Active ageing; Car dependence; Isolation; Seniors' health issues; Behavioural change; Environmental challenges; Internet of Things (IoT); Demand-responsive; Mobility as a Service (MaaS).

1 INTRODUCTION

1.1 Introduction background

Growing up and living in rural Ireland, surrounded by green fields, small villages, and working on the land, is viewed as having a very idyllic lifestyle. Seniors in rural Ireland depend on mobility and getting around to complete the basic daily chores. If access is reduced or removed, the daily tasks become very complicated, if not impossible, resulting in limited personal mobility. Walker defined 'personal mobility' as a 'degree of freedom,' this freedom results in 'ease of moving about' [1]. Demographically a fundamental change is taking place in society. The maturing sector of the population is statistically growing at a faster annual rate than ever before. This sector is dynamic, independent, and living longer; they are 'evolving as a major source of consumption, with extended periods of free time and a desire to travel' [2].

Those working and living in rural Ireland are more car-dependent than people living in urban areas. However, the picture is very different for Seniors in rural Ireland without access to a car or PT. The practical impact of poor or no access can result in not having the independence to get to the local shop, collect the pension, get to the doctor for a general check-up, or collect a prescription on time [3].

This research will review the impact of rural transport on Seniors who live in rural areas. Preliminary interviews indicated that accessibility to the community is critical. If Seniors are not mobile or do not have access to PT options, the long-term impact can be very detrimental, potentially resulting in isolation and loneliness. 'Mobility does not always generate movement, but it does generate happiness' [1]. In practical terms, poor accessibility can result in sections of the rural countryside not meeting or speaking to neighbours from one week to the next. The research paper will explore the mobility challenges and requirements of rural users of the PT Free Travel Scheme. Those entitled to the Free Travel Scheme card are entitled to 'bus, rail and Dublin's LUAS with some exceptions' in the 28 counties free of charge [4]. For this research paper, it is proposed to refer to any person over sixty-six as a 'Senior.' Sixty-six is the specific legal age at which Irish residents qualify for the Free Travel Scheme.

1.2 Research paper objectives

This research paper explores whether the current system can cope with the increased demand and pending challenges. The primary objective was to investigate and address the accessibility issues experienced by Seniors looking to access the PT Free Travel Scheme in rural Ireland. The research paper explores actual and perceived PT mobility challenges among Seniors and solutions that might bridge any gaps. The research will look at multiple factors which restrict or prevent Seniors from accessing the PT Free Travel Scheme. It will explore the dangers and risks to the well-being of Seniors when they become immobilised. The research paper will explore if a change needs to occur to address any potential accessibility challenges of rural users and explore technology opportunities to include 'user' technology supports and demand response transport options.

The five steps identified to deliver the research project's objectives are the following:

1. Carry out a literature review;
2. Define methodology;
3. Implement/carry out research;
4. Assess findings and provide discussion;
5. Provide conclusions.

2 LITERATURE REVIEW

2.1 Exploring existing research

The literature review aims to explore existing research concerning accessibility challenges and opportunities faced by Seniors in rural Ireland, particularly regarding their use of PT. The literature review explores:

- The value and benefits of PT accessibility within a rural locality.
- International best practice papers and journals highlighting and addressing rural PT accessibility issues.
- Behavioural changes required to address environmental challenges.
- International technology solutions that support the needs and wants of PT rural users and the benefits of independent mobility to support active ageing.
- The impact of the demographic shift on rural communities.

2.2 Motivation behind the research

The motivation behind the research - a significant population shift will occur in Ireland over the next fifteen years. The transport industry is evolving, and new technologies challenge how customers access and use PT in rural regions. The research investigated how other regions utilise technology solutions to address and solve mobility issues for older people. The investigated areas included Demand Responsive Transport (DRT) solutions and trip sharing services. A review of published literature was undertaken. The researcher explored what is known about the topic area and determined other researchers' approaches. A literature review determined whether this research was 'exploratory' and could help 'advance what is already known about the topic' [5].

- The literature review research findings were presented using the PESTEL framework.
- This framework helped present the extensive literature review in a formalised way.
- Topics reviewed included active ageing both in Ireland and mainland Europe. An extensive literature review was undertaken on transport economics, social change, and behavioural change interventions. Independent and global mobility for Seniors was also an area that was researched. Several international rural transport case studies were reviewed.
- Extensive online research was done regarding technology. MaaS and IoT were researched. A review of how these technologies could be leveraged to utilise existing state-owned assets was undertaken.
- This research paper explored the National Transport Authority and the Local Link program. It reviewed the Green Deal 2050 and the impact of environmental change on PT.
- The researcher found several gaps when compiling the literature review.
- Transport-related papers found limited resources when addressing social problems like transport poverty and isolation.
- There was little evidence to support the value and benefits of collaboration between different state organisations, such as transport access to hospitals and day-care centres.
- The researcher found limited literature on the use of MaaS in rural locations.

2.3 Goals of the literature review

A key objective of this section was to investigate existing literature concerning rural mobility and accessibility challenges in the context of Seniors using PT. Related topics, up-to-date papers, peer-reviewed articles, and published transport-related journals were reviewed. The European Union and government published reports also form part of the research literature review.

2.4 Structure and approach - PESTEL analysis

Using the PESTEL framework to structure literature review research, the researcher investigated the Political, Economic, Social, Technological, Environmental, and Legal factors (PESTEL) that influence Seniors accessing rural PT. The PESTEL framework process provides a practical approach to exploring the context of accessibility for Seniors in rural Ireland, areas of potential change such as population and technology. The literature review also looked at external and internal variables plus the strengths, weaknesses, opportunities, and threats (SWOT analysis) that could influence the research question. The literature review was strategically analysed and evaluated using the PESTEL framework in Figure 1.

Figure 1 PESTEL framework [6].

3 METHODOLOGY

3.1 Research methodology

Strategy/research design - Qualitative research methods explored the barriers experienced by users of PT services in rural areas. Time has been spent analysing target audiences and reviewing population demographic shifts over the next fifteen years. The methodology chosen for this research was based on using the funnelling process. The funnelling process helped 'frame' the research paper question [9]. Work experience and

background reading have shown the researcher the importance of awareness of the needs and wants of end-users.

- For this research paper, the researcher undertook primary qualitative interview research.
- Strategically the researcher created two stakeholder groups.
- Recorded interviews were completed with at least one member from each stakeholder subset. The interviewee subsets included PT rural Seniors, drivers, transport operators, rural transport policy stakeholders, non-transport stakeholders, an international transport advisor, national PT policy stakeholders - Minister of State, and European transport policy decision-makers - European MEP policymaker.
- The research findings found evidence of several gaps in published literature. From the primary qualitative research, PT users and drivers viewed isolation as a critical concern. The research did not find many published transport-related articles that addressed isolation's impact on Seniors.
- The findings indicated that MaaS was viewed as a potential transport influencer. However, many of the published articles on MasS were focused on urban areas. The findings show evidence that there is potential for further research to be undertaken and published to address the knowledge deficit to address demand-responsive trips and Rural-MaaS. These technology platform concepts show potential over the next 10-15 years to address rural PT requirements for Seniors.
- The research process was unable to find much-published literature to address the topic of interconnecting state-run services. The research findings indicate that benefits and synergies can be gained by collaboration between different government departments.
- The findings indicate a fantastic opportunity to do in-depth quantitative research on demographic shift, population density, and national census trends. This quantitative research could help create primary data to support a much-needed overarching strategy for the next 10 to 15 years.

3.2 Research philosophy – data collection

The focus of this research project was to utilise qualitative research methods. Qualitative research is a 'systematic inquiry into social phenomena' in naturalised settings [8]. Qualitative research focuses on 'human experience through systematic and interactive approaches' [9]. Qualitative research methods are used when 'little is known about the topic' and 'allows the researcher to explore meanings and interpretations of constructs rarely observed in quantitative research' [8]. The preferred approach was that all interviews would have been face-to-face 'in natural settings' to help 'provide a context to observed phenomena' [12]. Due to Covid-19 restrictions, research interviews were unable to be conducted face-to-face. The PT rural users' interviews focused on users' experience and the process undertaken to make a trip using PT. Interview responses were general and 'not specifically about facts and figures' [10]. Qualitative research approaches are 'phenomenology, ethnography, and grounded theory' [12]. The first stage of the qualitative research study identified a problem in the PT arena. The identified problem areas were then refined into a research question. 'Additional research questions 'emerged from the researcher's literature review and stakeholder feedback [12]. In the article 'Assessing the methodological quality of published papers', it was stated that 'qualitative research studies do not begin with a hypothesis'; however, 'some studies may result in the formation of hypotheses' which during the research process are 'tested using quantitative methods' [10]. The research paper explored 'how individuals and groups behave, how organisations function, and how interactions shape users' experience of PT in a rural setting [8]. The researcher was the 'primary data collector and used a qualitative research approach' [11]. The researcher used interviews to examine why certain actions occur when they happen and then interpret the impact positive or negative when those events occur as planned. Qualitative interview research tools were used to investigate and explore the research question. Interviews focused on the elements and events that supported rural PT 'from the perspectives of those involved' in the process [8].

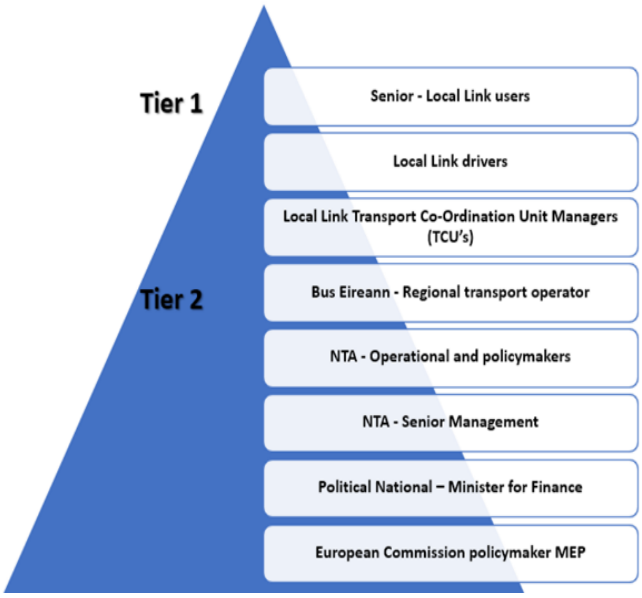

Figure 2 Tier 1 and Tier 2 research interview stakeholders.

The researcher undertook interviews at each stakeholder level, as highlighted in Figure 2. The interview numbers may not be exhaustive; however, the researcher believes that no link in the chain was omitted as per Figure 3. A significant limiting challenge was affording time to find interviewees and transcribing recorded interviews.

4 RESULTS/FINDINGS

4.1 Interview research themes

The research findings have been segmented into multiple themes. Each interview was transcribed and reviewed. Common themes were distilled and coded for the Tier 1 and Tier 2 stakeholders. The following Venn diagram Figure 4 highlights the research themes found during the thematical analysis phase. The findings explored first-hand interview references to support the primary research interview themes in greater detail.

Interview number	Stakeholder group	Stakeholder profile	Name of stakeholder interviewed:
No. 1	Stakeholder Group 1.	Local Link Senior customer	Dan X. Local Link customer
No. 2		Local Link Senior customer	Bernard X. Local Link customer
No. 3		Local Link Senior customer	Janette X. Local Link customer
No. 4		Local Link Senior customer	Michael X. Local Link Customer
No. 5	Stakeholder Group 1.	Accessibility wheelchair user	Evie X. Public transport wheelchair customer
No. 6	Stakeholder Group 1.	Local Link drivers	Joe X. Local Link Driver
No. 7		Local Link drivers	Mick X. Local Link Driver
No. 8	Stakeholder Group 1.	Regional transport manager	Mr Damien O' Neill TFI Local Link Longford Westmeath Roscommon Manager
No. 9		Regional transport manager	Mr Anthony Moroney TFI Local Link Tipperary Manager
No. 10		Regional transport manager	Mr Alan Kerry TFI Local Link Kildare South Dublin Manage
No. 11	Stakeholder Group 2.	National Seniors advocate group	Mr John McWeeney Age Friendly Ireland - Assistant Civil Defence Officer
No. 12	Stakeholder Group 2.	Transport Operator - Regional	Mr Robert O'Mahoney Head of PSO Contracts Bus Eireann
No. 13	Stakeholder Group 2.	Connecting Ireland planner	Mr Edward Rhys Thomas Transport Planner NTA
No. 14	Stakeholder Group 2.	National Local Link policy manager	Ms Blathin McElligott Local Link Programme Manager NTA
No. 15	Stakeholder Group 2.	National Transport Authority	Mr Declan Sheehan Chief Information Officer NTA
No. 16		National Transport Authority	Mr Bernard Higgins Director of Transport Technology NTA
No. 17		National Transport Authority	Mr Tim Gaston Director of Public Transport Services NTA
No. 18		National Transport Authority	Mr Hugh Creegan Director of Transport Planning & Investment, Deputy CEO NTA
No. 19		National Transport Authority	Ms Anne Graham Chief Executive Officer NTA
No. 20	Stakeholder Group 2.	International Transport Mobility expert	Mr Jason Clark Mobility Consultant ex Transport For London TFL
No. 21	Stakeholder Group 2.	National political policy maker	Mr Paschal Donohoe Minister for Finance of Ireland
No. 22	Stakeholder Group 2.	European political policy maker	Mr Ciarán Cuffe Member of European Parliament MEP for Dublin

Figure 3 Inverted Stakeholder organisational eco structure pyramid.

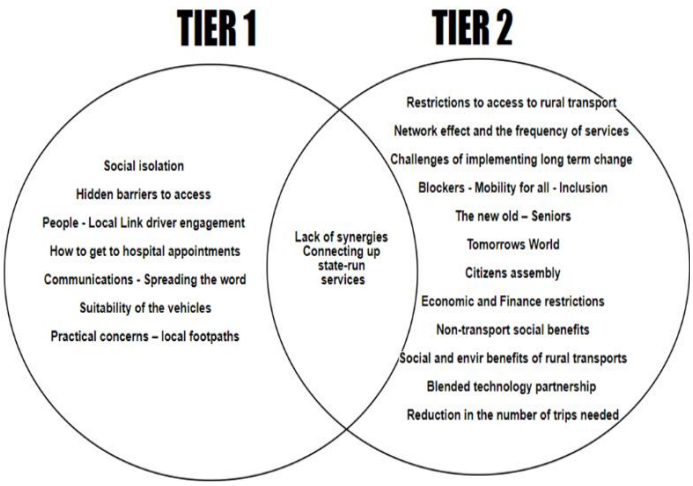

Figure 4 Venn diagram of research findings.

4.2 Tier 1 interview research themes - Social isolation

A recurring word that all Tier 1 interviewees repeated was the word isolation. The word isolation was not used in any of the interview questions. The researcher did not actively or purposely use the word to lead interviewees.

4.3 Discussion of research findings

The research findings indicate that health policy creates urban centres of excellence, staffed to provide a best-in-class medical system. However, the Tier 1 interviewee feedback spotlights that the PT network system does not exist for rural patients to access these hospitals.

There was no evidence from the Tier 2 research findings to show that health policymakers and transport planners are working to deliver a national transport solution to support patients getting access to hospital appointments.

Major strategic decisions need to be made regarding building a sustainable rural PT network to address access for Seniors to hospitals, day-care centres, and even step-down nursing homes.

The research findings uncovered the real and perceived barriers that Seniors in rural Ireland experience when accessing PT. Several research interviewees discussed the phenomenon of resistance and the perceived stigma of senior males using rural PT. Seniors living in rural Ireland have become car-dependent. Access to PT is critical for those without a car or a medical reason who can no longer drive.

The findings confirmed how valuable an excellent rural transport network is to every small village and rural community.

- The research indicated the importance of delivering the mobility services and trip destinations that Seniors need and want when using the Free Travel Scheme.
- A key research finding was that behavioural change and lifestyle initiatives are needed to help inform and educate Seniors to help reduce short car trip dependency.
- A key finding was the requirement to deliver new transport products and services for Seniors in rural areas. Examples are services to regional hospitals and day-care centres.

There were some boundary restraints. The researcher would have liked to have completed focus groups. However, due to Covid-19 restrictions, this was not possible.

4.4 Short, medium, and long term

The recommendations fall into three-time frame categories: short, medium, and long term. All concepts in the recommendations section are distilled ideas that have been evidence-driven. These ideas have been informed during the literature review, primary qualitative research, and reflection during the research process.

4.5 Short-term recommendations

- *Recommendation 1*

To deploy a rural real-time passenger information (RTPI) system for all Local Link services. A rural RTPI Global Positioning System (GPS) offering for all Local Link public services would improve confidence in arrival and departing times for Senior users. This rural RTPI product offering would build peace of mind for all Seniors looking to use the Local Link RTPI App service.

- *Recommendation 2*

To pilot a range of people-carriers or small accessible vehicles within the Local Link fleet. The findings indicated accessibility issues and concerns about the size of the Mercedes Sprinter. The pilot should only be run using electric vehicles (EV).

The pilot EV fleet should be tested for its suitability to address the first and last five kilometres' challenges and trialling access points to the new Connecting Ireland network. This pilot project would strive to deliver pockets of sustainability to the Local Link national service.

- *Recommendation 3*

To create a year-round advertising promotional campaign. Design local-based campaigns which could leverage local radio and regional press. A promotional campaign should highlight how to access the Local Link service and where and when they run. Seasonal campaigns should promote the actual Local Link services in each local area.

- *Recommendation 4*

To create branded marketing material to promote pickup and drop off zones for Local Link service locations. This physical bus stop infrastructure Local Link branding should be rolled out across the country. The Local Link branding needs to be visually identifiable throughout the country. This identity project will help promote confidence and build brand awareness across the marketplace.

- *Recommendation 5*

To review entry criteria to access the Free Travel System for those who need free transport but are under 66. It is evident that some people fall between the cracks and may need the Travel Pass before 66 in certain circumstances to address transport poverty.

- *Recommendation 6*

The final short-term recommendation would be to engage with the Citizen's Assembly network. This process would review how people live in rural Ireland, what they do, where they go and how they use rural PT to access services. The main objective should be to unearth the primary reasons that block the delivery of independent mobility in rural Ireland. This public process could potentially unlock and be transformative across many interlocking state organisations, not just the transport arena. The solutions-based process should look to roll out pilot test projects. Each solution needs to be scalable.

4.6 Medium-term recommendations

- *Recommendation 7*

The first medium-term recommendation looks at how the NTA could research and build a procurement tender to deliver a centralised national Local Link booking system. The centralised national booking system should be managed and financed by the NTA. A centralised system should manage each Local Link booking. A back-office prediction generator would potentially decide the most suitable vehicle type for each group or individual booking.

- *Recommendation 8*

Pilot options of a new Local Link vehicle type similar to the BRUCK. This multi-service vehicle would blend seat types for children and Seniors. The service could potentially support trips for schoolchildren in the morning, trips for Seniors and the delivery of small medical prescriptions throughout the day.

- *Recommendation 9*

Recommends a Business Intelligence (BI) gathering process that looks to collect quantitative research data. The research needs to track the travel patterns of Seniors who are independently mobile and support a healthy lifestyle. The data needs to map the active ageing population of the state. This data must inform and support the NTA strategy to deliver evidence-driven solutions for the next 10-15 years.

4.7 Long term recommendations

- *Recommendation 10*

A flexible and dynamic public-private model will build a long-term public-private procurement strategy. The blended model would strive to deliver defined outputs in a commercial platform partnership.

Two key deliverables would include the following:

Options to address a private hackney solution for hard to reach first-and-last One2Five KM rural trips.

Build a centralised customer experience entry point system. This system could operate the following platforms - contact centre, multi-platform Smartphone App and web-based platform.

- Recommendation 11

Significant changes will need to occur to the Local Link transport fleet. These changes need to deliver good quality, sustainable fit for purpose transport fleet. The NTA needs to set up a programme to migrate from the diesel-powered Mercedes Sprinter vehicle to a more environmentally friendly solution of mixed-use EVs.

- *Recommendation 12*

It is advised that the option to create a Rural-MaaS platform technical ecosystem should be looked at in the long term. Rural-MaaS could potentially deliver information to customers to help them access rural PT services.

In conjunction with the Rural-MasS project, autonomous EVs should also be piloted in remote locations. This project could help promote accessibility and remove car dependency for Seniors in hard-to-reach locations.

- *Recommendation 13*

The final long-term recommendation looks to a far more long-reaching subject of sustainable living. A national review needs to integrate more accessible services into rural villages by fostering public participation.

This environmentally sustainable research project needs to look at ways to promote how Seniors live independently in age-friendly villages and rural settlements. The project would need to investigate options to restructure our state services. Investigate systems that could deliver mobile services to rural villages and towns.

The final objective would restructure institutional systems to reduce or limit the number of trips required to access hospitals and day-care centres.

5 CONCLUSION

In conclusion, this research paper investigates Seniors' rural mobility and accessibility challenges using the Free Travel Scheme. The research objectives are to explore the rural PT system and how it delivers services to Seniors living in rural Ireland. The research paper reviews how the rural transport system might manage and address the demographic shift of Seniors living in Ireland over the next 10 to 15 years.

Parting glass a quote from the wise:

'In a world where we can expect to see more and more people leading significantly longer lives, innovative and creative thought around the ageing process will become increasingly important' [13].

REFERENCES

[1] Walker, J., "Human Transit," in *Human Transit How Cleaner Thinking about Public Transit Can enrich our communities and our lives*, Washington, Island Press, 2012: 19, p. 19.

[2] Banister, D. & Bowling, A., “https://www.sciencedirect.com/science/article/pii/S0967070X03000520,” 2004: 105-115. [Online]. Available: https://www.sciencedirect.com/science/article/pii/S0967070X03000520. [Accessed 1 Sept 2021].

[3] Maynooth University, “https://mural.maynoothuniversity.ie/1052/1/Flexibus_Booklet_MAy_2008.pdf,” 2008: 19. [Online]. Available: https://mural.maynoothuniversity.ie/1052/1/Flexibus_Booklet_MAy_2008.pdf. [Accessed 1 Sept 2021].

[4] Citizens Information, “https://www.citizensinformation.ie/en/social_welfare/social_welfare_payments/extra_social_welfare_benefits/free_travel.html#,” 2021. [Online]. Available: https://www.citizensinformation.ie/en/social_welfare/social_welfare_payments/extra_social_welfare_benefits/free_travel.html#. [Accessed 4 Sept 2021].

[5] Teherani et al., "https://doi.org/10.4300/JGME-D-15-00414.1," 2015: 669. [Online]. Available: https://doi.org/10.4300/JGME-D-15-00414.1. [Accessed 9 July 2021].

[6] Corporate Finance Institute, “https://corporatefinanceinstitute.com/resources/knowledge/strategy/pestel-analysis/,” 2021. [Online]. Available: https://corporatefinanceinstitute.com/resources/knowledge/strategy/pestel-analysis/. [Accessed 9 Nov 2021].

[7] Neveu, M., "https://digitalcommons.calpoly.edu/cgi/viewcontent.cgi?referer=https://scholar.google.com/&httpsredir=1&article=1045&context=arch_fac," 2008. [Online]. Available: https://digitalcommons.calpoly.edu/cgi/viewcontent.cgi?referer=https://scholar.google.com/&httpsredir=1&article=1045&context=arch_fac. [Accessed 9 July 2021].

[8] Neubauer et al., "http://dx.doi.org/10.4300/JGME-D-15-00414.1," 2019. [Online]. Available: http://dx.doi.org/10.4300/JGME-D-15-00414.1. [Accessed 5 July 2021].

[9] Burns, N., & Grove, S., “https://www.scirp.org/(S(351jmbntvnsjt1aadkposzje))/reference/ReferencesPapers.aspx?ReferenceID=574704,” 2007. [Online]. Available: https://www.scirp.org/(S(351jmbntvnsjt1aadkposzje))/reference/ReferencesPapers.aspx?ReferenceID=574704. [Accessed 5 July 2021].

[10] Greenhalgh, T., "https://www.bmj.com/content/315/7103/305?fb_xd_fragment," 1997. [Online]. Available: https://www.bmj.com/content/315/7103/305?fb_xd_fragment. [Accessed 6 July 2021].

[11] Roberts et al., "https://journals.sagepub.com/doi/full/10.1177/1757975918811093," 2019. [Online]. Available: https://journals.sagepub.com/doi/full/10.1177/1757975918811093. [Accessed 5 July 2021].

[12] Scharalda G. & Leonard J., “https://www.ncbi.nlm.nih.gov/pmc/articles/PMC3012622/,” 2010. [Online]. Available: https://www.ncbi.nlm.nih.gov/pmc/articles/PMC3012622/. [Accessed 1 Oct 2021].

[13] President Higgins, “https://tilda.tcd.ie/publications/reviews-newsletters/pdf/Newsletter_2016.pdf,” 2016. [Online]. Available: https://tilda.tcd.ie/publications/reviews-newsletters/pdf/Newsletter_2016.pdf. [Accessed 3 Dec 2021].

An overview of threat sources, vulnerabilities, and physical impact assessment of an Internet of Things enabled transportation infrastructure

Konstantinos Ntafloukas[1], Daniel P. McCrum[1], Liliana Pasquale[2]
1 School of Civil Engineering, University College of Dublin, Dublin 4, Ireland
2 School of Computer Science, University College of Dublin, Dublin 4 and Lero, Ireland
Author: Konstantinos Ntafloukas. Email at: konstantinos.ntafloukas@ucdconnect.ie

ABSTRACT: Critical transportation infrastructure is an appealing target for attackers due the level of impact and value that can be obtained from cyber-attacks. In recent years, more and more transportation infrastructure operate as a cyber-physical system. A cyber-physical system exists as an integration of physical and cyber space. Previous cyber-attacks in the transportation domain demonstrate that attackers of different characteristics (e.g., motives) can exploit cyber vulnerabilities (e.g., authentication mechanisms) and damage the physical space (e.g., loss of services). The inherent vulnerabilities of Internet of Things devices increase the risk of an Internet of Things enabled transportation infrastructure protection being jeopardized. The question arises as to how to protect such cyber-physical systems? Traditional risk assessment processes consider the cyber and physical space as isolated environments. Subsequently, the risk assessment process for stakeholders (i.e., operators, civil and security engineers) who act as assessors, becomes more complex due to cyber-related security issues. This paper presents for the first time the characteristics, that should be considered by stakeholders, to conduct an accurate cyber-physical risk assessment of their own system. These characteristics include the threat source, vulnerability and physical impacts considering both cyber and physical space. Additionally, the paper informs stakeholders about the role of control barriers, operating in cyber and physical space and describes the steps of cyber-physical attacks against an Internet of Things enabled transportation infrastructure, in its physical area. The results should be of great interest of stakeholders, who attempt to incorporate the cyber domain in risk assessment process.

KEY WORDS: Transportation infrastructure; Internet of Things; Cyber-attack; Risk; Threat source; Vulnerability; Physical impact; Control barriers

1 INTRODUCTION

Internet of Things (IoT) enabled transportation infrastructure operating in a city (i.e., bridge, roadways, highways, tunnels, embankments) exists to provide a variety of engineering services (e.g., wireless structural health monitoring) through IoT applications [1], [2], [3]. Its operation relies on wireless sensor networks (WSNs), that avail of the advances of IoT technology, in sensing and transmission of data [4]. The data processing depends on the constant cooperation of the IoT layers [5]. The basic IoT layer architecture, as shown in Figure 1, builds upon the sensing layer for data collection, that includes physically distributed IoT devices (e.g., sensors), that wireless sense and transmit data (i.e., data communication) availing of IoT technologies (e.g., ZigBee) in the network layer, until data are proceeded to the end-user for data analytics and process, through the application layer (e.g., cloud). Bringing together these technologies results in the integration of the physical world with computational facilities, as a cyber-physical system (CPS) [6]. The IoT upgraded transportation infrastructure as a CPS should be protected against attacks that threaten the main security attributes known as (1) confidentiality (i.e., disclosure of data), (2) integrity (i.e., modification of data), and (3) availability (availability of data), from cyber-attackers. With respect to a IoT enabled transportation infrastructure services, data confidentiality ensures that information (e.g., structural metrics, private data of users etc.) can only be accessed by authorized users with high level credentials (e.g., operators). The protection of data integrity ensures that information or the CPS configuration can be modified only by authorized users (e.g., civil engineers). The protection of data availability ensures that services and information are available at any time to the authorized users.

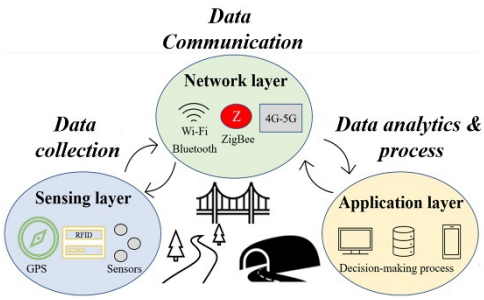

Figure 1. Basic IoT layer architecture

In the past, the physical and cyber space were considered as isolated environments, this is not the case anymore. Potential breach in the cyber space, of the security triad could lead to physical impacts (i.e., cyber-physical attacks) [7]. Previous cyber-attacks in the transportation domain against IT systems, demonstrate that successful cyber-attacks can result in adverse physical impacts (e.g., casualties) [8], [9]. The inherent technical weaknesses (e.g., limited energy resources) and vulnerabilities (e.g., lack of authentication) of IoT devices (e.g., sensors), that IoT applications in transportation domain are based upon, define the existing security risks. Studies and reports raise the awareness of security risks due to integration of IoT technology in vital critical infrastructure [10]. For example, if an adversary is able to intrude a WSN area of an IoT enabled transportation infrastructure, without being detected, then the risk of a Denial of Services (DoS) attack (i.e., the attacker floods the system with an amount of messages that cannot be proceeded resulting it in being disabled) that undermines availability of data and subsequently availability of transportation services is greater than ever [11]. However traditional risk approaches overlook the interdependency of the

cyber and physical space. Additionally, a lack of data related to cyber events due to underreporting for reputational reasons [12] and the rise of new threat sources and vulnerabilities in cyber domain [13], has made the risk assessment process a complex task for stakeholders. This paper targets to bridge the gap between the civil and security engineering domains, with respect to IoT enabled transportation infrastructure. Risk as a generic formula of likelihood and impact can be extended, with respect to cyber-physical attacks against physical infrastructure, as a product of threat source, vulnerability and physical impact, as shown in Equation 1 [14]. The deficiencies of traditional risk calculation of physical infrastructure (product of likelihood and impact) source from; i) the lack of data related to cyber-attacks against critical infrastructure [12], for reputational issues and; ii) the complex human characteristics that necessitate a more wholistic profile approach [13]. For example, the motivation and knowledge of the attacker are two characteristics that can impact the risk.

$$\text{Risk} = \text{Threat source} \times \text{Vulnerability} \times \text{Physical Impact} \quad (1)$$

For reasons of brevity, this paper will not present the wholistic cyber-physical risk assessment approach developed by the authors, but rather to give an overview of the identified characteristics that should be considered in every aspect (i.e., Threat source, Vulnerability, Physical Impact) of Equation 1.

Following the results of a latent content analysis, identification, and proposal of previously neglected characteristics in the three aspects (threat source, vulnerability & impact) is presented. Within this context, the sensing layer where cyber and physical space coexist is the area of focus. Additionally, the paper describes the role of control barriers as proactive measures against cyber-physical attacks and describe for the first time, a cyber-physical attack scenario against an IoT enabled transportation infrastructure that is based on the characteristics. The results of the presented characteristics are of interest to stakeholders who need to incorporate cyber threats in existing physical risk procedures for transportation infrastructure. Additionally, the control barriers presented can inform stakeholders of the role of proactive measures against types of cyber-physical attacks discussed in the paper

2 RELATED WORK

In this section a brief review of existing studies, standards and tools related to cyber risk in critical infrastructure are presented. Due to the relevantly recent integration IoT devices in the transportation domain has led to an absence of appropriate risk guidelines. A risk assessment process was presented by considering in-vehicle security vulnerabilities [15]. The process applies the NIST (National Institute of Standards and Technology) risk assessment approach (later described in this Section), that qualitatively assesses the risk through a likelihood-impact matrix. The study does not consider the physical infrastructure as a CPS but rather focused on raising security awareness among transportation operators, engineers for advanced vehicles. A container port subjected to four cyber-attack scenarios, was used as a case study in maritime transportation domain to demonstrate the applied risk assessment process [16]. Risk was qualitative described and quantitatively calculated as an aggregation of likelihood and impact, after the completion of a questionnaire based on experts' decision. Although, the study was oriented on assisting operators within the maritime domain in mitigating cyber risk, the assessment of threat source and vulnerability was based on limited abstract characteristics (e.g., skills) and on a predetermined questionnaire with potential vulnerabilities of assets (e.g., lack of employees training), respectively. Furthermore, the exploitation of vulnerabilities was not linked to physical impacts but rather assisted in prioritizing the risks per asset so as mitigation measures to be recommended. As stated in the NIST standard, risk for organizations can be qualitatively and quantitatively assessed by determining the likelihood and impact of a cyber event [17]. The NIST standard was created to focus on the organizational environment, as it guides assessors towards the identification of certain deficiencies (e.g., plan for organizations continuity) to assist them rank the cyber risk. Common Vulnerability Scoring System (CVSS) is a tool widely used by organizations (e.g., NIST), to measure the severity of cyber vulnerabilities [18]. CVSS adopts mathematical equations and experts' opinion addressed with qualitative and quantitative scores. However, CVSS measures the severity of a vulnerability and not the risk. Although current studies, standards and tools, succeed in raising security awareness, they overlook the cyber-physical nature of an IoT enabled transportation infrastructure, that is based on the presented characteristics of this paper. Specifically, previous studies focus on security issues related to other elements (i.e., vehicles, ports), are based on abstract threat source characteristics without associating them with the nature of infrastructure, are oriented on the preparedness of an organization (i.e., NIST) for attacks against IT systems or provide limited knowledge to the actual assessment of risk (i.e., CVSS).

3 RISK ASSESSMENT APPROACH

The proposed procedure of risk assessment to cyber-physical attacks on transportation infrastructure, initiates with the identification of an asset that could be attacked. In the case of an IoT enabled transportation infrastructure, assets refer to tangible (e.g., sensors) or intangible (e.g., communication protocol) entities of IoT technology that come with certain vulnerabilities that could be exploited by different threat sources, leading to physical impacts, as shown in Figure 2. For example, a threat source can target the communication protocol of IoT devices, exploiting vulnerabilities (poor authentication mechanisms), resulting in unavailability of data and denial of transportation services for a certain period of time. Essential and new characteristics in respect to the threat sources, vulnerability and physical impacts have been identified. Due to the lack of research into the cyber-physical nature of an IoT enabled transportation infrastructure, identified characteristics were mainly sourced from the cyber space. The identified characteristics were then adjusted to the cyber-physical nature of an IoT enabled transportation infrastructure, while the proposed ones, are functioning as a bridge between the security (i.e., cyber space) and civil engineering (i.e., physical space) domains.

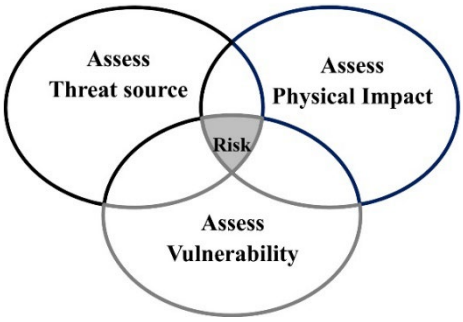

Figure 2. Cyber-physical risk assessment approach

3.1 Threat source

In order to assess a cyber-physical threat source, identification of characteristics that accurately define the source and adjustment of the threat's applicability to the cyber-physical nature of an IoT enabled transportation infrastructure should be accomplished. In this regard, it is common for expert opinion to be used. However, this is rarely available, and organization are not very amenable to highlighting their potential vulnerabilities. Therefore, a structured all available information from any publication in the research databases, of Springer Link Digital Library, IEEE Explore, ACM Digital Library, Wiley, Elsevier ScienceDirect, and Scopus were used. Keywords of (("attacker profile" OR "adversary profile" OR "attacker characteristics" OR "adversary characteristics") AND ("cyber-physical")), in a timeframe that was set between 2016 (i.e., after the Ukrainian power grid hack, the first publicly acknowledged cyber -attack to result in adverse physical impact) [19]) and 2021, was harvested. The key attacker characteristics that were identified and adjusted into an IoT enabled transportation infrastructure and should be considered towards a risk assessment approach are *Knowledge, Resources and Psychology. Knowledge* is associated with the expertise level and the understating of the system that is under attack, on behalf of the threat source. Expertise refers to knowledge of attack methods (e.g., spoofing) in any parts of IoT asset, and understanding of the system expresses the knowledge of the IoT asset that is under attack (e.g., protocol). *Resources* is associated with the belongings of the threat source. Belongings refer to practical capabilities of the threat source that describes the possession of manpower (e.g., acting alone or under group), tools necessary for a cyber-physical attack (e.g., modules with certain features) and of financial support necessary to perform an attack. *Psychology* is associated with motivational and behavioral aspects of the threat source. Motivational aspects describe the type of motivation that drives the threat source to conduct the attack (e.g., ideology, religious etc.). Behavioral aspects describe the dimensions of periodicity as the frequency with which the threat source will try to attack the system and determination as the effort which the threat source will show to accomplish the attack. However, all of the aforementioned characteristics source from the cyber space, overlooking the potential physical aspects of the critical infrastructure that attackers can target. Especially, transportation infrastructure is considered as a major target due to its societal value. Therefore, *Terrorism Experience* is a new proposed characteristics that should be additionally considered in cyber-physical risk assessment approaches that focus on critical infrastructure. Traditional terrorist organizations that used to act solely in physical space (e.g., bombing) have shown a great interest in cyber threats too [20]. IoT devices in the sensing layer of transportation infrastructure, are distributed in more or less secured physical areas that can be breached by terrorist organizations availing of their existing intruding experience.

3.2 Vulnerability

The vulnerability characteristics that were considered in this approach, were based both on exploitability metrics of CVSS tool and the cyber-physical perspective of an IoT enabled transportation infrastructure. These include: *Attack Vector*, *Attack Complexity, User Interaction* and *Interoperability*. *Attack Vector* describes the distance (i.e., Network, Adjacent, Local, Physical) between the attacker and the IoT asset in order to be considered as exploitable. However, while in CVSS the farther the attacker is from the asset, the greater the vulnerability score, this is not the case for IoT enabled transportation infrastructure. IoT assets that are deployed into a WSN, for example, can be accessed by the threat source physically or through a local network, without being detected, must be considered of great exploitability score due the high number of IoT inherent vulnerabilities. *Attack Complexity* describes whether the attacker can exploit the vulnerability at any time (i.e., Low complexity), or the attacker should carry out additional steps due to existence of conditions beyond the attacker's control (i.e., High complexity). In an IoT enabled transportation infrastructure, *Attack Complexity* should increase when conditions include the existence of advanced physical (e.g., advanced CCTV systems) or cyber (e.g., intrusion detection system) control barriers that can prevent or detect the threat source from exploiting the vulnerability. *User Interaction* describes whether the attacker can act alone (i.e., no interaction) or not (i.e., require interaction), to exploit the vulnerability. The lower the need for interaction the greater the vulnerability. *Privileges Required* describes whether the attacker should be authorized (i.e., low- or high-level privileges) or not (i.e., no privileges required) to exploit the vulnerability. The lower the need for authorization the greater the vulnerability score. For example, when the attacker targets to command a victim node, the latter can include a list of validated identities to whether the command will be forwarded or will be rejected.

The specific characteristics discussed in the previous paragraph capture the technical vulnerabilities of an IoT asset. However, in the case of IoT enabled transportation infrastructure, transportation services (e.g., monitoring) may rely on a high level of interoperability of data, as the interconnection of two or more IoT systems through the use of same IoT devices [23]. Interoperability can enable communication between heterogenous IoT devices and systems. Therefore, the level of *Interoperability* is a new proposed vulnerability characteristic, that should be considered in the risk assessment process. For example, two IoT systems in an IoT enabled transportation infrastructure may operate for structural health monitoring and monitoring of traffic flow. While IoT devices of both IoT systems harvest data from vehicles, in terms of induced loads (i.e., structural monitoring)

and number (i.e., monitoring of traffic flow), the intersection of data could be accomplished through *Interoperability*, either directly or with the use of an advanced application layer gateway [24]. Therefore, IoT devices that are part of two or more IoT systems, are more appealing target for attackers, to achieve a greater disruption.

3.3 Physical Impacts

While the confluence of IoT technology and transportation infrastructure is in its relatively early stages of widespread adaption, previous events have shown that cyber-attacks can adversely impact the physical space. With respect to IoT enabled transportation infrastructure, physical impacts describe the consequences in the physical space driven by the exploitation of IoT assets and the subsequent breach of confidentiality, integrity or availability of data (See Section 1). The physical impacts that should be considered in the risk assessment process, as described below, complies both with suggestions of risk assessment policies within EU members [25] and previous reported impacts: i) *User safety* reflects humans' safety and should be measured in terms of casualties. For example, a successful cyber-physical attack against the IoT system controlling the traffic flow could harm humans' safety; ii) *Economics (monetary loss)* reflects economic losses from both disruption of primary services for a period of time and of restoration services. Furthermore, blackmail is a usual technique from the side of attackers to gain financial profit. For example, a Denial of Services attack against sensors of WSN, could disrupt the traffic line for hours; iii) *Social and political impact* reflects violation of public security, and outrage within people, unstable environment. For example, a successful cyber-physical attack that leads to disclosure of data of passengers or blackmail of operators can result in unstable environment. While certain physical impacts (e.g., social impact), cannot be quantified, assessors should follow their own established criteria as part of their National Risk Assessment guidelines [26].

3.4 Control barriers

Control barriers operate individually in cyber or physical space or combined in both spaces at the same time. They operate in a proactive manner for preventing or detecting the threat source or in response way against a cyber-attack. Their action impacts the vulnerability characteristics and therefore should be appropriately considered in the risk assessment process. For example, physical control barriers, such as intelligent video surveillance systems and motion detectors can protect the physical area from intruders [27], and subsequently reduce the vulnerability brought by the *Attack Vector* characteristic. Cyber control barriers such as the ability of the victimized node to develop a blacklist, of misbehaving nodes [11], or the integration of advanced Intrusion Detection Systems that could detect attacks and alert the end-user [28], can increase the complexity of an attack against the WSN and subsequently reduce the vulnerability brought by the *Attack Complexity* characteristic. The above mentioned barriers can operate at the same time in their space as integrated control barriers. The use of solar panels, as a renewable energy for wireless sensors [29], has been successfully tested in a bridge. Such an application could be utilized in a response manner against an energy depletion attack on a sensor and subsequently reduce the vulnerability brought by the *Attack Complexity* characteristic.

3.5 Cyber-physical attacks against the sensing layer

Several studies have contributed to security awareness in each of the layers in a WSN [30]. These layer are; sensing layer, network layer application layer and. However, the role of sensing layer in the case of an IoT enabled transportation infrastructure should be considered potentially the most vulnerable to a cyber-physical attack. IoT devices that have a sensing layer, are exposed to attack. Therefore, ensuring constant and consistent operation of IoT devices is of vital importance. With respect to an IoT enabled transportation infrastructure e.g. sensor in a structural health monitoring system, a cyber-physical attack against the sensing layer that is based on the identified and proposed characteristics of previous sections (See Sections 3.1, 3.2, 3.3 & 3.4) and jeopardize its protection are described below. The sensing layer attack are focused on the disruption of an IoT asset (i.e., communication protocol) through energy depletion of a ZigBee WSN, widely used for monitoring purposes [29], [31], and are divided into the three steps of *Reconnaissance, Infiltration, and Conclusion*. *Reconnaissance* describes the necessary actions (e.g., gathering of information) made by the attacker, prior to the attack. *Infiltration* describes the necessary actions (e.g., attack methods) in the attack phase. The *Conclusion* describes the necessary actions that will lead to the final outcome.

3.5.1.a Energy depletion attack against the sensing layer

ZigBee devices operates with the use of four layers (i.e., Physical, MAC, Network, Application), each one of them responsible for certain operations (e.g., data addressing), using different security keys, that enables nodes to create the network [32]. The deployment of ZigBee WSN is accomplished under certain topologies (i.e., start, tree, mesh) and is based on the existence of devices (i.e., sensors), routers and coordinators. Coordinator acts as a gateway, a bridge between sensors and backbone network (e.g., antennas), until data have been transmitted to the end-user (i.e., application layer). In the described energy depletion attack, the attacker can target the victim nodes by flooding them with a significant number of bogus messages. The victim nodes can not prevent the attacker and are forced to proceed the bogus messages, spending an amount of energy, beyond the scheduled, until it the energy depleted (e.g. battery). Therefore, the victim nodes can not proceed the data related to transportation services. The deployment of IoT based WSN and the attack phases are demonstrated in Figure 3. The description of the attack does not target to assess the described characteristics but rather to provide an overview of the cyber-physical attack process against the sensing layer of an IoT enabled transportation infrastructure.

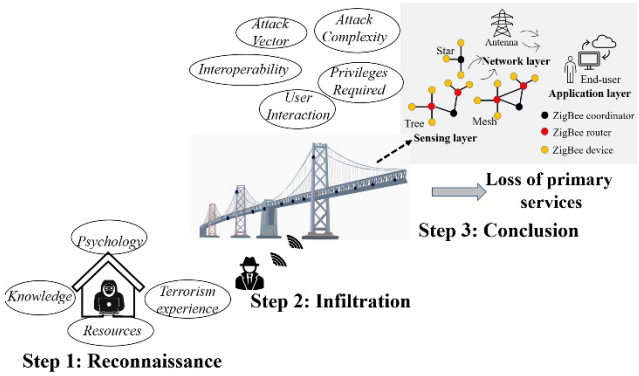

Figure 3. IoT based WSN and attack phases

Reconnaissance; This step is in the pre-attack phase, where the attacker identifies the target and collect information about its vulnerabilities. The attacker is motivated (*Psychology*) to launch a cyber-physical attack. The attacker uses their *Terrorism Experience* and *Knowledge* to physically visit the WSN area, evaluate the level of physical control barriers (see Section 3.4) that could prevent his attack and recognize the implemented IoT technology based on ZigBee modules. The attacker, by using remote connection through their laptop (*Resources*), can access available public vulnerability databases [33] or criminal cyber communities (e.g., Dark Web) to collect information through financial exchange (*Resources*) [34], and design their attack methods (*Knowledge*).

Infiltration; This step is in the attack phase. The attacker infiltrates the physical area, or the surroundings of ZigBee WSN (*Terrorism Experience*), that enables him to achieve the necessary proximity in order to locally interfere with the communication protocol of victim nodes (*Attack Vector*). The attacker is not aware of the security key that enables nodes to being authorized and participate in the network (*Privileges Required*). The attacker uses a module with adequate storage and computational capabilities (*Resources*), to broadcast bogus messages against the MAC layer of victim nodes (*Knowledge*). Even though, the bogus messages are rejected by integrity check (i.e., a message integrity code verification standard in MAC layer), nodes are spending an amount of energy to proceed and reject them. The victim nodes are unable to develop blacklists and avoid the bogus messages being processed (*Attack Complexity*). The attacker exploits this vulnerability and keep sending bogus messages until he depletes the energy of victim nodes and result in loss of packets or unavailability of data (*Knowledge*). The victim nodes can be elements of two or more IoT systems affecting them at the same time (*Interoperability*).

Conclusion; The attacker leads the victim nodes to energy depletion and results to loss of primary services (i.e., physical impact) for a period of time until restoration services take place.

4 CONCLUSION

Critical transportation infrastructure that is associated with IoT technology, should be considered by infrastructure stakeholders as an appealing target for cyber-attackers. The reason for this is that they are not typically risk assessed for cyber-attacks and due to their cyber-physical nature, the impacts of such attacks can be significant. A knowledge gap exists within both the security and civil engineering domain, and this is also combined with a lack of data of previous cyber-attacks against critical infrastructure being published. The main reason for this is to prevent future attacks and reputational damage. These issues have resulted in the cyber and physical space typically being treated as isolated environments in risk assessment methods. This paper aims to bridge this gap by identifying, adjusting and proposing cyber and physical characteristics in respect of the threat source, vulnerability and physical impact of cyber-physical threats. The specific characteristics can contribute into an accurate cyber-physical risk assessment approach. Control barriers in both spaces, target to inform stakeholders of potential actions against cyber-physical attacks targeting the sensing layer. A cyber-physical attack scenario is presented in the paper, to assist stakeholders understand the steps of a successful cyber-physical attack, by utilizing those characteristics that should be assessed towards the cyber-physical risk assessment process.

ACKNOWLEDGMENTS

This work is financially supported by a University College of Dublin Advanced PhD Scholarship Scheme.

REFERENCES

[1] M. Mishra, P. B. Lourenço, and G. V. Ramana, "Structural health monitoring of civil engineering structures by using the internet of things: A review," *Journal of Building Engineering,* p. 103954, 2022.

[2] E. Koursari, S. Wallace, Y. Xu, P. Michalis, and M. Valyrakis, "Smart bridge: Towards robust monitoring of environmental hazards," in *River Flow 2020*: CRC Press, 2020, pp. 886-890.

[3] Z. Zhao *et al.*, "Integrating BIM and IoT for smart bridge management," in *IOP Conference Series: Earth and Environmental Science*, 2019, vol. 371, no. 2: IOP Publishing, p. 022034.

[4] H. Landaluce, L. Arjona, A. Perallos, F. Falcone, I. Angulo, and F. Muralter, "A review of IoT sensing applications and challenges using RFID and wireless sensor networks," *Sensors,* vol. 20, no. 9, p. 2495, 2020.

[5] R. Mahmoud, T. Yousuf, F. Aloul, and I. Zualkernan, "Internet of things (IoT) security: Current status, challenges and prospective measures," in *2015 10th international conference for internet technology and secured transactions (ICITST)*, 2015: IEEE, pp. 336-341.

[6] S. K. Singh, Y.-S. Jeong, and J. H. Park, "A deep learning-based IoT-oriented infrastructure for secure smart city," *Sustainable Cities and Society,* vol. 60, p. 102252, 2020.

[7] G. Loukas, *Cyber-physical attacks: A growing invisible threat*. Butterworth-Heinemann, 2015.

[8] S. J. Templeton, "Security aspects of cyber-physical device safety in assistive environments," in *Proceedings of the 4th International Conference on PErvasive Technologies Related to Assistive Environments*, 2011, pp. 1-8.

[9] ENISA, "Security measures in the Railway Transport Sector," in "Railway Cybersecurity," European Union Agency for Cybersecurity, November 13, 2020 2020. [Online]. Available: https://www.enisa.europa.eu/publications/railway-cybersecurity

[10] P. Williams, P. Rojas, and M. Bayoumi, "Security taxonomy in iot–a survey," in *2019 IEEE 62nd International Midwest Symposium on Circuits and Systems (MWSCAS)*, 2019: IEEE, pp. 560-565.

[11] X. Cao, D. M. Shila, Y. Cheng, Z. Yang, Y. Zhou, and J. Chen, "Ghost-in-zigbee: Energy depletion attack on zigbee-based wireless networks," *IEEE Internet of Things Journal,* vol. 3, no. 5, pp. 816-829, 2016.

[12] L. Maschmeyer, R. J. Deibert, and J. R. Lindsay, "A tale of two cybers-how threat reporting by cybersecurity firms systematically underrepresents threats to civil society," *Journal of Information Technology & Politics,* vol. 18, no. 1, pp. 1-20, 2021.

[13] R. Gandhi, A. Sharma, W. Mahoney, W. Sousan, Q. Zhu, and P. Laplante, "Dimensions of cyber-attacks: Cultural, social, economic, and political," *IEEE Technology and Society Magazine,* vol. 30, no. 1, pp. 28-38, 2011.
[14] FEMA, "A How-To Guide To Mitigate Potential Terrorist Attacks Against Buildings," in "Risk management," Department Of Homeland Security, 2005. [Online]. Available: https://www.wbdg.org/FFC/DHS/fema452.pdf
[15] K. B. Kelarestaghi, M. Foruhandeh, K. Heaslip, and R. Gerdes, "Vehicle security: Risk assessment in transportation," *arXiv preprint arXiv:1804.07381,* 2018.
[16] B. Gunes, G. Kayisoglu, and P. Bolat, "Cyber security risk assessment for seaports: A case study of a container port," *Computers & Security,* vol. 103, p. 102196, 2021.
[17] NIST, "Guide for Conducting Risk Assessments," National Institute of Standards and Technology, 2012. [Online]. Available: https://nvlpubs.nist.gov/nistpubs/Legacy/SP/nistspecialpublication800-30r1.pdf
[18] FIRST. https://www.first.org/ (accessed February 1st, 2022).
[19] SANS, "Analysis of the Cyber Attack on the Ukrainian Power Grid. Defense Use Case," March 18, 2016 2016. [Online]. Available: https://media.kasperskycontenthub.com/wp-content/uploads/sites/43/2016/05/20081514/E-ISAC_SANS_Ukraine_DUC_5.pdf
[20] C. H. Malin, T. Gudaitis, T. Holt, and M. Kilger, *Deception in the Digital Age: Exploiting and defending human targets through computer-mediated communications*. Elsevier, 2017.
[21] D. Giantas and D. Stergiou, "From terrorism to cyber-terrorism: The case of ISIS," *Available at SSRN 3135927,* 2018.
[22] J. J. Plotnek and J. Slay, "Cyber terrorism: A homogenized taxonomy and definition," *Computers & Security,* vol. 102, p. 102145, 2021.
[23] R. Nawaratne, D. Alahakoon, D. De Silva, P. Chhetri, and N. Chilamkurti, "Self-evolving intelligent algorithms for facilitating data interoperability in IoT environments," *Future Generation Computer Systems,* vol. 86, pp. 421-432, 2018.
[24] E. Avelar, L. Marques, D. dos Passos, R. Macedo, K. Dias, and M. Nogueira, "Interoperability issues on heterogeneous wireless communication for smart cities," *Computer Communications,* vol. 58, pp. 4-15, 2015.
[25] M. Theocharidou and G. Giannopoulos, "Risk assessment methodologies for critical infrastructure protection. Part II: A new approach," *Scientific and Technical Research Reports,* 2015.
[26] M. G. Mennen and M. Van Tuyll, "Dealing with future risks in the Netherlands: the National Security Strategy and the National Risk Assessment," *Journal of Risk Research,* vol. 18, no. 7, pp. 860-876, 2015.
[27] G. Bocchetti, F. Flammini, C. Pragliola, and A. Pappalardo, "Dependable integrated surveillance systems for the physical security of metro railways," in *2009 Third ACM/IEEE International Conference on Distributed Smart Cameras (ICDSC)*, 2009: IEEE, pp. 1-7.
[28] F. Sadikin, T. Van Deursen, and S. Kumar, "A ZigBee intrusion detection system for IoT using secure and efficient data collection," *Internet of Things,* vol. 12, p. 100306, 2020.
[29] M. Chae, H. Yoo, J. Kim, and M.-Y. Cho, "Development of a wireless sensor network system for suspension bridge health monitoring," *Automation in Construction,* vol. 21, pp. 237-252, 2012.
[30] N. Mishra and S. Pandya, "Internet of things applications, security challenges, attacks, intrusion detection, and future visions: A systematic review," *IEEE Access,* 2021.
[31] T. Harms, S. Sedigh, and F. Bastianini, "Structural health monitoring of bridges using wireless sensor networks," *IEEE Instrumentation & Measurement Magazine,* vol. 13, no. 6, pp. 14-18, 2010.
[32] O. Olawumi, K. Haataja, M. Asikainen, N. Vidgren, and P. Toivanen, "Three practical attacks against ZigBee security: Attack scenario definitions, practical experiments, countermeasures, and lessons learned," in *2014 14th International Conference on Hybrid Intelligent Systems*, 2014: IEEE, pp. 199-206.
[33] CVE. "Common Vulnerabilities and Exposures." https://cve.mitre.org/cve/search_cve_list.html (accessed 10th of February, 2022).
[34] M. Schäfer, M. Fuchs, M. Strohmeier, M. Engel, M. Liechti, and V. Lenders, "BlackWidow: Monitoring the dark web for cyber security information," in *2019 11th International Conference on Cyber Conflict (CyCon)*, 2019, vol. 900: IEEE, pp. 1-21.

Resilience Methodological Framework for Critical Infrastructure Systems subjected to Cyber-Physical Threats

Lorcan Connolly[1], Emma Sheils[1], Alan O'Connor[1], Eugene OBrien[1]
[1]Research Driven Solutions Ltd, 1A St. Kevin's Avenue, Dublin, D08TX29
email: lorcan.connolly@researchdrivensolutions.ie, emma.sheils@researchdrivensolutions.ie, alan.oconnor@researchdrivensolutions.ie, eugene.obrien@researchdrivensolutions.ie

ABSTRACT: EU Critical Infrastructures (CIs) are increasingly at risk from cyber-physical attacks and natural hazards. Research and emerging solutions focus on the protection of individual CIs, however, the interrelationships between CIs has become more complex for example in smart cities and managing the impacts of cascading effects and enabling rapid recovery is becoming more pertinent and highly challenging. PRECINCT aims to connect private and public CI stakeholders in a geographical area to a common cyber-physical security management approach which will yield a protected territory for citizens and infrastructures. The project requires a single resilience measure for all CIs (e.g. transport, power, ICT) within the project "Precincts", which will be used as Living Lab Demonstrators of the methodology.
This paper focuses on the Resilience Methodological Framework of the PRECINCT project. The framework uses the measures of service for each CI mode as an indicator of resilience. The resilience is then measured as a reduction in this level of service before, during and after an extreme event. Measures of service may include persons served by a power network, persons transported by a railway system, safety of users etc. Resilience indicators are scored for various elements of the infrastructure including organisational indicators, environmental indicators, and indicators relating to the infrastructure itself.

KEY WORDS: Resilience, Cyber, Natural disaster, Hazard, Risk, Critical Infrastructure

1 INTRODUCTION

EU Council Directive 2008/114/EC [1] on the identification and designation of European critical infrastructures and the assessment of the need to improve their protection defines Critical Infrastructure (CI) as:
"…an asset, system or part thereof located in Member States which is essential for the maintenance of vital societal functions, health, safety, security, economic or social well-being of people, and the disruption or destruction of which would have a significant impact in a Member State as a result of the failure to maintain those functions;"

EU CIs are increasingly at risk from cyber-physical attacks and natural hazards. Research and emerging solutions focus on the protection of individual CIs, however, the interrelationships between CIs have become more complex, for example, in smart cities. The PRECINCT project aims to adopt a common cyber-physical security management approach to yield a protected territory for citizens and infrastructures. Cyber-physical threats in this context may refer to natural disasters (e.g. earthquakes, flooding, storm surges) and man-made hazards (e.g. terrorism and cyber attacks)

The project demonstrates a Resilience Methodological Framework (RMF) implemented in a serious gaming platform to test and validate new detection and mitigation approaches in present day real-life contexts (demonstrated in PRECINCT "Living Labs"). This paper provides an overview of the RMF

2 EVOLUTION OF RESILIENCE

2.1 Risk Assessment of CI Networks

For decades, advanced risk assessment has been the preferred methodology for managing and maintaining CI networks subjected to various natural and man-made hazards. One of the most universally accepted codes of practice is ISO 31000:2018 *Risk management — Guidelines* [2]. The prescribed risk management process involves the systematic application of policies, procedures and practices to the activities of communicating and consulting, establishing the context and assessing, treating, monitoring, reviewing, recording and reporting risk. It was noted in [3] that this necessary broadness for application across many sectors means that it often fails to capture context-specific issues which are particularly important for resilience; this over-standardization can all too often promote a 'rigidity-trap' which limits adaptability and flexibility [4]. Moreover, previous risk assessment approaches have been noted to be too focused on physical robustness of infrastructure systems and fail to consider the whole scheme of the disaster cycle over time, which must be considered at all stages of the threat considered (before, during and after the event), as illustrated in Figure 1.

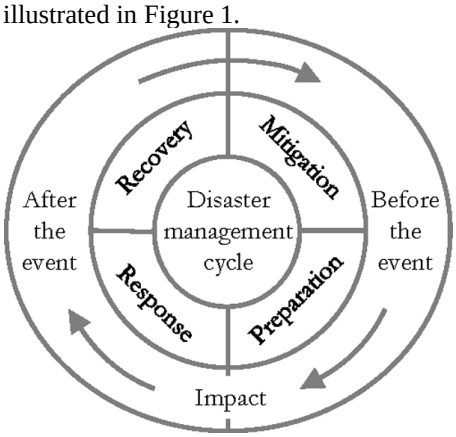

Figure 1. Disaster Management Cycle [5]

2.2 Resilience – Concept and Motivation

In order to address the previously identified shortcomings of traditional risk assessment, the concept of Resilience evolved in the 1970s as it pertained to studies of systems ecology [6]. More recently the concept has evolved in the realm of CI in order to address all aspects of the Disaster Management Cycle [7]. Resilience is generally considered as the capacity of a system, community or society potentially exposed to hazards to adapt, by resisting or changing to reach and maintain an acceptable level of function and structure. This may be in response to a climate hazard (e.g. flooding, hurricane), natural hazard (e.g. earthquake), or a man-made hazard such as a cyber-attack or terrorism. This consideration of the temporal aspects of the disaster cycle is key to the resilience concept. The idea was explained succinctly in [8], as shown in Figure 2. The performance of the system over time is shown by the heavy green line while the hazard intensity is shown by the dashed red line. Performance may be measured by one or more KPIs in relation to the network (e.g. passengers carried within a transport network). Prior to a threat occurring, the system can remain in equilibrium, without significant disruptions to service. The hazard defines the beginning of the "hazard phase". The system's resilience should define the ability to absorb, resist or accommodate this hazard. The performance reduces as the intensity of the hazard increases. This reduction in performance is dynamic, time varying and may take many shapes (e.g. linear, exponential etc.) depending on the system characteristics in terms of resilience. Once the perturbation is finished, the "recovery phase" begins; The resilience properties of the system should specify the ability to restore, return or recover from the hazard. This recovery action continues until the moment that a new system equilibrium is reached where the system can operate. The level of service associated with the new equilibrium point could be equal, better or worse than the previous level of service of the CI. Finally, the hazard phase and the recovery phase should be analysed in a specific time frame. The evaluation of the impact and the damages suffered in the system should always be evaluated with regard to time spent in each phase.

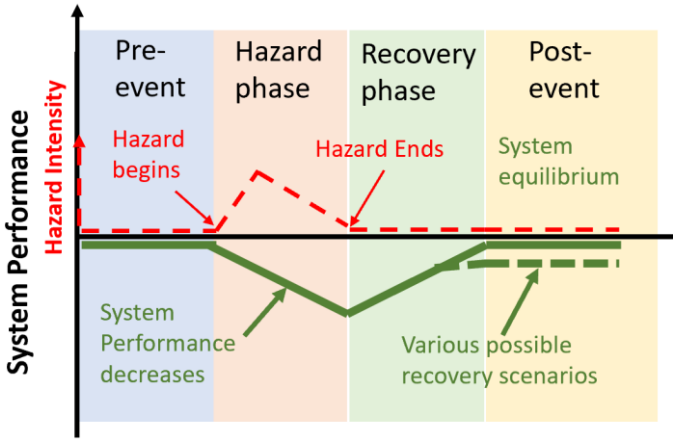

Figure 2. Resilience Evaluation (reproduced from [8])

This example highlights the concept of resilience in general and how it differs to that of risk assessment. The organisational / operational, asset management and technical levels are all considered over time, throughout the resilience disaster management cycle, in conjunction with the resilience cycle.

Many definitions of resilience exist in the literature, both for consideration of CI and in other industries / scientific domains. For the current work, the definition of resilience of the CEN publication, "Guidelines for the assessment of resilience of transport infrastructure to potentially disruptive events" [9], was adopted. This allows reasonable flexibility for the PRECINCT approach. Moreover, this is the most current codified document which prescribes guidelines for assessment of resilience. For this reason, the PRECINCT RMF directly adopted this definition of resilience:

"Resilience is the ability to continue to provide service if a disruptive event occurs"

In order to develop the PRECINCT RMF, an extensive review was carried out of the current state of the art in resilience frameworks of Critical Infrastructure.

3 REVIEW OF EXISTING FRAMEWORKS

Resilience Frameworks developed as part of previous projects of a similar nature to PRECINCT were reviewed and appraised in conjunction with the PRECINT project requirements. While over 20 European projects were appraised, a summary of some of the key fundings is presented in this section.

3.1 Resilens Project

Resilens [6] developed a Resilience Management Matrix and Audit Toolkit. This was a semi-quantitative combination tool of complementary methods designed to operate in logical progression as a "single functioning unit" to achieve the overall goal of providing a resilience assessment function, resulting in the scoring of the resilience level of any CI system evaluated. The tool was established focussing primarily on qualitative / semi-quantitative analysis, with the quantitative tools intended only to provide evaluation which complements the other toolkit approaches. This further helps to define the system and reduce subjectivity. The Resilens consortium suggested several issues associated with fully quantitative resilience assessment:

1. The identification of the most relevant Indices and Characterisations (I&C) describing the system, given that a complete scrutiny of all the I&C is impractical. The larger the number of I&C included, the more difficult and time consuming the tool will be.
2. The selected I&C should not overlap information, in order to avoid the consideration of the same aspects several times, overweighting their importance.
3. The selection of the most suitable weights to combine the selected I&Cs.
4. The validity of quantitative indicators for enhancing resilience is often not substantiated by empirical evidence and many technical and conceptual issues remain.

The Resilens consortium noted that quantitative, matrix approaches can be normative, discourage necessary adaption and lead to the focussing of resources on 'easy wins' rather than a more holistic conception of resilience. The consortium also concluded that many existing indices exhibit shortcomings in terms of robustness and problems in the aggregation of data to different scales. It was therefore suggested that greater importance should be placed upon context, scale and risk specificity in any measurement of resilience.

3.2 Resolute

The Resolute Resilience Guideline [10] is structured as a report which, when read, facilitates CI operators and organisations in thinking in terms of interdependencies and resilience headlines which can assist in identifying gaps or shortcomings / vulnerabilities in the system. It is structured according to four aspects of resilience (Anticipate, Monitor, Respond, Learn), with various subtopics under each. The formal European Resilience Management Guidelines (ERMG) then consists of a commentary on each subtopic including the background, general recommendations, examples of how each topic can be implemented, common conditions for achieving the requirements, interdependencies and limitations of the subtopic. The Resolute approach to resilience enhancement encourages collaborative oversight across various subtopics by providing a high-level description of the ways organisations can achieve resilience. This is an effective means of coordinating organisational impact in the resilience context. In this sense, the guidelines also aim to provide the user with a full-scale system overview, regardless of the organisational level or area from which the user may be operating, or of the role that the stakeholder plays towards the delivery of the service being provided by the CI.

This approach appears to be extremely beneficial to the resilience space. However, this did not lend itself well to the requirement to deliver quantitative resilience indicators which can be directly applied in the PRECINCT Living Labs.

3.3 Foresee

The Foresee resilience methodology is grounded on the principle of service levels, with resilience being principally measured in terms of how service is affected using each measure of service, and the cost of the interventions required to ensure that the infrastructure once again provides an adequate service. Resilience is therefore measured as the cumulative difference throughout the duration of the hazard/absorb and recovery phases between;

- the service provided by the infrastructure if no event occurs, (i.e. before an event occurs) and after the infrastructure has been restored, and the service provided by the infrastructure if an event occurs (illustrated in Figure 3 for the "travel time" measure of service), i.e. during the "hazard" and the "recovery" phase, and
- the costs of intervention if no event occurs and the costs of interventions if an event occurs.

It should be noted that different measures of service may be employed to measure resilience (e.g. injuries and fatalities during an interruption). The Foresee project dealt specifically in measures of service for transport infrastructure. Three possible ways to measure resilience are proposed 1) using simulations, 2) using indicators with differentiated weights and 3) using indicators with equal weights. Simulations have the highest level of precision but are difficult to use in a way that provides an overview of an entire situation. The accuracy of their results is, of course, also dependent on the quality of data and models used. Using indicators is less precise but provides a better overview of complex network situations.

The CEN publication "Guidelines for the assessment of resilience of transport infrastructure to potentially disruptive events" [9] is based upon the findings of the Foresee approach. As this document is likely to form the basis for European standardisation on the subject of resilience, it was identified as an excellent starting point for the PRECINCT approach.

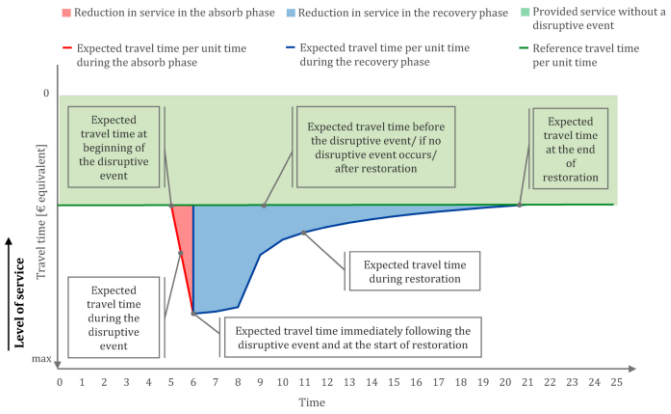

Figure 3. Illustration of transport infrastructure resilience using the "travel time" measure of service [9]

In conclusion, it was clear from the review of past research that some projects (Resilens / Resolute) developed qualitative and semi-quantitative frameworks which aimed to enhance the understanding of resilience and indirectly, the resilience of the system itself. The motivation for these forms of methodologies appears to be that quantitative, indicator-based approaches "can be normative, discourage necessary adaption and lead to the focussing of resources on 'easy wins' rather than a more holistic conception of resilience". It has also been noted that many of the existing indicator-based approaches "exhibit significant shortcomings in terms of robustness and problems in relation to the aggregation of data to different scales" [6]. However, examining the research space as a whole, this seems to have been the state of play 5-10 years in the past. More recent projects like Foresee and SmartResilience [11] have successfully implemented indicator-based approaches where indicator values are directly contextualised in terms of service levels. However, the shortcomings / difficulties with applying indicator-based approaches as outlined in the Resilens project should be closely considered. Due to space limitations, SmartResilience is not summarised as part of this paper but more information is available in [11].

The approach developed in the CEN publication [9] is directly relevant in terms of the PRECINCT requirements. This form of quantitative framework provides a unique platform to the operation of the PRECINCT serious game and Living Lab implementation. Furthermore, this document may form the initial basis for standardisation on the topic, and the understanding of resilience in terms of the service provided by the infrastructure, providing a unique method to combine the resilience score of multi-modal CIs. For this reason, the PRECINCT RMF was adopted from the approach of CEN CWA 17819 to the required context. Some initial work was required in order to facilitate adoption of the method for various CIs concurrently, rather than individual transport networks. Additionally, the framework was modified in order to consider multiple cascading hazards, with consideration of not only natural hazards, but also man-made hazards and cyber threats.

4 PRECINCT RMF

The PRECINCT RMF is outlined in Figure 4 below. Each step of the process is described in the following subsections.

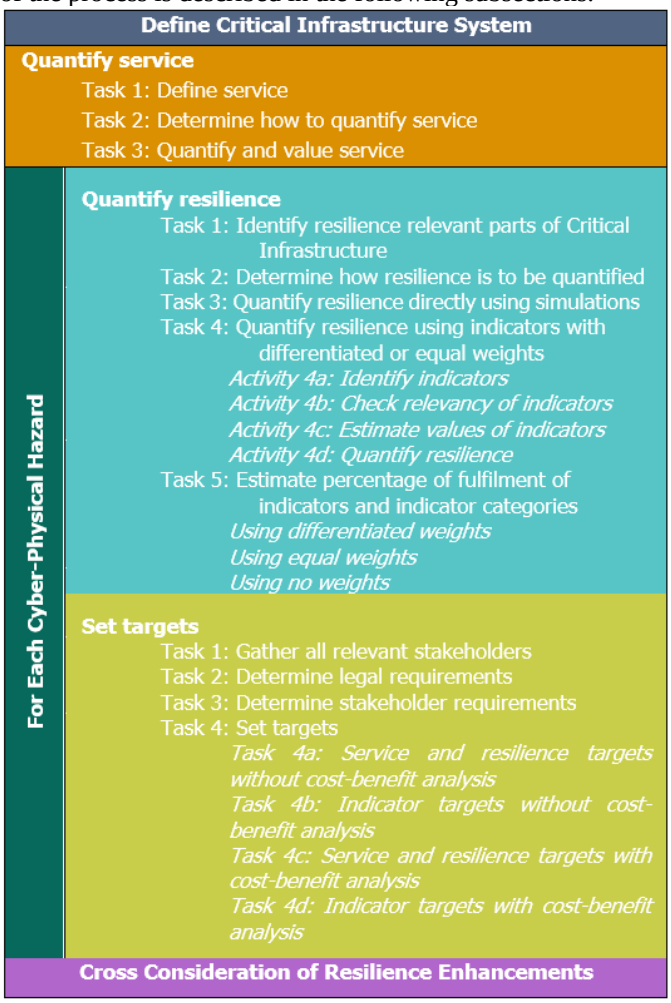

Figure 4. PRECINCT Resilience Methodological Framework

4.1 Define Critical Infrastructure System

The first step in the process is the definition of the CI system being assessed. The RMF can be used to assess the resilience of any CI including, but not limited to, energy, water, telecommunications, transport as well as multimodal combinations of these CIs. Organisations responsible for the resilience of the CI and the people served also contribute to the resilience of the CI and, as such, should be considered as part of the CI system. This may include police departments, first responders, emergency services, fire departments etc. The various parts of the infrastructure should be categorised according to Infrastructure, Environment and Organisation. This may need to be categorised separately for each CI being considered in the system.

Infrastructure describes the physical assets and cyber / data systems that are required to provide service and are considered in the assessment. Examples may include bridges and road sections forming part of a transport network, central control rooms forming part of a motorway Intelligent Transport System (ITS). The Environment consists of the physical environment in which the infrastructure is embedded that might affect the provision of service as well as the organisational environment in which the infrastructure management organisation is subject to. Items to be considered in the Environment category include the occurrence of floods or likelihood of deliberate physical attacks to infrastructure elements, as well as the regulations/codes impacting the infrastructure. The Organisation category covers the organisation(s) responsible for ensuring that the infrastructure provides service, as well as responders responsible for resilience. Indicators in this category include emergency plans, maintenance activities etc.

The Definition step should describe all resilience-relevant aspects of the CI, including contextual information such as spatial boundaries, geographic context, regulatory background etc. This step should also define the hazards of interest to the multimodal system of CIs. Interdependencies between events should also be considered where relevant. For example, an urban tram system which has sufficient flood defences may not be impacted by a 1 in 100-year flood event. However, the power network supplying electrification to trams may potentially be at risk of shutdown.

4.2 Quantify Service

In PRECINCT, Resilience is benchmarked against the service provided by the system being assessed. This may include time spent travelling, safety of users etc. The various steps in measuring the service within the PRECINT RMF are as follows:

1. Define the service that the CI system provides.
2. Determine how the service is to be quantified.
3. Quantify and value service.

The definition of the service provided by a CI requires consideration of the most basic reason for the system being in place. The service definition should ideally be obtained through discussion with the CI stakeholders. Stakeholders include not only the owners and managers of the system, but also the users for whom the service is provided. A sample definition of service for a fibre broadband network may be described as follows; the primary reason for the CI is to provide uninterrupted 50MB internet services to private dwellings and businesses. The primary measure of service in this case may be the length of time for which connection remains stable throughout the year. This may be further assigned a cost for simplicity (e.g. the supply of internet for a day is valued according the cost of the internet for private and business users throughout the day).

Next, the user must determine how to quantify the service. This requires a decision on whether service will be quantified using simulations or indicators. Should indicators be used, the assessor must also decide what indicators best model the service in question and determine how data for the indicators will be obtained. Measures of service should also include intervention costs, where relevant, being of interest to the overseeing organization in the context of resilience decision making. Other examples may include travel time for a transport network, safety of use for a gas supply network, as well as socio-economic measures for a power supply network (e.g. the breakdown in power supply may impact the supply of water and various other services to the community served).

The final step is the calculation / valuing of the service itself, either by way of simulations or indicators. In either case the

outcome is a numeric estimation of the service provided by the CI each year. An example may include a telecom system which is expected to deliver broadband to 100 users for 364 days in a year. The service provided is then equal to 36,400 user days. In order to allow comparison and equal consideration of intervention costs and different measures of service across different CI types, the units used to quantify service should be expressed in monetary values wherever possible. For example, if the provision of broadband per person day has a value of €2, the service provided in the previous example is quantified as 36,400 × €2 = €72,800. The estimation of the values should, as far as possible, be related to published values, which may be often found in codes, or collected using one or more valuation techniques, such as hedonic pricing [12]. The values associated with measures of service are solely to be used as reference values in measuring resilience.

4.3 Quantify Resilience

For the PRECINCT project, resilience is quantified in terms of relative reductions in the provision of each CI service during (and following) a disruptive event. After the CI system is sufficiently defined, as well as the relevant hazards outlined and associated service quantified, the tasks involved to quantify resilience are as follows, for each hazard:

1. Identify resilience relevant parts of the CI.
2. Determine how resilience is to be quantified.
3. Quantify resilience directly using simulations or…
4. Quantify resilience using indicators with differentiated or equal weights.
5. Estimate percentage of fulfilment of indicators and indicator categories.

It should be noted that Task 5 is an optional step in the process which clarifies areas for resilience enhancements.

The resilient relevant parts of the CI should be identified according to the global division listed for the parts of each CI assessed. This step allows consideration of the areas which impact on the service in general when carrying out the resilience analysis.

In determining how resilience is to be quantified, the assessor decides whether to directly quantify the reductions in level of service and the increased intervention costs due to a disruptive event, or to indirectly quantify these properties using indicators. The most time-consuming method which also requires significant expertise, resources and data availability, is the direct quantification of resilience using simulations. Should insufficient time, data or expertise be available, indicators may be used to quantify resilience. Indicators may be summarised in terms of equal or unequal weights, again, depending on the accuracy required, time and resources available. Where there are a number of complex interactions between different CIs (as is the case within PRECINCT), it is recommended that indicators be used. On this basis, the simulation method will not be discussed further in this paper.

Indicators are parts of the CI system that give an indication of the difference between the service provided, and the intervention costs, with and without the occurrence of the disruptive event. While some indicators may manifest in a similar fashion across multiple CIs and hazards, a separate list of indicators should be produced when analysing each hazard individually, as the weight assigned to each indicator may change depending on the hazard analysed. The steps involved in measuring resilience using indicators are as follows:

a) Identify indicators
b) Check relevancy of indicators
c) Estimate values of the indicators
d) Quantify resilience, either using differentiated weights, or equal weights.

An example of an indicator under the “Infrastructure” part of the CI would include the condition state of the infrastructure. This may be recorded on an individual asset basis, with one indicator per asset or as an average of all assets affecting the CI mode being analysed. As an example, this indicator may take a value of 1 – 5, with 5 being the best score and 1 being the worst (e.g.: 5 – like new, 4 - slightly deteriorated, 3 – average, 2 – poor, 1 – alarming).

Indicators must be checked for relevance to the system to ensure it is worthwhile to include them, and also to investigate if they provide a sufficient overview of the CI. This should be done by investigating how indicators change the measures of service being investigated and the intervention costs following the disruptive event.

The next step simply involves the selection of the indicator score for each indicator in the assessment. The number of scores possible for each indicator may vary for each hazard.

The final step of measuring resilience with indicators involves correlating indicator scores with measures of resilience, generally in monetary units representing differences in intervention costs or measures of service. The process for assigning monetary values to each indicator can be done assuming equal weights (i.e. each indicator has the same impact on service and intervention costs) or assuming differentiated weights. For differentiated weights, the relative impact of each indicator on resilience must be estimated. This is achieved as follows, for each indicator:

i. Set all indicators (for all CI modes considered) to their best values and estimate the reduction in service and additional intervention costs, if the disruptive event occurs.
ii. Set all indicators (for all CI modes considered) to their best values except one and set that indicator to its worst value, and then estimate the reduction in service and additional intervention costs, if the disruptive event occurs.
iii. Assuming a relationship, e.g. linear relationship, between the worst and best values for each indicator and using the actual values of the indicators, quantify the resilience in terms of expected total costs.

The weight of the indicator is then given by the difference between the value of reduction in service and intervention costs if the indicator has its worst value and the value of the reduction in service and intervention costs if the indicator has its best value. This essentially provides a monetary value for the minimum and maximum score for each indicator, allowing a monetary value to be allocated to the actual score assigned. Once the indicator values are assigned, they can be summed to give a quantification of resilience for each part of the system (i.e. infrastructure, environment and organization). These can further be summed to provide an overall representation of the resilience of the CI system, with various graphical representations possible to highlight problem areas for improvement.

4.4 Set Targets

The setting of targets for resilience is very useful to ensure the goals of the CI organisation are achieved, and to allow the framework to inherently consider codified norms which the bound the problem. The steps involved in setting targets are as follows, for each CI and each hazard:

1. Gather all relevant stakeholders.
2. Determine legal requirements.
3. Determine stakeholder requirements.
4. Set targets.

The first step in setting targets is the gathering of relevant stakeholders. As for earlier steps, this should include all users, managers and anyone affected by the any of the CI modes analysed in the CI system. Subsequently, relevant legal requirements should be identified in consultation with relevant stakeholders. Examples of legal requirements on indicators might include minimum condition states an infrastructure asset must achieve, minimum design / assessment load, legal requirements to practice emergency plans etc. These targets will quickly highlight areas where resilience enhancements must be put in place.

Finally, targets are set either against measures of service / resilience, or against indicators. Additionally, for each of these cases, targets can be set either with or without Cost Benefit Analysis (CBA). The most common approach developed within the PRECINCT project is the setting of indicator targets with CBA. The process is based on incrementally calculating the benefit / cost ratio of raising each indicator by 1 level. The indicator target is then selected as the one which maximises the benefit cost ratio while satisfying all legal and stakeholder requirements.

4.5 Cross Consideration of Resilience Enhancements

The final step in the RMF involves the consideration and putting in place of resilience enhancements to the CI system in question, considering the resilience quantification and targets. This step can be carried out either individually for each hazard or alternatively a cross consideration can be performed over multiple hazards. An example may include an assessment of a CI system for which the hazards of interest are a 1/20-year flood event, a 1/100-year flood event, and a terrorist threat. The cross consideration of resilience requires the likelihood of the hazards to be quantified. For physical / natural threats, this may be quantified by relating to the event probabilities as determined by climatological/meteorological modelling. The likelihood of cyber/terrorism hazards where human factors are a key input that may be more difficult to quantify. The determination of the likelihood of hazard events is outside the scope of this methodology.

Once the likelihoods of each threat have been determined, the resilience of the entire system may be weighted according to the likelihood of each event. This may be done on an individual measure of service / indicator level, for the various infrastructure parts, or for the entire resilience of the system. The delineation of appropriate resilience enhancements can then be performed by examining the statistical representation of resilience across all measures of service / indicators.

5 CONCLUSIONS AND FUTURE WORK

This paper presented the PRECINCT RMF, its motivation, development and operation. The framework marks a significant contribution to the state of the art in the application of quantitative resilience calculation for multimodal CIs subjected to Cyber-Physical Hazards. Further progress beyond the State of The Art will be achieved in the future PRECINCT Living Labs, which will demonstrate the framework within three urban locations subjected to hazard combinations. These will be developed in a serious gaming platform to provide training and guidance on resilience enhancement. Furthermore, the PRECINCT interdependency and cascading effects graphs will be used to model the impact of these hazards, the resilience indicators and the outcome resilience estimation.

ACKNOWLEDGMENTS

This work was part of the PRECINCT project, which received funding from the European Union's Horizon 2020 Research and Innovation Programme under Grant Agreement No. 101021668.

REFERENCES

[1] Council Directive 2008/114/EC of 8 December 2008 on the identification and designation of European critical infrastructures and the assessment of the need to improve their protection, Official Journal of the European Union, L345/7.

[2] ISO 31000:2018, Risk Management—Guidelines. Geneva: International Standards Organisation, 2018

[3] Little, R. (2012) Managing the Risk of Aging Infrastructure. [online] Available at: http://www.irgc.org/wp-content/uploads/2012/04/R.-Little_Risk-of-AgingInfrastructure_revision-Nov2012.pdf [Accessed: 03.12.21]

[4] Rogers, P. (2013) 'The Rigidity Trap in Global Resilience: Neoliberalisation Through Principles, Standards, and Benchmarks.' Globalizations, 10, p.383–395.

[5] Mauroner, Oliver & Heudorfer, Anna. (2016). Social media in disaster management: How social media impact the work of volunteer groups and aid organisations in disaster preparation and response. International Journal of Emergency Management. 12. 196. 10.1504/IJEM.2016.076625.

[6] Resilens Consortium (2016), Resilience Evaluation and SOTA summary report. Available at: http://resilens.eu/

[7] Bruneau, M., S. Chang, R. Eguchi, G. Lee, T. O'Rourke, A. Reinhorn, M. Shinozuka, K. Tierney, W. Wallace, and D. von Winterfelt (2003) A framework to quantitatively assess and enhance the seismic resilience of communities. Earthquake Spectra 19(4): 733–752.

[8] Martinez-Pastor, B., Resilience of Traffic Networks to Extreme Weather Events: Analysis and Assessment, Trinity College Dublin. School of Civil, Structural and Environmental Engineering, 2018

[9] Committée Européen De Normalisation (CEN) (2021), CWA 17819, Guidelines for the assessment of resilience of transport infrastructure to potentially disruptive events, ICS 03.220.01; 13.200.

[10] Resolute Consortium (2018), European Resilience Management Guidelines. Available at: https://www.resolute-eu.org/

[11] SmartResilience Consortium (2019), D3.8: Assessing Resilience Level of Smart Critical Infrastructures based on Indicators. Available at: https://resiliencetool.eu-vri.eu/home.aspx?lan=230&tab=2646&itm=2646&pag=3146

[12] Kask, S.B. and Maani, S.A., 1992. Uncertainty, information, and hedonic pricing. *Land Economics*, pp.170-184.

Gender Differences in Perceptions of cycling to school: A gender analysis of students' and parents'/guardians' perceptions of cycling to school factors

Ross Higgins[1], Aoife Ahern[2]
[1]School of Engineering, University of Limerick, Limerick, Ireland.
[2]School of Civil Engineering, University College Dublin, Dublin 4, Ireland.
email: Ross.Higgins@ul.ie, Aoife.Ahern@ucd.ie

ABSTRACT: Increasing the number of daily walking and cycling trips by 2030 is one of Ireland's objectives in achieving its 2030 emissions reduction targets. This will involve a reduction in car travel and an increase in active travel. There is scope to further increase the number of cycling trips as only approximately 3% of adults commute by bicycle with males accounting for more than twice the rate of females. A gender difference in cycling to school rates also exists. To design strategies to promote the uptake of cycling, especially to girls, the reasons for not cycling must be understood. This study comprises the surveys and qualitative focus group meetings with students and parents/guardians. Factors yielding significant differences between boys and girls were uniforms, bags, traffic concerns, physical efforts of cycling, effects on personal appearance, and peer- and parental-influences. Female parents/guardians rated factors significantly more negatively for their daughters compared to their sons, unlike the male parents/guardians. The focus group results affirmed the same factors while explaining the origins and effects of peer-influences where girls, it seems, are more peer-influenced than boys. Students were less concerned about traffic safety than their parents/guardians, who in most cases, insist on wearing helmets. Uniforms must change to encourage girls to cycle to school, heavy schoolbags should be eliminated using tablets and segregated cycle lanes need to be constructed to alleviate parents', especially mothers', traffic concerns. Further research is required to inform the design of measures to address the non-infrastructural enablers to cycling for secondary school students.

KEY WORDS: Cycling to school; gender; students; parents/guardians; barriers; sustainable travel; reducing emissions.

1 BACKGROUND

Limiting climate change is an agenda of many countries, including Ireland. Decarbonising transport is seen as important part of many countries' climate action proposals [1]. In Ireland, there are ambitious targets of reducing carbon emissions and the Irish government aims to achieve a 42 - 50% reduction in emissions from transport by 2030. Among measures, published in the Ireland's revised Climate Action Plan [2], is a target to significantly increase the number of daily walking, cycling and public transport trips by 2030. Cycling commuting rates have increased in Ireland recently; however, rates are still much lower (3% for workers) than those in other countries [3]. Gender differences in cycling rates are evident across the population with male adults more than twice as likely (3.9% v 1.7%) to cycle to work compared to females. An interesting phenomenon occurs as children progress from primary school to secondary school. At primary school (5-12 yo), boys again are approximately twice as likely to cycle than girls but at secondary school level (13 – 18 yo) the rate of cycling among boys more than doubles and the rate among girl halves [3].

Similarly, gender differences are found across many English-speaking countries [4, 5]; however, in parts of Europe, such as in the Netherlands, women account for 55% of all cycling trips [5].

Much research is available to account for the gender differences in cycling commuter rates among adults. Traffic volumes and speeds [6, 7], preferences for separation from traffic [6], personal safety [8, 9], bicycle handling skills [6, 10, 11], distance [12] and the requirements to look presentable [13, 14] generally are concerns more for woman then men.

Most research available on school children's behaviours relates to parents' perceptions rather than those of students. Mixing with traffic appeared to be a significant concern among parents. According to research from New Zealand, parents were more concerned with their children cycling compared to walking given the availability of footpaths for walkers [15].

Other research found that parents/guardians were significantly influenced by social norms, i.e., the perceptions of their friends' and family towards permitting their children to walk or cycle to school [16].

This paper summarises a significant component of PhD research and determines if cycling to secondary school rates differ by gender and if this is affected by weather conditions; examines the factors which affect girls more than boys in relation to cycling; determines if male and female parents'/guardians' perceptions differ and if these perceptions differ based on student gender.

2 METHODOLOGY

The study comprised two main parts: surveys and focus group meetings. Separate surveys were carried out for students and for parents/guardians. The authors have previously published a detailed account of the survey findings [17]. Contained in this paper is a summary of those survey findings along with an overview of the focus group methods and results.

2.1 Surveys

Surveys were taken by students across seven mixed post-primary schools in Limerick City and suburbs in 2019 and 2020. Students were asked questions related to their travel patterns and their perceptions towards cycling. A screening question - did you live greater than 8km away from school? - was introduced to eliminate the students who could not easily cycle to school. Research from Belgium [18] indicated that distance cycled to school by adolescents reduced significantly with commuting distances of greater than 8km. The students'

survey contained thirty-six questions relating to cycling to school. These Likert Scale questions asked students to indicate their level of agreement with statements. Strongly Agree = 1 to Strongly Disagree = 5 were the codes used. An analysis of the means indicates the average level of agreement with statements.

Parents/guardians were asked to offer their consent to allow their children participate in the study and also to participate in the parents'/guardians' survey by providing their email addresses. A total of 251 parents/guardians, (M = 47.4 years, SD = 5.9 years) ranging in age from 32 to 65 years, responded to the survey.

2.2 Qualitative Focus Group Meetings

Meetings were held with secondary school students and with parents/guardians.

Homogeneous groups formed naturally as student participants were from the same class and therefore were of similar ages. In all but one meeting, male and female participants were separated for a number of reasons; mainly, it allows for participants to feel more comfortable to contribute to a discussion [19].

The number of student participants varied from seven to thirteen as there was a limit to the access to students that could be provided due to practicalities of attendance, consent, and the teacher offerings. Extra time was provided to conduct the focus group of thirteen participants resulting in no apparent issues.

For the parents'/guardians' focus groups, between four and ten parent/guardian participants contributed to the meetings.

The parents/guardians that were recruited were not necessarily the parents/guardians of the students that took part in the students' focus groups. Parents/guardians that consented to complete the questionnaire by providing their email addresses were contacted during the recruitment process.

Access to students for focus groups was challenging during the Covid-19 pandemic. For the student focus groups, many schools had a no visitors policy. This meant that the supporting teachers had to set up online meetings to facilitate focus group meetings. The visual communication comprised videos of students' faces only. Despite participants wearing masks, the audio quality was good.

The online focus group meetings with parents/guardians were much improved. Participants did not have to wear masks and the nature of webcam videos meant that facial expressions and body language were easy to determine.

Notes were taken to actively summarise key points as well as recording non-verbal language. Transcripts were developed from the recordings. A discussion guide was developed to help guide the focus group meetings. This contained *inter alia* introductory questions and specific questions related to the research questions. New issues, relevant to the topic, were further explored.

The focus group meetings were conducted between September 2020 and February 2021 as outlined in Table 1.

Table 1: Qualitative focus group meeting details

Student or Parents/Guardians	Composition	Duration
Students	4 males, 9 females	1:12
Students	8 females	0:34
Students	7 males	0:34
Students	11 females	0:32
Students	8 males	0:34
Parents/Guardians	6 males	1:01
Parents/Guardians	10 females	1:50
Parents/Guardians	4 females	1:21

NVivo, which is qualitative data analysis software, was used to manage the analysis of the data. Two separate analyses were completed: an analysis of the five meetings with students and an analysis of the three meetings with parents/guardians; therefore, two separate *NVivo* files were created. The type of qualitative analysis used was thematic analysis where the focus group meeting transcripts and notes were analysed to reveal common themes. There are typically two different approaches to thematic analysis: inductive, where the data forms themes and deductive, where the analysis begins with an existing understanding, and therefore predetermined themes, on a subject [20]. The latter was adopted here as some knowledge of perceptions towards cycling to school by gender was already known. The coding of the data was completed systematically where common features were coded as nodes (*NVivo* terminology) and groups of nodes brought together as themes. Specifically, the coding comprised the tagging of quotations on particular points. Nodes were created and modified during the review of the transcripts. Following a final review of themes, the nodes were ordered by frequency of reference; the most referenced being indicative of the main barriers to cycling. Descriptions of the themes that emerged during the meetings were written with relevant quotations presented as evidence.

3 RESULTS

The main findings of both the surveys and the qualitative focus group meetings are described in this section.

3.1 Surveys

3.1.1 Cycling to/from school rates by gender and by weather

Table 2 shows the cycling to school rates by weather and by to/from secondary school. The analysis reveals that boys are almost eighteen times more likely than girls to cycle; while the CSO's figures indicate that boys are 24.3 times more likely to cycle than girls (4.69% v 0.19%) [3]. The discrepancy (18 v 24.3) is likely due screening question which eliminated those who lived greater than 8km from school.

The results of column proportion tests showed that for all four comparisons, there were statistically significant gender differences.

Table 2: Contingency table showing cycling to/from rates by weather, by gender for secondary school students (n = 457)

			Secondary School Travel		
To or From	Weather		Gender		
			M	F	Total
To	Good	No.	9a	0b	9
		%	5.7%	0.0%	2.7%
	Bad	No.	11a	0b	11
		%	7.2%	0.0%	3.4%
	Total	No.	20a	0b	20
		%	6.4%	0.0%	3.0%
From	Good	No.	15a	1b	16
		%	9.4%	0.6%	4.8%
	Bad	No.	9a	2b	11
		%	5.9%	1.2%	3.4%
	Total	No.	24a	3b	27
		%	7.7%	0.9%	4.1%
	Total	No.	44a	3b	47
Total		%	7.1%	0.4%	3.6%

Subscripts a and b indicate that, following a z-test, the column proportions are significantly different.

3.1.2 Barriers to cycling with significant gender differences

The results of the Mann-Whitney U tests, with Benjamini-Hochberg adjustments, for questions related to cycling to school, show that there were statistically significant gender differences ($p < .05$) in perceptions across a number of factors as shown in Table 3.

The factor with the largest difference between means was "my uniform does not lend itself to riding a bicycle". Girls must wear long skirts, at least, to "midcalf" in all of the schools that engaged with the study [21, 22]. This is the norm across many schools in Ireland.

Many of the factors that were significantly different by gender related to a lack of enthusiasm for the effort of cycling for girls. The "number of bags or weight of bags", being "too tired", being "too lazy", "not physically fit enough to cycle" or that cycling "involves too much planning ahead" were perceived as barriers for girls more than boys. Girls' perceptions of their bike handling and bike maintenance skills were also significantly different from those of boys.

Aligned with research among adults, female students reported being more conscious of their physical appearance with a significant difference in means between the genders in relation to: "cycling would ruin my hair especially if I wore a helmet". Traffic volumes and speeds seemed to affect girls more than boys with respect to cycling to school.

There was a significant difference between males and female students associated with the level of agreement with the statement, "cycling to school is uncool", indicating that girls are more peer-influenced than boys. Finally, a significantly higher rate of male students indicated owning or having access to a bicycle.

Table 3: Results of Mann-Whitney U tests with Benjamini-Hochberg adjustments comparing Likert Scales responses related to cycling to secondary school for boys and girls (n = 154 males, 174 females)

Factor	Male		Female		U	Z	Sig.	BH Adj.
	M	SD	M	SD				
There is too much traffic on the roads / traffic goes too fast to make cycling safe	3.06	1.23	2.66	1.25	10889	-2.843	.004	**.011**
I don't own or have access to a bicycle	3.97	1.22	3.54	1.39	10870	-2.916	.004	**.010**
I have to carry too many bags / my bags are too heavy	2.54	1.22	1.95	1.01	9638	-4.414	<.001	**<.001**
It involves too much planning ahead	3.38	1.27	2.88	1.14	10072	-3.832	<.001	**.001**
I would not be able to fix minor mechanical issues	3.30	1.29	2.76	1.23	10071	-3.822	<.001	**.001**
I am not physically fit enough to cycle	4.16	1.11	3.82	1.20	10967	-2.845	.004	**.011**
I do not feel confident handling a bike	4.06	1.09	3.37	1.19	8680	-5.570	<.001	**<.001**
I would get too hot and sweaty if I cycled	3.34	1.28	2.86	1.25	10474	-3.338	.001	**.003**
I often feel too tired to cycle	3.36	1.31	2.78	1.26	9924	-3.999	<.001	**<.001**
My uniform does not lend itself to riding	2.97	1.32	1.85	1.22	6888	-7.772	<.001	**<.001**
Cycling would ruin my hair esp. w/helmet	3.51	1.28	2.74	1.25	8880	-5.257	<.001	**<.001**
I would be afraid of being attacked by bullies or strangers on my way to / from school	3.90	1.17	3.58	1.16	10999	-2.745	.006	**.014**
It is uncool to cycle to school	3.71	1.13	3.17	1.18	9809	-4.177	<.001	**<.001**
I am too lazy to cycle	3.53	1.25	3.08	1.28	10588	-3.207	.001	**.005**
Walking is more sociable	2.59	1.12	2.30	1.11	11301	-2.376	.018	**.032**
Driving a car or getting a lift in a car is cooler	3.49	1.21	3.06	1.25	10639	-3.156	.002	**.005**
My parent(s)/guardian(s) think that it is unsafe	3.55	1.26	3.14	1.30	10837	-2.908	.004	**.010**

M: Means, SD: Standard Deviation, U: Test statistic for Mann-Whitney U Test, Z: Standardised Test Statistic, Sig. (2-t): p-values for Mann-Whitney U Test, BH Adj.: p-values following Benjamini-Hochberg adjustments (bold values indicate statistical significance at the $p<.05$ level).

3.1.3 Parents'/guardians' Effect on Cycling to School by student gender

Parents/guardians were asked questions related to their perceptions of cycling commuting and questions about their perceptions of their children cycling to school. The results show that parents'/guardians' barriers to cycling for their children relate to safety issues, especially, traffic volumes, traffic speeds and driver behaviour which aligns with other research on walking and cycling to school [23]. Parents/guardians also indicated that the number of bags and the weight of bags were factors affecting their children's ability to cycling to school.

Analysing the results by student gender reveals some interesting findings. "He/she would get too hot and sweaty if he/she cycled" was seen as more of an issue for girls than boys, as were uniforms and the effect of cycling on their physical appearance. They indicated on average that "it is uncool to cycle to school" for the girls not for their boys. There were no gender differences in relation to cycling being affected by pre- and post-school activities. Of particular note, parents/guardians, did not differentiate between their male and female children in relation to their personal safety concerns.

3.2 Qualitative Focus Group Meetings

Presented here is an abridged version of the main findings of the qualitative focus groups. Not all themes are mentioned.

3.2.1 Distance to School

Distance was a significant barrier to cycling to school which aligns with previous research [24]. A small proportion of students said that if the distance barrier was removed, they would consider cycling to school: "If I lived closer I probably would do it." Gender differences were not revealed during student and parent/guardians focus group discussions on the effect of distance on cycling to school.

3.2.2 Uniforms

Wearing a prescribed uniform was obligatory for all of the students in the schools in the study area. Boys must wear trousers and girls must wear skirts to about "mid-calf". Discussions across all qualitative focus groups indicated that the skirts do not support cycling. When asked "why don't you cycle to school?", a characteristic response was "because we wear really long skirts, and it would be very hard to cycle in it". The uniform appeared to be the main barrier to cycling to school: "I would cycle to school if I didn't have the skirt."

Parents/guardians offered comments suggesting that the long skirts are as restrictive as a long journey and that the low rates of cycling to school among girls in the study area, as a result of the skirts, was expected. One parent described the skirts as follows: "It's totally prohibitive. It's not just skirts, it's Limerick school skirts here you're handed this thing when you're 12 and told, by the way, you won't be cycling even if you want to because you have put this on and it's not just the length of the skirt. It's the weight of the skirt…It's just not safe to cycle in a skirt that length." One parent offered some context surrounding the culture of girls wearing skirts that are longer than required: "I wore a very long skirt, but it wasn't as long. I was in the same school, and it wasn't as long as it is now. My daughter's skirt fitted her this year, but she had to change it because it wasn't long enough. Another €70. The skirts have to hit the ground…I just am sickened by the fact that I have to buy another €70 contraption. It's archaic. It's like having to wear a corset; you can do nothing in these skirts."

Some proposals, which would require a change to school uniform policy, were outlined by parents/guardians. These included a free pass on PE days where students could be permitted to wearing their gym gear if they cycled: "If the schools could cooperate. I mean, on certain days they have their sports days where they have sports activities, they wear tracksuits."

Another suggestion from a parent/guardian would permit students to change from their uniforms upon arrival to school: "If I my daughter could wear a tracksuit and even had a changing facility when she gets into school, she could happily pack her uniform into her backpack."

3.2.3 School Bags and Gear Bags

Many students indicated that their main reason for travelling to school by car was because of the weight or awkwardness of their bags. Students must carry school bags for books and occasionally bags for PE classes or after-school activities including hurleys and hockey sticks.

The weight of the school bags, in particular, steers students away from cycling to school. One student who has a less than one-kilometre commute says that he walks instead of cycling because he has a bag on his back containing books, and he has to carry extra books in his arms. This describes a challenging commute even without a gear bag which many students would need up to "four times a week".

Some parents/guardians said that the bags are heavy especially for first to third-year students. The lighter bag of students in transition year (4th year in secondary school) would support more walking and cycling, according to some parents'/guardians' comment: "When they were younger, say first, second third year, they were more argumentative about walking because the bags were very heavy then and I found it easier, in transition year, that they were quite happy to walk and cycle because you'd less time constraints and bags were lighter".

Digital learning resources are becoming more readily available for students, suggesting that there may be lighter school bags in the future: "during the lockdown, the book companies have come on big time with digital versions of their books."

3.2.4 Infrastructure and Traffic

While students' concerns with road safety were not on par with those of their parents/guardians, there was still a number of comments related to traffic and infrastructure with respect to cycling to school.

Many of the parents/guardians, whose children did not cycle, said that their main barrier for their children cycling to school was road safety. One mother described her anxiety: "for parents, it's more safety, safety, safety. If it's not safe, straight away, we're anxious leaving our kids amongst the traffic." Parents/guardians made several comments on why they thought it was unsafe, mainly due to a lack of cycle lanes, inadequate cycle lanes or peak traffic.

Parents/guardians seemed to be more conscious of their children's safety than their children were about their own

safety: “He cycles occasionally, but like that, the infrastructure: I don't think it is an issue for him, but it is for us.”

As barriers to cycling were hypothetically broken down for students, one girl’s response, for not cycling, clearly illustrates a concern for mixing with traffic: “probably not because, like, it’s weird, like, I get nervous cycling in traffic”. This aligns with much research that says that women have stronger preferences for separation with traffic [6].

Dangers of peak traffic were highlighted by several parents/guardians describing an unequal competition between cyclists and drivers. “There’re about five schools in our area and there's a lot of traffic on the road and, even guiding them off our road onto another, you're taking your life into your hands. There's very little space there, especially at junctions. People are in such a hurry to go. They would speed up and knock your child down to save a minute getting into work, honest to God like.”

On the other hand, off-road cycling facilities were highly regarded by parents/guardians. One mother explained the infrastructure in her locality: “we are very, very lucky that we live within a 3-kilometre or thereabouts radius of the school and there are safe cycle routes. So, there's no worry about safety in relation to traffic or crossing roads.

3.2.5 Peer-Influences

Most students said that they would cycle to school if others from their area, cycled to school. Several contributions matched the following comment: “If all my friends were cycling to school, I’d probable cycle then myself.” Sometimes, barriers did not need to be hypothetically eliminated for a student to indicate that they would be influenced by friends’ behaviour, noting the additional safety benefits of group riding: “It would probably be safer; more people.”

A large proportion of the parents’/guardians’ comments across all focus groups related to peer-influence on cycling. The low rates of cycling to school particularly among female students means that cycling is simply not contemplated. One mother explained this as follows: “They don't see girls cycling so therefore they don't cycle. It’s a vicious circle. How we break that, I don’t know because the infrastructure is actually very good.”

Bolstering this point was another parent’s graphic imagery: “I'd say that the whole peer element I'd say. You know the way people are like sheep. One does it, they all do it, I think. I think if there were more cycling, more girls would be inclined to do it.”

Active commuting to school has been shown to be one of the behaviours that often continues throughout secondary school [24]. One mother believes that first-year students are the most sensitive: “when they come into first year, they find it very hard to settle in because they're making new friends. So, they might not want to cycle because they want to fit in and be doing what all you other girls are doing.”

3.2.6 Parental-Influences

Students acknowledged their parents’/guardian’s road safety concerns, particularly surrounding peak traffic, in relation to cycling to school: “Some parents might not want their kids to cycle at all 'cause they might be worried about them on the roads with so many cars trying to get to school at the same time.”

Helmets and high-visibility clothing were revealed as a conflicting issue among students and their parents/guardians as the following indicates: “Some parents might start saying that they want their kids to wear a helmet and the kids might not want to.”

There were a number of comments made by students that indicated that they would be able to cycle to school but their siblings, often younger, may not be. One student, when asked if he would get his parents’/guardians’ support to cycle, said: “I probably would, but they’d be more worried about my younger brother. I'd have to look after him on the roads.”

Parents/guardians mostly indicated that they would offer the same level of support to cycle to school to their sons and daughters. However, a number of female parents/guardians seemed to provide more support in the form of lifts to their daughters: “her bags can be so heavy, and she has so many of them and the boys are stronger than she would be. Now, she’s not a meek child by any stretch of the imagination”. Another mother admitted being more protective of her daughters than their sons due to, perhaps, increased vulnerabilities for girls: “I suppose, I sense more danger for her than for him. You know she's very young. I suppose I'm just more protective of her than him, but there's no real logical explanation. Simply, because she's a girl.”

4 DISCUSSION/CONCLUSION

The main of objectives of this paper were to determine if cycling to secondary school rates differed by gender and if this was affected by weather conditions; to examine the factors which affect girls more than boys in relation to cycling; to determine if male and female parents’/guardians’ perceptions differ and if these perceptions differ based on student gender.

The research showed that girls are less likely to cycle to secondary school boys. Bad weather affected cycling rates for both genders aligning with research on walking and cycling to school in Canada [25] but differing from findings from the Netherlands [26] where active travel rates to school are significantly higher.

Girls’ uniforms – long skirts – were a considerable barrier to cycling when compared with trousers for boys. However, a number of factors need to be considered together. Carrying school bags and mixing with traffic, which affect girls significantly more than boys, added to girls’ obligations to wear long skirts, described as “corsets” in focus groups, would seem to significantly affect bike handling. Indeed, girls on average rated their bicycle-handling skills less than those of boys. Perhaps, this would not be the case if girls were allowed to wear trousers. Most international research [10, 11, 27, 28] in the area focusses on females’ stronger preferences for separation from traffic. This research, however, suggests there are several factors that are barriers for girls more than boys, but the starting point of the requirement to wear skirts compounds other factors leading girls away from cycling to school.

Lower physically fitness levels among girls were reported more for girls than for boys aligning with research that suggests that that Irish schoolgirls undertake less physical activity than boys [24]. The physical work associated with cycling compared with traveling by car seems to affect girls more than boys.

Girls reported being more affected than boys by impact of cycling on their physical appearance aligning with research among adults [29].

Evidenced primarily from the qualitative focus group meetings was the view that girls were more peer-influenced than boys. One of the main priorities of girls, particularly first years, is to conform to social norms. The quote, "girls don't cycle because they don't see other girls cycling" by one mother illustrates this point. It seems that girls, even more than boys, are reluctant to engaged in an activity that would be considered unusual, leading to, "a vicious circle".

Aligning with other research [15], the results showed that parents/guardians reported that traffic volumes/speeds and lack of cycling infrastructure were barriers to cycling to school for their children.

There was some agreement between students and parents/guardians related to uniforms, school bags and fixing a bicycle; however, there were some differences where parents/guardians perceived their children's fitness, their ability to handle a bike, their tiredness/laziness, and their self-appearance as factors that should not affect cycling.

An interesting finding from the surveys was the differing perceptions that male and female parents/guardians had on their children cycling to school. Male parents'/guardians' perceptions were not significantly differentiated by the gender of their child, while the data from female parents/guardians showed significant differences between their daughters and sons across several factors. It seems that to increase the rates of cycling among female students, a change to female parents'/guardians' attitudes and perceptions is required. addressing the concerns of female parents/guardians on cycling to school may have significant impacts.

Girls should be permitted to wear trousers and there should be more segregated cycle lanes developed to alleviate concerns, especially among female parents/guardians, of the risks associated with the mixed with traffic. Finally, measures should be put in place to reduce the weight of the school bags. while there may be advantages and disadvantages to moving to a tablet/computer-based learning experience [30], it would help to mitigate the heavy school bag which is a barrier to cycling, especially girls.

REFERENCES

1. International Transport Forum. *How serious are countries about decarbonising transport?* 2021 [cited 2022 07/01/2022]; Available from: https://www.itf-oecd.org/how-serious-are-countries-about-decarbonising-transport.
2. Government of Ireland, *Climate Action Plan*. 2021.
3. Central Statistics Office. *Census of Population 2016 – Profile 6 Commuting in Ireland*. 2016 21/11/2017]; Available from: http://www.cso.ie/en/releasesandpublications/ep/p-cp6ci/p6cii/p6mtw/.
4. UK Government. *Statistical data set - Mode of travel* 2020 [cited 2020 24/08/2020]; Available from: https://www.gov.uk/government/statistical-data-sets/nts03-modal-comparisons#mode-by-age-and-gender.
5. Garrard, J., S. Handy, and J. Dill, *Women and cycling.* City cycling, 2012: p. 211-234.
6. Aldred, R., et al., *Cycling provision separated from motor traffic: a systematic review exploring whether stated preferences vary by gender and age.* Transport Reviews, 2017. **37**(1): p. 29-55.
7. Dill, J. and J. Gliebe, *Understanding and measuring bicycling behavior: A focus on travel time and route choice.* 2008.
8. Bopp, M., A.T. Kaczynski, and G. Besenyi, *Active commuting influences among adults.* Preventive Medicine, 2012. **54**(3): p. 237-241.
9. Heesch, K.C., S. Sahlqvist, and J. Garrard, *Gender differences in recreational and transport cycling: a cross-sectional mixed-methods comparison of cycling patterns, motivators, and constraints.* International Journal of Behavioral Nutrition and Physical Activity, 2012. **9**(1): p. 106.
10. Akar, G., N. Fischer, and M. Namgung, *Bicycling choice and gender case study: The Ohio State University.* International Journal of Sustainable Transportation, 2013. **7**(5): p. 347-365.
11. Misra, A., K. Watkins, and C.A. Le Dantec, *Socio-demographic influence on rider type self classification with respect to bicycling*. 2015.
12. Carroll, J., et al., *What drives the gender-cycling-gap? Census analysis from Ireland.* Transport Policy, 2020. **97**: p. 95-102.
13. Broache, A., *Perspectives on Seattle Women's Decisions to Bike for Transportation*. 2012, University of Washington.
14. Dalton, A., *Cycling experiences: Exploring social influence and gender perspectives*. 2016, University of the West of England.
15. Mandic, S., et al., *Differences in parental perceptions of walking and cycling to high school according to distance.* Transportation Research Part F: Traffic Psychology and Behaviour, 2020. **71**: p. 238-249.
16. Pang, B., S.R. Rundle-Thiele, and K. Kubacki, *An empirical examination of the ecological and cognitive active commuting framework: a social marketing formative research study.* Health Education, 2017.
17. Higgins, R. and A. Ahern, *Students' and Parents' Perceptions of Barriers to Cycling to School - An Analysis by Gender.* Sustainability, 2021. **13**(23).
18. Van Dyck, D., et al., *Criterion distances and correlates of active transportation to school in Belgian older adolescents.* International Journal of Behavioral Nutrition and Physical Activity, 2010. **7**(1): p. 87.
19. Krueger, R.A. and M.A. Casey, *Focus groups: a practical guide for applied research*. 5th ed. 2015, Thousand Oaks, California: SAGE.
20. Braun, V. and V. Clarke, *Using thematic analysis in psychology*. Qualitative research in psychology, 2006. **3**(2): p. 77-101.
21. Castletroy College. *School Uniform*. 2021 [cited 2021 17/05/2021]; Available from: https://www.castletroycollege.ie/page/School-Uniform/32563/Index.html.
22. Crescent College Comprehensive. *School Uniform*. 2021 [cited 2021 17/05/2021]; Available from: https://www.crescentsj.com/about/school-uniform/.
23. Aibar Solana, A., et al., *Parental barriers to active commuting to school in children: does parental gender matter?* Journal of Transport & Health, 2018. **9**: p. 141-149.
24. Woods, C., et al., *The Children's Sport Participation and Physical Activity Study 2018 (CSPPA 2018).* 2019.
25. Blanchette, S., et al., *Influence of weather conditions on children's school travel mode and physical activity in three diverse regions of Canada*. 2020.
26. Helbich, M., et al., *Natural and built environmental exposures on children's active school travel: A Dutch global positioning system-based cross-sectional study*. Health & Place, 2016. **39**: p. 101-109.
27. Dill, J. and N. McNeil, *Four types of cyclists? Examination of typology for better understanding of bicycling behavior and potential*. Transportation Research Record, 2013. **2387**(1): p. 129-138.
28. Wittmann, K., et al., *Cycling to high school in Toronto, Ontario, Canada: Exploration of school travel patterns and attitudes by gender*. Transportation Research Record, 2015. **2500**(1): p. 9-16.
29. Davies, D., et al., *Attitudes to cycling: a qualitative study and conceptual framework.* 1997: Transport Research Laboratory Crowthorne.
30. Marcus-Quinn, A., T. Hourigan, and S. McCoy, *The digital learning movement: How should Irish schools respond?* The Economic and Social Review, 2019. **50**(4): p. 767-783.

Planning Cycle Parking Trials in Dún Laoghaire-Rathdown: A Survey & GIS Approach

Dr. Robert Egan[1], Dr. Conor Dowling[2], Prof. Brian Caulfield[1]
[1]Centre for Transport Research, Department of Civil, Structural & Environmental Engineering, Trinity College Dublin
[2] Trinity Business School, Trinity College Dublin
email: eganr5@tcd.ie, conor.dowling@smartdunlaoghaire.ie, brian.caulfield@tcd.ie

ABSTRACT: Dún Laoghaire-Rathdown (DLR) has a considerable supply of unsheltered cycle parking for people cycling throughout the region in addition to a growing network of protected cycle infrastructure. With further high-quality developments being considered in expanding the cycle network in the county, cycle parking is one area of critical cycle infrastructure that can also be improved in order to attract more people to cycling as an alternative to car travel. In particular, cycle parking that enhances protection from theft and the natural elements could enable more people to cycle in the region who may be otherwise deterred by less protected forms of parking. We carried out a programme of research to plan a series of cycle parking trials with DLR County Council, in which new forms of cycle parking could be tested in optimal locations in the region. In this planning process, we collected and analysed data from an ArcGIS Survey123 survey questionnaire completed by people who have access to a cycle and live or visit the county. This survey primarily measured i) current and hypothetical mobility practices; ii) cycle parking practices, preferences and perceptions; iii) socio-demographics; and iv) locations in DLR where respondents would like to see cycle parking trialled. Through an analysis of these data and an investigation of survey-derived GIS (Geographic Information System) hotspot parking demand locations, we provide a basic outline of potential trials for enhanced cycle parking in the county.

KEY WORDS: CERI/ITRN 2022; Cycling; Cycle Parking; Transport Planning; Cycle Infrastructure; Public Transport Integration; Parking Policy; ArcGIS.

1 INTRODUCTION

Cycle parking is widely viewed as a primary component of a robust cycling system; a system that integrates cycling as a normal mode for both cycle-only journeys as well as multi-modal trips. Although cycle mobility infrastructure is often the focus in media discourse in relation to cycling promotion, the imperative of sufficient and good quality cycle parking for expanding ridership is visible across international transport policies [1][2][3][4][5].

Indeed, examining Irish cycling policy, the expanded availability of secure cycle parking is proposed as a major objective to promote cycling nationwide [6]. This policy states that high-quality cycle parking is as important as exemplary cycle mobility infrastructure, such as segregated cycle tracks. This perspective on the importance of cycle parking is actioned within the policy. Namely, it is not only proposed that unsheltered cycle parking stands should be made more widely available for cyclists, but also that efforts to provide dedicated, guarded and high-volume cycle parks as well as potential cycle parking stations – which are a notable characteristic of high-cycling contexts within Europe – should be enacted. These considerable cycle parking ambitions [6] arguably exceed recent policy and planning objectives emerging from the UK [1][7][8].

In this paper, we delineate a novel approach to planning secure cycle parking trials in the relatively high-cycling context of Dún Laoghaire-Rathdown (DLR) county. For this approach, we draw on i) survey questionnaire data, ii) Geographic Information System (GIS) data, and iii) hotspot investigation to derive the outlines of several location-specific secure cycle parking trials for the county – a county that has considerable unsheltered cycle parking coverage at present [9] and expanding cycle networks [10][11]. The research-based planning approach delineated in this paper provides a unique addition to existing parking planning guidance at a national [12] and local [13] level.

2 METHODOLOGY

This research was implemented using a two-step methodology involving, first, the construction, dissemination and analysis of an online survey for people who have access to a cycle who either live or visit DLR and, second, on-site investigation of cycle parking practices and potential sites at parking request hotspots derived from the analysis of geodata provided by survey respondents.

2.1 Online Survey:

A robust quantitative survey with GIS components was constructed via ArcGIS Survey123 in order to gather data from respondents to inform cycle parking planning. Primarily, questions were asked regarding the travel behaviour of respondents (e.g. mode of travel, cycle ownership, cycle destinations, cycle frequency, cycle parking practices), preferences for a suite of cycle parking types in DLR (e.g. open rack, cycle compound, cycle locker), and perceptions of cycle parking in DLR (e.g. security of existing cycle parking, likelihood of using cycling as an access mode if secure parking made available, willingness to walk/pay for more secure cycle parking). Crucially, respondents were also asked to provide three geopoints on a map of DLR indicating where they would like to see cycle parking facilities installed and important demographic data were collected to disaggregate these responses. This survey was disseminated via the DLR official twitter account and was circulated via email to relevant groups and authorities (e.g. Dublin Cycling Campaign, Smart Dublin, etc.).

First, sample characteristics and responses to categorical variables relating to mobility practices, cycle ownership and parking practices were examined. Second, scale responses to items relating to cycle parking preferences and perceptions regarding cycle parking in DLR were analysed using

descriptive statistics. Third and last, geopoints provided by respondents were analysed using the ArcGIS Online Map function. This provided useful visualisations of the aggregate and disaggregated (e.g. disaggregated by responses to questions such as gender, cycle parking duration, cycle type, etc.) geopoints provided by respondents, including functions such as heatmap and cluster points in particular.

2.2 Hotspot Investigation:

Following up from the ArcGIS analysis of geopoints provided by respondents requesting cycle parking, rough hotspot locations were identified for trialling cycle parking solutions. To determine more specific sites for trial measures, on-site observation of potential and current cycle locations took place within hotspots or near them (i.e. within 50 – 100m radius of them). In these exploratory observations of hotspot regions, nearby destinations were considered along with the suitability of specific locations for upgraded, additional or new cycle parking that was highly favoured in the survey (i.e. sheltered open cycle racks, guarded sheltered cycle compound and digital access cycle locker) depending on factors such as existing passive surveillance, spatial availability, and likely duration of parking in light of proximal destinations.

3 RESULTS

3.1 Basic Findings

This section presents the basic findings for the survey. In total, there were 574 valid respondents to the survey (58.12% men; 36.92% women). Roughly 65% of the sample were between 35 – 54 years old. 32% of respondents live in Dún Laoghaire, 13% visit or work in DLR but do not live there, and the remainder of respondents live in other regions of DLR county. Overall, 46% of respondents work in DLR. Of the sample, 49.1% use cycling as their usual commute mode; this stands in stark contrast to the rate of 1.5% for Ireland [14]. Similarly, the educational profile of the sample (44% of the sample have a postgraduate qualification as their highest form of education) contrasts with the rate of postgraduate qualification of those in DLR of ~20% [15].

The vast majority – 98.3% – of the sample owned a cycle; these cycles mainly consisted of urban bikes (51%), sport bikes (34.7%) and standard e-bikes (9.6%). The sample was primarily composed of people who cycled frequently, with 45.5% cycling about four or five days + per week, 26.3% cycling about two or three days per week, and 13.1% cycling about once per week. 66.5% of the sample mainly cycled solo; however, 14.7% cycled with their children, 7.18% with their friends/family and 6.5% with their partner.

The top three reported destinations for respondents were friend or family member home/residence (34.87%), shops (groceries) (33.16%) and 'there is no destination' (31.45%) – that is, cycling itself is the trip purpose; these top destinations were closely followed by workplace (31.11%) and shops (retail) (30.7%). However, for the question 'Where is your most frequent cycling destination in Dún Laoghaire-Rathdown?', a different distribution emerged. As shown in Table 1., 'Work/Education' scores highest at 23%, followed by 'Cycling' (20.2%), 'Shopping' (19%), and 'Outdoor Recreation' (13.8% - largely comprising open text responses relating to swimming and use of DLR beaches). At their most frequent destinations, respondents generally used open rack cycling facilities (56.41%) to park their cycles or street furniture (17.78%) as opposed to secure forms of cycle parking (e.g. key access cycle compound – 3.76%). Lastly, at their most frequent destination, respondents generally left their cycles parked between 30 minutes or less to 2 hours (66% of sample) whereas longer stay parking was less frequent – '2-4 hours' (10.26%), '4-6 hours' (5.13%) – except for the '6+ hours' response which 16.75% of respondents selected.

The final section of the survey involved questions relating to cycle theft. 23.93% of the sample (140 respondents) had their cycle stolen in DLR in the past, with nearly half of all thefts occurring in Dún Laoghaire while other thefts were more sparsely distributed across the other regions of DLR county. The vast majority of these respondents were using an open cycle rack at the time, primarily with a U-lock.

Table 1. Sample Survey Responses

Variable	Frequency	Percent
Usual Commute Mode		
- 'Not at work, school or college'	30	5.2
- 'On foot'	17	3.0
- 'Cycle'	282	49.1
- 'Bus, minibus or coach'	15	2.6
- 'Train, DART or LUAS'	46	8.0
- 'Motorcycle or scooter'	4	.7
- 'Driving a car'	106	18.5
- 'Passenger in a car'	3	.5
- 'Van'	2	.3
- 'Other - including lorry'	1	.2
- 'Work mainly at or from home'	68	11.8
Cycle Ownership		
- Yes	564	98.3
- No	10	1.7
Cycle Type		
- Utility Bike	293	51.0
- Sport Bike	199	34.7
- Folding Bike	3	.5
- E-Bike	55	9.6
- Alternative Cycle	24	4.2
Cycle Frequency		
- 'Less than once per month'	42	7.3
- 'About once or twice per month'	45	7.8
- 'About once per week'	75	13.1
- 'About two or three days per week'	151	26.3
- 'About four or five days per week'	261	45.5
Main Cycle Destination		
- Social/Care	58	10.1
- Work/Education	132	23.0
- Indoor Recreation	38	6.6
- Outdoor Recreation	79	13.8
- Sport/Fitness	30	5.2
- Shopping	109	19.0
- Public Transit	12	2.1
- Cycling	116	20.2

3.2 Descriptive Statistics

3.2.1 Cycle Parking Type Preferences

This section presents the findings from the survey that were subject to a simple descriptive statistics analysis. The results of numerous scale questions relating to the reported likelihood for a given respondent to use a particular type of public cycle parking are displayed in Table 2. in the form of descriptive statistics (i.e. mean, mode and standard deviation). Five responses were available, ranging from 'Highly Unlikely' (a

value of 1) to 'Highly Likely (a value of 5) with 'Unsure' (a value of 3) in the centre. Importantly, before asking this question, respondents were asked what cycle parking they generally use for their most frequent cycle journey parking in which we found that secure cycle parking was hardly used (e.g. key access cycle compound – 3.76%). In this respect, this question does not ask respondents what they are likely to use in DLR in relation to what is currently available but, rather, how likely they would be to use certain cycle parking types if hypothetically available. The fact that the mode value of 5 (i.e. 'Highly Likely') was recorded for each of the guarded cycle compound questions shows that this selection of questions was, for the most part, understood correctly as a hypothetical exercise.

Overall, one can see that 'Open Rack Sheltered' is the cycle parking type most highly ranked by respondents, with a mean of 3.99 (close to 'Likely') and a mode of 5 ('Highly Likely'), with the smallest level of standard deviation at 1.24 among all types. 'Open Rack Unsheltered' was the second highest cycle parking type in terms of mean score (3.75). Among 'secure' parking types, 'Cycle Compound – Sheltered and Guarded' was rated the highest by respondents with a mean of 3.66 and a mode of 5; this was closely followed by 'Cycle Compound – Indoor and Guarded' (mean: 3.6; mode: 5) and less closely followed by 'Cycle Compound – Unsheltered and Guarded' (mean: 3.51; mode: 5). Accordingly, sheltered cycle compound parking that is guarded by an attendant appears to be the most preferred secure cycle parking type for the sample, while the key access cycle compound variations appear less popular as demonstrated by their lower means and modes. Interestingly, both 'Cycle Bunker – Key Access' and 'Cycle Locker – Padlock' were rated the lowest amongst the options – both with modes of 1 ('Highly Unlikely'), thereby suggesting that such cycle parking types would not be particularly well used if installed for trial purposes. However, 'Cycle Locker – Digital Access' received more favourable responses with a mean of 3.07 (slightly above 'Unsure') and a mode of 4 ('Likely') but with the highest standard deviation across the questions of 1.45, suggesting the greatest variation in responses amongst the alternative forms of parking.

3.2.2 Cycle Parking Related Statements

The following results depicted in Table 3. present descriptive statistics for responses to various statements relating to cycle parking in DLR in which responses ranged from 'Strongly Disagree' (value of 1) to 'Strongly Agree' (value of 5), with 'Neutral' situated in the middle (value of 3). There is a clear result that the majority of participants do not perceive public cycle parking in DLR as secure (mean 2.24, mode 2 – i.e. 'Disagree'). However, on average, respondents were neutral regarding the accessibility of cycle parking in DLR (mean: 3.17). Interestingly, there appeared to be a small perception of unsafety when locking one's cycle in DLR cycle parking amongst respondents (mean: 2.53, mode: 2). Lastly, on average, respondents perceive that cycle parking in DLR is somewhat insufficient (mean: 2.59; mode: 2) in terms of available supply. On the basis of the responses to the aforementioned four statements, cycle parking is perceived by respondents in general as not particularly secure for cycles, not particularly sufficient in terms of supply, and not particularly safe for cyclists, but, on the other hand, basically accessible.

The next round of statements related to hypothetical cycling practices if secure cycle parking facilities were installed in DLR. First, respondents on average appear to nearly agree that they would cycle more if more secure cycle parking in DLR was provided (mean: 3.72; mode: 5 – 'Strongly Agree'). Second, and more definitively, respondents appear to agree that they would be more interested in accessing public transit by cycling if more secure options for parking were provided (mean: 3.94; mode: 5). Third, respondents were closest to 'Agree' in response to the statement that they would be more likely to use public transport if more secure cycle parking was provided in DLR near their route (mean: 3.85; mode: 5). For all three of these statements, the mode response was 5 – 'Strongly Agree' – indicating that the majority of respondents were in strong agreement with these three statements. In this respect, if we are to believe respondents, increased secure cycle parking would likely lead to more cycling and cycle-public transport integrated journeys in DLR.

The last round of statements relate to willingness to pay a cost for access to more secure cycle parking facilities (i.e. a monetary cost and an energy/time cost). Responses, on average, were closest to 'Neutral' (mean: 3.28) in relation to willingness to pay a small fee of 2.5 euros per week to use secure cycle parking over standard cycle parking in DLR, while the mode response was 'Likely' (value of 4). These responses had the highest standard deviation among all responses of 1.3, indicating less consensus amongst participants compared to other statement responses. Similarly, the mean response to willingness to walk a greater distance to one's destination to use secure cycle parking was closest to 'Neutral' (mean: 3.22), also with a mode of 'Likely'. Thus, these findings suggest that the sample is not particularly willing to pay for secure cycle parking facilities nor walk a greater distance to access them, despite – as presented earlier in this section – an overall interest in secure cycle parking over standard cycle racks currently available in DLR. Therefore, free access to cycle parking and maximum proximity to destination are significantly valued by respondents along with secure cycle parking, particularly considering that a very small fee for secure cycle parking is quoted (based on the 'bikelocker.ie' weekly rates) and no walking distance is specified when the cost is distance from destination.

Table 2. Cycle Parking Type Preferences

Cycle Parking Type	Mean	Mode	SD
Open Rack Cycle Parking - Sheltered	3.99	5.00	1.24
Open Rack Cycle Parking - Unsheltered	3.75	4.00	1.28
Cycle Compound - Unsheltered (Key)	2.98	4.00	1.34
Cycle Compound - Sheltered (Key)	3.19	4.00	1.42
Cycle Compound - Indoor (Key)	3.13	4.00	1.43
Cycle Compound – Unsheltered (Guarded)	3.51	5.00	1.39
Cycle Compound - Sheltered (Guarded)	3.66	5.00	1.39
Cycle Compound - Indoor (Guarded)	3.60	5.00	1.43
Cycle Locker - Padlock	2.87	1.00	1.41
Cycle Locker - Digital Access	3.07	4.00	1.45
Cycle Bunker - Key Access	2.90	1.00	1.43

Table 3. Cycle Parking Perception & Hypothetical Practices

Statement	Mean	Mode	SD
Public cycle parking in DLR is secure	2.24	2.00	.98
DLR public cycle parking is accessible	3.17	4.00	.96
I feel safe when locking my cycle to public cycle parking facilities in DLR	2.53	2.00	1.13
There is sufficient public cycle parking available in DLR	2.59	2.00	1.10
I would cycle more if there were more secure cycle parking facilities near my destination(s) in DLR	3.72	5.00	1.15
I would be interested in accessing public transport by cycling if there were more secure cycle parking facilities in DLR	3.94	5.00	1.09
I would be more likely to use public transport if there were more secure cycle parking facilities in DLR near my route	3.85	5.00	1.14
I would be willing to pay a small fee, such as 2.5 euros per week, to use secure cycle parking (e.g. locker, compound, bunker) rather than a standard cycle stand.	3.28	4.00	1.3
I would be willing to walk a greater distance to my destination to use secure cycle parking	3.22	4.00	1.17

3.3 Geopoints

In this section, the majority of the 1755 geopoints provided by respondents are mapped within the county boundary of DLR in response to the question 'Please place a pin at three locations where you would like to see cycle parking in DLR on the maps below.' These geopoints help us to decide what location or number of locations are suitable for trialling new forms of cycle parking in DLR through mapping respondent demand. A large body of mapping exercises – which cannot, due to space limitations, be displayed in this paper – demonstrated that Dún Laoghaire town and pier (particularly the central-eastern side) is an optimal trial location in term of respondent demand. One can see the majority of points from respondents concentrated in this location (Figure 1), which is more clearly visible in the heatmap representation of these points (Figure 2). Importantly, the pattern persisted when looking at women-only respondent points, geopoints placed by respondents that use non-typical cycles – namely e-bikes, cargo bikes and non-cargo cycles with trailers – and for respondents who generally park their cycle for long-stay parking. Likewise, the patterns persisted in clustered geopoints for respondents who selected likely or highly likely to use secure parking types. Based on our multi-faceted GIS analysis of respondent geopoints, the central-eastern region of Dún Laoghaire was selected by the team for further investigation (i.e. for 'Hotspot Investigation and Assessment') to select specific locations for specific cycle parking solutions where trails could take place.

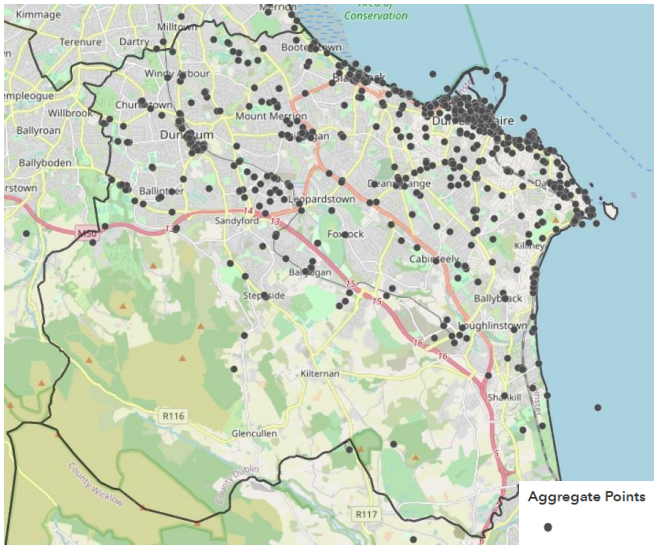

Figure 1. Respondent Geopoints in DLR County

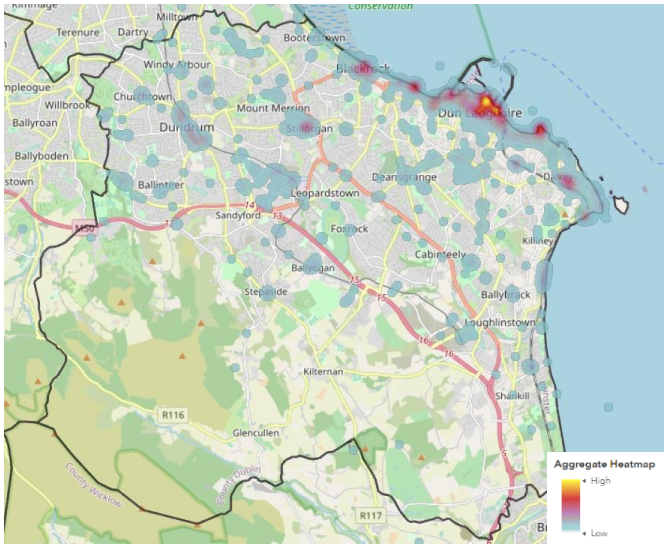

Figure 2. Heatmap of Respondent Geopoints in DLR County

3.4 Hotspot Investigation & Assessment

Following up from the ArcGIS analysis of geopoints provided by respondents requesting cycle parking, rough hotspot locations were identified for trialling cycle parking solutions. To determine more clearly specific sites for trial measures, on-site observation of potential and current cycle locations took place within hotspots or near them (i.e. within a 50 – 100m radius of these hotspots). In these exploratory observations of hotspot regions, nearby destinations were considered along with the suitability of specific locations for upgraded, additional or new cycle parking that was highly favoured in the survey (i.e. sheltered open cycle racks, guarded sheltered cycle compound and digital access cycle locker) depending on

factors such as existing passive surveillance, spatial availability, and likely duration of parking in light of proximal destinations.

As mentioned in the previous section, central-eastern Dún Laoghaire was selected as the most in demand location for respondent cycle parking. Consequently, this basic area was selected for an in-depth and exploratory on-site observation by members of the research team, taking into account the survey findings and the major directives for effective cycle parking planning originating from a previously conducted cycle parking literature review. Closer inspection of points of concentration was carried out and designated hotspots in this area were derived, along with a mapping of existing cycle parking in this area (see Figure 3). Clear hotspots within this subsection of the DLR county were identified for three locations in particular: near Dún Laoghaire train station (Hotspot 1), at the beginning of the Pier Walk beside Queen's Road (Hotspot 2), and at the intersection between Georges Street and the Marine Road in the town centre (Hotspot 3).

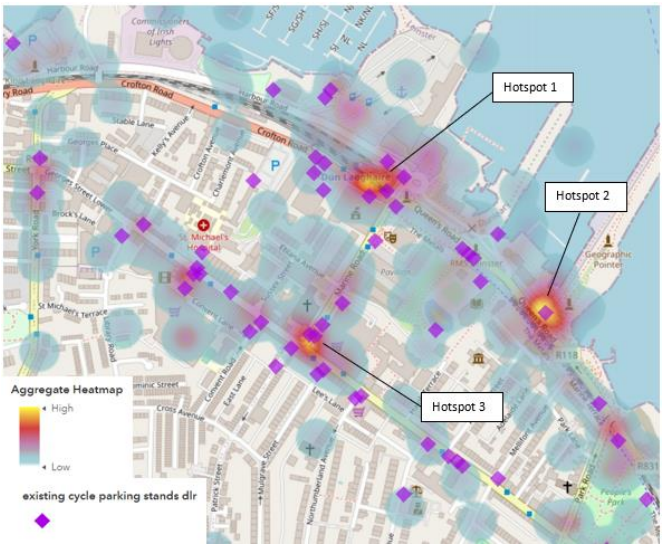

Figure 3. Hotspot Parking Demand Locations in Dún Laoghaire

In the team's inspection of the areas proximal to the hotspots, obvious nearby destinations were noted. For Hotspot 1, Dún Laoghaire train station was the most obvious destination, while being situated within close walking distance to bus services, a range of shops, cafés, restaurants and workplaces. Hotspot 2, on the other hand, was ideally situated for walking along Dún Laoghaire Pier and as a potential base for other recreational activities in Dún Laoghaire such as swimming. Lastly, Hotspot 3 was centrally located near a range of shops and workplaces. With these potential user destinations in mind, one can consider the likely duration and security requirements of cycle parking if such destinations were being accessed.

For Hotspot 1, there is a strong possibility that cycle parking may be relatively long-term (e.g. over 6 hours) considering journeys to other areas of Dublin, such as to one's workplace, may be made via the DART having accessed this service by cycling. In this respect, some form of secure cycle parking that is low cost for a long period would be reasonable to trial. Near this hotspot (as well as in Dún Laoghaire), there is already a considerable supply of cycle parking; however, all of this parking appears to be open and unsheltered, both of which are not ideal long-stay parking due to the long-term exposure to the elements and the lack of security besides passive surveillance and one's lock. There is no question that this particular rail station has a high level of demand with 4329 average daily boardings in 2019 – one of the highest levels for a rail station in Ireland [16]. Thus, trialling higher quality cycle parking near this station could potentially increase cycle access journeys (by replacing potential car access or car-only journeys), which is the most effective form of cycle-public transport integration [17]. Furthermore, this hotspot is also situated close to multiple bus routes, thereby opening up the possibility of further sustainable multi-modal journeys. With current and future public transport users in mind who may cycle as a mode of access, the installation of a sheltered cycle compound in this general location with some form of security could be a viable trial possibility (from the survey, guarded cycle parking is most favoured, but the possibility of digital or key access is also plausible).

For Hotspot 2, if cycle parking relates mainly to recreational activities such as a walk of the Pier, the Peoples Park, leisure-related retail, exploration of Dún Laoghaire town, or toward swimming spots further South, cycle parking duration may be short – medium term (e.g. from 1 – 4 hours). Such use is suggested by DLR Eco-Counter data. The DLR York Road Counter, for example, records an hourly average of 373 counts on Sunday for 12pm which is the peak hourly usage for the week. This is followed by 291 average counts for 12pm on Saturday and then much lower peak hourly averages of between 124 and 150 on weekdays which occur at 8am – suggesting commuter journeys. A similar pattern of use appears for the DLR Peoples Park Counter, which presents the highest hourly average counts in the last year of 941 at 3pm on Sundays, followed by 601 at 3pm on Saturdays. For weekdays, the peak hourly averages are much lower with 354 for 11am on Friday being the next peak. Once again, a pattern of leisure journeys appear prevalent for leisure amenities in the surrounding area rather than more long-term activities that may require more long-term cycle parking facilities in particular. In this respect, first, existing open rack cycle parking could be upgraded with shelters in this hotspot location; second, some form of digital access cycle lockers could be trialled. While digital access cycle lockers may be more expensive than traditional key access cycle lockers, they could potentially enable a great deal of flexibility through their app based access. With some users likely owning expensive cycles and engaging in relatively short-stay parking during weekends, these costs may be acceptable for such a pattern of use, as opposed to daily use during weekdays for long-stay parking (e.g. 8 hours per day).

Lastly, for hotspot 3, a mix of destinations are concentrated in Dún Laoghaire town centre that would likely involve a mix of potential cycle parking durations (e.g. cafés, shopping, restaurants, workplaces). However, there is also a great deal of open rack cycle parking available in the surrounding streets that – upon our midweek investigation – was largely unused, yet very visible to the public and therefore subject to a good deal of 'natural guardianship' [18]. However, once again, there are a lack of mixed cycle parking options (e.g. with shelter, with security features) despite the potential mix of cycle parking uses and preferences for different users cycling to this area. In

this respect, the provision of some long-term cycle parking facilities (such as a guarded cycle compound that is sheltered/indoors), and better quality sheltered open facilities may be warranted.

4 CONCLUSION

In this paper, we provided an account of a novel research-informed approach to planning cycle parking in DLR county, incorporating survey questionnaire data, GIS data, and on-the-ground hotspot investigation. Analysing these data and engaging in on-site observations of hotspots, we made several tentative and general recommendations for three hotspot areas in Dún Laoghaire to trial new and enhanced forms of cycle parking. These trials may increase ridership and promote modal shift from private car journeys to cycle and public transport cycle access journeys. If successful, such trials could be expanded to successive hotspots of stated or observed demand across the county. This unique approach may be useful for future cycle parking planning and policy efforts by national [12] and local authorities [13].

ACKNOWLEDGMENTS

This research was funded as part of a collaborative research project between SFI funded Enable, Connect research centre hosted by Trinity College Dublin and Dún Laoghaire-Rathdown County Council through the Smart Dún Laoghaire research programme.

REFERENCES

[1] Department for Transport (2014). *Cycling Delivery Plan*. Department for Transport. https://assets.publishing.service.gov.uk/government/uploads/system/uploads/attachment_data/file/364791/141015_Cycling_Delivery_Plan.pdf

[2] Director General for Passenger Transport (1999). *The Dutch Bicycle Master Plan : Description and Evaluation in an Historical Context*. Ministry of Transport, Public Works and Water Management. http://www.hembrow.eu/studytour/TheDutchBicycleMasterPlan1999.pdf

[3] Federal Ministry of Transport and Digital Infrastructure (2020). *Germany 2030 – A Cycling Nation: National Cycling Plan 3.0.* Federal Ministry of Transport and Digital Infrastructure. https://www.nationaler-radverkehrskongress.de/wp-content/uploads/NRVP_3.0_EN_RZ.pdf

[4] Le Gouvernement République Française (2018). *Plan Vélo & Mobilités Actives*. Le Gouvernement République Française. https://www.ecologie.gouv.fr/sites/default/files/Dossier%20de%20presse%20-%20Plan%20v%C3%A9lo%20-%20vendredi%2014%20septembre%202018.pdf

[5] Tour de Force (2017) *Bicycle Agenda 2017-2020*. Tour de Force. https://www.fietsberaad.nl/getmedia/1c52943f-8948-4539-8b0d-4fda6048b1a2/Tour-de-Force-Bicycle-Agenda-2017-2020.pdf.aspx.

[6] Smarter Travel (2009). *National Cycle Policy Framework*. Department of Transport. https://www.hse.ie/eng/about/who/healthwellbeing/our-priority-programmes/heal/healpublications/national-cycle-policy-framework.pdf.

[7] Transport Scotland (2017). *Cycling Action Plan for Scotland 2017 -2020: Cycling as a Form of Transport.* Transport Scotland. https://www.transport.gov.scot/media/10311/transport-scotland-policy-cycling-action-plan-for-scotland-january-2017.pdf.

[8] Welsh Government (2021) *Active Travel Act Guidance.* Welsh Government. https://gov.wales/active-travel-act-guidance.

[9] Dún Laoghaire-Rathdown County Council (2021). *Bicycle Parking Stands DLR.* DATA.GOV.IE. https://data.gov.ie/dataset/bicycle-parking-stands-dlr

[10] Dún Laoghaire-Rathdown County Council (2021). *DLR Connector: Pre-Design Consultation*. Dún Laoghaire-Rathdown County Council. https://www.dlrcoco.ie/en/news/public-consultation/dlr-connector-pre-design-consultation

[11] Dún Laoghaire-Rathdown County Council (2020). *Coastal Mobility Interventions*. Dún Laoghaire-Rathdown County Council. https://www.dlrcoco.ie/en/transportation-infrastructure/coastal-mobility-interventions

[12] National Transport Authority (2011). *National Cycle Manual.* National Transport Authority. https://www.nationaltransport.ie/wp-content/uploads/2013/10/national_cycle_manual_1107281.pdf.

[13] Dún Laoghaire-Rathdown County Council Municipal Services Department (2018). *Standards for Cycle Parking and associated Cycling Facilities for New Developments.* Dún Laoghaire-Rathdown County Council Municipal Services Department. https://www.dlrcoco.ie/sites/default/files/atoms/files/dlr_cycle_parking_standards_0.pdf

[14] Central Statistics Office (2019). *National Travel Survey 2019*. Central Statistics Office. https://www.cso.ie/en/releasesandpublications/ep/p-nts/nationaltravelsurvey2019/howwetravelled/

[15] Central Statistics Office (2016). *Census of Population 2016 – Profile 6 Commuting in Ireland*. Central Statistics Office. https://www.cso.ie/en/releasesandpublications/ep/p-cp6ci/p6cii/

[16] National Transport Authority (2020) *National Rail Census Report 2019*. National Transport Authority. https://www.nationaltransport.ie/wp-content/uploads/2020/08/NTA_Heavy_Rail_Census_Report_2019..pdf

[17] Martens, K. (2007). Promoting bike-and-ride: The Dutch experience, *Transportation Research Part A: Policy and Practice*, *41*(4), 326–338. https://doi.org/10.1016/j.tra.2006.09.010.

[18] Chen, P., Liu, Q. and Sun, F. (2018) 'Bicycle parking security and built environments', *Transportation Research Part D: Transport and Environment*, 62, pp. 169–178. doi: 10.1016/j.trd.2018.02.020

Environment

The Application of a Downscaled Economic Model for Sediment Management Projects in Ireland and The Netherlands

Harrington, J.[a], Wijdeveld, A. [b], Wensveen, M.[c], Hamilton A.[d], Lord R.[e], Torrance K.[e], Debuigne T. [f], Masson E. [g], Batel, B.[a]

[a] *Sustainable Infrastructure Research & Innovation Group, Munster Technological University, Cork, Ireland*
[b] *DELTARES, P.O. Box 177, 2600 MH Delft, Netherlands*
[c] *Port of Rotterdam, 3198 LK Europoort Rotterdam, Netherlands*
[d] *Scottish Canals, Canal House, Applecross St, Glasgow, G4 9SP, United Kingdom*
[e] *Department of Civil & Environmental Engineering, University of Strathclyde, Glasgow G1 1XJ, United Kingdom*
[f] *Ixsane, 23 Av. de la Créativité, 59650 Villeneuve-d'Ascq, Lille, France*
[g] *University of Lille, 42 Rue Paul Duez, 59000, Lille, France*

email: joe.harrington@mtu.ie

ABSTRACT: The management of dredged sediment is a challenge for Ports and is the focus of the EU NWE Interreg SURICATES Project which investigates aspects of sediment management. This paper focuses on a regionally downscaled economic model to assess impacts of sediment management options (including disposal, treatment and reuse) for dredged sediments. The model analyses the economic benefits associated with sediment use and specifically Gross Domestic Product (GDP) and jobs created and has been applied to sediment management projects across the SURICATES Partner Countries (Ireland, Scotland, France and the Netherlands) and the United Kingdom (excluding Scotland).

The model facilitates regional analysis of effects of sediment management projects on GDP and job creation. Methods for estimating economic induced impacts are based on industry specific Type I & Type II economic multipliers and coefficients, derived for the EU Interreg NWE SURICATES partner countries using Symmetric Input-Output Tables and application of the open Leontief model based on available economic data for the identified countries. The model has been validated against completed sediment management projects.

The model has been applied to sediment projects in Ireland (Maintenance dredging – Port of Fenit) and in the Netherlands (Dredged sediment reallocation – Port of Rotterdam) and estimates the direct contribution to GDP and direct jobs created and indirect and induced economic project impacts. The model provides valuable results into the benefits of sediment management projects.

More generally it allows impact analysis for economic aspects of sediment projects with potential to inform stakeholders.

KEY WORDS: Dredging, Sediment Management, Economic, Model, GDP, Jobs Created, Port of Fenit, Port of Rotterdam, Circular Economy

1 INTRODUCTION

This paper presents a regionally downscaled economic model developed to assess the impacts of the management of dredged sediments. The model provides an additional tool to support the sustainable use and management of dredged sediments which is an ongoing and major challenge for many ports, harbours and river authorities worldwide.

The process of dredging involves the removal of sediments from the aquatic environment, including port and harbours and is critical to providing navigable access to ports and waterways.

Sediment management approaches that may be practiced including disposal (at sea or on land) or beneficial use (engineering use, environmental enhancement or agricultural and product uses). These sediment management approaches are now focusing on increased beneficial use in the context of the Circular Economy and 'Working with Nature' solutions to the maximum extent practicable. Sediment management practice and challenges have been presented in an Irish context by, for example, by [1], [2], [3] and in a broader international context, for example, [4], [5] and [6].

The sediment management technique selected wlll depend on a range of factors including the sediment characteristics and contamination levels (if any), local site conditions, and national and international practice. These feasibility issues are generally dependent on a range of often inter-related technical, financial, environmental, legislative and societal factors with this paper focusing primarily on the regional economic aspects of dredge sediment management.

The downscaled economic model presented in this paper facilitates the regional analysis of the effect of a dredging project on Gross Domestic Product (GDP) and job creation. The economic model analyses the direct, indirect and induced effect on GDP along with the direct, indirect and induced jobs created. The economic effects were downscaled to a regional EU NUTS3 (EU Nomenclature of Territorial Units for Statistics - NUTS) level using Simple Location Quotients (SLQs) for a number of countries in North West Europe (the partner countries in the EU Interreg NWE SURICATES Project [7]). The model assesses the potential economic impact, accounting for costs and benefits, within the time period of the project. Longer-term economic benefits which may be derived from beneficial use projects are not included in the analysis and would require significant assumptions to

be made and such an analysis would be sensitive to the assumptions made and may not be sufficiently reliable or robust. Thus, the analysis presented in this paper is actually likely to underestimate the full longer-term economic benefits of dredge sediment management projects.

2 METHODS

2.1 Economic Modelling Framework

Project economic impacts can be developed based on multipliers derived from Symmetric Input-Output Tables (SIOT). For these tables the outputs of one industry sector correspond to the input of another industry allowing identification of the impact of activities within a sector(s) for an economy, at a national or regional level [8]. A multiplier index measuring the total effect of an increase in investment on employment or income can be generated with three types of multiplier effect; direct, indirect and induced. Direct effects refer to the impact on economic activity of the industry/development. Indirect effects refer to the impact arising from upstream or inter-sectoral linkages, such as the income or jobs accruing to suppliers. Induced effects are impacts arising from general household spending of those directly and indirectly employed by the industry/development. This approach is well established to model the economic impacts of developments [9], [10].

Figure 1 presents the overall modelling approach applied including the primary model inputs (including the Economic Impact Area, the project site, sediment characteristics and unit costs from an extensive unit cost database), the available sediment management options (the full logistical chain of project activity from dredge sediment generation through to ultimate placement or disposal) and the model outputs (direct, indirect and induced contributions to GDP and employment),

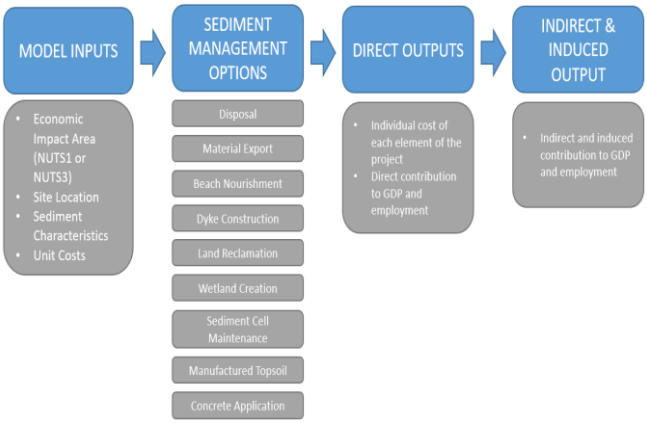

Figure 1. Overall Economic Model Structure – Inputs and Outputs

2.2 Direct Costs

The direct costs are the actual costs associated with completion of the project and it is the sum of all the individual process unit costs involved. The unit costs include essential processes of a dredging campaign such as design, environmental assessment, monitoring, dredging, sediment management, dewatering, treatment, transport, and any other relevant costs.

3 DIRECT, INDIRECT, AND INDUCED IMPACTS

The model generates the direct, indirect, and induced impacts in terms of the contribution to the Gross Domestic Product (GDP) and the resulting impact on jobs. GDP is the most common indicator of financial activity in a specific time period. It measures the total monetary value of all goods and services produced within country's borders [11]. The expenditure approach, used in the economic model developed, estimates the direct impact on GDP by how much money is invested in the specific dredging project. The direct jobs created include those directly associated with the dredging project and any additional jobs created.

An increase in the final demand for a particular industry results in an increase in demand for other linked industries further down the supply chain. This is called the indirect contribution to GDP. The indirect contribution to GDP is estimated by applying sector specific Leontief Type I multipliers to the corresponding sectoral GDP. The direct cost of the individual elements is then deducted from this value [8]. The indirect employment represents the number of full-time equivalent jobs that are created as a result of the economic activity generated by the dredging project.

The induced contribution to GDP is the result of increased personal income caused by the direct and indirect effect on GDP, or in other words, the spending of employees. A proportion of this increased income will be re-spent and returned to the economy. The induced effect is estimated using the Leontief Type II Output Multipliers. Similar to Type I Output Multipliers, the Type II Output Multipliers are also derived from SIOT tables [8].

The relevant equations for direct, indirect and induced economic impacts at a National level have previously been presented in detail by [12] and [13].

4 DEVELOPED MODEL

4.1 National and Regional Economic Areas

The economic model was developed for five countries: Ireland, France, the Netherlands, Scotland, and the United Kingdom (excluding Scotland). The set of output multipliers and employment coefficients was derived for each country individually based on available data from national statistics offices, OECD, and Eurostat. Furthermore, the economic and employment contributions were downscaled to a regional NUTS3 level.

There are often considerable regional differences in terms of economic performance and these can be reflected through a downscaling approach to a regional NUTS3 level (Figure 2). The SLQ method (Equation 1) is a common estimation procedure quantifying how concentrated a particular industry is on a regional NUTS3 level relative to the reference NUTS1 level [11]. Eurostat provides employment data for eleven NACE (a statistical classification of economic activities in the EU) categories to a NUTS3 level. The NUTS3 employment data form an 'asset' to generate the SLQ ratios which are applied to the national level multiplier and employment coefficients. In the case where a region is over-represented as a proportion of employment in a particular sector, the national multiplier and employment coefficients were used for that

region and where a region is under-represented the national multiplier was downscaled to reflect the degree of under-representation.

SLQ = (X/Y)/(X'/Y') (1)

where

SLQ – Simple Location Quotient

X - Amount of asset in a region (sectoral employment)

Y - Total amount of comparable asset in a region (total employment)

X' - Amount of asset in a larger reference region (sectoral employment)

Y - Total amount of comparable asset in a larger reference region (total employment)

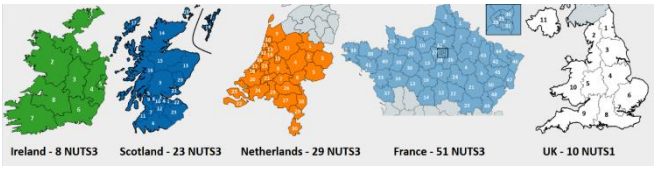

Figure 2. NUTS3 (& NUTS1) NWE Country Regions included in the Economic Model

4.2 Unit Costs and Treatment Methods

Unit costs were gathered from different dredging contractors and engineering consultants across the five countries identified. Treatment methods in the model include the most common applications that are widely used internationally. The economic model is flexible and allows customisation to satisfy various possible dredging scenarios.

5 MODEL APPLICATION

5.1 Background

The economic modelling tool developed has been validated against data from an actual dredging project. The validation involved comparing the model outputs with actual outputs in terms of the effect on GDP and jobs created. This validation exercise was initially presented for a Pilot Study Site where 533m^3 of sediment was dredged from a canal near Falkirk, Scotland and transported by road and placed at a bioremediation site. This Pilot Study formed part of the Interreg NWE SURICATES Project [7]. The validation exercise proved satisfactory with good comparison between real project data (direct cost and employment created) and the outputs from the economic model. A detailed description of the project site and the modelling work undertaken has previously been presented [13].

The model applications presented in this paper focus on two larger projects. One project is an innovative and large-scale sediment reallocation project within the Port of Rotterdam, The Netherlands, another Pilot Study as part of the Interreg NWE SURICATES Project. The second project is at a smaller scale and involves dredging and offshore disposal at the Port of Fenit, Co. Kerry, Ireland. In this case the sediment management approach implemented was assessed and compared with a number of other potentially feasible scenarios.

The following sections outline the modelling work undertaken.

5.2 Sediment Reallocation, Port of Rotterdam

The Port of Rotterdam in the Netherlands (Figure 3) is the largest seaport in Europe and a key asset in the international maritime supply chain. The Port has a large dredging requirement to maintain navigable access and it invests heavily in sediment management. As part of the EU NWE SURICATES Project the Port led a large-scale pilot project involving the dredging and reallocation of approximately 500,000m^3 of sediment. The overall aim of this pilot study was to assess the efficacy of sediment reallocation to support formation of wetland areas to provide erosion protection of channel banks and also to determine if such an approach could reduce the sailing distance of dredging equipment, thereby saving on CO_2 emissions.

The sediment was dredged by a Port-owned hydraulic dredger with an in-built hopper from the inner berthing areas of the Port (freshwater) and then reallocated approximately 10km downstream within a tidally controlled Port waterway area through a ‘rainbowing’ process, Figure 3 shows the dredged and sediment reallocation areas. The reallocation site (Figure 4) was selected based on numerical modelling work undertaken to mimic the behaviour and transport of the dredged sediments; this modelling work indicated a potential zone of sediment deposition.

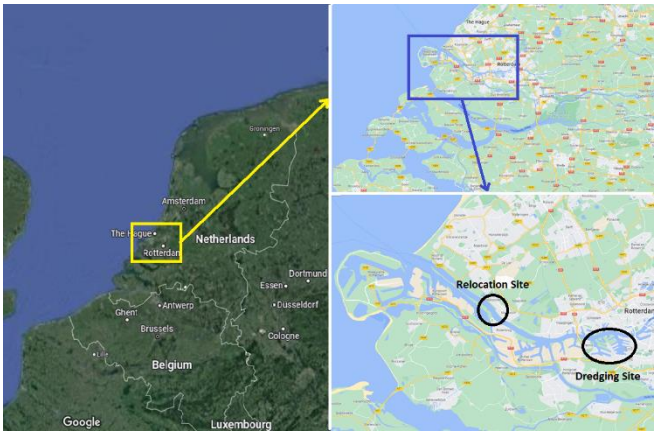

Figure 3. Port of Rotterdam Site Location

Figure 4. Hydraulic Dredger *Ecodelta* at the Reallocation Site

Deltares provided all the necessary information required to apply the economic model. This included the following project inputs: the type of dredging operation, beneficial use type and methods along with the outputs such as direct cost breakdown and total jobs created from the dredging project.

The economic model was applied to this sediment reallocation project. The actual cost of the dredging project was estimated at approximately €1million with 8 fulltime equivalent jobs created. The economic model was then applied and the impact on GDP and jobs created is presented in Figures 5 and 6, respectively. The economic model estimated a direct cost of €1.2m, which is approximately 20% higher than the actual direct cost of the dredging project. As this project involved the use of the Port-owned dredger the actual cost is likely to have been lower than if an external dredging contractor was used. The economic model estimated that the sediment allocation project would create 10.2 direct jobs. The comparison of such model output to actual project data is the first application for a large-scale project with differences of approximately 20% found, albeit with the mitigating proviso outlined above. The model predictions indicate the indirect and induced contributions to GDP (as a proportion of the direct contribution) at 56% and 5.1% respectively.

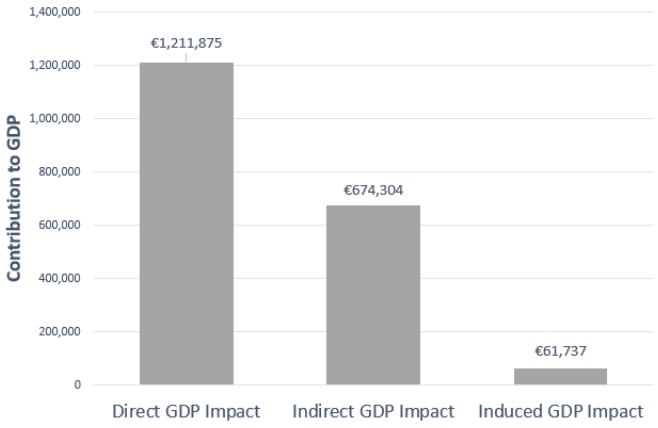

Figure 5. Sediment Reallocation Project – Modelled Effect on GDP

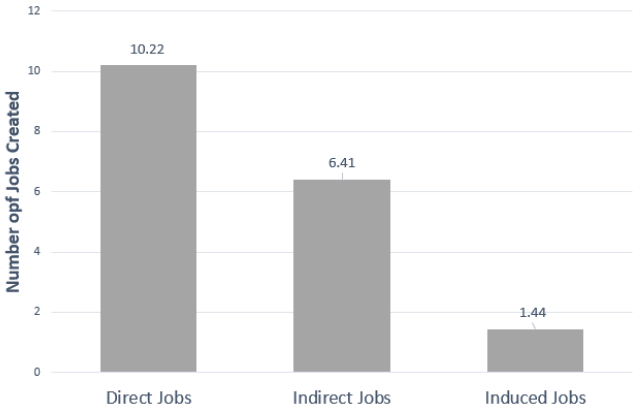

Figure 6. Sediment Reallocation Project – Modelled Number of Jobs Created

5.3 Sediment Management, Port of Fenit

Fenit Harbour is a mixed function seaport under the auspices of Kerry County Council. It the most westerly commercial port in Ireland and is located on the northern part of Tralee Bay (Figure 7). Maintenance dredging is an ongoing requirement to provide safe navigable access and berthage for commercial shipping and recreational craft.

Current harbour planning envisages dredging of approximately 1m tonnes of dredged sediment over the coming 8-year period with an initial phase of dredging completed in May 2021 when dredging was undertaken for 57,770 m^3 with offshore disposal to an EPA licensed site 7km sail distance. The dredging was undertaken by an external dredging contractor as a combination of primarily suction hopper dredger with some plough dredger activity (Figure 8).

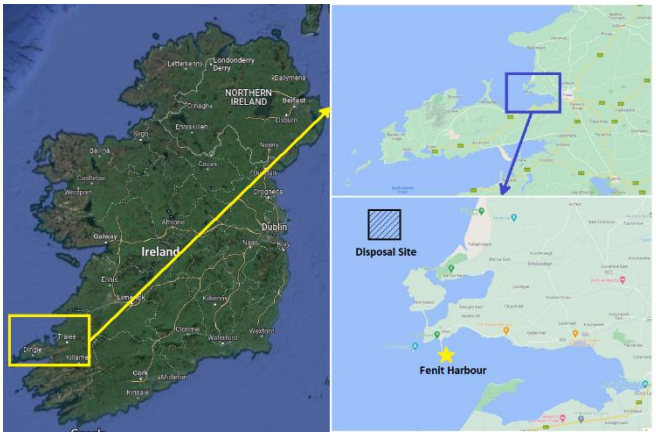

Figure 7. Port of Fenit Site Location

Figure 8. Hydraulic Dredger *Marbury* (left) and Plough Dredger (right) used at the Port of Fenit

The economic model was applied to assess a number of sediment management scenarios based on the dredging volume for the May 2021 dredging campaign as follows:

(1) The completed works of dredging and offshore disposal, (2) Construction of a flood protection dyke using dredged sediments and (3) Wetland restoration.

The flood protection dyke is proposed to be located on a coastal stretch approximately 7.6km from the Port dredging site where there is a high probability of flooding (Figure 9) based on predictions by the Irish Office of Public Works. It is assumed that all 57,770 m^3 of fine dredge sediment would be reused for the construction of the 2.1km long dyke with a dyke height of 3m and crest width of 2.5m, a geotextile filter layer and a rock armour outer layer requiring 6,000 m^3 of rock material supplied by the nearby Ardfert Quarry, a trucking distance of approximately 11km from the dyke construction site. It is assumed for purposes of this modelling work that the dredged sediment is suitable for such an application.

Figure 9. Proposed Dyke Location and Areas of High Flood Risk in Tralee Bay

Wetlands have a valuable and beneficial role in flood regulation, water purification and wildlife habitat and Tralee Bay is an internationally important wetland for wintering waders and wildfowl. Local wetland habitats include swamps, tidal marshes, peatlands and inter-tidal areas. The fine dredged sediment from the Port of Fenit is potentially suitable for nourishing and enhancing the existing Tralee Bay wetlands which are located approximately 2.5km sail distance from the Port of Fenit. It is a large wetland area covering 314 hectares and contains estuarine silts and clays (Figure 10).

The wetland restoration scenario involves the 57,770 m^3 of silty dredged sediment being transported via trailer suction dredger and placed into the designated wetland area via high-pressure discharge of dredged sediment. The thickness of the applied sediment layer is generally lower in the vegetated areas and higher in the open water areas. No berm or weir box installation is required. It is assumed for modelling purposes that the dredged sediment is appropriate for such use. This sediment application would of course require extensive site investigation, sampling and environmental assessment.

Figure 10. Identified Wetland Areas in Tralee Bay

The economic model was applied to the three sediment management scenarios, either implemented or proposed. Figure 11 presents the results of the model application for the different scenarios.

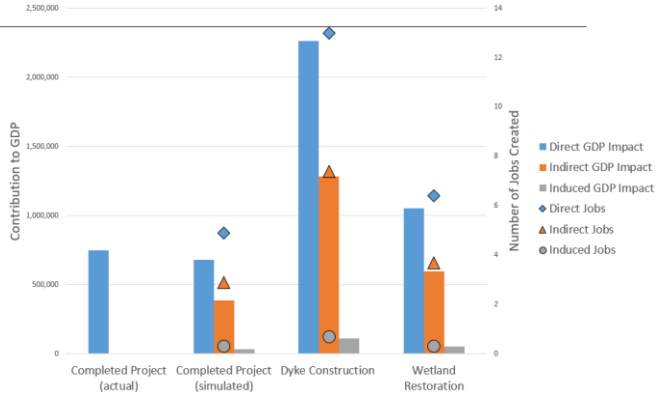

Figure 11. Port of Fenit Sediment Management Scenarios – Economic Modelling Results

The actual cost of the dredging and offshore disposal (completed project) was estimated at approximately €750k, no estimate of employment created by the project was available. The economic model estimated the direct cost at €681k, a difference of less than 10% which is considered satisfactory. The model predicts indirect and induced contributions to GDP of €385k and €34,600, 56% and 5% respectively of the direct GDP contribution. The model predicted direct, indirect and induced employment at 5, 3 and 0.3 Full Time Equivalent (FTE) jobs.

The application of the economic model to the different sediment management scenarios shows that the lowest direct cost approach is the offshore disposal option, confirming current practice and experience in Ireland. The positive economic impact is largest for the dyke construction scenario and the wetland restoration proposal also provides a greater economic benefit than disposal at sea.

The model predicts the contribution to GDP from dyke construction at approximately €2.3m, with indirect and induced contributions of approximately €1.3m and €113k respectively (56% and 4.9% of direct GDP contribution respectively). The estimated number of jobs created was 13FTE. Similarly, for wetland restoration the model predicts the contribution to GDP at approximately €1.05m, with indirect and induced contributions of approximately €597k and €53k respectively (57% and 5% of direct GDP contribution respectively). The direct number of jobs created was estimated at 6.4FTE.

These model estimates indicate the positive potential economic benefits that may be derived from sediment use projects, rather than the application of more traditional disposal at sea. This is in addition to a range of other non-economic benefits that can be achieved through such beneficial use applications.

6 CONCLUSION

This paper presents a regionally downscaled economic model that has been developed and can analyse, through the contribution to GDP and jobs created, the economic impacts of sediment management projects. The economic model is based on applying an open Leontief model to standardised symmetrical input-output tables based on national and regional statistical economic data. The model numerically

outputs the direct, indirect, and induced effect of GDP and jobs created.

The model has been applied to two sediment management projects; a large-scale sediment reallocation project at the Port of Rotterdam, The Netherlands and a smaller scale dredging project at the Port of Fenit, Ireland. Model predictions for the direct economic impacts for the Port of Rotterdam Project are within 20% of the estimated actual project values (but with the mitigating proviso regarding the likely reduced cost by the use of the Port-owned dredger). For the Port of Fenit project the model provides a satisfactory prediction of the actual cost of the dredging and offshore disposal project, within 10% of the actual cost. For both projects the indirect contribution to GDP has been found to be over 50% of the direct contribution which is considerable; the induced contribution is much smaller and estimated at approximately 5%.

A number of different sediment management scenarios are also modelled for the Port of Fenit project including dyke construction and wetland restoration. This modelling work shows that the traditional practice of offshore disposal provides the lowest direct cost and that the beneficial use scenarios provide greater positive economic impact. A range of other benefits will also be derived from the beneficial use of sediment (which may include environmental, ecological, CO_2 emission reduction, flood protection, societal and/or recreational). In the context of these potential benefits, the Circular Economy and the philosophy of 'Working with Nature' this economic modelling work provides further evidence to support the increased beneficial use of sediment.

The economic model developed is unique with application at a National and a Regional level. It has been applied in this paper to real dredge sediment management projects in Ireland and the Netherlands and highlights the positive economic impact of sediment projects. The model can facilitate and inform stakeholders across the sector but it is important to note that the model results must be considered in the context of broader environmental and societal impacts and industry needs.

ACKNOWLEDGEMENTS

The authors wish to acknowledge the funding received for the SURICATES Project through the INTERREG NWE programme and the European Regional Development Fund (ERDF).

The authors would like to thank the Irish Central Statistics Office, the United Kingdom Office for National Statistics, the Scottish Government's National Statistics Office, The Organisation for Economic Co-operation and Development (OECD), and Eurostat who provided economic data.

The authors would like to thank to Dr. Declan Jordan from University College Cork for advice and guidance.

The authors also wish to thank the other SURICATES project partners (Université de Lille Sciences et Technologies, France; IXSANE, France; Bureau de Recherches Géologiques et Minières, France; TEAM2, France; ARMINES, France; Deltares, The Netherlands; Port of Rotterdam, The Netherlands; University of Strathclyde, Scotland; Scottish Canals, Scotland; University College Cork, Ireland) for the provision of data and advice as appropriate.

REFERENCES

[1] Harrington, J., Sutton, S., Lewis, A. (2004). "Dredging and dredge disposal and reuse in Ireland – a small island perspective", Proceedings of World Dredging Congress XVII, B4-5, 1-14, Hamburg, Germany.

[2] Sheehan, C., Harrington, J., **(**2012**)** 'Management of dredge material in Ireland – a review'. Waste Management, Volume 32, Issue 5, Pages 1031-1044. https://doi.org/doi.org/10.1016/j.wasman.2011.11.014

[3] Harrington, J. and Smith, G. (2013). Guidance on the beneficial use of dredge material in Ireland, Environmental Protection Agency.

[4] Bortone, G., Palumbo, L., **(**2007**).** SedNet: Sustainable management of sediment resources - sediment and dredged material treatment. Elsevier, The Netherlands.

[5] Laboyrie, H.P.,, Van Koningsveld, M., Aarninkhor, S.G.J., Van Parys, M., Lee, M., Jensen, A., Csiti, A., Kolman, R., **(**2018**).** Dredging for sustainable infrastructure. CEDA/IADC, The Hague, the Netherlands.

[6] United States Army Corps of Engineers **(**2013**)** Dredging and dredged material management - engineering manual. Engineering Manual EM 1110-2-5025, Department of the Army, Washington DC, USA.

[7] SURICATES - Sediment Uses as Resources In Circular And Territorial EconomieS (2022). https://www.nweurope.eu/projects/project-search/suricates-sediment-uses-as-resources-in-circular-and-territorial-economies/. Accessed 5 May 2022.

[8] Leontief, W., (1951). Input output economics, Scientific American, 1951. 185, pp. 15-21.

[9] Hawdon, D. Pearson, P. (1995). Input-output simulations of energy, environment, economy interactions in the UK, Energy Economics, (1995) 17(1): p. 73-86.

[10] Ivanova, G., Rolfe, J. (2011). Using input-output analysis to estimate the impact of a coal industry expansion on regional and local economies, Impact Assessment and Project Appraisal, (2011). Beech Tree Publishing 29(4): p. 277-288.

[11] Carey, M.A., Johnson T.G., (2014), 'Ireland's Input-Output Framework – Where Are the Regions?', *Borderlands*, Issue 4.

[12] Harrington, J. R., Murphy, J., Coleman, M., Jordan, D., Debuigne, T. and Szacsuri, G. (2016) 'Economic modelling of the management of dredged marine sediments', Geology, Geophysics and Environment, 42(3), pp.311-324. doi: 10.7494/geol.2016.42.3.311.

[13] O' Sullivan R., Harrington, J., Hamilton, A., Batel, B., 'The Application of an Economic Modelling and Analysis Tool to Assess the Economic Benefits and Impacts of Beneficial Use of Dredged Sediment'; Civil Engineering Research Ireland (CERI) Conference, pp. 630-634, Cork Institute of Technology (Online), August 2020, ISBN 978-0-9573957-4-9.

Hydrodynamic Simulation of Navan Wastewater Treatment Plant: An adaptive approach to overcome future operational challenges

Mohammed Mahmoud[1*], Zeinab Bedri[1], Ahmed Nasr[1]
[1]School of Civil and Structural Engineering, TU Dublin, Bolton Street, Dublin 1, Dublin, Ireland.
Email : D20125723@mytudublin.ie, zeinab.bedri@tudublin.ie, ahmed.nasr@tudublin.ie.

ABSTRACT: Ireland's Climate Change Adaptation Strategy calls for developing an energy-efficient design for all new and upgraded assets, including wastewater treatment facilities. There is a huge potential to reduce greenhouse gas emissions associated with energy use in the wastewater treatment processes through adjusting the level of treatment to the assimilative capacity of the receiving water body. Currently, a conservative approach based on the lowest flow conditions is used to estimate the assimilative capacity of the receiving body. This approach results in the estimation of low permissible Emission Load Values (ELVs) that do not account for the dynamic variation of the receiving water body's dilution capacity. Maintaining such ELVs require intensive wastewater treatment processing all around the year. In this study, a hydro-environmental model was built using MIKE21 FM to assess the assimilative capacity of the Boyne River to Total Phosphorus (TP) and Ammonium (NH_4) under different effluent discharges from the Navan Wastewater Treatment Plant (WWTP) during high flow conditions. The modelling results showed the availability of sufficient assimilative capacity in this water body during high flow conditions, allowing for the use of higher ELVs and consequently the reduction of treatment levels and the associated carbon emissions. These results indicate the possibility of creating an adaptive wastewater treatment operation approach that considers different scenarios of future climate change and population growth.

KEYWORDS: Wastewater Treatment Plant, Hydrodynamic Model, MIKE21 FM, River Boyne.

1 INTRODUCTION

In Ireland, urban wastewater treatment plants (UWWTPs) produce annually around 1000 to 1500 kt CO_2 eq of Greenhouse Gases (GHG) which represents 1.6 percent of national GHG emissions according to the latest report of the Environmental Protection Agency [1]. This significant level of carbon footprint is attributed to the excessive use of energy in wastewater operations to produce conservative, high-quality effluents. Currently, there are over 1100 UWWTPs in Ireland, and hence lowering the carbon footprint of this sector will contribute to the achievement of the EU's 2030 GHG emission target [2]. Reducing CO_2 emissions associated with wastewater treatment must be carried out without violating any level of compliance specified by relevant legislation and policies.

The permissible Emission Load Values (ELVs) of Irish UWWTPs are currently estimated based on a conservative approach which uses one of the lowest flow indices in the receiving river body to quantify its dilution capacity. Such an approach results in a single ELV estimate and does not account for the assimilative capacity dynamics of the receiving water body. This approach results in conservatively low permissible ELVs, which require intensive wastewater treatment processing all around the year and will thus result in high GHG emissions. Using flow-dependent ELV estimates allows for optimising the level of treatment in the UWWTPs in such a way that the generated effluent will be proportionate to the ambient assimilative capacity in the receiving water body. Consequently, the UWWTP will operate more efficiently, and this will result in reducing GHG emissions while maintaining the environmental quality standard of the receiving water body.

This study investigates the use of a mathematical modelling approach to estimate dynamic ELVs based on the ambient flow conditions. The study uses a high flow condition as a case study to demonstrate the proposed approach. Such results constitute a gateway to further investigation on the possibility of easing the wastewater treatment level in order to obtain a reduction in energy usage and operation cost. In this study, Navan WWTP has been selected as a case study since it represents a typical example of a large wastewater treatment facility. The Navan WWTP discharges on the River Boyne which has a catchment area of 2694 km^2 [3]. The river catchment extends to include the majority of Co. Meath, the southern part of Co. Louth, an area in the southeast of Co. Cavan, the eastern area of Co. Westmeath and an area northwest of Co. Kildare. The main channel stretches 113 kilometres from its headwaters near Newbury Hall in Co. Kildare to its outlet to the Irish Sea at Momington, east of Drogheda. The source of the river is located at an elevation of about 140 m, and its average primary channel gradient is 1.24 m per kilometre. The River Boyne catchment has relatively flat terrain with predominant pasture land. The national importance of this study came from the fact that the main channel of the River Boyne is designated salmonid water under the Communities (Quality of Salmonid Waters) Regulations, 1988 (S.I. No. 293/1988). Also, the EPA considers this area as a Special Protection Area (SPA) and Special Area of Conservation (SAC) based on the EU Birds Directive (79/409/EEC) and EU Habitats Directive (92/43/EEC), respectively. On the other hand, based on the EPA river quality surveys, the water quality status is moderate.

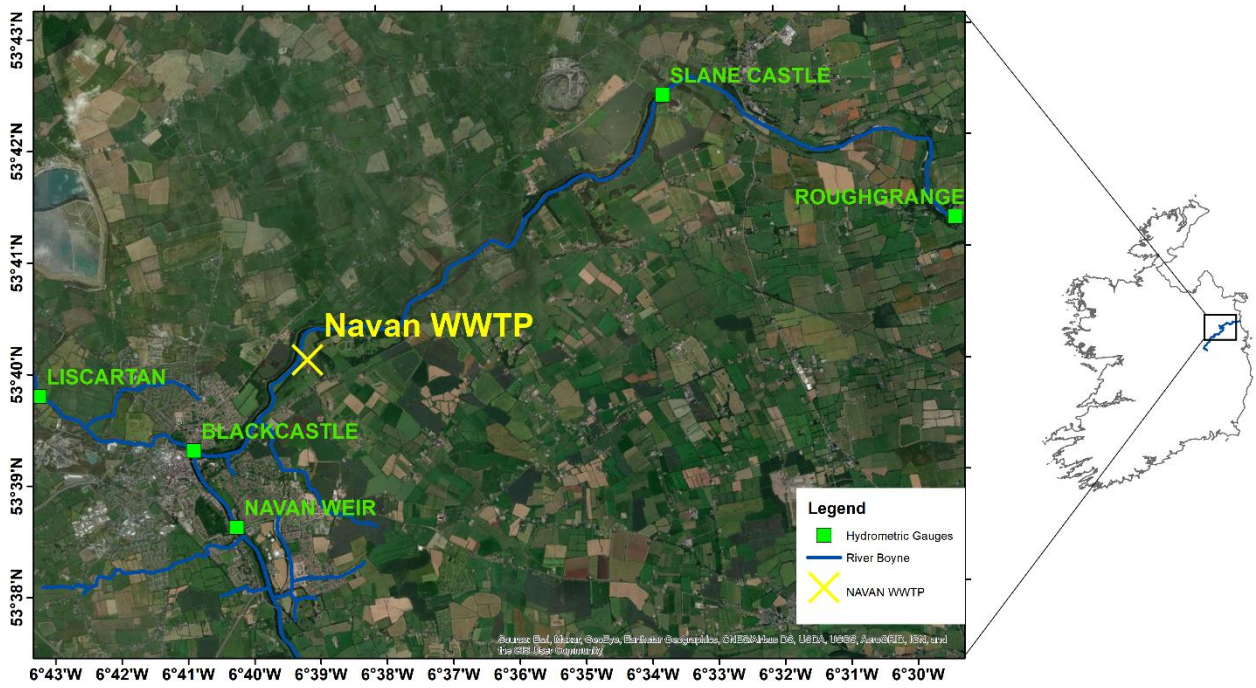

Figure 1: Study Area and hydrometric gauge locations.

2 METHODOLOGY

2.1 Study Area

The Navan Wastewater Treatment Plant (WWTP) is located 4 km east of Navan town centre, and it was built to serve the agglomeration of Navan town and its surrounding areas (see Figure 1). The plant occupies a 4.5-hectare site located close to the River Boyne to the south of the townland of Ferganstown and Ballymacon [4,5]. Between 1999 and 2001, the facility commenced operations in phases. Currently, the facility serves 50,000PE, but has a capacity of 60,000PE. The plant offers primary (screening and primary settlement), secondary (Activated Sludge diffused aeration), and tertiary treatment in the form of nutrient removal (Ferric Chloride Dosing).

2.2 Data Acquisition

Data required to build the mathematical model consisted of; a) Bathymetric data, b) Hydrometric data, and c) Measured effluent concentrations. The Office of Public Works (OPW) provided the bathymetric data through personal contact. The data were used to delineate the model boundaries (river banks) and the model ground elevation (river cross-sections). The hydrometric data – flow and water levels – was publicly accessed and downloaded for the hydrometric gauges in the study area from waterlevels.ie. Effluent concentrations were obtained from the EPA annual compliance report [4].

2.3 Modelling approach

The model used in this study is MIKE21 FM [6], a numerical modelling system developed by the Danish Hydraulic Institute (DHI) to simulate 2-Dimensional surface flows. The model employs a spatial discretisation method based on cell centric. It uses unstructured triangular elements, which give flexibility in creating a high-resolution grid for the system geometry [6]. . In this study, the Hydrodynamics Module of MIKE 21 FM is coupled to the Transport Module to simulate the transport of two water quality parameters (Total Phosphorus and Ammonium) in the waters of River Boyne.

2.3.1 Hydrodynamic model:

The hydrodynamic module is considered the core computing component of the MIKE 21 FM modelling scheme [7], as it forms the foundation for other modules, including the transport module. The hydrodynamic module of MIKE 21 FM is based on the numerical solution of the depth-averaged Navier-Stokes equations. A two-dimensional hydrodynamic model is used to simulate the hydrodynamic characteristics of the River Boyne. In this study, the simulations were conducted during a period of high flow conditions.

2.3.2 Transport module

The Transport Module uses the fluid transport and dispersion processes to simulate the spread of dissolved or suspended substances in any aquatic environment [7]. The module has the capability to stimulate and distinguish between conservative or nonconservative, organic or inorganic materials. As mentioned, the inputs of the transport module are based on the results of the hydrodynamic module calculations [6], [7]. The water quality and hydrodynamic models were coupled to simulate the spatial distribution of the variable concentration of pollutants along the mixing zone of the Navan WWTP through the transport equation. This study chose Total Phosphorus (TP) and Ammonium (NH_4) as pollutants of concern.

2.3.3 Model setup and Calibration

Setting up the MIKE21 FM model comprises three steps: (i) generating the mesh of the modelling domain; (ii) defining the time step and the simulation period; (iii) building the hydrodynamic model; and (iv) building the transport module. The mesh generator tool provided in Mike Zero was used to generate the non-structured mesh with a domain of 52735

elements and 29242 nodes for the study area (Figure 2). The model domain spans from Black Castel hydrometric gauge (upstream U/S Navan WWTP) to Roughgrange gauge downstream D/S Navan WWTP. These upstream and downstream boundaries were defined as open boundaries in the model. Slane Castle hydrometric station falls inside the model domain and has been included in the model as the calibration point. Hydrometric data were set as boundary conditions for the U/S and the D/S open boundaries, as flow measurements were set to the U/S boundary and water levels to the D/S boundary. A three-day simulation period was adopted to start from 14/01/2010 and finish on 17/01/2010 to match the period of high flows (5 percentile) based on the U/S flow records. The simulation period was selected based on the data availability as well as the reported event of the EQS exceedance during the study period. The rest of the hydraulic characteristics were set to defaults for a later stage to be calibrated. Finally, the effluent discharge point was specified in the model (location and effluent flow). Also, the edge of the mixing zone was pinpointed. This was necessary to determine the flows and surface water elevations at this point. The hydrodynamic model was calibrated by adjusting the bed resistance (Manning coefficient) and comparing the fit/match between the simulated and observed water levels at Slane Castle.

Following the calibration of the hydrodynamic module, the transport module was built up. Two pollutant sources were identified (TP and NH_4), and their concentrations were set based on a statistical analysis performed on the effluent concentrations provided in the annual evaluation document of 2010 [4]. Four scenarios were simulated based on the statistical analysis; S1: represents the maximum reported concentrations of TP and NH_4 during 2010, S2: represents the reported average concentrations of TP and NH_4, S3: represents the minimum concentrations reported for TP and NH_4, while S4: represents licenced ELV concentrations for TP and NH_4. The following Table 1 summarises the statistical analysis of the monitored effluent concentrations used to generate the concentration curves (Figures 4 – 7) for TP and NH_4.

Table 1: Concentrations of the pollutants of concern based on the statistical analysis of the measured effluent data in 2010.

	Concentrations (mg/l)			
	Max	Avg.	Min	License ELV (EQS)
Scenario	S1	S2	S3	S4
TP	2.1	0.8	0.3	1
NH_4	7	2	0.1	3

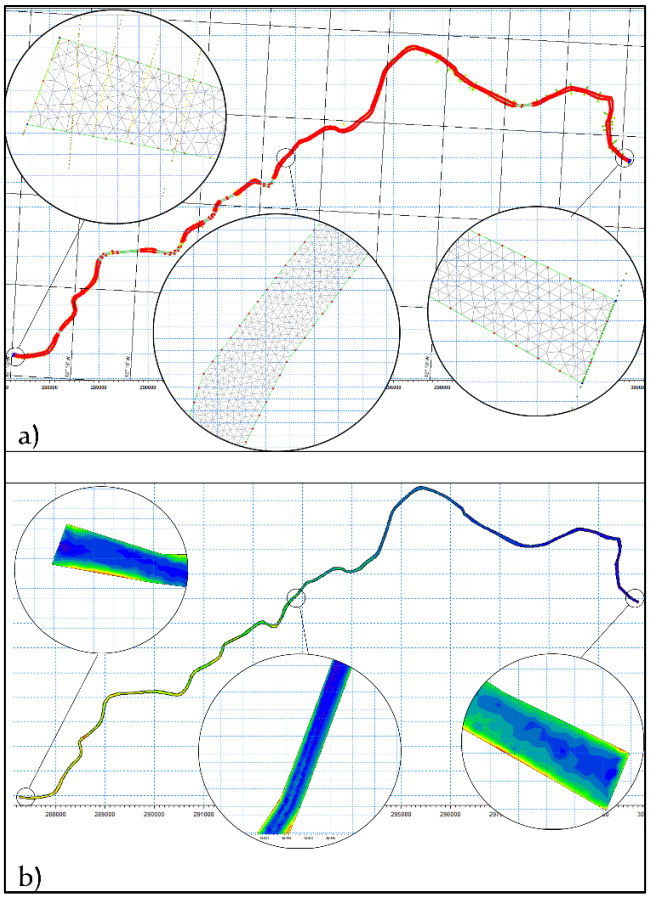

Figure 2: a) Unstructured mesh generated for the study domain (River Boyne), b) Interpolated bathymetry using the mesh generated.

3 RESULTS AND DISCUSSION

3.1 Hydrodynamic Model Calibration

The hydrodynamics model calibration was conducted by performing several simulations in which the main hydrodynamic model parameter (bed resistance) was adjusted. Following each hydrodynamic simulation, the simulated and observed surface water surface levels at Slane Castle hydrometric gauge were compared. A range of values for the bed resistance parameter "Manning's number" was tested (22 to 45 $m^{1/3}/s$), as shown in Table 2. Figure 3 shows the simulated water surface levels that resulted from the simulations outlined in Table 2. The best fit between simulated and observed water surface levels was based on; (i) visual inspection of the fit between simulated and observed water levels and (ii) four statistical measures, the Correlation Coefficient (CC), Mean Absolute Error (MAE), Root Mean Squared Error (RMSE) and BIAS to assess the goodness of fit (Table 2). From the visual inspection of the results trend, Run 1 to Run 3 tends to underestimate the surface elevation at the calibration point. Also, the results showed that Run 3 and Run 4 resulted in the best fit. However, based on the statistical measures, Run 4 (with a Manning coefficient of 22 $m^{1/3}/s$) resulted in the least errors (MAE = 0.072m and RMSE =0.085) and a high correlation coefficient (CC=0.99). Therefore, a Manning coefficient value of 22 $m^{1/3}/s$ was retained for the subsequent water quality simulations.

Table 2: Statistical analysis of the simulated water levels versus measured data at Slane Castle Station.

Run No	Bed Resistance (Manning $m^{1/3}/s$)	Errors			CC
		MAE	RMSE	BIAS	
1	32	0.296	0.300	-0.00735	0.996
2	45	0.470	0.470	-0.01166	0.997
3	25	0.134	0.143	-0.00309	0.996
4	22	0.072	0.085	-0.00048	0.995

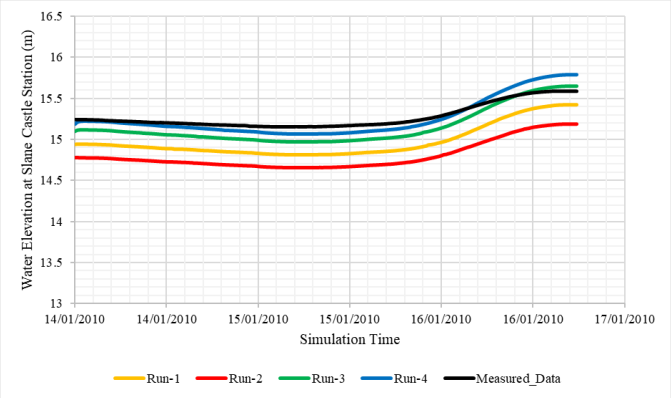

Figure 3: Calibration Curves based on the measured and simulated water level results at Slane Castle Station.

3.2 Transport Module Simulations -Total Phosphorus

Results of the water quality simulations for Scenarios S2 and S3 indicated that TP concentrations in the immediate vicinity of the discharge point, following initial dilution, were below the Environmental Quality Standards (EQS) (Figure 4). While concentrations of TP in the effluent for simulation S1 have exceeded the ELVs, simulated concentrations in the vicinity of the discharge location were still below the EQS limits for high-status rivers (<0.025 mg/l) and considered to be safe for discharge [8]. Similarly, TP concentrations at the boundary of the mixing zone (450 m downstream of the primary discharge location) were extremely low, <0.003 mg/l for the maximum measured TP (S1 simulation) (Figure 5). Overall, the results confirm that at high flow conditions in the Boyne River (5th percentile flow), the river has a significant capacity to dilute effluent discharges, even when the concentrations of TP in the effluent discharges exceed the ELV TP concentrations.

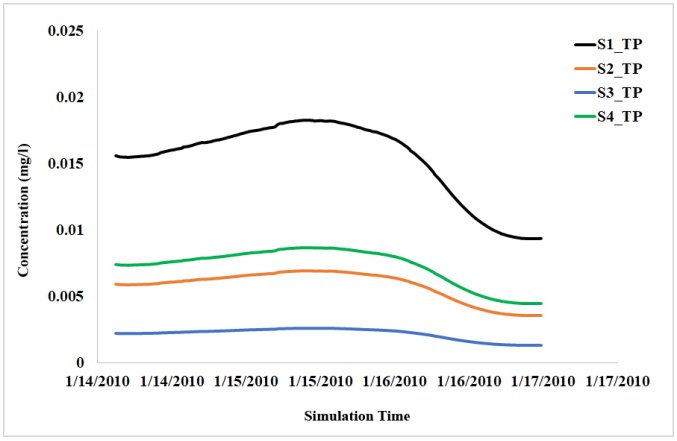

Figure 4: Total Phosphorus Concentrations in the immediate vicinity of the Discharge point.

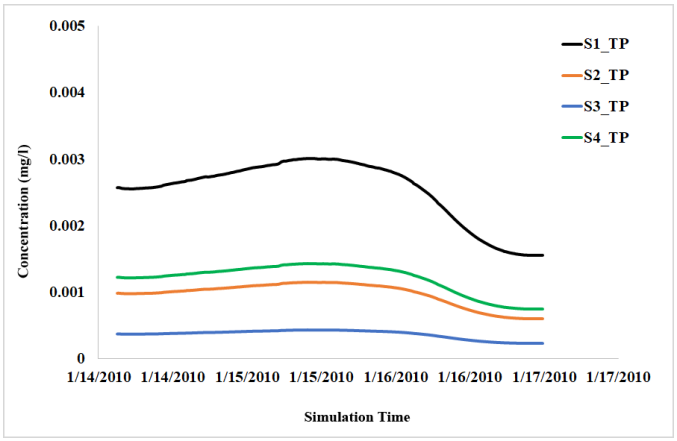

Figure 5: Total Phosphorus Concentrations at the boundary of the Mixing Zone 450m downstream of the discharge point.

3.3 Transport Module Simulations -Ammonium

Simulated Ammonium concentrations exhibited a similar pattern to TP concentrations. Results showed that the effluent in Scenarios S2 and S3 were significantly diluted following discharge due to the high river flow (Figure 6,7). The concentrations of Ammonium in the vicinity of the discharge point did not exceed the high-status limit of (0.04 mg/l) for S2 and S3. While for S1, a reported exceedance of the NH_4 ELV concentrations in effluent discharges resulted in high NH_4 concentrations in the vicinity of the discharge point (>0.04mg/l), which did not satisfy the high-status limit. However, the concentrations resulting from this scenario satisfy the limit of good status (<0.065). Likewise, to the TP pollutant, the results suggest that with high flow conditions, the river has the capacity to dilute NH_4 concentrations even when the effluent discharges exceed the high permissible NH_4 concentrations.

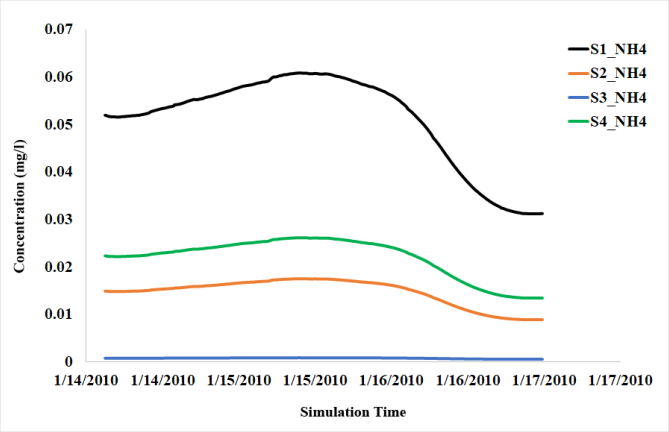

Figure 6: Ammonium Concentrations in the immediate vicinity of the Discharge point.

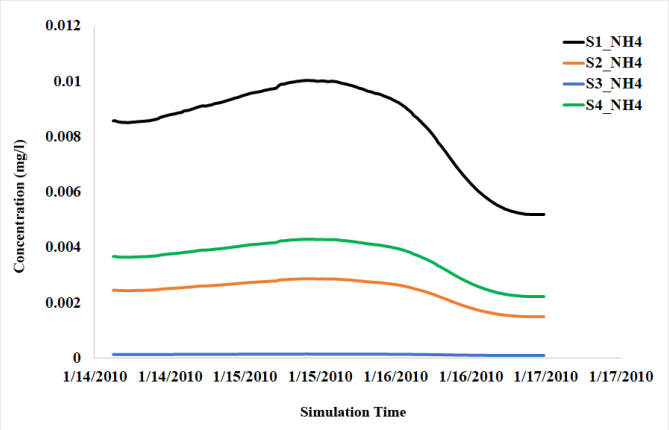

Figure 7:Ammonium Concentrations at the boundary of the Mixing Zone 450m downstream of the discharge point.

3.4 Study Limitation

This study provides a preliminary result based on a mathematical model to investigate the availability of sufficient assimilative capacity in the water body during high flow conditions. This may allow for higher ELVs than the lower limit estimated based on low flow conditions. The study, however, had some limitations:

- The study investigated only the dynamic flow dependent ELV concept in the high flow condition scenarios. The concept needs to be applied to a range of different flow conditions.
- The study also did not calibrate the transport model as it used a constant effluent discharge.
- Due to the limited information at the discharge vicinity, the study did not perform a validation process.

The limitations mentioned above will be averted in the full-scale study.

4 CONCLUSIONS

A hydrodynamic model was developed using MIKE21 FM to simulate the impact of effluent discharges from the Navan Wastewater Treatment Plant (WWTP) on the water quality of the receiving water body, Boyne River. The study aimed to investigate the use of flow-dependent ELVs based on river flow conditions. The hydrodynamic model was calibrated by adjusting the bed resistance coefficient and comparing the simulated surface elevations at Slane Castle station with the observed water levels. Following a number of simulations in which a range of values for bed resistance was tested, the best model was selected based on the highest correlation and low errors. Then a transport module was developed based on the calibrated hydrodynamic module. Two pollutants were simulated; TP and NH_4. The overall results suggested that with high flow conditions, the river has the capacity to dilute the TP and NH_4 even when the effluent discharges exceed the high permissible NH_4 concentrations.

REFERENCES

[1] Environmental Protection Agency, “Ireland’s National Inventory Report 2021,” 2021. [Online]. Available: www.epa.ie.

[2] European Commission, "Investing in a climate-neutral future for the benefit of our people SWD(2020) 176," 2020, [Online]. Available: https://eur-lex.europa.eu/legal-content/EN/TXT/?uri=CELEX:52020DC0562#footnote11.

[3] C. Moriarty, "Studies of rivers and lakes," p. 279, 1998.

[4] EPA, "Annual Environmental Report for EPA Waste Water Discharge Licence D0059-01," 2010.

[5] EPA, "Navan Waste Water Treatment Works - Annual Environmental Report For EPA Waste Water Discharge Licence D0053-001," 2011. [Online]. Available: http://www.epa.ie/licences/lic_eDMS/090151b2803d24d4.pdf.

[6] DHI, "Hydrodynamic and Transport Module Scientific Documentation," *User Man.*, p. 55, 2018, [Online]. Available: www.mikepoweredbydhi.com.

[7] DHI, "MIKE 21 & MIKE 3 Flow Model FM Oil Spill Module," *User Man.*, 2015.

[8] "European Communities Environmental Objectives (Surface Waters) Regulations 2009," no. 327, 2012, [Online]. Available: https://www.irishstatutebook.ie/eli/2009/si/272/made/en/print.

Life Cycle Sustainability Assessment of a Pedestrian Bridge Made from Repurposed Wind Turbine Blades

Angela J. Nagle[1,2*], Kieran Ruane[5], T. Russell Gentry[3], Lawrence C. Bank[3], Niall Dunphy[1,2,6], Ger Mullally[1,2,4], Paul G. Leahy[1,2]

[1]*School of Engineering, University College Cork, Western Road, Cork, Ireland*
[2]*Environmental Research Institute, University College Cork, Lee Road, Cork, Ireland*
[3] *School of Architecture, Georgia Institute of Technology , 245 4th Street, NW, Suite 351, Atlanta, Georgia, USA*
[4]*Department of Sociology and Criminology, University College Cork, Western Road, Cork, Ireland*
[5]*Department of Civil, Structural & Environmental Engineering, Munster Technological University, Cork, Ireland*
[6]*Cleaner Production Promotion Unit, University College Cork, Western Road, Cork, Ireland*
*Corresponding author email: **paul.leahy@ucc.ie**

ABSTRACT:
The disposal of decommissioned wind turbine blades is becoming a problem to the wind sector, with industry calling for a landfill ban by 2025, and recycling not yet commercially available. Repurposing of the blade material into second life applications is an option that is being explored. A 5.5m pedestrian bridge was commissioned by the County Council on a new cycleway in Cork, which utilized two N29 blades. A third blade was used for extensive reverse engineering. The blades replaced two steel girders, half of the handrail material, and offered reduced lifetime maintenance costs. For repurposing to take hold, it should not only be commercially viable, it must also be environmentally and socially beneficial, as can be measured through a life cycle sustainability assessment (LCSA). An LCSA includes environmental Life Cycle Assessment, Life Cycle Costing and Social Life Cycle Assessment. Comparing the BladeBridge to a conventional bridge showed an environmental impact reduction of 14% in the combined four end categories of Human Health, Climate Change, Ecosystem Quality, and Resources. The cost of the BladeBridge was more than a conventional bridge due to the reverse engineering required; however, second and subsequent BladeBridges made from the same blade model are expected to be 30% less expensive across the lifetime due to material substitution and reduced maintenance requirements. A social assessment indicated improvements against sub-indicators from SDGs 12 and 17, through the reduction of waste through repurposing, supporting green public procurement, raising awareness for reuse, and assisting with the decoupling of the increase of renewable energy production and waste generation.

KEY WORDS: Life Cycle Assessment, Life Cycle Sustainability Assessment, composites, waste, wind energy

1 INTRODUCTION

An increase in renewable energy across Europe is central to the Green Deal's goal of zero emissions by 2050, and continued development of wind energy is key to this. However, as wind energy capacity grows and older wind farms reach end of life, sustainable disposal options are needed for decommissioned turbine parts, particularly composite wind turbine blades, in order to prevent 'green energy' from becoming a significant generator of waste.

Initial studies show that end-of-service life blades have nearly the same properties as new blades (Beauson and Brøndsted, 2016). However, the fatigue resistance of the blade may be reduced after a service life of power generation. Thus, decommissioned wind blades may perform well in new applications, under low stresses where durability is the main concern (Alshannaq et al., 2021). Capitalizing on these attractive residual properties by re-purposing the blades into large structures has the potential to have lower environmental impacts than recycling, material recovery or co-processing in cement kilns. Several studies showed promising results in modelling the use of decommissioned blades in roofing (Bank et al., 2019; Gentry et al., 2020), electrical transmission towers (Al-Haddad et al., 2022; Alshannaq et al., 2021) and short span pedestrian bridges (Jensen and Skelton, 2018; Leahy et al., 2021; Ruane et al., 2022).

The pedestrian BladeBridge, designed by researchers in the Re-Wind Network (www.re-wind.info, (Ruane et al., 2022; Suhail et al., 2019) was recently constructed as part of a new greenway project in County Cork, Ireland (Stone, 2022). The 5.5m pedestrian bridge was commissioned by Cork County Council on the new Midleton to Youghal cycleway and utilized two decommissioned Nordex N29 blades as the girders. A third blade was used for extensive reverse engineering and testing. The wind blades replace an amount of raw material that would have been required in a typical bridge build, resulting in different cost and environmental impacts as compared to a conventional bridge. Technical feasibility was demonstrated through reverse engineering and load testing of the blades, detailed in a previous paper (Ruane et al., 2022). The Midleton to Youghal greenway is a 23km cycleway in the south of Ireland, near Cork City (McConnell, 2021). Cork County Council is managing the project, and chose to locate the BladeBridge at a stream crossing 2 km from the start of the greenway at the Midleton train station. The county council was interested in publicly displaying their efforts at material repurposing, and thereby chose the location for maximum exposure to users.

The BladeBridge project supports several Irish goals aligned with the EU Green Deal: (1) Green public procurement (GPP), which encourages reuse and repurposing of materials in government projects (European Commission, 2019). (2) Improved performance on the United Nations Sustainable

Development Goals (SDGs), particularly SDG 12 - Sustainable Consumption and Production, which is based partly on circular material use (Clark et al., 2020), in which Ireland is ranked 2nd last out of all 28 EU countries at 1.6% (Eurostat, 2018). (3) Improved performance on SDG 17, Partnership for the Goals, which among other things, encourages the production of renewable energy to be decoupled from the generation of waste. Secondly, the Irish program for government includes a pledge to spend the equivalent of €1 million euros/day on cycling and walking infrastructure, and develop an integrated national network of greenways across the country (DTTAS, 2018; Leahy et al., 2021). Due to the need to improve performance on SDGs 12 and 17, the push to build cycling infrastructure across the country (DTTAS, 2018), and the availability of decommissioned blade material (Delaney et al., 2021), an opportunity exists in Ireland to use repurposed blades in the construction of bridges on cycle ways. However, for repurposing of blade material into bridges to take hold, it should not only be commercially viable, it must also be environmentally and socially beneficial, as can be measured through a life cycle sustainability assessment (LCSA).

A life cycle sustainability assessment includes environmental Life Cycle Assessment (LCA), Life Cycle Costing (LCC) and social Life Cycle Assessment (s-LCA). A wide variety of LCSA methodologies exists, with some studies fully incorporating the three pillars of s-LCA, LCA, and LCC into multi-criteria decision making (MCDM) frameworks, and others studying the three separately (Kühnen and Hahn, 2017). The s-LCA framework, as defined by the UNEP Guidelines, has strong links with the UN SDGs (Benoît Norris et al., 2020). The SDGs have become a focus of public policy discussion, as citizens become more interested in social well-being and the environment, rather than just economic growth (Clark and Kavanagh, 2021). LCSA and the SDGs are also increasingly being combined in research (Maier et al., 2016; Wulf et al., 2018; Zeug et al., 2021).

2 METHODOLOGY

2.1 Life Cycle Sustainability Assessment

A comparative LCSA of the blade bridge against a conventional bridge is presented, using each of the three pillar frameworks separately to perform quantitative assessments, and then qualitatively discussing them as an integrated assessment. An LCA and LCC are first performed following the framework in ISO 21931-2 (ISO, 2019). LCA has four steps: (1) Goal and Scope definition, (2) Inventory, (3) Impact Assessment and (4) Interpretation (ISO, 2006). In step (3), the end categories of Human Health, Ecosystem Quality, Climate Change, and Resources will be assessed using IMPACT 2002+ life cycle impact assessment (Humbert et al., 2014). The LCC will follow the same four-step framework, but phase (3) will consider lifecycle cost rather than impact assessment.

Further details of the life cycle phases which inform phase (2) Inventory are given in Figure 1. The stages considered are Pre-Construction (A0), Production and Construction (A1-A5), and Maintenance (B2). Phases C and D are discussed qualitatively, but are not included in the quantified LCSA due to the uncertainties associated with them.

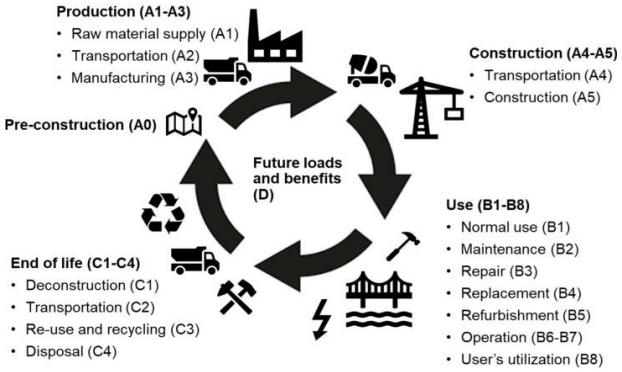

Figure 1: Life cycle phases of an infrastructure project (Ek et al., 2020)

S-LCA indicators are developed using the idea of 'thinking globally while acting locally' (Geddes, 1915). SDGs may be considered as the world's Key Performance Indicators, and therefore, can bring the 'global' aspect to s-LCA indicator selection. By identifying shortfalls in specific national SDG performance, and examining their intersection with the s-LCA indicators, the 'local' element can be added to the indicator selection. The s-LCA indicators in this study are developed by overlapping the SDGs which are categorised as socially-based (1, 2, 3, 4, 5, 8, 10, 12, 16, 17) in the Guidelines for s-LCA (Benoît Norris et al., 2020), with those in which Ireland is demonstrating a shortfall (2, 12, 13, 17) (Sachs et al., 2021) The resulting intersecting set contains SDGs 2, 12 and 17.

Figure 2: Ireland's performance against the SDGs (Sachs et al., 2021)

The BladeBridge and a conventional bridge structure are then qualitatively assessed against the sub-indicators under these three SDGs. Initial screening of the sub-indicators showed that only five of the 38 indicators are applicable to the construction of pedestrian bridges.

2.2 Goal and Scope Definition

The goal of this study is to compare the environmental, social and cost implications of a pedestrian bridge made using decommissioned wind turbine blades as girders against a bridge made with conventional materials. The functional unit is set as 'A 22m^2 pedestrian bridge with emergency vehicle load capacity of 12 tonnes, over 60 years'. The temporal boundary of 60 years was chosen based on the engineering design of the BladeBridge, combined with a UK guidance document on the design working life of a bridge with a primary load bearing structure of Glass Fibre Reinforced Polymer (GFRP) (CIRIA C779, 2018). The physical boundaries include the blades, cradles, superstructure, decking (Figure 3), and handrails. The

maintenance schedule includes repainting all steel surfaces every 20 years, and re-application of anti-graffiti coating every 5 years.

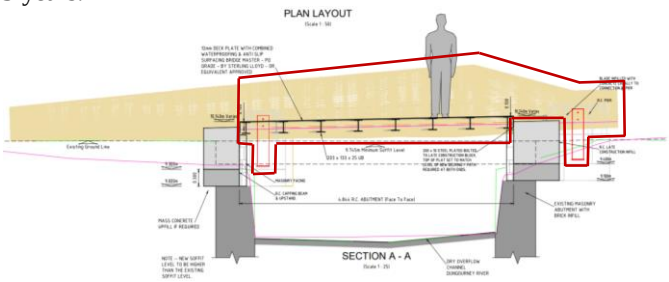

Figure 3: LCSA physical boundaries (Image generated by Kieran Ruane, MTU)

3 DATA

The three N29 blades replaced 289 kg of stainless steel in the parapet and 561 kg of recycled steel that would have been required in a 5.5m span conventional bridge, and as well as the corresponding transportation, galvanization and additional surface re-coating required of steel surfaces every 20 years. However, the blades required transport from the premises of the decommissioning contractor in Belfast to Cork, 30 hours of reverse engineering work, the fabrication of steel cradles to support the blades, and additional FRP end caps and repair work.

3.1 Life Cycle Inventory

The following section details the elements of the life cycle inventory of Blade Bridge (Table 1) and a conventional bridge (Table 2). These amounts were used to carry out the LCA and LCC.

Table 1. Inventory for BladeBridge

Module	Resource	Qty
A0	Oven type SNOL Model 12/1100, 30 hours @800C, would equal 1.5kW * 30 hours	45 kWh
A1-A3	FRP End Caps	25 kg
A1-A3	Cross & support beams, Connectors, cradles; Galvanised Steel with recycled content	1467 kg
A1-A3	Steel decking (1.5mx2m sheets); Galvanised Steel with recycled content	1628 kg
A1-A3	Parapets; Stainless Steel	289 kg
A2	3 x 0.75 tonne Blades transported 432 km	972 tkm
A3	3095 kg of Steel transported 1316 km by road and 126 km by ferry from Luxembourg	4073 tkm
A5	Concrete Abutments at tip & root; C40/C50 50% GBBS	0.6 m3
A5	Formwork; plywood	0.1 m2
B2	Anti-graffiti coating every 5 years @ 5kg each coat	55 kg
B2-B3	Painting Steel Surfaces ever 20 years and 40 years @26kg per 2 coats	52 kg

Table 2. Inventory for Conventional Bridge

Module	Resource	Qty
A1-A3	Girders, support beams, Connectors, bolts, cradles; Galvanised Steel with recycled content	2028 kg
A1-A3	Steel decking (1.5mx2m sheets); Galvanised Steel with recycled content	1628 kg
A1-A3	Parapets; Stainless Steel	578 kg
A3	3656 kg of Steel transported 1316 km by road and 126 by ferry.	4811 tkm
B2	Anti-graffiti coating every 5 years @ 5kg each coat	55 kg
B2-B3	Painting Steel Surfaces ever 20 years and 40 years @32kg per 2 coats	64 kg

3.2 Life Cycle Assessment Comparison

A single score LCA comparing BladeBridge to a conventional bridge shows an improvement of each of the four end categories: 7% on Ecosystem Quality, 13% on Human Health, 14% on Resources, and 17% on Climate Change (Figure 4), with an overall 14% reduction in environmental impact as compared to a conventional steel bridge. A second blade bridge, with the elimination of the reverse engineering work, and reduction in materials due to over-engineering of the first bridge, shows a further 1-2% improvement in the combined four end categories.

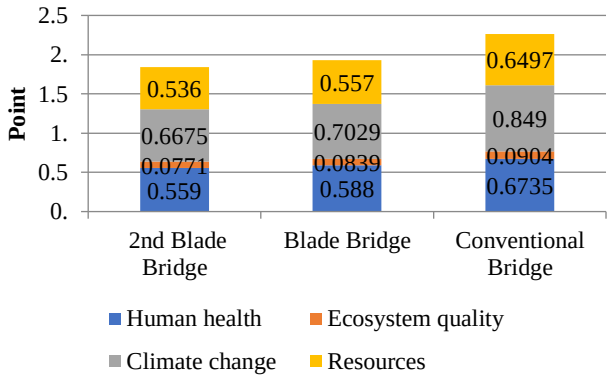

Figure 4: Single Score Comparison between blade-bridge and a conventional bridge

3.3 Life Cycle Cost Comparison

The cost of the first BladeBridge was 7% higher than the conventional bridge, predominantly due to the labour required to reverse engineer the blade. 70% of the cost of the

BladeBridge was labour, 29% was materials, and 1% was transportation of the blade. 21% of the labour cost was in reverse engineering the blade, included in the category A0 Pre-Construction work. However, a second bridge made using the same blade model can expect to be fabricated at approximately 30% less overall lifetime cost as compared to a standard bridge. The cost difference between the standard bridge and a second BladeBridge made from the same model blade would be due to a reduction in steel material and galvanising, half the required parapet material, and a reduction in the cost of maintenance at 20 and 40 years, due to the reduced surface area of steel that must be re-coated.

3.4 Social Life Cycle Assessment Comparison

A qualitative comparison of the BladeBridge and a conventional bridge against the five applicable SDG sub-indicators showed that the BladeBridge scored higher on all five indicators.

12.5 By 2030, substantially reduce waste generation through prevention, reduction, recycling and reuse:
Re-purposing of blades into pedestrian bridges has the potential to use 10% of the expected future volume of blade material in Ireland (Nagle et al., 2022). Therefore, it exceeds the requirement for compliance with current regulations, which allow landfill, but will not satisfy the impending requirements of the 2025 landfill ban. Conventional bridges may use recycled steel, which is in line with basic societal expectation, but do not currently prevent or reduce material use. BladeBridge scores higher.

12.7 Promote public procurement practices that are sustainable, in accordance with national policies and priorities
BladeBridges demonstrate circular material use and reduced environmental impacts, which is beyond current compliance for public procurement. However, the bridges are not zero waste or zero impact, and therefore there is still room for improvement. Conventional bridges are at basic compliance levels. BladeBridge scores higher.

12.8 By 2030, ensure that people everywhere have the relevant information and awareness for sustainable development and lifestyles in harmony with nature
BladeBridge offers sustainable development awareness raising by being a visible artefact in what is likely to be a highly-trafficked pedestrianised public realm setting. It is passively educational, and does not 'ensure awareness' but instead offers an awareness raising experience. A conventional bridge does not offer additional sustainable development awareness. BladeBridge scores higher.

17.14 Enhance policy coherence for sustainable development
The BladeBridge allows the wind energy to become cleaner and more circular by reducing waste, thereby improving performance under SDG 7 (Affordable and Clean Energy) while preventing a negative knock-on effect on SDG 12. Conventional bridges do not affect this. BladeBridge scores higher.

17.17 Encourage and promote effective public, public-private and civil society partnerships, building on the experience and resourcing strategies of partnerships
BladeBridge is an opportunity for bridge owners, managers and contractors to become educated on the potential for repurposing construction and demolition waste, and to upskill their supply chains in this respect. The project will encourage academic, public, private, and civic group collaboration. Conventional bridges do not affect this. BladeBridge scores higher.

4 DISCUSSION/CONCLUSIONS

Compared to a conventional bridge, the BladeBridge project demonstrates that overall environmental gains of 14% or more can be made through the use of decommissioned blades to replace steel girders in a pedestrian or cycleway bridge. The cost of the first bridge made from a specific blade model is more expensive due to the reverse engineering required. Most of this testing could be avoided with access to the Original Equipment Manufacturer (OEM) blade design data, which has thus far been unavailable to the ReWind project due to IP concerns. However, preliminary estimates show that cost reductions of up to 30% across the lifetime of the bridge could be achieved on second and subsequent bridges manufactured from the same blade model, as compared to the cost of a conventional bridge (Nagle, A., 2022).
The BladeBridge shows improvements on indicators based on socially aligned SDGs in which Ireland is exhibiting a shortfall in its performance. Therefore, as compared to a conventional bridge, Blade Bridge could support improvements in Irish performance against SDGs 12 and 17 by reducing waste volumes through blade repurposing, supporting green public procurement, raising public awareness for reuse, and contributing to the decoupling of increased renewable energy deployment with end-of-life waste generation.

4.1 Design Modifications to Improve LCSA

Design modifications that would improve upon the LCSA would include consuming more of the blade material, and substituting more steel material with blade material. Further cost reductions in labour could be gained by standardizing the deck to blade connections, thereby reducing engineering and fabricator design time. The size of blades that will be decommissioned will increase stepwise year on year, following the increase in turbine sizes that were installed in the last two decades. Currently, many of the available decommissioned blades are under 15m in length. The next increase in size will be to 22-25m in length. Blades of this size will have a proportionately wider maximum chord section, which results in the substitution of more handrail material. Larger blades will also be proportionately lighter in weight than their substituted steel parts. Installation of a conventional bridges with a span greater than 7m would likely require a heavier crane than would be required with an equivalent BladeBridge, thereby increasing the proportional gains made in the installation of a BladeBridge.

4.2 Overcoming Barriers

Cork County Council's willingness to facilitate a research project and their desire to commission something visibly different and sustainable on this particular greenway resulted in

the first bridge of this type in Ireland. The bridge was largely funded by Munster Technological University and, thus, the Council got the bridge at a heavily discounted price, though it is noted the Council provided the bridge approach works, parapets and general finishing works. The blades were donated by Everun Ltd, also reducing the overall cost of the bridge. The Council's concerns around the quality of the material were allayed by extensive testing of a spare blade which had come from the same wind farm and had been stored in the same location. This was one of the key outputs of the exercise, as it was an enabler of greater acceptability of repurposed blade materials in public infrastructural. Visual inspection of the test blade showed that it was in a similar condition to the blades to be incorporated in the bridge. Cutting of the blade and the testing method were developed based on collaboration between a team member with 25 years of bridge design experience, and two other team members with 30+ years of FRP composites expertise. The bridge foundation design was also developed through a similar process. This collaborative testing and reverse engineering process was documented in a peer reviewed paper (Ruane et al., 2022). Insurance and liability were covered by the bridge designer's own professional and public indemnity insurance.

4.3 Business Aspects of BladeBridge

A BladeBridge business model is two-sided, much like E-Bay, in that the business requires one customer to need to decommission blade material, and another customer to want to buy repurposed blade products. Scaling up a BladeBridge business will first require education of stakeholders on both sides of the business model. For example, wind asset owners will need to understand the impending landfill ban, and the lack of availability of recycling options for blade material, while public procurement specialists in county councils will need to be educated on the option of procuring pedestrian bridges made with repurposed material. The design of the BladeBridge was informed by extensive laboratory work. The performance of the bridge in-service will now be monitored over time so that further confidence may be gained in this concept and the results disseminated to potential procurers of pedestrian bridges.

LCSA of a pedestrian and cycle bridge incorporating wind turbine blades as structural elements demonstrates significant environmental, social advantages over conventional designs for these structures, based on steel. The benefits accrue from reduced resource requirements for the bridge fabrication, diversion of composite blade material which might otherwise end up in landfill or other environmentally undesirable material streams, social benefits, particularly in areas identified as those in which Ireland is under-performing by assessment against the UN Sustainable Development Goals. The BladeBridge can act as an exemplar to public and private bodies in green public procurement and in providing high-visibility sustainable infrastructure. The BladeBridge has also been shown to be cost-competitive with conventional solutions, and the cost advantages are expected to increase with further deployments as learning effects will reduce the need for materials testing, reverse engineering and over-engineering.

ACKNOWLEDGMENTS

This material is based upon work supported by InvestNI/Department for the Economy (DFE), Grant USI-116; by Science Foundation Ireland, Grant 16/US/3334; and by the U.S. National Science. Foundation under grants numbers 1701413 and 1701694, under the project "Re-Wind". A special thanks to Everun for the donation of the blades, Cork County Council for commissioning this project, Munster Technological University for funding, and Civil and Structural Engineering Advisors Ltd for the donation of both funding and design and drafting time.

REFERENCES

Al-Haddad, T., Alshannaq, A., Bank, L., Bermek, M., Gentry, R., Henao-Barragan, Y., Li, S., Poff, A., Respert, J., Woodham, C., 2022. Strategies for Redesigning High Performance FRP Wind Blades as Future Electrical Infrastructure, in: ARCC-EAAE 2022 INTERNATIONAL CONFERENCE IN MIAMI RESILIENT CITY: Physical, Social, and Economic Perspectives, March 2-5. Miami.

Alshannaq, A., Scott, D., Bank, L., Bermek, M., Gentry, R., 2021. Structural Re-Use of De-Commissioned Wind Turbine Blades in Civil Engineering Applications. J. Compos. Constr.

Bank, L.C., Arias, F.R., Gentry, T.R., Al-Haddad, T., Tasistro-Hart, B., Chen, J.-F., 2019. Structural Analysis of FRP Parts from Waste Wind Turbine Blades for Building Reuse Applications, in: SEMC Cape Town. DfE, Cape Town.

Beauson, J., Brøndsted, P., 2016. Wind turbine blades: An end of life perspective, in: MARE-WINT: New Materials and Reliability in Offshore Wind Turbine Technology. Springer International Publishing, pp. 421–432. https://doi.org/10.1007/978-3-319-39095-6_23

Benoît Norris, C.., Traverso, M.; Neugebauer, S.., Ekener, E.., Schaubroeck, T.., Russo Garrido, S.., Berger, M.., Valdivia, S.., Lehmann, A.., Finkbeiner, M.., Arcese, G., 2020. Guidelines for SOCIAL LIFE CYCLE ASSESSMENT OF PRODUCTS AND ORGANIZATIONS 2020.

CIRIA C779, 2018. Fibre-reinforced polymer bridges - Guidance for designers.

Clark, C., Kavanagh, C., Lenihan, N., 2020. Measuring Progress: The Sustainable Progress Index 2020, Social Justice Ireland.

Clark, C.M., Kavanagh, C., 2021. Measuring Progress: The Sustainable Progress Index 2021.

Delaney, E.L., McKinley, J.M., Megarry, W., Graham, C., Leahy, P.G., Bank, L.C., Gentry, R., 2021. An integrated geospatial approach for repurposing wind turbine blades. Resour. Conserv. Recycl. 170, 105601. https://doi.org/10.1016/j.resconrec.2021.105601

DTTAS, 2018. Government of Ireland - Strategy for the Future Development of National and Regional Greenways.

Ek, K., Mathern, A., Rempling, R., Brinkhoff, P., Karlsson, M., Norin, M., 2020. Life Cycle Sustainability Performance Assessment Method for Comparison of Civil Engineering Works Design Concepts: Case Study of a Bridge. Int. J. Environ. Res. Public Health 17, 1–34. https://doi.org/10.3390/IJERPH17217909

European Commission, 2019. The European Green Deal. Eur. Comm. 53, 24. https://doi.org/10.1017/CBO9781107415324.004

Eurostat, 2018. Circular material use rate, Statistical Office of the European Communities.

Geddes, P., 1915. Cities in evolution: An introduction to the town planning movement and to the study of civics. Williams & Norgate, London.

Gentry, T.R., Al-Haddad, T., Bank, L.C., Arias, F.R., Nagle, A., Leahy, P., 2020. Structural Analysis of a Roof Extracted from a Wind Turbine Blade. J. Archit. Eng. 26, 04020040. https://doi.org/10.1061/(asce)ae.1943-5568.0000440

Humbert, S., De Schryver, A., Bengoa, X., Margni, M., Jolliet, O., 2014. IMPACT 2002+: User Guide. https://doi.org/10.1007/BF02978505

ISO, 2019. ISO 21931-2:2019(en), Sustainability in buildings and civil engineering works — Framework for methods of assessment of the environmental, social and economic performance of construction works as a basis for sustainability assessment — Part 2: Civil engine.

ISO, 2006. ISO 14044: Environmental management — Life cycle assessment — Requirements and guidelines.

Jensen, J.P., Skelton, K., 2018. Wind turbine blade recycling: Experiences, challenges and possibilities in a circular economy. Renew. Sustain. Energy Rev. 97, 165–176. https://doi.org/10.1016/J.RSER.2018.08.041

Kühnen, M., Hahn, R., 2017. Indicators in Social Life Cycle Assessment: A Review of Frameworks, Theories, and Empirical Experience. J. Ind. Ecol. 21, 1547–1565. https://doi.org/10.1111/jiec.12663

Leahy, P., Zhang, Z., Nagle, A.J., Ruane, K., Delaney, E., McKinley, J.M., Bank, L.C., Gentry, R., 2021. Greenway bridges from wind blades Greenway pedestrian and cycle bridges from repurposed wind turbine blades. Irish Transp. Res. Netw. 82–89.

Maier, S.D., Beck, T., Vallejo, J.F., Horn, R., Söhlemann, J.H., Nguyen, T.T., 2016. Methodological approach for the sustainability assessment of development cooperation projects for built innovations based on the SDGs and life cycle thinking. Sustain. 8, 1–26. https://doi.org/10.3390/su8101006

McConnell, D., 2021. Completion of Youghal-Midleton Greenway delayed until 2023. Irish Exam.

Nagle, A.J., Mullally, G., Leahy, P.G., Dunphy, N.P., 2022. Life cycle assessment of the use of decommissioned wind blades in second life applications. J. Environ. Manage. 302, 113994. https://doi.org/10.1016/J.JENVMAN.2021.113994

Ruane, K., Zhang, Z., Nagle, A.J., Huynh, A., Alshannaq, A.A., Mcdonald, A., Leahy, P.G., Soutsos, M., McKinley, J.M., Russell Gentry, T., Bank, L.C., 2022. Material and Structural Characterization of a Wind Turbine Blade for use as a Bridge (Accepted for Jan, 2022 Conference), in: 102nd Annual Transportation Research Board. Washington D.C.

Sachs, J.D., Kroll, C., Lafortune, G., Fuller, G., Woelm, F., 2021. SUSTAINABLE DEVELOPMENT REPORT 2021:The Decade of Action for the Sustainable Development Goals.

Stone, M., 2022. Engineers are building bridges with recycled wind turbine blades. The Verge.

Suhail, R., Chen, J.-F., Gentry, R., Taristro-Hart, B., Xue, Y., Bank, L., 2019. Analysis and Design of a Pedestrian Bridge with Decommissioned FRP Windblades and Concrete, in: 14th International Symposium on Fiber-Reinforced Polymer Reinforcement of Concrete Structures (FRPRCS). Belfast, Northern Ireland, UK.

Transport Infrastructure Ireland, 2019. Technical Approval of Structures on Motorways and Other National Roads: DN-STR-03001, TII Publications.

Wulf, C., Werker, J., Zapp, P., Schreiber, A., Schlör, H., Kuckshinrichs, W., 2018. Sustainable Development Goals as a Guideline for Indicator Selection in Life Cycle Sustainability Assessment, in: Procedia CIRP. https://doi.org/10.1016/j.procir.2017.11.144

Zeug, W., Bezama, A., Thrän, D., 2021. A framework for implementing holistic and integrated life cycle sustainability assessment of regional bioeconomy. Int. J. Life Cycle Assess. 26, 1998–2023. https://doi.org/10.1007/S11367-021-01983-1/FIGURES/6

CERCOM - Adoption of the Circular Economy in Road Construction

Emma Sheils[1], Lorcan Connolly[1], Alan O'Connor[1], Eugene OBrien[1]
[1]Research Driven Solutions Ltd, 1A St. Kevin's Avenue, Dublin, D08TX29
email: emma.sheils@researchdrivensolutions.ie, lorcan.connolly@researchdrivensolutions.ie,
alan.oconnor@researchdrivensolutions.ie, eugene.obrien@researchdrivensolutions.ie

ABSTRACT: Implementation of the circular economy and resource efficiency has the potential to significantly contribute to decarbonisation targets, while using fewer natural resources, maintaining or enhancing biodiversity and providing regenerative design for generations to come. The CERCOM project has developed an innovative risk-based framework and management tool to facilitate a step change in the adoption of Resource Efficiency (RE) and Circular Economy (CE) principles in procurement and multi-lifecycle management by National Road Authorities (NRAs) across Europe. To develop the Risk-Based Analysis Framework (RBAF) and establish the system boundaries, risk-based decision analysis was first reviewed to establish current good practice. A review of risk-based approaches from previous research projects was completed. Building on processes developed in previous frameworks, the CERCOM Risk-Based Analysis framework is presented which utilises a weighted sum of the Risk Reduction Index, the Cost Potential Index and the various Key Performance Indicators developed in the work in order to delineate and rank various construction and maintenance activities in terms of circularity and risk. The framework considers technical, economic, environmental and social criteria, as well as RE / CE, to assess the change in risks in moving from a linear to a circular economy. The RBAF allows NRAs to decide on the level and scope of analysis they wish to complete and provides a tool to do so taking account the scale and nature of the project. The result is in an intuitive user-friendly framework for NRAs, providing trust and confidence in output results.

KEY WORDS: Risk analysis; Circular economy; Resource efficiency; Highway maintenance.

1 INTRODUCTION

Implementation of Circular Economy (CE) has the potential to tackle the root causes of global challenges such as climate change, biodiversity loss and pollution whilst at the same time providing regenerative design for generations to come. In the context of road construction and maintenance, several European National Road Authorities (NRAs) are already engaged with the circular agenda. A recent review has reported that while some progress has been achieved by the EU NRAs, particularly regarding maximising recycling and minimising waste, "not all NRAs and/or sector stakeholders seem to be adequately familiar with the Circular Economy concept" [1]. As road infrastructure accounts for an extensive use of resources, NRAs must become more material and energy efficient, moving beyond recycling, to reuse, repair/life extension and minimising use of materials. To make the process truly operable, a quantitative methodology is required which can adequately make the case for CE and Resource Efficiency (RE) in procurement and multi-lifecycle management.

In 2020, the Conference of European Directors of Roads (CEDR) issued a call for research on Resource Efficiency and Circular Economy and commissioned the project, 'Circular Economy in Road Construction & Maintenance' (CERCOM) [2]. CERCOM investigates how the circular economy could work in the context of highway construction and maintenance and what barriers and opportunities exist for its adoption. The aim of CERCOM is to deliver an innovative risk based framework and management tool to facilitate a step change in the adoption of RE & CE principles in procurement and multi-lifecycle management by CEDR NRAs. To develop the Risk-Based Analysis Framework (RBAF) and establish the system boundaries, risk-based decision analysis was first reviewed to establish current good practice.

2 OVERVIEW OF EXISTING RISK ANALYSIS FRAMEWORKS

2.1 Risk analysis

Design and maintenance of road networks aims to meet the required performance standards while also limiting the risk to road users and the infrastructure itself. In procurement of any design or maintenance strategy, consideration of risk is paramount in deciding upon the most appropriate solution for the scheme. That is, the solution which maximises safety and ensures the desired level of functionality while minimising cost. With the move towards a circular economy, there is an added objective to ensure RE & CE factors are integrated within this assessment. One of the objectives of CERCOM is to identify the fundamental characteristics of a risk-based framework to make it applicable to NRAs in their procurement processes. Risk management involves gaining an understanding of what may go wrong, the probability of this happening and the associated consequences. The primary source for the current work is ISO 31000:2018 Risk management – Guidelines [2]. The prescribed risk management process involves the systematic application of policies, procedures and practices to the activities of communicating and consulting, establishing the context and assessing, treating, monitoring, reviewing, recording and reporting risk. This process is illustrated in Figure 1.

The ISO 31000 framework should be considered when developing risk assessment frameworks for any specific need, and as such forms the basis for the development of the CERCOM RBAF. The framework enables rational decisions to be made around the adoption of RE & CE approaches, with the principles of risk assessment at its core.

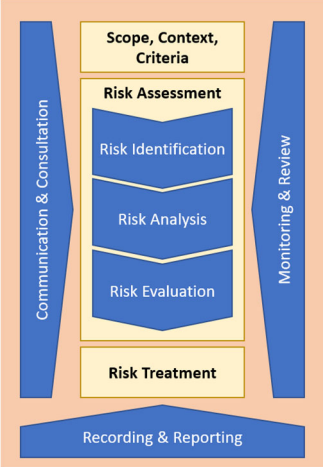

Figure 1. ISO 31000 Risk Management Process [2]

Within the scope of CERCOM, the Scope Context and Criteria, Risk Assessment and Risk Treatment headings of ISO 31000 are integrated directly into the core aspects of the RBAF. The other aspects of Communication and Consultation, Monitoring and Review and Recording and Reporting are continuous processes and occur throughout the procurement process.

The objective of CERCOM is to build upon risk-based assessment frameworks previously developed in the CEDR funded RE-GEN (Risk Assessment of Ageing Infrastructure) project as well as EU framework projects such RAIN (Risk Analysis of Infrastructure Networks) and INFRARISK (Novel Indicators for Identifying Infrastructure at Risk). These previous frameworks for assessment of transport infrastructure were reviewed to facilitate identification of good practice. While numerous examples exist in the literature and were considered as part of the overall review, an overview is provided of these projects based on their relevance to the CERCOM risk-based analysis framework requirements. These can be tailored to suit the CERCOM objectives.

2.2 INFRA-RISK

The INFRARISK project (www.infrarisk-fp7.eu/) aimed to develop reliable stress tests on European critical infrastructure using integrated modelling tools for decision-support. The project intention was to advance decision-making approaches leading to better protection of existing infrastructure while achieving more robust strategies for the planning of new infrastructure. Integrated risk mitigation scenarios and strategies were developed, using local, national and pan-European infrastructure risk analysis methodologies, taking into consideration multiple hazards and risks with cascading impact assessments. An operational framework with cascading hazards, impacts and dependent geospatial vulnerabilities was developed.

To develop the INFRARISK Risk Assessment Framework, a two-phased approach was undertaken. The initial definition of the INFRARISK Risk Assessment Framework had its basis in the global procedure of ISO 31000. This is key to any framework in order to keep the format in line with modern codes of practice. In the preliminary framework, the system boundaries are defined, including the spatial boundaries (e.g., the extent of the transport network to be assessed) and the temporal boundaries (i.e., the time period over which the risk assessment will take place, and the subdivisions of this time period over which the risk will be analysed).

Through engagement within the INFRARISK consortium and discussion on the specific requirements, an updated Risk Assessment Framework was defined by the project, which provided a more flexible and open methodology which could be adapted to not only road and rail infrastructure networks, but all infrastructure networks, allowing for the inclusion of cascading events and interdependencies. The Framework is illustrated in Figure 2.

Figure 2. INFRARISK Final Risk Assessment Framework

In the initiate stage, spatial boundaries and temporal boundaries within the system are considered. This step should also consist of an overview of how the assessment will be carried out, the levels of abstraction and the models and software to be used to determine if the infrastructure related risks are acceptable. Effort should also be made at this stage to define what an acceptable level of risk may be in the context of the organisation. It is important that some thought is put into this before the risk assessment is conducted to provide context to the results.

The Conduct Risk Assessment phase again consists of analysing the system by simulating its behaviour in specific situations and estimating and evaluating the risk. The INFRARISK approach recommends performing the assessment initially at a very high level of abstraction in order initially describe the process, followed by iteratively refining the level of abstraction until it is decided that the level of risk is either acceptable or not. The systems and models can be tested and benchmarked throughout the iteration process, and the level of detail in each model can be enhanced throughout each iteration. This saves time placing needless levels of detail on models that have a comparatively low impact on the risk. This may be a useful step in the CERCOM context as the priorities and capabilities to perform risk analysis incorporating CE and RE aspects may vary significantly between NRAs. The various sub tasks within this stage include (i) set up the risk assessment, (ii) determine approach, (iii) define system, including the definition/determination of the system boundaries, events, scenarios, relationships between events, and models, (iv) estimate risk, and (v) evaluate risk. The INFRARISK framework allowed for the application of various levels of risk assessment, from quantitative to qualitative approaches. The qualitative approach may be demonstrated by a risk matrix, with consideration of likelihood and consequences, but without formal quantification. In the context of the CERCOM approach, the level of complexity in the risk

assessment process may be dynamic and vary depending on the requirements of the NRA.

The Conduct Intervention Programme stage consists of developing measures to reduce the risk to an acceptable level and optimising to choose the most advantageous action or combination of actions. While the INFRARISK approach to risk analysis is more complex than what is required for NRAs to adopt CE & RE solutions in the procurement process, there are certain aspects of the tools and framework that will prove to be of benefit for the CERCOM RBAF.

2.3 RAIN

The RAIN project (http://rain-project.eu/) aimed to develop an analysis framework that identified critical infrastructure components impacted by extreme weather events and minimised the impact of these events on the EU infrastructure network. The project had a core focus on land-based infrastructure with a much wider consideration of the ancillary infrastructure network in order to identify cascading and inter-related infrastructure issues. A core component of the research considered the implications of climate change and the subsequent impacts that this may have on an already ageing and vulnerable infrastructure system.

The RAIN project is a particularly useful source for the development of the CERCOM approach in the development of quantitative tools which can be used for Risk analysis. The framework developed was fully probabilistic, with not only the hazards and impacts being modelled probabilistically, but also the consequences and "utility" of the associated impacts. As per the INFRARISK approach, while the methodology is complex and not directly applicable to the CERCOM objectives, many of the tools developed may be transferrable.

The framework consisted of 5 steps, globally divided into two phases; the inference phase and the decision phase. The first step of the inference phase, enumeration, consists of listing of all possible states that the infrastructure may be as well as all the possible actions that can be taken to manage these states This phase may be considered part of the "scope context and criteria" stage of the ISO 31000 risk management process.

The second step in the inference phase is the quantification phase. In this step, the hazards and associated vulnerabilities of the infrastructure are modelled in order to describe the likelihood of each state occurring. The quantification of the likeliness of the possible states of the system under consideration gives us the state probability distributions. The quantification step also contains the quantification of consequences of each state. This state consequence quantification is often based on historic data as well as estimates from key stakeholders.

The final step in the inference phase is the construction of the outcome probability distribution. This involves multiplication of the consequences and likelihoods at each state in the system. The risk is represented by a random variable representing the fact that the final risk is an uncertain value.

The first step in the decision phase is the construction of the "Utility" distribution. This is a distribution which describes the practicalities of a strategy in the context of the availability of budget to implement it. Choosing the action which optimizes the risk 'position' on this basis is therefore the final step in the process. This level of probabilistic utility estimation is not required for CERCOM, where deterministic outcomes of RBAF are preferable in order to be usable in the procurement process of most NRAs.

However, there may be scope to include a flexible approach whereby probabilistic tools may be employed where data is available.

2.4 Re-Gen

The primary objective of the Re-Gen project (Risk Assessment of Aging Infrastructure Networks - www.re-gen.net) was to provide Road Owners/Managers with best practice tools and methodologies for risk assessment of critical infrastructure elements such as bridges, retaining structures and steep embankments. The Re-Gen project sought to adopt a network-wide probabilistic risk-based approach to optimize lifecycle performance of the infrastructure, within the context of evolving traffic demands and climate change effects. The Re-Gen project therefore suggested using quantitative risk assessment tools (e.g. fault tree or BBNs) to model the risk of road infrastructure in respect of climate change and long-term traffic growth. If historical data is not available to perform such analysis, Re-Gen recommended that application of structured expert judgment to provide quantitative data.

The Re-Gen project provided guidance on deterministic calculation of failure consequences, considering both direct and indirect costs, including rehabilitation costs C_{Reb}, vehicle detour / running costs C_{Run}, travel time costs C_{Trav} based on the average person wage and Accident costs C_{Acc}. The risk is then computed according to Equation 1:

$$R = P_f \times (C_{Reb} + \dot{C}_{Run} + C_{Trav} + C_{Acc}) \quad (1)$$

Where P_f is the probability of a specific failure state occurring, computed from the fault tree analysis. The Re-Gen project also proposed risk optimization techniques which are of particular relevance to the CERCOM approach. To make effective decisions, the risk framework must be able to identify the action (or combinations of actions over time) which both minimise the risk and the required resources. Re-Gen proposed Multi-Attribute Optimization for this task. An example was provided of potential interventions to prevent a risk (R) of bridge failure. It was assumed that after the implementation of the i_{th} intervention the value of the residual risk would be R_i. As such, a Risk Reduction Index (RRI) can be defined for each intervention as [4]:

$$RRI_i = \frac{R - R_i}{R} \quad (2)$$

The RRI lies in the interval 0.0 – 1.0 for feasible interventions. The cost of each intervention can be estimated as C_i and includes but is not limited to the cost of materials and labour. Having the total budget allocated for risk optimization B, a Cost Potential Index (CPI) can be defined for each intervention as [4]:

$$CPI_i = \frac{C_i}{B} \quad (3)$$

Finally, the Net Risk Reduction Gain ($NRRG$) of the i_{th} intervention is defined in this work as:

$$NRRG_i = w_1 \times RRI_i + w_2 \times CPI_i \quad (4)$$

Where w_1 and w_2 are weighting factors, reflecting the preference of decision makers to either reduce the risk or to expend less money on interventions. It should be noted that $w_1 + w_2 = 1.0$, and *CPI* is considered negative in Equation (4), reducing the *NRRG* brought about by the intervention. The optimal intervention strategy is the one which maximizes the sum of $NRRG_i$; that is, the net gain of risk reduction should be the greatest after the application of the optimal intervention strategy under the constraint of the limited available budget.

Although the framework developed in Re-Gen had a different aim to the CERCOM project, the tools are a good starting point for evaluating risk while prioritising RE and CE uptake by NRAs in the procurement of road construction and/or maintenance activities. The flexibility to perform quantitative or qualitative risk assessment also lends itself well to NRAs, while the multi-attribute optimization appears to be an excellent tool for building the prioritisation of environmental goals, RE and CE approaches.

3 CERCOM FRAMEWORK

3.1 Framework Overview

The aim of the CERCOM framework is to facilitate procurement of circular solutions for road construction and maintenance while assessing the risk of doing so. In order to develop the basis of the framework, the system boundaries and general context were first established.

The CERCOM framework considers technical, economic, environmental and social criteria, as well as RE / CE, to assess the change in risks in moving from a linear to a circular economy. The framework is applicable to all road infrastructure elements under the maintenance remit (e.g., road pavements, bridges, retaining walls, cuttings and embankments and roadside infrastructure). The framework is adaptable to new construction and maintenance methodologies, lending itself to, for example, the evaluation of novel "green", circular and bio-based maintenance solutions, and has a means by which the RE and CE ranking of different solutions can be considered.

The RBAF framework is outlined in Figure 3. It is reflective of the universally accepted ISO 31000 approach, with the "Scope, Context, Criteria", "Risk Assessment" and "Risk Treatment" integral within the 5 steps of the framework.

Figure 3. CERCOM Risk-Based Analysis Framework

3.2 Establish context

This step involves a description of the primary goals of the assessment, the hazards involved, the potential actions to reduce risk, the consequences to be considered and how the hazards and consequences will be calculated. A qualitative approach to defining the context is advised within the framework. Expert judgement should be used to establish the nature of the assessment, the hazards, the actions which may be taken, the level of the analysis and the means of assessing RE / CE approaches (i.e., as KPIs or through quantitative cost representation).

3.3 Likelihood

Likelihoods are considered quantitatively within the RBAF, quantifying as accurately as possible, the probability of failure, or the probability of exceedance of a given damage state for given scenarios of hazard and action. This can be used to quantify possible increased risks associated with moving from linear to more circular materials and practices. An example may include quantifying the probability of a certain level of pavement wear for different products proposed as part of a resurfacing regime. By quantifying the probabilities associated with traditional methods and more innovative methods, the various risks associated with moving towards a circular economy can be assessed and optimized as part of the framework. It is important to highlight that the framework does not replace or override these minimum safety requirements set out in design standards, but rather, it aims to use the performance level associated with different methods to compare, rank, and optimize viable options. Probabilistic modelling can utilize Event Trees, Decision Trees and Bayesian Network Modelling to consider the complex interdependencies between different network elements. For NRAs who may not possess the level of data required to perform quantitative probabilistic modelling, Event Trees are also a useful tool to contextualize the problem and describe the processes leading to failure. Expert judgement can then be used rather than probabilistic modelling to input the likelihoods where required.

3.4 Evaluate consequences

Consequences evaluated in a risk assessment are directly related to the specific failure states considered in evaluating likelihood. Probabilities and consequences are combined as part of the final optimization step of the process to calculate the Risk associated with a proposed construction or maintenance scenario. Consequences should be considered quantitatively and expressed in monetary terms where possible.

3.5 Establish additional KPIs

Additional KPIs are established for the scheme in question and their values are quantified for each potential strategy. KPIs should be as orthogonal as possible to avoid double counting and should be determined in a collaborative way among all stakeholders. A range of scores are proposed for each KPI and values are assigned for each strategy. Weights are used to assign relative importance in the "Optimize" step. KPIs have a value between 0.0 and 1.0, with 0.0 having the lowest benefit on CE / RE and 1.0 having the highest benefit. Within the framework, these additional KPIs are divided into 3 categories, RE & CE, Environmental and Social. The framework is flexible to include as many KPIs as necessary in order to capture individual NRA requirements. A ranked interpolation approach of quantifying each KPI provides a robust and stable means to evaluate various RE / CE factors in an intuitive way, and is outlined as follows:

1. Determine the number of ranks required to quantify the KPI;
2. Set the minimum rank to a value of 0.0, and the maximum rank to a value of 1.0;
3. Determine the mathematical relationship between each KPI rank;
4. Score the KPI for the scenario being evaluated and interpolate according to ranked relationship.

In the simplest case, a linear relationship may be assumed between the first and final rank. Where a more complex response is required, a multi-linear or quadratic relationship may be established between different KPI ranks. This type of model may be developed, for example, where the benefit of increasing the rank raises the RE / CE, environmental or social value exponentially. In this case, linear interpolation should be carried out between each rank, as illustrated in Figure 4. An example of how ranks may be structured to reward innovation is outlined as follows:

- Rank 1 = minimum acceptable performance, KPI 0;
- Rank 2 = industry norm, established practice but not always applied, KPI 0.15;
- Rank 3 = industry leading performance, uncommon, KPI 0.6;
- Rank 4 = medium term goal, KPI 1.0.

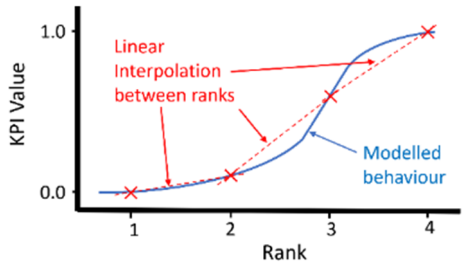

Figure 4. Interpolating KPI values

3.6 Optimize

To allow performance, cost, resource efficiency, environmental and social factors to be considered and integrated into a single index for optimization purposes, the Net Risk Reduction Gain (*NRRG*) is incorporated into the RBAF (Equation 5). This weighted sum involves calculation of the risk, costs and all KPIs to provide a means of scoring the various potential maintenance strategies. All weights assigned must sum to 1.0. For each potential action, the Risk associated with each strategy is calculated and used to generate the Risk Reduction Index (*RRI*), outlined in Equation 6. In terms of cost, the calculation of the Cost Potential Index (*CPI*) provides flexibility within the framework to allow NRAs to vary the level of complexity involved in the calculation of costs associated with each proposed strategy (Equation 7).

$$NRRG_i = w_1 \times RRI_i + w_2 \times CPI_i + w_3 \times KPI_{1,i} + w_4 \times KPI_{2,i} + \cdots \quad (5)$$

$$RRI_i = \frac{R - R_i}{R} \quad (6)$$

$$CPI_i = \frac{B - C_i}{B} \quad (7)$$

R = Risk associated with the "Do Nothing" option;
R_i = Risk associated with maintenance / construction option i;
B = Budget available for maintenance / construction activity;
C_i = Cost associated with maintenance / construction option i;
$KPI_{3,4,5\ldots,i}$ = Values of each KPI associated with maintenance / construction option i;
$w_{1,2,3\ldots}$ = Values of weights for each KPI. Note that all weights must sum to 1.0

The developed additional KPIs should ensure that contractors can be rewarded for producing a scheme that will be long lasting, cost effective to maintain, use limited amounts of raw materials, designed for multiple lifecycles and/or can be readily repaired for (multi) life extension. The intention is to add components to the scheme design considering reuse, recycling, demountability, etc. pointing towards closing the loop. The KPIs should also be sympathetic to the various maturity levels across NRAs. For example, staff in NRAs may have zero/low or medium levels of awareness of RE & CE. Another example is that the supply chain may have zero engagement between stakeholders, may just recognise the need for engagement or may be actively engaged.

The high-level indicators provide a means to rank strategies taking account of resource efficiency, environmental and social factors within the framework, while allowing for quantification of risk and multiple lifecycle performance. While performance and cost are encompassed within the *RRI* and *CPI*, further KPIs are required for RE & CE, environment and social considerations. It should be again noted that all weights will sum to 1.0, and the KPIs should be expressed in the interval of 0.0-1.0, with 1.0 being the maximum possible value achievable within each KPI. The minimum requirements of each KPI (as defined within the objectives and codified norms of the NRA) should be sustained for each option considered.

This approach allows for maintenance and construction costs and/or Whole Life Costing/multi-LCA to be incorporated. KPIs are utilized within the calculation of *NRRG* to integrate critical resource efficiency, environmental and social factors.

4 SAMPLE APPLICATION

A sample application of a resurfacing scheme for a section of road was considered to demonstrate the application of this framework and assess the stability and robustness. A brief outline of the example is summarized below. As well as the "do nothing" scenario as reference, 3 maintenance options were examined.

- Option 1 - Use of **standard asphalt** surface course with minimum recycled content in line with NRA requirements. This can be further recycled as a surface course at the end of its life, or downcycled into binder / base course.
- Option 2 - Use of asphalt containing **high-recycled content** surface course.
- Option 3 - The use of asphalt containing 10% **crushed glass** and 20% reclaimed aggregate, jointly replacing 30% of the aggregate within the surface course.

The goal is to assess the relative risks associated with adopting the more resource-efficient maintenance scenarios through the application of the developed framework. To assess the possible

risks associated with more innovative approaches, a probability of early failure is assigned to each option based on empirical evidence, as outlined in Figure 5. To calculate the risk, the probability of failure is multiplied by consequences which are defined in terms of cost. For this example, the consequence of a failure event is the emergency rehabilitation cost and is assumed to be equal for all 3 options. The *RRI* (Equation 6) is then generated for each scenario.

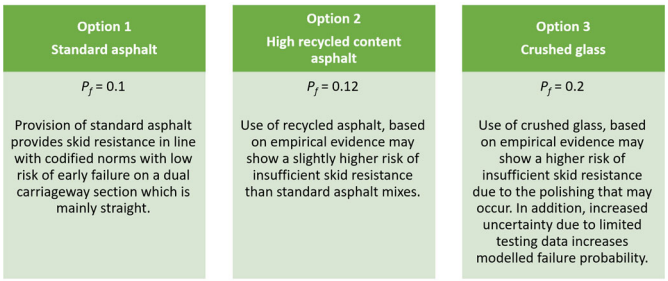

Figure 5. Probability of failure event for each option.

To calculate the *CPI* (Equation 7) for this sample application, it is assumed that the cost of carrying out maintenance options 1, 2 and 3 are €8 million, €7.5 million and €8.5 million, respectively (from an available maintenance budget of €20 million).

As the CERCOM project progresses, multi-Life Cycle Analysis will be integrated into the approach to directly take account of reuse, residual value and disposal of materials. This level of analysis may not be required for some NRAs or for certain schemes, so a more simplistic means to consider residual value of materials is suggested through the integration of an additional cost KPI (KPI_{RV}), which is assigned for each of the 3 scenarios in this example.

Option 1 is assigned KPI_{RV}= 0.5, assuming that materials are fit for re-use with extensive processing required. Option 2 would be similar to Option 1 in terms of residual value, but would require slightly more processing for reuse. As such, a value of KPI_{RV}= 0.45 is assumed. Option 3 is assigned KPI_{RV}= 0.25, assuming that crushed glass would limit the options available for subsequent reuse in surface course material.

For the current example, the following KPIs are also included in the analysis to account for circularity, resource efficiency and environmental factors, Energy Use (KPI_E), Recycled Content (KPI_{RC}) and Carbon Cost (KPI_{CC}). Based on data available, the construction Energy Use of dual carriageways vary from 5.6-12.6 TJ/km. For maintenance Option 1, the construction costs are assumed equal to 10 TJ/km. For Option 2, the construction material energy would be lower due to the lack of production and treating of raw material. For the purpose of this study, 1,200 TJ is assumed. For Option 3, an intermediate case of 1,400 TJ is assumed. Interpolating between upper and lower bounds yields values of KPI_E equal to 0.38, 0.63 and 0.45 for options 1, 2 and 3, respectively.

A recycled content of 20%, 60% and 30% is taken for the scenarios considered, yielding values of KPI_{RC} of 0.2, 0.6 and 0.3 for maintenance options 1, 2 and 3, respectively. For Carbon Content, based on empirical evidence associated with the maintenance scenarios considered and appropriate upper and lower bounds, values of KPI_{CC} of 0.62, 0.71 and 0.65 are interpolated for options 1, 2 and 3, respectively.

The *NRRG* (Equation 5) is calculated for each scenario using a weighted sum of all KPIs, the results are outlined in Table 1. For this example, the technical performance (*RRI*) is assigned twice the weight of each of the other KPIs. NRAs can alter weights to rank priorities when evaluating options. The results show that the option with high recycled content is considered the optimal maintenance scenario with the highest *NRRG*.

Table 1. *NRRG* for each maintenance option.

KPI		Standard asphalt	High recycled content	Crushed glass	KPI Weight
Risk Reduction Index		0.90	0.88	0.80	0.3
Cost	- Cost Potential Index	0.60	0.63	0.58	0.14
	- Residual Value	0.50	0.45	0.25	0.14
RE	- Energy Use	0.38	0.63	0.45	0.14
	- Recycled content	0.20	0.60	0.30	0.14
Environment	- Carbon Cost	0.62	0.71	0.65	0.14
Weighted Sum = NRRG:		**0.59**	**0.69**	**0.55**	1.00

Several sensitivity studies were carried out to check the robustness of the analysis and provide confidence in the basis for the risk-based analysis framework. The ranked interpolation method to quantify KPIs provides a robust and stable means of integrating quantitative measures of RE & CE into the analysis for the evaluation of construction and maintenance scenarios. This results in an intuitive user-friendly framework for NRAs, providing trust and confidence in output results.

5 CONCLUSIONS

The intrinsic value of road materials needs to be protected and if possible enhanced [5]. Climate change has led to the need to reassess road maintenance strategies. This RBAF achieves the objective to provide NRAs with a user-friendly tool that can be used in procurement of maintenance and construction schemes and adapted to suit the scope of the scheme and requirements of NRAs. It aims to support innovative use of new materials and methods to promote CE & RE while effectively managing associated risks. Crucially, the RBAF also has the scope to provide increased functionality as more data becomes available in terms of new materials and approaches. The framework is constructed in such a way as to allow NRAs on different stages of the journey towards circularity to progress over time, building on successful strategies and engaging with more circular approaches.

ACKNOWLEDGMENTS

This work was part of the CERCOM project, which is a CEDR project funded through the Call 2020 Resource Efficiency and Circular Economy.

REFERENCES

[1] Mantalovas, K.; Di Mino, G.; Jimenez Del Barco Carrion, A.; Keijzer, E.; Kalman, B.; Parry, T.; Lo Presti, D., (2020), 'European National Road Authorities and Circular Economy: An Insight into Their Approaches', Sustainability 2020, 12,7160. https://doi.org/10.3390/su12177160.

[2] CEDR (2020), https://www.cedr.eu/peb-call-2020-resource-efficiency-and-circular-economy).

[3] ISO 31000:2018, (2018), Risk Management—Guidelines, *Geneva: International Standards Organisation*.

[4] Yuan Z, Khakzad N, Khan F, Amyotte P. (2015), 'Risk-based optimal safety measure allocation for dust explosions', Safety Science, 74: 79-92.

[5] Flint, M., Bailey, H.K., (2017), 'Application of high recycled content mixtures on strategic roads', *The 16th Annual International Conference on Asphalt, Pavement Engineering and Infrastructure*, Liverpool John Moores University.

Timber construction in Ireland for the mitigation of climate change and the housing crisis in 2022

David Gil Moreno[1], Des O'Toole[2], Patrick J. McGetrick[1], Annette M. Harte[1]
[1]Timber Engineering Research Group, Ryan Institute. National University of Ireland Galway
[2]Forest Industries Ireland & Coillte
email: david.gil-moreno@nuigalway.ie, des.otoole@coillte.ie, patrick.mcgetrick@nuigalway.ie, annette.harte@nuigalway.ie

ABSTRACT: The current carbon footprint of the construction sector in Ireland together with the need for new homes to satisfy housing demand make it difficult to meet Ireland's commitments for the reduction of emissions. The challenge of increasing the number of homes while reducing emissions can be partially mitigated with an increased use of timber in the construction sector. This study analysed the potential of timber construction in Ireland to mitigate climate change while addressing the housing needs. The analysis drew different scenarios regarding the percentage of dwelling types in the coming years, and the share built with timber (timber frame and cross-laminated-timber) and masonry or concrete. Overall, scenarios with larger use of timber produced greater annual greenhouse gas abatement, although the type and mix of dwellings had a large influence, with larger emissions savings associated with the construction of apartments where masonry and concrete were substituted for mass timber. The best scenarios for the mitigation of climate changes while addressing the housing needs in Ireland combined a strong increment of timber scheme houses and apartments in the short term, with a larger presence of medium and high-rise buildings that produce less emissions than the equivalent in concrete.

KEY WORDS: Timber; CLT; LCA; Embodied carbon; Emissions.

1 INTRODUCTION

The goal of the Paris Agreement to limit global warming to 1.5°C above pre-industrial levels needs the construction sector to reduce its greenhouse gases (GHG) emissions. Building construction and operations accounted for 37% of energy-related carbon dioxide (CO_2) emissions in 2020 [1]. The GHG emissions of materials and/or processes associated with producing, transporting, installing and disposal are called embodied carbon (EC). The EC is quantified using Life Cycle Assessment (LCA) methodology [2, 3].

In 2020, as part of the European Green Deal, the European Commission announced plans to reduce the EU's GHG emissions by at least 55 % by 2030 compared to 1990 levels [4]. Ireland's emissions of GHG in 2019 were 59.8 Mt of CO_2e [5], 9.9% higher than emissions in 1990. These emissions were the second worst per capita in the EU, and 53% higher than the EU28 average of 7.9 tonnes [6]. The latest Irish Government commitment is for a 7% annual GHG emissions reductions for 2021-2030 [7]. In the transition to a climate neutral economy by 2050, the Climate Bill 2021 [8] states that the first two carbon budgets "*shall provide for a reduction of 51 per cent […] on December 31st, 2030, from the annual greenhouse gas emissions reported in 2018*". Ireland's emissions of GHG in 2018 were 60.9 Mt of CO_2eq [9].

Whereas the emissions need to be reduced, according to the Central Statistics Office (CSO), Ireland's population is expected to increase from 4.7 million to between 5.6 and 6.7 million by 2051 [10], depending on the assumptions, creating significant further demand for housing in the coming decades. To meet this demand, 30,000 additional housing units must be provided per annum (p.a.). The Central Bank of Ireland [11], using the high migration demographic projection of the CSO, estimates a demand of a*round 33,000 units per year from 2020-2039, falling to 26,000 per year from 2040-2051*. This is a total of 972,000 units. The Irish Business and Employers Confederation estimates 32,000 homes/year between 2019-2051 [12]. The National Development Plan 2021-2030 [13], states that 600,000 new homes will be required by 2040, planning to deliver almost 400,000 new homes between 2020 and 2031 (roughly 33,000 new homes p.a.), which will have *an embodied carbon cost of somewhere between four and six megatons of CO_2e, based on the current carbon intensity of construction* (Dr Kinnane, [14]).

Other scenarios draw even higher demands for new homes when considering obsolescence and changing household size [15]. In this regard, apartments can play an important role to address the housing crisis. Ireland has the lowest apartment rate in Europe at 12% [16] with the next lowest being Malta (22%) the Netherlands and Belgium (both 28%). Ireland has the highest percentage in Europe of population living in a house at 92% whereas the average in the EU is 53% [17].

The challenge of increasing the number of homes while decarbonising the construction sector can be partially mitigated with a larger use of timber as shown in Figure 1 and Figure 2. Wood and engineered wood products are bio-based materials of lower EC than concrete, masonry or steel [18-20] that can also store carbon (CS) for as long as the material is used. According to the Intergovernmental Panel on Climate Change (IPCC), not only that, *in the long term, a sustainable forest management strategy aimed at maintaining or increasing forest carbon stocks, while producing an annual sustained yield of timber, fibre or energy from the forest, will generate the largest sustained mitigation benefit* [21]. In Sweden, a study [22] analysed the emissions from the construction of a multi-storey building, and showed that the GHG mitigation efficiency of a wood-frame compared to a concrete-frame is higher even

if in the concrete-frame alternative the forests that would provide the timber are used for carbon storage. A study in the UK [23] compared the 100-year GHG mitigation achieved by newly planted commercial Sitka spruce (the main timber species in Ireland) and newly planted broadleaf conservation forests modelling the planting rate of 30,000 ha/year from 2020 to 2050 recommended by the UK Committee on Climate Change. The study found that harvesting and using the timber from Sitka spruce forests harvested in year 50 (a conservative rotation length for this species in Ireland) followed by replanting achieved better cumulative GHG balance than new broadleaf or Sitka spruce forests unharvested.

Currently in Ireland, about 24% of new builds are constructed using timber frame, far from the 83% used in Scotland [24]. In addition, building regulations in Ireland limit the use of combustible materials such as timber where the height of the top floor is over 10 m, equivalent to a building of 4 storeys [25]. The current study aims to show the potential of timber construction in Ireland to mitigate climate change. The study draws different scenarios that satisfy the demand for new builds for the period 2022-2050, using different combinations of dwelling types and construction materials. The ultimate aim is to compare the impact of timber construction, including modern engineered wood products, and the most common construction material and typologies in Ireland.

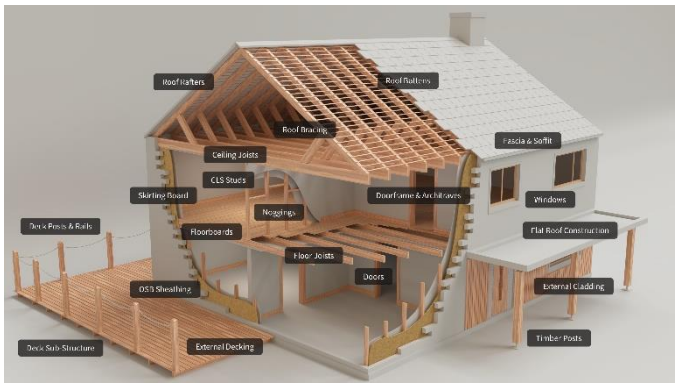

Figure 1. Potential applications of wood in domestic construction. Source [26]

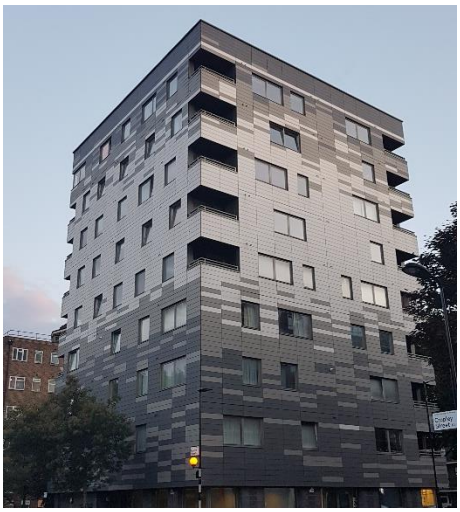

Figure 2. Murray Grove, London. Nine-storey CLT

2 MATERIALS AND METHODS

A study by the BioComposites Centre at Bangor University [27] analysed the EC and CS associated with the typical housing archetypes in the UK, very similar to those in Ireland. This study is used here (Table 1) as the basis to investigate the potential CO_2 emissions associated with satisfying the housing demand that Ireland faces in the coming decades. The calculations covered the product stages of the life cycle of the structural elements (modules A1-A3), according to EN15804 [28] (excluding internal finishes and fittings). For each housing archetype different building solutions were investigated. The functional units were matched within each archetype for identical floor plan, and matching wall, roof and glazed areas. Following the guidelines by RICS [3], the CS and EC are reported separately.

Table 1. EC and CS (kg CO_2e/m^2) of structural elements, A1-A3, for different archetypes and materials (TF: Timber frame; CLT: Cross-Laminated-Timber). Size shows the internal area and number of bedrooms (B). Low and medium-rise are 3 and 6 storey respectively. Values adapted from [27]

Archetype	Size (m^2, B)	EC	CS
Bungalow, masonry	58.5, 2B	264	-71
Bungalow, TF		235	-111
Detached house, masonry	117, 4B	177	-72
Detached house, TF		150	-109
Detached house, TF & clad		102	-126
Apartment, low-rise, masonry	70.1, 2B	176	-57
Apartment, low-rise, TF		132	-97
Semi- Detached, masonry	84.4, 3B	187	-67
Semi- Detached, TF		152	-105
Mid-terraced, masonry		161	-67
Mid-terraced, TF		137	-103
Apartment, low-rise, masonry,	50, 1B	176	-57
Apartment, low-rise, TF		132	-97
Apartment, medium rise, concrete		414	-61
Apartment, medium rise, CLT		158	-309
Apartment, medium rise, concrete	70.1, 2B	414	-62
Apartment, medium rise, CLT		158	-309

The CSO defines the dwelling types in Ireland as single, scheme and apartment. Table 2 shows the EC and CS using the values per living unit in Table 1 and adapted to the CSO housing archetypes. For that, it was assumed that 50% of single houses were bungalows and 50% 4-bedroom detached houses. For the scheme houses, the distribution from the CSO [29] was used: 12% detached, 17% mid-terrace, and 65% semi-detached houses, and adjusted relative to the 94% of the breakdown (the remaining 6% belongs to "others"). For the apartments, it was assumed that these were 2-bedrooms equally split between 3 and 6-storey unless otherwise stated.

Table 2. Average EC & CS per housing unit.

		Single	Scheme	Apartment
Traditional	EC, t CO_2e	18.09	16.03	20.68
	CS, t CO_2e	-6.3	-6.00	-4.185
Timber	EC, t CO_2e	15.64	13.21	10.17
	CS, t CO_2e	-9.59	-9.34	-14.26

The analysis draws different scenarios regarding the number of new homes, and the share built with timber. The new dwelling completions in the year 2019, which showed the largest construction activity of the last five years, was chosen as the most recent pre-Covid reference (Table 3). It must be noted that currently timber dwellings (24% of the total) only cover light frame construction. The scenarios assume that future emissions will remain the same as the baseline scenario.

Table 3. Dwelling types in 2019 in Ireland. Source: [29] and Timber frame industry data.

	Single	Scheme	Apartment
Traditional	4,817	7,863	3,407
Timber	250	4,650	100
Total	5,067	12,513	3,507

This study assumes a slight increment of units built in 2022 (22,000) compared to 2019 (21,087) and then 1,500 additional units per year to reach 33,000 units p.a. by 2030. This gradual increment is justified as to due to the limitations of the sector (workforce, machinery, etc.) it is unlikely that there will be a large increment in new homes in the short term. The level of new homes is maintained until 2040, falling to 30,000 per year from 2041-2050. The reason for drop to 30,000 per year, instead of the 26,000 projected by The Central Bank of Ireland, is to compensate for the lower growth in the initial years. Based on these assumptions a total of 881,000 units will be built in the period 2022-2050, with an average of 30,400 new homes p.a. For the period 2022-2040, the total is 581,000 units (the National Development Plan states that 600,000 new homes will be required in the period 2021-2040).

Regarding the percentage of dwelling types and share built with timber over the period studied, the analysis draws different scenarios. This is mostly based in the need to increase the proportion of apartments.

All scenarios maintain that in 2022 the mix of dwellings will be the same as in 2019, i.e. 24%, 59% and 17% for single houses, scheme houses and apartments. The models, except for scenario i), assume that the percentage of apartments increases by 1% p.a., from 17% in 2022 to 30% in 2035 and maintaining that percentage thereafter. The increment of apartments reduces the percentage of scheme houses. The percentage of timber units in 2022 remains the same as in 2019 at 24% of the total (1%, 22% and 0.5% single houses, scheme houses and apartments respectively) in i and ii, and in the rest of scenarios amounts to 26% where the 2% increment is proportionally spread among the dwelling. Details for each scenario (summary in Table 4) are:

i) The dwellings distribution (24%, 59% and 17% single houses, scheme houses and apartments respectively) and percentage of timber units within a dwelling (5%, 37% and 3% respectively as shown in Table 3) remains like in 2019 for the whole period studied. That is, nothing changes except the number of new units is larger.

ii) The percentage of timber units within a dwelling type remains the same as in 2019. The total percentage of apartments increases by 1% p.a., from 17% in 2022 to 30% in 2035.

iii) After 2022, there is an increment of 5% p.a. in the percentage of timber buildings within each dwelling type until reaching a maximum of 70%. This is only reached by the scheme houses by 2033.

iv) After 2022, there is an increment of 5% p.a. in the percentage of timber scheme dwelling and 10% p.a. in single and apartment dwelling until reaching a maximum of 70%.

v) After 2022, there is an increment of 5% p.a. in the percentage of timber scheme dwelling and 15% p.a. in single and apartment dwelling until reaching a maximum of 70%. From 2025 all the apartments are 6-storey.

vi) Like v but the apartments were considered the average between 3- and 6-storey for the whole period.

vii) The scenario aims to build 50% of all dwellings in timber in a maximum of 10 years. There is an increment of 5% p.a. in the percentage of timber scheme dwelling, 25% p.a. in single dwellings and 33% p.a. in apartments until reaching 50% within each dwelling type.

viii) Similar to scenario v but from 2025 there is a strong increment of 6-storey CLT apartments that by 2032 make 70% of the dwelling type.

ix) Similar to scenario v but the timber apartments are limited to 5% of the apartments from 2025. Between 2022-2025 apartments are 2-bedrooms equally split between 3 and 6-storey. From 2025 all the apartments are 6-storey, either CLT (5%) or concrete (95%).

Table 4. Summary of scenarios.

	2022 Timber / Total	% Increments in timber and CLT p.a.			Max % Timber within dwelling
		Single	Scheme	Apartment	
i	24%	-	-	-	-
ii	24%	-	-	-	-
iii	26%	5	5	5	70
iv	26%	10	5	10	70
v	26%	15	5	15	70
vi	26%	15	5	15	70
vii	26%	25	5	33	50
viii	26%	15	5	15	70
ix	26%	15	5	15	70 & 5

3 RESULTS

Overall, scenarios with larger use of timber produced greater annual GHG abatement, although the type of dwellings had a large influence. Table 1 and Table 2 showed that larger EC savings are associated with construction of apartments (more than 60% comparing 6-storey CLT and concrete buildings). For the most common semi-detached house the reduction in EC is almost 20%.

Figure 3 shows the variation in the EC emissions associated with the construction activity. Scenario i could be considered business as usual (BAU). It has less apartments (146,520) than the other scenarios (239,189). The drop in 2041 is associated with a reduction in the construction from 33,000 to 30,000 new housing units.

Figure 4 shows the EC emissions per dwelling unit. For scenario i, where the % of dwellings and timber buildings are like in 2019, the average housing unit produces 16.6 kt CO_2e. An almost identical EC emissions are produced by scenario iii, that built 36% of new dwellings in timber, and 7.1% of the apartments in timber or CLT (compared to 2.9% in scenario i). Scenarios iv and vi show a slow reduction in the EC in the first years, accelerated from 2035 when the apartments reach 30% of the dwellings. As the result of a larger increment in the number of timber units in scenario vi, the timber buildings from 2035 are 62% (against 49% in iv), and from 2045 amount to 70% of the total.

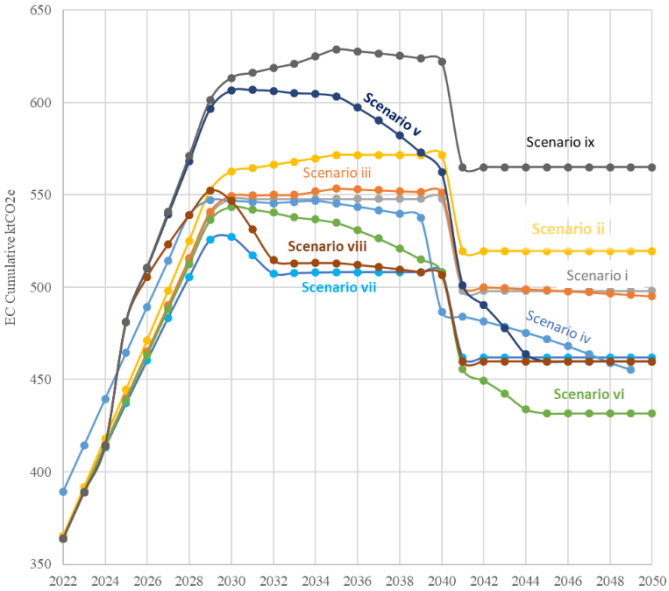

Figure 3. EC emissions for different housing scenarios between 2022 and 2050.

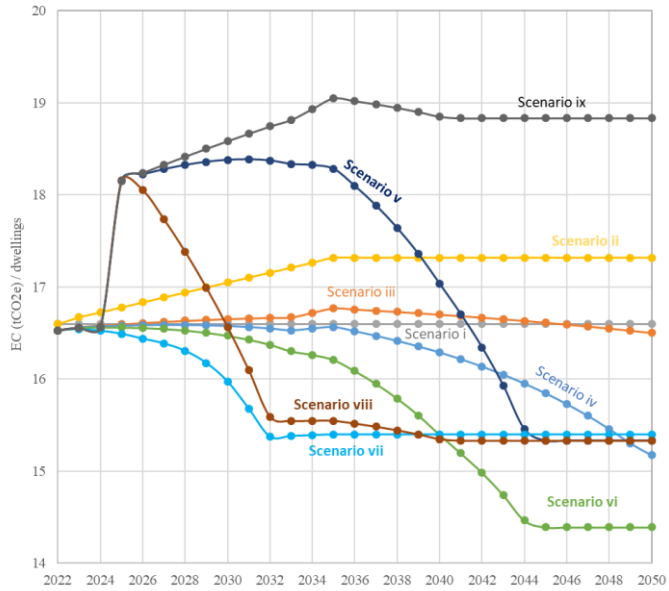

Figure 4. EC emissions per dwelling for different housing scenarios between 2022 and 2050.

Scenarios v and viii only include 6-storey apartments from 2025, which translates in the sharp EC shown in Figure 4. Afterwards, both scenarios increase the % of apartments until reaching 30% in 2035, which is maintained thereafter. In scenario v the % of timber increases until reaching 70% in 2045 whereas in scenario viii the 70% is reached in 2032 and therefore the number of CLT apartments over the period is larger.

The difference between v and vi is the type of apartments, where the EC of 6-storey concrete building are much higher than 3-storey. The largest reduction of EC in the next 10 years is described by scenario vii, in which 50% of all dwellings are built in timber in 2032, with schemes houses reaching this percentage in 2026.

However, the EC does not describe the whole picture of the GHG abatement. Table 5 shows the summary of accumulated EC and CS for the nine scenarios analysed. Scenario i has less apartments than the other scenarios and a low % of timber used that results in higher EC than other scenarios and very low potential for CS. The most beneficial scenario for GHG abatement is viii, which combines low EC and the largest CS giving the lowest cumulative net carbon. Scenario ix, that increases significantly the number of 6-storey concrete buildings, is the worst due largely to the high EC.

Scenarios vi and vii are the second most beneficial for GHG abatement. They describe the lowest EC and a high CS. Scenario vi, increases the use of timber until reaching 70% within each dwelling type. It builds more timber units (50%) than scenario vii (45%), but less apartments with timber. Scenario vii draws a sharp increment in the timber buildings in the first ten years that results in a strong reduction of EC and in a higher % of timber apartments over the full period.

The GHG abatement of scenarios iv and v is slightly better than the average due to a relatively low EC and high CS.

Scenario ii is the second least beneficial situation. It maintains the percentage of timber units in each dwelling type, but it reduces the total number of scheme houses (that bear most of the timber construction) as the result of building a larger percentage of apartments. This reduces to 20% the total percentage of timber units built in 2022-2050. The difference with scenario viii in the cumulative net carbon are 0.142 Mt CO_2e p.a. more in scenario ii.

The greatest CS occurs in the scenarios viii and v, with average of 0.105 Mt CO_2e p.a. and 0.07 Mt CO_2e p.a respectively. This is due to the large number of CLT apartments.

Table 5. Accumulated EC & CS for different housing scenarios between 2022 and 2050.

	Average % Timber	Timber apart (% total apart.)	EC	CS (-)	Net
			Mt CO_2e		
i	24	4,178 (2.9%)	14.6	5.8	8.8
ii	20	6,820 (2.9%)	15.1	5.6	9.6
iii	36	16,930 (7.1%)	14.7	6,1	8.6
iv	42	41,471 (17%)	14.3	6.4	7.8
v	50	82,883 (35%)	15.0	7.6	7.5
vi	50	82,883 (35%)	13.8	6.9	6.9
vii	45	99,971 (42%)	13.8	6.9	6.9
viii	57	141,117 (59%)	14.0	8.6	5.5
ix	42	11,790 (4.9%)	16.4	6.4	10

Figure 5 shows that when considering the cumulative net carbon effect (EC and CS together) scenarios viii, vii and vi are the most beneficial in the GHG abatement.

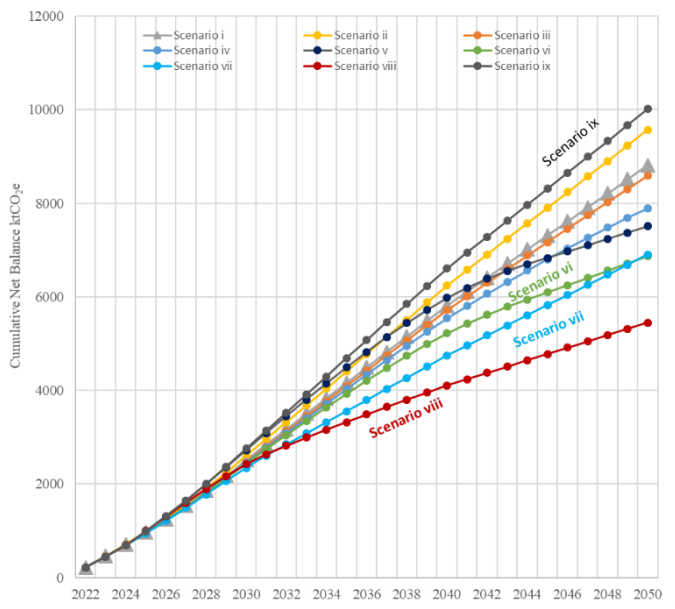

Figure 5. Cumulative net carbon for different housing scenarios between 2022 and 2050.

4 DISCUSSION

The best scenarios for the mitigation of climate changes while addressing the housing needs in Ireland are viii, vii and vi that combine a strong increment in the number of timber scheme houses with a larger presence of medium and high-rise buildings that can accommodate the housing demand while producing less emissions than the equivalent in masonry and concrete. In particular, scenario viii avoids 3.3 million tonnes CO_2e compared to scenario i that represents BAU.

According to the hypothesis formulated, Ireland would reach the highest rate of construction in 2030. At this time, total emissions of GHG should be reduced to at most 31,1 Mt CO_2e in agreement with Climate Bill 2021. For the period 2022-2030, the best scenario is described by scenario vii, where the net carbon emissions (EC minus CS) produced are 411 kt CO2e less than those produced by scenario ix, which increases significantly the number of 6-storey concrete buildings.

In the same period, scenario vii produces 61.4 kt CO_2e less EC than scenario i, BAU. Adding the CS in the period, the difference between scenarios vii and ix in the cumulative net is 164 kt CO_2e. For the year 2030 only, there are EC savings at 20.6 kt CO_2 compared to scenario i. This difference is roughly equivalent to the carbon sequestered by 3,700 ha of average Irish forest in one year [30].

The reductions of emission for the different scenarios may seem modest. However, it must be understood in the context of a sector which activity will likely increase in the next decades and that needs to reduce the GHG emissions with immediate effect. In addition, the case study only covered residential buildings. The differences in EC could be larger when using timber cladding instead of brick that reduces the EC significantly [31], even after several replacements, and can account for a reduction of 2.9% in EC and a 3.1% increase in CS using 25% timber cladding of the external wall area [27]. The current study considers a lower number of apartments than the housing needs according to Lyons [15] who regarding the lack of apartment home states: *it would be prudent for policymakers to cater for a slow transition over coming decades to a society with household sizes similar to Western European averages now*. The results show that the GHG abatement could be larger if more apartments are built. However, this will require a revision of the building regulations in Ireland to allow timber buildings of more than four storeys. The National Building Code in Canada for example allows for up to 12 stories, and the UK counts with many examples of timber frame buildings of six or seven storeys.

The presented analysis assumes that after the service life has been achieved, new dwellings will replace the old ones. Therefore, if the timber elements are not reclaimed and reused the CS released to the atmosphere is compensated by new construction. In this regard, it is important to highlight the relatively short rotation lengths used in Ireland for harvesting forest crops (35-45 years) in comparison to continental Europe. This is due to the growing conditions that allow to reach merchantable volumes earlier, and the poor quality of sites to which forestry is typically relegated (richer soils are used for agriculture) together with wind exposure of Ireland that advises against leaving trees standing for too long at the risk of being windthrows [32].

The savings of CO_2e using timber would be larger if assessing more stages of the life cycle. For a cradle-to-grave boundary (from production to end of life), Walsh and McAulliffe [33] estimated an annual savings of 460 kt CO_2e based on the construction of 25,000 new timber frame homes in Ireland in comparison to traditional masonry construction. The study covered stages A1 to C but found the largest difference in the stages A1-A3. The building materials used in the timber house produced a saving of 124.1 kg CO_2e/m^2, 41% less carbon than the masonry construction materials. This difference is larger than that used in the analysis of the current study. It is also important to notice that the end-of-life C1-C4 in the timber frame building produced 3.1 kg CO_2e/m^2 less, with the additional potential benefit of reclaiming timber for other projects [34]. The total EC (modules A1-A4, B4-B5, C1-C4) was 353 kg CO_2e/m^2 for the masonry house and 218 kg CO_2e/m^2 for the timber frame building. Including the effects at the end-of-life allows to account for the carbon sequestration [3], that amounted to 42 kg CO_2e/m^2 and 78 kg CO_2e/m^2 in the masonry and timber frame units respectively. Thus, the presented study uses conservative values of the GHG emissions associated with traditional and timber materials used as structural elements in construction compared to other studies, but it still shows significant evidence of the benefits that timber construction can bring to the mitigation of climate change. In support of this, the Timber Engineering Research Group at NUI Galway is leading the SAOLWood project, which aims to create a lifecycle inventory with data specific to harvested wood products used in construction in Ireland.

5 CONCLUSIONS

The decarbonisation of the construction sector is necessary in order to mitigate the effect of climate change and achieve the Irish Government commitment of GHG emissions reductions

while addressing the increasing demand for housing in the coming decades. This paper has shown that medium to strong increase in the construction of timber buildings, particularly apartments, delivers more GHG saving than scenarios with limited use of timber. Further research is needed to include and quantify the potential benefits of timber for reuse and recycling as part of the circular economy.

ACKNOWLEDGMENTS

This work was developed at National University of Ireland Galway within the WoodProps programme funded by the Forest Sector Development Division of the Department of Agriculture, Food and the Marine, Ireland.

REFERENCES

[1] United Nations Environment Programme, "2021 Global Status Report for Buildings and Construction: Towards a Zero-emission, Efficient and Resilient Buildings and Construction Sector ", Nairobi, 2021. [Online]. Available: https://globalabc.org/sites/default/files/2021-10/GABC_Buildings-GSR-2021_BOOK.pdf

[2] IStructE, "How to calculate embodied carbon," Second ed. London: The Institution of Structural Engineers, 2022.

[3] RICS, "Whole life carbon assessment for the built environment," 1st ed: Royal Institution of Chartered Surveyors (RICS) London, UK, 2017, p. 41.

[4] European Commission. "2030 climate & energy framework." https://ec.europa.eu/clima/policies/strategies/2030_en (accessed 27/04/2022.

[5] EPA, "Ireland's National Inventory Report 2021," in *Greenhouse Gas Emissions 1990-2019 Reported to the United Nations Framework Convention on Climate Change*, ed: Environmental Protection Agency 2021.

[6] CSO. "Environmental Indicators Ireland 2021 - Greenhouse Gases and Climate Change." Central Statistics Office. Available: https://www.cso.ie/en/releasesandpublications/ep/p-eii/environmentalindicatorsireland2021/greenhousegasesandclimatechange/ (accessed 27/04/2022.

[7] (2020). *Ireland's National Energy and Climate Plan 2021-2030*. [Online] Available: https://www.gov.ie/en/publication/0015c-irelands-national-energy-climate-plan-2021-2030

[8] Dáil Éireann (2021, 9 Jun 2021). *Climate Action and Low Carbon Development (Amendment) Bill 2021*.

[9] EPA, "Ireland's National Inventory Report 2020," in *Greenhouse Gas Emissions 1990-2018 Reported to the United Nations Framework Convention on Climate Change*, ed: Environmental Protection Agency 2020.

[10] CSO. "Population Projections Results." Central Statistics Office. https://www.cso.ie/en/releasesandpublications/ep/p-plfp/populationandlabourforceprojections2017-2051/populationprojectionsresults/ (accessed 12/01/2022.

[11] T. Conefrey and D. Staunton, "Population change and housing demand in Ireland," *Central Bank of Ireland Economic Letter*, vol. 14, pp. 1-16, 2019.

[12] IBEC, "Estimating Ireland's long-run housing demand," *Property Industry Ireland, IBEC*, 2019.

[13] DPER, "National Development Plan 2021—2030," *Department of Public Expenditure and Reform*, 2021.

[14] C. McCurry, "Housing For All plan could see embodied emissions almost double, says expert," *Independent.ie*, 26/04/2022. [Online]. Available: https://www.independent.ie/breaking-news/irish-news/housing-for-all-plan-could-see-embodied-emissions-almost-double-says-expert-41589059.html

[15] R. C. Lyons, "Ireland in 2040: Urbanization, demographics and housing. Symposium:'Where'will the Economy be in 2040? Delivering on the National Development Framework, 122-128," *Journal of the Statistical and Social Inquiry Society of Ireland*, vol. Vol. 47, Symposium: Where will the Economy be in 2040? Delivering on the National Development Framework, 2018.

[16] R. C. Lyons, "The role of apartments in meeting Irish housing requirements, 2018-2022," ed: Activate Capital, 2017.

[17] Eurostat. "Housing in Europe - House or flat – owning or renting." European Commission. Available: https://ec.europa.eu/eurostat/cache/digpub/housing/bloc-1a.html?lang=en (accessed 12/01/2022.

[18] C. De Wolf, F. Yang, D. Cox, A. Charlson, A. S. Hattan, and J. Ochsendorf, "Material quantities and embodied carbon dioxide in structures," in *Proceedings of the Institution of Civil Engineers-Engineering Sustainability*, 2015: Thomas Telford Ltd.

[19] A. M. Moncaster, F. Pomponi, K. E. Symons, and P. M. Guthrie, "Why method matters: Temporal, spatial and physical variations in LCA and their impact on choice of structural system," *Energy and Buildings*, vol. 173, pp. 389-398, 2018/08/15/ 2018, doi: https://doi.org/10.1016/j.enbuild.2018.05.039.

[20] A. H. Buchanan, S. B. J. E. S. Levine, and Policy, "Wood-based building materials and atmospheric carbon emissions," vol. 2, no. 6, pp. 427-437, 1999.

[21] IPCC, "Climate Change 2007: Mitigation. Contribution of Working Group III to the Fourth Assessment Report of the Inter-governmental Panel on Climate Change [B. Metz, O.R. Davidson, P.R. Bosch, R. Dave, L.A. Meyer (eds)]," in *Climate change 2007: Mitigation of climate change*: Cambridge University Press, Cambridge, United Kingdom and New York, NY, USA, 2007, ch. Chapter 9.

[22] P. Börjesson and L. J. E. p. Gustavsson, "Greenhouse gas balances in building construction: wood versus concrete from life-cycle and forest land-use perspectives," vol. 28, no. 9, pp. 575-588, 2000.

[23] E. J. Forster, J. R. Healey, C. Dymond, and D. Styles, "Commercial afforestation can deliver effective climate change mitigation under multiple decarbonisation pathways," *Nature Communications*, vol. 12, no. 1, p. 3831, 2021/06/22 2021, doi: 10.1038/s41467-021-24084-x.

[24] STA, "Annual survey of UK structural timber markets - Market report 2016," Structural Timber Association, October 2017 2016. [Online]. Available: http://www.forestryscotland.com/media/370371/annual%20survey%20of%20uk%20structural%20timber%20markets%202016.pdf

[25] NSAI, "IS 440:2009+A1:2014 Timber frame construction, dwellings and other buildings (including amendment 1,consolidated). National Standards Authority of Ireland, Dublin, p. 92," ed, 2014.

[26] "Forest Industries Ireland, Dublin." Available: https://www.ibec.ie/connect-and-learn/industries/energy-transport-and-resources/forest-industries-ireland (accessed 27/04/2022.

[27] M. Spear, C. Hill, A. Norton, C. Price, and G. Ormondroyd, "Wood in Construction in the UK: An Analysis of Carbon Abatement Potential. Extended Summary. Published as an annex to the Committee on Climate Change report" Biomass in a low-carbon economy"," 2019.

[28] CEN, "Sustainability of construction works. Environmental product declarations. Core rules for the product category of construction products. EN 15804: 2012+ A2: 2019. European Committee for Standardization, Brussels," p. 67, 2014.

[29] CSO. "New Dwelling Completions Q4 2020." Central Statistics Office. Available: https://www.cso.ie/en/releasesandpublications/er/ndc/newdwellingcompletionsq42020/ (accessed 12/01/2022.

[30] Forest Service, "Forest Statistics Ireland 2020," Department of Agriculture, Food & the Marine, Ireland, Wexford, Ed., ed, 2020.

[31] J. Monahan, J. C. J. E. Powell, and buildings, "An embodied carbon and energy analysis of modern methods of construction in housing: A case study using a lifecycle assessment framework," vol. 43, no. 1, pp. 179-188, 2011.

[32] Á. N. Dhubháin and N. Farrelly, "Understanding and managing windthrow," COFORD Connects, Silviculture/Management No. 23 ed: Department of Agriculture, Food and the Marine, Dublin, 2018.

[33] J. Walsh and B. McAulliffe, "Study of the Embodied Carbon in Traditional Masonry Construction vs Timber Frame Construction in Housing," ed: Jeremy Walsh Project Management, Tralee,, 2020.

[34] "InFutUReWood." InFutUReWood, 2020, Available: https://www.infuturewood.info (accessed 27/04/2022.

Investigating the Demand in Horticulture and Private/Recreational sectors for Recycling-Derived Fertilisers in North-West Europe

Aoife Egan[1], Niamh Power[1]
[1] Sustainable Infrastructure Research & Innovation Group and Department of Civil, Structural & Enviromental Engineering, Munster Technological University Cork, Bishopstown, Cork, Ireland.

email: aoife.egan@mtu.ie, niamh.power@mtu.ie

ABSTRACT: Horticulture including nursery stock, ornamental plants, fruit, and vegetables represents a thriving industry with the fruit and vegetable sector alone accounting for 18 % of the total value of agricultural production in the EU. In addition, 5.7% of land use in Europe is assigned to services and residential land, of which 35% is used for recreation, leisure, and sport. It is estimated that over 11 million tonnes of fertiliser were used in EU agriculture in 2018. The horticulture and recreational sectors are dependent on non-renewable sources of nutrients such as imported rock phosphate, of which its global reserves are being depleted. Considering the circular economy, it is important to increase nutrient recycling rates across North-West Europe in the agricultural sector and the horticulture and recreational sectors. The application of recycling-derived fertilisers such as compost, digestate or manure is an excellent mineral fertiliser alternative. This research aims to investigate regional nutrient demand within the North-West Europe target sectors by exploring agricultural statistics and regional databases to assess the area of crops grown per region, fertiliser recommendations, fertiliser sale rates and prices. Results obtained from the agriculture sector indicate that demand for nutrients from recycling is evident in North-West Europe, even in regions where animal manure is largely used as a nutrient source. It is envisaged that the nutrient demand will be equally evident in the horticulture and recreation sectors creating a niche area for the use of recycling derived fertiliser products, thus feeding into the circular economy and closing the nutrient cycle loop.

KEYWORDS: Circular economy; Recycling-derived fertilisers; Nutrient demand; Horticulture; Recreational sector.

1 INTRODUCTION

The use of recycling derived fertilisers (RDFs), which are sustainable recycled fertilisers that come from organic sources, in agriculture across Europe, has been slow to date. However, through greater awareness of the benefits of RDFs, emphasis on sustainable agriculture and the impact fertilisers have on emissions, coupled with current supply issues of mineral fertiliser due to sanctions on Russia, it is envisaged that the end-users such as farmers are more informed and encouraged to consider mineral fertiliser alternatives. However, there are markets other than the agricultural sector such as the horticulture and recreation sectors that have great potential to utilise RDFs. The benefits of which include that the RDFs can be applied to land that is not used for food production and therefore their application is not as constrained.

1.1 Global fertiliser reserves

Phosphorus (P), potassium (K) and nitrogen (N) are essential elements for plant nutrition and growth. Phosphorous cannot be substituted with any other mineral and it is of high economic importance. Phosphate rock minerals resources are the only significant global source of P. Globally there are approximately 71 billion metric tons of phosphate rock reserves, with the highest reserves located in Morocco with approximately 50 billion metric tons [1]. However, the mineral reserves of rock phosphate are being depleted globally and in 2014 the European Commission added rock phosphate to its critical raw materials list [2] as the supply security is at risk.

The majority of the world's reserves of K are recovered by underground mining methods. Canada has the world's largest potash reserves, which exceeded 3.7 billion metric tons in 2019 [3]. Nitrogen fertiliser is heavily dependent on natural gas for its production via the Haber-Bosch process, with consumes on average 1–2% of the world's annual primary energy supply and generates more than 300 Mt of fossil-derived carbon dioxide per year [4]. This energy-intensive process, therefore, incurs high fuel costs, which in turn drives up the costs of mineral fertiliser. Due to the Russia-Ukraine war, sanctions imposed on Russia, which is the major exporter of potash, ammonia and urea, by the West have disrupted exports, shipments and supply of these fertilisers globally [5].

1.2 Fertiliser sales

Global fertiliser costs are increasing annually due to a variety of factors including import and energy costs, distribution and supply chain, and as a result of a shortage of labour and the shutdown of several fertiliser plants due to the COVID 19 pandemic. The Russia-Ukraine war has also impinged on fertiliser sales due to sanctions imposed by the West, therefore affecting the fertiliser supply globally [5]. In 2020, the global fertiliser market summed to more than 158 billion euros. In addition, it is predicted that the fertiliser market will exceed 195 billion euros by 2027 [6].

However, on average, the annual fertiliser sales rate is decreasing across North-West Europe (NWE) with many farmers in Europe deciding to change or substitute chemical fertilisers with organic forms. It has been reported that sales of N have decreased by 12% between 2014 and 2019, with sales of P reducing by 21% between 2011 and 2019, and K sales decreasing by 5% between 2010 and 2019 [7]. Organic fertilisers have an important role in following sustainable organic farming by the farming community. Such sustainable fertilisers include RDFs.

1.3 Recycling derived fertilisers

Recycling derived fertilisers are a by-product of, not only the

farming industry but also domestic sources and commercial industries. These types of fertilisers are a rich source of NPK that are essential for crop growth. Also, some RDF products have the potential to increase the organic and humus content in the soil, increase the soil's microorganism communities and overall increase the soil fertility, making RDFs excellent sustainable alternatives to mineral fertilisers [8].

These recycled products come from several different sources, all of which are waste by-products, such as animal manure that has been used in agriculture as a soil improver for many years. Another source includes sewage sludge which comes from the treatment of wastewater. The application and use of sewage sludge in agriculture are regulated under S.I. NO. 267/2001 [9] which refers to waste management regulations in Ireland. Household waste and food industry waste are additional sources of RDFs, with over one million tonnes of food sent to landfills or digested and recycled, each year in Ireland [10].

There are many different RDF products derived from recycled sources, however, composting is one of the most commonly known and is typically used as an organic soil enhancer. It can be made from green waste, household waste, food industry waste [11] and sewage sludge [12]. Digestates are produced from various sources including animal manure, green waste, food industry by-products and household wastes [13] that have been digested in an anaerobic digester. Anaerobic digestion is considered to be a well-developed process across Europe [14] and is a growing solution for both waste recycling and green energy production [13] in the form of biogas. On the other hand, struvite is a less well known but excellent example of RDFs. Struvite is recovered P from wastewater treatment plants. It is recovered in a crystalised granular form and acts as an excellent slow-release fertiliser [15].

1.4 Horticulture and recreational sectors

There is a growing demand for sustainable mineral fertiliser alternatives in the agricultural sector, with previous research conducted by Egan et al. [8], to determine what properties farmers were looking for in RDFs, to encourage uptake of these recycled fertilisers. It was estimated that in Europe, the organic fertiliser market in 2016 had a value of 2,247 million euros and this market is expected to reach 2,988 million euros by 2023 [16]. However, there are further potential markets for RDFs other than in agriculture, including the horticulture and the recreational sectors.

The horticulture sector includes nurseries, gardening services, cemetery gardening, gardening supplies retailers, garden centres, florists and landscape gardening. In addition, the associated production of fruit, vegetables, salads, herbs and ornamentals contribute to this sector. The fruit and vegetable sector alone accounts for 18 % of the total value of agricultural production in the EU and is worth over 50 billion euros [17]. In addition, the EU is the biggest producer of flowers, bulbs and potted plants with 44 % of total global production. Also, the ornamental plant sector has an estimated turnover of 20 billion euros in production [18].

On the other hand, although not as big as the horticulture sector, housing, services and recreation made up a third of the overall increase in urban and other artificial land areas between 2000 and 2006, at a European level [18]. In addition, 5.7% of the total area of the EU in 2018 was used for services and residential purposes, of that 35% was associated with recreation, leisure and sport [19].

1.5 The circular economy

The circular economy aims to extend the normal life-cycle of products by reusing, sharing and recycling products for as long as possible. RDFs by their nature are recycled, reused and often shared products that contribute to the circular economy [8]. By using these recycled fertilisers in sectors other than agriculture and by expanding into new markets such as the horticulture and recreational sectors, there are more opportunities for producers and end-users to avail of and use these organic fertilisers. Thus further contributing to the circular economy.

2 METHODOLOGY

The data for this analysis was obtained from statistical databases available online. The global fertiliser price data were obtained from the World Bank Commodities Price Data (The Pink Sheet) [20]. The data is available from the year 1960 to 2021, however, for the scope of this research, the data for urea, DAP and potassium chloride from 2008 to 2021 was utilised. The data was displayed from 2008 to 2021 to assess how the global fertiliser price in euro per tonne, had fluctuated annually. The mean (average) value over 13 years was also included in the figure as a visual reference. The data referring to the price of fertiliser in Ireland was obtained from the Central Statistics Office [21]. The data is presented as the price of urea and potassium chloride in euros per tonne from the years 2008 to 2021 to assess how the fertiliser price in Ireland had fluctuated annually. The price of superphosphate data was only available from the years 2012 to 2017 and 2019 to 2021. Fertiliser sales data for NPK were obtained from the statistical office of the European Union, Eurostat. The data is available from the year 2008 to 2019 and are displayed per ‘000 tonnes, to assess how the fertiliser sales in NWE had fluctuated annually.

The land use and tenure data were obtained from Eurostat for the seven target countries across NWE, which are Belgium, France, Germany, Ireland, Luxembourg, the Netherlands and the United Kingdom [22]. Tenure data was used to assess how much land was used for horticulture in NWE in 2013 and 2016, whereas land use data were used to assess the land used for the arts, entertainment and recreational sector in 2015 and 2018 [19]. Although the recreation sector is one of the markets of interest, this data is not available as an entity on its own and therefore the data includes the arts and entertainment sectors. Fertiliser use data for NWE were obtained from Eurostat [23]. The mean NPK input in the utilised agricultural area (UAA), that is the total area taken up by agriculture including arable land, permanent grassland, permanent crops etc., was assessed between 2010 to 2019 for the seven NWE countries of interest in this study. Where applicable the standard error of the mean (SEM) was assigned to the data to measure how far the sample mean of the data is likely to be from the true population mean.

3 RESULTS AND DISCUSSION

3.1 Fertiliser prices

Globally the price of fertilisers is rapidly increasing since 2021, with an expected surge in price in 2022 due to the Russia-Ukraine war, an increase that hasn’t been observed since 2008.

The price of fertiliser in 2008 soared due to a global food and energy crisis, where supply could not keep up with the demand, particularly in Asia. Furthermore, there was a huge demand for fertilisers in the United States, Brazil, and Europe for biofuel production [24].

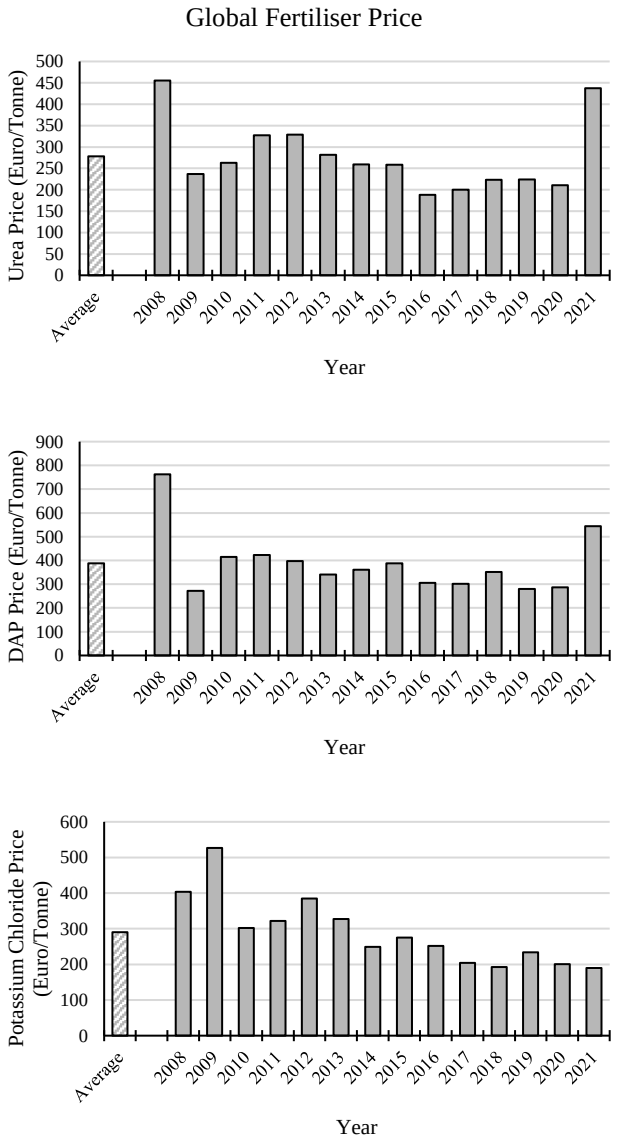

Figure 1. Global fertiliser price (euro/Tonne) of urea, DAP and potassium chloride between the years 2008-2021 (World Bank).

In addition, the production of livestock increased, thus increasing the demand for grain and subsequently for fertilisers. At that time, energy prices peaked, resulting in an increase in the price of natural gas which is essential for N fertiliser production. The demand for sulfur increased and therefore the price of phosphate increased which is necessary for the production of the world's most commonly used fertiliser Di-Ammonium Phosphate (DAP) and other types of phosphate fertilisers. Also, the supply of good quality phosphate rock diminished [24].

The peak in fertiliser price is evident in Figure 1, which displays the global fertiliser prices (euro/Tonne (t)) for urea (containing 46% N), di-ammonium phosphate (containing 49% P) and potassium chloride (containing 50% K) over the past 13 years. During this time, the price of fertiliser increased with N costing 456 euro/t, P was priced at 762 euro/t and K costing 403 euro/t in 2008, increasing to 527 euro/t in 2009.

In Ireland, the price of fertiliser also peaked in 2008 (Figure 2), with the price of urea costing 443 euro/t, and granular superphosphate containing 16% P was priced at 507 euro/t in 2008, increasing to 644 euro/t by 2009. There was no data available for the price of potassium chloride in Ireland in 2008. The subsequent years following the initial fertiliser price surge in 2008 resulted in a price drop (see Figure 1 and Figure 2), where the global price of urea had dropped to 237 euro/t by 2009 and in Ireland had decreased to 330 euro/t by 2010. In addition, the global price of potassium chloride decreased to 302 euro/t and in Ireland, it was down to 448 euro/t by 2010 respectively. This price reduction was due to the lack of demand as farmers were not willing to pay two or three times the price of fertiliser in early 2007. However, global fertiliser prices in 2022 are now higher than those recorded in 2008 according to the CRU marketing and analysis company [25].

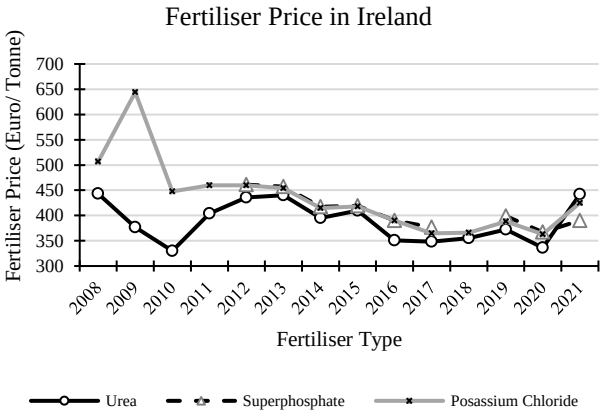

Figure 2. Fertiliser price (euro/Tonne) in Ireland of urea, superphosphate and potassium chloride from the years 2008-2021 (CSO).

This increased price is due to reduced supplies caused by the Russia-Ukraine war, a China export ban, Covid 19 and disruptions to the supply chain. The price of the raw materials component used in fertilisers, including ammonia, nitrogen, potash, urea, phosphates, sulphates, and nitrates, has risen 30% since the beginning of 2022, according to CRU [25]. The increase in fertiliser price is evident in Figure 1, where the price of urea globally increased by 107% and DAP increased by 90% between 2020 and 2021, however, the price of potassium chloride did not increase in this period. On the other hand in Ireland, the price of potassium chloride increased by 17% between the years 2020 and 2021 (Figure 2) and urea increased by 32% in Ireland at that time. It is evident at a regional level there are differences between the increased price rates of fertilisers. However, this data does not reflect the price increases of the current fertiliser market due to the sanctions imposed on Russia, as the official statistics are not keeping up with the reality of the situation or are not yet publically available.

3.2 Fertiliser sales rate

After the unprecedented peak in fertiliser prices in 2008, which

continued into 2010 for N and K and 2011 for P, the sale of fertilisers across NWE decreased (see Figure 3). The mean sale of N decreased by 6% between 2010 and 2012. However, N sales increased between 2012 and 2014 by 7%. Since 2014, the sales of N have plateaued between 2015 and 2017, with a marked decrease in 2019, 12% lower than the N sales in 2014.

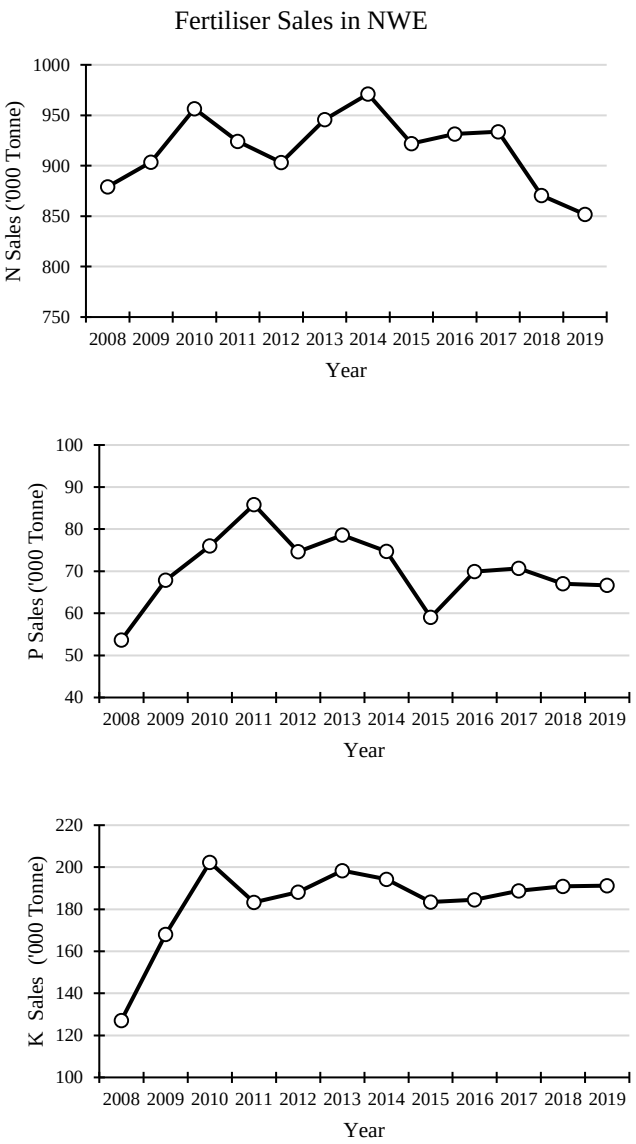

Figure 3. Fertiliser sales in North-West Europe, the mean NPK sales from 2008 to 2019 (Eurostat).

With regards to P, the mean sales decreased between 2011 and 2012 by 13%, with a slight increase in sales evident between 2012 and 2013 by 5%. Since then P sales have gradually plateaued and decreased by 15%. Potassium sales decreased between 2010 and 2011 by 9%, with an increase in sales by 8% evident between 2011 and 2013. However, between 2013 and 2019, K sales had decreased by 4%.

Overall the sales of NPK have decreased from 2008, until recently. However, there is a common trend of an increase in sales in NPK between the years 2012 and 2014. According to PhosAgro [26], one of the world's leading phosphate-based fertilizer producers they were able to increase their sales of fertilisers in containers, increasing their global customer market. In addition, in Ireland from 2013 to 2014, fertiliser demand increased due to a national fodder shortage [27].

With an increase in the global population, the growing demand for fertilisers is expected to increase [28]. In particular, more recently the Russia-Ukraine war and Covid 19 affected supply chains which will ultimately drive the market demand. In addition, however, currently and in the future, regulatory and environmental constraints coupled with high production costs are likely to act as drawbacks in the industry.

3.3 Land Use

Agricultural land accounted for 39 % of the total area in the EU in 2018 [7]. In terms of promoting RDF use in agriculture, there has been in-depth research into what farmers are looking for in these recycled products regarding the RDF properties [8]. However, to increase their use and the market demand for these sustainable fertilisers, it was important to explore other sectors, including horticulture and recreation. Horticulture tenure refers to the land that is owned by an individual that is used for horticulture purposes. Figure 4 describes the mean tenure of indoor, outdoor, citrus/fruit and other types of horticulture over two years. It is clear in Figure 4, that horticulture tenure in Germany increased by 12% and in Belgium increased by 10%. On the other hand, however, horticulture tenure decreased in Luxembourg by 37% and in the United Kingdom by 14%. Horticulture tenure in Ireland increased by 3% between the years 2013 and 2016.

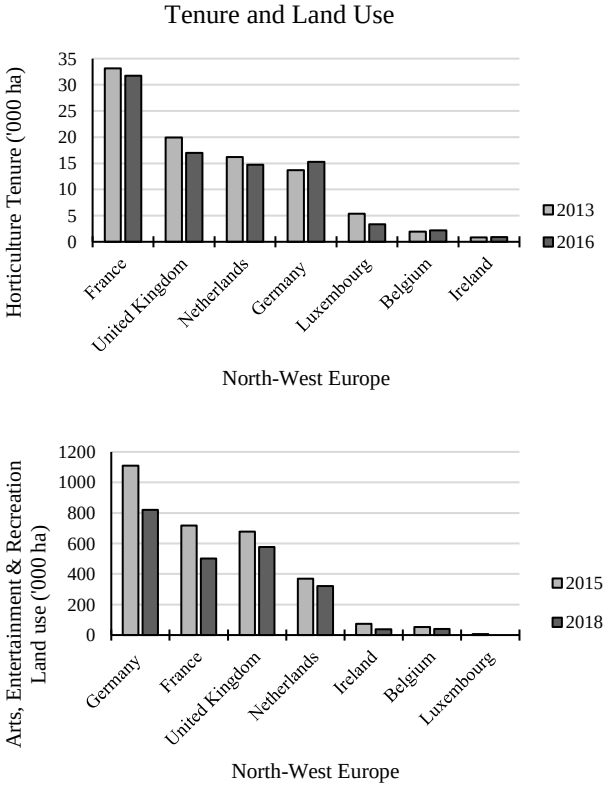

Figure 4. Tenure for horticulture and land use for the arts, entertainment and recreation sectors in NWE.

According to the European Parliament report [17], the fruit and vegetable sector represents 18% of the total value of

agricultural production in the EU, but only uses 3% of the EU's cultivated land. A report conducted by the European Parliamentary Research Service (EPRS) [27], assessed the share of EU farms that specialised in horticultural products and their agricultural area by farm size in hectares in 2016. They found that 77% of the farmers in the EU cultivated an area of fewer than five hectares and grew crops that could be classified as horticulture, which represented just 19% of the total area cropped with horticulture products. In addition, 150,000 ha of land in Ireland were assigned for horticulture use in 2016 (Figure 4). Horticulture in Ireland represented just 1.2% of overall agricultural output in 2002 [30].

Overall, 5.7% of land use in Europe is assigned to services and residential land, of which 35% is used for recreation, leisure, and sport. Land use in this instance refers to the amount of land managed and modified for the arts, entertainment and recreation sector. Figure 4 indicates that it has slowly decreased in NWE between the years 2015 and 2018. The amount of land used for this sector in Ireland decreased by as much as 50% and by 30% in France during the same period. Although, there is very little published information on land use in the recreational sector in NWE.

3.4 Fertiliser use

According to Fertilisers Europe, of the 179 million hectares of agricultural land available in the EU, 75 % are fertilised with mineral fertilisers. The European Commission [31] states that the EU market value of fertilisers has been increasing annually by 3% since 2005. The quantity of fertilisers used in the EU represents 10% of the total use at a global level. In terms of volume, N is the most used nutrient in the EU, representing more than two-thirds of the total use of NPK. Fertiliser use between 2010 and 2019 in NWE varied per country.

It is clear in Figure 5 that the Netherlands and Belgium are the dominant users of N and P, with a mean N input of 375 kg/ha and 312 kg/ha applied respectively. That is a 55% increase in N use in the Netherlands and a 29% increase in use in Belgium compared to the mean NWE value over that period. The minerals P and K are applied in much lower quantities in the EU and are representative of less than 20% each of the overall use in volume. The Netherlands and Belgium were the highest users of P (Figure 5) with a mean input of 35 kg/ha and 32 kg/ha applied respectively. That is, a 41% and a 30% increase compared to the mean NWE input of P respectively. In addition, Luxembourg was the third-highest county to apply N with a mean input of 250 kg/ha, whereas the United Kingdom are the third-highest applicant of P with 24 kg/ha.

3.5 RDFs and market demand in the horticulture sector

A market has been identified in the horticulture and recreation sectors for RDF use, however, according to Bergstrand [32], there are challenges involved with supplying horticulture crops with their full nutrient requirements by using only organic fertiliser due to high biomass production and EU regulations. Additional challenges include the limited volume of growing media in pots thus reducing the application of fertilisers. However other studies carried out by Succop and Newman [33] who focused on herbs fed with liquid organic fertilisers found no difference in fresh mass production. Although, longer growing greenhouse crops, such as tomatoes and peppers are reported to be more problematic as it is difficult to supply a sufficient amount of nutrients before starting the crop, therefore increasing labour costs [32]. There is a sufficient gap in the horticulture market for RDFs, to what extent RDFs would be required to fulfil this demand, needs to be further researched.

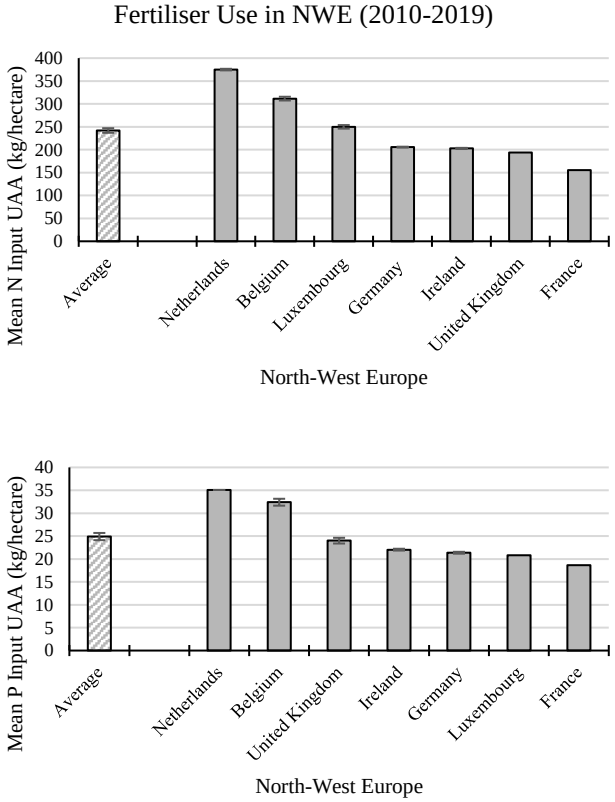

Figure 5. Fertiliser use UAA in North-West Europe, the mean N & P inputs from 2010 to 2019 (Eurostat).

4 CONCLUSION

With depleting global P reserves, the unsustainable production of N and security of supply issues, it is clear that the fertiliser industry and its current production must change. In addition, with increasing fertiliser prices, most recently with Covid 19 and the Russian-Ukraine war, the demand for more cost-efficient locally sourced fertilisers will increase. In the agricultural industry, fertiliser sales have been decreasing, with a growing interest in using more sustainably sourced fertilisers. Currently, there is a gap in the market for the use of RDFs, not only in the agricultural sector. The horticulture and recreational sectors are markets with great potential for expanding the use of RDFs and encouraging them to be used and accepted outside of the agricultural market. The acceptance and use of RDFs in these sectors would reduce the use of mineral fertilisers, and therefore, feed into closing the nutrient cycle loop and actively contributing to the circular economy.

ACKNOWLEDGMENTS

The authors would like to acknowledge the EU Interreg North-West Europe (NWE) Programme for funding the Nutrient Recycling – from pilot production to farms and fields ReNu2Farm Capitalisation NWE601.

REFERENCES

[1] Deloitte Sustainability, (2017) 'Study on the review of the list of Critical Raw Materials 2017', *British Geological Survey, Bureau de Recherches Géologiques et Minières and Netherlands Organisation for Applied Scientific Research*, European Commission, 1-9.

[2] European Commission, (2014). 'Communication from the Commission to the European Parliament the Council, the European Economic and Social Committee and the Committee of the Regions', *Review of the List of Critical Raw Materials for the EU*, European Commission, Brussels.

[3] Garside, M. (2021), 'Distribution of global potash reserves by select country 2019', *Chemicals & Resources, Mining, Metals & Minerals*, Statista. Available at: https://www.statista.com/statistics/604174/distribution-of-potash-reserves-worldwide-by-select-country/

[4] Tanabe, Y. and Nishibayashi, Y. (2013), 'Developing more sustainable processes for ammonia synthesis', *Coord. Chem.* Rev. 257 (17–18). https://doi.org/10.1016/j.ccr.2013.02.010.

[5] Polansek, T. and Mano, A. (2022), 'As sanctions bite Russia, fertilizer shortage imperils world food supply', Business, Reuters. Available at: https://www.reuters.com/business/sanctions-bite-russia-fertilizer-shortage-imperils-world-food-supply-2022-03-23/

[6] Fernández, L. (2021), 'Fertilizer market size worldwide 2020-2027', *Chemicals & Resources*, Chemical Industry. Statista. Eurostat. https://data.europa.eu/data/datasets/oba8ifzvjm0lhjkzm8moyq?locale=en

[7] Eurostat, (2021) 'Land use overview by NUTS 2 regions'. Land cover and land use, landscape (LUCAS). Available at:

[8] https://ec.europa.eu/eurostat/databrowser/view/lan_use_ovw/default/table?lang=en

[9] Egan, A., Saju, A., Sigurnjak, I, Meers, E, Power, N. (2022). 'What are the desired properties of recycling-derived fertilisers from an end-user perspective?', *Cleaner and Responsible Consumption*, Volume 5, 2022, https://doi.org/10.1016/j.clrc.2022.100057

[10] S.I. NO. 267/2001, (2001), 'Waste management (use of sewage sludge in agriculture) (amendment) regulations.', *Irish Statute Book*. http://www.irishstatutebook.ie/eli/2001/si/267/made/en/print

[11] Department of Communications, Climate Action and Environment.

[12] National waste prevention programme (NWPP). Food Waste. Available at:https://www.dccae.gov.ie/en-ie/environment/topics/sustainable-development/waste-prevention-programme/Pages/Stop-Food-Waste0531-7331.aspx

[13] Yadav, S.K., Kauldhar, B.S., Sandhu, Thakur, K., Sharma, S. and Sharma T. R. (2020). 'Retrospect and prospects of secondary agriculture and bioprocessing',*Journal of Plant Biochemistry and Biotechnology*, 29, 1–14.

[14] Gabira, M.M., da Silva, R.B.G., de Moura D'Andrea Mateus, C., Lyra Villas Boas, R. and da Silva, M. (2019), 'Effects of Water Management and Composted Sewage Sludge Substrates on the Growth and Quality of Clonal Eucalyptus Seedlings', *Floresta*, 50, 2, 1307-1314.

[15] Guilayn, F., Rouez, M., Crest, M., Patureau, D. and Jimenez, J. (2020), 'Valorization of digestates from urban or centralized biogas plants: a critical review', *Reviews in Environmental Science and Bio/technology*, 1-44.

[16] Corona, F., Hidalgo, D., Martín-Marroquín, J.M., Gregorio A. (2020), 'Study of the influence of the reaction parameters on nutrients recovering from digestate by struvite crystallisation', *Environmental Science and Pollution Research*,1-13.

[17] O'Donnell C, Barnett D, Harrington J and Power N. (2022). 'The extended effect of top-dressed recovered struvite fertiliser on residual Irish grassland soil Phosphorus levels compared to commercial Phosphorus fertiliser'. *Agronomy*, 12(1):8. https://doi.org/10.3390/agronomy12010008

[18] Roy, A. (2022), 'Europe Organic Fertilizer Market by Source (Plant, Animal, and Mineral), by Crop Type (Cereal & Grain, Oilseed & Pulse, Fruit & Vegetable, and Others), by Form (Dry and Liquid) and by Country (Germany, France, Italy, Spain, UK, and Rest of Europe) - Opportunity Analysis and Industry Forecast, 2017-2023', Allied Market Research.

[19] European Parliament. (2014), 'On the future of Europe's horticulture sector, strategies for growth'. Report 27.1.2014. Available at: https://www.europarl.europa.eu/doceo/document/A-7-2014-0048_EN.html

[20] EU-LUPA, (2012) 'European Land Use Pattern'. ESPON Applied Research 2013/1/8 Report. Available at:

[21] https://www.espon.eu/sites/default/files/attachments/DFR_Scientific_Report_EU-LUPA.pdf

[22] Eurostat. (2021), 'Land Use Statistics', Eurostat Statistics Explained. Available at https://ec.europa.eu/eurostat/statistics-explained/index.php?title=Land_use_statistics&oldid=529898

[23] Pink Sheet Data (May 2022), Commodity Markets, The World Bank. Available at: https://www.worldbank.org/en/research/commodity-markets

[24] CSO (2022), 'Fertiliser Price (Euro per Tonne), Agricultural Input and Output', Absolute Prices.AJA05. https://data.cso.ie/table/AJA05

[25] Eurostat, (2021), 'Tenure of agricultural holdings'. Management and practices'. Available at: (https://ec.europa.eu/eurostat/databrowser/view/ef_mp_tenure/default/table?lang=en

[26] Eurostat, (2021) 'Land use overview by NUTS 2 regions', Land cover and land use, landscape (LUCAS). Available at: https://ec.europa.eu/eurostat/databrowser/view/lan_use_ovw/default/table?lang=en

[27] Chand, R. (2008). 'The Global Food Crisis: Causes, Severity and Outlook', *Economic and Political Weekly*, 43(26/27), 115–122. http://www.jstor.org/stable/40278908

[28] Agriland (2022) 'International prices reach highest ever levels.' Fertilisers'. Available at: https://www.agriland.co.uk/farming-news/fertiliser-international-prices-reach-highest-ever-levels/

[29] PhosAgro (2012) 'Delivering stable growth and sustainable returns'. Annual Report. Available at: https://www.annualreports.com/HostedData/AnnualReportArchive/p/LSE_PHOR_2012.pdf

[30] Buckley, C., Dillon, E., Moran, B. and Lennon, J. (2018), 'Trends in fertiliser use' Teagasc Research 13 (3).

[31] Dawson, J and Hilton, J. (2011), 'Fertiliser availability in a resource-limited world: Production and recycling of nitrogen and phosphorus'. *Food Policy*, 36 (1), S14-S22. https://doi.org/10.1016/j.foodpol.2010.11.012.

[32] Rossi, R. (2019), 'The EU fruit and vegetable sector. Main features, challenges and prospects.' European Parliamentary Research Service (EPRS).Members' Research Service PE 635.563. Available at: https://www.europarl.europa.eu/RegData/etudes/BRIE/2019/635563/EPRS_BRI(2019)635563_EN.pdf

[33] Inter Trade Ireland, 'A Review of the All-Island Horticulture Industry'. The Trade and Business Development Body. Available at: https://intertradeireland.com/assets/publications/A-Review-of-the-All-Island-Horticulture-Industry.pdf

[34] European Comission, (2019), 'Fertilisers in the EU. Prices, trade and use', EU Agricultural Markets Briefs No 15. Available at: https://ec.europa.eu/info/sites/default/files/food-farming-fisheries/farming/documents/market-brief-fertilisers_june2019_en.pdf

[35] Bergstrand, K. J. (2022), 'Organic fertilizers in greenhouse production systems – a review', Scientia Horticulturae, 295, https://doi.org/10.1016/j.scienta.2021.110855.

[36] Succop, E. & Newman, S. (2004), 'Organic Fertilization of Fresh Market Sweet Basil in a Greenhouse' HortTechnology, 14 (2) 235-239

Energy

Tensile Mechanical Testing of Powder Epoxy Glass Fibre Composites with Embedded Optical Fibre Sensors

Brendan Kelley[1], Jamie Goggins[2,3], William Finnegan[2,3]
[1]Energy Systems Engineering, School of Engineering, National University of Ireland Galway, Galway, Ireland
[2] Civil Engineering, School of Engineering, National University of Ireland Galway, Galway, Ireland
[3]MaREI Research Centre for Energy, Climate and Marine, Ryan Institute, National University of Ireland Galway, Galway, Ireland
email: b.kelley1@nuigalway.ie, jamie.goggins@nuigalway.ie, william.finnegan@nuigalway.ie

ABSTRACT: Tidal energy is increasingly garnering attention as a viable renewable energy source. Faced with a hostile marine environment, components in tidal energy machines must withstand severe stresses from hydrodynamic loading and corrosive elements. Fibre reinforced composites have emerged as a promising material solution to these challenges, and the novel designs of tidal turbine blades now require certification through structural testing. Furthermore, the capacity to understand the material behaviour of the turbine blades throughout their lifetime provides an opportunity to mitigate repairs, maintenance costs, and operational downtime. Embedded sensors, a type of structural health monitoring system widely used in aerospace and structural applications, inform on these issues, but have not yet seen significant deployment in tidal energy. This study embeds optical fibre sensors into powder epoxy glass fibre composites and subjects the testing coupons to tensile testing. The effects on composite material tensile strength, modulus of elasticity, and shear modulus are examined by varying embedded optical fibre sensor diameter and orientation relative to the reinforcing fibres. The results of this study indicate no significant degradation of component mechanical strength caused by the embedded optical fibres. The impact of this study is a de-risking of embedded structural health monitoring systems of tidal energy components which can mitigate unpredicted failures and reduce the levelised cost of tidal energy.

KEY WORDS: Composite materials; Glass fibre; Powder epoxy; Embedded sensors; Fibre optics; Mechanical testing; Structures; Tidal energy.

1 INTRODUCTION

Although hydropower, wind and solar energy have dominated renewable energy supply, ocean energy technologies are emerging as a promising addition to the renewable energy toolbox. With a call for approximately €1 billion in investment funding for wave and tidal energy, the European Commission aims to deploy 100MW of ocean energy by 2025 and 1 GW by 2030; by the European Commission's estimates, ocean energy has the potential to supply up to 10% of Europe's energy needs [1]. As of 2020, tidal stream energy boasted 36.3 MW of cumulative installations worldwide, with 27.9 MW in Europe alone (shown in Figure 1) [2].

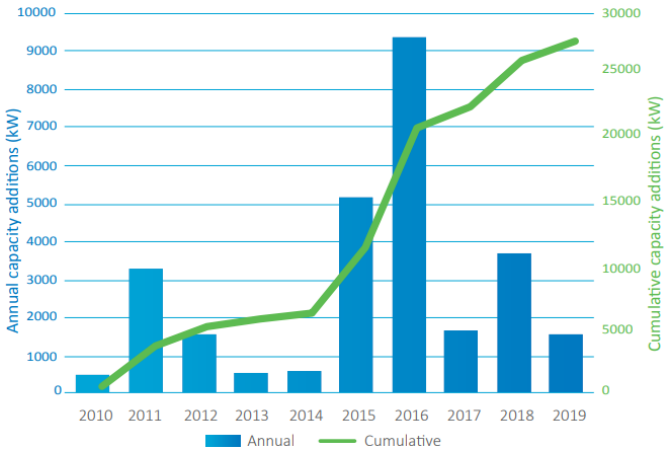

Figure 1. Annual and Cumulative Tidal Stream Capacity (in kW) from 2010-2019 in Europe [2]

Given the nascent stage of the tidal energy field, tidal energy device designs are afforded a high degree of experimentation and innovation. Tidal blades, a key component of tidal energy devices, must be designed to withstand harsh ocean forces for their life cycle deployment of up to 20 years. Because the density of sea water is roughly 800 times that of air, tidal turbine blades are subjected to static and fatigue loading forces roughly five times greater than those experienced by an equivalently powered wind turbine [3]. Tidal turbines must display excellent strength limits, fatigue endurance, and survivability as they are subjected to high cycle long-term fatigue loads and extreme weather events.

Glass fibre-reinforced polymer (GFRP) composites are strongly suited to meet these challenges making them an ideal material choice for tidal turbine blades. They offer a high specific strength and stiffness, resistance to saltwater corrosion, and a versatility in manufacturing of complex shapes at a lower cost than carbon fibre. GFRP material behaviour is highly anisotropic depending on the orientation, layout, and ply layering of the reinforcing glass fibres; thus, any areas devoid of glass fibres, known as resin rich regions, can cause weakness [4]. GFRP materials achieve highest tensile strength when the fibres are aligned with the load direction. The resin material used is also a critical design consideration; powder epoxies are an intriguing innovation in composite manufacture. In some applications, powder epoxies offer improved mechanical performance at reduced cost when compared with traditional liquid epoxies [5], [6].

Structural health monitoring (SHM) systems monitor component structural health and provide real-time data on machine operating conditions. SHM systems enable energy device operators to pre-emptively identify structural

weaknesses and failure potentials, thereby mitigating operational downtime and maximising power production capacity factor. SHM systems decrease device operating costs, extend component lifespans, reduce operational risks, and reduce inspection costs [7], [8]. Tidal energy devices in particular stand to strongly benefit from the deployment of SHM systems because of their inaccessibility in the marine environment; furthermore, SHM systems enable renewable energy systems to be deployed in more remote locations [9].

Optical fibre sensors are a promising SHM technology. When embedded in composite components, fibre optic sensors can provide structural health information on a variety of metrics including material deformation, non-uniform strain distribution, and microscopic damages. An example of a fibre optic SHM system with Bragg Grating sensors deployed in a wind turbine is shown in Figure 2 [10].

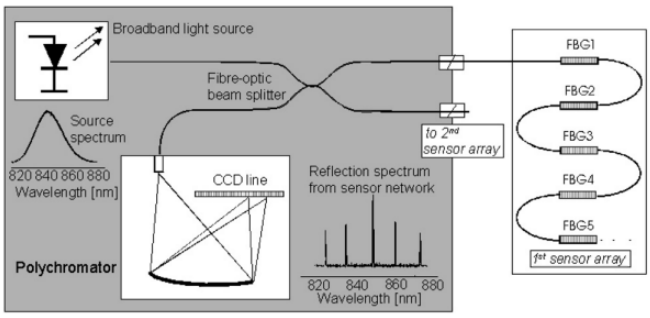

Figure 2. Wind Turbine Fibre Optic Sensor SHM System [10]

However, fibre optic sensors embedded in composite components can disturb the reinforcing fibre structure, thereby compromising mechanical strength. The literature has identified that the diameter size of the fibre optic cable can impact material behaviour response; small diameter fibre optic cables are less intrusive than standard sized optical fibre sensors (~ outer diameter 125 μm) [11], [12], [13], [14], [15], [16], [17]. Another driving factor in embedded sensor-host material behaviour is the orientation of the sensor in relation to the reinforcing fibres [11], [13], [16], [17], [18], [19]. The reinforcing fibres are increasingly disrupted as the orientation of the embedded sensor ranges from parallel to transverse; the ensuing resin rich region devoid of structural fibres can act as a stress concentration.

In this paper, the methodology used for manufacturing and testing specimens with embedded fibre optic cables of varying diameters and orientations is presented. The tensile test results are discussed. Additionally, microscopic images of the embedded sensors interacting with the composite material are presented and discussed.

2 METHODOLOGY

2.1 Aims and Objectives

The aim of this research is to investigate the impact of embedding optical fibre sensors on the tensile strength of powder epoxy glass-fibre composite samples. The effects on composite structural integrity of embedding optical fibre sensors of different sizes and with different orientations relative to the reinforcing fibres are examined. This work supports the larger aim of verifying novel material solutions and investigating SHM systems in the tidal energy sector. In order to achieve the aim of this study, the following objectives must be achieved:

- To embed fibre optic cables in powder epoxy glass-fibre composite samples, including:
  - Small and standard diameter fibre optics;
  - Fibre optics embedded both parallel and perpendicular to the reinforcing fibres.
- To manufacture tensile test specimens with embedded fibre optic cables.
- To perform tensile testing and microscopic examination of fibre optic/host material interaction.

2.2 Methodology

The two variables scrutinised in this research are fibre optic diameter and fibre optic orientation relative to the surrounding glass fibres. To investigate the effect of diameter, fibre optic cables with a standard diameter and small diameter are embedded. In regard to orientation, the extreme cases of embedding fibre optic cables parallel and perpendicular to the glass fibres are considered. Thus, the array of tensile test specimens studied in this research encompass the five following testing permutations:

1. **Control** sample with **no** embedded fibre optic cable.
2. **Standard** diameter fibre optic cable that runs **parallel** to glass fibres.
3. **Small** diameter fibre optic cable that runs **parallel** to glass fibres.
4. **Standard** diameter fibre optic cable that runs **perpendicular** to glass fibres.
5. **Small** diameter fibre optic cable that runs **perpendicular** to glass fibres.

2.3 Materials

The composite material used in this study is unidirectional (UD) glass fibres with the ÉireComposites CPET (Composites Powder Epoxy Technology) epoxy prepreg system [20]. The synthetic fused silica glass fibre optic cables were procured from CM Scientific in Dublin, Ireland. The standard diameter fibre optic cable is the Molex 1068000098 cable with core, cladding, and outer coating diameters of 100, 110, 124 micro-meters, respectively. The small diameter cable (Molex 1068001596) has core, cladding, and outer coating diameters of 50, 55, and 65 micro-meters, respectively.

2.4 Test Specimen Manufacture

The test coupons were designed according to ASTM D3039, the international standard for conducting tensile testing of composite materials [21]. The test coupons were designed with a width of 15mm, length of 250 mm, and thickness of 2mm. To ensure homogeneity of results, the parallel test specimens were all produced from the same panel (parallel panel layout with 4 control, 5 standard diameter, and 5 small diameter samples shown in Figure 3), and the perpendicular test specimens from the same panel (perpendicular panel layout with 3 control, 5 standard diameter, and 5 small diameter samples shown in Figure 4). The test coupons were designed to be loaded longitudinally along the length of the specimen in line with the UD glass fibres.

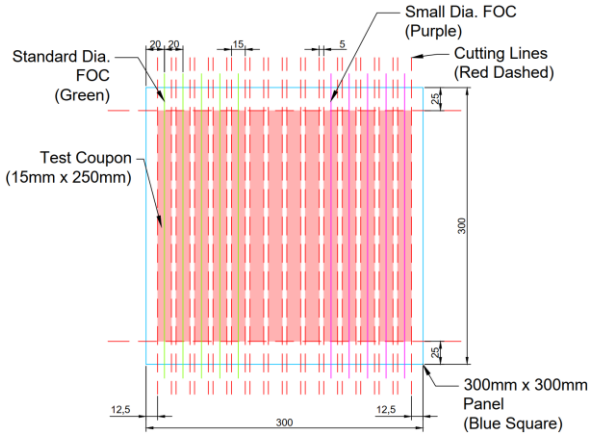

Figure 3. Parallel Panel Test Coupon Layout (units mm)

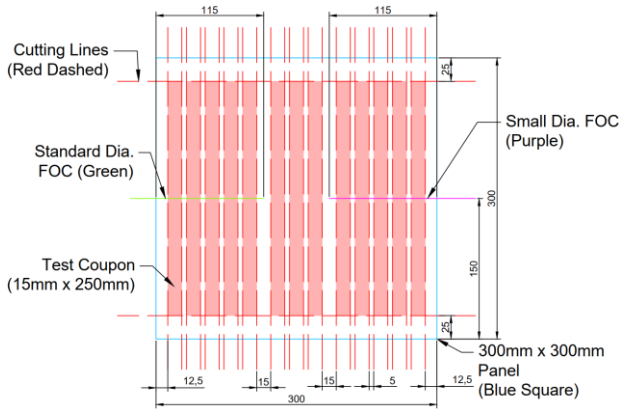

Figure 4. Perpendicular Panel Test Coupon Layout (units mm)

The test panels and coupons were manufactured at ÉireComposites Teo in County Galway, Ireland. In manufacturing the two panels, the first UD glass fibre ply was laid down flat on a Teflon-coated base plate. After being cleaned with isopropyl alcohol, the standard diameter and small diameter fibre optic cables were placed parallel or perpendicular to the UD glass fibres according to the appropriate panel. The ends of the fibre optics were taped down to secure them in place during the curing process (blue heat resistant tape used with the parallel panel visible in Figure 5). To complete the ply-cable-ply sandwich assembly, a second glass fibre ply was placed on top.

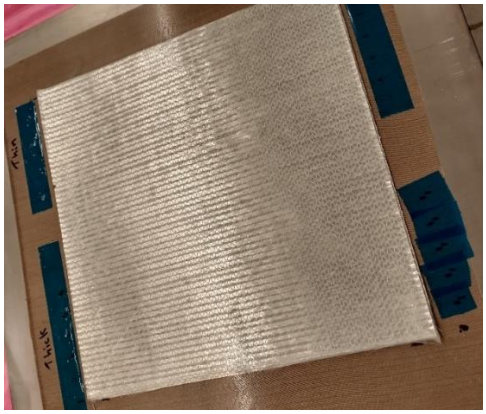

Figure 5. Glass Fibre Ply with Fibre Optic Cables Held by Heat-Resistant Tape

Release film, breather fabric, and vacuum bagging were then applied to the assemblies, and the seal was verified via vacuum drop test. After curing in the oven at 180° C, the completed panels were subjected to ultrasonic non-destructive testing using a MIDAS water-jet through-transmission rig (Model No: M1913). The resulting C-scans indicated successful panel consolidation with no major internal flaws. The test coupons were cut from the larger panels with a diamond edge blade surface grinder that used a water/Dromus oil coolant. The cut specimens were end-tabbed with square glass fibre-epoxy tabs and bonded to the test specimens with EA-9394 two-part paste adhesive (cut and tabbed specimen shown in Figure 6).

Figure 6. Cut and Tabbed Test Coupon

2.5 *Mechanical Testing*

Testing took place at the Composites Testing Laboratory (CTL) testing division of ÉireComposites Teo. ASTM D3039 test standards were followed [21]. Tensile testing was conducted with a Zwick/Roell Z400 universal testing machine in a controlled environment (23°C, humidity 57%). The specimens were held by hydraulic wedge grips with a grip pressure of 1500 psi. The applied force relative to the strain was continuously monitored during loading (constant displacement rate 2mm/min), and the maximum force and strain were recorded upon specimen failure. A biaxial extensometer determined elastic modulus between 0.1% and 0.3% strain.

2.6 *Microscopic Inspection*

To better understand how the fibre optic cables interacted with the glass fibres and resin matrix, one specimen from each fibre optic testing permutation (small diameter parallel, standard diameter parallel, small diameter perpendicular, and standard diameter perpendicular) was polished with diamond grit and then examined with an Olympus BX53M microscope.

3 RESULTS AND DISCUSSIONS

The tensile tests produced the following results: ultimate tensile strength, modulus of elasticity, and shear modulus. Due to a myriad of factors including manufacturing process and micro-scale material inconsistencies, composite material behaviour can vary from specimen to specimen, even within uniform testing groups. To isolate behaviour caused by the embedded fibre optic sensors from naturally occurring material flaws, the results from each test group are examined in aggregate.

3.1 *Tensile Strength*

The number of samples tested (n), average ultimate tensile strength, tensile strength range, standard deviation, and percent variance of each testing permutation group are shown in Table 1. The tensile strengths of the control groups from both panels overlap, although the ranges differ. There is some material property inconsistency between the two panels, as the range of

tensile strength values in the parallel panel control samples is wider than the perpendicular panel control samples.

To examine the effect of varying fibre optic diameter on the tensile strength, specimens from within the same panels are compared. The average tensile strengths of the test groups from the perpendicular panel all fall within one standard deviation of each other; this suggests no statistically significant difference in tensile strength between the perpendicular panel samples. Thus, there is no evidence of degradation in tensile strength caused by the embedment of either diameter fibre optic cable. Of note, the standard diameter specimens achieve both the lowest (390 MPa) and highest (454 MPa) tensile strength values of the perpendicular panel. It is clear that the standard diameter perpendicular fibre optic cables do not limit a specimen from reaching its maximum tensile strength potential. However, it is unclear whether the low tensile strength value can be attributed to the fibre optic cable or a material flaw.

Table 1. Tensile Strength

Test Group	n	Avg. Tensile Strength (MPa)	Range (MPa)	Std. Dev.	Var. (%)
Control Perpendicular	3	423	413 – 440	14.83	3.51
Standard Diameter Perpendicular	5	429	390 – 454	23.96	5.58
Small Diameter Perpendicular	5	425	411 – 444	12.43	2.92
Control Parallel	4	409	385 – 451	29.25	7.16
Standard Diameter Parallel	5	409	378 – 431	19.05	4.66
Small Diameter Parallel	5	425	406 – 438	13.03	3.07

The parallel panel control specimens display a wide spread of tensile strength values with a percent variance of 7.16%; the disparity between the lowest tensile strength from the parallel panel control group (385 MPa) and that of the perpendicular control group (413 MPa) suggests manufacturing process or microscopic material inconsistency between panels. The lowest tensile strength value of either panel is seen in the standard diameter samples from the parallel panel at 378 MPa. Again, however, the average tensile strengths of the parallel panel specimens fall within one standard deviation of each other; thus, there is no evidence of a statistically significant degradation in tensile strength caused by embedding the fibre optic cables of either diameter in the parallel panel samples.

To examine the effect on tensile strength of varying the orientation of the fibre optic cables relative to the glass fibres, it is necessary to compare the test groups from different panels. The maximum tensile strength values observed for the standard diameter and small diameter specimens from the perpendicular panel (454 MPa and 444 MPa, respectively) exceed those of the equivalent testing groups from the parallel panel (431 MPa and 438 MPa, respectively). However, the average tensile strengths of each similar testing group again are found within one standard deviation of one another. Thus, this data set has not demonstrated a statistically significant difference in tensile strength caused by varying fibre optic orientation. A limitation of this analysis worth noting is the fact that the tensile strength measurements come from different panels with material structures that will vary on a microscopic scale.

3.2 Modulus of Elasticity

Table 2 displays the modulus of elasticity values produced from the tensile testing. Similar statistical analysis as used with the tensile strength section is applied here. In scrutinising the effect of varying fibre optic diameter within panels, the average modulus values of the testing groups fall within one standard deviation of one another, demonstrating no statistically significant disagreement in modulus value. Furthermore, when comparing specimens between panels, the average modulus values are also within one standard deviation of each other; there is no evidence that fibre optic orientation degrades the material's modulus of elasticity. In regard to both fibre optic orientation and diameter size, the fibre optic cables are not shown to impact the modulus of elasticity values.

Table 2. Modulus of Elasticity (E)

Test Group	n	Avg. E (GPa)	Range (GPa)	Std. Dev.	Var. (%)
Control Perpendicular	3	19.19	18.62 – 19.65	0.52	2.73
Standard Diameter Perpendicular	5	19.42	19.21 – 19.65	0.17	0.87
Small Diameter Perpendicular	5	19.2	18.70 – 20.00	0.5	2.6
Control Parallel	4	19.6	18.43 – 20.77	0.96	4.88
Standard Diameter Parallel	5	19.64	18.81 – 20.10	0.52	2.66
Small Diameter Parallel	5	19.65	18.85 – 19.99	0.46	2.34

3.3 Shear Modulus

The shear modulus results from the tensile testing are shown in Table 3. The average shear modulus values for the small and standard diameter test groups from each panel fall within one standard deviation of their respective control groups indicating that shear modulus is not impacted by fibre optic diameter size. When isolating for fibre optic orientation between panels, the shear modulus values from like groups also overlap within one standard deviation. Thus, there is no evidence from this data that fibre optic diameter or orientation impact shear modulus. A discrepancy worth highlighting is that the control group averages from the different panels lie within two standard deviations distance of each other.

Table 3. Shear Modulus

Test Group	n	Avg. μ	Range	Std. Dev.	Var. (%)
Control Perpendicular	3	0.34	0.34 – 0.35	0.01	1.54
Standard Diameter Perpendicular	5	0.36	0.34 – 0.38	0.02	5.08
Small Diameter Perpendicular	5	0.34	0.31 – 0.37	0.02	5.71
Control Parallel	4	0.36	0.35 – 0.37	0.01	2.12
Standard Diameter Parallel	5	0.35	0.34 – 0.36	0.01	2.61
Small Diameter Parallel	5	0.36	0.36 – 0.37	0	0.99

3.4 Microscopic Examination

The images produced from the microscopic inspection inform on how the fibre optic cables interact with the glass fibres and resin matrix. The microscopic image taken from the specimen containing the standard diameter fibre optic cable embedded perpendicular to the glass fibres is shown in Figure 7. The long streaks crossing the middle of the picture are the longitudinal glass fibres (in the force load direction), while the small circles are the lateral reinforcing fibres coming in and out of the plane; the large circle in the middle is the fibre optic cable neatly sandwiched between two longitudinal bundles. There is a grouping of lateral glass fibres also located in between the longitudinal fibres, but the fibre optic cable clearly has driven displacement of the longitudinal fibres. Although there are other smaller resin pockets visible, the resin rich region caused by the fibre optic is the largest concentration of pure resin. The fibre optic cable creates a substantial area devoid of glass fibre reinforcement.

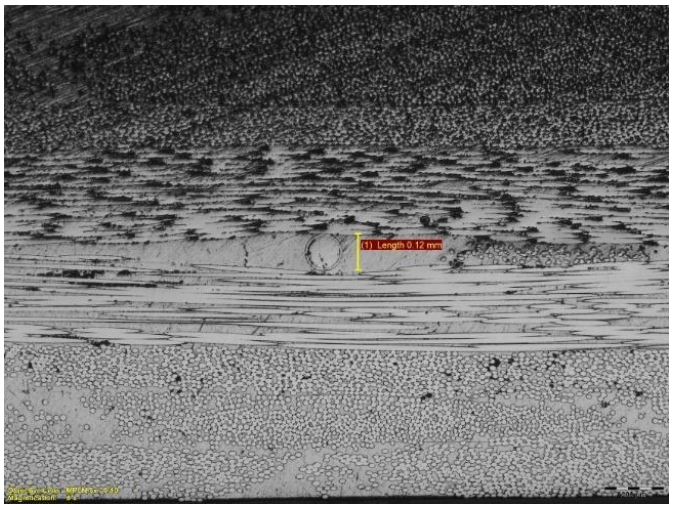

Figure 7: Standard Diameter Perpendicular Microscopic Image

Figure 8 shows the microscopic image produced from the small diameter perpendicular specimen. Again, the fibre optic cable is surrounded above and below by longitudinal fibres, and it is joined by several groupings of lateral fibres. However, in contrast with the standard diameter optical fibre, the small diameter cable does not seem to cause any additional displacement of the longitudinal fibres and comfortably fits in the space created by the lateral glass fibres. Furthermore, naturally occurring resin rich areas can be seen throughout that are larger than that next to the fibre optic cable.

Figure 8: Small Diameter Perpendicular Microscopic Image

The standard diameter fibre optic cable embedded parallel to the glass fibres is displayed in Figure 9. In the images of the parallel specimens, the long streaks across the picture are the lateral glass fibres, while the small circles are the longitudinal fibres (in line with the loading). Here, the standard diameter fibre optic cable comfortably nestles amongst the longitudinal glass fibres. Although minor resin rich areas are visible on either side of the cable, it is apparent that significantly larger resin rich areas have naturally developed elsewhere within the specimen without influence from the optical fibre.

Figure 9: Standard Diameter Parallel Microscopic Image

In Figure 10, a small diameter fibre optic cable running parallel to the longitudinal glass fibres is seen. Although a large resin rich area surrounds the fibre optic cable, it is uncertain whether the fibre optic cable caused the disruption. It is possible that the fibre optic cable simply settled into a naturally occurring resin rich region that would already have been devoid of glass fibres.

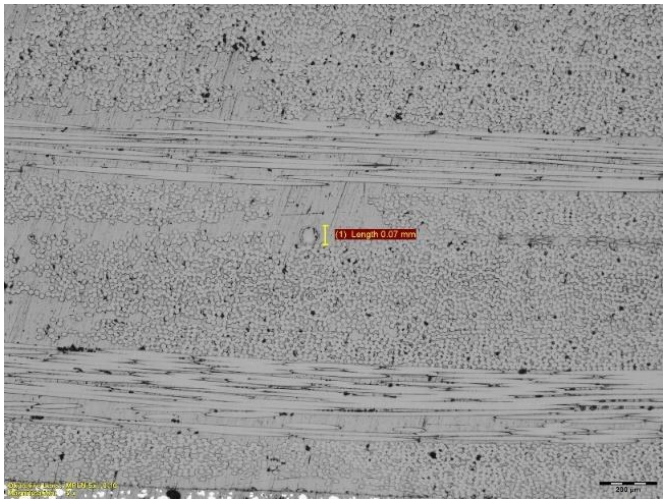

Figure 10: Small Diameter Parallel Microscopic Image

4 CONCLUSION

In this paper, the methodology used for manufacturing and tensile testing of powder epoxy glass-fibre composite specimens with embedded fibre optic sensors was outlined. An examination of the effect on composite tensile strength of varying fibre optic diameter size and orientation relative to the surrounding reinforcing fibres was presented and discussed. The data in this experiment did not indicate, in a statistically significant manner, that the embedded fibre optic cables resulted in a degradation in mechanical performance, in terms of ultimate tensile strength, modulus of elasticity and shear modulus. The impact of this work is expected to de-risk the use of embedded sensor SHM systems in tidal turbine blades. By implementing real-time, continuous, and reliable SHM systems, the need for onsite maintenance and operational downtime in tidal energy devices can be reduced thereby lowering the levelised cost of tidal energy.

ACKNOWLEDGMENTS

This research was funded in part by the European Commission through the H2020 CRIMSON project (grant agreement no.: 971209) and Science Foundation Ireland (SFI), through the MaREI Research Centre for Energy, Climate and Marine (Grant no. 12/RC/2302_2).

REFERENCES

[1] Implementation Working Group Ocean Energy, "SET-Plan Ocean Energy-Implementation Plan," 2021. Accessed: Feb. 23, 2022. [Online]. Available: https://setis.ec.europa.eu/implementing-actions/ocean-energy_pt

[2] R. Collombet, "Ocean Energy: Key trends and statistics 2020," 2021.

[3] P. Harper, S. Hallett, A. Fleming, and M. Dawson, "Advanced fibre-reinforced composites for marine renewable energy devices," *Marine Applications of Advanced Fibre-Reinforced Composites*, pp. 217–232, Jan. 2016, doi: 10.1016/B978-1-78242-250-1.00009-0.

[4] A. Godara and D. Raabe, "Influence of fiber orientation on global mechanical behavior and mesoscale strain localization in a short glass-fiber-reinforced epoxy polymer composite during tensile deformation investigated using digital image correlation," *Composites Science and Technology*, vol. 67, no. 11–12, pp. 2417–2427, Sep. 2007, doi: 10.1016/J.COMPSCITECH.2007.01.005.

[5] T. Flanagan, J. Maguire, C. Ó. Brádaigh, P. Mayorga, and A. Doyle, "Smart Affordable Composite Blades for Tidal Energy Smart Affordable Composite Blades for Tidal Energy," 2015.

[6] C. Floreani, C. Robert, P. Alam, P. Davies, and C. M. Ó. Brádaigh, "Mixed-mode interlaminar fracture toughness of glass and carbon fibre powder epoxy composites—for design of wind and tidal turbine blades," *Materials*, vol. 14, no. 9, May 2021, doi: 10.3390/MA14092103.

[7] J. Lian, O. Cai, X. Dong, Q. Jiang, and Y. Zhao, "Health monitoring and safety evaluation of the offshore wind turbine structure: A review and discussion of future development," *Sustainability (Switzerland)*, vol. 11, no. 2. MDPI, Jan. 18, 2019. doi: 10.3390/su11020494.

[8] M. A. Rumsey and J. A. Paquette, "Structural health monitoring of wind turbine blades," in *Smart Sensor Phenomena, Technology, Networks, and Systems 2008*, Mar. 2008, vol. 6933, p. 69330E. doi: 10.1117/12.778324.

[9] M. Martinez-Luengo, A. Kolios, and L. Wang, "Structural health monitoring of offshore wind turbines: A review through the Statistical Pattern Recognition Paradigm," *Renewable and Sustainable Energy Reviews*, vol. 64, pp. 91–105, Oct. 2016, doi: 10.1016/J.RSER.2016.05.085.

[10] K. Schroeder, W. Ecke, J. Apitz, E. Lembke, and G. Lenschow, "A fibre Bragg grating sensor system monitors operational load in a wind turbine rotor blade," *Meas. Sci. Technology*, vol. 17, pp. 1167–1172, 2006, doi: 10.1088/0957-0233/17/5/S39.

[11] E. J. Friebele *et al.*, "Optical fiber sensors for spacecraft applications," *Smart Materials and Structures*, vol. 8, no. 6, pp. 813–838, Dec. 1999, doi: 10.1088/0964-1726/8/6/310.

[12] N. Takeda, Y. Okabe, J. Kuwahara, S. Kojima, and T. Ogisu, "Development of smart composite structures with small-diameter fiber Bragg grating sensors for damage detection: Quantitative evaluation of delamination length in CFRP laminates using Lamb wave sensing," *Composites Science and Technology*, vol. 65, no. 15–16, pp. 2575–2587, Dec. 2005, doi: 10.1016/J.COMPSCITECH.2005.07.014.

[13] K. Levin and S. Nilsson, "Analysis of the local stress field in a composite material with an embedded extrinsic Fabry-Perot interferometer (EFPI) sensor," 1994.

[14] Y. Okabe, T. Mizutani, S. Yashiro, and N. Takeda, "Detection of microscopic damages in composite laminates with embedded small-diameter fiber Bragg grating sensors," 2002. Accessed: Nov. 26, 2021. [Online]. Available: www.elsevier.com/locate/compscitech

[15] K. Satori, Y. Ikeda, Y. Kurosawa, A. Hongo, and N. Takeda, "Development of small-diameter optical fiber sensors for damage detection in composite laminates," in *Smart Structures and Materials 2000: Sensory Phenomena and Measurement Instrumentation for Smart Structures and Materials*, Jun. 2000, vol. 3986, p. 104. doi: 10.1117/12.388097.

[16] S. S. J. Roberts and R. Davidson, "Mechanical properties of composite materials containing embedded fiber-optic sensors," in *Fiber Optic Smart Structures and Skins IV*, Dec. 1991, vol. 1588, pp. 326–341. doi: 10.1117/12.50193.

[17] G. Luyckx, E. Voet, N. Lammens, and J. Degrieck, "Strain Measurements of Composite Laminates with Embedded Fibre Bragg Gratings: Criticism and Opportunities for Research," *Sensors 2011, Vol. 11, Pages 384-408*, vol. 11, no. 1, pp. 384–408, Dec. 2010, doi: 10.3390/S110100384.

[18] K. Shivakumar and L. Emmanwori, "Mechanics of Failure of Composite Laminates with an Embedded Fiber Optic Sensor," Greensboro, Jul. 2003. doi: 10.1177/0021998304042393.

[19] D. W. Jensen, J. Pascual, and J. A. August, "Performance of graphite/bismaleimide laminates with embedded optical fibers. Part I: uniaxial tension," *Smart Mater. Strucl*, vol. 1, pp. 24–30, 1992.

[20] "EC1921-003-01 Technical data sheet - glass fibre powder epoxy composite (EXTERNAL DISTRIBUTION)." EireComposites Teo, Galway, Ireland.

[21] ASTM International, "Standard Test Method for Tensile Properties of Polymer Matrix Composite Materials," 2017. doi: 10.1520/D3039_D3039M-17.

A 2030 vision for renewable energy; The political landscape surrounding ocean energy for electricity in Europe

Zak Hawthorne [1], Peter Ryan [1] Thomas Dooley [1], Fergal O'Rourke [1]
[1]Department of Electronic and Mechanical engineering, Dundalk Institute of Technology, Dublin road, Dundalk, Ireland
Email : Zak.hawthorne@dkit.ie, Peter.Ryan@dkit.ie, Thomas.Dooley@dkit.ie, Fergal.Orourke@dkit.ie

ABSTRACT: The diversification of the energy supply worldwide is paramount to reducing harmful emissions and addressing climate change. Europe is rapidly moving towards the decarbonisation of energy in heat and transport, however these developments are often through electrification and as such commonly transfer the burden to the electrical grid. This increasing electricity demand, driven primarily by electric vehicles and heating/cooling systems, will require the supply of a diverse range of renewable energy sources. Furthermore, it is crucial that effective environmental policy is approved by the European Union to allow for the development of a greater range of renewable energy technologies and in doing so provide a greater diverse range of energy supply. The path toward a renewable electrical system has largely been dependent on solar and wind developments and whilst this has been quite successful, it neglects one of the greatest renewable assets, the ocean. Harnessing ocean energy is crucial to alleviating the extra load placed on the electrical grid from other decarbonisation efforts. This paper sets out to describe the various potential ocean energy technologies for harnessing both wave and tidal energy, and the political landscape surrounding ocean energy for electricity production. Additionally forecasting possible energy scenarios, by 2030, within the EU context in various countries is explored. Finally, this work provides details on the policy and political decisions required to make ocean energy a key component of the EU energy mix.

KEY WORDS: Ocean-energy, Policy,

1 INTRODUCTION

1.1 A history of ocean energy

The ocean has long been a coveted source of energy, with use of tidal mills going so far back as Ancient Greece and found as early as the first century in parts of Asia and Europe [1]. This innovation continued into the Middle Ages in places such as Nendrum Monastery in Ireland dated from AD 619 [2]. These are however all tidally based devices, the first use of ocean waves as an energy source was as early as 1799 in France by father and son Girard. This patent is documented in [3]. The idea of this first wave energy device, was to connect a lever to a floating body in the ocean, with it's fulcrum on the shore which when lifted and lowered by the wave would cause a reciprocating motion suitable for pumps or other mechanical means [3]. It seems that wave energy largely lay dormant, with some notable attempts listed by [4] in the form of a Wave power air compressing company in the 19th century and another French invention in the form of a test station using a 'barometric ram siphon'. Unfortunately, an economic crisis in 1929 would halt further research [4]. But it was another crisis, The oil crisis of 1973 that would reform the investigation into renewable energies [5], of which ocean energy in the form of wave and tidal was resurrected, largely attributed to Stephen Salter who was an engineer at Edinburgh university, and his wife Mrs Salter for such clear design objectives. [3]. From this point a number of interests were renewed including the innovation of previous ideas such as that of Yoshio Masuda, described by [5] as 'The father of modern wave energy technology'. His most famous contribution being the re-purposing oscillating water column technology to utilise a turbine for recharging batteries on ocean buoys, which until then had only been used for buoy whistles [6].

1.2 Current state of the art

Currently there are a number of different methods that may be used to extract energy from the ocean, largely these can be considered as either tidal or wave-based devices. Examples of each are given in Table 1,2 and are explained briefly thereafter.

Table 1: Wave energy harvesting devices [7]

Type	Operating principle
Attenuator	Relative motion between waves
Point absorber	Buoyancy
Oscillating wave surge	Wave particle motion
Oscillating water column (OWC)	Pneumatic conversion
Over-topping/terminator	Water capture
submerged ΔP	Pressure differential

This table is not a complete list of all wave energy converters

1.2.1 Attenuator

Wave attenuators extract energy from the relative position of a device floating on the ocean. The most well known example of

this system is the Pelamis, a large, segmented cylindrical construction anchored to the sea bed. Of note is the survivability of this device, outlined as having to withstand a much larger power input range than other forms of renewable energy systems, with stormy conditions being 100 times the levels of normal operation. It's streamlined form is attributed to the survival of extreme wave conditions, thought of in the same way that a surfer might dive under wave crests.[8] The economic viability of this system is interesting as during investigation it was found that Ireland had, compared to alternatives such as Portugal, a better power output. Unfortunately, it was found to not coincide with Irish demand, i.e. Output power was less during period of high demand. Ultimately however, Ireland still held the best economic results of a number of areas considered although these results relied heavily on both initial costs, and feed in tariff rates.[9] Regrettably the company behind the Pelamis went into administration in 2014, with their assets bequeathed to Wave Energy Scotland [10].

1.2.2 Point absorber

Point absorber devices are similar to attenuators in that they 'ride' the wave, however they are typically smaller than the wavelength of the wave. [11] They generate power through the use of a power take off system driven by the relative location of the device and a fixed reference.[12] One example of this type of device, was the Power-Buoy developed by Ocean Power Technology, with their innovation concerning monitoring and adaptation to environmental conditions [13]. To further this, the manufacturer's literature implies that the device was able to withstand hurricane conditions [14]. The economic viability of this device is unknown, with the company themselves even noting the uncertainty of this as mentioned in their annual report [15].

1.2.3 Oscillating wave surge

These devices, outlined as being shallow operating depth (10-20 metre) devices, exploiting enhanced horizontal fluid particle velocities. this is unique as typically devices extract energy from heaving modes of motion.[16] The best example of this style of converter is the Oyster, developed by Aquamarine Power Ltd. These devices, being placed in shallow water do not have to deal with quite as severe weather conditions, as the waves experience wave breaking and seabed friction before reaching the device [17]. This style of converter has been outlined as a serious contender for economic, reliable power from ocean waves [16].

1.2.4 Oscillating water column

The operating principle of oscillating water column devices is, in essence, a pneumatic conversion of the energy in the water waves. This is achieved through the use of a hollow opening in which ocean waves will be captured and the oscillating motion of the free surface firstly (moving upwards) will pressurise the volume of air within the chamber, causing a flow through a turbine usually at the top or side of the structure. The flow then receding, will now cause a lower pressure than atmospheric within the chamber, forcing air to re-enter through the same opening/turbine. This is shown graphically below in Figure 1

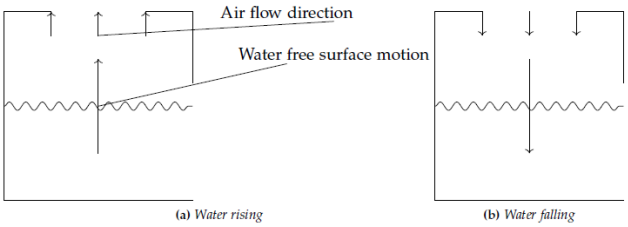

Figure 1: example of OWC motion

An example device being the the 'ocean energy buoy' (OE buoy) project [54]. Which is a floating structure utilising the same concept as shown in Figure 1 above.

1.2.5 Over-topping/terminator

Over topping devices are more akin to traditional hydro power systems, containing the water similar to a dammed river. These systems were outlined as having poor efficiency per characteristic length, meaning they are unlikely to be heavily used.[18] One example of a commercial over topping device is the 'wave dragon', advertised as being, scalable, low cost of maintenance, and using mature hydro turbine technology [19]. An economic analysis of the wave dragon device found it to be superior in power generation per wave energy flux to both the Pelamis and Aqua buoy systems by quite a substantial margin although no claims of the reflected economic viability were made [20]

1.2.6 Submerged pressure differential

This device uses the change in pressure as waves move over it to generate power.[21] These are similar to point absorbers although submerged [22] allowing for greater tolerance of difficult conditions [23] an example of this type of device is the 'Symphony WEC' and perhaps to make the device more cost effective, it is proposed to use existing offshore wind energy infrastructure [24]

Table 2: Tidal energy harvesting devices [8],[9]

Type	Operating principle
Turbine (tidal stream)	Direct tidal motion
Oscillating hydrofoil	Hydrodynamic lift and drag
Tidal Kite	Hydrodynamic lift
Tidal Barrage	Water height difference

This table is not a complete list of all tidal energy converters.

1.2.7 Turbine

Analogous to wind turbines, there are multiple types of turbines used for extracting wave energy from horizontal and vertical turbines and may be enhanced with a venturi. However, they are generally all using the same concept of using the tidal motion to drive the turbine as wind would drive a wind turbine. A recent example of a tidal turbine is the AR2000 developed by SIMEC Atlantis Energy, a 2-megawatt horizontal axial turbine [27]. this recently developed turbine is built upon

innovation from its predecessor (the AR1500) which is currently used in the MeyGen tidal stream energy project. [28]
2.0.7. Oscillating Hydrofoil
The oscillating hydrofoil is a very interesting design, with similar forces being developed by an aerofoil. A change in angle of attack allows for a change in lift and drag which causes the hydrofoil to alter direction. This is intentionally induced to form an oscillatory pattern. An example of this device is the 'Stingray' concept, which used two hydrofoils to produce hydraulic power for use in a hydraulic motor [29].

1.2.8 Tidal kite

The tidal kite is an eccentric design using a 'flying' structure resembling an aeroplane anchored to the seabed but operating as a kite would, using tides in this instance and being moved in a continuous `figure 8' pattern. electricity is generated through a turbine at the front of the craft (again, reminiscent of propeller driven aircraft) and provided through the anchoring cable [30] An example of a device is the minesto Deep Green 500, a 12 metre wing span, 500 kW device. a comprehensive life cycle assessment is given by [31]. In summary, the device as deployed in an array is similar in environmental credentials to wind power. although it is largely affected by capacity factor.

1.2.9 Tidal barrage

A tidal barrage is perhaps the most conventional of these systems, In essence it is essentially a time dependent dam, in that, at high tide water is allowed to flow into a basin, and during low tide when the water has receded it is allowed to flow back out through a number of turbines for electricity production. And indeed power can be extracted as the water enters, although this will impede the flow into the basin [32]. An example of a tidal barrage in operation is the Rance estuary barrage in Brittany, France. Which was completed in 1967 (refurbished in 1996) and is a 240MW plant. [33]

2 EUROPEAN POLICY

2.1 Introduction

This section will outline the European union (EU) and affiliates in terms of policy towards all renewable electricity sources, with an onus on the Irish perspective, and will aim to project where ocean energy projects may be fit into energy strategy for 2030.

2.2 Previous policy

In order to evaluate the efficacy of current policy It is important to evaluate the success of previous initiatives. The EU has for a long time been concerned with renewable energy going at least as far back as 2005 in setting out support for renewable energy through policy [10] This directive set out to achieve 21% electricity production from renewable sources by 2010 a goal that was not met. This criterion was amended in relation to the 2020 goals, set in 2010 and from then only stipulated that overall final energy production should be at least 20% by 2020 [11]. This allowed for more flexible targets for renewable electricity (RES-E) on a national basis. Of particular interest are the nations with the highest potential for ocean energy, these, and their targets are shown below in Table 3

Table 3: Promising nations for ocean energy and their RES-E 2020 targets

Country	%Target	% Achieved	Reference
Ireland	40	39.1	[39]
UK	30	43.1	[40],[41]
France	27	24	[42],[43]
Portugal	55.2	29.6	[42],[44]
Spain	40.2	43.6	[42],[45]

From this it can be seen that in terms of renewable electricity generation, substantial progress has been made towards the targets. Assuming that this trend continues this leads to a promising future for renewable energy and as such ocean energy may be re-examined as a viable resource. The main concern being the manner of device which is used to implement target goals.

3 CRITIQUE OF IRISH STRATEGY

Outlined in [19] the Irish intent is to reach 80% renewable electricity by 2030 through the increase of solar and wind energy. Naturally, given the context of this report, it seems absurd that ocean energy is completely neglected, this is evidently a shared view as per [20] which expresses the case for ocean energy to be included in the National Energy and Climate Plan. To that end, the Irish potential for ocean energy is outlined.

3.1 Irish Ocean energy

Ocean energy has a potential in Ireland of 27.5 -31.1 GW in wave and 1.5-3 GW in tidal energy [21]. This can be compared to the similar 11- 16 GW for onshore wind and 30 GW for offshore wind projected to be achievable by 2050 by the SEAI [22]. What makes the apparently neglect of ocean energy in 2030 strategy even more short sighted, is the continued funding in the area for many years as shown below in Figure 2.

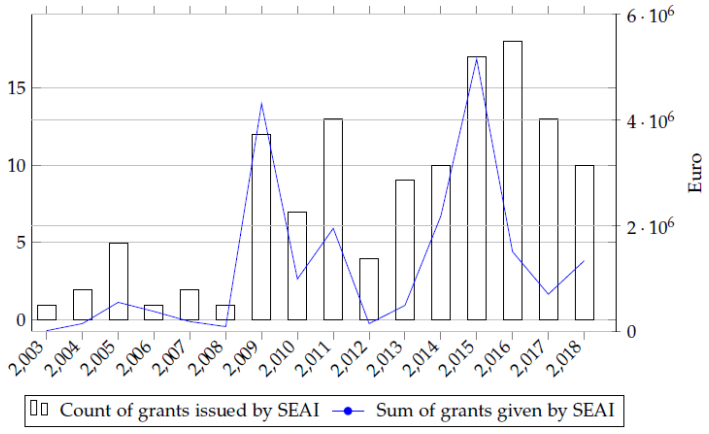

Figure 2: SEAI ocean funding data from [50]

And whilst the SEAI have outlined that there has been fewer applications and attribute this to a lack of funding which is limited by `EU state aid rules'. Even within these constraints,

developers of these technologies may reapply for funding once they reach higher technology readiness levels (TRL). This may not be a sufficient incentive as outlined by the SEAI as for technological readiness levels beyond 6 (demonstration) the costs rise to 10s of millions which at this time is not supported by funding [23]. As it seems that the 'EU state aid rules' are the most problematic element of this, and they will be relevant in all European union cases. It is important to understand these constraints more directly. Whilst these regulations are a quagmire of legal particularity. The EU for the longest time has allowed up to €200,000 in aid for a period of three (3) years with no need for notification of state aid measures, and for loans up to €1,500,000. However, there were previsions set out for aid in research and development up to €10,000,000. for industrial research [24]. This is subject to change in a positive way in 2022 as there is currently a draft of a Climate, Energy and Environmental Aid Guidelines (CEEAG) revision of state aid guidelines to increase funding to the climate, energy, and transport industries, including using private companies. estimated at 350 billion additional annual investment over 2011-2020 [25]. With this considered. The Irish strategy of focusing solely on wind and solar energy should be reconsidered. especially as there is scope in the future for combined wave and offshore wind devices. Be it through shared infrastructure or synergy as outlined by [26].

4 A DIFFERENT FUTURE

Whilst ocean energy may be absent from the Irish energy strategy, it should be seriously considered as a viable option. The question becomes what technology is most viable. based on the current funding as shown below in Figure 3 and the aforementioned ocean potentials, it is expected that wave energy will be the general technology type. Although selecting a specific device to harness wave energy is based most likely on which is the first to commercial viability. Outlined in [50] is that the highest TRL level achieved through SEAI funding is level 7, which also used US department of energy funding to reach this stage. Whilst not explicitly stated this is referring to the 'ocean energy buoy' (OE buoy) project. an OWC class WEC [54]. Specifically, the OE buoy is a 500kW floating OWC [55], this class of WEC has a large potential due to not being limited to coastlines. And as the Irish ocean potential is as high as 100kW/m in winter as laid out in the very comprehensive analysis by [56] this style of device is certainly a viable option. Although, this is only if wave power reaches maturity, in this way it is useful to look at previous trends in other renewable energy such as wind which has experienced huge growth since its beginning stages in 1992 as shown in Figure 4 Currently there is no installed capacity for wave energy in Ireland. However, based on similar growth from wind, it could expected that when wave energy begins to be implemented it should rise quickly. This is evidently similarly expected for other renewables, as solar energy in Ireland contributes only 1% of renewable electricity yet is a large part of the 2030 plan alongside wind [46]. Furthermore, the pressures of increased public consciousness of climate change, and the growing severity of its effects may in-fact make this growth even more rapid than wind.to this end, a forecast of where ocean energy may be by 2030 if they can replicate the growth trends of wind, is shown below in Figure 5

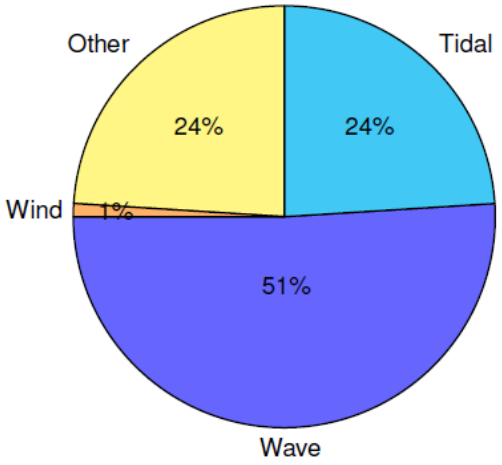

Figure 3: Grants issued for ocean sector by technology type [50]

4 A 2030 VISION

From Figure 5 ocean energy could have an installed capacity as high as 2500 MW by 2030 in Ireland. This potential is a significant portion of overall daily electricity demand. In order to achieve this goal, an investment in infrastructure is required to ensure that the west if Ireland is capable of supporting these ocean energy projects. Although as the SEAI plan to use offshore wind heavily in their 2030 plan, this is a required regardless. This further illustrates that ignoring Ocean energy despite the possibility of shared infrastructure is short sighted. Selecting a device that will be viable for the Irish environment is the largest challenge in achieving the development of these goals.

5 THE LIKELY CANDIDATE

As OWC systems seem to be the most likely candidate due to holding the highest TRL. It is prudent to discuss the advantages and disadvantages of this technology, and what may be the barriers to adoption

5.1.1 Advantages

OWC systems are versatile, with the ability to harvest wave energy while being coastal or, in the ocean (through floating structures), and more importantly, the electricity generating systems are not subject to the corrosive effects of ocean water. For coastal applications this reduces the maintenance difficulty as there is no need for heavy equipment to move a device from the ocean. And in any case maintenance should be required less frequently, as the actual turbine and its components will not be in the corrosive seawater environment.

5.1.2 Complications

OWC's bidirectional flow characteristics mean that traditional turbine designs cannot be used without air flow rectification systems. In place of this, with the sacrifice of some efficiency, a Wells turbine is commonly used. As such these devices hold a large data set for comparison. Although impulse turbines are heavily studied and hold advantages [12] at the cost of more difficult manufacture and analysis.

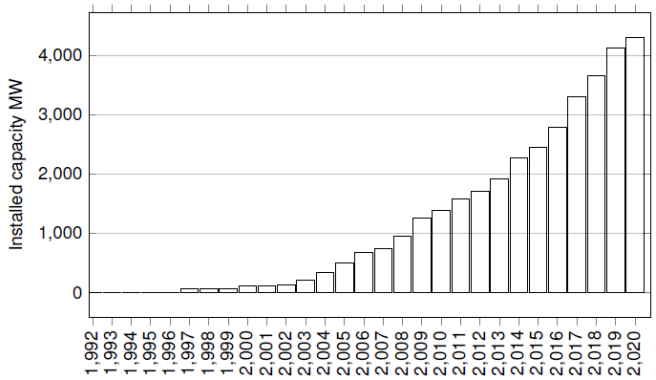

Figure 4: Wind installed capacity data from [30]

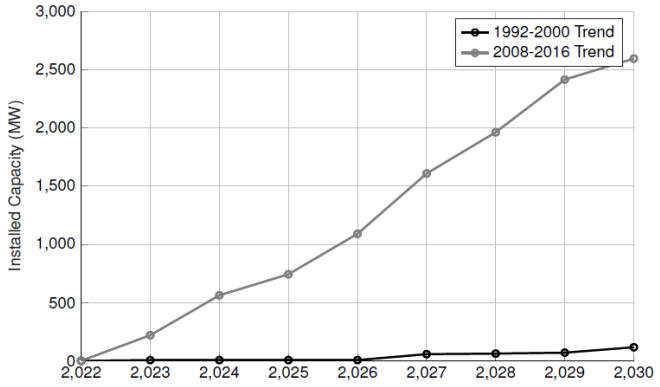

Figure 5: Ocean energy forecast from wind trends. Trends from [57]

6 CONCLUSION

In conclusion, Ireland holds great potential for ocean energy but unfortunately is likely to ignore it in favor of further wind and solar developments. One factor that may change this in favor of ocean energy developments is the adoption of a single technology that can be readily implemented. As of late this appears most likely to be in the form of an Oscillating water column, although reaching commercial viability is still a challenging prospect due to the need for additional funding of projects beyond the demonstration phase.

REFERENCES

[1] Roger H. Charlier and Loïc Menanteau. "The saga of tide mills". In: Renewable and Sustainable Energy Reviews 1.3 (1997), pp. 171–207. issn: 13640321. doi: 10 .1016/S1364-0321(97)00005-1. 5
[2] Thomas McErlean and Nroman Crothers. "HARNESSING THE TIDES : THE EARLY MEDIEVAL TIDE MILLS AT NENDRUM MONASTERY , STRANGFORD LOUGH". In: The Journal of the Royal Society of Antiquaries of Ireland137 (2007), pp. 165–167.
[3] David Ross. Energy from the waves. 1980. isbn: 0080267157.
[4] Judicael Aubry et al. "Wave energy converters." In: (2011). url: https://hal.archives-ouvertes.fr/hal-01156751.
[5] António F.de O. Falcão. "Wave energy utilization: A review of the technologies". In: Renewable and Sustainable Energy Reviews 14.3 (2010), pp. 899–918. issn: 13640321. doi: 10.1016/j.rser.2009. 11.003. [6] T. V. Heath. "A review of oscillating water columns". In: Philosophical Transactions of the Royal Society A: Mathematical, Physical and Engineering Sciences 370.1959 (2011), pp. 235–245. issn: 1364503X. doi: 10.1098/rsta.2011.0164.
[7] The European marine centre LTD. Wave devices: EMEC: European Marine Energy Centre. url: http://www.emec.org.uk/ marine-energy/wave-devices/.
[8] The European Marine Energy Center. Tidal devices : EMEC: European Marine Energy Centre. 2020. url: https : / / www.emec.org.uk/marine- energy/tidal-devices http://www.emec.org.uk/ marine - energy / tidal - devices/
[9] Tethys. Tidal | Tethys. url: https : / /tethys.pnnl.gov/technology/tidal
[10] European Commission. "Communication of the European Commission COM(2005) 627 final – The support of electricity from renewable energy sources". (2005).
[11] European Commission. Renewable Energy: Progressing towards the 2020 target. Tech. rep. 2010.
[12] Sustainable Energy Authority of Ireland. Renewables | Energy Statistics In Ireland | SEAI. url:https://www.seai.ie/data-and-insights/seai-statistics/key-statistics / renewables/ (visited on 01/12/2022).
[13] Department for Business Energy and Industrial Strategy. "UK Energy Brief in 2020". In: (2021). url: www . gov . uk/government / statistics / uk - energy - in-brief-2021.
[14] Angus Brendan MacNeil et al. Houseof Commons - 2020 renewable heat and transport targets - Energy and Climate Change Committee. Tech. rep. 2016
[15] EREC. "Mapping Renewable Energy Pathways towards 2020". In: European Renewable Energy Council (2011), p. 28.
[16] International Energy Agency. France 2021 - Energy Policy Review. Tech. rep. 2021.
[17] Instituto nacional de Estatística. The state of the environment 2020. Tech. rep. 2021. doi: 10.1179/isr.1985.10.4.376.
[18] RED eléctrica de España. "Year end forecast". In:(2021).
[19] The Sustainable Energy Authority of Ireland. Energy in Ireland 2021 report. Tech. rep. 2021. url: https : / / www . seai.ie/publications/Energy-in-Ireland- 2020.pdf.
[20] Marine Renewables Industry Association. "Submission to Public Consultation on Ireland's Draft National Energy and Climate Plan (NECP) 2021-2030". In: February 2019 (2019), pp. 2021–2030.
[21] Interreg North-west Europe. Ocean Energy and the Regions. Tech. rep. 2018, pp. 1–16.
[22] The Sustainable Energy Authority of Ireland. "Roadmap Introduction to the Wind Energy Roadmap to 2050 The development of renewable energy , including both offshore and onshore wind , is central to our energy policy ."
[23] Sustainable Energy Authority of Ireland.

"Review of funding supports to the Ocean Energy Sector" (2020).
[24] European Commission. "State aid : frequently asked questions concerning EU rules". In: 1998 (2008), pp. 6–10.
[25] European Commission. "Guidelines on State aid for climate, environmental protection and energy DRAFT".
[26] C. Pérez-Collazo, D. Greaves, and G. Iglesias. "A review of combined wave and offshore wind energy". In: Renewable and Sustainable Energy Reviews 42 (2015), pp. 141–153. issn: 18790690. doi: 10 . 1016 / j . rser . 2014 . 09 . 032
[27] Ocean Energy Systems. "WAVE ENERGY DEVELOPMENTS". In: (2021).
[28] Tony Lewis. Demonstration of the Ocean Energy (OE) Buoy at U.S. Navy's Wave Energy Test Site. Tech. rep. 2019, pp. 1–16.
[29] Sarah Gallagher et al. "The nearshore wind and wave energy potential of Ireland: A high resolution assessment of availability and accessibility". In: Renewable Energy 88 (2016), pp. 494–516. issn: 18790682. doi: 10.1016/j.renene.2015. 11.010.
[30] EirGrid. Wind-Installed-Capacities. url: https : / / www . eirgridgroup . com / site - files / library / EirGrid / Wind - Installed-Capacities.png
[31] Mohamad Kaddoura, Johan Tivander, and Sverker Molander. "Life cycle assessment of electricity generation from an array of subsea tidal kite prototypes". In: Energies 13.2 (2020), pp. 1–18. ISSN: 19961073. DOI: 10.3390/en13020456.
[32] Junqiang Xia, Roger A. Falconer, and Binliang Lin. "Impact of different operating modes for a Severn Barrage on the tidal power and flood inundation in the Severn Estuary, UK". In: Applied Energy 87.7 (2010), pp. 2374–2391. ISSN: 03062619. DOI: 10.1016/j.apenergy.2009.11.024. URL: http://dx.doi.org/10.1016/j.apenergy.2009.11.024.
[33] Aquaret. "Case Study : La Rance Barrage Technology Type Project Type / Phase". In: Aquaret December (2008).
[34] Greaves.Deborah and Gregorio Iglesias. Wave and Tidal Energy. Vol. 3. February 2004. 2011, pp. 53– 60. ISBN: 3904144987.
[35] Ant´onio F.O. Falcoã, João C.C. Henriques, and José J. Candido. "Dynamics and optimization of the OWC spar buoy wave energy converter". In: Renewable Energy 48 (2012), pp. 369–381. ISSN: 09601481. DOI: 10.1016/j.renene.2012.05.009.
[36] Manabu Takao and Toshiaki Setoguchi. "Air turbines for wave energy conversion". In: International Journal of Rotating Machinery 2012 (2012). ISSN: 1023621X. DOI: 10.1155/2012/717398.
[37] European Commission. "Communication of the European Commission COM(2005) 627 final - The support of electricity from renewable energy sources".
[38] European Commission. Renewable Energy: Progressing towards the 2020 target. Tech. rep. 2010.
[39] Sustainable Energy Authority of Ireland. Renewables Energy Statistics In Ireland—SEAI. URL: https: //www.seai.ie/data-and-insights/seai-statistics/key statistics/renewables/
[40] Department for Business Energy and Industrial Strategy. "UK Energy Brief in 2020". In: (2021). URL: www.gov.uk/government/statistics/uk-energy-in-brief-2021.
[41] Angus Brendan MacNeil et al. House of Commons – 2020 renewable heat and transport targets – Energy and Climate Change Committee. Tech. rep. 2016.
[42] EREC. "Mapping Renewable Energy Pathways towards 2020". In: European Renewable Energy Council (2011), p. 28.
[43] International Energy Agency. France 2021 - Energy Policy Review. Tech. rep. 2021.
[44] Instituto nacional de Estat´ıstica. The state of th environment 2020. Tech. rep. 2021. DOI: 10.1179/isr. 1985.10.4.376.
[45] RED el ´ ectrica de Espa˜na. "Year end forecast". (2021).
[46] The Sustainable Energy Authority of Ireland. Energy in Ireland 2021 report. Tech. rep. 2021. URL: https: //www.seai.ie/publications/Energy-in-Ireland-2020.pdf.
[47] Marine Renewables Industry Association. "Submission to Public Consultation on Ireland's Draft National Energy and Climate Plan (NECP) 2021-2030". In: February 2019 (2019), pp. 2021–2030. URL: www.oceanenergy-europe.eu.
[48] Interreg North-west Europe. Ocean Energy and the Regions. Tech. rep. 2018, pp. 1–16.
[49] The Sustainable Energy Authority of Ireland. "Roadmap Introduction to the Wind Energy Roadmap to 2050 The development of renewable energy , including both offshore and onshore wind , is central to our energy policy ." In: Wind Energy (2011), pp. 1–10. URL: http://www.seai.ie/Publications/Statistics_Publications/SEAI _2050_Energy_Roadmaps/Wind Energy_Roadmap.pdf.
[50] Sustainable Energy Authority of Ireland. "Review of funding supports to the Ocean Energy Sector".
[51] European Commission. "State aid : frequently asked questions concerning EU rules". In: 1998 (2008), pp. 6–10.
[52] European Commission. "Guidelines on State aid for climate, environmental protection and energy DRAFT".
[53] C. P´erez-Collazo, D. Greaves, and G. Iglesias. "A review of combined wave and offshore wind energy". In: Renewable and Sustainable Energy Reviews 42 (2015), pp. 141–153. ISSN: 18790690. DOI: 10.1016/ j.rser.2014.09.032..
[54] Ocean Energy Systems. "WAVE ENERGY DEVELOPMENTS". In: (2021).
[55] Tony Lewis. Demonstration of the Ocean Energy (OE) Buoy at U.S. Navy's Wave Energy Test Site. Tech. rep. 2019,
[56] Sarah Gallagher et al. "The nearshore wind and wave energy potential of Ireland: A high resolution assessment of availability and accessibility". In: Renewable Energy 88 (2016), pp. 494–516. ISSN: 18790682. DOI: 10.1016/j.renene.2015.11.010.
[57] EirGrid. Wind-Installed-Capacities. URL: https : / / www . eirgridgroup.com /

The development of hydrogen standards in Ireland

Niamh Conroy[1],
[1]National Standards Authority of Ireland, 1 Swift Square, Northwood, Santry, Dublin 9, Ireland, D09 A0E4
email: niamh.conroy@nsai.ie

ABSTRACT: Hydrogen gas is proposed as an alternative fuel for use in hard to decarbonise energy sectors in the transition to a net-zero carbon economy. Hydrogen is capable of being generated from renewable sources (green hydrogen) even though in the early stages of the transition, "blue" or "grey" hydrogen manufactured from reforming natural gas might be relied upon. To allow for the use of hydrogen gas in different energy segments, it must be delivered to the end-user either via new/existing transmission/distribution gas pipelines or via road transport as an intermediate step to a distribution point for consumption. In both cases, a number of standards must be developed or updated. This paper examines the history of how gas standards were developed in Ireland and summarises the current status of standards as they apply to hydrogen gas as a fuel. The paper then sets out the requirements for the development of standards for repurposing an existing distribution natural gas pipeline for use with hydrogen with a particular focus on civil and structural engineering matters, such as pipelines and pipe materials.

KEY WORDS: Hydrogen; standards; H_2; NSAI; ISO; CEN; GERG; IGEM.

1 INTRODUCTION

NSAI is Ireland's official standards body with responsibility for providing services for standardisation, conformity assessment and measurement. In 1996, the National Standards Authority of Ireland Act was passed. The NSAI formally came into existence in April 1997 and became Ireland's official standards body and a member of international and European standards bodies (ISO and CEN).

A Standard is defined by European Regulation (EU) 1025/2012 as: "a technical document designed to be used as a rule, guideline or definition". It is about establishing an agreed way of making a product, managing a process, delivering a service or supplying materials. Standards are voluntary specifications of good practice, and in the case of Gas Technical Standards, these specifications address the safe utilisation, distribution, and transmission of gas. As the national member of the international standards organisations, NSAI facilitates input to the development and publication of new standards through its consultative committee network and Irish representation on international standards committees. They operate in an open and transparent way to ensure that quality, safety and consistency are at the forefront of any new standard [1].

As the usage of hydrogen gas increases, the compliment of International, European and Irish Gas Standards will all require review, revision and, in some cases, whole new standards might be produced. In addition, a number of hydrogen experts from different sectors of society will be required to sit on the NSAI gas technical committees. This paper provides a brief history of the formation of the Gas Technical Standards Committees (GTSC), the evolution of European and Irish gas standards and the next steps required along the standards development journey.

2 IRISH GAS STANDARDS DEVELOPMENT

2.1 Formation and Evolution of the Gas Technical Standards Committees

The GTSC was established in 1982 to advise on what standards and codes of practice are necessary for products and processes used in the Irish gas industry with particular regard to safety. The GTSC initially set itself an ambitious programme to produce a complete set of gas industry standards suitable for Irish conditions. It achieved this as the first suite of public Standards were launched by the Minister for Energy in 1987. With the liberalisation of the gas market in 2000 (in adherence with the EU Gas Directive 98/30/EC), the work of the GTSC took on a new importance in providing the necessary checks and balances to ensure an efficient service to the public with due regard to safety. Article 5 of the Directive states that "Member States shall ensure that technical rules establishing the minimum technical design and operational requirements" are in place. The process of standardisation is an important function in the overall context of Gas Safety and open competition [1]. This had been greatly aided by the adoption of the European Gas supply standards. For example, with the launch of the CEN TC 234 EN standards in 2000, the Irish standards were brought in line with the CEN TC 234 EN suite of standards. Members of the GTSC were closely involved in the development of these standards on behalf of the Irish gas industry and the NSAI.

Throughout the years, the committees have evolved to meet the growing demands of industry, calling on various sectors of the industry to participate on committees as the need arises. The development of standards is largely done by industry itself with the assistance of the authorities whose role it is to represent public interest and safety. This process provides for the identification of potential hazards and workable solutions. The GTSC has established itself as the independent body for establishing and harmonising gas standards by a consultative process. Today, NSAI publishes as Irish Standards a large number of CEN standards relating to gas infrastructure. Hence

there is rarely any need now to refer to non-Irish standards, such as British Standards. It is important to note that the Institute of Gas Engineers and Managers (IGEM) standards are referred to occasionally where the need arises (e.g. IGEM SR.25).

2.2 Scope of the GTSC

The scope of NSAI/TC 01 Gas Technical Standards Committee (GTSC) covers all aspects of the supply and usage of natural gas, liquefied petroleum gas (LPG), liquefied natural gas (LNG), renewable gas (biomethane, bio LPG) and hydrogen as shown in Figure 1. The membership of the committee is composed of key stakeholders/collective bodies that provide an authoritative and representative voice or policy role in the gas sector.

GTSC members contribute their knowledge and expertise on a voluntary basis and advises the NSAI on what Irish standards and Codes of Practice are necessary for products and processes used in the gas industry, with particular regard to safety. The GTSC also supports the development of European (CEN) and International (ISO) gas related standards [1].

The role of the associated sub-committees is as follows:

- To advise the NSAI regarding Irish Standards and Codes of Practice necessary for the transmission, distribution and utilisation of natural gas, LPG, LNG, renewable gases (biomethane, BioLPG and hydrogen) with particular regard to safety and to make recommendations as required;
- To draft appropriate documentation including Standards, Codes of Practice, Amendments and Safety Recommendations as necessary;
- To ensure that interested parties are consulted in the drafting of these Standards and Codes of Practice;
- To liaise with similar bodies in other EU countries and in particular CEN (European Committee for Standardisation) and ISO (International Organisation for Standardisation); and
- To advise NSAI on how to vote on draft European and International Standards.

2.3 CEN/ISO Standards Development

ISO is an independent, non-governmental international organisation and officially came into existence in 1947. It has a membership of 165 national standard bodies. As ISO has members throughout the world as well as in Europe, it was not considered suitable to be responsible for drafting European standards. Furthermore, standards published by ISO are voluntary, not mandatory, for ISO members to adopt. For these reasons, the European Commission appointed CEN (the Comité Européen de Normalisation or European Committee for Standardisation) [3].

CEN was founded in 1961. The mission of CEN is to foster the economy of the European Union (EU) in global trading, the welfare of European citizens and the environment by providing an efficient infrastructure to interested parties for the development, maintenance and distribution of coherent sets of standards and specifications [4]. Benefits and opportunities have been achieved because the CEN TC 234 suite of standards have been adopted in all the CEN member countries. This has provided a common understanding and also a common 'language' for gas infrastructure design, maintenance and operations in Europe.

CEN's work of preparing standards is carried out by technical committees (TCs). CEN TC 234 oversees the development of the gas infrastructure standards. Over the years, CEN TC 234 has set up many working groups and task forces. These have involved mostly voluntary input from a large number of gas industry professionals – from consultants, contractors and research organisations and academia. Of relevance for the hydrogen industry is the recently formed WG 13 focusing on pre-normative research required for accommodating hydrogen blends onto the gas network. This study was commissioned by the European Commission and is being completed by the European Research Group (GERG).

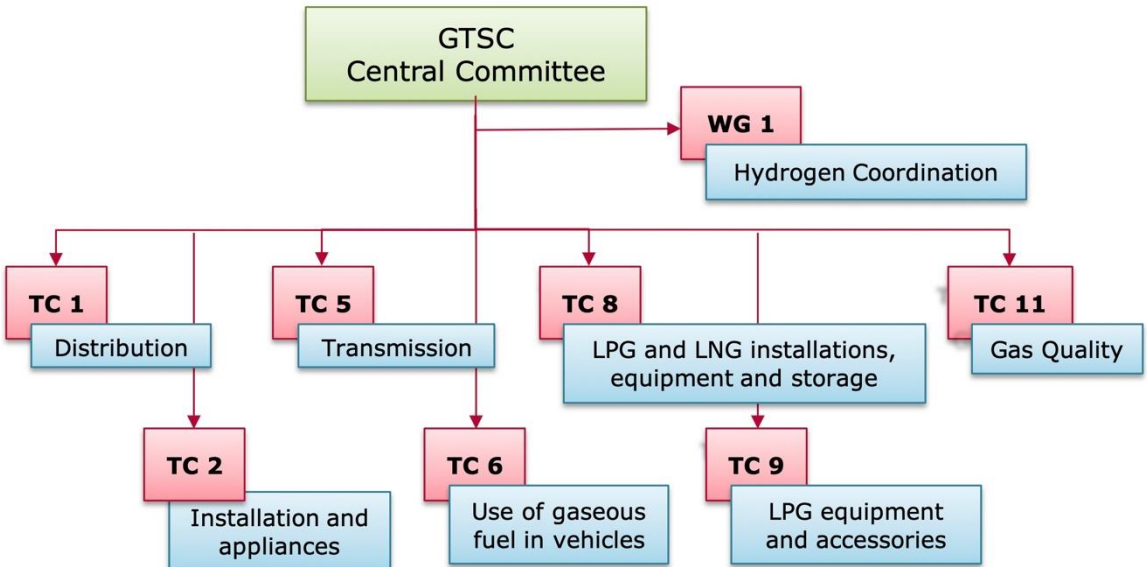

Figure 1. GTSC Structure [2]

2.4 EN Standards and Vienna Agreement

Once a standard is published by CEN as an EN, all the member bodies of CEN must adopt it as their national standard with national annexes if required and withdraw any competing national standards. CEN TC 234 suite of standards are the same standards used in all CEN countries. In contrast, standards published by ISO are not mandatory, unless they are adopted by CEN and published as EN ISO standards.

In order to avoid duplication of standardisation work, it was decided in 1991, under the Vienna Agreement, that when CEN and ISO both require a standard in a particular area, they would cooperate and not compete. There is ongoing collaboration between CEN and ISO in the preparation of various standards to accommodate the inclusion of hydrogen blends.

2.5 Irish Gas Standards

Table 1 shows the full suite of Irish gas standards produced by each of the Gas Technical Standard Committees.

Table 1. Irish Standards produced by GTSC committees

GTSC Committee	Irish Gas Standards Published
NSAI GTSC TC 1 Gas Distribution	I.S. 329, S.R. 12007-5, I.S. 370, I.S. 822
NSAI GTSC TC 2 Gas Installations and appliances	I.S. 813, I.S. 820. SWIFT 8
NSAI GTSC TC 5 Gas Transmission	I.S. 328
NSAI GTSC TC 6 Use of Gaseous Fuels in Vehicles	
NSAI GTSC TC 11 Gas Quality	

2.6 Hydrogen vs Natural Gas

At a high level, the properties that hydrogen and natural gas have in common are detailed in Table 2 and the differences between them are listed in Table 3.

Table 2. Common properties of hydrogen and natural gas

Characteristic	Methane (Natural Gas)	Hydrogen
Gaseous	Yes	Yes
Colourless	Yes	Yes
Odourless	Yes	Yes
Explosive	Yes	Yes
Flammable	Yes	Yes
Corrosive	No	No
Toxic	No	No

More interestingly, the properties that differ contribute to the biggest challenges that need to be overcome for widespread blending of hydrogen into a gas network. These are detailed in Table 3.

Table 3. General differences in properties between hydrogen and natural gas

Parameter	Methane (Natural Gas)	Hydrogen
Relative Density (air=1)	0.55	0.07
Flammability limits (Mol,-%)	4,4-17	4,0-77
Ignition energy (mJ)	0.26	0,0017
Combustion energy (MJ/m^3)	40/36	13/11
Wobbe number (MJ/m^3)	Upper: 54 Lower:48	Upper:48 Lower:41
Gross calorific value (kJ/mol @ 20°C)	891	286
Flame colour	blue	colourless
Molecular mass (g/mol)	16	2
Molecule size (pm)	220	75
Molecule size (pm)	220	75
Infrared absorption	yes	no
Joule-Thompson coefficient (K/bar)	0,4	-0,03
Sound velocity (m/s)	338	1203

The key differences in the properties of NG/H blends compared to NG include a slight increase in the probability of ignition, a slight increased leakage rate, an increase to hazardous areas and an increased flammability range. It is widely documented that transporting blends of 10% hydrogen in existing natural gas pipelines will not pose technical issues. However, there is large body of work being undertaken to understand the challenges that will face the industry at blends greater than 10% [5-9]. To develop standards, research studies and trials which address the scope of the existing standards and existing network are required. The majority of the research studies to date are to support specific trials [6,7]. A coordinated industry approach, rather than project specific research is required to achieve this.

2.6.1 Specific Material Issues

There are some common themes for knowledge gaps for all components across the distribution and transmission networks before revisions to standards can be completed. These knowledge gaps, including materials suitability, leak tightness and impact of increased flow in hydrogen (required to deliver the equivalent energy in natural gas), are listed in Table 4.

Table 4. List of relevant components and knowledge gaps

Topic	Knowledge Gap	Pre-Normative Research required
Valves	Tightness	Develop an understanding for hydrogen behaviour in regards to valve tightness and its long term effect on their materials
Meters	Flow calibration standards	Develop calibration methods for hydrogen blends and validate using accuracy tests with renewable gases and a reliable inter-comparison test campaign
Pressure regulators	Test data is very limited for blends more than 30 % for distribution network pressures and almost no test data available or blends as well as 100 % H_2 for transmission network pressures	Field test projects for pressures higher than 8 bar as well as for high blend H_2 at distribution network pressures
All components	Longer term testing of components in existing high pressure gas networks	Longer term testing to understand impact of operation on hydrogen mixtures in real networks

2.6.2 Implications for End Users (Mobility)

Focusing on one particular end user sector – Compressed Natural Gas vehicles (CNG). CNG vehicles are supplied from the existing natural gas distribution network in Ireland. There are several challenges here if H_2 blends are to be used widespread on the network and H_2 is to be used in CNG vehicles. The number of gaps of knowledge is high and several experimental studies are necessary before considering a potential increase of the 2% limit in standards and regulations [7]. Given the absence of consensus on the impact of hydrogen addition in CNG and the amount of unknown information, it is currently unclear if the development of H2/CNG fuel will need a modification of the available standards and regulations on both vehicles and fuels or if dedicated ones will be needed. It is thus very much advised to perform systemic and in-depth studies on this subject, as well as investigating on mitigation measures that can be taken to reduce the impact of H_2 over the different NGVs parts and operations that are subject to concerns.

2.7 Implications for European/International/Irish Standards

The existing standards of CEN/TC 234 can be amended to cover natural gas infrastructure used for hydrogen services. For some aspects, new CEN deliverables are needed.

The current EN gas standards are being reviewed for the implication for hydrogen blending by the following CEN committees. These are listed in Table 5.

Table 5. Standards under review and responsible CEN committees

CEN TC234 Working Group	Gas Standards requiring revision for the inclusion of hydrogen
WG1 (Gas Installation in buildings)	EN 1775
WG2 (Pipelines with MOP <=16 bar)	EN 12007 and EN 12327
WG3 (pipelines with MOP >16 bar)	EN 1594, EN 12732
WG5 (Gas Measuring)	EN 1776
WG6 (Gas Pressure Regulation)	EN 12186 and EN 12279
WG 7 (Gas Compressor)	EN 12583
WG 8 (Industrial Piping)	EN 15001
WG 10 (Service Lines)	EN 12007-5
WG 11 (Gas Quality)	EN 16727

2.8 Implications for GTSC

Currently, NSAI has several standards committees working in climate action related areas such as wind energy, solar energy, alternative fuels in transport, electrification of heat and transport, and the circular economy. More recently, the area of hydrogen energy is one in which NSAI is supporting new cross-disciplinary standards work. In June 2021, NSAI and Gas Networks Ireland started a two-year secondment to work on standardisation activities relating to hydrogen. Recognising the fuel as a relatively new area with great potential to be adopted nationwide, a Hydrogen Standardisation Expert was appointed. The key activities of the Hydrogen Standardisation Expert is to follow all international work and contribute to national areas of interest.

As well as participating in the GTSC sub-committees, the Hydrogen Standardisation Expert follows several international committees related to hydrogen standardisation activities, listed in Table 6.

Table 6. Related CEN and ISO hydrogen committees

Committee Reference	Committee Title
ISO/TC 197	Hydrogen Technologies
CEN/TC 234	Gas Infrastructure
CEN/CLC/JTC 6	Hydrogen in Energy Systems

2.8.1 Formation of Hydrogen Working Group

A Hydrogen working group was formed, which reports directly into the GTSC Central Committee. This working group provides a dedicated platform for the Hydrogen Standardisation Expert to update members on the ongoing hydrogen related activities and allow for discussion on this specific area. The

working group consists of the Chairs of each GTSC sub-committee and a number of members with an interest or expertise in hydrogen.

The current activities of the working group include:

- Monitoring the progress of the EC-CEN/GERG Pre-normative research project on hydrogen/natural gas blends where information is identified for circulation and discussion with relevant GTSC sub-committees, and
- Information gathering from Ireland relating to H_2 projects and studies, including engagement with stakeholders working in area of hydrogen and recruitment of experts onto the appropriate GTSC sub-committee.

3 DEVELOPMENT OF HYDROGEN STANDARDS

This paper now moves to consider the development of standards for repurposing an existing natural gas distribution pipeline for natural gas/hydrogen blends. The focus is largely on civil and structural engineering matters, such as pipeline and pipe materials. Table 7 (see end of paper) summarises the issues and concerns and the requirements that must be understood for the development of a hydrogen standard for repurposing of an existing distribution pipeline (PE/steel) for natural gas/hydrogen blends (<= 20% hydrogen blends). It is developed using the latest publicly available information and may include some conservative requirements which further research may deem not necessary. There are a number of questions here that research results will be required in order to formulate more guidance for Gas Operators to follow.

There are a number of factors at play which will inform and guide an overall roadmap for adapting existing irish gas standards to accommodate the blending of hydrogen. A hydrogen strategy for Ireland currently in development will provide a scope and timelines for how hydrogen will form part of the decarbonisation journey, the progression and completion of pre-normative research will address gaps required for standardisation and sufficient hydrogen expertise on the GTSC committees will all be key to the roll out of a suite of revised and new gas standards. Ireland and indeed NSAI are at the start of this journey.

3.1 Pre-Normative Research

Accepting hydrogen into the natural gas network requires input from many gas TCs at CEN, i.e. CEN/TC 234 and part particularly from the manufacturers of essential components, e.g. valves, gas pressure regulators, gas meters, safety control devices, leak detection devices, and many more. Many of these manufacturers are assessing the potential impact of hydrogen on existing components in natural gas service. Co-operation with these other CEN and ISO TCs for various essential components and applications will be necessary to ensure that projects to introduce hydrogen have all the essential elements of the gas chain fully co-ordinated into the plan. The positive co-operation of the component manufacturers will be particularly important. In the transition scheme to hydrogen, there is a large body of knowledge and experience available from the hydrogen industry for gas production and use. The long-established safety requirements in this sector will aid the amendment of natural gas standards and codes of practice and the development of any new standards. The European Research Group (GERG) is producing a hydrogen research roadmap which identifies the key gaps in knowledge for standardisation and timelines for addressing such gaps. There is potential here for partnering organisations/research bodies with knowledge in specific areas to work collaboratively together and receive European funding. The potential for Irish research in this topic is vast [10].

4 CONCLUSIONS

The Gas Technical Standards Committees have evolved over the years as the gas industry has evolved and they will continue to evolve as the gas industry adapts to meet the decarbonisation challenges that lie ahead. Engagement with hydrogen experts in other industries will be essential to ensure fully functioning Irish gas standards are produced. Depending on the percentage of hydrogen blend, there is a large body of pre-normative research required to inform updates to a number of standards. Through the NSAI facilitating collaboration between Ireland's policy makers, researchers and industry experts, the Authority can support Ireland's pursuit of climate neutrality by getting 'ahead of the curve' and ensuring best international practice through standards.

ACKNOWLEDGMENTS

The author acknowledges colleagues in NSAI, Gas Networks Ireland, GERG and IGEM who contributed to this paper.

REFERENCES

[1] NSAI GTSC Annual Activity Reports (1985-present), NSAI Archives.
[2] NSAI 2021 Annual Activity Report.
[3] ISO Website, ISO - Standards (May 2022, date last accessed).
[4] CEN Website CEN (May 2022, date last accessed).
[5] European Gas Research group website Removing the technical barriers to use of hydrogen in natural gas networks and for (natural) gas end users. - Gerg (May 2022, date last accessed).
[6] HyDeploy website. https://hydeploy.co.uk (21 February 2019, date last accessed).
[7] Isaac, T. (2019), HyDeploy: The UK's First Hydrogen Blending Deployment Project, Clean Energy.
[8] Altfeld, K, and Pinchbeck, D. (2013), HIPS project - Admissible hydrogen concentrations in natural gas systems, GERG website.
[9] Decarbonising the gas value chain – Challenges, solutions and recommendations, 2022, ENTSOG.
[10] Ekhtiari, A, Flynn, D, and Syron, E. (2020), Investigation of the Multi-Point Injection of Green Hydrogen form Curtailed Renewable Power into a Gas Network, University College Dublin.

Table 7. Requirements for the development of a hydrogen standard for repurposing an existing distribution pipeline.

	Issues	Considerations	Standard Requirements	Research Required
Introduction	What's required to facilitate the repurposing of a distribution natural gas network to hydrogen	Consider amendments being made in various CEN/IGEM standards Identify where modifications are required for Irish Gas Standards	All under review	
Legislation	Primary Legislation Gas Act Pressure Systems Regulations	Gas Quality Impact on material properties Control of Noise (higher velocities in NG/H_2 pipelines)		-Impurities resulting from the hydrogen production process -Release of impurities from existing network -Noise studies - Odorisation
Impact of Hydrogen Properties	Hydrogen Properties: Small Molecule Low Density High Buoyancy Low volume energy density High Mass energy density	Hazards: -Higher probability of ignition -Faster dispersion -Explosivity -Flame detection -High volume leak rate	Hazardous Area Venting Purging	
Material	Impact on materials: -Diffusion -Embrittlement -Joint Leakage	Probability of failure Increase pressure	Failure Data	Legacy Materials: -Cast/ductile iron -Mechanical joints -Leakage control
Design Assessment	Flowrate Demand Capacity	Assess the technical capacity of existing pipeline to transport hydrogen Determine new maximum allowable operating pressure and allowable pressure fluctuations		-Challenge design methodology of ASME B21:12 Quantitative Risk Assessment -Failure Mode: -Leak size -Failure Rate data -Consequences -Dispersion -Ingress into buildings -Probability of ignition -Explosion
	Ingress into building Detection Fatalities	Emergency Response Proximity to Buildings		
Integrity Management	-Existing Damage and Repairs -Repair Methods Isolations -Connections and Replacements	Assess current condition of existing network: -Isolations -Repair Methods -Live Welding -Cathodic Protection Produce pipeline design and integrity assessment		-Assessment of historical repair methods -Assessment if stopple, mechanical line stop, squeeze off methods suitable -Assessment of sealant, mechanical joint repairs, encapsulation methods, leak clamps -Investigate the feasibility of using current In-Line Inspection tools in various H_2NG mixtures
Operations	Equipment functionality and operability assessment	Non Routine Operations requirements	ATEX Classification	Trials required to assess turbulent flow, including noise, vibration, dust and debris

Modeling the effects of Construction Risks on the Performance of Oil and Gas Projects in Developing Countries: Project Managers' Perspective

M.K.S. Al-Mhdawi[1], Alan O'Connor[2] , Mario Brito[3], Abroon Qazi[4], H.A. Rashid[5]
[1,2] Department of Civil, Structural and Environmental Engineering, Trinity College, University of Dublin, Ireland
[3] Centre for Risk Research, University of Southampton, UK
[4]School of Business Administration, American University of Sharjah, Sharjah, United Arab Emirates
[5]Departement of Civil Engineering, Al-Nahrain University, Iraq

Email: almhdawm@tcd.ie, alan.oconnor@tcd.ie, M.P.Brito@soton.ac.uk, aqazi@aus.edu, hateem.a.rasheed@nahrainuniv.edu.iq

ABSTRACT: Oil and gas (O&G) construction projects are considerably prone to risk due to their complex nature, environment, and the involvement of numerous stakeholders. Additionally, the increase in global energy consumption makes it imperative for decision-makers to assess O&G risks and understand how they impact project performance (PP). This research seeks to (1)identify and assess the level of riskiness of the key risks facing O&G construction projects by considering the case of Iraq; and (2)capture the effects of O&G risks on construction PP from project managers' perspective. To achieve this, a mixed-method approach was adopted. First, we identified O&G project risks through a focus group session with six Iraqi project managers. Second, we rated the level of riskiness of the identified risks and their impact on PP by administrating a survey to 75 experts. Third, we quantitatively analyzed the identified risks under fuzzy-analytical hierarchy process environment. Fourth, we quantitatively analyzed the effects of the identified risks on PP under structural equation modelling environment. The findings show that the most significant O&G risks are poor communication, skilled workers shortage, unstable security, political instability, and contractor bankruptcy. Furthermore, the results of the SEM analysis show that management risks have the strongest effects on PP, followed by legal risks, financial risks, technical risks, and logistics risks. The findings of this investigation might be of interest to O&G decision-makers, as they offer insight into how these risks may affect PP. This should facilitate the development of mitigation strategies in the early stages of the project.

KEY WORDS: Oil and gas, project performance, risk management, developing countries

1 INTRODUCTION

Oil and gas (O&G) construction projects are complex and risky due to their dynamic environment, unique nature, complex technology, remote geographical locations, and involvement of numerous stakeholders and must adhere to a tight schedule and budget. There are numerous risks associated with O&G construction projects, including social, political, financial, and technical risks, as well as those associated with natural disasters. Understanding the risks associated with the energy sector is not only vital for the construction sector, but also for the upstream and downstream oil and gas sub-sectors [1].

Iraq, as a case study of oil-producing developing countries, is the fifth-largest oil producer in the world and the second-largest oil producer in OPEC. It contributes to approximately 65% of the country's gross domestic product (GDP), as well as, over 90% of its public income. Its importance makes it essential for the financial stability of the country, the vitality of the economy, and the ongoing construction and reconstruction efforts. The Iraqi government is therefore under considerable pressure to ensure that construction projects are completed on schedule, within the estimated budgets, and with the least amount of uncertainties and risks. Unfortunately, the construction sector in Iraq is not as advanced in assessing and managing risks as it is in developed countries [2]. This is due to management challenges such as lack of expertise in using modern technology for construction project management, and lack of awareness of risk management potential benefits, insufficient risk management resources, and insufficient familiarity with risk management processes. Along with the project management challenges, the country's ill security profile, fluctuating political conditions, and economic instability had resulted in a decline in petroleum prices on the global market. These challenges, in turn, have a continuing effect on the performance of the construction sector, particularly for critical infrastructure projects like O&G projects leading to cost deviation, failure to meet the expected work quality, and schedule delays. A handful of studies have investigated the impact of O&G risks on the construction sector. For example, Thuyet et al. [3] proposed strategies to address the key O&G construction risks in Vietnam in terms of their impact on project objectives. Al-Sabah et al. [4] evaluated the impact of O&G construction risks on project cost, schedule, and company performance in the Arabian Gulf region from the perspective of multinational architecture, engineering, and construction firms. Furthermore, Kassem et al. [5] assessed the level of impact of the critical risks facing Yemen's O&G construction projects in terms of their impact on project success. To the best of our knowledge, no study has examined the impact of O&G risks on construction projects' performance from the perspective of project managers. This research thus attempts to address the following research question: "What are the key risks facing the Iraqi O&G construction sector, and how do these risks affect project performance (PP)?" To address this

research question, we begin by identifying the key O&G construction risks in Iraq. Then we outline our proposed analytical methods to quantify the level of riskiness of the identified risks and their effects on PP under Fuzzy-Analytical Hierarchy Process (FAHP) and Structural Equation Modelling (SEM) environments. Finally, we discuss the outputs of the assessment models, their implications, suggestions for future research, and research limitations.

2 METHODOLOGY

In this study, we used a multi-phase methodology to achieve the research objectives. Details on each one of the implemented phases are presented in the following subsections.

2.1 Phase One: Data Collection

2.1.1 Focus Group Session

In this study, we held one focus group session with six experienced project managers working on O&G construction projects in Iraq to (1) identify the key O&G construction projects risks; (2) identify the key indicators of project performance; and (3) develop the hypothesized relationships between O&G construction risks and project performance. We chose this method of data collection since there have been few studies that examine O&G construction risks both internationally and locally (in Iraq). Moreover, this method offers the advantage of exploring and understanding phenomena and situations more deeply and has been extensively utilized in previous studies to identify risks and challenges associated with engineering and construction management [6].

2.1.2 Structured Questionnaire Survey

In this study, we developed a structured survey to (1) assess the level of riskiness (i.e. weights) of O&G risks; and (2) examine the effects of O&G risks on the performance of O&G construction projects. There were four sections in the questionnaire survey. The first section precedes the main body of the survey, and it sets forth the objectives of this study. In the second section, respondents provided demographic information, which comprised information about their working sector, their experience, and their educational background. The third section compared the values (i.e., relative weights) of each risk category and it risks with other risk categories and their risks in a set of pair-wise comparison matrices. Lastly, the four section examined the respondents' perceptions about the effects of O&G risks on project performance. To this end, 75 survey forms were distributed to project managers working on O&G construction projects in Iraq.

2.2 Phase Two: The Development of Risk Analysis Model

2.2.1 Background

Analytical Hierarchy Process (AHP) is one of the most widely used methods for multi-criteria decision-making developed by Saaty [7] to address complex decision problems. In this method, factors are categorized into groups and levels, and then weighted and prioritized accurately and consistently. This method is used to derive ratio scales from paired comparisons, both discrete and continuous. These comparisons can be made using actual measurements or a scale that reflects the relative strength of feelings or preference. Its key benefit resides in its ability to verify and decrease the inconsistencies in expert judgments; it provides a comprehensive view of the complex relationships arising from an event, and it examines the spread of influence from more critical to less critical factors [8]. Although AHP is widely used for multi-criteria decision making problems, particularly when qualitative assessment is needed, it involves subjectivity in pairwise comparisons and thus vagueness type uncertainty resulting from a lack of information or conflict of opinions dominates in this process. To address the deficiency of AHP, Fuzzy Sets Theory (FST) is integrated with AHP to capture this type of uncertainty. This integration was developed proposed by Buckley [9].

FST was developed by Zadeh [10] in the 1960s and has since become a major tool for analyzing and solving problems involving uncertain parameters. The value of FST lies in its ability to formalize and deal with human knowledge and uncertainties in decision-making. FST is used to handle complex and poorly defined problems as a result of a lack of precise and complete information that characterizes the real-world situation [8]. Further, Alhumaidi [11]stated that the use of FST does not only deal with incomplete and imprecise data, but also takes into account the vagueness and subjectivity inherent in linguistic terms. In contrast to numerical variables, linguistic variables have values that are expressed as sentences or words rather than as numbers.

2.2.2 Risk Analysis

In this section, we describe the methodological steps used to analyze the level of riskiness of the identified O&G construction risks under the FAHP environment (adapted from Li et al. [12]). **First**, we structured the elements of the problem into a three-level hierarchy. The first level is the target (i.e., the analysis of O&G risks). The second level is the criteria (the categories of O&G risks). Finally, the third level is the sub-criteria (i.e., O&G risks). **Second**, we administrated a structured survey to 75 Iraqi construction experts to conduct pairwise comparison of risks using fuzzy numbers (refer to section 2.1.2).
Third, we constructed a set of judgment matrices after synthesizing the experts' judgments. **Fourth**, we used the Eigen value method to determine the eigenvector or weighting vector for each pair-wise matrix. **Fifth**, we computed the consistency ratio for each of the developed matrices and the overall inconsistency for the hierarchy using Eq. (1) and Eq. (2). A CR of 10% or less indicates a consistent and valid matrix, and if it exceeds this threshold, the matrix is inconsistent and should not be further analyzed.

$$CR = \frac{CI}{RI} \quad (1)$$

$$CI = \frac{\lambda max - n}{n-1} \quad (2)$$

Where *CR* is the consistency ratio; *RI* is the consistency index of a pair-wise comparison matrix (obtained from Table 1); λmax is the maximum eigenvalue; n is the number of criteria.

Table 1. Consistency Index

n*	2	3	4	5	6	7	8	9	10
RI	0	0.58	0.90	1.12	1.24	1.32	1.41	1.45	1.49

Sixth, the weighting of the fuzzy matrixes was calculated using Eq. (3) and fuzzy arithmetic operations [11, 13].

$$\tilde{w}_{x_i} = \sum_{i=1}^{m} M_x^i \otimes \left[\sum_{i=1}^{m}\sum_{j=1}^{m} M_x^{i,j}\right]^{-1},\ i,j = 1,2,3,\dots,m \quad (3)$$

Where $\tilde{w}_{x_i}$ is the fuzzy weighting of the ith risk factor; m is the number of risk factors; M_x^i is the *i*th row of M_x; $M_x^{i,j}$ is the *i*th row and *j*th column of M_x.

Seventh, we calculated the composite fuzzy weighing vector of each risk factor using Eq.(4)

$$\tilde{W}_{RS_t} = \tilde{w}_{S_t} \otimes \tilde{W}'_{RS_t},\ t = 1,2,3,\dots m \quad (4)$$

Where $\tilde{W}_{RS_t}$ is the composite fuzzy weighting vector of the hierarchy criteria level; $\tilde{w}_{S_t}$ is the the fuzzy weighting of the criteria level;$\tilde{W}'_{RS_t}$ is the local fuzzy weighing vector of the sub-criteria level.

Eighth, since a fuzzy number consists of an interval of real numbers, comparing the fuzzy weighting of each risk factor may not produce reliable results. Consequently, we defuzzified the fuzzy weightings using α and β indices. The α index reflects the experts' knowledge and experience (i.e., understanding and familiarity with the risks involved), whereas the δ index reflects their risk taking attitude. A scale of six grades was used to represent the level of familiarity that experts had with the identified O&G risks. These grades were as follows: not familiar, low familiarity, medium familiarity, high familiarity, and very high familiarity, with the corresponding ratios of 0, 20%, 40%, 60%, 80%, and 10%, respectively.

Assuming *Y*= (x_1, x_2, x_3), the fuzzy interval for triangular membership function (x_1, x_3) will reduced to $[x_1^\alpha, x_3^\alpha]$ (refer to Eq. 5 and 6).

$$x_1^\alpha = x_1 + \alpha(x_2 - x_1) \quad (5)$$

$$x_3^\alpha = x_3 - \alpha(x_3 - x_2) \quad (6)$$

If the α value is equal to 1, this indicates that the experts are most experienced and confident in their evaluation, and the fuzzy interval will then be reduced to the crisp value x^2. In contrast, if the α value is equal to zero, then this indicates that the experts have the least experience and confidence in their judgment. The crisp weighting of the risk factors was computed by using Eq. (7)

$$x = \delta\, x_3^\alpha + (1 - \delta\,)x_1^\alpha \quad (7)$$

To this end, the average α was 0.83, suggesting that respondents had a high level of experience evaluating risks. Further, the δ was 0.5, reflecting the neutral risk attitude of the study experts.

2.2 Phase Two: The Development of Impact Assessment Model Under SEM Environment

In this research, we used Structural Equation Modelling (SEM) to analyze the relationships between the identified O&G construction risks and project performance. In contrast to other techniques like least square regression, logistic regression, and log-linear modeling, SEM has many advantages, such as estimating and evaluating the entire conceptual model instead of just testing individual hypotheses. During the focus group session, project managers identified the indicators of project performance, which were then used to develop the hypothesized model. Following the development of the hypothesized relationships among the constructs (i.e., O&G risks and project performance indicators), we administered a structured questionnaire survey to 75 Iraqi project managers as described previously in section 2.1.2. The survey output was analyzed using PLS-SEM by Smart PLS software package V. 3.

3 RESULTS

3.1 Profile of the Focus Group Participants

As mentioned in Section 2.1.1 of the research methodology, we conducted one focus group session with six Iraqi project managers. The session lasted 3 hours and took place in April 2022. The questions were grouped into three themes. The first theme focused on the respondents' role in construction, their working experience, and their educational background. The second theme focused on the identification and classification of the key O&G construction risks. Finally, the third theme investigated the respondents' perceptions about the impact of the O&G 19 risks on project performance. The profile of the focus group participants is presented in Table 2.

Table 2. Profile of Focus Group Participants

Number of Group Participants	Years of Experience	Education Level		
		BSc	MSc	PhD
Expert 1	17	1	-	-
Expert 2	22	1	-	-
Expert 3	19	-	1	-
Expert 4	26	-	-	1
Expert 5	16	1	-	-
Expert 6	20	-	-	1

3.2 Profile of the Survey Respondents

In total, 75 survey forms were administered online to O&G construction project managers in Iraq. Out of the 75 administered surveys, 63 were returned. However, only 56 responses were completed and considered for further analysis. Table 3 outlines the distribution of respondents among the public and private construction sectors, their range of experience, and their educational qualifications.

Table 3. Profile of survey respondents

	Category	Distribution (%)
Working Sector	Public Sector	19
	Private Sector	81
Range of Experience	1-5 Years	2
	6-15 Years	34
	16-25 Years	46
	>25 Years	18
Educational qualifications	BSc degree	71
	MSc Degree	21
	PhD degree	8

3.3 O&G construction risks and their level of riskiness

In this research, we identified and validated a set of O&G risks through a focus group session with key construction project managers in Iraq. To this end, the 47 identified risks were categorized under two categories, namely external risks and internal risks. The internal risks were categorized into five sub-categories, namely financial risks, legal risks, political risks, social risks, and environmental risks. The external risks, on the other hand, were categorized into six sub-categories, namely technical risks, logistics risks, zoning risks, human risks, design risks, and management risks. The identified O&G risks categories, sub-categories, and their risks are in columns 1 to 3 of Table 4.

In total, 22 reciprocal matrices were created to assist the respondents in performing pair-wise comparisons of the hierarchy's criteria and sub-criteria levels. Consistency ratios were computed to confirm the consistency of the experts' assessments throughout all reciprocal matrices. In the following subsections, we summarize the most significant O&G risks according to their weights (*W*) and rankings (*R*) as determined by the FAHP analysis (refer to columns 4 and 5 of table 4).

In the financial risks subcategory (*CR*=0.0726 <0.1), the most significant risk was contractor bankruptcy (*W*=0.68; *R*=5). In the legal risks sub-category (*CR*=0.0563<0.1), the most significant risk was bribery and corruption (*W*=0.64; *R*=7). In the political risks sub-category (*CR*=0.069<0.1), the most significant risk was unstable security (*W*=0.79; *R*=3). In the social risks sub-category (*CR*=0.035<0.1), the most significant risk was disturbance to local residence (*W*=0.39; *R*=32). In the environmental risks sub-category (*CR*=0.062<0.1), the most significant risk was pollution (*W*=0.58; *R*=11). In the technical risks sub-category (*CR*=0.020<0.1), the most significant risk was the use of defective materials (*W*=0.53; *R*=16). In the logistics risks sub-category (*CR*=0.072<0.1), the most significant risk was skilled workers shortage (*W*=0.82 ;*R*=2). In the zoning risks sub-category (*CR*=0.059<0.1), the most significant risk was remote site location (*W*= 0.62; *R*=8). Moreover, in the human risks sub-category (*CR*=0.0437<0.1), the most significant risk was construction site deaths and serious injuries due to poor safety measures (*W*= 0.43 ;*R*=27). Furthermore, in the design risks sub-category (*CR*=0.0812<0.1), the most significant risk was design delays (*W*= 0.65; *R*=5). Finally, in the management risks sub-category (*CR*=0.062<0.1), the most significant risk was poor communication (*W*= 0.83; *R*=1).

Table 4. Identified O&G construction risks and their level of riskiness

Category	Sub-category	Risk	*W*	*R*
	Financial risks	Insufficient contingences	0.42	28
		Inflation	0.29	43
		Contractor bankruptcy	0.68	5
		Resource monopolizing	0.49	20
		Economic instability	0.37	36
		Currency rate fluctuation	0.59	10
		Materials and Equipment price escalation	0.52	17
Internal Risks	Legal risks	Lack of clarity regarding contractual obligations	0.64	7
		Delays in resolving disputes	0.56	13
		Change in laws	0.35	38
		Bribery and corruption	0.61	9
	Political risks	Political instability	0.73	4
		Unstable security	0.79	3
		Appropriation and/or confiscation	0.36	37
	Social risks	Land acquisition problems	0.28	44
		Tribal conflicts	0.35	38
		Disturbance to local residence	0.39	32
	Environmental risks	Adverse weather conditions	0.42	28
		Natural disasters	0.27	45
		Pollution	0.58	11
		Construction debris	0.41	30
	Technical risks	Changes in the specification of materials	0.48	22
		The use of defective materials	0.53	16
		Poor constructability	0.39	32
		Equipment breakdown	0.44	26
		Inadequate QS/QC	0.3	42
	Logistics risks	Skilled workers shortage	0.82	2
		Materials and equipment shortage	0.38	35
		Lack of transportation facilities	0.47	24
	Zoning risks	Unforeseen site conditions	0.23	47
		Remote site location	0.62	8
		Artificial obstructs	0.45	25
External risks	Human risks	Deaths by natural causes	0.26	46
		Construction site deaths and serious injuries due to poor safety measures	0.43	27
		Strikes	0.31	41
		Illnesses	0.40	31
	Design risks	Poor design	0.39	32
		Rushed design	0.48	22
		Design delays	0.68	5
		Design changes	0.33	40
		Design complexity	0.52	17
	Management risks	Subcontractors deficiency	0.51	19
		Poor communication	0.83	1
		Poor equipment management	0.55	15
		Inefficient planning	0.57	12
		Inadequate scheduling	0.56	13
		Poor budgeting	0.49	20

3.4 Project performance indicators and hypotheses development

3.4.1 Performance Indicators

In this research, we identified 11 key performance indicators from the perspective of project managers during the focus group session. These indicators are as follows: team management, project coordination, conflict management style, communications and reporting, quality control system, quality assurance, risk and opportunity management, contract management, schedule management, stakeholders management, and health and safety management.

3.4.2 Hypotheses development

On the basis of the focus group session outputs, we developed 11 hypotheses that examine the impact of O&G construction risks on PP and its indicators. Listed below are the developed hypotheses:

H1. *Financial risks have a positive impact on PP.*
H2*. Legal risks have a positive impact on PP.*
H3. *Political risks have a positive impact on PP.*
H4. *Social risks have a positive impact on PP.*
H5. *Environmental risks have a positive impact on PP.*
H6. *Technical risks have a positive impact on PP.*
H7. *Logistics risks have a positive impact on PP.*
H8. *Zoning risks have a positive impact on PP.*
H9. *Human risks have a positive impact on PP.*
H10. *Design risks have a positive impact on PP.*
H11. *Management risks have a positive impact on PP.*

3.5 Assessment of the Measurement Model

The Measurement Model specifies the rules of correspondence between measured and latent variables and is assessed using internal consistency reliability, convergent validity, and discriminant validity.

3.5.1 Internal Consistency Reliability

Internal consistency reliability (ICR) refers to the degree to which test measurements remain consistent when performed under similar conditions repeatedly. ICR measured by Cronbach's alpha (i.e., a measure of tests' internal consistency) and composite reliability (i.e., a measure of internal consistency in scale items). the Cronbach's Alpha values ranged between 0.804 and 0.920. The composite reliability, on the other hand, ranged between 0.870 and 0.913. Both measures exceeded the threshold of 0.707, indicating accepted construct reliability [14].

3.5.2 Convergent Validity

Convergent validity refers to the degree to which a new scale is related to other measures and variables of the same construct, based on the outer loading of indicators and average variance extracted. To this end, the range of the outer loadings for the constructs' indicators was from 0.814 to 0.959, exceeding the minimum threshold of 0.60 for item reliability [15] . Furthermore, the CV values were deemed adequate ranging from 0.538 to 0.801, exceeding the recommended threshold of 0.5 [16].

3.5.3 Discriminant Validity

Discriminant validity refers to the degree of differentiation and independence between a set of factors. In this research, Heterotrait-monotrait Ratio of Correlations (HTMT) was used to measure discriminant validity. To this end, the range of the HTMT values was from 0.373 to 0.627, which was below the threshold of 0.90 [17]. Accordingly, the test results were deemed satisfactory.

3.6 Assessment of the Structural Model

The Structural Model (SM) examines the relationships among constructs and is assessed using the coefficient of determination, Cross-validated redundancy, and path coefficients

3.6.1 Coefficient of determination (R^2)

In this research, R^2 values were obtained using the bootstrap algorithm in SMART PLS 3.0 with the recommended iterations of 300. R^2 values for the effects of O&G risks on PP was 0.713, exceeding the minimum acceptable level of 0.1 as recommended by Falk and Miller [18]. Hence, indicating a satisfactory predicting capability.

3.6.2 Cross-validated redundancy (Q^2)

In this research, the Q^2 values were obtained using the blindfolding algorithm in SMART PLS 3.0 with the recommended iterations of 300 and an omission distance of seven. The Q^2 values for the effects of O&G risks on PP was 0.421 exceeding the minimum acceptable level of 0.00 as recommended by Hair et al. [19]. Hence, indicating a satisfactory predicting relevance level.

3.6.3 Path coefficients(β)

In the context of SEM, a path coefficient is a standardized version of a linear regression weight, which can be used to evaluate the hypothesized correlation between two variables. In order to accept the hypothesis, the T-valu (T) e must be greater than 1.96, while the P-value (P) must be less than 5%. In this research, H1 examines whether financial risks have a positive impact on PP. Results indicated that financial risks had a significant impact on PP (β =0.606, T =8.786, P<1%). Consequently, H1 was supported. H2 examines whether legal have a positive impact on PP. Results indicated that legal risks had a significant impact on PP (β =0.639, T =6.735, P<1%). Therefore, H2 was supported. H3 examines whether political risks have a positive impact on PP. Results indicated that political risks had a significant impact on PP (β =0.316, T =4.109, P<1%). Thus, H3 was supported. H4 examines whether social risks have a positive impact on PP. Results indicated that Social risks had a significant impact on PP (β =0.466, T =6.964, P<1%). Accordingly, H4 was supported. H5 examines whether environmental risks have a positive impact on PP. Results indicated that environmental risks had a significant impact on PP (β =0.452, T =6.119, P<1%). Hence, H5 was supported. H6 examines whether technical risks have a positive impact on PP. Results indicated that technical risks had a significant impact on PP (β =0.531, T =6.183, P<1%). Therefore, H6 was supported. H7 examines whether logistics risks have a positive impact on PP. Results indicated that logistics risks had a significant impact on PP (β =0.526, T =5.726, P<1%). Accordingly, H7 was supported. H8 examines whether zoning risks have a positive impact on PP. Results indicated that zoning risks had a significant impact on PP (β =0.470, T =5.732, P<1%). Consequently, H8 was supported. H9 examines whether human risks have a positive impact on PP. Results indicated that human risks had a significant impact on PP (β =0.512, T =5.875, P<1%). As a result, H9 was supported. H10 examines whether design risks have a positive impact on PP. Results indicated that design risks had a significant impact on PP (β =0.476, T =6.873, P<1%). Hence, H10 was supported. H11 examines whether management risks have a positive impact on PP. Results indicated that management risks had a significant impact on PP (β =0.728, T =7.745, P<1%). In light of this, H11 was supported.

4 CONCLUSIONS

O&G construction projects are complex and risky due to their dynamic environment, unique nature, complex technology, remote geographical locations, and the involvement of numerous stakeholders. In order to achieve the set goals of such projects with high performance, it is crucial to thoroughly examine the major risks associated with these projects. The aim of this paper is to quantify the effects of construction risks on the performance of O&G projects by considering the case of O&G construction projects in Iraq. In this research, we (1) identified the key risks facing O&G construction projects, as well as the key performance indicators from the perspective of Iraq project managers; (2) developed a set of hypotheses to capture the impact of O&G construction risks on project performance; (3) quantified the riskiness level of O&G risks; and (4) examined how construction project managers in Iraq perceive the impact of O&G risks on project performance. First, a focus group session was conducted with six construction project managers in Iraq to identify O&G risks and key project performance indicators, and to hypothesize the relationships between the O&G risks and PP. Second, a structured survey (i.e., AHP and SEM-based) was administered to 75 experts to assess the level of riskiness of O&G risks and their impact on project performance. Third, a FAHP model was developed to quantify the level of riskiness of O&G risks. Last, a SEM model was developed to quantify the direct effects of O&G risks on PP.

Based on the results of the FAHP analysis, the top 10 significant risks facing O&G construction projects were (high to low riskiness level): poor communication, skilled workers shortage, unstable security, political instability, contractor bankruptcy, design delays, bribery and corruption, remote site location, lack of clarity regarding contractual obligations, and currency rate fluctuation.

Based on the results of the SEM analysis, all analyzed risk categories had a significant impact on the performance of O&G construction projects in Iraq. In fact, management risks had the strongest effects on PP (β=0.728), followed by legal risks (β=0.639), financial risks (β=0.606), technical risks (β=0.531), logistics risks (β=0.526), human risks (β=0.512), design risks (β=0.476), zoning risks (β=0.470), social risks (β=0.466), environmental risks (β=0.452), and political risks (β=0.316), respectively. Ultimately, this study contributes to the body of knowledge by providing a useful aid to practitioners and researchers seeking a reference on common potential risks affecting the performance of O&G construction projects. For future work, the findings of this paper can be used by research scholars to (1) develop guidelines and strategies to respond to O&G risks; and (2) model the effects of O&G construction risks on developing versus developed countries.

4.1 Limitations

Despite its importance, this study has a number of limitations. First, this research relies on expert judgment, derived from focus group sessions and questionnaire surveys. Other inputs, such as historical data from previously achieved projects, should be considered to complement the results. Second, 47 risks were identified in this research and grouped into two categories and 11 subcategories. Other O&G risks should be identified and classified under the study's existing classification or under new construction categories and sub-categories. Last, the results of this study were based on the perspective of construction project managers in Iraq. The perspectives of other construction stakeholders (e.g., contractors, consultants, etc.) regarding the effects of O&G risks on project performance may differ.

REFERENCES

[1] De Maere d'Aertrycke, G., Ehrenmann, A. and Smeers, Y., 2017. Investment with incomplete markets for risk: The need for long-term contracts. *Energy Policy*, *105*, pp.571-583.

[2] Al-Mhdawi, M.K., 2020. Proposed risk management decision support methodology for oil and gas construction projects. In *The 10th International Conference on Engineering, Project, and Production Management* (pp. 407-420). Springer, Singapore.

[3] Thuyet N., Ogunlana, S., and Dey, P. (2007). "Risk Management in Oil and Gas Construction Projects in Vietnam." *International Journal of Energy Sector Management, 1* (2): 175–193.

[4] Al-Sabah, R., Menassa, C.C. and Hanna, A., 2014. Evaluating impact of construction risks in the Arabian Gulf Region from perspective of multinational architecture, engineering and construction firms. *Construction management and economics*, *32*(4), pp.382-402.

[5] Kassem, M., Khoiry, M., and Hamzah, N. (2020). "Factors on the Success of an Oil and Gas Construction Project." *Engineering Construction and Architectural Management, 27* (9): 2767–93.

[6] Al-Mhdawi, M.K.S., Brito, M.P., Onggo, B.S. and Rashid, H.A., 2022a. Analyzing the Impact of the COVID-19 Pandemic Risks on Construction Projects in Developing Countries: Case of Iraq. In *Construction Research Congress 2022* (pp. 1013-1023).

[7] Saaty, T. L. 1980. *Analytic Hierarchy Process*. Maidenhead, England: McGraw Hill Higher Education.

[8] Al-Mhdawi, M.K.S., Brito, M.P., Abdul Nabi, M., El-adaway, I.H. and Onggo, B.S., 2022b. Capturing the Impact of COVID-19 on Construction Projects in Developing Countries: A Case Study of Iraq. *Journal of Management in Engineering*, *38*(1), p.05021015.

[9] Buckley, J.J., 1985. Fuzzy hierarchical analysis. *Fuzzy sets and systems*, *17*(3), pp.233-247. Shackman, J.D., 2013. The use of partial least squares path modeling and generalized structured component analysis in international business research: A literature review. *International Journal of Management*, *30*(3), p.78

[10] Zadeh, L.A., 1965. "Fuzzy sets". *Information and Control*, 8: 338-353.

[11] Alhumaidi, H.M., 2015. Construction contractors ranking method using multiple decision-makers and multiattribute fuzzy weighted average. *Journal of Construction Engineering and Management*, *141*(4), p.04014092.

[12] Li, J. and Zou, P.X., 2011. Fuzzy AHP-based risk assessment methodology for PPP projects. *Journal of Construction Engineering and Management*, *137*(12), pp.1205-1209.

[13] Fayek, A.R., 2018. *Fuzzy Hybrid Computing in Construction Engineering and Management*. Emerald Publishing Limited

[14] Hair Jr, J.F., Matthews, L.M., Matthews, R.L. and Sarstedt, M., 2017. PLS-SEM or CB-SEM: updated guidelines on which method to use. *International Journal of Multivariate Data Analysis*, *1*(2), pp.107-123.

[15] Gefen, D. and Straub, D. (2005), "A practical guide to factorial validity using PLS-Graph: tutorial and annotated example", Communications of the Association for Information Systems, Vol. 16 No. 1, pp. 91-109

[16] Ringle, C.M., Sarstedt, M., Mitchell, R. and Gudergan, S.P. (2018), "Partial least squares structural equation modeling in HRM research", The International Journal of Human Resource Management, pp. 1-27, doi: 10.1080/09585192.2017.1416655.

[17] Henseler, J., Ringle, C.M. and Sarstedt, M. (2015), "A new criterion for assessing discriminant validity in variance-based structural equation modeling", Journal of the Academy of Marketing Science, Vol. 43 No. 1, pp. 115-135.

[18] Falk, R. and Miller, N.B. (1992), "A primer for soft modeling", Open Journal of Business and Management, Vol. 2 No. 4, p. 103.

[19] Hair, J. F., Hult, G. T. M., Ringle, C. M., and Sarstedt, M. (2017). A Primer on Partial Least Squares Structural Equation Modeling (PLS-SEM). 2nd Ed., Thousand Oakes, CA: Sage.

Performance Degradation in Electric Load Forecasting Models due to Heterogeneous Data Streams in Smart Grid

Muslim Jameel Syed[1], Jamie Goggins[1], Abdul Azeem[2]
[1]MaREI Centre, Ryan Institute & School of Engineering, National University of Ireland, Galway, Ireland
[2]Universiti Teknologi PETRONAS Seri-Iskandar, Electrical and Electronic Engineering Department, Perak,Malaysia
email: muslimjameel.syed@nuigalway.ie

ABSTRACT: Smart Grid (SG) is an advanced digitally enabled power grid for controlling the flow of electricity and enables the use of integration of different generative modalities (such as carbon, solar, river, ocean, and wind) to meet energy demands. Electric load forecasting is an essential element in the planning, periodical operation, and facility expansion in the electric industry. Whereas due to the amalgamation of different generative modalities, the SG's data streams are heterogeneous and operate in dynamic environments. In literature, numerous statistical, shallow learning (such as auto-regression linear regression, support vector machine), and memory-based (recurrent neural network ARMIA, LSTM, and other) electric-load forecasting models have been proposed. A study uses the PV generation for complex parameters for long-term forecasting, utilizing the nonlinearity, periodicity, and fluctuation of parameters over time. A recent study presents analysis over the multivariable data based on copula correlation to determine the optimal LSTM parameters for load forecasting. Few studies have criticized the static nature of traditional forecasting models and described it as a challenge for the SG environment. After comprehensive literature review and critical analysis, we identified the incompatibility of traditional electric load forecasting models are due to change in evaluation criteria (with respect to the different generative modalities), parameters selections, factors affecting forecast, and criteria for selection of model optimization and other. These limitations cause the model deterioration and make them obsolete for further use, hence are required a more dynamic self-adaptive, and continuous learning approach to avoid such performance degradations in the SG environment.

KEY WORDS: Smart Grid; Concept drift, Uncertainty, Electric Load Forecasting.

1 INTRODUCTION

load forecasting has been attracting a lot of research and industry interest due to its crucial role in energy management systems—which serves as a foundation for planning energy generation and distribution, supply operations, energy budgeting, and the development of the smart grid [1].

The smart meters are enablers to improvise the electric load forecasting, smart meters track and quantify energy use for residential and non-residential buildings, and results in more accurate forecasting. A research estimates that by 2024, the EU will have installed 51 million smart meters for gas and close to 225 million for electricity. By 2024, it is anticipated that roughly 77 percent of European consumers would have a smart electricity meter, representing a potential investment of €47 billion. 44 percent of people plan to use one for gas. In the EU, installing a smart meter typically costs between €180 and €200 [2]. One of the advantages of smart meters is the handling of heterogeneous data streams (adding a new appliance or a change in home occupants behaviour patterns will result in different energy consumption profiles), and different generative modalities (such as carbon, solar, river, ocean, and wind). In such scenarios, we often deal with streaming data that is sequentially collected over time. Due to the nonstationary nature of the environment, the streaming data distribution may change in unpredictable ways, which is known as concept drift [3].

To handle concept drift, previous methods first detect when/where the concept drift happens and then adapt models to fit the distribution of the latest data. However, there are still many cases that some underlying factors of environment evolution are predictable, making it possible to model the future concept drift trend of the streaming data, while such cases are not fully explored in previous work. These concepts change can occur in different applications, particularly it has great adverse impact over the electric load or smart grid environment. For example, traditional forecasting techniques need to be examined in respect to how they handle diverse energy consumption patterns present among individual energy consumers as well as changes in patterns over time. Deep Learning (DL) techniques have recently exhibited outstanding effectiveness in load forecasting due to automatic lower-level feature extractions, results more accurate generalizations, when the data is huge [4].

Interestingly, the deep learning models are found better than shallow learning models to get insight from smart meters data. However, the heterogeneity of the data handling is still a big challenge. This is because, the smart meter environment is online environment (the change in the input features or output features may take place), whereas the current load forecasting approaches are offline (all training data must be available for training) [5]. More precisely, offline machine learning is an approach that ingests all the data at one time to build a model, whereas online learning is an approach that ingests data one observation at a time.

Offline Machine Learning also is known as batch learning. In offline machine learning, the model is trained and tested (or deployed) on the dataset from the same data population. In offline machine learning, the feature of class-wise distribution does not change because the data population (features input and output are already known and cannot be updated). Initially, the model is first trained, and then is sent into production and runs without learning anymore. Compared to offline learning, online learning does not have the whole set of training data beforehand. Online learning is helpful when the data may be

changing rapidly over time. It is also useful for applications that involve an extensive collection of data that is continuously growing, even if changes are gradual. Similarly, the underlying distribution of smart meter data changes over time, producing what is referred to as concept drift [6].

When traditional machine learning approaches deals in concept drift scenario, the massive performance degradation is observed in the system, which can make model obsolete [7]. Therefore, the online forecasting approaches with adaptability features can be useful in such scenario [8].

A study [8] suggest that despite the fact, the online learning has proven to be more effective to handle concept drift scenario, but still, it is important to examine its effectiveness for electric load forecasting use case and determine the several types of concept drift can be present in electric load forecasting. The remainder of the paper is organized as follows: Section II presents the adopted methodology, Section III discusses the results and discussion, Section IV concludes the paper.

2 METHOD

The issue of the concept drift problem is not new but in literature, no significant contribution can be seen which provides a comprehensive view on this topic when dealing with the smart grid distribution environment. Therefore, to extract most of the relevant information for this topic we followed a Systematic Literature Review. In the planning phase, we design a six stages review protocol based on Systematic Literature Review guidelines. The mitigation strategies of concept drift are primarily depending on the types of datasets; hence a single framework is not valid for all kinds of data streams. Therefore, it is essential to survey a comprehensive literature review for finding the types of datasets and their related studies, this contribution can benefit the other researchers to correlate the concept drift effects on several kinds of dataset streams.

2.1 Review Process

The search strategy comprises search terms, literature resources, and search process, which are detailed one by one as follows.

The relevant literature search is a critical phase, to dig out all the relevant literature of the area of Concept drift issue this study takes some major steps. Initially, the search terms are derived from the research questions and their synonyms are identified both English and American spelling. Moreover, used the Boolean OR and AND to link the major term, as defined below. Machine Learning AND (stream OR online OR real-time) AND (classification OR clustering) AND (Concept drift OR Concept change OR ‘‘dynamic changes”, OR ‘‘adaptivity’’, etc. Most of the research papers were acquired from well-reputed high-quality journal papers from the electronic databases, including IEEE Xplore, Science Direct, Web of Science, Google Scholar and ACM digital library. The search process is dependent on four phases, in phase 1 we search around 150 research papers from the most reputed electronic libraries based on search terminologies. In phase two, we study the abstract of the 150 papers and segregated the relevant and not relevant candidates for full paper screening, here we found 35 papers that were relevant to the concept drift..

2.2 Quality Assurance Process

In phase 1, we downloaded the 150 papers based on identified search terms. In phase 2, we have gone through the shallow literature review for all 150 papers, in the shallow literature review we specifically identified the most relevant 35 research papers based on their titles and abstracts, these articles were related to concept drift. In phase 3, these 35 extracted papers were further refined to 20 papers after diagonal reading of the full paper, the selection criteria of relevancy were based on Big Data streams.

The quality assessment (QA) of selected studies is originally used as the basis for weighting the retrieved quantitative data in a meta-analysis, which is a typical data synthesis strategy. However, after the extraction of relevant research articles, we did not find the satisfactory numbers of a research article to be classified as obtained research papers according to the quality assessment results weightage, whereas we followed the quality assessment results to support our review findings.

There are some other papers, which directly do not participate to the problem area but are essential for defining the research methodology and supporting our argument, because these papers were not relevant to the subject matter, therefore, we did not present them as a part of the paper selection. The goal of data synthesis is to aggregate evidence from the selected studies for answering the research questions. A single piece of evidence might have a small evidence force, but the aggregation of many of them can make a point stronger. The data extracted in this review include both quantitative data (e.g., values of estimation accuracy) and qualitative data (e.g., strengths and weaknesses of concept drift mitigation techniques).

3 RESULT AND DISCUSSION

Smart Grid (SG) is an advanced digitally enabled power grid for controlling the flow of electricity and enables the use of integration of different generative modalities (such as carbon, solar, river, ocean, and wind) to meet energy demands. Also, changes with time from the residential and nonresidential building, such as adding a new appliance or a change in home occupants behaviour patterns will result in different energy consumption profiles Electric load forecasting is an essential element in the planning, periodical operation, and facility expansion in the electric industry [9]. Whereas due to the amalgamation of different generative modalities, the SG’s data streams are heterogeneous and operate in dynamic environments [10]. In literature [11], numerous statistical, shallow learning (such as auto-regression [12], linear regression [13], support vector machine [14]), and memory-based (recurrent neural network [15] ARMIA, LSTM, and other [16]) electric-load forecasting models have been proposed. A study [17] uses the PV generation for complex parameters for long-term forecasting, utilizing the nonlinearity, periodicity, and fluctuation of parameters over time. A recent study presents analysis over the multivariable data based on copula correlation to determine the optimal LSTM parameters for load forecasting [18]. Several studies [19][20] has criticized the static nature of traditional forecasting models and provided empirical evidence to prove that existing load forecasting models has a challenge for the SG environment due to change in evaluation criteria (with respect to the different generative

modalities), parameters selections, factors affecting forecast, and criteria for selection of model optimization [21]. These limitations cause the model deterioration and make them obsolete for further use, hence are required a more dynamic and adaptive approach to avoid such performance degradation in the SG environment, which is known as issue of concept drift.

The issue of concept drift is a common phenomenon in online machine learning when the statistical properties of a target domain (input data streams) arbitrarily change over time which causes the classification accuracy in deployed models and make them in-effective for further use. Thus, the deployed models must be dynamic enough to detect and adapt to such changes (concept drift) from the input streams. Concept drift handling strategies depend on the type of data streams, and there is no generic solution for different types of concept drift. In literature, the concept drift issue is classified into three (3) primary types of drift such as real drift, virtual drift and hybrid drift. However, some studies have derived some more types considering its frequency pattern, such as gradual, sudden, abrupt, blip and incremental. One of the major problems while dealing with concept drift handling is the possibility of reoccurrence of the previous concept drift. Therefore, the proposed models must contain a concept drift reoccurrence assumption. Also, the literature suggests considering four (4) aspects to handle concept drift efficiently, which are (1) future assumption (2) change detection and handler (3) dynamic model selection and (4) learner adaptability. Moreover, Concept drift detection is a prerequisite step of its adaptation. Concept drift detection methods can be classified as 1) Error-rate-based methods 2) data-distribution based methods and 3) parameter-based methods. However, most of the techniques are based on error-rate method. The existing concept drift detector models can be classified into four (4) types, such as 1) statistical models 2) window-based detectors models 3) block-based ensemble models 4) incremental-based ensemble models. However, all these solutions possess a common problem that they have overlooked noises as concept drift, and there is no particular way to distinguish the noise and potential concept drift. Concept drift handling solutions are categorized as shallow learning, deep learning and hybrid learning, which uses the four (04) different methods, such as single classifier, instance selection or window-based approach, weight-based approach, an ensemble of classifiers. Among all the proposed methods, the ensemble classifier approach is mostly adopted by the researchers due to its diversity feature to adapt to new changes. The concept drifted data can be categorized into the synthetic and real dataset. The support vector machine (SVM), random forest (RF), extensive learning machine (ELM) and convolutional neural network (CNN) are mostly used base classifiers for concept drift handling.

In literature, the majority of concept drift adaptation techniques addressed the non-imaging data. However, few recent studies have highlighted the issue of concept drift in the image data stream. The provided solutions in the literature either limited to one type of concept drift (new features arrival during greyscale image (1 channel) data stream or addressed only specific part of concept drift handling (such as detection or adaptation). Besides, to the best of the author's knowledge, there is no single existing solution which performs online training for adaptation (existing solution performs offline training).

4 CONCLUSION AND FUTURE CONSIDERATION

Power system operations rely heavily on electrical load forecasts. It is used to make various decisions about energy transactions and management. As a result, for decision-makers in the energy sector, accuracy and precision are critical. This article provided a thorough examination of various load forecasting models for various periods and sectors.

Although hybrid techniques were found to have higher forecasting accuracy, they still had drawbacks. The traditional methods of load forecasting, as well as their performance and limits, were examined. We explored the significance of various generation modalities in current power systems and offered an analysis to adjust existing load forecasting methods for DGM situations (SG and Smart city). Finally, noting limitations, trends, and research gaps will assist readers in selecting and evaluating models that meet their needs, as well as determining future working directions. Future work will concentrate on improving the constraints of existing load forecasting models, as well as their DGM and adaptability.

REFERENCES

[1] Y. Hong, Y. Zhou, Q. Li, W. Xu, and X. Zheng, ''A deep learning method for short-term residential load forecasting in smart grid,'' IEEE Access, vol. 8, pp. 55785–55797, 2020.

[2] European Commission, Directorate-General for Energy, Alaton, C., Tounquet, F., Benchmarking smart metering deployment in the EU-28 : final report, Publications Office, 2020, https://data.europa.eu/doi/10.2833/492070

[3] Fekri, Mohammad & Patel, Harsh & Grolinger, Katarina & Sharma, Vinay. (2020). Deep Learning for Load Forecasting with Smart Meter Data: Online Adaptive Recurrent Neural Network. Applied Energy. 282. 10.1016/j.apenergy.2020.116177.

[4] D. Gholamiangonabadi, N. Kiselov, and K. Grolinger, ''Deep neural net works for human activity recognition with wearable sensors: Leave-one subject-out cross-validation for model selection,'' IEEE Access, vol. 8, pp. 133982–133994, 2020.

[5] A. L'Heureux, K. Grolinger, H. F. Elyamany, and M. A. M. Capretz, ''Machine learning with big data: Challenges and approaches,'' IEEE Access, vol. 5, pp. 7776–7797, 2017.

[6] E. V. Z. E. Indr liobait, M. Pechenizkiy, and J. Gama, ''An overview of concept drift applications,'' in Proc. Big Data Anal., New Algorithms New Soc., 2016, pp. 114–191.

[7] H. M. Gomes, J. Read, and A. Bifet, ''Machine learning for streaming data: State of the art, challenges, and opportunities,'' ACM SIGKDD Explor. Newslett., vol. 21, no. 2, pp. 6–22, Feb., 2019.

[8] M. N. Fekri, H. Patel, K. Grolinger, and V. Sharma, ''Deep learning for load forecasting with smart meter data: Online adaptive recurrent neural network,'' Appl. Energy, vol. 282, Jan. 2021, Art. no. 116177.

[9] A methodology for Electric Power Load Forecasting. https://doi.org/10.1016/j.aej.2011.01.015

[10] Guerrero, J. I., García, A., Personal, E., Luque, J., & León, C. (2017). Heterogeneous data source integration for smart grid ecosystems based on metadata mining. Expert Systems with Applications, 79, 254-268. https://doi.org/10.1016/j.eswa.2017.03.007

[11] Tina, G. M., Ventura, C., Ferlito, S., & De Vito, S. (2021). A state-of-art-review on machine-learning based methods for PV. Applied Sciences, 11(16), 7550. https://doi.org/10.3390/app11167550.

[12] López, M., Sans, C., Valero, S., & Senabre, C. (2018). Empirical comparison of neural network and auto-regressive models in short-term load forecasting. Energies, 11(8), 2080. https://doi.org/10.3390/en11082080.

[13] G. Dudek, "Pattern-based local linear regression models for short-term load forecasting," Electric Power Systems Research, vol. 130, pp. 139-147, 2016. https://doi.org/10.1016/j.epsr.2015.09.001.

[14] Yang, J., Tang, Y., & Duan, H. (2022). Application of Fuzzy Support Vector Machine in Short-Term Power Load Forecasting. Journal of Cases

on Information Technology (JCIT), 24(5), 1-10. DOI: 10.4018/JCIT.295248

[15] W. Kong, Z. Y. Dong, Y. Jia, D. J. Hill, Y. Xu, and Y. Zhang, "Short-term residential load forecasting based on LSTM recurrent neural network," IEEE Transactions on Smart Grid, vol. 10, no. 1, pp. 841-851, 2017. DOI: 10.1109/TSG.2017.2753802.

[16] Farsi, B., Amayri, M., Bouguila, N., & Eicker, U. (2021). On short-term load forecasting using machine learning techniques and a novel parallel deep LSTM-CNN approach. IEEE Access, 9, 31191-31212. DOI: 10.1109/ACCESS.2021.3060290

[17] Ding, S., Li, R., & Tao, Z. (2021). A novel adaptive discrete grey model with time-varying parameters for long-term photovoltaic power generation forecasting. Energy Conversion and Management, 227, 113644. https://doi.org/10.1016/j.enconman.2020.113644.

[18] Zheng, J., Zhang, L., Chen, J., Wu, G., Ni, S., Hu, Z., ... & Chen, Z. (2021). Multiple-Load Forecasting for Integrated Energy System Based on Copula-DBiLSTM. Energies, 14(8), 2188. https://doi.org/10.3390/en14082188.

[19] A. Azeem, I. Ismail, S. M. Jameel and V. R. Harindran, "Electrical Load Forecasting Models for Different Generation Modalities: A Review," in IEEE Access, vol. 9, pp. 142239-142263, 2021, doi: 10.1109/ACCESS.2021.3120731.

[20] Luo, X., & Oyedele, L. (2022). A self-adaptive deep learning model for building electricity load prediction with moving horizon. Machine Learning with Applications, 100257. https://doi.org/10.1016/j.mlwa.2022.100257

[21] Panda, D. K., & Das, S. (2021). Smart grid architecture model for control, optimization and data analytics of future power networks with more renewable energy. Journal of Cleaner Production, 301, 126877. https://doi.org/10.1016/j.jclepro.2021.126877

Modelling human influences on the indoor environment in homes

Niti Saini[1], Roger P. West[1], Patrick Shiel[1], Ruth Kerrigan[2], Ricardo Filho[2], Ian Pyburn[2]
Department of Civil Structural and Environmental Engineering, Trinity College, College Green, Dublin 2.
[2]Intergrated Environmental Solutions, Castleforbes House, Castleforbes Road, Dublin 1.

Email : sainin@tcd.ie, rwest@tcd.ie, pat.shiel@verteco.ie, ruth.kerrigan@iesve.com, ricardo.filho@iesve.com, ian.pyburn@iesve.com

ABSTRACT: Providing a healthy indoor environment in A-rated homes is emerging as a major challenge for researchers and practitioners because low-carbon design is focussed on the reduction of energy consumption and air-tightness while recent research shows that control of the indoor climate through the perceived effects of occupier interventions can have a significant impact on comfort levels. The present study aims to critically analyse various parameters affecting the relative humidity and CO_2 levels in energy-efficient residential buildings in Ireland. A sample of A-rated residential dwellings were studied to gauge the consequences of occupant behaviour on the indoor air quality (IAQ). The data on selected IAQ parameters were collected, evaluated and modelled to provide meaningful insights into the consequences of occupier behaviour on the IAQ. An IES-VE model was created and calibrated using real on-site data by matching different variables in the data, including occupancy, heating schedules/profiles, equipment usage, door-window opening and ventilation schedules. Once calibrated, different simulations were run to identify the causes and solutions based on the different parameter exceedances. The findings suggest that higher accumulated humidity and CO_2 levels in different house zones can be relieved by using the internal doors, mechanical ventilation and trickle vents more efficiently without compromising the thermal performance, brought about by providing better occupier guidance at hand-over.

KEY WORDS: IAQ; A-rated homes; Human behaviour; Mechanical ventilation.

1 INTRODUCTION

IAQ is considered as one of the major issues that has evolved requiring attention for improving occupant comfort inside buildings. This is often exhibited by analysing the rate of air changes, the concentration level of CO_2, relative humidity and the temperature [1][2]. IAQ is mainly evaluated through its impact on human health, along with an analysis of comfort levels and human productivity inside the buildings. Past research has shown that poor IAQ inside school buildings tends to cause several health issues among children who are more prone to air pollution [3]. CO_2 is considered a common indicator of the status of air quality in buildings that has a major impact on the health of the occupants [4][5]. The air temperature and relative humidity are other major indicators of an occupant's perceived comfort [6]. The thermal insulation in building facades is influential in determining the indoor temperature and thermal comfort and temperature control provides the possibility for energy saving [7][8]. According to Arif [9] IAQ affects the comfort and well-being of occupants recognising that people spend much of their time indoors. Health and comfort related factors are influenced by building characteristics such as facade design, ventilation system, etc.

Poor indoor environments in places of work can significantly reduce the work performance of the occupants including cultural, psychological and sociological dimensions [9]. The adverse influence of a poor indoor environment on the occupant's health has been identified by various researchers [10][11]. Similar findings have been made by other studies claiming that the accumulation of multiple effects in buildings, such as the indoor environment, building characteristics, architecture and occupant's behaviour are attributed to the building-associated illness known as Sick Building Syndrome (SBS) [12][13]. The SBS is described as a situation in which the occupants of a building experience acute health- or comfort-related effects that seem to be linked directly to the time spent in the building. In this context it is recognised that occupants of air-tight A-rated residences can be more exposed to poor IAQ leading to SBS. Symptoms are not only related to houses or offices but also many public buildings such as schools and hospitals [14]. Uncomfortable indoor humidity, temperature and biological and chemical pollutants are some of the factors that cause SBS to develop among the occupants of airtight homes, with inadequate ventilation affecting their physical and psychological well-being [10]. SBS symptoms include eye, throat and nose irritation, wheezing, cough, headache, cognitive disturbances, pulmonary functions or flu like symptoms [15]. Takigawa [15] established that hypersensitivity, pneumonitis and asthma are also associated with inflammation and atopy problems, where one's immune system is more likely to develop allergic disease, triggered by exposure to indoor air contaminated with biological or fungal concentrations. Furthermore, Moreno-Rangel showed that indoor air quality has a significant impact on the health and well-being of the occupants residing in more modern airtight buildings [16].

In recent years, the problems associated with IAQ have become evident as higher standards of airtightness can affect occupants' health. Therefore, IAQ in airtight buildings is important in terms of an assessment of humidity and CO_2 levels along with VOC emissions and other air pollutants. Numerous researchers have shown that energy efficient houses and their ventilation systems have an impact on the IAQ, which is also dependent upon the occupant's actions, influencing thermal efficiency [17][18][19].

Thus, it is crucial that buildings be designed not only considering aesthetics, energy-efficiency, or operational performance but also considering the indoor environment impact of the relevant building characteristics and occupants' actions and behaviours. They pose an important bearing on the use of the thermal and ventilation systems through opening and

closing of door/windows, supplementing any HVAC systems, which impact the IAQ of buildings. Therefore, the aim of this study is to critically analyse various parameters affecting the relative humidity and CO_2 levels in energy-efficient residential buildings in Ireland. The data on selected IAQ parameters have been collected, evaluated and modelled to provide meaningful insights into the consequences of occupier behaviour on the IAQ. For the purpose of this paper, these measured factors (temperature, humidity and CO_2) are referred to collectively as IAQ here, even though some factors traditionally associated with this term are not going to be discussed, such as VOCs, dust, radon, etc. Only these three factors were measured on site and are reported on in this paper. The RH and CO_2 issues in particular, as faced by occupants, are modelled using purpose-designed software and recommendations are provided for improved user behaviour based on the simulation results.

Figure 1. Ceiling mounted LoraWAN sensors.

2 METHODOLOGY

A methodology was developed to record IAQ data in the likely most occupied rooms in each of the houses under consideration in this study. Data was gathered using LoraWAN battery-operated sensors (Figure 1), measuring CO_2, temperature and relative humidity (RH), transmitting every 5 minutes to a local Things Network (TTN) gateway. From the TTN, real-time data was gathered by a software analysis tool called iSCAN provided by project partners IES. As part of the AMBER project, data has been collected from 57 houses in Ireland from five rooms, namely the master bedroom and adjoining en suite, second bedroom, living room and kitchen. The typical layout and location of sensors for these sample houses is given in Figure 2.

Figure 2. Drawing indicating the locations of the five sensors provided in each typical house.

The collected data were analysed to study the IAQ parameters, in the context of Temperature (T), Relative Humidity (RH) and CO_2 emission levels during the different seasons. These three variables across different house zones and seasons were then mapped to external weather parameters, occupancy patterns and family structures in the analysis.

The monitored houses were in full compliance with the ventilation requirements (Part F-2009) and efficiency/materials requirements under energy conservation (Part L as per the 2011, 2017 amendments) in the Irish building regulations. Ventilation is provided to these homes using a combination of passive window frame-mounted trickle vents (TVs) in the living room and bedrooms, and (humidity) demand-controlled ventilation (DCV) centrally extracting from high humidity areas (bathrooms and kitchens). The mechanical extract fans were remotely triggered through the measurement points in the kitchens and bathrooms based on a 65% RH set point.

The extract operated as a variable speed fan that effectively changed the number of air-changes per hour (ACH) in each zone. Windows were fitted with Aereco trickle vents (EHM1276 Humidity Sensitive Air Inlet) in rooms that did not have ceiling extract, such as in kitchens and bathrooms. These vents could be closed, meaning they were actually 10% open, or completely open (100%) or run in auto mode where the measured RH varied and the opening gave minimum airflow below 65% RH to maximum airflow at 100% RH.

A virtual model was created in the IES-VE software entailing a number of steps, namely defining the geometry of the house, its orientation and house type (three and four bedroom mid and end terrace houses), solar parameters, material and elemental properties and various loading scenario inputs (Figure 3).

Once the model had been successfully constructed in the IES-VE software, the simulations of the internal environment of the project houses were performed. When calibrating, one day's data for a house with four occupants (two adults and two children) was linked with the real on-site data for that particular day for all three parameters, namely, T, RH and CO_2, within the four main house zones (kitchen, living room, master bedroom and second bedroom). Calibration was achieved by creating and matching different variables in the data, including occupancy, heating schedules/profiles, equipment usage, door-window opening and ventilation schedules. Once the model was calibrated, different simulations were run to solve the reported IAQ issues faced by different families. Due to space restrictions, only one house type, a three bedroom mid terrace house, is considered here.

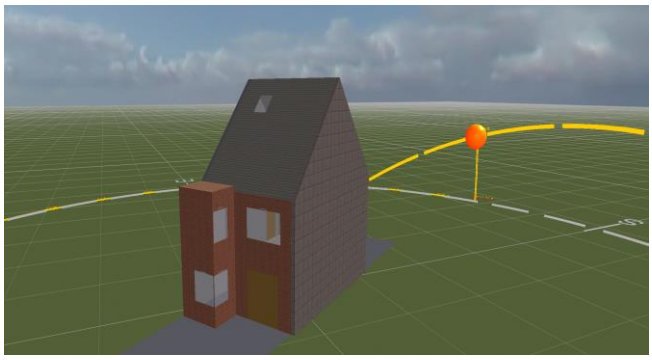

Figure 3. 3D view of a typical house in IES-VE.

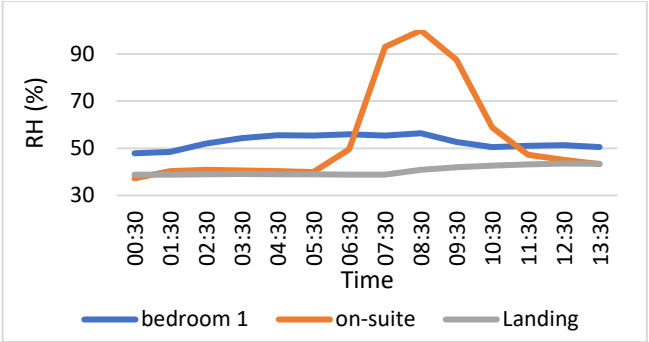

Figure 4. Impact of RH in different house zones when both nearby doors are closed after a shower.

3 RESULTS AND DISCUSSION

3.1 Relative Humidity (RH)

Generally, it is observed that the en suite bathroom witnesses higher RH as compared to any other zone, for obvious reasons. It is, therefore, advised that the adjoining door between the en suite and master bedroom be left open after taking a shower but not during. The rationale for the advice is that the accumulated pooled water and RH after a shower can be dissipated through mechanical ventilation but does so more effectively through the opening of the adjoining door which will more quickly alleviate the condensation issues in the en suite through vapour diffusion. To better understand the role of open doors to dissipate the RH, the following scenarios were considered:

Case A: This is the base case in which both the doors to the master bedroom (en suite and landing) are closed during and after taking a shower. This is the actual scenario in this selected house on one particular day and used for calibration of the model. The impact on RH is given in Figure 4 which shows that from 5.30 am until 10.30am, the RH in the en suite is elevated, rising to a peak at 8.30 am, signifying the periods when the occupants take a shower. With the door between the en suite and bedroom and between the bedroom and landing closed, it is observed that the maximum RH in the en suite was 99.9% at 8.30 am. At that time, the RH was at its maximum in the bedroom at 56.3% due to the transfer of some RH under the door from the en suite to the bedroom, added to overnight RH from the sleeping occupants. The maximum RH in the landing was noted at 43.5%, at about 10.30am, which is indicative of the fact that there is little if any transfer of RH from the en suite to the landing due to the closed doors. On average, the RH in the en suite, bedroom and landing were calculated to be 54.5%, 52.6% and 40.5% respectively, which are low although for two hours the RH was over 90% in the en suite. Thus, by keeping the doors closed, the impact on RH is negligible in the master bedroom and landing areas, but is of concern in the en suite.

Case B: In this case, the adjoining door between the en suite and master bedroom was kept open after the shower, while the door between the bedroom and landing was kept closed. The modelled effect on RH in all these three house zones is given in Figure 5. It can be observed that by opening the door after a shower, the accumulated RH in the en suite diffuses to the master bedroom, such that the level of RH is high in both the bedroom and en suite. However, there is not much impact on the RH in the landing area because the bedroom door into the landing is closed. The maximum RH in the en suite showed a slight decrease compared to the base case, falling from 99.9% to 88.2%, while the average RH in the bedroom rose marginally from 54.5% to 56.0%. Opening the door between the en suite and master bedroom deteriorates the IAQ in the bedroom considerably as the maximum RH in the master bedroom rose from 56.4% to 80% but does not improve the RH in the en suite by as much due to the relative volume of spaces involved.

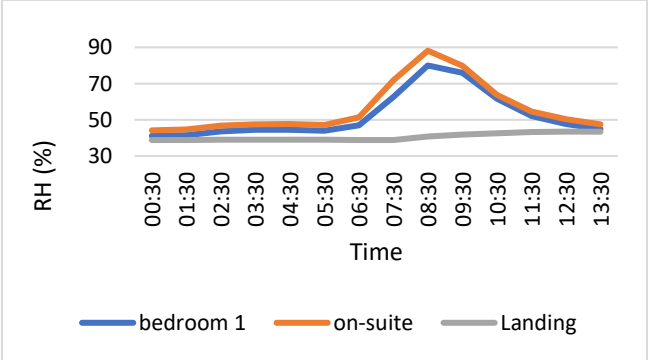

Figure 5. Impact of RH in different house zones (door between en suite and bedroom kept open after a shower).

Case C: In this case, the adjoining doors between the en suite and bedroom and between the master bedroom and landing area are kept open. The impact on the RH level in all three house zones is given in Figure 6 which shows that when both doors are opened, it leads to an increase in the RH level in the landing but improves the RH in the en suite and master bedroom. The maximum RH level in the bedroom was only slightly higher than the base case, at 60.8% as compared to 56.4% initially when all doors were closed. Moreover, the average RH in the master bedroom was the lowest of all three scenarios at 45.6% with some of the overnight RH also escaping. In the en suite, the maximum RH was the lowest of the three scenarios at 71.9%, as compared to 100% and 88.2% previously. In the landing area, the maximum RH rose to 60.6% due to dissipation of moisture from the en suite to the bedroom to landing, but this is within an acceptable range (Less than 65%) due to the extractor fan in the landing, which was inserted in a revised model to improve the overall IAQ.

Nonetheless, the maximum RH in the landing was still under the recommended threshold level and is not considered

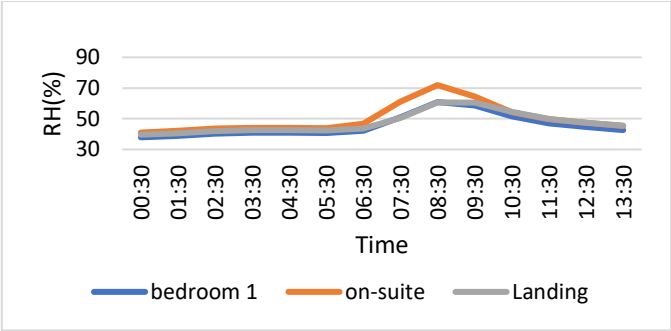

Figure 6. Impact of RH when both doors are kept open after shower.

problematic (Table 1). Thus, the opening of doors between the en suite, master bedroom and landing area (after a shower) is the preferred solution and recommended for maintaining good IAQ which can be further benefitted from by the continuous running of a new extractor fan in the landing area introduced to reduce the RH/CO_2 in the second bedroom (see below) .

Table 1 Maximum RH levels in all 3 cases of ventilation

Max RH (%)	Case 1	Case 2	Case 3
En suite	99.9	88.2	71.9
Bedroom	56.4	80	60.8
Landing	43.5	43.5	60.6

3.2 CO_2 in bedrooms

Case A – CO_2 in both bedrooms in similar conditions

It was observed from the real data in a typical case that CO_2 levels in the second bedroom could be noticeably higher than those in the master bedroom, despite similar conditions of doors, windows and vent closing. Subsequently, it was cross-checked in the model that higher CO_2 levels were observed to exist in the second bedroom despite this similarity with the main bedroom. The master bedroom was attached to the en suite, which was fitted with a mechanical extract fan which runs for 24 hours every day. However, gaps under a closed door between the en suite and master bedroom helped in reducing the level of CO_2 in the master bedroom due to air exchange, which is not the case in the second bedroom.

In this case, the base conditions entail that the master bedroom to landing door and the TV are closed. It should, however, be noted that the inbuilt factory setting of the TV keeps it open by about 10%, despite the fact that some occupants seal it with tape to avoid subsequent draughts.

Figure 7 shows typical actual values of CO_2 in the master and second bedroom for a single day assuming the above circumstances. The CO_2 levels were highest in the early morning (at 6.30 am in this case), which was most likely due to the accumulation of CO_2 in the room which had been occupied throughout the night. Later, at around 7.30am in this case, the occupants woke up, prepared themselves for the day's activities and left the room. The CO_2 levels started to reduce at a rapid pace through diffusion/dissipation, depending on whether the door to the landing was left open or not. Similar behaviour was noted in the evening, showing that CO_2 levels depended largely on the balance between occupancy (for CO_2 generation) and ventilation/dissipation (for CO_2 dissipation).

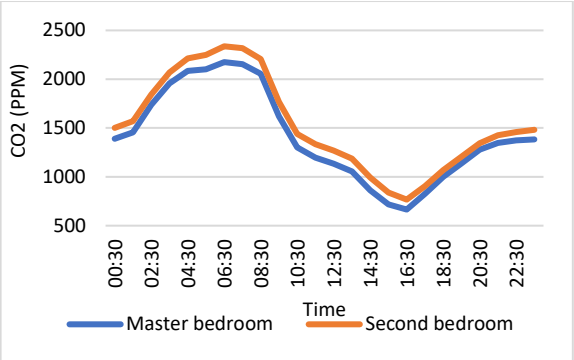

Figure 7. Actual CO_2 values in the master bedroom and the second bedroom over a day.

Moreover, it was found that the maximum difference in the CO_2 levels between the master bedroom (with double occupation) and second bedroom (with single occupation) was found to be circa 165 ppm at 7.30 am, noting that the en suite door had been left open during the night and the mechanical extract therein releasing some CO_2 externally. This scenario is not applicable in the second bedroom because there is no forced ventilation nearby, which causes the CO_2 levels to become so high.

Case B- Grill/opening in both bedroom doors

As observed in the previous scenario, it was established from actual data that the issue of high CO_2 levels in the bedrooms was observed to be the case in most of the houses. To address this problem, it was recommended by the authors that the house design be changed to provide an extra air grill in the partition above the bedroom door so that the CO_2 does not accumulate as much. It was also found that the CO_2 level increased with time when the room was occupied and, thus, it is advised that while sleeping at night, the occupants keep the main door of the room slightly open or a grill should be provided in the door which will lead to some air flow, and a lesser CO_2 accumulation. It is noted that the provision of an additional smoke detector in the bedrooms near that door would be highly recommended. The effect of this change to the ventilation is illustrated in the simulations shown in Figures 8 and 9 for the master bedroom and second bedroom respectively.

Figure 8 shows that the CO_2 levels in the landing were low before the door was opened or a grill inserted in the door. The average CO_2 levels on the landing were about 515 ppm, with the highest at 630 ppm at 10.30 pm. When the change was implemented, it was found that some of the CO_2 from the master bedroom diffused to the landing, increasing the average CO_2 to 735 ppm while the maximum CO_2 levels also increased to 830 ppm.

Similarly, when the change was implemented, the decrease in the maximum CO_2 was significant, from 2175 ppm to 1630 ppm. Therefore, the average reduction in CO_2 in the master bedroom due to the grill/door being open was estimated to be 20.3%, that is, from 1415 ppm to 1130 ppm.

Similarly, the change in CO_2 in the second bedroom, after implementing the advice is as follows: Figure 9 shows that the CO_2 levels in the landing were low before the advice of opening the grill/door was implemented. The average level in the landing near to the second bedroom was 755 ppm, with the

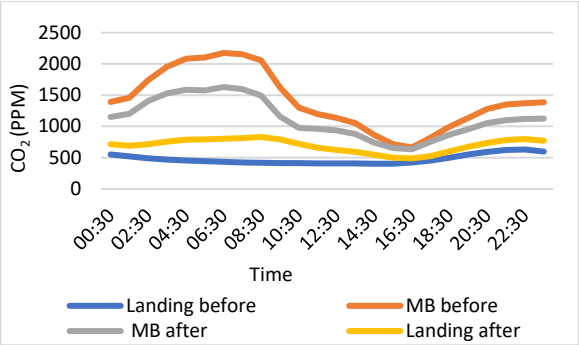

Figure 8. Effect of door opening on CO_2 levels in the master bedroom and landing.

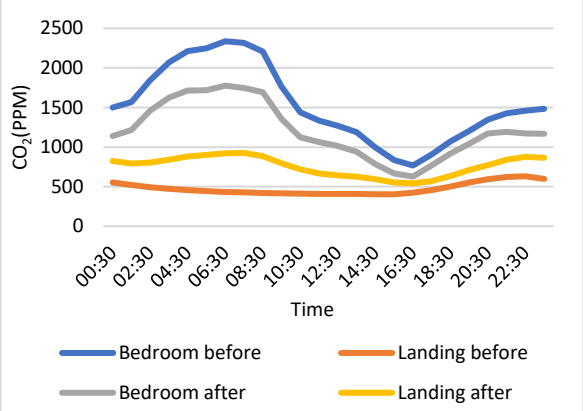

Figure 9. Effect of door open on CO_2 levels in the second bedroom and landing.

the highest at 630ppm at 7.30 am. Now when the advice was implemented, the simulation showed that the CO_2 from the second bedroom diffused into the landing, increasing the average CO_2 to some extent and the maximum CO_2 levels increased by about 300 to reach 925 ppm. Similarly, the corresponding decrease in the maximum CO_2 was significant, from 2335 ppm to 1775 ppm. Finally, the average reduction in CO_2 in the second bedroom due to the provision of a grill/door opening was estimated at 20.9%, from 1535 ppm to 1210 ppm.

Hence, the implementation of the advice has shown potentially positive results in enhancing the modelled IAQ for these rooms.

Case 3 Grill + extractor in landing

As observed in the previous case, when the doors of the two bedrooms are open, it causes the CO_2 levels in the bedrooms to fall and transfers some CO_2 to the landing. Even these CO_2 levels (typically greater than 1700 ppm) in any zone are not healthy for the occupants. Hence, in this case, a simulation is undertaken to examine the reduction in the CO_2 levels from the landing area by installing an additional extract fan in the ceiling of the landing area, in the same way that the en suite extractor fan keeps the CO_2 levels down in the master bedroom. Moreover, that fan must be operational for 24 hours. The impact of this change is illustrated in Figures 10 and 11 for the master and second bedrooms respectively.

The maximum CO_2 in the master bedroom, second bedroom and landing, before implementing any advice had been 2175 ppm, 2335 ppm and 630 ppm respectively. These levels, after all three changes were incorporated, fell to 970 ppm, and 945 ppm in the bedrooms and rose to 700 ppm in the landing (Table 2).

As the threshold level of CO_2 for any house for good IAQ is no more than 1000 ppm, these new design recommendations have reduced the peak levels, facilitating much better IAQ within the house throughout the day. Overall, these actions helped achieve better exchanges within different zones in the house, preventing CO_2 accumulation in the two worst rooms for CO_2 levels, diffusing or dissipating CO_2 through enhanced mechanical extract and door/grill openings.

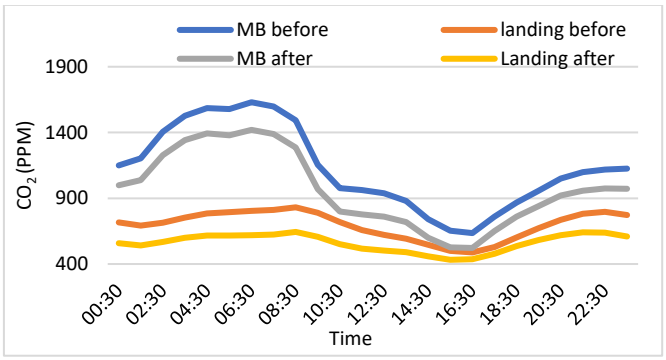

Figure 10. Impact of installing extract fan in the ceiling of landing, on CO_2 in the master bedroom and landing area.

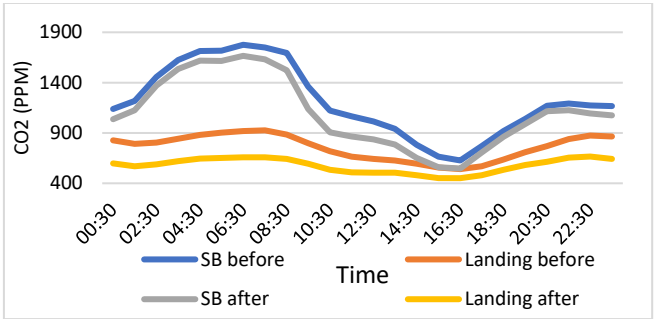

Figure 11. Impact of installing extract fan in the ceiling of landing, on CO_2 in second bedroom and landing area.

4 CONCLUSION

The observed high accumulation of CO_2 levels in the two bedrooms in reality can be relieved by opening the internal doors when leaving the rooms, according to the simulation in the calibrated model. By installing grills in the bedroom doors or keeping the internal door slightly open while sleeping at night (notwithstanding the fire consequences), accumulation of CO_2 in the rooms can be significantly reduced. By doing this, the CO_2 from the master bedroom will be dissipated to the landing area, which can further be removed by installing an extract fan in that area. This extract fan can be left operational throughout the day. The bedroom tickle vents should be left open throughout the night so that CO_2 is not unduly accumulated. However, if by doing so, the occupants experience a cold breeze/draught and close the vent, they should then re-open the TV in the morning at the time of

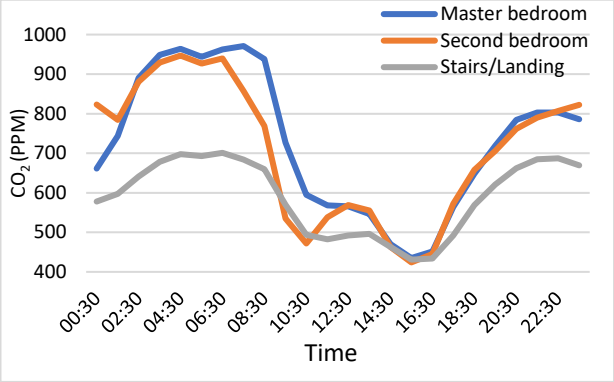

Figure 12. Impact of installing extract fan in the ceiling of landing, the grill at bedrooms and TV open on CO_2 levels.

Table 2 Maximum CO_2 levels in all 3 cases

Max CO_2 (ppm)	Case 1	Case 2	Case 3
Master Bedroom	2175	1630	970
Second Bedroom	2335	1775	945
Landing	630	830	700

leaving the room. This will dissipate the overnight accumulated CO_2 within a few hours although it will do nothing to reduce the overnight accumulations. The central mechanical ventilation system and trickle vents in the houses should always be kept on/open, so that the extraction of CO_2 and RH from the bathrooms and en suite lead to proper air exchange within the building, leading to compliance with Part F of the Irish Building Regulations.

Naturally, the relative humidity tends to be much higher in the en suite after taking the shower, which has the potential to cause persistent high moisture, condensation, and eventually mould formation issues. Thus, to mitigate this problem, it has been shown through simulations that opening the adjoining door between the en suite and master bedroom after showering will help dissipate the higher RH levels faster. Also, when the door between the master bedroom and landing is opened, the excess RH levels dissipate to the landing area, which can be removed by installing the extra extract fan in the landing.

Whilst it may be a reasonable expectation that a house with a continually running ventilation system with open trickle vents can deliver sufficient air change rates - and the performance data suggests that this results in compliant internal environmental conditions – a significant question remains as to what adverse conditions occur when occupants tend to interfere with the system as designed. Informing occupants as to what actions they should or should not undertake when living in an air-tight A-rated home is a vital part of maintaining good IAQ, as designed, and the authors have developed a guide for such purposes which is available on request.

REFERENCES

[1] Khoshbakht, M., Gou, Z., & Dupre, K. (2018). Energy use characteristics and benchmarking for higher education buildings. Energy and Buildings, 164, 61-76

[2] Psomas, T., Teli, D., Langer, S., Wahlgren, P. & Wargocki, P. (2021). Indoor humidity of dwellings and association with building characteristics, behaviours and health in a northern climate. *Building and Environment*, 198, 107885

[3] Clements-Croome, D. J., Awbi, H. B., Bakó-Biró, Z., Kochhar, N., & Williams, M. (2008). Ventilation rates in schools. *Building and Environment*, *43*(3), 362-367

[4] Persily, A. & de Jonge, L. (2017). Carbon dioxide generation rates for building occupants. *Indoor Air*, 27(5):868-879

[5] Ramalho, O., Wyart, G., Mandin, C., Blondeau, P., Cabanes, P.-A., Leclerc, N., Mullot, J.-U., Boulanger, G. & Redaelli, M. (2015). Association of carbon dioxide with indoor air pollutants and exceedance of health guideline values. *Build. Environ.*, 93:115–124

[6] Kavgic, M., Summerfield, A., Mumovic, D., Stevanovic, Z. M., Turanjanin, V., & Stevanovic, Z. Z. (2012). Characteristics of indoor temperatures over winter for Belgrade urban dwellings: indications of thermal comfort and space heating energy demand. *Energy and Buildings*, *47*, 506-514

[7] Bekkouche, S. M. E. A., Benouaz, T., Cherier, M. K., Hamdani, M., Yaiche, M. R., & Khanniche, R. (2013). Influence of building orientation on internal temperature in Saharan climates, building located in Ghardaïa region (Algeria). *Thermal Science*, *17*(2), 349-364

[8] Vilčeková, S., Apostoloski,I.Z., Mečiarová, L., Burdová, E.K. & Kiseľák, J. (2017). Investigation of Indoor Air Quality in Houses of Macedonia. Int J Environ Res Public Health, 14(1): 37

[9] Arif, M., Katafygiotou, M., Mazroei, A., Kaushik, A., & Elsarrag, E. (2016). Impact of indoor environmental quality on occupant well-being and comfort: A review of the literature. International Journal of Sustainable Built Environment, 5(1), 1-11.

[10] Joshi, S. M. (2008). The sick building syndrome. Indian journal of occupational and environmental medicine, 12(2), 61

[11] Mentese, S., Mirici, N. A., Elbir, T., Palaz, E., Mumcuoğlu, D. T., Cotuker, O., & Otkun, M. T. (2020). A long-term multi-parametric monitoring study: Indoor air quality (IAQ) and the sources of the pollutants, the prevalence of sick building syndrome (SBS) symptoms, and respiratory health indicators. Atmospheric Pollution Research, 11(12), 2270-2281

[12] Nag, P. K. (2019). Sick building syndrome and other building-related illnesses. In OfficeIn-Office Buildings (pp. 53-103). Springer, Singapore

[13] Brunekreef, B. &; Holgate, S.T. (2002). Air pollution and health. *Lancet* 2002, 360, 1233–1242

[14] Takeda, M., Saijo, Y., Yuasa, M., Kanazawa, A., Araki, A., & Kishi, R. (2009). Relationship between sick building syndrome and indoor environmental factors in newly built Japanese dwellings. International archives of occupational and environmental health, 82(5), 583-593

[15] Takigawa, T., Wang, B. L., Sakano, N., Wang, D. H., Ogino, K., & Kishi, R. (2009). A longitudinal study of environmental risk factors for subjective symptoms associated with sick building syndrome in new dwellings. Science of the total environment, 407(19), 5223-5228.

[16] Moreno-Rangel, A., Sharpe, T., McGill, G., & Musau, F. (2020). Indoor air quality in Passivhaus dwellings: A literature review. International Journal of Environmental Research and Public Health, 17(13), 4749

[17] Lin, Z.; Zhao, Z.; Xu, H.; Zhang, X.; Wang, T.; Kan, H.; Norback, D. Home Dampness Signs in Association with Asthma and Allergic Diseases in 4618 Preschool Children in Urumqi, China-The Influence of Ventilation/Cleaning Habits. PLoS ONE (2015), 10, e0134359

[18] Balvers, J., Bogers, R., Jongeneel, R., van Kamp, I., Boerstra, A., & van Dijken, F. (2012). Mechanical ventilation in recently built Dutch homes: technical shortcomings, possibilities for improvement, perceived indoor environment and health effects. *Architectural Science Review*, *55*(1), 4-14

[19] Hashemi, A., & Khatami, N. (2015). The effects of air permeability, background ventilation and lifestyle on energy performance, indoor air quality and risk of condensation in domestic buildings. *Sustainability*, *7*(4), 4022-4034

Indirect based approaches to assessing the heating behaviours of occupants in residential buildings

Masoud AzimiSechoghaei[1], Asit Kumar Mishra[1], Paul Moran[1], Jamie Goggins[1,2]
[1]MaREI Centre, Ryan Institute & School of Engineering, College of Science and Engineering, National University of Ireland, H91 TK33 Galway, Ireland
[2]Energy Resilience and the Built Environment (ERBE) Centre for Doctoral Training, National University of Ireland, H91 TK33 Galway, Ireland
email: m.azimisechoghaei1@nuigalway.ie, paul.t.moran@nuigalway.ie, asitkumar.mishra@nuigalway.ie, jamie.goggins@nuigalway.ie

ABSTRACT: Identifying occupants' heating behaviour in residences is important to understand how occupants drive heating energy demand and how heating demand varies across homes. Hence, several direct (e.g., heating appliance or heating energy use monitoring) and indirect (e.g., indoor environmental quality monitoring) approaches have been deployed to study and record heating behaviours. This paper presents a literature review of prominent indirect-based approaches for identifying the heating behaviours of occupants in buildings. Indirect approaches for examining the heating behaviour of building occupants can be applied where the installation of space heating monitoring equipment is not feasible. The paper discusses previous methodologies and subsequent metrics used for examining heating behaviours following a systematic literature review. The identified methods are examined and cross-compared in terms of their approaches and accuracy, with limitations identified for future research to address.

KEY WORDS: Heating behaviour; Residential buildings; Temperature; DEAP

1 INTRODUCTION

1.1 Irish building stock and greenhouse gas emissions

An average Irish home emits 60% more CO_2 than the average home in EU [1]. Multiple factors have an impact on the level of CO_2 emitted. Firstly, a substantial proportion of the housing stock was built before introducing and implementing the minimum standards for insulation, building and energy efficiency regulations [1]. Other factors include (i) a high average number of persons per dwelling in Ireland, (ii) large building floor areas, (iii) a large number of rooms per dwelling, (iv) a high proportion of detached dwellings and (v) extensive use of oil, gas, and solid fuels for heating [1].

1.2 Heating behaviour in standard assessment models

To help improve the energy efficiency of the building stock, EU member states were required to introduce a standard assessment procedure for the energy performance certification of new and existing buildings in their respective jurisdictions by the Energy Performance Building Directive (EPBD) [2]. The assessment would provide building owners with Energy Performance Certificates (EPCs). The EPCs act as an information tool for building owners, occupants and real estate actors on the energy demand of the building [3]. Additionally, collective EPC data for building populations can provide an important tool for policymakers and local civic in developing policies to achieve national energy reduction targets in the building sector [4].

Assumptions regarding heating behaviours in standard assessment procedures which produce EPCs have been questioned in previous studies. Field studies have shown that daily heating hours in residences [5]–[8] can be different from the assumptions in a standard assessment model [9]. According to Kane et al. [5], the number of heating hours ranged from 6.7-11.4 hours per day based on room air temperature, 2.9-3.3 hours per day based on radiator surface temperature, and 4.4 hours per day based on gas consumption. The assumed number of heating hours in BREDEM is 9 hours per day for weekdays and 16 hours per day during the weekend [9].

In UK homes, 60% of monitored living room temperature profiles over 3 months showed very different temperature profiles compared to those assumed in SAP (Standard Assessment Procedures) [10]. Huebner et al [6] found that a substantial proportion of UK homes had their space heating on between 09:00 and 16:00. SAP and DEAP [11], the standard assessment procedure in Ireland, assume the space heating to be off between 09:00 and 16:00.

Discrepancies between assumed and actual indoor temperatures has also been found in SAP and DEAP (Dwelling Energy Assessment Procedure) [7], [8]. Moran & Goggins [7] found theoretical energy demand was overestimated and theoretical average temperatures were underestimated in a study of 16 households. Based on the sample of houses in this study, the DEAP assumption of a 3°C temperature differential between the living area and the rest of the dwelling during heating hours is not representative of temperatures in actual buildings.

Studies have examined the differences in theoretical and actual energy demand of homes based on standard assessment procedures. An Irish study on the oil consumption of 145 houses pre-retrofit found that houses with a lower BER were poorer predictors of a household's oil consumption [12]. Based upon the post-retrofit data collected in this study, reasons for the differences in the theoretical and actual energy demand were believed to be due to the theoretical internal room temperatures of DEAP not being representative of the actual internal room temperatures and the underestimation of the usage of the secondary heating systems in the households.

1.3 Aim of paper

Monitoring the space heating patterns of householders has become more accessible in recent years through the development of smart metering technology. However, in certain instances, it is not possible to monitor space heating energy consumption without disrupting the energy supply to the house (e.g., houses with digital gas meters). Furthermore, in households that require solid fuel for their main space heating fuel, it is necessary for a householder to record detailed daily notes to establish accurate heating patterns. However, householders cannot be relied upon or imposed on to keep such detailed and accurate records [13].

The aim of this paper is to review indirect methods for assessing heating behaviour practices in residential buildings. The paper examines previous methods to establish the current state of the art practices in the area. This knowledge will feed into the development of a methodology for examining heating behaviours of occupants in residential buildings, in particular where installation of space heating monitoring equipment is not feasible. The developed methodology will be applicable for a number of applications including:

(i) Examining heating profiles of residential buildings compared to the heating profiles of standard assessment procedures.

(ii) Investigating whether the space heating behaviour of householders (e.g., heating period durations, indoor temperatures when heating is on and off, indoor temperatures when heating is turned on and off, etc.) change following an energy efficiency building retrofit.

(iii) Relaying space heating behaviour characteristics back to householders as part of energy consumption and IEQ feedback strategies and assess whether the information elicits any changes in the householders heating behaviour characteristics.

1.4 Systematic literature review methodology

The flowchart of the literature review methodology can be found in figure 1.

Keyword searches were conducted using the website's search engine of the NUI Galway university library. It should be noted that choosing articles from search results was conducted after reviewing the abstracts. The chosen keywords are similarly looked up using the combination shown in Table 1. The NUIG library website's advanced search engine settings were configured with two rows of terms. The first term refers to heating behaviour; the second is a synonym for "home" (see table 1). In table 1, each row includes a list of the articles that were found and those that were chosen.

A total of 4178 articles were found. The abstract of all articles was carefully reviewed, and after removing duplicates, 101 articles were identified for more detailed review. Also, six more articles were identified manually and added to the 101 selected articles. A total of 107 initially articles were selected in this step.

The abstract and methodology of 107 remaining articles were reviewed and 38 articles selected for detailed review. After reviewing all 38 articles, 23 related articles to indirect heating behaviour assessment in residential buildings were shortlisted for the presented systematic literature review.

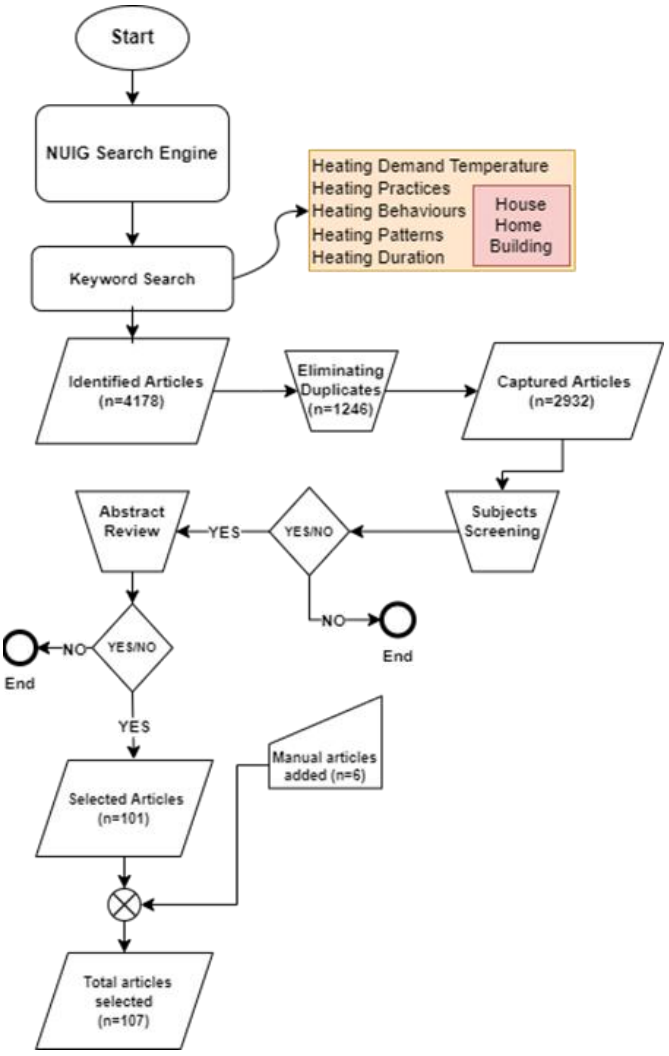

Figure 1 Systematic literature review methodology flowchart

Table 1 Keyword search

Keywords	Articles identified	Article captured for abstract review
Heating demand temperature & house	31	17
Heating demand temperature & home	25	0
Heating demand temperature & building	35	0
Heating practices, house	240	22
Heating practices, home	286	3
Heating practices, building	254	4
Heating Behaviors, house	218	16
Heating Behaviors, home	283	5
Heating Behaviors, building	434	3
Heating patterns, house	393	10
Heating patterns, home	418	3
Heating patterns, building	490	9
Heating duration, house	276	7
Heating duration, home	269	1
Heating duration, building	526	1
Total	4178	101

2 INDIRECT METHODS USED FOR RESIDENTIAL HEATING BEHAVIOUR ASSESSMENT

A method that directly monitors the heating system operation can involve monitoring how much energy is consumed by the heating appliance (e.g., electric heat pump), the fuel flowing to

the heating appliance with a flowmeter (e.g., oil, gas, etc.), or the fluid transferring heat to the heat distributors with heat flow meters. A method that indirectly monitors the operation of a heating system involves using sensors to monitor an element indirectly impacted as a result of the heating system being in operation. Studies have used radiator surface temperatures and indoor room temperatures for indirectly determining when a heating system is in operation [14]. Other approaches include the use of surveys/interviews.

Survey questions differed based on research design and hypothesis. While some studies used surveys designed by other researchers [15]–[17], others developed their own questionnaire [5], [18]. The first step to design a survey is how to measure parameters required by the study design. The second step is selecting the case study or study population. The third step is how to gather appropriate number of responses to the survey. The fourth step is analysis of responses [28].

Face to face, mailed, telephone, and web deliveries are common ways to collect data in surveys [29], with questions covering aspects of occupant behaviour [19], [20] such as heating system use, hours spent at home, appliance usage [9], [21], [22], window opening or ventilation related behaviour [20], etc. These are contextualised with other categories such as attitudes towards conservation (attitude to environment, concern regarding climate change, expenditure on energy etc.).

2.1 Statistical approaches in residential heating behaviour assessment

Shipworth et al. [19] designed an indoor temperature-based indirect method to determine a dwelling's heating profile and used a one-way analysis of variances (ANOVAs) for non-related case studies. Huebner et al. [6] developed a methodology based on time sequence comparison of indoor temperature to find when the heating is on or off in the residential building. Two years later, Huebner et al. [10] found a new relationship between human factors and building characteristics using a hierarchical cluster analysis (Ward's method).

Kane et al. [5] investigated heating and temperature profiles in residential buildings. Kane et al. [5] used seven different equations for assessing heating and temperature profiles including room air temperatures, radiator surface temperatures, gas meter data, peak thermostat temperatures and average thermostat temperatures. The profiles were developed based on data collected for five months in 20 dwellings.

Kelly et al. [23] developed a panel regression method, which is a development of standard regression method, with five statistical models to predict the mean internal temperature of residential dwelling. Bedir et al. [24] developed a hierarchical cluster analysis to investigate thermostat behaviours. This method provides a better understanding of thermostat control and the occupant's behavioural pattern. Becker et al. [25] developed a hidden Markov Model (HMM) for classification to find out how much energy could be saved in a residential building with an occupancy-based heating strategy. This method can be used while improving the building's characteristics parameters in the simulation.

Heating behaviour and temperature metrics can be classified into time-based and temperature-based metrics [26]. The most common metrics across reviewed articles are room air temperature [5], [6], [10], [17], radiator surface temperature [5], [27], number of under-heated days [15], [16], and daily mean temperature [16], [23]. A number of metrics are used in different equations across reviewed articles to assess heating and temperature profiles.

Shipworth et al. [19] developed a temperature-based metric equation to identify the state of the heating system in residential buildings:

$$Heating\ is\ active\ if\ T_{LR,i+1} - T_{LR,i} > 0 \quad (1)$$

where $T_{LR,i}$ is the living room temperature at time interval i.

Huebner et al. [6] developed a new approach three years later to show when the heating system is on or off based on the room air temperature. According to the Huebner et al. [6] technique, a change in the heating system's status (on/off) was considered to have happened if the temperature fluctuations in the room were at least 0.75° C.

Also, Kane et al. [28] used ANOVA to find variances among non-correlated case studies. Kane et al. [28] proposed an equation based on room air temperature to calculate heating hours and developed nine metrics that affect and characterise heating practices, including external air temperatures (warmer days requiring less heating), number of heating periods per day, start and end times of heating periods, duration of heating per day, number of under-heated days, mean winter temperature, the difference between the average temperature of the living room and bedroom, mean daily maximum temperature in the living room and, average temperature during heating periods.

Two years later, Kane et al. [5] upgraded the room air temperature equation he developed earlier [28].

Kane et al.'s [5] equation for assessing if the heating is operational based on room air temperature is as follows:

$$Heating\ is\ active\ at\ time't'\ if\ \left(T_{room,t} - T_{room,t-1} > 0\right) or\ (if(T_{room,t-1} - T_{room,t-2} > 0 \text{ or } T_{room,t-2} - T_{room,t-3} > 0\ and\ T_{room,t-1} - T_{room,t} > -0.05)) \quad (2)$$

where $T_{room,t}$ is the room air temperature at time t, $T_{room,t-1}$ is the room air temperature at the time step before time t, and $T_{room,t-2}$ is the room air temperature at the time step before time t−1.

Kane et al. [5] developed another equation to calculate when the heating is on and off based on radiator surface temperature. Heating state identification based on radiator temperature [5]:

$$Heating\ is\ active\ if$$

$$\left(\left(T_{rad,t} - T_{rad,t-1} > 3°C\right) or\ T_{rad,t} > 35°C\right)$$

$$unless\left(\left(T_{rad,t} - T_{rad,t-1} < -3°C\right) or\ T_{rad,t} < 18°C\right) \quad (3)$$

where $T_{rad,t}$ is the radiator surface temperature and $T_{rad,t-1}$ is the radiator surface temperature (◦C) at time the time step before time t.

According to Kane et al. [5], of the two indirect methods for assessing heating operation based on room air temperature and radiator surface temperature, the methodology based on radiator surface temperature is the most reliable. Figure 2, adapted from Kane et al. [5], provides the heating hours over five-months based gas consumption, radiator surface temperature, and room air temperature. The first column is the total heating hours calculated based on the gas consumption method, a direct heating hours calculation method. The second and third columns are total heating hours based on the radiator surface calculation metric (see Eq. 3). Because TRV sensors were not used (or were used) on the monitored radiators in Kane et al. [5], the second and third total heating hours estimations differed. The fourth and the fifth columns are total heating hours based on the room air temperature calculated by Eq. 1 and Eq. 2, respectively.

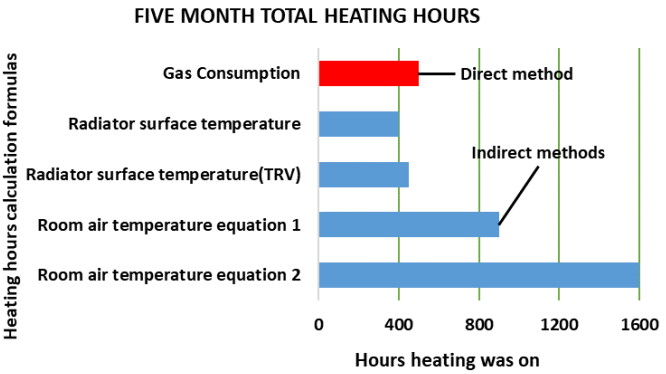

Figure 2. Total heating hour comparison based on direct and indirect methods (adapted from Kane et al. [5])

2.2 Machine Learning approaches in residential heating behaviour assessment

Among reviewed studies, some researchers used machine learning (ML) techniques rather than statistical methods. Xue et al. [21] provided an ML approach to improve characterizing energy performance of district heating and distinguished six heating patterns concerning the primary heat of the substation. Jang et al. [22] developed a hybrid Artificial Neural Network-Random Forest (ANN-RF) technique to predict building thermal energy consumption behaviours in a school building in South Korea.

Machine learning approaches can improve the heating and occupant behaviour prediction compared to statistical methods. Due to the more complex and comprehensive modelling that they utilise, ML algorithms can create a more feasible heating monitoring system by optimising the location of heating sensors and controllers [29]. However, compared to statistical techniques, ML algorithms require much larger datasets for analysis. Berliner et al. [14] developed a ML based method (ANN) to assess indoor heating, temperature, and humidity profiles in 39 case studies of indoor and outdoor temperature and humidity data. The indoor temp was measured based on radiator input and output temperature data. This approach was used for the first time on temperature and humidity data and can be used on the rest of the monitored time series data concerning the dwelling heating profile, such as electrical, gas boiler usage, or room temperature data. Berliner et al. [14] state a 78% accuracy of their model, which predicts the heating duration within one hour.

Becker et al. [25] developed a Hidden Markov Model (HMM) to predict when occupants are at home based on smart electricity meter data to provide an occupancy-based heating strategy and discovered that 9-14% of heating energy could be saved.

3 DISCUSSION

As highlighted in Figure 1, a high level of uncertainty can exist when using indirect methods to estimate heating behaviour. Reliable approaches that can indirectly and non-intrusively monitor heating patterns in residences, need to be carefully vetted and their results verified. Except for a few reviewed studies, validation of proposed methodologies was not clear from the information provided in the reviewed studies. In this section studies that have validated their approach through verification of results have been summarized. Validation was either performed against other approaches, including direct measurement of heating energy use, in the same study or through cross-comparison against results from other similar studies.

Some studies compare their developed methodologies against others approaches such as Kane et al. [5] as discussed above. Models and other machine learning based methods reported a 70-80% precision [14]. Jang et al. [22] found the ANN model can improve the quality of prediction comparing to other ML models [22].

Finding the best strategy becomes challenging as not all the examined research assess (based on the information in the articles) the accuracy of their methodology for indirectly assessing heating behaviours. Furthermore, due to the wide variations that can be caused by occupant behaviour, determining the best method based solely on the projected total heating hours and set point temperature is unreliable. As an illustration, the mean number of heating hours per weekday varies from 3.3 to 9.8 or more [5], [30], while the mean indoor temperature for the same period varies from 19.5 to 21.5°C [6], [31].

There is no simple way to validate all reviewed methodologies and find the most accurate method. Therefore, a comparison of existing developed methods with an independent set of data is needed to determine the optimum method for indirectly assessing heating behaviours and temperature profiles.

In addition, any developed indirect methods should be validated using a direct source of heating schedules such as those implemented in smart heating control systems [5]. Also, smart control and metering devices help monitor more challenging parameters by requiring a more advanced sensor. For instance, Becker et al. [25] predict the occupant's presence by using smart home metering devices and electricity consumption.

Performance of regression-based models can be assessed based on the model coefficient of determination (R^2) and other model accuracy checks such as mean absolute error (MAE) or root-mean-square deviation (RMSE). A panel-based regression model using the three assumptions of exogeneity of regressors, conditional homoskedasticity, and conditionally uncorrelated correlations to predict variance of residential indoor

temperature with $R^2 = 0.45$ is an example of this [23]. Another example is a simple linear regression model for mean internal temperature based on standardized daily external temperature [32].

Similar to regression-based models, the output of ML or AI based models can also be verified against the input data set to check the validity and utility of these models. Studies have used Artificial Neural Network (ANN) models [14], [22] arriving at 70-80% precision [14]. Among the ML approaches used, ANN was shown to have improved prediction, compared to random forest model [22].

4 CONCLUSIONS & FUTURE WORK

This literature review discusses different indirect heating behaviour assessment aspects across the most related articles. The aim of this paper is to review indirect methods for assessing heating behaviour practices in residential buildings. Following a systematic literature review which included the in-depth review of 38 studies, the following conclusions were drawn:

- Based on one study comparing methods based on radiator surface temperature, room air temperature, peak thermostat temperatures and average thermostat temperatures, a method based on radiator surface temperature was identified as the most approach for indirectly assessing residential heating and temperature behaviours.
- The high level of uncertainty when using indirect methods for assessing heating behaviours mean any developed approaches should be validated with direct measurements of heating behaviours.
- ML approaches are starting to become more common in developing methods for indirectly assessing residential heating behaviours.
- The number of dwellings and the monitoring duration can significantly impact the generality of results on a larger scale.
- A comparison of existing developed indirect methods with an independent set of data is needed to determine the optimum method for indirectly assessing heating behaviours and temperature profiles.

ACKNOWLEDGMENTS

The authors would like to acknowledge the financial support from the Sustainable Energy Authority of Ireland (SEAI) through the HEAT CHECK project (grant agreement 19/RDD/492).

REFERENCES

[1] SEAI, “Energy in the residential sector,” 2018. [Online]. Available: https://www.seai.ie/publications/Energy-in-the-Residential-Sector-2018-Final.pdf

[2] T. H. E. E. Parliament, T. H. E. Council, O. F. The, and E. Union, “Directive 2002/65/EC of the European Parliament and of the Council,” *Fundam. Texts Eur. Priv. Law*, pp. 65–71, 2020, doi: 10.5040/9781782258674.0021.

[3] A. Arcipowska, F. Anagnostopoulos, F. Mariottini, and S. Kunkel, *Energy Performance Certificates (EPC) across the EU Mapping of national approaches*. 2014. [Online]. Available: http://bpie.eu/publication/energy-performance-certificates-across-the-eu/#.VDZi_vmSx9V

[4] I. E. Agency, “Energy Performance Certification of Buildings - Policy Pathway,” p. 64, 2010, [Online]. Available: https://iea.blob.core.windows.net/assets/b496e040-a9d4-4d6e-b98b-ec3cfb02a3eb/PolicyPathway-EnergyPerformanceCertificationofBuildings.pdf

[5] T. Kane, S. K. Firth, T. M. Hassan, and V. Dimitriou, “Heating behaviour in English homes: An assessment of indirect calculation methods,” *Energy Build.*, vol. 148, pp. 89–105, Aug. 2017, doi: 10.1016/j.enbuild.2017.04.059.

[6] G. M. Huebner, M. McMichael, D. Shipworth, M. Shipworth, M. Durand-Daubin, and A. Summerfield, “Heating patterns in English homes: Comparing results from a national survey against common model assumptions,” *Build. Environ.*, vol. 70, pp. 298–305, Dec. 2013, doi: 10.1016/j.buildenv.2013.08.028.

[7] P. Moran and J. Goggins, “Can DEAP help us to predict the energy demand and indoor temperature of homes before and after renovation ? A case study from Dublin,” *Civ. Eng. Res. Irel. 2020*, pp. 371–376, 2020.

[8] G. Hunter, S. Hoyne, and L. Noonan, “Evaluation of the Space Heating Calculations within the Irish Dwelling Energy Assessment Procedure Using Sensor Measurements from Residential Homes,” in *Energy Procedia*, Mar. 2017, vol. 111, pp. 181–194. doi: 10.1016/j.egypro.2017.03.020.

[9] J. Henderson and J. Hart, “BREDEM 2012-A technical description of the BRE Domestic Energy Model,” p. 37, 2015, [Online]. Available: www.bre.co.ukOtherBREpublicationsareavailablefromwww.brebookshop.com

[10] G. M. Huebner, M. McMichael, D. Shipworth, M. Shipworth, M. Durand-Daubin, and A. J. Summerfield, “The shape of warmth: Temperature profiles in living rooms,” *Build. Res. Inf.*, vol. 43, no. 2, pp. 185–196, Mar. 2015, doi: 10.1080/09613218.2014.922339.

[11] SEAI, “Domestic Energy Assessment Procedure (DEAP) 4.2.2,” no. July, p. 195, 2020, [Online]. Available: https://www.seai.ie/energy-in-business/ber-assessor-support/deap/.

[12] KajLeonhart Petersen, “SERVE Energy Monitoring Project – Report on Implementation and Analysis CONCERTO INITIATIVE Sustainable Energy for the Rural Village Environment,” no. October, 2012.

[13] E. Network, “Energy Consulting Network and Tipperary Energy Agency, SERVE (Sustainable Energy for the Rural Village Envrionment) Energy Analysis, 2013.No Title,” 2013, [Online]. Available: https://scholar.google.com/scholar?q=Energy Consulting Network and Tipperary Energy Agency, SERVE Energy Analysis, 2013.

[14] N. Berliner, M. Pullinger, and N. Goddard, “Inferring room-level use of domestic space heating from room temperature and humidity measurements using a deep, dilated convolutional network,” *MethodsX*, vol. 8, Jan. 2021, doi: 10.1016/j.mex.2021.101367.

[15] P. Beagon, F. Boland, and J. O’Donnell, “Quantitative evaluation of deep retrofitted social housing using metered gas data,” *Energy Build.*, vol. 170, pp. 242–256, Jul. 2018, doi: 10.1016/j.enbuild.2018.04.022.

[16] S. H. Hong, T. Oreszczyn, and I. Ridley, “The impact of energy efficient refurbishment on the space heating fuel consumption in English dwellings,” *Energy Build.*, vol. 38, no. 10, pp. 1171–1181, Oct. 2006, doi: 10.1016/j.enbuild.2006.01.007.

[17] G. M. Huebner, M. McMichael, D. Shipworth, M. Shipworth, M. Durand-Daubin, and A. Summerfield, “The reality of English living rooms - A comparison of internal temperatures against common model assumptions,” *Energy Build.*, vol. 66, pp. 688–696, 2013, doi: 10.1016/j.enbuild.2013.07.025.

[18] R. V. Jones, A. Fuertes, C. Boomsma, and S. Pahl, “Space heating preferences in UK social housing: A socio-technical household survey combined with building audits,” *Energy Build.*, vol. 127, pp. 382–398, Sep. 2015, doi: 10.1016/j.enbuild.2016.06.006.

[19] M. Shipworth, S. K. Firth, M. I. Gentry, A. J. Wright, D. T. Shipworth, and K. J. Lomas, “Central heating thermostat settings and timing: Building demographics,” *Build. Res. Inf.*, vol. 38, no. 1, pp. 50–69, Jan. 2010, doi: 10.1080/09613210903263007.

[20] D. Mora, C. Carpino, and M. De Simone, “Energy consumption of residential buildings and occupancy profiles. A case study in Mediterranean climatic conditions,” *Energy Effic.*, vol. 11, no. 1, pp. 121–145, Jan. 2018, doi: 10.1007/s12053-017-9553-0.

[21] P. Xue, Z. Zhou, X. Chen, and J. Liu, “An application of data mining in district heating substations for improving energy performance,” in *E3S Web of Conferences*, Nov. 2017, vol. 22. doi: 10.1051/e3sconf/20172200192.

[22] J. Jang *et al.*, "Development of an improved model to predict building thermal energy consumption by utilizing feature selection," *Energies*, vol. 12, no. 21, 2019, doi: 10.3390/en12214187.

[23] S. Kelly *et al.*, "Predicting the diversity of internal temperatures from the English residential sector using panel methods," *Appl. Energy*, vol. 102, pp. 601–621, 2013, doi: 10.1016/j.apenergy.2012.08.015.

[24] M. V. D. S. Bedir, "for a Renewable Future, Germany (CD)," in *Analysis of thermostat control in dutch dwellings: occupants' behavioral profiles*, 2018, pp. 155–186.

[25] V. Becker, W. Kleiminger, V. C. Coroamă, and F. Mattern, "Estimating the savings potential of occupancy-based heating strategies," *Energy Informatics*, vol. 1, pp. 35–54, Oct. 2018, doi: 10.1186/s42162-018-0022-6.

[26] T. Kane, "Indoor temperatures in UK dwellings: investigating heating practices using field survey data," 2013, [Online]. Available: https://dspace.lboro.ac.uk/dspace-jspui/handle/2134/12563

[27] S. Paine, P. James, A. B. Bahaj, and A. Waggott, "Heating and controls use resulting from shared-cost charges in communal network social housing," *Build. Serv. Eng. Res. Technol.*, vol. 41, no. 3, pp. 315–331, May 2020, doi: 10.1177/0143624420911170.

[28] T. Kane, S. K. Firth, and K. J. Lomas, "How are UK homes heated? A city-wide, socio-technical survey and implications for energy modelling," *Energy Build.*, vol. 86, pp. 817–832, 2015, doi: 10.1016/j.enbuild.2014.10.011.

[29] Z. Liu *et al.*, "Accuracy analyses and model comparison of machine learning adopted in building energy consumption prediction," *Energy Exploration and Exploitation*, vol. 37, no. 4. SAGE Publications Inc., pp. 1426–1451, Jul. 01, 2019. doi: 10.1177/0144598718822400.

[30] A. Bruce-Konuah, R. V. Jones, A. Fuertes, and P. De Wilde, "Central heating settings in low energy social housing in the United Kingdom," in *Energy Procedia*, 2019, vol. 158, pp. 3399–3404. doi: 10.1016/j.egypro.2019.01.941.

[31] A. Bruce-Konuah, R. V. Jones, and A. Fuertes, "A method for estimating scheduled and manual override heating behaviour and settings from measurements in low energy UK homes," *Int. J. Build. Pathol. Adapt.*, 2021, doi: 10.1108/IJBPA-05-2021-0074.

[32] A. J. Summerfield, R. J. Lowe, H. R. Bruhns, J. A. Caeiro, J. P. Steadman, and T. Oreszczyn, "Milton Keynes Energy Park revisited: Changes in internal temperatures and energy usage," *Energy Build.*, vol. 39, no. 7, pp. 783–791, Jul. 2007, doi: 10.1016/j.enbuild.2007.02.012.

One-Stop-Shops: Are they effective in delivering energy retrofit of homes in Ireland?

Orlaith McGinley[1,2], Paul Moran[1], Jamie Goggins[1,2]
[1]MaREI Centre, Ryan Institute & School of Engineering, College of Science and Engineering, National University of Ireland, Galway, University Road, Galway, Ireland
[2]Energy Resilience and the Built Environment (ERBE) Centre for Doctoral Training, National University of Ireland, Galway
email: o.mcginley2@nuigalway.ie, paul.t.moran@nuigalway.ie, jamie.goggins@nuigalway.ie

ABSTRACT: The European Commission's Renovation Wave Strategy aims to enable deep retrofit and double the annual rate of energy retrofit by 2030. Ireland has a role in achieving this ambition with Ireland's Climate Action Plan setting a target of retrofitting 500,000 homes to a B2 Building Energy Rating (BER) or better by 2030. To accomplish this, persistent retrofit barriers must be addressed. Both the Commission's Renovation Wave Strategy and Ireland's Climate Action Plan emphasise the importance of One-Stop-Shop (OSS) retrofit models in alleviating these barriers. In fact, several Irish OSSs exist, with the National Home Retrofit scheme in place to assist their growth and new OSS development. A fundamental understanding of existing Irish OSS and retrofit services is required to support this. This paper presents the findings of ongoing research which evaluates existing Irish OSS and retrofit services. Householder experiences of engaging with existing Irish OSSs are discussed, based on the findings of surveys with householders who have completed (and partially completed) their retrofit journey using their services. The paper reveals that while householders generally have positive experiences with OSSs, there are several areas for improvement. More pressingly, householders agree that there are systemic issues not yet addressed in existing OSSs that not only impact householder satisfaction with the retrofit process, but also impact the effectiveness of OSSs in supporting retrofit uptake.

KEY WORDS: One-Stop-Shop; Retrofitting; Energy Efficiency; Retrofit Barriers

1 INTRODUCTION

Circa 1% of Europe's existing building stock is retrofitted annually, with around 0.2% undergoing deep retrofit [1]. The European Commission's Renovation Wave Strategy [1] proposes to at least double the annual energy retrofit rate of European residential buildings by 2030, with 35 million buildings to be retrofitted by 2030. Ireland's Climate Action Plan [2] sets equally ambitious targets, including retrofitting 500,000 dwellings to a B2-Building Energy Rating (BER) or better by 2030, in addition to the installation of 400,000 heat pumps in existing homes. In 2020, however, just 18,400 homes were retrofitted in total, of which just 4,000 achieved a B2-BER, and 1,600 installed a heat pump [2]. While COVID-19 certainly impacted retrofit activity in 2020 [2], from 2013-2019, approximately 23,000 retrofits were completed on average per annum, with just 2,600 dwellings in 2019 achieving a B2-BER or better [3]. Current projections state that around 75,000 homes will need to be retrofitted annually from 2026-2030, to achieve the targets set [2]. This will require thousands of Irish homeowners to make the (often complex) decision to retrofit. Significant retrofit barriers must be alleviated to achieve this ambition. For homeowners, these barriers might be financial, associated with the high upfront costs of retrofits, difficulties accessing grants and financing, and the complexity of funding structures [4], [5], [6]. Moreover, homeowners often lack awareness and knowledge of retrofit measures, their benefits, and of the retrofit schemes and providers available [6]-[13]. In addition, homeowners may face difficulties accessing the information they need, and question the trustworthiness and credibility of different information sources [7], [8], [9], [10], [11], [12], [13]. Homeowners also face difficulties in finding appropriately skilled contractors with availability to conduct the works [9], [14], [15], and are often concerned about the quality, reliability, and trustworthiness of these retrofit professionals [10], [13], [14], [16], [17]. Furthermore, the disruption, hassle, and stress associated with retrofit implementation can also prevent homeowners from implementing works, particularly when homeowners have to manage the process and coordinate multiple actors across a fragmented supply chain [11], [18], [19], [20].

Both the Renovation Wave strategy [1] and Ireland's Climate Action Plan [2] emphasise the important role of One-Stop-Shop (OSS) retrofit models in addressing retrofit barriers and supporting retrofit uptake. OSSs are designed to offer and support full-service retrofitting, providing householders with a single point of contact who guides householders through the process, acts as project manager, and takes responsibility for the process [21]. Across Europe, around 100,000 retrofits are completed annually through OSSs [22], with OSSs emerging in Ireland supported by the National Home Retrofit Scheme in place to support their growth [23].

Literature has discussed OSS business models [18], [22], [24], [25], [26], [27], [28] and their proposed benefits [18], [19], [21], [24], [29], [30], [31]. From a householder perspective, the benefit of OSSs lies in their support of retrofit decision-making, and as a single contact for trusted, reliable advice and information [18], [30]. Consequently, householders could implement deeper retrofits than they would otherwise consider [18], [29], [30], with project management reducing the hassle they traditionally face [18], [19]. OSSs can also provide access to financing and grants, while also managing repayments, reducing the likelihood of multiple repayments for the householder [18], [24]. By integrating the supply side, OSSs allow supply side stakeholders to achieve economies of

scale, and promote knowledge, skill, and innovation transfer among the supply side [18]. Moreover, by pooling supply chain capacity, OSSs can enable single service providers to extend their offerings and enter wider market segments [18]. They can also act as a representative for the supply side [18].

Others, however, note potential disadvantages including the reduced ability for homeowners to choose preferred suppliers, while the retrofit measures available to householders, may be limited to only those offered by the OSS [26]. There may also be higher costs associated with their use [29], while conflicts of interest can arise between the different disciplines involved. Having a single point of contact might also introduce potential biases [26]. Furthermore, any issues between the homeowner and the OSS will impact the entire project [26].

While the business models and benefits of OSSs are increasingly discussed in literature, there is a distinct lack of studies which empirically examines householders' experiences with OSSs. Some studies investigate various factors (including socio-demographics), that relate to interest in OSS models, [24], [29], [30], but less frequently examine actual engagement with OSSs. Yet, such research is considered vital to validate the effectiveness of OSSs and ensure their continuous improvement. For instance, Bjørneboe et al. [30] found that while there were benefits of the OSS model, the concept was not a sufficient motivator for houseowners to undertake extensive renovations. Moreover, it could not be said whether the OSS model made renovation more accessible to those without an already vested interest in retrofitting to begin with [30]. They also state that OSSs should offer householders the freedom to choose the contractors they would like to do the works, and ultimately conclude that the focus should be on enhancing the role of independent energy advisors within the retrofit industry, rather than moving towards OSSs, to improve impartiality in the retrofit process [30].

The success of the Irish OSS model in contributing to the achievement of the Climate Action Plan targets relies on many householders being willing to undertake deep retrofits. Moreover, the supply side must be encouraged to undertake this role. Yet, no research exists which examines the Irish householders' interest in engaging with OSSs, nor their experiences in doing so. Moreover, there is no research which examines the interest and ability of Irish supply-side stakeholders in taking on this role. Yet, this is vital to ensuring the necessary supports are in place to encourage and enable their development. Thus, questions remain as to whether an OSS model is enough to solve the slow progress of retrofitting in Ireland, and fast enough to meet ambitious government targets.

This paper presents the initial findings of ongoing research evaluating Irish OSS and retrofit services, from the perspective of retrofit professionals and experts in the industry, and from the perspective of householders who have completed (or partially completed), their retrofit journey using OSSs. Semi-structured interviews with retrofit professionals/experts and householder surveys have been used to evaluate these services. While the householder surveys collect a broad range of information, this paper focusses on findings from six householders (hereafter, Householder 1 to Householder 6), specifically focussing on their experiences of engaging with Irish OSSs during their retrofit journey.

2 DATA COLLECTION

Householder surveys were conducted with householders from six households that had retrofitted their dwellings using Irish OSSs. Surveys were conducted from July 2021 to January 2022. Householders were recruited from referrals from professionals within existing OSSs, and from personal contacts. Prior to the surveys, householders were provided with a project information sheet and consent form. The surveys lasted approximately 1 hour and were recorded and transcribed verbatim. In these surveys, data was gathered on householders' experiences with OSS and retrofit services in Ireland, including detailed accounts of their retrofit journey, the quality of the OSS services and customer relationships throughout the process. Information was also gathered on householders' perception of the technical quality of the implemented retrofits, their overall satisfaction with the process, and any benefit they perceive to have obtained.

3 HOUSEHOLDER EXPERIENCES WITH IRISH OSS

Figure 1 presents householders' responses to various statements relating to their OSS experience. The remainder of this section will discuss their responses in more detail and highlight important themes emerging from the surveys, including the importance of independence, transparency, and accountability within OSSs and the difficulties householders face in understanding the retrofit grant process. Householders' overall ratings of their OSS experiences and the quality of the implemented works are also presented.

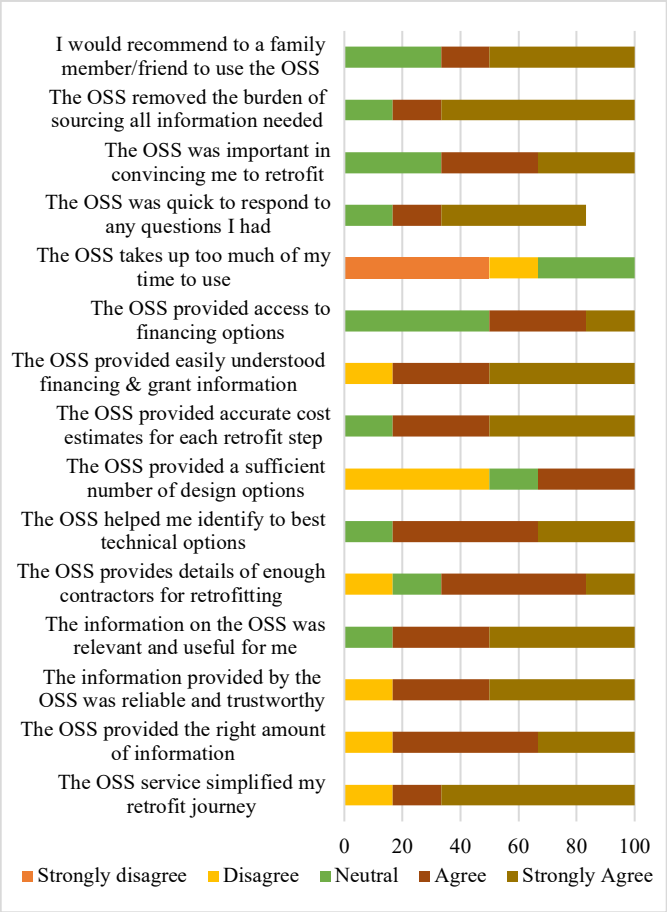

Figure 1. Householder experiences with Irish OSSs

3.1 The importance of independence, transparency, and accountability

OSSs are expected to act as a single point of contact for trusted, reliable retrofit information and advice [18], [30]. Most householders felt that the OSS removed the burden of sourcing the information needed, and that the information provided was relevant, useful, reliable, and trustworthy. However, one householder (Householder 2) disagreed that sufficient information was provided, noting that more information on the measures, their benefits, and the reasons for all technical and design decisions was required. They also expressed their scepticism regarding the trustworthiness of information provided. In their case, the OSS completed all aspects of the retrofit (including advice, design, and works implementation) in-house. The householder questioned the trustworthiness of information provided by such an OSS relative to an independent body. They stated:

"…I'm not particularly sure that I believe a lot of what I'm being told…when it is being advocated as a better option by a builder, I'm wondering do I believe this person or not?" [Householder 2]

In addition, Householder 2 noted that the lack of transparency in such an OSS model can have particularly negative consequences if anything goes wrong.

"…anything that happens through the OSS…the relationship is with the OSS…triple alarm bells ringing, very bad system. No transparency…because my builder [also the OSS] messed up, and because my builder [also the OSS] isn't taking responsibility, I have no comeback…" [Householder 2]

Comparatively, Households 1,3,5 and 6 used OSSs which were independent from the contractors that would be implementing the works. In such OSSs, contractors were recommended to householders, with the OSS providing advice, project management and co-ordination of all aspects of the retrofit process. Householder 5 emphasised the benefits of such a model in terms of the trustworthiness of the information provided.

"*…the fact that [the OSS] aren't contractors…I've never felt that they were trying to sell me something, so I've never felt that they benefit financially from the more I do, because they're independent and they're…providing a project management service…in many ways they told me ways to save money…" [Householder 5]*

Independence of the OSS was not only found to be an important factor in householders' perception of the trustworthiness of information provided, but in their satisfaction with the number of technical and design options offered. The OSSs used by Householders 1, 3, and 5 provided householders with the choice of several contractors that could conduct the works. Householder 6 noted that as a result, several technical and design options were offered, allowing the householder to avoid significant disruption during the installation of their heating system. They stated:

"While we used a One-Stop-Shop, they…came back with more than one quote [from multiple contractors], particularly for the heating system, which was very useful…Initially, when one of the companies did an assessment for the heating system, they told us…they might have to replace underfloor piping...When a second contractor came…their chief engineer…had a solution that…wouldn't have to have any piping changed which was attractive…" [Householder 6]

However, one householder noted the importance of transparency in how and why OSSs recommend contractors to householders and the relationships between OSSs and recommended contractors. For instance, the OSS used by Householder 1 offered a choice of three contractors to the householder. The householder noted that while they trusted that all three would have been equally good, they questioned whether the OSS was independent from the contractors they recommend. They questioned the OSSs criteria for inclusion on their recommended list, and the need for visibility in this process.

"*There were only three listed [by the OSS] …I don't know if they [OSS]…qualify the builders…but the [building surveyor] and the builders should be strictly independent from the [OSS], but I'm not sure that that is the case…I don't doubt that they should be on the list, but does it create a monopoly if they're the only ones eligible?" [Householder 1]*

On the other hand, however, the OSS used by Householder 5 selected the contractors for the householder. However, Householder 5 stated that this was not necessarily an issue, but a benefit of OSSs. They stated:

"…the contractors would have been selected for me…given the choice I wouldn't even know who to pick…I'm just as happy that someone else has the responsibility…if something goes wrong…somebody else is looking after it…" [Householder 5]

3.2 Access to grants & financing: The importance of information and transparency in the grant process

A benefit of OSSs is their ability to provide or arrange access to grants and loans [18], [24]. Most householders felt that the OSS provided easy to understand information on grants and financing. However, several householders expressed the difficulty they encountered in understanding the grant process, including the calculation of grant and energy credits. For instance, Householder 6 disagreed that the OSS provided easy to understand information on grants and financing, stating that they remained uncertain as to how much they had obtained and how it was calculated. They stated:

"…more information about the details of getting the grants, and the amount of the grants…I shouldn't have had to ask for that...everything was going so quickly…we got an invoice, and we would just pay it…towards the end…I would be thinking, well, where do the grants actually figure in all this…?" [H6]

"…their communication with us could have been better and their invoicing could have been…more transparent. [The OSS] figures and my figures don't match…" [Householder 6]

Householder 2 agreed that the OSS provided easy to understand information on financing and grants, however, they later stated that they were uncertain as to the amount of grants and energy credits they got.

"*…I'm unclear…it [the cost] was presented [as] energy credits…how much it cost…how much you saved…Maybe I'm just not very good at math…The information…was a bit unyielding…" [Householder 2]*

They also expressed concerns regarding the lack of transparency in the grant and energy credit calculation. This was particularly important, given that the issues they

experienced with their implemented works reduced their overall faith in the OSS. They stated:

"Seemingly, I'm on the SEAI grant, and you get credits off the price…I'm just told by the building contractor how many grant credits have been used…So, I'm trusting a contractor [also their OSS] [to provide this information], which would be fine if I trusted my contractor which I no longer do, so that is the issue." [Householder 2]

"…the builder [also their OSS] is calculating credits, that the [grant authority] cannot validate, so there is no independent advisor to advise me on this…" [Householder 2]

"…if you go with a One-Stop-Shop, the grant goes directly to the One-Stop-Shop, it doesn't go to the client at all…" [Householder 2]

Householder 1 noted other issues with the grant process, whereby difficulties in obtaining the grants delayed their works. However, they were not entirely clear as to why, given their uncertainty as to how the process operates. However, they felt this was not an area for improvement within the OSS, but a wider issue within the Irish grant process.

Three householders agreed that the OSS provided access to financing options. However, the householders did not use these services. Others were neutral on this point, stating that it was either not offered by their OSS, or not relevant to them. As a wider issue, Householder 2 expressed that finance providers currently offering retrofit loans required more training in the area.

"…I was completely underwhelmed when I spoke to [financing provider] about…green loans…the staff were at the inception of the project and not trained in properly…" [Householder 2]

3.3 *The overall experience of Irish OSSs and perceptions of the quality of implemented works*

Figure 2 presents householders' overall ratings of the OSS service and the quality of the implemented works. Householders generally rated their overall experience of the OSS services and the quality of the works quite highly, with several noting no areas for further improvement. However, while Householder 6 rated the quality of the implemented works as excellent, they rated the overall OSS service used slightly lower on the scale at 6 out of 10. This was primarily a result of issues the householder encountered with transparency in the grant calculation and in the OSSs invoicing.

Householder 2, however, struggled to rate their experience, given the issues they encountered post retrofit. They also felt that wider issues remain unaddressed by OSSs.

"…I bought into 'there must be something I don't know about a OSS and a retrofit', and I am still questioning why…The systemic problem is why are people currently being advised to do deep retrofit when there is no accountability…no transparency…I understand we are on doomsday times, but honestly, unless there is some…accountability and transparency for the SEAI, the builders, and independent evaluators, I wouldn't advise anyone to do a deep retrofit at this point in time…" [Householder 2]

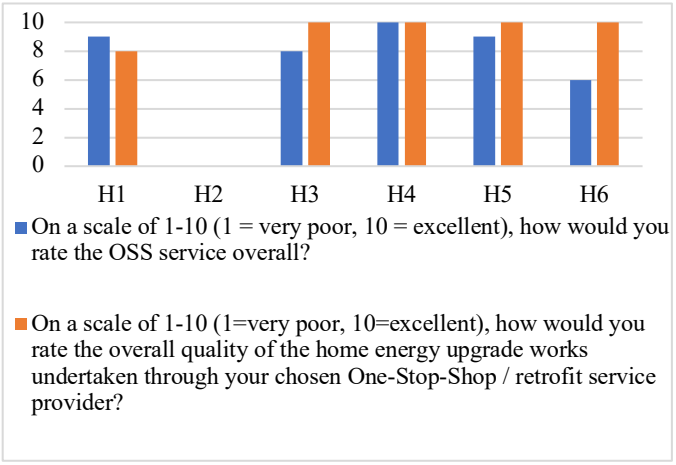

Figure 2. Householder ratings of their overall experience of the OSS service and the quality of the works

4 DISCUSSION & CONCLUSION

Thousands of Irish householders will have to retrofit their homes if Ireland's Climate Action Plan targets are to be achieved. However, the barriers householders face must be addressed. Information on and access to grants and financing must be improved, while the complexity in their use must be reduced. The awareness and knowledge of householders on what to do, how to do it, retrofit measures and their benefits must be increased on a national basis. To do so, easily accessible, coherent, and trustworthy information must be provided by credible sources. Householders must be able to easily access skilled and trustworthy contractors, to reduce their concerns around the reliability of retrofit professionals and quality of the works, while the difficulties associated with managing a disruptive and inconvenient process with many actors, must be removed. OSSs are a proposed solution for alleviating these barriers.

This paper examines householders' experiences of engaging with Irish OSSs. The paper found that householders generally have positive experiences with OSSs. Most householders agreed that the OSS simplified their retrofit journey. Most felt that their OSS was a trusted contact for reliable retrofit information and advice, and that OSSs improved the accessibility of the information they needed. Most agreed that the OSS provided easily understood information on grants and financing, provided accurate retrofit costs, and could provide access to finance options if required by the householder. In addition, most householders agreed that the OSSs provided details of enough technical options for their home, suggesting that OSSs are well positioned to increased householders' awareness of retrofit technologies and their benefits. However, they did not always offer enough design options. In addition, several householders felt that OSSs provided details of enough contractors available to do the works, suggesting that OSSs can effectively reduce barriers associated with the accessibility and availability of skilled retrofit professionals. However, while these findings suggest that OSSs can, as stated by other authors, remove persistent retrofit barriers for householders, this is not always the case. This is reflected in Householder 2's particularly negative experience of engaging with their OSS, and by the fact that other householders highlighted several

areas for improvement that they see necessary for OSSs to successfully support householders through their retrofit journey.

The findings reveal several key factors for OSS success, including the OSSs independence from the contractors that will be implementing the works, and quite crucially, increased transparency and oversight not just of the OSS and its operations, but within the retrofit industry at large.

By design, OSSs effectively blur lines between various actors in the retrofit process, including contractors, suppliers, retrofit designers and surveyors, and even, grant authorities and finance bodies. While this reduces the effort required from householders in sourcing and managing each of these actors and the retrofit process, householder experiences suggest that there must be transparency in the OSSs relationship with these actors, their roles, and their responsibilities, to reduce the likelihood of project biases that could ultimately impact the householder. This includes transparency in how contractors are chosen and recommended by OSSs, clear and tangible explanations in why retrofit measures are recommended over other technical and design options, and in how grants and energy credits are applied to the costs of the works throughout the retrofit process.

Moreover, householders' experiences suggest that if the OSS itself is not an independent body from these actors, then oversight of the OSS is critical. This is particularly the case for OSS models in which all aspects of the retrofit are conducted in-house, given the lack of fall back a householder has if something goes wrong. Such was the case in Householder 2's experience. It is critical that this oversight is provided to ensure quality in the retrofit process, and to limit the occurrence of negative retrofit experiences that when perpetuated, can prevent others from implementing retrofits. Such findings largely support Bjørneboe et al.'s [30] conclusion that the role of independent bodies in the retrofit industry be bolstered oversee and ensure that OSSs conduct quality works. In addition, the findings also somewhat agree that at the least, OSSs should offer householders the freedom to choose between the contractors with which they are affiliated, in line with Bjørneboe et al. [30].

A further point of interest is that two of the six householders interviewed, neither agreed nor disagreed that the OSS was important in convincing them to conduct their works. This could suggest that, in line with Bjørneboe et al. [30], the OSS concept itself is not a sufficient motivator for homeowners to undertake retrofits. Thus, more research is required to confirm whether the establishment of OSSs (and their associated benefits) is enough to encourage householders to embark on, and complete, their retrofit journey.

While the findings of this paper are based on the experiences of a small sample of householders, this ongoing research project will continue to gather insights on householder experiences of engaging with Irish OSSs, as well as that of the retrofit experience of householders that have not engaged with OSSs, to draw comparisons between these experiences. This research will also gather insights as to the readiness of supply-side stakeholders to take on this role, and the future directions for success. This research will inform the continuous improvement of OSSs as they develop over time and contribute towards their success in incentivising householders to engage in deep retrofit until the end of the decade and beyond.

ACKNOWLEDGMENTS

The authors acknowledge the financial support of the European Union's Horizon 2020 research and innovation programme (Grant agreement No. 839134), Science Foundation Ireland for the ERBE Centre for Doctoral Training (Grant agreement No. 18/EPSRC-CDT/3586) and the MaREI Centre (Grant agreement No. 12/RC/2302_P2).

REFERENCES

[1] European Commission, "Communication from the commission to the European Parliament, the Council, the European Economic and Social Committee and the Committe of Regions - A Renovation Wave for Europe - greening our buildings, creating jobs, improving lives. COM/2020/662 final," European Commission, Brussels, 2020.

[2] Government of Ireland , "Climate Action Plan," Government of Ireland , Dublin, 2021.

[3] Sustainable Energy Authority of Ireland , "National BER Research Tool," [Online]. Available: https://ndber.seai.ie/BERResearchTool/Register/Register.aspx . [Accessed 21 April 2022].

[4] M. Collins and J. Curtis, "An examination of the abandonment of applications for energy efficiency retrofit grants in Ireland," *Energy Policy,* vol. 100, pp. 260-270, 2017.

[5] R. Desmaris, O. Jauregui, O. McGinley and J. Volt, "D 2.1 Market and PESTLE Analysis," TURNKEY RETROFIT Consortium, 2019.

[6] M. Collins and J. Curtis, "Identification of the information gap in residential energy efficiency: How information asymmetry can be mitigated to induce energy efficiency renovations," Economic and Social Research Institute (ESRI), Dublin, 2017.

[7] Sustainable Energy Authority of Ireland , "Policy insights for encouraging energy efficiency in the home A compilation of findings from a research fellowship co-funded by SEAI and ESRI," Sustainable Energy Authority of Ireland, Dublin, 2018.

[8] C. Wilson, L. Crane and G. Chryssochoidis, "Why do people decide to renovate their homes to improve energy efficiency," Tyndall Centre for Climate Change Research, Norwich, 2013.

[9] B. Risholt and T. Berker, "Success for energy efficient renovation of dwellings - Learning from private homeowners," *Energy Policy,* vol. 61, pp. 1022-1030, 2013.

[10] H. Ebrahimigharehbaghi, Q. Qian, F. Meijer and H. Visscher, "Unravelling Dutch homeowners' behaviour towards energy efficiency renovations: What drives and hinders their decision making?," *Energy Policy ,* vol. 129, pp. 546-561, 2019.

[11] C. Klockner and A. Nayum, "Specific Barriers and Drivers in Different Stages of Decision-Making about Energy Efficiency Upgrades in Private Homes," *Frontiers in Psychology ,* vol. 7, p. 1362, 2016.

[12] I. Kastner and E. Matthies, "Investments in renewable energies by German households: A matter of economics, social infleunces and ecological concern?," *Energy Research & Social Science ,* vol. 17, pp. 1-9, 2016.

[13] S. Priest, T. Greenhalgh, H. Neill and G. Young, "Rethinking Diffusion Theory in an applied context: Role of Environmental Vlaues in Adoption of Home Energy Conservation," *Applied Environmental Education & Communication,* vol. 14, no. 4, pp. 213-222, 2015.

[14] J. Baginski and C. Weber, "A Consumer Decision-making Process? Unfolding Energy Efficiency Decisions of German Owner-Occupiers," House of Energy Markets and Finance , Essen, 2017.

[15] R. Baumhof, T. Decker and K. Menrad, "A Comparative Analysis of House Owners in Need of Energy Efficiency Measures but with Different Intentions," *Energies,* vol. 12, no. 12, p. 2267, 2019.

[16] B. Mallaband, V. Haines and V. Mitchell, "Barriers to domestic retrofit - learning from past home improvement experiences," in *Retrofit 2012 Conference* , Salford , 2012.

[17] G. Cerinsek, D. Bancic, D. Podjed, S. D'Oca, J. Vetrsek, S. Dolinsek and P. op't Veld, "Boosting affordability, acceptability, and attractiveness of deep energy renovations of residential buildings - a people centred ethnographic approach," in *ES3 Web of Conferences, vol. 111, p. 03026. EDP Sciences* , 2019, 2019.

[18] B. Boza-Kiss and P. Bertoldi, "One-Stop-Shops for energy renovations of buildings," European Commission, Ispra , 2018.

[19] E. Mlecnik, I. Kondratenko, J. Cre, J. Vrijders, P. Degraeve, J. Aleksander van der Have, T. Haavik, S. Aabrekk, M. Gron, S. Hansen, S. Svendsen, O. Stenlund and S. Paiho, "Collaboration Opportunities in Advanced Housing Renovation," *Energy Procedia ,* vol. 30, pp. 1380-1389, 2012.

[20] T. Long, W. Young, P. Webber, A. Gouldson and H. Harwatt, "The impact of domestic energy efficiency retrofit schemes on householder attitudes and behaviours," *Journal of Environmental Planning and Management ,* vol. 58, no. 10, pp. 1853-1876, 2015.

[21] O. McGinley, P. Moran and J. Goggins, "Key Considerations In The Design Of A One-Stop-Shop Retrofit Model," in *Civil Engineering Research in Ireland 2020*, 2020.

[22] P. Bertoldi, B. Boza-Kiss, B. Valle and M. Economidou, "The role of one-stop shops in energy renovation - a comparative analysis of OSSs cases in Europe," *Energy and Buildings ,* vol. 250, p. 111273, 2021.

[23] Sustainable Energy Authority of Ireland , "One Stop Shop Service," [Online]. Available: https://www.seai.ie/grants/home-energy-grants/one-stop-shop/. [Accessed 13 April 2022].

[24] K. Mahapatra, L. Gustavsson, T. Haavik, S. Aabrekk, S. Svendsen, L. Vanhoutteghem, S. Paiho and M. Ala-Juusela, "Business models for full service energy renovation of single family houses in Nordic countries," *Applied Energy,* vol. 112, pp. 1558-1565, 2013.

[25] D. Brown, "Business models for residential retrfoti in the UK: a critical assessment of five key archetypes," *Energy Efficiency ,* vol. 11, pp. 1497-1517, 2018.

[26] K. Balson, M. Moreira and L. Simkovicova, "Description of one-stop-shop models for step by step refurbishments," EuroPHit, 2016.

[27] R. Moschetti and H. Brattebo, "Sustainable business models for deep energy retrofitting of buildings: state-of-the-art and methodological approach," in *SBE16 Tallinn and Helskini Conference: Build Green and Renovate Deep* , Tallinn and Helsinki , 2016.

[28] J. Volt, S. Zuhaib and S. Steuwer, "Benchmarking of promising experiences of integrated renovation services in Europe," TURNKEY RETROFIT project , 2019.

[29] G. Pardalis, K. Mahapatra, G. Bravo and B. Mainali, "Swedish House Owners' Intentions Towards Renovations: Is There a Market for One-Stop-Shop?," *Buildings ,* vol. 9, no. 7, p. 164, 2019.

[30] M. Grøn Bjørneboe, S. Svendsen and A. Heller, "Using a One-Stop-Shop Concept to Guide Decisions When Single-Family Houses are Renovated," *Journal of Architectural Engineering ,* vol. 23, no. 2, 2017.

[31] Sustainable Energy Authority of Ireland , "Behavioural insights on energy efficiency in the residential sector," Sustainable Energy Authority of Ireland , Dublin, 2017.

[32] C. Aravena, A. Riquelme and E. Denny, "Money, comfort or environment? Priorities and determinants of energy efficiency investments in Irish households," *Journal of consumer policy,* vol. 39, no. 2, pp. 159-186, 2016.

[33] J. P. Clinch and D. J. Healy, "Domestic energy efficiency in Ireland: correcting market failure," *Energy Policy,* vol. 28, no. 1, pp. 1-8, 2000.

Can Irish buildings become net energy-producing carbon-sinks?

Brian Norton[1, 2, 3]
[1]IERC, International Energy Research Centre, Tyndall National Institute, University College Cork, Cork, Ireland
[2]Dublin Energy Lab, Technological University Dublin, Dublin, Ireland
[3]MaREI: the SFI Centre for Energy Climate and Marine
email: brian.norton@ierc.ie

ABSTRACT: Embodied GHG emissions will become an increasingly significant part of the total GHG emissions from buildings as operating emissions reduce in future. An immediate increase in cumulative emissions occurs at the time of renovation because of the embodied emissions in the additional materials and components used. Coordinated updating of existing policies together with well-targeted and innovative initiatives are required integrate decarbonisation of electricity and heat produced by, and supplied to, buildings with decarbonisation of industry and transport, (iii) reuse and recycle to reduce embodied GHG emissions in building materials, components and processes used in both the construction of new buildings and in building renovations.

KEY WORDS: Buildings, Energy, Renovation, Decarbonisation

1 INTRODUCTION

Buildings' greenhouse gas emissions (GHG) summarised in Table 1 (Norton et al, 2021), arise from operational energy use, production of that energy used and from emissions embodied in the energy used to produce, transport and install materials, components, and systems during building, maintenance, renovation and demolition. The largest embodied emissions are in foundations, floor slabs and in structural components that contain steel and cement.

Table 1. Processes Leading to GHG Emissions from Buildings

Operational	Direct	Fossil fuels combustion on site to provide heating and hot water
	Indirect	Use of district heat produced from fossil-fuels
		Use of fossil-fuel generated electricity
Embodied		Extraction and processing of construction materials. Manufacturing building components
		Transportation to site; Construction processes
		Demolition processes

Technology improvements, energy retrofits of existing buildings and enhanced building regulations for new buildings combined with macroeconomic factors to reduce domestic energy use in Ireland from 1990 to 2015 by 32% in raw figures; equivalent to 37% when correcting for the warming climate over that period. However, the average Irish home still has high energy consumption compared with elsewhere in the EU. Direct GHG emissions produced by burning fuels for energy use depend on a particular building's form, fabric and systems. These vary daily and annually with weather conditions, number of occupants and their activities, internal temperatures, equipment and appliances used and their control settings. A wide range of interventions, summarised in Table 2, can improve building fabrics, enable energy generation as well as store and more-efficiently use energy.

Table 2 Opportunities and Challenges for the Adoption of Key Technologies (adapted from Norton et al, 2021)

Technology	**Opportunity**	**Challenges**
Thermal insulation	Low heat losses through building envelope	Can be disruptive to retrofit in existing buildings
Mechanical ventilation with heat recovery	Lower heat losses by controlled ventilation and air-tightness	Regulations required to ensure regular cleaning to avoid airborne virus transmission
Heat pumps	Replace boilers or electric heaters	Rate and cost of introduction
District heating	Can use heat pumps, biogas, solar, geothermal and/or waste heat. Large heat stores can balance supply and demand	Installation of heat networks. Without carbon capture and storage, district heating can no longer use fossil fuels.
Building-integrated PV	Provides local electricity generation	Shading from trees and adjacent buildings
Solar water heating	Can offers 30% of hot water supply.	Uncompetitive with other renewable energies
Biogas	When replacing natural gas, it avoids assets becoming stranded in supply infrastructure and existing gas boilers	Role limited by sustainable biogas resources
Green hydrogen		Green hydrogen more expensive than green electricity used for its production, so not viable in electrifiable building applications.
Geothermal heat	Use directly or via heat pumps.	Geothermal heating largely unexploited.
Energy-efficient lights	Lower electricity use.	Control to switch-off artificial lighting when daylight is available

2 REDUCING GHG EMISSIONS BY RENOVATING EXISTING BUILDINGS

The largest potential for reducing GHG emissions is in increasing the depth and rate of energy-efficient renovation. In Ireland, it is intended to make grant-supported energy retrofits of 500,000 homes to B2 Energy Performance Certificate (EPC) standard by 2030. The opportunities and barriers are summarised in Table 3.

Table 3. Opportunities for, and barriers to more energy-efficient existing buildings (Norton et al, 2021)

Action	Impact	Barriers
Deep energy renovation	Reduces energy use and GHG emissions	Access to affordable finance, confidence in renovation outcomes and occupants to vacate and/or accept disruption
Energy renovation of rented housing		Disincentive of benefits accruing to tenant. Needs regulations obliging landlords to renovate.
Use prefabricated renovation components	High quality control; lower embodied GHG emissions; year-round indoor jobs	Investment in manufacturing facilities requires long-term addressable renovation market
Renovate neighbourhoods	Economies of scale	Enables bundling of renovations to be more easily funded. Easier in areas with similar buildings.
	District heating use, positive-energy homes can export energy to neighbours; collective action/support	
Intensify occupancy	Lower energy use per unit building area	Resistance to downsizing,
Leave fewer buildings vacant		Property market conditions; Planning constraints

Cumulative GHG emissions from local combustion of fuels and those produced in supplying electricity and heat for both residential and non-residential buildings in the EU have been calculated for the two scenarios given in Table 4 (EASAC, 2021).

Cumulative emissions from both scenarios as shown in Figure 1, are broadly similar until around 2030, when they start to diverge. The carbon budgets for the EU buildings sector to deliver its share (i.e., about 25% of EU's carbon budget) of the GHG emissions reductions needed to limit climate warming to 1.5 and 2 degrees Celsius are also shown in Figure 1.

Table 4. Scenarios examined for projecting cumulative emissions from EU buildings to 2050 (EASAC, 2021)

Scenario	Features	Assumptions
Renovation wave	Decarbonisation of electricity and heat supplied to buildings, (as in no renovation scenario). Energy renovation decreases the operational GHG emissions from buildings but increases their embodied GHG emissions.	Operational GHG emissions for each building (or floor area) decrease to zero after renovation. Average 3.3% (630,000,000 m2/a) of total EU floor area renovated annually from 2021 to 2050. Total floor area unchanged after renovation. Each floor area is renovated only once. Renovations incur embodied GHG emissions when renovated, falling from 125 kgCO2e/m2 in 2021 to zero in 2050 (due to use of zero-carbon energy).
No renovation (Business as usual – BAU)	Annual emissions from buildings decrease year-on-year with decarbonisation of electricity. In 2050 there are still emissions from combustion of fuels in buildings.	Consistent with EU targets, assuming that GHG emissions from electricity and district heat production will fall by 55% (compared to 1990) by 2030 and reach net-zero by 2050. GHG emissions from combustion of fuels within buildings remain at their mean level between 2010 and 2018 as heating systems within buildings are not renovated.

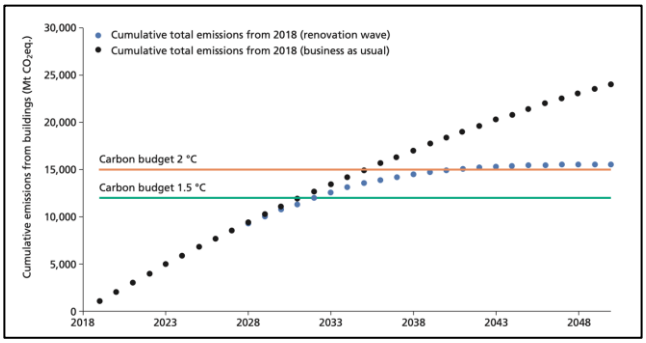

Figure 1. Impact of a European renovation wave on the cumulative emissions from EU buildings

As indicated in Figure 1, that If building renovation rates are increased to deliver an average of 3.3% per year with a bell curve distribution between 2021 and 2050, and each renovation reduces building operational emissions to zero, while producing embodied GHG emissions (e.g.: 125 kgCO2e/m2 in 2021 declining to zero by 2050), then the EU buildings sector could deliver its share of the GHG emission reductions needed to limit climate warming to 2 degrees Celsius. Renovation reduces operational GHG emissions from buildings but increases emissions in the short-term due to embodied carbon emissions. The trade-off between reducing operational emissions but adding embodied emissions, depends on the amount of GHG emissions embodied in renovation. This is shown in Figure 2 where cumulative emission curves are presented for different levels of embodied GHG emissions (kgCO2e/m2 of floor area) and for business-as-usual (BAU) but all other parameters remain unchanged.

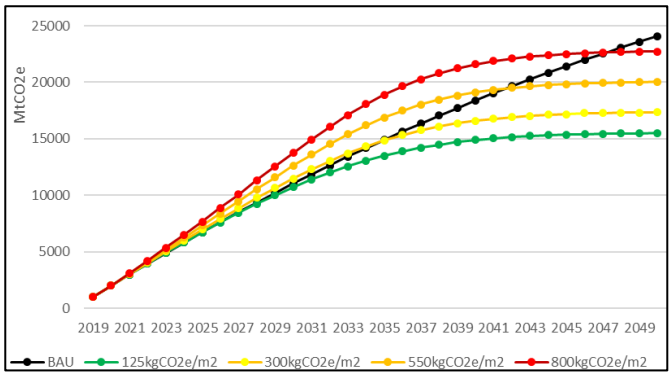

Figure 2. Sensitivity of cumulative GHG emission trajectories to embodied GHG emissions

An implication of this analysis is that for a particular building energy retrofit,

(i) maximum operational energy use reduction per unit embodied energy should be achieved that may require refurbishing to higher than the current B2 EPC target, and

(ii) embodied emissions must be included in design choices, materials selection and construction techniques.

Reducing embodied GHG emissions requires (i) improved availability and quality of embodied GHG emissions data for building materials and components, (ii) improved documentation on embodied GHG emission from new buildings and renovations, (iii) setting limits for embodied GHG emissions per m2 floor area of both new and renovated buildings, (iv) more use of recycled building materials and components and (v) designing components for re-use and recycling if they have high embodied GHG emissions. With treatments and installation that limit fire risks, timber can be engineered to replace concrete and steel and is well-suited for prefabrication. By using timber, carbon absorbed by trees can be locked into a building, delaying the negative impacts on forest carbon sinks caused by cutting down trees. However, as less than half the carbon in harvested trees can end-up in wood products with a long lifetime, the carbon footprints of all timber sources need to be closely monitored.

Energy renovations of domestic (Ahern and Norton, 2019) and non-domestic (Norton and Lo, 2020) buildings usually also improve air quality, access to daylight, comfort, sound insulation, disabled access and/or access to outdoor space. Wider social benefits also accrue through new renovation businesses creating jobs. Economic cases for investments in energy renovations should therefore aggregate both direct and indirect benefits.

Deeper energy renovations to reduce GHG emissions to nearly-zero have significantly higher investment costs that typically take up to about 30 years to recover through savings in energy costs, so providing affordable initial finance becomes essential. Underprivileged vulnerable groups need others to invest to raise them out of energy poverty. Investing in the deep renovation of buildings whose occupants are in energy poverty could be a better use of public funds than social welfare interventions paying high energy bills for energy inefficient homes over extended periods. Energy poverty interconnects policies on energy use, family welfare, social housing, social care, housing tenure, income support and economic development.

3 ENERGY SUPPLY TO BUILDINGS

Given that fossil-fuelled heating systems typically last up to about 25 years, it is urgent to set clear deadlines for their installation to cease by 2029 as implied in the REPowerEU plan (EC, 2022), Indeed projections shown in figure 3, from the most recent report of the Intergovernmental Panel on Climate Change (Clarke at al. 2022), indicates that steeper reductions in greenhouse gas emissions from buildings require a significantly rising share of electricity, almost no gas as well as much lower energy requirements.

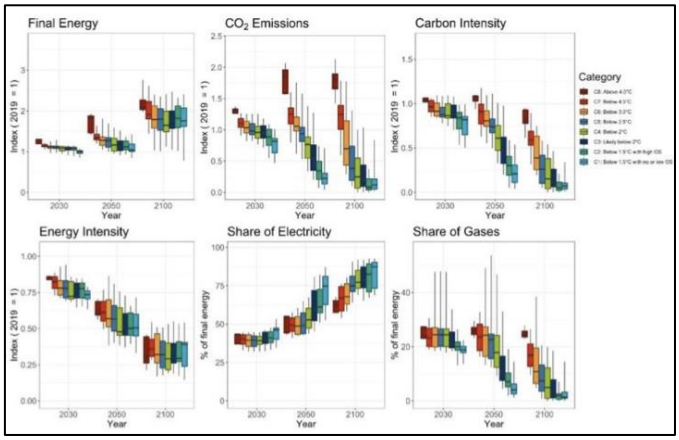

Figure 3. Projections of energy use and emissions from buildings by the Intergovernmental Panel on Climate Change (Clarke at al. 2022).

Renewable energies will provide low GHG emission heating and electricity through grid and building-integrated photovoltaics, heat pumps and district heating networks. The challenges and requirements for low-carbon electrification of buildings are summarised in Table 5.

4 TOWARDS BUILDINGS AS CARBON SINKS

For truly environmentally sustainable buildings it is important to (i) focus on energy used by a building instead of primary energy demand, (ii) include embodied GHG emissions from building materials, components and processes, and (iii) separate renewable energy exports and energy consumption

Table 5. Meeting the challenges of low-carbon building electrification (Adapted from Norton et al, 2020)

Challenge	Requires
Electrified building heating at competitive cost	Mass use of heat pumps with cost-reductions through economies of scale
Balancing electricity demand from buildings with variable supplies of electricity coming from renewable generation.	Battery electricity storage in buildings Coupling buildings to batteries in electric vehicles Storing excess electricity as heat for future use Coordinated aggregated approach to grid flexibility management, with up-dated electricity market rules On-site generation of renewable electricity Reinforcement of electricity transmission and distribution grids Large-scale flexible electricity generation
Minimising total and peak demands for electricity from buildings	Maximising number of low-energy renovated existing buildings Use of district heating/cooling systems in urban areas Storage and use of waste heat, solar heat and excess renewable electricity generation Load-shifting of equipment and appliances Time-dependent tariffs and smart-metering to encourage self-generation and self-consumption.
Intersector Coupling	Greater interconnection between sectors as low-carbon energy supplies to buildings are optimised at the energy system level with those for transport and industry.

when making building energy performance assessments to avoid perverse incentives that might discourage the reduction of underlying building energy demand. Key priorities to decarbonise new and existing buildings are summarised in Table 6.

5 CONCLUSION

Buildings in Ireland can indeed become net energy producing carbon sinks if, and when, the following prerequisites are in place:

- Net zero energy design with building integrated PV, heat pumps and heat recovery from ventilation air and, where feasible, waste-water
- Local storage of PV and solar heat energy generation
- Use of low embodied energy materials
- Forest products inventories that ensure wood used in buildings is a net CO_2 sink
- Wind and photovoltaic electricity generation linked efficiently to energy storage and hydrogen production to ensure winter peak electrical loads are met

Table 6. Key priorities to decarbonise new and existing buildings (adapted from Norton et al ,2020)

Priority	Action	
Improve health and wellbeing by deep-energy renovation	Ensure deep energy renovations provide high air quality, good access to daylight, and avoid draughts and overheating.	
Deliver new and renovated buildings operating with nearly zero GHG emissions	Refocus regulations, certification schemes and incentives Legal/regulatory obligations on building owners or their energy suppliers Facilitate and support commitments by public authorities. Increase deep renovation rates 2 to 3 times	
Reduce embodied GHG emissions	Make available certified data on energy and GHG emissions	for new and renovated buildings
		in materials and components
	Promote recycled materials, re-used building components, and renovation instead of demolition.	
Expand and modernise the building industry	More circular business models and innovation in construction processes for new and renovated buildings with lower GHG emissions	
Phase-out fossil fuels by 2030	Legislate for energy industries to phase-out use of fossil fuels and accelerate introduction of new decarbonised energy supplies. Integrate decarbonised supplies of electricity and heat to buildings, industry and transport.	
Legislation should be updated with	National targets, and eventually limits per m2 of floor area for both operating and embodied GHG emissions in new buildings and renovations, Separate accounting of (a) embodied plus operating GHG emissions and (b) positive energy contributions of a building by generating and exporting electricity and/or heat A new focus on final energy consumption and GHG emission data (instead of primary energy consumption data) for setting building performance limits and determining financial returns on environmentally-sustainable investments in specific buildings and renovations.	

- Inter-building heat and electricity networks linked to heat and electricity storage to match local supply and demand (Saif et al, 2022).

The challenge is to make technically feasible options economically viable. Coordinated updating of existing policies together with well-targeted and innovative initiatives are required that (i) ensure that measures to reduce energy and GHG reductions also enhance the health and well-being of

building occupants, (ii) integrate decarbonisation of electricity and heat produced by, and supplied to, buildings with decarbonisation of industry and transport, (iii) reuse and recycle to reduce embodied GHG emissions in building materials, components and processes used in both the construction of new buildings and in building renovations. Decarbonising buildings is an opportunity to develop and produce new products and services that create new high-quality jobs.

ACKNOWLEDGEMENTS

The author wishes to thank the European Academies Science Advisory Committee for insights reported in this paper gained in producing the report "Decarbonisation of buildings: for climate, health and jobs". The development of this paper was partially supported by MaREI, the SFI Research Centre for Energy, Climate and Marine [Grant No. 12/RC/2302_P2].

REFERENCES

[1] Ahern, C. and Norton, B., 2019. Thermal energy refurbishment status of the Irish housing stock. Energy and Buildings, 202, p.109348.

[2] Clarke, L., Wei, Y-M., Navarro, A. D. L. V., Garg, A., Hahmann, A. N., Khennas, S., Azevedo, I. M. L., Löschel, A., Singh, A. K., Steg, L., Strbac, G., Wada, K., Ameli, H., de La Beaumelle, N. A., Bistline, J., Byers, E., Calvin, K., Chawla, K., Cui, Y., ... Veldstra, J *Climate Change 2022: Mitigation of Climate Change. Working Group III Contribution to the IPCC Sixth Assessment Report* Cambridge University Press.

[3] Cohen, R., Eames, P.C., Hammond, G.P., Newborough, M. and Norton, B., 2022. Briefing: The 2021 Glasgow Climate Pact: steps on the transition pathway towards a low carbon world. Proceedings of the Institution of Civil Engineers-Energy, pp.1-6.

[4] EASAC 2021 Decarbonisation of buildings: for climate, health and jobs, EASAC Secretariat German National Academy of Sciences Halle, Germany

[5] EC, 2022, REPowerEU Plan, Communication from the Commission to the European Parliament, the European Council, the Council, the European Economic and Social Committee and the Committee of the Regions, 18th May 2022

[6] Norton, B. and Lo, S.N., 2020. Atria, Roof-space Solar Collectors and Windows for Low-energy New and Renovated Office Buildings: a Review. SDAR* Journal of Sustainable Design & Applied Research, 8(1), p.4.

[7] Norton, B., Gillett, W.B. and Koninx, F., 2021. Briefing: Decarbonising buildings in Europe: a briefing paper. Proceedings of the Institution of Civil Engineers-Energy, 174(4), pp.147-155.

[8] Saif, A., Khadem, S.K., Conlon, M. and Norton, B., 2022. Hosting a community-based local electricity market in a residential network. *IET Energy Systems Integration*. In Press.

Hydrodynamic modelling of marine tidal turbines: A state of the art review

Kai Xu[1, 2], William Finnegan[1, 2], Fergal O'Rourke[3], Jamie Goggins [1, 2]
[1]Department of Civil Engineering, National University of Ireland Galway, Galway, Ireland
[2]MaREI Centre, Ryan Institute, National University of Ireland Galway, Galway, Ireland
[3]School of Engineering, Dundalk Institute of Technology, Dundalk, Ireland
email: k.xu1@nuigalway.ie, william.finnegan@nuigalway.ie, fergal.orourke@dkit.ie, jamie.goggins@nuigalway.ie

ABSTRACT: With increasing reliance on renewable energy, tidal energy has attracted increased attention and investment due to its potential, in terms of reliability and predictability. This paper reviews the recent progress in key issues of tidal turbines and discusses the methods used in present research. In the development of tidal current turbines, theoretical and computational hydrodynamic modelling are quite essential. Some simplified approaches, such as Blade Element Momentum Theory (BMET), can provide a quick predication of a device's hydrodynamic performance and power output. However, with growing computational capabilities, Computational Fluid Dynamics (CFD) has gained popularity due to its accuracy and versatility. Meanwhile, due to the significant development of marine energy, laboratory tests and field trials of large-scale prototypes of tidal turbines have been conducted. In addition to hydrodynamic performance, some other system components such as supporting structures and device clusters, are also addressed in the literature. Despite the large number of studies over the last decades, marine tidal device technology is still not a fully mature technology. To this end, the fatigue performance of turbine blades still lacks detailed investigation, which plays an important part in the overall performance of the turbine over its design life, especially in complex submarine environments. This paper describes the state-of-the-art of both the numerical and physical modelling of tidal turbine rotors. A discussion, based on results from the H2020 MaRINET2 project, on fluctuations due to thrust loadings on turbine blades in current and wave conditions has also been presented.

KEY WORDS: Blades; Fatigue; Hydrodynamic modelling; Structures; Tidal energy.

1 INTRODUCTION

Despite lockdowns and worldwide supply chain disruptions, Europe still witnessed a 2.2 MW of new tidal stream capacity installations in 2021 [1]. Ocean Energy Europe (OEE) considers in a high growth scenario, 2.9 GW of ocean energy capacity can be deployed globally by 2030, which includes both tidal stream and wave energy and of which 92% (2.6GW) will be in European waters [2]. Ocean energy, in the form of tidal energy, can play an important part in balancing Europe's electricity grid as it is 100% predictable. Marine tidal devices are designed to convert the kinetic energy of tidal currents into electrical power by means of complex mechanical parts that undergo rotational motions in reaction to flow-induced hydrodynamic forces. During the 20-year in-service design life, tidal turbine blades must be capable of contending the harsh submarine conditions [3] and the challenge of cyclic loads of tides and waves, which poses a high demand of the durability of turbine structures.

Marine devices can be typically classified as turbine systems when moving parts consist of rotor blades and non-turbine systems, while marine turbines are further classified based on the orientation of turbine axis with respect to the dominant direction of the current, i.e., horizontal axis turbines and vertical axis turbines separately [4]. According to an EU report by Corsatea and Magagna [5], 76% of research and development in the tidal energy sector are related to horizontal axis tidal turbines (HATT). A HATT's rotor axis is parallel to the incoming water stream (employing lift or drag-type blades) and is very similar to modern day wind turbines from a concept and design point of view [6], as is shown in Figure 1. This paper mainly reviews the research on horizontal axis tidal turbine technologies and discusses the findings on turbine system components.

Figure 1. Demonstration of horizontal axis tidal turbine [7].

The aim of this paper is to present a state of the art review on hydrodynamic modelling of tidal turbines. However, to achieve this aim, the following objectives are completed in this study:

- To systematically review the numerical and physical methods used in present research on tidal turbines,
- To briefly review the latest progress and findings in research on some energy capturing system components,

- To review the fatigue problems of tidal turbine blades and reveal the relative amplitudes of thrust force fluctuation.

As the world's energy supply moves to a greater reliance on ocean energy resources, the complex interaction between the tidal flow, turbine blades and support structures has attracted a lot of research and investigations. Different research methods have been developed and many key system components are researched, which are comprehensively covered in this paper.

2 NUMERICAL MODELLING

Firstly, theoretical and computational modelling play an important role in the development of tidal turbines.

2.1 Blade Element Momentum Theory (BEMT)

Primarily, numerical methods are taken to validate concepts preliminarily, at which stage, energy capturing mechanisms are investigated, while the estimation of power output is obtained. In that case, simplified system layouts and ideal operating conditions are usually assumed, e.g., an isolated turbine rotor in uniform uniaxial flow [4].

The power of HATTs is generated by means of a lifting surface subject to blades' rotary motions. The prediction of hydrodynamic forces generated on the blades is obtained by computational models with different levels of approximation in describing relevant dynamics mechanisms. Because of the similarities in energy capturing mechanisms and layouts, some mature computational methods for wind turbine modelling are introduced to simulate HATT.

Some simplified approaches, such as Momentum theory, Blade Element Method (BEM) and their combination, Blade Element Momentum Theory (BEMT), can provide a quick predication of a HATT's hydrodynamic performance and power output capability by momentum and energy balancing of the water mass flowing through the device. Fast estimations of hydrodynamics and power output can be given with basic representations of geometry and operating conditions. Bahaj et al. compared numerical results by two BEMT models with the experimental data in his research [8, 9], demonstrating the capability of BEMT to give reliable performance estimations at an early stage of HATT design. In present research, BEMT has been widely used; for example, the time-dependent reliability analysis for the blades of a HATT can be done with BEMT to develop the limit-state function of the turbine over its design life period [10]. And the BEMT is used to assess the presence of stall and corroborate the performance data attained from the fluid analysis in a full fluid-structure interaction analysis of a range of composite, bend-twist coupled blades [11]. Some improvements have been made to increase the accuracy of BEMT, such as with Prandtl tip and hub loss corrections [12]. However, because the blade is simplified to multiple beam elements, the full-field stress distribution cannot be simulated and the behaviour of composite material under multi-axial stress states is not able to be captured, which means that the reduction in accuracy of BEMT cannot be avoided.

2.2 Computational Fluid Dynamics (CFD)

In recent years, with the increased computational capabilities, computational fluid dynamics (CFD) is gaining ground due its higher accuracy and applicability under a range of operating conditions. There exist a number of publications applying CFD models to investigate the performances of HATTs, which are summarised in Table 1.

Many commercial codes such as ANSYS CFX and ANSYS Fluent are widely used in present research. Among various CFD approaches, the Reynolds-averaged Navier Stokes equations (RANSE) models are the most commonly used due to its computational efficiency. However, in large-scale turbulence structures, these models cannot accurately resolve the turbulence near-wake region due to its anisotropic nature [32].

Table 1. Summary of previously published studies using CFD to examine the operation of horizontal axis tidal turbines.

Reference	Numerical method	Modelling Tool	Turbulence model	Flow
Liu et al. [13]	LES	N/A	N/A	Current
Finnegan et al. [14]	RANSE	ANSYS CFX	SST	Current
Ouro et al. [15]	LES	N/A	N/A	Current
Badshah et al. [16,17]	RANSE	ANSYS CFX	SST	Current
Aparna et al. [18]	RANSE	ANSYS Fluent	SST	Current
Gebreslassie et al. [19]	RANSE IBF	OpenFOAM	k-ω SST	Current
Kulkarni et al. [20]	RANSE	ANSYS CFX	k-ε SST	Current
Tatum et al. [21]	RANSE	ANSYS CFX	SST	Current/Wave
Frost et al. [22]	RANSE	ANSYS CFX	SST	Current
Noruzi et al. [23]	RANSE	ANSYS CFX	SST	Current
Holst et al. [24]	RANSE	ANSYS CFX	SST	Current/Wave
Mason-Jones et al. [25]	RANSE	ANSYS Fluent	RSM	Current
Jo et al. [26]	RANSE	ANSYS CFX	SST	Current
hee Jo et al. [27]	N/A	ANSYS CFX	SST	Current
Kang et al. [28]	LES CURVIB	N/A	Smagorinsky model	Current
Turnock et al. [29]	Coupled RANSE-BEMT	ANSYS CFX	k-ε	Current
Faudot and Dahlhaug [30]	RANSE	ANSYS CFX	SST	Current/Wave
O'Doherty et al. [31]	RANSE	ANSYS Fluent	RSM	Current

Alternately, Large Eddy Simulations (LES) models solve the spatially averaged Navier-Stokes equations and directly resolve large turbulence structures (eddies). Thus, LES models can represent the full spectral distribution of blade bending moments [33-35], although LES models are computationally more expensive compared with RANSE models and greater mesh accuracy is required. The Shear Stress Transport (SST) model is a combination of k-ω model near walls and the standard k-ε model away from walls using a blending function, utilising the advantages of both models. Thus, it is commonly used to obtain the closure of the Navier-Stokes equations and has been successfully used to model the near wake of tidal turbines [36-38]. The computational modelling provides reference data for the design of full-scale prototypes to be deployed in open water and is highly efficient in researching on various turbine system components, especially in addressing multiple device operations.

3 PHYSICAL MODELLING

The collections of experimental data measuring turbine performance under different operating conditions provide datasets, which could be beneficial in validating computational and numerical models.

3.1 Laboratory-based Experiment Work

Representative experimental studies investigating the marine tidal energy capturing mechanisms and device operation have been discussed in this section, some of which are summarised in Table 2.

Table 2. Summary of previously published studies on physical modelling of horizontal axis tidal turbines.

Reference	Facility Type	Flow
Glennon et al. [3]	Mechanical loading	N/A
Bahaj et al. [7]	Towing tank	Current
Liu et al. [12]	Flume	Current
Xu et al. [39]	Towing tank	Current
Gaurier et al. [40, 41]	Towing tank /Circulating tank	Current/Wave
Gaurier et al. [42]	Flume	Current/Wave
Mycek, et al. [43-45]	Flume	Current
Lust et al. [46]	Towing tank	Current/Wave
Milne et al. [47]	Towing tank	Wave
Maganga et al. [48]	Circulating tank	Current
Wang et al. [49]	Cavitation tunnel	Current

Recently, inter-laboratory tests have been undertaken using similar testing devices and subjected to the same testing conditions to identify the influence of test environment on the device's performance, referred as Round Robin Tests (RRTs) in the framework of the EC-funded R&D project MaRINET2 and former successful MaRINET Infrastructures Network [40, 41]. In that programme, the exact same 0.724 m diameter HATT is tested in three tanks, i.e., the wave and current flume tank of IFREMER, the towing tank of CNRINM and the FLOWAVE circular combined wave and current test tank. The turbine performance is measured in facilities of different type (towing tanks, flume tanks and circulating water channels) and the impact of testing energy capturing devices towed in calm water or fixed in an onset flow with non-negligible turbulence levels is investigated.

3.2 Field Trials

Though it is still a long way for the large-scale commercial utilisation of marine tidal energy, yet tidal turbine technology can be expected to develop rapidly during the next decades considering the number of projects in progress and the obtained funding in the last few years.

MCT SeaGen deployed a 1.2 MW HATT since 2008 at Strangford Lough, Northern Ireland, which was the world's first commercial-scale tidal turbine [50]. This project reached an important milestone in 2012 by producing up to 5GWh of electricity in service, equal the electricity required by 1,500 households annually.

Many ongoing projects give results of open-sea field tests for device's pre-commercial deployment assessment. A 5.3m diameter turbine with three symmetrically shaped blades for operation in bi-directional tidal currents has been tested for three months off the coasts of South Korea near the island of Jindo, which is a 1:3 scaled pilot installation [51]. Similarly, a 1:3 scaled prototype in open sea is being tested in Norway for more than five years. Several full-scale 1 MW unit prototypes have been tested at the European Marine Energy Centre (EMCE) in the Orkney Islands, Scotland and worldwide.

Orbital Marine Power (OMP)'s prototype, the SR200 was installed in 2017 with a rated capacity of 2 MW and generated around 3 GWh in its first year of operation despite mainly being an R&D platform. In 2021, OMP deployed its next generation product, O2-2000 turbine with twin rotors with a diameter of 20 meters in a 74-meter-long platform, which is projected to meet the demand of round 2,000 homes and offset approximately 2,200 tonnes of CO_2 production per year over the next 15 years, as shown in Figure 2.

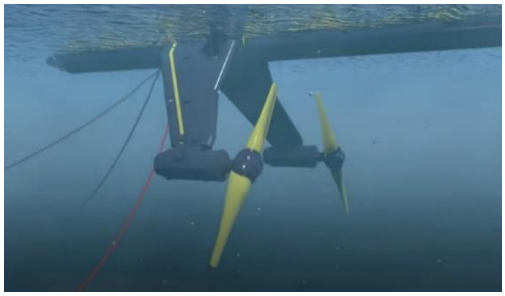

Figure 2. Orbital Marine Power O2-2000 tidal turbine [52].

4 FINDINGS ON TURBINE SYSTEM COMPONENTS

In existing research, details of the flow-field around the device are analysed, and parametric studies are performed to investigate device performance on different operating conditions and to optimise power output. Many more detailed representations of energy capturing system components are addressed in addition to hydrodynamic performance, e.g., blockage, supporting structures and device clusters.

Whelan et al. [53] implied that the blockage corrections are unnecessary when blockage area ratios (the projected structure area to the domain area) are less than 5%, while

Gaurier et al. [41] suggested that it might not be reliable for prediction of power coefficient at high TSR for which thrust coefficients are high.

Mason-Jones et al. [25] found that with the addition of a support structure, the amplitudes of the peak torque, power and axial thrust were shown to increase, but with reduced average values over a rotation cycle via the use of quasi-static CFD models.

Ouro et al. [15] revealed that the rotor loadings, e.g., thrust, flapwise and edgewise bending moments, power efficiency are influenced by array spacing of tidal stream turbines, a spacing of 8D is considered insufficient. Liu et al. [12] found that the blade root vortex shedding can cause a serious vortex influence area behind the upstream rotor, and suggested the device rotor should avoid this region; otherwise, the rotor's system performance will be severely degraded. Mycek et al. [45] also presented a qualitative and quantitative characterisation of the interactions between turbine groups concerning both the wake and the performance of the downstream turbine, in which the upstream turbulence intensity conditions have an influence, and suggested that a compromise between individual performance and the number of energy converters needs to be made wisely when considering array design. Myers et al. [52] found that close lateral separation increases the thrust of adjacent rotor disks, and the accelerated flow passing between adjacent rotor disks could be utilised to improve the kinetic energy of downstream turbines by 22%.

4.1 Fatigue

According to Finnegan et al. [14], the magnitude of fatigue loading on tidal turbine blades is very significant, which can be up to 43% of the maximum total thrust force on the blade, and fatigue should be taken into consideration in all stages of design, testing, operational and maintenance phases of tidal turbine development.

Tatum et al. [21] found that in a pure tidal current situation, load fluctuation on each blade is approximately 17%, while in a current/wave situation, the fluctuation could range from 32% and 36% of the mean thrust on each blade. The results of Noruzi et al. [23] showed that when the ratio of installation depth from the ocean surface to the total depth of water at the point of installation is smaller than 20%, the surface wave has a great role in performance of tidal turbine. The uneven distribution of power and thrust spikes could lead to non-uniform loading and eventually fatigue.

4.2 Thrust variation

In the datasets created at IFREMER during the MaRINET2 project [55], the result of a series of flume tests is given in different current and wave conditions. The thrust force of rotor and blade in test "run003" and "run054" within one wave circulation is illustrated in Figure 3 and Figure 4. To explain, the frequency of wave is 0.6Hz and the sampling frequency is 128Hz, so around 213 data is used to demonstrate the force variation in one circulation of wave. As can be seen in Figure 3, the fluctuation turns much bigger after the addition of wave, from round 3% of the mean thrust to 28%. It is noted that for a tidal turbine of 42 RPM, 1.67 secs could contain over one rotations of turbine blades, yet the huge fluctuation of thrust in one turbine blade is still meaningful as illustrated in Figure 4. This shows that the fluctuation of thrust loading on turbine blades is even larger, and it is essential to combine fatigue into the design of tidal turbine blades.

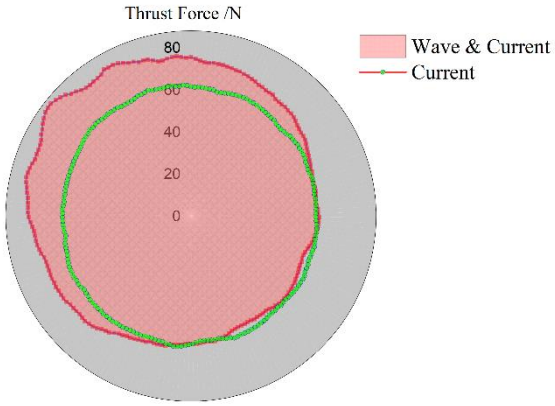

Figure 3. Variation of thrust force on tidal turbine rotor in only current (velocity 0.8m/s, turbulence 1.5%) and current/ wave conditions (0.155m amplitude, 0.6Hz frequency) within one wave period.

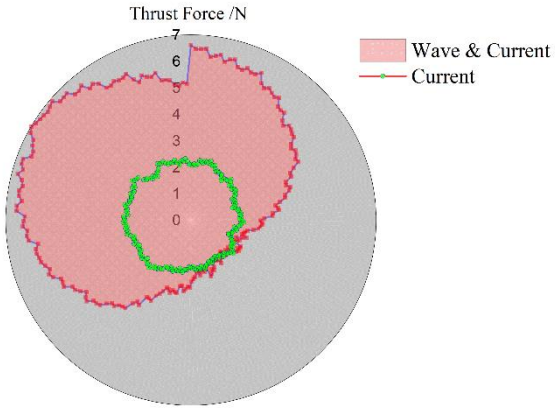

Figure 4. Variation of thrust force on one blade of tidal turbine in only current (velocity 0.8m/s, turbulence 1.5%) and current/ wave conditions (0.155m amplitude, 0.6Hz frequency) within one wave period.

5 DISCUSSION

Recent numerical simulations and experimental data analysis have proven that the magnitude of fatigue loading on tidal turbine blades is quite significant, especially under wave and tidal current conditions in shallow water or for floating turbines. However, the fatigue test recommendations in present DNVGL-ST-0164 [56] and the IEC design requirements for marine energy systems IEC TS 62600e2:2016 [57] are unverified since the technology needed to conduct high-cycle fatigue testing that does not exist. And though low-cycle fatigue testing is managed, it is not sufficient to propose confident measures for long-term blade endurance. New protocols for introducing complex cyclic loading spectra during fatigue testing of tidal turbine rotor blades need to be developed.

6 CONCLUSION

Tidal energy has potential to supply clean reliable and predictable renewable energy into the electricity grid, with many studies carried out to investigate the performance and energy capturing mechanism of tidal turbines. Usually, numerical methods such as BEMT can give a quick estimation of hydrodynamics and power output capacity with basic representations of geometry and operating conditions. Due to increased computational capabilities, CFD is widely used in present simulation of tidal turbines. Commercial codes, such as ANSYS CFX, and simplified models, such as RANSE, are utilised as they are less computational expensive, while some more complex methods like LES offer other options.

With increased investment in ocean energy, many physical modelling and field tests have been performed in the past decade, providing useful experimental datasets for validating computational and numerical models. Some great achievements and milestones have been made, and some prototypes have been in practical use.

Many parametric studies have been performed to investigate key influencing facts on tidal turbines such as supporting structures and device clusters. During tidal turbine operation, the fluctuation of forces on turbine blades is inevitable, leading to serious fatigue problems, especially when the surface wave has a great role in the performance of a tidal turbine. Preliminary research has been conducted on fatigue of tidal turbine rotors. However, when it comes to detailed mechanisms and testing protocols, more work needs to be done.

ACKNOWLEDGMENTS

This research was funded in part by Science Foundation Ireland (SFI) through the MaREI Research Centre for Energy, Climate and Marine (Grant no. 12/RC/2302_2) and the European Commission through the H2020 CRIMSON project (grant agreement no.: 971209).

REFERENCES

[1] Rémi C., *Ocean Energy Key trends and statistics 2021*, Brussels: Ocean Energy Europe, 2021.

[2] Cagney D., *2030 Ocean Energy Vision Industry analysis of future deployments, costs and supply chains*, Brussels: Ocean Energy Europe, 2020.

[3] Glennon, C., Finnegan, W., Kaufmann, N., Meier, P., Jiang, Y., Starzmann, R., and Goggins, J. (2022), 'Tidal stream to mainstream: mechanical testing of composite tidal stream blades to de-risk operational design life', *Journal of Ocean Engineering and Marine Energy*, 1-20.

[4] Day, A.H., Babarit, A., Fontaine, A., He, Y.P., Kraskowski, M., Murai, M., Penesis, I., Salvatore, F. and Shin, H.K. (2015), 'Hydrodynamic modelling of marine renewable energy devices: A state of the art review', *Ocean Engineering*, 108, 46-69.

[5] T.D. Corsatea and D. Magagna, *Overview of European Innovation Activities in Marine Energy Technology*, European Commission, Brussels, Belgium, 2013

[6] Khan, M. J., Bhuyan, G., Iqbal, M. T. and Quaicoe, J. E. (2009), 'Hydrokinetic energy conversion systems and assessment of horizontal and vertical axis turbines for river and tidal applications: A technology status review', *Applied energy*, 86, 1823-1835.

[7] The maritime executive. (2015), 'Tidal Energy Project Cleared off U.K.'.

[8] Bahaj, A.S., Batten, W.M.J. and McCann, G. (2007a), 'Experimental verifications of numerical predictions for the hydrodynamic performance of horizontal axis marine current turbines', *Renewable Energy*, 32, 2479–2490.

[9] Bahaj, A.S., Molland, A.F., Chaplin, J.R. and Batten, W.M.J. (2007b), 'Power and thrust measurements of marine current turbines under various hydrodynamic flow conditions in a cavitation tunnel and a towing tank', *Renewable Energy*, 32, 407–426.

[10] Hu, Z. and Du, X. (2012). 'Reliability analysis for hydrokinetic turbine blades', *Renewable Energy*, 48, 251-262.

[11] Nicholls-Lee, R.F., Turnock, S.R. and Boyd, S.W. (2013). 'Application of bend-twist coupled blades for horizontal axis tidal turbines', *Renewable Energy*, 50, 541-550.

[12] Masters, I., Chapman, J.C., Willis, M.R. and Orme, J.A.C. (2011), 'A robust blade element momentum theory model for tidal stream turbines including tip and hub loss corrections', *Journal of Marine Engineering & Technology*, 10, 25-35.

[13] Liu, X., Feng, B., Liu, D., Wang, Y., Zhao, H., Si, Y. and Qian, P. (2022), 'Study on two-rotor interaction of counter-rotating horizontal axis tidal turbine', *Energy*, 241, 122839.

[14] Finnegan, W., Fagan, E., Flanagan, T., Doyle, A. and Goggins, J. (2020), 'Operational fatigue loading on tidal turbine blades using computational fluid dynamics', *Renewable Energy*, 152, 430-440.

[15] Ouro, P., Ramírez, L. and Harrold, M. (2019), 'Analysis of array spacing on tidal stream turbine farm performance using Large-Eddy Simulation', *Journal of Fluids and Structures*, 91, 102732.

[16] Badshah, M., Badshah, S., VanZwieten, J., Jan, S., Amir, M. and Malik, S.A. (2019), 'Coupled fluid-structure interaction modelling of loads variation and fatigue life of a full-scale tidal turbine under the effect of velocity profile', *Energies*, 12, 2217.

[17] Badshah, M., Badshah, S. and Kadir, K. (2018), 'Fluid structure interaction modelling of tidal turbine performance and structural loads in a velocity shear environment', *Energies*, 11, 1837.

[18] Aparna, D.L., Naayagi, R.T. and Ramadan, M. (2017), 'CFD analysis of tidal turbine blades', *TENCON IEEE Region 10 Conference*, 2708-2711.

[19] Gebreslassie, M.G., Sanchez, S.O., Tabor, G.R., Belmont, M.R., Bruce, T., Payne, G.S. and Moon, I. (2016), 'Experimental and CFD analysis of the wake characteristics of tidal turbines', *International Journal of Marine Energy*, 16, 209-219.

[20] Kulkarni, S.S., Chapman, C. and Shah, H. (2016), 'Computational fluid dynamics (CFD) mesh independency study of A straight blade horizontal Axis tidal turbine'.

[21] Tatum, S., Allmark, M., Frost, C., O'Doherty, D., Mason-Jones, A. and O'Doherty, T. (2016), 'CFD modelling of a tidal stream turbine subjected to profiled flow and surface gravity waves', *International Journal of Marine Energy*, 15, 156-174.

[22] Frost, C., Morris, C.E., Mason-Jones, A., O'Doherty, D.M. and O'Doherty, T. (2015), 'The effect of tidal flow directionality on tidal turbine performance characteristics', *Renewable Energy*, 78, 609-620.

[23] Noruzi, R., Vahidzadeh, M. and Riasi, A. (2015), 'Design, analysis and predicting hydrokinetic performance of a horizontal marine current axial turbine by consideration of turbine installation depth', *Ocean Engineering*, 108, 789-798.

[24] Holst, M.A., Dahlhaug, O.G. and Faudot, C. (2014), 'CFD analysis of wave-induced loads on tidal turbine blades', *IEEE Journal of Oceanic Engineering*, 40, 506-521.

[25] Mason-Jones, A., O'Doherty, D.M., Morris, C.E. and O'Doherty, T. (2013), 'Influence of a velocity profile & support structure on tidal stream turbine performance', *Renewable energy*, 52, 23-30.

[26] Jo, C.H., Kim, D.Y., Rho, Y.H., Lee, K.H. and Johnstone, C. (2013), 'FSI analysis of deformation along offshore pile structure for tidal current power', *Renewable energy*, 54, 248-252.

[27] hee Jo, C., young Yim, J., hee Lee, K. and ho Rho, Y. (2012), 'Performance of horizontal axis tidal current turbine by blade configuration', *Renewable Energy*, 42, 195-206.

[28] Kang, S., Borazjani, I., Colby, J.A. and Sotiropoulos, F. (2012), 'Numerical simulation of 3D flow past a real-life marine hydrokinetic turbine', *Advances in water resources*, 39, 33-43.

[29] Turnock, S.R., Phillips, A.B., Banks, J. and Nicholls-Lee, R. (2011), 'Modelling tidal current turbine wakes using a coupled RANS-BEMT approach as a tool for analysing power capture of arrays of turbines', *Ocean Engineering*, 38, 1300-1307.

[30] Faudot, C.L. and Dahlhaug, O.G. (2011), 'January. Tidal turbine blades: Design and dynamic loads estimation using CFD and blade element momentum theory', *International Conference on Offshore Mechanics and Arctic Engineering*, 44373, 599-608.

[31] O'Doherty, T., Mason-Jones, A., O'doherty, D.M., Byrne, C.B., Owen, I. and Wang, Y.X. (2009), 'September. Experimental and computational analysis of a model horizontal axis tidal turbine', *8th European Wave and Tidal Energy Conference (EWTEC)*, Uppsala, Sweden.
[32] Tedds, S., Owen, I., Poole, R. (2014), 'Near-wake characteristics of a model horizontal axis tidal stream turbine', *Renew Energy*, 63, 222–235.
[33] Ahmed, U., Apsley, D., Afgan, I., Stallard, T.J., Stansby, P.K. (2017), 'Fluctuating loads on a tidal turbine due tovelocity shear and turbulence: Comparison of CFD with field data', *Renew Energy*, 112, 235–246.
[34] Ouro, P., Harrold, M., Stoesser, T. and Bromley, P. (2017), 'Hydrodynamic loadings on a horizontal axis tidal turbine prototype', *Journal of Fluids and Structures*, 71, 78-95.
[35] Ouro, P. and Stoesser, T. (2019), 'Impact of environmental turbulence on the performance and loadings of a tidal stream turbine', *Flow Turbulence and Combustion*, 102, 613-639.
[36] Badshah, M., VanZwieten, J., Badshah, S. and Jan, S. (2019), 'CFD study of blockage ratio and boundary proximity effects on the performance of a tidal turbine', *IET Renewable Power Generation*, 13, 744-749.
[37] Sufian, S.F., Li, M. and O'Connor, B.A. (2017), '3D modelling of impacts from waves on tidal turbine wake characteristics and energy output', *Renewable energy*, 114, pp.308-322.
[38] Tian, W., VanZwieten, J.H., Pyakurel, P. and Li, Y. (2016), 'Influences of yaw angle and turbulence intensity on the performance of a 20 kW in-stream hydrokinetic turbine', *Energy*, 111, 104-116.
[39] Xu, Y., Zhao, J., Sun, S. and Liu, P. (2022), 'Tidal Turbine Apparatus Vibration and Its Effect on Power Production Measurement', *Journal of Marine Science and Engineering*, 10, 172.
[40] Gaurier, B., Ordonez-Sanchez, S., Facq, J.V., Germain, G., Johnstone, C., Martinez, R., Salvatore, F., Santic, I., Davey, T., Old, C. and Sellar, B. (2020), 'MaRINET2 Tidal Energy Round Robin Tests—Performance Comparison of a Horizontal Axis Turbine Subjected to Combined Wave and Current Conditions', *Journal of Marine Science and Engineering*, 8, 463.
[41] Gaurier, B., Germain, G., Facq, J.V., Johnstone, C.M., Grant, A.D., Day, A.H., Nixon, E., Di Felice, F. and Costanzo, M. (2015), 'Tidal energy "Round Robin" tests comparisons between towing tank and circulating tank results', *International Journal of Marine Energy*, 12, 87-109.
[42] Gaurier, B., Davies, P., Deuff, A. and Germain, G. (2013), 'Flume tank characterization of marine current turbine blade behaviour under current and wave loading', *Renewable Energy*, 59, 1-12.
[43] Mycek, P., Gaurier, B., Germain, G., Pinon, G. and Rivoalen, E. (2014), 'Experimental study of the turbulence intensity effects on marine current turbines behaviour. Part II: Two interacting turbines', *Renewable Energy*, 68, 876-892
[44] Mycek, P., Gaurier, B., Germain, G., Pinon, G. and Rivoalen, E. (2014), 'Experimental study of the turbulence intensity effects on marine current turbines behaviour. Part I: One single turbine', *Renewable Energy*, 66, 729-746.
[45] Mycek, P., Gaurier, B., Germain, G., Pinon, G. and Rivoalen, E. (2013), 'Numerical and experimental study of the interaction between two marine current turbines', *International Journal of Marine Energy*, 1, 70-83.
[46] Lust, E. E., Luznik, L., Flack, K. A., Walker, J. M. and Van Benthem, M. C. (2013), 'The influence of surface gravity waves on marine current turbine performance', *International Journal of Marine Energy*, 3, 27-40.
[47] Milne, I. A., Day, A. H., Sharma, R. N. and Flay, R. G. J. (2013), 'Blade loads on tidal turbines in planar oscillatory flow', *Ocean engineering*, 60, 163-174.
[48] Maganga, F., Germain, G., King, J., Pinon, G. and Rivoalen, E. (2010), 'Experimental characterisation of flow effects on marine current turbine behaviour and on its wake properties', *IET Renewable Power Generation*, 4, 498-509.
[49] Wang, D., Atlar, M. and Sampson, R. (2007), 'An experimental investigation on cavitation, noise, and slipstream characteristics of ocean stream turbines', *Proceedings of the Institution of Mechanical Engineers, Part A: Journal of Power and Energy*, 221, 219-231.
[50] Fraenkel, P.L. (2010), 'Development and testing of Marine Current Turbine's SeaGen 1.2MW tidal stream turbine', *Proceedings of Third International Conference on Ocean Energy (ICOE)*, Bilbao, Spain.
[51] Ruopp, A., Daus, P., Biskup, F. and Riedelbauch, S. (2015), 'Performance prediction of a tidal in-stream current energy converter and site assessment next to Jindo, South Korea', *Journal of Renewable and Sustainable Energy*, 7, 061707.
[52] Christopher McFadden. (2021), 'The world's most powerful tidal turbine is almost complete', *Interesting Engineering*.
[53] Whelan, J. I., Graham, J. M. R., and Peiro, J. (2009), 'A free-surface and blockage correction for tidal turbines', *Journal of Fluid Mechanics*, 624, 281-291.
[54] Myers, L. E., and Bahaj, A. S. (2012), 'An experimental investigation simulating flow effects in first generation marine current energy converter arrays', *Renewable Energy*, 37, 28-36.
[55] Gaurier, B., Ordonez-Sanchez, S., Facq, J.V., Germain, G., Johnstone, C., Martinez, R., Salvatore, F., Santic, I., Davey, T., Old, C. and Sellar, B. (2021), 'MaRINET2 Tidal "Round Robin" dataset: comparisons between towing and circulating tanks test results for a tidal energy converter submitted to wave and current interactions', SEANOE.
[56] DNV GL, Tidal Turbines, DNV Standard, DNVGL-ST-0164, Oslo, Norway, 2015.
[57] I.E.C. (IEC), IEC TS 62600-2:2016 Marine Energy - Wave, Tidal and Other Water Current Converters - Part 2: Design Requirements for Marine Energy Systems, International Electrotechnical Commission (IEC), Geneva, Switzerland, 2016.

High cycle dynamic testing of marine hydrokinetic blades

Conor Glennon[1,2], William Finnegan[1,2], Patrick Meier[1,2], Yadong Jiang[1,2], Jamie Goggins[1,2]
[1]Civil Engineering, School of Engineering, National University of Ireland Galway, University Road, Galway, Ireland
[2]SFI MaREI Research Centre for Energy, Climate and Marine, Ryan Institute, National University of Ireland Galway, University Road, Galway, Ireland
email: conor.glennon@nuigalway.ie, william.finnegan@nuigalway.ie, patrick.meier@nuigalway.ie, yadong.jiang @nuigalway.ie, jamie.goggins@nuigalway.ie,

ABSTRACT: River and tidal current energy can play a substantial role in the de-carbonisation of Europe's electricity production. In recent years several companies have been developing technology to harness the power of the world's waterways. One such developer is the Ocean Renewable Power Company (ORPC) who have developed a range of marine hydrokinetic devices to provide reliable electricity to remote communities who are normally dependent on local diesel-powered electricity generation. The latest generation of ORPC devices use high efficiency carbon fibre reinforced epoxy foils to extract energy from flows with diurnal variations in flow speed, subjecting the device to a wide envelope of blade loading. Technology to harness water current energy is still at a relatively early stage of development, hence de-risking of components plays a vital role on the road to commercialisation. In this study, planned testing of a demonstrator foil from the ORPC device in a novel dynamic loading setup is presented where the load will be generated by the rotation of an offset mass by an electric motor fixed to the blade. Such a test setup will allow for efficient testing up to very high cycle numbers not normally achieved in classic hydraulically actuated testing. Dynamic modelling of the blade response will be used to help predict the natural frequencies and relate the frequency of rotation to the load response in the blade. Data generated from the testing will contribute to the modelling and validation of future tidal blades, as well as the overall goal of electricity de-carbonisation.

KEY WORDS: CERI/ITRN 2022; marine energy; renewable energy

1 INTRODUCTION

Tidal flows are created by the changing gravitational pull of the sun and moon as the earth rotates causing predictable flows of water. Tidal energy is the utilisation of these moving masses of water to generate electricity. Tidal flows are an ideal source of renewable energy because their periods and durations are easy to predict accurately, allowing grid operators to effectively plan grid generation. Tidal energy devices are very site-sensitive due to the localised nature of the water current in a specific location, hence tidal energy devices are best suited to sites with a natural means of increasing the local water flow. For example, the fastest water currents may be found in bays where the surrounding landscape naturally funnels the water or between relatively close islands which would have the same effect.

Unlike the wind power industry which has arrived at a 'standard' 3-bladed horizontal axis design, the tidal energy industry is generally at an earlier stage of technical development which sees a variety of design philosophies coming to market. With this range of designs it is essential that testing of key components takes place in order to prove and qualify designs prior to field deployment. This testing is essential to increase confidence and investment in the industry.

Ireland has a strong development potential of 3000 MW across several sites in Irish waters [1]. Figure 1 shows the variety of tidal energy devices under consideration which including 'sea-snakes', underwater tidal stream generators, paddle generators and kite generators [2].

Figure 1. The wide variety of tidal energy devices under development [2]

2 CRIMSON PROJECT

2.1 Project Overview and Facilities

In an era where single point thermal generation of electricity appears to have peaked [3], the industry must look at all available options in the move to distributed generation. One such company contributing to the solution is the Ocean Renewable Power Company (ORPC) with their development of marine hydrokinetic (MHK) devices. The latest work in MHK development is part of the wider CRIMSON project [4] which comprises NUI Galway, ÉireComposites, Consiglio

Nazionale delle Ricerche (CNR), and Mitsubishi Chemical Advanced Materials (MCAM).

CRIMSON stands for the **C**ommercialisation of a **R**ecyclable and **I**nnovative **M**anufacturing **S**olution for an **O**ptimised **N**ovel marine turbine and has the objective to develop, test and manufacture MHK devices using recycled carbon fibre material.

The project draws from the expertise of experienced players in the fields of materials recovery and production (MCAM), advanced composites manufacturing (ÉireComposites), MHK turbine development, installation and operation (ORPC) plus the research expertise, resources and facilities provided by NUI Galway and CNR.

NUI Galway will lead the work package on structural testing of the MHK turbine assembly with the demonstrator foil, once received from manufacturer ÉireComposites. Testing will take place in the Large Structures Test Laboratory located in the Alice Perry Engineering Building at NUI Galway, see Figure 2 and Figure 3. The test lab is under the management of the Sustainable and Resilient Structures Research Group (nuigalway.ie/structures) and has overseen the testing of several marine renewable energy devices in recent years, including static and fatigue testing of the world's largest tidal turbine blade in 2020 which saw a peak load of 1 MN borne by the blade [5].

Figure 2. The Large Structures Test Laboratory at NUI Galway operated by the Sustainable and Resilient Structures research group

2.2 Existing developments in marine hydrokinetic devices

OPRC have a track record of MHK design, installation and operation, most notably through the ACCORD project [7] in 2018. In 2019 ORPC deployed its RivGen power system in a river feeding Iliamna Lake beside the remote Alaskan village of Igiugig. Igiugig village operates in own electrical micro-grid, fuelled by diesel electric generators. The diesel for these generators is delivered by air periodically to the village's airstrip, from where it is transported to the generating station.

Igiugig has seen its fair share of attempts at de-carbonising its electrical grid by well-meaning developers but none have seen the success of the RivGen device. In October 2020, the RivGen device was announced as being the longest operating river current energy converter in the US [8] during which it dealt with frazil ice debris strikes from the spring break up of ice in Alaska's largest lake. ORPC is now looking at further deployments in the Americas and Europe. Figure 4 shows the RivGen system on-site in Igiugig, prior to its immersion.

Figure 3. A sample installation of hydraulic actuators at the Large Structures Test Laboratory, NUI Galway.

2.3 RivGen Power System

The RivGen power system comprises a horizontal shaft mounted on specially designed bearings with an electrical generator at one end. Three blades are mounted on this shaft in a helical pattern as if they are wrapped around the shaft. Helically twisted blades are a development that levels out the torque response from the shaft as it rotates and are an improvement from previous iterations with straight blades. Manufacturing helical blades represents enormous challenges over straight blades and it is a challenge for which carbon fibre is particularly suited.

The existing blade design uses a high performance carbon fibre material combined with ÉireComposites' proprietary CPET (composite powder epoxy technology) giving a high performance hydrodynamic blade with excellent saltwater immersion characteristics [9] [10].

Figure 4. RivGen power system on-site, ready for commissioning in Igiugig, Alaska [6]

2.4 CRIMSON project goals

The CRIMSON project aims to build on the progress made by past developments with the ACCORD project by placing additional focus on sustainability in the material selection process. The stated aims of the project are to "bring to market a reliable, sustainable marine energy turbine through the application of novel materials and technologies over the complete life cycle of the product" [4]. Since the project kick-off in 2021, work has begun at ÉireComposites on testing recycled carbon fibre (rCF) material received from MCAM to evaluate their suitability for use in such a high performance application. It is hoped that breakthroughs made in CRIMSON in the use of rCF material will pave the way for its use in other applications and industries. Ultimately, the best outcome for the test programme is that rCF material can be depended on for the key turbine components.

ÉireComposites will manufacture a demonstrator turbine blade which be sent to the Large Structures Test Lab at NUI Galway for a full test programme to validate the design lifetime.

3 METHODS

3.1 Aim and objectives

The overarching aim of this paper is to lay out the work planned at the Large Structures Test Lab at NUI Galway to evaluate the novel tidal bade.

In order to achieve this aim, the following key considerations will be discussed:

- Load prediction and modelling plus and overview of the planned suite of testing
- Data collection and the instrumentation planned for this purpose
- The proposed dynamic, static and fatigue testing

3.2 Load prediction and modelling

Modelling of the test assembly by researchers in the Sustainable and Resilient Structures research group in conjunction with ORPC will output the loads, displacements and strains expected during at operating speeds. The performance of the carbon fibre blades will be monitored under a controlled maximum strain type setup. This means the blade must be able to perform at operational conditions without exceeding the materials maximum strain limit. The testing outlined in the following sections is expected to confirm the stains predicted by the computational modelling.

3.3 Testing overview

Testing of the blade will be guided by industry standards DNV GL ST-0164 and IEC62600-3, as with previous test programmes in the Large Structures Test Lab. Loading information will be informed by design analysis carried out by ORPC in co-operation with ÉireComposites and MCAM.

The test programme will aim to validate the blade's design lifetime by replicating 20 years' worth of loading in an accelerated test programme of static and fatigue testing as well as a dynamic analysis of the blade's natural frequency and damping behaviour.

A representative blade of the newly-developed turbine design will be installed in the Large Structures Test Lab in a similar fashion to Figure 5.

Testing will commence with a dynamic analysis to determine the blade's natural frequency and damping coefficients. The blade will then be statically loaded incrementally up to its maximum operational load during which displacement and strain sensors will be compared to expected performance.

Fatigue testing will follow and will be provided by a novel 'rotating mass' arrangement, further described in Section 3.7.

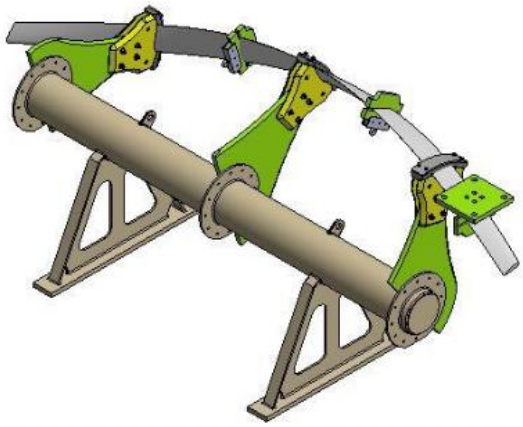

Figure 5. Representative test fixture

3.4 Instrumentation

Enormous amounts of data can be collected from test of this scale so it is crucial to know what should be recorded and what can be left out, or inferred from collected data.

Single axis accelerometers will be rigidly mounted on key parts of the blade span to record the frequency and damping response of the blade to excitations. A minimum of 3 accelerometers will be required to collect data in the x, y and z axes. Endevco piezoelectric sensors with a range of 1-8000 Hz and sensitivity of 100 mV/g will provide ample granularity of data.

Displacement will be recorded using linear variable displacement transducers (LVDTs) installed at the blade tip and mid-span locations as well as at the mounting brackets to record any movement and the fixed points. The displacement range required of the LVDTs will be determined in prior analysis of the blade design and material performance.

Loading will be recorded using suitably sized load cells connected to the main data acquisition system. In the case of

hydraulically actuated testing the load cells are already incorporated in the hydraulic actuator assembly, as shown in Figure 6.

Figure 6. In-line load cell mounted on a hydraulic actuator at the Large Structures Test Laboratory, NUI Galway

Strain will be monitored using linear and rosette electrical resistance strain gauges from the Tokyo Measuring Instruments Lab. Analysis of the blade design by ORPC and ÉireComposites will reveal the expected locations of maximum strain to guide the positioning of the strain gauges.

3.5 Dynamic analysis

A dynamic analysis of the blade will be conducted prior to any loading of the blade. This will involve fixing the blade to its hub supports in a manner representative of what will be applied in the field. The blade will be excited by means of a hammer strike while the acceleration response will be recorded. Post processing of this data will reveal the blade's natural frequency and damping characteristics.

3.6 Static testing

The purpose of static testing is to prove the blade's capability to reach its maximum operational load without any obvious failure or breaches of design limits. Static testing commences by applying loads incrementally to the blade until the maximum operational load is reached. At each loading increment, the blade will be held for a defined time period as defined in [13] and [14] and observed for any discrepancies from expected behaviour. When the test assembly has held the operational load for the required dwell period without any major issues, the static test will be considered complete and allow progression to fatigue testing.

Load may be applied to the blade using a choice of electronically controlled hydraulic actuators available in the test lab at NUI Galway. A displacement controlled loading regime will be used to mitigate the risk of damage to the blade or personnel in the event of unexpected behaviour. Once static testing has been passed satisfactorily the blade can progress to fatigue testing.

3.7 Fatigue testing

A large part of the research impact of the testing work packages lies in the novel test method planned for fatigue testing. It is proposed to test the blade to 10,000,000 cycles during testing. Achieving this number of cycles with standard electrically powered hydraulic actuators would require a prohibitive amount of laboratory time as well as a huge amount of energy. To overcome this, a rotating mass will be used to generate the required load at a suitably high frequency. In a first order system, the force generated by a rotating mass is described by equation (1) where F is the force in Newtons, m is the mass of the rotating mass in kg, ω is the angular velocity of the mass in rad/sec and r is the radius at which the mass is mounted, in metres

$$F = m\omega^2 r \tag{1}$$

This rotating mass then generates a response in the "fixed" blade which interacts with the initial excitation causing a second order response.

A geared electric motor with inverter has been sourced to rotate the mass at a controllable and measurable rate. Loading data will be provided by a load cell mounted between the electric motor and the blade. The data acquisition system will simultaneously monitor load, displacement and strain data as they are generated.

Figure 7. 3 phase electric motor with gearbox used to rotate a mass at a measurable, controllable rate [15]

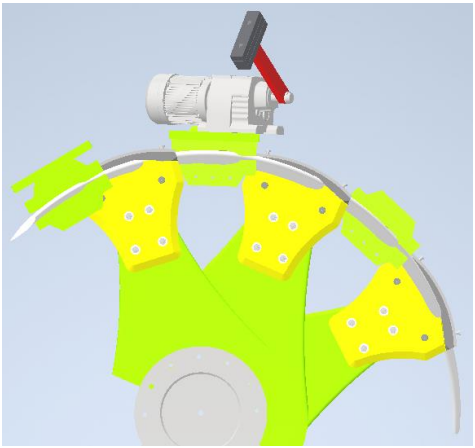

Figure 8. Representative test fixture with rotating mass fatigue test equipment mounted on the blade.

4 DISCUSSION

4.1 Expected outputs

Testing on this scale generates vast quantities of data which will be used to confirm assumptions and validate the design.

Static testing of the blade up to its maximum operational load will yield valuable data on the load-displacement response of the blade and give an effective means of comparison to the modelled blade. Results at this stage can be used to fine tune the fatigue test programme before it starts.

The instrumentation used in fatigue testing of the blade will reveal how the displacement response of the blade changes as the test develops. A divergence in displacement about the neutral axis as the cycles increase would indicate that the testing is having a weakening effect on the blade structure, as expected, and this data can in turn be used to estimate residual fatigue life in the blades. If the blade successfully survives the fatigue programme, a final static test to failure may be done to determine the remaining capacity of the blade.

An earlier generation of the foil was tested previously at the facility in NUI Galway, which was performed using two vertical actuators, as shown in Figure 9. The actuator at the cantilever section was attached directly to the foil, while the actuator at the mid-span section used a wire rope connection to load the foil towards the centre of rotation. A comprehensive set of static tests, along with low-cycle fatigue testing, was performed. The full details of the results from this testing programme for the device are given in [12].

Figure 9. A helical foil installed at the Large Structures Testing Laboratory undergoing structural testing using two actuators.

A comprehensive static testing programme was first completed on the helical foil, where the deflection and strain along the foil under the maximum static load profile is given in Figure 10. The maximum deflection is at the cantilever tip of the blade of 23 mm, where the mid-span deflection was approximately 4 mm. The maximum strain on the foil is approximately -1.2×10^{-3} in compression and approximately 1.05×10^{-3} in tension, Figure 11. These strains aligned well with the predictions used in the foil design and were lower than the conservative strains given in the DNVGL-ST-0164 standard.

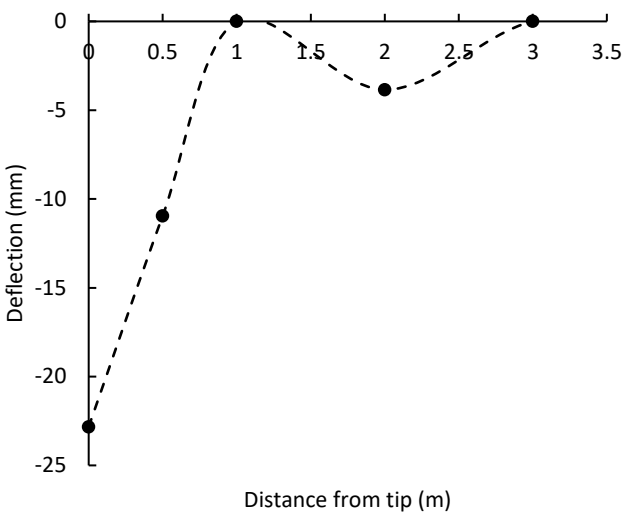

Figure 10. Selected testing results from the structural testing of a helical foil under the maximum static load, showing the foil deflection

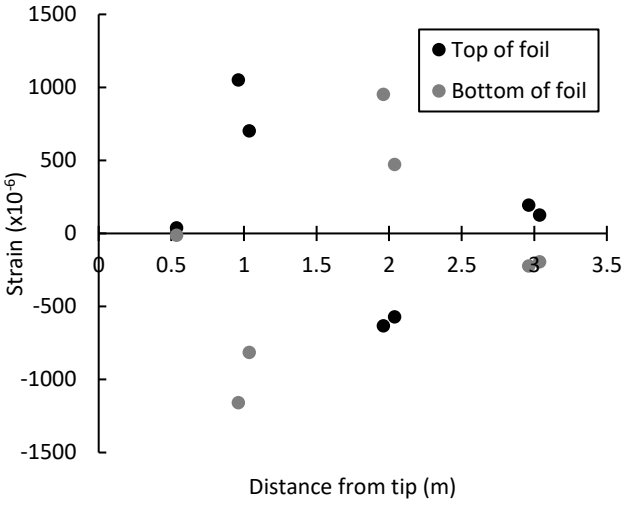

Figure 11. Selected testing results from the structural testing of a helical foil under the maximum static load, showing the strain at the top and bottom outer surfaces along the length of the foil.

4.2 Impact of this research

The purpose of the test programmes was to prove the structural integrity of rCF material of the MHK blades for an operational lifetime in a laboratory environment using recognised international standards (DNVGL-ST-0164 and IEC-TS-62600–3). The net result of the CRIMSON project will be a contribution to marine hydrokinetic energy as a serious player in the de-carbonisation of electrical grids in Europe. As an ever increasing amount of virgin carbon fibre material is produced every year it is imperative that industry and research should combine to improve its environmental impact. By their nature, carbon fibre parts are often designed for high impact, high value components so using a recovered (recycled) material will naturally experience roadblocks to commercial application. Funding mechanisms such as the Horizon 2020 Fast Track to

Innovation help companies and research institutions to prove the capabilities of these materials.

5 CONCLUSION

This paper summarises the planned test programme of a recycled carbon fibre blade for a novel tidal turbine design. The work is funded as part of the CRIMSON project which brings together the capabilities of several companies and institutions operating in the tidal energy field. A new tidal turbine blade will be design using data and modelling techniques optimised for the inclusion of recycled carbon fibre. A full-scale test programme will then be carried out at NUI Galway on a demonstrator blade with the intention of qualifying the blade for its 20 year design life. The long term goal for projects such as CRIMSON is the widespread of adoption of tidal energy as a means of producing environmentally-friendly electricity in Europe.

ACKNOWLEDGMENTS

This project is being carried out as part of the Horizon 2020 Fast Track to Innovation funding mechanism for the CRIMSON (**C**ommercialisation of a **R**ecyclable and **I**nnovative **M**anufacturing **S**olution for an **O**ptimised **N**ovel marine turbine) project and would like to acknowledge the support from Science Foundation Ireland (SFI), through the MaREI Research Centre for Energy, Climate and Marine (Grant no. 12/RC/2302_2). The authors would like to thank the other project partners for their valuable input throughout.

REFERENCES

[1] *Ocean Energy*. Sustainable Energy Authority Of Ireland. (n.d.). Retrieved May 4, 2022, from https://www.seai.ie/technologies/ocean-energy/

[2] National Geographic Society. (2012, October 9). *Tidal Energy*. National Geographic Society. Retrieved May 4, 2022, from https://www.nationalgeographic.org/encyclopedia/tidal-energy/

[3] IEA, World electricity generation by fuel, 1971-2019, IEA, Paris https://www.iea.org/data-and-statistics/charts/world-electricity-generation-by-fuel-1971-2019

[4] CRIMSON CONSORTIUM. (2021, January). Commercialisation of a Recyclable and Innovative Manufacturing Solution for an Optimised Novel marine turbine. H2020.

[5] Y. Jiang, E. Fagan, W. Finnegan, A.K. Vanhari, P. Meier, S. Salawdeh, C. Walsh, J. Goggins, 2022. Design and Structural Testing of Blades for a 2MW Floating Tidal Energy Conversion Device. *Materials Research Proceedings.* 20 (2022) p74-80 DOI: 10.21741/9781644901731-10

[6] Technologies, T. (n.d.). *RivGen® power system by Ocean Renewable Power Company (ORPC)*. by Ocean Renewable Power Company (ORPC). Retrieved May 4, 2022, from https://orpc.co/our-solutions/scalable-grid-integrated-systems/rivgen-power-system

[7] *ACCORD*. MaREI. (n.d.). Retrieved July 6, 2022, from https://www.marei.ie/project/accord/

[8] Kist S (2020 RivGen® power system now longest operating current energy converter in US https://www.orpc.co/uploads/news/orpcrivgen-power-system-now-longest-operating-current-energyconverter-10-05b-2020_637375865099902799.pdf. Accesses 9 Jun 2021

[9] Glennon C, Flanagan T, Doyle A, Kelly G, O'Bradaigh C, Finnegan W, (2018), "Development of Novel manufacturing Techniques for Composite Tidal Turbine Blades", SAMPE Europe Conference 18 Southampton, https://www.research.ed.ac.uk/en/publications/development-of-novel-manufacturing-techniques-for-composite-tidal

[10] Finnegan W, Allen R, Glennon C, Maguire J, Flanagan M, Flanagan T. Manufacture of High-Performance Tidal Turbine Blades Using Advanced Composite Manufacturing Technologies. Appl Compos Mater (Dordr). 2021;28 (6):2061-2086.

[11] Finnegan W, Fagan E, Flanagan T, Doyle A, Goggins J, (2020), "Operational fatigue loading on tidal turbine blades using computational fluid dynamics", Renewable Energy, Volume 152, Pages 430-440,

[12] Meier P, Finnegan W, Cronin P, Donegan J, Barrington M, Hung L C, Goggins J. (2020), "Static and Fatigue Testing of A Full Scale Helical River Turbine Foil," in Proceedings of Civil Engineering Research in Ireland 2020 (CERI2020), 625 Cork, Ireland, 2020, pp. 271-276. https://sword.cit.ie/cgi/viewcontent.cgi?article=1046&context=ceri

[13] DNV GL (2015), "Tidal turbines," in DNV Standard, DNVGL-ST0164, ed. Oslo, Norway.

[14] International Electrotechnical Commission (IEC) (2020), IEC TS 62600-3:2020 Marine energy - Wave, tidal and other water current converters, in Part 3: Measurement of mechanical loads, ed,.

[15] https://www.artisantg.com/PLC/91139-2/SEW-Eurodrive-R17-DRS71S4-Helical-Gearmotor

A study of wind-wave misalignment for the Irish coastline and its effect on the wind turbine response

Shubham Baisthakur[1], Breiffni Fitzgerald[1]
[1] Department of Civil, Structural and Environmental Engineering, Trinity College Dublin, Ireland
email: baisthas@tcd.ie, Breiffni.Fitzgerald@tcd.ie

ABSTRACT: A wind turbine is one of the largest rotating structures on earth. More wind turbines are now being developed with taller towers and longer blades, making them more flexible. As a result, an offshore wind turbine can exhibit a significant dynamic response. The wind turbines are subjected to a time-varying, highly turbulent loading environment. The wind and wave loads may not always act in the same direction during the wind turbine operation. The misaligned wind-wave loading can excite the less damped side-to-side mode of vibration for a wind turbine, exhibiting an amplified response for a prolonged period. Therefore, the assumption of co-directionality of wind and wave forces may not always represent conservative wind turbine design. The wind-wave misalignment is a local phenomenon, and it depends on the properties of the coast and wind profile. This paper studies the characteristics of wind-wave misalignment for the East Coast of Ireland and its impact on the system loads and deformations. The environmental data from Irish Marine Weather Buoy Network (IWMBN) is used in this study. This study uses environmental data from the Irish Marine Weather Buoy Network (IWMBN). This network of five offshore buoys monitors weather and oceanographic conditions for the Irish coast in real-time. The method of bins is used to study the statistical properties of wind speed and wind-wave misalignment. The response of the IEA 15MW reference wind turbine model with a monopile foundation for co-directional and misaligned wind-wave loading is simulated using OpenFast. It has been observed that misaligned wind-wave loading amplifies the wind turbine response for some operating conditions.

KEY WORDS: Wind-wave misalignment, Irish coastline, IEA 15MW reference wind turbine

1 INTRODUCTION

The concerns around the climate crisis and greenhouse gas emissions are driving the demand for renewable energy worldwide. Offshore wind energy, in particular, is pursued as a domain of high potential as it offers access to a richer wind resource and the least disturbance to the built urban environment. Researchers are pushing boundaries to achieve higher hub heights and larger rotor diameters to exploit the richer wind resource available at higher altitudes. With increasing hub heights, wind turbines are becoming more and more flexible. The increasing turbine heights and rotor lead to increased aerodynamic loads; the wind turbine foundation systems are getting larger to support this increased load. Due to the increased dimensions, the foundation system attracts higher wave loading. The combination of reduced natural frequency and increased hydrodynamic loads lead to a hydrodynamically sensitive structure. A detailed performance analysis under a range of possible operating conditions is necessary to ensure that there is no unanticipated resonance during the wind turbine operation. The misaligned loading can impact both the ultimate and the fatigue loads.

A wind turbine model is designed to produce a specific power output (power rating). The power rating governs the wind turbine features, i.e., the number of blades, rotor diameter and hub height. The structural design of a wind turbine structure is then performed for a set of Design Load Cases [1]. The standard wind turbine model, designed using this approach, is then installed at different locations for power generation. However, many parameters, for example, the load spectrum and natural frequency of the wind turbine, may vary from location to location [2, 3]. The local parameters influencing the wind turbine operation should be identified, and the wind turbine response should be simulated for local conditions to ensure reliable performance. During the operation of a wind turbine, the wind and wave load may not always act in the same direction [4]. Small misalignments between wind and wave loads are observed at all wind speeds, while large misalignments can be seen at higher speeds [5]. For large misalignments, the wave periods are closer to the first modal frequency of the support structure, resulting in higher dynamic amplification. The misaligned loading pattern can also excite the less damped side-to-side vibrations in wind turbine towers and cause vibrations over an extensive period, even for moderate excitations [6, 7]. Many researchers have studied the impact of wind-wave misalignment on various aspects of wind turbine operation [8-11].

Since wind-wave misalignment is a local phenomenon, it may exhibit different patterns at different locations. In this study, the nature of wind-wave misalignment is studied for the Irish coastline. The environmental data from Irish Marine Weather Buoy Network is used in this study.

2 METHODOLOGY

2.1 Modelling of wind-wave misalignment

Ocean waves are primarily generated as a result of momentum exchange between wind and the sea surface. Since wind and waves travel at different speeds, the waves generated by a specific wind profile reach a specific point later than the wind. Therefore, there is a high probability of misalignment in wind

and waves. The formation of wind waves depends on various parameters such as the fetch length, wind speed, wind duration, width of fetch and water depth. The geometrical parameters such as fetch length and width are constant for a particular geographic location. Therefore, while studying the wind-wave misalignment for a specific location, the wind-wave misalignment angle can be modelled as a function of the wind speed alone. The wind speed can be modelled as an independent variable for all practical purposes. Under these assumptions, the joint distribution for wind speed and wind-wave misalignment can be given as

$$p(U,\beta) = p(U)p(\beta|U) \quad (1)$$

where, U is the wind speed, and β is the wind-wave misalignment angle. This statistical model is further used in this study.

The Irish Marine Weather Buoy Network (IMWBN) data is used to study the variation of wind speed and the misalignment angle for the Irish coast. The location of weather buoys in the Irish sea is shown in Figure 1. This study focuses on the East Coast of Ireland. The data from weather buoys M2, M3 and M5 is used for the analysis. More than 20 years of wind and wave data measurements are available for these buoy locations. The wind speed is averaged over a 10min period and is reported every hour.

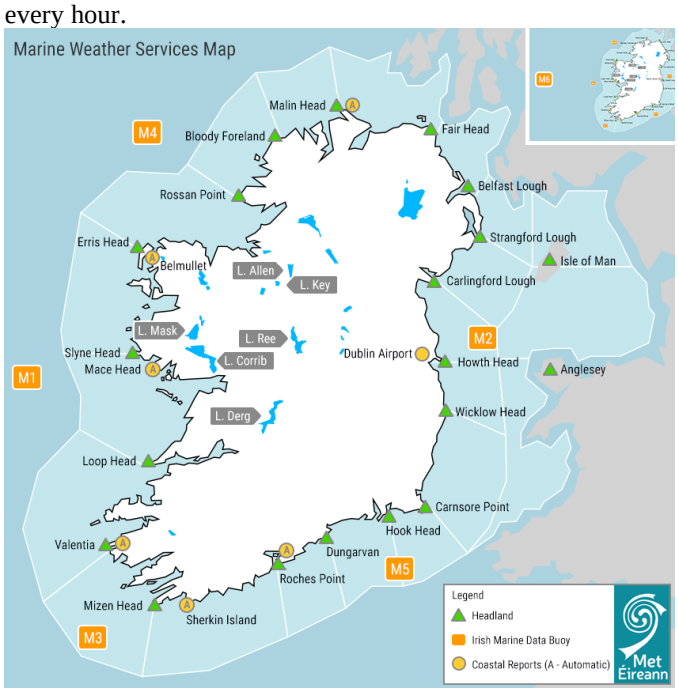

Figure 1. Location of weather buoys in the Irish Sea

2.2 *Metocean Data Analysis*

The wind speed data obtained from the buoys M2, M3 and M5 is analyzed using the method of bins. The method of bins is a statistical method for the analysis of random data. In this method, a number of bins (NB) are defined with a lower and upper limit. The number of observations falling within this range compared to the total number of observations (N) is called the frequency of bin, f. The difference between the lower and upper limits is bin-width(w), while the average is the mid-point(m). A bin width of 1m/s is used for wind speed analysis.

The histogram plot for the wind speed distribution at the selected locations is shown in Figure 2. The height of a histogram is proportional to the frequency of the corresponding bin. A probability distribution curve is obtained by normalizing the histogram heights and joining the histograms' centres, as shown in Figure 2.

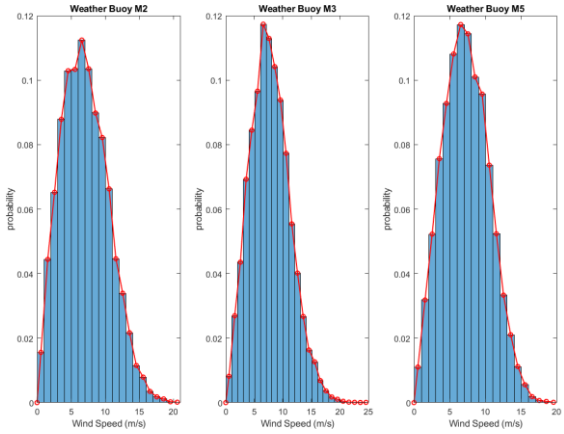

Figure 2. Probability Distribution of wind speed obtained using Method of Bins

This study aims to develop a generic model of wind-wave misalignment for the Irish coast. The data from a single weather buoy may not adequately represent the variations along the entire coast. The data from three weather buoys, M2, M3 and M5, are combined to capture the nature of wind-wave misalignment at different locations across the coast and take into account the information obtained from different locations. The histogram plot in Figure 2 shows that the wind speed at these locations shows similar characteristics. In this study, wind-wave misalignment is modelled as the function of wind speed alone. In this context, the data from these locations are combined to simplify the analysis. The Weibull distribution is found to best represent the wind speed data by performing a goodness of fit analysis. The Weibull distribution parameters for wind speed on the East Coast of Ireland are given in Table 1.

Table 1. Wind Speed Distribution Parameters.

Quantity	Type of Distribution	Shape Factor	Scale Factor
Wind Speed	Weibull	2.17	7.90

After defining the wind speed model, wind-wave misalignment data is studied for its dependence on wind velocity. A wind-rose analysis is performed, which shows the recorded values of the wind-wave misalignment at different wind speeds [12]. Figure 3 shows that at lower wind speeds, an extensive range of wind-wave misalignment can be observed; however, as the wind speed increases, the wind-wave misalignment narrows down to a small range. The wind-wave correlation at high wind speeds is often combined with fully developed sea states and weather regimes. Also, the ocean waves generated at low wind speeds are weaker and travel at

low speed. However, stronger waves generated at higher wind speeds can travel at higher speeds and exhibit a better correlation with wind speeds.

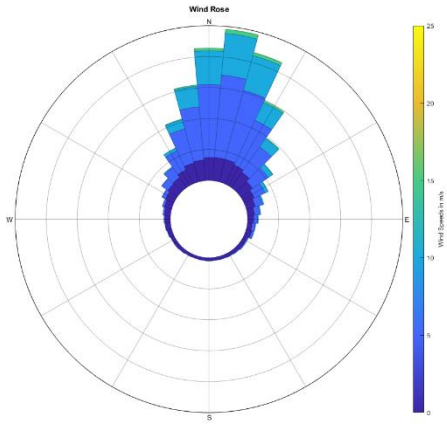

Figure 3. Wind Wave Misalignment on East Coast

The 2D method of bins is used to study the wind-wave misalignment data conditioned over wind speed. The wind speed data is categorized into different wind speed bins of width 1m/s, and the wind-wave misalignment angles observed for a given wind speed bin are recorded. The resulting joint histogram of wind-speed and wind-wave misalignment is shown in Figure 4. The high-intensity pixel shows the high probability of joint occurrence of (U, β) pair. Figure 4 shows that the probability of aligned wind-wave loading increases with an increase in wind speed up to a specific wind speed and decreases with a further increase in wind speed. However, there is not enough data available at high wind speeds, and a more detailed analysis is required to ascertain this phenomenon.

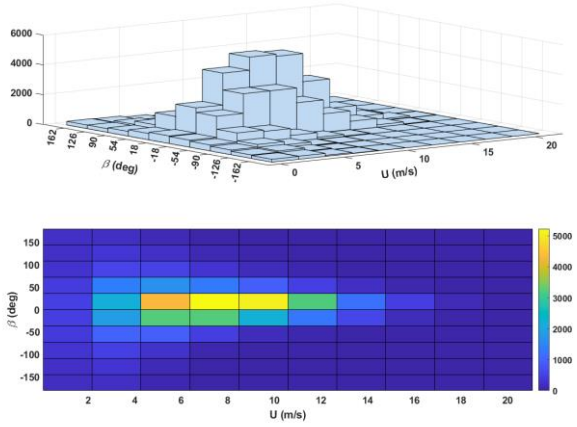

Figure 4. Joint histogram plot of wind speed and wind-wave misalignment

Marginal pdf of wind-wave misalignment angle $(p(\beta|U))$ is presented in Figure 5 to examine the gradual change in the nature of misalignment angle with the increase in wind speed. The wind-wave misalignment for each wind speed bin is shown in Figure 5, where the x-axis represents the wind-wave misalignment angle in degrees.

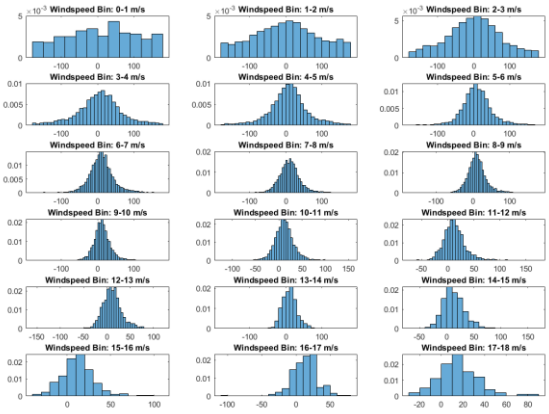

Figure 5. Variation of wind-wave misalignment angle at different wind speeds

From Figure 5, it can be inferred that at low wind speeds, the wind-wave misalignment angle is very weakly dependent on wind speed, whereas, at higher wind speeds, a better correlation is observed. In this context, using a single distribution to model the marginal pdf of wind-wave misalignment $(p(\beta|U))$ may not represent the actual nature of its variation. A critical wind-speed range can be defined below which the wind-wave misalignment angle can be modelled as an independent variable following a uniform distribution. Further study needs to be carried out to check if the critical wind speed can be defined as a characteristic of a particular coastal location. For the Irish coast, the weak correlation between wind-wave misalignment angle and wind speed is observed below 3m/s, the cut-in wind speed of the IEA-15MW reference wind turbine, so this phenomenon is not discussed in depth. From the statistical analysis, the mean and standard deviation of wind-wave misalignment angle at different wind speeds is mentioned in Table 2. The mean (μ_β) and standard deviation (σ_β) parameters are calculated by following formulas:

$$\mu_\beta = \frac{1}{N}\sum_{i=1}^{N} U_i \qquad (2)$$

$$\sigma_\beta = \sqrt{\frac{1}{N-1}\sum_{i=1}^{N}(U_i - \mu)^2} \qquad (3)$$

Further study is required to find the best fit distribution to represent the marginal pdf of wind-wave misalignment angle at different wind speeds.

Table 2. Mean and Standard Deviation of wind-wave misalignment angle at different wind speeds.

Wind Speed	μ_β	σ_β
3.5	4.98	61.92
4.5	7.71	53.98
5.5	8.27	44.00
6.5	9.95	38.00
7.5	10.23	32.50
8.5	11.00	28.50
9.5	11.83	25.42
10.5	11.66	21.90
11.5	12.93	22.65
12.5	11.12	21.55
13.5	10.67	24.00
14.5	13.00	21.00
15.5	12.40	20.00
16.5	12.83	19.40
17.5	15.40	19.25

3 EFFECT OF WIND-WAVE MISALIGNMENT ON THE RESPONSE OF IEA-15MW REFERENCE WIND TURBINE

To study the severity of the impact of wind-wave misalignment on wind turbine response, the wind-turbine response is simulated for co-directional and misaligned wind-wave loading, and the deformation and reactions under these conditions are compared. The wind speed and wave direction parameters mentioned in Table 2 are used for the simulation. This reference wind turbine is chosen for this study as it represents the largest standalone wind turbine model and is a leap ahead of current generation wind turbines. [13]. The IEA-15MW reference wind turbine is an IEC Class 1B direct-drive machine with a rotor diameter of 240 meters (m) and a hub height of 150 m. The wind turbine response is simulated using OpenFast, a computer-aided aero-servo-hydro-elastic tool widely used to model the horizontal axis wind turbines [14]. This tool uses the AeroDyn module to compute the aerodynamic forces and HydroDyn to compute the hydrodynamic loads. This simulation assumes that the rotor always faces the inflow wind, and the mean wave direction is equal to the wind-wave misalignment angle. A pictorial representation of the loading configuration is shown in Figure 7. The wave coming from the positive Y-axis is considered positively misaligned and vice versa.

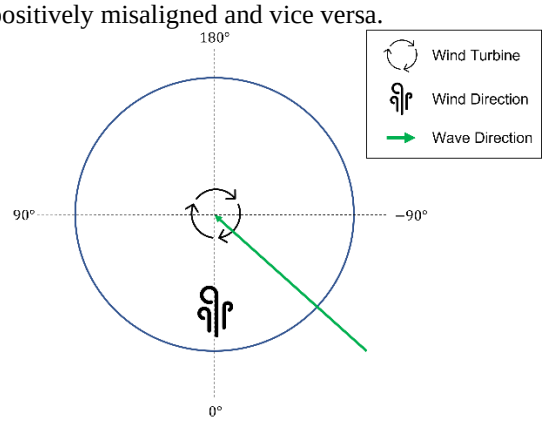

Figure 6. Wind-Wave loading configuration

The effect of misalignment on the tower side-to-side deformation and the forces generated at the tower base in the Y direction (perpendicular to inflow wind) are shown in Figure 7 and Figure 8, respectively.

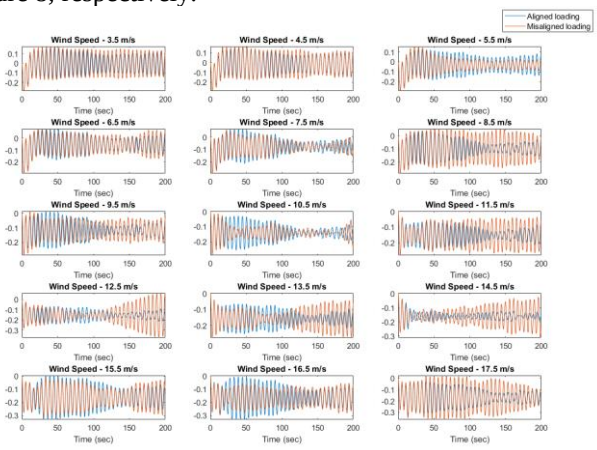

Figure 7. Effect of wind-wave misalignment on tower side-to-side deformation

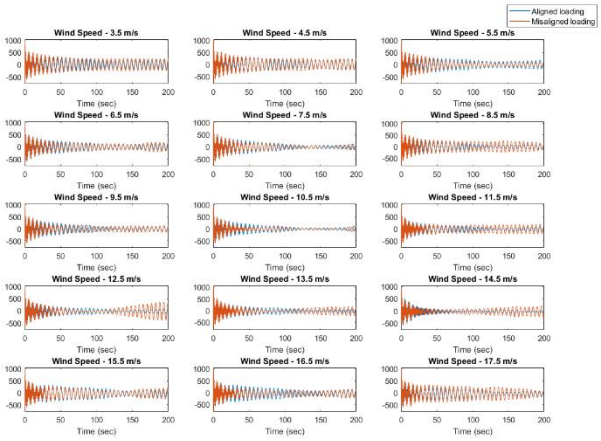

Figure 8. Effect of wind-wave misalignment on tower base reaction in Y-direction

4 CONCLUSION

Figures 7 and 8 show that the misaligned loading pattern creates high amplitude oscillations in tower side-to-side forces and deformation at certain wind speeds. These high amplitude fluctuations in tower forces will increase the range of stress reversal and can adversely impact the fatigue life of the wind turbine. A detailed analysis is required to quantify the effect of wind-wave misalignment on the fatigue life of the structure. These simulations show that the co-directionality of wind and waves may not always lead to a conservative design. The misalignment in the wind and waves should be accounted for to achieve a reliable fatigue life of the structure.

ACKNOWLEDGMENTS

This work has been supported by the SEAI RD&D Projects SEAI/19/RDD/511 and SEAI-21/RDD/601 . The authors are grateful for the support.

REFERENCES

1. CHANGE, T.S.T. and M. BE, *Wind energy generation systems–Part 3-1: Design requirements for fixed offshore wind turbines.*
2. Bhattacharya, S., *Design of foundations for offshore wind turbines*. 2019: John Wiley & Sons.
3. AlHamaydeh, M. and S. Hussain, *Optimized frequency-based foundation design for wind turbine towers utilizing soil–structure interaction.* Journal of the Franklin Institute, 2011. **348**(7): p. 1470-1487.
4. Li, X., et al., *Effects of the yaw error and the wind-wave misalignment on the dynamic characteristics of the floating offshore wind turbine.* Ocean Engineering, 2020. **199**: p. 106960.
5. Bachynski, E.E., et al., *Wind-wave misalignment effects on floating wind turbines: motions and tower load effects.* Journal of Offshore Mechanics and Arctic Engineering, 2014. **136**(4).
6. Fitzgerald, B., D. Igoe, and S. Sarkar. *A Comparison of Soil Structure Interaction Models for Dynamic Analysis of Offshore Wind Turbines*. in *Journal of Physics: Conference Series*. 2020. IOP Publishing.
7. Fischer, T., et al., *Study on control concepts suitable for mitigation of loads from misaligned wind and waves on offshore wind turbines supported on monopiles.* Wind Engineering, 2011. **35**(5): p. 561-573.
8. Verma, A.S., et al., *Effects of Wind-Wave Misalignment on a Wind Turbine Blade Mating Process: Impact Velocities, Blade Root Damages and Structural SafetyAssessment.* Journal of Marine Science and Application, 2020. **19**(2): p. 218-233.
9. Stewart, G.M. and M.A. Lackner, *The impact of passive tuned mass dampers and wind–wave misalignment on offshore wind turbine loads.* Engineering structures, 2014. **73**: p. 54-61.
10. Koukoura, C., et al., *Cross-wind fatigue analysis of a full scale offshore wind turbine in the case of wind–wave misalignment.* Engineering structures, 2016. **120**: p. 147-157.
11. Hildebrandt, A., B. Schmidt, and S. Marx, *Wind-wave misalignment and a combination method for direction-dependent extreme incidents.* Ocean Engineering, 2019. **180**: p. 10-22.
12. Pereira, D., *Wind Rose*. 2022: Matlab Central File Exchange.
13. Gaertner, E., et al., *IEA wind TCP task 37: definition of the IEA 15-megawatt offshore reference wind turbine*. 2020, National Renewable Energy Lab.(NREL), Golden, CO (United States).
14. Marshall Buhl, G.H., Jason Jonkman, Bonnie Jonkman, Rafael Mudafort, Andy Platt, Mike Sprague, *The New Modularization Framework for the FAST Wind Turbine CAE Tool*. 2022.

Pedagogy

Education for Sustainable Development: Mapping the SDGs to University Curricula

Thomas_Adams[1,2], Jamie_Goggins[1,2,3]
[1]School of Engineering, National University of Ireland Galway, University Road, Galway, Ireland
[2]MaREI, the SFI Research Centre for Energy, Climate and Marine, National University of Ireland, Galway
[3]Ryan Institute, National University of Ireland, Galway
email: t.adams4@nuigalway.ie, jamie.goggins@nuigalway.ie

ABSTRACT: Education for sustainable development is a growing research field, particularly over the last decade. This paper expands on previous research titled "Embedment of the SDGs in engineering degree programs", in which a keyword scanning tool was created to quantify the level of SDG coverage within a list of learning outcomes. The methodology in this paper refines this tool further by reviewing the performance of keywords from three reputable sources. A total of 6,681 SDG related keywords were compiled and a team of reviewers conducted a critical analysis on the relevancy of the context in which the keywords were found when scanned for. This process reduced the list to 214 keywords each labelled either as SDG focussed or SDG supportive. This list was used to perform a cross-institutional scan on Civil Engineering programmes, in a collaboration between seven Irish Higher Education Institutions. This paper also presents results from a survey of NUI Galway lecturers within the College of Science and Engineering. The survey asked staff to rate the level of SDG coverage within their own modules, in their own opinion. This gave results which could be compared with the keyword scanning tool. Findings show success in improving the accuracy of the keyword tool, and its capability of being applied to many institutions. There is consistency across trend in SDG coverage in the 6 Civil Engineering programmes, with high coverage of SDGs 6, 13, 11 and 7 and in the results from the survey.

KEY WORDS: Sustainable Development Goals; Pedagogy; Education For Sustainable Development; Curriculum Mapping; Learning Outcomes.

1 INTRODUCTION

The Sustainable Development Goals (SDGs) were launched in 2015, superseding the Millennium Development Goals. The goals were part of the Agenda 2030, which was adopted by all United Nations (UN) member states in 2015 [1]. The world is on an accelerating path towards sustainable development (SD) since. The SDGs cover a wide range of issues connected to society, economies, and the environment and one of the most fundamental aspects of the goals lies in SDG 4, Education for Sustainable Development (ESD).

Education for Sustainable Development (ESD) is a long-established field of research and international collaboration. Lozano et. al [2] summarises a history of eleven global declarations, charters and partnerships for sustainability in Higher Education Institutions (HEIs), which goes back as far as 1990. One the most important of these was the UNs Decade for Education for Sustainable Development, which spanned from 2005 to 2014.

Several bibliometric literature reviews have been published since showing the growth of the research field [3]–[9]. These literature reviews detail the various directions the research has taken as well as the most cited authors, documents, and most active journals. A prevalent point is the importance of holistic, whole of institution, and horizontal implementation of ESD for best results. Also, the precept of "What gets measured gets done" alluding to the many sustainability assessment tools that have been created for HEIs to gain a baseline sustainability evaluation.

Many schools, universities and governments are attempting to align their education systems with the SDGs [10]. The Irish Government released an interim report on the National Strategy on Education for Sustainable Development in Ireland in 2020 [11], before going about a public consultation process in 2021 on the ESD Strategy to 2030 [12]. NUI Galway's Sustainability Strategy, like many others, has the objective to embed sustainability principles and practices into all programme delivery at all levels of research, learning and events [13].

UNESCO [14], the Commonwealth [15], and the Sustainable Development Solutions Network (SDSN) Australia Pacific [16] have all released comprehensive guides for the incorporation of sustainability into education institutions. These guides agree that mapping the curriculum to the SDGs is useful as a baseline to build this incorporation from. The Irish Governments ESD consultation report claims that the UNESCO framework [14] should be considered and adapted to the Irish context.

This paper is placed in the field of sustainability assessment in Higher Education Institutions (HEIs) and focusses on curriculum assessment. It aims to address an acknowledged gap within sustainability assessment tools which is a lack of methodologies for assessing of the education of sustainability [17]. The SDGs are used as a framework for sustainability and this paper aims to present two easy and accessible methods for mapping the SDGs to a university curriculum.

This is specifically relevant to Colleges of Engineering in Ireland due to the accreditation body, Engineers Ireland. Engineers Ireland provide an accreditation for all 3rd level engineering courses in Ireland to ensure they meet international standards, the needs of the engineering profession and broader responsibilities of society, the environment and economy. As of 2021, the accreditation criteria now include sustainability as a Programme Area [18]. Engineers Ireland have determined that the study of seven Programme Areas is necessary if graduates are to achieve the Programme Outcomes. This gives relevance to the assessment of curriculum material of engineering modules, as these should facilitate the engineering graduate's achievement of the Programme Outcomes [18].

2 LITERATURE REVIEW

2.1 Introduction

The next two sections explain the literature behind the methodology presented in this paper. The first method pursued was to create a tool that could scan curriculum material for a list of SDG related keywords, resulting in a baseline measure of SDG related teaching in a university. Keyword lists were sourced online and critically analysed as the basis for this tool. The second method aimed to gather input from lecturers through a survey which asked for staff to self-rate their modules in terms of SDG coverage.

2.2 Sustainability Assessment Tools

In terms of the assessment of sustainability in curricula, there are few published open access tools available for use. A 2012 study conducted a review of 16 sustainability assessment tools to examine trends in issues and methodologies [17]. It found that these tools mainly focussed on the environmental impacts of university operation and issues related to governance, lacking the measurement of curriculum, research, and outreach aspects. A 2019 review of 19 sustainability assessment tools found that these tools tend to neglect the impacts HEIs have outside of their organizational boundaries [19]. There is a need for further research on the educational and outreach aspects of sustainability in HEIs. There are several guides available which offer advice to HEIs for implementing sustainability into education [14]–[16]. However, these guides do not provide a tool with which to assess the current level of education for sustainable development within a university's curriculum. This initial step of quantifying the level of ESD within a university allows for the identification of each institutions' unique pathway of further ESD implementation. This research paper aims to add to the literature surrounding the measurement of sustainability education in HEIs.

2.3 Keyword Method Theory

One methodology of curriculum assessment which has been trialled by some universities is a keyword scan [26]–[29]. This is carried out by searching for a list of SDG related keywords in curriculum material, resulting in SDGs being assigned to certain modules or programs. There are variations in the methodology followed for the creation of the keyword lists. This study compares three of the most cited lists of keywords. The first of these is the Compiled Keywords for SDG Mapping, created during a collaboration between Monash University and SDSN Australia/Pacific in 2017 [27]. This list contains 915 keywords spanning from SDGs 1-17 with an added miscellaneous category of keywords also. The second keyword list was produced in 2019 by SIRIS Academic [28]. This list was built by extracting key terms from the UN SDG indicators document, before being both manually and automatically enriched. A literature review around the SDGs informed the manual enrichment and a machine learning model based on neural networks was also utilized to automatically add to the database. This list contains 3,445 keywords spanning SDGs 1-16. The third list under review in this project was put together by the University of Auckland [29], which was based on Elsevier's SDG search query for published research. The University of Auckland used an n-gram text-mining model on abstracts of SDG related academic publications to develop the list with additional search terms added thanks to input from the Sustainable Development Solutions Network (SDSN) and the UN [29]. This list contains 2,321 keywords ranging from SDGs 1-16. This research critically analysed these keyword lists.

A machine learned approach was used by Elsevier in the "Mapping Research Output to the SDGs" initiative [30]–[32]. These models use handpicked research publications that relate to an SDG to create a "golden set" for the machine learning methodology. This is a significant step forward in SDG mapping, but the initiative is applied to research only, not curricula.

2.4 Survey Method Theory

Another method of assessing the level of sustainability education in HEIs is through surveys. The survey used in this paper was adopted from an SDG Curriculum toolkit created by University College Cork (UCC) [33]. The SDG Curriculum Toolkit was created by a team at UCC and offers excel spreadsheets for students or staff to manually map modules, courses, or research to the SDGs. In this study, lecturers were asked to rate the coverage of the SDGs within their modules, but with an added step of noting the level that their modules covered each SDG. Modules could either be marked as not related, supportive of or focussed on an SDG, based on definitions laid out in the STARS 2.2 Technical Manual [34]. The survey was sent to lecturers of modules in the College of Science and Engineering at NUI Galway.

3 METHODOLOGY

3.1 Introduction

The methodology for this paper is broken into two distinct sections. Firstly, a method of scanning for a list of SDG related keywords in curriculum material. This followed a process of critically analysing a compiled list of keywords, created from three different keyword lists. Members of the universities sustainability academic working group formed a team to review the performance of the keywords. The second method utilised a survey to ask module owners to rate, in their opinion, how well their modules covered each SDG. The purpose of these different SDG measuring techniques was to compare the resulting lists of SDG-rated modules to verify how accurate and automated each method was to implement.

3.2 Keyword Scanning Tool

Using Microsoft Excel, a tool was developed to crosscheck a list of learning outcomes for the presence of keywords. These keywords and learning outcomes were input, they were then operated on by equation 1 and 2 below, creating the output of learning outcomes now labelled with keywords and SDGs. Equation 1 operates by scanning a cell containing a learning outcome for the contents of another cell containing a keyword. If the keyword is present the equation prints this keyword, if not the cell remains blank. Equation 2 gathers the keywords that were printed into one cell. Equation 1 would then be used again to scan this cell for the keywords and print the SDG label.

$$= IF(ISNUMBER(SEARCH("cell","range")),"cell","")$$

$$= TEXTJOIN(",",,"row\ of\ cells")$$

3.3 Keyword and Module Sources

The tool was used to compare the three keyword databases seen in Table 1. SDG related keyword lists are available online, and this study chose three of the most cited lists. One produced by Monash University [27], one from SIRIS Academic, Barcelona [28] and the last from the University of Auckland [29]. These lists make a total of 6,681 keywords that were analysed.

Table 1 – Keyword Sources

Source	No. Keywords	Span
Monash University	915	SDG 1-17
SIRIS Academic	3445	SDG 1-16
University of Auckland	2321	SDG 1-16

A list of 1,103 modules was provided by the IT department of the University which spanned all Colleges in NUI Galway. This study focusses on the College of Science and Engineering, but to include keywords relevant to other Colleges, some modules from all Colleges were input. Learning outcomes were the chosen module material for the scan. Some studies include module titles and descriptions also. The Engineers Ireland accreditation document, mentioned in the above sections, associates learning outcomes with the successful achievement programme areas and programme outcomes, so scanning learning outcomes alone was the chosen method [18]. Table 2 shows the number of modules divided into the various Colleges at NUI Galway.

Table 2 – No. of Modules in each College

College of	No. of Modules
Arts, Social Sciences & Celtic Studies	280
Science and Engineering	513
Medicine, Nursing, & Health Sciences	102
Business, Public Policy, & Law	90
Adult Learning and Profess Development	69
Acadamh na hOllscolaíochta Gaeilge	49
Total	1,103

3.4 Keyword Critical Analysis

These 1,103 modules were then scanned for the presence of all 6,681 keywords using the excel tool described above. The lists were reduced through four stages of review, as described in Table 3 below. First, all words not hit were removed, which accounted for 91% of all words, leaving just 601 keywords. Second, keywords that appeared in multiple SDGs were moved into their own column of "multiple SDG words". For example, *"Biodiversity"* which appears under SDG 14 and 15 in the SIRIS list, was moved to the "multiple SDG words" column and labelled as SDG 14 & 15.

Table 3 - Stages involved in reducing the keyword lists

Stage	Description
Start	Full lists from three sources scanned for in modules
1	Removed words not hit
2	Bundled words under many SDGs into one group
3	Removed words covered by a shorter root word
4	Compiled the three lists and removed duplicates

The third step involved removing all words for which a shorter root word was present. Using *"Biodiversity"* as an example again, the Monash list contains the following four terms which were all removed under this process *"Coastal biodiversity, Biodiversity loss, Marine biodiversity, Strategic plan for biodiversity"*. The excel tool operates such that these longer text strings are not necessary and will end up giving more than one hit if the longer term is present. The final stage involved compiling the remaining words into one list and removing duplicates. At this point, an in-depth review was carried out on the remaining words to evaluate the context each keyword was in. This analysis was performed by members of the Universities Sustainability Academic Working Group, whereby each member of the team would read through a list of learning outcomes and judge if the keyword found in the learning outcome was in the context of the associated SDG. Once the context was understood, a relevancy score was given to the keyword for each learning outcome reviewed. The relevancy scores can be seen in Table 4 below.

Table 4 - Description of Relevance Scores

Score	Relevancy Description
0	Not relevant to assigned SDG
1	Supportive of assigned SDG
2	Focussed on assigned SDG
3	Supportive of an SDG other than the SDG assigned
4	Focussed on an SDG other than the SDG assigned

The definitions for an SDG "supportive" or "focussed" learning outcome were adopted from the STARS 2.2 Technical manual [34]. Using these definitions means the tool could be used in future STARS applications, where a list of modules which are sustainability focussed, or supportive is required. After all learning outcomes for a keyword had been analysed, it's relevancy scores were totted up to see if the context it was found in was mostly focussed, supportive or irrelevant. If the keyword received the same relevancy score for at least 70% of the learning outcomes, it would be assigned this relevancy label. If the relevancy labels did not reach a consensus, a keyword would settle for the lower of the scores, i.e., if it received 50% "1 – supportive" and 50% "0 – irrelevant", it would be deemed irrelevant. Words labelled irrelevant were removed, words labelled with scores 3 or 4 in the table above were moved to the more relevant SDG category. This critical analysis produced two final lists. One of SDG supportive keywords and one of SDG focussed keywords, as per the STARS definitions [34].

3.5 Survey

A survey was circulated among lecturers in the College of Science and Engineering in NUI Galway with responses received from 33 of them. An SDG rating spreadsheet for modules was adopted from UCC [33]. The spreadsheet was included in the survey and asked lecturers to rate whether they thought their module(s) as per the STARS definitions [34]. This gave the opportunity for comparison with the results from the keyword critical analysis.

3.6 Limitations

There is a potential for bias in the keyword critical analysis, as there is a level of interpretation involved in the assigning of

relevancy scores. Using a team of people to review the keywords was an attempt to overcome this, however there is still a level of bias present. As a result, the keyword scanning tool is not definitively accurate and should not be used to define whether a module is SDG supportive or focussed. It should be used as a guide baseline measure of SDG coverage which should then be reviewed by the module owner. However, given the methodology used, the keyword list can be continuously reviewed and updated, based off module owner's feedback, and could be developed to an acceptable level of accuracy.

4 RESULTS

4.1 Introduction

This section presents results from two distinct sections. Firstly, the analysis of the three keyword lists, showing how many words made it through each reducing process and the critical analysis. Secondly, trends in SDG coverage are presented from both the keyword method and the survey method. The keyword method was applied to Civil Engineering programmes from seven Irish HEIs and to 87 modules from the College of Science and Engineering at NUI Galway.

4.2 Keyword Critical Analysis

As described in the methodology section above, three lists of keywords went through the process described in Table 3, to reduce the lists down to one list of useful words. Table 5 on the next page shows the resulting reduction in the number of keywords in each list at each stage of the process.

4.3 Trends in SDG Coverage

This section presents trends in SDG coverage using these 214 keywords and the keyword tool. Firstly, Figures 1 and 2 show the trend keyword hits for Civil Engineering Programmes from seven Irish higher-level institutions. Figure 1 shows the results from the focussed keywords and Figure 2 the supportive. Figures 3 and 4 give a comparison of the keyword method and the survey method. From the 33 responses to the survey a total of 87 modules were submitted with SDG ratings. These 87 modules were then put through the keyword tool for a direct comparison. Figures 3 and 4 show the trend in SDG coverage for focussed modules and supportive modules respectively. Table 6 below shows the data presented in the graphs above. It also shows the number of modules scanned for each institution and the percentage of these modules that contained keywords

Table 5 - Civil Programme data for 7 Irish HEIs

HEI	Foc hits	Supp hits	# Mods	% Hit
NUIG	70	26	40	60%
UCD	25	32	76	47%
WIT	34	23	46	46%
UCC	41	53	61	56%
TCD	30	50	65	55%
UL	40	36	60	50%
GMIT	19	18	34	50%
Average:	**37**	**34**	**55**	**52%**

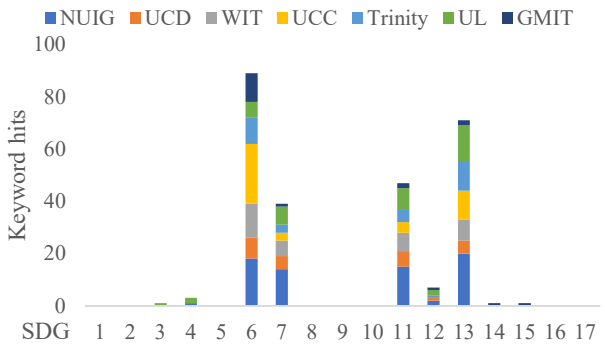

Figure 1 - SDG focussed trend for Civil Eng in 7 Irish HEIs

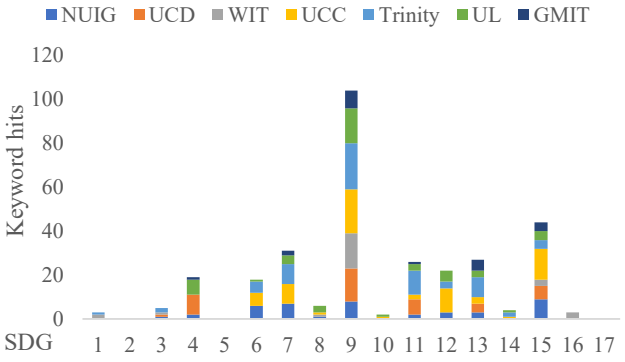

Figure 3 - SDG supportive trend for Civil Eng in 7 Irish HEIs

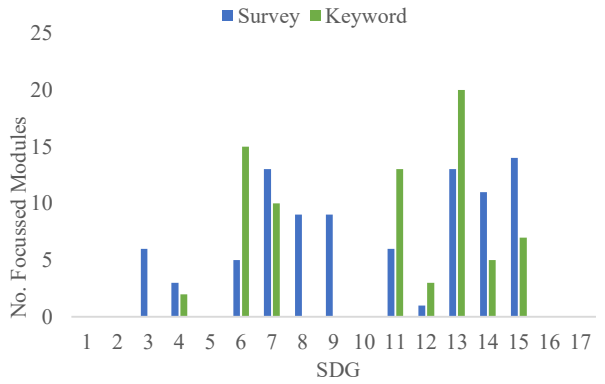

Figure 2 - Survey Vs Keyword Scan, Focussed Modules

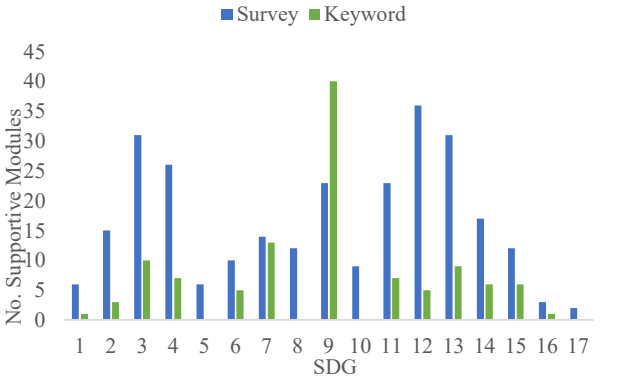

Figure 4 - Survey Vs Keyword Scan, Supportive Modules

Table 6 – Stages of reducing keyword lists

Stage	Monash	SIRIS	Auckland	Sum	Removed
Start	915	3,445	2,321	6,681	
1	215	222	164	601	6,080
2	154	187	137	478	123
3	132	174	109	415	63
4				261	154

Table 4 in the methodology section shows the criteria involved in a critical analysis that was carried out on the remaining 261 keywords. From this critical analysis, a further 42 keywords were removed due to mostly irrelevant hits. Sixty-two were labelled as "focussed" keywords and 152 as "supportive keywords, resulting in a final list of 214 keywords, split 29% focussed and 71% supportive.

5 DISCUSSION

5.1 Intro

This section will discuss the results in the same two distinct sections, firstly the keyword analysis, secondly the SDG trends.

5.2 Keyword Analysis

The keyword analysis was successful in producing a list of keywords tailored to the needs of the Irish third level education system. The initial reduction of keywords was necessary to reduce the number of words the excel tool would have to scan for, reducing computing demands. The list of 261 keywords was critically analysed by a team of reviewers. The group review was successful in removing irrelevant words and in labelling any remaining words as either supportive or focussed, as per the STARS definitions. Each reviewers' labels were cross checked, finding an acceptable consistency of 70%. As well as improving the accuracy of the keyword scanning tool, it also gives the tool the added capability of indicating whether modules are sustainability supportive or focussed, which is necessary when completing a STARS application. It is important to note that the keyword scanning tool is not definitive and is only intended to give an indication to a modules SDG coverage. It has the potential to take in large amounts of data and produce these indications, which should then be reviewed by the individual module owners for accuracy before a module is officially labelled as sustainability supportive or focussed.

5.3 Trends in SDG Coverage

The collaboration between Civil Engineering departments from seven Irish higher-level institutions was a successful part of this study, and the results show the keyword scanning tool's capability of being applied to other institutions. The consistency in the SDG trend across the institutions shows the tool is not NUI Galway biased and can be used to provide a baseline measure of SDG coverage at any HEI. Table 6 shows that while NUIG did receive the most keyword hits overall, UCC was a close second and TCD and UL also performed very well. Most programs received hits in at least half of their modules, with only UCD and WIT falling just under 50%. It can also be seen that there was almost an even split of focussed to supportive hits (52:48), even though in terms of keywords the split is 29:71. There is no correlation between the number of modules submitted and the number of hits received, meaning the tool successfully sifted through the large amount of data to identify key modules. In terms of where the SDG coverage sits within the programmes, there was a general trend of a peak in year 4, with year 3 following close behind and year 5 containing most of the rest of the modules. Years 1 and 2 contained very little SDG coverage.

The trend in SDG focussed modules is what one might expect from Civil Engineering programmes, with a large focus on SDGs 6 (clean water), 13 (climate action), 11 (sustainable cities) and 7 (clean energy). SDG 12 (consumption & production), 4 (education), 3 (health & wellbeing) 14 (life below water) and 15 (life on land) received minimal coverage and the other 8 SDGs didn't see any hits in terms of focussed keywords. The trend in SDG supportive modules was more spread-out bar the obvious outlier of SDG 9 (industry, innovation & infrastructure). Only SDGs 2 (zero hunger), 5 (gender equality), and 17 (partnership for the goals) didn't receive hits. The high coverage of SDG 9 was due to four keywords receiving a lot of hits: *Technology*, *Industry*, *Business,* and *Infrastructure*. The top five words hit overall were *Soil* (SDG 15 supportive), *Water* (SDG 6 focussed), *Technology* (SDG 9 supportive), *Sustainable* (SDG 7, 11 & 13 focussed) and *Wastewater* (SDG 6 focussed).

The results from comparing the survey to the keyword tool could give a basis for carrying out another review of the supportive keywords. On average, the keyword method scored 0.8 focussed keywords per module and 1.3 supportive, while the survey method scored 0.9 focussed keywords per module and 3 supportive, meaning in terms of focussed modules, the survey method gave 1.2 times more hits and in terms of supportive modules it gave 2.4 times more. In terms of the SDG trend, the survey tended to cover more SDGs overall. The keyword method gave higher scores for SDG 6, 11, 12 and 13 in the focussed modules and SDG 9 in the supportive modules, the survey method gave higher scores in all other SDGs. In terms of the top 10 modules identified by each method, 5 were common in the focussed group and 6 were common in the supportive group. SDGs 4, 6, 7, 13, 14 and 15 were all scored relatively similarly by both methods, again showing the keyword tool has a decent level of accuracy. However, the discrepancy in scores in the other SDGs gives grounds for further investigation, into both why the keywords scored lower and why the survey scored higher.

6 CONCLUSIONS

This research successfully presented a methodology for measuring a baseline of SDG teaching in a university's curriculum. The consistency in the trend of SDG coverage among Civil Engineering programmes shows the capability of the keyword tool in being applied to many institutions. The group review of keywords was successful in increasing the accuracy of the keyword list. The survey produced an SDG focussed trend consistent with the keyword tool, showing the focussed keyword list can provide results that agree with input from 33 lecturers. The supportive keyword list is only half as accurate unfortunately, leaving opportunity for further review.

7 FUTURE ASPECTS

There is a future aspect of this research in the use of artificial intelligence as curriculum mapping tool. Given its proficiency for analysing the context of a string of text, it could be utilized to scan learning outcomes for the context of SDGs. The keyword tool and survey methods could be used for comparisons. Collaboration with HEIs on more programmes could be pursued, expanding the measure of SDGs in curricula.

ACKNOWLEDGMENTS

This research was funded by Science Foundation Ireland (SFI) through the MaREI Centre (Grant no. 12/RC/2302_2). Learning outcome data was provided by the NUI Galway. Thanks to members of the CUSP academic WG who contributed to the critical analysis of the keywords and lecturers in the College of Science and Engineering who did the survey.

REFERENCES

[1] K. V. Sarabhai, "ESD and Global Citizenship Education," *J. Educ. Sustain. Dev.*, vol. 7, no. 2, pp. 137–139, 2013, doi: 10.1177/0973408214527309.

[2] R. Lozano, R. Lukman, F. J. Lozano, D. Huisingh, and W. Lambrechts, "Declarations for sustainability in higher education: Becoming better leaders, through addressing the university system," *J. Clean. Prod.*, vol. 48, pp. 10–19, 2013, doi: 10.1016/j.jclepro.2011.10.006.

[3] G. Grosseck, L. G. Tîru, and R. A. Bran, "Education for sustainable development: Evolution and perspectives: A bibliometric review of research, 1992-2018," *Sustain.*, vol. 11, no. 21, pp. 1992–2018, 2019, doi: 10.3390/su11216136.

[4] P. Hallinger and C. Chatpinyakoop, "A bibliometric review of research on higher education for sustainable development, 1998-2018," *Sustain.*, vol. 11, no. 8, 2019, doi: 10.3390/su11082401.

[5] P. L. Côrtes and R. Rodrigues, "A bibliometric study on 'education for sustainability,'" *Brazilian J. Sci. Technol.*, vol. 3, no. 1, p. 8, 2016, doi: 10.1186/s40552-016-0016-5.

[6] A. Zutshi, A. Creed, and B. L. Connelly, "Education for Sustainable Development: Emerging Themes from Adopters of a Declaration," *Sustainability* , vol. 11, no. 1. 2019, doi: 10.3390/su11010156.

[7] M. Tang, H. Liao, Z. Wan, E. Herrera-Viedma, and M. A. Rosen, "Ten Years of Sustainability (2009 to 2018): A Bibliometric Overview," *Sustainability* , vol. 10, no. 5. 2018, doi: 10.3390/su10051655.

[8] T. Wright and S. Pullen, "Examining the Literature: A Bibliometric Study of ESD Journal Articles in the Education Resources Information Center Database," *J. Educ. Sustain. Dev.*, vol. 1, no. 1, pp. 77–90, Mar. 2007, doi: 10.1177/097340820700100114.

[9] S. Menon and M. Suresh, "Synergizing education, research, campus operations, and community engagements towards sustainability in higher education: a literature review," *Int. J. Sustain. High. Educ.*, vol. 21, no. 5, pp. 1015–1051, 2020, doi: 10.1108/IJSHE-03-2020-0089.

[10] A. Wiek, L. Withycombe, and C. L. Redman, "Key competencies in sustainability: A reference framework for academic program development," *Sustain. Sci.*, vol. 6, no. 2, pp. 203–218, 2011, doi: 10.1007/s11625-011-0132-6.

[11] DE, "'Education for Sustainability' The National Strategy on Education for Sustainable Development in Ireland Report of Interim Review and Action Plan for Q4 2018-Q4 2020," 2020.

[12] DE, "Joint Public Consultation on a National Strategy on Education for Sustainable Development (ESD) to 2030," Dublin, 2021. [Online]. Available: https://www.gov.ie/en/consultation/8bce5-joint-public-consultation-on-a-national-strategy-on-education-for-sustainable-development-esd-to-2030/.

[13] NUI Galway, "NUI Galway Sustainability Strategy," *2021*. https://www.nuigalway.ie/sustainability/strategy/ (accessed Feb. 23, 2022).

[14] UNESCO, *Education for Sustainable Development Goals - Learning Objectives*, vol. Volume-2, no. Issue-1. Paris, 2017.

[15] The Commonwealth, "Curriculum Framework for Enabling the Sustainable Development Goals," no. July, 2017.

[16] SDSN, "Accelerating Education for the SDGs in Universities: A guide for universities, colleges, and tertiary and higher education institutions.," New York, 2020. [Online]. Available: https://irp-cdn.multiscreensite.com/be6d1d56/files/uploaded/accelerating-education-for-the-sdgs-in-unis-web_zZuYLaoZRHK1L77zAd4n.pdf.

[17] M. Yarime and Y. Tanaka, "The Issues and Methodologies in Sustainability Assessment Tools for Higher Education Institutions: A Review of Recent Trends and Future Challenges," *J. Educ. Sustain. Dev.*, vol. 6, no. 1, pp. 63–77, 2012, doi: 10.1177/097340821100600113.

[18] D. Owens and R. Manton, "Accreditation criteria," 2021. doi: 10.1016/b978-075064843-1/50010-9.

[19] F. Findler, N. Schönherr, R. Lozano, and B. Stacherl, "Assessing the Impacts of Higher Education Institutions on Sustainable Development—An Analysis of Tools and Indicators," *Sustainability*, vol. 11, no. 59, 2019, doi: https://doi.org/10.3390/su11010059.

[20] T. Waas, K. Ceulemans, W. Lambrechts, J. Vandenabeele, R. Lozano, and T. Wright, "Sustainable Higher Education - Understanding and Moving Forward," Brussels, 2012.

[21] E. M. Barrella and M. K. Watson, "Comparing the Outcomes of Horizontal and Vertical Integration of Sustainability Content into Engineering Curricula Using Concept Maps," *World Sustain. Ser.*, pp. 1–13, 2016, doi: 10.1007/978-3-319-32933-8_1.

[22] S. P. Trad, "A framework for mapping sustainability within tertiary curriculum," *Int. J. Sustain. High. Educ.*, vol. 20, no. 2, pp. 288–308, 2019, doi: 10.1108/IJSHE-09-2018-0151.

[23] R. Lozano, M. Y. Merrill, K. Sammalisto, K. Ceulemans, and F. J. Lozano, "Connecting competences and pedagogical approaches for sustainable development in higher education: A literature review and framework proposal," *Sustain.*, vol. 9, no. 10, pp. 1–15, 2017, doi: 10.3390/su9101889.

[24] R. Lozano, M. Barreiro-Gen, F. J. Lozano, and K. Sammalisto, "Teaching Sustainability in European Higher Education Institutions: Assessing the Connections between Competences and Pedagogical Approaches," *Sustain. 2019, Vol. 11, Page 1602*, vol. 11, no. 6, p. 1602, Mar. 2019, doi: 10.3390/SU11061602.

[25] R. Lozano and M. Barreiro-Gen, "Analysing the factors affecting the incorporation of sustainable development into European Higher Education Institutions' curricula," *Sustain. Dev.*, vol. 27, no. 5, pp. 965–975, 2019, doi: 10.1002/sd.1987.

[26] A. Kuros, A. D. Rockcress, J. L. Berman-Jolton, and ..., "Critiquing and Developing Benchmarking Tools for Sustainability," no. December, 2017, [Online]. Available: https://digitalcommons.wpi.edu/iqp-all/2169/.

[27] Monash University, "Compiled-Keywords-for-SDG-Mapping_Final_17-05-10," *Australia/Pacific Sustainable Development Solutions Network (SDSN)*, 2017. http://ap-unsdsn.org/wp-content/uploads/2017/04/Compiled-Keywords-for-SDG-Mapping_Final_17-05-10.xlsx (accessed Feb. 03, 2020).

[28] N. Duran-Silva, E. Fuster, F. A. Massucci, and A. Quinquillà, "A controlled vocabulary defining the semantic perimeter of Sustainable Development Goals," *[Data set]*, vol. Zenodo, Dec. 2019, doi: https://doi.org/10.5281/zenodo.3567769.

[29] J. Mu and K. Kang, "The University of Auckland SDG Keywords Mapping," 2021. https://www.sdgmapping.auckland.ac.nz/ (accessed Nov. 03, 2021).

[30] M. Vanderfeesten, R. Otten, and E. Spielberg, "Search Queries for 'Mapping Research Output to the Sustainable Development Goals (SDGs)' v5.0.2," *Zenodo*, Jul. 2020, doi: https://doi.org/10.5281/zenodo.4883250.

[31] F. Schmidt and M. Vanderfeesten, "Evaluation on accuracy of mapping science to the United Nations' Sustainable Development Goals (SDGs) of the Aurora SDG queries," Jun. 2021, doi: 10.5281/ZENODO.4964606.

[32] M. Rivest *et al.*, "Improving the Scopus and Aurora queries to identify research that supports the United Nations Sustainable Development Goals (SDGs) 2021," vol. 4, 2021, doi: 10.17632/9SXDYKM8S4.4.

[33] J. Barimo *et al.*, "SDG Curriculum Toolkit," 2021. https://www.ucc.ie/en/sdg-toolkit/teaching/tool/ (accessed Mar. 24, 2022).

[34] AASHE, "STARS Technical Manual Version 2.2," no. June, pp. 1–322, 2019, [Online]. Available: https://stars.aashe.org/wp-content/uploads/2019/07/STARS-2.2-Technical-Manual.pdf.

Shrinking Sports Socks and Cracking Concrete Slabs

Roger P West[1], Stephen W. West[2]
[1]Department of Civil, Structural and Environmental Engineering, Trinity College, College Green, Dublin 2
[2] Sport Injury Prevention Research Centre, Faculty of Kinesiology, University of Calgary, Calgary, Alberta, Canada
email: rwest@tcd.ie, stephen.west@ucalgary.ca

ABSTRACT: In the teaching of materials science to undergraduate engineering students, it can be effective to pose them with an everyday problem which they have an intuition as to how to solve, but in the absence of a full understanding of the science underpinning the solutions. A good knowledge of science should be a pre-requisite for utilising many forms of engineering technology. This paper will describe how, by drawing an analogy from everyday life, the principles behind the causes of drying shrinkage of concrete slabs can be better understood. By introducing a tutorial problem on how to quickly dry a pair of saturated sports socks for use that day, in the absence of electricity, to over 250 first year engineers, imaginative and practical suggestions were made based on common sense and creative ideas, but, in many cases, without an appreciation of the underlying physical phenomena. In particular, over the course of a 50-minute tutorial, parallels between drying socks and concrete slabs were regularly drawn, including the physical effects of capillary suction, diffusion, evaporation, phase changes and latent heat capacity, temperature/humidity regimes, laminar flow, wind speed, surface to volume ratio and, ultimately, the shrinkage phenomenon itself which leads to concrete cracking worldwide. Two mind maps describing the indoor and outdoor factors which may be used to solve the sock-drying problem are combined with the correspondences between this and the concrete slab drying problem, leading to an engaging and motivating dialogue with the students. This learning exercise emphases the importance of a deeper understanding of the underlying science when solving many physical problems in engineering or in any other technological discipline.

KEY WORDS: Concrete cracking; Evaporation and diffusion; Drying rates.

1 INTRODUCTION

This paper is concerned with a case study involving a novel approach to teaching and learning during a tutorial in advance of covering all the associated theory in lectures [1]. In a staged approach, an early intervention during the teaching session makes the students more aware of and sensitive to their surroundings [2], thereby controlling their own learning through future duplication of the method in other topics and disciplines [3]. In essence, as shall be illustrated, despite the apparent simplicity of the problem presented, a complex real-world problem is used as a vehicle to promote student learning of concepts and principles [4].

When introducing students to any concept with which they may not yet be familiar, it is sometimes convenient to use an every-day analogy with which they are not only familiar but for which they have an intuition, albeit perhaps not fully grounded in the inherent scientific principles. The use of an analogy to explain subject-specific concepts is not exclusive to engineering alone. For example, consider two cars which have travelled the same distance, with their known corresponding fuel consumptions. Based on the car characteristics, they have achieved the same output (external 'load'), but with a different efficiency (internal 'load'). This analogy has been used in the discipline of sport science [5] to outline the concept of internal vs external training load, which demonstrates that in any group of athletes doing the same training session (ie, an external load), one might expect to observe a very different response between athletes (e.g. heart rate, an internal load). Substituting this sporting concept for a more familiar analogy allows students to garner an understanding outside of the discipline within which they are working.

In the teaching of engineering materials to first year engineering students, in the absence of early lectures on the topic of concrete technology, it can be difficult to have meaningful early technical discussions at tutorials on water/cement ratios, pore structures, moisture transport, shrinkage and shrinkage induced cracking [6]. However, most students will have a view on the options to dry out wet clothes quickly and which of these are most effective even though they may not be familiar with the nuances of the underlying sciences. In some cases, the methods may be based on misconceptions which would need to be dispelled.

This paper will describe one such tutorial exercise delivered to over 250 engineering students, where in the first day of the concrete section of the materials module, in smaller tutorial groups, students were posed with a problem to solve as a means of introducing principles which had wider applicability in tackling the problems associated with the drying out of freshly poured concrete slabs. The problem posed was as follows: "*The power in your house has been cut off while washing sports socks in a washing machine and they are saturated with water. You need to use them for a game later in the day. Use your knowledge of physical phenomena to dry the socks as quickly as possible".*

In splitting the students into groups of two or three and allowing them time to discuss firstly how this problem could be tackled indoors, then later on in the same session how it might be tackled outdoors, the students were invited to offer their practical solutions one by one, whereupon the lecturer would then explain the science behind the proposed solution and give an analogy as to how the same principle might be applied in concrete technology, recognising that concrete, for all its appearances, is a highly porous material which is saturated with water when manufactured, albeit it with a much longer timescale on its drying characteristics than socks. In the treatment of the student ideas in this paper, their offered suggestions will be listed first (shown in Figures 1 and 2 in yellow for indoor and outdoor effects, respectively and in *italics* in the text), then the explanation given to them on the underlying physical effect (shown in red in these figures and in **bold** in the text) will be described to support or refute their suggestion, then an analogous concrete example (shown in blue in these figures and underlined in the text) will be described where appropriate. The culmination at the end of each tutorial is a sound basis for the use of an industry-standard means of assessing the likelihood of plastic shrinkage cracking of slabs based on environmental physical phenomena, all of which have parallels in the drying of sports socks.

2 DRYING INDOORS

2.1 Physical measures

Before *laying socks out to dr*y in the environment, given they are saturated when taken out of the washing machine, there are some obvious physical actions which can remove the surplus water held in the coarse voids in the socks. At the end of these various physical processes the socks are still damp, but no longer saturated.

Squeezing: If *socks are held up*, gravity will cause some of the surplus water to **flow** out of the bottom of the sock, which might be considered to be governed by **D'Arcy's law**. But, as suggested by the students, this liquid flow process can be accelerated by *squeezing the sock*, leading to much faster water flow. In concrete analogy terms, the process of bleeding is when surplus water is squeezed to the surface by the settling of the heavier particles (see Figure 1).

Wrapping up: The suggestion of *wrapping the socks in a towel* or *kitchen roll* is one in which the absorbent properties of a **hydrophilic** material are exploited. This process is based on **capillary suction**, a phenomenon easily seen by touching the corner of a sugar cube onto the surface of coffee in a cup. This fact was elucidated on by noting the effectiveness of different fabrics, including competitive and optimized alternative kitchen rolls, is determined by **pour size**. For example, the height of rising damp in a concrete or stone ground floor wall, in the absence of a damp proof course (a water-proofing membrane), is determined by this physical feature. The case of using *newspaper as an absorbent material* stuffed into shoes to dry them had resonance with the students. In concrete terms the process of vacuum dewatering to remove bleed water and reduce the near-surface water to cement ratio is analogous in concept to this wrapping of socks process

Rotation: Most students have a sense of the radial thrust which exists on a playground roundabout and used this knowledge not to explain the workings of a standard tumble dryer (there was no electricity to run one in the problem), but the rather charming example was posited of using a "*salad tosser*" to use the **centrifugal force** to expunge any free water. The suggestion of *rotating the socks one at a time* was dismissed as an outdoor solution due to the need to avoid wet interior surfaces, although the example of using a *spinner to dry togs in a swimming pool* was a good one, albeit requiring electricity.

2.2 Environmental measures

Inevitably there was a suggestion of *laying out the socks to dry on a clothes horse*, but the causes of drying in this scenario needed careful explanation. Firstly, the definition of when some material is dry is one which is open to misunderstanding as dryness, per se, does not mean there is no moisture in the porous solid. It is best defined by the ideal state whereby the **moisture vapour contained within all the voids in the element are in equilibrium with moisture in the surrounding air**. If both are at the same temperature, this translates into the relative humidities being identical, noting that the **relative humidity** is the percentage of moisture in the air compared to when it is fully saturated (**the dew point**) at that temperature. It follows that for a given amount of moisture in the air in an enclosed volume, if the temperature increases the relative humidity falls because the capacity of the air to hold moisture increases with increasing temperature. Surprisingly, this means that if the relative humidity in the area, say the kitchen, is already almost 100%, then the socks are almost "dry" before the drying process even begins, although it will still feel damp to the user! With this in mind, as a new concept to some students, though understood by every mechanical or facade engineer, the following scenarios were posed by the students and were explained to and understood by them:

Exposed surface: The **volume to exposed surface ratio** is important for drying rates. *Thicker socks laid flat on a table will be slower to dry that thin socks* if they have the same void structure. In lay*ing out socks on a clothes horse* to dry, if they are spread over just one wire so that the halves hang right beside the other then a high humidity equilibrium is set up between the two layers and moisture loss is from the outer surfaces only. Therefore, *spreading the socks over at least two wires* will expose all external surface and speed up drying, The students also suggested *turning the socks inside out at some point* to further speed up the drying. This is not unlike the notion that to dry out a suspended concrete slab one should strip the shutters early to allow two-way drying, a luxury not afforded to slabs on grade which can only dry out in one direction and, therefore, are effectively twice as deep [7].

Temperature: Placing the socks in a warm room would be expected to dry them more quickly. Partly this is because there is a **greater capacity to hold more water in the air** (due to lower relative humidity, to be discussed below) but also because if the sock is warm, assisted perhaps by solar gains, it will have **more (heat) energy to allow it phase change** from water as a liquid into water as a vapour, and thus evaporate off

the surface. This energy term is known as the **latent heat of vapourisation** and is one of the reasons why cold socks dry less quickly and why building contractors turn on a hot-air blower to dry out a concrete floor slab more quickly prior to covering it [8]. Incidentally, as the moisture evaporates off the surface of the socks, there will be a **difference in the concentration of moisture vapour in the voids** within the socks and moisture will now **diffuse to the surface**, as it proceeds to dry out internally. This is very much like the much slower migration of moisture between voids in a concrete floor slab under a vapour concentration gradient, governed by **Fick's law**.

Humidity: Given the foregoing, it follows that the *lower the relative humidity in the room, the faster the drying will be* and so placing the socks in a room that already has a high relative humidity, such as in a poorly ventilated bathroom, will not assist in this matter. Thus, using **well ventilated spaces** will aid with drying, but surprisingly, this will only be the case if the relative humidity outside the house is lower than that inside – if it is a damp day outside (possibly with close to 100% humidity), ventilating the space may allow moisture ingress not egress. In the case of a contractor who is under pressure to lay a floor slab early, something that needs to be assessed carefully because early application can lead to covering delamination or buckling, the use of a dehumidifier can assist in reducing the relative humidity of pores close to the surface but will do little to dry out the pores deep in the concrete because the diffusion rate in concrete is so slow [8]. Such fast drying of floor slabs can also lead to shrinkage and, due to the restraints, subsequently either to overnight plastic shrinkage cracking of uncured surfaces or long term drying shrinkage cracking, both of which may need repair. This is not unlike drying socks, which also shrink, but in an unrestrained way, and so **socks (and other clothes) can feel tighter fitting when put on after drying**.

Finally, the students were informed that regularly drying clothes in this way in a house will raise the average relative humidity internally and may, in excess, promote mould growth in the longer term with its attendant adverse health implications.

3 DRYING OUTDOORS

3.1 Exposure

As was the case of drying socks indoors, *placing socks on a washing line, over several wires and turning them inside out* occasionally will **expose the maximum area** and promote faster drying. In the case of concrete slabs in the open environment, after a suitable period of curing, slabs on grade have one-way drying only and so are vulnerable to ground restraint, shrinkage movement and cracking and drying is inevitable in any given environment. Overnight plastic shrinkage cracking is avoided foremostly by curing.

3.2 Environmental measures

Many of the observations which came up in student discussions for the indoor scenario are equally applicable here:

Temperature: Whether due to *sunshine or high ambient temperature, a warm day is intuitively a good clothes drying day*, although as explained previously it does depend also on the relative humidity. In essence, in cold weather there is lower **thermal energy for evaporation** and **less capacity for the moisture to be retained in the air** due to higher relative humidity at low temperature, giving rise to slower drying. On hot days, the opposite is true, and the drying of the socks will be promoted for these two reasons, enhanced if the humidity is also low. For drying of concrete slabs, the same principles of surface evaporation and internal diffusion from within a porous material apply, although diffusion is at a very slow rate because of the closed nature of the pore structure in concrete. Also externally, the rate at which bleed water is evaporated, potentially causing overnight plastic shrinkage cracking, depends heavily on both the atmospheric and concrete temperatures, as explained above.

Humidity: With an understanding of what the term "dry" means, *the lower the environmental humidity, the faster the moisture evaporates off the surface of the sock* and, hence, the faster moisture diffuses to the surface, just like concrete slabs. However, as the relative humidity profile inside the sock (concrete) approaches the ambient, **the concentration gradient decreases and the drying slows down**. Indeed, as stated previously, if the environment is damp (in high humidity), such as immediately after fine rain, then **drying will be slow or even stop, even though the sock is still damp to touch**. For a concrete slab, over time, it will not only reach hygric equilibrium with the environment, but as the environment humidity fluctuates, which it does continuously, the concrete will swell and shrink slightly as it absorbs and evaporates moisture from the surrounding air.

Wind: The final important environmental element affecting drying is the *existence of wind and its speed*. While some students mentioned a *hairdryer* as an indoor solution (which was discarded as there was no electricity source in the problem poised), outdoors the drying principles are the same. Accepting now that **if the concentration gradient in humidity is greater, evaporation/drying occurs faster**, if there is no wind then very close to the surface there is a **laminar layer of gradually changing humidity** from high just inside the socks (when drying) to the ambient humidity a short distance away. If on the other hand a wind is blowing, then this laminar layer is removed by the wind and the two humidities exchange moisture over a very short distance, which happens more quickly due to the higher gradient. Thus, as is well known and as the students identified, *wind accelerates drying considerably*. It also significantly increases the risk of a concrete surface drying out soon after pouring and thus increases the risk of overnight cracking of a new slab, which is why proper curing is essential if wind is expected.

3.3 Concrete protection in practice

When a concrete slab is exposed to the environment immediately after a pour, it is essential to cover it by some means (water, plastic, curing membrane, etc) if the

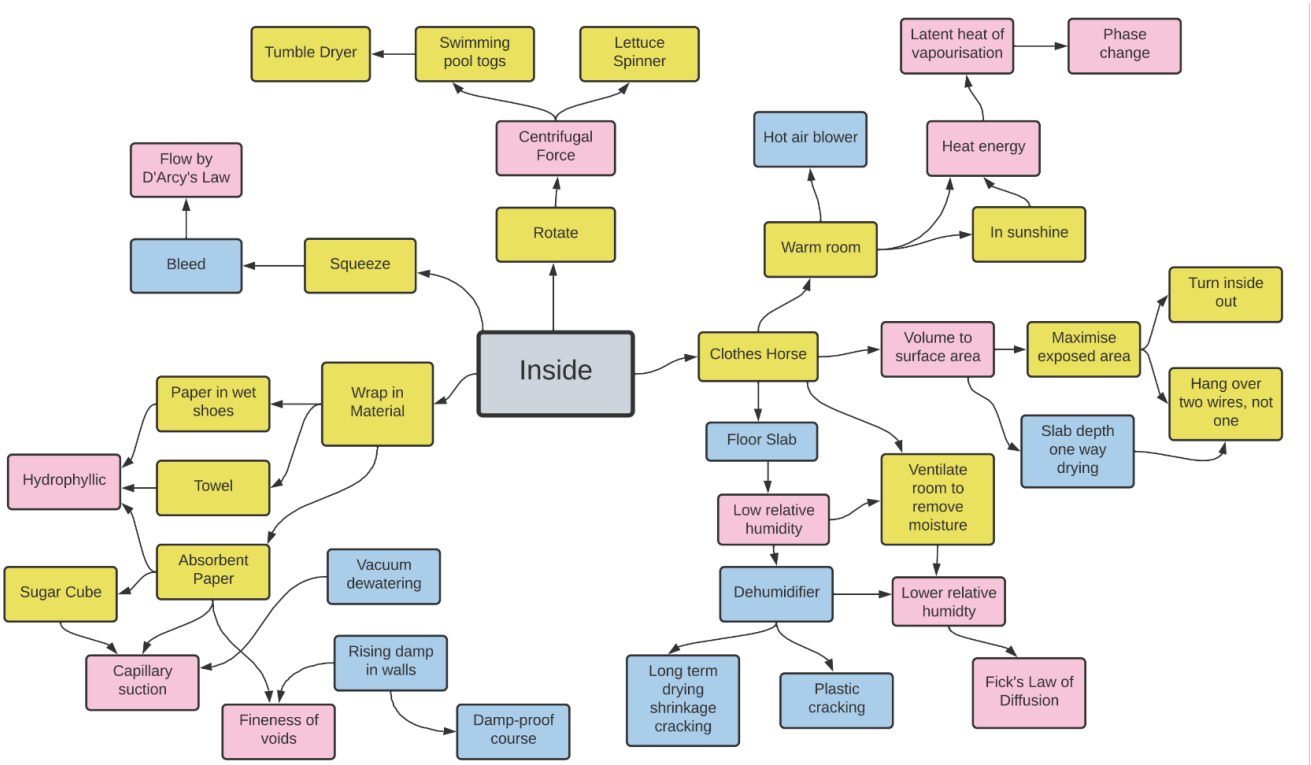

Figure 1. Mind map of indoor factors

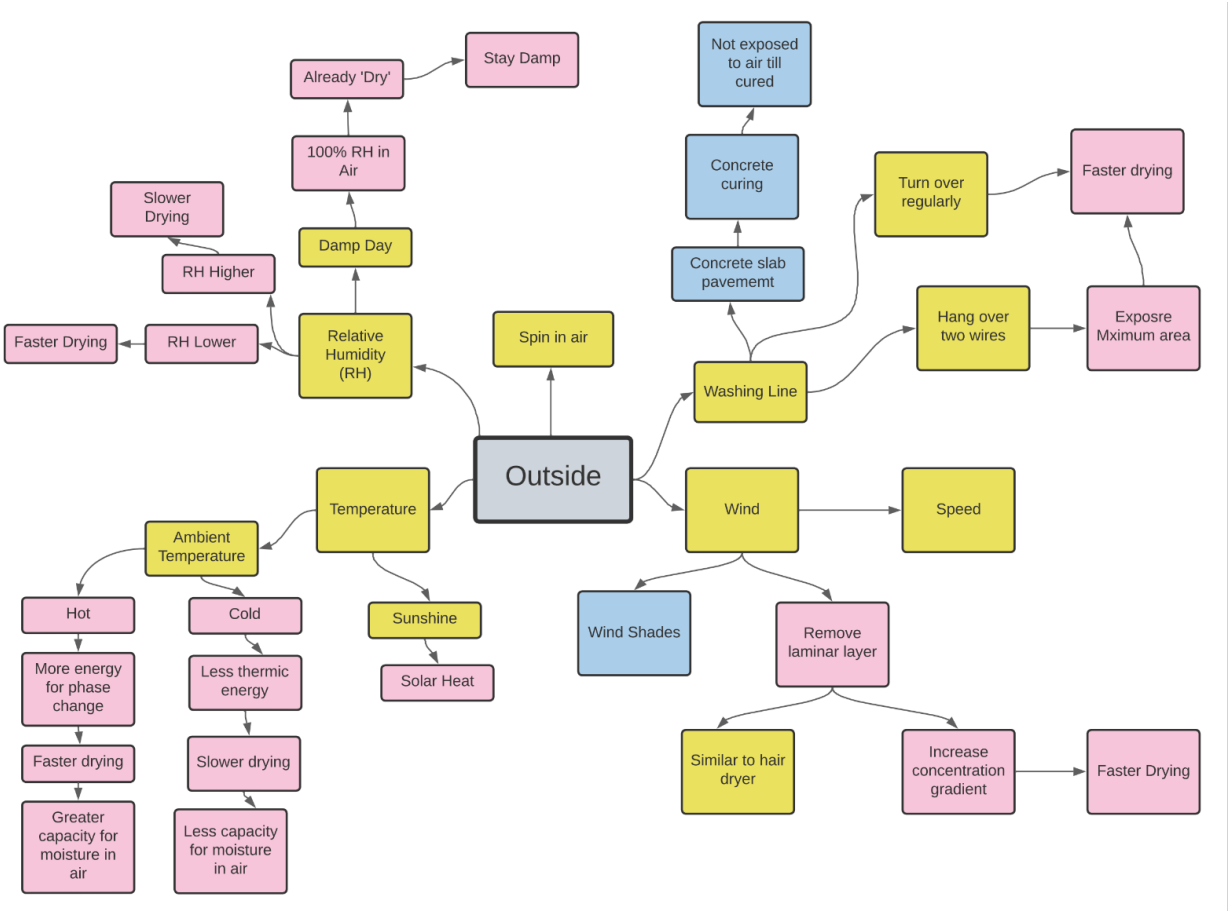

Figure 2. Mind map of outdoor factors

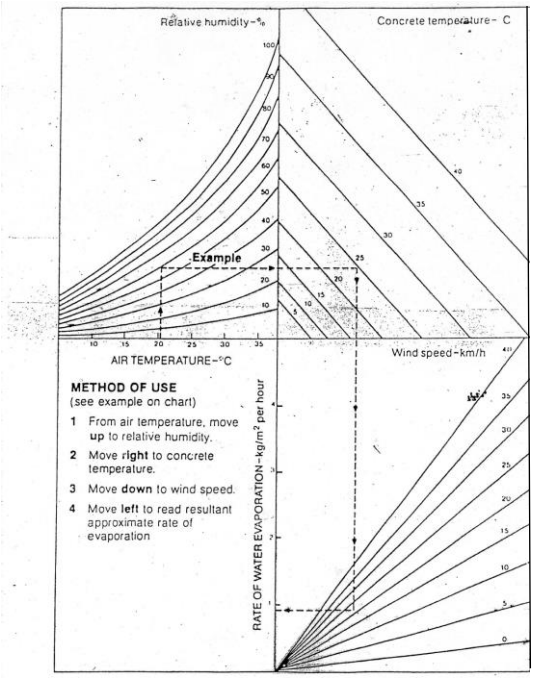

Figure 3. Effect of ambient drying conditions on the rates of evaporation of bleed water from a concrete surface [9].

Figure 4. Typical concrete footpath to avoid cracking caused by pavements drying out over time.

environmental conditions are adverse such that plastic shrinkage cracking is promoted. The ACI manual [9] has a useful nomograph in this regards (Figure 3), in which a quantitative evaluation of the relative importance of the air temperature and relative humidity, concrete temperature and wind speed can be made. A traditional rule of thumb exists that water evaporation rates of less than 1kg/m^3/hour are less likely to cause cracking, while above this, measures must be put in place to protect the concrete surface from drying. It also clearly explains to the students the concrete technology and environmental physics background as to why movement joints are necessary in pavements every 5 to 6m (Figure 4) to avoid long-term drying shrinkage cracking.

These two latter figures are presented to the students at the end of the tutorial, as described, so that they can observe how the simple concepts collaboratively developed during the tutorial can be used in earnest in practice to prevent the expensive and surprisingly frequent problem of plastic shrinkage cracking.

CONCLUSIONS

Through the use of a common every-day problem for which many people believe they have an instinctive, if sometimes misinformed, solution, it was possible to engage first year engineering students with the minimum of concrete technology knowledge in realising the key physical and environmental determinants in the drying out of socks and thus also drying out of concrete slabs and what the drying process involves in practice.

Over the course of a 50-minute tutorial, without delving into the minutiae of the various physical phenomena, the students realised that they need to base their understanding of the different solutions on sound physics appropriate to the relevant phenomena and they need to improve their awareness of the engineering characteristics of any such problem, not just relying on their instincts.

Student feedback after the session included their observations about how their perceptiveness of every-day events and how to approach a common but complex problem had been transformed by the experience.

This approach to learning is highly transferrable into other disciplines, of course, such as the example cited in sports science in which a familiar problem (car specification and performance) can be used as an illustrative analogy for a more involved and complex biological and anatomical phenomena (delivering human sports performance without injury).

REFERENCES

[1] Biggs, J. (1999) Teaching for quality learning at university. Buckingham, UK: SRHE and Open University Press.
[2] Healey M, Jenkins A. (2009). Developing undergraduate research and inquiry. York: Higher Education Academy.
[3] Pintrich, P. R. (2002) The role of metacognitive knowledge in learning, teaching, and assessing, theory into practice, 41:4, 219-225, DOI: 10.1207/s15430421tip4104_3.
[4] Moallem M, Hung W, Dabbagh N. (Eds.) (2019). The Wiley handbook of problem-based learning. Hoboken, NJ: John Wiley & Sons, Inc.
[5] McKay, C. and West, S., (2022), 'Stress, coping and the missing link in training load: Camel, meet straw', In: "*The mental impact of sports injury*", Ed. C. McKay, Routledge, Oxon, 45-60.
[6] West, R.P., Taylor, D., Burke, M. and Grimes, M., (20200, 'Teaching Engineering Materials through experiential learning' , *Civil Engineering Research in Ireland (CERI20)*, Cork, 412-417.
[7] West, R.P. and Holmes, N., (2005), 'Predicting moisture movement during the drying of concrete floors using finite elements', *Construction and Building Materials*, 19, 674-681.
[8] Holmes, N. and West, R.P., (2013), 'Enhanced accelerated drying of concrete floor slabs', *Magazine of Concrete Research*, 65, 19 (2013)
[9] ACI, (2015), *American Concrete Institute Manual of Concrete Practice*, pp 172.

Delivering materials laboratory sessions to large classes during the COVID-19 pandemic

Roger P. West, Declan O'Loughlin, Amir Pakdel, Michael Grimes and Shane Hunt
School of Engineering, Trinity College, University of Dublin, Dublin 2, Ireland
email: rwest@tcd.ie, d.oloughlin@tcd.ie, pakela@tcd.ie, michael.grimes@tcd.ie, huntsf@tcd.ie

ABSTRACT: Traditional modules on engineering materials usually have accompanying laboratory exercises of some sort, often involving many students working in groups, overseen by demonstrators and technical staff. During the pandemic, academic staff were encouraged to continue with laboratory sessions while lectures were moved on-line. This paper describes how a 10 ECTS Engineering Materials module was adapted to give more than 250 first year engineering students weekly exposure to a materials project which was closely aligned with the lecture material. The overall objective was to examine the feasibility of a sustainable bamboo reinforced concrete beam in three phases, in mechanical, electrical and civil departments, involving bamboo mechanical property evaluation, the construction of a temperature sensor and logger and the flexural response of a bamboo concrete beam in flexure when cured under different temperature regimes. The first component involved inventive home testing of provided bamboo culms, the second working on prototype sensors in 54 small groups over several weeks in a laboratory. The third involved 10 minute waves of small bubbles of individual groups following multiple tasks demonstrated in pre-prepared videos at 12 concrete testing stations over a 12 hour period each week, observed and marked by socially distanced demonstrators. The team dynamics changed completely from previous years, where interdependencies, acting on constructive peer feedback for the benefit of the group, sharing draft report documents and introducing new project management skills were all in evidence. This was achieved while simultaneously successfully observing the bond or tensile failures of the recycled aggregate GGBS under-reinforced bamboo beams in flexure, depending strongly on the (monitored) thermal curing regime.

KEY WORDS: Concrete; Bamboo; Materials; Teaching; COVID-19 Pandemic.

1 INTRODUCTION

As part of the offered curriculum in first year engineering at Trinity College, a 10 ECTS module (1E12 Engineering Materials and their Applications) gives an opportunity for synergy between an applications-based lecture/tutorial series on engineering materials and a related problem-based project which is undertaken by students in groups [1]. The module content and organisation before the pandemic has been previously described [2], whereby the lecture topics cover the fundamental mechanical, thermal and electrical properties of a variety of engineering materials used. In this context, facilitating student inquiry and independent thinking, using lecture material associated with a problem based-project is an effective way of learning, leading to a deeper understanding of not just learning outcomes but life-skills, as shall be seen [3, 4].

The lectures were complemented by a parallel series of weekly laboratories in which bamboo, as a renewable material, was examined to establish its key properties, and then its utilisation in a sustainable bamboo reinforced concrete beam in flexure was explored. In particular, by design, two different failure modes in flexure emerged, prompted by the degree of thermal curing to which the beam had been exposed: For weaker cement pastes cured at a lower temperature, the failure was by debonding and anchorage failure of the bamboo, while at a higher curing temperature the matrix strength was sufficiently strong to bond well to the bamboo, thereby causing tensile snapping failure of the bamboo instead. The beams were designed to be under-reinforced, which was confirmed by the failure mode and by checking that the concrete compression was below the cube strength when the bamboo snapped.

To fully monitor this behaviour, the student groups, of which there were 54, with a cohort of more than 250 students, each manufactured their own temperature sensors and logging devices using Arduino and then made and tested their own plain and reinforced concrete beams, each receiving their own data on temperature and load-deflection values over time for subsequent analysis.

However, the rapid arrival of the Covid-19 pandemic caused the cancellation of most engineering laboratories country-wide, which in Trinity College resulted in there being no laboratories in computing, physics, chemistry and engineering science in 2020. However, in the case of the engineering materials module, a scheme was devised by the three lecturers involved to enable the weekly laboratory programmes to proceed safely and this paper describes how this was achieved and the consequences thereof on the learning experience. In particular, there was a significant shift to student-driven solutions to the problems posed, either individually or within groups. It shall be shown how team work, team dynamics and collective responsibility played an enhanced part in improved delivery of the module learning objectives.

It should be kept in mind that the engineering students who experienced this module were in their first term at college, with a very limited knowledge of engineering materials, which makes their achievements all the more remarkable.

2 THE ENGINEERING MATERIALS MODULE

2.1 Overview

The semester was split into three parts, where lectures and project work were run by a lecturer from Mechanical Engineering for the first three weeks, Electronic Engineering for three weeks and Civil Engineering for five weeks.

The weekly staff contact hours breakdown is shown in Table 1 in which it can be observed that, while the number of weeks of contact are low per student (6 hours in fact) , the staff contact hours are potentially high (19 hours). The extensive use of postgraduate demonstrators for the laboratory and tutorial sessions is normally essential and was extended in this programme, noting that lecturers attended the laboratory session in full also, as appropriate.

Table 1. Module timetabled hours per week.

Session	Hours
Lecture	3
Lab. brief	1
Tutorial	3
Laboratory	Up to12

2.2 Laboratory overview

2.3.1 Mechanical component

To commence the laboratory testing in week 1 of the semester, the students were given a free choice of how to establish the bending strength and stiffness of the bamboo type (Moso) being used in the mechanical and civil components. For Covid 19 reasons, two samples bamboo culms were given to every student to take home and to inventively use any implements found in the home to undertake the given tasks. These could include buckets, kitchen weighing scales, water or books as measured loads, builder or measuring tape to measure deflections, etc. Each student wrote their own report explaining how the objectives were met and citing the properties they measured and the bamboo's failure mode in flexure. These simple exercises tied in well with the parallel lectures on strength, stress-strain behaviour and how to establish Young's modulus of elasticity of different materials.

2.3.2 Electronic component

The Electronic laboratories featured the design, manufacture and testing of a data-logging temperature sensor, suitable for monitoring the thermal curing of concrete mixed in the Civil component, described in the following section.

Due to social distancing and ventilation requirements, each student attended the laboratory for 45 minutes a week across nine sessions, in hour-long blocks over two days. Although working in groups, students were distanced from each other in accordance with the College guidelines at the time. To maximise the student achievement during the restricted contact time, the work was demonstrated during the supporting laboratory briefings and though pre-recorded videos demonstrating key skills such as soldering, health and safety requirements and sample testing procedures.

The overall design work was achieved over four sessions as follows:

- an introductory session including open-ended instruction and tasks for programming a microcontroller, sampling from an analogue-to-digital converter (ADC) at regular and configurable intervals and reading from a commercial temperature sensor (LM35, Texas Instruments, Dallas, TX, USA);
- practical electronic skills in soldering, laboratory equipment use, such as multimeters and sealing and testing of the soldered designs;
- design and assembly of a combined sensor consisting of a current source (LM334, Texas Instruments) driving a five-diode chain and circuitry to monitor the voltage across the diode chain using a microcontroller;
- testing and characterisation of the combined sensor with reference to the commercial temperature sensor and recording of the values to an SD card using the microcontroller to enable data logging.

Supporting laboratory briefings covered basic characterisation and data analysis techniques, such as elementary line fitting and error analysis. Students were encouraged to research and apply more advanced model fitting and error analysis techniques as appropriate. Lecture material supported the student experience in the laboratories, including theoretical concepts, such as the response of materials to electric and magnetic fields, the electronic structure of solids and semiconductors, doping of semiconductor materials and p-n junctions.

Groups were responsible for preparing a group report of approximately ten pages in length which had to be professionally typeset, including all graphics, schematics, calculations and results. Additionally, each student was responsible for preparing a short individual personal reflection on the project work. Each group member received the same mark except for isolated examples where a group member did not engage at all. Reports were assessed on quality in terms of the description of the aims of the overall project, the methods, results and the overall conclusions in the context of the module as a whole.

2.3.3 Civil component

The Civil laboratories had the aim of testing composite bamboo reinforced concrete beams in flexure, while also undertaking a series of other international standardised tests including fresh and hardened density, workability, compressive concrete cube strength and tensile strength from beams. This culminated in observing how a group's recycled aggregate bamboo reinforced beam with 50% slag cement behaves under flexure. It was a different experience to the free-form bamboo testing undertaken in the first few weeks as here following strictly the international test standards was emphasised and assessed.

Week by week, these tests included:

- Week 1: Mixing concrete, sampling, slump and fresh concrete density testing, making a cube
- Week 2: Hardened concrete density, testing a cube, including recording load deflection data, making a plain concrete beam
- Week 3: Flexural testing of that beam, making the bamboo reinforced beam and a cube with the novel mix

- Week 4: Cube testing, beam density testing and flexural testing of the reinforced beam

Due to the pandemic, the normal delivery method of a demonstrator instructing a large cohort (circa 30 students at a time), who then proceed to undertake the same test in groups, had to be abandoned due to the restrictions on social distancing, of 1.5m, in place at the time. Therefore, for the 12 test stations planned for the students over the four weeks of laboratory contact in Civil Engineering, a series of eight individual test methods were identified and the responsible Technician produced a video of each, published on YouTube, which were accessible to the students in advance using a QR code.

To avoid unnecessary contact, student groups became their local bubble whereby during the laboratory, no group would come into contact with any other group. Student groups would arrive at 10 minute intervals (Figure 1) and all necessary PPE was given out to protect the students from laboratory and Covid19 hazards. A one-way system using the building's fire escape was put in place so no groups had to cross-over in any spaces as they moved from station to station around the building.

After induction, they moved on from station to station every ten minutes until their session was finished. In detail, student groups were assembled separately outside the building by a staff member and individually-owned masks were worn mandatorily throughout the time in the building. The first (induction) station each day involved electronic contactless signing in, hand sanitisation, glove distribution and a reminder of the sessions planned for that day for each individual of the group and for each group as they arrived in turn throughout the day.

Having collected their own concrete samples pre-mixed for them, at the stations the demonstrators were deployed to observe and mark the students on how well they performed the allocated task at each station, based on the student's viewing and understanding of the video procedure as watched in advance. Groups nominated their own project manager who ensured every group member had been allocated their tasks within the group – namely technical responsibility for conducting and writing up one of: density, slump, cube and beam tests.

Only one member of the group needed to perform the specific task at each station, one of three on that day. However, other group members, socially distanced, were allowed to interject to correct any student colleague who was not conducting the test properly. In this way every team members was engaged all the time (as they too stood to lose marks for an improper procedure executed by an exhibiting colleague).

The key outcome of the technical aspects was to observe how a normal strength under-reinforced concrete beam with

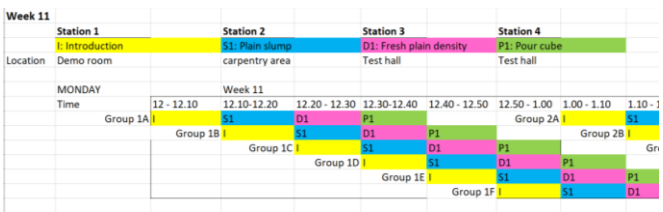

Figure 1. Partial typical Civil concrete laboratory timetable.

renewable bamboo as reinforcement fails by snapping of the bamboo in tension (Figure 2). On the other hand, a low strength cement matrix (low by virtue of testing at 7-days, the presence of slower reacting 50% slab cement cured at a given temperature and naturally weaker 100% recycled aggregates) would promote a premature bond failure of the cement matrix with the bamboo, as evidenced by the bamboo slipping into the beam at its ends (Figure 3). Which mode of failure would pertain was not known to the students in advance which added to the sense of anticipation. Which failure mode occurred largely depended on the curing regime - the higher curing temperature matured the cement hydration and caused tensile failure while the lower curing temperature promoted a weak matrix and debonding of the cement paste and bamboo. These quite subtle influences of the main parameters would normally be difficult to convey in the lecture theatre but were quickly assimilated and reported on by the majority of the students.

This laboratory regime was supported by the lecture programme, which included concrete fresh and hardened properties, especially vulnerability to shrinkage, creep and thermal movement, its weakness in tension and the benefits of an under-reinforced concrete-steel composite.

Each member of each group had their own task and the group report submitted at the end of the term was assembled by the project manager and proof-read by all members of the group. They had all been briefed in every topic and stood to lose out if errors by a weaker team group member were not identified by the rest of the group prior to submission.

Every 10 minutes, on prompting between demonstrators by walky-talky, each group moved on to the next station, circulating around the building. Furthermore, by virtue of every student wearing gloves and all equipment being washed down by demonstrators between groups, the risk of passing on a Covid-19 infection was minimised.

Figure 2. Bamboo tensile failure during flexural test.

Figure 3. Bamboo bond failure during flexural test.

In the four weeks of the Civil laboratories, with a throughput of over 250 students every week, only one case of Covid-19 was reported (in week 3) and that student's group was isolated for the remaining week although none of his colleagues contacted the virus.

3 STUDENT TEAMWORK

3.1 During the Civil laboratory sessions

Normally laboratory exercises would be demonstrated first, then multiple groups would test their own specimens using duplicate equipment. Due to the Covid-19 restrictions, no large group demonstrations were possible so, as previously described, the key tests were recorded on video and posted up for the students to watch alone and in advance of attending the sessions. In review, this appeared to have been preferred by the students because they could learn in their own time, replay the instructions and did not suffer from being disinterested at the back of a large group when demonstration occurred, as can occasionally be the case.

When a single group arrived at a station with their own concrete to undertake a test to an international standard, a single member of the group would perform the test in front of the others in his/her group, who observed the test, suitably socially distanced. However, the students were surprisingly engaged in every test because the system for marking ensured each group was allocated ten marks at the start of each test and the student undertaking the test could lose marks either by making a mistake in the procedure, or by being forced to ask a question of the demonstrator whose primary role was to observe and mark. This latter would arise if nobody in the group knew what to do next, or, if the former arose, then any member of the group could interject with advice to the exhibitor to stop them making a mistake and losing the team some marks. In this way, if an exhibitor performed poorly, the group members as much as the student exhibiting were to blame. The demonstrator gave immediate feedback, telling each group their allocated mark as they left for the next station, explaining why they lost their marks. Only the Project Manager (PM)of the group could challenge the apportionment of marks.

The sense of being in a team together, helping each other to maximise their collective marks was evident. Every student PM was asked to reflect on their experience of the team dynamics in their portion of the group report.

3.2 During the Civil report writing

In a similar vein, the appointed PM would issue a Word template to all the group so they could type up their own individual parts using the one format. Thus, when each student submitted their own section of the report to the PM for compilation, which they generally only had seven days to complete, there was some uniformity to the report presentation, which made it appear more professional and easier to edit. The front cover of the group report was individually designed by the PM as part of his/her responsibilities which gave rise to some interesting creations.

More importantly, if there was a member in the group who was less skilled at report writing, then when the PM circulated the compiled draft report to all group members, everybody read each other's work and this opened up individuals to accept and respond to positive feedback from their peers. Furthermore, it became clear to the group members that if the group did not receive a high mark for their report, then this was as much the fault of every group member for not proofing and correcting the draft as it was the fault of the student who wrote the errant section. This included critical observations on data plotting and beam and bamboo tensile capacity calculations.

In this way, the students learnt quickly the benefit of collective and individual effort and the responsibilities inherent in being part of a team with members with disparate skills and abilities. This was particularly the case as all members of the group were guaranteed to be given the same mark, provided the attendance criterion (minimum 75%) was met.

However, in one exceptional case, two members of a group complained that three others were not carrying their weight in the delegated work and this has also been observed to be the case for this group in the earlier phases of the project. The solution to this, in the third phase in Civil engineering, was to inform the group members that every section of the report would be assessed separately and if one section, provided by any one of the five students, was seen to be abnormally weak, then that student would receive their own mark for this phase while the average of the remaining parts of the report written by his/her colleagues would be given to the other four group members. After this system was put in place, and had been accepted by all the students involved, all individual section marks turned out to be reasonable and, thus, every member of the group received the same mark. In this way, the weaker student had to respond, while the complainants believed their mark to be enhanced by virtue of all members of the team performing better.

The collective team effort within groups, led by the PM, ensured that not only were significant lessons learnt about how to conduct internationally recognized concrete tests, but also the benefits and drawbacks of working in teams with disparate individuals were gleaned.

4 CONCLUSIONS

While the laboratory sessions as part of the materials module were well established and integrated with the lecture content and learning outcomes from previous years, the sudden imposition of restrictions due to the onset of the pandemic made it much more challenging to continue with laboratories for very large numbers of first year engineering students. Nonetheless, a scheme was devised for weekly laboratory sessions, as described herein, which complied with the Covid restrictions in full.

In Civil engineering in particular, this was achieved by ensuring the selected student groups worked in pods, which visited test stations one at a time in sequence without crossover. With prior viewing of the test method on purpose-made videos, a group dynamic developed to attempt to maximise their marks both for the tests themselves and also for their collective group report. While the marks awarded for their reports appeared to be high (an average of 73%, which is not unusually high for project-based laboratory work) compared to the previous year [1], two year's data is not sufficient to comment on this further. However, it is noteworthy that when the pandemic restrictions were lifted in the 21/22 academic year, this same model for

delivery of the engineering materials module was chosen to be used by the staff involved and the students were similarly enthused and engaged.

Important lessons on teamwork, responsibility, interdependence and comraderie were learnt by the students, as evidenced in their reflective comments in the project reports. In addition to the fundamental technical themes on bond and tension/compression in beams and failure modes of under-reinforced bamboo reinforced beams, the overarching theme of sustainability immediately caught the student's attention. The prospect of uniquely combining recycled concrete as aggregate, GGBS as a low carbon cement and bamboo reinforcing as a net carbon absorber in their concrete beam projects piqued their interest and featured heavily in the reflective section of their project reports. In all, the feedback from the fledgling student cohort was that this was an enriching, motivating and fun way to learn about sustainability, data gathering, material behaviour, report writing and teamwork.

REFERENCES

[1] Moallem M, Hung W, Dabbagh N. (Eds.) (2019). *The Wiley handbook of problem-based learning.* Hoboken, NJ: John Wiley & Sons, Inc.

[2] West, R., Taylor, D., Burke, M., Grimes, M. and Hunt, S. (2020). 'Teaching engineering materials through experiential learning', *Proc of CERI & ITRN 2020*, Cork, 412-417.

[3] Healey M, Jenkins A. (2009). *Developing undergraduate research and inquiry.* York: Higher Education Academy.

[4] Banta, T.W., Jones, E.A. and Black, K.E., (2009), *Designing Effective Assessment: Principles and Profiles of Good Practice,* John Wiley & Sons, San Francisco.

New Frontiers

Investigating the accuracy and reliability of UAV photogrammetry on railway infrastructure

Aimee McCabe, Dr. Daniel McPolin, Dr. Sreejith Nanukuttan
School of Natural and Built Environment, Queens University Belfast, David Keir Building, Stranmillis Road, BT95AG
email: amccabe19@qub.ac.uk, d.mcpolin@qub.ac.uk, s.nanukuttan@qub.ac.uk

[1]ABSTRACT: 3D scanning systems have become more commonly used for geometrical data capture, especially with the increased uptake of new technologies within the industry, coupled with the advances in computer systems. 3D scanning is a wide, encompassing term that relates to the non-contact, non-destructive process of digitally capturing the shape and form of physical elements. Within the industry, this is most commonly carried out using a laser scanner, which uses a line of laser light to scan an element and return a set of points, or coordinates. However, with advances in technology and consumer drones, UAV photogrammetry is quickly becoming more popular. Photogrammetry can be defined as the use of photography to obtain measurements between objects to define points in space. When combined with drones, this technique allows rapid, inexpensive scanning of the built environment. Critical to the use of photogrammetry is the establishment of accuracy and reliability. As laser scanners are generally accepted as being accurate for this work it is necessary to compare the two technologies to establish how accurate UAV photogrammetry is and if it can be used as a suitable tool for 3D data capture.
For this project, drone technology has been used to photograph railway infrastructure to provide a basis for comparison to other survey methods and to test the technology on a varied landscape. The accuracy of models was evaluated by determining measurements within the scene and comparing these results to measurements obtained from a laser scan survey. Results shows a minimum difference in measurements of 0.33mm and a maximum average of 37.5mm.

KEY WORDS: CERI/ITRN 2022; UAV; Photogrammetry; 3D Data; Infrastructure; Laser Scanning; Built Environment; Drone; Structures

1 INTRODUCTION

In the developed world it is generally regarded that 50% of our wealth is contained within the built environment. As such there is a requirement for the management and monitoring of our critical infrastructure. Methods of structural health monitoring come in many forms, from installed sensors to surveys (by various means) over a period of time. All commonly used methods are expensive and time consuming such that they are deployed sparingly and the majority of our infrastructure is in an unknown state of repair. This was tragically demonstrated by the Genoa bridge collapse in Italy in 2018 and less dramatically, the closure of the Forth Road bridge in Scotland in 2015.

3D scanning systems have been employed more readily in recent years, due to their accessibility and ease of use as well as their assumed high level of accuracy. However they can also be expensive and time consuming to use. This research aims to investigate the various methods of 3D scanning currently available on the market and quantify the accuracy, focusing on laser scanning and UAV photogrammetry used for site surveys and large object modelling. As new technology becomes available it is necessary to ensure that it is an adequate tool for the job and can perform to high accuracy standards as needed in the construction industry.

2 3D SCANNING TECHNIQUES

2.1 Lidar

Lidar is an acronym for light detecting and ranging and can also be known as laser scanning. It is a remote scanning technique in which beams of light or lasers are shone from the scanner onto an object. The time taken for the laser beam to be reflected back from the object is measured and from this, the distance from scanner to object can be calculated. Scanners can shine hundreds of thousands of laser pulses a second and each of these returned pulses can be processed into a 3D point cloud. [1] These point clouds are made up of millions of single points, each with a designated coordinate. When viewed together, they represent a 3D replica of the captured object. Laser scanning is generally accepted as being very dimensionally accurate, with some machines able to accurately measure to 3mm at 50m[2]

2.2 Photogrammetry

Photogrammetry is a method of obtaining 3D about physical objects and environments through the means of a 2D medium, e.g., photographs. The core idea behind photogrammetry is triangulation, where in a line of sight can be calculated from the camera using 2 or more images of the same object or environment point. These lines of sight are then intersected to produce a three-dimensional coordinate of the point of interest [3]. Triangulation is also the principle behind another surveying method, theodolites. Theodolites have been used for hundreds

of years and although they are a trusted method of surveying, they can only measure one point at a time (single point triangulation) whereas photogrammetry can measure multiple (multiple point triangulation).Figure 1 below shows how single point and multiple point triangulation works, using images from 2 different locations. As can be seen, photogrammetry allows for numerous points to be triangulated at once, allowing for a more expansive environment to be scanned in a single pass. Combining this technique with UAVs expands the range of objects and environments that can be captured in 3D in a short time period.

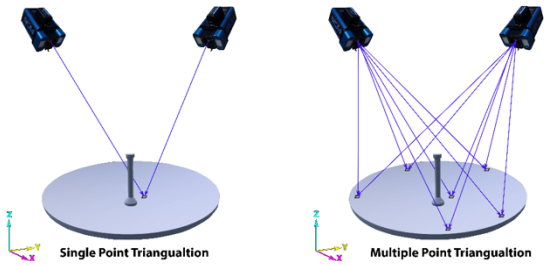

Figure 1. Single and Multiple Point Triangulation Diagram[4]

Using multiple images from multiple locations ensures complete coverage of the object and produces a more accurate XYZ coordinate and complete 360 movement around the object provides the ability to create a full 3D model.

2.3 UAV Photogrammetry

Combining the technique of photogrammetry with aerial based cameras allows for a larger range of movement around an object, especially on constructions sites where the objects may be large bridges or buildings. This is relevant particularly in inaccessible areas such as structures at heights, the underside of bridges or where there would be a danger to the survey team. By creating photogrammetry models, it provides both a record of the 2D images of the site but also a 3D model partner, which can enhance the BIM (Building Information Modelling) process [5]. The speed of model creation and the ability to survey large areas in a short space of time opens up new opportunities for monitoring our infrastructure and provides improved asset management by monitoring over time. Through the uptake of small consumer drones or UAVs, photogrammetry is quickly becoming a readily available tool within the construction industry for site surveys, recording of historical data and for the quick creation of a 3D model. With BIM being used across the vast majority of all construction projects, a photogrammetry model removes the need for an original 3D model to be built from scratch. A photogrammetry model can be used as the base for a new construction model, as a record of construction and for asset management facilitation.

3 METHOD

This study considers two methods of 3D scanning rail infrastructure sites which are currently in the process of, or are ear marked for, remedial work. The 3D scanning methods in question will be a laser scanner and UAV photogrammetry. The study will analyse the differences in each scanning method including time taken and speed of processing as well as comparing the accuracy of the UAV photogrammetry recorded data against the laser scan data. The accuracy of the laser scanner will not be investigated as their accuracy specifications are set by the parent company and they are generally regarded as highly accurate within the industry. This will allow for a conclusion to be drawn on the accuracy of UAV photogrammetry and their ability to be used as a survey tool within the industry.

10 railway infrastructure sites were identified by Translink, the railway network provider in Northern Ireland. These sites were specifically railway bridges, which would be suitable for the project. The sites were chosen based on their current work stage and applicability to the project. At each site a UAV will be used to capture images of the bridge from both sides and these images will be processed into a 3D model. A laser scanner will also be used at the same sites so that both methods can be compared to each other across a number of variables and to test how accurate the created models are. The laser scanning and initial post processing of the collected data will be carried out by an independent consultant who is an expert in their field. This is to ensure the highest accuracy of the captured data and best use of the equipment. The UAV photogrammetry and all further processing will be carried out by the researcher.

3.1 Test Programme

Approximately 6 rail infrastructure sites were identified based on the plan for their future remedial work, their current dataset, if any, and the suitability for the project. This list includes railway bridges of single and multiple spans, various construction materials and in populated and rural locations. The details of these bridges can be seen in Table 1. All sites were surveyed using two different 3D scanning techniques; UAV photogrammetry and laser scanning, and the 3D models created from each method were compared. The models were compared across several factors including accuracy, time taken and interoperability. All 3D datasets were processed the same way, to ensure reliability and repeatability of the investigation.

Table 1 - Selected Bridge Information

Bridge Name	Form	Material	No of Spans	Approx. Height
Auld's Bridge	Segmental Arch	Concrete	1	4m
Newry Canal	Deck and Girder	Steel	1	6m
Valentine's Glen	Semi-Circular Arch	Masonry	2	12m
Three Mile Water	Segmental Arch	Concrete	7	14m
Braid Water	Segmental Arch	Masonry	4	6m
Craigmore Viaduct	Arch	Masonry	18	Varies.

3.2 Data Collection Methodology

At all sites, a take-off and landing zone was identified on each side of the bridge, to allow for flights to be conducted on either side of the railway line. This area was identified using

local maps and will be shown on the flight information plan. Once on site, the UAV (A Phantom 4 Pro) was set up and on initial take off, the UAV moved to the highest appropriate level to begin the survey. The UAV will take photos at the highest heigh level first, positioned close to the bridge (between 10m and 15m to the face) and moving from left to right in a horizontal path. The UAV will stop approximately every 1m to take a photograph. Once this flight line is complete, the height will be reduced, and the flight will continue in a horizontal path in the opposite direction. This path is followed until the UAV is below the arch of the bridge and it can no longer be seen in the camera viewfinder. At this stage, the UAV will focus on the pillars of the bridge, using the same horizontal flight method as before. Each pillar will be surveying individually. Once complete, the UAV will return to high level and will be positioned further from the bridge (approximately 20-30m) and will use the same survey method as before. This is to ensure that the bridge is captured in as much detail as possible, both up close and further away within context of its surrounding environment. Any distinct features on the bridge such as date plates and carvings will be specifically photographed by the UAV once the overall flight has been completed. Depending on the size of the site, it is envisaged that each flight will return a minimum of 100 photos with this volume increasing as the size of the site increases.

The Lidar scans were carried out by an external professional with a high level of experience in carrying out surveys. At each site, it was estimated to have a minimum of 5 set up positions for the scanner. This would depend on the size of the site as well at the limitations of access and ideally each position would be 10m. The scanner used was a FARO Focus S 150 Laser Scanner which has a range of 0.6 – 100m and a 3D point accuracy of 2mm over 10m and 3.5mm over 25m. The scanner is secured to a level tripod and placed in a chosen position on site. The scanner will then rotate 360 on its base while scanning the environment. For this project, it will be assumed that the laser scanner is 100% accurate, in order to compare the photogrammetry measurements.

3.3 Model Creation

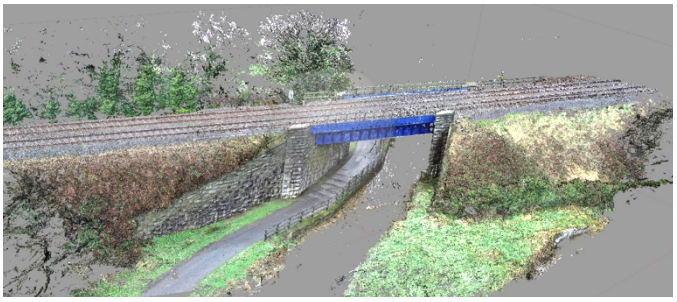

Figure 2. Newry Canal Dense Point Cloud – Photogrammetry Model

Photogrammetry modelling took place within Agisoft Metashape with all photos being uploaded and aligned on medium quality setting and a dense point cloud created, also on medium setting. This ensured that the quality was high enough without having to spend a significant portion of time modelling. At this stage, the point cloud gives a rough idea of how the model will look when fully complete. Figure 2 above shows the dense cloud for this the Newry Canal bridge and as can be seen, there are clearly defined features visible, such as the blue of the bridge and the steep embankments.

Once the dense cloud was complete, a surface mesh was then created. This mesh is created from small triangles and connects the points to each other, while following the geometry of the physical environment. It is likened to putting a blanket over a shape, while the shape can be seen it is not an exact replica. This mesh can be refined and accuracy enhanced by reducing the size of the triangle and maximising the amount of triangles within the mesh itself. This finer mesh allows for greater detail to be captured and modelled. This mesh acts as the surface of the model, and when complete, provides a clear reconstructed image of the photogrammetry model.

The lidar point cloud was created by the external professional who undertook the survey. The scans were initially registered and indexed using the FARO Scene software and then processed using Autodesk ReCap. This allowed for the point cloud to be built and viewed and at this stage, the file was passed to the researcher. Figure 3 below shows the dense point cloud resulting for the laser scan of Newry Canal.

Both models were viewed with Autodesk ReCap for the purpose of taking measurements along selected lines and comparing the resulting values.

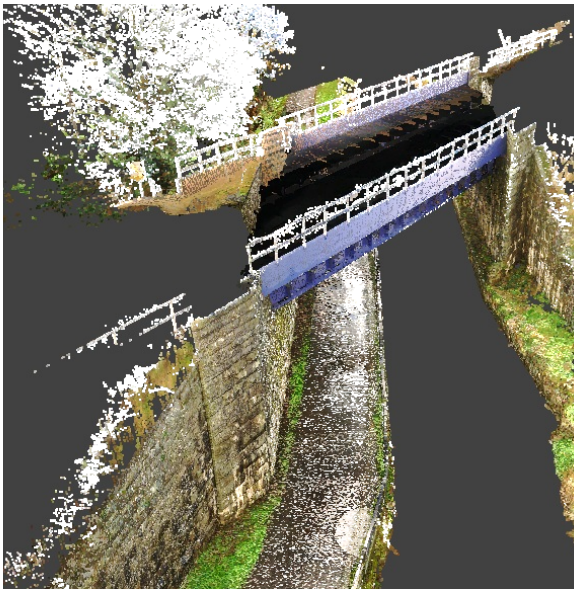

Figure 3. Newry Canal Dense Point Cloud - Lidar Model

4 RESULTS

For the purpose of this writing, the results of only two case studies will be looked at.

Within each case study, comparisons will be made between the two models where the accuracy of the photogrammetry model will be compared to the Lidar model. When taking dimensional readings from the scans, 3 measurements were taken at each location and averaged. This ensures a more accurate reading as

human error can allow for slight differences in measurements, due to the selection of different points within the point cloud. This is common practice when working with point clouds, especially those with a large volume of points.[6] Measurements were taken at 8 locations within each scan and each location chosen was a permanent feature of the site, e.g. Width of the bridge deck, Height of archway. This ensured that measurements could be taken again in the future, if necessary, at the exact same location. It will be noted if the accuracy of each measurement is over the pre-designated acceptable tolerances which are 25mm for a high accuracy topographic survey or 50mm for standard topographic surveys, as set out by The RICS[7]. In order to establish this, it is assumed that the Lidar scans are 100% accurate, which allows for the photogrammetry model to be compared effectively.

4.1 Newry Canal

Newry Canal is a steel deck and girder bridge which spans a pedestrian footpath and small river. The UAV flight took 248 photos over 27 minutes while the Lidar scanner set up at 8 stations and took 90 minutes to complete the survey. Both models took approximately 2.5 hours to build.

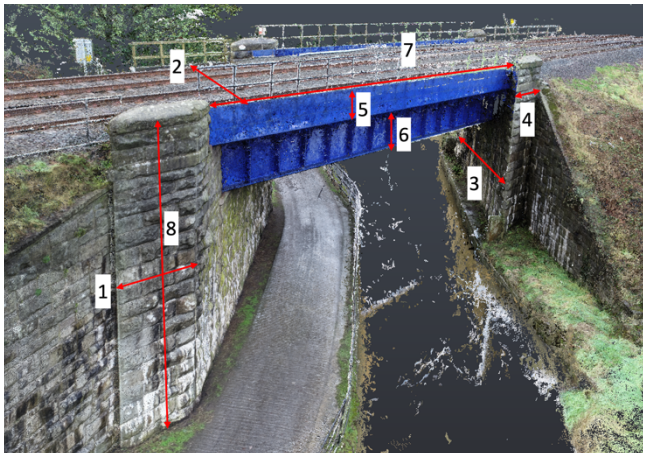

Figure 4. Measurement Locations Newry Canal Model

Within the results table, Table 2, locations are numbered (1) to (8) and refer to the location at which measurements were taken at each model. Figure 4 above shows these numbered locations for reference. As can be noted the difference in average measurements ranges from 0.33mm at location (8), the span width, up to 31.33mm at location (3), the support wall width.

Table 2. Newry Canal Model Results

	Model	Measurement (m)			Av. (m)	Difference in Averages (mm)
(1)	Lidar	2.11	2.10	2.09	2.10	7.00
	Photo	2.11	2.11	2.10	2.11	
(2)	Lidar	8.39	8.40	8.41	8.40	11.67
	Photo	8.42	8.42	8.40	8.41	
(3)	Lidar	15.97	15.98	16.0	15.98	31.33
	Photo	16.02	16.02	16.0	16.01	
(4)	Lidar	2.06	2.04	2.10	2.07	14.67
	Photo	2.06	2.00	2.09	2.05	
(5)	Lidar	1.01	1.02	1.00	1.01	16.00
	Photo	1.03	1.04	1.00	1.02	
(6)	Lidar	1.57	1.62	1.70	1.63	19.00
	Photo	1.61	1.61	1.61	1.61	
(7)	Lidar	8.02	8.02	8.01	8.01	15.00
	Photo	8.02	8.04	8.03	8.03	
(8)	Lidar	17.01	17.04	17.06	17.03	0.33
	Photo	17.01	17.02	17.08	17.03	
				Average Difference		14.37

All measurements, apart from one at location 3, are within the allowed tolerance for a high accuracy survey and all are within the +/-50mm tolerance for standard topographic surveys. This larger difference is understood to have occurred due to the UAV being unable to fly under the bridge and so it is relying on the meshed model to accurately bind the two sets of photos from either side of the bridge correctly. It may also be down to human error in selecting the correct points on the model due to the stonework being uneven. The overall average difference across the model equates to 14.37mm which is within tolerance and provides a realistic expectation for the accuracy of UAV models when compared to Lidar models.

4.2 Three Mile Water

Three Mile Water is one of two bridges located at Bleach Green Viaducts. It is a concrete, segmental arch bridge with a total of 7 spans and an approximate height of 14m. The bridge itself is within 13m of a second bridge which made the UAV flight higher risk. For this study, only one span was surveyed. The UAV took 371photos over a total flight time of 35 minutes while the lidar scanner was set up at 7 stations and took 95 minutes to complete. Figure 5 shows locations (2) to (8) where measurements were taken on both models, with the results displayed in Table 3. Location (1) is not displayed within this image, but it is the width of the bridge deck. Both models took approximately 3 hours to build.

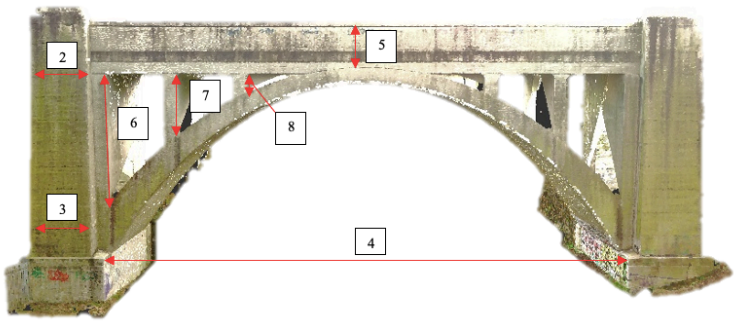

Figure 5. Measurement Locations: Three Mile Water

Table 3. Three Mile Water Model Results

	Model	Measurement (m)			Av. (m)	Difference in Averages (mm)
(1)	Lidar	5.19	5.19	5.2	5.19	64.52
	Photo	5.13	5.15	5.11	5.13	
(2)	Lidar	2.81	2.76	2.81	2.79	49.00
	Photo	2.82	2.82	2.88	2.84	
(3)	Lidar	3.02	3.03	2.99	3.01	49.33
	Photo	3.06	3.08	3.05	3.06	
(4)	Lidar	27.20	27.18	27.24	27.21	35.33
	Photo	27.22	27.26	27.25	27.25	
(5)	Lidar	2.55	2.59	2.52	2.56	11.33
	Photo	2.59	2.51	2.53	2.55	
(6)	Lidar	6.80	6.81	6.81	6.80	17.33
	Photo	6.80	6.81	6.86	6.82	
(7)	Lidar	3.32	3.28	3.29	3.29	25.67
	Photo	3.32	3.35	3.29	3.32	
(8)	Lidar	1.02	1.08	1.06	1.05	35.67
	Photo	1.09	1.08	1.09	1.09	
				Average Difference		37.56

From looking at the results, the measured dimensions are showing a much lower range of accuracy. Over half of the measured locations results in an average difference that is above the 25mm tolerance for a high-quality topographic survey. However, all but one location is within the 50mm tolerance for a standard topographic survey. Location (1), the width of the bridge deck, which is showing an average difference of over 64mm can be explained by noting that the bridge deck was not entirely modelled within the lidar model due to the scanner being ground based. It was only able to capture the underside of the bridge which can lead to measurement difficulties. This lack of data can be seen in Figure 6 which is an image of the Lidar model.

Figure 6. Image of Lidar Model: Three Mile Water

This lack of modelled data can be directly related back to the measurements where the lidar data cannot be taken as 100% accurate. In this case, a manual dimension would need to be taken to allow both scanning techniques to be compared.

Other measurements are relatively high, notably location (2) and (3). At each of these locations, large vegetation was growing at the side and made its way into the photogrammetry model making it more difficult to accurately pinpoint the edge of the column. The mortar at the joints measured also made it more difficult to pick up points. The photogrammetry model can be seen in Figure 7 below.

Figure 7. Photogrammetry Model - Three Mile Water

Overall, the average difference of 37.56mm is within tolerance for a standard topography survey but outside of a high accuracy survey. However, for this scale of survey, especially one at height on a high safety risk site such as a railway bridge, it provides a clear and accurate representation of the area and its key features. The model can be used to plan for restoration work and as a tool for ongoing asset management but may be limited in its use as an accurate, as built, 3D representation.
This case study is a good example of how UAVs can be used in large, hard to reach areas where lidar scans may miss data, but how their accuracy is not fully accepted in today's industry.

5 CONCLUSION

Due to the lidar scanning equipment being ground based, vital information cannot be captured above the height of the parapet.. This lack of possible movement from the scanner means that only data that can be seen from ground level, can be collected. So, while the data collected is highly accurate and portrays a realistic impression of the site, it does not convey the full information. To capture data above ground level, the scanner would have needed to be placed on the tracks themselves. This would involve track closures and a significant time expenditure, and so was not undertaken as part of this study. The scanners did, however, capture the underside of the bridge in great detail, which the UAV was incapable of doing as the camera cannot physically rotate high enough on its axis to look up. These situations show both an advantage and disadvantage of the ground-based scanners compared to UAV based surveys.

Current results show that UAV photogrammetry can be extremely accurate over railway infrastructure sites and provide a beneficial dataset for any future work. However they can also

give larger errors than Lidar scanning and this would need to be acknowledged and allowed for within a survey. They have proven to be quicker and more efficient across large sites when compared to laser scanning and showcase the ability to create workable, substantial structured datasets of real infrastructure sites in a number of hours. An additional benefit of UAV scanning is the lost cost of the equipment compared to a laser scanner. The drone used within this project cost under £2,000 with an additional £500 used for pilot training and CAA approval. The laser scanner used was bought in 2019 for £45,000. This large expense is not feasible for all sites, especially those which are small, inaccessible or where there is no budget for a high accuracy survey. It shows how UAV photogrammetry could be a more appealing technique for the industry.

6 FURTHER WORK

Additional work is being carried out on a much larger site, Craigmore Viaduct, which will test both scanners in all of the compared states. To further the project, it would also be beneficial to return to sites and carry out additional surveys and compare these to the originals to see if the equipment is as accurate to itself as it is to each other. This would provide greater reliability and evidence the repeatability of the project.

Although outside the scope of this project, it is noted that a higher resolution camera could also be used, which would increase the accuracy of the models and therefore provide better dimensional data. Bespoke cameras can also be utilised to conduct overhead photography which would allow for data to be collected from the underside of bridges by the UAV.

ACKNOWLEDGMENTS

This research presented in this paper is part of an ongoing Engineering and Physical Sciences Research Council (EPSRC) funded project. The authors would like to Robert Best at Translink for allowing the surveys to be carried out on the railway assets as well as to John Meneely of QUB for facilitating the lidar Surveys.

REFERENCES

[1] GeoSlam, “What is LiDAR and How Does it Work?,” 2021. https://geoslam.com/what-is-lidar/ (accessed May 04, 2022).

[2] Leica Geosystems, “Leica RTC360 3D Laser Scanner,” 2019. https://leica-geosystems.com/en-gb/products/laser-scanners/scanners/leica-rtc360 (accessed May 04, 2022).

[3] J. Horswell, “Recording,” *Encyclopedia of Forensic Sciences: Second Edition*, pp. 368–371, Jan. 2013, doi: 10.1016/B978-0-12-382165-2.00207-5.

[4] “Basics of Photogrammetry – Geodetic Systems, Inc.” https://www.geodetic.com/basics-of-photogrammetry/ (accessed Sep. 28, 2021).

[5] J. J. Lin, K. K. Han, and M. Golparvar-Fard, “A framework for model-driven acquisition and analytics of visual data using UAVs for automated construction progress monitoring,” in *Congress on Computing in Civil Engineering, Proceedings*, 2015, vol. 2015-January, no. January, pp. 156–164. doi: 10.1061/9780784479247.020.

[6] J. Tuley, N. Vandapel, and M. Hebert, “Analysis and Removal of Artifacts in 3-D LADAR Data,” Jan. 2005, doi: 10.1184/R1/6551939.V1.

[7] Royal Institution of Chartered Surveyors, “Measured surveys of land, buildings and utilities : RICS guidance note, global.,” 2014.

Sustainable cities and climate change

Improving the sustainability of fibre-reinforced polymer composite structures

William Finnegan[1,2], Tomas Flanagan[3], Conor Kelly[3], Jamie Goggins[1,2]
[1]Civil Engineering, School of Engineering, National University of Ireland Galway, Galway, Ireland
[2]MaREI Research Centre for Energy, Climate and Marine, Ryan Institute, National University of Ireland Galway, Galway, Ireland
[3]ÉireComposites Teo, An Choill Rua, Inverin, Co. Galway, Ireland
email: william.finnegan@nuigalway.ie, t.flanagan@eirecomposites.com, c.kelly@eirecomposites.com, jamie.goggins@nuigalway.ie

ABSTRACT: As technologies for manufacturing with fibre-reinforced polymer composites have advanced, more applications are being found in the aerospace, automotive and renewable energy sectors, which is due to their combination of lightweight and high-strength properties. Traditionally, fibre-reinforced thermoset composites have been preferred for many of these applications, including flight surfaces and wind turbine blades, where no sustainable solution has been resolved for their end-of-life disposal. As a result, the current end-of-life strategies for composite structures is disposal at landfill or, at best, incineration resulting in heat recovery. However, neither option offers a sustainable solution in terms of resource usage. Therefore, in this paper, an initial study into incorporating environmental impact into the design of composite structures is presented. An example has been detailed for replacing a thermoset-based composite material with a recyclable thermoplastic-based composite material, where finite element analysis is used to model the stiffness of the two materials and lifecycle assessment is used to evaluate environmental impact, in terms of its global warming potential of manufacturing a composite panel from each of the two materials. Strategies for reducing the environmental impact are discussed through optimising the energy usage, in particular during curing. Other end-of-life strategies and the use of bio-based resins for composite materials are also discussed. As the world strives to reach net zero emissions, the efficient use and sustainable end-of-life strategies of resources will play a key role.

KEY WORDS: Composite materials; End-of-life strategies; Renewable energy; Sustainability.

1 INTRODUCTION

As the world moves towards a more sustainable future, considerations for sustainability at initial design stages for products and infrastructure becomes even more prevalent. In recent decades, the use of fibre-reinforced polymer composite materials has grown due to its lightweight and high-strength properties. In particular, these materials have been widely used in the aerospace, automotive and renewable energy sectors, where other applications are continuing to be found. However, a drawback with using composite materials is their disposal at end-of-life that has been disposal at landfill in most cases. An example of this is shown in Figure1 for wind turbine blades at their end-of-life. Therefore, if these materials are to continue to be used, a more sustainable solution for their end-of-life strategies must be found, which should be part of the design stage for composite structures.

When designing or modelling composite structures, finite element analysis (FEA) provides a relatively quick, low-cost insight into the mechanical performance of a given design, where extensive details on using finite element analysis for composite materials is provided by Barbero [1]. However, a key aspect of the modelling is model validation. A recent example of model development using FEA for modelling a 13m composite wind turbine blade and its validation through static and dynamic testing has been presented by Finnegan et al. [2]. Learnings from this study will form the FEA presented in this paper.

However, this type of analysis only gives insights into the mechanical performance of the composite structure. Lifecycle assessment (LCA) offers a standardised methodology for assessing the environmental impact of a design. Previously, Tapper et al. [3] performed a review of the current literature to evaluate the LCA framework and its ability to accurately determine the benefits of closed-loop composite recycling. This study found that the use phase offers the greatest potential for emissions savings in the transport sector but recycling may possibly provide net environmental savings gains in the production phase over traditional materials.

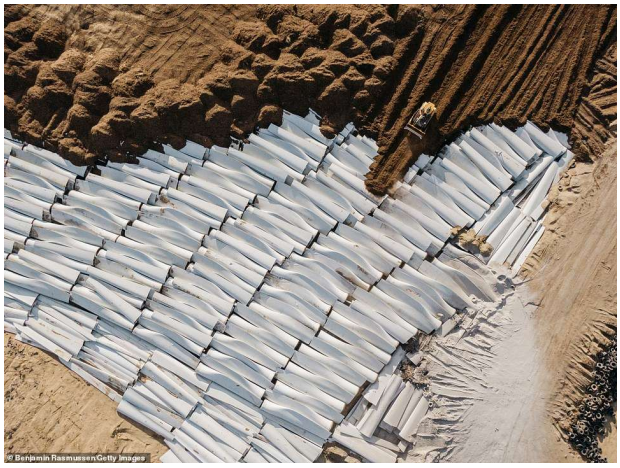

Figure 1. Wind turbine blades, made from composite materials, being disposed of at landfill at their end-of-life

Ead et al. [4] performed a review of LCA for green composites, in particular the use of natural fibres and biopolymers as an alternative to the commonly used synthetic composites. This study found that green composites are a viable alternative to synthetic composites in many applications. Therefore, LCA is a framework that has been shown to provide an insight into the environmental impact of using composite materials for a range of applications and is suitable for use in the present study.

Traditionally, fibre-reinforced thermoset composites have been preferred for many of these applications, including flight surfaces and wind turbine blades, where no sustainable solution has been resolved for their end-of-life disposal. As a result, end-of-life strategies need to be developed to ensure the sustainability of composite structures allows for their continued use in the future.

In this paper, an initial study into incorporating environmental impact into the design of composite structures is presented. An example has been detailed for replacing a thermoset-based composite material, glass-fibre reinforced powder epoxy (GFRPE), with a recyclable thermoplastic-based composite material, glass-fibre reinforced polypropylene (GFRPP), where LCA is used to evaluate environmental impact, in terms of its global warming potential of manufacturing a composite panel from each of the two materials. Strategies for reducing the environmental impact are discussed through optimising the energy usage, in particular during curing. Other end-of-life strategies and the use of bio-based resins for composite materials are also discussed.

2 MATERIALS AND METHODS

2.1 Aim and objectives

The overarching aim of this paper is to investigate end-of-life strategies of fibre-reinforced polymer composite structures to improve their sustainability. In particular, a study examining the impact of replacing a thermoset-based composite material with a recyclable thermoplastic-based composite material is detailed. However, in order to achieve this aim, the following objectives must be completed:

- To perform mechanical testing on composite materials to assess their material properties
- To investigate the stiffness of components manufactured from composite materials
- To estimate the environmental impact of technologies with varying end-of-life strategies using LCA
- To investigate other end-of-life strategies and sustainable composite materials in order to improve the sustainability of composite structures

2.2 Methodology

The methodology for the research presented in this paper first assesses the performance of two materials using a finite element analysis (FEA) in order to design a component with similar stiffness with each material. In this analysis, due to the difference in material properties, there will be a difference in thickness of the component between the materials used in order to ensure the component's performance is consistent. The reason for using an alternative composite material is to provide a more sustainable alternative and, therefore, the sustainability of the solution needs to be assessed. LCA is then used to estimate the environmental impact of each composite material applied in order to determine the sustainability of the solution. The social and economic impacts of each technology are also contributors to sustainability but are not included in the present study, as they are not expected to be significant in a comparative LCA.

FEA is used to evaluate the performance and quantify the amount of alternative materials needed by varying the thickness of the composite panel in the presented study. The FEA model has been developed using ANSYS WorkBench 17.1, where it will combine a number of the ANSYS software packages, including DesignModeler and Mechanical (ADPL) [5]. The ADPL solver is based on the finite element method, where ADPL incorporates the layup details of the composite material.

LCA is used to estimate the environmental impact of each of the two composite technologies, GFRPE and GFRPP, in accordance with ISO 14040 [6]. The functional unit will be a single composite panel of dimension 0.5m x 0.5m. The system boundary will be cradle to manufacturing plant gate, which will include the manufacture of the composite materials and their processing into a final product, which is the composite panel in this study. For the purpose of this study, only the global warming potential impact will be assessed using the IPCC 2013 methodology. However, cumulative energy demand, eutrophication potential (freshwater and marine) and acidification potential are other impact categories that would be relevant when exploring the environmental impact of composite structures. The impact factors used to calculate the impact in this study are based on the Ecoinvent v3.5 database [7].

2.3 Composites materials

In order to demonstrate the FEA-LCA combined approach presented in this paper, two composite material technologies have been selected: GFRPE and GFRPP.

GFRPE is an advanced thermoset polymer reinforced with glass fibre and has a number of advantages over traditional composite materials, including small through-thickness wet out requirement of the composite layers, good fibre volume fraction control at material manufacture stage, low exotherm during cure and it requires a vacuum bag only, out-of-autoclave cure, where further details on GFRPE is presented in Finnegan et al. [8].

GFRPP is a thermoplastic polymer reinforced with glass fibre and has been selected for this study as it can be heated and re-shaped at its end-of-life. This gives the option of recycling, which cannot be easily done with thermoset-based composites. In addition to its recyclability, GFRPP has a number of other advantages, including good impact strength, high stiffness, very good mould filling capability and low creep at elevated temperatures.

In order to evaluate the material properties of the composite materials, mechanical testing was performed, in line with the ISO 527, ASTM D6641 and ASTM D3518 to investigate the tensile, compressive and shear properties, respectively. In order to manufacture the test specimens, 2mm composite panels were manufactured and tests specimens were then machined from this panel, where the coupons used for the GFRPE tensile tests are shown in Figure 2. An Instron tensile testing machine,

which may be used for both static and fatigue tensile testing of material coupons is also shown in Figure 2.

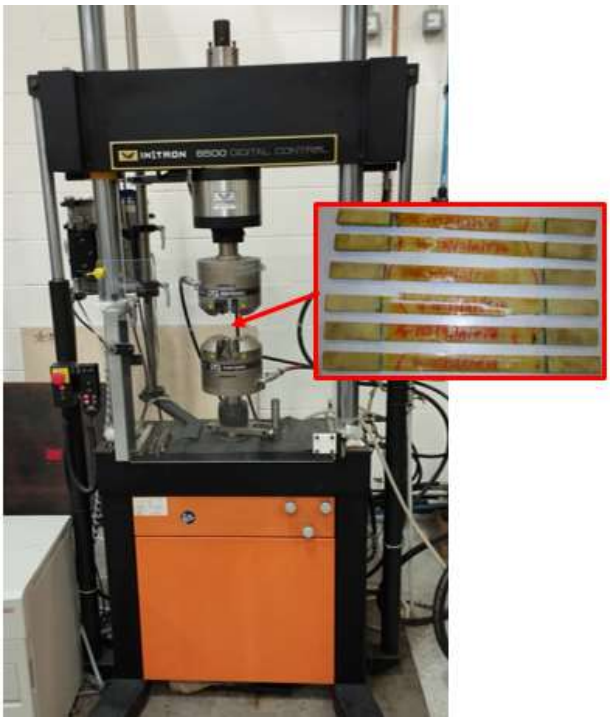

Figure 2. Tensile testing machine and test coupons used for tensile testing of GFRPE

3 RESULTS AND DISCUSSION

3.1 Mechanical testing results

Coupon mechanical testing trials were performed for each of the two composite materials, where unidirectional fibres were used, detailed in Section 2.3: GFRPE and GFRPP. A summary of the mechanical properties for each of these materials that were derived from the results from the mechanical testing of test coupons is presented in Table 1. It is evident from Table 1 that GFRPE has superior mechanical properties, when compared to GFRPP, where 0° tensile and 0° compressive strengths are 57% and 60% higher, respectively. These difference will be incorporated into the design of a composite panel using the FEA in Section 3.2.

Table 1. Summary of the material properties of GFRPE and GFRPP, based on the results from mechanical testing.

Property	Unit	Standard	GFRPE	GFRPP
0° tensile strength	MPa	ISO 527	782	498
0° tensile modulus	GPa	ISO 527	39.7	33.7
90° tensile strength	MPa	ISO 527	46.5	11.3
90° tensile modulus	GPa	ISO 527	11.9	5.4
0° compressive strength	MPa	ASTM D6641	643	402
0° compressive modulus	GPa	ASTM D6641	37.9	34.2
90° compressive strength	MPa	ASTM D6641	185	53.3
90° compressive modulus	GPa	ASTM D6641	14	5.4
In-plane shear strength	MPa	ASTM D3518	53.7	22
In-plane shear modulus	GPa	ASTM D3518	3.7	1.1

The material properties for GFRPE and GFRPP, presented in Table 1, are used as inputs for the FEA model, discussed in Section 3.2.

3.2 FEA results

For the purpose of this study, a FEA was performed on the coupons being used for the mechanical testing in order to compare the performance of the two composite materials.

Initially, a FEA was performed on each coupon with a 2mm thickness, where loads were applied to each coupon up to 10kN, where the results are presented in Figure 3. There is a significant difference between the stiffness of the two composite materials, which can be seen from the two "2mm" plot lines in Figure 3. Therefore, in order to match stiffness, the thickness of the GFRPP coupon was increased to 2.85mm, where it can be seen to perform in a similar way to the 2mm GFRPE coupon, up to a 10kN loading. It is also expected to perform in a similar way in compression within this range.

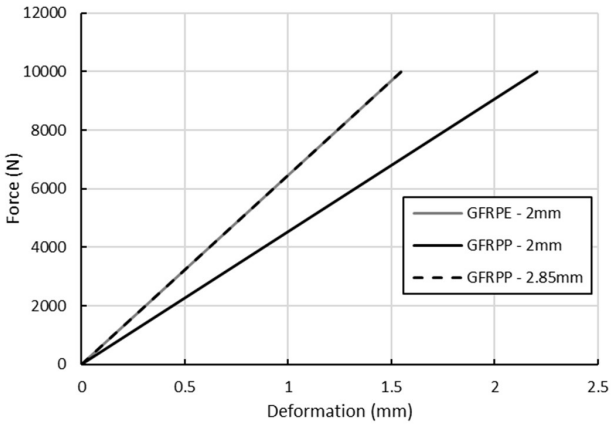

Figure 3. Results from FEA of composite material coupons, where the thickness was varied from 2 to 2.85mm for GFRPP

This examples takes a basic case of a test coupon to illustrate the use of FEA to estimate the design changes necessary to improve the stiffness of a component manufactured with GFRPP to be comparable to one manufactured with GFRPE.

3.3 LCA results

The results from the FEA in Section 3.2 are then used to inform the design of the two composite panels that will be compared using LCA. Each composite panel is 0.5m x 0.5m with differing thicknesses to ensure comparable stiffness, where the GFRPE panel has a thickness of 2mm and the GFRPP panel has a thickness of 2.85mm. In order to complete the LCA of the two composite materials, a lifecycle inventory for composite panels manufactured using each of the two material has been compiled, which is summarised in Table 2.

Table 2. Lifecycle inventory for GFRPE and GFRPP that is used to perform the LCA in this study

	GFRPE	GFRPP
Composite material (kg)	0.95	1.35
Waste material (kg)	0.095	0.135
Manufacturing consumables:		
Bagging (kg)	0.08	0.08
Sealant tape (kg)	0.06	0.06
Breather membrane (kg)	0.02	0.02
Energy:		
Oven (kWh)	19.3	3.5
Vaccuum pump (kWh)	2	2
Kitting: Power Cutter (kWh)	0.017	0.017
Lay-Up: Heat Gun (kWh)	0.367	0.367
End of life:		
Composite material recovery (kg)		-1.49
Reheating recovery (kWhr)		0.64
Landfill	1.045	

As discussed in Section 3.2, additional material is required for manufacturing the GFRPP panel, where waste composite material is estimated at 10% for each material, which is a reasonable estimate for the composite manufacturing industry in producing a standard shaped panel. Other inputs to the manufacturing process are manufacturing consumables, namely nylon bagging, sealant tape and breather membrane, and energy inputs, consumed by the oven, vacuum pump, power cutter and heat gun, which are based on data collected at a composites manufacturing site.

Impact factors, based on the Ecoinvent v3.5 database, are then applied to the lifecycle inventory to estimate the global warming potential, in kg CO_2 eq./panel, and the comparative results are presented graphically in Figure 4.

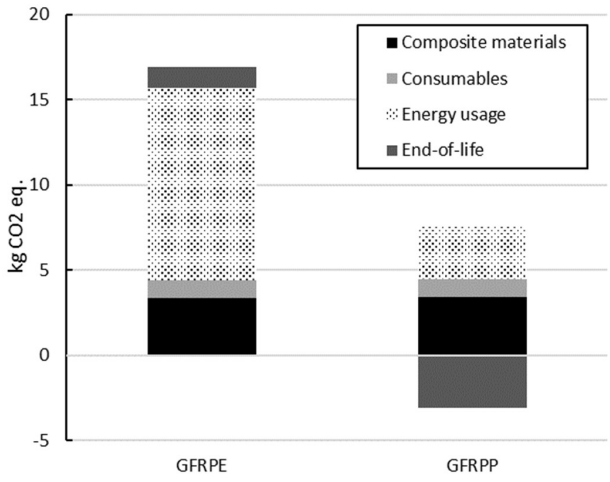

Figure 4. Comparison of the global warming potential of manufacturing a 0.5m x 0.5m panel from GFRPE and GFRPP

The overall global warming potential for each panel, when end-of-life strategies are accounted for, is approximately 16.9 kg CO_2 eq./GFRPE panel and is approximately 4.5 kg CO_2 eq./GFRPP panel. The most significant contributor to the overall impact is the energy usage, where the oven during the cure of the panel is the main energy user. Further optimisations for energy efficient use during curing may significantly reduce the overall global warming potential for each composite material. The next most significant contributor is the end-of-life strategy, where a positive impact on emissions of approximately -3.1 kg CO_2 eq./GFRPP panel is seen, as it is assumed that all of the composite material can be recycled at its end-of-life. However, as this may not always be the case, a best case scenario is presented in this paper.

The impact of manufacturing consumables on the global warming potential is calculated to be approximately 1 kg CO_2 eq./panel, regardless of the composite material used, and the impact of the composite material itself before manufacture is calculated to be approximately 3.3 kg CO_2 eq./GFRPE panel and approximately 3.4 kg CO_2 eq./GFRPP panel.

3.4 Discussion

The study presented in this paper takes one strategy for improving the sustainability of fibre-reinforced polymer composite structures by using a composite material that can be recycled at its end-of-life, as it uses a thermoplastic-based resin rather than a thermoset. A drawback of this strategy, which can be seen in the analysis presented in this paper, is that there is a reduction in stiffness of GFRPP, compared to GFRPE, resulting in additional GFRPP being required to manufacture a panel, or component, of similar stiffness. However, even with this additional material, there is still a significant reduction in global warming potential when producing a 0.5m x 0.5m panel, i.e. 16.9 kg CO_2 eq./GFRPE panel and 4.5 kg CO_2 eq./GFRPP panel. The most significant contributor to the overall global warming potential for each composite material is energy use, with improved cure cycles and more efficient ovens, along with using electricity generated from a renewable low carbon source, would significantly reduce the environmental impact of using composite materials. This end-of-life strategy is being explored as part of the RAREPlastic and MI-Drone projects, where thermoplastic-based composite materials will be demonstrated on full-scale wind turbine blades and deliver drones, respectively.

Another strategy that is currently being explored with regard to end-of-life strategies is recycling of the reinforcing fibres. Due to its high value, this strategy is currently being investigated for carbon fibre, rather than glass fibre. Mitsubishi Chemical Advanced Materials (MCAM) [9] are using innovative processes to recover carbon fibre from composites at its end-of-life and recycle it into fabric to be used for renewable energy and other applications. This technology will be incorporated into the Ocean Renewable Power Company (ORPC) tidal energy technology and demonstrated at full-scale during the H2020 CRIMSON project [10]. A further technology being explored in the H2020 CRIMSON project is the use of bio-based resins for composite materials, which uses a more sustainable and renewable resource for the manufacture of the resin. A graphical summary of the potential applications of these technologies is summarised in Figure 5.

Figure 5. Technologies currently being explored for use of sustainable composite material technologies, through the MI-Drone, RAREPlastic and H2020 CRIMSON projects

4 CONCLUSION

This paper summarises an initial study into incorporating environmental impact into the design of composite structures. An example has been presented for replacing a thermoset-based composite material, GFRPE, with a recyclable thermoplastic-based composite material, GFRPP, where LCA is used to evaluate environmental impact, in terms of its global warming potential of manufacturing a composite panel from each of the two materials. Strategies for reducing the environmental impact are discussed through optimising the energy usage, in particular during curing. In addition, other end-of-life strategies and the use of bio-based resins for composite materials are discussed. This study will be expanded further during a number of ongoing research projects, including the MI-Drone, RAREPlastic and H2020 CRIMSON projects.

The main impact of this study is the investigation into alternative end-of-life scenarios for composite structures, other than landfill. The key enabler of the proposed technologies is their reduction in costs, provided that the reduction in energy costs is greater than the increased costs for the composite material required to achieve the same mechanical performance. As the world strives to reach net zero emissions, which is targeted to be achieved by 2050, the efficient use and recycling of resources will play a key role.

ACKNOWLEDGMENTS

This research was funded in part by the European Commission through the H2020 CRIMSON project (grant agreement no.: 971209) and the Department of Business, Enterprise and Innovation and administered by Enterprise Ireland under the Disruptive Technologies Innovation Fund, MI-DRONE Project (Contract Ref: DT 2020 0221). The first and last authors would like to acknowledge the support from Science Foundation Ireland (SFI), through the MaREI Research Centre for Energy, Climate and Marine (Grant no. 12/RC/2302_2). The second and third authors would like to acknowledge the support from the Environmental Protection Agency (EPA) for the RAREPlastic project.

REFERENCES

[1] E. J. Barbero, *Finite element analysis of composite materials*. CRC press, 2007.

[2] Finnegan, W., Jiang, Y., Dumergue, N., Davies P. and Goggins, J. (2021), 'Investigation and validation of numerical models for composite wind turbine blades', *Journal of Marine Science and Engineering* 9(5):525.

[3] Tapper, R. J., Longana, M. L., Norton, A., Potter, K. D. and Hamerton, I. (2020), 'An evaluation of life cycle assessment and its application to the closed-loop recycling of carbon fibre reinforced polymers', *Composites Part B: Engineering*, 184.

[4] Ead, A. S., Appel, R., Alex, N., Ayranci, C. and Carey, J. P. (2021), 'Life cycle analysis for green composites: A review of literature including considerations for local and global agricultural use', *Journal of Engineered Fibers and Fabrics*, 16.

[5] Thompson, M.K. and Thompson, J.M. *ANSYS Mechanical APDL for Finite Element Analysis*, Butterworth-Heinemann: Oxford, UK, 2017.

[6] International Organization for Standardization, *ISO 14040: Environmental Management – Life Cycle Assessment – Principles and Framework*. Geneva, Switzerland, 2006.

[7] Wernet, G., Bauer, C., Steubing, B., Reinhard, J., Moreno-Ruiz, E. and Weidema, B. (2016), 'The ecoinvent database version 3 (part I): overview and methodology', *The International Journal of Life Cycle Assessment*, 21(9), 1218-1230.

[8] Finnegan, W., Allen, R., Glennon, C., Maguire, J., Flanagan, M. and Flanagan, T. (2021) 'Manufacture of high performance tidal turbine blades using advanced composite manufacturing technologies', *Applied Composite Materials*, 277.

[9] Mitsubishi Chemical Advanced Materials, URL: www.mcam.com, accessed: 06/05/2022

[10] Gardiner, G. (2021) 'ÉireComposites and ORPC to use recycled carbon fibre in tidal turbine foils', *Composites World*.

Methods of strengthening CLT manufactured using Irish Sitka Spruce

Emily McAllister[1], Daniel McPolin[2], Jamie Graham[3], Grainne O'Neill[4]
[1]Department of Civil Engineering, Queens University of Belfast, Northern Ireland
email: emcallister48@qub.ac.uk, d.mcpolin@qub.ac.uk, jgraham74@qub.ac.uk, goneill1990@qub.ac.uk

ABSTRACT: Climate change is a current global issue which must be addressed in order to create a sustainable future. The construction sector is a major contributor to climate change, specifically through the use of manmade materials such as steel and concrete. While European countries have embraced the use of naturally sourced materials, such as cross laminated timber, their use in the UK and Ireland is much more limited. Currently, cross laminated timber (CLT) is only manufactured in mainland Europe with transportation to the UK and Ireland adding to costs. Domestically producing CLT from home-grown Sitka Spruce will result in CLT panels which have lower mechanical strengths relative to their EU counterparts. Within the UK, timber is growing with a high moisture content, leading to lower strength timber. This research investigates the drying and conditioning methods used to reduce the timber moisture content to 12%, which is required to produce CLT panels of the highest strength characteristics. The research also investigates how the addition of a strengthening material, glass fibre mesh, improves the panels overall performance in bending and shear tests.

KEY WORDS: Cross Laminated Timber; Composite; Drying; Conditioning.

1 INTRODUCTION

The use of natural resources as a reputable building material is rapidly developing, particularly with timber. Cross laminated timber (CLT) is becoming an increasingly favourable building material within Europe.

CLT is an engineered product of timber which is formed by the arrangement of lengths of timber placed in layers, with each layer positioned perpendicular to one another. CLT panels are composed of an odd number of layers, typically three or five layers (Swedish Wood, 2019). The principal benefit of the use of CLT as a building material within the construction industry is the ability it has to replace traditional building materials such as steel or concrete products. These materials commonly have higher levels of carbon embedded within them relative to CLT. The continued use of high carbon materials would drastically impact the sustainability of the future due to global warming (Younger et al. 2008). It is important that the construction industry have a suitable alternative with a less detrimental impact on the environment.

CLT is a suitable alternative building material which has become increasingly popular within Europe (CBI, 2017). This promising building material has been favoured by the construction industry within the United Kingdom and Ireland. However, with no suitable CLT production plant in the region, the product cannot be sourced locally and must be imported from other parts of Europe. This transportation adds to the overall carbon footprint of the product as well as adding approximately 10% to the costs, deeming it less sustainable as initially anticipated. (Waugh Thistleton Architects, 2018).

To overcome this problem, CLT can be manufactured using timber supplies sourced locally within the UK and Ireland (Sikora et al 2016). Sitka Spruce has been regarded as a favourable source product for CLT manufacture through past research due to its abundance in regions of Ireland and Scotland (Crawford et al. 2015). This study investigates the feasibility of the use of timber of strength class C16 instead of C24 as a source material for the production of CLT. Timber within a strength class of C16 has typically lower strength characteristics that C24 timber but is lower in cost due to its abundance.

2 THE IMPORTANCE OF THE CONSTRUCTION INDUSTRY WITHIN THE UNITED KINGDOM AND IRELAND:

The current shortage of housing units within the United Kingdom has reached over one million. More than 69,000 houses need to be constructed every year for the next 15 years to eradicate this demanding issue (BBC Housing Briefing, 2020).

With these vast shortages, new-builds and existing households are becoming increasingly unaffordable. According to Sirius, a property finance company, a traditional build with a timeframe of 12 months would have an estimated loan interest of £252,000 over a year whereas a modular build with a timeframe of 6 months would have an estimated loan interest of £126,000 (Sirius, 2021). Any existing houses and new-builds rely on heavily on 'man-made' materials such as steel and concrete blockwork, which have an immense carbon footprint, directly associating today's construction with climate change due to carbon dioxide emissions. The process of concrete production alone is currently responsible for 5% of anthropogenic global CO2 production per annum. (Chemistry World, 2008)

With the vast majority of construction involving the use of concrete, the effect on global warming is exigent leading to disastrous implications, such as extreme droughts, flash flooding and storms. With the high demand for housing, it is important to seek new materials which can be used to replace the traditional methods of construction. The alternative methods and materials will need to provide low cost, sustainable housing for the future.

The use of timber in construction has a plethora of benefits including a low carbon production, high insulating properties and when used correctly and similar structural abilities to blockwork, when used correctly (BK Structures, 2022). With a great focus being placed on the search for a low carbon building materials, there has been an increase in timber import levels since 2007, showing the demand for timber in the construction industry (Federation TT, 2021).

According to a study carried out in 2021, the predicted demand for CLT use in the US and Canada alone was estimated to be 800,000m^3/year by the year 2030 (Brandt et al., 2021). According to 'Checkatrade UK', a CLT panel would typically cost £30/m^2 to manufacture for a typical house in the UK and Ireland. With domestic manufacture of the CLT panels, some production and transportation costs are eliminated and so CLT manufactured using home-grown timber sources is much more viable for housing in terms of costs. In addition, it has the significant benefit of arriving on-site fully machined allowing for rapid on-site assembly

3 CONDITION OF RAW TIMBER FOR CLT MANUFACTURE

In the past, CLT panels have been manufactured in the laboratory to replicate those manufactured in eastern European factories such as 'KLH Massivholz' and 'Metsawood'. Before the panels are assembled, the raw timber is dried and conditioned under highly controlled settings to ensure the timber has a suitable moisture content and has dried at the correct pace to allow the moisture to fully leave without distorting the timber. Also, panels manufactured in industrial settings are subject to high amounts of vertical and lateral pressure to ensure maximum bonding between the joins of timber sections. This high pressure also forces any remaining moisture out of the fibres of the timber before the adhesive dries. Both these factors appear to be of high importance in the manufacture of CLT panels, however, with past investigations, the drying and conditioning phase appears to be the control which is the most difficult to adapt. Studies show that the fundamental rule for timber drying is that the end quality of timber depends on the rate of drying (Reeb et al., 2007).

However, in an industrial setting, adding to manufacturing time respectively loses profits and so a balance between the drying time and condition of the timber is established. The moisture content of the timber for CLT is required to be 10-12% (BS EN 16351, 2015). However, it is important that this moisture content is the same throughout the whole section of the timber and not only at the section extremities. As Trada (2011) explains, the moisture first evaporates from the surface of the timber, creating a gradient in the moisture content with a high degree of moisture in the core of the section. The moisture gradient then causes the water to be drawn to the surface which in turn evaporates (Trada, 2011).

A set of CLT panels were manufactured in the laboratory under replicated conditions as in a factory setting. The timber was allowed to air dry for 3-4 days in an area of high ventilation and temperature of 18-20 ºC. The moisture content of the timber was checked daily using a moisture probe and the panels were manufactured once the timber had a moisture content reading of 12-15%. Within hours after manufacture, gaps started appearing in the panels as shown in Figure 1. These gaps resulted in insufficient bonding between the layers, leading to a reduction in panel strength. The average modulus of elasticity of five panels manufactured in the laboratory is shown within Table 1 below and is compared with industrial CLT panels, manufactured using C24 timber sources.

Figure 1. CLT panels made within the laboratory which showed gaps between lamella over time

Table 1. Data provided by Metsawood Leno and KLH CLT on the moisture content of timber used to manufacture CLT panels along with corresponding modulus of elasticity (Leno Metsawood, 2012), (KLH UK, 2012).

Source of Data	Average Modulus of Elasticity (N/mm^2)	Moisture Content before assembly (%)
Metsawood (Leno)	10,590	10% (+/- 2%)
KLH	12,000	12% (+/- 2%)
CLT manufactured in the laboratory	5,496	12% - 15%

The gaps between the lamella were measured daily using a feeler gauge and grew over time as shown in Figure 2. These gaps formed as a result of insufficient drying and conditioning before manufacture. When moisture testing using the moisture probe, the timber appeared successfully dried, however the inner core of the timber remained high in moisture. During the manufacture, with the pressure being applied for successful adhesion of the glue, the moisture was forced to the outer parts of each lamella, which then subsequently dried off with time, resulting in the shrinkage. These results show the high importance of the drying and conditioning stage in the manufacture of CLT panels.

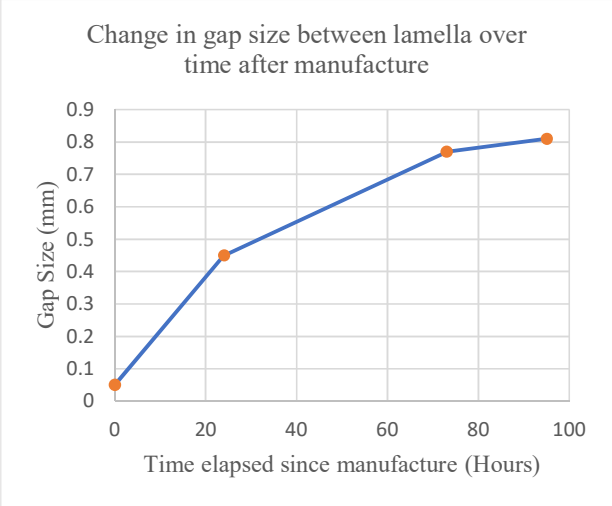

Figure 2. The change in gap size (mm) at a given time after manufacture of the panel

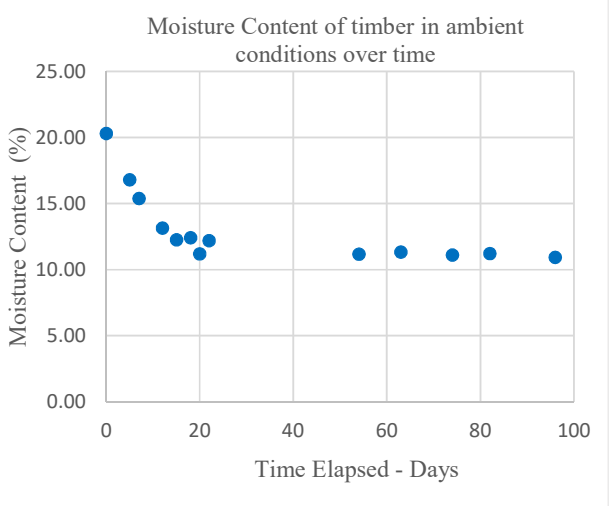

Figure 4. Change in moisture content of timber in ambient conditions over time

4 METHODS OF DRYING AND CONDITIONING

In order to determine the patterns in timber drying and the rate it occurs in different conditions, some timber samples were dried in ambient conditions and some in a humidity and temperature controlled cabinet.

4.1 Drying in ambient conditions

As shown in Figure 3, timber samples were arranged and left to naturally dry in ambient conditions. The room temperature fluctuated between 18-22ºC and the humidity was ever changing. The moisture content was determined using the oven drying method, as explained in Section 5.2. With the ambient conditions, the timber samples took around 40 days to reach the equilibrium moisture content of around 12% and it was observed that distortion had occurred in the timber during this time. The rate of drying of the timber samples is as shown in Figure 4.

Figure 3. Arrangement of C16 timber samples drying in ambient conditions

4.2 Drying in controlled conditions

An airtight drying cabinet was constructed to replicate the drying of timber within a controlled factory setting in Europe. A temperature and humidity controlling unit was installed to maintain a temperature of 20ºC and 65% relative humidity.

These conditions would give an equilibrium moisture content of 12%. The timber was strapped using small ratchet straps to reduce twisting during the drying process. The set-up is as shown in Figure 5.

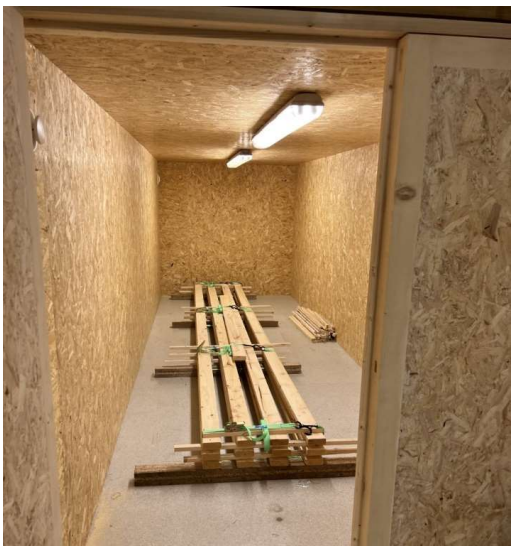

Figure 5. Arrangement of C16 timber drying in controlled conditions; 20ºC and 65% relative humidity

5 METHODS OF MEASURING MOISTURE CONTENT

5.1 Use of handheld device

A handheld device can be used to get instant readings of moisture content from a sample of timber. Moisture meters can either have probes to penetrate the timber or can be pinless and non-invasive to the timber using electromagnetic sensors to read the moisture content. For readings in this project, an Orion 910 pin-less moisture meter was used. This meter was suitable for timber with moisture between 4.0% and 32.0%. To ensure accuracy of the hand held moisture meter it was verified with the oven drying method, as outlined in Section 5.2.

5.2 Oven drying method

The oven drying method is the most accurate form of testing the moisture content of a piece of raw timber as it directly measures the mass of moisture in the sample. The method is described in BS EN 13183-1 and involves taking samples of a length of timber, each being 20mm in thickness. The first sample should be taken 300mm in from the end of the sample and this piece should be discarded. In this case, a selection of 10 samples were cut. Immediately after being cut, these samples are weighed and recorded and then placed in an oven at 103ºC (±2ºC) and left for two hours, as shown in Figure 6. The samples are weighed every two hours until the difference between two successive weighing's is less than 0.1%. The moisture content of the timber to which the samples were cut from is calculated using Equation (3) from BS EN 13183-1.

$$\omega = \frac{m_1 - m_0}{m_0} \, x \, 100 \qquad (3)$$

where ω is the moisture content as a percentage; m_1 is the mass of the test slice before drying (in grams); m_0 is the mass of the test slice after being oven dried (in grams) (BS EN 13183-1, 2002).

Figure 6. Oven drying method used to determine moisture content of timber before manufacture of CLT panels

6 DETERMINING THE PERFORMANCE OF A CLT PANEL

In order to determine how feasible it is to replace traditional materials with CLT made from C16 home-grown timber sources, the mechanical and strength characteristics of the panels must be identified. This will allow the capabilities to be compared with traditional materials. Table 2 below shows the elastic modulus of the materials which can be used in CLT panels.

Table 2. Elastic Modulus of various materials (Martynova et al. 2018).

Material	Elastic Modulus, E_m, (kN/mm^2)
C16 timber (parallel to grain)	8.0
C16 timber (perpendicular to grain)	0.27
Glass Fibre Mesh	72

In past research, the bending capacity of CLT panels has been found using the stiffness values of each individual length of timber in the CLT panel (Sikora et al., 2016). Using this method, the stiffness of any 'timber-only' CLT panel can be calculated at a predictive level. Equations (1) and (2) based on BS EN 310, can be used to obtain the modulus of elasticity (in N/mm^2) and bending strength (in N/mm^2) of CLT panels (BS EN 310, 1993).

$$E_m = \frac{{L_1}^3 (F2 - F1)}{4bt^3 (a2 - a1)} \qquad (1)$$

$$f_m = \frac{3F_{max} L_1}{2bt^2} \qquad (2)$$

where L_1 is the distance between the support centres; b is the width of the test piece (mm); t is the thickness of the test piece (mm); $F2 - F1$ (in N) is the increment of load on the straight-line portion of the load-deflection curve; $a2 - a1$ (in mm) is the increment of deflection at the mid-length of the test piece (corresponding to F2 - F1); and F_{max} is the max load applied (N).

However, different theoretical calculations were used in past research including the layered beam theory, gamma beam theory and shear analogy theory to determine strength characteristics of the panels (Sikora et al., 2016).

In most previous studies, strength and stiffness characteristics were only determined on a panel manufactured from timber only and do not allow for consideration if an additional material is introduced in the panel (Sikora et al., 2016). Within this study, it is anticipated that by adding a layer of strengthening mesh, the overall performance of the panel will be improved; thus providing higher strength and stiffness despite the use of a lower strength timber source.

Panels will be made at a variety of spans and will have either three or five layers. They will firstly be manufactured on a timber only basis and then with the added strengthening layer of glass fibre polymer mesh. The two forms of panels will then be tested in shear and bending tests to determine their strength and stiffness capacities.

The theoretical strength and stiffness of a CLT/GRP composite panel strength has been established. This was achieved by homogenizing the composite using the Young's

modulus of the materials in each layer of the panel and transforming it into a single material using modular ratios. From this, the parallel axis theorem can then be used to calculate the moment of inertia for the cross section of the panel. Thus, bending stresses on positions of the panel can simply be calculated for various loads. However, it is important to note that at this point this theoretical modelling is only suitable for the calculation of strength characteristics up to the moment of failure of the outermost component in the CLT panel. Post elastic behaviour, most notably in the outmost compression zone is not yet considered in the model. This theoretical modelling technique can also be used to calculate the same characteristics when the panel has an existing strengthening layer.

Figure 7 below shows the experimental and theoretical deflection results for a three layer, 'timber-only' CLT panel with a span of 2000mm. The results illustrate the accuracy which can be achieved by using the theoretical model to get an idea of the physical performance of a CLT panel during experimental testing.

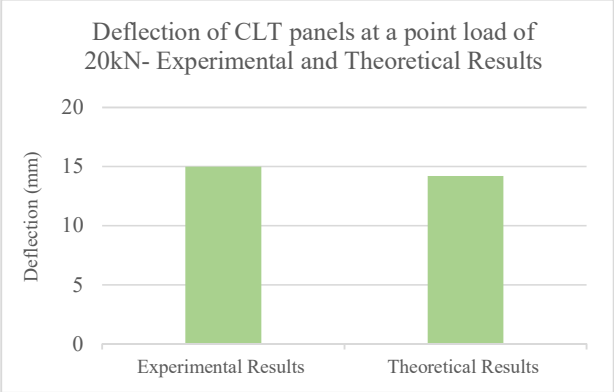

Figure 7. The experimental and theoretical results for a three-layer timber only panel, with a span of 2000mm, deflecting under a load of 20kN.

From this, the same theoretical modelling programme was then used to determine the performance for a range of panels including composite panels with the added strengthening layer. Figure 8 below shows how various panels would theoretically deflect when a typical domestic floor load of 1.5kN/m^2 is applied. The panels compared are; a three-layer 'timber-only' CLT panel and a three-layer GRP mesh composite CLT panel. Again, the panels considered are 2000mm in span. The layer of GRP mesh in the composite panel is 10mm in thickness-a typical grade of mesh used in construction works involving plasterboard.

The results show that with the presence of the additional material layer, the same load applied results in a reduced deflection, by 33%. This indicates that with the additional strengthening layer, the performance of the panel is greatly improved resulting in panels with similar strength characteristics to those made in central Europe using C24 timber.

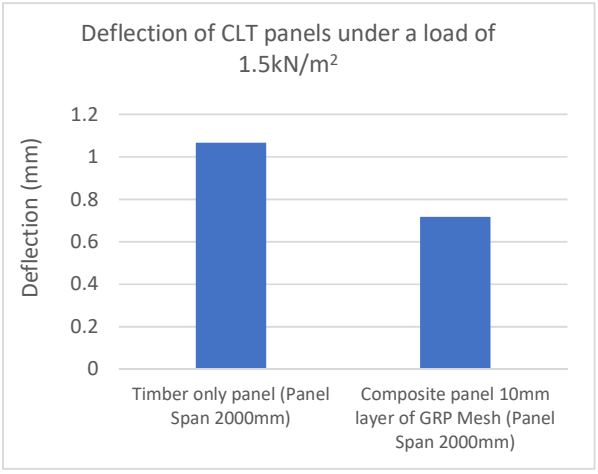

Figure 8. The comparison of theoretical deflection results of a three-layer 'timber only' panel and three-layer GRP mesh composite CLT panel, under a load of 1.5kN/m^2.

7 IMPROVING THE PERFORMANCE OF CLT

7.1 Additional layer

As determined from the predicted values from the theoretical modelling programme, the addition of a layer of GRP mesh improves the strength of the CLT panel; thus reducing the deflection caused upon loading.

With the same load of 1.5kN/m^2 applied each time, the presence of the additional 10mm layer of GRP mesh resulted in a deflection reduction of 33% on average. This additional layer is required when using the C16 timber as a source material for the CLT panels. The panel strength is improved as the tensile forces acting on the bottom of the panel are not only resisted by the overlapping pattern of the CLT but also by the additional material which has a high tensile force resistance. The use of GRP mesh can be substituted using any layering material and the modelling programme can calculate the strength parameters when the value for the Young's modulus for the additional material is imputed. This programme can therefore determine the combination of materials which produces panels with the highest performance, saving time and waste of timber and other materials.

8 CONCLUSIONS

From the work undertaken to date, it is confirmed that the CLT panels manufactured using home-grown C16 Sitka Spruce results in panels with a lower modulus of elasticity to those manufactured using C24 timber sources. However, the addition of a layer of GRP mesh would increase the overall panel strength properties. Through the theoretical calculations, it is confirmed that with the addition of a layer of GRP mesh, a 2000mm panel deflects 33% less during a loading of 1.5kN/m^2.

It is also confirmed that theoretical calculations within a modelling programme can be used to get an idea of the panel strength characteristics, allowing the best combination of materials to produce higher strength panels. It is also important

to note the importance of the drying and conditioning stage before manufacture of the CLT panels. If the timber is not at the correct moisture content, the structure releases or absorbs moisture, resulting in shrinkage or swelling, thus leading to gaps forming in the CLT panel. In order to get the timber to a moisture content of 12%, the timber must be placed in an environment of 20ºc and 65% relative humidity. It has also been noted that the most accurate method of determining the moisture content in a timber sample is by using the oven drying method as outlined in BS EN 13183-1.

REFERENCES

[1] BBC Briefing-Housing (2020) [Online] Available at: PowerPoint Presentation (bbci.co.uk) (Accessed Date: 10/09/2021)

[2] BK Structures (2022) CLT [Online] Available at: CLT | Our Services | Cross Laminated Timber | B&K Structures (bkstructures.co.uk) (Accessed Date: 20/01/22)

[3] Brandt, K., Latta, G., Camenzind, D., Dolan, J., Bender, D., Wilson, A., and Wolcott, M. (2021). "Projected cross-laminated timber demand and lumber supply analysis," (PEER-REVIEW ARTICLE (ncsu.edu)), (Accessed Date: 20/02/2022)

[4] BSI, British Standards Institutions. (2015). BS EN 16351 - Timber structures — Cross laminated timber — Requirements

[5] BSI, British Standards Institutions. (2002) BS EN 13183-1 – Moisture content of a piece of sawn timber

[6] BSI, British Standards Institutions. (1993). BS EN 310 - Wood-based panels — Determination of modulus of elasticity in bending and of bending strength

[7] CBI Ministry of Foreign Affairs (2017) "Exporting cross laminated timber (CLT) to Western Europe" [Online] Available at: Exporting cross laminated timber (CLT) to Western Europe | CBI (Accessed Date: 22/06/2022)

[8] Chemistry World (2008) "The concrete conundrum" [Online] Available at: CW.03.08.Concrete.indd (rsc.org) (Accessed Date: 14/09/2021)

[9] Crawford. D, Hairstans. R, Smith. S, Papastavrou. P (2015) "Viability of cross-laminated timber fromUK resources" [online] Available at: Viability of cross-laminated timber from UK resources (icevirtuallibrary.com) Accessed Date: 14/04/2021

[10] Federation TT, (2011) Statistical Review [online] Available at: Timber industry well positioned to meet demand in 2022, says TTF - Timber Trade Federation (Accessed Date: 05/01/2022)

[11] J.E. Reeb and T.D. Brown (2007) "Air- and Shed-drying Lumber" [online] Available at: Air- and Shed-drying Lumber (oregonstate.edu) (Accessed Date: 14/12/2021)

[12] KLH UK. (2012). *Sustainability*. [online]Available at: http://www.klhuk.com/sustainability.aspx (Accessed date: 05/11/2021)

[13] Leno Metsawood (2012) Technical Knowledge 2012-Cross Laminated Timber CLT Available at: Leno - Metsäwood - PDF Catalogs | Documentation | Brochures (archiexpo.com) (Accessed Date: 04/11/2021)

[14] Martynova. E, Cebulla. H (2018) "Inorganic and Composite Fibers" [Online] Available at: Glass Fibre - an overview | ScienceDirect Topics (Accessed Date: 26/03/2022)

[15] Sikora, K. S., McPolin, D. O., & Harte, A. M. (2016). "Effects of the thickness of cross-laminated timber (CLT) panels made from Irish Sitka spruce on mechanical performance in bending and shear" [online] Available at: https://www.sciencedirect.com/science/article/pii/S0950061816307000 (Accessed Date: 10/01/2021)

[16] Sirius Property Finance (2021) "Modular building could save developers hundreds of thousands in funding interest" [Online] Available at: MODULAR BUILDING COULD SAVE DEVELOPERS HUNDREDS OF THOUSANDS OF POUNDS IN FUNDING INTEREST – Sirius Property Finance (siriusfinance.co.uk) (Accessed Date: 25/06/2022)

[17] Swedish Wood (2019) The CLT Handbook [Online] Available at: Swedish-Wood-CLT-Handbook.pdf (woodcampus.co.uk) (Accessed Date: 22/06/2022)

[18] Trada Technology. (2011). Drying and Moisture Content of Timber

[19] Waugh Thistleton Architects (2018) 100 PROJECTS UK CLT [Online] Available at: CLT 100 UK Projects (thinkwood.com) (Accessed Date: 26/03/2022)

[20] Younger, M., Morrow-Almeida, H. R., Vindigni, S. M., Dannenberg, A. L. (2008) "The Built Environment, Climate Change, and Health Opportunities for Co-Benefits" [Online] Available at: doi:10.1016/j.amepre.2008.08.017 (ajpmonline.org) Accessed Date: 22/06/2022

Optimising heating costs in low-occupancy offices

Erica Markey[1], Roger P. West[2], Niti Saini[2]
[1]Department of Mechanical, Manufacturing and Biomedical Engineering, Trinity College, College Green, Dublin 2
[2]Department of Civil, Structural and Environmental Engineering, Trinity College, College Green, Dublin 2
email: markeye@tcd.ie, rwest@tcd.ie, sainin@tcd.ie

ABSTRACT: From the growing number of international agreements, such as the Kyoto Protocol, Paris Accord and most recently the Glasgow Pact, it may be observed that there is an increasing global focus on reducing carbon emissions and reducing energy waste. In Europe, buildings are one of the largest energy consumers, with space heating accounting for the majority of this consumption. As more flexible working models become the norm, especially during and post-pandemic times, office occupancy is likely to remain substantially lower than pre-pandemic levels. In the absence of suitable interventions, this is likely to lead to the heating of unoccupied rooms, wasted energy, money and unnecessary generation of greenhouse gases. The main aim of the project on which this paper is based was to design and manufacture a device that sits on a conventional radiator valve and which can turn it on and off remotely with a view to saving energy, while still ensuring a comfortable working environment when it is required. Research into the occupancy rates and heating regimes of offices in two buildings in Trinity College Dublin are presented in this paper. This research involved occupier questionnaires and data collection from sensors placed in these offices to establish temperature and occupancy histories. A physical prototype device was built and placed in one office with the sensors still present to demonstrate the personal control and responsibility which office users could have over their office heating costs in the future. Estimates were made, through modelling, as to the potential extent of energy savings which could arise through the use of such radiator control devices.

KEY WORDS: Optimising heating costs, Low occupancy offices, Sustainable buildings.

1 INTRODUCTION

According to the "International Energy Outlook" published by the US Energy Information Administration [1], 20% of the total energy consumed worldwide is consumed by buildings, including residential and commercial buildings. The UK Department of Energy and Climate Change found that space heating accounted for 60% of domestic energy consumption, while heating water added an additional 15% [2]. Modern living standards require high thermal comfort, increasing the demand for energy. This demand is not constant and varies with outdoor environmental conditions, the physical characteristics of the building, the orientation, and the behaviour of the occupants [3], [4].

When evaluating indoor air quality, CO_2 levels are taken as a proxy for ventilation quality, as poor ventilation can lead to excessive accumulation of CO_2 and indicates the possibility of other harmful pollutants building up. The indicators used for thermal comfort are indoor temperature and relative humidity [5]. According to ASHRAE Standards 62.1 (for ventilation), CO_2 levels should be limited to 700 ppm above outdoor CO_2 levels, which is usually 300-500 ppm, and relative humidity should be below 65% [6]. Similarly, the ASHREA Standards 55 (thermal comfort) state that the indoor temperature should be within a range of 18-22°C [6].

Being aware of the challenges around sustainability and high energy consumption, particularly within buildings, Trinity College Dublin is continuously examining alternative ways to be more sustainable. The university has identified that an area with a large scope for improvement is to reduce the energy waste associated with heating rooms when they are not occupied or with continuously heating rooms when they are already at an acceptable temperature, which studies have shown to be 20 °C [7].

The thermal energy in Trinity is predominantly supplied by natural gas. According to the 2017 Annual Report of Estates and Facilities [8], Trinity consumes 34 million kWh annually. Despite the significant drop in occupancy rates during the Covid-19 restrictions, the heating requirements of most buildings did not change. This is due to many buildings moving to extended opening hours to facilitate requirements of exceptional Covid-19 demands and many of the buildings needing to be kept at a minimum temperature in order to protect their fabric and structure. Trinity's campus is unusual as more than 60% of the buildings are more than 100 years old, and 25% are over 200 years old [8]. Although Trinity recognises the importance of preserving these buildings, they also highlight that the lower occupancy rates of the buildings during the Covid-19 restrictions required a disproportionate amount of heating compared to occupancy levels [9]. Furthermore, in most buildings, the heating is switched on daily and centrally at the beginning of the heating season and radiators are on in individual rooms unless turned off manually by occupants.

2 METHODOLOGY

This project consists of three sections, a faculty questionnaire, a sensor survey of sample offices and the design and manufacture of a prototype radiator controller.

2.1 Faculty questionnaire

A questionnaire was designed, validated and distributed to faculty members within the Civil and Mechanical Engineering departments at Trinity College Dublin. The questionnaire was designed to collect information on the occupancy rates and heating regimes of offices on the Trinity campus. Participants were asked to consider how their occupancy had changed during the Covid-19 pandemic. The faculty chosen to participate in this questionnaire were based in two different buildings on campus. The Simon Perry Building, built circa the

early 1990s, and the Parsons Building, whose construction spans from 1895 to the 1990s, have been selected due to their difference in age. This is reflected in the insulation specifications and the types of radiators within them all of which had radiators with local manual control valves.

2.2 Room survey

Following the questionnaire, specific rooms were selected to be sensored, selected on the basis of room size and room orientation. A varied distribution would allow for the influence of solar gain on the room temperature to be examined. LoRaWAN network operated sensors measuring the air temperature and the CO_2 levels were placed in the rooms. Each room had two sensors installed, one on the workstation and one beside the radiator, with one acting as a backup in case of a fault and as a method of cross-referencing the exact timing of switching on/off of the radiators. The CO_2 readings from the sensor at the workstation acted very effectively as an occupancy sensor. The data collected during this survey was used to calculate the potential savings in energy and to produce a set of guidelines for the faculty at Trinity College on the best practices for reducing heat waste.

2.3 Design and manufacture of prototype

In parallel to the sensor experiment, a mechanical prototype was built which can physically turn radiators on and off. The prototype is electronically controlled by an app which allows the user to input his/her calendar and operate it manually and remotely. The occupancy schedule that is developed will ensure that the heating in the room will only be on when the occupant is scheduled to be present. The app's manual override system is in case the calendar does not correctly reflect the user's actual schedule. The device also has a temperature sensor built-in which provides it with the current room temperature with a view to preventing overheating.

3 FACULTY QUESTIONNAIRE

The survey was sent to the 36 faculty members in the Simon Perry Building and the Parsons Building that have their own offices, which elicited a 50% response rate. The survey was structured in two parts, the first section dealing with the time spent by the faculty both on campus and in their offices and the second on their interaction with the heating system. The first part was intended to gather information on the frequency and duration of these time frames. This section compared the faculties' pre-Covid timetable and the restricted timetable that was in place during the survey. The survey was completed in October 2021 and the government guidelines at the time were to work from home as much as possible with only a few lectures in person. The purpose was to compare how office occupancy rates had changed during the pandemic and to establish where potential savings could be made.

The second section of the survey dealt with the heating regime of offices. The purpose was to gather information on the level of engagement individuals had with the heating system in their offices. It examined some of the reasons for turning off or not turning off their radiators.

3.1 Occupancy

Figure 1 plots the mean number of weekly hours the faculty spend both on campus and in their offices, based on the responses, pre and post the pandemic. It is clear from this graph that there has been a significant drop in the number of hours faculty spend on campus. This is not surprising, as at the time the government was still strongly encouraging people to work from home as much as possible.

This graphs also compares the number of hours spent on campus and in the office. It is not surprising that the number of hours spent in the office is lower each week than the time spent on campus. Many academics spend time in lectures, tutorials, laboratories, or meetings that require them to leave their offices. Before Covid-19 arose the faculty spent on average seven hours per day on campus but not in their offices. This is lower than expected but it is, however, consistent with the results found during the sensor survey. This result may limit the potential savings gained by turning the radiator off for short periods throughout the day.

Figure 1 also shows that there is a drop in the number of hours the faculty spend on campus but not the proportion in their offices. This reflects the fact that many lectures, etc. were still conducted online during this period but when people came in they tended to spend longer per day on campus.

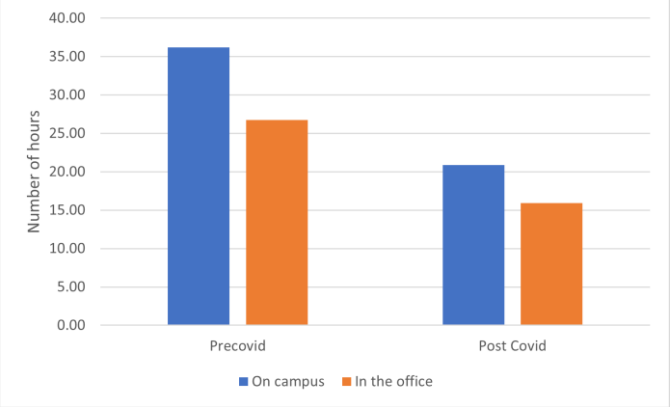

Figure 1. Mean number of hours on campus and in offices

3.2 Heating regime

It is evident from Figure 2 that a large majority of respondents had no interaction with their heating systems, with nearly 80% stating that they either never turned the heating off or never turned it on. The effectiveness of a radiator controller is highly influenced by the interaction of the occupant with the controls. Having a system that worked independently of the occupant interaction would be beneficial as it removes this factor.

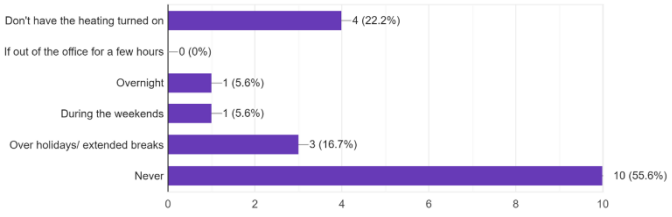

Figure 2. Level of interaction with heating system

There were 15 respondents who answered the question exploring the reasons why people did not turn off the heating in their offices. More than 45% of the respondents said that they rely on the college's management of the building to control the heating. One respondent was unable to easily access the radiator valve and, as a result, did not turn off the heating. Five respondents, representing 33%, said they were concerned about returning to a cold room.

Eight people responded to the question about why they turn off the heating. The main motivation cited by more than 60% was that they wanted to contribute to the college's green initiatives. Two responded that they turn off the heat when the room becomes too warm. It is surprising that this is not a greater number; however, it is assumed that the other respondents were thinking about non-reactive reasons for turning off the heating. This is verified in the next question, where the respondents are asked how they react to excess heat, where a much bigger proportion say they turn off the radiator.

When asked how they react to excess heat, 60% of the respondents opened the window, and of this group only three also turned off the radiator. Opening the window while the heating is still on is a wasteful habit, but one that also delivers fresh air A less wasteful method of heat dissipation is to open the office door and allow heat to dissipate through the rest of the building. Encouragingly, some of the respondents already use this method.

3.3 Conclusions from the faculty survey

Comparing the time spent on campus before any Covid restrictions with the time during restrictions shows a clear and significant drop. This is not surprising as the government guidelines at the time encouraged people to work from home as much as possible. Based on the feedback obtained from the occupants, there is a poor level of interaction with the heating system. Nearly 80% of the respondents had no interaction with the heating system, and a large majority of this group is dependent on building management to control the heating. It is not possible for building management to maintain the optimum heating level in individual rooms and they must assume that each office will be occupied every day, leading to wasted energy when the office is not. This highlights the importance of individual, automated room controls that do not rely solely on the interaction of the occupants to reduce heat waste. It is clear from the feedback that many of the occupants are dissipating excess heat in a wasteful manner. Guidelines outlining the best practices for radiator use and heat dissipation should be compiled and distributed to all faculties in the College.

4 ROOM SURVEY

Sensors were installed in nine of the surveyed offices in the last week in January and were monitored continuously for eleven weeks. During the sensor installation, the dimensions and physical features of the office were recorded. Only two of the nine offices had thermal radiator control and none a local room thermostat.

4.1 Influence of solar gain on the room temperature

Rooms that are south facing will experience more solar gain than rooms facing north. Figure 3 compares the room temperature of two similar rooms, the only physical difference between the two being their orientation. The data presented here is for a Saturday when the building heating is turned off and both rooms were unoccupied. The room temperature for the South facing office is consistently higher than the North facing room. While the temperature of both rooms increase, the south facing room increases by more than 4°C compared to just 0.5°C in the north facing office. This difference can be attributed to the solar gain experienced by the south facing office by comparison with days when no solar gain exists.

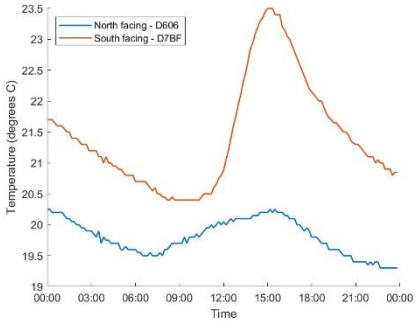

Figure 3. Examining the influence of solar gain on room temperature

4.2 Influence of window size on room temperature

The size and number of windows can have a significant influence on the temperature of a room. Figure 4 is a comparison between two south facing offices, one room has a window area of 10.8 m^2 and the other has 1.5 m^2. As both rooms are south facing they both experience solar gain, which is observed to be the reason for the increase in temperature. The room with the larger window is able to capture more sunlight and therefore experiences more solar gain and observed in the more significant temperature rise. However, as windows have less thermal insulation than walls, the temperature drops more sharply than in the small window room and so the early morning temperature is lower in this room.

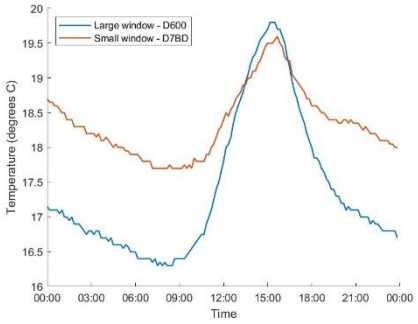

Figure 4. Examining the influence of window size on room temperature

4.3 Eliminating over heating of the rooms

Research has indicated that heating offices above 20°C is unnecessary [7]. Figure 5 is an example of a room where the occupant interacts well with the heating system, as it can clearly be seen that the heating is turned on and off when the occupant enters and exits the room (as shown by the CO_2 data). However, the room has been heated to excess with much of the day spent with temperatures above 20°C. Switching off the heating once the room is at 20°C in this situation would save

approximately 10% of energy use. Most offices in this study were observed to spend a significant portion of the day at temperatures above 20°C and much larger saving are possible.

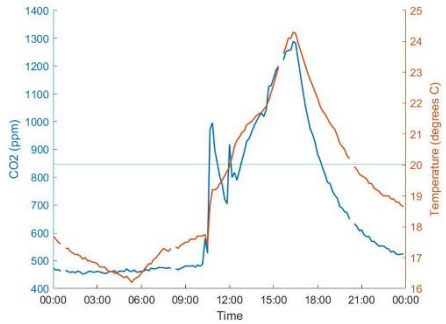

Figure 5. Example of a high occupancy room with good interaction with heating system

4.4 Reducing the heating period

The clearest example of heat waste comes from the heating of unoccupied rooms. Modelling was undertaken to calculate the proposed heating period which would reduce the time the room is unoccupied while the heating is on. This was achieved simply by creating simulated heating windows during which heat was provided based on the heating and cooling rates in the room from their acquired temperature data signatures. The specific heating and cooling rate was calculated for each individual room which depend on many factors, such as the difference between the room and the outside air temperature and the time since the heating was turned off. To maintain consistency across each of the calculations, the cooling rate was calculated using the data from the six hours before the heating was turned on. The heating rate was calculated using the data from the first three hours the heating was turned on. The analysis for this section assumes that the room temperature is above 18°C while occupied.

A day is considered high occupancy if the occupant is present for more than two hours before and after lunch. The temperature and CO_2 for a high occupancy day is presented in Figure 6, where it is evident that the occupant first enters the room at 10 am and departs at 12 pm., to return at 4pm. The modelling for this situation found that the heating should be on for no more than three hours, from 9am to 12pm. The proposed heating period is highlighted in the purple box in Figure 6. Implementing this new heating schedule would result in a 75% saving for this room on this day.

Due to the nature of an academic's work, on that day there are times where they must leave their offices to deliver lectures, attend laboratories or attend meetings. During this time there may be a saving if the heat is turned off while they are out of the room. Figure 7 is an example where the occupant has left the room for three hours in the middle of the day with two heating periods.

The results of this modelling indicate that the heating for the latter room should be turned on at 7am and turned off between 10am and 3pm, where it is turned on again for an hour. This proposed heating schedule would reduce the heating period by six hours, representing a 50% saving. However, analysing this example using a single heating phase also results in a 50% saving, with a heating period from 7am to 11am.

A day is considered to be low occupancy if the occupant of

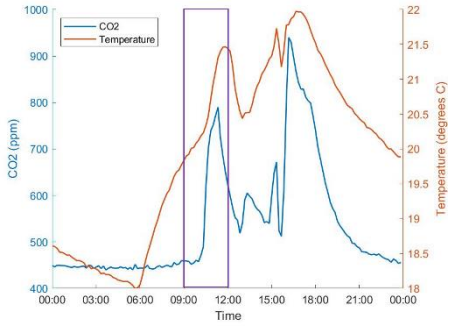

Figure 6. Proposed heating period for a high occupancy room

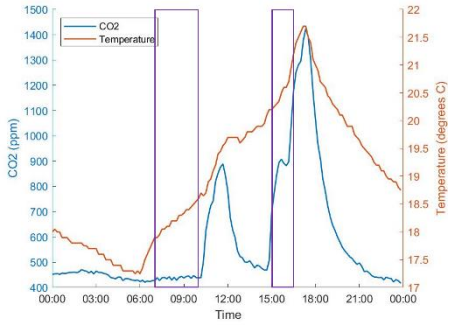

Figure 7. Proposed heating period for a medium occupancy room

the room is not present throughout the day. wherein the heating should not be on during these days. Figure 8 is an example in which the occupant is not present but the heating is on for 12 hours, which is entirely wasteful. The potential savings for this room and all low occupancy rooms are 100% as the heating should not be on. On average, the offices surveyed were unoccupied 54% of the weekdays, and on the majority of these days the heating had been left on. Eliminating this situation will result in dramatic savings.

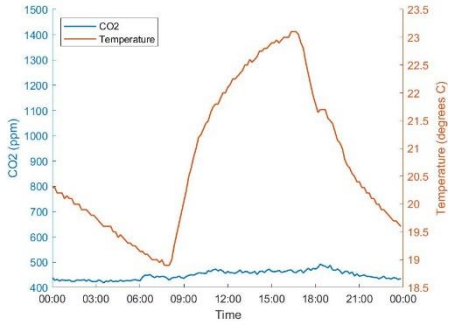

Figure 8. Example of a low occupancy room where the heating is on

4.5 Conclusions from the survey study

The orientation of rooms has a clear influence on room temperature, and this effect will be especially prominent in the Spring and Summer months as the intensity of the sun light increases. South facing rooms experience more solar gain, which significantly increases the room temperature, with more scope for sensored switching of radiators. The offices have, to

some extent, been designed with this in mind, and so the north facing offices are better insulated by reducing the window size. As windows are less thermally insulating than walls, rooms with larger windows decrease in temperature much faster than rooms with smaller windows. However, they are also more adept at capturing solar gain, so their room temperatures rise much more throughout the day.

There are two situations that lead to heat waste. The first is continuing to heat rooms that are already at a comfortable temperature; the second is heating unoccupied rooms. It is clear from the data collected during this study that the offices in the Simon Perry and Parsons buildings are heated to excess. Most of the offices spent some time at temperatures greater than 20°C. Reducing the maximum room temperature will result in large savings for the university. About 25% average saving can be achieved through reducing the maximum room temperature.

The average occupancy rates for these offices were 24% high occupancy, 22% medium occupancy, and 54% low occupancy. With all levels of occupancy, there are potential savings to be gained by reducing the heating period. High and medium occupancy rooms can achieve savings up to 60%. As the occupant is not present on low occupancy days, the heating should not be on at all, and therefore, these have potential savings of 100% accepting that pre-heating temperature will be lower on subsequent days.

5 PROTOTYPE

Smart radiator valves (SRV), such as the one proposed in this project, are not a novel idea. There are many SRV options on the market to improve a home heating system. They are, however, different from the smart thermostat, which controls the heating directly from the boiler; an SRV controls the heating by switching individual radiators on and off. Many of the SRVs have been designed to be used in conjunction with a smart thermostat or a central hub, which would not scale from domestic settings to academic buildings. The key reason that these devices are not suitable for use in Trinity is that they are not compatible with the manual radiator valve that it frequently found in Trinity. These devices have been designed to be used on thermostatic radiator valves which control the flow by pushing a pin down or releasing it. As a result they use a linear actuator to move the pin vertically. Manual radiator valves use a rotational motion to open and close the valve and so the linear motion cannot be easily converted.

To cause rotational motion, the motor must be braced against something; when you turn a valve by hand, your wrist acts as a brace. If the motor was not securely braced against something it would simply rotate itself and the force would not be transferred to the valve. Several concepts for mounting the motor to the radiator were considered, and it was decided to mount the motor on the pipes of the radiator. Prototypes for two different pipe configurations were built (Figure 9).

Several concepts for connecting the motor to the valve were considered. The final cap design is a replacement cap that is connected to and turns the valve using the same mechanism and principles as the original cap. The cap also has the larger gear attached to the top.

Gears were needed to increase the torque produced by the motor, to ensure that it would be sufficient to turn the radiator valve. The gears were designed in a 4-1 ratio and are a helical

Figure 9. Prototypes with rotational restraint in a same pipe or adjacent pipes configuration

design to reduce the risk of vertical slippage. All of the components were designed using solidworks and were 3D printed.

5.1 Hardware

The motor used in the prototype was a Nema 17 stepper motor, which was controlled by an Arduino Nano IOT 33 microcontroller. The Nema 17 is a commonly used stepper motor capable of supplying high torque at low speeds. The Arduino Nano IOT 33 was chosen as it allowed for the prototype to be connected to a WIFI network, which allows the user to control the device remotely from an app written specifically for that purpose.

5.2 App design

A basic app was designed and built using the Arduino Cloud IDE. This app allowed the user to input a personalised work schedule for the heating and provided an override function, in case this schedule did not match the actual movements of the user. The scheduling function used did not satisfy all of the functionality desired and so a fit-for-purpose app was developed which was connected to the Arduino API and successfully demonstrated the override function from any user's phone operated remotely. Unfortunately, due to time constraints, this ap could not be developed to connect to an online calendar, such as google calendar, and data scrape the occupancy schedule from this, though in principle it has the capability to do this. An automatic scheduling function such as this will reduce the need for the user to interact with the heating controls although it is important because studies have found that user interaction with a heating control is the greatest factor in the effectiveness of that controller [10]. It should also be noted that occupiers occasionally open windows for fresh air, which is especially thermally inefficient in Winter.

5.3 Conclusions from the prototype

The key design consideration for the mount is that the motor must be securely locked in place to ensure that it does not rotate when in operation. Several concepts for the motor mounts and the valve attachments were considered and sketched with the most promising being manufactured and tested. The final design was successfully tested both in the vertical and horizontal arrangement.

The app was successfully trialled during a demonstration and offered some basic functionality for the device; however, it is

not complete and should the project be continued the remaining functionality can be added. The app also requires an Arduino account, which means that it cannot be downloaded by multiple people. The fit-for-purpose app, in early stages of development, was successfully used to control the motor over the network, switching on/off an office occupant's radiator on demand.

6 CONCLUSIONS

A questionnaire completed by faculty members located in the Simon Perry and Parsons buildings quantified the drop in office occupancy rates during the Covid-19 restrictions. It also showed that a significant proportion of individuals do not interact with their heating systems when present in their offices. When dissipating excess heat, the methods that are currently used are wasteful and guidelines describing the best practices should be distributed to all who are working on the campus.

Sensors monitoring the occupancy and room temperature/CO_2 levels within the offices of two buildings on campus exposed the factors affecting the room temperature. The results from the survey were that despite the lifting of the Covid restrictions many people were choosing to work remotely and occupancy levels have remained well below the pre pandemic levels. The calculations produced estimates for the level of heat waste in heating offices on campus. With all levels of occupancy there are potential savings that could be gained, ranging from 100% savings for low occupancy rooms to 10% for high occupancy rooms.

SRVs are not a novel idea, with many devices currently available on the market. However, they are not suitable to be used in large non-domestic settings, such as academic buildings. An early stage prototype was designed, manufactured and successfully tested during brief demonstrations. This device acts as a proof of concept that a radiator controller can be remotely used on a manual radiator valve. Two apps were developed, one using the Arduino IDE which was straightforward to build but restricted in its functionality. A second fit-for-purpose app was designed to switched on/off a radiator remotely using a mobile phone, and which, if further developed, will allow the user to set up an automated electronic personal diary schedule without direct user input, with a manual remote override. Versions of both apps were successfully used to control the motor over WIFI connections.

6.1 Future considerations

The device built during this project is an early stage prototype with many possible improvements that could be made. The first and largest improvement would be to incorporate a proportional integral derivative (PID) controller. It is important that a universal mount is designed as it is not feasible to create bespoke mounts. Once a universal mount is designed, it will be possible to optimise the size of the prototype as it is currently a bulky device. After an optimised mount has been created, alternative materials can be used to manufacture the mount. It is possible to avoid the limitations of 3D printing and the risk of plastic degradation due to the heat of the radiator by machining parts from metal or a heat resistant plastic. Currently, the number of revolutions needed to rotate the valve fully is hard coded and cannot be adjusted for each radiator. A useful functionality for the prototype would be to have a way of measuring the resistance the motor is experiencing so it would know if the valve is fully open or closed. This, along with a universal mount, would make the device more adaptable. Along with the adjustments to the device it is recommended that the faculty questionnaire and the room survey should be extended to different participants, in order to build on the findings of this project and verify that the results are consistent.

6.2 Alternative solutions

Although a device such as this would reduce the heat waste, it is not the only method nor the most effective. Increasing the efficiency of the overall system is likely to have a significant reduction on the heat waste experienced. The results of the room survey highlighted the effect of insulation, window size and room orientation on overall room temperature. A well-insulated building would require much less energy to keep it at a comfortable temperature for the occupants.

SRVs are only suitable for systems that operate using radiators; however, many offices rely on underfloor heating or heat pumps to heat the building. It may be more beneficial to design a device that can work across many different heating systems.

Often it is not the solution that produces the greatest savings that is the best overall solution. The cost of the solution and the speed at which it can be implemented are two further considerations when implementing changes to a system. The greatest justification for a heating system managed by radiator controllers, such as the one prototyped here, is that they are retrofit devices. There are also significant carbon emissions associated with renovations, from the manufacturing of new parts to transporting of materials. These emissions cannot be discounted when choosing the best overall solution.

REFERENCES

[1] US Energy Information Administration, "International energy outlook," *US Energy Information Administration, Washington, DC*, 2011.

[2] Department of Energy and Climate Change (DECC), "Smarter heating controls research programme." Government of Ireland, 2012.

[3] A. Figueiredo, R. Vicente, J. Lapa, C. Cardoso, F. Rodrigues, and J. Kämpf, "Indoor thermal comfort assessment using different constructive solutions incorporating PCM," *Applied Energy*, vol. 208, pp. 1208–1221, Dec. 2017, doi: 10.1016/j.apenergy.2017.09.032.

[4] M. Taleghani, M. Tenpierik, and A. van den Dobbelsteen, "Indoor thermal comfort in urban courtyard block dwellings in the Netherlands," *Building and Environment*, vol. 82, pp. 566–579, Dec. 2014, doi: 10.1016/j.buildenv.2014.09.028.

[5] P. T. B. S. Branco, M. C. M. Alvim-Ferraz, F. G. Martins, and S. I. V. Sousa, "Children's exposure to indoor air in urban nurseries-part I: CO2 and comfort assessment," *Environmental Research*, vol. 140, pp. 1–9, Jul. 2015, doi: 10.1016/j.envres.2015.03.007.

[6] American Society of Heating, Refrigerating and Air-conditioning Engineers, "ASHRAE Standard 55-2019 Thermal environmental conditions for human occupancy." American Society of Heating, Refrigerating and Air-conditioning Engineers, 2019.

[7] K. Parsons, "5 - Thermal comfort in buildings," in *Materials for Energy Efficiency and Thermal Comfort in Buildings*, M. R. Hall, Ed. Woodhead Publishing, 2010, pp. 127–147. doi: 10.1533/9781845699277.1.127.

[8] Trinity College Dublin Estates and Facillities, "Estates & Facilities Annual Report 2016 – 2017." 2017.

[9] Trinity College Dublin, "Sustainability Report 2019/20." 2020.

[10] S. Kelly *et al.*, "Predicting the diversity of internal temperatures from the English residential sector using panel methods," *Applied Energy*, vol. 102, pp. 601–621, Feb. 2013, doi: 10.1016/j.apenergy.2012.08.015.

Floodplain restoration: opportunities to use nature in the solution of complex challenges impacting urban areas in Ireland for adaptation to a changing climate.

Mary-Liz Walshe[1], Laurence Gill[2]
[1]Department of Civil, Structural and Environmental Engineering, Trinity College Dublin, Dublin 2, Ireland
[2]Department of Civil, Structural and Environmental Engineering, Trinity College Dublin, Dublin 2, Ireland
Email: walsheme@tcd.ie, Laurence.Gill@tcd.ie

ABSTRACT: Floodplain restoration in urban areas is becoming increasingly important in Ireland as we face a changing climate and devise sustainable responses. The influence of water on the evolution of Irish settlements is notable with major towns and cities typically sited at the mouths of rivers and on their floodplains. Pursuing sustainable climate resilient strategies in our most populous areas is likely to require some floodplain restoration elements. Preserving serviced urban land for, or returning it to, floodplain status prompts some exciting but challenging conversations around urban land management.

The approach to river restoration must be appropriately selected and the dynamics governing each river system must be carefully understood so that the intended outcomes can be realised and unintended consequences minimised. The research suggests that benefits of urban floodplain restoration are significant, e.g. potential for restoration of urban ecosystems, access to nature, links with urban regeneration, renaturalising the shape and flow of river systems, increased resilience to climate change, etc. and opportunities must be recognised, investigated, and better understood and communicated so that informed decisions can be made.

This paper outlines the findings of the literature review undertaken to date for research that aims to devise a new protocol to deliver sustainable/integrated and achievable restoration plans for urban rivers. This paper also highlights two exciting Dublin City Council projects that embody these approaches, *The Camac River Flood Alleviation Study* and *Planning the River Corridors of Dublin City,* and that reflect the real-life constraints that currently face such efforts in urban areas.

KEY WORDS: CERI/ITRN2022; Urban river restoration; Floodplain restoration; Water Framework Directive; Hydromorphology; Natural flood management; Climate resilience.

1 INTRODUCTION

Many cities around the world are located along or near rivers, due to the proximity of water, transportation, food, energy and other resources they provide [1]. Many of Ireland's historical settlements exhibit a similar pattern. The relationship is complex, however and typically, the city has squeezed the river, altering its morphology and reducing its capacity to deliver ecosystem services, as well as adding excess runoff and diffuse pollution loads. River flooding damages the city in return. However, there are many potential benefits in both directions. With good management, the city and its people can gain aesthetic and recreational opportunities, increased land values and economic development in river corridors [2].

'In many cities, encroachment of floodplains with urban development led to a stance of flood defence that posited that city and river were in a fight for territory, and the perception that the measure of success was exclusively in our ability to keep the flooding river "at bay", behind levees or within concrete channels [...] Shifting paradigms now force us to confront this ambition with the environmental consequences of these "gray" solutions.' [3]

From the late 1700's to the mid-20th century, urban riverbanks saw the widespread and accelerated introduction of industry, linear infrastructure (e.g. railways and roads) and harbour infrastructure. In parallel, natural floodplains were raised to produce development land next to the river. These forms of encroachment on the river corridor tended to displace flood waters and often resulted in more severe urban flooding, which in turn promoted the introduction of hard flood protection infrastructure, further severing the city from the river [3]. The services provided by the natural channel and wetlands to inhabitants were also lost [2].

Today, as a result of these legacy issues, urban flooding can threaten citizens' quality of life, produce socioeconomic losses, and act as a driver of urban decay [4]. Conversely, the role of restored river floodplains is one that also enhances the resilience of the river basin against climate and anthropogenic change, as well as increasing flood safety, improving water quality and increasing its ecosystem services for society [5]. The potential for urban river restoration to act as a driver for urban renewal is also acknowledged and in the last few decades, the progressive relocation of industries, harbours and other historical riverside land-uses provides opportunities for cities to rethink their relationship with the river, possibly giving it more space and embracing it as an ecological and aesthetic asset rather than as a problem [2].

River restoration has many definitions and can have many context- or location-specific goals but in general, the activity seeks to bring about sustainable environmental enhancements, returning a river system and processes to a more natural state. River restoration in the urban environment is a complex undertaking. The volumes and timing of flows have been altered by urbanisation [6], water and habitat quality has diminished [7], flood risks and morphological modifications are more pronounced and the lack of public open space made it more difficult to apply the concept of full renaturalisation [1]. It is often clear that it is impossible or infeasible to completely reverse these impacts and so the initial challenge is often in establishing what water management interventions or physical habitat changes are possible that can re-establish natural river process and sustain freshwater ecosystems [6]. Current thinking suggests that even partial river restoration in the urban environment can bring about myriad benefits to the

urban environment through enhanced reintegration of the river as a valuable feature of the landscape [1].
The current climate and biodiversity crisis prompts a particular examination of urban floodplains and ecosystems and an improved understanding of flooding as an important natural process. As the importance of the hydrologic and ecological functions of natural floodplains becomes better understood, there are increasing calls to restore connectivity of floodplains, so that they actively flood [8].

Pan-European research undertaken in 2017 found a statistically significant positive link between the presence of natural areas on river floodplains and 'good status' under the Water Framework Directive (WFD) [9]. The same research confirmed similarly significant inverse links between the density/presence of i) infrastructure and ii) urban areas on river floodplains and estimated that the renaturalisation of between 10% and 20% of river floodplains together with improvement management of nutrients could see a significant proportion of European rivers achieve 'Good Status' under the WFD.
The impacts of a changing climate and the need to protect and enhance ecosystems coupled with the pressures for continued urbanisation and competing water demands [7] are such that those in pursuit of healthy, vibrant sustainable cities must examine their land-use management policies and give careful regard to these discussions.

Two projects in Dublin commenced in 2019 are assessing the extent to which these land use management principles can be embraced: The Camac Flood Alleviation Scheme and Planning the River Corridors of Dublin City. This paper also summarises a selection of typical approaches to river restoration, how they relate to the Water Framework Directive and climate adaptation/resilience and assesses the potential and limitations of each in the context of these two Dublin projects.

2 WHAT IS RIVER RESTORATION AND NATURAL FLOOD MANAGEMENT?

The practice of river restoration has generally evolved from a primary focus on form (and the physical shape of the channel e.g. creating river meanders) or definitions of static conditions (e.g., implementing a minimum instream flow) to its current focus on dynamic hydrologic, geomorphic, and ecological processes [6, 7]. In recent decades, the application of river restoration techniques commenced with a focus on small-scale actions in headwater streams to a new focus on the challenges posed by addressing larger rivers and their floodplains [6], which has brought river restoration into the urban domain. The majority of restoration interventions target headwaters and small tributaries [7] but the most severe habitat and land-use alterations are typically in lowland floodplains and deltas [7]: Urban stream restoration presents unique problems: there is minimal space for rehabilitation [10].
The Water Framework Directive (WFD) is potentially a key driver of river restoration across entire river systems, including urban reaches and sub-catchments with its focus on the need to address diffuse pollution and hydro-morphological pressures but progress across Europe seems to have been moderate [11]. It is accepted that in urban areas, the measures to address these pressures often have important co-benefits such as flood protection, biodiversity improvements and recreational benefits and in highlighting these aspects, it can be helpful to frame them in terms of ecosystems services [11].
The role of floodplains as a place for water retention during extreme discharges caused by intense precipitation and the supply of water in times of drought is essential under conditions of global climate change. The related ecosystems have a value also. In order to increase the ability of floodplains to perform these key functions, it is critical that the connectivity of rivers with its surrounding floodplains be preserved and human activities adapted to support this and to restore river ecosystems [12].
The selected targets of, a) improved flood control and the enhancement of ecological conditions through copying nature and, b) supporting the recreational value of small water bodies, all in cooperation with people living there, were the focus of a study of ecological restoration of small water courses in Asia and central Europe [13]. Most of the assessed river systems showed deficits in the hydromorphological status. The restoration projects, mostly linked with flood control projects, were found to improve the ecological status of water bodies as well as the diversity of animals and plants in the river landscape [13].

3 A SELECTION OF APPROACHES TO RIVER RESTORATION

Urban waterfront development has been a feature of the developed world but the success of these interventions, not just ecologically but architecturally, is regularly in question.
That doesn't mean, however that aesthetic improvements cannot form part of a more holistic river restoration undertaking. Appreciating what did not work elsewhere may provide insights needed to improve future endeavours. The results of a Pinto and Kondolf study in 2020 show that poorly conceived projects failed for several different but predictable reasons. To bring about more successful interventions, future designs should reflect the local context, the morphology of the river valley, the time and budget needed to deliver a set of solutions, and select uses and functions that embrace diversity *'and provide multiple benefits, including good flood management performance and the restoration of the rivers' natural connectivity*.' [3]

Another approach to river restoration was to undertake works to support selected individual high-value species or habitats (and the WFD includes measures for the support and protection of 44 key water-dependent natural habitats and 22 species) but this was also found to have its limitations.
Overly specific conservation and restoration aims often proved inappropriate and ultimately had a negative impact, restricting diversity and eroded ecosystem resilience [6].
Many past restoration actions are based on subjective positions on what habitats are good/desirable or on an overly narrow approach. Criticism has been levelled at legal mandates in both the USA and Europe (including the WFD) for their role in narrowly defining particular aspects of river ecosystems to be restored (e.g. water quality, species, or structural features). It has been shown that, following this narrow focus, interventions often fail to address the basic

causes of habitat loss and therefore cannot bring about meaningful results [7].

Worse still, an inappropriate intervention could have negative consequences: efforts to achieve particular conditions for certain locations or ecological functions could compromise key natural processes that need support for wider ecosystem benefits [6].

There is a clear basis for the need to '*define restoration actions by their potential to maintain ecological integrity or to support diverse and productive ecosystems that are resilient to change as opposed to specific native species or reference conditions'* [7] if river restoration efforts are to be more successful and demonstrate sustainability in the longer term.

This leads us to the more current approach, process-driven restoration. Process-oriented restoration aims to address the root causes of degradation, and to understand and characterize the primary processes driving habitat conditions and ecosystem dynamics [7]. It is believed that the '*restoration of critical processes also allows the system to respond to future perturbations through natural physical and biological adjustments, enabling riverine ecosystems to evolve and continue to function in response to shifting system drivers (e.g., climate change)'*[7].Actions thus conceived help avoid the limitations associated with the more static interventions described earlier.

An idea posed by G.M. Kondolf in a 2011 article is centred around allowing rivers to "heal themselves" [14]. He posits that this is the most sustainable approach to the restoration of the ecological value of rivers and it also focuses on facilitating or restoring the following physical processes: flooding, sediment transport, erosion, deposition, and channel changes in the creation and maintenance of complex river forms. This approach requires room for the river to move and sufficiently recover its flow regime and sediment load. This is a particular challenge for urban rivers where, in general, their catchments are fundamentally altered in a way that makes us question the feasibility and merits of affording the necessary time and space required for this river healing to take place [1, 14]. Kondolf has devised a framework based on current stream power/sediment supply and encroachment of development in river floodplains of land so that the most appropriate actions for individual situations might be considered at an early stage [14].

A related approach to river restoration that is process-driven is one that also considers flows. Traditionally, river restoration approaches either physically change the landscape or channel (channel-floodplain manipulation) or adjust hydrology (to achieve environmental flows e.g. through the removal of dams or weirs), and such actions are often independent. Current research points to the benefits of coupling channel-floodplain manipulation and environmental flow actions to achieve process-based goals [6]. Such a combined approach supports comprehensive river restoration efforts aimed at supporting resilient ecosystems within human-dominated landscapes in a non-stationary climate. A recent article by Whipple and Viers (2019) encapsulates this thinking and identifies four elements of combined approaches for restoring highly modified rivers:

(1) identify physical and ecological process potential given interactive effects of altered landscapes and flows;

(2) consider capacity for sustaining identified processes under potential future change;

(3) model alternatives for coupled restoration actions to support identified processes; and

(4) evaluate alternatives using metrics representing integrative effects of coupled actions. [6]

The authors suggest these emergent elements contribute to the development of standard practices for restoring highly modified rivers [6].

It is closely related to the Kondolf's river healing approach but outlines the links with engineering and climate adaptation/resilience even more directly, stating that re-establishing the geomorphological and hydrological conditions necessary to sustain ecosystems is a central challenge for restoration within highly altered systems. Whipple and Viers stress that meeting this challenge requires simultaneously addressing multiple and interacting stressors within the context of irreversible changes and socio-economic constraints [6]. The paper states that the removal of lateral barriers (e.g. embankments or flood defences) in a highly regulated river may be insufficient alone to restart the floodplain inundation dynamics known to be important for key species. Hence, recognition that restoring only the morphological elements, without addressing the flow/landscape interactions that complete the larger picture, the measures are unlikely to produce the necessary space and time variability and resulting complexity of environmental conditions that define successful ecological restoration [6]. An assessment to identify aspects of the river system that are fundamentally altered and the most appropriate suite of restoration actions that can align with current limitations is important in highly modified rivers but in addition, a wider landscape-scale perspective is increasingly important to understand climate change implications and to support and sustain diverse and healthy ecosystems under a range of possible future scenarios [6]. Absent geomorphic elements may prevent the reestablishment of certain dynamic physical processes and therefore make it difficult to meet ecological objectives, e.g. bringing about a more natural flood regime with high-magnitude, long-duration floods can potentially move sediments in a positive way but if that sediment is no longer available, that positive result may not result. It has also been acknowledged that in certain cases the reinstatement of historical flow regimes could have a negative impact on some ecosystems. [6]

Other constraints, such as land availability for floodplain reconnection and the potential timing and duration of associated flood pulses within modified floodplains, are increasingly recognized as important components of environmental flow assessments [6], which is not news to many in the engineering and hydrology professions.

Defining a natural flow regime for a highly modified river is not considered a straightforward task. Some have even queried whether it is possible in all cases. Reaching agreement on whether a 'natural flow regime' is that of a past state or whether it is one newly defined for its assessed potential within an existing physical setting and changing climate [6].

The most recent debates on this topic posit that non-static conditions also highlight the need for dynamic and process-based responses to bring about ecosystem resilience [6].

4 WHAT ABOUT THE SOCIO-ECONOMIC FOCUS? ECOSYSTEM SERVICES APPROACH?

The challenges of urban river restoration are significant. The volumes and timing of flows have been altered by urbanisation [6]. This can vary from the regulation of water courses (e.g. for water supply), to an increased rate of surface water run-off resulting and a shorter hydrologic response time due to the presence in urban areas of impervious surfaces and storm water drainage infrastructure. A feature of urban catchments is that water and habitat quality has diminished [7]. On account of human activities in the river corridor and across urban river catchments, flood risks and morphological modifications are more pronounced and in parallel, the lack of public open space made it even more difficult to apply the concept of full renaturalisation [1]. It is often obvious that the complete reversal of these impacts is either impossible or infeasible so the initial challenge is often in establishing what water management interventions or physical habitat changes are possible that can re-establish natural river process and sustain freshwater ecosystems [6]. Current thinking suggests that even partial river restoration in the urban environment can bring about myriad benefits to the urban environment through enhanced reintegration of the river as a valuable feature of the landscape [1].

Urban river restoration is a uniquely challenging undertaking as outlined in previous sections but one aspect is in its favour: it receives the support and increasing interest of the urban population in living on the borders of urban rivers. On the flip side of this, the available space for URR is limited [15].

The results of a study undertaken by A. Zingraff-Hamed *et al.*[15] show that urban river restoration comprises a wider range of goals and measures than its rural counterpart: it includes the restoration of riparian habitats, and integrates ecological and social goals (flood protection is an obvious inclusion here). This same study recommends the categorisation of URR projects into various typologies, based on the project goals. And while other restoration expects caution against specifying goals that are too narrow and fixed, the Zingraff-Hamed *et al.* study does allude to the need for some metrics by which past projects can be assessed and support can be leveraged for future restoration projects through improved communication [15]. The paper also highlights the need for clarity with the language surrounding restoration activities, particularly in relation to terms such as *ecological restoration*, which focuses on re-establishing a pre-existing state in terms of species composition and community structure, to *rehabilitation*, which focuses on re-establishing ecosystem processes, productivity, and services and highlights the frequent absence of the goal of enhancement of the social function of rivers in accepted definitions [15].

It seems clear that river restoration projects around the world are delivering advantages, but urban examples are less frequent. High property values, the relatively small sizes of land-holdings, and high density of human infrastructure (sewers, roads, railways) limit the available space, thus limit the restoration options available [15]. In urban areas, the scarcity of open spaces is a great drawback and attempts to reconnect them, where they do exist, must respect human needs for housing and safety. It is suggested that in developed areas, river restoration must be adapted and possibly reinterpreted by the authorities to designate parks or green corridors as flood-prone areas, and to prevent new occupation [1].

As our cities continue to evolve, there may be additional opportunities to increase the available space in our urban river corridors. Especially in Europe, we see a trend away from heavy industry inside cities with the result that many of these sites are now brownfields. Typically, as serviced sites, they are ready for redevelopment and are often seen as opportunities for economic stimulation of the economy. This also provides the opportunity for these urban quarters to rethink their relationship with the river, possibly giving it more space and embracing it as an ecological and aesthetic asset, rather than as a problem [2].

Another factor that influences the need for increased space for the river is that on account of intense urbanisation, the space now required to restore the river function in urban areas is even greater than in its previous natural condition [1]. This also relates to the earlier discussion on environmental flows and understanding the hydrology in the past, present and future.

The city must resolve many conflicts: the approach to the development of river corridors must be supportive of the river's ecological health, which is in turn beneficial to the city. There are conflicts and synergies. The higher value of riverside land can help fund/facilitate regeneration but the development of this land can make flooding worse and reduce the space available for ecological improvements and benefits. [2]

In these complex decision-making processes, the concept of ecosystem services can facilitate a more informed discussion and the services provided by improved flood control and greater access to nature in the urban environment are two that grab the headlines in recent times. The WFD provides for and supports partial restoration in cases where socio-economic considerations mean that full ecological restoration is unfeasible. Such water bodies can be formally designated as heavily modified water bodies (HMWB).

5 CONVENTIONAL FLOOD DEFENCE & RESTORATION

Conventional flood risk management techniques are characterised by structural measures (e.g. embankments or flood walls, reservoirs, and engineered channels) that limit river processes and cut them off from their floodplains, with negative environmental repercussions. The use of flood defences, by preventing the floodwaters from dissipating out across floodplains, can concentrate the flow and can increase flood risks both downstream and upstream [9]. It has further been suggested that the presence of structural flood defences has the effect of increasing development on urban floodplains as the risk of flooding is perceived as having been eliminated [9]. Modifying rivers in this way also limits the natural floodplain capacity to store floodwaters, improve water quality, provide habitat for invertebrates and fish during periods of high flow, and support a multitude of cultural services. '*As the importance of the hydrologic and ecological*

functions of floodplains becomes better understood and communicated, there are increasing calls to restore connectivity of floodplains, so that they actively flood' and policies are being adopted to encourage projects that both reduce flood risks and restore floodplain ecosystems, while acknowledging the social ecological context [9].

Considering climate change, structural measures also tend to be more fixed and not easily adapted [9].A recent article by Serra-Llobet *et al.*[8] examines four floodplain management projects for multi-benefits (located in Europe and the USA) that were selected for their well-documented successes both in flood risk reduction and ecological preservation or restoration. The findings were that interventions that both reduce flood risk and restore ecosystems are clearly possible and often cost-effective, and that they could be more widely implemented. Grizetti *et al.* [9] suggest that such projects could also bring about gains in status under the WFD although, as discussed above, consideration of the wider catchment issues and the extent to which self-sustaining river processes can be re-established would dictate the longer-term successes of such endeavours as true river restoration projects. Nonetheless, as protection from flooding and access to an enhanced natural environment are considered key ecosystem services for urban dwellers currently, even a partial restoration that enhanced these elements would be worth considering.

In Ireland the policy to ensure that flood risk management informs place-making by avoiding the siting of inappropriate development in flood risk areas is embedded in planning at all levels from national to local. The National Planning Framework contains such a policy objective in accordance with The Planning System and Flood Risk Management Guidelines for Planning Authorities"[17].In its remit under the Floods Directive, the OPW is also advocating the use of Sustainable Drainage Systems (SuDS) across entire catchments, and Land Use Management and Natural Flood Risk Management among other no-regret measures in the pillars of prevention and of preparedness and resilience (part of wider Government policy regarding climate action). The OPW has undertaken to work with partners at project level and at a catchment-level to identify any measures, such as natural water retention measures, that can have benefits for Water Framework Directive, flood risk management and biodiversity objectives [17].

6 TWO DUBLIN RIVER RESTORATION-ORIENTED PROJECTS

Two novel Dublin projects are outlined briefly below that have been guided by and reinforce the findings of the previously discussed literature above.

6.1 Camac Flood Alleviation Scheme

The background to this live project is as follows:

1) A long history of flooding in the urban centres along this river (severe flooding occurred in October 2011). Areas of pluvial and/or network flooding identified. River is not currently considered 'defended'.

2) Hard engineering options or 'structural measures' largely proposed by Eastern Catchment Flood Risk Assessment and Management Study (CFRAMS) but the designs failed the project Cost Benefit Assessment.

3) Irish understanding of WFD/hydromorphology has evolved since the CFRAMS: For a highly urbanised catchment and potentially designated heavily modified waterbody such as this, a river-restoration approach to flood risk management is worth investigating.

4) Flooding currently occurring in developed areas.

5) Location of flood risks currently not aligned with low vulnerability and uses: modelling suggested some historical residential areas potentially flood more frequently than riverside public parks.

This project commenced in 2019 and is led by DCC in partnership with South Dublin County Council and the OPW. A key output is a fully integrated catchment model (the river and its full catchment). Another key deliverable is the establishment of a baseline ecological condition as well as a baseline hydromorphological condition. A hydromorphology assessment was devised to facilitate the identification of restoration opportunities to manage flooding and to mitigate the impacts of urbanisation on current and future flood risks (fluvial and pluvial).The findings of the hydromorphology assessment and mapping of historical surface flow paths examined together with the full catchment model should facilitate a full catchment and river-restoration oriented response to existing flood risks and potentially a discussion about defining environmental flows. Any improvement in the management of urban run-off for flooding through natural means should include benefits for water quality. Key nature-based solution opportunities currently being investigated (to better reintegrate the river with the surrounding landscape and to support its natural processes while keeping people and property safe) include the reconnection of the river with its historical floodplains to the extent possible within the current constraints. The safe reinstatement of floodplains, or even partial restoration of floodplains combined with the siting of proposed complementary structural elements set back from the river channel, is a key aim. An obvious first step is the reimaging of existing riverside public parks in the river corridor. This also offers a potential role for privately-owned lands on existing and historical floodplains, with a particular focus on brownfield sites and the benefits of river and floodplain restoration in these areas, which will also be assessed in the selection of appropriate design options. The scheme must demonstrate a positive cost-benefit relationship, which will be another critical consideration. Residents are well informed regarding benefits of a restorative and ecologically friendly approach to the management of flooding despite recent flood events.

Currently anticipated limitations on restoration: Availability of land and land-ownership patterns; timescales relating to availability of land; costs (project design outputs are to be subject to CBA so large-scale land acquisition unlikely to be possible); Some hydromorphologically-indicated interventions (e.g. removal of bank protection) won't be possible until flows are adequately managed across the catchment (attainment of e-flows) and returned to a more natural range through sustainable means.

6.2 Planning the River Corridors of Dublin City

As one of the key limiting factors for urban river restoration is space, an exciting new project was undertaken in Dublin city

to establish (1) what additional space might be required for meaningful river rehabilitation, (2) what new planning policies were needed to support this long-term endeavour, (3) identification of co-benefits/constraints.

Various hydrological and geomorphological approaches were used to define and map the river corridors but the project found that significant development has taken place on our city's river floodplains/corridor over the centuries and the corridors were too large to be zoned in their entirety for river restoration or green infrastructure purposes. The exercise highlighted how the city's rivers were often cut off from their natural historical floodplains even in riverside public parks and other open space. It was found that available existing public open space was insufficient to permit full restoration of the city's rivers. It was also felt that where river restoration involved the potential conversion of a portion of historical floodplains lands in recreational use to floodplain use that this would require a partnership with local residents. The project also found that to fully assess the potential for each of the city's rivers to be meaningfully restored, further investigations and a detailed plan for each would be required in partnership with the community and stakeholders. The potential for rehabilitated rivers to support ecotourism given the wealth of built heritage on their banks was also noted. A portion of the Camac was featured in more in-depth study and some potential flagship restoration projects (including brownfield sites) were assessed in terms of their importance for WFD improvements, ecology, and NFM or climate resilience. The need to define and ultimately achieve environmental flows through catchment-wide measures was also highlighted as a potential constraint on the restoration potential of the Camac in the City Area. The importance of river restoration and outcomes from the project are reflected in the draft Dublin City Development Plan 2022-2028: a) the specification of geomorphologically indicated setback distances for development from the top of the riverbank; b) the rezoning of a section of a large industrial site from industrial to 'open space and green networks' that can permit the daylighting of the Camac River and the creation of floodplain storage; c) a stated commitment to complete detailed river restoration strategies/masterplans for the city's rivers that will bring together the many strands to maximise synergies; d) several Camac sub-catchments have been designated for growth in the draft Plan and opportunities to enhance river corridors are to be pursued as part of this. The elements and findings of this project are being examined to create a draft protocol to derive integrated, sustainable and achievable river and floodplain restoration plans for smaller urban rivers. The scoping of the next phases of this project is underway, taking account of the findings of the first phase and also the published literature.

7 CONCLUSIONS

Urban river restoration is a hugely complex undertaking with myriad cause and effect relationships to be understood and potentially difficult choices to make. The potential benefits are also of great significance as our cities continue to grow and the pressures on the natural environment are set to increase. As climate change adaptation/resilience and the need to support biodiversity for the socio-economic benefit of urban dwellers are key challenges facing governments and local governments, the evidence for floodplain and river rehabilitation (even partial restoration) is compelling. The derivation of short term and long term interventions and plans/policies requires a detailed examination and understanding of complex hydrological and hydraulic responses and consistent approaches to storm water management throughout river catchments, to enable the co-benefits and synergies of river restoration to be realised. A protocol to chart some of the outline steps could be a valuable contribution to urban river restoration.

REFERENCES

[1] Guimarães, Luciana & Teixeira, F.C. & Pereira, Jéssica & Becker, Beatriz & Oliveira, A.K.B. & Lima, A.F. & Verol, Aline & Miguez, Marcelo. (2021). The challenges of urban river restoration and the proposition of a framework towards river restoration goals. Journal of Cleaner Production. 316. 128330. 10.1016/j.jclepro.2021.128330.

[2] Lerner, D.N.; Holt, A. (2012) How should we manage urban river corridors? *Procedia Environ. Sci. 13*, 721–729

[3]Pinto, P. &Kondolf, G. M. (2020). The Fit of Urban Waterfront Interventions: Matters of Size, Money and Function. Sustainability. 12. 4079. 10.3390/su12104079.

[4] Veról AP, Bigate Lourenço I, Fraga JPR, Battemarco BP, Linares Merlo M, Canedo de Magalhães P, Miguez MG. River Restoration Integrated with Sustainable Urban Water Management for Resilient Cities. *Sustainability*. 2020; 12(11):4677.

[5] Kiedrzyńska, E., Kiedrzyński, M. & Zalewski, M. (2015). Sustainable floodplain management for flood prevention and water quality improvement. Nat Hazards, 76: 955.

[6] Whipple, A. A., &Viers, J. H. (2019). Coupling Landscapes and River Flows to Restore Highly Modified Rivers. Water Resources Research, 55, 4512–4532.

[7] Beechie, T. & Sear, D. & Olden, J. & Pess, G. & Buffington, J. & Moir, H. & Roni, P. & Pollock, M. (2010). Process-Based Principles for Restoring River Ecosystems. BioScience. 60. 10.1525/bio.2010.60.3.7.

[8] Serra-Llobet, A. & Jähnig, S. & Geist, J. &Kondolf, G.M. & Damm, C. & Scholz, M. & Lund, J. & Opperman, J. & Yarnell, S. & Pawley, A. & Shader, E. & Cain, J. &Zingraff-Hamed, A. & Grantham, T & Eisenstein, W. & Schmitt, R. (2022). Restoring Rivers and Floodplains for Habitat and Flood Risk Reduction: Experiences in Multi-Benefit Floodplain Management From California and Germany. Frontiers in Environmental Science. 9. 10.3389/fenvs.2021.778568.

[9] Grizzetti, B., Pistocchi, A., Liquete, C. *et al.* Human pressures and ecological status of European rivers. *Sci Rep* **7,** 205 (2017).

[10] Violin, C. & Cada, P. & Sudduth, E. & Hassett, B. & Penrose, D. & Bernhardt, E. (2011). Effects of Urbanization and Urban Stream Restoration on the Physical and Biological Structure of Stream Ecosystems. Ecological applications : a publication of the Ecological Society of America. 21. 1932-49. 10.2307/41416629.

[11] COWI, 2014. Support Policy Development for Integration of an Ecosystem Services Approach with WFD and FD Implementation. Resource document.

[12] Jakubínský, J., Prokopová, M., Raška, P., Salvati, L., Bezak, N., Cudlín, O., Cudlín, P., Purkyt, J., Vezza, P., Camporeale, C., Daněk, J., Pástor, M., & Lepeška, T. (2021). Managing floodplains using nature-based solutions to support multiple ecosystem functions and services. *Wiley Interdisciplinary Reviews: Water*, 8(5), e1545.

[13] Binder, W. &Göttle, A. & Shuhuai, D. (2015). Ecological restoration of small water Courses, Experiences from Germany and from Projects in Beijing. International Soil and Water Conservation Research. 3. 10.1016/j.iswcr.2015.04.004.

[14] Kondolf, G.M. (2011). Setting Goals in River Restoration: When and Where Can the River "Heal Itself"?. In Stream Restoration in Dynamic Fluvial Systems (eds A. Simon, S.J. Bennett and J.M. Castro).

[15] Zingraff-Hamed, A. & Greulich, S. & Pauleit, S. & Wantzen, K. (2017). Urban and rural river restoration in France: A typology. Restoration Ecology. 25. 10.1111/rec.12526.

[16] Bernhardt, E. & Palmer, M. (2007). Restoring Streams in an Urbanizing World. Freshwater Biology. 52. 738 - 751. 10.1111/j.1365-2427.2006.01718.x.

[17] Office of Public Works (OPW), 2021, The Review of the Flood Risk Management Plans

Cost of Retrofit Solutions to Improve the Heat Loss Indicator of Buildings

Paul Moran[1], Jamie Goggins[2]
[1]MaREI Centre, Ryan Institute & School of Engineering, College of Science and Engineering, National University of Ireland, H91 TK33 Galway, Ireland
[2]Energy Resilience and the Built Environment (ERBE) Centre for Doctoral Training, National University of Ireland, H91 TK33 Galway, Ireland

email: paul.t.moran@nuigalway.ie, jamie.goggins@nuigalway.ie

ABSTRACT: To install a heat pump in a residential home, is it recommended to improve the thermal efficiency of the building fabric through the installation of various retrofit measures such as wall insulation, roof insulation, etc. To obtain a grant from the Sustainable Energy Authority of Ireland to install a heat pump, a building fabric is required to achieve a heat loss indicator of 2 W/Km^2 or better. This paper examines the cost of retrofit solutions for buildings constructed prior to the introduction of energy performance regulations in Ireland to meet the heat loss indicator target of 2 W/Km^2 or better with the implications of the results on the design of building retrofits discussed. The results highlight that for detached, semi-detached and terraced houses, it is possible to achieve the heat loss indicator performance targets without the need to install floor insulation. For bungalow houses, the low wall to floor ratio and large floor area of the houses means that it can be more difficult to achieve the heat loss indicator performance targets without installing floor insulation.

KEY WORDS: Building Retrofit, Heat Loss Indicator, Energy Efficiency, Retrofit Costs, Heat Pump.

1 INTRODUCTION

Ireland's Climate Action Plan [1] has set an ambitious target, of retrofitting 500,000 dwellings to a B2 equivalent Building Energy Rating (BER) standard by 2030, in addition to the installation of 400,000 heat pumps in existing homes. This will require thousands of homeowners in Ireland to retrofit their homes. Many barriers exist though for homeowners to improve the energy efficiency of their home with the cost required to retrofit among the most prominent [2]. Cost estimates from 2014 found retrofit packages to achieve BER standards ranging from A2-C2 depending on the typology and construction year of homes in Ireland could range from €5,000-€75,000 [6].

To help address the cost barrier to retrofitting, the Irish government provides grants to private homeowners to upgrade the energy efficiency of their home. The grant system is managed by the Sustainable Energy Authority of Ireland (SEAI). The grant system provides varying levels of economic aid for building fabric, heating system and renewable energy measures depending on the construction year of the home, the typology of the home, the socio-demographic and socio-economic status of the building occupants, and the management of the retrofit upgrade works [3].

As the generation of electricity in Ireland is expected to be decarbonised [1] and the efficiency of a heat pump heating system generally greater than other heating appliances available (e.g. boilers, stoves, etc.) [4], heat pumps are expected to be a key measure introduced into buildings as Ireland transitions to a low carbon economy. Homeowners can access grants to upgrade their heating systems to heat pump based heating systems [3].

Domestic heat pump heating systems can operate in a more efficient manner in a dwelling with low fabric and ventilation heat losses as lower space heating distribution temperatures are required [5]. Therefore, to obtain a grant for a heat pump system from SEAI, a dwelling is required to achieve a specific heat loss standard. A dwelling must achieve a Heat Loss Indicator value of 2 W/Km^2 or better [5]. The Heat Loss Indicator (HLI), which is based on the total of the fabric and ventilation loss for a dwelling divided by the total floor area, is calculated by DEAP [4]. DEAP is the Domestic Energy Assessment Procedure which is the assessment procedure used in Ireland for determining the energy performance certification of a dwelling, also known as Building Energy Ratings [4].

Unlike early construction practices in Ireland, building elements are now required to meet specific thermal fabric efficiency standards, as specified in Part L of the Irish energy performance building regulations [6,7]. This has resulted in increasing levels of insulation materials being used in the construction of building elements since the first draft of building regulations introduced in 1976 and 1981 [6]. The 2016 Census revealed there are over 2 million housing units in Ireland with 1.7 million occupied [8]. The Irish housing stock mainly consists of single-family dwellings (over 80%). In 2016, 42% of all occupied dwellings in Ireland were detached houses while 12% were apartments. 42% (figure based on houses built up to 1980) of the occupied building stock was constructed prior to the introduction of building regulations.

The aim of this paper is to determine what package of retrofit measures can achieve the fabric and ventilation loss requirements to receive a grant for a heat pump for common typologies constructed in Ireland prior to the introduction of the first energy performance regulations. Furthermore, the cost of retrofitting to improve the HLI standards of the residential buildings is also examined.

2 METHODOLOGY

2.1 Residential Typologies

The TABULA study identified 34 typical Irish house and apartment typologies [6]. The 34 Irish dwelling typologies are

spread across 10 age bands and include detached, bungalow, semi-detached and terraced houses, and an apartment. The 34 typologies include a range of building wall types including

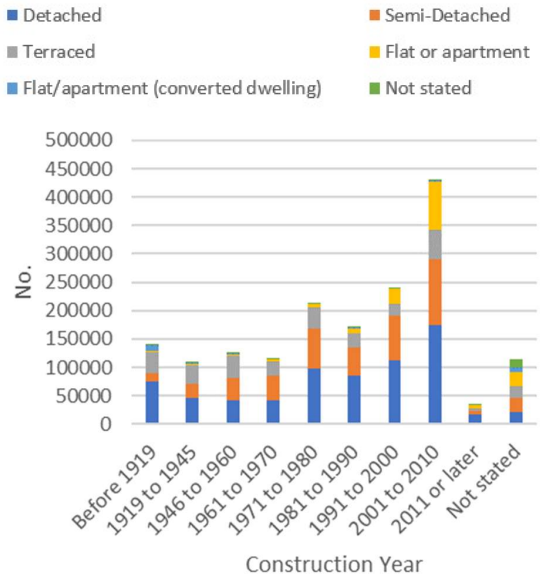

Figure 1. Construction year and typology of housing constructed in Ireland [8].

stone, mass concrete, solid brick, hollow block, cavity and timber frame with insulation levels varying from none to NZEB standards. The 10 construction age bands were identified based on distinct construction types prior to building regulations in 1976 and subsequent changes to building regulations. This paper focuses on five external wall types identified prior to the introduction of building regulations; stone wall, 225mm solid brick wall, 330mm solid brick wall, mass concrete wall and hollow block wall. Characteristics of the typologies (wall area, floor area, U-values, etc.) are taken from the TABULA Webtool [9] which provides all the building data used for developing the results of the TABULA study in Ireland [6].

For this paper, houses identified as end terrace in the TABULA study are classified as semi-detached. The TABULA study includes 11 stone wall, 225mm-330mm solid brick wall, mass concrete wall and hollow block wall typologies. However, it does not include a detached, bungalow, semi-detached and terrace typology for each wall type. For example, there is a detached and semi-detached typology for a stone wall building constructed in 1900. To include a detached, bungalow, semi-detached and terrace typology for each wall type, two different approaches were used. If a typology was missing for a specific wall type, the dimensions of the missing typology are taken from a typology in the prior or proceeding age band. The building fabric and heating system characteristics of the existing typology case studies are used. For example, as mentioned above, a detached and semi-detached typology for a stone wall building constructed in 1900 are included in the TABULA study. The dimensions of the bungalow case study from 1900-1929 are used to represent a bungalow house pre-1900. The building fabric and heating system characteristics for the stone wall detached house constructed in 1900 are assumed the same for the bungalow case study.

The second approach is applied to semi-detached and terraced houses. If a semi-detached typology exists, an area of wall representing the party wall is removed to represent a terraced house. In the scenario where a terrace typology exists, an area of wall representing a party wall is added. Overall, there are 20 typologies included as part of this study. The pre-retrofit U-values for the building elements are provided in Table 1 for each wall type.

2.2 Retrofit Packages

Three retrofit packages are applied to the 20 typology buildings, referred to as 'Basic', 'Intermediate' and 'Advanced'. The 'Basic' retrofit package introduces roof insulation, external wall insulation, double glazed uPVC windows and doors, and passive wall vents as shown in Table 2. The 'Intermediate' package of retrofit measures increases the level of external wall insulation and introduces demand control ventilation. The 'Advanced' package of retrofit measures introduces floor insulation, triple glazed uPVC windows and doors and heat recovery ventilation.

Table 1. U-Values (W/m^{2}K) of building elements pre-retrofit

	Building Element				
Wall Type	Wall	Roof	Floor	Windows	Doors
Stone Wall	2.1	0.68	0.65-0.80	4.8	3
Solid Brick-225mm	2.1	0.68	0.69-0.84	4.8-5.7	3
Solid Brick-325mm	1.64	0.68	0.61-0.79	4.8-5.7	3
Mass Concrete	2.2	0.68	0.61-0.84	4.8-5.7	3
Hollow Concrete Block	2.4	0.68	0.69-0.79	4.8-5.7	3-5.7

Table 2. Retrofit measures applied to the building elements

		Retrofit Package		
Building Element	Retrofit Measure	BAS	INT	ADV
Roof	MW	250mm	250mm	250mm
Wall	External EPS Insulation	150mm	200mm	200mm
Windows & Doors	uPVC	DG	DG	TG
Floor	Suspended floor insulation-MW and/or Solid floor insulation, EPS	-	-	100mm
VENT		PWV	DCV	HRV

Abbreviations

ADV-Advanced
BAS-Basic
DCV-Demand Control Ventilation
INT-Intermediate
HRV-Heat Recovery
MW (λ: 0.04 W/mK)

DG-Double Glazed (λ: 1.2 W/m^{2}K)	PWV-Passive Wall Vents
EPS-Expanded polystyrene insulation (λ: 0.032 W/mK)	TG-Triple Glazed (λ: 0.7 W/m^{2}K)
	VENT-Ventilation

The retrofitted building elements meet the minimum U-value requirements for building retrofits [7]. Furthermore, it is assumed that the buildings achieve the minimum level of air-tightness recommended to introduce mechanical ventilation systems as part of a retrofit [10].

2.3 Cost & Grant Information

The costing of retrofit measures was collected in collaboration with SCSI (Society of Chartered Surveyors Ireland), KSN Construction Consultants and a number of material suppliers and contractors in the building sector. This market research was carried out between February 2021 and July 2021. Regarding the costing information, (i) costs are based on a traditional 3-bed house as referenced in the SCSI House Reinstatement Guide, (ii) costs would not apply for period/ protected houses, (iii) costs are based on a supply and fit rate, (iv) all costs are budget only, (v) costs are budget and do not allow for regional variations and (vi) cost exclude VAT.

As part of the roof retrofit works, roof ventilation tiles are included to provide sufficient airflow to the attic. The water tank is insulated and half the attic floor area is transformed into a platform for storage with OSB boards. The external wall insulation is finished with a wet render finish and paint. Aluminium window sills are also accounted for.

As part of the floor retrofit works, it is assumed half the previous floor surface is reinstated with the other half requiring a new floor finish. Floor screed is also included as part of the upgrade works for solid floor insulation. An air-tightness membrane is included as part of the works for suspended timber floors.

The current level of grants available for retrofit measures are sourced from SEAI [3]. The levels of grant aid currently available depends on the construction year of the home, the typology of the house, the socio-demographic and socio-economic status of the building occupants and the management of the retrofit upgrade works [3]. As part of this paper, the grants available for homeowners who use a One Stop Shop retrofit service [2] are included. Additional costs the One Stop Shop service can charge including project management fees, home energy assessments, etc. are not accounted for.

3 RESULTS

Figure 2 shows the average HLI of the typologies for each of the retrofit packages. The error bars highlight the maximum and minimum HLI achieved. For the 'Basic' retrofit package, the average HLI ranges from 2-2.8 W/Km^2. The 'Intermediate' retrofit package achieves an average HLI ranging from 1.5-2.2 W/Km^2 while the 'Advanced' Retrofit Package achieves an average HLI ranging from 0.9-1.4 W/Km^2. The average HLI of the existing buildings are 5.0 W/Km^2 for detached houses, 5.5 W/Km^2 for bungalow houses, 4.3 W/Km^2 for semi-detached houses and 4.1 W/Km^2 for terraced houses, respectively.

40 of the 60 retrofit buildings achieve a HLI of ≤ 2 W/Km^2. The technical guidance also allows for a HLI between 2 and 2.3 W/Km^2 where it is not economically feasible to upgrade the home further [5]. A HLI ≤ 2.3 W/Km^2 can be accepted where the following requirements are met:

- Maximum exposed wall U-value of 0.37 W/m^{2}K
- Maximum roof U-value of 0.16 W/m^{2}K or 0.25 W/m^{2}K where not accessible (e.g. flat roof or rafters)
- Maximum Window U-value of 2.8 W/m^{2}K* (and double glazed)
- Maximum Adjusted Infiltration Rate of 0.5 ac/h

52 of the 60 case study buildings achieve a HLI ≤ 2.3 W/m^2 while also meeting the additional requirements. Eight of the case study buildings achieve a HLI > 2.3 W/m^2. Seven of the eight buildings that achieve a HLI > 2.3 W/m^2 are bungalows. Seven of the nine buildings that fail to achieve a HLI ≤ 2.3 W/m^2 received a 'Basic' retrofit package with the remaining two receiving an 'Intermediate' retrofit package.

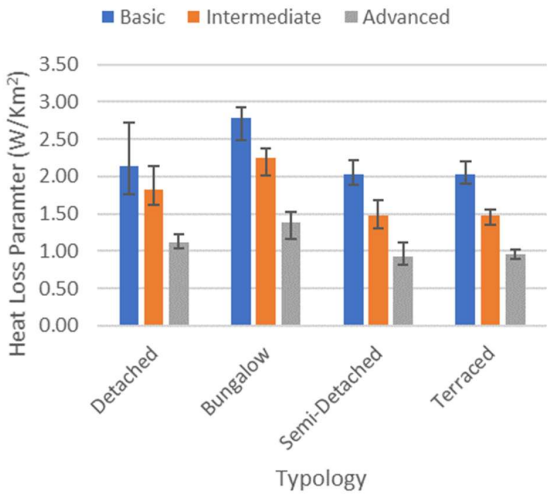

Figure 2. Heat loss indicator (HLI) of the typologies for each of the retrofit packages.

Figure 3 gives the average overall cost of each retrofit package for the four typologies. The average cost for the 'Basic' retrofit package ranges from €21,200 for terraced houses to €41,600 for detached houses. The error bars highlight the maximum and minimum overall cost. On average, an additional €5,400 is required for the 'Intermediate' retrofit package and €16,200 for the 'Advanced' retrofit package relative to the 'Basic' Package. The advanced retrofit package for a terraced house costs, on average, €6,100 less than the 'Basic' retrofit package for a detached house.

Figure 4 gives the average overall cost of each retrofit package for the four typologies accounting for the available grants from SEAI. The level of grant available ranges from €8,100 to €20,100 depending on the retrofit package and the typology. The level of grant covers 23%-65% of the cost for the retrofit packages. Similar to the results of Figure 3, an 'Advanced' retrofit package for a terraced house costs less on average compared to a 'Basic' package for a detached house. After accounting for grants, the 'Advanced' retrofit package for

a bungalow also costs less than the 'Basic' package for a detached house.

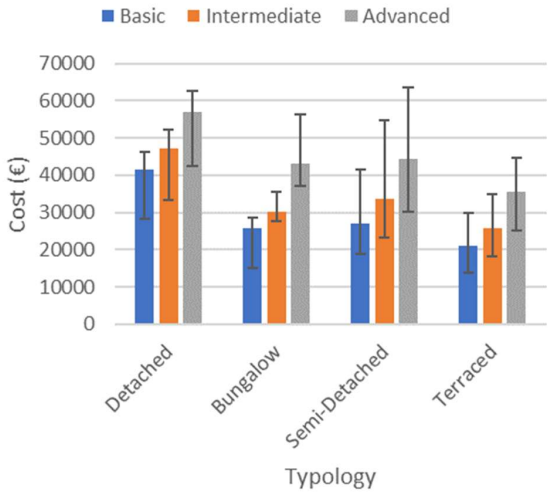

Figure 3. Cost of the retrofit packages for each of the typologies.

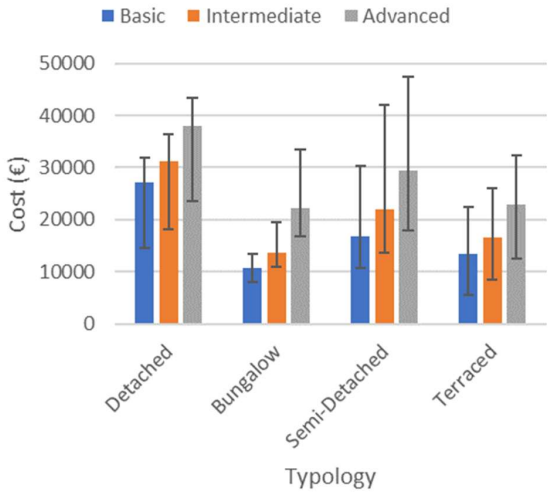

Figure 4. Cost of the retrofit packages including grants for each of the typologies.

4 DISCUSSION

52 of the 60 case studies achieve a HLI that meets the requirements for a heat pump. Bungalow houses are the main typology that do not achieve the HLI performance targets. The low wall to floor ratios and large floor areas of bungalow houses result in many of the retrofit packages without floor insulation not being able to achieve the HLI targets.

Given the larger surface areas of building elements in detached houses, the cost of retrofitting detached houses is shown to be larger than other typologies. For homes built before 2011, for the retrofit measures considered and with the retrofit project managed by a One Stop Shop Service, grant aid worth up to €20,100, €16,900 and €13,100 is available for detached, semi-detached and terraced houses, respectively. For the 'Advanced' retrofit packages which all achieve the HLI targets, on average 35-38% of the cost for detached, semi-detached and terraced houses is covered by the retrofit grants available for roof insulation, wall insulation, floor insulation, windows and doors, and mechanical ventilation. For bungalow houses, 48% of the average cost for the advanced retrofit package is covered by the SEAI grant. Therefore, while a larger percentage of the cost is covered for bungalow homes, bungalow homes are more likely to require floor insulation to meet the HLI requirements. The introduction of floor insulation as part of a retrofit solution will cause more disruption for the homeowners. Alternatively, external wall insulation greater than 200mm thick could achieve the HLI targets. For homeowners who manage the retrofit project themselves, SEAI do not provide funding for floor insulation, windows and doors, and mechanical ventilation. Homeowners can potentially lose out on €8,400-€10,600 worth of economic aid.

The retrofit strategy for walls examined as part of this paper focused on external wall insulation. However, external wall insulation may not be an option for some homeowners with these types of facades as they may live in protected structures or do not wish to lose the architectural value of the property such as those with solid brick facades. As installing internal insulation greater than 100mm may not be possible from a practical standpoint (loss of internal floor area, application of insulation, hygrothermal performance of wall, etc.), installing floor insulation will be required to compensate for the lower U-values of the walls to attempt to achieve the HLI targets. However, examining internal insulation as part of a retrofit strategy for achieving HLI targets is outside the scope of this paper.

4.1 Study Limitations

While the study provides useful costing information for various retrofit packages, the costing information is based on market research carried out between February 2021 and July 2021. Inflation increases since then has seen the rise in construction costs [11]. Therefore, the costs included as part of this paper are expected to be less than current market rates. In addition, the grant results presented in this paper focus on the grants available for homeowners who rely on a One Stop Shop service to manage the upgrade works.

5 CONCLUSION

This papers presents the HLI and cost results of 60 retrofitted stone wall, brick wall, mass concrete and hollow block wall residential buildings built prior to the introduction of energy performance regulations. The results highlight that for detached, semi-detached and terraced houses, it is possible to achieve the HLI performance targets to receive a grant for a heat pump without the need to install floor insulation. For bungalow houses, the low wall to floor ratio and large floor area of the houses means that it can be more difficult to achieve the HLI performance targets without installing floor insulation.

For homeowners intending to install a heat pump as part of a building retrofit in Ireland through a One Stop Shop retrofit service, they will have to invest on average between €13,400 to

€28,000, depending on the typology of their home, to meet the current HLI targets.

ACKNOWLEDGMENTS

This optional section contains acknowledgments. The authors would like to acknowledge the financial support from the European Union's Horizon 2020 research and innovation programme under grant agreement no. 839134, and support from the Sustainable Energy Authority of Ireland (SEAI) through the HEAT CHECK project (grant agreement 19/RDD/492).

REFERENCES

[1] DECC, CLIMATE ACTION PLAN 2021 Securing Our Future, Department of the Environment, Climate and Communications, 2021.

[2] O. Mcginley, P. Moran, J. Goggins, Key considerations in the design of a One-Stop-Shop retrofit model, in: Civ. Eng. Res. Irel. 2020, 2020: pp. 354–359.

[3] Sustainable Energy Authority of Ireland, SEAI-Home Energy Grants, (n.d.). https://www.seai.ie/grants/home-energy-grants/#comp00005b3cd2ca000000b2ba5132 (accessed November 2, 2018).

[4] SEAI, Domestic Energy Assessment Procedure (DEAP) Version 4.2.2 Ireland's official method for calculating and rating the energy performance of dwellings, Sustainable Energy Authority of Ireland, 2020.

[5] SEAI, Better Energy Homes Technical Assessment Process for Heat Pump System Grants, Sustainable Energy Authority of Ireland, 2022.

[6] M. Badurek, M. Hanratty, B. Sheldrick, D. Stewart, Building Typology Brochure Ireland, TABULA, 2014.

[7] DHPLG, Part L Building Regulations 2019 Technical Guidance Document: Conservation of Fuel and Energy-Dwellings, Department of Housing, Planning and Local Government, 2019. https://www.housing.gov.ie/sites/default/files/publications/files/tgd_l_dwellings_2019.pdf.

[8] Central Statistics Office, Ireland Census of Population 2016: Profile 1-Housing in Ireland, (2018). https://www.cso.ie/px/pxeirestat/Database/eirestat/Profile 1 - Housing in Ireland/Profile 1 - Housing in Ireland_statbank.asp?SP=Profile 1 - Housing in Ireland&Planguage=0 (accessed January 10, 2019).

[9] T. Loga, J. Calisti, B. Stein, TABULA WebTool, (2017). https://webtool.building-typology.eu/?c=all#bm (accessed May 4, 2022).

[10] NSAI, Standard Recommendation S.R. 54:2014 Code of practice for the energy efficient retrofit of dwellings, National Standards Authority of Ireland, 2014.

[11] SCSI/PwC, SCSI/PwC Construction Market Monitor 2022, The Society of Chartered Surveyors Ireland (SCSI) and PwC, 2022. https://www.pwc.ie/reports/scsi-pwc-construction-survey-2018.html.

Carbon Footprint of an Irish University, Scope 3 emission factors and COVID-19 trends

Thomas_Adams[1,2], Eoghan Clifford[1,3,4], Stephen Canny[1], Jamie_Goggins[1,2,3]
[1]School of Engineering, National University of Ireland Galway, University Road, Galway, Ireland
[2]MaREI, the SFI Research Centre for Energy, Climate and Marine, National University of Ireland, Galway
[3]Ryan Institute, National University of Ireland, Galway
[4]NexSys, the SFI Next Generation Energy Systems Partnership Programme, National University of Ireland, Galway
email: t.adams4@nuigalway.ie, eoghan.clifford@nuigalway.ie s.canny5@nuigalway.ie, jamie.goggins@nuigalway.ie

ABSTRACT: Many universities have not yet measured their carbon footprints. With Ireland's Government's increasing climate ambition under the newly constructed carbon budgets, all sectors of the Irish economy will soon be required to report on and reduce greenhouse gas emissions. Scope 3 is the most neglected area of emissions measurement, even though on average it accounts for more than 70 percent of an organisation's carbon footprint. According to the Greenhouse Gas Protocol (WRI), scope 3 emissions are attributable to sources such as purchased goods and services, waste, business travel, student and staff commuting, water usage, etc. Organisation specific emission factors, or national values, for many of these areas do not exist, making the accurate calculation of scope 3 emissions difficult. This paper compares methodologies for calculating scope 3 emissions for (i) commuting and (ii) purchased goods and services, two of the largest portions of an organisation's carbon footprint. For purchased goods and services, the main suppliers were contacted to open a discussion about supplier specific emission factors. For commuting, a survey was used to capture a more accurate dataset of emissions. The results show that sector emissions for goods and services can be up to 46.5% lower through the adoption of supplier specific emission factors when compared to global sector emission factors, while increasing the accuracy of commuting emission calculations resulting in a 34% increase. These large margins show the importance of accurate emissions reporting, especially in scope 3.

KEY WORDS: Carbon Footprint; COVID-19 Impact; Scope 3 Emissions; Supplier Specific Emission Factor.

1 INTRODUCTION

Society is set to rapidly decarbonise over the coming decades. Between COP26, IPCC reports, EU agreements and legally binding decarbonisation commitments by the Irish Government, it's clear now that this pathway has been agreed upon. Dublin and Cork have both been selected as part of the EU's 100 Climate-Neutral and Smart Cities by 2030 Mission [1] and there is an opportunity for universities to be leaders in this transition.

Society must follow science-based pathways for this decarbonisation, although before these pathways can be fully laid out, challenges must be addressed in the measuring of Greenhouse Gas (GHG) emissions. GHG emissions are grouped into three scopes, and while a lot of progress has been made in the measurement of scope 1 and 2, progress is still needed in scope 3. Scope 1 and 2 emissions refer to the direct burning of fossil fuels and purchased electricity, respectively. Scope 3 emissions cover a wide range of other potential sources and currently, as per the GHG Protocol, which is the most used carbon counting standard, estimating and reporting scope 3 emissions are optional [2]. Most organisations omit counting any scope 3 emissions [3], [4], even though for the organisations that include scope 3, it is usually the largest portion of emissions by far [5], [6]. There is a need for a standardised methodology for calculating these emissions, particularly for the categories of purchased goods & services and capital goods [7]–[10].

For scope 1 and 2, many countries now have national emission factor databases [11], [12], which allow organisations to accurately capture the GHG emissions associated with these sources. Scope 3 contains 15 different categories, each relating to a different part of the value-chain. Emission factors are available for some categories, whether these are regional, national, or international databases depends on the category. There are various tools available online to help organisations to gather an approximate estimate of their emissions [13], but these can have severe inaccuracies. This study utilised one of these tools for scope 3 categories 1 and 2, which refer to purchased goods and services and capital goods. The tool in question is the GHG Protocol's Scope 3 Evaluator [14]. The tool was used to give an estimate of these emissions, which can then be compared with more accurate methods of calculation. It was deemed more important to obtain an approximate estimate of these emissions even if there is a degree of inaccuracy present, so that steps can be taken towards both increasing the accuracy of the calculation method and decreasing emissions.

This paper uses NUI Galway as a case study for carbon footprint calculation methods, comparing quicker methods to more accurate methods and overall highlighting the importance of scope 3 emissions. For an organisation with a full-time equivalent of over 18,600 students and 2,300 staff, most scope 3 emissions can be tracked from two data sources. Firstly, the university's financial accounts track the spending on the following emission categories: Purchased Goods & Services, Capital Goods, and Business Travel. Secondly, a survey of staff and students gathered data for calculating the commuting emissions of the organisation. This paper aims to highlight the importance for universities to include scope 3 categories 1 (purchased goods & services), 2 (capital goods), 6 (business travel), and 7 (commuting) and present a proposed methodology to begin counting these emissions. It will also present results for the change in emissions between 2019 and 2020, analysing the impact of the COVID-19 pandemic restrictions on each emission category.

2 LITERATURE REVIEW

2.1 History of Carbon Footprint

A literature review on carbon footprint research was conducted based on 7,450 articles from between 1992 and 2019 [15], which found the year 2008 is the main node in carbon footprint research. This is backed up by the term carbon footprint being defined in 2008 [16]. Studies from 2009 and 2011 mention the need for standards and guidelines for carbon footprints, discussing the importance of Life cycle assessments (LCA) [17] & [18]. In addition, it is worth noting that carbon footprint research is showing a trend of merging with Economics research [15]. This paper is concerned with the need for standards and guidelines for carbon footprints, the importance of LCAs and the merging of carbon accounting with economic accounting.

2.2 Importance of Suppliers and Supply-Chain Emissions

As mentioned above, the GHG Protocol Corporate Standard is one of the most used emission calculation standards globally. This standard is split into 3 scopes, and only scope 1 and 2 are required to be reported on by this standard. As mentioned above also, scope 1 & 2 emissions are easier to calculate, even though usually they account for less emissions than scope 3 combined. A 2009 study found that on average, more than 75% of an industry sector's carbon footprint is attributed to scope 3 [5]. The results show that enterprises can capture a large portion of their total upstream carbon footprint by collecting full emissions information from only a handful of direct suppliers, and Scope 3 footprint capture rates can be improved considerably by sector-specific categorisation. Another study looking at the UK's supermarket sector found that 75-90% of a food product's carbon footprint occurs upstream of the point of sale, i.e. Scope 3 [6]. A methodology that has been emerging in recent years is to calculate emissions associated with purchased goods and services through a combination of LCA for appropriate products and spend based emission factors to estimate emissions for the remaining supplier base [7]–[10]. For LNG supply chains, it was found that supplier specific calculations of GHG emission intensities are estimated to be 30−43% lower than other analyses employing national or regional average emission profiles [10]. Suppliers have an important role to play in scope 3 emissions. In an ideal world, suppliers would provide LCAs of their products/services or at the least to an emissions intensity per € spent on their product/service. This would allow for carbon to be transferred from supplier to buyer, while money is transferred in the opposite direction.

2.3 University Carbon Footprints

Looking at the literature on carbon footprints in Higher Education Institutions (HEIs), there have been a few recent publications comparing HEI carbon footprints [3], [4], [19]–[21]. Findings show there is limited consistency between them [3] with a wide range of CO_2 per student when comparing from HEIs across the globe [4]. Some of the reasons for this include a lack of standardisation in time metric (year, semester), functional unit (student, employee, area) and data collection boundary (scope 1, 2, 3). Most of these carbon footprint reports do not include the purchased goods and services or capital goods categories, with only slightly more coverage of emissions from commuting and business travel. The general trend seen is that carbon footprints are improving over time. However, the methodology requires further improvements and solutions to several challenges, including the definition of representative emission sources, the creation of a robust emission factor database and the development of tools/methodologies that cover all the needs of this type of organisation, especially emissions associated with scope 3. A number of tools are being developed to aid HEIs with their carbon footprints [13]. However, none of these include the full scope 3 categories of purchased goods & services, capital goods, business travel and commuting.

2.4 COVID-19 Impact Studies

There is relatively limited literature on the impact of COVID-19 on carbon emissions. However, in Italy it was found that the average Italian's carbon footprint was 20% lower than the previous national average during the lockdown period [22]. A study of a UK university, results showed that the overall carbon footprint of the university decreased by almost 30% [23].

3 METHODOLOGY

3.1 Introduction

This methodology followed in this study saw two phases. First, a baseline carbon footprint measurement was completed which followed the most widely used carbon accounting standard globally, the GHG Protocol Corporate Standard. In this phase of the project, accuracy was somewhat sacrificed for speed in three of the scope 3 emissions categories (purchased goods & services, capital goods and commuting). This laid the basis for phase two of the methodology which was to pursue more updated calculation methods for these categories and compare the results.

3.2 Baseline Carbon Footprint

A baseline carbon footprint was calculated for 2017, as this was as far back that data could be collected to capture all scopes. The full methodology followed in creating this baseline is published on the NUI Galway website [24]. Full scope 1 and 2 emissions were calculated by the Buildings Office as per the ISO50001 Energy Management System [25]. For scope 3, the categories included are as follows: category 1: Purchased Goods & Services; category 2: Capital Goods; category 3 Fuel and energy related activities; category 5 Waste; category 6 Business Travel; category 7 Commuting; and category other Water. Other scope 3 categories were deemed negligible or irrelevant for a university as an educational institution. The SEAI provide emissions factors for scope 1, scope 2 and category 3 of scope 3 emissions [11]. In the baseline calculation, the UK Governments conversion factors for company reporting of greenhouse gas emissions were used for scope 3 categories 5 (waste), 6 (business travel) and 7 (commuting) and other (water) [12], as there were no Irish databases as granular or up to date. Emission factors from the GHG Protocol's Scope 3 evaluator were used for scope 3 categories 1 (purchased good & services) and 2 (capital goods) [14]. The emission factors used in the baseline calculation are known as global sector emission factors and aim to estimate the intensity of emissions from broad sectors in the global economy, such as construction. These are not very accurate

when applied to a specific organisation but were used in this baseline calculation to produce a guide from which to strive for more accurate and granular emission factors.

3.3 Supplier Specific Emission Factors

With the baseline measured, phase two of the methodology involved updating the calculations for the categories mentioned. Categories 1 (purchased goods & services) and 2 (capital goods) were grouped under the same heading because the data came from the same source, which is the university's financial accounts and will be collectively referred to as PG&S from here on. The method pursued to increase the accuracy in PG&S was to engage with the university's largest suppliers, requesting from them their carbon footprint. If a supplier had a full GHG emissions inventory, a supplier specific emission factor (SSEF) could be calculated by dividing the company's carbon footprint by their revenue, giving a carbon intensity per € spent on their products/services. This was the lowest level of accuracy to be accepted as an official SSEF, but it could get more accurate. The ideal solution would be for suppliers to provide LCAs for all products/services, giving an exact, cradle-to-grave figure for carbon associated with a certain product/service. The industry is some ways off this, however, and as is the financial accounting system used at NUI Galway. There has been work in recent years on the financial accounting system to allow for the inclusion of carbon emission factors, which would give the accounting system the ability to also account carbon alongside finances. However, currently this can only be done at the level of what's called a product code. The trail that a user of this system follows when purchasing a product/service is as follows: General Ledger code, Product Code, Supplier, Product Description. An example of this would be COMP, COMP202, Dell Inc, Latitude 5510. So, COMP is a General Ledger code under which there are several product codes such as COMP202. COMP202 is a product code which refers to a windows laptop. Dell Inc is the selected supplier, and the product description is up to the user of the system to fill in as accurately as possible, where the example has put the laptop model "latitude 5510". Considering this hierarchy, the ideal solution as mentioned would be to insert an LCA emissions figure after the product description as given by the supplier. In the baseline calculation, general ledger codes were used with the global average emission factors, for an initial estimate. The goal here is to move from the general global average EF method towards the supplier or product specific LCA values. To achieve this, there needs to be cooperation between the supplier, the buyer, and the accounting system.

3.4 Commuting Survey 2021

The baseline commuting emissions were calculated based off data from a 2015 commuting survey completed by NUI Galway staff and students. Gathering data for a carbon footprint was not factored into the creation of this survey. Thus, some assumptions had to be made. The distance of a commute being one, as the survey asked the distance of commutes in ranges such as 5-10kms or 10-20kms. To calculate a final distance figure, the mean of these distances was used (e.g., 7.5km and 15kms). A second average used was the emission factor for cars. The survey did not specify the fuel type or engine size when a respondent indicated that they drove, so an average emission factor for all car sizes and fuel types was used, excluding electric as a fuel type as this was deemed minimal at this stage. An updated commuting survey was circulated to staff and students in January 2022. The survey focused on travel habits to and from NUI Galway before the COVID pandemic, during the pandemic, in January 2022 and remote working preferences. Respondents completed details including modal choice for commuting (the number of times a particular mode was used per week was ascertained) and distance travelled. In terms of vehicle used respondents could choose bus, train, private vehicle, motorcycle, electric bicycles and scooters, bicycles, and walking. Multi-modal journeys were also tracked. In relation to private cars detailed of the age of the car, engine size and type (i.e. petrol, diesel, battery electric, plug-in hybrid or full hybrid). The survey comprised a detailed set of other questions which are not the focus of this study. Survey response from 1359 students (out of 18,000 students) and 777 staff (out of 2,500 staff). Emissions calculations were based on the survey responses and emission factors from the EcoInvent v3.8 database 2021 and were extrapolated to the full staff and student cohort.

4 RESULTS

4.1 Introduction

The results are in three sections. Firstly, findings from engaging with suppliers on emissions information and the impacts of this on the institutions carbon footprint. Secondly, changes in commuting emissions from the updated commuting survey. Thirdly, changes in the carbon footprint are shown comparing 2017-2019 (pre-covid) with 2020-2021 (covid).

4.2 PG&S Analysis: Scope 3 Categories 1 & 2

Firstly, this section will show a breakdown of the emissions associated with PG&S by general ledger code as per the baseline calculation method, in Figure 1. This shows the four general ledger codes that carry most of the emissions. These codes relate to the following sectors: BUILD to Building, Estates and Facilities Management; COMP to Computing, IT and Telecommunications Systems and Services; SERVE to Services - Professional/General; and LAB to Laboratory Equipment, Supplies and Services. Suppliers were contacted from all sectors with particular attention to the four mentioned above. Results from the first round of engagement reflected the findings of this paper. This being that most organisations had no emissions data and of those that did, all reported scope 1 and 2 emissions but most did not include scope 3. Nine suppliers replied in total, and the coverage of scopes by these suppliers is shown in Table 1. These were significant suppliers however and they amount to 9.7% of the expenditure from 2017-2021 and 5.9% of the entire emissions from 2017-2021, 12.4% of the PG&S emissions. There is one ideal case here also where a supplier has full LCAs completed for each individual product. However, as most of the suppliers did not include full scope 3 emissions, the resulting emission factors will not capture the full scope of the suppliers' emissions. This is reflected in Table 2. This table shows the results from calculating supplier specific emission factors using the data provided as it was. There is a correlation between the drop in emission factor and the amount of data provided, where the less info given the more the emission factor dropped by. The drops in emissions are calculated for all five years of data, with a drop of 15.15 $ktCO_2e$

found over the 5 years. The total emissions for these nine suppliers dropped from 18.6 $ktCO_2e$ to 3.4 $ktCO_2e$, showing an 82% reduction, a reduction of 10.1% in the entire PG&S category, and a 4.8% reduction in the entire carbon footprint over 5 years. Most of these emission factors of course are not very accurate and could be more inaccurate than the global emission factors. There is a significant difference in the first two suppliers. The first of which appearing the most realistic, with a 40% drop in emissions, the second showing a less realistic 88.1% drop, but including the full scope 3 emissions did separate it from the others who all dropped over 95%. Taking a closer look at the supplier that provided the ideal information, it can be seen how even though the provided data was ideal, the limitation in the accounting system means the carbon figure is still not perfectly accurate. As mentioned earlier, the accounting system does specify to the product level, only product codes. So, the data in the table above shows a representative sample of data that was manually sifted through for the relevant product code, counting how many of certain product models were purchased. This allowed the above, supplier-specific average emission factor to be calculated. This can be inserted into the accounting system at the product code level and may be more accurate than the global average emission factor, but for certainty the accounting system needs to account for purchases at the product level.

Table 3 shows how the emission factor was calculated for this supplier.

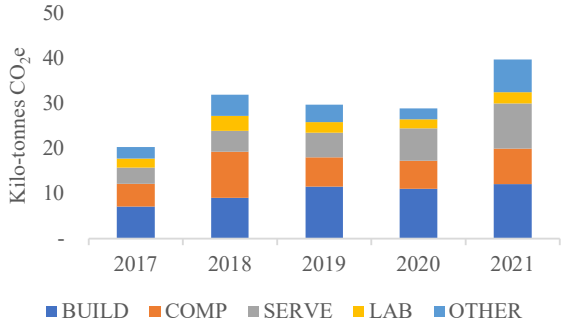

Figure 1 - 2017-2021 Emissions from Purchased Goods & Services by General Ledger Code

Table 1 – Scopes and GL Codes covered by Suppliers

Supp	GL Code	Scope 1	Scope 2	Scope 3	LCA
1	COMP	Y	Y	Y	Y
2	COMP	Y	Y	Y	
3	COMP	Y	Y		
4	COMP	Y	Y		
5	BUILD	Y	Y	Cat 6 & 7	
6	BUILD	Y	Y	Cat 7	
7	BUILD	Y	Y		
8	SERVE	Y	Y		
9	CATER	Y	Y		

Table 2 – Changes due to Supplier Specific Emission Factors

Supp	GL Code	% Drop in EF	Drop in $ktCO_2e$	% Drop in CF
1	COMP	40	2.0	0.63
2	COMP	88.1	1.5	0.46
3	COMP	95.3	3.2	1.03
4	COMP	99.6	0.2	0.06
5	BUILD	99.0	4.5	1.44
6	BUILD	99.4	1.5	0.48
7	BUILD	95.3	1.1	0.36
8	SERVE	99.9	0.8	0.26
9	CATER	98.2	0.3	0.09
Total		**82%**	**15.2**	**4.83**

As mentioned earlier, the accounting system does specify to the product level, only product codes. So, the data in the table above shows a representative sample of data that was manually sifted through for the relevant product code, counting how many of certain product models were purchased. This allowed the above, supplier-specific average emission factor to be calculated. This can be inserted into the accounting system at the product code level and may be more accurate than the global average emission factor, but for certainty the accounting system needs to account for purchases at the product level.

Table 3 – Emission Factor Calculation for LCA data

Product Model	No.	LCA EF ($kgCO_2e$)	($kgCO_2e$)	Cost (€)	($kgCO_2e$/€)
A	34	348	11,832	€ 23,645	0.50
B	7	403	2,821	€ 4,680	0.60
C	35	326	11,410	€ 33,342	0.45
D	54	315	17,010	€ 25,506	0.51
E	24	300	7,200	€ 16,645	0.43
F	15	296	4,440	€ 10,645	0.42
			Average EF		**0.49**
			Global EF		**0.81**
			Reduction		**40%**

4.3 Commuting Analysis: Scope 3 Category 6

Overall, the survey showed no significant changes in modal % choices between the previous survey in 2015 with of staff using a car as their primary mode of transport compared to 26% of students who used a car (walking was the most frequent modal choice for students) in January 2022. It is notable that for staff and particularly for students the distances travelled to campus increased significantly with 31% of students travelling more than 20 km in January 2022 compared to 13% in 2015 (for staff the figures were 24% in 2015 and 33% in 2022). Accommodation availability was a key factor in this increased travel distance. If sustained these long-term trends could present difficulties in reducing emissions due to commuting. Overall annual emissions due to commuting are shown in Figure 2. Reflecting the modal share staff emissions were 2.4 times higher/km than student emissions. In total 85% of commuting emissions were due to transport by car.

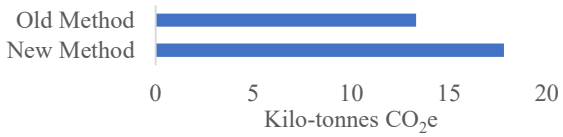

Figure 2 - Change in commuting emissions after updating the calculation methodology

4.4 Carbon Footprint Trends for a University 2017-2021

This section shows general trends in the carbon footprint for the University, and the impacts of COVID-19 restrictions, highlighting the changes between the 2019-2020 and 2020-2021. Figure 3 shows the carbon footprint by scope from 2017-

2021. The updated figures for commuting were included, but for PG&S the baseline method remains as there wasn't enough supplier data. Figure 4 shows the change in emissions by category due to COVID-19 restrictions, the clear outlier here being PG&S which increased substantially from 2020-2021, whereas all others decreased. The change bar represents the total change in emissions each year, which shows 14 $ktCO_2e$ were avoided going from 2019-2020, but 10.3 $ktCO_2e$ were gained the following year. These equate to a 23% fall in emissions initially followed by a 16.9% jump. The biggest carbon savings can be seen in commuting and business travel, with commuting falling by 6. $ktCO_2e$ and remaining dropped for the second year and business travel falling by 3.5 $ktCO_2e$ the first year before dropping a further 0. $ktCO_2e$ the following year. Scope 1 emissions fell by 1 $ktCO_2e$ and then by 0.23 $ktCO_2e$. Scope 2 fell by 1.8 $ktCO_2e$ before rising by 0. $ktCO_2e$. PG&S fell by 0.8 $ktCO_2e$ initially before rising by 10.8 $ktCO_2e$.

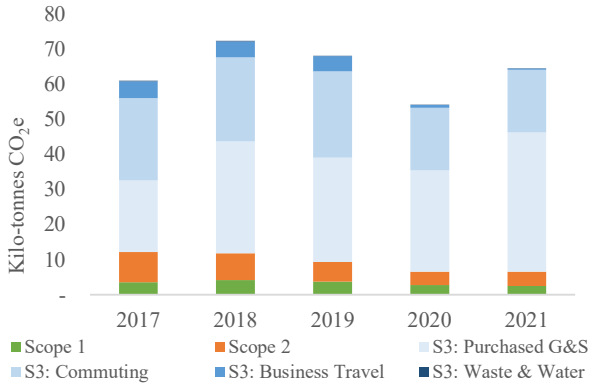

Figure 3 - NUI Galway Carbon Footprint 2017-2021 using rough method for PG&S and updated method for commuting

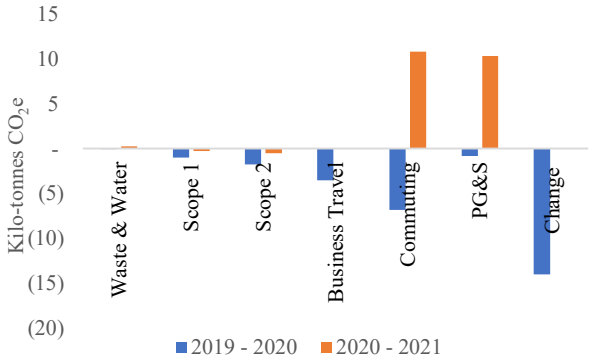

Figure 4 - Change in emissions due to COVID-19 restrictions by category

5 DISCUSSION

5.1 PG&S Discussion

This paper presents results from the first round of supplier engagement on emission factors. The findings are that at the time, most suppliers didn't have enough emissions information available to calculate accurate emission factors specific to their product/service. Looking at Tables 1 and 2, it can be concluded that at the very minimum a full scope 1, 2 and 3 GHG inventory is needed to confidently calculate and assign a supplier specific emission factor. There is a clear trend of unrealistically large drops in emissions associated with suppliers who didn't give full inventories. There is also the outlier of the supplier who had LCAs for their products. As explained in the results section, these LCAs could not be applied to their full affect due to the limitation of the accounting system, and the spend-based average emission factor was calculated above. Even so, this methodology produced a much more realistic figure of a 40% drop in emissions for this supplier compared to the global average emission factors. This aligns with [10], who found supplier specific calculations of GHG emission intensities are estimated to be 30−43% lower than other analyses employing national or regional average emission profiles. If a 40% drop was found to be the margin across the board for PG&S, NUI Galway's carbon footprint would see a 13% drop in the baseline and up to a 26% drop in 2021 emissions. These large margins show the importance of ensuring the most accurate carbon calculation methodology available is used for PG&S.

5.2 Commuting Discussion

Updating the method for calculating commuting emissions resulted in a 34% increase. This is partly due to the updated method having a wider scope, including cradle-to-grave emissions for vehicles. It is also due to more accurate picture that was captured in terms of car fuel, engine size and distances travelled. This large change in emissions again highlights the importance of applying best practice methods to the commuting category. The analyses also calculated "tail pipe emissions" to estimate the immediate impacts of remote working on transport emissions. In this scenario cycling would not be associated with any emissions and such emissions for private cars can be about 40% of the total vehicle emissions over a 100,000 km life cycle (it will vary between vehicles and for electric vehicles). Remote working (if implemented as per stated staff preferences) could reduce fuel consumption associated with staff commuting to NUI Galway by up to 40% (assuming no bounce back due to staff doing other trips instead).

5.3 Carbon Footprint Trends Discussion

Taking an average of the carbon footprint from 2017-2021, scope 1 equates to 5.2%, scope 2 to 9.3%, scope 3 to 85.5%. Scope 3 breaks down into PG&S at 47%, commuting at 33.7%, business travel at 4.7%, and waste & water at 0.1%. As mentioned above, there is a degree of uncertainty in the largest section, this being PG&S. It's likely that this figure will fall by somewhere between 30-43%, but for now as there is consistency in using the global average emission factor method, this will be used until a more accurate method can be widely applied. The commuting figures here have been calculated using the updated methodology and have a high degree of accuracy. Looking at the trend year on year in Figure 3, there are quite significant changes in the total carbon footprint, which again is largely due to the degree of inaccuracy in the PG&S calculation method. 2020 is the first year that saw a reduction in comparison to the baseline, with a drop of 11.4%, but the trend did not continue into 2021, with emissions 5.6% above the baseline. Pre-COVID-19 and excluding PG&S, all categories remained fairly static bar scope 2 which saw substantial reductions year on year. PG&S has quite a volatile trend as shown in Figure 1, again reflecting the degree of

inaccuracy. In terms of the COVID-19 impact, Figure 4 shows that commuting emissions provided the biggest savings, which dropped by 28% within its category from 2019-2020 and remained that low for 2021. Business travel dropped by 81% from 2019-2020 and by another 61% from 2020-2021. Scope 1 & 2 dropped by 27% and 32% respectively from 2019-2020. From 2020-2021 scope 1 dropped by a further 8% and scope 2 increased by 6%. PG&S dropped by 3% in 2020 and then rose by 38% in 2021. PG&S, commuting and business travel make up 99.8% of Scope 3 emissions for NUI Galway, with emissions from waste & water making up 0.2%. This breakdown of emission shows the importance for organisations to include scope 3 emissions in their carbon footprint, particularly from financial accounts and commuting behaviour.

6 CONCLUSIONS AND FUTURE WORK

This paper presents results from the calculation of an Irish university's carbon footprint, showing trends pre and throughout the COVID-19 pandemic. It also analyses the calculation methods behind the two largest sections of the scope 3 emissions, purchased goods and services and commuting. Using supplier specific emission factors as opposed to global sector emission factors, it was shown that PG&S emissions for one sector were 40% lower. However, using more accurate tracking of commuting emissions resulted in a 34% increase in the emissions figure. These large margins show the importance of an accurate carbon calculation methodology. This paper also makes a case for the importance of scope 3 emissions, due to the portion of the total carbon footprint it accounts for. More research is needed to standardise methodologies and emission factors for scope 3 emissions, particularly for purchased goods and services. A methodology for engaging with suppliers on supplier specific emission factors was shown to have limited success due to the lack of comprehensive emissions being captured by suppliers. The impact of COVID-19 saw the University's carbon footprint fall by 23% in 2020 but rise back to baseline levels in 2021.

Future aspects of this research lie in further updating the methodology for calculating emissions associated with purchased goods and services, which is needed in two areas. One is the carbon accounting system. Ideally, the system would track purchases at the product level, meaning LCA emission factors could be directly assigned to each product/service. The second area is the suppliers. It's evident that progress is needed in the widespread accounting of full scope 1, 2 and 3 GHG inventories, which will aid companies to progress towards LCAs of their products/services. Workshops on carbon measuring for suppliers could be a next step.

ACKNOWLEDGMENTS

This research was funded by Science Foundation Ireland (SFI) through the MaREI Centre (Grant no. 12/RC/2302_2). Data for the calculation of emissions was provided by NUI Galway's Buildings Office, Procurement & Contracts Office, and the Accounts Office.

REFERENCES

[1] E. Commission *et al.*, *100 climate-neutral cities by 2030 - by and for the citizens : report of the mission board for climate-neutral and smart cities*. Publications Office, 2020.

[2] GHG Protocol, "Calculation Tools | Greenhouse Gas Protocol," *ghgprotocol.org*, 2020. https://ghgprotocol.org/calculation-tools (accessed Dec. 15, 2020).

[3] E. Helmers, C. C. Chang, and J. Dauwels, "Carbon footprinting of universities worldwide: Part I—objective comparison by standardized metrics," *Environ. Sci. Eur.*, vol. 33, no. 1, p. 30, 2021, doi: 10.1186/s12302-021-00454-6.

[4] K. Valls-Val and M. D. Bovea, "Carbon footprint in Higher Education Institutions: a literature review and prospects for future research," *Clean Technologies and Environmental Policy*, vol. 23, no. 9. pp. 2523–2542, 2021, doi: 10.1007/s10098-021-02180-2.

[5] Y. A. Huang, C. L. Weber, and H. S. Matthews, "Categorization of scope 3 emissions for streamlined enterprise carbon footprinting," *Environ. Sci. Technol.*, vol. 43, no. 22, pp. 8509–8515, 2009, doi: 10.1021/es901643a.

[6] M. Tidy, X. Wang, and M. Hall, "The role of Supplier Relationship Management in reducing Greenhouse Gas emissions from food supply chains: Supplier engagement in the UK supermarket sector," *J. Clean. Prod.*, vol. 112, pp. 3294–3305, Jan. 2016, doi: 10.1016/j.jclepro.2015.10.065.

[7] R. Frost, N. Hewitt, and M. Berners-Lee, "Using supplier reported emissions information to enhance an EEIO model to estimate the GHG emissions of businesses," in *Paper presented to the 22nd International Input-Output Conference (Lisbon, Portugal: 14-18 July 2014).*, 2012, p. 7pp, Accessed: Apr. 21, 2022. [Online]. Available: www.oanda.com.

[8] K. E. King, "Improving Supplier Engagement as a Means to Reduce Greenhouse Gas Emissions of a Global Company Improving Supplier Engagement as a Means to Reduce Greenhouse Gas," 2017.

[9] P. Dhamankar, J. Kehoe, and E. Schwab, "Scope 3 Emissions Inventory and Supplier Engagement for Steelcase, Inc.," *Masters thesis Univ. Michigan*, no. April, 2021.

[10] S. A. Roman-White *et al.*, "LNG Supply Chains: A Supplier-Specific Life-Cycle Assessment for Improved Emission Accounting," *ACS Sustain. Chem. Eng.*, vol. 9, no. 32, pp. 10857–10867, 2021, doi: 10.1021/acssuschemeng.1c03307.

[11] SEAI, "Conversion factors," 2021. https://www.seai.ie/data-and-insights/seai-statistics/conversion-factors/ (accessed Apr. 27, 2022).

[12] DBEIS, "UK Government Greenhouse gas reporting: conversion factors 2020," *Department for Business Energy & Industrial Strategy*, 2021. https://www.gov.uk/government/publications/greenhouse-gas-reporting-conversion-factors-2021 (accessed Jun. 15, 2021).

[13] K. Valls-Val and M. D. Bovea, "Carbon footprint assessment tool for universities: CO2UNV," *Sustain. Prod. Consum.*, vol. 29, pp. 791–804, Jan. 2022, doi: 10.1016/j.spc.2021.11.020.

[14] Quantis, "Scope 3 Evaluator," 2019. https://quantis-suite.com/Scope-3-Evaluator/ (accessed Dec. 15, 2020).

[15] S. Shi and J. Yin, "Global research on carbon footprint: A scientometric review," *Environ. Impact Assess. Rev.*, vol. 89, p. 106571, Jul. 2021, doi: 10.1016/j.eiar.2021.106571.

[16] T. Wiedmann and J. Minx, "A definition of 'carbon footprint,'" *Ecol. Econ. Res. trends*, vol. 1, pp. 1–11, 2008.

[17] M. Finkbeiner, "Carbon footprinting-opportunities and threats," *International Journal of Life Cycle Assessment*, vol. 14, no. 2. pp. 91–94, 2009, doi: 10.1007/s11367-009-0064-x.

[18] D. Pandey, M. Agrawal, and J. S. Pandey, "Carbon footprint: Current methods of estimation," *Environ. Monit. Assess.*, vol. 178, no. 1–4, pp. 135–160, 2011, doi: 10.1007/s10661-010-1678-y.

[19] F. Samara, S. Ibrahim, M. E. Yousuf, and R. Armour, "Carbon Footprint at a United Arab Emirates University: GHG Protocol," *Sustain.*, vol. 14, no. 5, 2022, doi: 10.3390/su14052522.

[20] P. Yañez, A. Sinha, and M. Vásquez, "Carbon footprint estimation in a university campus: Evaluation and insights," *Sustain.*, vol. 12, no. 1, pp. 1–15, 2020, doi: 10.3390/SU12010181.

[21] S. T. DAĞLIOĞLU, "Carbon Footprint Analysis of Ege University within the Scope of Environmental Sustainability," *Commagene J. Biol.*, vol. 5, no. 1, pp. 51–58, 2021, doi: 10.31594/commagene.865194.

[22] B. Rugani and D. Caro, "Impact of COVID-19 outbreak measures of lockdown on the Italian Carbon Footprint," *Sci. Total Environ.*, vol. 737, p. 139806, Oct. 2020, doi: 10.1016/J.SCITOTENV.2020.139806.

[23] V. Filimonau, D. Archer, L. Bellamy, N. Smith, and R. Wintrip, "The carbon footprint of a UK University during the COVID-19 lockdown," *Sci. Total Environ.*, vol. 756, p. 143964, Feb. 2021

[24] T. Adams and J. Goggins, "NUI Galway Carbon Footprint Report," 2021. https://www.nuigalway.ie/sustainability/sustainabilityreports/nuigalwaycarbonfootprintreport/ (accessed Apr. 27, 2022).

[25] NUI Galway's Energy Team, "Energy Reports - NUI Galway," 2021. https://sustainability.nuigalway.ie/learn-live-lead-model/live/energy/energyreports/ (accessed Apr. 27, 2022).

Opportunities to design for Sustainability through our physical, educational and professional structures

Jennifer Boyer[1] and Lorraine D'Arcy[2]
[1]Vice President for Sustainability, Technological University Dublin, Grangegorman Campus, Dublin 7, D07 H6K8, Republic of Ireland
[2]Sustainability Action Research & Innovation Lead, Technological University Dublin, Grangegorman Campus, Dublin 7, D07 H6K8, Republic of Ireland
Email: Jennifer.Boyer@tudublin.ie, Lorraine.Darcy@tudublin.ie

ABSTRACT: This paper outlines opportunities to address the Sustainable Development Goals 2030 afforded through practiced-based professional education and research using multi-level stakeholder engagement in the areas of Architecture Engineering and Construction for wholistic, accelerated, and transformational impact being implemented at TU Dublin, Ireland's first Technological University.

KEY WORDS: Professional Education, Climate Action, Practice-based Pedagogies, Sustainability, Sustainable Cities & Communities.

1 GENERAL GUIDELINES

Founded upon the pillars of People, Planet, and Partnership, Ireland's first Technological University, TU Dublin, set out its inaugural University strategy to extend beyond the typical time-horizon of a University strategy to align with the United Nations Sustainable Development Goals 2030. In doing so, *Strategic Intent 2030* [1] aims to deliver on Sustainability '*through practice-based research'* using '*education as our engine'* by building upon our heritage as three former Institutes of Technology. Doing this allows TU Dublin's students to learn alongside industry and community through innovative learning and teaching models, within an inclusive and accessible environment that offers apprenticeships through to PhD level degrees.

The 1987 report of the United Nations World Commission on Environment and Development [2], highlighted that there are many challenges when reorganising societies and economies in response to increasingly evident existential sustainability challenges. At TU Dublin, the merging of three Institutes of Technology has meant significant transformation and reorganisation at a time when these environment and development challenges could not be ignored. Using the UN SDG framework of targets and indicators as a guide, TU Dublin have identified key interdependencies between global challenges and University capabilities to bring students, educators, industry, community and government together to develop our curriculum and research. Through new models of collaborative and participatory engagement we have created pilots for achieving 'common good' [3] through Quality Education (UN SDG 4).

Since the UN SDGs were published in 2016, industries have responded in different ways to the intertwined concerns of sustainability. Some industries, such as Food and Fashion, have leveraged effective customer feedback loops and moved quickly ahead of legislation to work proactively with new technologies to change business priorities, create new value propositions, and reshape supply chains. However there have been a number of innovation barriers [4] to the Architecture, Engineering, and Construction (AEC) industry, which are predicated upon longer time horizons for value realisation. Operating within a highly regulated and litigious environment, often at a distance from end users, has meant the industry has been slow to change to address sustainability challenges. The *European Green Deal* [5] recognises that the built environment sector has a vital role to play in responding to the climate emergency. With buildings responsible for 40% of global carbon emissions, decarbonising the sector is prioritised as an effective way to mitigate the worst effects of climate breakdown. As the global population approaches 10 billion people in the coming decade, global building stock is projected to increase to meet demand [6]. Building locations and their supporting infrastructure will also influence climate impacts, so challenges need to be addressed with consideration for their societal context. Without substantial changes to the AEC industry, the amount of natural resources consumed to meet population growth will only increase the construction sector's carbon emissions impact. Therefore, change to address global sustainability concerns within the AEC industry is no longer an economic and environmental, but also an urgent moral and societal imperative.

According to the World bank, the AEC industry has an economic value of 13 trillion USD as of 2021 [7]. This constitutes 15% of gross world product estimated at 85 trillion USD. Within the industry design professionals play a critical role as change agents. One opportunity to lever change in response to sustainability is through deep disciplinary channels across the AEC industry professions. Engaged and informed design professionals at initial design stages, can influence primary project decisions which affect downstream and upstream value chain activities which impact sustainable outcomes. Ensuring that our AEC workforce is ready to meet these challenges is central to our approach in engaging apprentices, undergraduates, postgraduates and researchers, staff and community and industry partners in our sustainability initiatives.

2 PROFESSIONAL BODIES RESPOND TO UN SDGS

Alongside educational institutions it is vitally important that professional bodies within the AEC industry support sustainable practices by playing a key role in protecting legal professional status and supporting industry development. These bodies act as regulators of quality, protecting public consumer interest and their members, by providing national level professional codes of conduct, and through the accreditation of professional academic programmes by discipline. They act as an assurance bridge connecting professional education to the act of real-world practice. Within the professional bodies, each contain unique longstanding cultural norms which reflect the values of their membership [8]. Sustainability values bring together particular and common concerns, which challenge professions to rethink strategic priorities. To do this requires deep consideration of the complex sociological understanding of responsibility as related to professional legitimacy [9] that traditionally has promoted competition between professions, moderate to little environmental concerns, and reticence towards a greater level of multi-disciplinary cooperation and collaboration.

Over the last two years with the popularisation of the UN SDGs, we have seen individual professional bodies within the construction industry respond differently in how they aim to address sustainability. Until recently, the outlier voice of grass-roots movements within the professions, such as Architects Declare[1], Quantity Surveyors Declare[2], etc. have acted as vehicles for creating awareness within the professions of structural systemic changes required. Recently, an increase in sanctioned European wide initiatives such as the New European Bauhaus[3] alongside the adoption of the EU Taxonomy[4] reinforce the potential for substantial structural and potential legislative change to professions and as such prompt professions to pursue a review of the *European Professional Qualifications Directive (2005/36/EC) 2005* [10] competencies to reflect sustainability concerns.

Examples of these changes include the Royal Institute of the Architects of Ireland (RIAI) who have a Sustainability Taskforce which serves under the Practice & Membership Services sub-committee of the RIAI Council. In 2019, it launched the first Policy on Sustainability [11] in response to the Global Climate Crisis. This policy was developed separately by the Taskforce to support the RIAI Strategy 2018-2022 by promoting five principles for members to adopt within their practice to *'build in*' sustainability concerns, a practice they summarise as *'commit, lead, develop, educate, and implement'*.

In 2020, Engineer's Ireland launched their annual 'barometer of the profession' report [12], a publication aimed at capturing professional trends. This time a dedicated section to World Engineering Day for Sustainable Development summarised five years of member (employers and academics) responses to the extent to which UN SDGs should be covered in engineering education. Through this research, six UN SDGs (and corresponding targets) were identified.

In 2022, the Society of Chartered Surveyors Ireland (SCSI) launched an independent report developed by TU Dublin researcher Dr. Roisin Murphy titled *Sustainable Development in the Surveying Profession* [13] to capture the breadth of this profession's knowledge and practices, and the extent to which sustainable development was embedded within academic programmes nationwide, to provide key recommendations and actions spanning across key stakeholders.

These professional bodies from the AEC industry are responding to sustainable development concerns each in different ways. By engaging members, revising policies, reviewing practices, and recognising the reach and influence of higher education on the industry the need for closer collaboration and coordination is necessary to ensure a more sustainable future for us all. One method for doing this is through practice-based pedagogies.

3 PRACTICED-BASED PEDAGOGIES

Professional education values the combination of theory and practice in tandem. It provides an educational experience through practice-based learning to simulate the professional industry workplace. An example from architectural education, with similar examples evident in other design professions, is the unique pedagogy of problem-based learning through applied projects which offers students an opportunity to propose solutions to complex briefs through iterative development and critique. Students become immersed in and committed to the study of architecture and other building design professions in part due to the attractive applied learning model afforded by such pedagogies. This experiential model of learning [14], actively responds to emergent societal concerns, and has evolved in architectural education into what is now an internationally adopted module called the Architectural Design Studio (ADS). ADS constitutes more than half of learning hours distributed across the five-year professional curriculum, and as the primary location for synthesizing knowledge and skills through architectural enquiry, it is therefore well positioned to take on the complex problems posed by sustainability and make its ethical concerns central to an architect's education.

By 2019, one particular UN SDG, that of 13 Climate Action was also attracting student attention and extra-curricular activism. Significant and regular media coverage of global climate activism was embraced by younger generations, with the likes of figureheads such as Greta Thunberg organising protests for global and governmental systems change. This awakening of youth voice reinforced the need to provide greater student agency at the heart of any curricular changes within the professional education model which was also an opportunity to utilise the established practiced-based pedagogies to offer to demonstrate and design a new future for the professions.

Therefore, between the inherent predisposed characteristics of PBL modules in AEC education which can centralise sustainability challenges into the curriculum and the desire of

[1] https://ie.architectsdeclare.com/

[2] https://scsi.ie/members-area/my-professional-journey/surveyors-declare/#:~:text=The%20Surveyors%20Declare%20document%20is,within%20our%20practices%20and%20homes.

[3] https://europa.eu/new-european-bauhaus/index_en

[4] https://ec.europa.eu/info/business-economy-euro/banking-and-finance/sustainable-finance/eu-taxonomy-sustainable-activities_en

students to create change for the future of their profession, practiced-based pedagogies offer a unique opportunity in accelerating multi-level stakeholder action for sustainability.

4 TECHNOLOGICAL EDUCATION & RESEARCH

Since the signing of the *Technological Universities Act* in Ireland in 2018 a new sector of higher education has now emerged nationally where the positioning of research and education for sustainability are supported by new agile structures designed to embed innovation practice into institutional systems and cultures. This promises to ensure a greater level or organisation learning and continuous improvement through the flow of cores activities for greater societal benefit [15]. Using technological innovation is one route that enables transformational change for sustainability rapidly across the industry. Its definition by the OECD in 2002 [16], refers to '*new products and processes and significant technological changes of existing products and processes*' which are initiated to increase the volume of knowledge in society at an accelerated rate.

In its role to serve the interest of greater society, TU Dublin has an obligation and duty of care to respond directly to industry and society needs by providing new relevant sustainable technological skills and knowledge through the education and research it offers. New models for delivering technological innovation which bind practical ethical concerns for sustainability and industry impact can be achieved through the application of the quadruple helix open innovation models to initiate meaningful change [17].

By bringing together key stakeholders from universities, government, industry, and communities across society together (Figure 1) through into an open forum of engagement which promotes open debate can generate an active ecosystem of co-creation to take action quickly and collectively to address critical sustainability challenges. In this model, existing industry professionals (educators and industry professionals) and future industry professionals (students) are treated as equal citizens facilitated to collaborate to realign professional missions and create change (Figure 2). In this model traditional hierarchy, siloed expertise, lack of transparency on decision making, are mutually disarmed to promote partnership, entrepreneurship, collective ownership, and individual responsibility.

Such processes utilise alternative modes of development and decision-making models to ignite, enact, and embed change through a public contract empowering local level ownership and purpose to enact change, When practiced within university environments, open innovation models prove the benefit of engaging learners across all levels of experience as the process can quickly reveal a variety of barriers to change that exist across industry, professional bodies, industry regulators and within higher education and research norms.

5 ACADEMIC CASE STUDIES FROM ARCHITECTURE ENGINEERING & CONSTRUCTION

This section outlines two case studies from TU Dublin. They demonstrate how education and research models can create

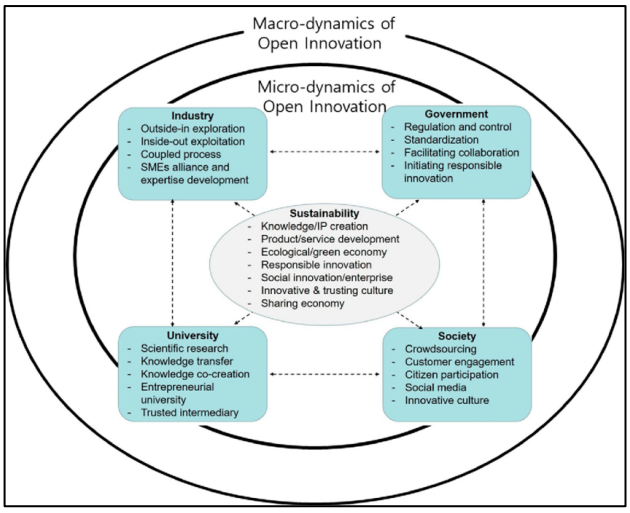

Figure 1 The roles of the quadruple-helix model for open innovation micro- and macro-dynamics [17].

Figure 2 Design for Climate Workshop, Dublin School of Architecture, TU Dublin May 3rd, 2019 [17]

catalyst effects in accelerating transformation to address sustainability by creating multi-level stakeholder engagement focused on single UN SDGs. Each case study utilises aspects of the quadruple helix open innovation model to, in the first instance engage discipline level stakeholders (in architecture) to prompt both academy and industry change and in the second instance, by bringing together a breadth of inter-disciplinary expertise to promote a single quite fundamental activity (that of walking) and foster coherent multi-disciplinary action to generate greater policy coherence.

5.1 Resilient Design for Climate

In May 2019, the TU Dublin School of Architecture initiative *Architectural Design for Climate Change* invited 300 students, 45 educators, the professional body (RIAI), and external industry experts in green building[5] to come together and revise the architectural curriculum. The forum hosted over 350 stakeholders in a structured participatory design workshop, offering collective non-hierarchical discussion and decision making to propose new priorities within the Architectural Design Studio (ADS) modules for addressing climate change in architecture. This forum provided a public contract that

[5] https://www.igbc.ie/

created shared ownership and local level responsibility, through a focused and accelerated curriculum change process outside of annual institutional programme review processes. The initiative highlighted challenges within existing pedagogies, skills and knowledge gaps, and promoted student voice as agency for change [18]. Outcomes of the initiative provided studio design project pilots in each of the five years within the Bachelor of Architecture programme focusing on topics such as *Reuse* and *Densification, Material Stewardship, Adaptation* and *Mitigation*, as well as *Carbon Neutral Cities and Towns*. The initiative reflected the student body's desire for an education experience that supported a culture of greater climate responsibility. However, to support and enable the development of such change, the academic programme team, would require a new level of investment.

In November 2019, the invitation to join a European Erasmus Plus project which focused on a digital climate curriculum arose through the *ARCH4CHANGE*[6] project where TU Dublin would lead the design and development of the work package delivering the educator toolkit. In December 2019, the Higher Education Authority (HEA) in Ireland launched the Human Capital Initiative (HCI)[7] which called for higher education transformation proposals to support enterprise engagement through cross institutional partnerships. By April 2020, TU Dublin proposed an alliance which included all schools of Architecture within Ireland to work together to address the twin crisis of Climate and Housing through a joint proposal under the HCI call for a *Resilient Design Curricula for 21st Century Design Professionals*. Adopting a federated partnership model to promote engagement across key local level stakeholders, the project proposes professional curriculum pilots to address climate and housing through the development of new skills, knowledge, and pedagogy by connecting students, educators, industry, local government and communities in a national cooperation. Both the ARCH4CHANGE and Resilient Design Curricula projects were secured at a critical time when resources for educators and their institutions was necessary to support curriculum revision in time to respond to urgent crisis. Collectively, all three projects provide examples of how the multilevel education needs of students, educators, industry professionals, and enterprise can be accelerated in response to global sustainability challenges.

5.2 Walkability in Cities & Communities

In September 2022, TU Dublin will host the 22nd annual international Walk21 conference. The conference presents an opportunity to engage with international experts and practitioners to empower local authorities, agencies and community groups, whether they are from rural, suburban or urban settings, to make places more walkable and liveable. The activity of walking provides for an example of the UN SDG framework in action, where the intersection a physical activity and enjoyment (SDG 3) meets sustainable transport (SDG 11).

An increasing emphasis is being placed on the importance of research to understand the determinants of walking behaviour; what prevents people walking in their neighbourhood, the role of walking and nature for good physical and mental health, the role of neighbourhood in social connectedness and participation in civic society. The Walk21 conference covers academic research but a greater emphasis is placed on showcasing real projects and programmes rolled out by local authorities and organisations all over the globe. Delegates are expected to attend from every continent and is likely to reach an audience of 5,000+ people.

The potential impact from this event is far reaching from National and International Policy and collaboration right down to grassroots implementation and community engagement and ownership. Workshops and walkshops locally hosted around Ireland with contributions from international experts with contexts relatable to many practitioners home and abroad will be a key feature of the event. The increasing publicly funded local workforce in this space will benefit greatly.

The key uniqueness of the Irish approach for Walk21 2022 is the interdisciplinary approach with a national focus. This was a key aim from the start of discussions around the Irish conference and enabled Irish government departments and agencies to develop a vision for the event together. Walking, walkability and liveability are topics of relevance to many disciplines and greater collaboration in this space will lead to better value for investment and greater collaborative working. Walking is an activity that is available to all. Good design and provision for walking (walkability) serves those that wish to walk, run, push or roll. Good walkability and liveability in cities and communities are central to the Irish Programme for Government as they…

- contribute to a better quality of life for all
- are key considerations for neighbourhood and regional planning within the National Development Plan (NDP)
- are important for domestic and international tourism
- can reduce transport related carbon emissions and improve air quality
- walking is an equitable form of transport available to all at no cost
- allow greater appreciation of our natural and built heritage and biodiversity
- contribute to greater wellbeing and has a role in preventative medicine
- contribute to urban regeneration and makes urban centres more attractive for living and commerce
- provide opportunities for rural development and community participation projects
- are social provision, especially offering opportunities for community interactions and activity for those marginalised in society
- lead to safer communities with greater social connectiveness
- afford greater physical access to education and more attentive students from active commuting
- are global topics of relevance for all climates, cultures and communities where we can learn from each other
- are topics of relevance for a number of state departments, agencies and sections within our local authorities creating greater opportunities for collaborative interdisciplinary projects

The Walk21 conference provides evidence for relevant implementation of National Policies and Strategies post-Covid19 including National Climate Action Plan, National

[6] https://www.arch4change.com/

[7] https://hea.ie/skills-engagement/human-capital-initiative/

Planning Framework, Our Rural Future, Healthy Ireland Framework, Sustainability Mobility Policy, National Sports Policy among others and contribute to Ireland's whole government approach to delivering on UN SDG 11 through the creation of sustainable cities and communities.

5.3 Case Studies Summary

The case studies provided offer examples of higher education curriculum revisions and research arising from the unique pedagogical attributes of the AEC industry by creating real action for sustainability through multi-level stakeholder interactions premised upon practice-based enquiry. Each use different approaches to mobilising change within society to address sustainability. By using a deep discipline approach in Architecture to address climate change, a shared intergeneration purpose enabled traditional barriers to change to reduce through recognition of the need for a multi-level learner approach [19]. The example provided by the universal activity of walking invites a wide range of interdisciplinary approaches to create accessible, sustainable, enjoyable and healthy means of transport. UN SDG targets and indicators provide multiple ways of engaging people in sustainability action through discipline depth and interdisciplinary breadth. Be it through professional curriculum revision or action research for policy impact the case studies demonstrate scalable solutions and multiplier effects to creating a more sustainable built environment/future.

6 DISCUSSION

With the most recent issue of the IPCC Report in April 2022, greater levels of action are needed from all areas of industry working more coherently and collaboratively now. Increased social consciousness, relative appetites across society to enact change, and increasing external environment pressures may provide increased likelihood for climate action if curated through open innovation models. However, existing embedded cultures must not be underestimated.

Will higher education for all levels of learners at the same time and in a shared 'space' where local concerns and global challenges meet, deliver greater levels of collaboration within the education sector and across government, industry, and enterprise organisations to achieve Quality Education and address industry level challenges that enable diffusion into wider society [20]?

Will/can greater levels of participatory engagement using quadruple helix open innovation models enable the opportunity to (re)align professional values to sustainability principles if they necessitate new ways of working that challenge existing governance and decision-making practices?

What is the new (or refreshed) role of research in the context of developing new knowledge and skills to address existential global challenges? Can greater levels of action research and technological innovation demonstrate a new practiced-based ethical value to society through the closing of the theory and practice gap?

If applied learning and active practice afford an opportunity to increase societal cohesion through greater collaborative dialogue and partnerships at national and international level, will impact to progress Policy Coherence for Sustainable Development (SDG target 17.14) be achieved quickly enough to save our planet?

7 CONCLUSIONS

The combination of practiced-based pedagogical and action-oriented research environments provided by the Technological University have a unique role to play in creating accelerated impact for sustainability through deep discipline and multi-disciplinary approaches which utilise open innovation practices. In order to support sustained impact at a global scale, there are further areas to be considered.

Each of the 17 UN SDGs are reliant upon interdependent targets and indicators of other UN SDGs to be achieved. The UN SDG framework by design dissolves industry boundaries and prompts greater levels of joined up thinking and collaboration to meet each goal and achieve global level sustainability by 2030. As both a conceptual and practical tool, the UN SDG framework offers organisational, disciplinary, and industry lessons yet to fully realised if operationalised at scale.

Each professional field, organisation, and individual begins at different starting points when engaging with Sustainability. Engagement and participatory practices through supportive learning and education environments are an essential ingredient for creating an inclusive experience for all participants. Developing sustainability mind-sets involve significant cultural and behavioural change. To enable this involves creating opportunities for greater individual ownership at local level to enact and be responsible for enacting meaningful and lasting impact.

To maintain open innovation practices within an organisation at scale and enable sustained transformational impact requires new agile organisational structures and resource flows (new systems) with dedicated ongoing project management and performance evaluation. Strong communications and dynamic feedback loops to support participatory practice models in real time have struggled to articulate the value of such practices to cover the additional resources required to deliver them [21] until now.

Technological Universities offer society a neutral territory to accelerate change through multi-level stakeholder engagement for piloting, developing and deploying new solutions through human-centred approaches to address the critical time cost [22] of sustainability.

Change requires leadership. Within the greater sustainability movement taking place across industry globally, leadership is found across all levels of organisations and society. Leith Sharpe, Director of Executive Education for Sustainability Leadership at Harvard University, describes the critical role of students, middle managers and senior leaders working across organisations to create new governance structures and create sustained impact [23]. With our students as advocates sitting in the driving seat as agents of their destiny, greater alignment is possible between the actions taken now within a discipline, an industry, and society in order to meet sustainability challenges.

It is possible to accelerate sustainability efforts by taking a combined approach to reach all levels within a profession and collaboratively with other professions through educational institutions, professional bodies and community stakeholders to revisit standards and competencies as more recently evident through individual initiatives. A greater level of collaboration

across disciplines through shared objectives rooted in UN SDGs are needed to tackle the grand challenge of our time.

REFERENCES

[1] TU Dublin Strategic Intent pdf website source https://www.tudublin.ie/explore/about-the-university/strategicintent/2030/ accessed on XXXX

[2] Report of the World Commission on Environment and Development: Our Common Future, Unite Nations World Commission on Environment and Development. Also known as 'the Brundtland Report', 1987

[3] Aristotle, 1984 [Pol.], Politics, Carnes Lord (trans.), Chicago: University of Chicago Press.

[4] Jannik Giesekam, John R. Barrett & Peter Taylor (2016) Construction sector views on low carbon building materials, Building Research & Information, 44:4, 423-444, DOI: 10.1080/09613218.2016.1086872

[5] European Green Deal https://ec.europa.eu/info/strategy/priorities-2019-2024/european-green-deal_en

[6] Construction Global Market Report 2022, Research and Markets, Dec 2021, ID 5515088

[7] https://data.worldbank.org/indicator/NY.GDP.MKTP.CD

[8] Susskind, R. E., & Susskind, D. (2015). The future of the professions: How technology will transform the work of human experts.

[8] Blau,1984)Blau, J.R.(1984). Architects and Firms: A Sociological Perspective on Architectural Practices (pp. 27-35) The MIT Press

[9] European Professional Qualifications Directive (2005/36/EC) 2005, https://eur-lex.europa.eu/legal-content/EN/TXT/?uri=celex:32005L0036

[10] https://www.riai.ie/uploads/files/general-files/Sustainability_for_the_Current_Global_Crisis_RIAI_2019.pdf

[11] https://www.engineersireland.ie/LinkClick.aspx?fileticket=QIJJm-hwkgSs%3d&portalid=0&resourceView=1

[12] https://scsi.ie/wp-content/uploads/2022/03/SCSI_SustainableDevelopment_FINAL.pdf

[13] Kolb, D. A. (1984). Experiential learning: Experience as the source of learning and development. Englewood Cliffs, New Jersey: Prentice-Hall.

[14] Diaconu, Mihaela. (2011). Technological Innovation: Concept, Process, Typology and Implications in the Economy. Theoretical and Applied Economics. XVIII(2011). 127-144.

[15] https://stats.oecd.org/glossary/detail.asp?ID=2688#:~:text=OECD-%20Statistics,the%20market%20(product%20innovation)

[16] Yun, Jinhyo & Liu,. (2019). Micro- and Macro-Dynamics of Open Innovation with a Quadruple-Helix Model. Sustainability. 11. 3301. 10.3390/su11123301.

[17] Boyer, Jennifer E. (2022) "Design for Climate - A Case Study from Architectural Education," Irish Journal of Academic Practice: Vol. 10: Iss. 1, Article 2., Available at: https://arrow.tudublin.ie/ijap/vol10/iss1/2

[18] Emily F. Pomeranz, Daniel J. Decker, William F. Siemer, Arthur Kirsch, Jeremy Hurst & James Farquhar (2014) Challenges for Multilevel Stakeholder Engagement in Public Trust Resource Governance, Human Dimensions of Wildlife, 19:5, 448-457, DOI: 10.1080/10871209.2014.936069

[19] De Vries, H.A., Tummers, L.G., and Bekkers, V.J.J.M. (2018). The diffusion and adoption of public sector innovations: A meta-synthesis of the literature. Perspectives on Public Management and Governance

[20] Velden, Maja & Mörtberg, Christina. (2014). Participatory Design and Design for Values. 10.1007/978-94-007-6994-6_33-1.

[21] Inyim, Peeraya & Zhu, Yimin & Orabi, Wallied. (2016). Analysis of Time, Cost, and Environmental Impact Relationships at the Building-Material Level. Journal of Management in Engineering. 32. 04016005. 10.1061/(ASCE)ME.1943-5479.0000430.

[22] Sharp, L. (2009) Higher education: the quest for the sustainable campus, Sustainability: Science, Practice and Policy, 5:1, 1-8,

Influential determinants of indoor humidity in homes and the impact of retrofits

[1]A K Mishra, [1]P Moran, [1, 2]J Goggins
[1]MaREI Centre, Ryan Institute & School of Engineering, College of Science and Engineering, National University of Ireland Galway, Galway, Ireland
[2]ERBE Centre for Doctoral Training, National University of Ireland, Galway, University Road, Galway, Ireland.

email: asitkumar.mishra@nuigalway.ie, paul.t.moran@nuigalway.ie, jamie.goggins@nuigalway.ie

ABSTRACT: Climate change and carbon emission concerns have reinforced focus on retrofitting residential buildings in Ireland. The climate action plan targets to retrofit 500,000 homes by 2030. While this drive has mostly focused on the energy and carbon emission reduction impact, the impact on indoor thermal environment and air quality also deserves attention. The Irish climate causes moisture in homes to be a major concern. Indoor humidity levels can impact building integrity, occupant comfort, and health due to mould growth. This work compares the indoor humidity in 23 homes in the Dublin region pre- and post-retrofit. The homes were monitored in 2015 and 2016, with retrofits taking place in summer of 2015. Using mixed-effects models, the impact of retrofitting on indoor humidity was assessed. Some of the most important factors influencing indoor humidity in the homes examined. Results from this work can help understand how building retrofits can affect indoor humidity, and consequentially occupant wellbeing and comfort.

KEY WORDS: energy retrofits; relative humidity; indoor humidity; outdoor humidity; indoor air quality.

1 INTRODUCTION

For the European Union (EU), including Ireland, energy efficiency focused retrofits of buildings are a key action towards reducing energy use and emissions of the building sector [1, 2]. The rationale of this focus is apparent from the fact that in Ireland, homes account for 25% of the energy use and nearly 29% of the carbon emissions [3]. To mitigate the energy demand and carbon emissions of the residential sector, Ireland has set an ambitious goal of retrofitting 500,000 homes by 2030 to a building energy rating (BER) of B2 or better (less than 125 kWh//m^2/year) [2].

In addition to the energy usage in homes, one in three European children are likely to be living in homes with unhealthy indoor air quality (IAQ) [4]. In Ireland, nearly 380,000 people live with chronic obstructive pulmonary disorder (COPD) [5]. Asthma is the most common chronic disease in Ireland, and both asthma and COPD are associated with poor indoor air quality [6]. People spend nearly 90% of life indoors and about 75% of that time is spent inside homes [7], and as such home indoor environments have a crucial impact on our wellbeing [8]. The Energy Performance of Buildings Directive in the EU obligates that member states' building energy policies account for healthy and comfortable indoor climate [9].

While studies have examined how retrofitting impacts home energy use in Ireland, not a lot of attention has gone towards understanding the impact of retrofits on indoor climate – indoor temperature, humidity, and air quality – using actual monitored data [10-13]. Beyond the concerns related to structural impacts of humidity [14], indoor humidity levels are important determinants of health and wellbeing [15]. Humidity levels impact mould growth, which in turn has an impact on respiratory health [16]. More importantly, in view of the ongoing pandemic, indoor humidity affects transmission of multiple respiratory viral infections [17], resulting in a more acute impact on health and wellbeing. Studies have examined how outdoor humidity levels impact indoor humidity levels in dwellings [18] and commercial buildings [17].

Taking into consideration a range of factors in indoor air such as pathogens, allergens, mites, and mould, an optimal indoor humidity zone is predicated between 30 and 60% RH [15, 16]. While large commercial buildings can have dedicated systems for humidification and dehumidification, as part of their indoor climate control system, similar facilities with dedicated humidification/dehumidification for residences are not an economical option. The residential indoor humidity balance depends on indoor activities, outdoor conditions, and home ventilation system. Ventilation can be tasked with getting rid of the humidity being generated by internal sources such as occupants and occupant activities (e,g, cooking, showering, etc.). Traditionally, most Irish homes depend on natural ventilation, primarily using passive wall vents, windows, and trickle vents. More recently, with retrofits targeting airtight building envelopes, it is becoming necessary to provide homes with mechanical ventilation approaches including extraction ventilation in wet rooms, whole house extraction ventilation, and in certain cases, mechanical ventilation (with or without heat recovery).

In this study, the impact of standard retrofit solutions on the indoor humidity in a specific group of observed homes are examined, while accounting for the variations in outdoor conditions. The results provide an understanding of how retrofits can affect indoor climate, specifically humidity.

2 METHODS

2.1 Field study and data collection

Indoor temperature and humidity data were logged in rooms of 23 homes in Dublin County, during 2015, 2016, and 2017. In this work we utilize pre-retrofit data from 2015 and post-

retrofit data from 2015-16, constituting 22 months of continuous monitoring data. In each home, temperature and relative humidity data loggers were set up in four or five rooms. Lascar EL-USB-2+ monitors were used in this study (temperature accuracy: ±0.45 °C; relative humidity accuracy: ±2.5%). Data logging interval was one hour, pre-retrofit and 15-minute post-retrofit. Logging frequency was decided based on the onboard memory of the monitors and how frequently householders could be approached to download the data and reset the monitor. Taking into consideration availability of an unobtrusive location, avoiding pets and children, and accessibility, loggers were installed at heights between 0.5 m and 2 m. The homes monitored were all within 15 km of the Dublin airport, hence, for outdoor temperature and humidity, the weather data from Dublin airport's meteorological stations was used [19].

Due to factors such as householders moving the data loggers, data loggers running out of battery or memory, etc., some of the data was missing. The level of data missing varied for the different homes. Indoor temperature for the homes was taken as the average of the temperature from the different rooms monitored in each home. To obtain average humidity for each home, relative humidity values were used to obtain partial pressure of water vapour in air, based on the Arden Buck equation [20]. The average partial pressure of water vapour was converted back into a relative humidity value, at the average home temperature. The conversion from relative humidity and temperature to partial pressure of water vapour is provided in Equation 1.

$$p_w = \frac{RH}{100} \times 0.61121 \exp\left(\frac{\left(18.678 - \frac{T}{234.5}\right)T}{257.14+T}\right) \quad (1)$$

In Equation 1, p_w is the partial pressure of water vapour (kPa), T is the temperature (°C), and RH is the relative humidity (%). Using p_w, the absolute humidity (AH) was calculated, illustrated in Equation 2.

$$AH\ (\frac{kg\ of\ water}{kg\ of\ dry\ air}) = \frac{0.6219907 \times p_w}{101 - p_w} \quad (2)$$

In Equation 2, AH is the absolute humidity (kg of moisture per kg of dry air) and p_w is the partial pressure of water vapour (kilopascals).

2.2 Home retrofit measures

Each home that was part of this study received an upgrade to the building fabric and heating system. Attic insulation, wall insulation, doors and windows were upgraded. Window and external door frames were upgraded to double-glazed uPVC. The heating system upgrade included a new boiler, hot water tank and controller for setting boiler operation schedule and temperature set point. The homes had passive ventilation, utilizing wall vents, trickle window vents, opening and closing of windows and doors, and extraction fans in bathrooms and kitchens. Mechanical extract fans were installed in the kitchen and bathrooms. Passive wall vents were installed in each room of the houses constructed in 2000. For the houses constructed in 1994, the existing vents were cleaned. For further details on the retrofit measures, refer to [21].

2.3 Data processing and modelling

Data was collated in Excel files and all subsequent processing and modelling was carried out in R [22]. Data was resampled, by averaging all readings within the specific hour, to have all readings at hourly intervals. Descriptive statistic values were calculated initially, including distribution characteristics of the data, mean values, and binning humidity data. The impact of the retrofits on indoor humidity was assessed using linear mixed-effects models (LMEs). LME models are an extension of linear regression models. In this case, there are multiple data points belonging to each home (implying non-independence of data) and data is missing for some of the homes. Hence, LMEs are the suitable choice instead of linear regression which cannot deal with data non-independence. Each home was assigned a House ID, a random number assigned to each home, preceded by the letter H. The House ID served as the random effect in the models. Random, in this instance, is not about mathematical randomness. The House ID is a random effect since how it affects the indoor relative humidity has a less systematic explanation than factors such as outdoor humidity (a fixed effect). Factors associated with individual homes, such as number of occupants, how occupants use their home, will have an impact on the humidity levels. The starting models were comprehensive and controlled for multiple confounders including outdoor temperature (Toutdoor, °C), outdoor humidity levels (RHoutdoor, %), average indoor temperature of the homes (Tindoor, °C), construction year (ConYear, 1994 or 2000), typology (BuiltType, mid terrace or end terrace), number of people living in each home (OccupantNumbers), income of the household (HouseholdIncome, Euros per annum), household number (HouseID, a random ID assigned to homes for anonymity), and the retrofit status (RetrofitStatus, pre- or post-retrofit). The model includes outdoor temperature and humidity as parameters, thus taking into consideration the variations in outdoor conditions over the extended period. As these variables have different units and a wide range of magnitudes, they were scaled before being fitted into the models.

$$RHindoor, average \sim RHoutdoor + Toutdoor + Tindoor + ConYear + BuiltType + OccupantNumbers + HouseholdIncome + RetrofitStatus + (1 + RetrofitStatus|HouseID) \quad (3)$$

In Equation 3, the last term represents the random effect HouseID, while specifying that for each home, the relation developed can have a different intercept and a different slope, from all the other homes. These types of LMEs are referred to as LMEs with random slopes.

Starting with the comprehensive model in Equation 3, the model was gradually simplified, moving towards simpler models with similar or the same prediction error as the initial model. To compare two models, ANOVA was used. Prediction errors were compared using Akaike Information Criteria (AIC) [23]. To check specifically the impact of the retrofit, the simplest model arrived at was compared with a model without the retrofit status. The null hypothesis in this case was that addition of retrofit status as an effect does not significantly improve the model, implying retrofits did not affect indoor humidity levels. Models with and without retrofit status

included were compared by ANOVA to test this null hypothesis. When significant differences emerge between models, a pairwise comparison of pre- and post-retrofit data was done using "lsmeans" package in R [24].

3 RESULTS AND DISCUSSION

3.1 Summary statistics

Table 1 provides the mean and standard deviation (s.d.) of temperature and humidity for all homes combined, during the pre- and post-retrofit periods.

Table 1. Indoor conditions, pre- and post-retrofit, averaged across all homes. Representation: Mean (s.d.)

	Temperature (°C)	RH (%)
Pre-retrofit	19.5 (2.3)	52 (7)
Post-retrofit	20.6 (2.0)	57 (7)

On average, homes got warmer post-retrofit. This was expected since the retrofits improved the thermal properties of the building fabric. At the same time, a small increase in humidity levels was also noted. It must be clarified that these mean values do not consider outdoor weather. These confounding effects are accounted for in the LME.

Figure 1 provides a stacked bar plot for humidity in each home, binned across five humidity range categories. Each home's assigned ID is on the x-axis while the y-axis provides the relative humidity values. Each stack on the bar-plots is annotated with the percentage of readings that were within the specified humidity bin. From the comfort point of view, low humidity has little effect on thermal comfort, but skin dryness, and eye and throat irritation can increase when humidity levels are under 30% [25]. Such situations were rare both pre- and post-retrofit. For all homes except one, the fraction of readings in the 60-80% increased post-retrofit. Pre-retrofit, 17 homes spent 80% or more time in the 40-60% relative humidity bin. Post-retrofit the number of such homes droped to nine. The 40-60% humidity band is a recommended "optimum" zone for avoiding a range of issues ranging from respiratory pathogens, fungi, mould, allergies and asthma, mites, and chemical interactions [26, 27]. Following the retrofit upgrade work, this noted increase in humidity levels in multiple homes presents a concerning pattern. Following the retrofit, there were very few instances (two homes, H21 and H12) where RH exceeded the 80% mark.

3.2 Mixed effects models

Following model simplifications, the model form arrived at is shown in Equation 4.

$$RHindoor,average \sim RHoutdoor,average + Toutdoor + RetrofitStatus + Tindoor + (1 + RetrofitStatus|HouseID) \quad (4)$$

The model in Equation 4, while being much simpler in form, led only to a small change in AIC value (1689860 vs 1689850). For AIC values, smaller is better. For comparison, the LME (Equation 4) had a notably better AIC value than the linear model that took all the factors in Equation 3 into account (1689860 vs 1794033). A similar model was also constructed which used outdoor absolute humidity instead of the outdoor relative humidity, as in Equation 4. The absolute humidity-based model was discarded as the RH based model was significantly better ($\chi^2 = 5864$, $p < 0.0001$).

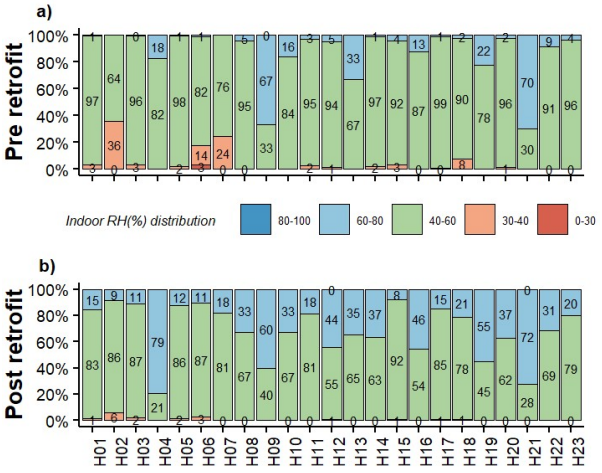

Figure 1. Indoor RH distribution binned, a) pre-retrofit and b) post-retrofit.

In the simplified LME, building and socio-economic factors including construction year, built type, number of occupants, and income of the household, were all excluded. It is likely that by considering the homes as a random effect, several of these factors are being inherently considered in the model. The study gathered multiple building and socio-economic factors. However, there are always aspects of occupant behaviour like cooking, showering, drying clothes, that cannot be surveyed without compromising privacy. It would be difficult to have a model that explicitly accounts for these factors. The LME helps the case by providing an option to implicitly account for multiple behavioural, building, and socio-economic factors.

Comparing LMEs with and without the retrofit status included affected the model significantly ($\chi^2(1)=23.7$, $p<0.0001$). The lsmean estimates for pre- vs post-retrofit values of humidity indicated a 3.5% increase ($p< 0.0001$, std. error = 0.6, z-ratio = 6.16). The humidity lsmean for homes pre-retrofit was 53.0% (95% confidence interval: 51.1-54.9%). Similarly, the post-retrofit lsmean was 56.5% (95% confidence interval: 55.2-57.8%). It must be noted here that unlike the values provided in Table 1, the estimates for lsmean consider the confounding effects due to change in outdoor weather and change in indoor temperatures. Hence, the lsmean values are a better and more unbiased indicator of the impact of retrofits on indoor humidity. Post-retrofit, indoor conditions had warmed up. Warmer indoor conditions would have led to lowered RH values if the absolute water content of the indoor air had remained the same. However, what is noted is that even accounting for the change in indoor temperature, the relative humidity levels rose.

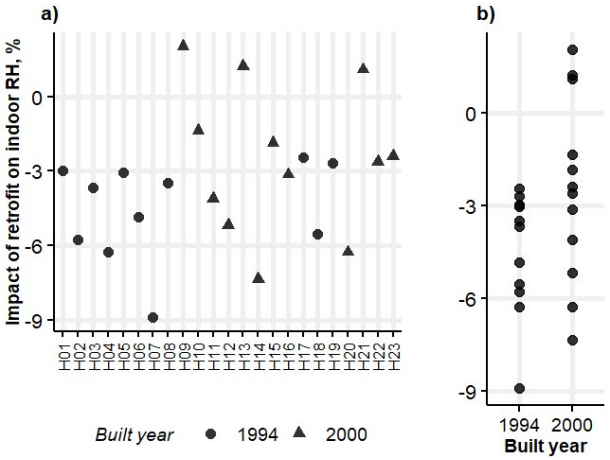

Figure 2. The estimated shift in indoor humidity levels due to the energy retrofits, using the LME a) for each home b) for homes grouped by the built year.

Based on the coefficients of the LME, the external temperature had the strongest impact (coefficient = 4.6), followed by external RH (3.6), and indoor temperature (-1.6) on the model for predicting indoor humidity levels. This is aside of the shift found for indoor humidity due to the retrofit. Since the variables had been scaled for the model, the coefficients are a direct representation of the relative importance of the different parameters in predicting indoor humidity levels.

Figure 2 provides the estimated shift in average indoor humidity, from the pre-retrofit to the post-retrofit period, based on the LME. From Figure 2 b), it may be noted that the only homes where the estimated average humidity reduced were built in 2000. Also, the homes built in 2000 had a wider spread of the estimated change in relative humidity. For 13 of the homes, the humidity shift was 3% or more.

Figure 3 provides plots of indoor relative humidity against outdoor relative humidity, for each home. Similar correlations have been provided in previous studies [17, 18]. However, unlike the previous works, LMEs developed as part of this study consider the data from each home independently instead of trying to create one uniform model for the whole data set. Additionally, retrofit status is also introduced as an additional parameter. From Figure 3, it is apparent that across retrofit status and for each individual home, indoor humidity levels related well to outdoor humidity, as suggested by the previous works.

Given the inherent differences between homes, the mixed effects models are the statistically appropriate choice for the available data sets. In Figure 3, the predicted data, based on the LME in Equation 4, has been provided in the form of linear fits. The lines represent linear fits for predicted values from the LME in Equation 4. The predicted values have been differentiated into pre- and post-retrofit parts. As the LMEs are random slopes models, the lines for each home have differing slopes and intercepts. These differences indicate that indoor humidity of each home responds differently to changes in outdoor humidity. These differences are due to a combination of factors such as differences in the building and materials, occupancy, occupant behaviour, and demographics, which are subsumed into the random effect, i.e., home ID.

The dashed lines, representing predicted post-retrofit data are almost consistently over the pre-retrofit predicted data linear fit. This further illustrates that the indoor humidity increased post-retrofit, and this increase was noted through the entire range of outdoor humidity levels experienced.

The analysis consistently showed that post-retrofit indoor relative humidity increased, even after considering variations in outdoor weather and indoor temperature over the monitoring duration. This is likely due to the energy retrofits also create more airtight facades for the homes.

3.3 Householder feedback

Of the 20 households for which feedback could be obtained, 17 indicated a presence of mould in their homes before the retrofit work, based on visual inspection of the indoor surfaces. Post-retrofit, 11 of these 17 households did not have a presence of mould based on visual inspection. For most of these houses, where an improvement in the mould situation was noted, householders referred to the mould growth around the frames of the windows being remedied. This could be due to the frames having been replaced with uPVC since many householders still reported condensate on the windows. Mould along the junctions of ceilings and walls also persisted. Six houses had a mould presence both before and after retrofits. Two houses, which did not have mould pre-retrofit, reported issues of mould along the ceiling-wall junction and walls in the bathrooms despite the new extractor fans. The mould issue at the ceiling-wall junction could be related to thermal bridging issues in these junctions. There are two humidity levels of importance regarding mould growth. While mould germination requires RH of 80%, mould survival and growth requires RH levels above 60% [28]. It is important to note here that even though indoor humidity levels above 80% were not encountered during the period when readings were taken, RH of air near indoor surfaces can still be higher than 80%. The lower temperature of these surfaces, due to inadequate insulation, faulty workmanship, or thermal bridging, decreases the local air temperature, thus increasing the RH and causing moisture to condense on the material surfaces leading to optimum conditions for mould growth. The local RH can exceed 80%, leading to favourable conditions for mould germination.

Some householders also reported draft issues with the newly installed wall-vents, especially the ones on the walls exposed to prevailing winds. This led some householders closing or blocking them, adversely impacting the ventilation in these homes. Some householders also switched the extract fans in the kitchen and bathrooms to manual mode. They did not appreciate the auto mode fans being operational a ‘long time’ after using the shower in the bathroom or cooking in the kitchen. The kitchen extractor had the further issue of the fan being ‘shaky’ and ‘noisy’ during windy weather. Householders with this issue blocked off these vents. Due to these range of issues, ventilation during operation was often inadequate.

Passive ventilation can be effective, but this does require active cooperation of the householders, e.g., opening windows, keeping vents open. Mechanical ventilation removes some of the responsibility of homeowners but still needs occupants to be educated in their use and necessity. Occupants can still

adversely impact mechanical ventilation set-ups, as was seen with some of the kitchen extractor fans. Thus, a suitable technical solution in combination with educating householders on the importance of ventilation is critical to prevent mould growth problems [28].

3.4 Study limitations

The small sample size is a limitation of this work. Homes in a specific region and with similar designs and era of construction made up our entire sample space. Progressing to cover a wider range of residence typologies and geographical regions can provide further, unbiased insights regarding moisture issues in retrofits. For a larger sample size, models could examine the influence of demographic, socio-economic, and regional parameters. In the current model, the random effect subsumes a lot of these variations implicitly.

In this study, seasons and heating periods were not included in the model. Similarly, the difference between different rooms of the homes was also not modelled. These factors will be part of the further analysis being carried out on the data.

4 CONCLUSION

Using linear mixed effects models, the impact of energy retrofits on indoor humidity levels was examined. While home retrofit programs are driven by energy and CO_2 emission reduction goals, it is important to acknowledge that they also impact the indoor environment of homes. Indoor humidity is an important parameter of indoor thermal environment and air quality and can impact several aspects related to occupant health and building structural integrity. Hence, such investigations into the impact of retrofits on indoor environmental parameters are useful to understand the scope of impact due to energy retrofits in dwellings.

The LME model analysis showed that post-retrofit, indoor humidity levels showed a statistically significant increase. Outdoor temperature and humidity were important predictors for indoor humidity levels.

The increase was consistent even after considering the variations of outdoor weather and indoor temperature across pre- and post-retrofit periods. The post-retrofit homes had relative humidity levels which were greater than the 40-60% RH zone, considered to be optimum from multiple perspectives, more frequently than in pre-retrofit homes. Humidity levels post-retrofit did not exceed the 80% mark. However, the increased humidity levels are not ideal from the point of view of health as well as localized mould formation. Even though the room air humidity levels are under 80%, humidity in air close to cold surfaces can go beyond 80%, starting mould problems. The increased humidity could partly be a consequence of the more airtight facades resulting from energy retrofits. Following the tenet of "build tight and ventilate right", the post-retrofit homes did have improved ventilation features. However, occupant use meant that the ventilation system may not have been able to achieve its goal. Householders blocked passive vents and did not use extractor fans as advised.

With the homes becoming more airtight, our results suggest that retrofit measures should focus on suitably designed ventilation system and a smooth handover of homes to occupants. Occupant cooperation and understanding of the home heating and ventilation is a necessity for smooth operation and health indoor environment in post-retrofit homes. This may require a policy level move. Such a move can not only aid with any humidity issue but will also contribute to improved overall air quality in homes.

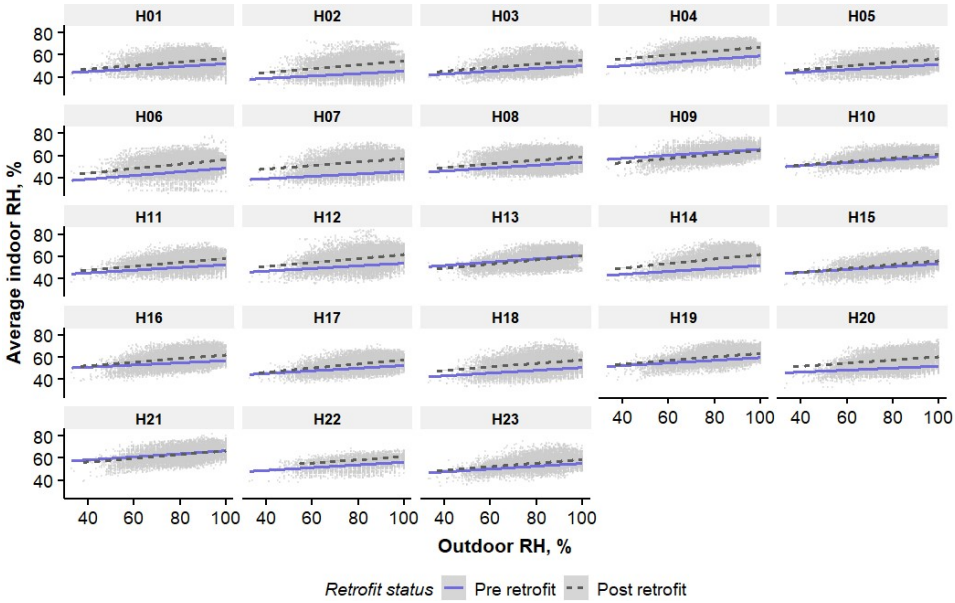

Figure 3. Average indoor relative humidity data plotted against outdoor relative humidity for each home, represented by grey dots.

ACKNOWLEDGMENTS

The authors wish to acknowledge the financial support from Sustainable Energy Authority of Ireland (SEAI) through Grant No. RDD/492. The authors would also like to acknowledge financial support from the Science Foundation Ireland (grant no. 13/CDA/2200).

REFERENCES

[1] European Commission, COMMUNICATION FROM THE COMMISSION TO THE EUROPEAN PARLIAMENT, THE EUROPEAN COUNCIL, THE COUNCIL, THE EUROPEAN ECONOMIC AND SOCIAL COMMITTEE AND THE COMMITTEE OF THE REGIONS The European Green Deal, 2019. https://doi.org/10.2307/j.ctvd1c6zh.7.

[2] DCCAE, Climate Action Plan 2019 To Tackle Climate Breakdown, Department of Communications, Climate Action and Environment, 2019. https://doi.org/10.5860/choice.46-0890.

[3] Sustainable Energy Authority of Ireland (2017), Ireland's Energy Statistics – Key Statistics, Residential sector. https://www.seai.ie/data-and-insights/seai-statistics/key-statistics/residential/ (accessed Apr. 02, 2022).

[4] Velux (2020) Healthy homes Barometer 2020 Ensuring a green recovery post-Covid-19 with sustainable buildings https://velcdn.azureedge.net/-/media/com/healthy-homes-barometer/hhb-2020/hhb_main_report_2020.pdf [accessed 02/11/2021]

[5] HSE (2022) About COPD, National Clinical Programme https://www.hse.ie/eng/about/who/cspd/ncps/copd/about/about-copd.html [accessed 28/04/2022]

[6] Asthma Society of Ireland (2017) Asthma & Indoor Air Quality. https://www.asthma.ie/sites/default/files/files/document_bank/2017/Dec/Indoor%20Air%20Quality%20Report.pdf [accessed 28/04/2022]

[7] Kleipeis NE, Nelson WC, Ott WR, Robinson JP, Tsang AM, Switzer, P, Behar JV, Hern SC, Engelmann WH, (2001), The National Human Activity Pattern Survey (NHAPS): a resource for assessing exposure to environmental pollutants. Journal of Exposure Science and Environmental Epidemiology, 11(3), 231-52

[8] Asikainen, A., Carrer, P., Kephalopoulos, S., de Oliveira Fernandes, E., Wargocki, P., Hänninen, O. (2016) Reducing burden or disease from residential indoor air exposures in Europe (HEALTHVENT project) Environmental Health, 15:S35 https://doi.org/10.1186/s12940-016-0101-8

[9] European Commission, Energy Performance of Buildings Directive https://ec.europa.eu/energy/topics/energy-efficiency/energy-efficient-buildings/energy-performance-buildings-directive_en [accessed February 2022]

[10] J. Scheer, M. Clancy, S.N. Hógáin, Quantification of energy savings from Ireland's Home Energy Saving scheme: An ex post billing analysis, Energy Effic. 6 (2013) 35–48. https://doi.org/10.1007/s12053-012-9164-8.

[11] A. Byrne, G. Byrne, G. O'Donnell, A. Robinson, Case studies of cavity and external wall insulation retrofitted under the Irish Home Energy Saving Scheme: Technical analysis and occupant perspectives, Energy Build. 130 (2016) 420–433. https://doi.org/10.1016/j.enbuild.2016.08.027.

[12] A. Byrne, G. Byrne, A. Davies, A.J. Robinson, Transient and quasi-steady thermal behaviour of a building envelope due to retrofitted cavity wall and ceiling insulation, Energy Build. 61 (2013) 356–365. https://doi.org/10.1016/j.enbuild.2013.02.044.

[13] M. Collins, J. Curtis, Value for money in energy efficiency retrofits in Ireland: grant provider and grant recipients, Appl. Econ. 49 (2017) 5245–5267. https://doi.org/10.1080/00036846.2017.1302068.

[14] British Standards Institution (2021), Management of moisture in buildings — Code of practice. BSI Standards Publication.

[15] P. Wolkoff (2018), 'Indoor air humidity, air quality, and health – An overview', *International Journal of Hygiene and Environmental Health*, vol. 221, no. 3, pp. 376–390, doi: 10.1016/j.ijheh.2018.01.015.

[16] R. Quansah, M. S. Jaakkola, T. T. Hugg, S. A. M. Heikkinen, and J. J. K. Jaakkola (2012), 'Residential Dampness and Molds and the Risk of Developing Asthma: A Systematic Review and Meta-Analysis', *PLOS ONE*, vol. 7, no. 11, p. e47526, doi: 10.1371/journal.pone.0047526.

[17] J. Pan *et al.* (2021), 'Correlating indoor and outdoor temperature and humidity in a sample of buildings in tropical climates,' *Indoor Air*, vol. 31, no. 6, pp. 2281–2295, doi: 10.1111/ina.12876.

[18] J. D. Tamerius *et al.* (2013), 'Socioeconomic and Outdoor Meteorological Determinants of Indoor Temperature and Humidity in New York City Dwellings,' *Weather, Climate, and Society*, vol. 5, no. 2, pp. 168–179, doi: 10.1175/WCAS-D-12-00030.1.

[19] Met Éireann, Met Éireann Dublin Airport Monthly Weather Data, (2016). http://www.met.ie/climate/monthly-data.asp?Num=532 (accessed April 6, 2017).

[20] Buck, A. L. (1981). New equations for computing vapor pressure and enhancement factor. *Journal of Applied Meteorology and Climatology*, 20(12), 1527-1532.

[21] Moran, P., & Goggins, J. (2020). Can DEAP Help Us To Predict The Energy Demand And Indoor Temperature Of Homes Before And After Renovation? A Case Study From Dublin. Civil Engineering Research in Ireland 2020. Cork, Ireland.

[22] R Core Team (2021). R: A language and environment for statistical computing. R Foundation for Statistical Computing, Vienna, Austria. https://www.R-project.org/

[23] B. Winter (2013), Linear models and linear mixed effects models in R with linguistic applications, University of California, Merced, Cognitive and Information Sciences.

[24] R. V Length (2016), Least-Squares Means: The R Package lsmeans, J. Stat. Softw. 69, 1–33. https://doi.org/10.18637/jss.v069.i01

[25] Derby, M. M., Hamehkasi, M., Eckels, S., Hwang, G. M., Jones, B., Maghirang, R., & Shulan, D. (2017). Update of the scientific evidence for specifying lower limit relative humidity levels for comfort, health, and indoor environmental quality in occupied spaces (RP-1630). *Science and Technology for the Built Environment*, 23(1), 30-45.

[26] Arundel, A. V., Sterling, E. M., Biggin, J. H., & Sterling, T. D. (1986). Indirect health effects of relative humidity in indoor environments. *Environmental health perspectives*, 65, 351-361.

[27] Baughman, A., & Arens, E. A. (1996). Indoor humidity and human health--Part I: Literature review of health effects of humidity-influenced indoor pollutants. *ASHRAE Transactions*, 102, 192-211.

[28] Su, B. (2006). Prevention of winter mould growth in housing. *Architectural Science Review*, 49(4), 385-390.

A Review of Methods for Examining Behaviours of Occupants in Residential Buildings

Lala Rukh Memon[1,2], Paul Moran[1], Jamie Goggins[1, 2]
[1]MaREI Centre, Ryan Institute & School of Engineering, College of Science and Engineering, National University of Ireland, H91 TK33 Galway, Ireland
[2]Energy Resilience and the Built Environment (ERBE) Centre for Doctoral Training, National University of Ireland, H91 TK33 Galway, Ireland
Email: l.memon1@nuigalway.ie, paul.t.moran@nuigalway.ie, jamie.goggins@nuigalway.ie

ABSTRACT: The energy transition is a technological as well as a societal challenge. It is unknown to what extent are we ready to change our behaviours pertaining to energy consumption. Buildings can play a pivotal role in reducing global energy consumption, and greenhouse gas (GHG) emissions, as well as bringing a global clean energy transition. Occupant behaviours, being complex and dynamic, significantly impacts building energy performance, as well as occupant comfort. Diverse sociological and psychological factors influence how and why occupants use energy within buildings. The dynamic nature of human behaviour makes this area of research a challenge. Occupant behaviour can be described with higher accuracy by understanding human-building interactions. This study systematically reviews existing methods currently used for examining occupant behaviour with a focus on the impact on heating and cooling in residential buildings, including hot water consumption patterns and ventilation patterns. The review helps in understanding the importance of using individual or share approaches aiming to integrate human behaviour with indoor/outdoor conditions. It is realised that however occupancy alone has been repeatedly analysed to understand the human behaviour. Several other energy demand drivers remain mainly unaddressed.

KEY WORDS: Cooling; Energy consumption patterns; Energy Demand Practices; Heating; Occupant behaviour; Residential buildings; Room air conditioner; Ventilation.

1 INTRODUCTION

Buildings are among the major economic sectors of energy use globally, accounting for about one-third of final energy use [1]. The share of energy consumption in buildings has been consistent in the last decade leading up to 2020, until the global COVID-19 pandemic caused shifts in building energy demand away from commercial and industrial activities to residential buildings [2]. This provided an opportunity to witness changes in energy demand patterns in buildings from a new perspective. On average, a reduction of 20% was observed in countries with full lockdown measures, whereas in places with partial lockdowns, the reduction was less significant [1]. After easing lockdown measures, a significant increase in demand for higher ventilation rates (for health reasons) was also observed [1].

By reducing energy demand of the building sector, energy and climate crisis can be potentially addressed [4]. With growing concerns over the implementation of building energy codes; building energy policies have also been improving over the last decade [4]. Consequently, energy intensity in the building sector has also reduced substantially by 0.5% to 1% each year from 2010 to 2019 [5]. However, annual floor area growth and resulting energy service demands outpaced the efficiency gains [4].

Occupant behaviour, despite being complex, significantly impacts building energy performance, as well as occupant comfort. As a result, it causes uncertainty in building energy performance [6]. The performance gaps between predicted and actual energy consumption in residential buildings are considerable and also attributed to occupant behavioural factors [7]–[14], among other parameters such as uncertainty in modelling, and poor operational practices.

To avoid uncertainty caused by occupant behaviour, it is essential to determine the impact of dynamic occupant behaviours (including social and psychological drivers) on building energy demand including energy demand behaviours such as indoor temperature requirements, fresh air volume per person, hot water consumption per person, space heating duration, etc. Accurate information for understanding human behaviours can help improve the energy performance contracting framework by incorporating social and psychological factors thereby seeking more energy saving benefits.

Occupant behaviour and associated parameters have been treated as boundary conditions, like weather [15]. Recently, occupant behaviour in buildings has drawn attention of researchers as more evidence is recognised about human-buildings interaction and impact of occupancy, movement, and diverse choice of comfort on energy use in buildings [16], [17].

Therefore, understanding occupant behaviour, and choosing scientific methods to define occupant behaviour for building energy performance evaluation is becoming more important to narrow this gap [17]. A better understanding of occupant behaviour shall lead to suitable building architecture design, system choice and equipment adoption. Through which, not only energy and environmental costs can be saved but it shall help achieve better air quality, thermal comfort, economic and social development.

This study is aimed at providing an analysis of the literature of methods used for examining the occupant behaviour in residential buildings focusing on the impact on heating and cooling loads. The case studies, survey studies, and building simulation methods paired with fieldwork are particularly targeted to narrow the scope of this study.

2 METHODOLOGY

A systematic literature review was carried out to analyse the methods used for occupant behaviour examination in residential buildings. The search question mainly focused on occupant behaviour and its impact on energy consumption in residential buildings pertaining to heating and cooling. Thus, the keywords used for the search are Occupant behaviour' OR 'Occupant Behavior' AND 'Energy demand practices' OR 'Energy consumption patterns' AND 'residential' AND NOT 'fire hazard' AND NOT 'office' AND NOT 'evacuation'.

The flow chart shown in Figure 1 provides a summary of the inclusion/exclusion of bibliographic records used for this study. In the first step, 27 studied are excluded which did not meet the aim of the study, based on title and abstract reading. In the second step, only studies with case studies and field work and surveys are included. Finally, in third step, all studies not addressing heating and cooling demand are excluded. Also, at this stage of screening process only peer reviewed and journal papers are included, and conference proceedings, book chapters are excluded due to inaccessibility.

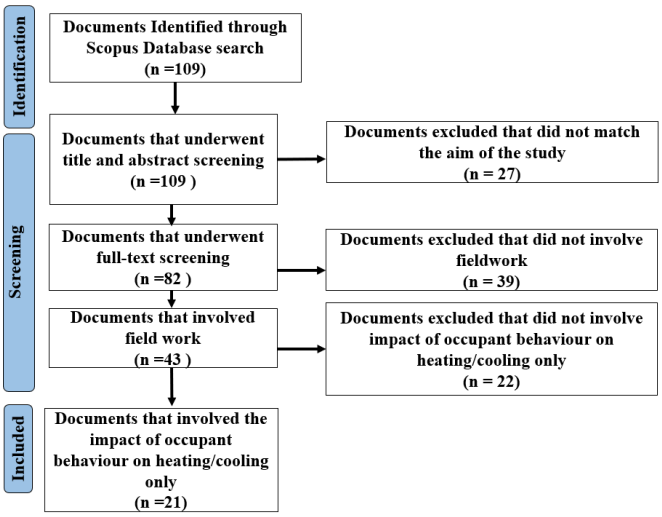

Figure 1. Literature Screening Process

3 METHODS FOR EXAMINING OCCUPANT BEHAVIOUR IN RESIDENTIAL BUILDINGS

3.1 Overview

The occupant behaviour being a not very old concept in the field of energy in buildings, the studies are very young, 2017 and onwards except for one study. Majority of the reviewed studies are based on analysis of Chinese residential buildings (11), followed by Denmark (2), Italy (2), Australia (1), Cyprus (1), Finland (1), Portugal (1), Spain (1), and Switzerland (1).

As only case studies, fieldwork, and survey studies are reviewed, sample size and period of data collection are key factors. It is highlighted that even in such a small pool of studies under consideration, the sample size, as well as the period of data collection, varies significantly from 1 residential building [18] up to 8,293 [19]. Similarly, the time of data collection varies from 6 days [20] up to 7 years [19]. The sample size and period in occupant behaviour analysis impact the results significantly, as occupant behaviour can be dynamic and results from a few households cannot be the true representation of bigger population groups. Similarly, in a data collection period as big as 7 years, many dependent variables such as age, the number of occupants in a building, income, education, and health status can potentially change over time.

In changing global times, other changes such as lockdowns imposed by pandemics can occur, which significantly change occupants' energy profile. One of the studies under review is conducted during COVID-19 lockdown period, which represents changing occupant behaviour towards energy consumption [18]. However, the results of this study cannot be generalised for typical times, the method stands valid. Another reasonable consideration is if the energy is provided through renewable energy resource [20]. Which may impact the consumption behaviour [21].

From the literature, the following common goals were identified:

- To group occupants based on behaviours such as on/off times, the duration of each operation, AC 'run-over-night' probability, consumption intensity and representative pattern for analysing energy saving potential [22] [23] [24] [25] [26] [27] [19]
- To integrate the occupants' behaviour into hot water systems control [28] [20]
- To identify household socio-demographic characteristics contributing to development of energy-user profiles [29]
- To predict AC on/off behaviour and relationship with indoor environmental conditions, building characteristics, mean outdoor temperature [30] [31] [32] [33]
- To identify relationship between thermal comfort needs over healthy indoor air quality [34]
- To identify relationship between occupants' actions and characteristics of the built environment [35] [36]
- To identify the influence of family income, number of children, and building age on heating patterns [37]
- To build correlations between occupant actions and local seasonal changes [38] [39]

Table 1 describes the purpose of reviewed studies and the approach taken in terms of data collection. These are categorised as survey for data collection through questionnaires (online or in person) and data loggers for data collection through real-time field measurements. It is evident that (seven) studies aiming to develop relationships, or integrate behaviour with indoor or outdoor conditions, typically use multiple approaches, for example survey and measurement. However other studies with single approach studies focus on building parameters or socioeconomic factors only.

Table 1. Aims and data collection method of reviewed studies

Ref	Aim	Survey	Data Loggers
[28]	Integrate the occupants' behaviour into hot water systems control	x	x
[30]	Build the relationship of air conditioner performance with occupant behaviour and service space properties	x	x
[22]	Analyse energy saving potential based on occupant heating behaviour	x	x
[34]	Build a relationship of occupant's choice (mechanical vs natural ventilation) with thermal comfort needs and indoor air quality	x	x

[23]	Assess energy performance of buildings considering real use of energy	x	x
[20]	Determine hot water usage patterns	x	x
[38]	Analyse changed electricity consumption pattern in response to the environment air temperatures	x	x
[35]	Determine occupant behavioural patterns associated with heating and cooling energy consumption	x	
[36]	Build a relationship of occupants' actions with characteristics of the built environment	x	
[37]	Determine impact of family income, number of children, and building age on heating patterns	x	
[24]	Measure room-wise heating demands		x
[31]	Predict air conditioner on/off behaviour		x
[32]	Predict indoor environmental conditions and energy consumption based on air conditioner operation patterns		x
[25]	Identify temperature-setting behavioural patterns through cluster analysis		x
[26]	Develop a methodology for heating behaviour characterization		x
[29]	Develop clusters for daily on/off times, the duration of each operation, and air conditioner 'run-over-night' probability		x
[27]	Analyse energy saving potential based on occupant heating behaviour		x
[19]	Develop clusters based on consumption intensity and representative pattern		x
[39]	Build correlations between occupant groups and different seasons on DHW use		x
[33]	Analyse the influence of heating set-point preferences on indoor environmental quality and heating demand in residential buildings		x

The aimed and well achieved goals of the reviewed studies incorporate different occupant behaviours in different studies but a holistic framework that addresses social and psychological energy demand drivers in residential buildings is still missing. Occupant behaviour and actions towards energy-related building control can be induced by several dynamic factors, external to the occupant (environmental conditions), internal (personality, background, etc.), and (building characteristics) including heating/cooling devices and ventilation systems [40]. Also, the occupant actions impact several different energy-related expenses, such as hot water consumption, use of air conditioners, use of heating and cooling systems, and ventilation system which are discussed in the following sections.

3.2 Domestic Hot Water Consumption

Hot water consumption is a highly stochastic occupant behaviour leading to higher energy demand for water heating purposes. In one study, a hot water control framework using Reinforcement Learning is proposed, claiming to learn occupants' behaviour and act objectively according to the energy use needs [18]. The proposed methodology requires minimum number of sensors to measure only four parameters, i.e., temperature, water flow, and power use of the heat pump are measured. Reducing the error margin and increasing economic feasibility. Only occupancy and water consumption patterns are analysed as drivers of energy demand for hot water. Whereas the drivers behind occupant behaviour can be physical, environmental, contextual, psychological, and social in nature [41]. However, comparing with a similar study [42] (conducted before lockdown), and depending on survey regarding occupancy prior to pandemic. The results show that the occupant's behaviour during lockdown certainly does not follow the same consumption trends as during typical times and the correlation between weekdays and weekend days is weaker. As the duration and frequency of hot water consumption is observed to be increased throughout the week during study period. The number of occupants also varies between 3 and 5 over the study period. These unexpected changes make machine learning model training and thus prediction of occupant's behaviour difficult.

Similarly, another study of 86 apartments for 52 weeks with 191 occupants proposes a bottom-up model (using R language to build the correlations) in hot water consumption patterns via analytical formulas [43]. This study also does not include any other drivers besides occupant's schedule for hot water consumption without real-time monitoring of the temperature. Only hourly consumption data for cold and hot water with 1-hour time resolution and accuracy ±2% is considered [43].

It is observed that if the study is conducted for smaller period, such as six days, in case of study [20]. It becomes feasible to investigate more participants (4714 occupants in 16 buildings) and include more factors for analysis such as shower frequency, duration of hot water use, and the experience and expectations of the hot water system in the survey.

From a review of methods for analysing the impact of occupant behaviour on hot water consumption patterns, it is found that shared approach (using data loggers and survey together) helps in understanding occupant behaviour [18], [20]. But shared approaches can be limited by number of factors such as either by number of buildings (only 1 in case of [18]), number of participants, or period of analysis [20]. Also, these methods however building the relationship between occupant behaviour and hot water demand, cannot be generalised as limiting factors involve, if the study is carried out during COVID-19 lockdown period [18] or carried out in buildings with solar water heating systems [20].

3.3 Energy Use Profile with a focus on heating/cooling

Rinaldi et al. [36] conducted multivariate regression analysis to relate the construction year with heating and cooling set points, fuel consumption, the adaptive behaviour of occupants, and family monthly income. This study was based on data from an online survey (comprising sections for background information of buildings, family general information, behaviours, common preferences and fuel consumption). The result of this study shows that the set-point temperature of heating system varies with respect to construction year of the building, i.e., lower in newer (after 2000s) buildings. Furthermore, survey results also show that the occupants in these newer buildings react adaptively to meet thermal comfort [36]. For example, by change of clothes according to weather and drinking hot or cold drinks respectively. These adaptive

preferences are further reflected through reduction in overall fuel consumption for heating systems.

In contrast to a survey only based study, Cipriano et al. [23] provides a quantitative and qualitative framework. A (questionnaire) survey (consisting of predefined 43 questions further classified into household information, economic data, consumption of water & energy, comfort, occupancy, and use of appliances) is followed by a field survey of energy-related data, which included gas and electricity bills, and equipment inventory along with monitoring of indoor and outdoor temperature and electricity half-hourly consumption. The study results have corelated the family income with type of space heating system, number, and use of energy appliance [23]. As results show sufficient difference in energy consumption with a difference of at least 36% in monthly income of two groups [23].

3.4 Heating & Cooling

For energy saving in residential buildings, the heating/cooling system must be designed and selected as per the occupant's actual demand, which makes understanding the user demand even more important. Heating and cooling demands are irregular and part-time, part-space heating and cooling have the potential to meet the thermal comfort and save energy [24]. Like many other survey-based studies, Ozarisoy and Altan [35] also relies on the respondent's response only, without conducting Realtime measurement for developing energy consumption profiles. Various methods are used as represented in Table 2 to examine occupant behaviour related direct and indirect factors impacting space heating and cooling demand in residential buildings. For example, J. P. Gouveia et al. [38] have investigated power consumption attributed to space heating/cooling, minimum and maximum daily outdoor temperatures in addition to a survey. With the variation in power consumption in response to change in outside temperature during a day, authors have developed proxy for occupants' behaviour pertaining to space heating and cooling [38].

Table 2. Methods used for examining direct and indirect factors that relate (heating/cooling) energy demand in response of occupant behaviour

Behaviour (data collection method)	Ref
– Occupancy patterns (Survey) – Window-opening patterns (Survey) – Heating consumption patterns (Survey)	[35]
– Indoor air temperatures (temperature loggers; WZY-1A, Tianjian Hua Yi Co., China) – (on/off information, mode, temperature setting, power, fan speed, and other operating information) (Dataloggers)	[24]
– Indoor air temperature and humidity (iButtons)	[32]
– Total natural gas consumption (Meter) – Temperature (Sensors) – Relative Humidity (Sensors) – CO_2 (Sensors)	[26]
– Heating patterns (district heating consumption data	[19]
– Demographical data (Survey)	[37]
– Electricity consumption profile (Survey and Smart meter)	[38]
– Setpoint for heating (simulation tool IDA ICE (Indoor Climate and Energy; ICE 4 2009)	[33]

3.5 Use of Air Conditioners

Table 3 provides an overview of the methods used for examining direct and indirect factors that relate (air conditioner) energy demand in response of occupant behaviour. From the review, it is recognized that Artificial Neural Network and a Gradient Boosting Decision Tree algorithms provide better prediction results as compared to logistic regression [44]. Also, drivers like indoor relative humidity and CO_2 concentration significantly affect the model accuracy, thus these must be considered while modelling occupant behaviour for air conditioners [31]. Another critical factor in energy consumption in residential buildings is the set-point temperature of room air conditioners [25]. The studies carried out in China represents a significant correlation between the operating hours and energy required for cooling. Which supports the part-time, part-space use mode for energy saving potential, in contrast to much popular full-time, full-space mode in China [27].

Table 3. Methods used for examining direct and indirect factors that relate (air conditioner) energy demand in response of occupant behaviour

Behaviour (data collection method)	Ref
– Temperature, relative humidity, CO_2 concentration, and PM2.5 concentration (Ikair, sensor module) – AC power data at the corresponding time (Smart meter)	[31]
– Refrigerant (refrigerant temperature sensors) – Temperature (Temperature sensors) – Environment temperature (environment temperature sensor) – Humidity (humidity sensors) – Unit and compressor electricity consumption (unit and compressor electricity consumption testing devices) – Compressor frequency (compressor frequency testing devices)	[30]
– Set-point temperature (sensors) – Indoor air temperature (sensors) – fan speed (sensors) – Total operation hours energy consumption (An integrated chip with a Wi-Fi module)	[25]
– Outdoor daily mean temperature (observation average)	[45]

– Temperature setting (Survey) – The daily/ hourly usage (Survey)	
– Real-time power consumption data (smart meter) – AC on/off status (Zigbee smart sockets)	[29]
– Real-time power, accumulated power, operation mode, indoor temperature, humidity, and temperature settings (Monitored, calculated, and investigated)	[22]
– Cooling/heating data of each FCU (A thermal energy metering system) – Metered data of FCUs (Chuntsuan Energy-saving Technology Company of Zhengzhou)	[27]

3.6 Ventilation

The properties (sliding-, pivoted-, side- or top hung windows) of window opening predefine the related window opening behaviour [46] and other factors such as opening angle, size and placement within facade impact air exchange rate significantly [47], requiring more energy. Ventilation behaviour has been analysed through shared approach by using on-site measurement for twelve months followed by an (online six questions based) survey [34]. The collected parameters for drivers' identification include, mechanical ventilation operation status, window (opening and closing) actions, indoor environmental parameters, outdoor environmental parameters.

A recorder with a differential pressure meter and magnetic sensors (mounted on the window casement and frame) has been custom designed to measure the mechanical ventilation operation status and the window-opening respectively. The survey inquiring the preferred method of ventilation in different outdoor environments and the reason for preference further helps to understand the ventilation duration and motivation behind using natural or mechanical ventilation systems. However, it is pertinent to mention that the questionnaire did not define different outdoor environments to the participants which can cause discrepancy in results.

4 DISCUSSION

Occupant behaviour is one of the main causes of the gap between building energy demand prediction and actual consumption. Diversity in the stochastic nature of occupant behaviour is a bottleneck in the development, implementation, monitoring, and evaluation of building energy policies. From the systematic literature review of methods for examining behaviours of occupants in residential buildings, it is observed that the seemingly simple occupant actions that influence energy demand patterns in buildings, such as opening/closing of the window, setpoint temperature preference, temporal preferences are driven by several complex interacting factors. It is further recommended that efforts should be made to address the dynamics of relationship among people's behaviour, indoor environmental conditions, thermal comfort, health, and wellbeing. Finally, using shared approaches, robust occupant behaviour models need to be developed, that address the socio-economic and psychological drivers.

5 CONCLUSION

The occupant behaviour in residential buildings is driven by building age and characteristics. Level of family income is a major driver that influences an occupant to sustain the desired or comfortable indoor environment. Further, the income levels may also impact the decision of making any improvements [22]. The analysis of the literature highlights those studies aiming to integrate occupant behaviour with indoor or outdoor conditions tend to implement shared approaches (survey, field measurements, or simulation) as shown in Table 1. However, these may be limited by sample size, period of data collection. In that case, smaller sample size (1 building) or a short period (few days) study cannot be generalised for a general population. Whereas if implementing single approach, building parameters or socioeconomic factors alone are analysed. Occupancy/occupant schedule/profile has been repeatedly analysed (in 16 out of 21 reviewed studies) and in 11 of them as the only occupant behaviour related factor whereas motivations behind the same are omitted.

ACKNOWLEDGMENTS

The authors highly acknowledge the Science Foundation Ireland (SFI) financial support for the ERBE Centre for Doctoral Training under grant agreement no.18/EPSRC-CDT/3586 and the financial support from the Sustainable Energy Authority of Ireland (SEAI) through the HEAT CHECK project (grant agreement 19/RDD/492).

REFERENCES

[1] A. Zervos, "Renewables 2021 Global Status Report," 2021. Accessed: Mar. 24, 2022. [Online]. Available: https://www.ren21.net/wp-content/uploads/2019/05/GSR2021_Full_Report.pdf

[2] IEA, "Global Energy Review 2020," Paris, 2020. Accessed: May 04, 2022. [Online]. Available: https://www.iea.org/reports/global-energy-review-2020

[3] M. Lu and J. Lai, "Review on carbon emissions of commercial buildings," *Renewable and Sustainable Energy Reviews*, vol. 119, 2020, doi: 10.1016/j.rser.2019.109545.

[4] S. Hu, D. Yan, E. Azar, and F. Guo, "A systematic review of occupant behavior in building energy policy," *Building and Environment*, vol. 175, p. 106807, 2020.

[5] IEA, "Tracking Buildings 2020," 2020.

[6] W. O'Brien and H. B. Gunay, "The contextual factors contributing to occupants' adaptive comfort behaviors in offices–A review and proposed modeling framework," *Building and Environment*, vol. 77, pp. 77–87, 2014, Accessed: Feb. 22, 2022. [Online]. Available: https://doi.org/10.1016/J

[7] P. de Wilde, "The gap between predicted and measured energy performance of buildings: A framework for investigation," *Autom Constr*, vol. 41, pp. 40–49, 2014, Accessed: Feb. 22, 2022. [Online]. Available: https://doi.org/10.1016/J.AUTCON.2014.02.009

[8] G. Killip, T. Fawcett, and K. B. Janda, "Innovation in low-energy residential renovation: UK and France," *Proceedings of the Institution of Civil Engineers-Energy*, vol. 167, no. 3, pp. 117–124, 2014, Accessed: Feb. 22, 2022. [Online]. Available: https://doi.org/10.1680/ener.14.00011

[9] T. Forman *et al.*, "Improving building energy performance in universities: the case study of the university of cambridge," in *Handbook of Theory and Practice of Sustainable Development in Higher Education*, Springer, 2017, pp. 245–266. Accessed: Feb. 22, 2022. [Online]. Available: https://doi.org/10.1007/978-3-319-47868-5_16

[10] G. Dermentzis, J. Schnieders, R. Pfluger, D. Pfeifer, W. Feist, and F. Ochs, "An overview of energy district tools in Europe and the importance of an equivalent heating reference temperature for district simulations," *Bauphysik*, vol. 39, no. 5, pp. 316–329, 2017,

Accessed: Feb. 22, 2022. [Online]. Available: https://doi.org/10.1002/bapi.201710036
[11] L. Gu, Y. Zhang, and Y. Wang, "Comparison of building energy efficiency standards of China and some developed countries," 2014.
[12] N. DellaValle, A. Bisello, and J. Balest, "In search of behavioural and social levers for effective social housing retrofit programs," *Energy and Buildings*, vol. 172, pp. 517–524, 2018, Accessed: Feb. 22, 2022. [Online]. Available: https://doi.org/10.1016/j.enbuild.2018.05.002
[13] S. J. Quan, Q. Li, G. Augenbroe, J. Brown, and P. P.-J. Yang, "Urban data and building energy modeling: A GIS-based urban building energy modeling system using the urban-EPC engine," in *Planning support systems and smart cities*, Springer, 2015, pp. 447–469.
[14] M. J. Pelenur and H. J. Cruickshank, "Closing the energy efficiency gap: a study linking demographics with barriers to adopting energy efficiency measures in the home," *Energy*, vol. 47, no. 1, pp. 348–357, 2012, Accessed: Feb. 22, 2022. [Online]. Available: https://doi.org/10.1016/j
[15] D. Yan, T. Hong, D. Dong, and A. Mahdavi, "Definition and simulation of occupant behavior in buildings," *International Energy Agency EBC Annex 66 Text*, pp. 1–14, 2014, Accessed: Feb. 22, 2022. [Online]. Available: https://doi.org/10.1016/j.enbuild.2017.09.084
[16] T. Buso, V. Fabi, R. K. Andersen, and S. P. Corgnati, "Occupant behaviour and robustness of building design," *Building and Environment*, vol. 94, pp. 694–703, 2015, Accessed: Feb. 22, 2022. [Online]. Available: https://doi. org/10.1016/j.buildenv.2015.11.003
[17] P. Hoes, J. L. M. Hensen, M. G. L. C. Loomans, B. de Vries, and D. Bourgeois, "User behavior in whole building simulation," *Energy Build*, vol. 41, no. 3, pp. 295–302, 2009, Accessed: Feb. 22, 2022. [Online]. Available: https://doi.org/10.1016/j.enbuild.2008.09.008
[18] A. Heidari, F. Maréchal, and D. Khovalyg, "An occupant-centric control framework for balancing comfort, energy use and hygiene in hot water systems: A model-free reinforcement learning approach," *Applied Energy*, vol. 312, p. 118833, 2022.
[19] P. Gianniou, X. Liu, A. Heller, P. S. Nielsen, and C. Rode, "Clustering-based analysis for residential district heating data," *Energy Convers Manag*, vol. 165, pp. 840–850, 2018.
[20] X. Feng, D. Yan, R. Yu, and Y. Gao, "Investigation and modelling of the centralized solar domestic hot water system in residential buildings," in *Building Simulation*, 2017, vol. 10, no. 1, pp. 87–96.
[21] P. Wicker and S. Becken, "Conscientious vs. ambivalent consumers: Do concerns about energy availability and climate change influence consumer behaviour?," *Ecological Economics*, vol. 88, pp. 41–48, 2013.
[22] Y. Wang, Z. Xu, Z. Wang, and H. Li, "Analysis of thermal energy saving potentials through adjusting user behavior in hotel buildings of the Yangtze River region," *Sustainable Cities and Society*, vol. 51, p. 101724, 2019.
[23] X. Cipriano, A. Vellido, J. Cipriano, J. Martí-Herrero, and S. Danov, "Influencing factors in energy use of housing blocks: A new methodology, based on clustering and energy simulations, for decision making in energy refurbishment projects," *Energy Effic*, vol. 10, no. 2, pp. 359–382, 2017.
[24] X. Ding, R. Ma, M. Shan, X. Wang, and X. Yang, "Occupants' on-demand control of individual heating devices in rural residential buildings: an experimental scheme and on-site study," *Energy and Buildings*, p. 111862, 2022.
[25] L. Yan, M. Liu, K. Xue, and Z. Zhang, "A study on temperature-setting behavior for room air conditioners based on big data," *Journal of Building Engineering*, vol. 30, p. 101197, 2020.
[26] M. Laskari, S. Karatasou, M. Santamouris, and M.-N. Assimakopoulos, "Using pattern recognition to characterise heating behaviour in residential buildings," *Advances in Building Energy Research*, pp. 1–25, 2020.
[27] J. An, D. Yan, and T. Hong, "Clustering and statistical analyses of air-conditioning intensity and use patterns in residential buildings," *Energy and Buildings*, vol. 174, pp. 214–227, 2018.
[28] M. Amayri, A. Arora, S. Ploix, S. Bandhyopadyay, Q.-D. Ngo, and V. R. Badarla, "Estimating occupancy in heterogeneous sensor environment," *Energy and Buildings*, vol. 129, pp. 46–58, 2016.
[29] D. Xia, S. Lou, Y. Huang, Y. Zhao, D. H. W. Li, and X. Zhou, "A study on occupant behaviour related to air-conditioning usage in residential buildings," *Energy and Buildings*, vol. 203, p. 109446, 2019.
[30] Z. Yang, L. Ding, H. Xiao, B. Wang, and W. Shi, "Field performance of household room air conditioners in Yangtze River Region in China: Case studies," *Journal of Building Engineering*, vol. 34, p. 101952, 2021.
[31] H. Liu, H. Sun, H. Mo, and J. Liu, "Analysis and modeling of air conditioner usage behavior in residential buildings using monitoring data during hot and humid season," *Energy and Buildings*, vol. 250, p. 111297, 2021.
[32] B. Jeong, J. Kim, Z. Ma, P. Cooper, and R. de Dear, "Identification of Environmental and Contextual Driving Factors of Air Conditioning Usage Behaviour in the Sydney Residential Buildings," *Buildings*, vol. 11, no. 3, p. 122, 2021.
[33] V. Fabi, R. V. Andersen, and S. P. Corgnati, "Influence of occupant's heating set-point preferences on indoor environmental quality and heating demand in residential buildings," *HVAC&R Research*, vol. 19, no. 5, pp. 635–645, 2013.
[34] D. Lai, Y. Qi, J. Liu, X. Dai, L. Zhao, and S. Wei, "Ventilation behavior in residential buildings with mechanical ventilation systems across different climate zones in China," *Building and Environment*, vol. 143, pp. 679–690, 2018.
[35] B. Ozarisoy and H. Altan, "Significance of occupancy patterns and habitual household adaptive behaviour on home-energy performance of post-war social-housing estate in the South-eastern Mediterranean climate: Energy policy design," *Energy*, vol. 244, p. 122904, 2022, doi: https://doi.org/10.1016/j.energy.2021.122904.
[36] A. Rinaldi, M. Schweiker, and F. Iannone, "On uses of energy in buildings: Extracting influencing factors of occupant behaviour by means of a questionnaire survey," *Energy and Buildings*, vol. 168, pp. 298–308, 2018.
[37] Y. Cui, D. Yan, and C. Chen, "Exploring the factors and motivations influencing heating behavioral patterns and future energy use intentions in the hot summer and cold winter climate zone of China," *Energy and Buildings*, vol. 153, pp. 99–110, 2017.
[38] J. P. Gouveia, J. Seixas, and A. Mestre, "Daily electricity consumption profiles from smart meters-Proxies of behavior for space heating and cooling," *Energy*, vol. 141, pp. 108–122, 2017.
[39] I. Kurniawan, Faridah, and S. S. Utami, "Characterizing of climate chamber thermal environment using the CFD simulation method using IES VE," in *AIP Conference Proceedings*, 2020, vol. 2223, no. 1, p. 050010.
[40] R. V. Andersen, J. Toftum, K. K. Andersen, and B. W. Olesen, "Survey of occupant behaviour and control of indoor environment in Danish dwellings," *Energy and Buildings*, vol. 41, no. 1, pp. 11–16, 2009.
[41] V. Fabi, R. V. Andersen, S. Corgnati, and B. W. Olesen, "Occupants' window opening behaviour: A literature review of factors influencing occupant behaviour and models," *Building and Environment*, vol. 58, pp. 188–198, 2012.
[42] A. Heidari, N. Olsen, P. Mermod, A. Alahi, and D. Khovalyg, "Adaptive hot water production based on Supervised Learning," *Sustainable Cities and Society*, vol. 66, p. 102625, 2021.
[43] A. Ferrantelli, K. Ahmed, P. Pylsy, and J. Kurnitski, "Analytical modelling and prediction formulas for domestic hot water consumption in residential Finnish apartments," *Energy and Buildings*, vol. 143, pp. 53–60, 2017.
[44] H. Liu, H. Sun, H. Mo, and J. Liu, "Analysis and modeling of air conditioner usage behavior in residential buildings using monitoring data during hot and humid season," *Energy and Buildings*, vol. 250, p. 111297, 2021.
[45] L. M. X. K. J. T. Y. L. Zhang Ziwei, "Prediction model of energy consumption based on the actual monitoring data of room air conditioner usage rate and setting temperature," *Journal of Civil and Environmental Engineering* , vol. 42, no. 3, pp. 165–173, 2020.
[46] A. Roetzel, A. Tsangrassoulis, U. Dietrich, and S. Busching, "A review of occupant control on natural ventilation," *Renewable and Sustainable Energy Reviews*, vol. 14, no. 3, pp. 1001–1013, 2010.
[47] D. Lai, Y. Qi, J. Liu, X. Dai, L. Zhao, and S. Wei, "Ventilation behavior in residential buildings with mechanical ventilation systems across different climate zones in China," *Building and Environment*, vol. 143, pp. 679–690, 2018.

A comparative study of the environmental impact of alkali activated and traditional materials

O. Alelweet1[1], S. Pavia[1]
[1]Department of Civil Engineering, University of Dublin, Trinity College, College Green, Dublin 2, Ireland.
[1]Department of Civil Engineering, University of Dublin, Trinity College, College Green, Dublin 2, Ireland
e-mail : alelweeo@tcd.ie; PAVIAS@tcd.ie

ABSTRACT: Many construction materials carry significant environmental impacts because they require high energy input and non-renewable materials for production, contributing to material depletion and greenhouse gas emissions. In particular, Portland cement (PC), the binder most widely used, is often considered a main contributor to emissions. Most PC environmental impact is due to clinker production which requires burning rocks at 1400^0C releasing abundant CO_2 from fuel combustion and rock decarbonization. Alkali-activated materials (AAMs) do not require clinker manufacturing but are produced at low temperature (ambient-100◦C). Hence, they yield low emissions and have low embodied energy (EE). Most AAMs are made with waste which further lowers their EE and the raw materials and fuel consumption for their making. Savings up to 75% CO_2 emissions are reported compared with PC products, and additional environmental benefits (water consumption reduction and no requirement for superplasticizers). This paper calculates the EE and carbon footprint (EC) of AAMs made with wastes including slag (GGBS), fly ash (FA), bauxite and red mud (RM). The values are compared with equivalent CEM II products. Their environmental impact is set against their strength to assist the design of optimum mixes at lower impact. It is evidenced that the right activator procures a strength similar to CEM II at approximately half the EE and EC, while a wrong activator increases the environmental impact and lowers strength. Pyroprocessing waste at relatively low temperature slightly increases environmental impact but can greatly increase strength: sintering bauxite at 800^0C enabled strength two times greater than the CEM II product.

KEY WORDS: fly ash; GGBS; red mud; bauxite; alkali activation; embodied energy; carbon footprint.

1 INTRODUCTION

The construction industry is one of the largest contributors to greenhouse gas emissions, and a great consumer of energy and non-renewable natural resources [1]. The fabrication of building materials such as aluminium, steel and PVC implies high energy consumption and environmental impact [2]. As a result of severe environmental problems, the construction industry needs to adapt. Using construction materials of low environmental impact worldwide would considerably lower the greenhouse gas emissions and improve the sustainability of construction. PC is the binder most widely used in construction. It is held responsible for major contributions to greenhouse gas emissions worldwide in multiple publications. Most of the environmental impact of PC is due to clinker production which requires burning rocks at c.1400°C releasing abundant CO_2 from the fuel combustion and the decarbonization of the carbonate rocks used as raw materials. Alkali-activated materials (AAMs) do not require clinker manufacturing but are produced at low temperatures, usually ranging from ambient to 100°C. Most alkali activated cements are produced at ambient temperatures, and others with a small energy input usually ranging from 60°C (curing) to 100°C (drying) or 400-600°C (thermal activation of certain wastes) [3-5]. Hence, they yield low carbon emissions and have low embodied energy (EE). Furthermore, most AAMs are made with industrial waste which further lowers their EE as well as the raw material and fuel consumption for their making. The reduction in emissions, and the use of waste for the production of AAMs, can elicit their wide uptake in the markets [6-9]. Industrial by products such as GGBS and ash residues such as FA are used instead of clinker for the production of AAMs. These wastes contain abundant silicates and/or aluminates that can be activated with alkali metals. On successful activation, the wastes' active components generate Si^{4+}, Al^{3+} and (sometimes) Ca^{2+} that become available to form cementing products [6-10].

Most authors agree that AAMs have lower EE and carbon emissions that their equivalent PC products. Duxon et al. [11] calculated the CO_2 emissions of AA FA and metakaolin cements using the CO_2 evolved during the production of Na_2O and SiO_2 in the alkali process as the primary inputs, and found savings of 80% in CO_2 emissions when compared to PC. However, there is a great divergence of results due to both a disparity in the data used and the different formulations. Wimpenny [12] and Provis and Deventer [13] state that the carbon footprint of AA binders is 30% of the PC print, but according to Zhang et al. [14], AA cement can be produced with 60% lower values of energy and CO_2 emissions than PC. Pacheco Torgal et al. [15] found several authors claiming 44-70% reductions in CO_2 emissions for several AAMs compared with similar PC mixes. Cunningham & Miller [16] account for AAMs having 10%–80% lower EE than their equivalent PC materials. Davidovits [17] states that geopolymers, a subset of AAMs where the binding phase is almost exclusively aluminosilicate, have 10-20% lower carbon footprint than PC, while other geopolymer formulations [18] have shown a 60% reduction in CO_2 emissions compared to their PC equivalents.

Using nine LCA (life cycle analyses) Lolli and Kurtis [19] conclude that AAMs show a 50% reduction in CO_2 production

when compared to PC and PC+SCM (supplementary cementitious material) binders, while providing the required compressive strength for pavement applications (30 MPa). The carbon emissions and EE of AAMs depend on their formulation. Ouellet-Plamondon and Habert [20] state savings up to 75% CO_2 emissions for certain formulations when compared with equivalent PC products. They also highlight further environmental benefits such as reducing water use and no requirement for superplasticizers. Ouellet-Plamondon and Habert [20] claim that sodium silicate activators can contribute up to 80% of the total impact of an AAM, while Anvekar et al. [21] report EE 48% greater than equivalent PC material due to the alkali activator energy demand. Several authors agree that the main source of CO_2 impact for AAMs is the production of sodium silicate activator from sodium carbonate [22-23]. However, the carbonate can be either mined from evaporite deposits or produced through the Solvay process. Mining implies 1/10 of the Solvay process CO_2 production, hence the impact of silicate activator is often overestimated [19].

Matheuet al [24] state that the global warming potential of AAMs is c. 25% lower than PC equivalents. They demonstrate that, in ten LCA categories (global warming potential, acidification, human health, air pollutants, ecotoxicity, smog, natural resource depletion, indoor air quality, water intake and ozone depletion) AAMs have less impact than PC materials. They found that, in seven categories, the AAMs impact was 40% lower than PC equivalents. In two categories PC material performed better: eutrophication and habitat alteration, due to the use of potassium-based activators. Potassium hydroxide can emit nutrients into waterways (eutrophication) and hence alter habitats. In this paper, potassium activator is replaced with sodium silicate/hydroxide.

As the environmental impact of AAMs depends on their formulation, not only is it important to use activators of low impact, but it is also important to use wastes that do not require calcination or any other high-energy processing to render them reactive. The processing of the wastes in this paper is minimal, based on previous work by the authors that determined the minimum processing that renders maximum reactivity [4-5, 25].

This paper calculates the embodied energy (EE) and carbon footprint (EC) of AAMs made with several industrial wastes including granulated blast furnace slag (GGBS), fly ash (FA), bauxite and red mud (RM) from Ireland and Saudi Arabia. These wastes have been successfully activated and used to produce AAMs by the authors. Most of the resultant AAMs showed satisfactory physical and mechanical properties, and others displayed outstanding mechanical strength and durability [26]. The outstanding performance of the AAMs in aggressive environments enhances their life cycle, hence reducing their environmental impact. Other authors have also found superior durability for certain AAM formulations including better corrosion resistance [7-9, 27]. The EC and EE of the AAMs produced is compared with equivalent PC materials made with CEM II A/L, a limestone cement of lower environmental impact than other members of the PC family.

2 MATERIALS AND METHODS

2.1 Materials

The AAMs were fabricated with wastes including GGBS, FA and RM sourced from Ireland and Saudi Arabia. A natural rock (bauxite), mined principally as an aluminium ore, was also used to fabricate some of the AAMs. The GGBS is a byproduct of the steel industry while the FA is a residue of burning coal in power stations. The RM is also a waste, generated during the refining of bauxite to produce aluminium

The wastes were used as precursors and activated with sodium hydroxide (NaOH) and sodium silicate (Na_2SiO_3), which dissolved the active components generating Si^{4+}, Al^{3+} and Ca^{2+} that become available to form cementing products. The sodium hydroxide activator (NaOH) was used in pellet form with 98% purity. It was mixed with distilled water to attain different molarities to suit the different AAMs: a 6 molar (M) solution was used for the RM, 8 M solutions for the GGBS, and 8-10M solutions for the bauxite. The molarities are chosen according to previous research [4-5, 25]. The composition of the AAMs is included in tables 1-3. A sodium silicate activator (Na_2SiO_3) in liquid form was used, with a viscosity ranging from 800 to 1400 cps; PH 11-14, chemical composition of 14-17% Na_2O; 31-35% SiO_2 and silicate modulus (MS = SiO_2/Na_2O) of 2.20. The activators (NaOH, Na_2SiO_3) are used in liquid form, however they are included in the calculations as solids because water accounts for neither EE nor EC [28].

As aforementioned, wastes that rendered the maximum reactivity [4-5, 25] with minimum processing were selected. The bauxite required grinding to enhance fineness and specific surface area. The bauxite was mined from a deposit located in the region of Ha'il, central/northern Saudi Arabia. It was oven-dried at 105 °C for 24 hours and ground in a digital ball mill at 150 r.p.m with 20mm Ø stainless steel balls. Finally, it was calcined at c.800 °C to enhance reactivity [4]. For the same reason, the RM was calcined at c.400 °C [5]. The DOE software was used to develop an optimum mix for the AA bauxite materials. The GGBS and FA were unprocessed.

2.2 Mixing, curing and compaction

The mix design (Tables 1-3) was based on existing literature and previous research by the authors. The sand to precursor ratio is constant at 3:1. The precursors were dry mixed for 3 min and the activator solution added and mixed for a further 5 minutes. The sand was then added and mixed for 6 min. The mortars were cast into prismatic molds of 160*50*50 mm, vibrated for 1 min, and sealed with plastic sheets to prevent moisture loss during curing. The specimens were demolded after 24 hours. The software determined curing in isothermal chambers at 20 ± 2 °C for 28 days for the AA bauxite materials. Some of the AA GGBS materials were cured in an oven at 60 °C for 24 h. The CEM II A/L-based control materials were fabricated according to EN 196-1[29]. The percentage composition is calculated from the mass fitted in a 3-gang prismatic mold to attain densities between 1842 and 1966 g/m^3 for the AA RM materials, 1676-1759 g/m^3 for the AA GGBS materials and 1685-1895 g/m^3 for the AA bauxite materials which is approximately 2 kg. As aforementioned, the activators are included in the calculations as solids because water accounts for neither EE nor EC.

2.3 Methods

Only the production stage is included in the calculations. Therefore, the life stages included in the EE and EC calculations are raw materials extraction, manufacturing and related transport, which in a LCA is equivalent to the cradle to gate system boundary. The scenarios for the production stage are usually defined in environmental product declarations (EPD). However, no EPDs were found for some AAM components. Therefore, some values are from the literature and others calculated with data provided by the producers-Table 4.

The EE and EC of the FA and GGBS are based on existing published data (Table 4). The EE and EC of the bauxite was calculated with the details of the mining process provided by the Ma'aden industries (Sidiya, Kaolin Processing and Management, Ma'aden 2021), and it is based on the quarrying of the Az Zabirah and Al Bai'tha mines. The Al Bai'tha supplies high-grade bauxite for aluminium production while the Az Zabirah mine supplies kaolin to the phosphate industry and low-grade bauxite to local cement companies. The environmental impact of quarrying this bauxite was calculated by Alelweet and Pavia [4] as summarized below. The primary energy used for quarrying is diesel, and the CO_2 emissions are estimated based on the quantity of diesel and the activity of the mine, amounting to 3.3 kg CO_2/t bauxite. This calculation considers a diesel consumption of 3144 l/day producing 8237.3 kg CO_2. The mining process starts with overburden stripping of a 0.5–1 m soil cap which is removed with a bulldozer. The strip waste is loaded into dump trucks and hauled to landfills outside the pit. Once exposed, the bauxite is ripped and piled in heaps with a bulldozer. The ore is then screened with wheel loaders and mobile screens and blended to meet customer requirements in terms of size and chemistry. The loaders collect the material passing the sieve and stockpile it as the final product. Auxiliary equipment includes one grader and one compactor for road maintenance. Finally, the product is loaded into trucks and dispatched to costumers. The red mud is produced as a waste during the refining of the quarried bauxite to produce aluminium. As a byproduct, the energy required for its manufacturing is zero. It is also produced locally; therefore, no transport is accounted for at the production stage.

Table 4. EE/ EC of the materials used to fabricate the AAMs.

	EE(MJ/kg)	EC(kgCO_2/kg)	Ref.
PC (CEM II A/L)	4.80	0.842	[30], [31]
PC (CEM I)	4.50	0.730	[32]
FA	0.10	0.008-0.010	[32-33]
GGBS	1.60	0.083	[32]
Bauxite	0.05	0.003-0.005	[4]
NaOH	3.50	0.632	[34]
Na_2SiO_3	4.60	0.430	[35]
Water	0	0	[28]
Quartz sand	0.85	0.020	[36]
Fine aggregate	0.17	0.025	[37]
	0.004	0.081	[32]
Coarse aggregate	0.12	0.006	[30]
Compaction	0.009	0.001	[38]

The embodied energy was measured, as Mega-Joules (MJ) per unit area (m^2) or per unit weight (kg or ton), according to Anvekar *et al.* [21]. The embodied energy and carbon were calculated with equations 1 and 2 [39].

$$EE = \sum_{i=1}^{n} (EE_i \times m_i) \quad (1)$$

$$E_{CO_2} = \sum_{i=1}^{n} (E_{CO_{2i}} \times m_i) \quad (2)$$

Where: EE_i is the embodied energy of each material component (MJ/kg), $E_{CO_{2i}}$ the embodied Carbon (kgCO_2/kg), and m the mass of each component.

As aforementioned, some of the components were processed (milled or heated). The impact of this processing appears in Table 5. According to Kim [40], ball milling is a grinding method of low environmental impact because it uses no chemical catalysts or any other substances. A ball mill of 0.15 kWh power capacity was used for grinding some of the wastes. The embodied energy of the grinding process $EE_{ball\ mill}$ was calculated with equation (3) [41]:

$$EE_{ball\ mill} = \frac{(P_{kWh} \times t)}{m \times 1000} \quad (3)$$

Where: P_{kWh} is the power capacity of the ball mill, (m) the mass in kg, and (t) the time in hours.

The RM was ground for 3h, the $EE_{\text{ball mill}}$ was 0.001 MJ/kg. The embodied energy of the grinding process for the bauxite $EE_{\text{ball mill}}$ was greater (0.009 MJ/kg) because it was longer. The EE and EC of the heating and calcination processes were also calculated (Table 5) [42-43].

Table 5. EE and EC of the dry and calcined RM and bauxite.

Materials	T (°C)	Time (h)	EE (MJ/kg)	EC (Kg-CO_2/kg)
RM_{dry}	105	24	0.14	0.017
$RM_{sintered}$	400	3	0.94	0.118
$Bauxite_{dry}$	105	24	0.14	0.017
$Bauxite_{sintered}$	800	3	2.19	0.277
GGBS (G4-G6)	60	24	0.02	0.002

3 RESULTS AND DISCUSSION

The EE and EC calculations used the data in Tables 1–5 and equations 1-3. As aforementioned, the calculations refer to material production. Therefore, the life stages included are raw material extraction or supply, manufacturing and extraction-related transport which are usually included in EPD's. The EE and EC of the AAMs are reported as the arithmetic mean of all the mixes investigated. The strength of the resultant AAMs (tables 6-8) is set against their environmental impact to optimize their design for lower environmental impact.

The strength results of the alkali-activated RM and GGBS materials are experimental while the strength of the AA bauxite materials comes from both experimental data and an optimization of the mix design modelled with software. The strength values are the arithmetic mean of 6 tests each, and the results are reliable, showing a small dispersion, with COVs ranging from 0.04 (RMG1) to 0.23 (RMFA5). The COV of the CEM II equivalent is 0.10. The alkali activators are the main

responsible for the environmental impact of AAMs [44]. It can be seen from the results that rising the concentration and molar ratio of activator increases environmental impact. However, it doesn't significantly increase the strength, sometimes it even reduces it (Table 6).

In the AA RM materials, the results show that growing RM substitution with FA, from 6 to 10%, nearly doubles the 28-d compressive strength of the resultant AAMs without increasing their environmental impact (Table 6). The same effect is evident for GGBS replacement when the main activator is NaOH. However, with silica activator, the strength drops despite the increase of GGBS.

The AA GGBS materials including NaOH-rich activators can reach strengths comparable to their CEM II equivalents (~26-34MPa compared with 37MPa for CEMII)-Table7. However, their environmental impacts are considerably lower: The EE of the AA GGBS materials is 53.78 % lower that the CEM II and the ECO2 66.67 % lower (Table 8). Therefore, the right activator can provide a similar strength at half the emissions and half the EE than a similar CEM II mix.

Sintering the bauxite precursor at 800ºC has slightly raised the environmental impact (Table 7-8) but has nearly doubled strength when compared to the equivalent CEM II product. The high strength of the GGBS blended bauxites (60MPa) is due to the combined reactions involving the pozzolanic transition aluminas in the bauxite, with the latent hydraulic phases of the GGBS, enhanced with the high surface areas of both precursors.

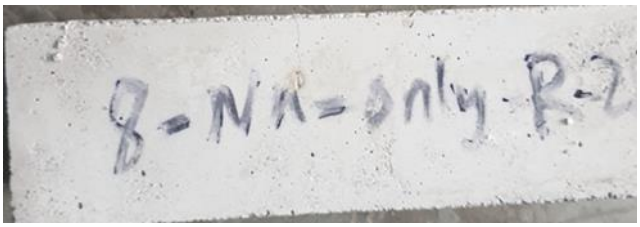

Figure 1. Typical appearance of AAGGBS materials studied.

Figure 2. Typical appearance of AA RM materials.

Figure 3. Typical appearance of AA bauxite materials

The results are comparable with others in the literature. Mathew et al. [45], calculated EE 40% under equivalent PC products for AAMs of formulation: 75%FA, 25%GGBS, NaOH (15M), Na_2SiO_3/NaOH=2.33 and ratio activator / FA+GGBS = 0.42. Kalaw et al. [46] report the EE of AA FA/PC materials at 3.52 MJ/kg (for 25% PC replacement with FA) and 2.43 MJ/kg (50% replacement). Their environmental impact is higher than the mixes in this paper because their PC has a greater EE than CEM II. Faridmehr et al. [47] also state comparable values for AAM mixtures made with high-volume FA which emitted 45.5 kg CO_2/m^3 and consumed 881.2 MJ/m^3. They report GGBS mixes reaching higher values at 70.6 kg CO_2/m^3 and 1534.5 MJ/m^3. The impact of their AAMs is significantly lower than their benchmark mortars made with PC (CEM I) which carry 436.8 kg CO_2/m^3 emissions and 2793 MJ/m^3 EE.

As aforementioned, most of the AAMs showed satisfactory properties and some displayed outstanding mechanical strength and durability [26]. Representative specimens appear in figures 1-3. Other authors have also found superior durability for certain AAM formulations including better corrosion resistance [2-4], [23]. An increased resilience enhances the life cycle of a material, hence reducing environmental impact.

4 CONCLUSION

The EE and EC of AAMs was calculated and compared with other materials. The results evidence that, in alkali activation technology, an appropriate design leads to lower environmental impact and superior strength.

From the AA GGBS material results, it was clear that the right activator procured a strength similar to the equivalent CEM II mixes at approximately half of their embodied energy and carbon emissions. Activators constitute the main environmental impact of AAMs. An excessive activator concentration or wrong molar ratio can increase the environmental impact while simultaneously lowering strength. Therefore, they must correctly selected and formulated.

In addition, sintering the bauxite at 800ºC only slightly raised the environmental impact of the resultant material, but it nearly doubled the strength when compared to the equivalent CEM II product. Consequently, pyro-processing waste precursors at relatively low temperature can report great strength increase with a low increase in environmental impact.

The importance of blending waste precursors is also acknowledged: increasing FA in the AA RM materials, from 6 to 10%, nearly doubles the 28-day compressive strength without increasing the environmental impact.

Therefore, three design variables particularly impact the results including:

1- Using adequate blends of waste precursors.
2- Using the right activator formulation for a given waste precursor.
3- An adequate processing (activation) of waste precursors.

ACKNOWLEDGMENTS

The authors thank Ma'adem Industries, for valuable information and for providing materials for the investigation. The authors also thank the Government of Saudi Arabia, Technical & Vocational Training Corporation and the Saudi Arabian Cultural Bureau for their support and for financing the project. We thank our colleagues in the Civil Engineering laboratories: M. O'Shea, M. Grimes, M. Gilligan, P. Veale and Chief Technician D. McAuley for their assistance with testing.

REFERENCES

[1] K. Ahmed Ali, M. I. Ahmad, and Y. Yusup, "Issues, impacts, and mitigations of carbon dioxide emissions in the building sector," *Sustainability*, vol. 12, no. 18, p. 7427, 2020.

[2] Z. Zhongming, L. Linong, Y. Xiaona, Z. Wangqiang, and L. Wei, "Using materials efficiently can substantially cut greenhouse gas emissions," 2020.

[3] T. Luukkonen, Z. Abdollahnejad, J. Yliniemi, P. Kinnunen, and M. Illikainen, "One-part alkali-activated materials: A review," *Cem. Concr. Res.*, vol. 103, no. October 2017, pp. 21–34, 2018.

[4] O. Alelweet and S. Pavia, "Pozzolanic and hydraulic activity of bauxite for binder production," *J. Build. Eng.*, vol. 51, p. 104186, 2022.

[5] O. Alelweet, S. Pavia, and Z. Lei, "Pozzolanic and Cementing Activity of Raw and Pyro-Processed Saudi Arabian Red Mud (RM) Waste," *lidsen*, no. 2689–5846, 2021.

[6] C. Shi, D. Roy, and P. Krivenko, *Alkali-activated cements and concretes*. CRC press, 2003.

[7] G. Habert, J. B. D'Espinose De Lacaillerie, and N. Roussel, "An environmental evaluation of geopolymer based concrete production: Reviewing current research trends," *J. Clean. Prod.*, vol. 19, no. 11, pp. 1229–1238, 2011.

[8] R. Unless, P. Act, W. Rose, T. If, and W. Rose, "Advances in understanding alkali activated materials," 2015.

[9] S. H. Teh, T. Wiedmann, A. Castel, and J. de Burgh, "Hybrid life cycle assessment of greenhouse gas emissions from cement, concrete and geopolymer concrete in Australia," *J. Clean. Prod.*, vol. 152, pp. 312–320, 2017.

[10] F. Pacheco-Torgal, J. A. Labrincha, C. Leonelli, A. Palomo, and P. Chindaprasirt, "Handbook of Alkali-Activated Cements, Mortars and Concretes," *Handbook of Alkali-Activated Cements, Mortars and Concretes*. pp. 1–830, 2014.

[11] P. Duxson, J. L. Provis, G. C. Lukey, and J. S. J. van Deventer, "The role of inorganic polymer technology in the development of 'green concrete,'" *Cem. Concr. Res.*, vol. 37, no. 12, pp. 1590–1597, 2007.

[12] D. Wimpenny, "Low Carbon Concrete – Options for the Next Generation of Infrastructure Concrete Solutions 09 Paper 4a-1," *Concr. Solut. 09*, no. February, pp. 1–10, 2009.

[13] J. L. Provis and J. S. J. Van Deventer, *Geopolymers: structures, processing, properties and industrial applications*. Elsevier, 2009.

[14] Z. Zhang, Y. Zhu, T. Yang, L. Li, H. Zhu, and H. Wang, "Conversion of local industrial wastes into greener cement through geopolymer technology: A case study of high-magnesium nickel slag," *J. Clean. Prod.*, vol. 141, pp. 463–471, 2017.

[15] F. Pacheco-Torgal, J. Labrincha, C. Leonelli, A. Palomo, and P. Chindaprasit, *Handbook of alkali-activated cements, mortars and concretes*. Elsevier, 2014.

[16] P. R. Cunningham and S. A. Miller, "Quantitative assessment of alkali-activated materials: environmental impact and property assessments," *J. Infrastruct. Syst.*, vol. 26, no. 3, p. 4020021, 2020.

[17] J. Davidovits and S. France, "Properties of Geopolymer Cements," 2018, no. October 1994, pp. 131–149.

[18] G. Habert, J. B. D'Espinose De Lacaillerie, E. Lanta, and N. Roussel, "Environmental evaluation for cement substitution with geopolymers," *2nd Int. Conf. Sustain. Constr. Mater. Technol.*, pp. 1607–1615, 2010.

[19] F. Lolli and K. E. Kurtis, "Life Cycle Assessment of alkali activated materials: preliminary investigation for pavement applications," *RILEM Tech. Lett.*, vol. 6, pp. 124–130, 2021.

[20] C. Ouellet-Plamondon and G. Habert, "Life cycle assessment (LCA) of alkali-activated cements and concretes," in *Handbook of alkali-activated cements, mortars and concretes*, Elsevier, 2015, pp. 663–686.

[21] S. R. Anvekar, L. R. Manjunatha, S. R. Anvekar, S. Sagari, and K. Archana, "An Economic and Embodied Energy Comparison of Geo-polymer , Blended Cement and Traditional Concretes," *J. Civ. Eng. Technol. Res.*, vol. 1, no. November, pp. 33–40, 2014.

[22] H. H. Weldes and K. R. Lange, "Properties of soluble silicates," *Ind. Eng. Chem.*, vol. 61, no. 4, pp. 29–44, 1969.

[23] U. A. Against *et al.*, "Safety data sheet," *Science Lab.com*, 2014. [Online]. Available: https://www.sciencecompany.com/Sodium-Silicate-Solution-16oz-P6375.aspx.

[24] P. S. Matheu, K. Ellis, and B. Varela, "Comparing the environmental impacts of alkali activated mortar and traditional portland cement mortar using life cycle assessment," in *IOP Conference Series: Materials Science and Engineering*, 2015, vol. 96, no. 1, p. 12080.

[25] O. Alelweet and S. Pavia, "An Evaluation of the Feasibility of Several Industrial Wastes and Natural Materials as Precursors for the Production of Alkali Activated Materials," *Int. J. Civ. Environ. Eng.*, vol. 13, no. 12, pp. 741–748, 2019.

[26] O. Alelweet and S. Pavia, "Durability of Alkali-Activated Materials Made with a High-Calcium, Basic Slag," *Recent Prog. Mater.*, vol. 3, no. 4, pp. 1–1, 2021.

[27] and P. K. Shi, Caijun, Della Roy, *Alkali-activated Cements and Concretes*. 2003.

[28] R. Jones, M. McCarthy, and M. Newlands, "Fly ash route to low embodied CO2 and implications for concrete construction," in *World of Coal Ash Conference, Denver, Colorado, USA*, 2011.

[29] B. STANDARD, "BS EN 196-10:2016 Methods of testing cement. Determination of the water-soluble chromium (VI) content of cement." BSI, p. 37, 2016.

[30] M. A. Nisbet, M. G. VanGeem, J. Gajda, and M. Marceau, "Environmental life cycle inventory of portland cement concrete," *PCA R&D Ser.*, no. 2137a, 2000.

[31] MPA, "Fact Sheet 18 Embodied CO 2 e of UK cement , additions and cementitious material," 2019.

[32] ICE, "Embodied Carbon-Inventory of Carbon and Energy (ICE)," 2014.

[33] N. Hepworth and M. Goulden, "Climate change in Uganda: Understanding the implications and appraising the response.," 2008.

[34] L. Thannimalay, S. Yusoff, and N. Z. Zawawi, "Life cycle assessment of sodium hydroxide," *Aust. J. Basic Appl. Sci*, vol. 7, no. 2, pp. 421–431, 2013.

[35] M. Fawer, M. Concannon, and W. Rieber, "Life cycle inventories for the production of sodium silicates," *Int. J. Life Cycle Assess.*, vol. 4, no. 4, pp. 207–212, 1999.

[36] J. Chen, P.-L. Ng, R. Jaskulski, and W. Kubissa, "Use of Quartz Sand to Produce Low Embodied Energy and Carbon Footprint Plaster," *J. Sustain. Archit. Civ. Eng.*, vol. 21, no. 4, 2018.

[37] R. Ranade, "Advanced cementitious composite development for resilient and sustainable infrastructure." University of Michigan, 2014.

[38] L. K. Turner and F. G. Collins, "Carbon dioxide equivalent (CO2-e) emissions: A comparison between geopolymer and OPC cement concrete," *Constr. Build. Mater.*, vol. 43, pp. 125–130, 2013.

[39] A. Adesina, "Performance and sustainability overview of alkali-activated self-compacting concrete," *Waste Dispos. Sustain. Energy*, pp. 1–11, 2020.

[40] S. Kim, "Engineering Sustainability of Mechanical Recycling of Carbon Fiber Composite Materials." p. 6, 2014.

[41] E. Petrakis and K. Komnitsas, "Effect of Grinding Media Size on Ferronickel Slag Ball Milling Efficiency and Energy Requirements Using Kinetics and Attainable Region Approaches," *Minerals*, vol. 12, no. 2, p. 184, 2022.

[42] Engineeringtoolbox.com, "Carbon Dioxide - Specific Heat of Gas vs. Temperature," 2001. [Online]. Available: https://www.engineeringtoolbox.com/carbon-dioxide-d_974.html.

[43] B. Sonesson, U., Janestad, H., & Raaholt, "Energy for preparation and storing of food: models for calculation of energy use for cooking and cold storage in households," *SIK Institutet för livsmedel och bioteknik.*, 2003. .

[44] B. C. Mendes *et al.*, "Application of eco-friendly alternative activators in alkali-activated materials: A review," *J. Build. Eng.*, vol. 35, p. 102010, 2021.

[45] B. J. Mathew, M. Sudhakar, and C. Natarajan, "Strength , Economic and Sustainability Characteristics of Coal Ash – GGBS Based Geopolymer Concrete," *International Journal Of Computational Engineering Research*, vol. 3. pp. 207–212, 2013.

[46] M. E. Kalaw, A. Culaba, H. Hinode, W. Kurniawan, S. Gallardo, and M. A. Promentilla, "Optimizing and characterizing geopolymers from ternary blend of philippine coal fly ash, coal bottom ash and rice hull ash," *Materials*, vol. 9, no. 7. 2016.

[47] I. Faridmehr, M. L. Nehdi, M. Nikoo, G. F. Huseien, and T. Ozbakkaloglu, "Life-Cycle Assessment of Alkali-Activated Materials Incorporating Industrial Byproducts," *Materials (Basel).*, vol. 14, no. 9, p. 2401, 2021.

Table 1. Composition of the AA RM materials (3:1 – sand: RM/FA/GGBS).

	RM		FA		GGBS		sand		Density	water		NaOH (6M)		Na_2SiO_3	
	(g)	(%)	(g)	(%)	(g)	(%)	(g)	(%)	kg/m^3	(g)	(%)	(g)	(%)	(g)	(%)
RM-1	450	20.23	—	—	—	—	1350	60.68	1853.84	252.49	11.35	68.67	3.09	103.45	4.65
RM-2	450	19.71	—	—	—	—	1350	59.13	1902.53	247.75	10.85	72.20	3.16	163.08	7.14
RM-3	450	19.07	—	—	—	—	1350	57.21	1966.53	230.24	9.76	75.13	3.18	254.47	10.78
RMFA1	315	14.24	135	6.10	—	—	1350	61.05	1842.78	244.60	11.06	66.53	3.01	100.21	4.53
RMFA2	315	13.88	135	5.95	—	—	1350	59.50	1890.68	240.46	10.60	70.07	3.09	158.29	6.98
RMFA3	315	13.44	135	5.76	—	—	1350	57.59	1953.58	223.85	9.55	73.04	3.12	247.41	10.55
RMFA4	225	10.17	225	10.17	—	—	1350	61.05	1842.78	244.60	11.06	66.53	3.01	100.21	4.53
RMFA5	225	9.98	225	9.98	—	—	1350	59.88	1878.86	233.19	10.34	67.95	3.01	153.49	6.81
RMFA6	225	9.53	225	9.53	—	—	1350	57.21	1966.53	230.24	9.76	75.13	3.18	254.47	10.78
RMG1	315	14.16	—	—	135	6.07	1350	60.68	1853.84	252.49	11.35	68.67	3.09	103.45	4.65
RMG2	315	13.88	—	—	135	5.95	1350	59.50	1890.68	240.46	10.60	70.07	3.09	158.29	6.98
RMG3	315	13.44	—	—	135	5.76	1350	57.59	1953.58	223.85	9.55	73.04	3.12	247.41	10.55
RMG4	225	10.17	—	—	225	10.17	1350	61.05	1842.78	244.60	11.06	66.53	3.01	100.21	4.53
RMG5	225	9.98	—	—	225	9.98	1350	59.88	1878.86	233.19	10.34	67.95	3.01	153.49	6.81
RMG6	225	9.60	—	—	225	9.60	1350	57.59	1953.58	223.85	9.55	73.04	3.12	247.41	10.55
CEM II	450	22.22	—	—	—	—	1350	66.67	1687.50	225.00	11.11	—	—	—	—

Table 2. Composition of the AA GGBS materials (3:1 - sand: GGBS).

	GGBS		sand		Density	water		NaOH (8M)		Na_2SiO_3	
	(g)	(%)	(g)	(%)	kg/m^3	(g)	(%)	(g)	(%)	(g)	(%)
G1	450	21.9	1350	65.69	1712.56	124.37	6.05	64.08	3.12	66.62	3.24
G2	450	22.37	1350	67.11	1676.25	100.46	4.99	111.04	5.52	—	—
G3	450	21.31	1350	63.92	1759.88	128.25	6.07	41.85	1.98	141.75	6.712
G4	450	21.90	1350	65.69	1712.56	124.37	6.05	64.08	3.12	66.62	3.24
G5	450	22.37	1350	67.11	1676.25	100.46	4.99	111.04	5.52	—	—
G6	450	21.31	1350	63.92	1759.88	128.25	6.07	41.85	1.98	141.75	6.712

Table 3. Composition of the AA bauxite materials (3:1 - sand: bauxite/FA/GGBS).

	Bauxite		FA		GGBS		sand		Density	water		NaOH (6M)		Na_2SiO_3	
	(g)	(%)	(g)	(%)	(g)	(%)	(g)	(%)	Kg/m^3	(g)	(%)	(g)	(%)	(g)	(%)
Bauxite +GGBS	225.00	11.12	—	—	225.00	11.12	1350	66.74	1685.71	127.46	6.30	41.10	2.03	54.29	2.68
Bauxite +FA	225.00	9.89	225.00	9.89	—	—	1350	59.36	1895.37	238.55	10.89	85.39	3.75	150.50	6.62

Table 6. Compressive strength and environmental impact of the AA RM materials (3:1 - sand: RM/FA/GGBS). Arithmetic means of CS = 11.76 N/mm^2 at 28 days, COVs =0.04-0.21. COV of PC mix = 0.1.

	CS MPa	% RM	% FA	% GGBS	% NaOH	% Na_2SiO_3	EE MJ/kg	**EC** $kgCO_2/kg$
RM-1	4. 53	20.23	—	—	3.09	4.65	1.43	0.18
RM-2	4.68	19.71	—	—	3.16	7.14	1.71	0.21
RM-3	1.69	19.07	—	—	3.18	10.78	1.88	0.20
RMFA1	6.87	14.24	6.10	—	3.01	4.53	1.27	0.16
RMFA2	10.85	13.88	5.95	—	3.09	6.98	1.55	0.19
RMFA3	5.74	13.44	5.76	—	3.12	10.55	1.72	0.18
RMFA4	9.90	10.17	10.17	—	3.01	4.53	1.18	0.15
RMFA5	11.54	9.98	9.98	—	3.01	6.81	1.43	0.17
RMFA6	8.90	9.53	9.53	—	3.18	10.78	1.66	0.17
RMG1	13.21	14.16	—	6.07	3.09	4.65	1.50	0.17
RMG2	9.52	13.88	—	5.95	3.09	6.98	1.75	0.20
RMG3	8.02	13.44	—	5.76	3.12	10.55	1.92	0.19
RMG4	27.48	10.17	—	10.17	3.01	4.53	1.52	0.16
RMG5	33.65	9.98	—	9.98	3.01	6.81	1.77	0.19
RMG6	12.59	9.60	—	9.60	3.12	10.55	1.97	0.18
CEM II	37.18	—	—	—	—	—	3.31	0.45

Table 7. Compressive strength and environmental impact of the alkali-activated GGBS and bauxite materials (3:1 - sand: GGBS/bauxite/FA/GGBS). COVs $_{AA\ GGBS}$=0.01-0.48; COVs $_{AA\ bauxites}$ = 0.41-0.63.

	GGBS (%)	Bauxite (%)	FA (%)	Curing t (°C)	NaOH (6M) (%)	Na2SiO3 (%)	CS (MPa)	EE (MJ/kg)	E_{CO2} - $kgCO_2/kg$
G1	21.90	—	—	20	3.12	3.24	25.70	1.48	0.14
G2	22.37	—	—	20	5.52	—	17.56	1.34	0.14
G3	21.31	—	—	20	1.98	6.71	5.21	1.75	0.16
G4	21.90	—	—	60	3.12	3.24	33.69	1.49	0.14
G5	22.37	—	—	60	5.52	—	12.03	1.35	0.14
G6	21.31	—	—	60	1.98	6.71	2.92	1.76	0.16
Bauxite + GGBS	11.12	11.12	—	20	2.03	2.68	60.41	1.52	0.16
Bauxite + FA	—	9.89	9.89	20	3.75	6.62	33.12	1.78	0.22
CEM II	—	—	—	20	—	—	37.18	3.31	0.45

Table 8. Summary of environmental impact vs strength results (MPa). EE (MJ/kg), EC (kgCO2/kg). E COVs = 0.06 – 0.62. % Δ -Arithmetic mean of the percentage variation compared with CEM II equivalent.

	AA RM materials			AA GGBS materials			AA Bauxite + GGBS			AA Bauxite + FA			PC equivalents		
	EE	ECO_2	CS	EE	ECO_2	CS	EE	ECO_2	CS	EE	ECO_2	CS	EE	ECO_2	CS
	1.62	0.18	11.76	1.53	0.15	16.19	1.52	0.16	60.41	1.78	0.22	33.12	3.31	0.45	37.18
% Δ	-50	-22	-65	-54	-67	-55	-54	-64	+40	-46	-53	0			

Authors Index

SPONSORED BY:

ROD
ROUGHAN & O'DONOVAN

THE IRISH CONCRETE SOCIETY

ARUP

CEMENT MANUFACTURERS IRELAND

IRISH CONCRETE FEDERATION
Set for life

ecocem IRELAND

roadstone

The Institution of Structural Engineers

MATTEST
MATTEST (IRELAND) LIMITED

Kingspan

Kilsaran

HOSTED BY:

DUBLIN
OLLSCOIL TEICNEOLAÍOCHTA BHAILE ÁTHA CLIATH
TECHNOLOGICAL UNIVERSITY DUBLIN

Trinity College Dublin
Coláiste na Tríonóide, Baile Átha Cliath
The University of Dublin